BASIN ANALYSIS

Principles and Applications

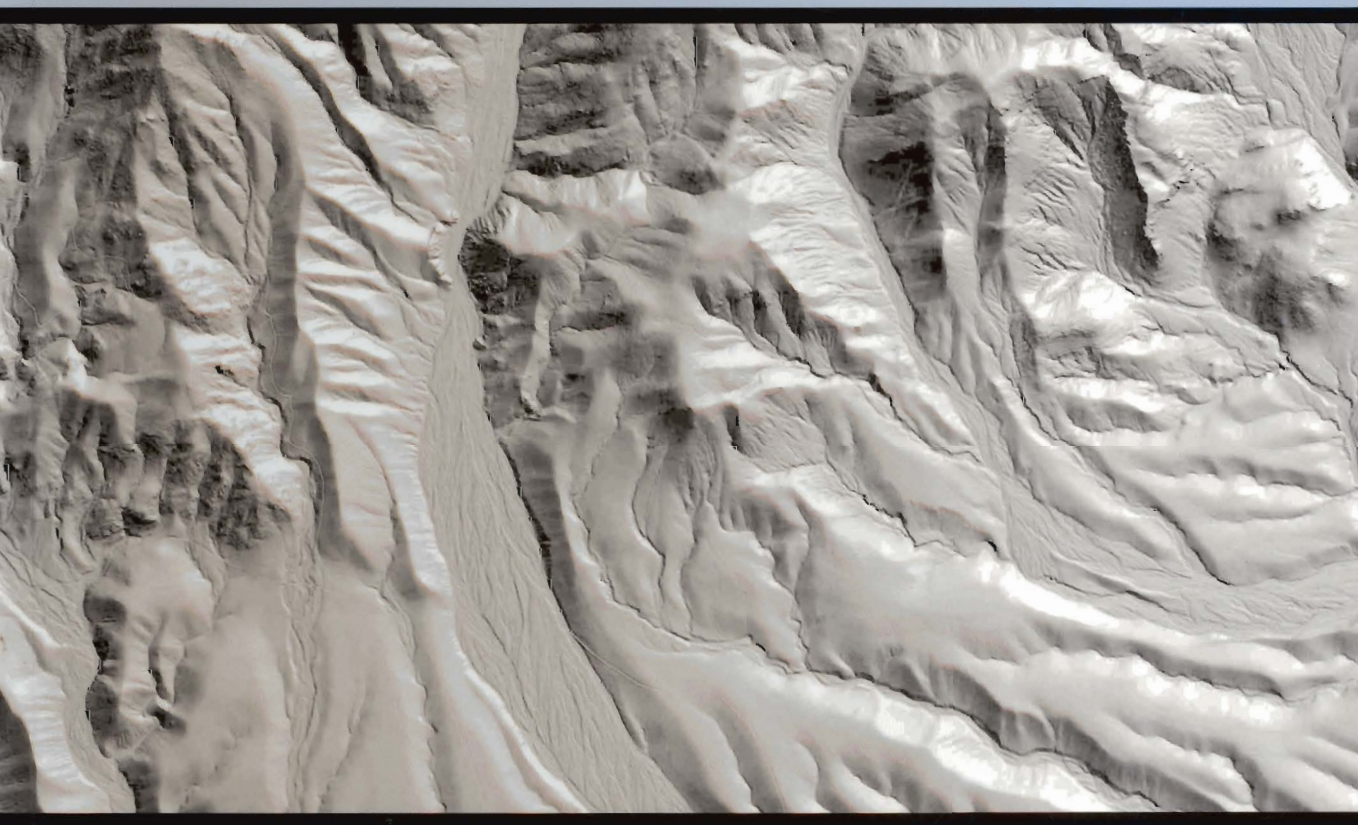

Philip A. Allen and John R. Allen

SECOND EDITION

Blackwell Publishing

BASIN ANALYSIS

Basin Analysis

Principles and Applications

Second Edition

Philip A. Allen
Department of Earth Sciences,
ETH Zürich

John R. Allen
BHP Billiton,
Australia

Blackwell
Publishing

BLACKWELL PUBLISHING
350 Main Street, Malden, MA 02148-5020, USA
9600 Garsington Road, Oxford OX4 2DQ, UK
550 Swanston Street, Carlton, Victoria 3053, Australia

First edition published 1990
Second edition published 2005 by Blackwell Publishing Ltd

3 2006

Library of Congress Cataloging-in-Publication Data

Allen, P. A.
Basin analysis: principles and applications/ Philip A. Allen and John R. Allen – 2nd ed.
p. cm.
Includes bibliographical references and index.
ISBN 0-632-05207-4 (pbk. : alk. paper)
1. Sedimentary basins. 2. Petroleum – Geology. I. Allen, John R. (John Richard), 1953– II. Title.

QE571.A45 2005
552'.5–dc22

2004005965

ISBN-13: 978-0-632-05207-3 (pbk. : alk. paper)

A catalogue record for this title is available from the British Library.

Set in 9/11 pt Baskerville
by SNP Best-set Typesetter Ltd, Hong Kong
Printed and bound in Singapore
by Fabulous Printers Pte Ltd

Contents

Preface to second edition

The first edition of *Basin Analysis* was written in 1988 and 1989 and published in 1990. A decade and a half have therefore passed since the writing of the first edition. Fifteen years is a long time between any two editions of a popular textbook, but in the field of basin analysis it is an eternity. The field has exploded with new data, new technology, and new concepts. This second edition attempts to take account of these new developments while retaining the successful basic structure and philosophy of the original text.

We originally defined basin analysis as the integrated study of sedimentary basins as geodynamic entities. This is even more the case today. It is now realized that the geodynamic system involving basin development must also include the processes of rock exhumation, erosion and sediment transport in the source terrains of sedimentary basins. In other words, the sediment supply to a basin is more than simply a boundary condition. The sediment efflux of eroding catchments is a thread linking intimately coupled process systems governed by a whole spectrum of driving mechanisms. Tectonics affect catchment topography as well as basin subsidence. Climate affects weathering and erosion as well as depositional environments and sedimentary products. Base-level change affects river incision and sediment transport as well as accommodation in the basin. To understand a basin as a geodynamic entity therefore requires an appreciation of the coupling between mantle, lithosphere, oceans, atmosphere, and land surface. The perspective is expansive and multidisciplinary. Basin analysis is no more the preserve of the geophysicist than the stratigrapher. It is the classic integrative topic in the curriculum and in our research portfolios.

The second edition of *Basin Analysis* is a major updating and reassessment of the first edition. We have retained the basic structure of first considering the fundamental physical state of the lithosphere before discussing the two grand classes of lithospheric deformation relevant to basin development – stretching and flexure. We have added a chapter on the effect of mantle dynamics, since it is now generally accepted that flow in the mantle related to the subduction of oceanic slabs, plume activity, and the slow incubation of heat beneath supercontinental assemblies impinge on basin development. Basins related to strike–slip motion continue to be treated in their own chapter because of their specific, intimate linkage to deformation within the principal displacement zone. The chapters on the basin-fill have been radically revised. A new chapter on the erosional engine for sediment delivery to basins has been included to reflect the massive and exciting advances in this area in the last decade. The discussion of basin stratigraphy highlights its structure or architecture and proposes explanations in terms of the external driving mechanisms or of the unforced, internal dynamics responsible. The techniques now used routinely in approaching problems in basin analysis have much expanded. We have updated subsidence analysis and measurements of thermal maturity of organic and nonorganic components of the basin-fill as the staple diet of basin analysts, but have included new thermochronological and exposure dating tools that have revolutionized our understanding of the rates of denudation of source regions, storage, and transfer to basins. Finally, the section on the application to the petroleum play has been retained, condensed, and updated to include the important petroleum system concept. It remains a useful summary of the scientific basis for petroleum geology and how many of the concepts and techniques discussed earlier in the book can be applied in a commercial arena.

The educational or intellectual philosophy adopted in *Basin Analysis* is that it is necessary to build up understanding by examining the underlying principles for the way in which basins function, rather than by presenting a blizzard of detail on the variability of the real world. We do not mean to be sectarian in the deductive *versus* inductive debate. The messy ground-truth of sedimentary basins, their structure, thermal and subsidence history, and stratigraphic architecture, is that each example has its own set of attributes, or to be anthropomorphic, its "individuality." But it is not an easy task to induct the functioning of basins from such a blizzard of detail. We therefore present wherever possible a simplified but useful physical analysis, backed up where appropriate with elementary calculus, as the means to enhance our understanding of basins generically. A further advantage of this approach is that students become armed with a wider range of scientific tools that can be used in a spectrum of other Earth Science and non-Earth Science applications. This is important in our current climate of fostering "transferable skills." The use of this first-principles approach is necessarily uneven in the text. Where a mathematical derivation is an optional extra, it is boxed separately from the rest of the text so as not to interrupt the flow. In most cases, however, the student will benefit from working through the simple mathematical analysis, inserting typical parameter values, and deriving a quantitative result. We have tried to encourage this "interactiveness" by providing practical examples with solutions on freely accessible web pages at ETH Zürich (www.erdw.ethz.ch/Allen).

Our perspective on developments over the last 15 years is that some hot issues have become luke warm, whereas others that were previously invisible or dormant have become widely debated. Such is scientific progress. As an example of the former, the art of sequence stratigraphy, with its controversial overemphasis on eustatic sea-level changes as the driving forces for stratigraphic packaging, has matured into a valuable observational tool with interpretation founded on a far better appreciation of the dynamics of accommodation generation and sediment supply. As an example of the latter, numerical models of a multilayer lithosphere now provide new insights into a range of problems involving the dynamics of lithospheric contraction and extension. A forceful and exciting community of scientists is simultaneously providing key observations and models to enable such improved solid-Earth models to be coupled to basin development *via* the critical interface of the Earth's surface. Such a successful merging of geomorphology, geophysics, isotope geochemistry, sedimentology, and structural geology sends a powerful message of the value of multidisciplinary approaches in the Earth Sciences.

The book is intended for undergraduates who have done the prerequisite set of introductory courses in the Earth Sciences. Those who have emerged from a sound physical sciences background will find this book more to their liking, but those entering Earth Science from the life or environmental sciences should not despair. The book should also prove to be useful to postgraduate students either as a text for taught courses in basin analysis and petroleum geology, or as a synthesis for doctoral students grappling with research problems across a wide range of Earth Science subdisciplines.

The writing of a textbook is a long, difficult road to tread. Goodness knows why anyone volunteers to do it. Any attempt at "completeness" has to be abandoned at an early stage. First, completeness can mean vast documentation of trivia. Second, attempts at completeness generally end in noncompletion. The book project then becomes a never-ending introspective diary. So to the academic staff using this book, please be understanding if sufficient credit is not given to your work. To the student, please do not think that you should not be visiting the library for supplementary reading.

Apart from primary sources in research papers, there are a number of textbooks and compilations or reviews that we have found valuable to consult and use. In the general area of basin analysis is Ingersoll and Busby's very useful compilation *Tectonics of Sedimentary Basins* (1995). Einsele's *Sedimentary Basins* (second edition, 2000), despite its title, is strongly focused on sedimentary geology. Leeder's *Sedimentology and Sedimentary Basins* (1999) is a stimulating text whose subtitle "From Turbulence to Tectonics" perfectly reflects its contents. The edited textbook by Reading (*Sedimentary Environments*, third edition, 1996) continues to be the best comprehensive source of all matters sedimentological. In the area of surface processes, useful material can be found in Summerfield's *Global Geomorphology* (1990) and its reincarnation as a multiauthor compilation in *Geomorphology and Global Tectonics* (2000). Allen's *Earth Surface Processes* (1997) provides a physically based approach to sediment routing and depositional processes, and Burbank and Anderson's *Tectonic Geomorphology* (2001) trail-blazes the important area of neotectonics and geomorphology. Turning to geophysics and dynamics, there is little competition for the mighty *Geodynamics* by Turcotte and Schubert (second edition, 2002). Very valuable material is also found in Fowler's *The Solid Earth* (1990) and *Isostasy and Flexure of*

the Lithosphere by Watts (2001) is very helpfully focused on some of the key issues underpinning basin development. *Diagenesis: A Quantitative Perspective* by Giles (1997) is a *tour de force* in the area of compaction and diagenesis of the basin-fill. Magoon and Dow's edited volume *The Petroleum System* (1994) is a valuable addition to the literature in the field of petroleum geology.

The journal *Basin Research* has published a number of important thematic sets that provide ideal hunting grounds for students of basin analysis: some examples are *Foreland Basins* edited by Allen, England, Watts and Grotzinger (1992), *Cratonic Basins* (1994) edited by Allen, Watts, Grotzinger and Royden, *Supradetachment Basins* edited by Friedmann and Burbank (1995), *Sediment Supply to Basins* edited by Hovius and Leeder (1998), *Interactions of Tectonics and Surface Processes in Landscape Evolution* edited by Burbank and Pinter (1999), *Processes and Controls in the Stratigraphic Development of Extensional Basins* edited by Gupta and Cowie (2000), and *Numerical and Physical Experimental Modelling of Stratigraphy* edited by Burgess and Paola (2002). Readers are also referred to the compilation of papers entitled *Tectonics and Topography*, edited by Ellis and Merritts, in the *Journal of Geophysical Research* (1994), and *Quantitative Dynamic Stratigraphy* (1990) edited by Cross, which together kick-started many quantitative approaches to the coupling of tectonics, surface processes, and stratigraphy.

We are grateful for the help of many colleagues, especially those who found time to look at drafts of book chapters, including Alex Densmore and Nick Richardson (ETH Zürich), and Peter Burgess (Shell, Rijswijk). Alex Densmore has cotaught a basin analysis class with PAA for several years and has provided much helpful input. Sonia Scarselli and Chris Krugh helped to assemble the practical exercises and solutions available on the web. Maja Reichenbach kindly provided much secretarial help. We are once again grateful for the support of staff at Blackwell Publishing, particularly Delia Sandford and Rosie Hayden in production and editor Debbie Seymour. Finally, we dedicate this volume to our families, Carolyn, Lorna, Frances, and Richard spread across England and Switzerland, and Annette, Michael, and Robert in Melbourne, Australia.

PAA, JRA, Zürich

PART

1 *The foundations of sedimentary basins*

CHAPTER 1

Basins in their plate tectonic environment

Assumptions, hasty, crude and vain,
Full oft to use will Science deign;
The corks the novice plies today
The swimmer soon shall cast away

(A.H. CLOUGH, POEM (1840))

SUMMARY

Sedimentary basins are regions of prolonged subsidence of the Earth's surface. The driving mechanisms of subsidence are principally related to processes within the relatively rigid, cooled thermal boundary layer of the Earth known as the lithosphere. The lithosphere is composed of a number of plates which are in motion with respect to each other. Sedimentary basins therefore exist in a background environment of plate motion.

The Earth's interior is composed of a number of compositional and rheological zones. The main compositional zones are between crust, mantle and core, the crust containing relatively low density rocks overlain by a sedimentary cover. The mechanical and rheological divisions do not necessarily match the compositional zones. A fundamental rheological boundary is between the lithosphere and the underlying asthenosphere. The lithosphere is sufficiently rigid to comprise a number of relatively coherent plates. Its base is marked by a characteristic isotherm (*c.* 1330 °C) and is commonly termed the *thermal lithosphere*, or alternatively *mechanical lithosphere*. The upper portion of the thermal lithosphere is able to store elastic stresses over long time scales and is referred to as the *elastic lithosphere*. The continental lithosphere has a strength profile with depth which suggests that a weak, ductile zone exists in the lower crust, separating a brittle upper crust and upper mantle, giving a jam-sandwich type structure. The oceanic lithosphere, however, lacks this low strength layer, its strength increasing with depth to the brittle–ductile transition in the upper mantle.

The relative motion of plates produces deformation, vulcanicity, and seismicity concentrated along their boundaries, which are classified as *divergent boundaries*, such as the mid-ocean ridge spreading centres of the ocean basins, *convergent boundaries* associated with large amounts of shortening, such as continental collision zones, and *conservative boundaries* characterized by strike–slip deformation. Although the theory of plate tectonics has the premise that deformation is concentrated along plate boundaries, the continental lithosphere deforms far from plate boundaries, and appears to behave at geological time scales more like viscous sheets than as rigid stress guides.

Sedimentary basins have been classified principally in terms of the type of lithospheric substratum (i.e., continental, oceanic, transitional), their position with respect to the plate boundary (intracratonic, plate margin), and type of plate motion nearest to the basin (divergent, convergent, transform). The formative mechanisms of sedimentary basins fall into a small number of categories, although all mechanisms may operate during the evolution of a basin:

- *Isostatic consequences of changes in crustal/lithospheric thickness*, such as caused mechanically by lithospheric stretching, or purely thermally, as in the cooling and subsidence of the oceanic lithosphere as it moves away from oceanic spreading centres;
- *loading (and unloading)* of the lithosphere causes a deflection or flexural deformation and therefore subsidence (and uplift), as in foreland basins;
- viscous flow of the mantle causes nonpermanent subsidence/uplift known as *dynamic topography*.

From the point of view of lithospheric processes there are two major groups of basins: (i) Basins due to lithospheric stretching, belonging to the rift-drift suite, and (ii) basins formed primarily by flexure of continental and oceanic lithosphere.

Inspection of any map showing hydrocarbon occurrences (e.g., St John et al. 1984) reveals their clustered pattern. In general, provinces of hydrocarbon occurrence correspond to the locations of sedimentary accumulations greater than about 1 km thick. These accumulations include sedimentary basins in the strict sense, implying zones of pronounced subsidence (Bally and Snelson 1980) but also carbonate bank build-ups on elevated oceanic crust, cratonic arches, and so on which become fossilized in the geological record. However, sedimentary basins located at sites of prolonged and substantial subsidence are of overriding importance.

Historically, basin studies have developed from a number of distinct viewpoints such as that of stratigraphic sequences and their relation to sea-level fluctuations (Sloss 1950, 1963), the geosyncline (Kay 1947, 1951; Aubouin 1965), and, more recently, the concept of plate tectonics (Dickinson 1974; Ingersoll 1988). The location of sedimentary basins and their driving mechanisms are intimately associated with the motion of discrete, relatively rigid slabs, which together represent the cooled thermal boundary layer of the Earth, and with the convective flow of the underlying mantle. The outer shell of the Earth comprises a relatively small number of these thin, relatively rigid plates, and they are in a state of motion with respect to each other. Such motions set up plate boundary forces that may be transferred considerable distances into the interior of the plates, so that sedimentary basins exist in a background environment of stress set up by plate motion. The lithospheric plates are the surface manifestation of a slow thermal convection in the mantle, and are subject to differential thermal stresses along their bases. The mantle and lithosphere therefore do not operate as independent systems. We see spectacular evidence for the interaction of mantle processes and the lithosphere in the volcanic and topographic expression above plumes that have risen from the core–mantle boundary. We also discern, though less spectacularly, the effects on mantle flow of the subduction of cold slabs of oceanic crust at ocean–continent boundaries.

Some basic ideas on plate tectonics and Earth structure are introduced in this chapter in so far as they help to explain the location and evolution of sedimentary basins. More exhaustive summaries can be found in Wyllie (1971), Cox (1973), Le Pichon et al. (1973), Smith (1976), Bird (1980), Cox and Hart (1986), and Kearey and Vine (1996). Ingersoll and Busby (1995) is a collection of individually written chapters of relevance to basin analysis and plate tectonics.

The Earth's interior is composed of a number of essentially concentric zones that are defined on the basis of either compositional changes, or mechanical/rheological changes.

1.1 COMPOSITIONAL ZONATION OF THE EARTH

There are three main compositional units; the crust, mantle, and core (Fig. 1.1).

1.1.1 Oceanic crust

The *crust* is an outer shell of relatively low density rocks. The oceanic crust is thin, ranging from approximately 4 to 20 km in thickness, 10 km being "normal," and with an average density of about 2900 kg m^{-3}. It comprises a number of layers that reflect its mode of creation: an upper veneer (layer 1) of unconsolidated or poorly consolidated sediments, generally up to 0.5 km thick; an intermediate layer 2 of basaltic composition, consisting of pillow lavas and associated products of submarine eruptions; and a layer 3 of gabbros and peridotites that may form the parent rocks which upon differentiation give rise to the basalts of layer 2. The oceanic crust has been thought to be distinctly layered in terms of velocity of seismic waves, but more recent views are that it possesses a more gradual and continuous increase in velocity with depth.

The lifetime of oceanic crust is short, despite the fact that it occupies about 60% of the surface of the Earth (*c.* 3.2×10^9 km^2). This is because as the oceanic crust cools during aging it becomes gravitationally unstable with respect to the mantle; as a result it is consumed. This explains why the oldest oceanic crust in today's oceans is as young as Jurassic in age (*c.* 150 Ma). Compared to the continents, the oceanic crust therefore has a very short lifespan.

1.1.2 Continental crust

The continental crust is thicker, ranging from 30 to 70 km, but with an "average" thickness of perhaps 35 km. It was originally thought to be divided into two layers, each with a distinct composition and density: (i) An upper layer with physical properties similar to those of granites, granodiorites, or diorites overlain by a thin veneer of sedimentary rocks. This so-called "*granitic layer*" has a thickness of between 20 and 25 km and a density of 2500–

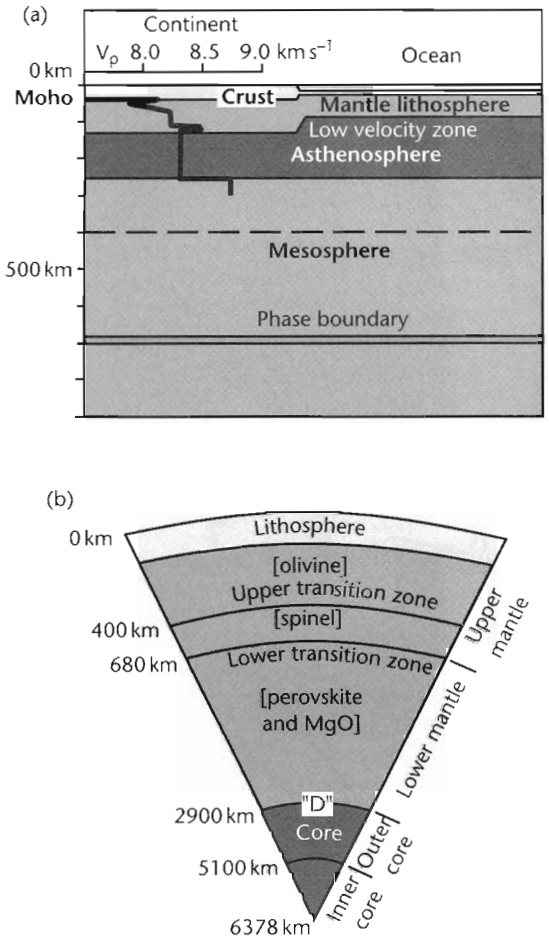

Fig. 1.1 The main compositional (a) and rheological (b) boundaries of the Earth. The most important compositional boundary is between crust, mantle, and core. There are strong compositional variations within the continental crust and compositional variations caused by phase changes in the mantle. V_p is velocity of **P** wave. The main rheological boundary is between the lithosphere and the asthenosphere. **P** wave velocities increase markedly beneath the Moho, but decrease in a low velocity zone representing the weak asthenosphere. The lithosphere is rigid enough to act as a coherent plate. **P** wave velocity in (a) from western Europe after Hirn (1976).

2700 kg m^{-3}. The term "granitic" is, however, misleading, since average densities are greater than that of granite; (ii) a lower layer of primarily basaltic composition, but the pressure and temperature at depths in excess of 25 km imply that the rocks are granulites, or their high pressure, high temperature equivalents, eclogites or amphibolites. The density of this lower layer is 2800–3100 kg m^{-3}. These layers may not in reality be well defined, and instead a more continuous variation of composition with depth may exist.

Information on the density of crustal rocks has been obtained largely by observations on seismograms of the speed of seismic waves passing through the various layers, coupled with laboratory experiments on rock materials. The existence of a low velocity crust was discovered by the geophysicist Mohorovicic shortly after the turn of the century. At the crust–mantle boundary, seismic **P** (longitudinal) wave velocities increase markedly; this abrupt increase in velocity may reflect a corresponding increase in rock density (Fig. 1.1). This horizon is known as the Mohorovicic discontinuity or Moho. The Moho varies in depth considerably. The continental crust thickens under orogenic belts, thins under zones of rifting, and attenuates completely at continental margins (Fig. 1.2).

In some regions, particularly the attenuated margins of continents, the crust is intermediate in character and thickness between typical oceanic and continental varieties. This may be due to the injection of dense intrusions, to metamorphism, or to other processes accompanying stretching. In particular, the depth to the Moho may be abnormally great due to the igneous underplating of the crust during plume activity. Several kilometers of underplate emplaced in the Early Tertiary over the head of the Iceland plume have been interpreted from seismic experiments carried out on the northwest European continental margin.

1.1.3 Mantle

The *mantle* is divided into two layers: the upper and lower mantle. The upper mantle extends to about 680 km ± 20 km and is punctuated by phase transitions. The inner mantle extends to the outer limit of the core at 2900 km, with an increasing density with depth.

Although there are of course no *in situ* measurements of the composition of the mantle, it can be estimated from the chemistry of volcanic and intrusive rocks derived by melting of the mantle, from tectonically emplaced slivers of mantle rock preserved in orogenic belts known as ophiolites, from nodules preserved in volcanic rocks, from minerals brought to the surface explosively in kimberlites, and importantly, from the remote

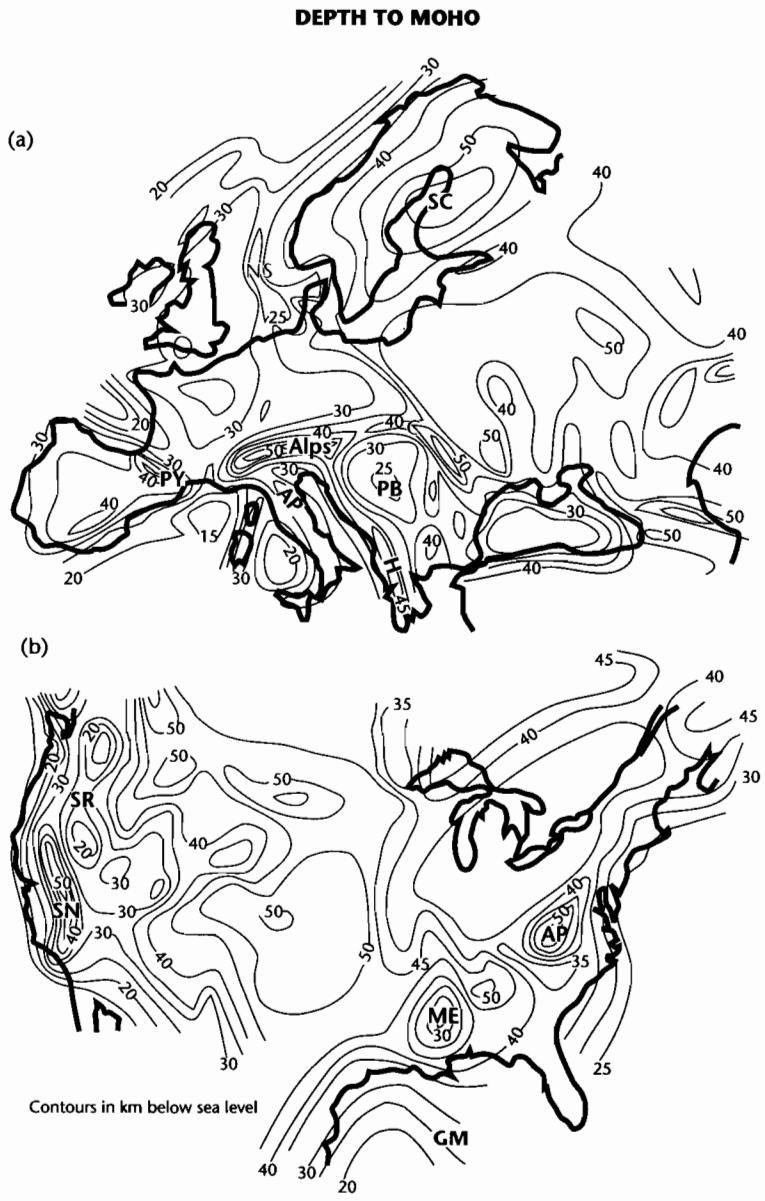

Fig. 1.2 Depth to the Moho below sea-level from (a) Europe and (b) North America, after Allenby and Schnetzler (1983) and Meissner (1986). In Europe, thick continental crust occurs in the Pyrenean–Alpine–Carpathian orogenic belt and in the Scandinavian Shield. Thin continental crust occurs along the Atlantic margin and in regions of continental stretching, such as the North Sea, western Mediterranean, Pannonian Basin, and Black Sea. In North America, thick continental crust is associated with the batholiths of the Sierra Nevada region, the Appalachian orogenic belt, the American midcontinent and the Canadian–NE USA shield. Thin crust is associated with the plateau basalts of the Snake River area, sites of rifting such as the Mississippi Embayment, and along the western active continental margin, eastern passive continental margin and the Gulf of Mexico. NS, North Sea; SC, Scandinavian Shield; PY, Pyrenees; AP, Apennines; PB, Pannonian Basin; H, Hellenides; SR, Snake River; SN, Sierra Nevada; ME, Mississippi Embayment; AP, Appalachians; GM, Gulf of Mexico. Reproduced courtesy of Elsevier.

but sophisticated measurement of the mantle using seismic waves. The main constituent of the mantle is thought to be olivine, mostly the Mg-rich variety forsterite.

Olivine is known to undergo phase changes to denser structures at pressures equivalent to depths of 390–450 km and *c.* 700 km in the Earth. At 390–450 km olivine is thought to change to spinel *via* an exothermic reaction involving a 10% increase in density. At *c.* 700 km spinel changes to perovskite and magnesium oxide in an endothermic reaction. These phase changes can be recognized by changes in the velocity of **S** waves (McKenzie 1983) and may determine the scale of convection in the mantle (Silver et al. 1988).

1.2 RHEOLOGICAL ZONATION OF THE EARTH

The mechanical or rheological divisions of the interior of the Earth do not necessarily match the compositional zones. One of the rheological zonations of primary interest to students of basin analysis is the differentiation between the lithosphere and the asthenosphere. This is because the vertical motions (subsidence, uplift) in sedimentary basins are principally a response to the deformation of this uppermost rheological zone of the Earth.

1.2.1 Lithosphere

The *lithosphere* is the rigid outer shell of the Earth, comprising the crust and the upper part of the mantle. It is of particular importance to note the difference between the *thermal* and *elastic* thicknesses of the lithosphere. It is generally believed (e.g., Parsons and Sclater 1977; Pollack and Chapman 1977) that the base of the lithosphere is represented by a characteristic isotherm (1100–1330°C) at which mantle rocks approach their solidus temperature. This defines the *thermal lithosphere.* Typical thicknesses of lithosphere under the oceans varies from *c.* 5 km at mid-ocean ridges to *c.* 100 km in the coolest parts of the oceans. The lower boundary of the lithosphere is poorly defined under continents, depths of 100 to 250 km being typical. The stepwise increases in velocities of **S** and **P** waves with depth through the lithosphere suggest that it contains compositional boundaries within it.

The rigidity of the lithosphere allows it to behave as a coherent plate but only the upper part of the lithosphere is sufficiently rigid to retain elastic stresses over geological time scales (say 10^7 years). Below this upper *elastic lithosphere* creep processes efficiently relax elastic stresses, so that there is a physical and conceptual difference between the elastic lithosphere and the thermal lithosphere. The lithosphere below the upper elastic portion must therefore be sufficiently soft to relax elastic stresses but sufficiently rigid to remain a coherent part of the surface plate.

The oceanic and continental lithosphere differ in their strength (Fig. 1.3). The strongest part of the oceanic lithosphere occurs in the mantle between 20 and 60 km depth, below which it becomes increasingly ductile. The continental lithosphere, however, appears to be markedly zoned rheologically. In particular, the upper seismically active brittle zone overlies a generally aseismic zone that may deform by ductile processes. This mid-lower crustal ductile zone has been invoked as a level of detachment of major upper crustal faults (e.g., Kusznir and Park 1987) (§3.5.2 and §3.5.3). There is a second, deeper strong layer in the mantle part of the continental lithosphere where earthquakes occasionally occur (Chen and Molnar 1983).

There are also heterogeneities in the mantle part of the lithosphere, although they are small compared with the crust. Seismological studies of western Europe (Hirn 1976) suggest a highly stratified lithosphere beneath the Moho (Fig. 1.1). In particular, a "channel" of reduced **P** wave velocities has been interpreted between 10 and 20 km below the Moho. This 10 km thick layer cannot be explained in terms of partial melting since the solidus temperature is far in excess of the actual temperature – the hydration (serpentinization) of peridotites has been postulated as a possible mechanism. Whatever the cause, this upper low velocity channel may serve as a zone of decoupling of the upper lithosphere from the lower portion of the lithosphere when acted upon by tangential tectonic forces. There are few examples, however, where a process of decoupling can be unambiguously demonstrated at these levels.

1.2.2 Sublithospheric mantle

The underlying region, the *asthenosphere* is weaker than the lithosphere and is able to undergo deformation relatively easily by flow. The upper part of the asthenosphere is known as the low velocity zone where **P** and **S** wave

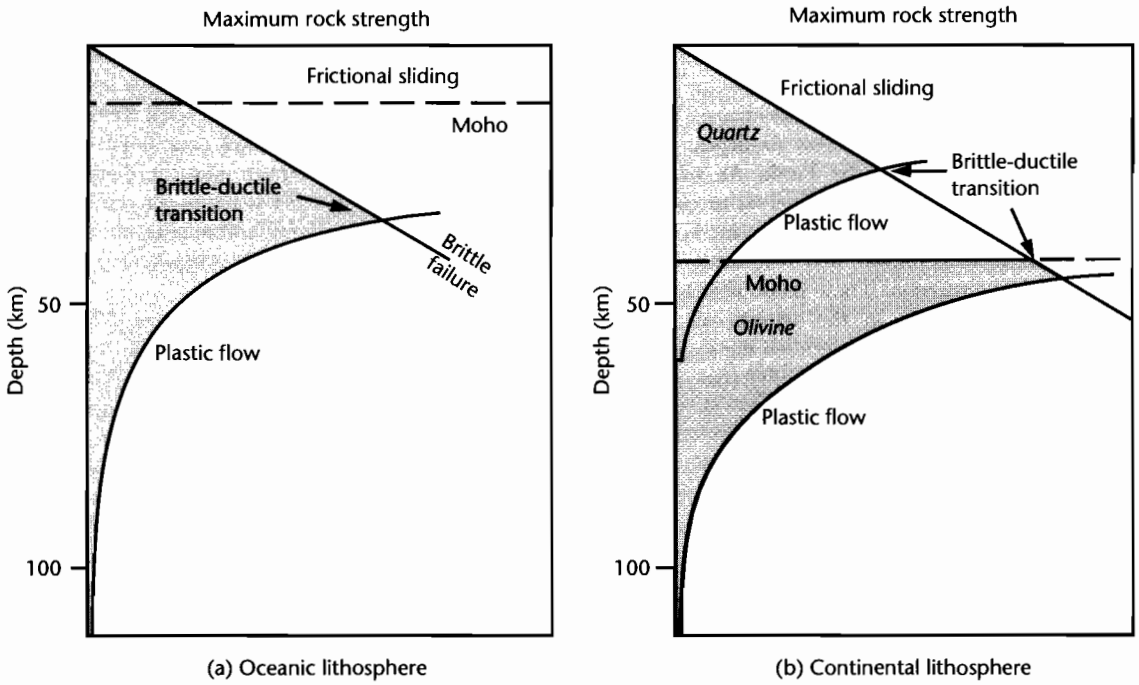

Fig. 1.3 Strength profiles for the oceanic (a) and continental (b) lithosphere, based on Molnar (1988) and Sammonds (1999). The yield strength of the continental and oceanic lithosphere is plotted as a function of depth. The olivine rheology of the oceanic lithosphere provides a strong elastic core extending to depths of over 50 km. The quartz or quartz-felspar rheology of the continental lithosphere causes a weak, ductile layer at equivalent depths. A second brittle–ductile transition occurs in the mantle lithosphere because of the compositional change to an olivine rheology. The elastic lithosphere is the upper portion that is able to store elastic stresses over long time periods. The base of the thermal lithosphere is a mechanical boundary separating the relatively strong outer shell of the lithosphere from the very weak asthenosphere.

transmission speeds drop markedly, presumably due to partial melting (Fig. 1.4).

Studies of minute variations in the transmission speeds of seismic waves has allowed the structure of the deep mantle to be visualized and mapped (Dziewonski and Woodhouse 1987), a topic known as *seismic tomography*. Zones of faster than average seismic velocity are attributed to propagation through denser rock which in turn is most likely due to a cooler temperature. Zones with slower than average seismic velocity are likewise thought to be due to warmer temperatures. Variations in temperature are probably caused by large-scale convection. Far from being inert, the mantle represents a vast volume of rock which dynamically interacts with the lithosphere. Instabilities rise from the core–mantle boundary as *plumes* of hot material which impinge on the base of the overlying lithosphere and may have a major role in continental break-up (Burke and Dewey 1973; White and McKenzie 1988). The thermal effects of the subduction of cold oceanic lithosphere and the insulating effects of supercontinental assemblies are also thought to be recognizable in the thermal structure of the mantle (Gurnis et al. 1996).

1.3 PLATE MOTION

Plate tectonics can operate because the lithosphere is composed of a number of coherent rheological "plates" (Fig. 1.5). The underlying concepts of relative plate motion come from studies of focal mechanism solutions of large earthquakes and observations of the distribution of earthquake epicenters, and from studies of magnetic lineations in the ocean basins. The nature and rates of

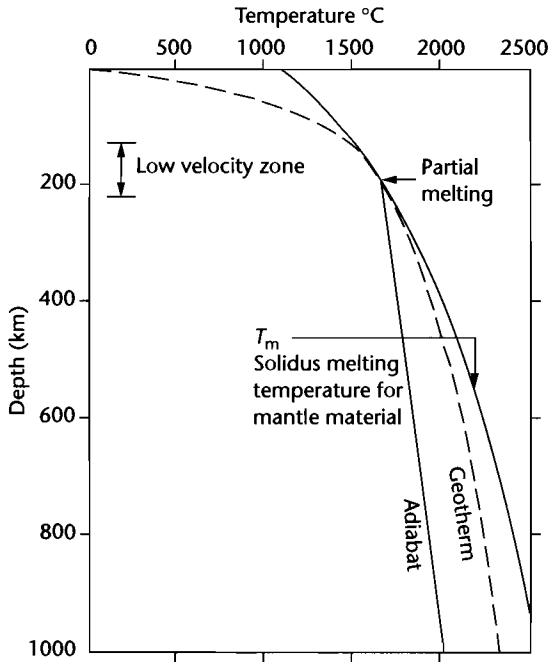

Fig. 1.4 Variation of temperature with depth, or geotherm, and the solidus temperature for mantle material (peridotite). Where the solidus curve (T_m) and the geotherm become tangential, partial melting in the mantle is likely to take place, resulting in a zone of low seismic wave velocities (low velocity zone).

relative plate motion (Minster and Jordan 1978) govern many aspects of the geodynamic environment of basins. Increasingly, reliable information on motion within plates is provided by measurement of *geodetic* strains involving the long-term occupation of triangulation networks and the use of ground position satellite (GPS) technology (Clarke et al. 1998).

The global pattern of seismic activity is of continuous and narrow belts of high frequency of earthquakes, bounding extensive regions of relative stability (Barazangi and Dorman 1969). The narrow zones of earthquake activity define plate margins. Oceanic plate boundaries are very sharply defined whilst continental boundaries are rather more diffuse.

The fact that earthquake epicenters occur at depths as great at 650 to 700 km along some plate boundaries suggests that a process exists that is capable of transferring brittle material to depths normally associated with deformation by flow. This process of plate subduction is responsible for both the relative youth of the oceanic crust and the distribution of earthquake epicenters. The fact that the interiors of plates experience only infrequent earthquake activity reflects the concentration of large relative motions of plates along their boundaries. However, this does not mean that the interiors of plates do not experience significant deformation. Continental plates clearly undergo extensive deformation a long way from plate boundaries (England 1987). In such cases, the driving force is believed to be the excess potential energy of elevated continental crust.

The lithospheric plates can be easily deformed by bending about a horizontal axis, but are highly resistant to torsion about steeply inclined axes. This latter property of strength allows the motion of plates over the Earth's surface to be modeled assuming no internal deformation, except at plate boundaries. But how do the oceanic and continental lithosphere compare in terms of flexural strength? Different views exist on this problem. On the one hand, oceanic plates are stronger because they consist of more mafic mineral assemblages, whereas the continents contain quartz which shows ductile flow at lower temperatures than olivine (see Fig. 1.3). They also contain fewer intrinsic weaknesses such as old fundamental fault systems. On the other hand, the oceanic plates are thinner and hotter, and therefore bend more easily under an applied force system. Whether continental or oceanic lithosphere is stronger in terms of their resistance to bending, or flexure, is therefore controversial and the strength must at least in part depend on parameters such as geothermal gradient and strain rate. Continental crust, however, appears to be weaker than oceanic crust when subjected to extensional stresses (Steckler and ten Brink 1986).

Three classes of plate boundary exist: divergent, convergent, and conservative (Fig. 1.6):

Divergent boundaries are typified by the mid-ocean ridge spreading centres of the ocean basins. Here, the recognition of magnetic bands correlated with a magnetic reversal chronology (Vine and Matthews 1963; Cox 1973) allows the rate of divergent plate motion to be estimated. Transform faults with strike–slip displacement offset the divergent boundaries, producing a highly segmented pattern.

Convergent boundaries are of two classes:

- Subduction boundaries where oceanic lithosphere constitutes the downgoing plate. Ocean–ocean

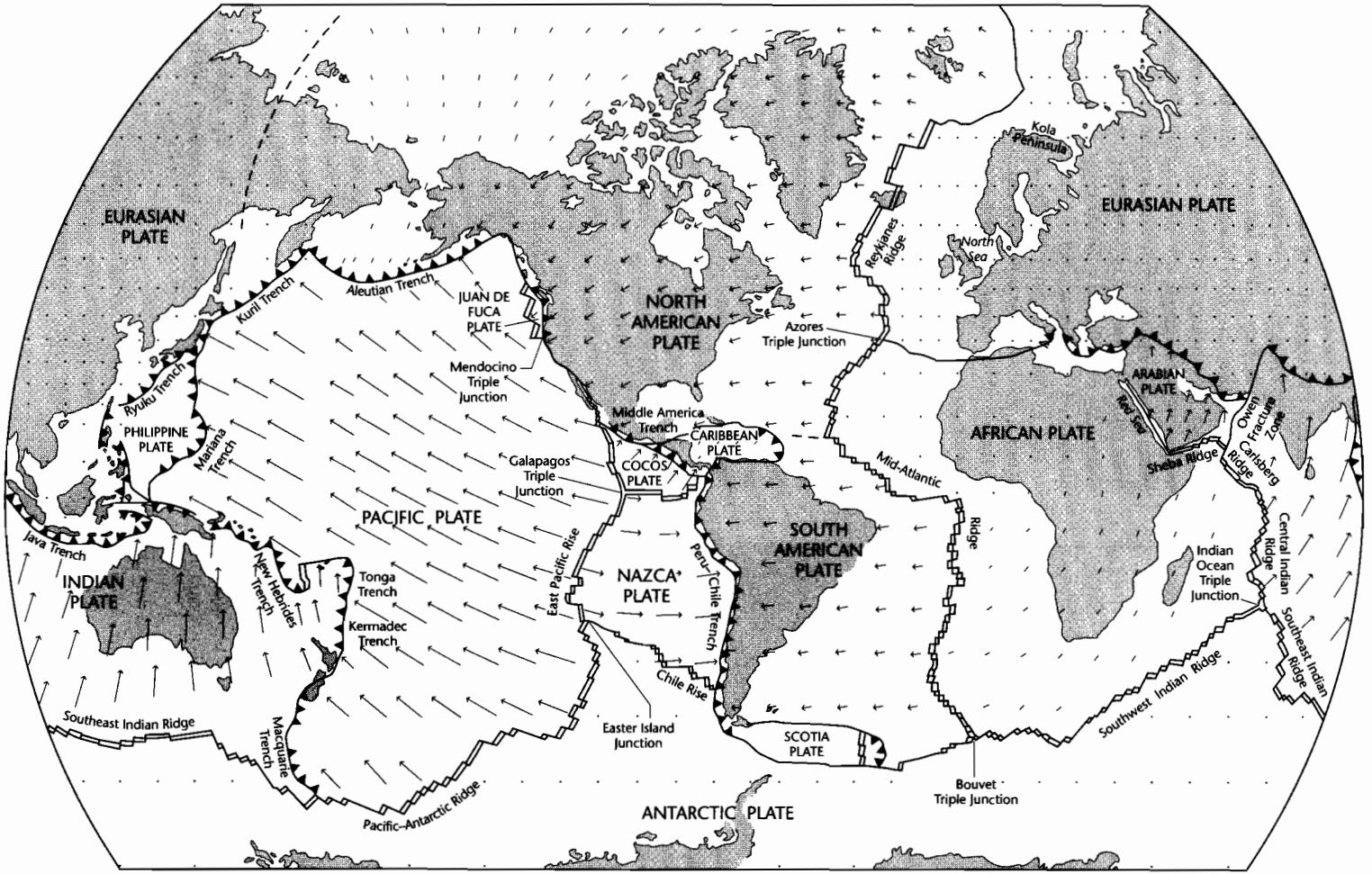

Fig. 1.5 The lithospheric plates, showing mid-ocean ridges, trenches, and transform boundaries (Le Pichon et al. 1973) and absolute motion vectors from Minster and Jordan (1978). Length of arrows is proportional to the plate speed. The fastest plate motion is in the western Pacific and Indian Oceans, whereas Africa, Antarctica, and Eurasia are almost stationary with respect to the mantle reference frame. Reproduced courtesy of American Geophysical Union.

boundaries, as for example, in the Mariana Islands, are characterized by a well-developed ocean trench and volcanic island arcs, whereas ocean–continent boundaries such as along the west of the Andes consist of an ocean trench with an associated continental magmatic arc with intense plutonic activity.

- Collisional boundaries where continental lithosphere constitutes the downgoing plate. Where both plates are continental, as in the Alps or Himalayan zones, the buoyancy of the downgoing plate resists subduction, leading to intense and widespread deformation. Less commonly, oceanic lithosphere may override continental lithosphere attached to subducting oceanic lithosphere, as in Taiwan.

Conservative boundaries occur where the adjoining plates are moving parallel to each other and are therefore dominated by strike–slip or transform faults.

The relative movement between plates causes earthquakes, a fact demonstrated by the concentration of seismic activity along plate boundaries. Earthquakes occur along trenches, ridges, and transforms, but they are distinctly different along the three types of boundary:

- Ridges are characterized by small to moderate earthquakes generated at shallow depths of <10 km;
- transforms experience larger earthquakes originating from depths of <20 km;
- subduction zones are sites of very large and deep earthquakes, with foci occurring as deep as 700 km.

The disappearance of earthquakes at relatively shallow levels along transforms and ridges is thought to be due to the change in rheology from brittle (capable of storing elastic stresses before rupture) to ductile (flowing by creep). This transition takes place in the range 600–900 °C, which corresponds to a depth of 20–30 km at transforms, but at shallower levels of about 10 km at ridges where temperatures are elevated. In contrast, at subduction zones, if the plate is descending quickly it remains cool relative to its surroundings and is capable of brittle deformation to large depths. Hence, earthquake foci along subduction zones (Fig. 1.7) may be very deep. The rate of slab subduction may affect the depth of earthquakes, however. If the slab is only slowly subducted, it may heat up sufficiently to prevent the occurrence of earthquakes at great depths.

It is possible to study the type of motion that occurred during a particular earthquake and to work out the stresses released at the time of the earthquake, and thereby the direction of plate motion that gave rise to the stresses. These methods are called *first motion* or *focal mechanism* studies, since it is the first motion of the ground surface, whether it is up/away from the source of the earthquake or down/towards the focus. Distinct radiation patterns result from first motion on strike–slip, normal, and reverse faults.

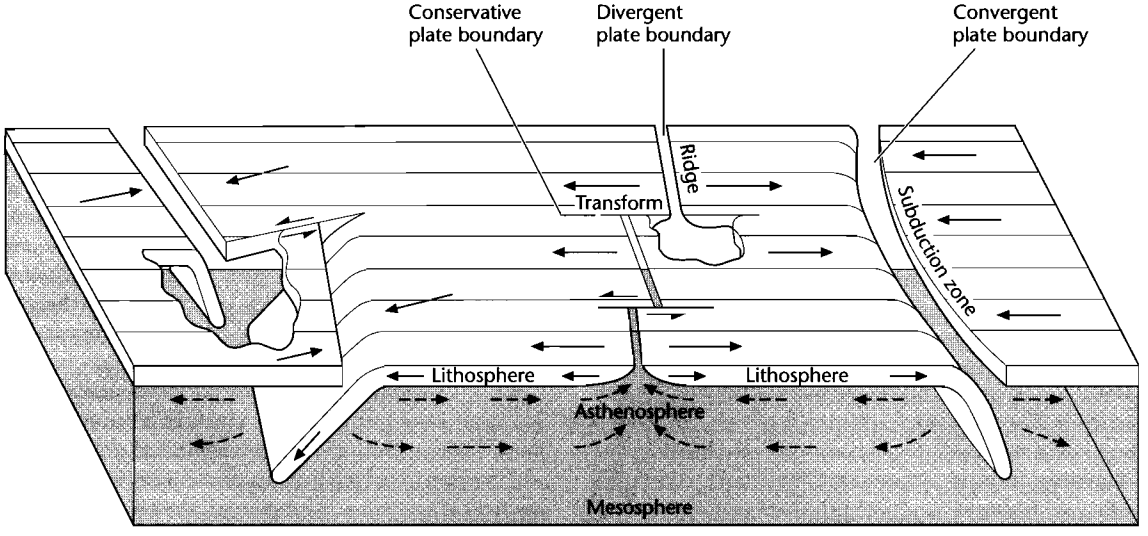

Fig. 1.6 The three types of plate boundary: convergent, divergent, and conservative (after Kearey and Vine 1996). Reproduced courtesy of Blackwell Publishing Ltd.

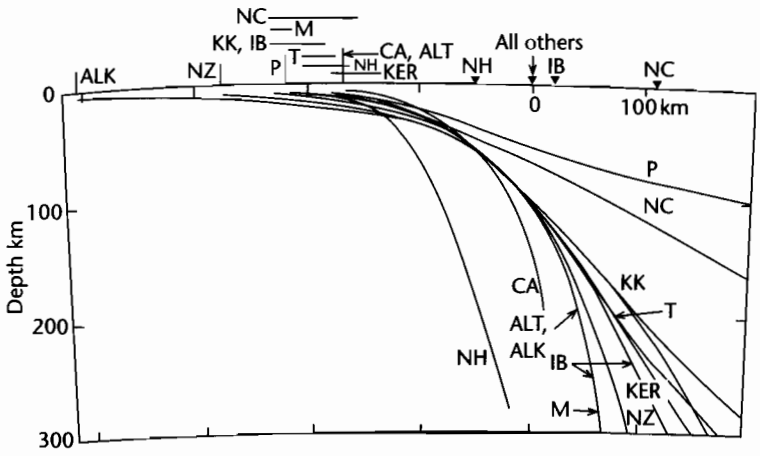

Fig. 1.7 Distribution of earthquake foci along Benioff zones, after Isacks and Barazangi (1977). NH, New Hebrides; CA, Central America; ALT, Aleutians; ALK, Alaska; M, Marianas; IB, Izu-Bonin; KER, Kermadec; NZ, New Zealand; T, Tonga; KK, Kuril-Kamchatka; NC, North Chile; P, Peru.

Sykes (1967) studied the first motion of earthquakes along mid-Atlantic ridge transforms and suggested that the motion was strike–slip, to the east on the northern blocks and to the west on the southern blocks. This is right lateral motion – opposite to that indicated by the offsets of the ridge – but the correct relative movement to support the plate tectonic interpretations of transforms as actively shearing only between the ridge segments and not beyond. The earthquakes originating from spreading centres are quite different from those being produced at transforms. First motion studies suggest that faults in the mid-ocean ridge are dip–slip and extensional. The situation at trenches is more complex. First motion studies of earthquakes along the *Benioff Zone* show that faulting takes place at roughly 45° to the inclined surface of the downgoing slab. At depths of greater than about 300 km, the focal mechanisms are compressional, but at shallower depths they are tensional. This pattern supports the view that in the lowermost part of the subducting slab, the plate experiences compression as it is forced into a zone of greater viscosity or strength at depth. The upper part, however, is in a state of tension because of the gravitational body forces on the cool plate "hanging" from its upper edge. This force constitutes slab-pull. Isacks et al. (1969) provide a detailed analysis of the use of seismological studies at sites of subduction.

The relative motion of plates with constructive, conservative, and destructive plate margins creates a continually changing picture of continental splitting, ocean basin creation, ocean closure, and continental collision. This cycle of plate motion involving the birth and closure of oceans is termed the Wilson cycle since it is based on early ideas of the opening and closing of the Atlantic ocean by John Tuzo Wilson (Wilson 1966) (Fig. 1.8). Many sedimentary basins can be fitted into a particular phase of the Wilson cycle.

1.4 CLASSIFICATION SCHEMES OF SEDIMENTARY BASINS

Ideally, classifications are theories about the basis of natural order rather than dull catalogues compiled only to avoid chaos (Gould 1989, p.98, quoted in Ingersoll and Busby 1995, p.2). In this sense, classification schemes for sedimentary basins should both reveal something of the underlying mechanisms for basin development and reflect the natural variability of the real world.

Recent classification schemes of sedimentary basins based on plate tectonics have much in common. Their lineage derives from Dickinson's influential work in 1974 which emphasized the position of the basin in relation to the type of lithospheric substratum, the proximity of the basin to a plate margin, and the type of plate boundary nearest to the basin (divergent, convergent, transform) (Fig. 1.9). The evolution of a basin could then be

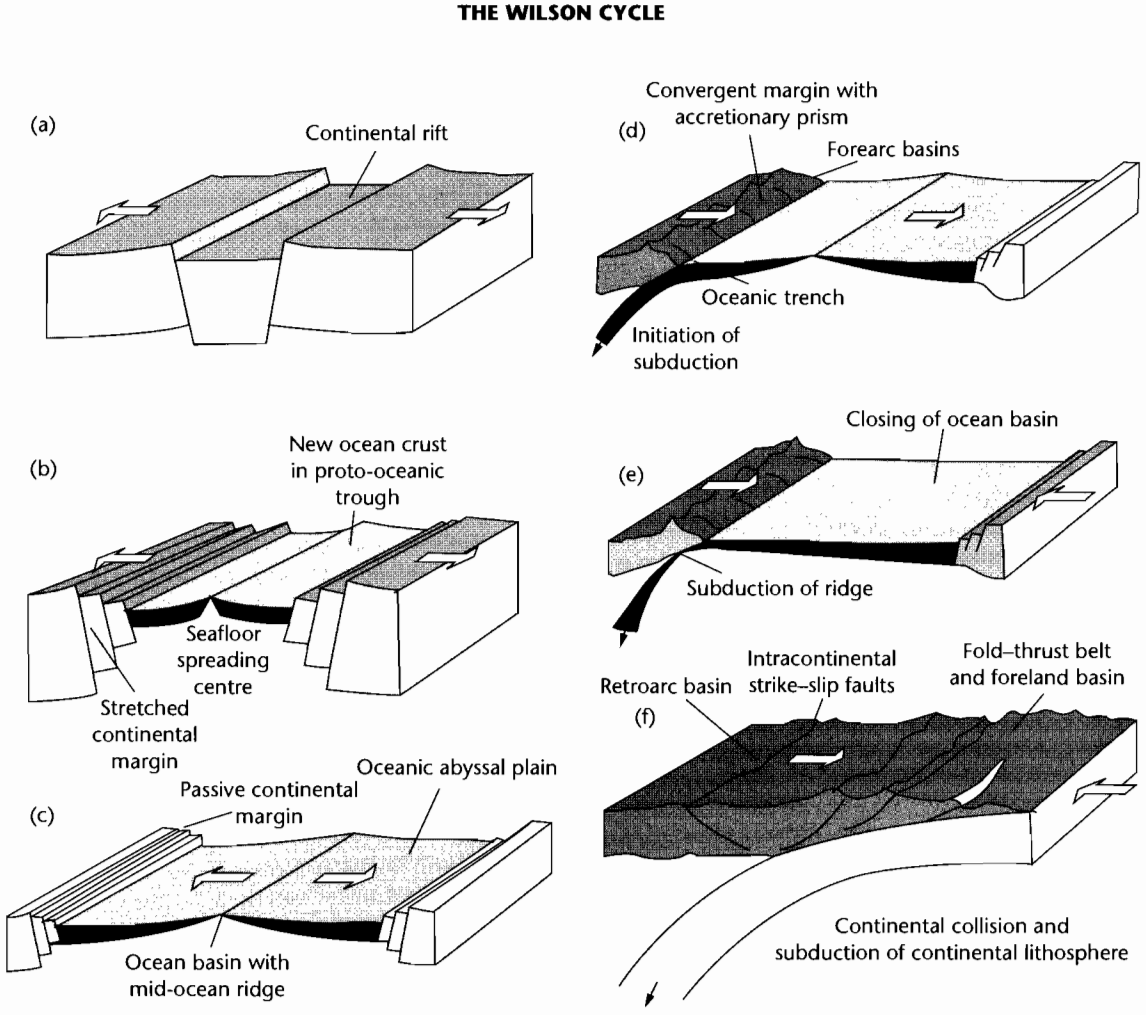

Fig. 1.8 The Wilson cycle of ocean formation and ocean closure. Continental extension (a) is followed by the creation of a new oceanic spreading centre (b) and ocean enlargement (c). Subduction of ocean floor (d) leads to closure of the ocean basin. Subduction of the oceanic ridge (e) takes place before continent–continent collision (f).

explained by changing plate settings and interactions. Dickinson (1974) recognized five major basin types on this basis: (i) Oceanic basins, (ii) rifted continental margins, (iii) arc–trench systems, (iv) suture belts, and (v) intracontinental basins.

Strike–slip or transform related basins were conspicuously missing as a distinct basin type in this classification, a deficiency corrected in Reading (1982). Bally (1975) and Bally and Snelson (1980) differentiated three different families of sedimentary basins based on their location in relation to megasutures, which in this context can be defined to include all the products of orogenic and igneous activity associated with predominantly compressional deformation. The boundaries of megasutures are often associated with subduction, whether it be of slabs of oceanic lithosphere (Benioff or B-type subduction) or of relatively buoyant continental lithosphere (Amferer or A-type subduction) and may also be the sites of impor-

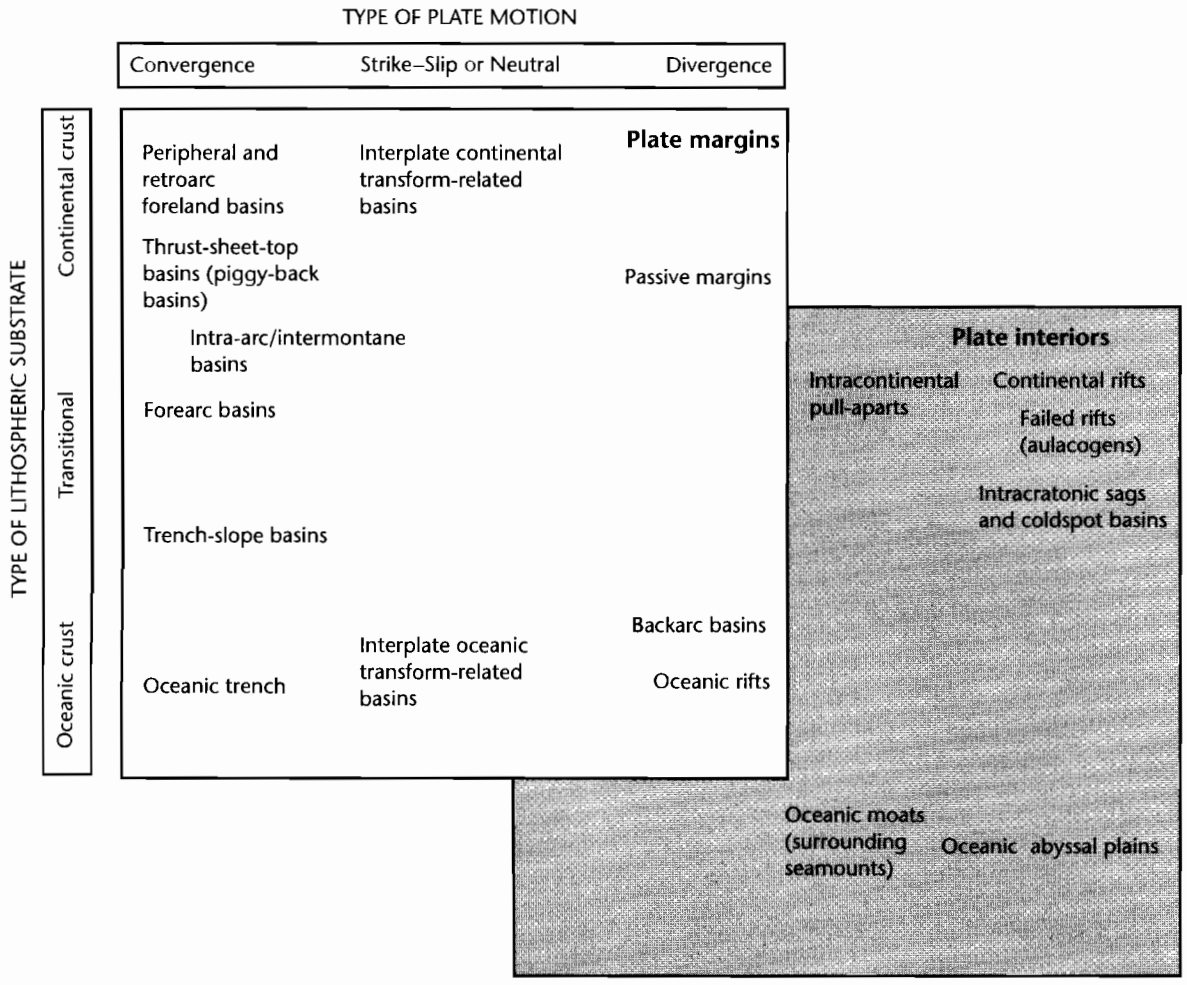

Fig. 1.9 Classification of basins using the type of lithospheric substrate, type of plate motion, and location with respect to the plate boundary.

tant wrench tectonism along transform faults. Ingersoll and Busby (1995) developed the classifications of Dickinson (1974) and Ingersoll (1988) to recognize 26 different types grouped into classes of divergent settings, intraplate settings, convergent settings, transform settings, and hybrid settings.

Industry-based classifications are typified by the scheme suggested by Halbouty et al. (1970) and later developed by Fischer (1975) and Klemme (1980). Klemme's scheme recognizes eight main types of basin based on their architectural characteristics such as linearity, asymmetry, cross-sectional geometry, which are themselves related to the tectonic setting and basin evolution. The goal of categorizing a sedimentary basin and thereby gaining some predictive insights into frontier basins is common to industry classifications such as those of Huff (1978) and Klemme (1980). It is pursued by an Exxon group (Kingston et al. 1983a, b) to the extent of devising a formula for each basin, thereby facilitating easy comparisons between basins and providing an "instant" idea of hydrocarbon potential. This classification system (Fig. 1.10) once again places basins primarily in their plate tectonic setting (lithospheric substrate, type of plate motion, and location on plate), reminiscent of Dickinson's analysis over a decade earlier, and categorizes a basin according to three critical factors:

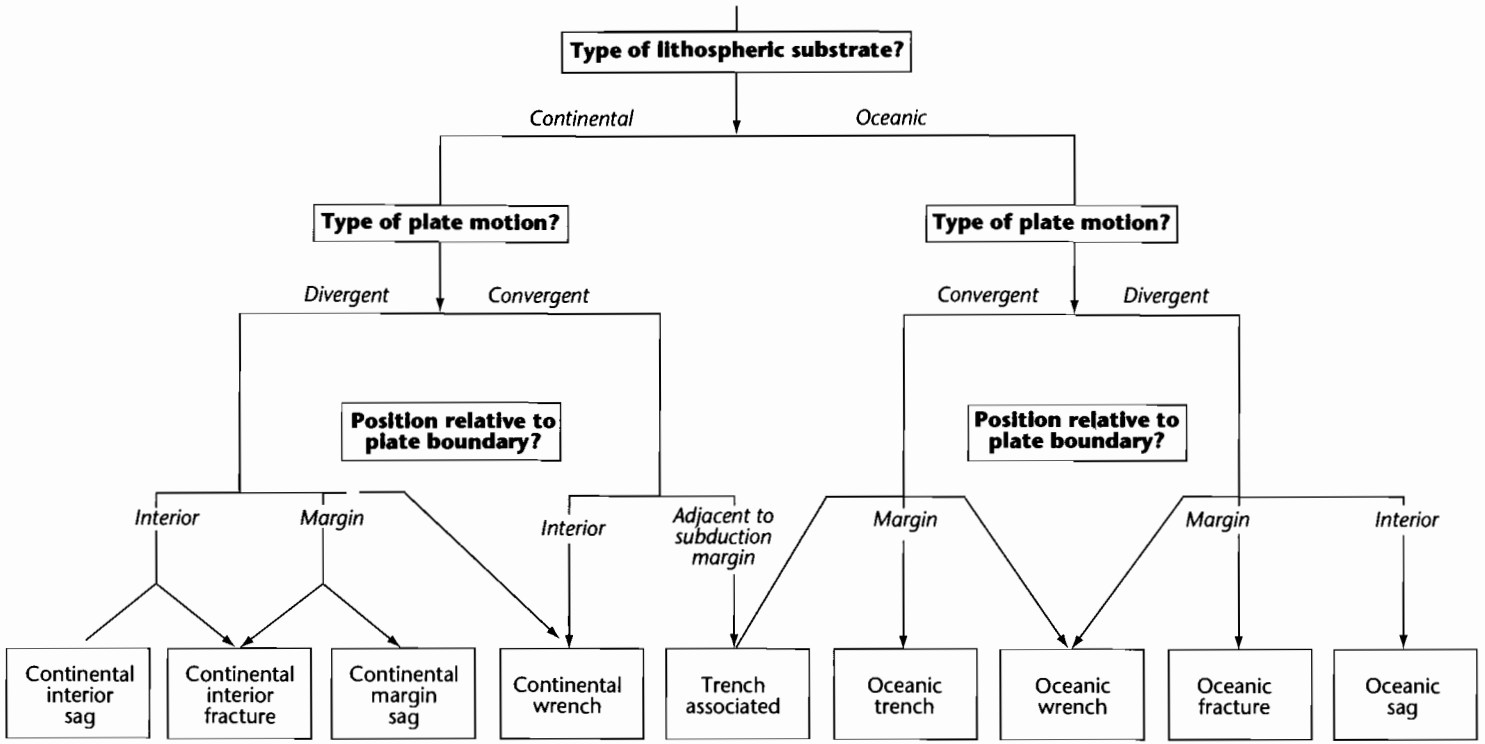

Fig. 1.10 Basin classification scheme based on Kingston et al. (1983a, b). Not all basin types appear in this scheme. Most notably, foreland basins are missing.

the basin-forming tectonics, the depositional sequences filling the basin, and the basin-modifying tectonics.

1.4.1 Basin-forming mechanisms

Although the classifications outlined above undoubtedly have their uses, particularly in predicting source presence, reservoir quality, availability of traps, etc., they have the effect of scrambling some of the essential differences and similarities between basins from the point of view of lithospheric mechanisms. Ingersoll and Busby (1995) recognized six subsidence mechanisms, operating to different degree in their 26 basin types (Table 1.1), which can be summarized as:

- Crustal thinning, such as caused primarily by stretching or surface erosion;
- lithospheric thickening, such as caused by cooling following stretching or accretion of melts derived from the asthenosphere;
- sedimentary and volcanic loading causing isostatic compensation;
- tectonic (supracrustal) loading causing isostatic compensation;
- subcrustal loading caused by subcrustal dense loads such as obducted mantle flakes or crustal densification due to phase changes;
- asthenospheric flow primarily due to the subduction of cold lithospheric slabs.

From the point of view of fundamental lithospheric processes, the major mechanisms for regional subsidence and uplift (*isostatic*, *flexural*, and *dynamic*) can be summarized as follows (Fig. 1.11):

Isostatic consequences of changes in crustal and lithospheric thickness; the thickness changes may be brought about purely thermally by *cooling* of lithosphere, for example where new oceanic lithosphere moves away from spreading centres. Thickness changes causing *thinning* may be caused by mechanical stretching, subaerial erosion or at depth by delamination or the removal (stoping) of a deep lithospheric root. Mechanical *thickening* of crust and lithosphere, as in zones of continental convergence, generally causes isostatic uplift. Thickening of the lithosphere by cooling, however, causes subsidence.

Loading and unloading at the surface and in the subsurface, including the far-field effects of in-plane stresses; *loading* of the lithosphere may take place on a small scale in the form of volcanoes or seamount chains, and on a large scale in the form of mountain belts, causing *flexure* and therefore subsidence. The sediment infilling a basin also acts as a sedimentary load, amplifying the primary driving mechanism.

Dynamic effects of asthenospheric flow, mantle convection, and plumes; subsidence or uplift are caused by the buoyancy effects of changes in temperature in the mantle. Since these temperature changes are transmitted by viscous flow, the surface elevation changes may be termed *dynamic*.

For a given basin type, some or all of the mechanisms given above may have a major or minor role. Consequently, rather than attempting an encyclopedic coverage of all basin types, we focus on the main lithospheric processes in Part 2 of this book. After an introductory chapter on the fundamentals of lithospheric mechanics (Chapter 2), basin forming processes are considered by investigating basins primarily caused by lithospheric stretching (Chapter 3) and basins primarily caused by flexure (Chapter 4). Chapter 5 discusses the role of mantle–lithosphere interactions in basin development. Basins related to strike–slip deformation are considered in Chapter 6.

Basins formed by stretching or thinning of the continental lithosphere fall within an evolutionary sequence (Kinsman 1975; Veevers 1981). The early stages of the sequence correspond to the development of intracratonic rifts often associated with crustal doming. Such rifts may evolve into oceanic spreading centres or may be aborted to form failed rifts or aulacogens. With seafloor creation and drifting of the continental edge away from the spreading centre, passive margin basins develop. The sequence has been termed the *rift-drift suite* of sedimentary basins. The mechanisms of interest within this evolutionary sequence are therefore primarily the thermal and mechanical behavior of the lithosphere under tension, and the thermal contraction of the lithosphere following stretching.

Basins formed by flexure fall into two groups. Flexure of oceanic lithosphere as it approaches subduction zones is responsible for the formation of deep oceanic trenches. It was the investigation of the deflection of the oceanic lithosphere at arc–trench boundaries that provided much of the framework for the general theory of lithospheric flexure. Flexure of the continental lithosphere in continental collision zones gives rise to foreland basins. The force system that causes flexure can be varied. In the case of ocean trenches, it is probably a combination of gravitational body forces on the downgoing oceanic slab and

Table 1.1 Basin classification adapted from Ingersoll and Busby (1995), modified from Dickinson (1974, 1976) and Ingersoll (1988), with modern and ancient examples.

Relative plate movement	Basin type	Basin description	Modern example	Ancient example
Divergent settings	Terrestrial rift valleys	Rifts in continental crust, commonly with bimodal volcanism	Rio Grande Baikal Rhine-Bresse Graben	Keeweenawan (Precambrian) Karoo (Jurassic) Viking and Central Grabens (Mesozoic)
	Proto-oceanic rift troughs	Incipient ocean basins floored by new oceanic crust, flanked by young rifted continental margins	Red Sea Gulf of California	East Greenland (Jurassic)
Intraplate settings	Continental rises and terraces	Mature rifted intraplate continental margins at continental–oceanic boundary	East coast, USA	Early Paleozoic of USA and Canadian Cordillera
	Continental embankments	Progradation of sedimentary wedges at edge of rifted continental margins	Mississippi, Gulf Coast, USA	Early Paleozoic Meguma terrane, Canadian Appalachians (?)
	Intracratonic basins	Broad cratonic basins, commonly with underlying rifts	Chad Basin (Cenozoic) Congo Basin	Paleozoic Michigan Basin Illinois Basin Williston Basin (USA)
	Continental platforms	Stable cratons with thin, extensive sedimentary cover	Barents Sea	Middle Paleozoic, North American Midcontinent
	Active ocean basins	Basins floored by oceanic crust at active divergent plate boundaries	Pacific Ocean	Various ophiolite-bearing complexes (Semail, Oman), Neoproterozoic Arabian Shield
	Oceanic islands, aseismic ridges and plateaus	Sedimentary aprons and platforms in intra-oceanic settings	Emperor–Hawaii seamounts	Mesozoic Snow Mountain Volcanic Complex (Franciscan, California)
	Dormant ocean basins	Basins floored by oceanic crust, neither spreading nor subducting	Gulf of Mexico	Phanerozoic Tarim Basin (China)
Convergent settings	Trenches	Deep troughs formed by subduction of oceanic lithosphere	Chile Trench	Cretaceous, Shumagin Island (Alaska)
	Trench–slope basins	Structurally confined basins on subduction complexes	Central America Trench	Cretaceous Cambria slab (California)
	Forearc basins	Basins within arc–trench gaps	Sumatra	Cretaceous Great Valley (California)
	Intra-arc basins	Basins along arc platform, including superimposed and overlapping volcanoes	Lago de Nicaragua	Early Jurassic, Sierra Nevada (California)

Table 1.1 *Continued*

Relative plate movement	Basin type	Basin description	Modern example	Ancient example
	Backarc basins	Oceanic basins behind intra-oceanic magmatic arcs, and continental basins behind continental margin magmatic arcs without foreland fold–thrust belts	Marianas	Jurassic Josephine ophiolite (California)
	Retroarc foreland basins	Foreland basins on continental sides of continental margin arc–trench systems	Andes foothills	Cretaceous Sevier foreland (Wyoming-Utah)
	Remnant ocean basins	Shrinking ocean basins between colliding continental margins and/or arc–trench systems (eventually subducted or deformed)	Bay of Bengal	Pennsylvanian-Permian Ouachita Basin
	Peripheral foreland basins	Foreland basins superimposed on rifted continental margins during continental collision	Persian Gulf Indo-Gangetic Plain Po Basin (Italy)	Tertiary North Alpine Foreland Basin (Switzerland)
	Piggy-back (thrust sheet top) basins	Basins carried above moving thrust sheets	Peshawar Basin (Pakistan)	Neogene, Apennines (Italy) Meso-Hellenic Trough (Greece)
	Foreland intermontane basins (broken forelands)	Basins formed among basement cored uplifts in foreland settings	Sierras Pampeanas (Argentina)	Laramide basins (USA)
Transform settings	Transtensional basins	Basins formed by local extension along strike–slip fault systems	Salton Sea, California	Carboniferous Magdalen Basin (Gulf of St Lawrence)
	Transpressional basins	Basins formed by local compression along strike–slip fault systems	Santa Barbara Basin (California)	Miocene Ridge Basin (California)
	Transrotational basins	Basins formed by rotation of crustal blocks about vertical axes within strike–slip fault systems	Western Aleutian forearc	Miocene Los Angeles Basin, California
Hybrid settings	Intracontinental wrench basins	Basins on continental crust associated with strike–slip tectonics caused by distant collisional processes	Qaidam Basin (China)	Pennsylvanian-Permian Taos Trough (New Mexico)
	Aulacogens	Former failed rifts reactivated during convergent tectonics	Mississippi Embayment	Paleozoic Anadarko Basin (Oklahoma)
	Impactogens	Rift basins caused by stresses transmitted from convergent plate margin	Baikal Rift (Siberia)	Rhine Graben (Europe)
	Successor basins	Basins in intermontane settings following cessation of orogenic activity	Southern Basin and Range (Arizona)	Paleogene Sustut Basin (British Columbia)

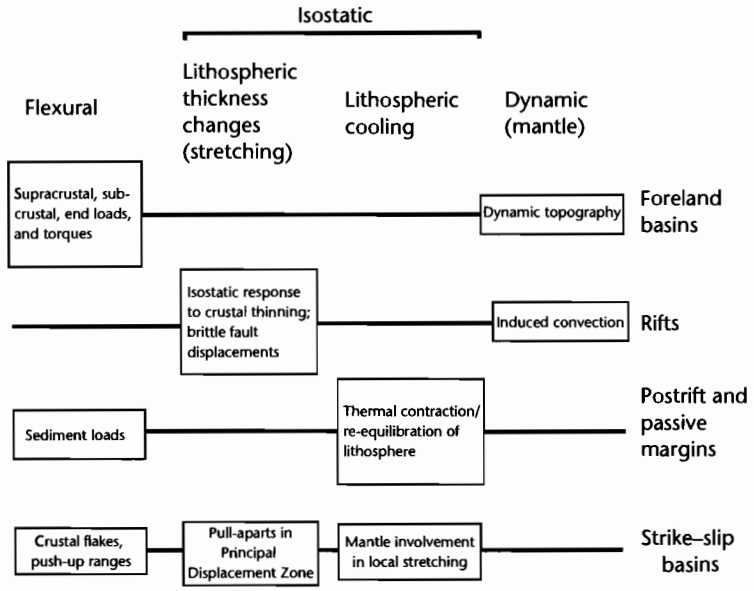

Fig. 1.11 Fundamental mechanisms of basin formation: flexural, isostatic, and dynamic. The importance of these mechanisms in foreland, rift, postrift and passive margin, and strike–slip basins is indicated by the size of the boxes.

the excess in mass of the magmatic arc. In the case of foreland basins it is a combination of topographic loads represented by the mountain belt, lateral density variations of lithospheric material (caused, for example, by prior stretching of the continental lithosphere in the overridden plate or by obduction of dense mantle flakes) and horizontal "in-plane" forces set up by the shallow "end-on" collision of buoyant continental lithosphere.

Processes within the mantle have an important role in basin development. Mantle plumes originating at the core–mantle boundary impinge on the base of the lithosphere and spread out laterally over a length scale of 10^3 km. They are instrumental in continental splitting and the formation of new ocean basins, and have a major role in igneous underplating and isostatic regional uplift. Present day *hotspots* over plumes or ascending limbs of mantle convection systems are characterized by topographic doming and commonly rifting. Basins located over downward limbs of convection systems, *cold-spot basins*, appear to be broad, gentle sags. The onset of subduction of cold oceanic slabs at ocean–continent boundaries causes far-field tilting of the continental plate towards its margin and therefore has a potentially major effect in forearc, intra-arc, and retroarc settings. In addition, it is believed that supercontinental assemblies in the geological past have experienced very long wavelength topographic doming caused by elevated sublithospheric temperatures generated by an overlying insulating lid.

CHAPTER 2

The physical state of the lithosphere

The kindly Earth shall slumber, lapt in universal law
(ALFRED LORD TENNYSON, *IN MEMORIAM* (1850))

SUMMARY

A knowledge of the behavior of the lithosphere is essential if we are to understand the initiation and development of sedimentary basins. Lithospheric processes are responsible for the highly dynamic nature of the tectonic processes near the surface of the Earth. The Earth's outer layer or lithosphere can be regarded as a thermal boundary layer between the cool atmosphere or oceans and the hot interior. The lithosphere is therefore a thermal entity but it also has a physical significance. The upper half of the lithosphere is sufficiently rigid that it is able to store and transmit stresses. Because the deformations caused by applied forces are generally recoverable, this outer zone is known as the elastic lithosphere.

Applied forces of whatever origin cause stresses which result in deformation or strain. The simplest view of applied forces is of those due simply to the weight of an overlying rock column, known as *lithostatic stress*. The difference between the actual stress and the lithostatic stress is a tectonic contribution known as *deviatoric stress*. Deviatoric stresses can be either tensile or compressive.

In an elastic solid there is a clear relationship between the stresses and resultant strains. The exact relationship depends on material properties known as Young's modulus and Poisson's ratio. Where only one of the principal axes is nonzero, a *uniaxial* state of stress is said to occur and the relation between stress and strain is called *Hooke's law*. If there are two nonzero components of principal stress, we have the condition termed *plane stress*. In an analogous fashion, *uniaxial strain* and *plane strain* refer to the coordinate system of principal strains. In a state of stress where all the principal stresses are equal, an *isotropic* state of stress, the fractional volume change caused by isotropic compression is given by the *bulk modulus* or its reciprocal, the *compressibility*.

The lithosphere is able to bend. The shape of the flexure of the lithosphere depends on its rigidity and the nature of the applied force or load causing the bending. Bending is accompanied by longitudinal stresses and bending moments in the plate. The bending moment is related to the local radius of curvature by a coefficient called *flexural rigidity*.

Whereas the upper 15–50 km of the Earth is thought to behave more or less elastically over geological time scales, rocks below this level deform with a creep-like behavior and thus relax stresses.

In order to understand the mechanical behavior of the Earth it is necessary to understand its thermal structure, since this determines its rheology. In the lithosphere, heat transfer is predominantly by conduction, whereas in the mantle convection is extremely important. Convection is the natural result of differential heating above a critical Rayleigh number and estimates for Earth's mantle strongly suggest that convection must be taking place. A thermal boundary layer develops along the upper surface of the convecting fluid because heat is lost by conduction to the surface. This cool boundary layer, the lithosphere, detaches and sinks due to gravitational instability along subduction zones. For conduction, the heat flux is related to the temperature gradient by a coefficient, the *thermal conductivity*. Heat fluxes in the continents are determined primarily by conduction from radioisotopic heat sources, whereas in the oceans they reflect cooling of newly created oceanic lithosphere. The variation of temperature with depth is known as the *geotherm*. Measurements of continental heat flows indicate a linear relationship between radiogenic heat generation and surface heat flow, with the intercept

equivalent to the "reduced" or basal heat flow from the mantle.

The reference equipotential surface for the Earth is termed the *geoid*. Some geoid anomalies probably represent density differences in the Earth set up by plate tectonic processes. The reduction of surface gravity data (*Bouguer anomalies*) provides important information on the way in which topography is compensated isostatically. The Airy model assumes that surface topography is compensated by variations in the depth of the underlying crust, whereas the Pratt model assumes variations in the density of the underlying crust. Periodic loads are supported by the flexural strength of the lithosphere, the degree of compensation depending on the flexural rigidity of the plate, and the wavelength of the load. Techniques such as admittance and coherence allow the flexural rigidity to be estimated from a correlation of the Bouguer gravity anomaly with the spectral wavelength of the topography.

Mantle convection is thought to take place by means of a thermally activated creep. *Diffusion creep* and *dislocation creep* are both strongly temperature dependent processes, but the latter is more rapid since it is driven by shear stresses acting on crystal imperfections. Crustal rocks may also behave in a ductile manner by pressure-solution creep, or they may deform in a brittle manner by fracturing (*Byerlee's law*). The occurrence of earthquake foci, and laboratory experiments on rock mechanics, suggest that that at depths of about 15 km and temperatures of *c.* 300 °C the continental crust starts to become ductile or plastic. The rheology of the crust is complex because of its compositional heterogeneity. The onset of ductility in the middle crust may serve mechanically to decouple the upper crust from the lower crust and mantle lithosphere. The lower lithosphere may deform as an elastic solid on short time scales but viscously on longer time scales. The time scale of the viscous relaxation of stresses is not fully understood but may be estimated from studies of postglacial rebound. In the case of a flexed plate, plastic deformation may take place if a critical elastic curvature is exceeded.

The key to understanding the deformation of the lithosphere is the profile of lithospheric strength with depth. Oceanic and continental lithospheres have different strength profiles. Continental lithospheric strength is strongly controlled by geothermal gradient and by thickening/thinning of the crust. Strain rate affects whether the lithosphere undergoes a net weakening or net strengthening over time, and therefore has an important role in determining the evolution through time of continental deformation.

Sedimentary basins represent a physical deformation of the lithosphere. In order to understand how basins are initiated and evolve through time, it is necessary to have some appreciation of the physical state of the lithosphere. This physical state can be thought of in terms of its thickness, mineralogy, thermal structure, and consequently its strength when acted upon by tangential forces or its rigidity when flexed by orthogonal forces. This chapter introduces some fundamental ideas on the physical state of the lithosphere and how this determines its deformation or flow. In the succeeding chapters in the next section, the particular cases of the stretching (extension) of the lithosphere (Chapter 3) and the bending (flexure) of the lithosphere (Chapter 4) are considered before investigating the large scale interaction of the lithosphere and mantle in Chapter 5 and processes in zones of strike–slip deformation in Chapter 6.

A large number of texts cover topics addressed in this chapter. The reader is particularly directed towards Fowler (1990), Middleton and Wilcock (1994) and Turcotte and Schubert (2002) for a wealth of further details on heat flow, gravity, linear elasticity and flexure, and rheology.

2.1 STRESS AND STRAIN

2.1.1 Stresses in the lithosphere

Body forces on an element of a solid act throughout the volume of the solid and are directly proportional to its volume or mass. For example, the force of gravity per unit volume is the product of ρ, the density and g, the acceleration of gravity. The body forces on rocks within the Earth's interior depend on their densities, but density is itself a function of pressure. If we normalize rock densities to a zero-pressure value, typical mantle rocks would have densities of about $3250\,kg\,m^{-3}$, ocean crust (basalt and gabbro) would have densities of about $2950\,kg\,m^{-3}$, whereas continental granites and diorites would be in the range 2650 to $2800\,kg\,m^{-3}$. Sedimentary rocks are highly variable, ranging from $2100\,kg\,m^{-3}$ for some shales to $2800\,kg\,m^{-3}$ for very compact marbles (Table 2.1).

Surface forces act only on the surface area bounding a volume and arise from the interatomic stresses exerted

Table 2.1 Common physical properties of rocks (after Turcotte and Schubert 2002).

	Density $kg\,m^{-3}$	Young's modulus E 10^{11} Pa	Shear modulus G 10^{11} Pa	Poisson's ratio ν	Thermal conductivity $K\,Wm^{-1}K^{-1}$	Coefficient of thermal expansion α, $10^{-5}K^{-1}$
Sedimentary						
Shale	2100–2700	0.1–0.7	0.1–0.3	0.1–0.2	1.2–3	
Sandstone	1900–2500	0.1–0.6	0.04–0.2	0.1–0.3	1.5–4.2	3
Limestone	1600–2700	0.5–0.8	0.2–0.3	0.15–0.3	2–3.4	2.4
Dolomite	2700–2800	0.5–0.9	0.2–6.4	0.1–0.4	3.2–5	
Metamorphic						
Gneiss	2600–2850	0.4–0.6	0.2–0.3	0.15–0.25	2.1–4.2	
Amphibolite	2800–3150		0.5–1.0	0.4	2.1–3.8	
Marble	2670–2750	0.3–0.8	0.2–0.35	0.2–0.3	2.5–3	
Igneous						
Basalt	2950	0.6–0.8	0.25–0.35	0.2–0.25	1.3–2.9	
Granite	2650	0.4–0.7	0.2–0.3	0.2–0.25	2.4–3.8	2.4
Diabase	2900	0.8–1.1	0.3–0.45	0.25	2–4	
Gabbro	2950	0.6–1.0	0.2–0.35	0.15–0.2	1.9–4	1.6
Diorite	2800	0.6–0.8	0.3–0.35	0.25–0.3	2.8–3.6	
Pyroxenite	3250	1.0	0.4		4.1–5	
Anorthosite	2640–2920	0.83	0.35	0.25	1.7–2.1	
Granodiorite	2700	0.7	0.3	0.25	2.0–3.5	
Mantle						
Peridotite	3250				3–4.5	2.4
Dunite	3000–3700	1.4–1.6	0.6–0.7		3.7–4.6	
Miscellaneous						
Halite			0.3	0.15	5.4–7.2	13
Ice	917		0.092	0.31–0.36	2.2	5

from one side of the surface to the other. The magnitude of the force depends on the surface area over which the force acts and the orientation of the surface. The normal force per unit area on horizontal planes increases linearly with depth. That due to the weight of the rock overburden is known as *lithostatic stress* or *lithostatic pressure*. This concept of surface forces in the Earth's interior is made use of in considering the way in which hydrostatic equilibrium (Archimedes Principle) influences the support of the oceanic and continental plates by the mantle, an important application known as *isostasy*.

The surface force acting on a unit area at the base of a vertical column of rock is given by

$$\sigma_{yy} = \rho g y \tag{2.1}$$

where ρ is the density of the rock column, g is the acceleration of gravity, and y is the height of the column. For equilibrium to be maintained, we can equate the surface forces due to the differing rock columns under continental and oceanic lithosphere. The isostatic balance at a depth equivalent to the base of the continental block (Fig. 2.1a) is expressed

$$h\rho_c g = b\rho_m g \tag{2.2}$$

and the elevation of the continental block above the mantle is given by

$$h - b = h\left(1 - \frac{\rho_c}{\rho_m}\right) \tag{2.3}$$

Putting $\rho_c = 2700\,kg\,m^{-3}$, $\rho_m = 3300\,kg\,m^{-3}$ and $h = 35\,km$, the elevation of the continental block is 6.4 km.

For the more realistic case of a continental block with its surface at sea level flanked by oceanic crust and an overlying water column (Fig. 2.1b), the isostatic balance at a depth equivalent to the base of the continental block is

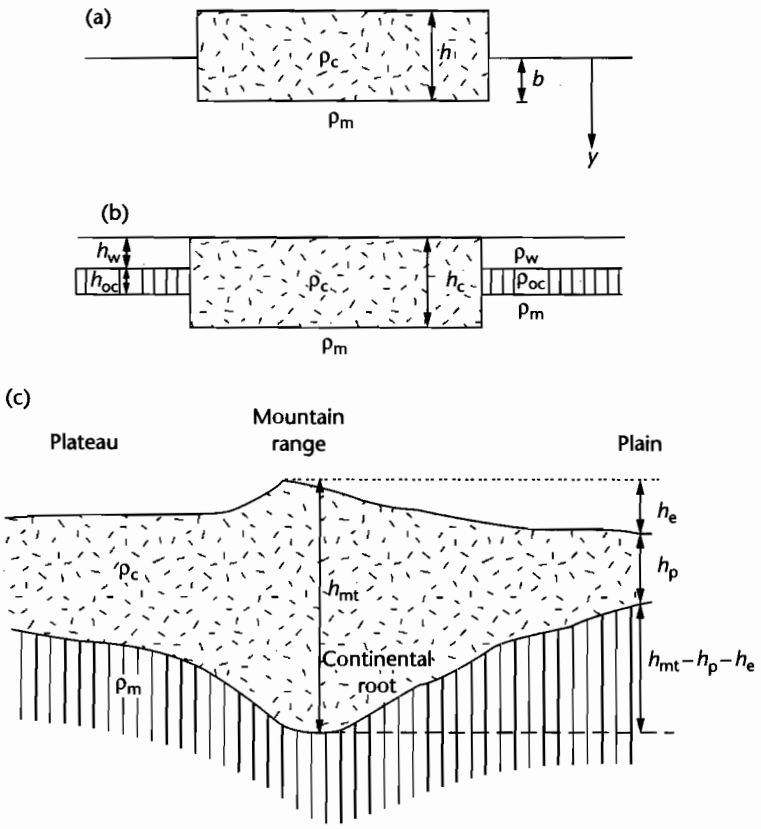

Fig. 2.1 Schematic diagrams illustrating the concepts of isostasy. (a) Continental block "floating" in a fluid mantle; (b) continental block flanked by oceanic crust and overlying water column; (c) continental mountain belt with a root surrounded by a plateau and low-lying plain. Notation explained in text.

$$h_c\rho_c g = h_w\rho_w g + h_{oc}\rho_{oc} g + (h_c - h_w - h_{oc})\rho_m g$$
$$h_{oc}(\rho_m - \rho_{oc}) + h_w(\rho_m - \rho_w) = h_c(\rho_m - \rho_c) \qquad (2.4)$$

Putting $\rho_c = 2700\,\mathrm{kg\,m^{-3}}$, $\rho_{oc} = 2950\,\mathrm{kg\,m^{-3}}$, $\rho_m = 3300\,\mathrm{kg\,m^{-3}}$, $h_c = 35\,\mathrm{km}$, and $h_{oc} = 20\,\mathrm{km}$, the water depth is 6 km. This is roughly the depth of the ocean we should expect above the oceanic abyssal plains.

A more familiar parameterization for isostasy is of a mountain belt with a "root," the excess mass in the elevated continental crust being compensated by the mass deficit at depth of the continental root replacing mantle. The isostatic balance at a depth equivalent to the base of the continental root (Fig. 2.1c) is

$$h_{mt}\rho_c g = h_p\rho_c g + (h_{mt} - h_p - h_e)\rho_m g$$

$$h_{mt} = h_p + h_e\left(\frac{\rho_m}{\rho_m - \rho_c}\right) \qquad (2.5)$$

Putting $h_p = 35\,\mathrm{km}$, $h_e = 5\,\mathrm{km}$, $\rho_m = 3300\,\mathrm{kg\,m^{-3}}$, $\rho_c = 2700\,\mathrm{kg\,m^{-3}}$, the thickness of crust in the mountain belt h_{mt} is 62.5 km. A very deep "granitic" root is therefore required to support a mountain range with an elevation of 5 km.

We will examine a simple application of isostasy in studying the bending of lithosphere in §2.1.4.

Normal surface forces can also be exerted on vertical planes (Fig. 2.2). If the normal surface forces, σ_{xx}, σ_{yy}, and σ_{zz} are all equal and they are also equal to the weight of overburden, the rock is said to be in a *lithostatic state of stress*. The normal surface forces σ_{xx}, σ_{yy}, and σ_{zz} are rarely

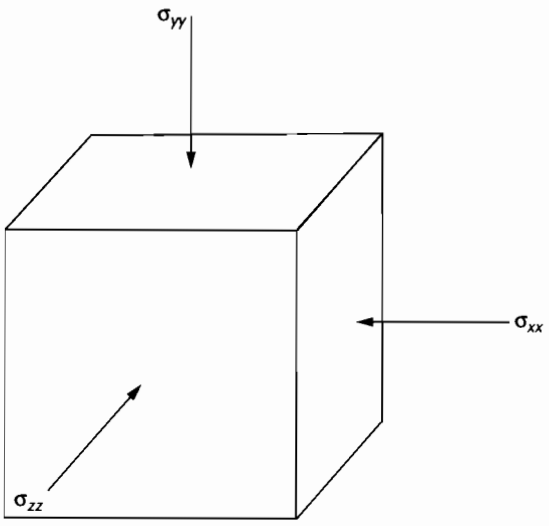

Fig. 2.2 Normal surface forces acting on vertical and horizontal planes.

equal when a rock mass is being subjected to tectonic forces. In such a case the total horizontal surface force (normal stress) acting on a continent, for example, would be made up of two components, a lithostatic term and a tectonic contribution known as a deviatoric stress ($\Delta\sigma_{xx}$),

$$\sigma_{xx} = \rho_c g y + \Delta\sigma_{xx} \tag{2.6}$$

where ρ_c is the density of the continent. Normal stresses can be either *tensile* when they tend to pull on planes or *compressive* when they push on planes. Horizontal deviatoric stresses may result from uplift producing excess potential energy or may be transmitted from plate boundaries, when they are commonly referred to as *in-plane* or *intraplate stresses* (see Chapters 3 and 8).

Surface forces acting parallel to a surface are known as *shear stresses*. Examples are provided by a thrust sheet with a lower fault plane that experiences a frictional resistance, or the gravitational sliding of a rock mass down an inclined plane.

Stress components can be generalized at any point in a material by using the x, y, z coordinate system. At any point we can envisage three mutually perpendicular planes on which there are no shear stresses. Perpendiculars to these planes are known as *principal axes of stress* and can be labeled

σ_1 = maximum principal stress
σ_2 = intermediate principal axis
σ_3 = minimum principal axis,

where convention is that σ is positive for compressional stress and negative for extensional stress. There are certain states of stress that can be described by use of the principal axes notation:

- *Uniaxial stress* has a finite σ_1, and $\sigma_2 = \sigma_3 = 0$
- *biaxial* or *plane stress* has $\sigma_1 > \sigma_2$ and $\sigma_3 = 0$
- *triaxial stress* is the general state $\sigma_1 > \sigma_2 > \sigma_3$.

If the principal stresses σ_1, σ_2, and σ_3 are identical, the state of stress is isotropic and any principal stress is equal to the pressure. In such a case, any set of orthogonal axes qualifies as a principal axis coordinate system. This is known as a *hydrostatic state of stress*. Where the state of stress is not isotropic, the pressure is equal to the mean of the normal stresses

$$p = \frac{1}{3}(\sigma_1 + \sigma_2 + \sigma_3) \tag{2.7}$$

Subtraction of the mean stress (that is, pressure) from the normal stress component reveals the *deviatoric normal stresses*. It is common for two of the principal stresses to be nonzero, giving the state of plane stress. Such a system is suggestive of the horizontal stresses in the lithosphere caused by tectonic processes.

2.1.2 Strain in the lithosphere

Strain is the deformation of a solid caused by the application of stress. We can define the components of strain by considering a rock volume with sides δ_x, δ_y, and δ_z which changes in dimensions but not in shape, so that the new lengths of the sides after deformation are $\delta x - \varepsilon_{xx}\delta x$, $\delta y - \varepsilon_{yy}\delta y$, and $\delta z - \varepsilon_{zz}\delta z$ where ε_{xx}, ε_{yy}, and ε_{zz} are the strains in the x, y, and z directions (Fig. 2.3). As long as the deformation of the volume element is relatively small, the volume change, or *dilatation*, is simply the sum of the strain components ($\varepsilon_{xx} + \varepsilon_{yy} + \varepsilon_{zz}$). Volume elements may also change their position without changing their shape, in which case the strain components are due to *displacement*.

Shear strains, however, may distort the shape of an element of a solid. In the case of a 2-D rectangular element which is distorted to a parallelogram (Fig. 2.4), the shear strain is dependent on the amount of rotation of the sides of the rectangular element. Thus, shear strain in the two dimensions x and y is determined by the

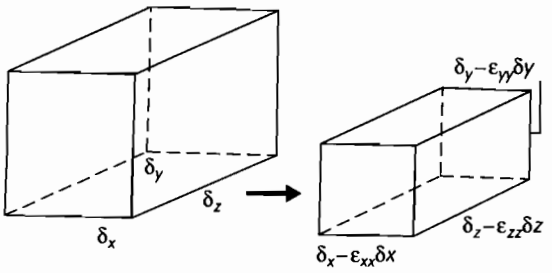

Fig. 2.3 A rectangular block that changes its dimensions but not its shape: this is a deformation involving no shear.

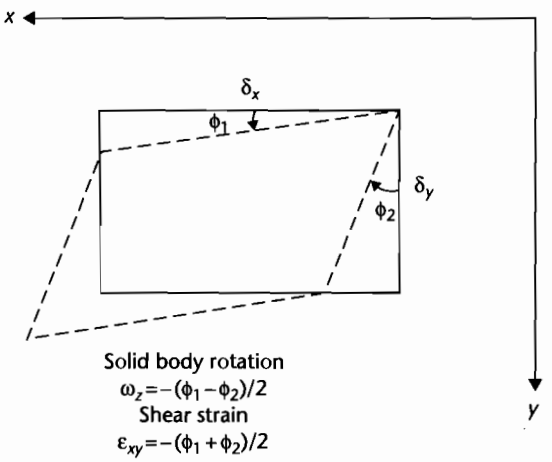

Fig. 2.4 Deformation of a rectangle into a parallelogram by a strain field involving shear.

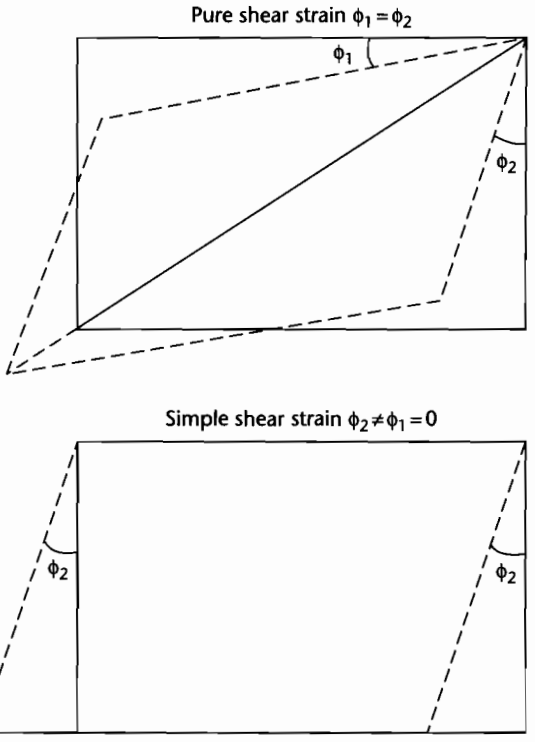

Fig. 2.5 Difference between pure shear strain (no solid body rotation) and simple shear strain (solid body rotation is $\phi_2/2$).

angles through which the sides of the rectangle are rotated (Fig. 2.4).

If the angles through which the sides of the rectangle are rotated (ϕ_1 and ϕ_2 in Fig. 2.4) are not equal, *solid body rotation* is said to have occurred. Solid body rotations do not involve changes in the distances between neighboring elements of a solid and therefore do not reflect strain.

The deformation of any element can now be described according to the shear strain and the solid body rotation. If no solid body rotation occurs, $\phi_1 = \phi_2$ and the deformation is a result only of shear strains, it is known as *pure shear*. If there is solid body rotation but $\phi_1 = 0$, the element has undergone *simple shear*. Figure 2.5 illustrates the two circumstances. We shall see how models of pure shear (e.g., uniform extension with depth) and simple shear (e.g., asymmetrical extension associated with translithospheric shear zones) have been applied to the formation of extensional basins (Chapter 3).

As in the case of shear stresses, shear strains can be described with reference to a coordinate system that is orientated such that shear strain components are zero. Such a system contains the *principal axes of strain*. The fractional changes in length along the directions of the principal strain axes are the *principal strains*. In the 3-D case the condition of isotropic strain is satisfied by

$$e = (\varepsilon_1 + \varepsilon_2 + \varepsilon_3)/3 = \Delta/3 \qquad (2.8)$$

where Δ is the dilatation and e is the mean normal strain.

It is very rare, however, for strain to be homogeneous. *Deviatoric strain* components are strains that are the difference between the actual strain and the mean normal strain. Deviatoric strains invariably result from

the operation of tectonic processes. Their analysis therefore greatly aids the interpretation of lithospheric deformation.

In an analogous fashion to the treatment of states of stress, we can define different states of strain.

- *Uniaxial strain* is where there is only one nonzero component of principal strain, that is, assuming the nonzero axis to be ε_1, $\varepsilon_2 = \varepsilon_3 = 0$.
- *Plane strain* is where only one of the principal strain components is zero, for example $\varepsilon_3 = 0$ and ε_1 and ε_2 are nonzero. It is a common starting point for studying lithospheric deformation, since it can be assumed that the strain in the direction of an infinite plate will be zero.

2.1.3 Linear elasticity

It is clearly important to know the relationship between the stress and the strain in a piece of lithosphere. These relationships reflect the basic flow laws of Earth materials.

Elastic materials deform when they are subjected to a force and regain their original shape and volume when the force is removed. For relatively low temperatures, pressures and applied forces, almost all solid materials behave elastically. The relation between stress and elastic strain is linear. However, at high temperatures and pressures or high levels of stress rocks do not behave elastically (§2.4). In near-surface regions where temperature and pressures are low, rocks deform by brittle fracture at high levels of stress. Deeper in the Earth, high temperatures and pressures cause the rock to deform plastically under an applied force, with no fracturing. Brittle materials that have exceeded their yield strength and plastic materials do not regain their original shape when the force is removed.

Because much of the lithosphere behaves as a strong material over geological (i.e. $>10^6$ yr) periods of time, it is able to bend under surface loads, to store the elastic stresses responsible for earthquakes, and to transmit stresses over large horizontal distances. This fundamental property of the lithosphere is crucial to an understanding of the formation of sedimentary basins.

The theory of linear elasticity underpins a very great deal of thought on lithospheric mechanics and often constitutes the basic assumption in models of lithospheric behavior.

In a linear, isotropic, elastic solid the stresses are linearly proportional to strains, and mechanical properties have no preferred orientation. The principal axes of stress and the principal axes of strain coincide. The relation between the principal strain and the components of principal stress can be stated as follows.

$$\varepsilon_1 = \frac{\sigma_1}{E} - \frac{\nu\sigma_2}{E} - \frac{\nu\sigma_3}{E} \tag{2.9}$$

$$\varepsilon_2 = -\frac{\nu\sigma_1}{E} + \frac{\sigma_2}{E} - \frac{\nu\sigma_3}{E} \tag{2.10}$$

$$\varepsilon_3 = -\frac{\nu\sigma_1}{E} - \frac{\nu\sigma_2}{E} + \frac{\sigma_3}{E} \tag{2.11}$$

The exact partitioning of stresses to give a resultant strain is clearly strongly influenced by E and ν, which are material properties known as *Young's modulus* and *Poisson's ratio* respectively. In general terms, a principal stress produces a strain component σ/E along the same axis and strain components $-\nu\sigma/E$ along the two other orthogonal axes.

Where only one of the principal stresses is nonzero (uniaxial stress), a shortening in the direction of the applied compressive stress will be accompanied by an extension in the two orthogonal directions (Fig. 2.6), and *vice versa*. Under these conditions where, let us say $\sigma_2 = \sigma_3 = 0$ and $\sigma_1 \neq 0$, there is a simple relation along the axis of uniaxial stress

$$\sigma_1 = E\varepsilon_1 \tag{2.12}$$

This well-known relationship is called *Hooke's law*.

There is a fractional volume change or dilatation due to uniaxial stress, but the contraction in the direction of uniaxial stress is compensated by expansion by half as much in the two other orthogonal directions.

In an isotropic state of stress, all the principal stresses and principal strains are equal. The pressure under these conditions is related to the dilatation by K, the *bulk modulus* or its reciprocal β, the *compressibility*. These parameters therefore give the fractional volume change during isotropic compression under a given pressure. If there is a volume change, in order that matter is conserved, there must be an increase in density. Such a density increase $\delta\rho$ is given simply by

$$\delta\rho = \rho\beta p \tag{2.13}$$

where p is the pressure, ρ is the density of the solid element and β the compressibility. In terms of the

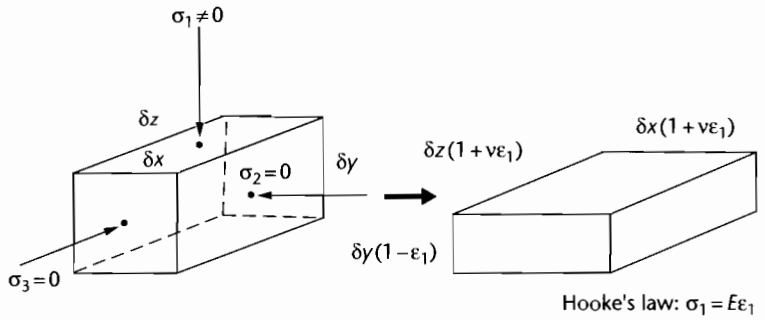

Fig. 2.6 Deformation under a uniaxial stress. Contraction in the direction of the compressive stress σ_1 is compensated by extension in the two orthogonal directions.

previously defined Young's modulus E and Poisson's ratio v,

$$K = \frac{1}{\beta} = \frac{E}{3(1-2v)} \tag{2.14}$$

showing that as v approaches 1/2 the bulk modulus tends to infinity, that is, the material becomes essentially incompressible.

2.1.4 Flexure in two dimensions

Because the lithosphere behaves elastically, it is able to bend when force systems or loads are applied to it. We will return to this topic in considerable detail when considering the initiation and maintenance of foreland basins (Chapter 4). The aim here is to provide a brief theoretical background of the way the lithosphere responds by flexure to these applied force systems. A full analysis is provided by Turcotte and Schubert (1982, 2002). The concepts involved in the flexure of an elastic solid may be briefly summarized as follows:

- Flexure results from vertical forces, horizontal forces, and torques (bending moments) in any combination. Horizontal loads are commonly neglected, perhaps unwisely, in geodynamical problems;
- the bending moment is the integration of the fibre (normal) stresses on cross-sections of the plate acting over the distance to the midline of the plate. The bending moment is related to the local radius of curvature of the plate by a coefficient called the *flexural rigidity*. Flexural rigidity is proportional to the cube of the equivalent *elastic thickness*. When applied to the lithosphere the equivalent elastic thickness does not represent a real physical discontinuity;
- a general flexural equation can be derived which expresses the deflection of the plate in terms of the vertical and horizontal loads, bending moment and flexural rigidity. This equation can readily be adapted for use in the study of geological problems.

BOXED TEXT 2.1: Derivation of Flexural Rigidity and the General Flexure Equation

In the simplest terms the flexure of a plate depends on its thickness, elastic properties, and the nature of the applied load. Imagine a plate of thickness h and width L which is fixed at both ends and which is subjected to a line load at its midpoint (Fig. 2.7). In order to attain a force balance, the vertical line load V_a must be counteracted by vertical forces $V_a/2$ at both ends. Assuming that both plate thickness h and deflection w are small compared to the width of the plate L (as required by linear elastic theory), we can study the

Continued

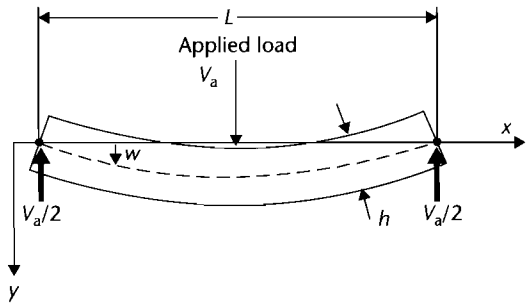

Fig. 2.7 Configuration and notation for a thin plate, pinned at both ends, bending under an applied load.

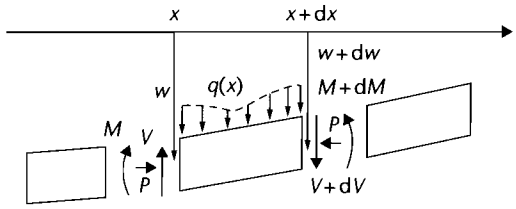

Fig. 2.8 Forces on a small element of a flexed plate. The forces can be balanced vertically and in terms of their tendency to rotate the element (moments or torques).

forces and torques on a small element of the plate. A downward force per unit area $q(x)$ is exerted on the plate by the applied load and on the end sections there is a net shear force per unit length V and horizontal force P per unit length, the latter being independent of x (Fig. 2.8). A bending moment M also acts on the end section related to the effects of normal stresses on the cross-section, σ_{xx}. These normal stresses are known as *fiber stresses* (Fig. 2.9).

The bending moment M is related to the curvature of the plate, since forces on the end section exert a torque about the midpoint of the plate. If the force on an element of thickness dy on the end of the plate is $\sigma_{xx}dy$, then this force will exert a torque about the midpoint ($y = 0$) of $\sigma_{xx}y\,dy$. Integrated over the entire end section we obtain the bending moment

$$M = \int_{-h/2}^{h/2} \sigma_{xx} y dy \tag{2.15}$$

The fiber stresses σ_{xx} result in longitudinal strains in the plate, contractional in the upper half and extensional in the lower half (Fig. 2.9). In the 2-D case

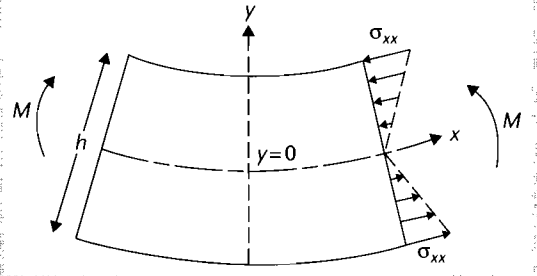

Fig. 2.9 Normal stresses on an end section of a flexed plate. These normal or fiber stresses exert torques about the midpoint of the plate, which when integrated over the end section (from $-h/2$ to $+h/2$) gives the bending moment.

we assume that the plate is infinite in the plane normal to the figure, so there is no strain in the direction perpendicular to the xy plane, that is, $\varepsilon_{zz} = 0$. This is the situation of *plane strain* (§2.1.2). If the plate is thin, it is possible to make the further assumption that stresses normal to the plate's surface are zero ($\sigma_{yy} = 0$). The relations between stress and strain can then be restated as (cf. eqn 2.9)

$$\varepsilon_{xx} = \frac{1}{E}(\sigma_{xx} - \nu\sigma_{zz}) \tag{2.16}$$

and from equation (2.10)

$$\varepsilon_{zz} = \frac{1}{E}(\sigma_{zz} - \nu\sigma_{xx}) \tag{2.17}$$

If the bending is 2-D (there is no strain in the direction perpendicular to the page in Fig. 2.10), $\varepsilon_{zz} = 0$, then (2.16) and (2.17) give

$$\sigma_{xx} = \frac{E}{(1-\nu^2)}\varepsilon_{xx} \tag{2.18}$$

which is the relation between fiber stresses and longitudinal strains. The bending moment can now be related to longitudinal strains by substitution of (2.18) in (2.15)

$$M = \frac{E}{(1-\nu^2)}\int_{-h/2}^{h/2} \varepsilon_{xx} y\, dy \tag{2.19}$$

The bending moment M can also be related to the deflection w. The local radius of curvature R is inversely

proportional to the rate of change in slope of the deflection, or $-d^2w/dx^2$ (if strains are small and $dw/dx \ll 1$, and where the negative sign simply states that w is positive downwards) (Fig. 2.10a). In addition, the longitudinal strain is also related to the radius of curvature. This relation can be derived by geometrical similarity (Fig. 2.10b), since the length of the plate is dependent on the local radius of curvature and ϕ ($l = R\phi$), and the change in length of the plate (Δl) is determined by the distance from the midline of the plate (y) and ϕ ($\Delta l = \phi y$). Using this result, the longitudinal strains ($\Delta l/l$) can be expressed in terms of the deflection,

$$\varepsilon_{xx} = \frac{\Delta l}{l} = \frac{y}{R} = -y\frac{d^2w}{dx^2} \tag{2.20}$$

The bending moment can therefore be rewritten

$$M = \frac{-E}{(1-\nu^2)}\frac{d^2w}{dx^2}\int_{-h/2}^{h/2} y^2\, dy \tag{2.21}$$

which when evaluated between the limits $-h/2$ and $h/2$ gives

$$M = \frac{-Eh^3}{12(1-\nu^2)}\frac{d^2w}{dx^2} \tag{2.22}$$

The coefficient of $-d^2w/dx^2$ in equation (2.22) is defined as the *flexural rigidity*, D. Note that the flexural rigidity D is proportional to the cube of the elastic thickness of the plate h. Flexural rigidity is commonly expressed as this length term. When applied to the lithosphere, the term equivalent elastic thickness Te is preferred, since the value of Te does not reflect the depth of a real physical discontinuity in the lithosphere; it is simply the equivalent thickness of a purely elastic beam.

The bending moment can therefore be written in terms of the curvature,

$$M = -D\frac{d^2w}{dx^2} = \frac{D}{R} \tag{2.23}$$

We can now proceed to establish the general flexural equation by carrying out a force balance on a segment of the plate. The force balance (Fig. 2.8) on a flexed plate with a downward force caused by loading $q(x)$ and horizontal forces (P) on the end sections is as follows.

Equating the forces in a vertical direction we have

$$q(x)dx = -dV$$

$$q(x) = -\frac{dV}{dx} \tag{2.24}$$

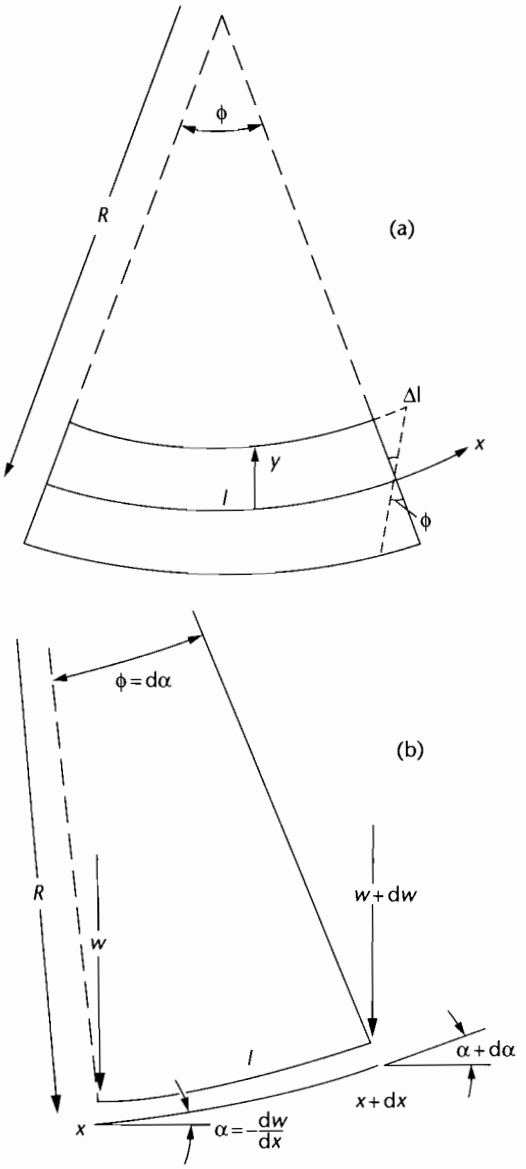

Fig. 2.10 Geometrical aspects of plate bending. (a) Longitudinal strain (extension below the midplane and contraction above the midplane of the plate) is a function of the distance from the midplane of the plate y, and the angle ϕ; (b) Notation to show that the second derivative of the deflection (d^2w/dx^2) gives the rate of change of slope of the plate; this is inversely related to the local radius of curvature R of the plate.

Continued

Balancing torques we have in the counterclockwise direction a force P acting over a moment arm of $-dw$ and the torque dM. In the clockwise sense we have $(V + dV)$ acting over a moment arm of dx. Since the term dV is small we can write

$$-Pdw + dM = Vdx \tag{2.25}$$

Differentiating (2.25) twice, so that (2.24) can be substituted into (2.25) gives

$$-P\frac{d^2w}{dx^2} + \frac{d^2M}{dx^2} = -q(x) \tag{2.26}$$

Since we have already expressed the bending moment in terms of the flexural rigidity and the local curvature, (2.26) can be rewritten as

$$D\frac{d^4w}{dx^4} = q(x) - P\frac{d^2w}{dx^2} \tag{2.27}$$

which is the *general flexure equation* for the deflection of a plate.

In the context of an elastic plate overlying a fluid-like mantle, this equation must be modified to account for a restoring force (buoyancy) acting upwards on the deflected plate (see below).

There will be different bending stresses under situations where the plate is pinned at one or both ends and according to whether it is point loaded (for example, at its free end) or uniformly loaded along its length, or loaded in some other fashion. However, the general flexural equation provides the basic starting point for more specific analyses.

When an applied load flexes a plate, the deflected region is filled either with water, as in the case of oceanic lithosphere or a starved continental basin, or with sediment, as in the case of most basins adjacent to hinterlands undergoing erosion. This infilling material has a smaller density than the mantle that is being replaced (Figs. 2.11, 2.12). The density difference can be denoted by $\Delta\rho$. The magnitude of the restoring force on the base of the deflected plate can be estimated by considering a balance of pressure (ρgh) under the region of maximum deflection and under the unaffected region. This upward restoring force is $\Delta\rho gw$, and the net vertical force acting on the plate is the applied load less this restoring hydrostatic force. The general flexural equation (2.27) therefore becomes

$$D\frac{d^4w}{dx^4} + P\frac{d^2w}{dx^2} + \Delta\rho gw = q_a(x) \tag{2.28}$$

where $\Delta\rho$ is $(\rho_m - \rho_w)$ for a purely water-filled basin (Fig. 2.11) and $\Delta\rho$ is $(\rho_m - \rho_s)$ for a fully sediment-filled basin (Fig. 2.12). The analytical solution of the general flexure equation in the context of a foreland basin is given in Chapter 4.

The lithosphere has a different flexural response according to the spatial distribution of the load $q_a(x)$. If the wavelength of a load of a certain mass, say excess topography, is sufficiently short, the vertical deflection of the lithosphere is small, and the lithosphere can be regarded as infinitely rigid for loads of this scale.

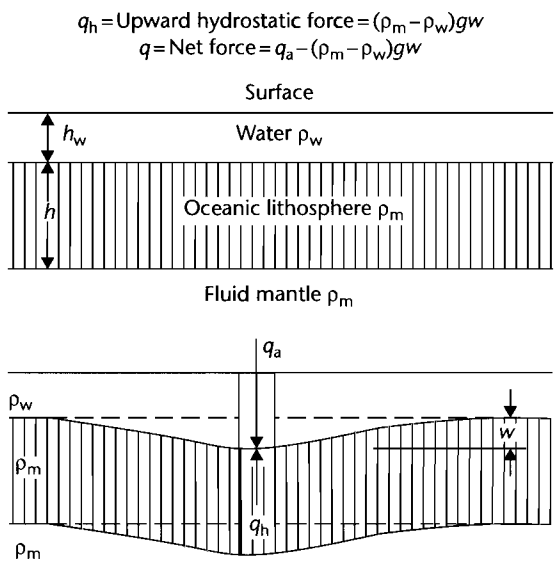

Fig. 2.11 Model for calculating the upward-acting hydrostatic restoring force on an oceanic plate, overlain by water, deflected by an applied force q_a.

However, if the wavelength of a load of the same mass is sufficiently long, there is an effective isostatic response towards hydrostatic equilibrium and the lithosphere appears to have no rigidity. These two situations must

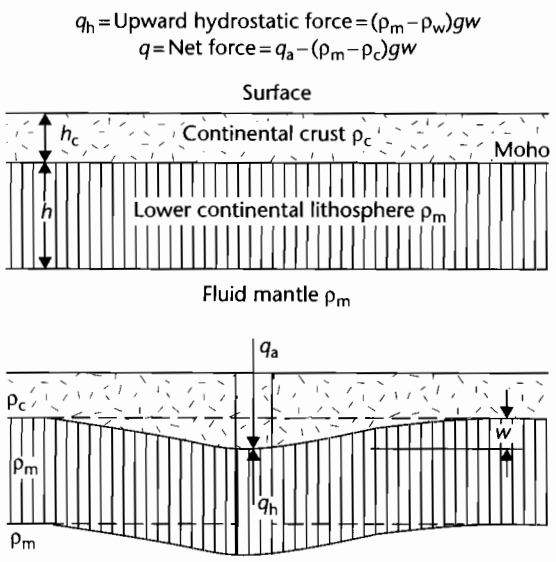

Fig. 2.12 Model for calculating the hydrostatic restoring force on the base of some continental crust where the deflection caused by the applied load q_a is assumed to be filled with material of the same density as the continental crust. This therefore approximates the case of a sediment-filled sedimentary basin on continental lithosphere.

be regarded as end members. The degree of compensation of the topographic load is the ratio of the deflection of the lithosphere to its maximum or hydrostatic deflection. The response of the lithosphere to an applied load such as the excess mass in a mountain belt is identical to its response to sediment loads in a basin. The degree of compensation for sediment loads of varying wavelength is dealt with in §2.3.3 and revisited in §9.3.

For reasonable values of plate thickness and flexural rigidity it is found that horizontal forces applied at the end of a plate are generally inadequate to cause buckling. Horizontal forces as buckling agents may, however, be much more important where the lithosphere has been strongly thinned in regions of high heat flow or where it is rheologically layered (§4.4).

The general features of basins such as oceanic trenches and foreland basins adjacent to mountain belts can be explained by flexural models. Applications of the foregoing discussion of elasticity and flexure to sedimentary basin analysis are given in Chapter 4.

2.2 HEAT FLOW: CONDUCTION AND CONVECTION

2.2.1 Fundamentals

To understand the mechanical behavior of the Earth it is necessary to know something of its thermal structure, since rock rheologies depend on temperature, itself a function of depth. The temperature distribution of the Earth must reflect the inputs and outputs of heat to the Earth system. In other words, there is a heat transfer or flow, achieved by processes of conduction, convection, and radiation. The essential differences between these processes are as follows. Conduction is a diffusive process whereby kinetic energy is transferred by intermolecular collisions. Convection on the other hand requires motion of the medium to transmit heat. Electromagnetic radiation, such as that of the Sun, can also transmit heat, but it is of relatively minor importance in the Earth's *internal* heat budget. It is of paramount importance in determining Earth's *surface* heat budget.

The processes of conduction and convection are of differing importance in different zones. In the lithosphere heat is transported primarily through conduction, whereas in the mantle convection of heat from the Earth's deep interior is dominant. Convection is a much faster process of heat transfer than conduction.

The fundamental relation for conductive heat transport is given by *Fourier's law*. It states that the heat flux Q is directly proportional to the temperature gradient and takes the mathematical form

$$Q = -K\frac{dT}{dy} \tag{2.29}$$

where K is the coefficient of thermal conductivity, T is the temperature at a given point in the medium and y is the coordinate in the direction of the temperature variation.

The heat flux at the Earth's surface gives a good indication of processes within the interior. Temperature measurements can be made on land in caves, mines, and better still, in deep boreholes and allow the heat flux to be calculated as long as the thermal conductivity K is known (see § 9.6.1). K can be measured in the laboratory on rock samples by subjecting them to a known heat flux and measuring the temperature drop across the sample (Table 2.1). The large range of values for sedimentary rocks is due, to a large extent, to large

variations in porosity (see also §9.3.1). Heat flow is in units of $mW\,m^{-2}$ or $cal\,cm^{-2}\,s^{-1}$. Surface heat fluxes are sometimes expressed in heat flow units where 1 HFU is equivalent to $10^{-6}\,cal\,cm^{-2}\,s^{-1}$ or $41.84\,mW\,m^{-2}$. Thermal conductivity is measured in units of Watts per meter per degree Centigrade ($W\,m^{-1}\,°C^{-1}$), and occasionally in $cal\,cm^{-1}\,°C^{-1}$.

Temperature measurements of the ocean floor can also be made by penetrating seafloor sediments with a temperature probe. The same probe contains a heater which enables the *in situ* thermal conductivity to be calculated.

The results of heat flow measurements of the oceans and continents reveal important variations (Table 2.2, Sclater et al. 1980a, 1981). Regions of high heat flow on the continents generally correspond to active volcanic areas, such as the Andes, or to regions of extensional tectonics like the Basin and Range province of western USA. Continental collision zones typically have low to normal surface heat flows (further details in §9.9). In areas devoid of active tectonics and vulcanicity, the heat flow appears to be inversely correlated to the age of the rocks (Jessop and Lewis 1978). This can be explained by the decreasing abundance with age of the radioactive heat-producing isotopes of uranium, thorium and potassium. Surface heat flows are also determined by the underlying rock type. Granites produce large amounts of radiogenic heat, whereas basalts and peridotites produce almost no radiogenic heat (Table 2.3).

In the oceans the surface heat flows are related not to the concentration of radioisotopes but to the age of the seafloor. Newly created oceanic crust cools by conduction as it travels away from the mid-ocean ridge, thereby explaining this relationship. Mean oceanic surface heat

Table 2.2 Regional variations in surface heat flow (data from Sclater et al. 1980a).

	Mean surface heat flow	
	$mW\,m^{-2}$	HFU
Continents:	56.6	1.35
Africa	49.8	1.19
North America	54.4	1.30
Australia	63.6	1.52
Oceans:	78.2	1.87
North Pacific	95.4	2.28
Indian Ocean	83.3	1.99
South Atlantic	59.0	1.41
Worldwide	69.9	1.67

Table 2.3 Typical concentrations of radioactive elements and heat generation from typical rock types comprising the continental and oceanic crust and undepleted mantle (from Fowler 1990).

	Granite	Tholeiitic basalt	Alkali basalt	Peridotite	Average continental upper crust	Average oceanic crust	Undepleted mantle
Concentration by weight							
U (ppm)	4	0.1	0.8	0.006	1.6	0.9	0.02
Th (ppm)	15	0.4	2.5	0.04	5.8	2.7	0.10
K (%)	3.5	0.2	1.2	0.01	2.0	0.4	0.02
Heat generation ($10^{-10}\,W\,kg^{-1}$)							
U	3.9	0.1	0.8	0.006	1.6	0.9	0.02
Th	4.1	0.1	0.7	0.010	1.6	0.7	0.03
K	1.3	0.1	0.4	0.004	0.7	0.1	0.007
Total	9.3	0.3	1.9	0.020	3.9	1.7	0.057
Density ($10^3\,kg\,m^{-3}$)	2.7	2.8	2.7	3.2	2.7	2.9	3.2
Heat generation ($10^{-6}\,W\,m^{-3}$)	2.5	0.08	0.5	0.006	1.0	0.5	0.02

Table 2.4 Relative abundance of isotopes and crustal heat generation as a function of age (from Jessop and Lewis 1978).

	Relative abundance					Heat generation	
Age (Ma)	^{238}U	^{235}U	U*	Th	K	Model A†	Model B‡
Present	1.00	1.00	1.00	1.00	1.00	1.00	1.00
500	1.08	1.62	1.10	1.03	1.31	1.13	1.17
1000	1.17	2.64	1.23	1.05	1.70	1.28	1.37
1500	1.26	4.30	1.39	1.08	2.34	1.48	1.64
2000	1.36	6.99	1.59	1.10	2.91	1.74	1.98
2500	1.47	11.4	1.88	1.13	3.79	2.08	2.43
3000	1.59	18.5	2.29	1.16	4.90	2.52	3.01
3500	1.71	29.9	2.88	1.19	6.42	3.13	3.81

Notes:

* Assuming a present isotopic composition of 99.2886% ^{238}U and 0.7114% ^{235}U.

† Model A based on Th/U = 4, K/U = 20,000.

‡ Model B based on Th/U = 4, K/U = 40,000.

flows are somewhat larger than their continental counterparts (Table 2.2). Expressed somewhat differently, the Earth's average surface heat flow corresponds roughly to one household light bulb (100 W) over an area of a tennis court. Approximately 60% of the heat loss of the Earth takes place through the ocean floor (Parsons 1982).

Since radioactive isotopes decay to stable daughter products, there must be a steadily decreasing heat production with time from radioactive decay. The rate at which heat is being transferred to the Earth's surface is therefore also decreasing with time, in turn slowing down the mantle convection system. Analysis of the abundance of the heat-producing radioisotopes and their stable daughter products suggests that heat production was twice the present value 3000 million years ago (Table 2.4), with ^{238}U and ^{232}Th taking over from ^{235}U and ^{40}K as the main heat producers because of the latters' relatively short half-lives.

2.2.2 One-dimensional heat conduction

Heat travels down temperature gradients (eqn 2.29). The lithosphere is subjected to changes in temperature with time, particularly associated with tectonic processes. Consequently, it is important to be able to develop a rule for the heat loss or gain of an element of lithosphere (Boxed text 2.2). Once such a rule is established, it can be modified to account for 3-D variations in heat flow.

BOXED TEXT 2.2: The 1D Heat Conduction Equation

Consider a volume element of vertical dimension δy with a cross-sectional area a (Fig. 2.13). A heat flow $Q(y)$ enters the element across its top surface. The element has an internal heat generation and is composed of material of density ρ and thermal capacity (specific heat) denoted by c. The specific heat is the amount of heat needed to raise the temperature of 1 kg of material by 1 °C (with units therefore of $Wkg^{-1}°C^{-1}$).

In a unit of time, the heat entering the volume element is $aQ(y)$ and the heat leaving the element is $aQ(y+\delta y)$.

$Q(y+\delta y)$ can be expanded in a Taylor series to give

$$Q(y+\delta y) = Q(y) + \delta y \frac{\partial Q}{\partial y} + \ldots \qquad (2.30)$$

Taking the first two terms only of the Taylor series, the net gain or loss of heat is therefore the difference between the heat fluxes through the top of the element and out of the bottom,

Continued

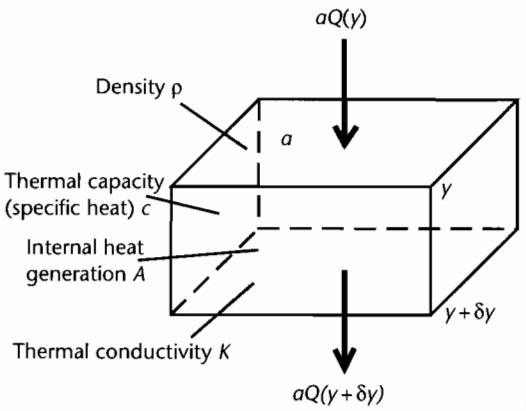

Fig. 2.13 Set-up and notation for conductive heat flow through a volume element of thickness δy, cross-sectional area a, density ρ, thermal capacity (specific heat) c, thermal conductivity K and internal heat generation A. Heat is conducted across the shaded faces only (it is perfectly 1-D).

$$aQ(y) - a\left\{Q(y) + \delta y \frac{\partial Q}{\partial y}\right\} = -a\delta y \frac{\partial Q}{\partial y} \tag{2.31}$$

Let the heat generated internally per unit volume and unit time be A. The heat generated in the element of volume $a\delta y$ is therefore $Aa\delta y$. The total heat gain or loss per unit time is then

$$Aa\delta y - a\delta y \frac{\partial Q}{\partial y} \tag{2.32}$$

If the material making up the volume element has specific heat c and density ρ and undergoes a small temperature change δT in a small time δt, the rate at which heat is gained or lost is

$$ca\delta y\rho \frac{\partial T}{\partial t} \tag{2.33}$$

Equating (2.32) and (2.33),

$$ca\delta y\rho \frac{\partial T}{\partial t} = Aa\delta y - a\delta y \frac{\partial Q}{\partial y} \tag{2.34}$$

which when simplified gives

$$c\rho \frac{\partial T}{\partial t} = A - \frac{\partial Q}{\partial y} \tag{2.35}$$

Substituting Fourier's law (equation 2.29) into (2.35),

$$\frac{\partial T}{\partial t} = \frac{A}{\rho c} + \frac{K}{\rho c}\frac{\partial^2 T}{\partial y^2} \tag{2.36}$$

which is the *1-D heat conduction equation*. We can define the *thermal diffusivity* as $\kappa = \dfrac{K}{\rho c}$. The thermal diffusivity expresses the ability of a material to gain or lose heat by conduction.

Certain boundary conditions can be applied to the 1-D heat conduction equation in order to simplify it for certain physical situations in the lithosphere:

(a) *Steady state solution* where there is no temperature change with time, i.e. $\partial T/\partial t = 0$,

$$\frac{\partial^2 T}{\partial t^2} = -\frac{A}{K} \tag{2.37}$$

(b) *no internal heat generation*, $A = 0$,

$$\frac{\partial T}{\partial t} = \frac{K}{\rho c}\frac{\partial^2 T}{\partial y^2} = \kappa \frac{\partial^2 T}{\partial y^2} \tag{2.38}$$

which is the *diffusion equation*. An equation of this form is used in a wide range of physical problems.

The volume element may be in motion relative to its surroundings and may therefore move through a region where the temperature varies with depth. If the volume element moves at a velocity u_y in the y direction (vertically in the lithosphere), its depth after time t will be $y + u_y t$, and the associated temperature change will be $u_y \partial T/\partial y$. The 1-D heat conduction equation therefore needs to be modified. The temperature change after a small time period δt is given by

$$\frac{\partial T}{\partial t} = \frac{K}{\rho c}\frac{\partial^2 T}{\partial y^2} + \frac{A}{\rho c} - u_y \frac{\partial T}{\partial y} \tag{2.39}$$

The temperature change of a piece of lithosphere is therefore seen to be made of three components: a basal heat flow term, an internal heat generation term; and an *advective term*. The advective term may be the movement towards the surface of a volume element of rock associated with the downcutting action of erosion. Or, with a different sign, it could be the velocity of deposition.

2.2.3 Geotherms

The variation of temperature with depth is called the *geotherm*. In the boxed text, we solve the 1-D conduction equation to derive the geotherm.

Taking reasonable parameter values, it is possible to calculate the temperature as a function of any depth in the crust ($0 \leq y \leq y_c$) using equation (2.43): thermal conductivity $K = 3\,\mathrm{W\,m^{-1}\,°C^{-1}}$, radiogenic heat generation A (in top 30 km) = $1.25\ 10^{-6}\,\mathrm{W\,m^{-3}}$, surface heat flow Q_0 (global average) = $70\,\mathrm{mW\,m^{-2}}$, and surface temperature $T_0 = 10\,°\mathrm{C}$. Extrapolating downwards, the temperatures calculated would cause the mantle to be fully molten below depths of about 100 km, since the geotherm would intersect the solidus for olivine, yet the mantle is able to propagate shear waves. Setting the radiogenic heat generation A to zero leaves the same problem. We conclude that the conduction geotherm in equations (2.43) and (2.46) does not apply to the bulk of the mantle where convection is taking place (§2.2.6).

Nevertheless, a conductive temperature profile appears to match continental geotherms where radiogenic heat production and conductive heat transport safely apply. The radiogenic heat production cannot be assumed to be uniform with depth. The abundances of the heat-producing radiogenic isotopes in a number of common rock types is given in Table 2.3. The heat gen-

BOXED TEXT 2.3: The Geotherm

In the case where there is no advective term and a constant heat flux, we have the equilibrium situation where $\partial T/\partial t = 0$. In this case

$$\frac{\partial^2 T}{\partial y^2} = -\frac{A}{K} \tag{2.40}$$

where A is the internal heat generation and $K/\rho c$ is the diffusivity κ. We can calculate the geotherm as long as we can provide some boundary conditions. Two boundary conditions are that the surface temperature is T_0 ($T = T_0$ at $y = 0$) and that the surface heat flow is $-Q_0$ at $y = 0$. Integrating (2.40) gives

$$\frac{\partial T}{\partial y} = -\frac{A}{K}y + c_1 \tag{2.41}$$

where c_1 is a constant of integration. Since $\partial T/\partial y = Q_0/K$ at $y = 0$, the constant c_1 must be equal to Q_0/K. Equation (2.41) after further integration therefore becomes

$$T = -\frac{A}{2K}y^2 + \frac{Q_0}{K}y + c_2 \tag{2.42}$$

Since $T = T_0$ at $y = 0$, c_2 must be equal to T_0. The temperature as a function of depth is therefore

$$T = T_0 + \frac{Q_0}{K}y - \frac{A}{2K}y^2 \tag{2.43}$$

There are instances where it would be more useful to calculate the geotherm with knowledge of the heat flow from the mantle rather than the surface heat flow (the reason for this is that the basal heat flow may be provided by a forward model of lithospheric stretching – Chapter 3). In this case, we have a pair of new boundary conditions. Firstly, $T = T_0$ at $y = 0$ and secondly, $Q = -Q_m$ at $y = y_c$, where y_c is the depth to the base of the crust, and Q_m is the basal heat flow from the mantle. Since $\partial T/\partial y = Q_m/K$ at $y = y_c$, the constant of integration c_1 in (2.41) is given by

$$c_1 = \frac{Q_m}{K} + \frac{A}{K}y_c \tag{2.44}$$

Substituting into (2.41) and integrating again,

$$T = -\frac{A}{2K}y^2 + \frac{(Q_m + Ay_c)}{K}y + c_2 \tag{2.45}$$

Since $T = T_0$ at $y = 0$, $c_2 = T_0$. Consequently, the geotherm in the region $0 < y < y_c$ is given by

$$T = T_0 + \frac{(Q_m + Ay_c)}{K}y - \frac{A}{2K}y^2 \tag{2.46}$$

Equations (2.43) and (2.46) give the geotherms where we have information of either the surface heat flow or the basal heat flow from the mantle. It would be possible to choose any depth in the lithosphere and apply the appropriate boundary conditions.

eration of the crust, being "granitic" in composition, far exceeds that of the mantle. Despite the fact that the very large volume of the mantle means that it contributes 80% of the Earth's radiogenic heat, it is the crustal contribution that is of importance in basin analysis and that determines the continental geotherm. The question is how we model the radiogenic heat generation in the continental crust. There are essentially two ways in which it can be treated (Boxed text 2.4):

- The lithosphere and sedimentary cover can be dealt with as "slabs" of constant internal heat generation;
- the internal heat generation can be modeled as decreasing exponentially with depth.

BOXED TEXT 2.4: Radiogenic Heat Production

Slab models for radiogenic heat generation

The simplest slab model is to have a single layer of radiogenic crust above a nonradiogenic mantle. The solution is given by equation (2.46) where y_c is the thickness of the crust. In a multilayer model, the same equations would be used but individual layers treated separately. For a two-layer model with a highly radiogenic upper crust, a less radiogenic lower crust and a nonradiogenic mantle (Fig. 2.14), we let

$A = A_1$ over the depth range $0 \le y < y_1$
$A = A_2$ over the depth range $y_1 \le y < y_2$
$Q = -Q_2$ at $y = y_2$
$T = T_0$ at $y = 0$

The solutions for temperature with depth are: for the depth range between $y = 0$ and $y = y_1$,

$$T = T_0 + \left\{\frac{Q_2}{K} + \frac{A_2(y_2 - y_1)}{K} + \frac{A_1 y_1}{K}\right\} y - \frac{A_1}{2K} y^2 \qquad (2.47)$$

and for the depth range between y_1 and y_2,

$$T = T_0 + \left\{\frac{Q_2}{K} + \frac{A_2 y_2}{K}\right\} y + \left\{\frac{A_1 - A_2}{2K}\right\} y_1^2 - \frac{A_2}{2K} y^2 \qquad (2.48)$$

Using this two-layer model, with $A_1 = 2.5 \times 10^{-6}\,\mathrm{W\,m^{-3}}$ in the upper crust ($y_1 = 20\,\mathrm{km}$) and $A_2 = 0.8 \times 10^{-6}\,\mathrm{W\,m^{-3}}$ in the lower crust ($y_2 = 35\,\mathrm{km}$) and the basal heat flow from the mantle $Q_2 = 30 \times 10^{-3}\,\mathrm{W\,m^{-2}}$, the geotherm is as sketched in Figure 2.14. The two-layer solution is compared to a one-layer crustal model with $A = 1.25 \times 10^{-6}\,\mathrm{W\,m^{-2}}$.

Exponential distribution of radiogenic heat generation

In an alternative model, the distribution of radiogenic heat production can be assumed to be exponential with depth (Fig. 2.14). If A_0 is the surface heat generation per unit volume, we can introduce a length scale for the exponential decrease in radiogenic heat production a_r such that the radiogenic heat generation per unit volume A at any depth is given by

$$A = A_0 \exp(-y/a_r) \qquad (2.49)$$

where a_r is between 4.5 km and 16 km for a range of continental heat flow provinces (Table 2.2, Sclater et al. 1980a).

One of the consequences of the exponential distribution of radiogenic heat is a linear relationship between the surface heat flow and the radiogenic heat content of surface rocks. This relationship has been demonstrated from many measurements in continental regions. The reason for this predicted linear relationship is as follows. The steady state solution for 1-D heat conduction (2.37) can be modified to account for an exponential radiogenic heat production to give

$$0 = K\frac{\partial^2 T}{\partial y^2} + A_0 \exp(-y/a_r) \qquad (2.50)$$

Integrating this once gives

$$c_1 = K\frac{\partial T}{\partial y} - A_0 a_r \exp(-y/a_r) \qquad (2.51)$$

Using Fourier's law (equation 2.29), (2.51) can be modified slightly,

$$c_1 = -Q - A_0 a_r \exp(-y/a_r) \qquad (2.52)$$

The constant of integration can be found by applying an appropriate boundary condition. Let us assume that as the depth becomes large ($y \to$ infinity), the heat flow is the basal heat flow from the mantle Q_m. Consequently, (2.51) shows that $c_1 = Q_m$. The heat flux at any depth is therefore

$$Q = -Q_m - A_0 a_r \exp(-y/a_r) \qquad (2.53)$$

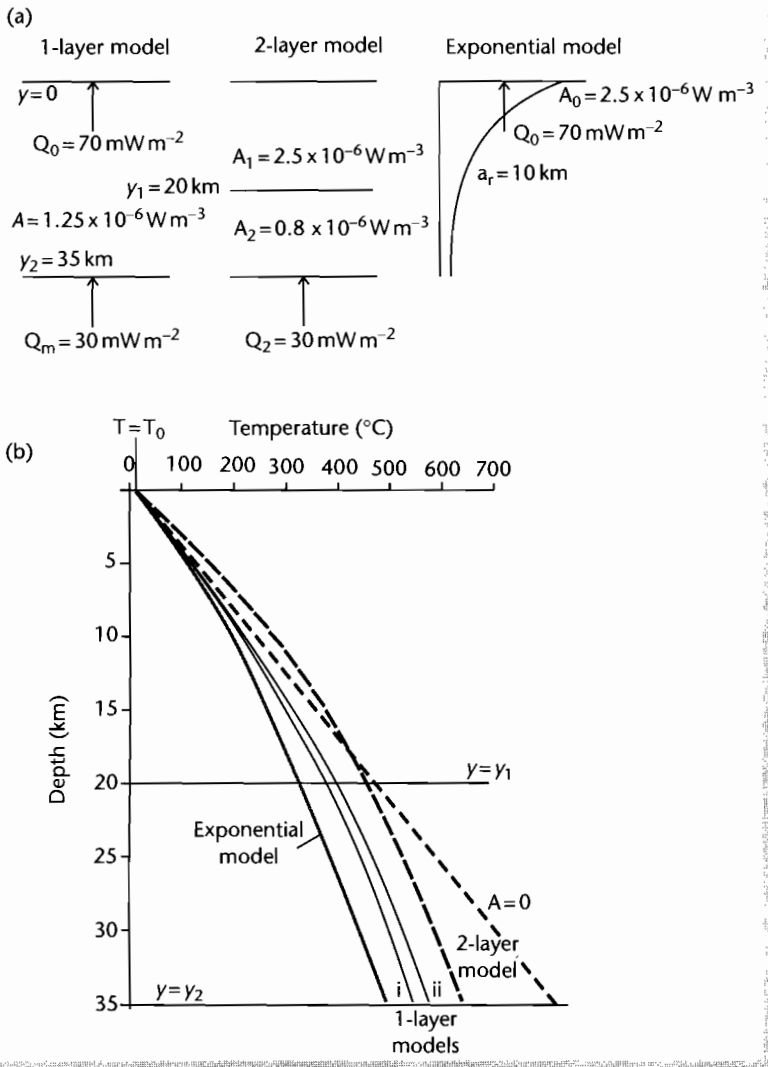

Fig. 2.14 Geotherms for the continental crust. (a) Model set-up; one-layer model with a constant internal heat generation for a 35 km-thick crust, with (i) a surface heat flow of 70 mW m^{-2}, and (ii) a basal heat flow of 30 mW m^{-2}; a two-layer model with a highly radiogenic 20 km-thick upper crust and a weakly radiogenic 15 km-thick lower crust; and a model with an exponentially decreasing radiogenic heat production with depth; (b) Resultant geotherms, with a linear geotherm for zero radiogenic heat production ($A = 0$) and surface heat flow of 70 mW m^{-2} shown for comparison.

or in terms of the surface heat flow, where $Q_0 = -Q$ at $y = 0$, is

$$Q_0 = Q_m + A_0 a_r \qquad (2.54)$$

showing that there is a linear relationship between the surface heat flow and the radiogenic heat production of surface rocks, with an intercept equal to the mantle heat flow and a slope of a_r. The example shown in

Continued

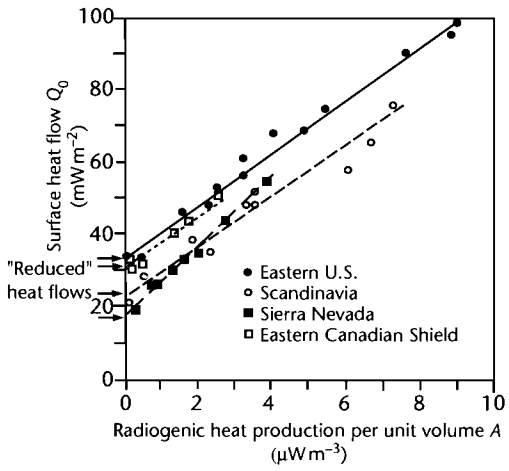

Fig. 2.15 The dependence of the surface heat flow Q_0 on the internal radiogenic heat production rate A in a number of geological provinces. The intercept on the y-axis gives the so-called "reduced" heat flow (20–30 mW m^{-2}). Derived from Roy et al. (1968), Turcotte and Schubert (2002). Reproduced courtesy of Cambridge University Press.

Figure 2.15 from granite plutons in eastern North America (Roy et al. 1968) gives a mantle heat flow, or *reduced heat flow*, Q_m of 30 mW m^{-2} and a length scale a_r of 7.5 km.

A further integration of (2.52) gives the temperature profiles at any depth. Using the boundary condition $T = T_0$ at $y = 0$,

$$T = T_0 + \frac{Q_m}{K} y + \frac{A_0 a_r^2}{K} \{1 - \exp(-y/a_r)\} \qquad (2.55)$$

or in terms of the surface heat flow, by integrating equation (2.53)

$$T = T_0 + \frac{Q_m}{K} y + \frac{(Q_0 - Q_m) a_r}{K} \{1 - \exp(-y/a_r)\} \qquad (2.56)$$

A typical geotherm with $A_0 = 2.5 \times 10^{-6}$ W m^{-3}, $Q_0 = 70$ mW m^{-3}, $K = 3$ W m^{-1} °C^{-1}, $T_0 = 10$ °C, and $a_r = 10$ km, is shown in Figure 2.14.

In some cases, it is possible that heat is conducted in more than one direction, an application common in regions of large lateral variations in surface temperatures. Such lateral variations might be due to topographic effects or to sea–land boundaries. The problem also arises where the lithosphere is stretched over a relatively narrow zone, as is common in strike–slip basins (Chapter 6), so that there is both upward and lateral loss of heat by conduction.

2.2.4 Time-dependent heat conduction: the case of cooling oceanic lithosphere

Many problems involve heat flows that vary in time. An obvious example is the heat flow associated with the intrusion of an igneous body, but the example used here is the cooling of the oceanic lithosphere and its consequent subsidence. This process finds great application in sedimentary basins experiencing a period of cooling following rifting (Chapter 3). Heat sources *within* the medium are unimportant in the time-dependent problem of the cooling of oceanic lithosphere (that is, $A = 0$).

At the crest of an ocean ridge, hot mantle rock injected in dykes and extruded as lava flows is suddenly subjected to a cold surface temperature and then continues to lose heat to the cold sea water as the seafloor spreads away from the ridge. The initial cooling can be treated as instantaneous. We know from the 1-D conduction equation (equation 2.38) where $A = 0$ that

$$\frac{\partial T}{\partial t} = \kappa \frac{\partial T^2}{\partial y^2} \qquad (2.57)$$

where $\kappa = K/\rho c$, which is the diffusion equation. We can define a characteristic time scale τ as the time necessary for a temperature change to propagate a distance l in a material with a thermal diffusivity κ (units of length^2 time^{-1}):

$$\tau = \frac{l^2}{\kappa} \qquad (2.58)$$

The length scale $l = \sqrt{\kappa\tau}$ gives the distance that a temperature change propagates in time τ. It is known as the *thermal diffusion distance.*

Let the surface plates move away from the ridge with a velocity u (Fig. 2.16). The cooling rocks form the oceanic lithosphere and the boundary between this relatively rigid upper layer and the easily deformed mantle is an isotherm

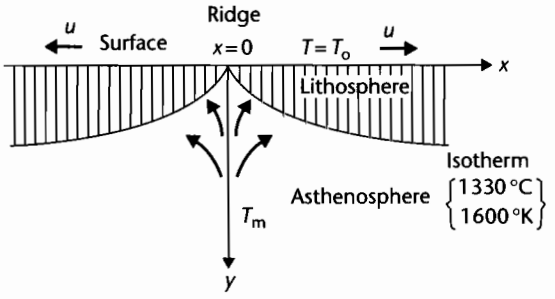

Fig. 2.16 Schematic diagram of the cooling oceanic lithosphere at a mid-ocean ridge. The oceanic plate moves away from the ridge at a velocity u. Its age is therefore determined by x/u, where x is the horizontal distance from the ridge crest.

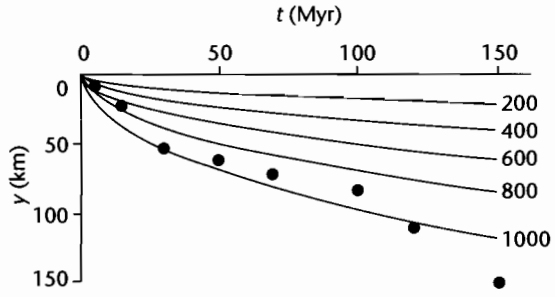

Fig. 2.17 Calculated isotherms for an oceanic lithosphere that is instantaneously cooled. The values of the isotherms are T–T$_s$ °K. The dots are the estimated thicknesses of the oceanic lithosphere in the Pacific, from Leeds et al. (1974).

with a value of about 1600 °K (1300 °C). The thickness of the oceanic lithosphere is clearly a function of its age, where age can be expressed in terms of x/u.

Using a time-dependent instantaneous cooling model, the isotherms below the seafloor as a function of age are parabolic (Fig. 2.17). The surface heat flow as a function of age is based on the 1-D conduction equation. It is compared with actual heat flow measurements of the ocean floor in Fig. 2.18 (Sclater et al. 1980a). The regions of poor correspondence between the predicted and observed surface heat flow measurements is probably due to temperature changes associated with hydrothermal circulation of sea water through the oceanic crust. These effects become less important with age as impermeable sediments blanket the ocean floor. For large ages (> 80 Myr) however, an additional heat source appears to

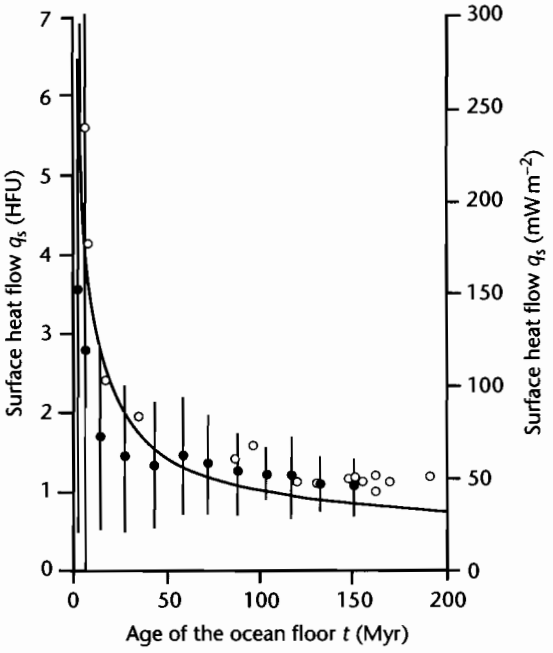

Fig. 2.18 Comparison of measured ocean heat flows (mean and standard deviation) and those predicted using the instantaneous cooling model, as a function of age. Black circles, data from Sclater et al. (1980a). Open circles, data from sediment covered regions of the Atlantic and Pacific Oceans, from Lister et al. (1990).

be recognizable, which may be mantle convection beneath the lithospheric plates.

The solution for the temperature as a function of age is given by

$$\theta = erfc\left(\frac{x}{2\sqrt{\kappa t}}\right) \tag{2.59}$$

where it can be seen that the denominator is in the form of a thermal diffusion distance, *erfc* is the complementary error function, x is the horizontal distance from the mid-ocean ridge crest, t is the age of the oceanic crust, and θ is a dimensionless temperature ratio given by

$$\theta = \frac{T - T_a}{T_s - T_a} \tag{2.60}$$

where T_a is the initial temperature (the asthenospheric temperature), T_s is the constant temperature of the space

into which the ocean lithosphere is emplaced (the sea water temperature), and T is the temperature at time t.

The cooled oceanic material forms a thermal boundary layer equivalent to the thickness of the new oceanic lithosphere. It is a largely arbitrary choice of the definition of the boundary layer, but if we define it as the thickness to where $\theta = 0.1$, it is found that the thermal boundary layer is 2.32 times the thermal diffusion distance $\sqrt{\kappa t}$ or $\sqrt{(\kappa x/u)}$. The thickness of the oceanic lithosphere at an age of 50 Myr is therefore approximately 92 km taking $\kappa = 10^{-6}\,m^2 s^{-1}$. The oceanic lithosphere should increase parabolically in thickness with age, and therefore also with distance from the ridge crest.

As it moves away from the ridge crest, the oceanic lithosphere cools and contracts. This increases the density of the oceanic lithosphere and causes a higher lithostatic stress on the underlying mantle. An isostatic balance (§2.1.1) shows that the seafloor must subside. Any column through the oceanic lithosphere can be balanced isostatically to give the depth of the ocean floor as a function of distance from the ridge crest, or age of the oceanic crust (Fig. 2.19). The mass per unit area in a column of any age is made up of two components: the contribution of the rock column and that of the water column. At the ridge crest, however, there is just the effect of the overlying column of mantle, $w + y_L$ thick.

The observed heat flows in the oceans, such as the Atlantic and Pacific Oceans (Parsons and Sclater 1977), and the observed bathymetry, are in general agreement with a model of instantaneous cooling of new oceanic material and its loss of heat through time by conduction, resulting in subsidence (Fig. 2.20). The general form of the relationship between the bathymetry of the ocean floor and its thermal age for oceanic lithosphere less than 70 Myr old is

$$h = h_{ridgecrest} + Ct^{1/2} \tag{2.61}$$

where h is the depth of the ocean floor, $h_{ridgecrest}$ is commonly in the region of 2.5 km, t is the age of the oceanic lithosphere, and C is a coefficient approximately equal to 0.35. This is commonly termed a *root age relationship*. If $h_{ridgecrest} = 2.5$ km, and $C = 0.35$, the ocean depth h at $t = 20$ Myr is 4 km, and at $t = 50$ Myr is 5 km. The heat flow Q ($10^{-3}\,W\,m^{-2}$) for oceanic lithosphere younger than 120 Myr old follows a similar but *inverse root age* relationship:

$$Q = 473t^{-1/2} \tag{2.62}$$

Since the age of the oceanic lithosphere is directly related to its distance from the ridge crest by the spreading rate, the oceanic bathymetry increases gradually away from the site of spreading and the heat flow decreases gradually away from the site of spreading. The isostatic balance and the root age relationship are affected by the presence of marine sediments overlying the ocean crust. However, in the deep sea the cover of pelagic sediments is generally only a relatively thin veneer.

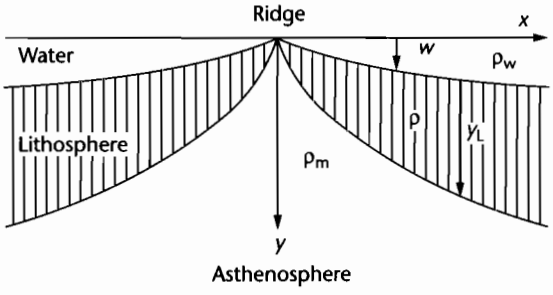

Fig. 2.19 The principle of isostasy requires the ocean to deepen with age to offset the effects of thermal contraction of the oceanic lithosphere. The water depth below the level of the ridge crest is w, the thickness of the oceanic lithosphere is y_L and ρ_m, ρ_w, and ρ are the mantle, water, and lithospheric densities respectively.

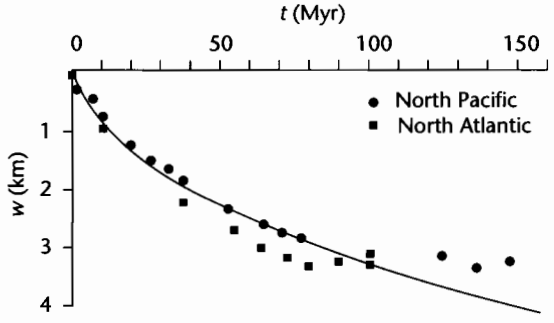

Fig. 2.20 Depth of the ocean floor below the level of the ridge crest as a function of age of the seafloor (Parsons and Sclater 1977). The solid line shows the theoretical result for an instantaneous cooling model. It is in close agreement with observations from the North Pacific and North Atlantic. The oceanic bathymetry follows a root–age relationship.

2.2.5 Thermal expansion

The laws of thermodynamics say that the equilibrium state of a material is governed by any two state variables, examples being temperature T, pressure p, and density ρ.

If a material is subjected to a change in pressure with temperature held constant, its volume will change. The change in volume for a certain pressure change is determined by the *isothermal compressibility* β. The fractional change in specific volume ($v = 1/\rho$) (volume per unit mass) with pressure at constant temperature can be written

$$\beta = -\frac{1}{v}\left(\frac{\partial v}{\partial p}\right)_T = \rho\left(\frac{\partial v}{\partial p}\right)_T \tag{2.63}$$

If pressure is held constant and temperature is varied, there will also be a fractional change in specific volume. This time, the factor determining the volume change is known as the *volumetric coefficient of thermal expansion* α_v. The fractional change in specific volume with temperature at constant pressure can be written

$$\alpha_v = \frac{1}{v}\left(\frac{\partial v}{\partial T}\right)_P = \rho\left(\frac{\partial v}{\partial T}\right)_P \tag{2.64}$$

β and α_v are material properties that can be found from laboratory experiments, typical values for rock being $\beta = 10^{-11}\,\mathrm{Pa}^{-1}$ and $\alpha_v = 3 \times 10^{-5}\,^{\circ}\mathrm{K}^{-1}$. β and α_v can be related since any changes in specific volume are due to changes in both temperature and pressure. The total volume change is therefore the net change resulting from the pressure change ($-V\beta \mathrm{d}p$, where $\mathrm{d}p$ is the pressure change) and from the temperature change ($+V\alpha_v\,\mathrm{d}T$, where $\mathrm{d}T$ is the temperature change). Note the opposing signs. With the material properties β and α_v given above, a 100 K change in temperature will result in a pressure change of 3 kbar (300 MPa), implying large changes in pressure and therefore stress for moderately small temperature changes. This is an important result since sedimentary basins are commonly associated with thermal disturbances (see especially Chapter 3).

Let a material have a reference density ρ^* corresponding to the temperature T^*. The difference in density between the material at its reference temperature and the same material at its new temperature T is related to the temperature difference $\mathrm{d}T = T - T^*$ through the volumetric coefficient of thermal expansion:

$$\rho - \rho^* = -\rho^*\alpha_v(T - T^*) \tag{2.65}$$

which by slight rearrangement gives

$$\rho = \rho^*(1 - \alpha_v \mathrm{d}T) \tag{2.66}$$

We could for example set the reference temperature to be 0 °C, or it could be the oceanic crust at the reference temperature of the asthenosphere, as in the mid-ocean ridge spreading problem. Since α_v for rock is typically $3 \times 10^{-5}\,\mathrm{K}^{-1}$, a 100 K temperature change produces a 0.3% change in density. Halite on the other hand has a α_v of $13 \times 10^{-5}\,\mathrm{K}^{-1}$, so a 100 K temperature change causes a 1.3% change in density. Temperature changes therefore cause large changes in stress but relatively small changes in density.

The thermal-associated strains for an isotropic body are the same along each of the principal axes of strain, and it is known from the discussion above that the magnitude of the volume change is proportional to the temperature change by α_v (i.e., $\varepsilon_1 = \varepsilon_2 = \varepsilon_3 = -1/3\ \alpha_v \mathrm{d}T$). The minus sign implies an extensional strain by convention. However, it is convenient to consider strains as linear quantities, so it is necessary to introduce a new coefficient, the *linear coefficient of thermal expansion* α_l. This coefficient relates the thermally induced strains to the temperature change, where $\alpha_l = 1/3\ \alpha_v$ (i.e., $\varepsilon_1 = \varepsilon_2 = \varepsilon_3 = -\alpha_l \mathrm{d}T$ for an isotropic material). The linear coefficient of thermal expansion is therefore the change in strain per degree of change in temperature.

2.2.6 Thermal structure of the upper mantle: effects of convection

Whereas the thermal structure of the lithosphere is dominated by conduction, that of the mantle is determined primarily by convection. The lithosphere simply serves as a thermal boundary layer exhibiting high temperature gradients. Extensional basins, other than thin-skinned varieties, involve upwelling of convecting asthenosphere. We therefore present here a very brief account of the thermal structure of the upper mantle. Further information is given in Chapter 5.

In the interior of a vigorously convecting fluid, the mean temperature increases with depth along an *adiabat*, so that the *adiabatic temperature gradient* is the rate of temperature increase with depth caused by compression due to the overlying rock column. The compressional pressure forces cause a decrease in volume and therefore an

increase in density. The relationship between the density and pressure changes is given by the *adiabatic compressibility*, β_a. For a solid it is somewhat smaller than the isothermal compressibility β given in equations (2.14) and (2.63). The purely adiabatic expressions for the variations of density and pressure with depth in the mantle do not perfectly match observed values based on seismic velocities (Fig. 2.21). In particular, at about 400 km there is a density discontinuity thought to be due to the phase change of olivine. This change to the denser spinel structure is thought to occur at a pressure of 14 GPa or 140 kbar and a temperature of 1900 °K. The phase change is *exothermic*, causing heating of the rock by *c.* 160 °K. The olivine–spinel phase change probably enhances mantle convection rather than blocks it. There is a second discontinuity in density at about 680 km, but its origin is less clear – it is probably also due to a change in mantle composition to perovskite. There is a sharp change in **P** wave velocity at about 680 km.

If a substance is *incompressible*, its volume is incapable of contracting, so adiabatic heating cannot take place. Rocks, however, are sufficiently compressible that adiabatic temperature changes are extremely important under the large pressure changes in the mantle. The adiabatic geotherms in the upper mantle underlying oceanic and continental lithospheres are different since continental lithosphere has its own near-surface radioactive heat source. Below this near-surface layer the heat flow is assumed to be constant at about 30 mW m^{-2} (Fig. 2.22). There is an important feature underlying Fig. 2.22, namely that the continental lithosphere as a thermal entity extends to about 200 km below the surface (§1.2).

It has been suggested that mantle convection takes place across the 400 km temperature and density discontinuity, essentially because subducted lithosphere appears to descend smoothly through this discontinuity. The influence of the 680 km discontinuity is less certain. Deep focus earthquakes provide evidence that convection takes place to 680 km but there is no direct evidence below this depth. Two contrasting models of mantle convection are therefore possible, one involving convection of the whole mantle, and one involving two major convecting systems, one shallow system linked to plate tectonics and a deeper system extending to the outer margin of the core. Smaller convecting cells may be superimposed on these major systems.

The *onset of convection* is a threshold above which the influence of the temperature difference in the fluid layer exceeds that of the viscous resistance to flow. The temperature difference is conventionally evaluated as the

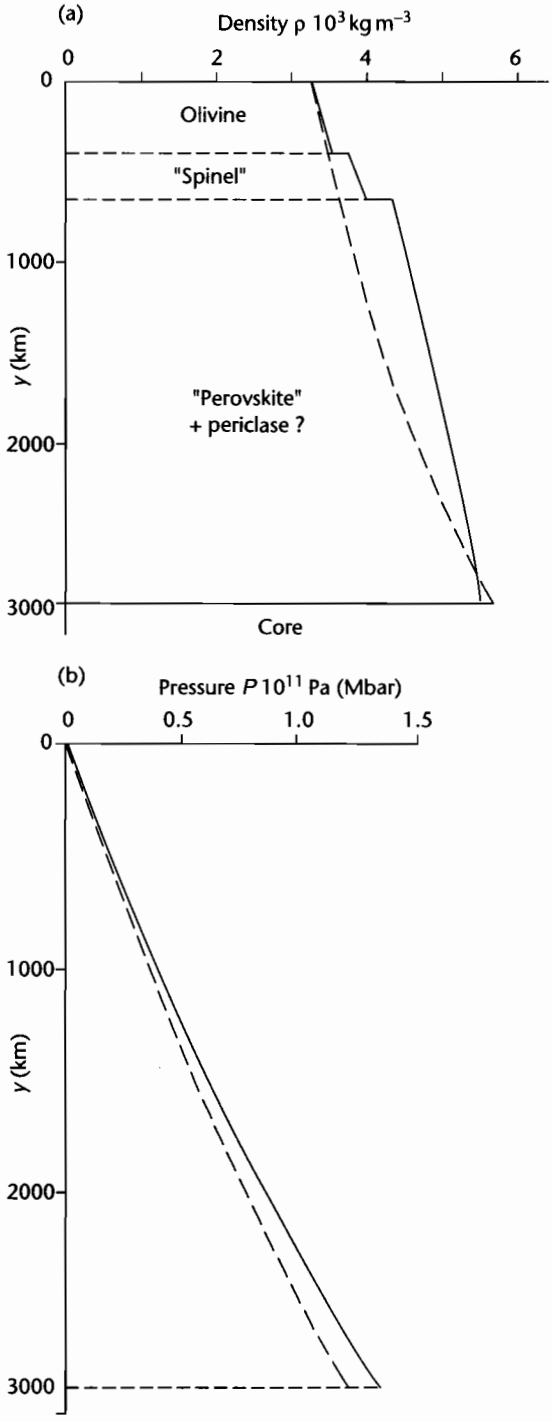

Fig. 2.21 Depth profiles of density (a) and pressure (b) in the mantle. Observed values are shown in solid lines; values calculated for a purely adiabatic behavior are shown in dashed lines.

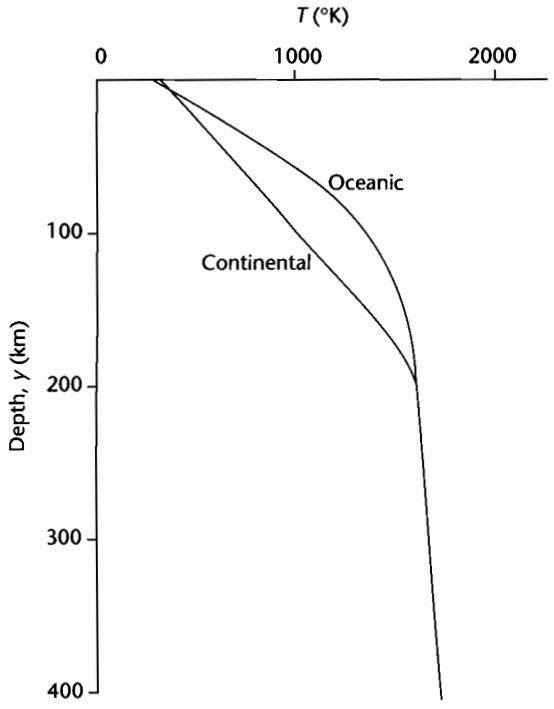

Fig. 2.22 Representative oceanic and continental geotherms in the shallow upper mantle.

fluid temperature at a point as a departure from the temperature expected from a purely conduction profile. The onset of convection is marked by a critical dimensionless number known as the *Rayleigh number*, *Ra*. A Rayleigh number analysis of Earth's mantle suggests that it must be fully convecting (more details in §5.1.2).

There are also large *lateral* temperature heterogeneities in the mantle, such as where cold lithospheric plates are subducted at ocean trenches. These lateral temperature variations are extremely important in providing a driving force for mantle convection. In the case of a descending cold lithospheric slab, the low temperatures of the plate cause it to be more dense than surrounding mantle, providing a gravitational body force tending to make the plate sink. A second factor is the distortion of the olivine–spinel phase change since the pressure at which this phase change occurs depends on temperature. The upward displacement of the phase change in the cold descending plate provides an additional downward-acting body force, helping to drive further plate motion. These two processes are often referred to as *trench pull*. If trench pull forces are transmitted to the oceanic plate as a tensional stress in an elastic lithosphere with a thickness of 50 km, the resultant tensional stress would be as high as 1 GPa.

The forces arising through the elevation of the ridge crest relative to the ocean floor constitute a *ridge push* force, also helping to drive plate motion. Ridge push is an order of magnitude smaller than trench pull, but since the latter is countered by enormous frictional resistances, the two agents of net trench pull and ridge push may be comparable.

2.2.7 Mantle viscosity

One of the fundamental differences between fluids and solids is their response to an applied force. Fluids deform continuously under the action of an applied stress whereas solids acquire a finite strain. Stress can be directly related to strain in a solid, but in fluids applied stresses are related to *rates* of strain, or alternatively velocity gradients. In Newtonian fluids there is a direct proportionality between applied stress and velocity gradient, the coefficient of proportionality being known as *viscosity*. (In non-Newtonian fluids there may be complex relationships between applied stresses and resultant deformations.) The problem of direct relevance to sedimentary basin analysis is the viscous flow in the mantle. One way in which the viscosity of the mantle can be estimated is by studying its response to loading and unloading (see also Chapter 4).

Mountain building is an example where the crust–mantle boundary is depressed through loading, but orogeny is so slow a process that the mantle manages to constantly maintain hydrostatic equilibrium with the changing near-surface events. In contrast, the growth and melting of ice sheets is very rapid, so that the mantle adjusts itself dynamically to the changing surface load: the way in which it does so provides important information on mantle viscosity. The displacement of the surface leads to horizontal pressure gradients in the mantle which in turn cause flow. In the case of positive loading, fluid is driven away from the higher pressures under the load, the reverse being true on unloading. The surface displacement decreases exponentially with time as fluid flows from regions of elevated topography to regions of depressed topography. If w is the displacement at any time and w_m is the initial displacement of the surface, the

form of the exponential decrease in surface topography with time is

$$w = w_m \exp(-t/\tau_r) \tag{2.67}$$

where τ_r is the characteristic time for the exponential relaxation of the initial displacement. It is given by

$$\tau_r = (4\pi\mu)/(\rho g\lambda) \tag{2.68}$$

where μ is the viscosity and λ is the wavelength of the initial displacement. Mantle viscosity can therefore be estimated from postglacial rebound if this relaxation time can be found.

Elevated beach terraces that have been dated (usually by ^{14}C) provide the basis for quantitative estimates of the rate of postglacial rebound. Large lateral variations in rebound rates are found. For example, the northern shore of Lake Superior is rising relative to the south by as much as 0.46 m per century following the Canadian glaciation (Kite 1972). The Baltic region of Scandinavia is also renowned for its raised beaches. After correcting the uplift of Swedish beaches for absolute (eustatic) changes in sea level, a relaxation time of $\tau_r = 4400$ years is found. Assuming a reasonable wavelength of the displacement for the Scandinavian glaciation to be $\lambda = 3000$ km, the viscosity of the mantle is estimated to be $\mu = 1.1 \times 10^{21}$ Pa s (10^{22} poises) (Fig. 2.23). However, this approximate analytical solution does not take into account: (i) the flexural rigidity of the elastic lithosphere, and (ii) the depth-dependency of mantle viscosity. A summary of the possible distribution of viscosity in the mantle (Cathles 1975) is given in Table 2.5.

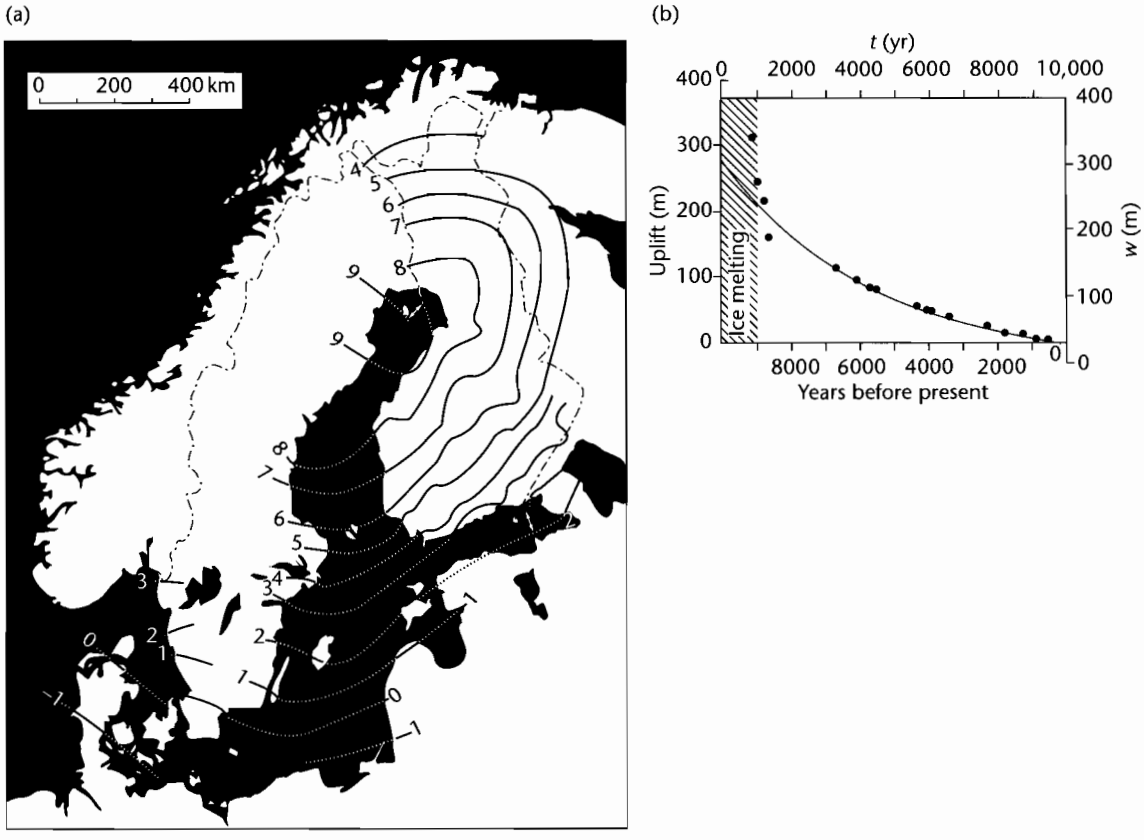

Fig. 2.23 Postglacial rebound of Scandinavia. (a) Present day rates of uplift occurring in Scandinavia (after Flint 1971), reproduced courtesy of John Wiley & Sons; (b) Postglacial uplift of the mouth of the Angerman River, Sweden over the last 10 000 years compared with the exponential relation in equation (2.67) with a constant viscosity of 10^{21} Pa s (after Turcotte and Schubert 2002).

Table 2.5 Viscosity of the mantle from glacial rebound studies (Cathles 1975).

		Dynamic or absolute viscosity	
Region	**Depth (km)**	**(Pa s)**	**(Poise)**
Lithosphere	0–100	Elastic	
Asthenosphere	100–175	4×10^{19}	4×10^{20}
Mesosphere	175–2848	10^{21}	10^{22}

2.3 GRAVITY AND ISOSTASY

2.3.1 Gravity anomalies and the geoid

The reference gravitational field of the Earth is that of an *oblate spheroid*. Topographic effects and density differences within the solid Earth cause local variations in the gravity measured at the Earth's surface. These are known as *gravity anomalies*. Topography causes a positive anomaly because of the mass of rock elevated above the oblate spheroid. However, the fact that the continents do not have positive gravity anomalies suggests that the influence of topography may be compensated by other effects. High topography, for example, is commonly associated with a deep crustal root. Crustal roots cause negative gravity anomalies because of the presence of a density deficit at depth. At large wavelengths, if the topography and root are perfectly balanced in hydrostatic equilibrium, there is a zero surface gravity anomaly.

From Newton's law of gravitation we know that the gravitational acceleration of a point outside a spherical mass such as the Earth is directed radially inwards and is given by

$$g_m = \frac{GM}{r^2} \tag{2.69}$$

where G is the universal gravitational constant (equal to $6.673 \times 10^{-11}\,\mathrm{m^3\,kg^{-1}\,s^{-2}}$), M is the mass of the Earth (73.483×10^{21} kg) and r is the radial distance from the center of mass to the point of interest.

A mass within or outside the Earth has a *gravitational potential energy*, which is the work done in bringing the mass from infinity to its position in the gravitational field. The gravitational potential energy per unit mass is the *gravitational potential*. Gravitational equipotential surfaces are where the gravitational potential is everywhere equal. In the absence of barometric and dynamic effects in the ocean–atmosphere system, the sea surface is a gravitational equipotential surface. This reference equipotential surface is known as the *geoid*. Over the ocean the geoid is the mean sea level. Over the continents the geoid is more difficult to recognize, but would be the water elevation in imaginary canals cut through the continents (Fowler 1990, p. 165). The geoid is close to being a spherical surface, with a certain eccentricity (flattening). Small departures from the reference geoid are called *geoid anomalies*. The largest geoid anomaly is about 100 m – small compared with the 21 km difference between the polar and equatorial radii of the reference geoid. A map of geoid anomalies (Fig. 2.24) (Lemoine et al. 1998) shows that some of them can be attributed to density variations related to plate tectonics. For example, geoid highs occur over some subduction zones where dense, cold lithosphere penetrates hot upper mantle (Chile–Peru).

Surface gravity anomalies are caused by mass anomalies on the surface of the Earth or within the solid Earth. From equation (2.69) it can be seen that the gravitational attraction scales on the mass and the square of the distance. Consequently, a mass anomaly of a given magnitude causes a much greater surface gravity anomaly if it is buried at a shallow depth in the upper crust than if it occurs in the upper mantle. Surface gravity anomalies are commonly produced by the gravitational effects of the mass represented by topography. The surface gravity anomaly at a point is given by the *Bouguer gravity formula*

$$g_y = 2\pi G \int_0^h \rho(y)\,\mathrm{d}y \tag{2.70}$$

where g_y is the surface gravity anomaly at a point, G is the universal gravitational constant ($6.673 \times 10^{-11}\,\mathrm{m^3\,kg^{-1}\,s^{-2}}$) and the integral gives the mass excess or deficiency below that point, h is the height of the body of anomalous density and y is the vertical coordinate. For the case of topography, h is the height of the topography and $\rho(y)$ is the crustal density ρ_c. The Bouguer gravity formula therefore becomes

$$\Delta g = 2\pi\rho_c G h \tag{2.71}$$

where Δg is the gravity anomaly due to topography. From equation (2.71) it can be seen that if crustal density is $2750\,\mathrm{kg\,m^{-3}}$, a 5 km high topography produces a gravity anomaly of $5.6\,\mathrm{mm\,s^{-2}}$. A more convenient unit of measurement is the *milligal*, equal to $10^{-5}\,\mathrm{m\,s^{-2}}$. Another unit is the *gravity unit*, which is $10^{-6}\,\mathrm{m\,s^{-2}}$. The 5 km high topography therefore produces a gravity anomaly of 560 milligal. Alternatively, if a 5 km high volcanic seamount

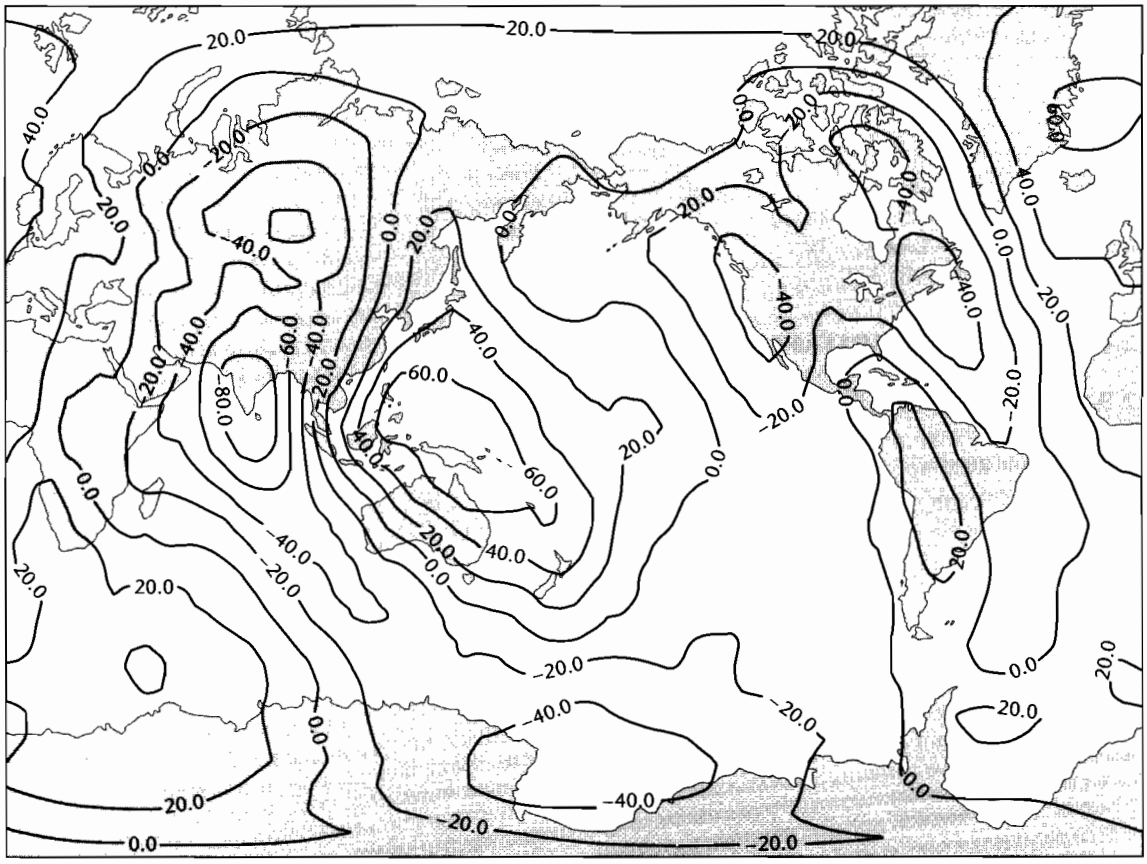

Fig. 2.24 The geoid height above the reference ellipsoid (Lemoine et al. 1998). Reproduced courtesy of NASA.

of density $2900\,kg\,m^{-3}$ replaced sea water with density $1000\,kg\,m^{-3}$, the gravity anomaly would be $4.0\,mm\,s^{-2}$, or 400 milligal.

A number of corrections are applied to surface gravity measurements in order to obtain the surface gravity anomaly.

- The reference gravity field is firstly subtracted, which contains a *latitude correction*;
- the variation of gravity with height is then subtracted (*elevation or free-air correction*). This correction is 3.07 mm s^{-2} for an elevation of 1 km. The resulting anomaly after this second step is called a free-air gravity anomaly;
- the gravitational attraction of local (short-wavelength) topography is removed with the Bouguer gravity formula to give the *Bouguer gravity anomaly*. If the topography is particularly steep, a *terrain correction* is also applied.

The Bouguer gravity formula does not account for any compensating changes in mass at depth, such as a light root beneath a mountain chain. Therefore Bouguer anomalies over mountain ranges are strongly negative. Since the mass of the topography is compensated over a long wavelength by the presence of a light root, so that there is no net mass difference beneath the observer, the free-air anomaly over mountain belts should be roughly zero (see also §2.3.3 and Fig. 2.28).

2.3.2 Models of compensation

The simplest way in which the mass excess of topography can be compensated is by the development of a deep, low-density root (Fig. 2.1c). Compensation for topography by changes in the thickness of the underlying crust

(Fig. 2.25a) is termed *Airy compensation* or *Airy isostasy*. From the principle of hydrostatic equilibrium, we can balance the pressure at the base of a lithospheric column through the mountain belt with that at the base of a column through adjacent lowlands at sea level. This gives

$$b = \frac{\rho_c h}{\rho_m - \rho_c} \tag{2.72}$$

where b is the thickness of the root, h is the height of the mountain belt, and ρ_m and ρ_c are the mantle and crustal densities respectively. If ρ_c is 2800 kg m^{-3} and ρ_m is 3300 kg m^{-3}, a 5-km high mountain would require a root thickness of $b = 28$ km. If the topography is negative (h is negative), representing a marine basin, the balancing of lithospheric columns gives

$$b = \left(\frac{\rho_c - \rho_w}{\rho_m - \rho_c}\right) h \tag{2.73}$$

where ρ_w is the density of ocean water. Using the same density terms as above and ρ_w is 1000 kg m^{-3}, the "anti-root" beneath a marine basin of depth 1 km is 3.6 km. The crust must be thinned by 4.6 km under the marine basin compared to the coastal plain at sea level.

An alternative model for isostatic compensation invokes lateral density variations over a depth range to a depth of compensation W (Fig. 2.25b). This model is known as *Pratt compensation*. The variable density ρ_p of lithospheric columns elevated at h is given by

$$\rho_p = \rho_0 \left(\frac{W}{W + h}\right) \tag{2.74}$$

where ρ_0 is the reference density for a lithospheric column with its surface at sea level. For a mountain elevated at 5 km, and taking the depth of compensation W as 125 km, requires a reduction of density beneath the mountain to 96% of ρ_0. Although this is a relatively small density change, there seems little evidence to support its existence. For negative topography (h is negative), the variable density of lithospheric columns below sea level is given by

$$\rho_p = \frac{\rho_0 W + \rho_w h}{W + h} \tag{2.75}$$

The Pratt model of compensation should be suitable where there are lateral density variations at depth, as for instance caused by the presence of plume-related swells. The Hawaiian swell (Crough 1978) reaches water depths of 4 km at its crest (seamounts of course reach sea level). The swell is situated in an abyssal plain at −6 km. What density change is required to elevate the Hawaiian swell 2 km above the adjacent abyssal plain? Putting $\rho_0 =$ 3300 kg m^{-3} under the abyssal plain and $W = 150$ km, the density of the column under the swell crest is 3281 kg m^{-3}, representing a density reduction of 0.6% of the reference density for oceanic rock under the abyssal plain. Since the volumetric coefficient of thermal expansion of oceanic lithosphere is *c.* 3×10^{-5} K^{-1}, this is equivalent to an average heating of the section down to 120 km by *c.* 190 °C. This is a reasonable result since plumes

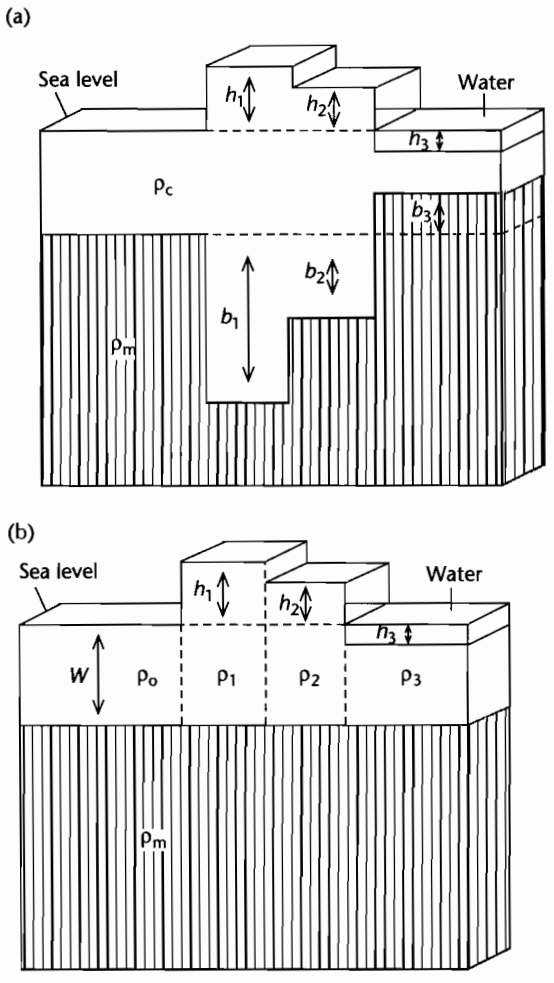

Fig. 2.25 Airy (a) and Pratt (b) models of isostatic compensation. Notation explained in text.

are known to cause excess temperatures of 100–200 °C above the normal asthenospheric temperature.

Whereas the Airy model is a good approximation of isostatic compensation in areas of active tectonics, such as mountain building and sedimentary basin formation, the Pratt model is a good predictor where lateral density variations are caused by temperature changes. Both models make use of the idea of hydrostatic equilibrium, envisaging notional lithospheric blocks able to float freely on a fluid asthenosphere. This in turn implies that the lithosphere is very weak and responds locally to any loads. An alternative model involving a stronger lithosphere able to store elastic stresses for considerable periods of time makes use of the concept of flexural rigidity developed in §2.1.4. In *flexural isostasy*, loads are compensated regionally by a lithosphere approximating an elastic sheet overlying a fluid substratum.

2.3.3 Flexural isostasy

The problem of flexural isostasy can be tackled by considering the way the lithosphere supports periodic topography. This simplified analysis can then be extended to the case of a sedimentary basin of a certain wavelength and amplitude.

BOXED TEXT 2.5: Flexural Isostasy

We start by assuming that topography is represented by a sinusoidal periodic load (Fig. 2.26) given by:

$$h = h_0 \sin(2\pi x/\lambda) \qquad (2.76)$$

where h_0 is the maximum height of the topography and λ is its wavelength. The load actually exerted on the lithosphere has the form of pressure or stress of the form ρgh, so the distribution of pressure under this periodic topography is

$$q_a(x) = \rho_s g h_0 \sin(2\pi x/\lambda) \qquad (2.77)$$

where ρ_s is the density of sedimentary rocks constituting the load. Assuming no horizontal applied forces (i.e., $P = 0$), and returning to the general flexural equation (eqn 2.28), we have

$$D\frac{d^4w}{dx^4} + (\rho_m - \rho_s)gw = \rho_s g h_0 \sin(2\pi x/\lambda) \qquad (2.78)$$

Since the load is sinusoidal and periodic, the deflection of the lithosphere will also be sinusoidal and periodic. The solution for the deflection w can therefore be assumed to be of the type

$$w = w_0 \sin(2\pi x/\lambda) \qquad (2.79)$$

where w_0 is the maximum deflection. Substituting (2.79) into (2.78) and rearranging, the amplitude of the deflection of the lithosphere is

$$w_0 = \frac{h_0}{\left\{D\frac{d^4w}{dx^4}\frac{1}{\rho_s g w} + \frac{\rho_m}{\rho_s} - 1\right\}} \qquad (2.80)$$

The fourth differential of w from (2.79) is $(2\pi/\lambda)^4 w$, so (2.80) simplifies to

$$w_0 = \frac{h_0}{\frac{\rho_m}{\rho_s} - 1 + \frac{D}{\rho_s g}\left(\frac{2\pi}{\lambda}\right)^4} \qquad (2.81)$$

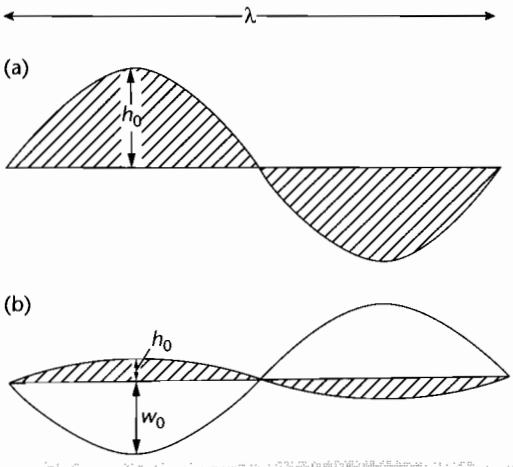

Fig. 2.26 Deflection of the lithosphere under a periodic (sinusoidal) load. In (a) the wavelength of the load is short and there is no deflection of the lithosphere. in (b) the wavelength of the load is long, leading to isostatic compensation of the load by a deflection of the lithosphere. w_0 is the maximum deflection, h_0 is the maximum elevation of the load (after Turcotte and Schubert 1982).

If the wavelength of the load is short, the deflection is very small compared to the maximum height of the load ($w_0 < h_0$). The lithosphere therefore appears to behave very rigidly to loads of this scale. If, however, the wavelength of the load is long, the deflection can be written

$$w = w_{0\infty} = \frac{\rho_s h_0}{(\rho_m - \rho_s)} \qquad (2.82)$$

which is the result obtained for a purely vertical isostatic balance (Airy isostasy) (§2.1). This means that for sufficiently long wavelengths, the lithosphere appears to have no rigidity and periodic loads should be in hydrostatic equilibrium. It is clearly desirable to be able to predict where we are in this range of complete to no compensation. The degree of compensation C of the load (Fig. 2.27) is the ratio of the actual deflection compared with the maximum (Airy) or hydrostatic deflection

$$C = \frac{w_0}{w_{0\infty}} \qquad (2.83)$$

Substituting (2.81) and (2.82) into (2.83)

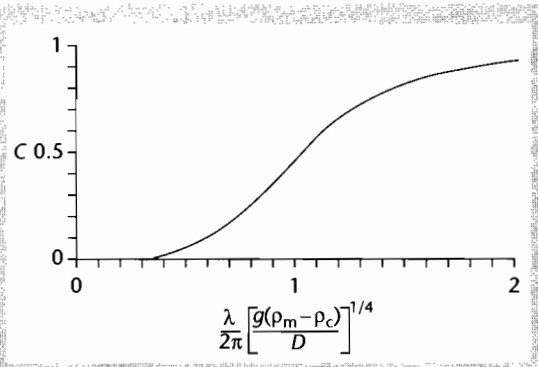

Fig. 2.27 Dependence of the degree of compensation C, on the nondimensional wavelength of periodic (sinusoidal) topography (after Turcotte and Schubert 1982). D is the flexural rigidity, λ is the wavelength of the load, ρ_m and ρ_c are the mantle and crustal densities respectively and g is the gravitational acceleration.

$$C = \frac{(\rho_m - \rho_s)}{\rho_m - \rho_s + \frac{D}{g}\left(\frac{2\pi}{\lambda}\right)^4} \qquad (2.84)$$

$(2\pi/\lambda)$ is sometimes termed the *wave number* (e.g., Watts 1988).

Gravity measurements can be used to test the state of isostasy in a region. Imagine a mountain elevated with respect to a coastal plain at sea level (Bott 1982) (Fig. 2.28). In the case of Airy isostasy, the Bouguer anomaly will be strongly negative over the mountain belt because there is a mass deficiency below sea level beneath the mountain belt. The Bouguer correction has removed the gravitational effect of the mountainous topography. However, the free-air anomaly should be weakly positive, but much smaller in magnitude than the Bouguer anomaly. This is because the gravity effect, measured at the surface, of the crustal rocks elevated above sea level in the mountain belt is stronger than the gravity effect of the more distant compensating root. When the structure is very wide compared to the compensation depth, the free-air anomaly reduces to zero.

If the imaginary mountain belt is only partially compensated, the Bouguer anomaly is reduced but remains negative and the free-air anomaly becomes more strongly positive. Where the mountains are completely uncompensated, that is, they rest on an infinitely rigid lithosphere, the Bouguer anomaly is zero, but the free-air anomaly is strongly positive.

The very common negative Bouguer anomalies associated with mountain belts suggests that they are compensated to some degree, depending on the flexural rigidity of the lithosphere. In present-day settings, the extent of this compensation can be estimated from the correlation of Bouguer gravity anomalies with topography as a function of its wavelength (Fig. 2.29) (Dorman and Lewis 1972). Topography with a wavelength of less than 100 km is not compensated, whereas topography with a wavelength of greater than 1000 km is fully compensated. The relationship between Bouguer gravity anomaly and topography as a function of its wavelength is called *admittance*. From Fig. 2.29, it can be seen that different curves are predicted for different flexural rigidities. The best fit for data from western United States is for a flexural rigidity of just 10^{21} Nm (equivalent elastic thickness of *c.* 6 km).

A related spectral technique is the conversion of both the topography and Bouguer gravity field by a fast

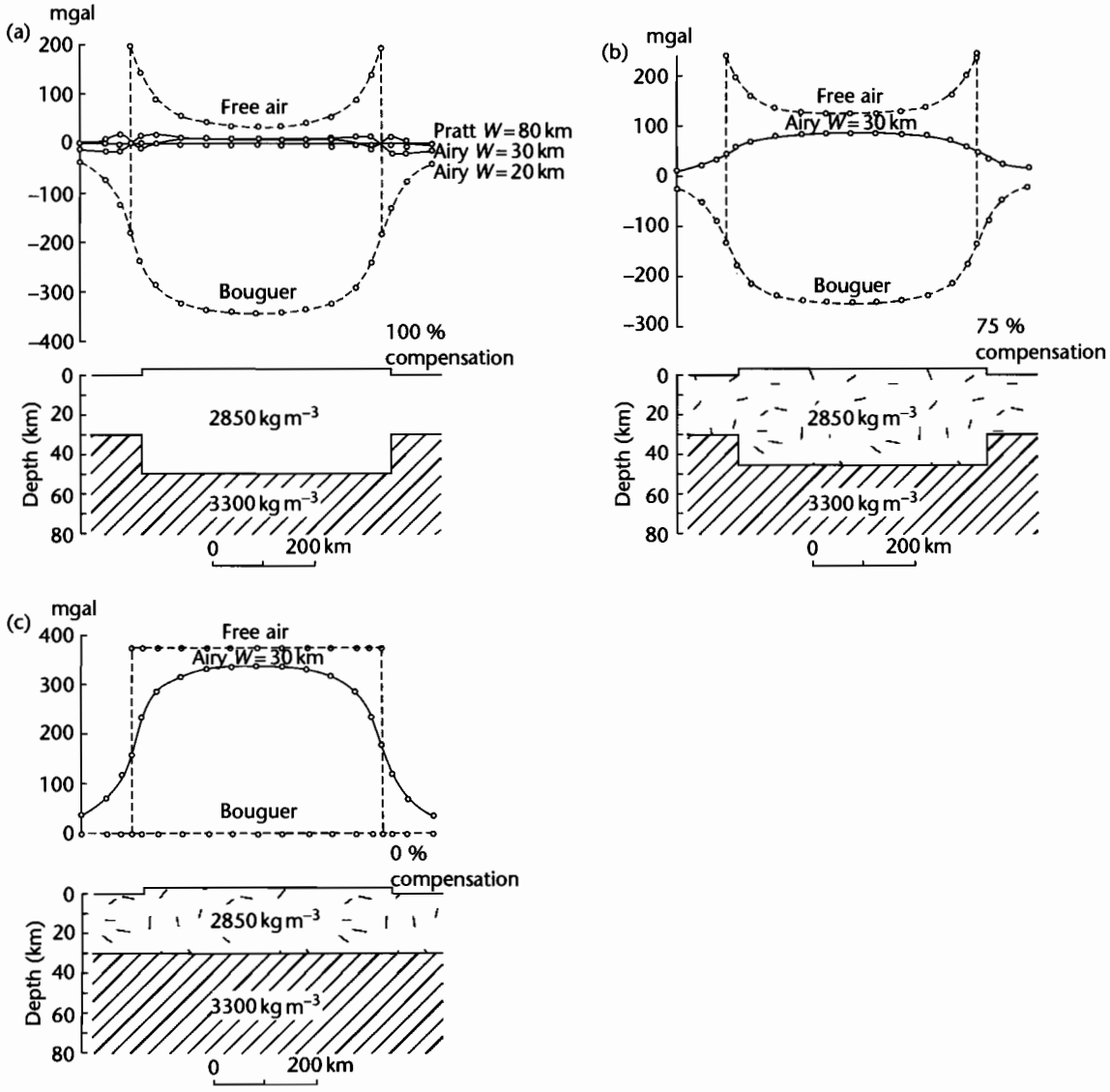

Fig. 2.28 Gravity anomalies over a schematic mountain range (Bott 1982 in Fowler 1990). In (a) the mountain range is 100% compensated (Airy isostasy); in (b) it is 75% compensated (Airy,) and in (c) the mountain range is uncompensated. Solid lines: isostatic anomalies calculated for the different density models shown using Pratt compensation depth $W = 80$ km, Airy compensation depths $W = 20$ km and 30 km. Dashed lines, free-air and Bouguer anomalies that would be measured over the mountain range. Reproduced courtesy of Elsevier.

Fourier transform (Forsyth 1985). The *coherence* function is the square of the correlation coefficient between the topographic and gravity signals. The coherence indicates the degree of compensation for any topographic loads or density contrasts. It can be thought of as the fraction of the gravity field that can be predicted from the topography using a given isostatic response function. A coherence of 1 indicates complete compensation on a plate

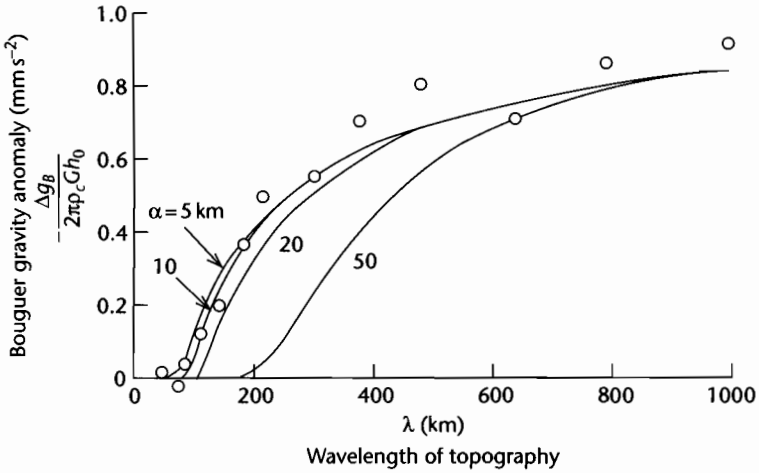

Fig. 2.29 Correlation of Bouguer gravity anomalies with topography (admittance) for the United States (Dorman and Lewis 1972), compared with the gravity formula for loading by periodic topography for different values of the flexural parameter $\alpha = [4D/(\rho_m - \rho_i)g]^{1/4}$ in km. The best agreement is with $\alpha \cong 20$ km, or flexural rigidity $D \cong 10^{21}$ N m, which with $E = 60$ GPa and $\nu = 0.25$, gives an equivalent elastic thickness Te of 6 km. Reproduced courtesy of Cambridge University Press.

with no flexural strength, and a coherence of 0 indicates that the load is completely supported by the strength of the plate. On a plot of coherence versus wavenumber ($k = 2\pi/\lambda$), the roll-over from a coherence of 1 to 0 gives a measure of the flexural rigidity or equivalent elastic thickness. Lowry and Smith (1994) mapped flexural rigidity variations across the Basin and Range-Colorado Plateau-Rocky Mountain area using coherence analysis. They found that areas of low flexural rigidity (average of 9×10^{21} Nm, $Te = 10$ km) correlated with areas of high surface heat flows in the Basin and Range. The highest flexural rigidities were in the Rocky Mountains (average of 3×10^{23} Nm, $Te = 33$ km), with areas of Archaean cratons reaching elastic thicknesses of 77 km.

The good correspondence of flexural rigidity with heat flow indicates that the flexural rigidity of the continental lithosphere is related to the thickness of the elastic layer overlying a temperature-dependent ductile layer. This elastic layer thickness also contains almost all earthquakes on the continents (Maggi et al. 2000), so there is a close correspondence between the seismogenic crust, the thickness of the strong elastic layer and the effective elastic thickness (§4.3).

The same idea of compensation as a function of wavelength can be used to investigate the flexural support for the sediment loads in sedimentary basins (§9.3.4). The sediment load is assumed to have a characteristic wavelength. Taking the example of a sedimentary basin 200 km wide ($\lambda/2 = 200$ km) with a sinusoidal sediment load and an underlying lithosphere of flexural rigidity 10^{24} Nm, $(\rho_m - \rho_s) = 800$ kg m^{-3}, the degree of compensation C is about 0.12. This suggests that the lithosphere behaves very rigidly to this kind of wavelength of load. Changing the wavelength of the load such that $\lambda/2$, the width of the basin, is now 400 km, $C = 0.68$, indicating that the sediment load is only weakly supported. In this case of large compensation, Airy-type isostasy is approached. It must be stressed, however, that rarely can C be estimated accurately in geological situations.

2.4 ROCK RHEOLOGY

2.4.1 Fundamentals

Joints and faults are evidence that rocks can behave as *brittle* materials, that is, they behave elastically up to a limit, beyond which they fail by fracturing. On the other hand, the widespread occurrence of folds suggests that rocks can also behave in a *ductile* manner. Three parameters are important in determining the brittle to ductile transition (Paterson 1958; Heard 1960): pressure, temperature, and strain rate.

Within the crust, rocks commonly deform by brittle fracture, but may also exhibit ductile behavior under stress by *pressure solution creep* (Rutter 1976, 1983) (§2.4.3). Dissolution of minerals in zones of high pressure and their precipitation in areas of low pressure causes creep even at low temperatures and pressures. Otherwise at low temperatures and pressures rocks may deform in a brittle manner by fracturing.

Mantle convection is thought to be attributed to two processes that allow rocks to deform by thermally activated creep: (a) *diffusion* processes operate at very low stress levels, in which the crystalline solid behaves as a Newtonian fluid with a viscosity that depends exponentially on pressure and the inverse absolute temperature; (b) motion of *dislocations* is more effective at higher stress levels. It is a non-Newtonian fluid behavior with the same exponential pressure and inverse temperature dependence. Creep also takes place in the lower lithosphere where it can relax elastic stresses. In this case the rheology is a combination of an elastic and viscous behavior – a *viscoelastic* rheology (§2.4.4).

The viscosities of both diffusion creep and dislocation creep are temperature dependent. If dislocation creep is the dominant mechanism of flow in the mantle, then the effective viscosity of the mantle will be *stress dependent* as well as temperature dependent. This dependence of effective viscosity on stress is well illustrated by the flow of a power-law rheology fluid in a channel (Fig. 2.30).

For a power-law fluid the strain rate or velocity gradient is proportional to the power n of the stress. Velocity gradients and therefore strain rates are greater near the walls of the channel where shear stress is a maximum, whereas a core region experiences small strain rates. This plug-flow appearance of the velocity profiles for large n is a direct consequence of the stress dependency of the effective viscosity μ_{eff} which changes from low at the walls to high at the center of the flow. This must be true because

$$\mu_{eff} = \tau \Big/ \frac{du}{dy} \tag{2.85}$$

i.e., the viscosity is the coefficient linking the shear stresses to the resultant velocity gradient or strain rate.

The idea can be applied to shear flow in the asthenosphere, which can be treated as having a heated lower boundary and an upper cooler boundary at the base of the rigid lithosphere. Shear in the asthenopheric velocity profile is concentrated in zones close to the lower boundary of the asthenosphere where the fluid is hottest and

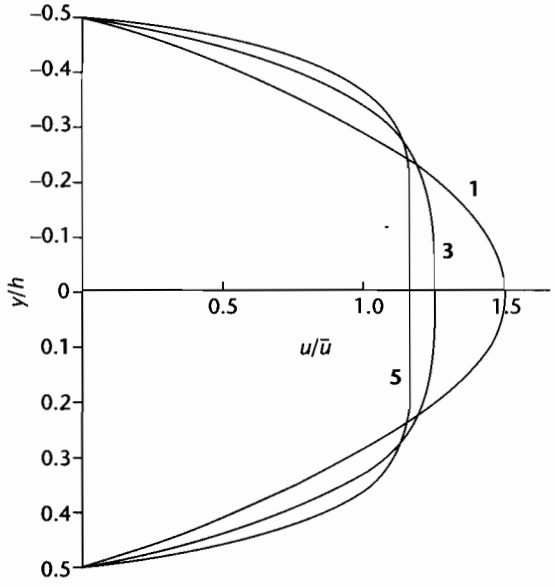

Fig. 2.30 Velocity profiles in a channel of thickness h for power-law fluid rheologies with $n = 1$ (Newtonian), $n = 3$, and $n = 5$. Distance from the channel wall is expressed by y/h. The velocity u is scaled by the average velocity $\bar{u}$.

viscosity the smallest. The upper part of the asthenosphere on the other hand tends to behave like a rigid extension of the overlying lithosphere as a result of this temperature and stress dependency of viscosity. Frictional heating can also have important consequences for shear flow of a fluid with a strongly temperature-dependent viscosity.

2.4.2 Rheology of the mantle

It was initially believed that at the high temperatures and low strain rates of the upper mantle, Newtonian (linear) flow would take place (e.g., Orowan 1967). Alternatively, the mantle may act as a power-law fluid, in which case the mantle's viscosity would be the stress-dependent effective viscosity associated with dislocation creep.

Most views of mantle rheology, however, come from laboratory studies. Since the mantle is composed primarily of olivine, laboratory studies of the creep of olivine at high temperatures are particularly relevant to mantle rheology. The strain rate in dry olivine $\dot{\varepsilon}_{xx}$ (or $-\dot{\varepsilon}_{yy}$) at 1400 °C as a function of stress appears to follow a cubic

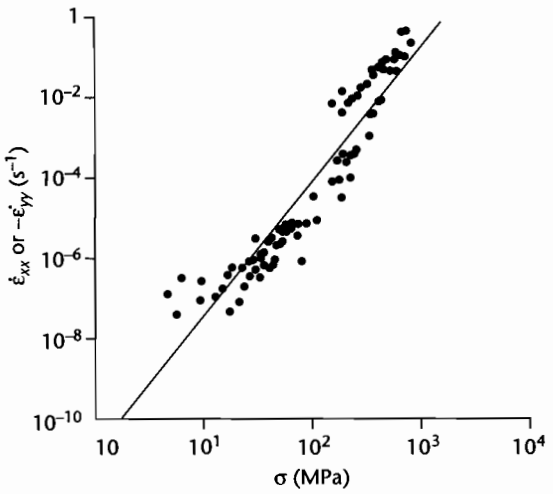

Fig. 2.31 Observed dependence of strain rate on stress for olivine at a temperature of 1400 °C (after Ashby and Verall 1977). Dry olivine obeys an approximate cubic power law rheology in these laboratory experiments.

power-law rheology reasonably well (Ashby and Verall 1977) (Fig. 2.31). Other rocks deform in a nonlinear way at high temperatures in the laboratory, with slightly different coefficients in the power law (ice $n = 3$, halite 5.5, limestone 2.1, dry quartzite 6.5, wet quartzite 2.6, basalt 3). The theoretical formula connecting strain rate and stress in dislocation creep closely matches the empirical relation for dry olivine in the laboratory, suggesting that dislocation creep is the dominant deformation mechanism. Although the laboratory experiments were at strain rates several orders of magnitude greater than mantle strain rates, the dislocation creep process is also thought to be dominant in the mantle. Only at exceptionally low strain rates, considerably smaller than those expected in the mantle, would diffusion creep become dominant.

It is reasonable therefore to assume that the mantle has a power-law rheology. This power-law effect is likely to be small, however, compared with the temperature dependence of mantle rheology.

2.4.3 Rheology of the crust

As every field geologist knows, crustal rocks exposed at the Earth's surface are strongly fractured and faulted at a range of scales. The occurrence of brittle failure depends on the stress overcoming the frictional resistance of the rock (Atkinson 1987 and Scholz 1990 for more details). This resistance to brittle failure increases with pressure and therefore depth.

It has been known for a considerable time that there is a roughly constant ratio between the frictional force on a potential failure plane F and the normal stress N. This ratio is equal to the coefficient of friction f, or the tangent of the angle of sliding friction ϕ

$$\frac{F}{N} = f = \tan\phi \qquad (2.86)$$

Byerlee (1978) found a large range of friction coefficients for different rock types at low pressures, but at moderate pressures (5–100 MPa, 50–1000 bar) the correlation was poor, and at high pressures (200–2000 MPa, 2–20 kbar) there was no rock type dependence at all. *Byerlee's law* states

$$F = aN + b \qquad (2.87)$$

where the coefficients a and b are 0.6 and 0.5 kbar at normal pressures of >2 kbar (200 MPa). Byerlee's law has the same form as the Navier–Coulomb failure criterion

$$\tau_c = C + \sigma\tan\phi \qquad (2.88)$$

where the shear stress acts in the direction of and balances the frictional force on a fracture plane, τ_c is the critical shear stress for failure, σ is the normal stress, ϕ is the angle of internal friction (in the range 0.7–1.7 for compact, coherent rocks), and C is the strength that exists even at zero normal stress (pressure) called *cohesion*. The shear stress needed to produce failure increases as the confining pressure increases. For initiation of a new fracture σ should be higher than for slip on an existing fracture.

Byerlee (1978) suggested that at normal pressures greater than 200 MPa (2 kbar), C is 50 MPa (0.5 kbar) and f is *c.* 0.6–0.85 for a wide variety of rock types (Fig. 2.32). Where in the crust would we expect to find normal pressures of 200 MPa? The weight of a column of rock of density 2800 kg m^{-3}, height 1 km and g = 10 m s^{-2}, is 28 MPa. We would expect to find 200 MPa of pressure at depths of 7–8 km in the crust. Earthquake foci are found at depths up to 15 km in the continental crust, equivalent to about 420 MPa (4.2 kbar). Between the surface and 15 km therefore, we should expect brittle deformation on unlubricated faults. Below 15–20 km

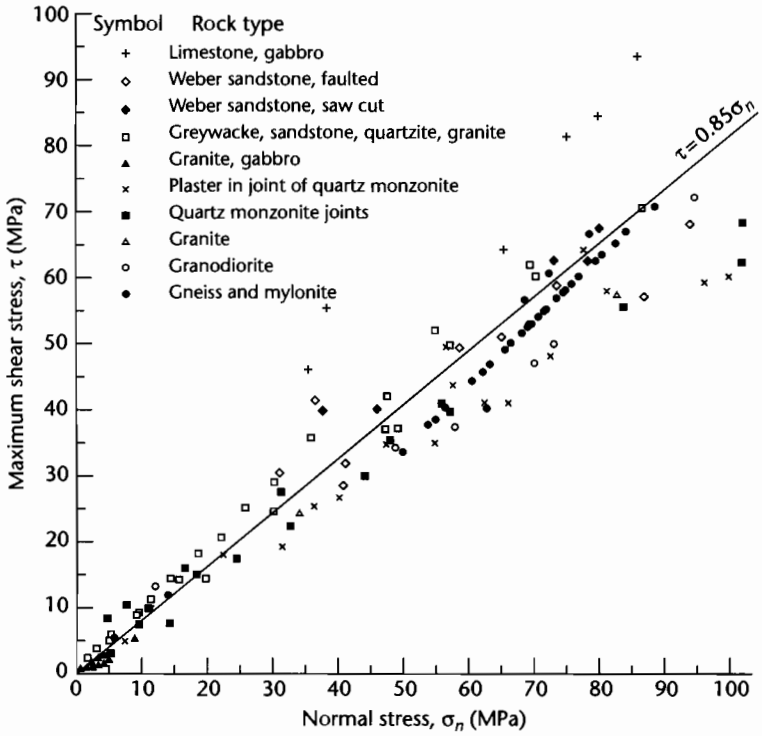

Fig. 2.32 Byerlee's law for the maximum shear stress τ to initiate sliding as a function of the normal stress σ_n, for a variety of rock types. The linear fit defines a maximum coefficient of static friction of 0.85 (Byerlee 1977). Reproduced courtesy of Cambridge University Press.

however, earthquakes are much less common, and the rheology is ductile or "plastic." Depths of about 10–15 km correspond with a temperature of 300 °C in continental crust.

Although faulting of the brittle upper crust is very familiar, there is also observational evidence that near surface rocks deform in both a plastic and fluid-like manner. The texture of many folded rocks suggests that the deformation responsible for the folding was the result of diffusive mass transfer. But the lower temperatures involved preclude the thermally activated diffusion processes discussed in §2.3.1. Instead, the diffusive processes take place through *pressure solution* whereby material is transported in solution from areas of high intergranular pressure and stress and precipitated in regions of low pressure and stress, leading to creep. Point and line contacts between grains in a sand would represent such high pressure/stress zones. The presence of water around the grains acts as the solvent and facilitates the transport of dissolved material. The pressure solution process also leads to compaction (§9.2.1).

Strain rate is linearly proportional to applied stress in pressure solution creep, so the deformation is equivalent to that of a Newtonian fluid. It explains viscous folding of rocks at quite low temperatures.

Although pressure solution probably dominates as the main ductile mechanism at low temperatures in the upper crust, the rheology of the crust is likely to be complex as a result of the many compositional changes taking place within it. Seismic refraction velocities have been used, for example, to interpret an amphibolite facies upper crust, granulite facies middle crust, and ultramafic lower crust in NW Britain (Hall and Al-Haddad 1976; Bamford 1979). Other authors have suggested much higher quartz contents, with significant proportions of acid and intermediate rocks metamorphosed to granulite and amphibolite facies in the lower crust (Fountain and Salisbury 1981). The layering of the continental crust

affects its strength as a function of depth (§2.4.6). In particular, a ductile region in the middle crust is thought to be the location of detachment of major extensional faults (Kusznir et al. 1987). This topic of decoupling in mid-crustal regions is dealt with in greater depth in considering extensional basins in Chapter 3.

In summary, the consideration of rock deformation textures, laboratory studies of quartz-bearing rock and continental seismicity suggests that a seismogenic upper crust characterized by discontinuous frictional (brittle) faulting passes below *c.* 15 km (*c.* 300 °C) depth into an aseismic continuous quasi-plastic region where dislocation creep takes place in mylonitic fault zones (Sibson 1983; Scholz 1990). In the deep crust at temperatures greater than 450 °C fully ductile continuous deformation is thought to dominate in gneissose shear zones (Grocott and Watterson 1980). The vertical zonation of deformation mechanism envisaged by Sibson (1983, p. 744) is shown in Fig. 2.33.

2.4.4 Viscoelasticity

The fact that seismic shear waves can be propagated through the mantle suggests that it is an elastic solid, yet it also appears to flow like a viscous fluid, enabling, for example, postglacial rebound to take place. A material that behaves as an elastic solid on short time scales but viscously on long time scales is known as a viscoelastic or *Maxwell* material.

In a Maxwell material, the rate of strain $\dot{\varepsilon}$ is the sum of the linear elastic strain rate $\dot{\varepsilon}_e$ and a linear viscous strain rate $\dot{\varepsilon}_v$. The elastic strain of a material under a uniaxial stress is

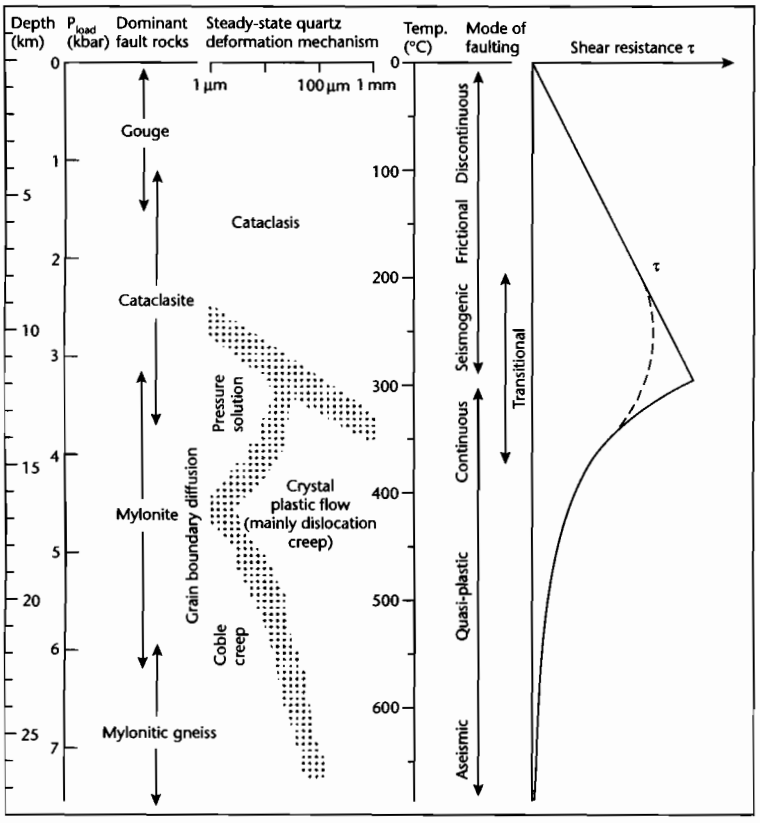

Fig. 2.33 Sibson's (1983) conceptual model for a major fault zone in the continental crust showing the dominant deformation mechanisms.

$$\varepsilon_e = \sigma/E \tag{2.89}$$

as will be recalled from Hooke's law (equation (2.12)), where E is Young's modulus. The rate of strain is therefore the time derivative of ε_e, $d\varepsilon_e/dt$. The rate of strain in a viscous Newtonian fluid subjected to a deviatoric normal stress σ is a velocity gradient $\partial u/\partial x$. The effective viscosity μ is taken as the ratio between stress and twice the strain rate. Therefore

$$\frac{d\varepsilon_v}{dt} = -\frac{\partial u}{\partial x} = \frac{\sigma}{2\mu} \tag{2.90}$$

(where the minus sign simply indicates a tensional strain by convention). Since the total strain is the sum of the elastic and viscous fluid strains, the total strain rate is

$$\frac{d\varepsilon}{dt} = \frac{1}{2\mu}\sigma + \frac{1}{E}\frac{d\sigma}{dt} \tag{2.91}$$

This is the fundamental rheological equation relating strain rate, stress and rate of change of stress for a *Maxwell viscoelastic* material. When a strain is initially rapidly applied to the viscoelastic medium, the time-derivative terms in (2.91) dominate and the material behaves elastically. Subsequently, if there is no change in the strain, the stress relaxes to $1/e$ of its original value in a time $2\mu/E$ which is known as the *viscoelastic relaxation time*. For the asthenosphere this relaxation time is of the order of 30 to 40 years, that is, longer than the period of seismic waves but shorter than the duration of postglacial rebound. The stress relaxation time is a strong function of temperature, rheological parameters, and initial stress and its range of values for the lithosphere is controversial. Some workers believe that the relaxation time is very short ($<10^6$ yr) while others believe it to be sufficiently long (20–30 Myr) to have a major impact on sedimentary basin geometry and subsidence. A viscoelastic rheology with a long relaxation time was used in early models of foreland basin evolution in particular (Beaumont 1978, 1981; Quinlan and Beaumont 1984).

2.4.5 Elastic–perfectly plastic rheology

When confining pressures approach a rock's brittle strength a transition takes place from brittle (elastic) behavior to plastic behavior (Fig. 2.34a). This transition is at the rock's yield stress σ_0. The elastic strain can be regarded as recoverable, but the deformation in the plastic field is not recoverable when the stress or load is removed (Fig. 2.34b). If the deformation continues indefinitely without any addition of stress above σ_0, the material is said to exhibit an *elastic–perfectly plastic* behavior (Fig. 2.34c). Laboratory studies of the mantle rock dunite show that it conforms closely to the elastic–perfectly plastic rheology (Griggs et al. 1960). A typical depth at which the brittle–plastic transition would occur for dunite is about 17 km; below this the rock should yield plastically under large deviatoric stresses.

The above discussion can be applied to the bending of a plate. If the plate is flexed, a yield stress in the plate may be attained, marking the onset of plasticity. This onset corresponds to a characteristic plate curvature and has associated with it a characteristic bending moment. Consider the situation where the bending moment exceeds the critical value for the onset of plasticity. We have previously seen that the longitudinal strains in a flexed plate are large in its outer parts but small in the interior. As a result, the outer regions may deform plastically while the interior core deforms elastically. After the bending moment for the onset of plasticity is attained there is a rapid increase in plate curvature due to a process known as *plastic hinging*. The plate then bends further, up to a maximum bending moment that is 1.5 times the critical moment for the onset of plasticity (Turcotte and Schubert 1982, p. 344). The observed profile across the Tonga Trench, which shows a curvature far in excess of that predicted of a purely elastic plate, may be due to this process of plastic hinging. A similar process is discussed in §4.3 in relation to the bending of continental plates in mountain belts.

2.4.6 Strength profiles of the lithosphere

Lithospheric strength is controlled by lithospheric rheology, which itself is dependent on the heat flow or geothermal gradient, and the composition of lithospheric rocks. The thickness of the crust and lithosphere and the geothermal gradient therefore interact to produce distinctive strength profiles. We should expect these profiles to be dramatically different between oceanic and continental lithosphere (Lynch and Morgan 1987).

The lithosphere can deform by brittle (faulting) and ductile mechanisms, each with its own yield strength. The yield stress (strength) of the lithosphere at any depth is conventionally calculated as the lesser of the two yield

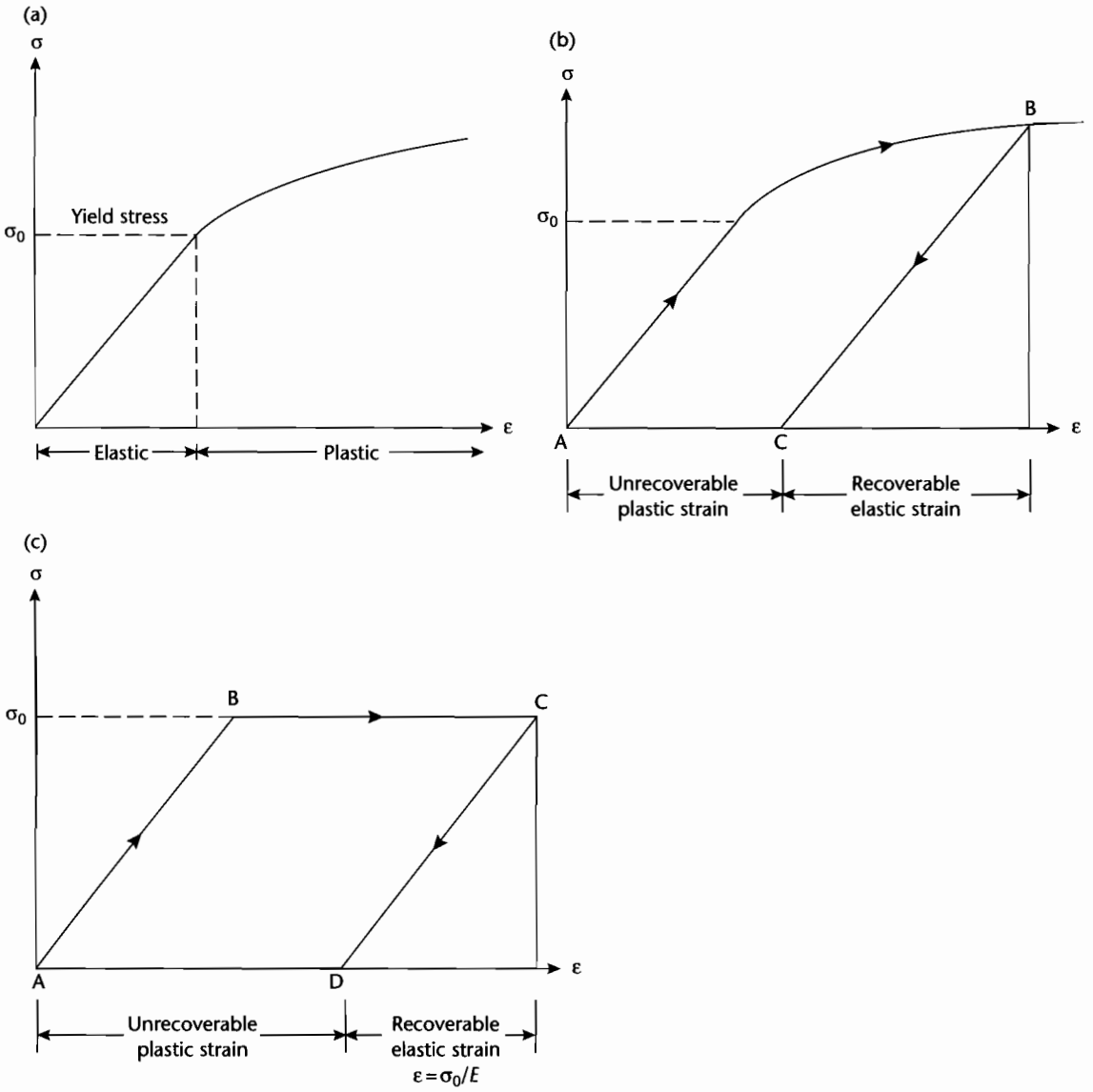

Fig. 2.34 Stress-strain trajectories for (a) a solid showing a transformation from elastic to plastic behavior; (b) loading and unloading of an elastic–plastic material. Unloading of the material once it has passed into the plastic field results in an unrecoverable deformation, or plastic strain; (c) a material with an elastic–perfectly plastic rheology. Plastic strain continues indefinitely without any addition of stress above the yield stress.

strengths for brittle failure and ductile creep (Brace and Kohlstedt 1980). The integral of the yield stress profile over depth is the total yield stress of the lithosphere, equivalent to the horizontal deviatoric force required to cause nonelastic strain. At one or several points in the profile, the brittle and ductile yield strengths may be equal. These points or depths are known as the *brittle–ductile transition.*

The brittle yield strength is assumed to be related to the pressure and therefore depth in the crust. It is independent of strain rate, temperature, and rock type. The ductile yield stress, however, is strongly dependent on strain rate, temperature, and rock composition. Let us firstly take the relatively straightforward case of the oceanic lithosphere.

The Anderson theory of faulting expresses the dip of a fault in terms of the coefficient of static friction. The tectonic stress required to cause faulting under tension is then

$$\Delta\sigma_{xx} = \frac{-2f_s(\rho g y - p_w)}{(1+f_s^2)+f_s} \tag{2.92}$$

and under compression is

$$\Delta\sigma_{xx} = \frac{2f_s(\rho g y - p_w)}{(1+f_s^2)-f_s} \tag{2.93}$$

where $\Delta\sigma_{xx}$ is the deviatoric stress, f_s is that static coefficient of friction, $\rho g y$ is the lithostatic stress and p_w is the pore pressure. To find the failure stress of the oceanic crust, we assume the pore pressure is hydrostatic so $p_w = \rho_w g y$, $\rho = 3300\,\mathrm{kg\,m^{-3}}$, and $\rho_w = 1000\,\mathrm{kg\,m^{-3}}$, and $f_s = 0.6$. The results for tension and compression are sketched in Fig. 2.35.

But how far downwards in the oceanic lithosphere does the Anderson theory extend? Power law creep as a function of temperature is given by an equation of the form (see also §3.6.4)

$$\dot{\varepsilon} = A\sigma^n \exp\left(\frac{-E_a}{RT}\right) \tag{2.94}$$

For olivine, $A = 4.2 \times 10^5\,\mathrm{MPa^{-3}\,s^{-1}}$, E_a is the activation energy $= 523\,\mathrm{kJ\,mol^{-1}}$, and $n = 3$. Taking strain rates of $10^{-12}\,\mathrm{s^{-1}}$ and $10^{-14}\,\mathrm{s^{-1}}$, the stress as a function of depth for a geothermal gradient of $25\,\mathrm{K\,km^{-1}}$ can be found (Fig. 2.35). We then assume that the lower of the frictional stress and the creep stress determines the strength of the oceanic lithosphere. The change from a frictional stress to a power law stress takes place at a depth of *c.* 28 km for the conditions given above. This is the brittle–ductile transition. Note that its depth depends on the geothermal gradient and strain rate, as well as on the "sign" of the deviatoric stress (tension or compression).

The same concepts apply to the continental lithosphere, but geothermal gradients are likely to be more complex because of the internal heat generation of radiogenic minerals.

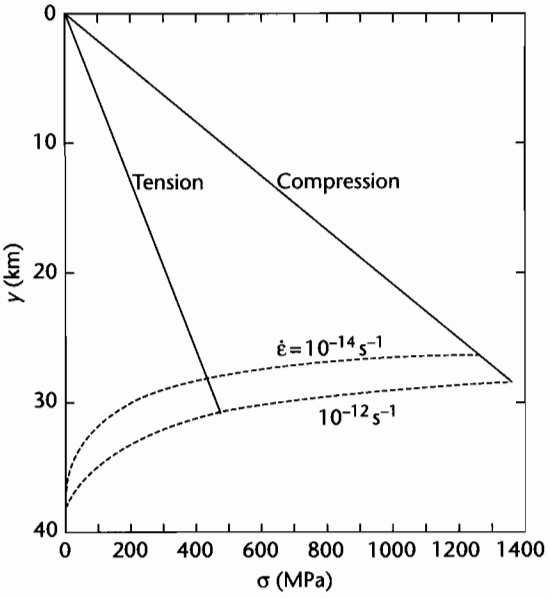

Fig. 2.35 Strength profile for the oceanic lithosphere calculated using equation (2.92) for tension and equation (2.93) for compression. The dashed lines are the stresses associated with creep in the lithosphere at the strain rates indicated. Reproduced courtesy of Cambridge University Press.

The effects of variations in geothermal gradient are illustrated in Figure 2.36 using reduced heat flows of $25\,\mathrm{mW\,m^{-2}}$ representing a cold continental shield, and $59\,\mathrm{mW\,m^{-2}}$ representing the high geothermal gradients typical of the Basin and Range province, USA (Lynch and Morgan 1987) ($K = 2.5\,\mathrm{Wm^{-1}\,K^{-1}}$, $A_0 = 2.1\,\mu\mathrm{W\,m^{-3}}$, $a_r = 10\,\mathrm{km}$). There are a number of points to note. First, there are two high strength brittle regions in the lithosphere, one in the upper crust and one in the upper mantle, each underlain by brittle–ductile transitions. Second, the brittle–ductile transition occurs at a much shallower level in the crust for the hot geotherm than for the cold geotherm. Third, the area to the left of the strength profile, representing the total yield strength of the lithosphere, is much greater for the cold lithosphere. We should expect cold lithosphere to be "stronger" than hot lithosphere when flexed or subjected to horizontal extensional or compressional deviatoric stresses. The total yield strength of the lithosphere is con-

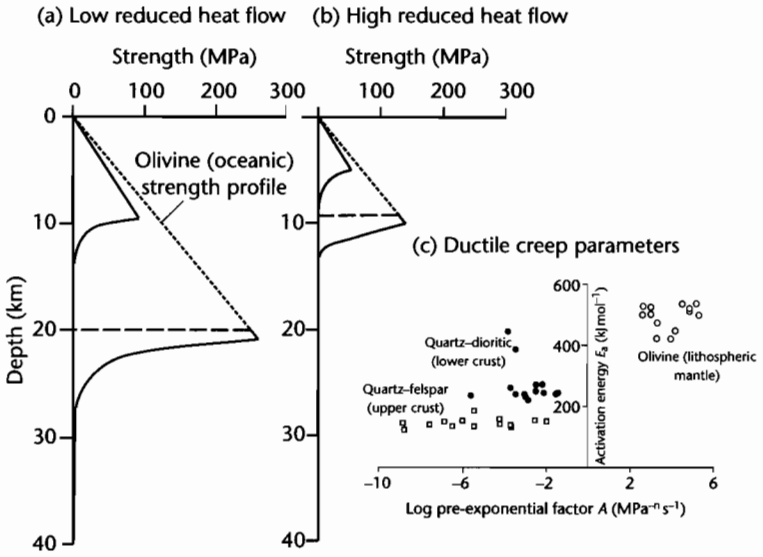

Fig. 2.36 Strength profiles of the continental lithosphere for different geothermal gradients, using (a) a low reduced heat flow of 25 mW m^{-2} for a cold continental shield area, and (b) a higher reduced heat flow of 59 mW m^{-2} for an area undergoing extension. $K = 2.5$ W m^{-1} K^{-1}, $A_0 = 2.1$ mW m^{-3}, $T_0 = 15$ °C, Universal Gas Constant = 8.31451 J mol^{-1} K^{-1}, strain rate is 10^{-12} s^{-1}, $n = 3$. For the olivine rheology, $A = 10^4$ MPa^{-3} s^{-1}, $E_a = 500$ kJ mol^{-1}; for brittle failure under tension $f_s = 0.6$, $\rho = 3300$ kg m^{-3}. For the lower crustal rheology, $A = 100$ Pa^{-3} s^{-1}, $E_a = 300$ kJ mol^{-1}, and for brittle failure under tension $f_s = 0.6$ and $\rho = 2750$ kg m^{-3}; (c) shows plot of activation energy E_a versus the pre-exponential factor A for a range of rock types typical of the lithospheric mantle, lower crust, and upper crust (derived from Table 1, Fernandez and Ranalli 1997).

siderably smaller (about half) under tension than under compression.

Oceanic lithosphere has a yield strength that is a strong function of its age. The entire oceanic crust is brittle, and the yield strengths of oceanic lithosphere older than about 10 Myr under both extension and compression are considerably higher than any likely imposed tectonic forces. Continental lithospheric strength is strongly dependent on the basal heat flow or geothermal gradient. For a low heat flow (25 mW m^{-2}) the strength under extension is an order of magnitude greater than any likely imposed forces; consequently, cold continental lithosphere is unlikely to undergo significant deformation. At higher heat flows the strength under extension is much reduced, making the continental lithosphere susceptible to extensional deformation. For example, the actively extending crust in the Basin and Range province, USA is 30 km thick with a reduced heat flow of 70 mW m^{-2} (Lachenbruch and Sass 1978), whereas in the eastern USA, which is tectonically inactive, crustal thickness is 40 km and reduced heat flow is 33 mW m^{-2}. A global comparison of tectonic activity and reduced heat flows shows that regions with high heat flows (>60 mW m^{-2}) such as the Rhine Graben (western Europe) and Shansi Graben (China) undergo rifting, whereas regions with lower heat flows (<50 mW m^{-2}) do not show signs of active extensional deformation (Kusznir and Park 1987, Fig. 8, p. 42).

Crustal composition is an important factor particularly at high geothermal gradients. The quartz rheology of the upper crust is weaker than the plagioclase rheology of the lower crust, which is in turn much weaker than the olivine rheology of the mantle. The thicknesses of upper and lower crust are therefore important in determining strength profiles. Crustal thickening has the effect of weakening the lithosphere, since the weaker quartz–plagioclase rheologies may replace the stronger olivine rheology at the depths normally associated with the lithospheric mantle. At crustal levels, a strong plagioclase or ultramafic lower crustal rheology may be replaced by a weaker quartz rheology during thickening. Thickened

crust in zones of convergence may therefore be prone to extensional collapse.

During extension of the lithosphere at a finite strain rate, an increase in geothermal gradient weakens the lithosphere, whereas the thinning of the crust simultaneously strengthens it. The balance between net strengthening and net weakening is strongly affected by the strain rate. At high strain rates ($\dot{\varepsilon}$ of 10^{-13} to $10^{-14}\,s^{-1}$) there is less opportunity for heat loss and re-equilibration of the geothermal gradient, leading to net weakening, whereas slow strain rates ($\dot{\varepsilon}$ of $10^{-16}\,s^{-1}$) promote net strengthening. Fast strain rates therefore lead to intense localized extension and high heat flows, whereas slow strain rates generate broad regions of extension with low surface heat flows.

PART

2 *The mechanics of sedimentary basin formation*

CHAPTER 3

Basins due to lithospheric stretching

When Earth breaks up and heaven expands
How will the change strike me and you
In the house not made with hands?

(ROBERT BROWNING, *BY THE FIRE SIDE* (1855))

SUMMARY

Intracontinental sags, rifts, failed rifts, and passive continental margins fall within an evolutionary suite of basins unified by the process of lithospheric stretching. Rifts are areas of crustal thinning, demonstrated by the shallow depth to the Moho, high surface heat flows, volcanic activity, seismic activity with predominantly extensional focal mechanism solutions, negative Bouguer gravity anomalies, and commonly elevated rift margin topography.

The nature of the fault systems and associated sedimentary basins within extending continental lithosphere depends on the initial crustal structure and geotherm, strain rate and total amount of strain. Discrete, localized continental rifts appear to form on normal thickness crust and extend slowly over long periods of time. At higher strain rates, localized rifts may evolve into passive margins. Wide extended domains with supradetachment basins occur on previously thickened crust that extends quickly over a short period of time. Local anomalies in the ductile lower crust may be amplified to produce core complexes within these wide extended terranes.

Passive continental margins are in general seismically inactive, and tectonics are dominated by gravity-driven collapse, halokinesis, and growth faulting. Heat flows are near-normal in mature examples. Passive continental margins can be divided into two types: (i) volcanic margins are characterized by extensive extrusive basalts and igneous underplating and significant surface uplift at the time of break-up, and (ii) nonvolcanic margins lack evidence for strong thermal activity, and consist of extensive sediment drapes overlying a strongly rifted basement. On conjugate margins, the extended continental lithosphere may lie at considerable oceanic depths beneath a very thin drape of sediment, or may be covered by sediment prisms over 10 km thick. There may be considerable asymmetry between conjugate margins, especially in the ductile lower crust.

Early investigations suggested that rifting fell into two end-member classes. Active rifting involves the stretching of the continental lithosphere in response to an active thermal process in the asthenosphere, such as the impingement of a hot mantle plume on the base of the lithosphere. Passive rifting, however, involves the mechanical stretching of the continental lithosphere from distant extensional forces, with passive upwelling of asthenosphere. Subsidence in rifts is an isostatic response to the stretching of the continental lithosphere. The postrift stage of failed rifts and the postrift or drift stage of passive continental margins is due to thermal contraction during cooling of the stretched lithosphere. The sediment loads are supported flexurally during this long phase of cooling. Dynamical models of the lithosphere incorporate a rheological understanding of a layered lithosphere undergoing extension. These numerical models make predictions of strain rate evolution as a function of the changing temperature field and viscosity within this layered lithosphere.

The simplest formulation of continental extension is the uniform stretching model of McKenzie (1978a) and its derivatives. The prototype uniform stretching model involves uniform stretching with depth, instantaneous extension, 1-D heat transport by conduction, no magmatic activity, no internal radiogenic heat sources, and the operation of Airy isostasy throughout. The uniform stretching model makes important first-order predictions. Initial fault-controlled subsidence is dependent on the initial crustal to lithospheric thickness ratio and on the stretch factor β. The subsequent thermal subsidence has

the form of a negative exponential, and depends on the stretch factor β alone. The uniform stretching model serves as a useful approximation for subsidence and paleotemperature in rifted basins such as the North Sea, and in sediment-starved passive margins, such as the Bay of Biscay and the Galicia margin of the eastern central Atlantic. However, sediment-nourished passive margins require the postrift subsidence to be modeled with flexural rather than Airy isostatic support. Volcanic margins require the effects of melt segregation, igneous underplating, and transient dynamic uplift to be accounted for.

Subsequent modifications to the prototype uniform stretching model have investigated the effects of depth-dependent stretching, extension by simple shear along transcrustal detachments, protracted rifting periods, elevated asthenospheric temperatures, magmatic activity, induced mantle convection within the upwelled asthenosphere, radiogenic heat sources, greater depths of lithospheric necking, and flexural support. These modifications affect the predictions of synrift and postrift subsidence, and in particular predict elevated synrift topography in the form of topographic swells or rift margin uplifts.

Dynamical approaches to lithospheric extension involve plane-stress or plane-strain models with various boundary conditions, and initial conditions. Dynamic models are especially instructive in explaining why rifts remain narrow, with small bulk extensional strains, or develop into oceanic spreading centres. One set of dynamic models indicates that at moderate to low initial strain rates, extension is limited by an increase in viscosity in the mantle lithosphere below the Moho. In contrast, at high initial strain rates, complete rifting results from the concentration of the extensional force on a progressively thinner high-strength layer within the lithosphere. Analogue models are able to replicate the narrow, localized rifts and extensive, tilted fault block terranes observed at passive margins as a function of strain rate. Analogue models also show that gravity spreading of weak, previously thickened crust leads to wide extended terrains and exhumed ductile lower crust in core complexes.

Igneous activity is a common feature of some continental rifts and passive margins at the point of break-up. Igneous activity is caused by adiabatic decompression due to one or a combination of lithospheric stretching, elevated asthenospheric temperatures, and presence of volatiles. Hot plumes derived from the core–mantle boundary have a profound effect on asthenospheric temperatures, melt generation by adiabatic decompression and surface uplift. Plume heads occupy areas of the asthenosphere generally 1000–2000 km across with temperature anomalies of 100–200 °C, and in the oceans are responsible for bathymetric swells 1–2 km above the surrounding seafloor. The elevation of sublithospheric temperatures over a mantle plume may generate large amounts of melting and the upward migration of melts to form igneous underplates and extrusive basalts. Transient surface uplift is caused by the dynamic effects of hot asthenospheric flow, whereas permanent uplift results from igneous underplating of the crust. Consequently, volcanically active passive margins and continental rifts stand elevated topographically compared to nonvolcanic equivalents. The amount of melt generated and its composition is related to the plate thickness, excess temperature, stretch factor, and percentage of volatiles.

The amount of extension (stretch factor β) and the strain rate history can be estimated by a number of techniques. The thermal subsidence history of boreholes allows the amount of lithospheric stretching and strain rate history to be estimated. Crustal stretching can be calculated from imagery of the depth to the Moho using gravity and seismic data. Stretch factors can also be estimated from forward sequential tectonostratigraphic modeling using well-constrained crustal and basin profiles derived from deep seismic reflection and refraction data.

3.1 INTRODUCTION TO RIFTS, FAILED RIFTS, AND PASSIVE CONTINENTAL MARGINS

Rifts, failed rifts, intracratonic sags, and passive margins form part of an evolutionary sequence of basins unified by the processes of lithospheric extension (Dietz 1963; Dewey and Bird 1970; Falvey 1974; Kinsman 1975; Veevers 1981). Two linked mechanisms explain the majority of observations in these basins: (i) brittle extension of the crust, causing extensional fault arrays and fault-controlled subsidence, and (ii) thermal relaxation following ductile extension of the lithosphere, leading to regional postrift subsidence.

The main difference between rift basins and basins experiencing regional subsidence but lacking major extensional faulting (sags) can be simply explained as follows (Fig. 3.1). In true rifts, tensile deviatoric stresses due to uplift, thinning, or regional stress fields are sufficient to overcome rock strength, and therefore cause

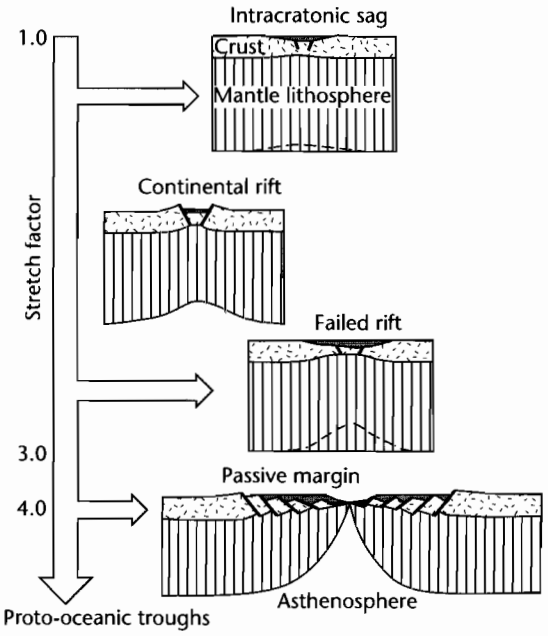

Fig. 3.1 Basins in the rift–drift suite as a function of increasing amounts of continental stretching.

faulting. If the deviatoric stresses are insufficient to cause brittle fracture, then uplift or subsidence may occur without fracturing. If the thermal "supply" is switched off and not renewed, the thermal contraction effect causes subsidence, so that sags can be regarded as immature continental basins that have failed to develop into either rifts or spreading centres, whilst rift basins that have experienced a subsequent sag phase can likewise be regarded as having failed to develop fully into oceanic spreading centres. The evolution of a rift system into a passive continental margin takes place when new oceanic lithosphere is created at a spreading centre, the rift–drift transition. In terms of mechanisms for basin formation, continental margin wedges record the response of the lithosphere to its continued cooling and to the considerable loading of the sediment itself.

In this chapter, the mechanisms of lithospheric extension are focused upon as a means of explaining the rift–drift suite of sedimentary basins. This suite of sedimentary basins is characterized by a distinctive set of geological, geophysical, and geomorphological observations that are strongly suggestive of elevated heat flows, volcanicity, extensional faulting, and thinned crust. Embedded within the overarching theme of lithospheric extension are complexities caused by the total amount of stretching, strain rate, and thermal and mechanical properties of the continental lithosphere undergoing extension.

3.2 GEOLOGICAL AND GEOPHYSICAL OBSERVATIONS IN REGIONS OF CONTINENTAL EXTENSION

3.2.1 Rifts

Rifts are areas of crustal extension and seismic studies show them to overlie thinned crust. Regions of rifting at the present day are characterized by negative Bouguer gravity anomalies, high heat flow, and volcanic activity, all of which suggest that in addition to crustal extension, a thermal anomaly exists at depth. The essential observations in zones of continental extension are summarized below.

Heat flow: The presence of active volcanoes and elevated heat flows in rift zones demonstrates active thermal processes. However, the measured values of heat flow are often difficult to interpret, because of complications due to convective heat transport, shallow magmatic intrusions, groundwater convection, and variability of conductive sediments and rocks. In general, rift zones have heat flows of 90–110 $mW m^{-2}$. This is up to a factor of 2 higher than in surrounding unstretched terranes (Fig. 3.2). Values are higher in volcanic rifts such as the Eastern Rift, Kenya, and lower in nonvolcanic rifts such as those of Malawi, Tanganyika, and the Jordan–Dead Sea Rift zone of the Middle East. In areas devoid of active tectonics and volcanicity, continental heat flow values appear to be strongly correlated with the type of underlying crust. In NE North America, for example, the higher heat flows over the Appalachians (average 58 $mW m^{-2}$) than over the North American Shield (average 29 $mW m^{-2}$) may be explained by the different thicknesses of underlying tonalitic crust (Pinet et al. 1991) containing the radiogenic heat producing elements uranium, thorium, and potassium (§2.2). In general, granitic terranes have high surface heat flows, whereas basic and ultrabasic igneous rocks and many sedimentary rocks are associated with low surface heat flows. The large variations caused by this internal radiogenic heat production makes the interpretation of surface heat flows in terms of continental stretching problematical.

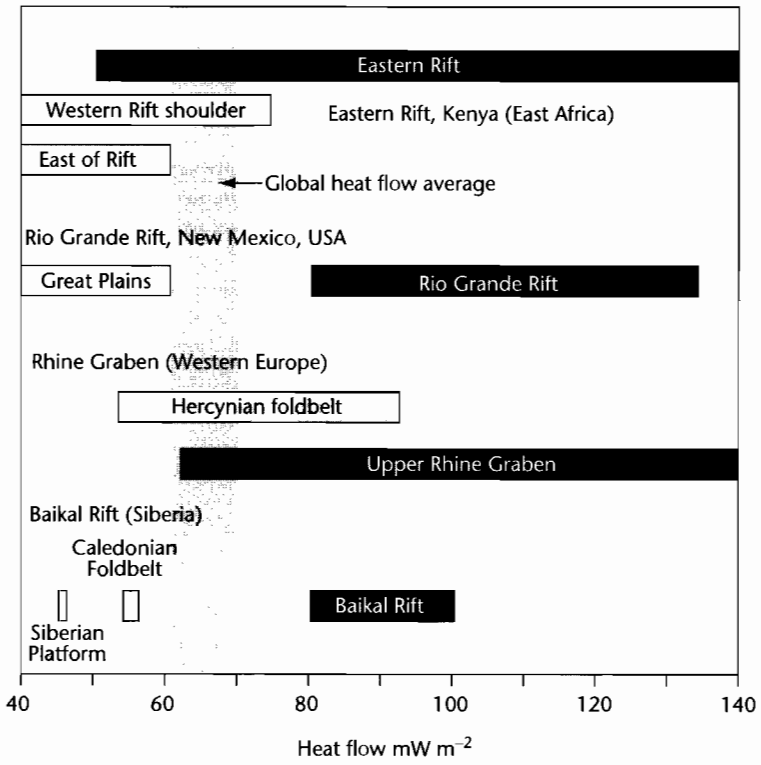

Fig. 3.2 Heat flows in some continental rifts and surrounding regions, compared to the global heat flow average. Dark boxes are rift zones; light boxes are rift flanks or adjacent unstretched regions.

Seismicity: Rift zones are characterized by high levels of earthquake activity. On the continental lithosphere, earthquake epicenters commonly delineate active rift zones or reactivated orogenic belts, as in southern Africa. Focal mechanism solutions in general indicate normal dip–slip faulting with orientations roughly parallel to the long-axis orientation of the rift. In some continental rifts, such as the Rhine Graben, strike–slip focal mechanisms dominate dip–slip solutions by 3:1. Although earthquakes are common in regions of continental rifting, they typically have moment magnitudes of up to 5.0 (Rhine Graben) or 6.0 (East African Rift), with shallow focal depths of < 30 km, indicating that the earthquakes are located in the brittle mid-upper crust.

Crustal thickness: Scismic studies show that the Moho is elevated beneath rift zones. The southern Rhine Graben is an example (Fig. 3.3). The Moho reaches a depth of 24 km near the Kaiserstuhl volcano due west of Freiburg, Germany directly beneath the centre of the graben. The Moho is dome-shaped, deepening to the north, NW and NE to about 30 km. Approximately 3 km of synrift sedimentary rocks are found in the graben, so the continental crust has been thinned from 30 km to 21 km, that is, by a factor of *c.* 1.4. In the North Sea failed rift, the crust (pre-Triassic) is > 31 km thick beneath the Shetland Platform and Scandinavian Shield, but is < 16 km thick beneath the Viking Graben (Klemperer 1988). The continental crust has therefore been thinned by a factor of approximately 2 immediately beneath the deepest part of the Viking Graben (Fig 3.4). An important observation, however, is that some regions of extensive, diffuse extension such as the Basin and Range, SW USA, are located on previously thickened crust. The Moho was therefore anomalously deep at the onset of extension, and extension/thinning has brought the Moho back to "normal" depth. This is also the case for the Tibetan Plateau, which is undergoing

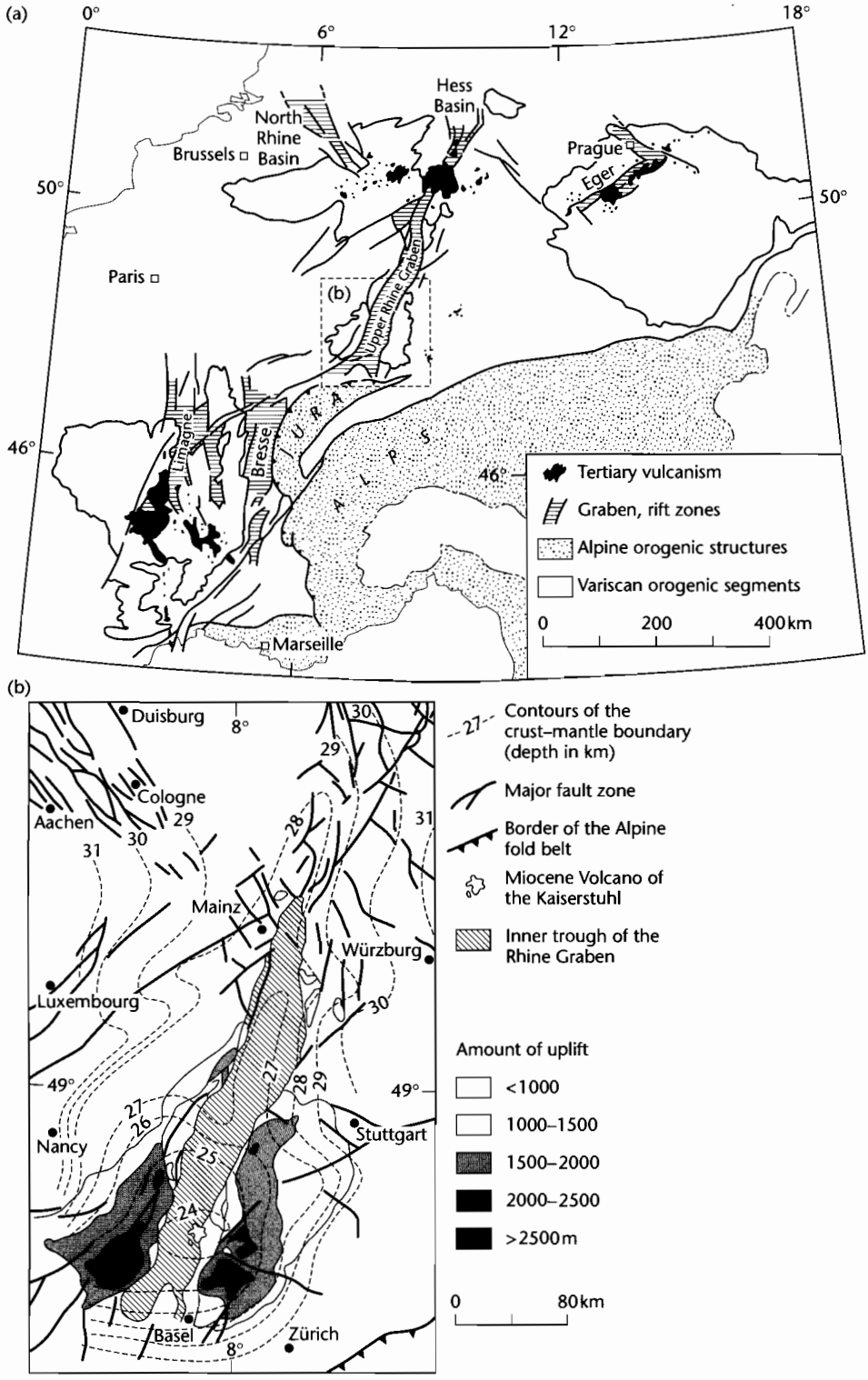

Fig. 3.3 (a) Location of main elements of the late Eocene–Recent Western European Rift System, with sites of Tertiary volcanicity; (b) Depth to the Moho below sea-level (in km), showing a mantle bulge in the southern Rhine Graben centred on the Kaiserstuhl volcano (Illies 1977). The largest amounts of denudation are found on the rift flanks above the shallow mantle. Reproduced courtesy of the Board of the Stichting Netherlands Journal of Geosciences.

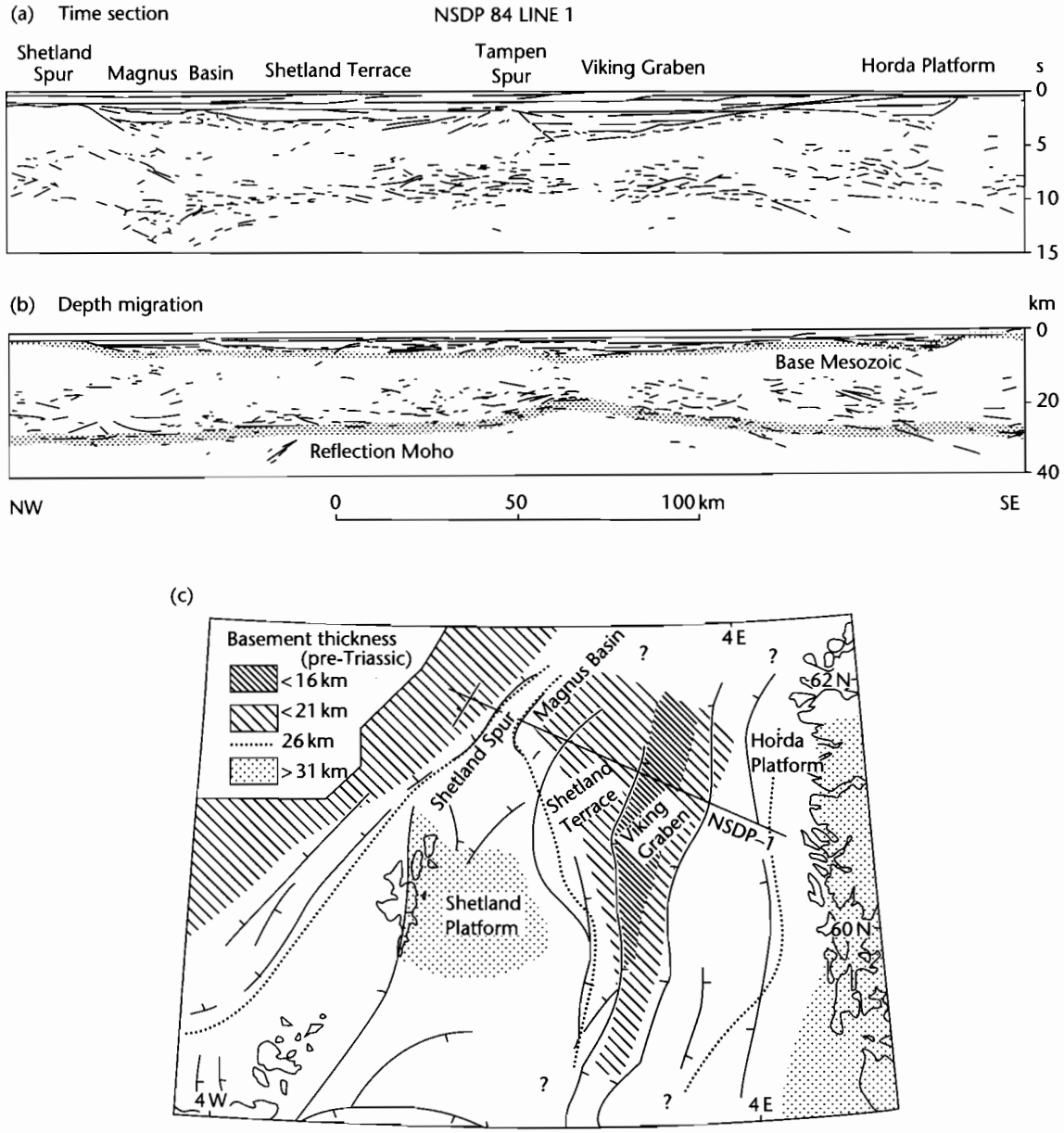

Fig. 3.4 Crustal thickness changes in the North Sea area as a result of Mesozoic rifting (after Klemperer 1988). (a) Unmigrated line drawing in two-way travel time of NSDP line 1 from the Shetland Spur to the Norwegian coast (location in (c)); (b) Depth-migrated version showing the depth of the reflection Moho; (c) Contour map of the interpreted thickness of the prerifting basement (pre-Triassic) showing that the Viking Graben has been stretched by a factor of 2 compared to the Shetland Platform.

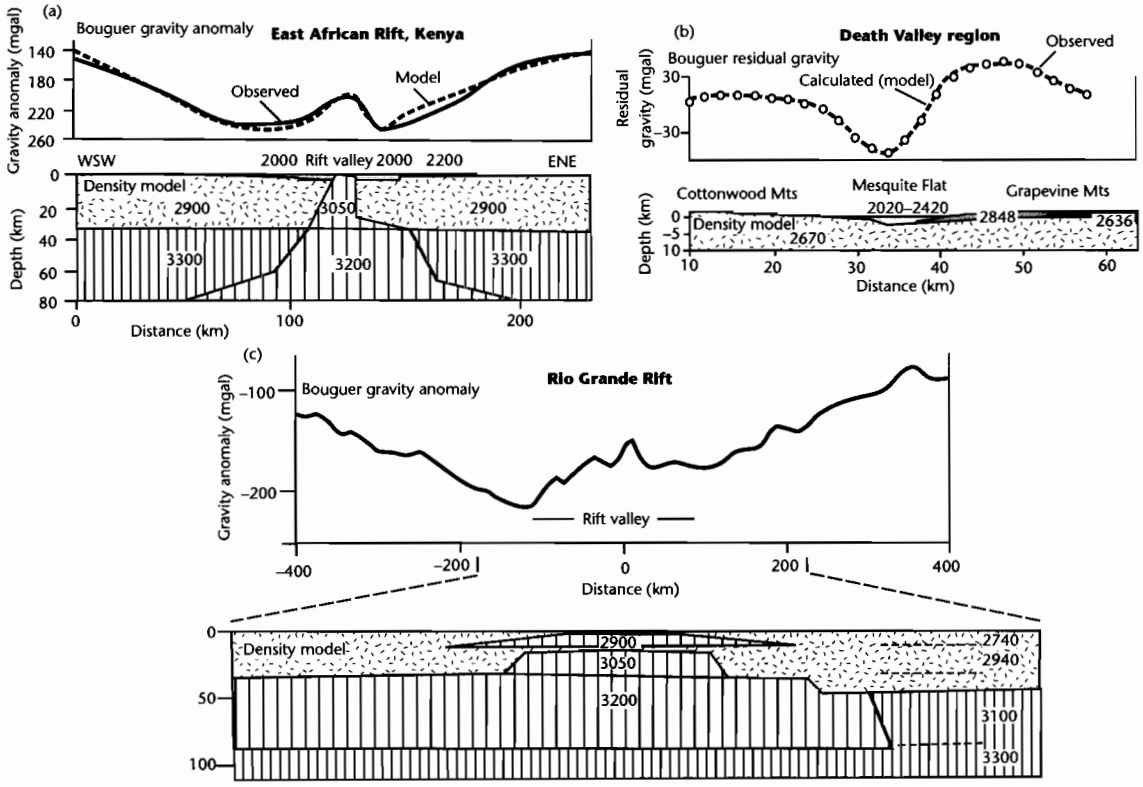

Fig. 3.5 Gravity profiles across rift zones. (a) Gravity profile and density model across the Gregory Rift, Kenya. The secondary gravity high is modeled as due to the intrusion of dense magma bodies beneath the rift valley (after Baker and Wohlenberg 1971); (b) Gravity profile and density model for a profile across Mesquite Flat, northern Death Valley, California (after Blakeley et al. 1999); (c) Gravity profile (*c.* 33 °N) and density model for the Rio Grande Rift of New Mexico (after Ramberg 1978). The secondary gravity high is thought to be due to the presence of dense igneous bodies beneath the rift. Densities shown in $kg\,m^{-3}$.

active extension and overlies crust as much as 70 km thick.

Gravity: It has been recognized for some time that rift zones have characteristic gravity signatures – typically a long wavelength Bouguer gravity low (Fig. 3.5) with sometimes a secondary high located in the centre of the rift zone (Fig. 3.5a, c). The conventional explanation is that rift zones have anomalously hot material in the mantle beneath the rift, producing a mass deficit and therefore a negative gravity anomaly. The subsidiary gravity high is thought to be due to the intrusion of dense magma bodies within the continental crust. Regions of widespread, diffuse extension such as the Basin and Range province of SW USA show a series of gravity highs corresponding to basement blocks, and *c.* 20 km-wide gravity lows corresponding to sedimentary basins (Fig. 2b). The gravity lows most likely reflect the mass deficit of light basin sediments.

Faults: Rift zones are typified by normal dip–slip faults with a variable number of strike–slip faults depending on the orientation of the rift axis in relation to the bulk extension direction. Consequently, the central Death Valley Basin is close to orthogonal to the extension direction and is typified by dip–slip normal faults, whereas the northern Death Valley Basin is more oblique and has faults with important strike–slip motion (Burchfiel and Stewart 1966). Faults in rifts are not infinite in extent: instead there is a displacement–length relationship, with most of the

slip being taken up on a small number of interacting major fault segments. Fault displacement dies out towards the tips of fault segments. The Jurassic Brent–Strathspey–Statfjord fault array system in the North Sea Basin (McLeod et al. 2000), the Neogene fault array of the Gulf of Suez in eastern Sinai (Sharp et al. 2000) and the modern fault array of the Lake Tanganyika Basin (Rosendahl et al. 1986) are all excellent examples. Most major border faults dip steeply inwards towards the basin centre and are planar as far as they can be imaged. However, some rift bounding faults are low-angle and listric, taking up very large amounts of horizontal extension, as in the supradetachment basins of SW USA. Metamorphic rocks may be unroofed from <25 km depth in these "core complexes" (Wernicke 1985).

Topography: Currently or recently active rift zones typically have elevated rift flank topography bordering a depositional basin. There may be two length scales of surface uplift. The best examples of the large length scale (several hundred km) are the >3 km-high topographic swells of Ethiopia and East Africa (Baker et al. 1972; King and Williams 1976) (Fig. 3.6). Other domal uplifts are found in northern Africa such as those in the Tibesti and Hoggar regions. These swells are commonly associated with widespread volcanic activity. Whereas the large

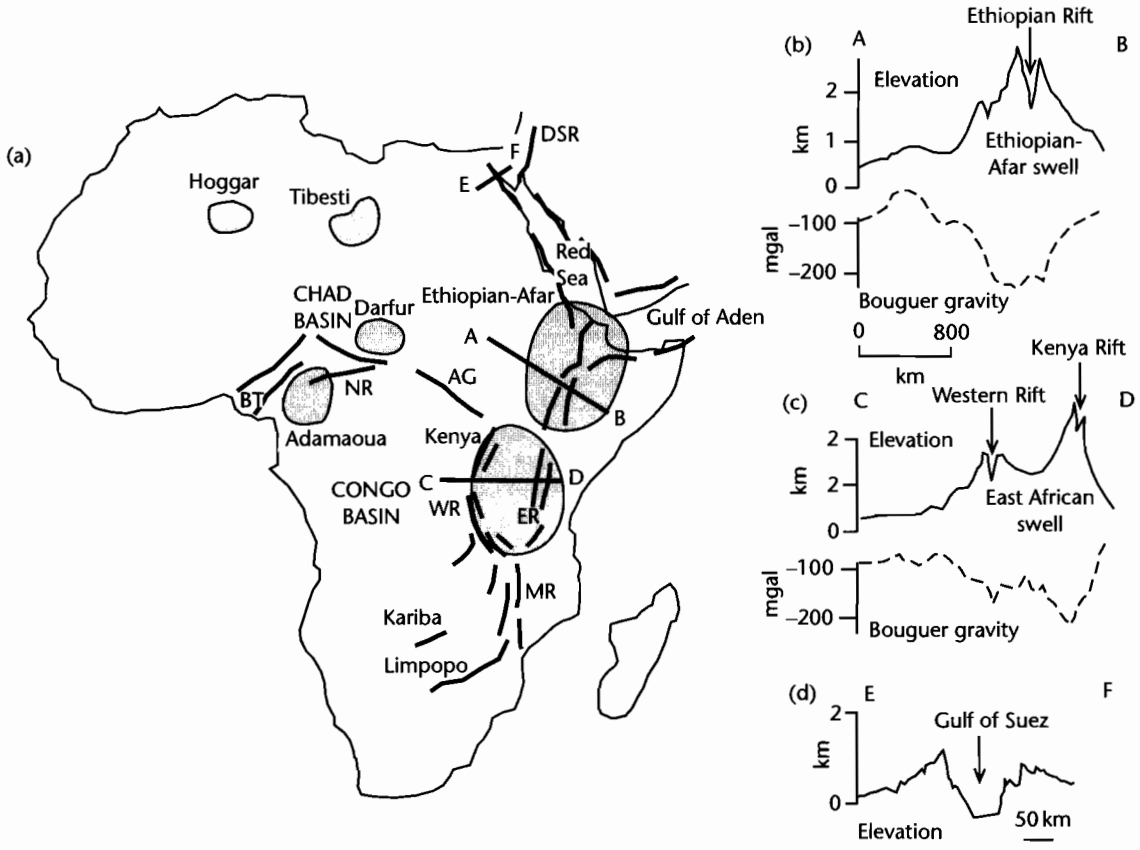

Fig. 3.6 (a) The major domal uplifts of Africa (Afar and East African domes) are due to uplift over hotspots in the mantle. Also shown are the smaller topographic uplifts of central Africa, and the main rift systems: AG, Abu Gabra Rift; BT, Benue Trough; DSR, Dead Sea Rift; MR, Malawi Rift; ER and WR, Eastern and Western Rifts; NR, Ngaoundere Rift. Topographic and Bouguer gravity profiles across the Afar (A–B) and East African (C–D) swells are shown in (b) and (c). (d) Topographic profile along E–F showing rift flank uplift along the Red Sea and Gulf of Suez. After Ebinger et al. (1989).

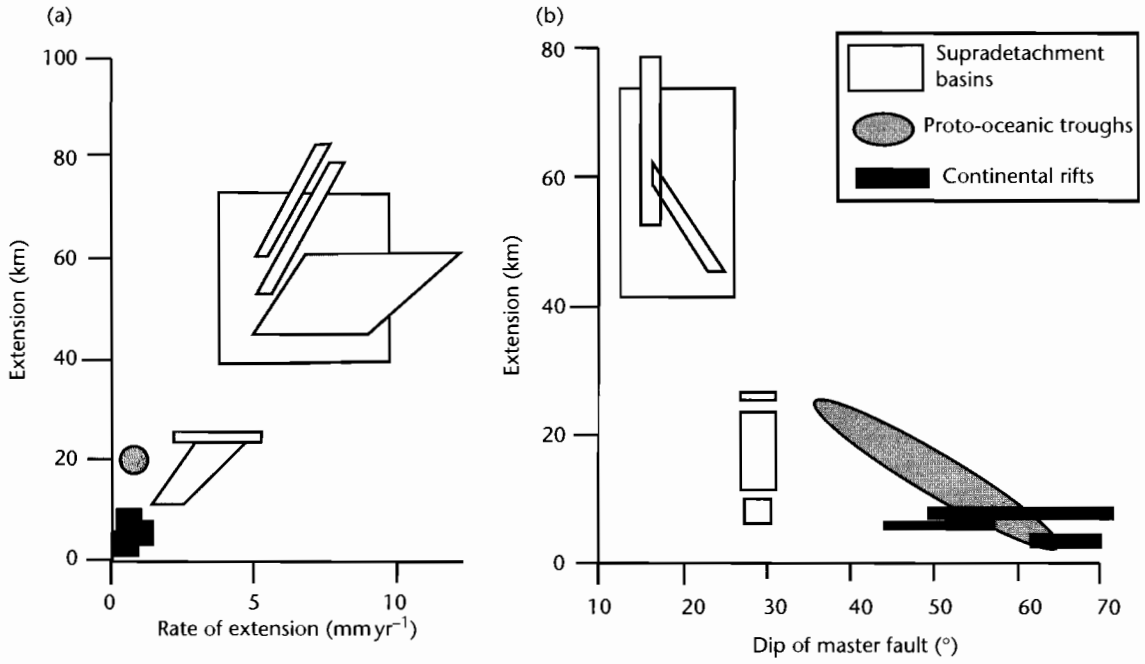

Fig. 3.7 Rifts, supradetachment basins, and proto-oceanic troughs in terms of their strain rate, total extensional strain, and dip of master faults, based on Friedmann and Burbank (1995). Reproduced courtesy of Blackwell Publishing Ltd.

domes of eastern and northeastern Africa are currently undergoing rifting, the smaller domes of north-central Africa are not. At a smaller length scale (<100 km) are the linear rift flank uplifts associated with border fault arrays. The <1 km-high highlands bordering the Gulf of Suez are a good example. Border fault footwalls involve upward tectonic fluxes, leading to enhanced denudation. In the southern Rhine Graben, tectonically driven exhumation of the rift flank has resulted in 2–3 km of erosion, exposing Hercynian crystalline basement in the Vosges of Alsace (France) and the Black Forest of Germany. Regions of extensive, diffuse extension are associated with plateau-type topography, such as the Basin and Range, USA and especially Tibet. In the first case, shallow subduction of relatively buoyant oceanic lithosphere beneath the North American Plate, and in the second case, thickening of continental lithosphere during India Asia collision, are the driving forces for extensive topographic uplift and extension.

Time scale and amount of extension: Extensional basins vary greatly in their duration of subsidence, total extensional strain, and therefore in their strain rate. Friedmann and Burbank (1995) believed there were two distinct families of basins, which could be recognized according to their strain rate, total extensional strain (or stretch factor β), and the dip of master faults (Fig. 3.7):

- Discrete continental rifts located on normal thickness crust (such as the Rhine Graben, Baikal Rift, Rio Grande Rift) extend slowly (<1 mm yr^{-1}) over long periods of time (10–>30 Myr), with low total extensional strain (generally <10 km). Master fault angles are steep (45–70°). Seismicity suggests that crustal extension takes place down to mid-crustal levels. At higher strain rates, narrow rifts may evolve through increased stretching into passive margins;
- supradetachment basins occur within wide extended domains with thickened crust. They typically extend quickly (<20 mm yr^{-1}) over short periods of time (5 12 Myr) with a high amount of total extensional strain (10–80 km). Master faults (detachments) are shallow in dip (10–30°), but may have originated at higher angles. Local anomalies in the ductile lower crust are amplified to produce core complexes (Wernicke 1985).

Table 3.1 Conjugate margins of the Atlantic.

Western margin	Eastern margin	Start of main rifting and duration
Southern Grand Banks	Iberia/Galicia	Valanginian (137 Ma) 15–25 Myr
Flemish Cap	Goban Spur	Barremian (127 Ma) 15–20 Myr
Labrador	SW Greenland	Barremian (127 Ma) 40–65 Myr

3.2.2 Passive continental margins

Passive continental margins involve strongly attenuated continental crust stretched over a region of 50–150 km, and exceptionally as much as 400–500 km (Keen et al. 1987), overlain by thin or thick sediment prisms. They are in general seismically inactive, and in mature examples heat flows are near-normal. Passive continental margins (also known as Atlantic-type margins) are characterized by seaward thickening prisms of marine sediments overlying a faulted basement with synrift sedimentary sequences, often of continental origin. The postrift seaward-thickening sediment prisms consist predominantly of shallow marine deposits. Seismic reflection sections show some passive margins to be underlain by linked listric extensional fault systems which merge into low-angle sole faults. The postrift or drifting phase in contrast is typically dominated by gravity-controlled deformation (salt tectonics, mud diapirism, slumps, slides, listric growth faults in soft sediments).

Passive margins overlie earlier rift systems that are generally subparallel to the ocean margins, or less commonly at high angles to the ocean margin (as in the case of failed arms of triple junctions such as the Benue Trough, Nigeria), or along transform fault zones (e.g., Grand Banks and Gulf of Guinea). The early synrift phase of sedimentation is commonly separated from a later drifting phase by an unconformity (the "break-up" unconformity of Falvey 1974). Some passive margins exhibited considerable subaerial relief at the end of rifting (leading to major unconformities), as in the case of the Rockall Bank, northeastern Atlantic, whereas in others the end of rifting may have occurred when the sediment surface was in deep water, as in the Bay of Biscay and Galicia margin of Iberia (Montadert et al. 1979).

Two end-members of passive margin can be identified based on the thickness of sediments (Fig. 3.8): (i) starved margins (2–4 km thick), and (ii) nourished margins (generally 5–12 km thick). In the central Atlantic, the American margin is nourished whilst the European margin is starved. In addition, some passive margins are associated with strong volcanic activity (Fig. 3.8), generally tholeiitic, at the time of break-up (White and McKenzie 1989). This volcanicity is commonly associated with subaerial emergence, as in the northern North Atlantic in the Early Tertiary (e.g., Skogseid et al. 2000).

Since passive margins represent the rifted edges of a piece of continental lithosphere, now separated by an ocean basin, it is possible to identify the original matching margins on either side of the ocean. These are known as *conjugate margins*. They are particularly well developed on either side of the northern Atlantic (Table 3.1).

Comparison of conjugate margins is informative regarding the geometry of extension prior to ocean basin development. For example, deep seismic reflection profiles show some conjugate pairs of passive margin to be symmetric, with seaward dipping, rotated fault blocks, whereas other deep profiles suggest the presence of a flat-lying or landward-dipping detachment or shear zone, producing a markedly asymmetrical pattern (Fig. 3.9). The profiles across the Labrador and SW Greenland margins show that although the brittle upper crust has been extended symmetrically, the lower crustal extension is particularly asymmetrical. Some margins show thin sediment covering wide regions of highly faulted, upper crust, commonly separated from underlying serpentinized upper mantle by a horizontal detachment (e.g., Iberia, Galicia, and SW Greenland margins). Other margins with thick sediment prisms consist of one or two major tilted crustal blocks and lack a horizontal detachment (e.g., Labrador margin).

In summary, these observations collectively suggest that there are a number of different archetypes of passive margin (Fig. 3.8):

- *Volcanically-active margins* are characterized by extrusive basalts, lower crustal igneous accretions, and significant uplift at the time of break-up. Continental extension and ocean spreading are thought to be intimately related to mantle plume activity;
- *nonvolcanic margins* lack evidence of high thermal activity at the time of break-up. Margins may be: (i) sediment-starved, with thin sediment veneers of 2–4 km draping large arrays of rotated synrift fault blocks above a subhorizontal detachment, as in the Bay

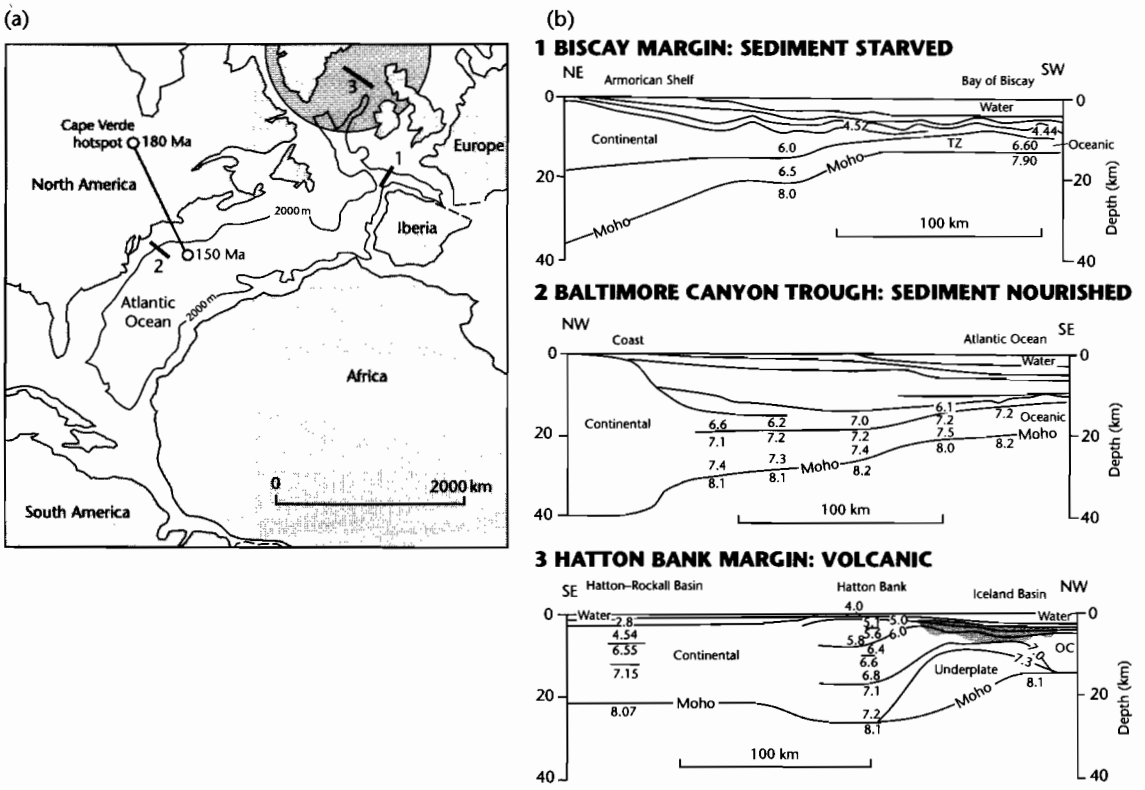

Fig. 3.8 Volcanic, sediment-nourished, and sediment-starved margins (after White and McKenzie 1989). (a) Location of margins in the central-north Atlantic region on a Middle Jurassic reconstruction (170 Ma), shortly after the onset of seafloor spreading; (b) Biscay margin, which is sediment starved; (c) Baltimore Canyon Trough margin, which is thickly sedimented; (d) Hatton Bank margin, which is characterized by important magmatic activity. Shaded area shows extent of extrusive basalts. Moho is overdeepened due to presence of igneous underplate. TZ, ocean–continent transition zone; OC, ocean crust. Reproduced courtesy of American Geophysical Union.

of Biscay, or (ii) sediment-nourished, with very thick (<15 km) postrift sedimentary prisms overlying a small number of tilted upper crustal fault blocks and a wide region of mid–lower crustal extension, as in the Baltimore Canyon region of the Eastern Seaboard of North America and the Labrador margin.

3.3 INTRODUCTION TO MODELS OF CONTINENTAL EXTENSION

3.3.1 Active and passive rifting idealizations

Early investigations of lithospheric extension suggested that rifting fell into two classes (Sengör and Burke 1978; Morgan and Baker 1983; Turcotte 1983; Keen 1985; Bott 1992), active and passive (Fig. 3.10). In *active rifting* deformation is associated with the impingement on the base of the lithosphere of a thermal plume or sheet. Conductive heating from the mantle plume, heat transfer from magma generation, or convective heating may cause the lithosphere to thin. If heat fluxes out of the asthenosphere are large enough, relatively rapid thinning of the continental lithosphere causes isostatic uplift. Tensional stresses generated by the uplift may then promote rifting. In *passive rifting* tensional stresses in the continental lithosphere cause it to fail, allowing hot mantle rocks to penetrate the lithosphere. Crustal doming and volcanic activity are only secondary processes. McKenzie's (1978a) widely accepted model for the origin of sedimentary basins belongs to this class of passive rifting. If

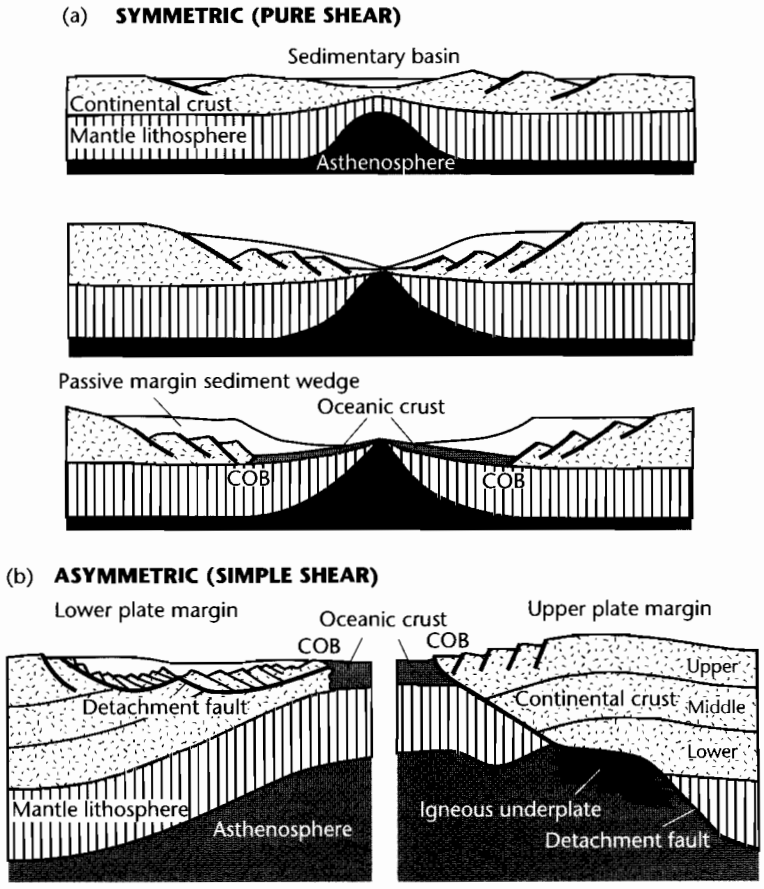

Fig. 3.9 Conjugate margins based on deep seismic information (after Lister et al. 1986; Louden and Chian 1999). (a) Symmetric margin (pure shear), and (b) asymmetric (simple shear) with a lithospheric detachment fault. COB is ocean–continent boundary. Reproduced courtesy of Royal Society London.

passive rifting is occurring, rifting takes place first and doming may follow but not precede it. Rifting is therefore a passive response to a regional stress field. It is not easy to determine whether a given rift is either active or passive, since for small mantle heat flows the amount of uplift may be minimal. In addition, it should be understood that active and passive models are idealized abstractions that represent "end-members." Real world cases may exhibit aspects of each (Khain 1992). The East African Rift appears to be a good candidate for active rifting whereas it has been suggested that the Rio Grande Rift may be due to passive rifting.

Some rifts are at high angles to associated plate boundaries, such as orogenic belts (Burke 1976, 1977). Some of these rifts appear to be linked to arms of triple junctions associated with the early stages of ocean opening – these failed rifts are termed *aulacogens*. Others are aligned at high angles to associated collision zones and are termed *impactogens* (Sengör et al. 1978) or *collision grabens* (Fig. 3.11). Whereas aulacogens are formed contemporaneously with the ocean opening phase, impactogens clearly postdate this period, being related temporally with collision. The Upper Rhine Graben has been cited as an example of an impactogen (Sengör et al. 1978) and collision in the Grenville orogeny has also been invoked as a cause of the Keweenawan Rift in North America (Gordon and Hempton 1986). The effects of compressional in-plane stresses on extensional basin development is discussed in §3.6.3.

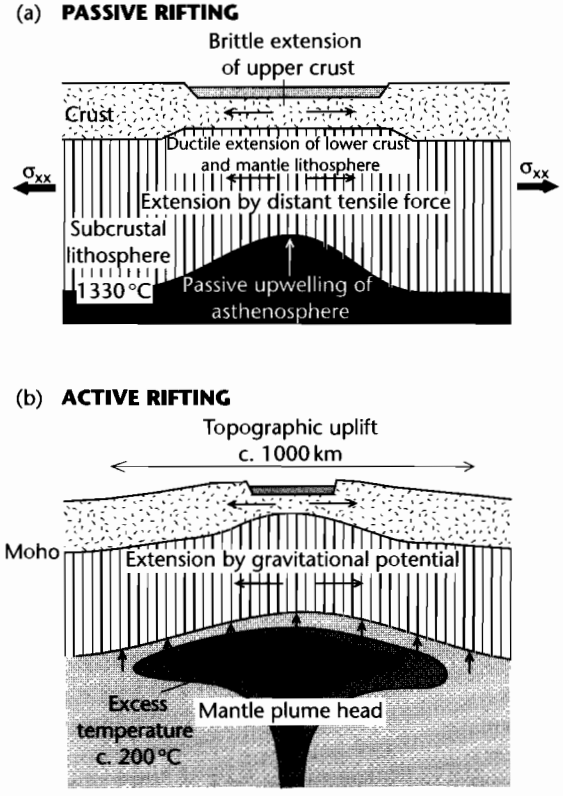

Fig. 3.10 Active and passive rifting end-member idealizations. (a) Passive rifting caused by a distant tensile deviatoric force σ_{xx} causes thinning of the lithosphere and passive upwelling of hot asthenosphere; (b) Impingement on the base of the lithosphere of a mantle plume causes long wavelength topographic doming and gravitationally driven extension of the lithosphere.

3.3.2 Postrift subsidence at passive continental margins

The synrift subsidence during stretching of the lithosphere is caused by brittle extension of the crust. Several mechanisms have been postulated as influences on the subsidence characterizing the postrift (or syn–drift) phase of passive margin development (§ 3.2.2).

It is universally agreed that the main mechanism for subsidence is cooling following lithospheric thinning: the upwelling of asthenosphere (McKenzie 1978a) is followed by thermal contraction (for detailed treatment see §3.4). Lithospheric stretching, however, may be accompanied by important magmatism, producing dyke swarms, plutons and extensive basaltic sheets (Royden et al. 1980; White and McKenzie 1989). Emplacement of large volumes of basaltic melt into the crust (or along its base) should produce transient uplift, followed by subsidence as the extruded, intruded, and underplated material cools. The result, long after emplacement, is determined by the density and thickness of the igneous additions to the lithosphere. Commonly, these igneous additions have a higher density than the crust but lower density than the mantle. Assuming that the bulk of the igneous accretion replaces lithospheric mantle, passive margins with large amounts of magmatic activity should remain relatively elevated compared to nonmagmatic margins (Fig. 3.12) (§3.7.2).

It has been postulated that subsidence may also result from phase changes (gabbro to eclogite) in lower crustal or mantle–lithosphere rocks. It is not known whether this process can be widespread enough to be responsible for significant amounts of subsidence at passive margins.

The growing sediment prism acts as a load on the lithospheric substrate and is supported isostatically. This may be by lithospheric flexure (Beaumont et al. 1982; Watts et al. 1982), as long as the wavelength of the load is sufficiently short. Historically, there was much debate as to whether flexural support involved an elastic plate or a viscoelastic (Maxwell) plate overlying a weak substratum (Watts et al. 1982). Since active faulting and high heat flows accompany the early stages of rifting, it has been assumed that an Airy isostatic model is most applicable during this period. However, postrift sediments are gently dipping and of wide extent, suggesting that flexure takes over at some stage after the end of rifting. Watts (1982) believed that the characteristic pattern of stratigraphic onlap on the eastern Atlantic and other margins suggested an increasing rigidity of the lithosphere with time – the expected result of an elastic lithosphere heated during the rifting stage and subsequently cooling.

3.3.3 Dynamical models involving lithospheric strength and rheology

In the last decade, emphasis has shifted away from active and passive rifting models and towards an understanding of the dynamics of stretching a piece of continental lithosphere with a particular strength and viscosity structure (Houseman and England 1986; Sonder and England 1989; Newman and White 1999). Increasingly, sophisticated numerical model predictions are examined alongside high-resolution 3-D seismic reflection data sets. The

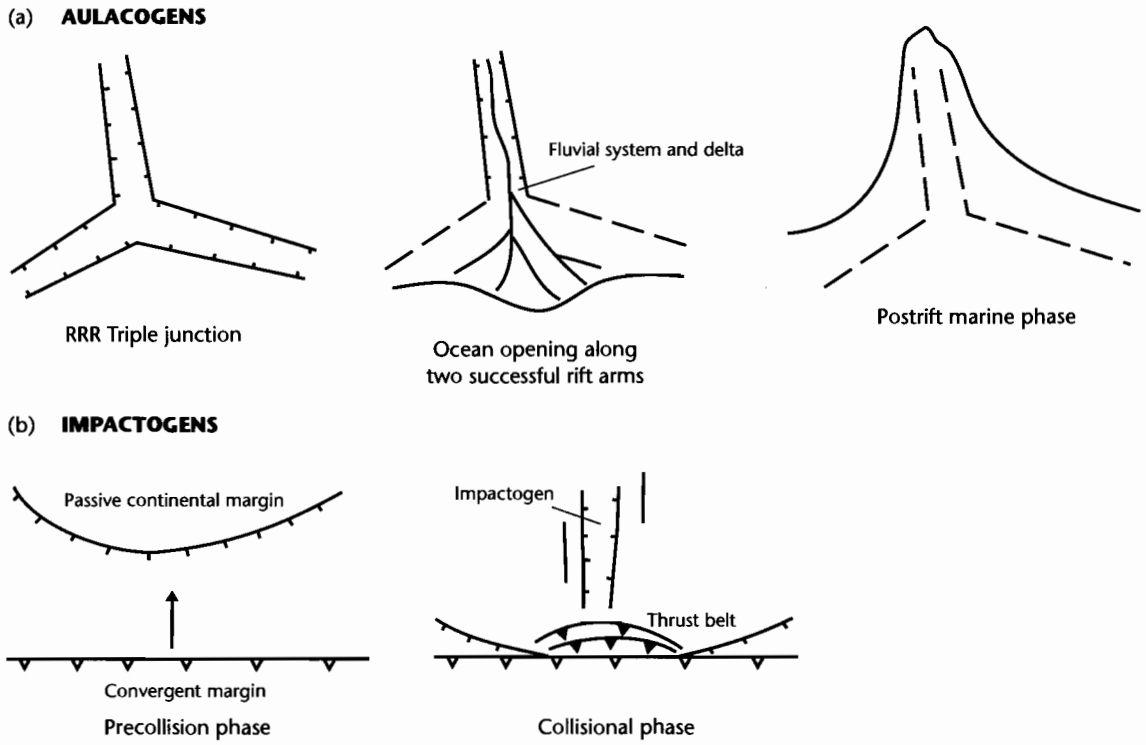

Fig. 3.11 Schematic diagrams to illustrate the development of (a) aulacogens and (b) impactogens, based on Sengör et al. (1978). In (a), successful opening of an ocean basin along two rift arms at a triple junction causes the development of a rift–sag basin along the third, failed rift arm. In (b), collision with a passive continental margin causes an extensional graben at high angles to the orogenic front.

fundamental infrastructure of these numerical models is the description of the rheology of the continental lithosphere (Fernandez and Ranalli 1997).

The *strength of the lithosphere* can be judged from laboratory experiments (e.g., Kohlstedt et al. 1995), though there is the problem of "scaling-up" laboratory experiments to the strain rates experienced by rocks in the lithosphere. The concept of the *strength envelope* (Goetze and Evans 1979; Ranalli 1995), which is the profile of lithospheric strength as a function of depth, underpins the rheological modeling of lithospheric extension and is discussed in greater detail in §2.4.6.

The *rheology of the lithosphere* and its response to extensional deformation is most strongly controlled by its temperature and its mineralogy. A material can only maintain stresses over geological time if the ratio of actual temperature to its melting temperature (known as the *homologous temperature*) is less than about 0.4. This implies that only the upper parts of the crust and upper mantle are capable of supporting elastic stresses over long periods of time. Most dynamic models of lithospheric extension use laboratory data for the dominant mineral comprising crust and mantle – that is, quartz + felspar for the crust, and olivine for the mantle. On a graph of stress at which failure takes place (σ_1–σ_3) versus depth in the continental lithosphere, two brittle–ductile transitions and two stress-supporting regions are predicted, one in the upper–midcrust, and the other in the upper mantle lithosphere (Figs. 1.3, 3.13). Since the quartz + felspar rheology of the continental lithosphere is weak at high temperatures, zones of orogenic thickening are prone to collapse by extension – an idea originally proposed by Tapponnier and Molnar (1976).

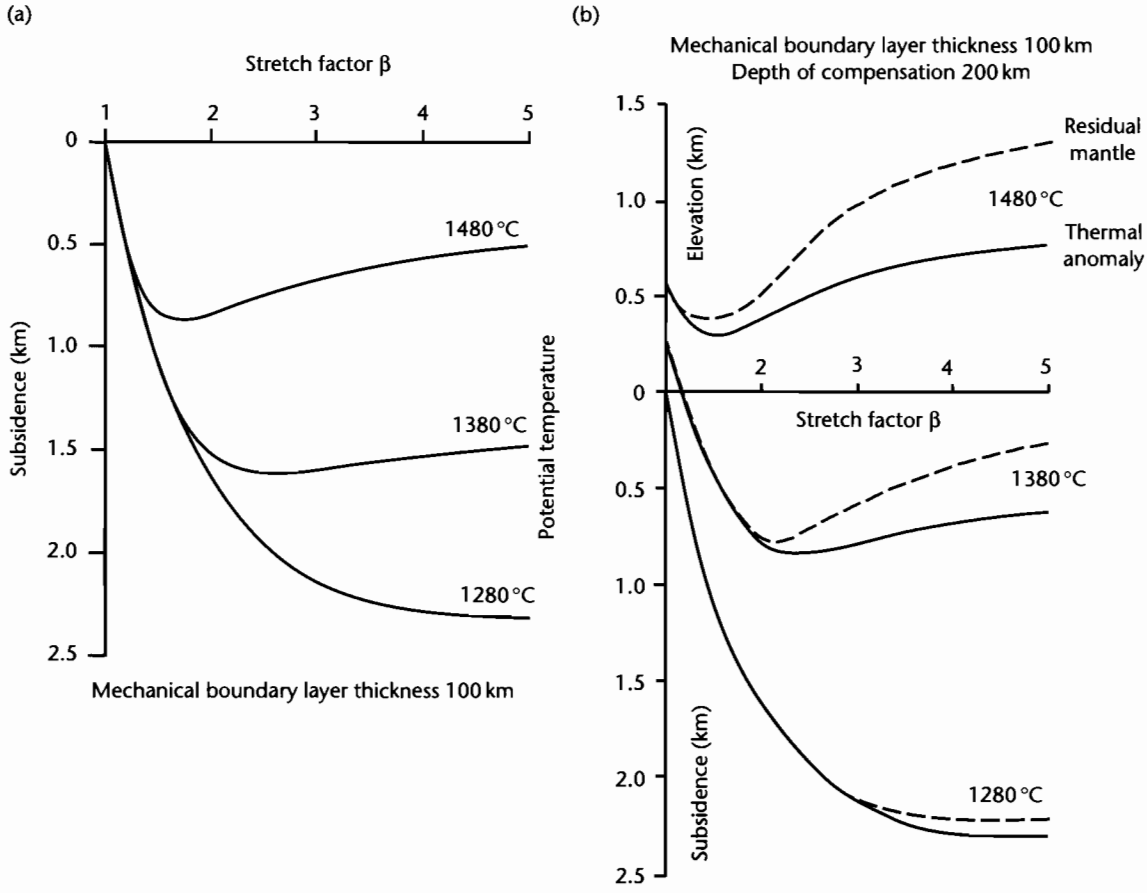

Fig. 3.12 Uplift and subsidence associated with plume activity at a spreading margin (after White and McKenzie 1989). (a) Subsidence at the time of rifting as a function of the stretch factor for potential temperatures of 1280 °C (normal), 1380 °C, and 1480 °C. Each curve incorporates the effects of lithospheric thinning, and crustal additions of melts caused by decompression of the mantle; (b) The effects of the reduced density of the abnormally hot asthenosphere (thermal anomaly) and the reduced density of the depleted mantle from which melt has been extracted (residual mantle) for three potential temperatures, as in (a). Plume activity causes the lithosphere to be elevated well above the level expected for an asthenosphere of normal temperature. The depth of compensation of 200 km is typical of the depth over which anomalously hot mantle is likely to extend. Reproduced courtesy of American Geophysical Union.

We will examine the results of numerical models of lithospheric extension in §3.6. One of the major results of numerical modeling is that the changing temperature field of lithospheric particles during extension results in a changing viscosity of the mantle lithosphere over time. Consequently, dependent on the initial strain rate, the extending lithosphere may extend rapidly into a runaway state, or may stop extending. This may explain dynamically the strain rate and bulk strain history of narrow rifts, wide rifts, and passive margins.

3.4 UNIFORM STRETCHING OF THE CONTINENTAL LITHOSPHERE

3.4.1 McKenzie's (1978a) uniform stretching model

Falvey (1974) proposed that the subsidence histories of various continental rift basins and margins could be explained qualitatively by extension in both crust and subcrustal lithosphere. The crust was assumed to fail by

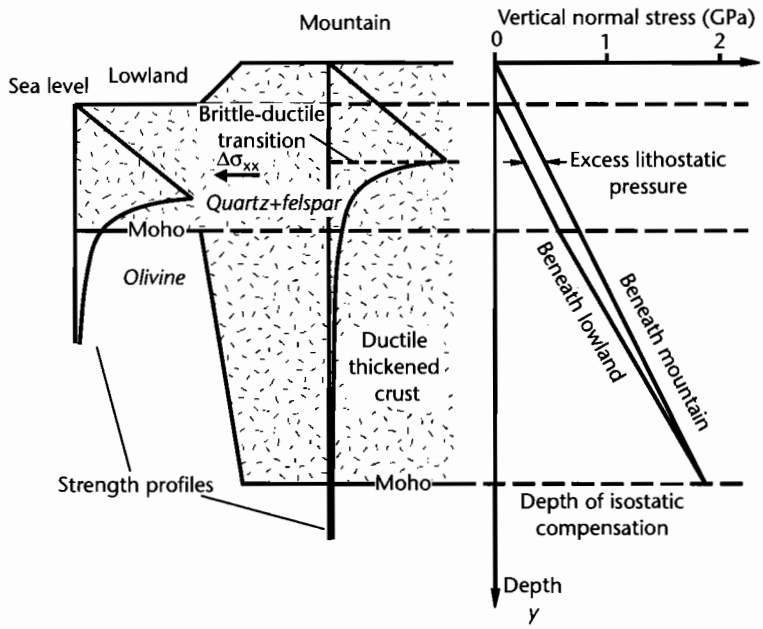

Fig. 3.13 Strength of the continental lithosphere and extensional collapse of thickened continental lithosphere. Thickened crust collapses for two reasons: (i) the quartz-felspar crust is rheologically weak, and (ii) the lithostatic stress is higher under the mountain than under the lowland region, causing it to spread laterally under a horizontal deviatoric stress (130 MPa at 10 km beneath the lowland). If the brittle yield strength of granite is 400 MPa, the brittle–ductile transition should be at a depth of *c.* 15 km beneath the mountain (density of granite 2750 kg m^{-3}).

brittle fracture and the subcrustal lithosphere to flow plastically. The isostatic disequilibrium caused by the crustal extension leads to a compensating rise of the asthenosphere, and consequent regional uplift. Partial melting of upwelled asthenosphere leads to volcanism and further upward heat transfer. Eventually, after the continental lithosphere has been extended and thinned to crustal levels, new oceanic crust is generated as the rift evolves into a continental margin.

McKenzie (1978a) considered the quantitative implications of a passive rifting or mechanical stretching model, assuming the amount of crustal and lithospheric extension to be the same (*uniform stretching*). The stretching is symmetrical, no solid body rotation occurs, so this is the condition of *pure shear*. He considered the instantaneous and uniform extension of the lithosphere and crust with passive upwelling of hot asthenosphere to maintain isostatic equilibrium (Fig. 3.14). The initial surface of the continental lithosphere is taken to be at sea-level and since the lithosphere is isostatically compensated throughout (Airy model), the subsidence or uplift consequent upon mechanical stretching can be obtained.

The results of McKenzie's (1978a) quantitative model of uniform stretching can be summarized as follows:

- The total subsidence in an extensional basin is made of two components: an initial *fault controlled subsidence* which is dependent on the initial thickness of the crust and the amount of stretching β; and a subsequent *thermal subsidence* caused by relaxation of lithospheric isotherms to their prestretching position, and which is dependent on the amount of stretching alone;
- whereas the fault-controlled subsidence is modeled as instantaneous, the rate of thermal subsidence decreases exponentially with time. This is the result of a decrease in heat flow with time. The heat flow reaches 1/e of its original value after about 50 Myr for a "standard" lithosphere, so at this point after the cessation of rifting, the dependency of the heat flow on β is insignificant.

The assumptions, boundary conditions, and development of the model are elaborated in the boxed text.

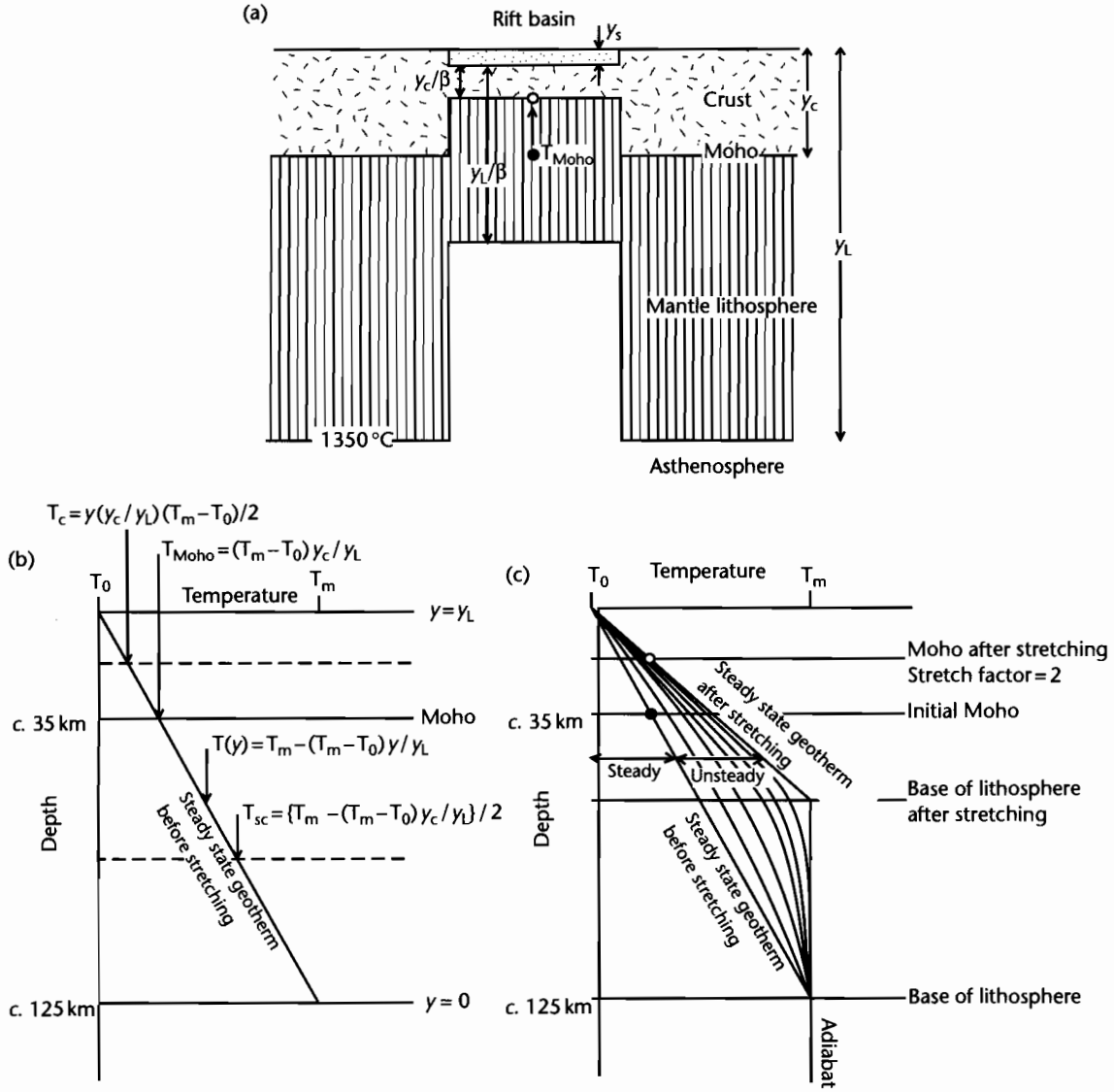

Fig. 3.14 Set-up for McKenzie's (1978a) uniform stretching model. (a) The crust and subcrustal lithosphere stretch horizontally and thin vertically uniformly with depth; (b) Derivation of average crustal and subcrustal temperatures from the steady state geotherm; (c) Geotherm following instantaneous stretching. The total temperature is made of steady and unsteady (transient) components. The transient temperature is shown as curves as a function of time.

BOXED TEXT 3.1: McKenzie's (1978a) Uniform Extension Model

The lithostatic column before rifting is made up of two components (see §2.1)

$$y_c\rho_c g + (y_L - y_c)\rho_{sc} g \tag{3.1}$$

where y_c and y_L are the thicknesses of the crust and lithosphere respectively, ρ_c and ρ_{sc} are the average densities of the crust and subcrustal lithosphere and g is the gravitational acceleration, which, because it is common to all lithospheric columns, can be ignored in the following analysis. These densities are assumed to have a linear relationship to temperature, and the geotherm is also assumed to be linear from T_m at the base of the lithosphere to T_0 at the surface (Fig. 3.14). As a result the average densities are given by

$$\rho_c = \rho_c^*(1 - \alpha_v T_c) \tag{3.2}$$

and

$$\rho_{sc} = \rho_m^*(1 - \alpha_v T_{sc}) \tag{3.3}$$

where ρ_c^* and ρ_m^* are crustal and mantle densities at 0 °C, α_v is the volumetric coefficient of thermal expansion and T_c and T_{sc} are the average crustal and subcrustal temperatures. Since the geotherms are linear, T_c and T_{sc} can be easily obtained as

$$T_c = \frac{(T_m - T_0)}{2}\frac{y_c}{y_L} \tag{3.4}$$

and

$$T_{sc} = \frac{1}{2}\left\{T_m - \frac{y_c}{y_L}(T_m - T_0)\right\} \tag{3.5}$$

By assuming that the surface temperature is 0 °C, these expressions simplify to

$$T_c = \frac{T_m}{2}\frac{y_c}{y_L} \tag{3.6}$$

and

$$T_{sc} = \frac{T_m}{2}\left(1 - \frac{y_c}{y_L}\right) \tag{3.7}$$

After rifting there are four components to the lithostatic stress at the depth of the original lithospheric thickness:

$$y_s\rho_s + (y_c/\beta_c)\rho_c + \{(y_L/\beta_L) - (y_c/\beta_c)\}\rho_{sc} + \{y_L - (y_L/\beta_L) - y_s\}\rho_m \tag{3.8}$$

where the new terms introduced are y_s, the thickness of sediment, water or air filling the rift axis; β_c and β_L, the stretch factors for the crust and lithosphere (for uniform stretching $\beta_c = \beta_L$); ρ_s, the average sediment, water, or air bulk density; ρ_{sc}, the subcrustal, lithospheric mantle density, equal to $\rho_m^*(1 - \alpha T_m)$ where ρ_m^* is the mantle density at 0 °C.

Balancing the columns before and after uniform stretching ($\beta_L = \beta_c = \beta$)

$$y_c\rho_c + (y_L - y_c)\,\rho_{sc} = y_s\rho_s + (y_c/\beta)\,\rho_c + (y_L - y_c)\,(1/\beta)\,\rho_{sc} + (y_L - y_s - y_L/\beta)\,\rho_m$$

Regrouping the terms

$$y_s = \frac{(1 - 1/\beta)}{(\rho_m - \rho_s)}\{\rho_m y_L - y_c\rho_c - (y_L - y_c)\rho_{sc}\} \tag{3.9}$$

Substituting the correct terms for ρ_c, ρ_{sc}, ρ_s, and ρ_m into (3.9) we have after rearrangement

$$y_s = \frac{y_L\left\{\left(\rho_m^* - \rho_c^*\right)\frac{y_c}{y_L}\left(1 - \alpha_v\frac{T_m}{2}\frac{y_c}{y_L}\right) - \frac{\alpha_v T_m \rho_m^*}{2}\right\}(1 - 1/\beta)}{\rho_m^*(1 - \alpha_v T_m) - \rho_s} \tag{3.10}$$

where β is the stretch factor, y_L is the initial thickness of the lithosphere, y_c is the initial thickness of the crust, ρ_m^* is the density of the mantle (at 0 °C), ρ_c^* is the density of the crust (at 0 °C), ρ_s is the average bulk density of sediment or water filling the rift, α_v is the thermal expansion coefficient of both crust and mantle, T_m is the temperature of the asthenosphere, and y_s is positive for subsidence, negative for uplift. Typical values for the above parameters, mostly derived from oceanic lithosphere studies (Parsons and Sclater 1977), are $y_L = 125$ km, $\rho_m^* = 3330\,\text{kg m}^{-3}$, $\rho_c^* = 2800\,\text{kg m}^{-3}$, $\alpha_v = 3.28 \times 10^{-5}\,°\text{C}^{-1}$, and $T_m = 1333$ °C.

For all values of the stretch factor, the initial subsidence S_i is positive for values of crust/lithosphere thickness ratio of greater than 0.12, corresponding to a crustal thickness y_c greater than about 15 km within a lithosphere of 125 km (parameter values as above, and sediment density of $2000\,\text{kg m}^{-3}$). McKenzie's model therefore predicts an initial subsidence with no uplift where continental crusts are "normal" in thickness (Fig. 3.15). The initial subsidence caused by isostatic

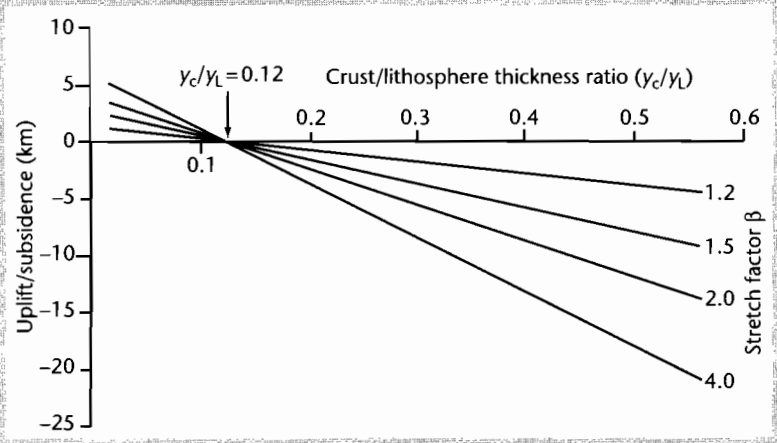

Fig. 3.15 Synrift subsidence as a function of the crustal/lithosphere thickness ratio y_c/y_L for stretch factors β between 1.2 and 4, using the uniform stretching model. Crustal, mantle and sediment densities are 2700 kg m^{-3}, 3300 kg m^{-3} and 2000 kg m^{-3} respectively. At a crust/lithosphere thickness ratio of 0.12 (corresponding to a crust of 15 km in a lithosphere 125 km thick), there is neither uplift nor subsidence during rifting. For thinner crusts, uplift occurs, and for thicker crusts, subsidence occurs. Since crustal thicknesses are typically 30–35 km, the synrift phase should be characterized by subsidence.

adjustment to mechanical stretching is followed by a long-term gradual subsidence caused by cooling and thermal contraction of the lithosphere following extension. This *thermal subsidence* is dependent on β alone.

The stretching of the lithosphere causes two responses: (i) the thinning of the crust and the fault-controlled subsidence is *permanent*, i.e., the brittle crust cannot regain its original thickness, and (ii) the thinning of the mantle lithosphere and any elevation changes caused by the presence of hot asthenosphere are *transient*.

In order to predict the cooling of the lithosphere following rifting that causes the thermal subsidence, we must know the heat flow through time. Following the *instantaneous* increase in heat flow accompanying rifting in the McKenzie (1978a) model, the heat flow decreases exponentially with time. We know two boundary conditions and we make two assumptions:

Boundary conditions:
(1) $T = 0$ at $y = y_L$
(2) $T = T_m$ at $y = 0$

Assumptions:
(1) lateral temperature gradients are much smaller than vertical gradients;

$$\left(\frac{\partial T}{\partial x} \approx 0 \approx \frac{\partial T}{\partial z}\right)$$

(2) internal heat production from radioisotopes is ignored.

The 1-D unsteady (that is, time-dependent) heat flow equation is

$$\frac{\partial T}{\partial t} = K\frac{\partial^2 T}{\partial y^2} \tag{3.11}$$

where the second derivative gives the curvature of the geotherm as it relaxes to its prestretching gradient. The temperature at any depth and time ($T(y, t)$) is made up of a steady-state solution $s(y) = T_m(1 - y/y_L)$ which applies to a linear geotherm in the lithosphere, and an unsteady-state component $u(y, t)$. The general solution for the unsteady term is

$$u(y,t) = \sum_{n=0}^{\infty} An \sin\left(\frac{n\pi y}{y_L}\right) \exp\left(\frac{-n^2\pi^2\kappa t}{y_L^2}\right) \tag{3.12}$$

where A is a constant and n is an integer that expresses the order of the harmonic of the Fourier transform, and κ is the thermal diffusivity. Therefore, as n increases, the negative exponential becomes very small and ceases to contribute to the unsteady temperature field. As a gross approximation it is frequently satisfactory to consider only $n = 1$. The constant A depends on the asthenospheric temperature (T_m) and the amount of stretching.

Continued

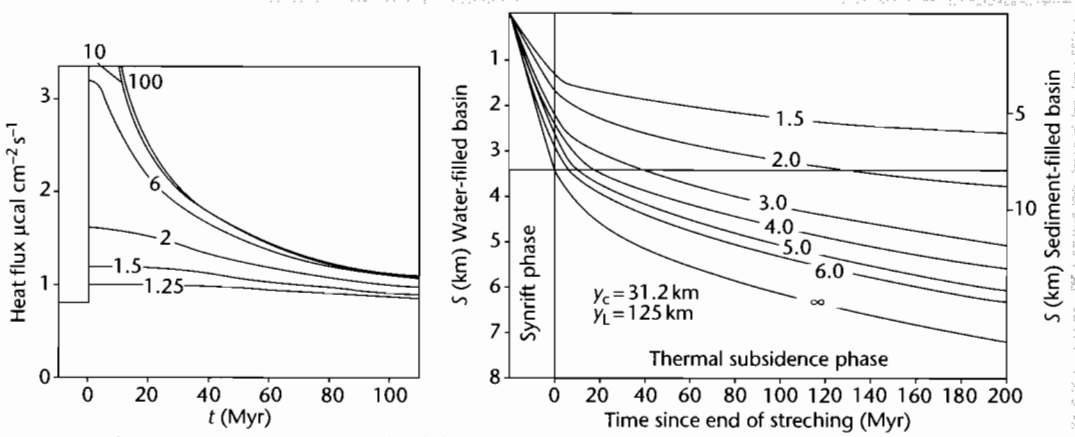

Fig. 3.16 Heat flow and subsidence as a function of the stretch factor using the uniform stretching model. (a) Heat flux against time (after McKenzie 1978a, p.28). After *c.* 50 Myr, the heat fluxes are similar for all values of stretch factor; (b) Elevation change (subsidence) against time for water-filled and sediment-filled basins, showing the negative exponential form of the subsidence history during the postrift, thermal contraction phase (after Sclater et al. 1980a).

At $t = 0$,

$$An = \left\{\frac{2}{n}(-1)^{n+1}\frac{\beta}{n\pi}\sin\left(\frac{n\pi}{\beta}\right)T_m\right\}$$

so if $n = 1$, An simplifies to $\frac{2}{\pi}\frac{\beta}{\pi}\sin\left(\frac{\pi}{\beta}\right)T_m$

The full solution for $T(y, t)$ is therefore the sum of the steady and unsteady components,

$$T(y,t) = T_m\left(1-\frac{y}{y_L}\right)+\left\{\frac{2}{\pi}\frac{\beta}{\pi}\sin\left(\frac{\pi}{\beta}\right)T_m\right\} \exp\left(-\frac{\pi^2\kappa t}{y_L^2}\right)\sin\left(\frac{\pi y}{y_L}\right) \quad (3.13)$$

or regrouping and simplifying

$$\frac{T(y,t)}{T_m} = \left(1-\frac{y}{y_L}\right)+\frac{2}{\pi}\frac{\beta}{\pi}\sin\left(\frac{\pi}{\beta}\right)\exp\left(-\frac{t}{\tau}\right)\sin\left(\frac{\pi y}{y_L}\right) \quad (3.14)$$

where $\tau = y_L^2/\pi^2\kappa$, and is known as the *thermal time constant* of the lithosphere.

The surface heat flux is given by Fourier's law (§2.2.1) which states that the flux is the temperature gradient times the thermal conductivity ($q_{y=L} = K\delta T/\delta y$). For $n = 1$, this is

$$q = \frac{KT_m}{y_L}\left\{1+\frac{2\beta}{\pi}\sin\left(\frac{\pi}{\beta}\right)e^{-t/\tau}\right\} \quad (3.15)$$

The subsidence caused by the thermal contraction is then given by

$$S(t) = E_0\frac{\beta}{\pi}\sin\left(\frac{\pi}{\beta}\right)\left(1-e^{-t/\tau}\right) \quad (3.16)$$

where

$$E_0 = 4y_L\rho_m^*\alpha_v T_m/\pi^2\left(\rho_m^*-\rho_s\right) \quad (3.17)$$

and ρ_s is the average density of the water or sediment filling the basin, ρ_m^* is the mantle density at 0 °C, α_v is the volumetric coefficient of thermal expansion, and the remaining terms are defined above.

The result of equation (3.15) is that heat flux is strongly dependent on the amount of stretching, the dependency becoming insignificant after about one thermal time constant (τ), or 50 Myr. At times younger than ~20 Myr, higher harmonics ($n = 2, 3 \ldots$) should be used in equation (3.12). Heat flux is sketched in Fig. 3.16a. Subsidence due to thermal relaxation is shown in Fig. 3.16b for comparison. If the subsidence history of a basin is known, it is therefore possible to estimate β from the thermal subsidence curve (§3.8.1).

Heat flux and subsidence calculated from the above uniform stretching model is provided in a Matlab exercise at www.erdw.ethz.ch/Allen.

3.4.2 Uniform stretching at passive continental margins

The uniform stretching model has been applied to the formation of passive margins (e.g., Le Pichon and Sibuet 1981). For the situation where stretching of the whole lithosphere occurs instantaneously at time $t = 0$ (or within a period of 20 Myr according to Jarvis and McKenzie 1980), heat production from radioactivity is ignored, local (Airy) isostatic compensation is maintained throughout, and the continental surface is initially at sea-level, the initial subsidence is given by equation (3.10). But since we are now dealing with passive margins, it is important to investigate the subsidence S_∞ at time $t = \infty$. The initial subsidence S_i (eqn 3.10) is a linear function of $(1 - 1/\beta)$ and S_∞ can also be expressed as a linear function of $(1 - 1/\beta)$. By introducing new parameters ρ'_{sc} and ρ'_c as the average densities of the subcrustal mantle part of the lithosphere and crust at time t_∞, the final subsidence S_∞ can be expressed

$$S_\infty = \frac{y_L(\rho'_{sc} - \rho_{sc}) + y_c\{\rho_{sc} - (\rho'_{sc}/\beta) + (\rho'_c/\beta) - \rho_c\}}{(\rho_m - \rho_w)} \quad (3.18)$$

The average densities of the subcrustal, mantle part of the lithosphere and the crust at time t_∞ are

$$\rho'_{sc} = \rho_m^*\left(1 - \frac{\alpha_v}{2}T_m - \frac{\alpha_v}{2}T_m\frac{y_c}{\beta y_L}\right) \quad (3.19)$$

and

$$\rho'_c = \rho_c^*\left(1 - \frac{\alpha_v}{2}T_m\frac{y_c}{\beta y_L}\right) \quad (3.20)$$

where, as a reminder y_L is the initial lithospheric thickness, y_c the initial thickness of the continental crust (at $t = 0$), the temperature at the base of the lithosphere is equal to the temperature of the asthenosphere T_m, ρ_m^*, and ρ_c^* are the densities of the mantle material and continental crust at 0 °C, ρ_w is the density of the seawater, α_v is the coefficient of thermal expansion. The average densities of the mantle part of the lithosphere, the crust before stretching and the asthenosphere are ρ_{sc}, ρ_c, and ρ_m.

From (3.18) to (3.20),

$$S_\infty = y_c(1 - 1/\beta)\left\{\frac{\rho_{sc} - \rho_c + \rho_m^*(\alpha_v/2)T_m + \varepsilon}{\rho_m - \rho_w}\right\} \quad (3.21)$$

where

$$\varepsilon = \left(\frac{\rho_m^* - \rho_c^*}{\beta}\right)\left(\frac{\alpha_v}{2}T_m\frac{y_c}{y_L}\right) \quad (3.22)$$

or by slight rearrangement,

$$S_\infty = y_c(1 - 1/\beta)\left\{\frac{(\rho_m^* - \rho_c^*)[1 - (\alpha_v/2)T_m(y_c/y_L)]\varepsilon}{(\rho_m - \rho_w)}\right\} \quad (3.23)$$

In fact, neglect of the additional term ε introduces an error of less than 0.5%.

The difference between the initial subsidence S_i and the final subsidence S_∞ is the subsidence caused by the progressive return to thermal equilibrium, i.e., that due to thermal contraction on cooling. The latter is termed thermal subsidence S_t and of course $S_t = S_\infty - S_i$.

3.4.2.1 Application to the sediment-starved Bay of Biscay and Galicia margins

As an example of this kind of analysis, it is possible to examine seismic reflection profiles across the northern Bay of Biscay and Galicia continental margins (Montadert et al. 1979) (Fig. 3.8a) and to test whether the uniform stretching model accurately predicts the observed subsidence. Active extensional tectonics started in the Late Jurassic–Early Cretaceous (*c.* 140 Ma). Extension extended outwards from a central region, creating new fault blocks which were progressively tilted. By the time oceanic crust was emplaced (120 Ma) the subsiding trough had reached a depth of about 2.4 km, and simultaneously active tectonics ceased, giving way to thermal subsidence. The Bay of Biscay is relatively starved of sediment, minimizing the effects of sediment loading compared to, say, the US Atlantic continental margin.

The following constants were chosen to fit the Biscay and Galicia data (Le Pichon and Sibuet 1981): $y_L = 125$ km (from Parsons and Sclater 1977); $y_c = 30$ km (from refraction data); $\rho_m^* = 3350\,\mathrm{kg\,m^{-3}}$; $\rho_c^* = 2780\,\mathrm{kg\,m^{-3}}$; $\rho_w = 1030\,\mathrm{kg\,m^{-3}}$; $\alpha_v = 3.28 \times 10^{-5}\,^\circ\mathrm{C}^{-1}$ (from Parsons and Sclater 1977); $T_m = 1333\,^\circ\mathrm{C}$ (from Parsons and Sclater 1977). Using these constants, the initial fault controlled subsidence simplifies to

$$S_i = 3.61(1 - 1/\beta)\,\mathrm{km} \quad (3.24)$$

and the final subsidence becomes

$$S_\infty \sim 7.83(1-1/\beta)\,\text{km} \tag{3.25}$$

so the thermal subsidence is the difference between S_i and S_∞,

$$S_t \sim 4.21(1-1/\beta)\,\text{km} \tag{3.26}$$

However, since the Bay of Biscay margin is 120 Myr old rather than being infinitely old, S_{120} is somewhat smaller than S_∞. As a result, the total subsidence at 120 Myr is

$$S_{120} \sim 7.23(1-1/\beta) \tag{3.27}$$

and the thermal subsidence at 120 Myr is

$$S_{t120} \sim 3.64(1-1/\beta) \tag{3.28}$$

Mid-ocean ridge crests are generally at about 2.5 km water depth, suggesting that zero-age oceanic lithosphere under 2.5 km of water is in equilibrium with a "standard" continental lithospheric column. Therefore during rifting, the asthenosphere should theoretically not be able to break through the thinned continental lithosphere as long as S_i is less than 2.5 km. Using equation (3.24) for the initial subsidence, the stretch factor required to produce 2.5 km of subsidence is 3.24; the crust by this time will be reduced in thickness to 9.25 km and will most likely be highly fractured – it is likely therefore that the asthenosphere would break through when this depth was reached. This represents the continent–ocean transition.

In the Bay of Biscay the estimated total subsidence at 120 Myr since rifting (S_{120}) for $\beta = 3.24$ is 5.2 km (eqn 3.27) and the final subsidence (S_∞) for an infinitely large β is 7.8 km (eqn 3.25). One should therefore expect to find continental crust in the Bay of Biscay at water depths of 5.2 km or shallower in the absence of sedimentation. [With the addition of a sediment load driving further subsidence, the entire sedimentary column could be as much as 15 to 20 km thick.] Oceanic crust should not be found at shallower water depths.

The extension estimated from fault block geometries in the upper crust is relatively high (*c.* $\beta = 2.6$) based on migrated seismic reflection profiling, indicating that the crust is substantially thinned and close to the value at which the asthenosphere could break through. Along the seismic profile the depth to the surface of the continental block is 5.2 km, which suggests that the model very satisfactorily explains the main features of the Biscay margin.

A regional synthesis suggests that water depth varies linearly with the thinning of the continental crust, following a relation close to

$$S_w = 7.5(1-1/\beta) \tag{3.29}$$

which is almost identical to the model prediction (eqn 3.27).

It is perhaps surprising that the Biscay and Galicia data fit the simple uniform stretching model so well. This is probably because during phases of rapid stretching, and in the absence of large sediment loads, the lithosphere is compensated on a local scale rather than responding by flexure.

3.4.2.2 The sediment-nourished eastern US and Canadian passive margin

It has been known for decades that the US and Canadian Atlantic margin is very thickly sedimented, with over 10 km along most of the margin, and considerably more in areas such as the Baltimore Canyon where a deep offshore well (COST B-2) was drilled in March 1976 (Poag 1980). The subsidence history of thickly sedimented margins such as this is profoundly affected by the *sediment load*. The sediment load is supported by the rigidity of the plate, and the borehole records (and seismic reflection profile data) need to be *backstripped* to obtain the tectonic subsidence (§8.3.3).

The main structural regimes of the US continental margin are shown in Fig. 3.8b. From landward to seaward, the *coastal plain* contains a seaward-thickening wedge of sediments. Basement depth increases rapidly in the *hinge zone*, thought to represent the transition between relatively undeformed continental crust and the highly attenuated and heated crust that has been modified by rifting. Seaward of the hinge zone lies the locus of the thickest sediment accumulations and still further seaward lies the true *oceanic crust*.

The backstripped COST B-2 well can be compared with theoretical curves to estimate the amount of extension. Using a simple uniform extension model, β varies from 3–3.5 for Airy isostasy, to 5 (up to mid-ocean ridge values) using a flexural isostatic model. The Airy results and the flexural results probably bracket a realistic estimate of about $\beta = 4$, which would suggest that the continental crust has been thinned to almost the oceanic

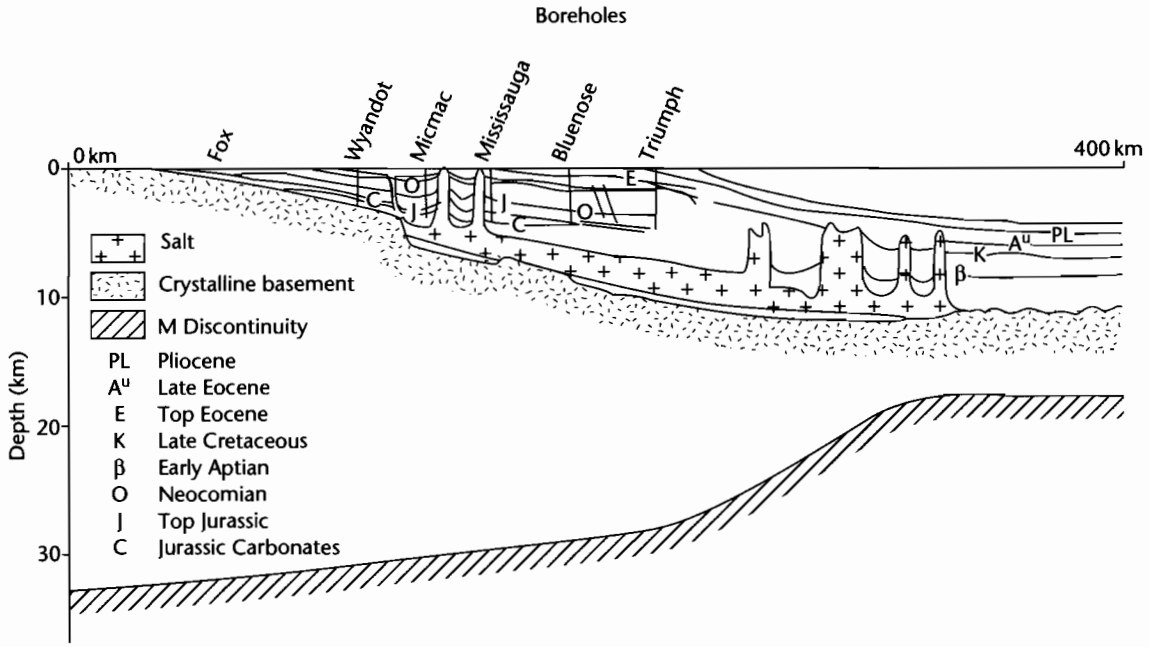

Fig. 3.17 Composite cross-section of the Scotian basin and crust. The sediment–basement interface is based on wells that penetrate it in addition to seismic reflection and refraction observations (Jansa and Wade 1975). After Beaumont et al. (1982).

thickness. This is supported by gravity modeling of crustal thickness (Grow et al. 1979).

The magnitude of the tectonic subsidence (and extension) varies systematically across the margin. Extension seaward of the hinge zone reaches values as great as $\beta = 4$, whereas the hinge zone has suffered much less extension ($\beta = 1.5$–2.0), and there is no synrift extension landward of the hinge zone, postrift subsidence being accomplished by thermal contraction and flexure.

The passive margin off Nova Scotia is one of the best studied mature examples available. The margin underwent rifting between 200 and 180 Ma. Its thick stratigraphy is well known from deep exploratory boreholes and seismic reflection data, and the deepest parts of the basin together with the variation in crustal thickness in the ocean–continental transition are known from seismic refraction. The composite cross-section is shown in Fig. 3.17.

In general, passive margins such as the US Atlantic and Scotian margins are adequately explained by a uniform stretching model coupled with melt segregation from the asthenosphere and migration into the crust (see §3.5.5), with postrift subsidence influenced by flexural support for thick sediment loads (§3.5.8). The importance of nonuniform, depth-dependent stretching is assessed in §3.5.1.

3.5 MODIFICATIONS TO THE UNIFORM STRETCHING MODEL

It is clear that there are a number of observations in regions of continental extension that suggest that the assumptions in the uniform stretching model should be re-examined. As a summary, these assumptions (some are implicit rather than stated) are as follows:

1. Stretching is uniform with depth;
2. stretching is instantaneous;
3. stretching is by pure shear;
4. the necking depth is zero;
5. Airy isostasy is assumed to operate throughout;
6. there is no radiogenic heat production;
7. heat flow is in one dimension (vertically) by conduction;

8 there is no magmatic activity;
9 the asthenosphere has a uniform temperature at the base of the lithosphere.

Modifications to the uniform stretching model invariably result in departures from the expressions for synrift and postrift subsidence given in equations 3.10 and 3.16. We briefly consider modifications to the uniform stretching model under the following headings:

- *Nonuniform (depth-dependent) stretching*: the mantle lithosphere may stretch by a different amount to the crust;
- *pure versus simple shear*: the lithosphere may extend along trans-crustal or trans-lithospheric detachments by simple shear;
- *protracted rifting*: continental rifts typically have synrift phases lasting 20–30 Myr;
- *elevated asthenospheric temperatures*: the base of the lithosphere may be strongly variable in its temperature structure due to the presence of convection systems such as hot plumes;
- *magmatic activity*: the intrusion of melts at high values of stretching modifies the heat flow history and thermal subsidence at passive margins;
- *induced mantle convection*: the stretching of the lithosphere may induce secondary mantle convection in the region of upwelled asthenosphere;
- *radiogenic heat production*: the granitic crust provides an additional important source of heat;
- *depth of necking*: necking may be centred on strong layers deeper in the midcrust or upper mantle lithosphere;
- *flexural compensation*: the continental lithosphere has a finite elastic strength and flexural rigidity, particularly in the postrift thermal subsidence phase.

3.5.1 Nonuniform (depth-dependent) stretching

Two families of models have been proposed to deal with the possibility of nonuniform stretching (Fig. 3.18):

- *Discontinuous* models, in which there is a discontinuity or decoupling between two layers with different values of the stretch factor β;

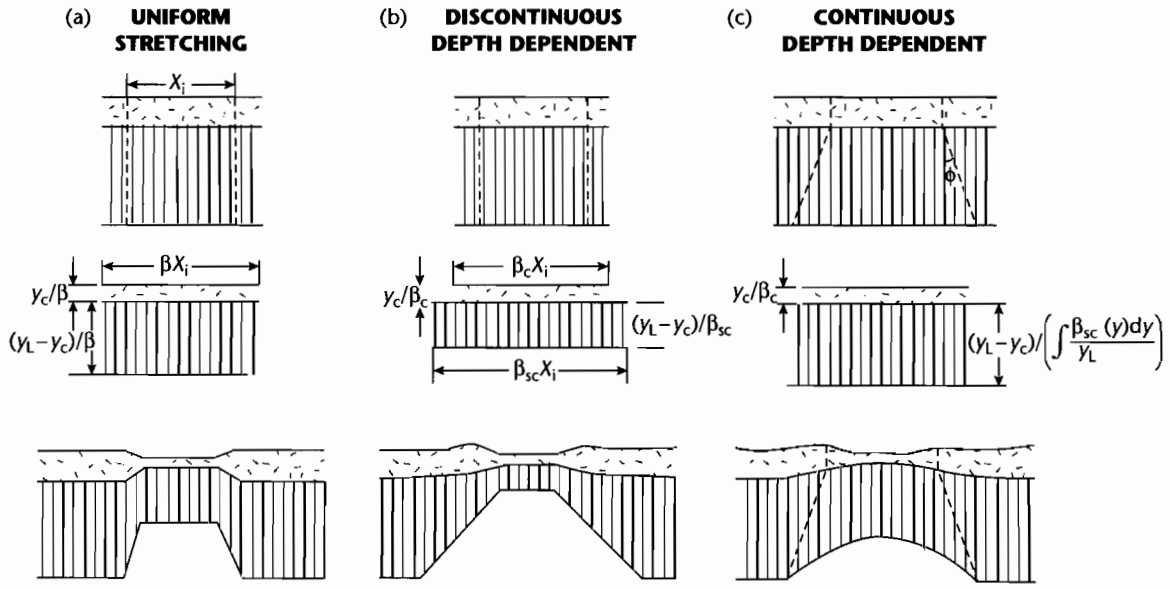

Fig. 3.18 Schematic diagrams to illustrate differences between (a) uniform, (b) discontinuous, and (c) continuous depth-dependent stretching. (a) Uniform extension in which the crust and subcrustal lithosphere extend by identical amounts; (b) Discontinuous depth-dependent extension in which the crust extends by a different amount to the subcrustal lithosphere, necessitating a decoupling between the two layers. The crustal and subcrustal extensions are independent but are uniform throughout the crust and subcrustal lithosphere (Royden and Keen 1980; Beaumont et al. 1982; Hellinger and Sclater 1983); (c) Continuous depth-dependent extension in which the stretching is a continuous function of depth in the subcrustal lithosphere and the crustal stretching is the same as in (a) and (b) (Rowley and Sahagian 1986).

- *continuous* models, where there is a smooth transition in the stretching through the lithosphere.

Critically, both sets of models make a first-order prediction – that zones of continental stretching should be characterized by elevated rift margin topography.

3.5.1.1 Discontinuous stretching with depth

Extension may not be uniform with depth because of the changing rheologic properties of the lithosphere. If the lithosphere extends inhomogeneously and discontinuously, there must be a depth d at which the upper and lower parts of the lithosphere are decoupled. This zone of detachment or shear is where listric faults in the overlying brittle zone sole out (Montadert et al. 1979; Kusznir et al. 1987). Structural evidence (e.g., seismic studies of the Basin and Range Province, Bay of Biscay and northwestern European continental shelf) demonstrates that some steep faults near the surface become listric into near-horizontal detachments where a transition to ductile behavior takes place. The focal depths of earthquakes in old cratons further suggest that while the upper part of the lithosphere has relatively high strength and is seismically active, the lower part is aseismic, probably due to the operation of ductile deformation mechanisms (Sibson 1983; Scholz 1988). In some instances at least, there may therefore be decoupling of the upper and lower zones at about midcrustal levels, allowing the two rheologic layers to extend by different amounts, giving a nonuniform discontinuous stretching.

The initial subsidence and thermal subsidence for the case of depth-dependent extension where the zone above d extends by β_c and the zone below d extends by ductile deformation by a different amount β_{sc}, is given by Royden and Keen (1980). If the lower zone stretches by ductile deformation more than the brittle upper zone, uplift should occur if the depth to decoupling approximates the crustal thickness ($d \approx y_c$). This uplift occurs at the same time as extension, and is an attractive feature of the model in view of the updoming characteristic of many present-day rift systems such as East Africa.

As an example of discontinuous depth-dependent stretching, in the centre of the Pattani Trough, Gulf of Thailand, the stretch factors for crust β_c and lithosphere β_L derived from subsidence plots were 2.35 and 1.90, indicating that crustal thinning was 20% greater than lithospheric thinning in the graben region (Hellinger and Sclater 1983).

The temporal relationship between faulting and rift flank uplift and the wavelength and amplitude of the rift flank uplift provide important constraints on the lithospheric stretching model. For example, if prerift sedimentary rocks are preserved in the graben but eroded from the flanks, it is a good indication that crustal uplift did not precede rifting. Footwall uplift may be due to coseismic strain along border faults, in which case the wavelength of the uplift (*c.* 10 km) will be smaller than the fault spacing. However, if the rift flank uplift has a much larger wavelength, it might imply that the subcrustal lithosphere was extended over a larger region than the more confined crustal extension. At first the crustal thinning, causing subsidence, outstrips the uplift from subcrustal thinning in the graben area, but the reverse is true beyond the graben edge. Later, after extensional tectonics has ceased, both flanks and graben should subside due to cooling and thermal contraction of the upwelled asthenosphere.

Regions initially at sea-level that are uplifted, such as graben flanks, are subject to erosion and theoretically should subside to a position below sea-level after complete cooling. But a second effect is the added crustal uplift caused by isostatic adjustment to the removed load. These two processes govern how much erosion will take place before the rift flanks subside below sea-level and erosion effectively stops. In the southern Rhine Graben, the present day surface uplift of the rift flanks is about 1 km. The erosional exhumation of footwall rocks is, however, of the order of 2.5 km (Illies and Greiner 1978). A further implication of rift flank erosion is an increase in the area of subsidence, so nonuniform extension models incorporating erosional effects predict larger subsiding basins than uniform extensional models. Regions that are not initially at sea-level prior to rifting, such as the Tibet Plateau and the Basin and Range province, have a different, lower base level for erosion.

A comparison of the stratigraphies generated by the uniform (one-layer) stretching model and the two-layer (depth-dependent) stretching model from the passive margin off New Jersey, USA is shown in Fig. 3.19. Both models show a well-developed coastal plain, hinge zone and inner shelf region underlain by a thick sequence of seaward dipping strata. The main difference is in the stratigraphy of the coastal plain, the one-layer model over-predicting synrift sediment thickness. The two-layer model, however, explains the lack of synrift (Jurassic) stratigraphy by the lateral loss of heat to the flanks of the rift, causing uplift and subaerial emergence.

3.5.1.2 Continuous stretching with depth

The implication of different amounts of stretching in the crust and mantle lithosphere is that there must be a

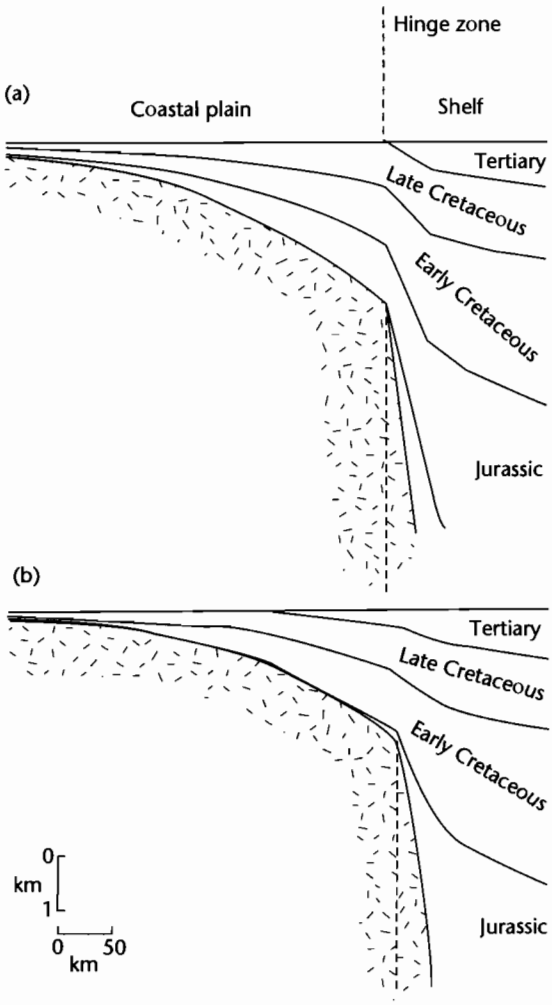

Fig. 3.19 Synthetic stratigraphy along profiles crossing the coastal plain and shelf off New Jersey constructed using the flexural loading model of Watts and Thorne (1984). (a) One-layer uniform stretching model; (b) two-layer model in which the lithosphere and crust are thinned by equal amounts seaward of the hinge zone, but only the mantle lithosphere is thinned landward of the hinge zone. The lithospheric thinning promotes early uplift of the zone landward of the hinge line, and helps to explain the absence of Jurassic strata from this region (after Steckler et al. 1988).

surface or zone of discontinuity separating the regions with the different values of β. Although such models are successful in explaining the common rift flank uplift that accompanies extension (e.g., Nova Scotian and Labrador continental margin, East African Rift, Red Sea, Rhine Graben), they have a number of requirements:

- The existence of an intralithospheric discontinuity, which although evident in some settings (e.g., Biscay Margin), is by no means universally "proven";
- a mechanism by which the mantle is detached and stretched by a different amount to the overlying crust, and a means of solving the attendant space problem in the mantle.

If the stretching is nonuniform but *continuous* with depth, these objections are removed (Rowley and Sahagian 1986). It is possible that the mantle may respond to extension as a function of depth, the strain rate decreasing as the extension is diffused over a wider region. This can be modeled by considering a geometry of an upward tapering region of stretching (Fig. 3.20). If ϕ is the angle between the vertical and the boundary of the stretched region in the mantle lithosphere, the amount of stretching depends on the depth beneath the crust and angle ϕ. The variation of β_{sc} with depth can then be integrated from the base of the crust to the base of the lithosphere to obtain estimates of initial and total subsidence in a similar fashion to the uniform stretching case. For large values of ϕ, the initial subsidence is increased but the amount of postextension thermal subsidence is decreased. The wider zone of mantle stretching results in uplift of the rift shoulders, and the horizontal length scale of the uplift is an indication of the value of ϕ. In the Gulf of Suez region, the horizontal width over which the topographic uplift occurs is about 250 km. Since the thickness of the subcrustal lithosphere is likely to be approximately 90 km, the taper angle ϕ is given by $\phi = \tan^{-1}(250/90) = 70°$. In the Rhine Graben, ϕ is approximately $\tan^{-1}(80/90) = 40°$.

A point in the rift shoulder region should therefore initially experience rock uplift, followed by a comparable amount of subsidence; if erosion has occurred, the final elevation of the point will be below its initial height. The same general pattern is observed where the crustal stretching varies from a minimum at the rift margin to a maximum at the rift centre (Fig. 3.20) (White and McKenzie 1988). The implications of stretching the mantle over a wider region than the crust (but with equal total amounts of extension) is that stratigraphic onlap should occur over previous rift shoulders during the

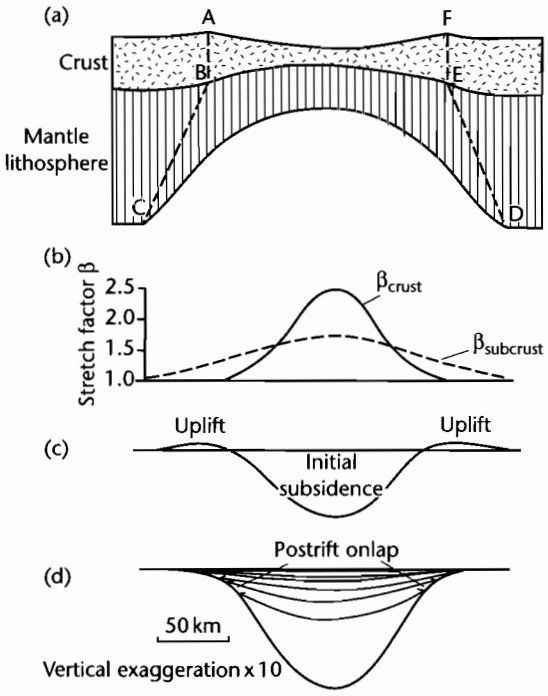

Fig. 3.20 Basin filling pattern resulting from continuous depth-dependent stretching (Rowley and Sahagian 1986; White and McKenzie 1988). (a) Geometry of a tapering region of extension in the subcrustal lithosphere; (b) Stretch factors in the crust and subcrustal lithosphere as a function of horizontal distance; (c) Initial subsidence and uplift immediately after stretching, showing prominent rift flank uplift; (d) Total subsidence 150 Myr after rifting, showing progressive onlap of the basin margin during the thermal subsidence phase, giving a "steer's head" geometry.

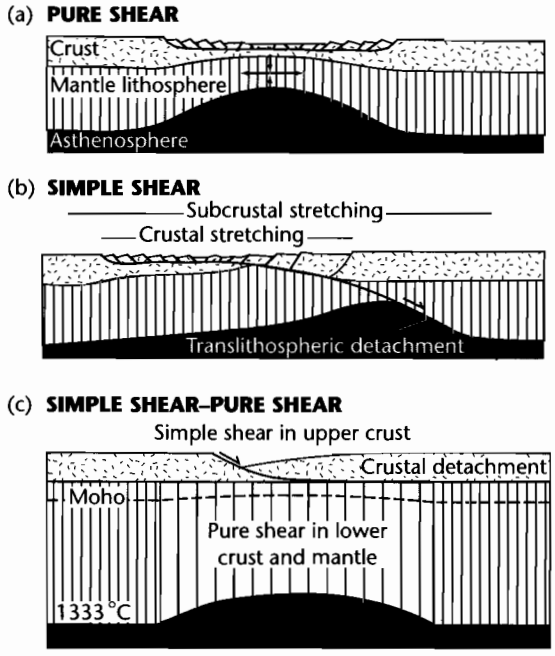

Fig. 3.21 Models of strain geometry in rifts (Coward 1986; Buck et al. 1988). (a) Pure shear geometry with an upper brittle layer overlying a lower ductile layer, producing a symmetrical lithospheric cross-section with the initial fault-controlled subsidence spatially superimposed on the thermal subsidence. The ductile stretching may be accompanied by dilation due to the intrusion of melts (Royden et al. 1980); (b) Simple shear geometry with a through-going low-angle detachment dividing the lithosphere into an upper plate or hangingwall, and a lower plate or footwall. Thinning of the lower lithosphere is relayed along the detachment plane, producing a highly asymmetrical lithospheric cross-section (after Wernicke 1981, 1985). Initial fault-controlled (synrift) subsidence is spatially separated from the thermal subsidence; (c) Hybrid model of simple shear in the upper crust on listric (shown) or planar faults, and pure shear in the ductile lower crust and mantle lithosphere (Kusznir et al. 1991).

postrift phase, a feature commonly found in "rift-sag" or "steer's-head" type basins.

3.5.2 Pure versus simple shear

The lithosphere may extend asymmetrically where the zone of ductile subcrustal stretching is relayed laterally from the zone of brittle crustal stretching (Buck et al. 1988 and Kusznir and Egan 1990 for quantitative analyses) (Fig. 3.21). This is the situation of *simple shear*. Wernicke (1981) proposed such a model, based on studies of Basin and Range tectonics, envisaging that lithospheric extension is accomplished by displacement on a large scale, gently dipping shear zone that traverses the entire lithosphere. Such a shear zone transfers or relays extension from the upper crust in one region to the lower crust and mantle lithosphere in another region. It necessarily results in a physical separation of the zone of fault-controlled extension from the zone of upwelled asthenosphere.

Wernicke (1981, 1985) suggested that there are three main zones associated with crustal shear zones (Fig. 3.22):

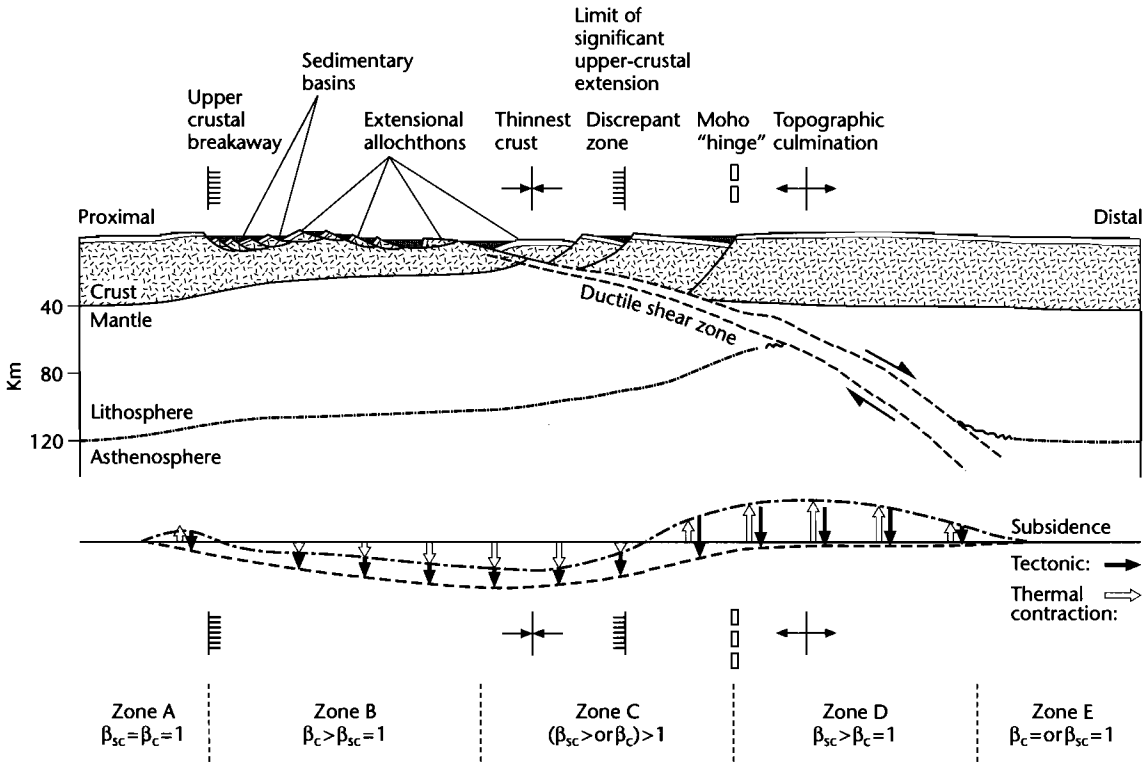

Fig. 3.22 Normal simple shear of the entire lithosphere, developed from the Basin and Range province of SW USA (Wernicke 1985). This geometry takes of the order of 10–15 Myr to develop. Midcrustal rocks in the hangingwall may initially pass through greenschist or amphibolite metamorphic conditions in the ductile shear zone, followed by uplift, cooling, and deformation in the brittle field.

(i) a zone where upper crust has thinned and there are abundant faults above the detachment zone, (ii) a "discrepant" zone where the lower crust has thinned but there is negligible thinning in the upper crust, and (iii) a zone where the shear zone extends through the subcrustal (mantle) lithosphere.

Since crustal thinning by fault-controlled extension causes subsidence but subcrustal thinning produces uplift, we should expect subsidence in the region of thin-skinned extensional tectonics but tectonic *uplift* in the region overlying the lower crust and mantle thinning (the discrepant zone of Wernicke). Subsequent asthenospheric cooling may result in one of two things. Thermal subsidence of the region above the discrepant zone may simply restore the crust to its initial level. However, if subaerial erosion has taken place in the meantime, thermal subsidence will lead to the formation of a shallow basin above the discrepant zone. The basement of the basin should be unfaulted. However, beneath the zone of thin-skinned extensional tectonics there should be minimal thermal subsidence.

Stretching of the lithosphere combined with unloading along major detachment faults can result in the unroofing of mantle rocks in their footwalls. These are called *core complexes* and *gneissic domes*. The turtlebacks of the Death Valley region and the Whipple Mountains of Nevada are examples (Wright and Coleman, 1974; Lister and Davis 1989).

Tectonic unloading may also result in flexural uplift of adjacent footwall areas along major detachment faults (Fig. 3.23). Kusznir et al. (1991) refer to this as the *flexural cantilever effect*. They use a model of simple shear in the

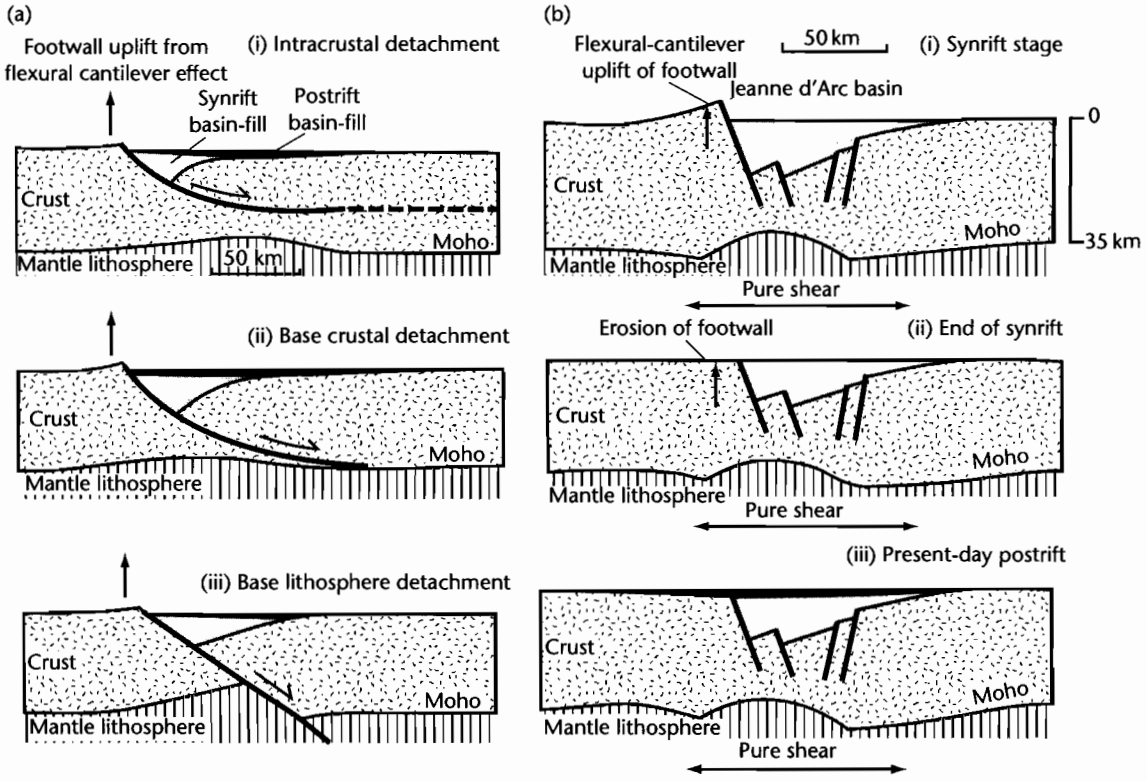

Fig. 3.23 Sedimentary basin geometry and crustal structure predicted by a simple shear–pure shear model including the flexural cantilever effect (Kusznir and Egan 1990; Kusznir et al. 1991). (a) Crustal structures after 100 Myr and 30 km extension with an equivalent elastic thickness of 5 km, for an intracrustal detachment (i), a base-crustal detachment (ii), and a base-lithosphere detachment (iii); (b) Sequential development of the Hibernia-Ben Nevis profile of the Jeanne d'Arc basin, showing flexural uplift and erosion of the unloaded footwall of the main detachment fault. The total amount of extension is 18 km, initial fault dip = 60°, initial crustal thickness is 35 km, and Te = 10 km. Reproduced courtesy of Geological Society of London.

crust and pure shear in the lithospheric mantle. The scale of the flexural cantilever effect depends on the depth at which the detachment soles out. The model has been successfully used to explain footwall uplift and erosion in the Jeanne d'Arc Basin, Grand Banks of Newfoundland, and Viking Graben, North Sea (Marsden et al. 1990; Kusznir et al. 1991), and Tanganyika Rift of East Africa (Kusznir and Morley 1990).

Models involving large-scale simple shear do not explain basins that have a thermal subsidence spatially superimposed on a fault-controlled subsidence, as in the North Sea (Klemperer 1988). Such examples are more suggestive of pure shear.

3.5.3 Protracted rifting and lateral heat conduction

The quantitative model of McKenzie (1978a) assumed instantaneous rifting of the lithosphere followed by thermal subsidence as the lithosphere re-equilibrates to its pre-extension thickness. This is an attractive assumption since it gives a simple, well-defined initial condition for the thermal calculations. Jarvis and McKenzie (1980) revised this 1-D model by allowing for protracted periods of stretching. If the duration of stretching is large compared with the diffusive time scale of the lithosphere ($\tau = y_L^2/\pi^2\kappa$), which is 50–60 Myr for a standard litho-

sphere, some of the heat diffuses away before the stretching is completed. In the general case, if the time taken to extend the continental lithosphere by a factor β is less than $60/\beta^2$ Myr, the results are similar to those of the uniform stretching model with instantaneous stretching. However, the sensitivity of the results depends on the value of the stretch factor and whether total subsidence or heat flow is being considered.

Considering total subsidence, if $\beta < 2$, the duration of extension must be less than $60/\beta^2$ Myr for the instantaneous stretching model to be a reasonable representation. If $\beta > 2$, the duration of extension must be less than $60(1 - 1/\beta)^2$.

Considering heat flow, if $\beta < 2$, the duration of extension must be less than 60 Myr for the instantaneous stretching model to be a reasonable representation. If $\beta > 2$, the duration of extension must be less than $60(2/\beta)^2$.

Stretching in the Pannonian Basin is thought to have lasted for up to 10 Myr (Sclater et al. 1980b), and stretch factors are <3. Consequently, the instantaneous model is a reasonable representation of the subsidence in the Pannonian Basin since the critical duration of extension is $60(1 - 1/3)^2 = 27$ Myr. It is also a reasonable representation of the heat flow history since the critical duration of extension is also 27 Myr. However, many sedimentary basins appear to have undergone protracted periods of rifting, considerably in excess of $60/\beta^2$ Myr (about 20 Myr for a stretch factor of 1.75). The Paris Basin, for instance, rifted in the Mid-Permian and sedimentation was restricted to elongate rift troughs until close to the end of the Triassic. The rift phase was therefore close to 60 Myr in duration. The Triassic (Carnian–Norian, 212–200 Ma) continental red beds and evaporites of the Atlantic margin of northeastern USA and Canada were deposited in fault-bounded rifts, but seafloor spreading did not commence until the Bajocian at about 170 Ma. The stretching in the Red Sea (Cochran 1983) appears to have occurred diffusely through a combination of extensional block faulting and dyke injection over an area of the order of 100 km wide. This phase of diffuse extension has lasted for 20–25 Myr in the northern Red Sea and is still occurring. A phase of rifting took place in the North Sea in the Permo-Triassic. There was another phase in the Jurassic which lasted until the Early Cretaceous. The duration of this major phase of extension was of the order of 50 Myr.

Taking the North Sea as an example, the stretch factor for the Jurassic extensional phase rarely exceeds 1.5, except along the axis of the Viking Graben (§3.8.2). Using $\Delta t = 50$ Myr and $\beta = 1.5$, the critical duration of rifting from Jarvis and McKenzie (1980) is about 27 Myr. Consequently, on this basis, we should expect the protracted duration of extension during the Jurassic phase in the North Sea to have had significant effects on the heat flow and subsidence history. Despite this, the North Sea appears to be satisfactorily explained by the uniform stretching model (Sclater and Christie 1980; Wood and Barton 1983).

The effect of a finite time of rifting is to cause a loss of heat and thus additional subsidence prior to the end of rifting or the onset of seafloor spreading. It effectively transfers a portion of the cooling from the postrift phase to the synrift phase.

Lateral heat loss during prolonged periods of rifting is caused by the large lateral temperature gradients set up by lithospheric thinning (Steckler 1981). The longer the rifting event, the more important lateral heat loss and uplift of basin margins are likely to be. Lateral heat conduction is also important in narrow basins such as pull-aparts in strike–slip zones. Effects of lateral heat flow are greatest near the basin edge ("hinge-zone" between strongly extended lithosphere and little-extended lithosphere) where horizontal temperature gradients are largest (Cochran 1983). The effects decrease towards the centre of the basin (Fig. 3.24).

In Cochran's (1983) models, the postrift subsidence near the centre of the basin is decreased (relative to the instantaneous case) by a minimum of 10–15% for a 10 Myr rifting event and by about 25% for a 20 Myr rifting event. Since the synrift subsidence is increased at the expense of the postrift subsidence, the effect is to flatten the postrift subsidence curves relative to those predicted by the instantaneous 1-D model. This should lead to underestimates of the stretch factor β. The model subsidence curves cross-cut the lines of equal β because of the lateral transport of heat out of the basin. The basin may be filled with sediment rather than water and the effects of the load of the sediments distributed by flexure. For a 20 Myr rifting time, about 70% of the sedimentary column is represented by synrift sediments in the finite rifting time model. In the North Sea Grabens, however, the synrift subsidence is only *c.* 40% of the total subsidence, which is more typical of the prototype uniform stretching model.

3.5.4 Elevated asthenospheric temperatures

The prototype uniform stretching model of McKenzie (1978a) envisages an asthenosphere with a laterally uniform temperature (1330 °C), which rises passively to

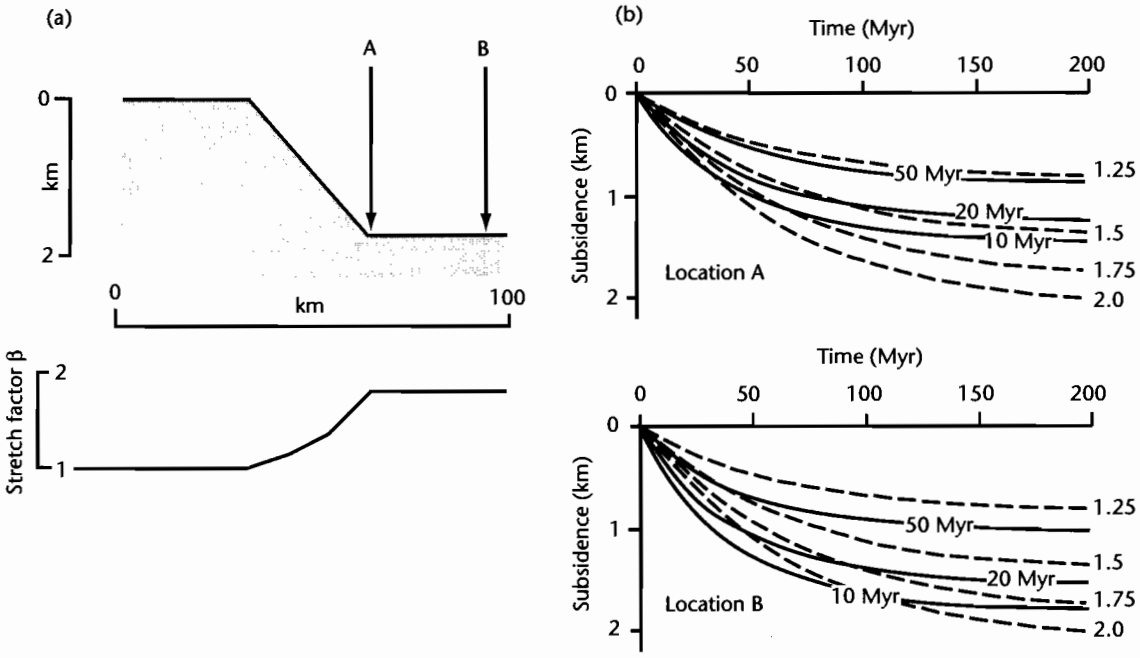

Fig. 3.24 Thermal subsidence for locations A and B in a water-filled basin as a function of time since the end of rifting, for stretch factors of 1.25–2.0, for finite rifting times of 10, 20, and 50 Myr (after Cochran 1983). Dashed lines are subsidence curves for the instantaneous uniform stretching model with $\beta = 2$ in the basin centre. Note that the two sets of curves cross-cut, making estimates of the amount of stretching from postrift thermal subsidence problematical unless the duration of stretching is known.

fill the region of lithospheric stretching. Some workers have suggested that continental stretching is in some cases associated with mantle plume activity (Spohn and Schubert 1983; Houseman and England 1986). Such activity may raise the local asthenospheric temperatures by *c.* 200 °C. Plume heads typically have diameters in the region of 1000 km (Griffiths and Campbell 1990) (§3.7). Laboratory experiments indicate that starting plumes may generate *c.* 600 m of surface uplift (R.I. Hill 1991) – insufficient to solely explain the 3 km-high swells of eastern Africa. However, mantle plume activity may drive continental extension by elevating the lithosphere, including its surface, thereby giving it excess potential energy compared to its surroundings (Houseman and England 1986).

The driving stress caused by the uplift may exceed a threshold value, causing *run-away or accelerating extension*, eventually leading to ocean crust production. Alternatively, the driving stress may be considerably lower than (about half of) the threshold value, causing *negligible extension*, as in many low-strain continental rifts. If the driving stress is intermediate in value, the extension is thought to be *self-limited* by the cooling of the ductile portion of the lithosphere. This produces aborted rift provinces such as the North Sea. These ideas are further developed in §3.7.

One of the complexities of this type of model is the *time scale of the plume*. Removal of the plume head at early, intermediate, or late stages has major effects on basin development. Another aspect is the *volcanicity* generated by the anomalously high asthenospheric temperatures. Mantle plumes are therefore commonly associated with very high volume basaltic igneous provinces such as the Karoo, Deccan, and Parana examples.

Plume activity has been invoked as a particularly effective mechanism of generating new ocean basins, such as the Atlantic. The opening of the northern Atlantic in the Paleocene has been related to the impingement of the Icelandic plume on the base of the lithosphere (White and McKenzie 1989). Mantle plume effects may have been common during supercontinental break-up of

Rodinia (*c.* 750 Ma), Gondwana (*c.* 550 Ma), and Pangea (*c.* 250 Ma).

3.5.5 Magmatic activity at passive margins

The simple uniform extension model does not address the problems of the formation of oceanic crust at passive margins and the nature of the continental to oceanic crustal transition, since as $\beta \rightarrow \infty$ continental lithosphere is thinned to zero and replaced by asthenosphere at the solidus temperature. This would imply enormously large initial subsidence for the oceanic region. This cannot be the case, since newly formed oceanic crust occurs at about 2.5 km depth at mid-ocean ridges. Large amounts of stretching are likely to promote the segregation of melts and their migration into the overlying crust. Melt segregation models involve greater heating (Royden and Keen 1980) than the conduction-based uniform model of McKenzie (1978a).

The melt segregation model assumes that a basaltic melt segregates from asthenosphere that has upwelled to replace stretched lithosphere. The segregated melt can be considered to either constitute new oceanic crust, or to be intruded into or to underplate the stretched lithosphere. The stretching β controls the amount of segregated melt available so that in the case of a laterally varying stretching (with β increasing towards the rift centre), the thickness of segregated melt increases towards the site of ocean floor creation, compensating to some extent for the rapidly thinning continental crust.

Figure 3.25 compares the uniform extension model with $\beta = 4$, the effects of a finite rifting period of 25 Myr (Cochran 1983), and the effects of greater heating by melt segregation (Royden and Keen 1980) on the eastern USA margin. All three curves fit the tectonic subsidence of the postrift phase of the COST B-2 well, although synrift subsidences differ by a factor of 2 between the finite case and the maximum (mid-ocean ridge) heating case.

3.5.6 Induced mantle convection

Models involving an active asthenospheric heat source should predict *uplift before rifting*. At present there is no consensus on the temporal relationships between uplift and extension. However, Steckler (1985) suggested that

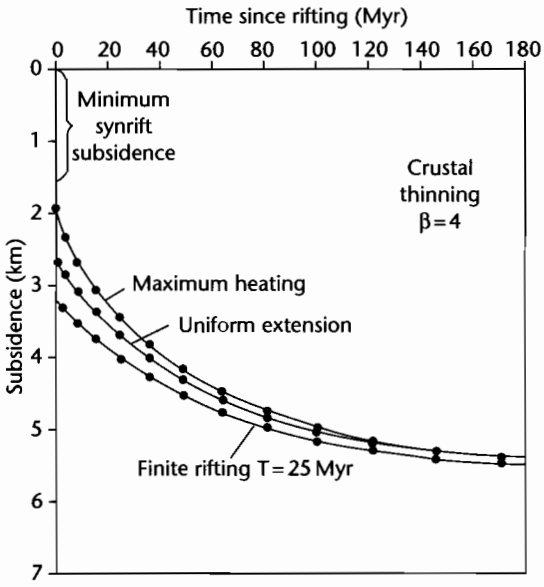

Fig. 3.25 Plot of tectonic subsidence versus time for uniform extension, rifting over a finite period of 25 Myr, and uniform extension with additional heating caused by melt segregation. In all cases the crust is thinned by a factor of 4, as suggested by the COST B-2 borehole. Note that there is minimal difference between the three curves at long time periods following rifting, suggesting that the "memory" of the initial rifting event fades with time (after Steckler et al. 1988).

in the Gulf of Suez, the rift flank uplifts were *not* formed as a precursor doming event prior to rifting, but rather formed *during* the main phase of extension (Fig. 3.26). The rift appears to have initiated (by Miocene times) at near sea-level, since the tilted fault blocks associated with early rifting experienced both subaerial erosion and marine deposition. The Early Miocene topography of the Gulf of Suez region was subdued and stratigraphic thicknesses are uniform over the area (Garfunkel and Bartov 1977). However, at the end of the Early Miocene, 8–10 Myr after the onset of rifting, a dramatic change took place – there is a widespread unconformity, and conglomerates appear at the rift margins suggesting major uplift and unroofing at this time.

The two main causes of vertical movements during rifting are: (i) uplift caused by heating of the lithosphere, and (ii) subsidence caused by thinning (or densification) of the crust. The lithospheric and crustal extensions needed to produce the observed uplift and rift subsidence

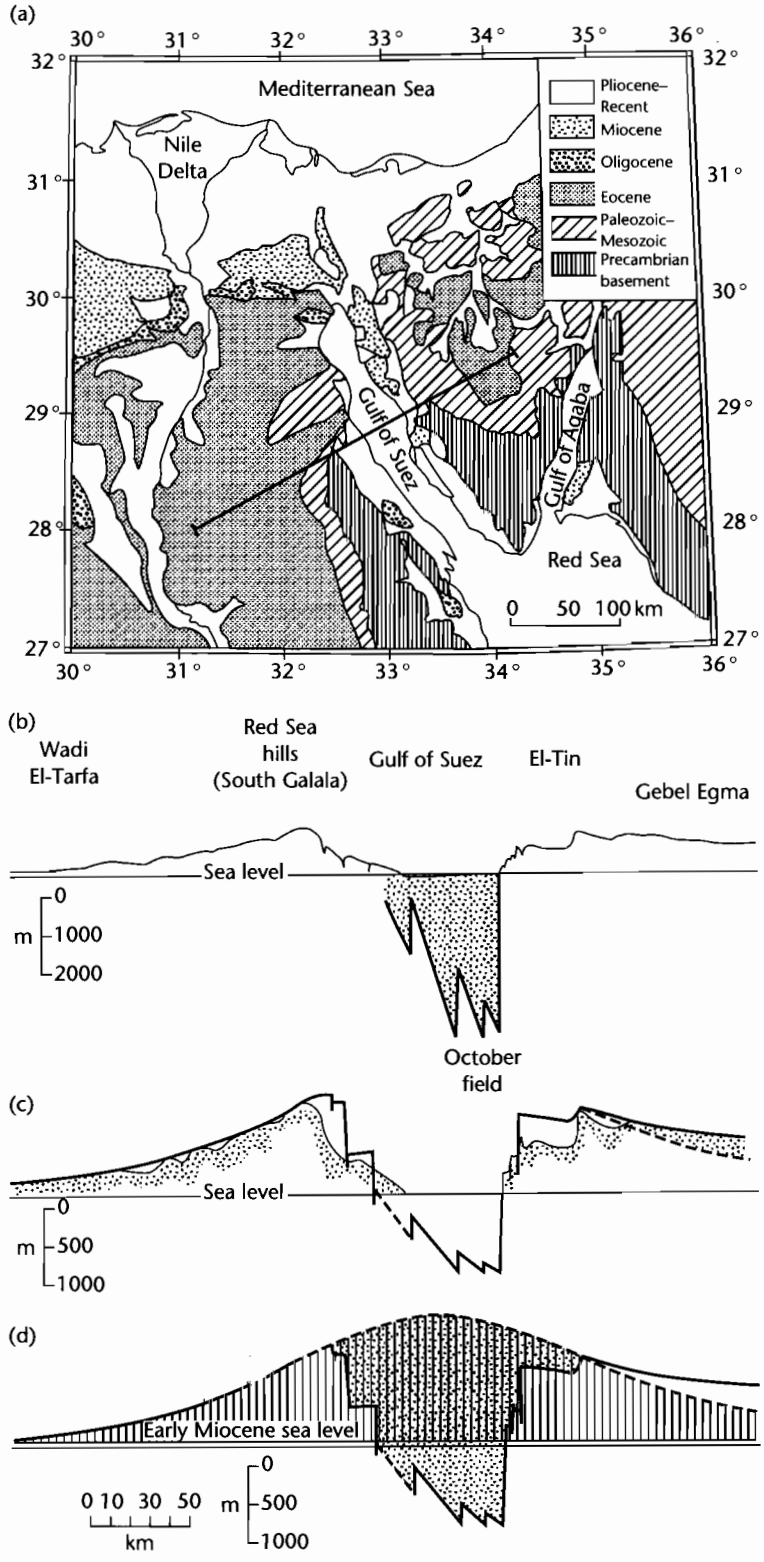

Fig. 3.26 (a) Geological map of the Gulf of Suez region, showing location of topographic profile shown in (b); (b) Topographic profile, vertical exaggeration 20:1. The stippled area represents the sedimentary fill of the Gulf; (c) Reconstructed profile with the effects of erosion and sedimentation removed using Airy isostasy, vertical exaggeration 40:1; (d) Interpretation of profile in (c) involving tectonic uplift due to thermal expansion of the lithosphere (vertical lines) and downfaulting of the rift axis caused by crustal stretching (stipple). After Steckler (1985).

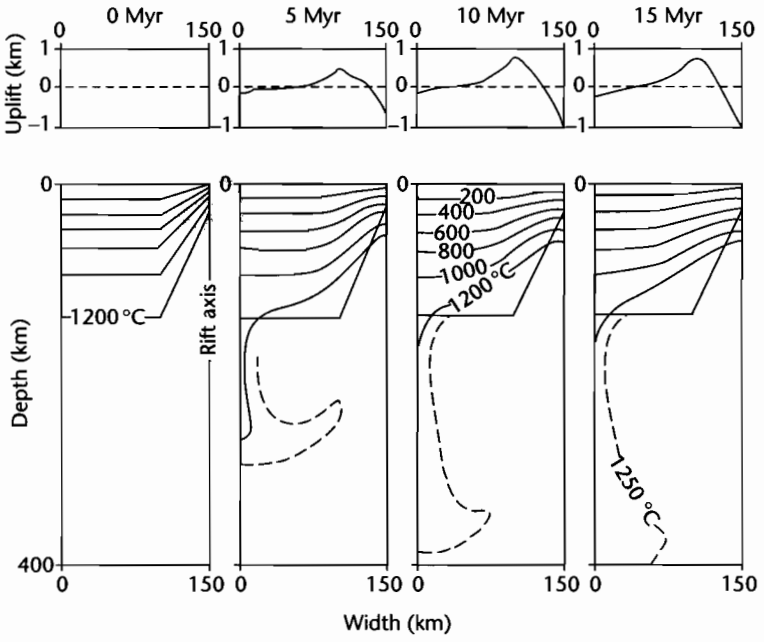

Fig. 3.27 Development of small-scale convection beneath rifts from the numerical experiments of Buck (1984). The rift is assumed to be symmetrical, with an initial half-width of 50 km. The average stretch factor is 1.6 and the internal temperature of the asthenosphere is 1300 °C. Comparison of the 1200 °C isotherm for the four time steps (0 Myr, 5 Myr, 10 Myr, and 15 Myr) shows how the rift flank is progressively heated through time, causing rift shoulder uplift. Top boxes show the topography caused by combined convection and conduction.

can be calculated using Airy isostasy. For the Gulf of Suez, the lithosphere must have extended by 2.5 times as much as the crust to explain the uplift and rift subsidence. This brings the uniform extension model seriously into doubt in terms of its ability to predict the lithospheric heating. How then does one explain the additional amount of heating that the lithosphere under the Gulf of Suez has undergone? This extra heat may have resulted from convective flow induced by the large temperature gradients set up by rifting. Numerical experiments confirm that secondary small-scale convection should take place beneath rifts (Buck 1984). Convective transport should heat the lithosphere bordering the rift, causing uplift of rift shoulders concurrent with extension within the rift itself (Fig. 3.27). If this mechanism is correct, it removes the need for active, sublithospheric heat sources. It also removes the requirement for two-layer extension to explain high heat flows at rift margins.

3.5.7 Radiogenic heat production

Although the very large volume of mantle contributes 80% of the Earth's radiogenic heat, it is the crustal contribution that determines the continental geotherm and which is of importance in basin analysis. The crustal radiogenic heat production can be modeled either as a series of slabs of different internal heat production, or as an exponential that decays with depth (§2.2.3). As a rule of thumb, the radiogenic heat production may be of roughly equal importance to the basal heat flow in determining the continental geotherm.

In practice, this makes little difference to the shape of the subsidence curves predicted by the uniform stretching model of McKenzie (1978a), though it potentially strongly affects paleotemperature estimations. It is therefore very important to include radiogenic contributions to the heat flow in modeling of thermal indicators in sedimentary basins such as vitrinite reflectance (Chapter 9).

3.5.8 Flexural compensation

It is likely that at low to moderate values of stretching the lithosphere maintains a finite strength during basin development (Ebinger et al. 1989), so that it responds to vertical loads by flexure. The degree of compensation (between the end members of Airy isostasy for a plate with no flexural rigidity and zero compensation for an infinitely rigid plate) depends on the flexural rigidity of the plate and the wavelength of the load (§2.3.3). There are two situations where flexure is likely to be important: (i) tectonic unloading by extension along major detachments leading to a regional cantilever-type upward flexure (Kusznir and Ziegler 1992), causing the footwall region to be mechanically uplifted, and (ii) downward flexure under the accumulating sediment loads in the synrift and especially postrift phase. Flexural compensation of sediment loads should be particularly important in passive margin evolution because of the secular increase in flexural rigidity and where sediment loads are narrow, as in pull-apart basins.

On the young (<24 Myr) Gulf of Lion's margin in the western Mediterranean, a local Airy model fitted the subsidence history data well. Thermal subsidence is exponential, of the form $e^{-t/\tau}$ where τ is the thermal time constant of the lithosphere (50–60 Myr), as in the uniform extension model of McKenzie (1978a). At higher values of stretching, the thermal subsidence more closely approximates the oceanic half-space cooling model, with subsidence related to root time. However, thickly sedimented old margins such as that of the Baltimore Canyon region of eastern USA (Steckler and Watts 1978, 1981) show departures from the subsidence history expected of Airy isostasy. In this case, a flexural model with the onset of thermal subsidence at 170 Ma fits the data very well with a $\sqrt{t}$ relationship.

3.5.9 The depth of necking

Necking is the very large scale thinning of the lithosphere caused by its mechanical extension. Necking should take place around one of its strong layers (Braun and Beaumont 1987; Weissel and Karner 1989; Kooi et al. 1992). The *depth of necking* is defined as the depth in the lithosphere that remains horizontal during thinning if the effects of sediment and water loading are removed. For the McKenzie uniform stretching model, the necking depth is implicitly 0 km. That is, all depths below the surface experience an upward advection during thinning (when sediment/water loading is removed). However, the necking depth may be deeper in the shallow mantle lithosphere. In this case, there is advection of material upwards from below the necking depth, but advection of material downward from above the necking depth.

The regional isostatic response to the different necking depths is shown in Fig. 3.28. If the necking depth is in the strong mantle lithosphere, there is a regional flexural uplift, causing a pronounced rift shoulder. We would expect a deep necking depth where the lithosphere is cold and strong, with a strong subcrustal mantle, such as in the Transantarctic Mountains and Red Sea region (Cloetingh et al. 1995). However, if the necking depth is within the upper–midcrust, there is a downward regional flexure, promoting subsidence of the rift margins. This should occur where the lithosphere is weak, or where the crust is thickened, as in the Pannonian Basin of eastern Europe (Horvath and Cloetingh 1996). The level of necking therefore controls the amount of rift shoulder denudation, and consequently, the sediment delivery to the basin during the synrift phase (van Balen et al. 1995; ter Voorde and Cloetingh 1996). There is theoretically an equilibrium depth of necking where there is no net flexural response. For a sediment-filled basin and initial crustal thickness of 33 km within a 100 km-thick lithosphere, this equilibrium depth is *c.* 10 km. Odinsen et al. (2000) used a necking depth of 18 km for their analysis of the northern North Sea, which therefore can be viewed as a relatively deep necking depth, promoting regional flexural uplift.

3.6 A DYNAMIC APPROACH TO LITHOSPHERIC EXTENSION

3.6.1 Generalities

Dynamic approaches to the modeling of continental extension use the constitutive laws of lithospheric materials to describe the 3-D deformation of the continental lithosphere under extension. A number of *plane strain* models making a range of assumptions of lithospheric rheology (Keen 1985, 1987; Buck 1986; Braun and Beaumont 1987; Dunbar and Sawyer 1989; Lynch and Morgan 1990; Bassi 1991) show, in general, that the style of deformation is controlled by strain rate, initial geotherm and rheologic structure. Consequently, any initial heterogeneities causing variability in the mechanical and

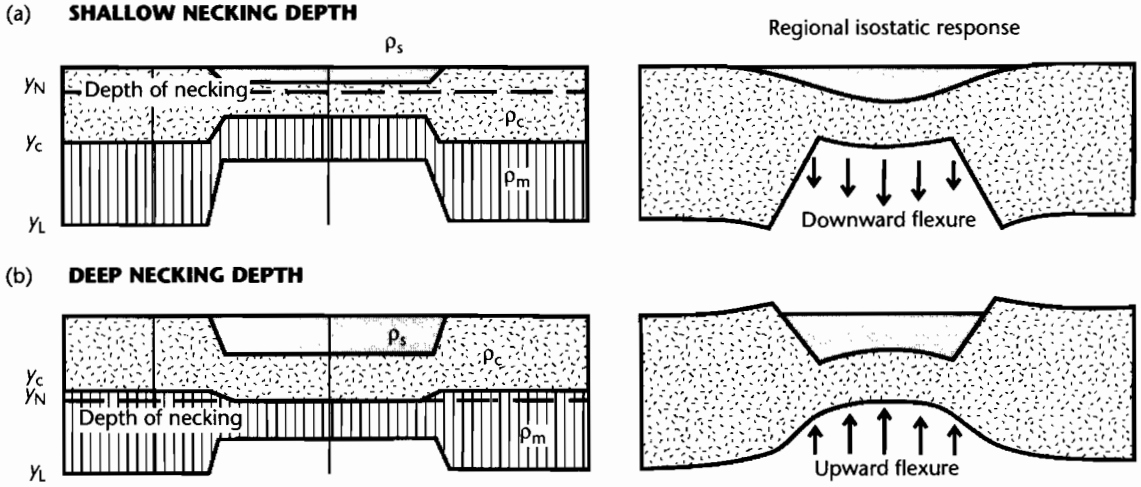

Fig. 3.28 Regional isostatic response to different depths of necking, based on Braun and Beaumont (1989), Kooi et al. (1992), Cloetingh et al. (1997). y_c, y_L and y_N are the initial thicknesses of the crust and lithosphere and the necking depth respectively; ρ_c, ρ_m, and ρ_s are the densities of the crust, mantle, and sediments respectively. In (a) a shallow depth of necking results in a net downward acting force on the lithosphere, causing a regional downward flexure. In (b) the necking depth is deep, resulting in an upward acting force on the lithosphere that causes flexural uplift of the rift flanks.

thermal properties of the lithosphere are likely to be highly influential in determining the resulting deformation. These initial perturbations that cause lateral strength variations might be thickness variations, pre-existing deep faults, thermal anomalies or rheologic inhomogeneities (Fernandez and Ranalli 1997).

Plane stress models approximate the lithosphere to a thin viscous sheet, in which the rheologic properties of the sheet are vertically averaged (examples are England and McKenzie 1982, 1983; Houseman and England 1986; Sonder and England 1989; Newman and White 1999). A single power-law rheology is used in these models to describe lithospheric deformation.

Dynamic models require *boundary conditions* on the margins of the extending lithosphere (Fig. 3.29). The choice of boundary conditions has important implications for the evolution through time of parameters in the model. As examples, the implications of five different boundary conditions are given below:

1 *Constant velocity boundary condition*: if L_0 is the initial width and v_0 is the extension velocity, the width of the extending zone after time t is

$$L = L_0 + v_0 t \tag{3.30}$$

and the extensional strain rate is

$$\dot{\varepsilon}(t) = (1/L)(\mathrm{d}L/\mathrm{d}t) \tag{3.31}$$

The extensional strain rate clearly decreases with time for a constant velocity boundary condition. A constant velocity boundary condition might be applicable to a situation where the extension is driven by relative plate motion, which over the duration of the extension has a constant vector.

2 *Constant strain rate boundary condition*: the width of the extending zone must vary in time as

$$L = L_0 \exp(\dot{\varepsilon} t) \tag{3.32}$$

and the extension velocity $v = (\mathrm{d}L/\mathrm{d}t)$ must increase as a function of time. For a constant strain rate boundary condition the extensional velocity would accelerate unreasonably.

3 *Constant stress boundary condition*: the result of a constant tectonic force boundary condition is to concentrate the

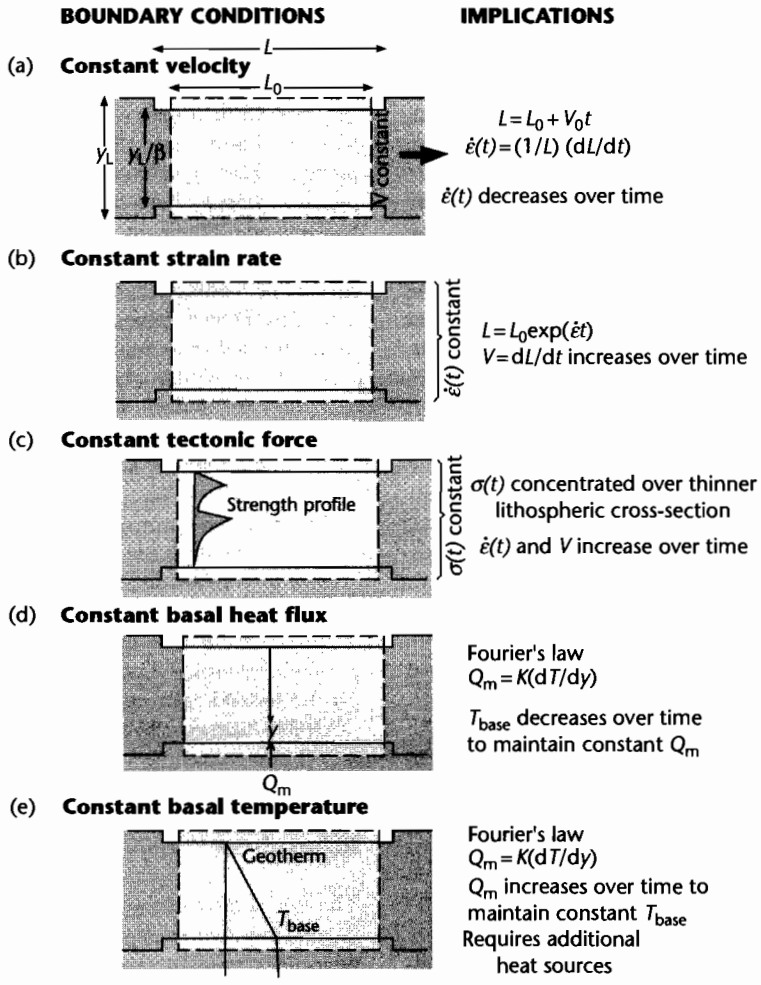

Fig. 3.29 Boundary conditions for dynamic models of lithospheric extension. (a) Constant velocity of extension over time, which implies that the strain rate must decrease over time; (b) Strain rate constant over time, which implies that the extension velocity must increase over time; (c) Constant tectonic force (deviatoric stress) over time, which causes the same force to be concentrated over a thinner lithospheric cross-section over time. This force becomes concentrated in the strong layers in the lithosphere, which undergo large scale necking. The strain rate therefore increases over time; (d) Constant basal heat flux over time, which implies, *via* Fourier's law, that the temperature at the base of the lithosphere must decrease over time; (e) Constant basal temperature over time, which implies that the basal heat flux must increase with time, as in the uniform stretching model of McKenzie (1978a). This requires additional heat sources to increase the basal heat flux.

stress on a progressively thinner lithosphere, especially on those parts of the lithosphere that are most resistant to deformation, such as the strong upper–midcrust or lithospheric mantle (Kusznir 1982). Tensile deviatoric stresses would therefore increase with time at the site of lithospheric necking, leading to accelerating strain rate, unless a "hardening" process prevents it. Such a "hardening" process might be cooling causing an increase in viscosity.

4 *Constant basal heat flux boundary condition*: if it is assumed that there are no additional heat sources in the asthenosphere such as plume heads and secondary convective

cells, the heat flux at the base of the lithosphere can be assumed to be constant as extension proceeds. If so, since $Q = K(dT/dy)$, and the thickness of the lithosphere decreases by extension, the temperature at the base of the lithosphere should decrease by the stretch factor β with time.

5 *Constant basal temperature boundary condition*: in similar fashion, a constant basal temperature implies that the basal heat flow increases (by a factor β) through time. Since the base of the lithosphere is usually taken as the solidus temperature of peridotite (Pollack and Chapman 1977), which is a constant temperature, this is a commonly applied boundary condition, and is implied in the uniform stretching model of McKenzie (1978a). However, it requires additional heat fluxes from the lithosphere, such as those caused by secondary convection, as stretching proceeds.

3.6.2 Modes of continental extension: narrow and wide rifts

There appear to be two different modes of continental extension (Fig. 3.30):

1 *Narrow rifts* with normal thickness crust (e.g., Rhein Graben; Gulf of Suez; Baikal; East Africa) are due to relatively small amounts of extension ($\beta < 2$). Narrow rifts may evolve into passive margins (e.g., Eastern Seaboard USA; Biscay–Armorican margin) alongside oceanic spreading centres. In crust with normal thickness (30–40 km) and geothermal gradient (30 °C km^{-1}), the process of lithospheric stretching is by a very large scale, localized thinning of the lithosphere or *necking* (Kooi et al. 1992). At early stages of lithospheric necking, rifts are 30–40 km wide, with the Moho elevated immediately beneath the rift. Some early rifts, such as those of East Africa, are wider (60–70 km). At late stages of necking, passive margins develop, with widths of 100–400 km and with the Moho shallowing from 30–40 km under the undisturbed lithosphere to 8–10 km at the continent–ocean boundary.

2 *Wide extended domains* where extension follows earlier crustal thickening by *c.* 20 Myr or more, providing time for the thickened brittle crust to spread gravitationally under its own weight over a weak layer in the lower crust (Jones et al. 1996). The width of the extending region can be as wide as the region of previously thickened crust – as much as 1000 km in the Basin and Range, USA. As a result of spreading, crustal thicknesses return to "normal" (*c.* 30 km), at which point extension stops. Local zones of exhumed ductile lower crust are termed *core complexes*. Core complexes are common in the Aegean (Greece) (Lister et al. 1984) and the Basin and Range province (Lister and Davis 1989), and have been interpreted in orogenic belts as diverse as the Alps of Austria–Switzerland (Frisch et al. 2000), the Variscan of west-central Europe (Burg et al. 1994a) and the Pan-African of western Saudi (Blasband et al. 2000). Flat-lying detachments associated with core complexes have been interpreted as initially low-angle faults that traversed the entire lithosphere. More recent studies suggest that they are initially steep and progressively rotated to a very shallow dip during extension, with a flat Moho undisturbed by any translithospheric faults/shear zones.

An important set of questions immediately springs to mind: what controls the duration and total stretching of a piece of continental lithosphere? Do rifts stay narrow because the driving force for extension is removed? Or is it because the mantle lithosphere gains in strength and self-limits extension (England 1983)? The first possibility can be termed "*force-controlled extension*" and the second possibility "*viscosity-controlled extension.*"

3.6.3 Forces on the continental lithosphere

The combination of forces causing stretching of the continental lithosphere may be varied. Extension of the lithosphere must be caused by a set of forces that have a resultant horizontal component that overcomes rock strength. It is known that stresses may be transmitted through the continental lithosphere over large lateral distances. These deviatoric stresses are termed in-plane stresses, since they are in the plane of the plate. For example, the World Stress Map of Zoback (1992) shows that the North Sea, Gulf of Lion, and Pannonian Basin, all of which were extensional tectonic provinces, are in a state of compressional stress at the present day.

Imagine a slab of continental lithosphere acted upon by *distant extensional forces*. Changes in the distant extensional force should cause the region to experience variations in the strain rate at the same time, regardless of location. If the crust varies in thickness across our slab of lithosphere, *buoyancy forces* caused by these thickness variations should interfere with the distant extensional forces.

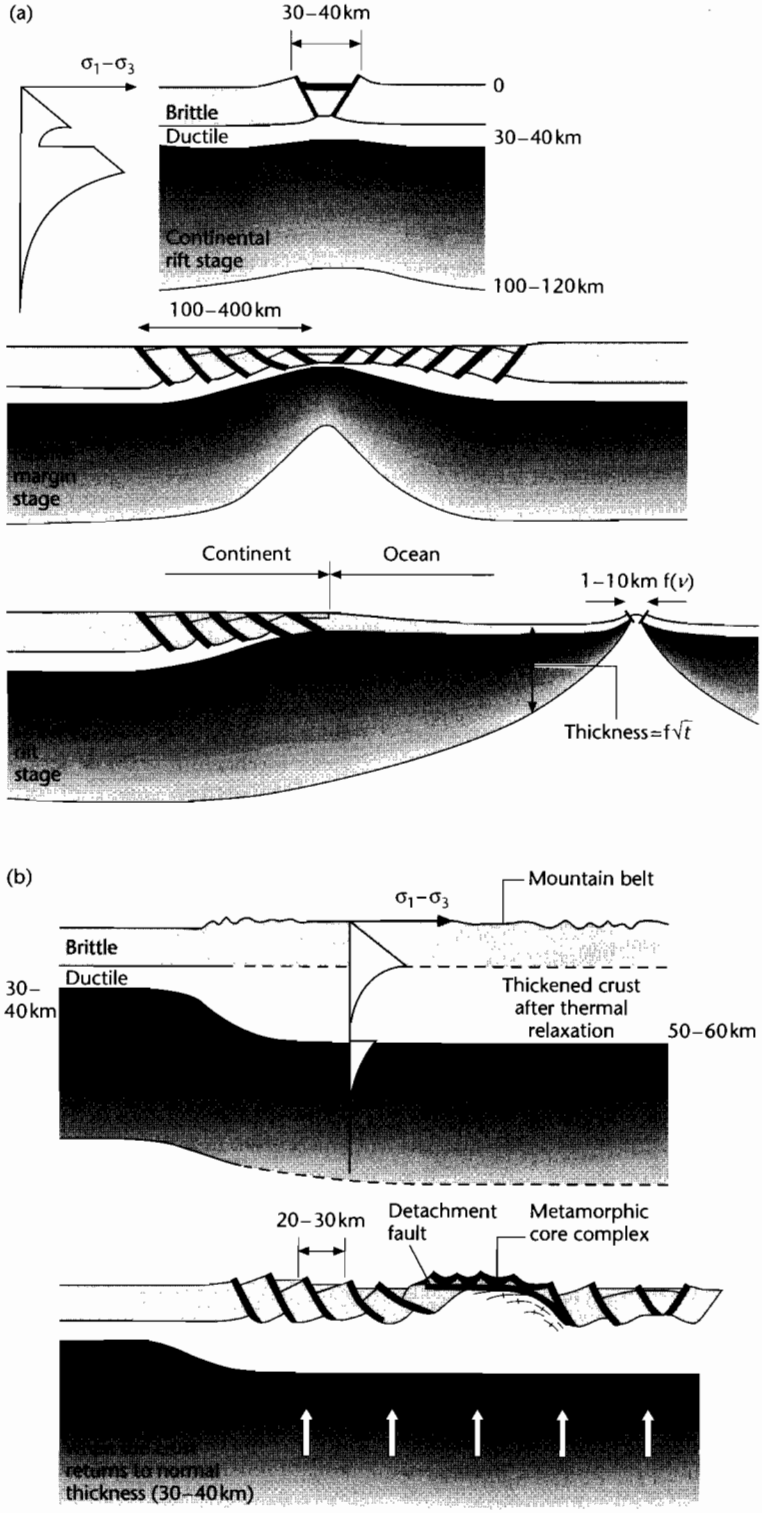

Fig. 3.30 Geological and structural differences between (a) narrow and (b) wide rifts, after Brun (1999). Wide rifts typically develop where the lithosphere has been previously thickened, with a Moho at >50 km. Extension leads to the unroofing of metamorphic core complexes. Reproduced courtesy of Royal Society, London.

Where the crust is thick, buoyancy forces assist the distant force to promote extension. But where the crust is thin, buoyancy forces oppose the distant extensional forces and resist extension. Could extension therefore be stopped by thinning the crust to a critical point? It is also possible that buoyancy forces may operate in the absence of a strong distant extensional force. For example, if the crust is thick, or if the lithosphere is elevated above a mantle plume, the buoyancy forces alone may drive extension. A further source of extensional stresses is the application of shear stresses to the base of the lithosphere, for example from the convectional motion in the mantle, with extension occurring above the divergent flow of a convection cell. However, these stresses are likely to be relatively minor because the asthenosphere has a very low viscosity.

Lateral transmission of mechanical energy through the lithosphere as a result of plate collision has been proposed as a cause of continental rifting by Molnar and Tapponnier (1975). For example, the Baikal Rift of central Asia may be influenced by plate collision along the Himalayan front in the south, and a further convergent plate boundary exists in the Pacific on the east, both boundaries being roughly 3000 km distant from the rift itself. The Rhine Graben has the collision boundary of the Alps in closer proximity in the south and the opening Atlantic (1000 km distant) and subsiding North Sea (500 km distant) in the west and north. However, the frequency of collision boundaries compared to the large number of modern and ancient rifts is negligible. It therefore seems inconceivable that collision events have a *primary* role to play in providing the deviatoric in-plane forces necessary for the rifting of the continents. A numerical model of a plate of constant thickness loaded horizontally by an indenter (Neugebauer 1983), using limits of lithospheric stress under compression and extension (Brace and Kohlstedt 1980), indicates that the predicted stress regime falls considerably short of that required of a self-sustaining mechanism for rifting in the Baikal and Rhine Rifts.

In addition to the forces applied at the edge of a continental plate by relative plate motion, there is an additional set of buoyancy forces set up by crustal thickness contrasts (England 1983; England and McKenzie 1983). The elevation of the continental lithosphere causes pressure differences to exist between it and neutrally elevated lithosphere. The relative importance of this driving force compared to that caused by applied forces at the plate boundaries can be gauged by an *Argand number* Ar (see §4.6). If the Argand number is small, that is, the effective viscosity is large for the ambient rate of strain, the deformation of the continental lithosphere will be entirely due to boundary forces. If Ar is large, however, the effective viscosity will appear to be small and the medium will not be strong enough to support the elevation contrasts, so the forces due to crustal thickness changes will dominate deformation. Numerical modeling using this approach explained the tectonic styles of major crustal shortening in the Himalaya and extension in Tibet (England and Houseman 1988, 1989) (Fig. 3.31).

3.6.4 Rheology of the continental lithosphere

The linkage between the forces on the lithosphere and its deformation is the rheology of lithospheric materials (§2.4). The rheology of the lithosphere controls its deformation under any set of initial and boundary conditions. Consequently, rheology underpins all dynamical models of basin development. Key to the correct treatment of rheology is the concept of the strength envelope (Goetze and Evans 1979; Ranalli 1995). A strength profile of the lithosphere must account for two different deformational mechanisms – brittle (or frictional) and ductile. The high strength regions of stabilized or "standard" continental lithosphere (with a Moho temperature of about 600 °C) occur in the midcrust and mantle lithosphere immediately beneath the Moho. Two low strength regions also occur – in the lower crust, and at greater depths in the mantle lithosphere. The continental lithosphere is therefore, at its simplest, a four-layer model (Fig. 3.32).

Information on rock rheology necessary for basin modeling essentially comes from laboratory experiments of rock deformation. Ignoring for the moment brittle failure (§2.4.3), the constitutive laws derived from these experiments express strain rate as a function of temperature, pressure, and deviatoric stress. Although laboratory experiments may not be fully representative of conditions in the lithosphere, the strain rate of rocks in the lithosphere is thought to obey a *power law creep* relationship as follows:

$$\dot{\varepsilon} = A\tau^n \exp(-E_a/RT) \tag{3.33}$$

where τ is the deviatoric stress, T is the absolute temperature, R is the universal gas constant (8.3144 J mol^{-1} K^{-1}), and A, E_a, and n are constants dependent on the type of material undergoing deformation (Fernandez and Ranalli 1997). The activation energy E_a ranges from

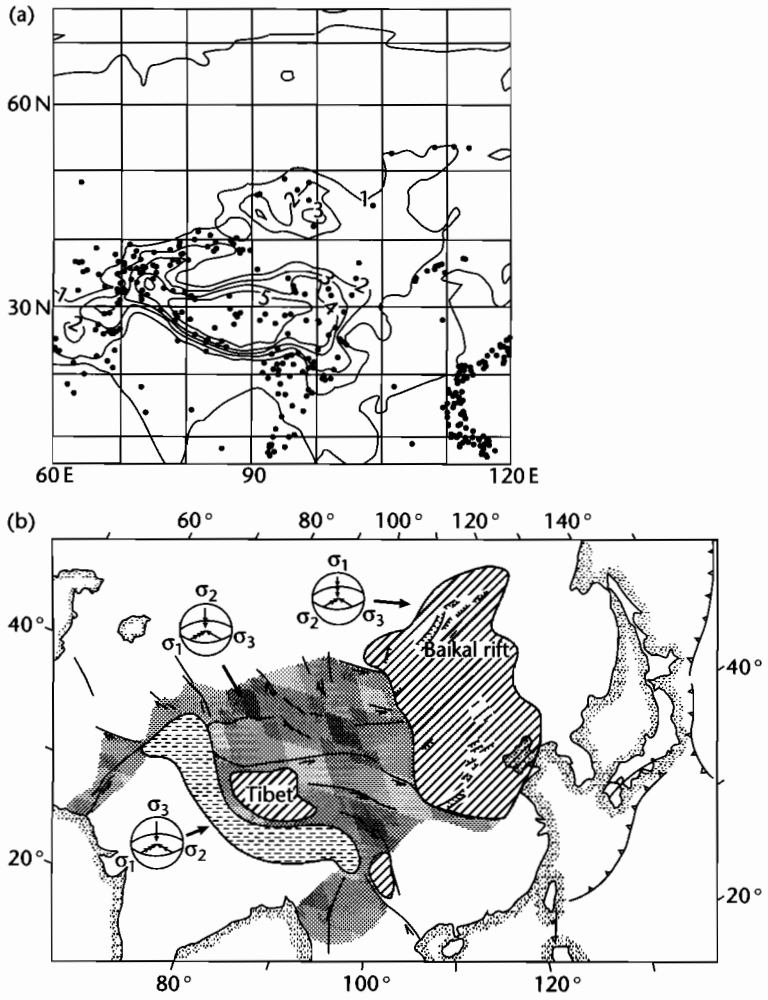

Fig. 3.31 (a) Average topographic elevation of Asia, with locations of earthquakes recorded by at least 50 stations between 1961 and 1977. Note that earthquakes occur diffusely over a very wide region of the Asian continent; (b) The major tectonic regimes for Asia (Tapponnier and Molnar 1976) are explained well by a numerical model of a viscous plate subjected to a collisional force along its southern boundary and gravitational forces arising from its thickness contrasts (England 1983; England and McKenzie 1983). Horizontal ornament, compression; stipple, strike–slip; diagonal hatch, extension.

about $500\,\mathrm{kJ\,mol^{-1}}$ for dry olivine to about $160\,\mathrm{kJ\,mol^{-1}}$ for quartz. The power exponent n is in the range 3–5. Equation (3.33) is in fact the common form of many temperature-activated processes, for example the maturation of organic matter to form petroleum.

It is a simple matter to calculate the difference in strain rate for dry olivine in the uppermost mantle lithosphere for a 20° temperature change from 600 °C to 580 °C (873 K to 853 K). We assume that the driving deviatoric stress τ, exponent n and material coefficient A are constant. A temperature change of just 20 °C causes over an order of magnitude change in the strain rate. This is because *viscosity* is highly dependent on temperature.

Although it is possible to measure strain rates of the surface of the Earth using techniques such as Global Positioning System geodesy (e.g., Bennett et al. 1997; Clarke et al. 1998), it is not known how representative this is of longer time scales and of the lithosphere as a

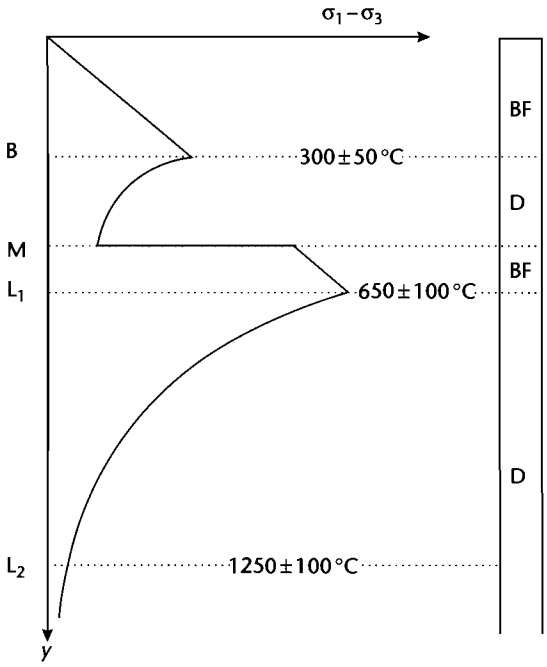

Fig. 3.32 Strength envelope for a four-layer lithosphere, after Fernandez and Ranalli (1997), with critical temperatures and typical rheology for a uniform felsic crust and low geothermal gradient. B, crustal brittle–ductile transition; M, Moho; L_1, mantle brittle–ductile transition; L_2, lithosphere–asthenosphere boundary; BF, brittle frictional; D, ductile power law. Reproduced courtesy of Elsevier.

whole. Whereas deformation of the upper crust is by brittle faulting, it is not known whether this fault-related upper crustal extension follows the same strain rate pattern as the ductile lower crust and lithospheric mantle. In some parts of the world (such as the Basin and Range province of SW USA, and the Aegean region of Greece and Turkey) upper crustal extension is diffuse and widespread, being distributed on very many individual faults. This suggests that extension of the ductile layers of the lithosphere may control the brittle extension of the upper crust. The strain rate of ductile deformation is determined by viscosity. It is open to question whether the amount of extension varies as a function of depth, but in the general case it can be assumed that strain and strain rate are independent of depth, representing the case of *pure shear*. The entire lithosphere is then assumed to extend at a rate determined by the depth-integrated viscosity.

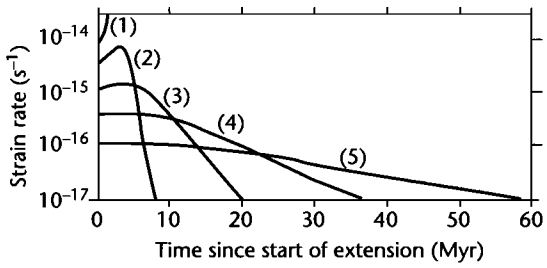

Fig. 3.33 Variation of the strain rate with time based on a set of 1-D numerical experiments (Newman and White 1999). Each experiment uses the same rheology, but the driving force varies, resulting in different initial strain rates. At very high initial strain rates (1), complete, rapid rifting of the lithosphere occurs. In (2) and (3) the strain rate rises at first because the same driving force acts on a progressively thinner lithosphere. Strain rate then falls because of the effect of cooling on viscosity in the mantle lithosphere. In (4) and (5) initial strain rates are low, so the mantle cooling effect dominates. Apart from passive margins, peak strain rates in extensional sedimentary basins rarely exceed $2 \times 10^{-15} s^{-1}$. Reproduced courtesy of Royal Society, London.

3.6.5 Numerical experiments on strain rate during continental extension

Using a relatively simple rheologic model of a low viscosity crust (not temperature-dependent) and a power law creep lithospheric mantle, Newman and White (1999) showed the strain rate history of a piece of extending continental lithosphere assuming pure shear. A number of scenarios are possible, depending on the initial strain rate/magnitude of distant driving force (Fig. 3.33):

- At *high initial strain rate*, complete rifting of the lithosphere takes place before any significant heat loss. The strain rate increases through time because the same distant driving force acts on progressively thinner lithosphere;
- at *lower initial strain rate*, strain rate rises at first because of the same lithospheric thinning effect, but mantle cooling becomes important and reduces the strain rate. The time taken for the strain rate to become negligible (less than about $10^{-17} s^{-1}$) depends on the initial strain rate – it is short for high initial strain rates and long for smaller initial strain rates. In other words, extension continues longer where the strain rate was lower.

How likely is it that the mantle lithosphere will cool sufficiently to significantly increase viscosity and stop

extension? Let us take equation (3.33) and derive an expression for the temperature change at the Moho of a piece of continental lithosphere extending with a stretch factor β required to cause a fall in the strain rate from an initial value $\dot{\varepsilon}_0$ to a new value $\dot{\varepsilon}_1$

$$\log_e \dot{\varepsilon}_0 - \log_e \dot{\varepsilon}_1 = \frac{E_a \Delta T}{R T_{MOHO}^2} - n \log_e \beta \tag{3.34}$$

where T_{MOHO} is the temperature at the Moho and the other parameters are as defined above. The temperature change, ΔT_r, required to lower the strain rate by an order of magnitude is then

$$\Delta T_r = \{2.3 + n \log_e \beta\} \frac{R T_{MOHO}^2}{E_a} \tag{3.35}$$

If the lithospheric stretch factor β is 1.2, $E_a = 500\,\mathrm{kJ\,mol^{-1}}$, $T_{MOHO} = 580\,^{\circ}\mathrm{C}$ (853 K), $n = 3$, $R = 8.314\,\mathrm{J\,mol^{-1}\,K^{-1}}$, the temperature change required to lower the strain rate by an order of magnitude is 34 °C. If the stretch factor β is 2.5, the answer is 61 °C. This is because with the higher stretch factor, the driving force is concentrated on a thinner slab of lithosphere, which causes the deviatoric stress to increase by a factor β as the lithosphere thins. This effect offsets the increase in viscosity caused by cooling.

How long should it take to accomplish the temperature reduction causing an order of magnitude fall in the strain rate? To answer this question requires us to know something about the geothermal gradient in the lithospheric mantle γ_m, the thermal conductivity of crust k_c and mantle lithosphere K_m, the radiogenic heat production of the crust A_c, the thermal time constant of the lithosphere τ, the initial thickness of the crust y_{c0} and initial Moho temperature T_o. The expression for the time period required, t_r, simplifies to

$$t_r = K(\dot{\varepsilon}_0)^{-1/2} \tag{3.36}$$

where the coefficient K is equal to 4×10^{-7} for the following parameter values: initial geotherm $\gamma_m = 25\,^{\circ}\mathrm{C\,km^{-1}}$, lithospheric time constant $\tau = 60$ Myr, initial Moho temperature $T_o = 580\,^{\circ}\mathrm{C}$, thermal conductivity of crust $k_c = 2.5\,\mathrm{W\,m^{-2}\,K^{-1}}$, thermal conductivity of mantle $K_m = 3.0\,\mathrm{W\,m^{-2}\,K^{-1}}$, crustal radiogenic heat production $A_c = 1.1\,\mu\mathrm{W\,m^{-3}}$, initial crustal thickness $y_{c0} = 33$ km, initial lithospheric thickness $y_{L0} = 120$ km.

The striking result is that the time taken to reduce the strain rate by an order of magnitude depends on the inverse square root of the initial strain rate. That is, if the initial strain rate is high, the time taken to reduce it by an order of magnitude is short. If the initial strain rate is low, the time taken to reduce the strain rate by an order of magnitude is long. If the initial strain rate is $3 \times 10^{-15}\,\mathrm{s^{-1}}$, the strain rate reduces to an order of magnitude smaller than this initial value in 7 Myr. When the initial strain rate is $3 \times 10^{-16}\,\mathrm{s^{-1}}$, this time scale becomes 23 Myr. This compares favorably with the observed time scale of rifting known from the geological record.

If the initial strain rate is less than *c.* $10^{-16}\,\mathrm{s^{-1}}$, it may take as much as 60 Myr for the extension to stop. It is likely that during this long period of time the driving force may be removed, for example, by changes in relative plate motion, or by changes in the convectional motion in the mantle (see also §3.7).

The subsidence history of sedimentary basins allows the stretch factor and peak strain rate of the underlying continental lithosphere to be estimated. White (1994) and Newman and White (1999) developed this technique and applied it to literally thousands of borehole subsidence records. They discovered that there was a strong relationship between the peak strain rate and the final stretch factor in all of the sedimentary basins studied (Fig. 3.34).

If continental extension is controlled by a distant driving force, we would expect large variations in this relationship between peak strain rate and stretch factor, since continental lithosphere is heterogeneous. However, if viscosity controls extension, we should expect just the relationship observed. Differences caused by variations in the magnitude of the distant driving forces are much smaller than the effects of viscosity (or values of the activation energy E_a, which may vary significantly).

If our viscosity-controlled extension model is correct, previously stretched lithosphere should be *stronger* than "normal" lithosphere. That is, for a given peak strain rate, we should expect a smaller stretch factor in the case of the previously stretched lithosphere. This appears to be supported by the data of Newman and White (1999). However, there is still an unanswered question: do previously rifted pieces of lithosphere tend to rift again? The geological record suggests "yes." The numerical model suggests perhaps "no."

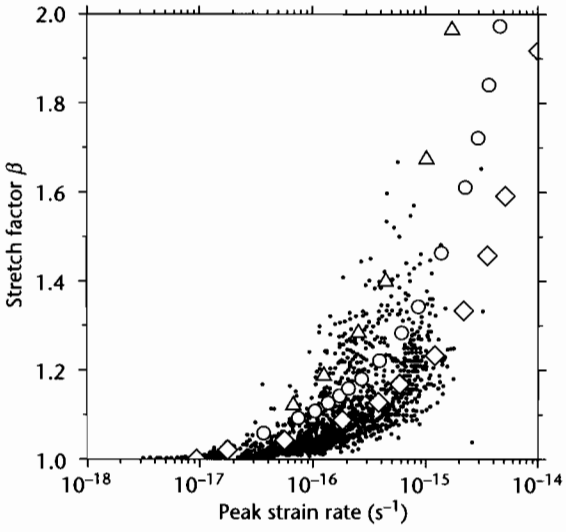

Fig. 3.34 Relation between peak strain rate and stretch factor for 2195 separate rifting episodes (small dots). Model results are for activation energies E_a of $300\,kJ\,mol^{-1}$ (triangles), $500\,kJ\,mol^{-1}$ (circles) and $1200\,kJ\,mol^{-1}$ (diamonds). After White (1994), and Newman and White (1999). Reproduced courtesy of Royal Society, London.

3.6.6 Insights from analogue models

Analogue models are experiments conducted with materials of carefully chosen viscosities, strengths and densities, scaled in such a way as to represent the deformation of a layered lithosphere at the appropriate strain rates. These models are informative about lithospheric stretching under a variety of conditions. Different results are obtained dependent on the strength profile of the lithospheric model and the scaled strain rate of the analogue experiment. The analogue experiments replicate many of the different styles of continental extension, particularly narrow, localized rifts versus extensive tilted fault block terranes (Brun 1999) (Fig. 3.30):

- For a simple two-layer model (brittle upper layer over a ductile lower layer), at low strain rates (and therefore low ductile strengths), deformation remains localized in an asymmetric graben; at high strain rate, the faulted zone is much wider, with highly tilted fault blocks;
- for a simple two-layer model with constant strain rate, small brittle layer thicknesses (therefore low brittle strength) produced extensively faulted models, whereas high brittle strength resulted in localized rifts;
- where the two-layer analogue model is able to extend under its own weight, faulting invades the whole model, producing a wide rift with highly tilted fault blocks rather than horsts and graben.

These results therefore suggest that ductile and brittle strengths and spreading under gravity have major roles in style of deformation. Horsts and graben appear to typify regions of slow strain rate, whereas tilted fault blocks are typical of high strain rate regions.

In four-layer models (two high-strength zones, corresponding to the upper crust and upper mantle lithosphere), low strain rates produce a narrow rift whose delimiting faults sole out into the brittle–ductile interface. Whereas a single zone of necking develops at low strain rates, at higher strain rates multiple necking (that is, *boudinage*) causes a widening of the extending zone, as in the passive margin stage. A local, low viscosity heterogeneity beneath the brittle–ductile interface (such as caused by the thermal effects of a large pluton, or by partial melting) causes an increase in stretching and allows the ductile layer to exhume to form core complexes. Initially steep normal faults are rotated into flat-lying detachments. In wide rifts therefore, local anomalies are prone to amplification to produce strong variations in extension and exhumation.

3.7 MANTLE PLUMES AND IGNEOUS ACTIVITY ASSOCIATED WITH CONTINENTAL EXTENSION

It is beyond doubt that some regions of continental stretching are unrelated to any "active" thermal processes. However, in other instances, continental stretching and break-up is associated with voluminous basaltic volcanism, as in the Deccan of India, the Karoo of southern Africa, and the Parana of South America. Magmatically active rifts and continental margins are commonly associated with anomalously high temperatures in the asthenosphere caused by the presence of mantle plumes (White and McKenzie 1989). We therefore turn our attention to mantle plumes before considering a model for melt generation and emplacement associated with plume activity.

3.7.1 Plumes

Far from their margins, oceanic plates are marked by long chains of volcanic islands (e.g., Emperor–Hawaiian seamount chain) and bathymetric swells elevating the seabed 1–2 km above the adjacent abyssal plains (e.g.,

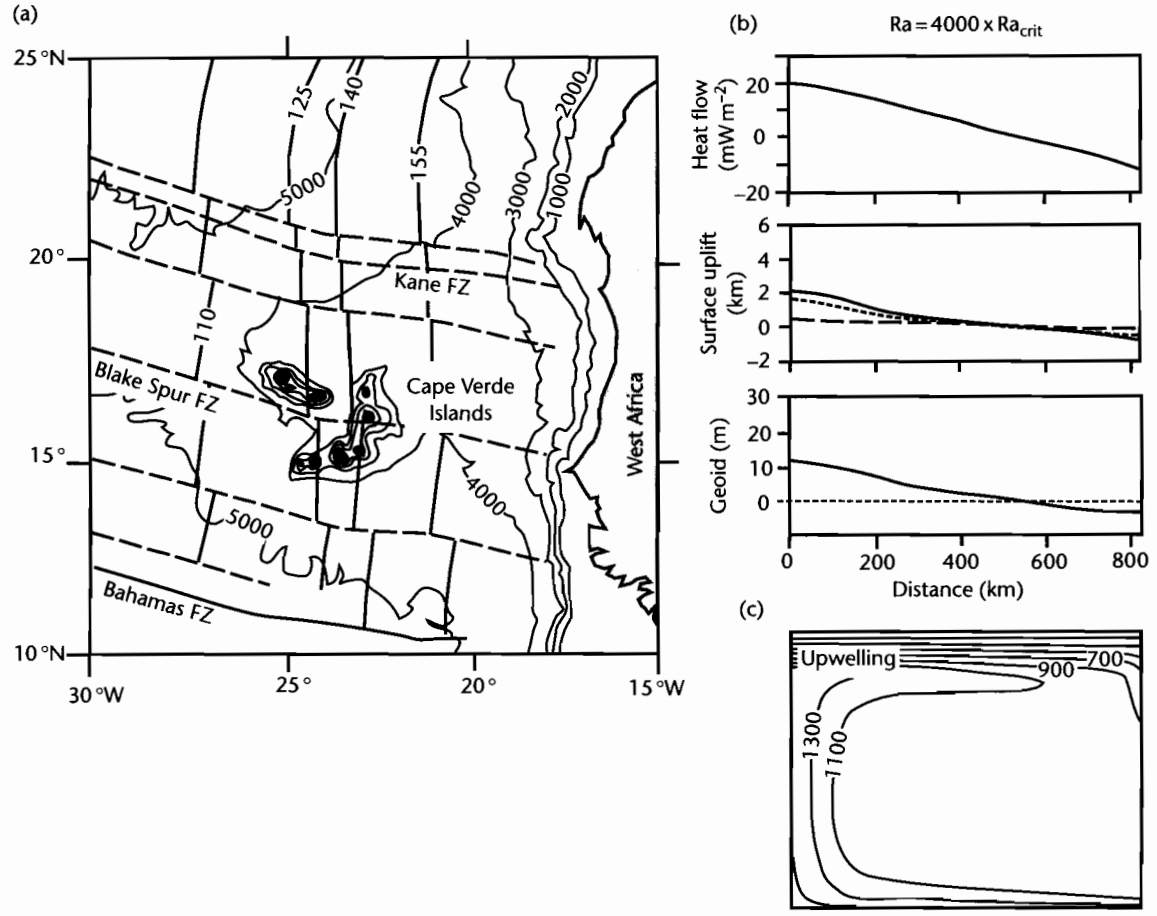

Fig. 3.35 Cape Verde hotspot. (a) Bathymetric map (in m) of the Cape Verde Rise, with isochrons in Ma. Fracture zones are shown in dashed lines; (b) Heat flow, surface uplift, and the geoid for a convection cell at 4000 times the critical Rayleigh number for convection. The total uplift is shown as a conductive component (dashed) and a convective component (dotted); (c) Temperature distribution responsible for the results shown in (b). After Courtney and White (1986). Reproduced courtesy of Blackwell Publishing Ltd. for Royal Astronomical Society.

Cape Verde, Reunion, and Iceland swells) (Wilson 1963; Morgan 1981). The equivalent chains and swells on land are less easy to discern because of the effects of erosion. However, all of these intraplate features are associated with the eruption of extensive basalts, whose geochemistry indicates that they originate by melting of mantle elevated above the normal temperature of the asthenosphere. They can be explained by the rising of hot plumes from the thermal boundary layer at the core–mantle boundary (see also §5.2.4).

The Cape Verde swell typifies plume-related temperature anomalies and bathymetric relief (Courtney and White 1986) (Fig. 3.35). The best fitting convection model to explain the temperature distribution involves a plume neck of 150 km diameter feeding a mushroom-like head of hot mantle material 1500 km across. The temperature anomaly in the plume head at the base of the plate is generally in the region of 100 °C, with the neck of the plume in excess of 300 °C above ambient asthenospheric temperatures. The centre of the Cape Verde swell is elevated by 1900 m relative to the normal oceanic depth: most of this relief can be attributed to dynamic uplift over the convecting plume head.

Geoid anomalies suggest that plume upwellings are spaced at about 2500–4000 km in the upper mantle beneath the oceans (McKenzie et al. 1980), but their distribution beneath the continental lithosphere is more speculative. The highspots associated with alkaline volcanism in north-central Africa, such as the Hoggar and Tibesti domes, may be related to activity in the underlying mantle (Thiessen et al. 1979; Sahagian 1980). Doming over hot plumes has also been interpreted as responsible for particular centrifugal paleodrainage patterns (Cox 1989), as well as for the eruption of vast piles of basalts.

The lithospheric plates move relative to the major mantle upwellings, though the question of whether the upwellings are stationary is unresolved. Two sorts of uplift pattern and igneous activity should result from plume activity depending on whether the lithosphere migrates over a plume head or plume tail. Plume head provinces should be areally extensive and equant (1500 km to 2500 km across), whereas plume tail provinces should be narrow (<300 km wide) and linear, that is, they should be hotspot tracks.

3.7.2 Melt generation during continental extension

Igneous activity in sedimentary basins is diagnostic of basin-forming mechanisms. In the prototype uniform stretching model of McKenzie (1978a), no melts are generated because the geotherm does not intersect the solidus for crustal and mantle materials. However, it is well known that rift provinces are associated with minor (e.g., Western Rift, Africa, North Sea) to major (e.g., Eastern Rift, Africa, Rio Grande) volcanism. Most importantly, continental break-up at high values of stretching is commonly associated with vast outpourings of flood basalts, indicating major melting of the asthenosphere by adiabatic decompression. Melts liberated by decompression are assumed to separate from their residue and to travel upwards to either be erupted at the surface, or to be emplaced as igneous bodies in the crust. McKenzie and Bickle (1988) showed how the amount of melt generated depends on the potential temperature of the asthenosphere – defined as the temperature the asthenosphere would have if brought to the surface adiabatically without melting – and the amount of stretching (Fig. 3.36). For example, if a 100 km-thick lithosphere is stretched by a factor of 2, we would expect a melt thickness of about 2 km for a potential temperature of 1400 °C. At higher values of stretching ($\beta = 5$), we would expect a melt thickness of 10 km for the same potential temperature. The normal potential temperature of the asthenosphere is 1280 ± 30 °C, so the examples above refer to an excess temperature of the order of 100 °C attributable to plume activity.

The conditions at the site of partial melting are reflected in the composition of the erupted basalts. Stretching at infinitely high values at a normal asthenospheric potential temperature of 1280 °C produces melt with the composition of a mid-ocean ridge basalt (MORB). However, increasing the potential temperature to 1480 °C causes an increase in MgO and a decrease in Na_2O. Consequently, we would anticipate the generation of first alkali basalts and then tholeiitic basalts as stretching increases over an asthenosphere with a potential temperature of 1480 °C.

The presence of a hot asthenosphere affects the subsidence experienced at the Earth's surface caused by lithospheric stretching. This is mainly caused by two effects: the addition of igneous bodies beneath the crust, and the dynamic uplift from the mantle plume.

3.7.2.1 Uplift due to igneous underplating

The density of igneous rock generated by adiabatic decompression of the mantle depends on the potential temperature at the site of partial melting, and ranges between 2990 and 3070 kg m^{-3} (at a depth of 10 km) for potential temperatures of 1280 °C and 1480 °C respectively. This range of density is midway between the density of the continental crust and the density of the mantle, so there is a strong likelihood that melts will be trapped and underplated beneath the crust. Since these igneous additions replace lithospheric mantle (density 3300 kg m^{-3}), the net effect is uplift relative to the depth expected from uniform stretching of the lithosphere without magmatic activity (§3.4) (Fig. 3.37).

Assuming Airy isostasy, the amount of underplating X required to generate an amount of surface uplift U can be found by balancing two lithospheric columns. In the undisturbed column, crust of thickness y_c and density ρ_c occurs within a lithosphere of thickness y_L and subcrustal density ρ_m. In the underplated lithospheric column, crust of the same thickness is underlain by a layer of basaltic underplate with thickness X and density ρ_x. The total thickness of this lithospheric column is y_L plus the surface uplift U.

Balancing the pressures at a depth of compensation at the base of the lithosphere yields

$$U = X\left(1 - \frac{\rho_x}{\rho_m}\right) \tag{3.37}$$

The density of the mantle lithosphere can be taken as $3300\,\mathrm{kg\,m^{-3}}$ and density of basaltic underplate as $3000\,\mathrm{kg\,m^{-3}}$. The rock uplift for an underplate thickness of 5 km is therefore 455 m, or approximately one-tenth of the underplate thickness. This is also the surface uplift without any erosion. We can incorporate erosion in the simplest way as follows (Brodie and White 1994). Consider a piece of lithosphere underplated with basalt of thickness X which is eroded so that the surface elevation change is zero. The crust therefore has a thickness of y_c minus the denudation D. We can once again perform an isostatic balance, giving

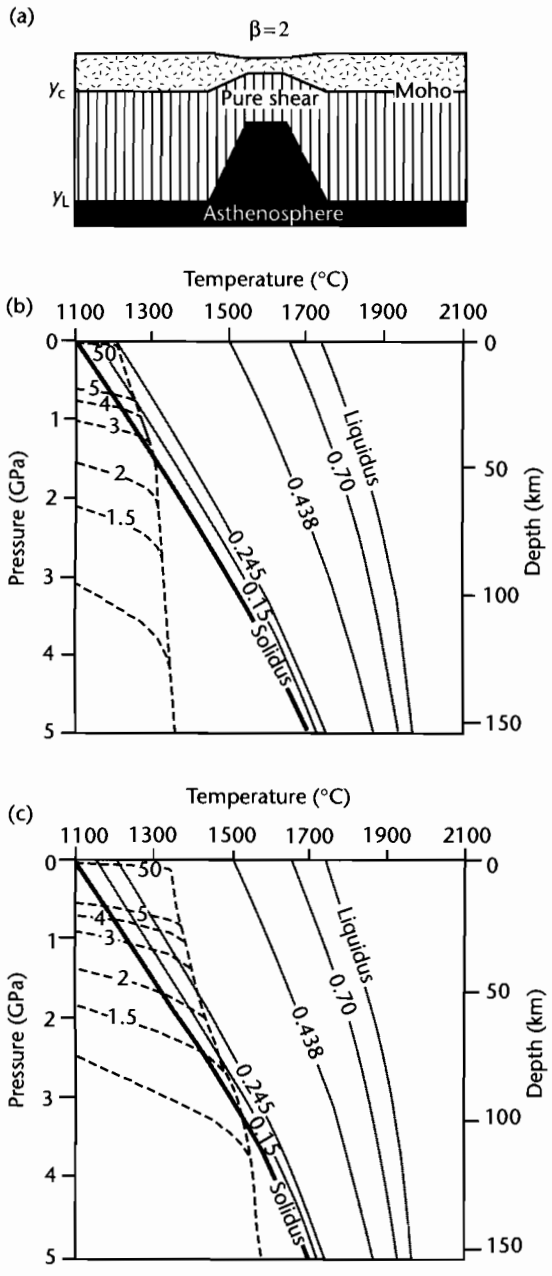

Fig. 3.36 Melt generation by adiabatic decompression during pure shear extension, based on McKenzie and Bickle (1988), White and McKenzie (1989), and Latin and White (1990). (a) Uniform stretching of the lithosphere by a stretch factor β of 2; (b) Adiabatic upwelling due to stretching at different values of β from 1.5 to 50. Potential temperature of the asthenosphere 1280 °C, mechanical boundary layer thickness of 100 km, kinematic viscosity $4 \times 10^{15}\,\mathrm{m^2\,s^{-1}}$. Curves between the liquidus and solidus show the melt fraction by weight. Only small amounts of melt can be produced at high values of stretching; (c) As for (b), but with a potential temperature of 1480 °C, showing that large amounts of melt can be liberated at relatively low values of the stretch factor β. Reproduced courtesy of Geological Society of America.

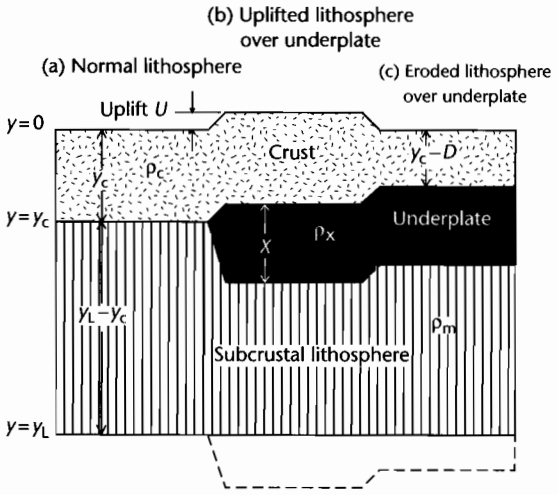

Fig. 3.37 Isostatic effects of igneous underplating as a result of plume activity. Normal lithosphere is shown in (a). An uplifted region results from the emplacement of an igneous underplate in (b). The effects of surface erosion are shown in (c).

$$D = X\left(\frac{\rho_m - \rho_x}{\rho_m - \rho_c}\right) \tag{3.38}$$

where D is the total denudation of crust caused by the emplacement of a basaltic underplate of thickness X. The total denudation for an underplate thickness of 5 km if there is no change in the surface elevation is 2.5 km, if crustal rocks of density 2700 kg m^{-3} are eroded. We therefore have the maximum erosion case and the no-erosion case. Reality is probably in between. Clearly, magmatic underplating can have significant effects on surface uplift and on the delivery of erosional products to neighboring sedimentary basins (White and Lovell 1997). The uplift caused by magmatic underplating is permanent.

3.7.2.2 Dynamic support produced by mantle plume

The circulation in the mantle plume maintains anomalously high temperatures that cause a dynamic uplift. The amount of dynamic uplift can be approximated by assuming that hot mantle replaces normal mantle down to a depth of compensation. This depth of compensation is most likely 150–200 km. The volumetric coefficient of thermal expansion of mantle rock is about 3.4 $\times 10^{-5}$ °C^{-1}, so there is a 0.34% change in the mantle density for every 100 °C change in its temperature. Dynamic uplift of 500–1000 m is therefore predicted for potential temperatures 100–200 °C hotter than normal. This dynamic uplift is transient, and disappears when the overlying plate migrates away from the anomalously hot asthenosphere, or changes in response to variations in the heat flux into the plume head.

The combined effect of underplating and dynamic support is to elevate the continental plate to sea-level or above during the rifting process for excess asthenospheric temperatures of 100–150 °C. This is entirely supported by the observation that the basalts erupted at rifted continental margins are commonly subaerial rather than submarine, and flow for large distances downslope to produce extensive flood basalt provinces.

3.7.3 The northern North Atlantic and the Iceland plume

The northern Atlantic contains extensive basalts covering *c.* 500 $\times 10^3$ km^2 on both sides of the ocean in Greenland and in northwest Britain, Ireland and the Faeroes. The basalts range from 52 to 63 Ma in age, with a main eruption phase at 59 Ma (Mussett et al. 1988). The thermal anomaly responsible for these igneous provinces is now located beneath Iceland. The Iceland region continues to be dynamically supported by the underlying plume over an area of anomalously shallow seafloor with a radius of 1000 km.

In the subsurface seismic record, extrusive basalt sheets can be recognized as seaward-dipping reflectors along both the east Greenland and Rockall–Faeroes–Norwegian margin (Fig. 3.38). Volumetrically smaller basaltic volcanism can be seen in onshore exposures such as the Tertiary igneous province of northwest Scotland and northeast Ireland. Thick (<8 km) prisms of accreted igneous rocks with seismic velocities >7.2 km s^{-1} have been imaged across the Hatton Bank and Voring Plateau beneath thinned continental crust, most likely representing underplated igneous rocks. White and McKenzie (1989) estimate the combined underplate and extrusive basalt volume as <10^7 km^3.

The Icelandic plume has been identified as the "smoking gun" for the widespread surface uplift of the North Atlantic area in the Early Tertiary (Paleocene). The regional surface uplift caused by underplating and dynamic support is thought to have promoted high rates of denudation and transport of particulate load into the deep sea environments of the North Sea and NW Atlantic margin basins. High rates of denudation in large areas of northwestern Europe during the Early Tertiary can be inferred from apatite fission track analysis (papers in Doré et al. 2002). In the neighboring sedimentary basins, such as the Faroes–Shetland Basin and the Rockall–Porcupine troughs, sandstones were episodically delivered from this exhuming continental landmass. White and Lovell (1997) suggested that the main pulses of submarine fan deposition correspond to the main phases of magmatic activity during the time period 62–54 Ma.

3.7.4 Low-volume melts in the Mesozoic North Sea Rift

We know from the preceding sections that adiabatic decompression is unlikely to be significant for low stretch factors and normal asthenospheric temperatures. Over a "normal" temperature asthenosphere (1280 °C), it is not possible to generate melts until very high amounts of stretching have taken place, by which time the parent material melts at very shallow depths, producing small melt volumes (McKenzie and Bickle 1988). It is therefore interesting to test whether the igneous activity noted in continental rifts with small stretch factors can also be

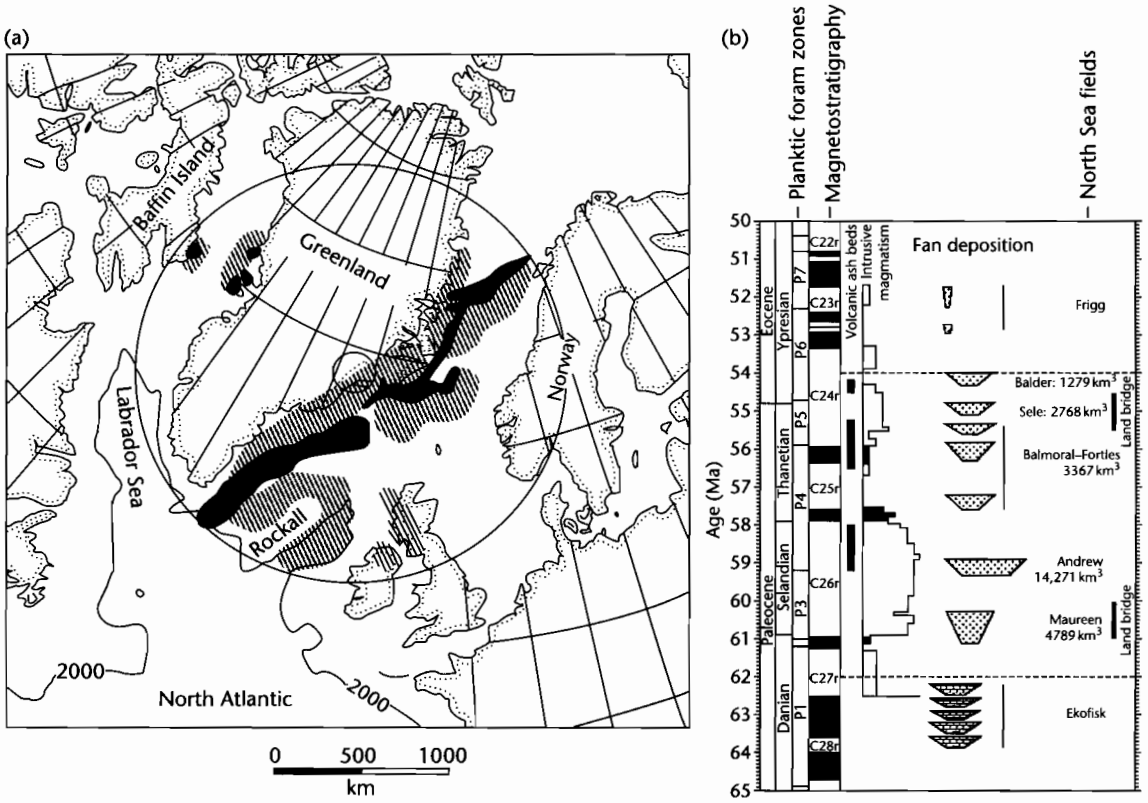

Fig. 3.38 (a) Reconstruction of the northern North Atlantic region just after the onset of ocean spreading (magnetic anomaly 23), showing the extent of the Iceland plume (White and McKenzie 1989). Solid shading shows position of extrusive volcanic rocks, hatching shows extent of Early Cretaceous igneous activity. Uplift over the plume head can be recognized in thermochronologic data such as apatite fission tracks. Reproduced courtesy of American Geophysical Union; (b) Pulsing of the Iceland plume is thought to have caused episodic deposition of sands in the deep sea (White and Lovell 1997). Periods of deep sea fan deposition correspond to times of high levels of intrusive igneous activity. Time scale from Berrgren et al. (1995). Reproduced courtesy of Macmillan Journals.

investigated using the approach outlined in §3.7.2 (Latin and White 1990).

Partial melting can only be achieved by the intersection of the solidus and geotherm. This may be promoted by: (i) high amounts of lithospheric stretching, (ii) presence of volatiles, and (iii) high asthenospheric temperatures, or a combination of factors (Fig. 3.39).

In the North Sea, low volume (*c.* 0.5 km melt thickness) synrift alkali basalts are found in the triple junction area, where the Viking, Central, and Moray Firth Grabens intersect (Fig. 3.4). They postdate the start of rifting by *c.* 30 Myr. The McKenzie and Bickle (1988) model suggests that:

- A combination of a mantle plume (1480 °C) and stretch factor of 1.4–1.6 (estimated from subsidence histories in North Sea Rifts) would give 5 km of tholeiites rather than 0.5 km of alkali basalts. In the triple junction region where β is >2, the model predicts even larger melt thicknesses;
- a combination of stretch factor 1.4–1.6 (observed/calculated), potential temperature of 1280 °C (that is, normal), mechanical boundary layer thickness of 70 km (that is, the lithosphere has been previously thinned/stretched) and a volatile (H_2O) content of 1%, would satisfactorily explain the alkali basalts in the Forties area near the triple junction of the North Sea rifts;
- if the potential temperature was 1380 °C (a "warm plume") and the mechanical boundary layer was 80 km (less previously thinned), the model would explain the

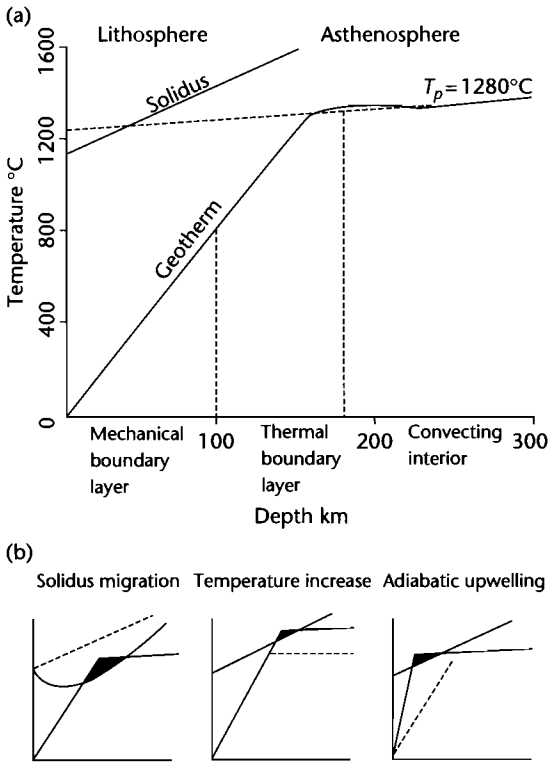

Fig. 3.39 Causes of partial melting related to lithospheric extension (after McKenzie and Bickle 1988, Latin et al. 1990, and Leeder 1995). (a) Geotherm for a potential temperature of 1280 °C and solidus for mantle material. The potential temperature is the temperature on an adiabatic gradient extrapolated to surface pressure; (b) Adiabatic decompression may be facilitated by migration of the solidus caused by the presence of volatiles such as water, by a temperature increase due the presence of a plume in the asthenosphere, or by mechanical thinning of the lithosphere and asthenospheric upwelling.

magmatism *and* the regional uplift over a diameter of *c.* 1000 km.

3.8 ESTIMATION OF THE STRETCH FACTOR AND STRAIN RATE HISTORY

An estimate of the amount of extension that has taken place can be obtained from a number of methods (Fig. 3.40). Knowledge of the strain rate history or total stretch factor is important as a basis for predicting the geothermal gradient and heat flow history of basin sediments, as well as in showing the role of rift structures in accommodating basin sediments.

3.8.1 Estimation of the stretch factor from thermal subsidence history

It has previously been shown (§3.1) that the lithospheric stretching model of the type formulated by McKenzie (1978a) predicts initial uplift or subsidence depending on the ratio of crustal to lithospheric thickness y_c/y_L and the stretch factor β. If y_c/y_L is known for a particular basin, the fault-controlled initial subsidence could in theory be used to estimate the amount of stretching. However, the extreme variations in synrift thicknesses make this a very unreliable technique.

The thermal subsidence in a basin generated by uniform stretching is dependent on the stretch factor alone. The postrift thermal subsidence phase of sedimentary basins also lacks the extreme thickness variations characteristic of synrift deposits. The standard technique is the construction of a set of subsidence curves for different values of the stretch factor β. Curves can be constructed for a water-loaded basin, where the density of the infill is $\rho_w = 1000\,kg\,m^{-3}$. In this case the postrift sediment thicknesses need to be decompacted and backstripped to reveal the water-loaded tectonic subsidence history (Chapter 9). The observed backstripped postrift subsidence can then be compared with the model curves to reveal the best-fitting stretch factor. Alternatively, model curves can be constructed that show the thermal subsidence for different values of the stretch factor β for a sediment-loaded basin. Construction of such curves requires estimation of the bulk density of the sediment column as a function of time. The model sediment-loaded curves can then be compared with the decompacted total subsidence curve derived from borehole data or outcrop sections.

3.8.2 Estimation of the stretch factor from crustal thickness changes

In some circumstances the attenuation of the crust can be estimated from deep seismic (refraction and wide angle reflection) results. For example, the Moho rises by 5 km in the southern part of the Rhine Graben and 3 km of sediment has accumulated. The crust has therefore thinned by 8 km (Emter 1971; Mueller et al. 1973). Simi-

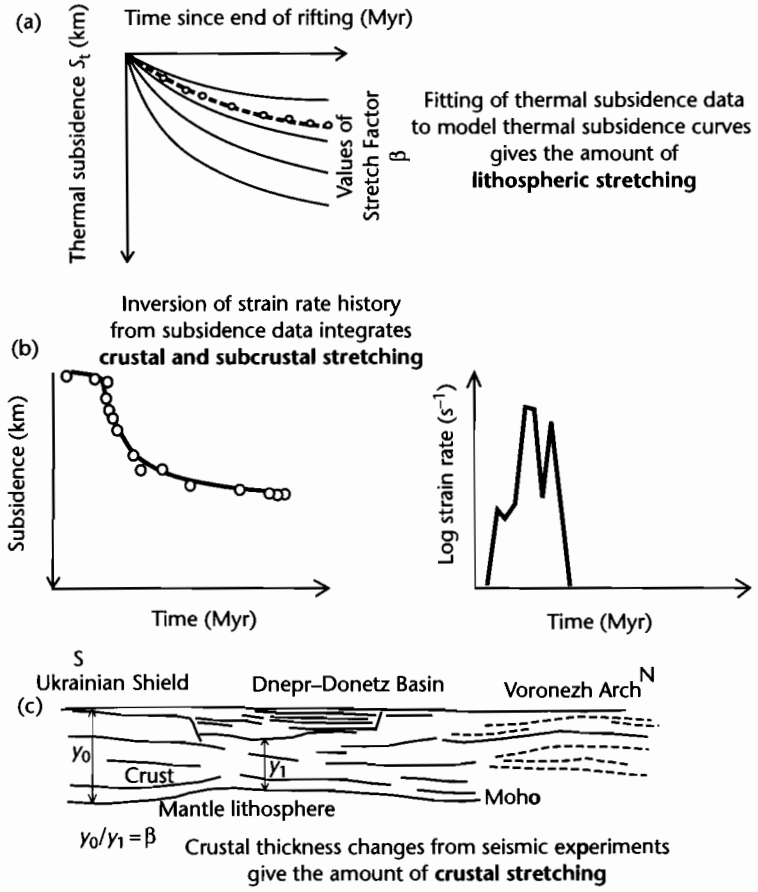

Fig. 3.40 Methods for calculation of the amount of stretching. (a) Calculation of the lithospheric stretch factor from thermal subsidence curves; (b) Inversion of strain rate history of the lithosphere from subsidence curves; (c) Calculation of the crustal stretching from mapping of the Moho.

larly, the nearby Limagne Graben (France) contains 2 km of sediments and the Moho rises to within 24 km of the surface (Hirn and Perrier 1974). Since the crust is about 30 km thick in the Massif Central, which separates the Rhine–Bresse Rift system from the Limagne Graben, the amount of crustal attenuation in these two cases can be estimated to be between 1.2 and 1.3.

The North Sea is a failed rift that underwent rifting in the Jurassic–Early Cretaceous. Regional deep seismic reflection profiles and gravity profiles in the Viking Graben–Shetland platform area have been used to estimate the depth to the Moho (Barton 1986; Klemperer 1988) (Fig. 3.4). More recently, the deep structure of the Viking Graben and adjacent areas of the northern North Sea (60–62 °N) has been investigated based on an integrated study of deep seismic reflection and refraction data, gravity and magnetic data (Christiansson et al. 2000) (Fig. 3.41). Where unaffected by Caledonian crustal roots and by Mesozoic stretching, the Moho lies at a depth of 30–32 km. It shallows to about 20–22 km beneath the Viking Graben. Since the graben is filled with approximately 10 km of Triassic to Cenozoic sedimentary rocks, the thickness of crystalline and Paleozoic crustal rocks in the Viking Graben is only about 10 km. This represents a stretch factor of over 3. In contrast, the East Shetland and Horda Platforms have stretch factors of less than 1.5. These values reflect the cumulative effects of several post-Caledonian stretching events.

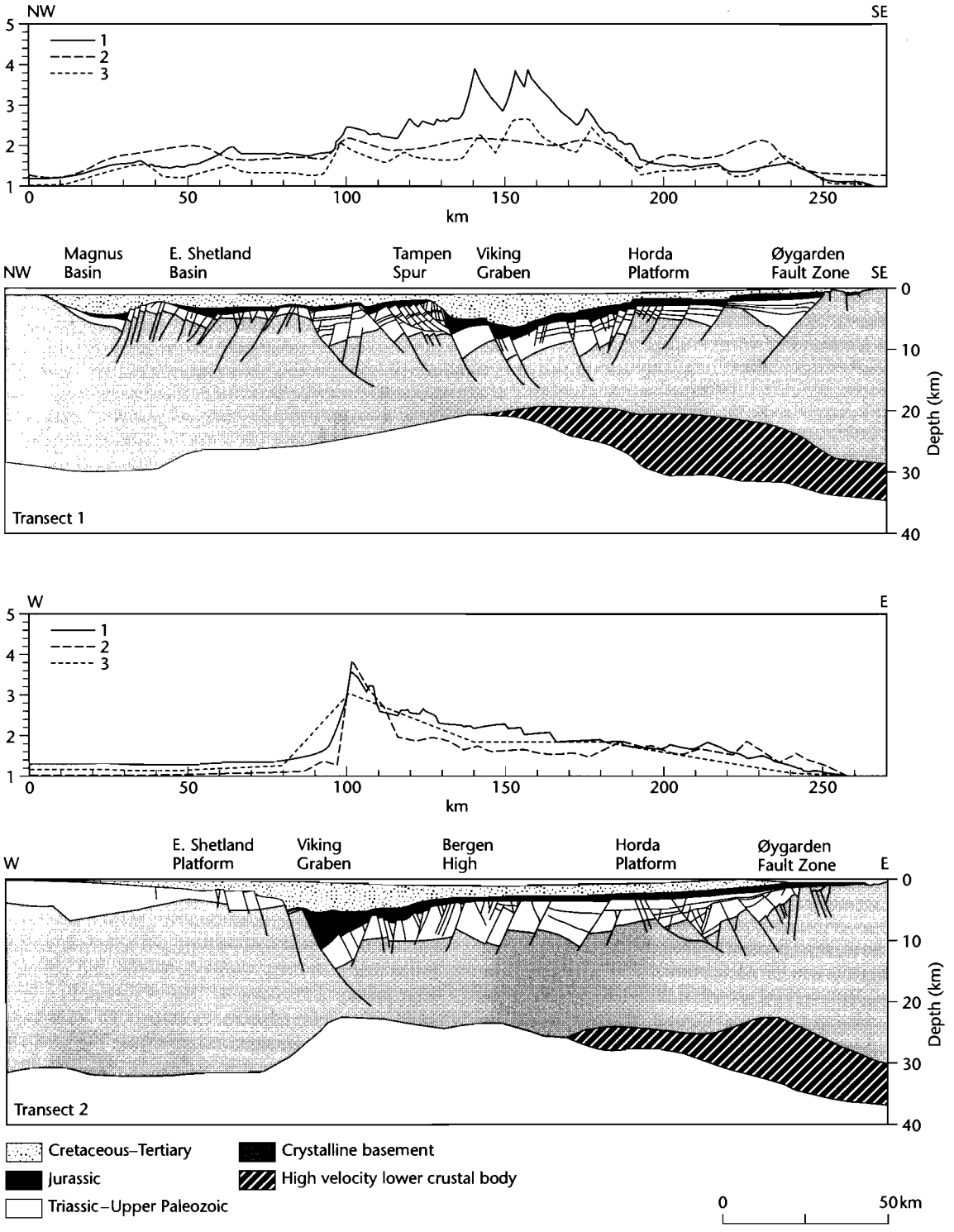

Fig. 3.41 Two crustal transects across the Viking Graben, northern North Sea (from Christiansson et al. 2000; Skogseid et al. 2000), based on the integration of all available geological and geophysical information, with estimates of crustal stretch factor. For each transect, line 1 indicates crustal thinning assuming an initial crustal thickness of 36 km; line 2 is derived from reverse modeling; and line 3 is derived from forward tectonostratigraphic modeling. Reproduced courtesy of Geological Society of London.

The estimates of crustal stretching derived from mapping of the Moho have been compared with estimates from subsidence analysis (Giltner 1987; Badley et al.1988, Christiansson et al. 2000) and forward tectonostratigraphic modeling (Odinsen et al. 2000). The former are somewhat higher than the stretch factors derived from the other two methods, which emphasizes the care that needs to be taken in the interpretation of β estimates. A similar exercise in the Rockall, mid-Norway and SW Barents Sea areas also showed large discrepancies between the crustal stretching estimated from deep seismic imagery and subsidence analysis (Skogseid et al. 2000) (Fig. 3.41).

3.8.3 Estimation of the stretch factor from forward tectonostratigraphic modeling

Stretch factors have been estimated along transects of the northern North Sea where the crustal profile, stratigraphic thicknesses and faults are very well constrained (Odinsen et al. 2000). Forward tectonostratigraphic models simulate crustal structure and basin development through time using a rheologic model of the lithosphere with a finite flexural strength based on Braun and Beaumont (1989) and Kooi et al. (1992) (§3.6). The forward model has the advantage of discriminating the stretching from each rifting event. Odinsen et al. (2000) compared the stretching in the Permo-Triassic (maximum of $\beta = 1.41$ in the Viking Graben) versus Jurassic (maximum of $\beta = 1.53$ in the Viking Graben) rifting events in the northern North Sea. The calculated distribution of stretch factors along two well-constrained crustal transects matches well earlier estimates based on 1-D subsidence analysis (Giltner 1987; Badley et al. 1988) (Fig. 3.41).

3.8.4 Inversion of strain rate history from subsidence data

White (1993, 1994) has taken the novel approach of calculating the strain rate history from the subsidence history of sedimentary basins using inverse methods. The stretch factor β can be viewed as representative of the total strain integrated over the time scale of extension. The stretch factor is therefore related to the vertical strain rate $G(t)$ by

$$\beta = \exp\left(\int_0^{\Delta t} G(t)dt\right) \tag{3.39}$$

where Δt is the duration of stretching. If the strain rate is constant, $\beta = \exp(G\Delta t)$. In the inverse method, the subsidence as a function of time is solved iteratively to give the strain rate as a function of time $G(t)$. Multiple stretching episodes can be resolved by this technique.

CHAPTER 4

Basins due to flexure

Every valley shall be exalted, and every mountain and hill shall be made low: and the crooked shall be made straight, and the rough places plain.

(ISAIAH 40:4)

SUMMARY

Flexure is the long wavelength deflection of a lithosphere of finite strength caused by the application of an external force system. A general flexural equation can be established for the case of a thin elastic plate overlying a weak fluid subjected to vertical applied forces, horizontal forces, and torques or bending moments. The general flexural equation can then be used in different geodynamic situations by applying different boundary conditions.

Flexure of the lithosphere is most clearly demonstrated at oceanic islands, seamount chains, ocean trenches, and foreland basins. Lithospheric flexure also supports sediment loads in most sedimentary basins. The characteristic signature of lithospheric flexure is a negative free air gravity anomaly (at sea) or a negative Bouguer anomaly (on land). The flexural basins associated with ocean–continent and continent–continent plate margins are particularly well represented in the geological record. In an Andean-type setting the flexural basin on the subducting oceanic plate is the ocean trench and the flexural basin on the upper plate is a retroarc foreland basin. In Alpine-type settings the flexural basin on the subducting plate or lower plate is called a peripheral- or pro-foreland basin, whereas the flexural basin on the overriding or indenting plate is termed a retro-foreland basin. Some foreland basins are related to subduction zone roll-back (subduction zone retreat) and are associated with prominent backarc extension. The formation and evolution of foreland basins is intimately related to the processes of shortening, exhumation, and extensional collapse in the adjacent orogenic wedge.

The deflection of the oceanic lithosphere along seamount chains such as the Hawaiian Islands can be explained by either the flexure of a continuous plate loaded by a vertical applied force (representing the excess mass of the seamount chain), or by the flexure of a plate broken beneath the vertical applied force. Some useful and simple expressions for the geometry of the deflection can be derived that involve the maximum amplitude of the deflection, the width of the basin, the location of the forebulge, and the height of the forebulge. In particular, the wavelength of the deflection is dependent on the *flexural rigidity* of the plate, or *flexural parameter*. The maximum deflection is dependent on the flexural rigidity and the magnitude of the applied load.

The bending of the ocean lithosphere at trench–arc systems can be explained by the flexure of a broken elastic plate by a combination of vertical and horizontal forces and bending moments. These forces cannot, however, be directly determined. Forebulges (or outer rises) are very well developed seaward of deep trenches in the northwestern Pacific.

Many studies of continental flexure have been made in collisional zones. Bouguer gravity anomaly profiles across mountain belts and foreland basins suggest a great variability in the make-up of the force systems deflecting the continental plate. This is primarily because of the complexity of crustal and mantle wedging and slab dynamics within and beneath collision zones. Although line load configurations provide reasonable deflections of the continental lithosphere, orogenic wedge loads, and sedimentary basin-fills need to be treated as spatially distributed loads.

There has been much debate about the flexural rigidity of the oceanic and continental lithosphere. The oceanic lithosphere appears to become stronger as it ages and cools, but it does not weaken in its ability to support loads with time since loading. This suggests that any

viscous relaxation that takes place, does so very quickly (less than 10^5 or 10^6 years), after which flexural rigidity approaches an asymptotic value. The factors determining the flexural rigidity of the continental lithosphere are less clear, and there is no relationship between flexural rigidity and its age. A number of factors may be responsible, such as differences in geothermal gradient caused by strong variations in the crustal radiogenic heat production, decoupling between a strong upper crust and strong underlying mantle lithosphere during bending, plastic yielding at high curvatures, and viscoelastic relaxation. The lithosphere approaching collision zones may also be segmented, producing a stepped, compartmentalized deflection. Strong spatial variations in flexural rigidity have been measured in the forelands of many mountain belts.

Although linear elasticity suggests that lithospheric buckling should not take place, analogue experiments and numerical models using more realistic lithospheric rheologies consistently reproduce long wavelength (several hundred km) antiforms and synforms. The topography of basins in, for example, central Asia, supports the existence of lithospheric buckles. Sedimentary basins located at buckle synforms may be difficult to discriminate from backbulge depositional zones.

Orogenic wedges act as primarily vertical loads on the deflected plate in collision zones. The movement of a line load or distributed load over a foreland plate forces a wave-like deflection ahead of it. The orogenic wedge is viewed as a dynamic unit with critical surface slopes in which the gravitational and deviatoric forces strive to achieve a steady state. Disturbances of equilibrium by externally imposed forces (such as changes in convergence rate) may result in major changes in the rates of shortening or extension of the wedge. These processes in turn influence the erosion of the mountain belt to provide detritus for the foreland basin and the configuration of the load causing the deflection of the overridden plate. Critical taper models modified to allow for brittle–ductile behavior suggest that the topographic profiles of some mountain belts, such as the Andes, can be explained by the changing ratio of basal shear stress in the decollement zone and strength of rocks in the lower part of the wedge. Ductile behavior in the hotter part of the wedge and within the deep basal shear zone cause a shallow foothills region, steeper intermediate segment, and elevated plateau physiography.

Analogue models using scaled physical experiments are successful at visualizing major crustal structures produced during convergence, including major crustal buckles, conjugate shears, and bivergent wedges. Early numerical models focused on diagnostic basin stratigraphy, treated erosion, sediment transport and deposition as a diffusional problem. Later 3-D plane strain numerical models illustrate the complex links between plate convergence, tectonic fluxes within bivergent wedges, and exhumation. The mechanics of these wedges can be investigated using the Argand number and Ampferer number. Two dynamical end members are the indentation model and the subduction model. Plane strain numerical models show that erosion of the surface of the orogenic wedge is of major importance to wedge dynamics as well as to the filling of adjacent foreland basins. Such models now provide a mechanical explanation for the topography, distribution of high grade metamorphic rocks and thermochronology of rocks in orogenic belts.

In Chapter 4 we focus on the process of lithospheric flexure with the goal of better understanding the behavior of the lithosphere when acted upon by applied force systems or loads. This is of relevance in a number of situations in basin analysis. First, flexure of the lithosphere may cause the primary subsidence or uplift in a sedimentary basin. The most important example is the downflexing of a continental plate by force systems set up during mountain building. This produces *foreland basins*. Second, the lithosphere may undergo a long wavelength flexure in supporting sediment loads. This takes place in basins of all types, including those due to stretching of the lithosphere (Chapter 3).

Foreland basins are elongate or arcuate, highly asymmetrical basins closely associated with continental collision zones. The alternative term "foredeep" was introduced by Price (1973). Dickinson (1974) proposed two genetic classes of foreland basin (Fig. 4.1): (i) Peripheral foreland basins situated against the outer arc of the orogen during continent–continent collision (e.g., Indo–Gangetic Plain, north Alpine foreland basin). (2) Retroarc foreland basins situated behind a magmatic arc linked with subduction of oceanic lithosphere (e.g., Andean examples, Late Mesozoic–Cenozoic Rocky Mountain Basins, North America). Both classes of foreland basin overlie cratonic lithosphere and are associated with crustal shortening in tectonically active zones. Some highly arcuate thrust belts and spatially restricted foreland basins are related to *subduction zone roll-back* and are commonly associated with important backarc extension (Fig. 4.1). The Apennines–Tyrrhenian Sea of the western Mediterranean is an example.

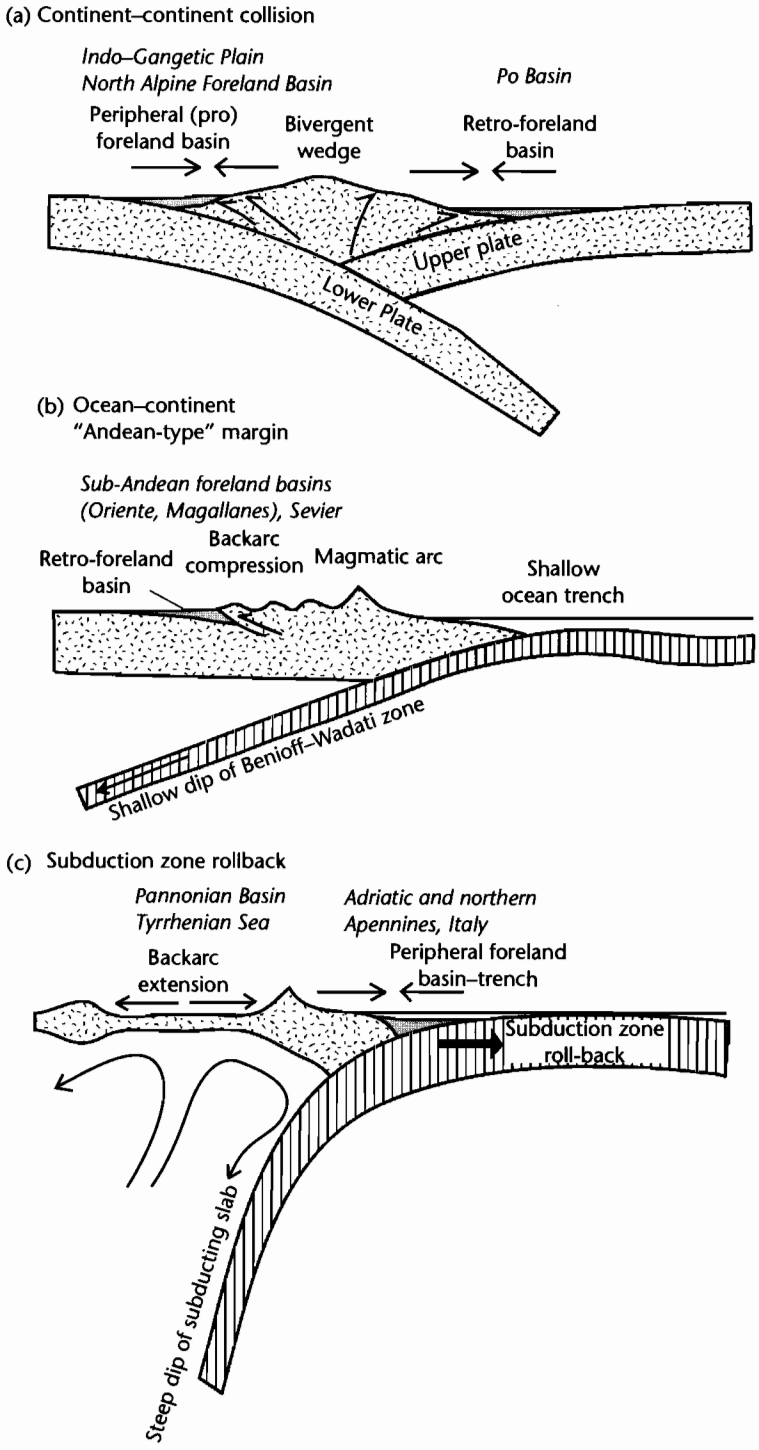

Fig. 4.1 Schematic illustration of peripheral foreland basins, retro-foreland basins, and basins related to subduction zone roll-back.

A mechanically similar situation to continental collision zones exists at ocean–ocean and ocean–continental collision zones where oceanic lithosphere is subducted. The complex plate boundary zone contains many structurally controlled basins. The mechanical equivalent of the orogenic wedge on continental lithosphere is the accretionary prism, with a forearc basin on its retro-flank, and an oceanic trench on its pro-flank.

The lithosphere is capable of distributing forces imposed by a load by a horizontal transmission of stresses. A general flexural equation (eqn 2.29) involving vertical applied loads, horizontal pressure forces, and torques or bending moments can be established for the case of a thin linear elastic plate in a state of plane strain, a reasonable approximation for the lithosphere. In the case of foreland basins, continental lithosphere is bent under the sum total of loads imposed by orogenesis. In the case of ocean trenches and forearc basins, the oceanic lithosphere is bent prior to subduction. We shall now examine these cases in more detail in order to investigate the precise nature of the basin-forming forces.

The reader is referred to §2.1.3 and §2.1.4 for some of the fundamentals of flexure of linear elastic materials. §2.4 contains background to more complex rheologies. In this chapter we concentrate on the application of ideas on flexure to the geometry of ocean trenches and particularly foreland basins. §8.3.1 discusses the stratigraphic patterns in basins of this type.

4.1 BASIC OBSERVATIONS IN REGIONS OF LITHOSPHERIC FLEXURE

Both oceanic and continental lithosphere are capable of a long wavelength bending termed flexure. Flexure of the oceanic lithosphere takes place at ocean trenches, mid-ocean ridges, seamount chains and individual oceanic volcanic islands. Flexure of the continental lithosphere takes place at sites of rifting, strike–slip faulting, at passive margins, and most emphatically at sites of plate convergence. The sedimentary basins caused by flexure of continental lithosphere located adjacent to zones of tectonic shortening commonly occur as pairs, separated by an orogenic belt or magmatic arc (Fig. 4.1). Flexural basins are elongated along the tectonic strike, with an asymmetrical cross-section deepening towards the orogenic belt or magmatic arc. On the continental lithosphere, Bouguer gravity anomalies are negative, indicating the presence of a mass deficit at depth, caused by the downward penetration of relatively light "granitic" material, replacing mantle. Flexural basins on continental lithosphere are close to strongly eroding source areas, and are typically filled with large thicknesses of synorogenic sediment. Ocean trenches, however, may be well-nourished or starved of sediment depending on the proximity of major sediment routing systems. Heat flows in regions of lithospheric flexure are close to normal, or slightly reduced due to crustal and lithospheric thickening during plate convergence.

In the following sections we separately consider some of the basic observations supporting flexure at ocean trenches and foreland basins.

4.1.1 Ocean trenches

At ocean–ocean and ocean–continent convergent boundaries, there is strong evidence that the oceanic lithosphere is bent to high curvatures. Seaward of the ocean trench is a positive free-air gravity anomaly (Watts and Talwani 1974) which corresponds to relatively elevated seafloor. The trench and accretionary prism are characterized by a large negative free-air gravity anomaly, and the island arc by a large positive anomaly (Fig. 4.2). These anomalies can be explained by the bending of the oceanic plate by an applied force system. The shape of the plate at depth can be imaged from the foci of the earthquakes that define Benioff–Wadati zones (Fig. 1.7). First motion studies of these earthquakes show different solutions according to location in the downgoing slab. On the outer wall of the trench the earthquakes are tensional and located down to 25 km depth. This is thought to be a response to outer arc bending stresses in the highly curved oceanic lithosphere. The contact between the upper surface of the downgoing plate and the overriding plate is marked by reverse fault focal mechanism solutions, due to the frictional contact and compressive deformation between the two plates. At much greater depths earthquakes occur at 30–40 km below the top of the slab, suggesting that they occur as the result of internal deformation of the downgoing plate, rather than as a result of compression against the opposite plate. The focal mechanism solutions suggest that the descending plate at these depths is in a state of either down-dip compression or extension (Isacks et al. 1969; Isacks and Molnar 1971), depending perhaps on the net effect of slab pull and ridge push forces on the plate (Spence 1987).

The ocean trenches of the world are remarkably uniform in their bathymetry and wavelength (Fig. 4.3). They are generally 50–100 km in width and 2–4 km below the general level of the adjacent ocean floor. They are asymmetrical in cross-section with a steeper limb

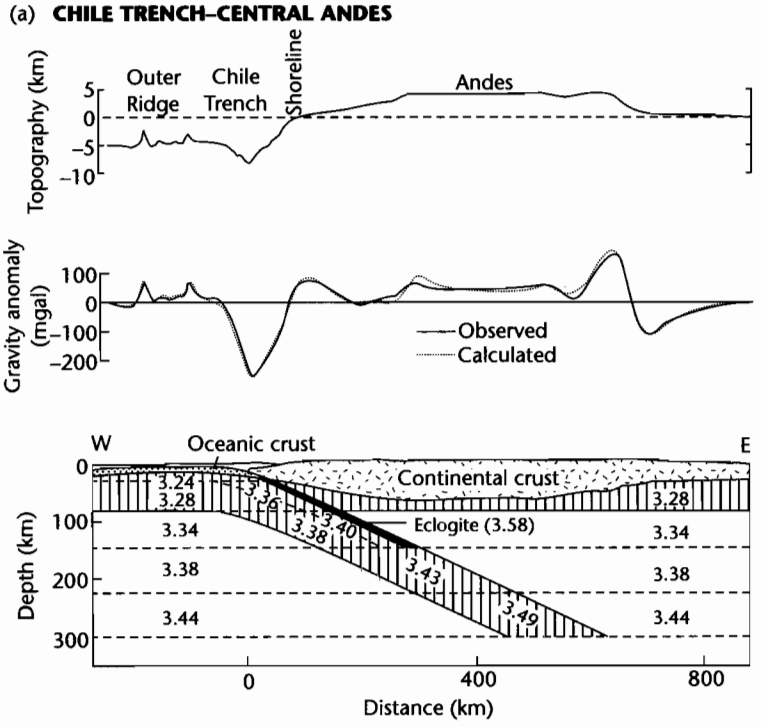

Fig. 4.2 Cross-sections of the arc–trench systems of the Andes and northwestern Pacific. (a) Topography, free-air gravity anomaly, and density model for a cross-section of the Chile Trench and central Andes at 23 °S, after Grow and Bowin (1975). Reproduced courtesy of American Geophysical Union; (b) Topography, free-air gravity anomaly, and crustal density model for the Japan Trench and arc, after Yoshii (1979), Matsuzawa et al. (1986), and van den Beukel and Wortel (1986). Reproduced courtesy of Cambridge University Press.

flanking the overriding plate, and a shallow slope on the side of the downgoing plate. Most trenches are relatively starved of sediment (e.g., Tonga), whereas others are filled with sediment (e.g., Lesser Antilles, and northern part of Burmese–Sunda Trench) and therefore lack a pronounced bathymetric expression. The key control is the availability of a major source of sediment; for example, the Ganges–Brahmaputra and Irrawaddy systems are responsible for the filling of the Burma Trench, while the same trench in Sumatra is relatively deficient in sediment fill.

Cross-sections of the Andes indicate that where the dip of the downgoing slab is shallow, as in Ecuador, there is very little volcanism and weak but widespread seismicity (Pilger 1984). Deformation extends from the active plate margin huge distances (up to 700 km) into the center of the plate, giving rise to crustal shortening and earthquake activity in fold–thrust belts facing the craton. Where the plate is being subducted at a high angle, there is active recent volcanism, seismicity is restricted to a narrow Benioff zone, and a well-developed longitudinal median sedimentary trough (Altiplano) is developed. The cause of the locally shallow angle of the downgoing slab may be the subduction of relatively buoyant oceanic ridges or of very young oceanic lithosphere.

4.1.2 Foreland basins

There are also elongate to arcuate basins located at ocean–continent and continent–continent collision zones (Fig. 4.1) where they are situated on continental lithosphere (Dickinson 1974). In an Andean-type setting (ocean–continent), the basin on the lower plate is the ocean trench, and the basin on the upper plate is a foreland basin, commonly termed of *retroarc type*. In a

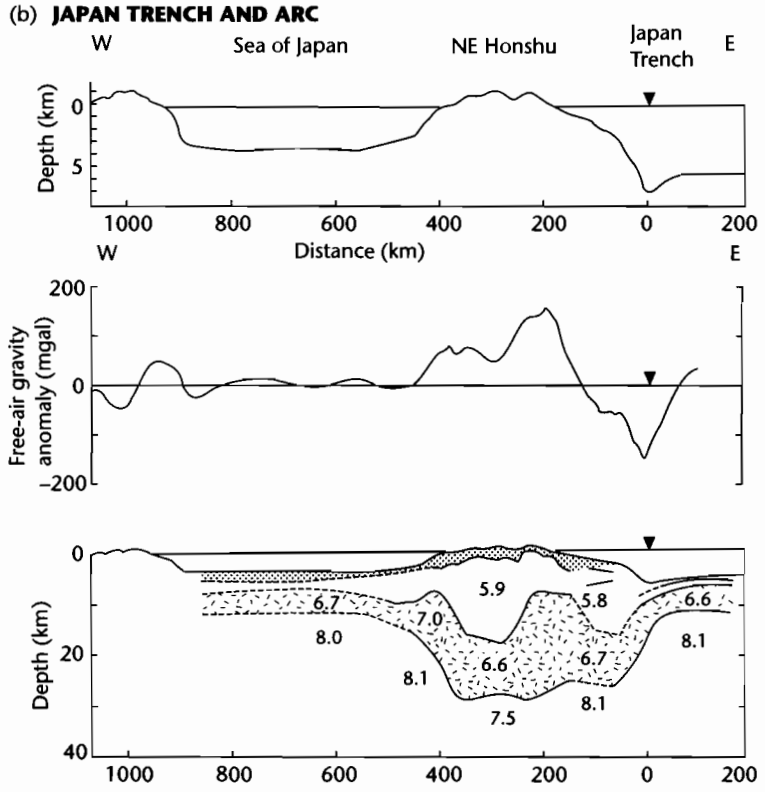

Fig. 4.2 *Continued*

Himalayan-type or Alpine-type setting (continent–continent), the foreland basin on the lower plate is of *peripheral* or *pro-foreland* type, and the basin on the upper plate is of *retro-foreland* type (Willett et al. 1993). Some orogenic belts contain large *intramontane basins*, as is classically displayed in the Andes of South America (Horton et al. 2001). However, these intramontane basins are caused by localized extensional and strike–slip tectonics rather than lithospheric flexure. Foreland basins may be partitioned by the uplift of crustal blocks cored by basement rocks (Schwartz and DeCelles 1988), as in the Laramide uplifts of the Rocky Mountains of the western interior of USA.

Foreland basin systems are dynamically linked to adjacent convergent orogenic belts. These convergent orogens are zones of considerable (hundreds of km) crustal shortening, achieved by translations along thrust faults and by ductile thickening. The thrust belts characteristic of orogenic belts are typically parallel to the strike of the orogenic belt, but in detail comprise salients and reentrants (syntaxes). The Appalachians of eastern North America and the Himalayas of India–Pakistan are Paleozoic and Cenozoic examples respectively. Many orogenic belts are also characterized by ductile extensional detachment faults and shear zones that facilitate rapid rates of exhumation of high grade rocks. The South Tibet Detachment System of the Himalayas (Burg et al. 1984) and the Simplon Fault of the Swiss Alps (Mancktelow 1985) are examples.

Some thrust belts and foreland basins are related to *subduction zone roll-back*, or *subduction zone retreat* (Royden 1993), where the rate of subduction exceeds the rate of plate convergence. Subduction roll-back produces short, highly arcuate thrust systems such as the Apennines and Carpathians of Europe. Foreland basins developed in such systems may be associated with regions of retroarc extension (e.g., Pannonian Basin) or the creation of new oceanic basins (Apennines–Tyrrhenian Sea, Malinverno and Ryan 1986; Doglioni et al. 1998).

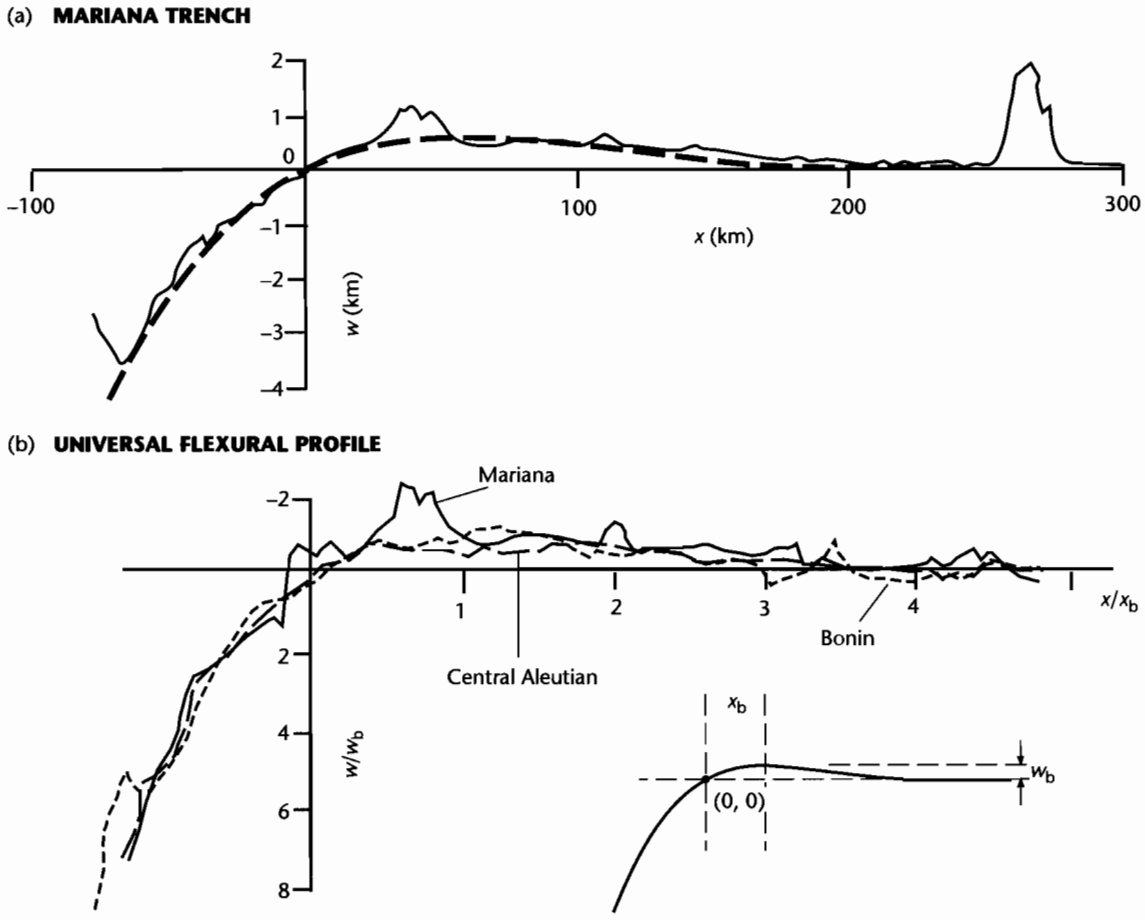

Fig. 4.3 (a) Bathymetry of the Mariana Trench (Watts and Talwani 1974) compared to that predicted by the universal flexural equation with x_b taken as 55 km, and w_b as 0.5 km (after Turcotte and Schubert 1982, p. 130); (b) Nondimensional comparison of the bathymetric profile of the Mariana, Bonin, and Central Aleutian oceanic trenches with a universal flexural profile (after Caldwell et al. 1976). The bathymetric profiles are normalized as described in §4.2.3. Reproduced courtesy of Cambridge University Press.

There are a number of well-documented orogenic belts and foreland basin systems related to Cenozoic orogenesis, such as the Pyrenees of Spain, Alps of France and Switzerland, Apennines of northern Italy, Himalayas of India and Pakistan, and Andes of South America. These examples provide benchmarks of the close linkage between lithospheric flexure, convergent tectonics, and basin development. As an example, the Himalayas are the world's highest and largest orogenic belt. A classic foreland basin (Burbank et al. 1996) with >6 km of sedimentary fill is found to the south of the Main Boundary Thrust of the Himalayan system (Fig. 4.4). The Himalayas are 250–350 km wide and extend for thousands of kilometers around the site of indentation of India with Asia. Convergence between the Indian indenter and Asia is currently *c.* 60 mm y^{-1} (Bilham et al. 1997). Shortening in the Himalayan fold–thrust belt is in excess of 700 km (DeCelles et al. 1998). Focal mechanism solutions of earthquakes (Molnar and Chen 1982) show that the Indian shield in the south is undergoing weak extensional faulting, the Lower Himalaya is experiencing thrust fault deformation, and the High Himalaya has a mixture of extensional and strike–slip deformation. Seismic imaging shows that

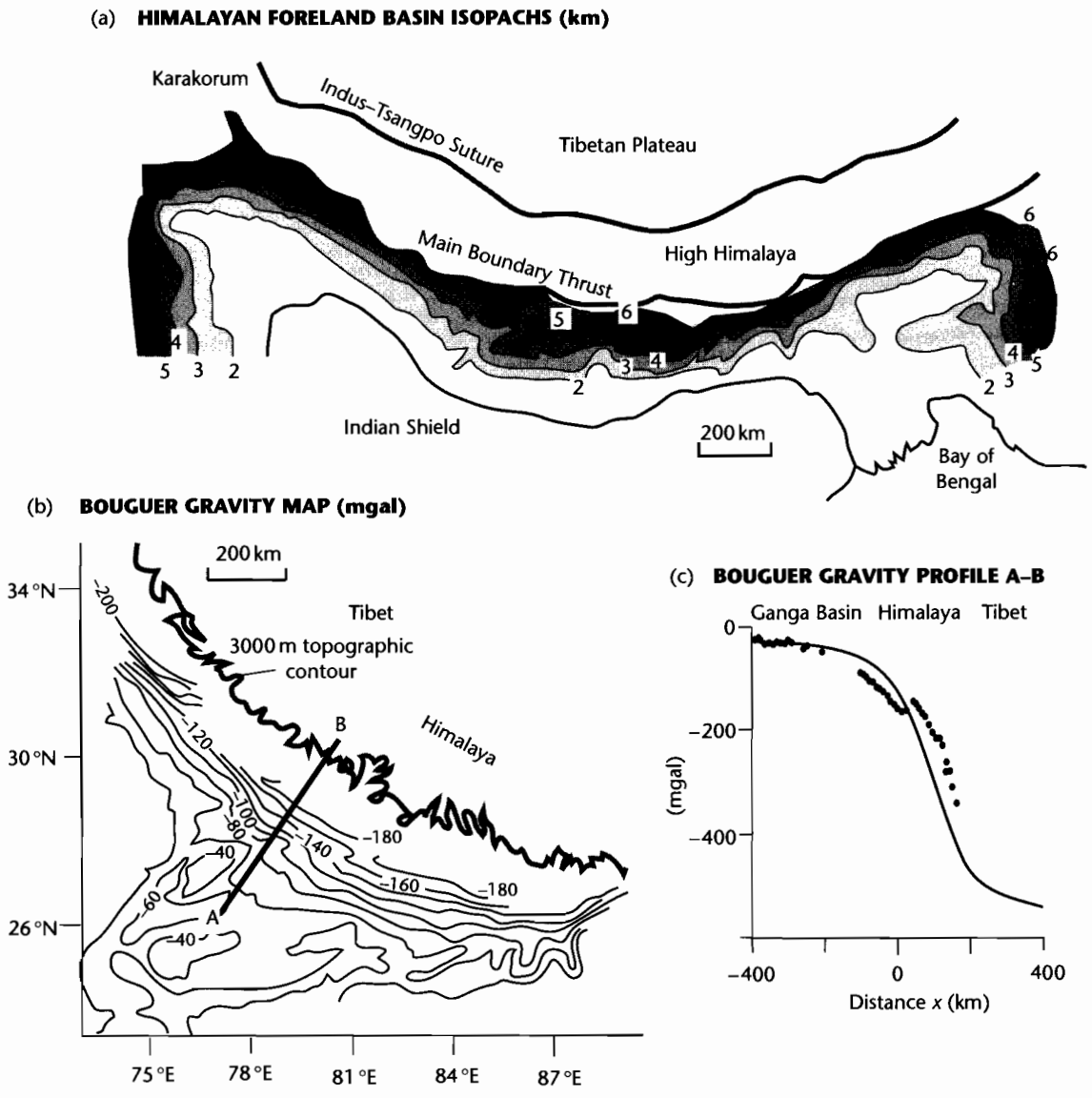

Fig. 4.4 The Himalaya and Ganga Basin. (a) Isopach map of sediment thicknesses in the Himalayan foreland basin, based on Raiverman et al. (1983); (b) Contours of Bouguer gravity anomaly over the Ganga Basin, and (c) observed Bouguer gravity anomalies along profile A–B, compared with the anomalies computed assuming the topography is locally compensated (Airy model) by thickening of the crust beneath central India. Note that there is an apparent mass excess in the Himalaya and a mass deficit over the Ganga Basin (after Lyon-Caen and Molnar 1985).

the Moho descends from about 35 km under the Indian shield, *via* a number of steps, to 70 km under Tibet. Although it is unlikely that the Indian plate slides smoothly under Asia, the gravity data in the Ganga Basin and Himalaya (Lyon-Caen and Molnar 1985) can be explained by the flexure of the Indian plate beneath the topographic load of the mountain belt (Fig. 4.4).

Foreland basins are therefore emphatically syn-orogenic. The bulk of the sediments in foreland basin systems (DeCelles and Giles 1996) are found in a *foredeep*, extending from the thrust front across the foreland plate (see also §8.3.1). The foredeep is classically asymmetrical, with subsidence rates at a maximum close to the thrust front. Sedimentation is dominated by sediment delivery from the orogenic belt, but significant sediment discharges may come from the opposite side of the basin, particularly early in basin development. Proximal foredeep deposits are progressively incorporated into the orogenic wedge as the thrust belt migrates over the foreland. Sediments also accumulate in *wedge-top* or *piggy-back basins* located on top of the deforming thrust wedge. These basins are commonly involved in thrust deformation, and may be eroded as the orogenic wedge is exhumed.

4.2 FLEXURE OF THE LITHOSPHERE: GEOMETRY OF THE DEFLECTION

Since the oceanic lithosphere has a relatively simple thermal structure and is relatively simple rheologically, it is the appropriate starting place for the consideration of flexure. Early measurements of free-air gravity anomalies in the ocean were highly influential in explaining the bathymetry of the seafloor, particularly adjacent to oceanic islands and seamount chains. Where there is negligible sediment loading, the bathymetry of the ocean floor and its free-air gravity anomalies can be explained by a model involving a line load acting on either a continuous plate (§4.2.1) or on the end of a broken plate (§4.2.2). The effect of a load system that has a significant spatial distribution is discussed in §4.2.3.

4.2.1 Deflection of a continuous plate under a line load

Some general concepts of flexure can be appreciated by considering the bending of oceanic lithosphere under loads acting a long way from the edge of the plate. A geological situation of this type is the flexure of the lithosphere under the load of mid-plate oceanic islands such as the Hawaiian archipelago (Vening-Meinesz 1941, 1948; Watts and Cochran 1974). The Hawaiian ridge is a long (thousands of km) line of volcanic islands of about 150 km width. The ridge therefore approximates a line load. The ridge is flanked by a depression, the Hawaiian Deep and then an outer rise

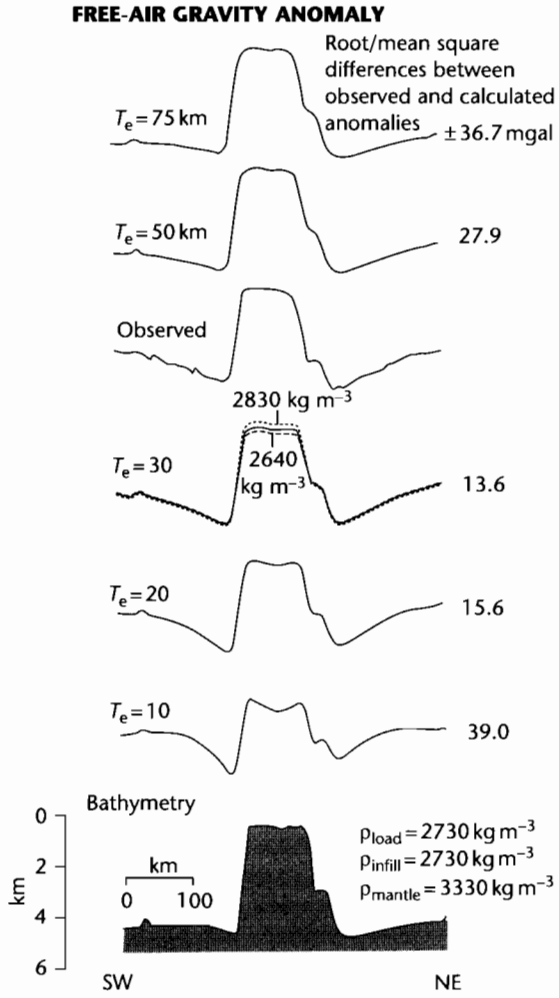

Fig. 4.5 Free-air gravity and bathymetry along a transect that intersects the Hawaiian Islands between Oahu and Molokai (Watts and Cochran 1974; Watts 2001). The seamount chain is associated with a free-air gravity high and the fringing moat by a free-air gravity low. Beyond a lateral distance of about 150 km the free-air anomalies become positive in the outer rise, which gives an indication of the width of the flexural depression. Calculated profiles using an elastic plate model are shown for a range of equivalent elastic thicknesses (10–75 km). The best fit is for a *Te* of 30 km. Reproduced courtesy of Cambridge University Press.

(Fig. 4.5). These three morphological elements (load, basin, and outer rise or forebulge) are a constant theme in flexural problems.

Taking the boundary conditions for the flexural force balance (eqn. 2.29) as follows:

The applied vertical load, $q_a(x) = 0$, except at the location of the Hawaiian ridge ($x = 0$), and

$P = 0$ since no horizontal forces are applied, then

$$D\frac{d^4w}{dx^4} + \Delta\rho g w = 0 \tag{4.1}$$

where w is the deflection, x is the horizontal scale, D is the flexural rigidity, and $\Delta\rho$ in this case is the difference in density between mantle and infilling ocean water.

The general solution for a fourth order differential equation such as this is accomplished by breaking it into exponential, sine and cosine components (it is in the form of damped sinusoids)

$$w = e^{x/\alpha}(C_1 \cos x/\alpha + C_2 \sin x/\alpha) + e^{-x/\alpha}(C_3 \cos x/\alpha + C_4 \sin x/\alpha) \tag{4.2}$$

where the constants C_1, C_2, C_3, and C_4 are determined by the boundary conditions and α is the *flexural parameter* (Walcott 1970), given by

$$\alpha = \left\{\frac{4D}{\Delta\rho g}\right\}^{1/4} \tag{4.3}$$

Following from the determination of the constants for the case of a line load bending the plate symmetrically (see Turcotte and Schubert 2002, pp.124–6), some useful and simple expressions emerge for the geometry of the deflection (Fig. 4.6). If the maximum deflection (w_0 at $x = 0$) is known, the profile of the deflection of the plate obeys

$$w = w_0 e^{-x/\alpha}(\cos x/\alpha + \sin x/\alpha) \tag{4.4}$$

The half-width of the depression (x_0) can be found since it is defined by the horizontal distance from the maximum deflection ($x = 0$) to the point where the deflection is zero ($w = 0$). Setting $w = 0$, equation (4.4) gives

$$x_0 = \frac{3\pi\alpha}{4} \tag{4.5}$$

The distance from the line load ($x = 0$) to the highest part of the forebulge (x_b) can be found since at the forebulge crest, the slope of the deflection is zero. That is, $dw/dx = 0$ at $x = x_b$. Equation (4.4) then gives

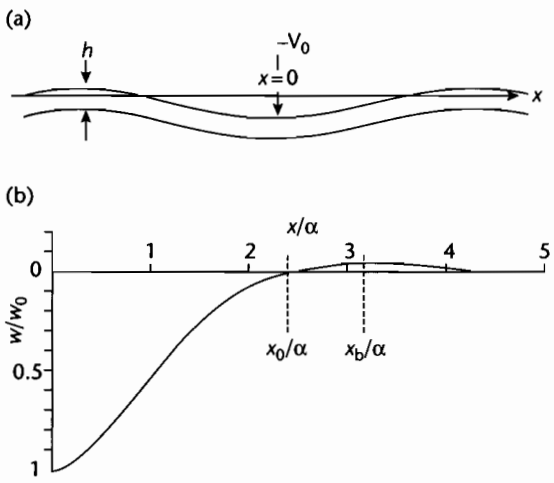

Fig. 4.6 (a) Deflection of a continuous elastic plate under a line load; (b) Theoretical deflection of the elastic lithosphere under a line load applied at the centre of an infinitely extensive plate. Parameters are defined in the text. The deflection w is scaled against the maximum deflection w_0. The horizontal distances are scaled against the flexural parameter α. Bending moments and horizontal in-plane forces are zero.

$$x_b = \pi\alpha \tag{4.6}$$

The height of the forebulge w_b above the datum of zero deflection can also be found using the condition that $x = \pi\alpha$ at the point where $w = w_b$. As a result equation (4.4) reduces to

$$w_b = -w_0 e^{-\pi} = -0.0432 w_0 \tag{4.7}$$

If the deflection under a line load approximates a sedimentary basin, the half width of the basin is represented by x_0 if base level is taken as $y = 0$. However, the half-width enclosed by the deflection is represented by x_b.

By comparison of the observed with the theoretical bathymetric or free-air gravity profiles, something can be said about the thickness of the equivalent elastic lithosphere (defined in §2.1.4) under the Hawaiian islands, always assuming the theory to be an adequate representation of the geodynamics (Watts and Cochran 1974). For example, the bathymetric profile suggests that the crest of the outer rise is about 250 km from the line load of

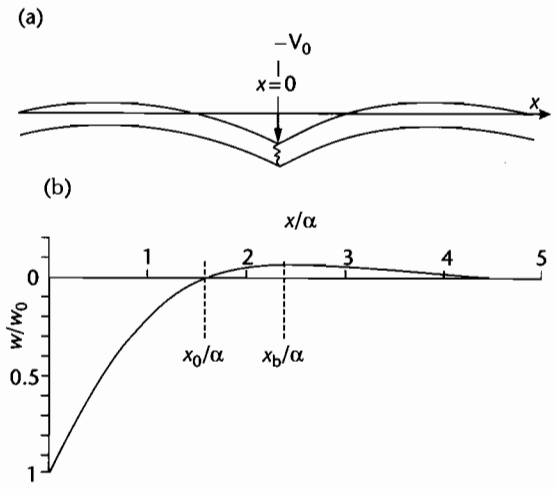

Fig. 4.7 (a) Deflection of a broken elastic plate under a line load applied at its end. Horizontal in-plane forces and applied bending moments are again zero; (b) Theoretical deflection of the broken plate under a line load applied at its end. Note that the half-width of the basin is narrower than for the unbroken plate, and that the elevation of the forebulge is greater than for the unbroken plate. Vertical and horizontal axes are scaled by w_0 and flexural parameter α respectively.

the Hawaiian Islands, i.e., $x_b = 250$ km. Assuming the moat to be water-filled, $\Delta\rho = 2300\,\mathrm{kg\,m^{-3}}$. With a gravitational acceleration of $10\,\mathrm{m\,s^{-2}}$, the flexural parameter from (4.6) is 80 km, which gives from (4.3) a flexural rigidity of 2.4×10^{23} Nm. If Young's modulus E is 70 GPa and Poisson's ratio $\nu = 0.25$, this gives an equivalent elastic thickness of 34 km.

4.2.2 Deflection of a broken plate under a line load

If the Hawaiian plate were broken under the Hawaiian Islands, the boundary conditions of the model of the lithosphere would need to be modified (Walcott 1970). In this case, we would consider the deflection of a semi-infinite elastic plate subjected to a line load $V_0/2$ applied at its end (Fig. 4.7). Assuming that no external torque is applied at $x = 0$, simple expressions describing the geometry of the deflection can be obtained as follows.

The maximum deflection for a broken plate of the same flexural rigidity and under the same vertical load is twice that of an unbroken plate (Turcotte and Schubert 2002, p.126). If the maximum deflection is known, the deflection as a function of x for a broken plate loaded at its end is given by (Turcotte and Schubert 2002, pp.127–9)

$$w = w_0 e^{-x/\alpha} \cos x/\alpha \tag{4.8}$$

The half width of the basin (at $w = 0$) is given by

$$x_0 = \frac{\pi\alpha}{2} \tag{4.9}$$

showing that the basin is narrower for the case of a broken plate. The distance to the crest of the forebulge (where $dw/dx = 0$) is given by

$$x_b = \frac{3\pi\alpha}{4} \tag{4.10}$$

showing that narrower forebulges characterize broken plates. Finally, the height of the forebulge (where $x_b = 3\pi\alpha/4$) is given by

$$w_b = w_0 e^{-3\pi/4} \cos 3\pi/4 = -0.0670 w_0 \tag{4.11}$$

indicating a considerably larger forebulge amplitude for a broken plate.

Returning to the case of the Hawaiian Islands with $x_b = 250$ km (see above), equation (4.10) gives 106 km for the flexural parameter, and flexural rigidity is therefore 7.26×10^{23} Nm. The equivalent elastic thickness with $E = 70$ GPa and $\upsilon = 0.25$ is 49 km.

Seismic refraction studies (Shor and Pollard 1964) suggest that the Moho is deflected downwards by approximately 10 km under the center of the Hawaiian Islands. If 10 km is the maximum deflection w_0, the height of the outer rise above the undeflected seafloor can be found from equation (4.7) for the unbroken plate and equation (4.11) for the broken plate. The results are 432 m and 670 m respectively. Measurements of the bathymetry of the seafloor surrounding the Hawaiian Islands indicate that the outer rise is elevated above regional by about 500 m (Chase et al. 1970) but this does not permit us to tell whether the continuous or broken plate best fits the observational data.

Submarine processes such as erosion or draping with sediment, volcanism and tectonics may cause significant changes to the bathymetric profile. Gravity profiles have

therefore been used to investigate the deflection curve across the Hawaiian area (Fig. 4.5). Free-air gravity anomalies in several profiles across the Hawaii–Emperor seamount chain (Watts and Cochran 1974) show a conspicuous gravity high (<250 mgal) corresponding to the positive bathymetry of the volcanic islands. This is because the free-air gravity anomaly records the excess density of the volcanic edifices relative to seawater. Flanking the central gravity high is a pair of long wavelength gravity lows (<−100 mgal), corresponding to the topographic moat surrounding the seamount chain. Beyond the gravity lows, at a distance of 150–200 km from the line of volcanic islands, are free-air gravity anomaly highs (<50 mgal), once again corresponding to the elevated seafloor of the outer rises.

A good fit was found between the observed free-air gravity anomalies and those calculated for the continuous elastic plate if $D = 5 \times 10^{22}$ Nm, and for the broken elastic plate if $D = 2 \times 10^{23}$ Nm. These values are close to the flexural rigidities estimated from the wavelength of the deflection given above.

Another geological situation is of the bending of oceanic lithosphere at arc–trenches. This configuration is similar to that of an end load on a broken plate, but in this case we cannot ignore the bending moments acting on the subducting plate. Subducting oceanic slabs are subject to a large number of forces. There is a large force acting downwards due to the negative buoyancy of the cold oceanic lithosphere. This may be enhanced at depths of 200–300 km where the olivine to spinel phase change takes place. The oceanic slab also experiences resistance to its downward motion at its tip, which may have a horizontal and rotational (torque) component. It also experiences resistance along its upper contact with the overriding plate, which also has a horizontal component, as has been suggested for the Taranaki–Wanganui region of New Zealand, where the Pacific plate becomes "locked" against the Australian plate (Stern et al. 1992).

Turcotte and Schubert (2002, pp.127–9) give the solution for the deflection by applying the boundary conditions for an ocean trench to the general flexural equation. This solution incorporates the contribution of vertical forces and bending moments to the deflection. Whatever their origin, they cannot be directly determined. However, it is possible to obtain some estimates of the geometrical aspects of the flexural depression by expressing the trench profile in terms of the height of the forebulge (w_b) and the half-width of the forebulge ($x_b - x_0$) (Fig. 4.8). The solution for the latter is

$$x_b - x_0 = \pi\alpha/4 \tag{4.12}$$

In other words, the half-width of the forebulge is a direct measure of the flexural parameter. A forebulge is well developed seaward of deep sea trenches in the northwestern Pacific (Watts and Talwani 1974). The observed bathymetric profile across the Mariana Trench (Fig. 4.3) suggests that the half-width of the forebulge (measured on the flank facing the trench) is about 55 km. Equation (4.12) then gives 70 km for the flexural parameter. Using $E = 70$ GPa, $\nu = 0.25$, and $\Delta\rho = 2300\,\mathrm{kg\,m^{-3}}$, from equation (4.3) the flexural rigidity of the Pacific plate at the Marianas Trench using the broken plate model is 1.35×10^{23} Nm, equivalent to an elastic thickness of 28 km.

Both the deflection w and the height of the forebulge w_b are functions of the flexural parameter and bending moment. Dividing the expression for w by the expression for w_b (i.e., w/w_b) eliminates the unknown parameters and gives a universal flexure profile of the type shown in Fig. 4.8. This universal profile applies to any 2-D elastic flexure under end loading, so can be applied to a variety of geological contexts.

As an example of its application, let us return to the case of oceanic trenches, such as the Mariana, Bonin and Central Aleutian Trenches (Fig. 4.3). For the Mariana Trench, taking horizontal distances from the point $x = 0$ at the oceanward intersection of the plate surface with sea level, the distance to the crest of the forebulge is approximately 55 km and its height is taken as 0.5 km (Fig. 4.3a). The three trenches are shown in terms of dimensionless depth versus dimensional horizontal distance in Fig 4.3b. Although the fit between the theoretical deflection and the observed bathymetry is not perfect, particularly where volcanoes have built cones in the forebulge region, the correspondence is generally good, suggesting that the lithosphere at ocean trenches can indeed be modeled in this way.

The flexure of a semi-infinite elastic oceanic plate at trenches was studied by Watts and Talwani (1974). Although the bathymetry of the Mariana Trench could be explained by purely a vertically applied force at the end of the plate, the Aleutian and Kuril Trenches were better explained by a model involving both a vertical applied force (V) and a horizontal applied force (P, where $P = 5\,V$). However, a bending moment at the end of the plate would reduce the necessity of a horizontal force to explain the deflection (Hanks 1971).

The same approach can initially be taken to the flexure of the continental lithosphere. As in the case of the

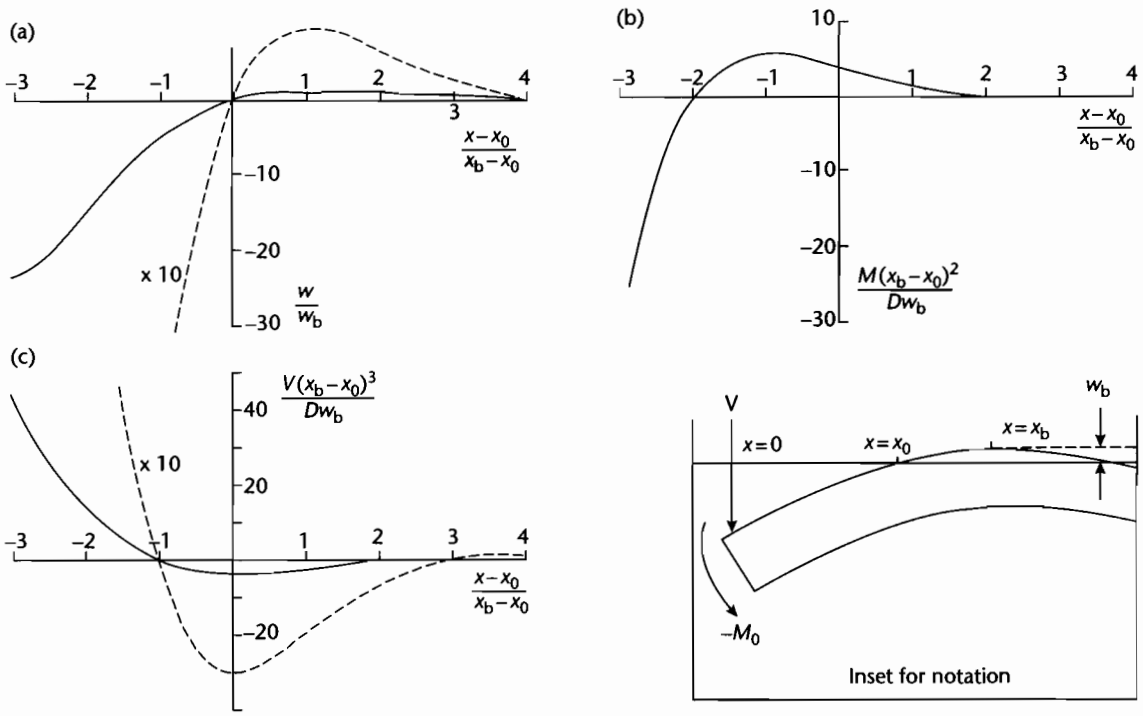

Fig. 4.8 Universal solution for the deflection of an elastic lithosphere under a vertical end load and a bending moment, approximating to the situation at ocean trenches. (a) Dependence of the nondimensional displacement w/w_b on the nondimensional position $(x-x_0)/(x_b-x_0)$. Dashed line shows vertical exaggeration of 10:1 to show geometry of forebulge; (b) The nondimensional bending moment $(M(x_b-x_0)^2/Dw_b)$ versus nondimensional position. Note that the maximum bending moment is found roughly one-third of the distance from $x=x_0$ to the maximum deflection; (c) The nondimensional vertical shear force $(V(x_b-x_0)^3/Dw_b)$ as a function of nondimensional position, showing that it reaches a maximum at the point of maximum deflection. Dashed line is at vertical exaggeration of 10:1. Inset shows notation.

oceanic lithosphere, the universal flexural profile of Figure 4.8 should be applicable, but since regions of continental collision are characterized by mountains acting as source areas for large volumes of detritus, basins occupying the flexural depressions tend to be rapidly filled with sediment. As a result $\Delta\rho$ in the flexural parameter (eqn 4.3) is the difference between mantle and sediment densities, $\rho_m - \rho_s$.

As in the case of the Mariana Trench, it is possible to match a theoretical deflection to the observed depth of basement in a region of continental flexure such as the Appalachians (Fig. 4.9). The best fit of the theoretical curve to the basement shape is by choosing $x_b - x_0 =$ 122 km (half-width of forebulge) and $w_b = 0.29$ km (height of forebulge). As must be obvious when considering a Paleozoic foreland basin, much information has been lost through erosion and the choice of parameters above is therefore neither unique nor verifiable. The close match between theory and observation in Fig. 4.9 merely gives some confidence in treating the geodynamic problem as essentially one of flexure. The flexural rigidity implied by the Appalachian profile in Fig. 4.9 is 10^{24} Nm (equivalent elastic thickness of 54 km). This suggests that the flexural rigidity of continental lithosphere can be greater than that of oceanic lithosphere.

4.2.3 Deflection of a continuous plate under a distributed load

Flexural basins on the continental lithosphere, such as foreland basins, are generally loaded by a force system that has a spatial distribution far removed from a line-load approximation. Consequently, it is necessary to con-

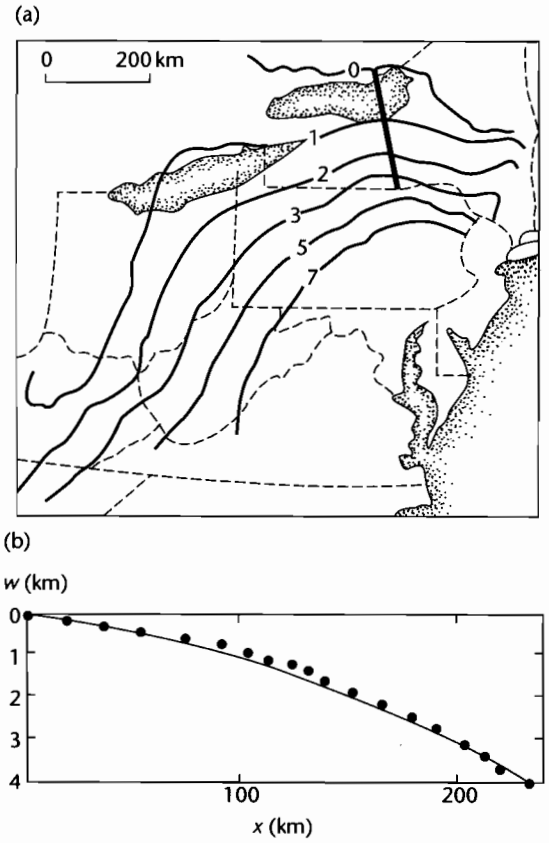

Fig. 4.9 Contours of basement (in km) in the Appalachian basin of the eastern United States, based on borehole records and seismic reflection studies (Turcotte and Schubert 1982, p. 131); (b) Depths of basement below sea level along the profile given in (a) as a function of distance from the point at which the basement rocks crop out at the surface. The heavy line is the theoretical deflection given by the universal flexure equation with $x_b - x_0$ equal to 122 km and w_b equal to 0.29 km.

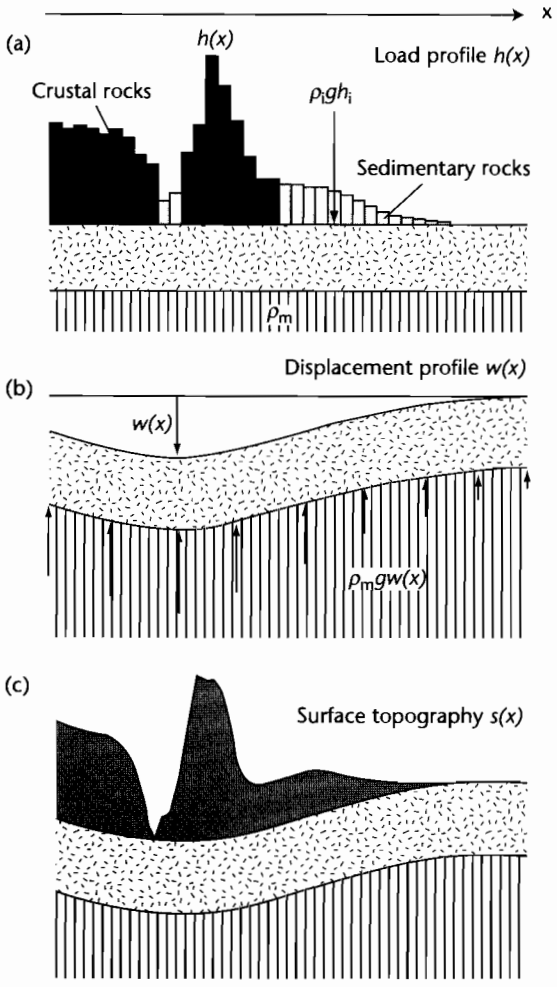

Fig. 4.10 Flexure under a distributed load. (a) The individual deflections caused by load blocks of given height h, density ρ, and width are solved analytically, and summed to give the displacement profile $w(x)$ in (b). The upward restoring force is shown by arrows. The distributed load then "sinks" into this displacement profile to give the resultant topographic profile $s(x)$ (c). Based on Jordan (1981) and Cardozo and Jordan (2001).

sider the solution of the general flexural equation for the case of an applied load $q_a(x)$.

Jordan (1981) made an early attempt to forward model the deflection of the continental lithosphere in the western interior of USA during the Late Jurassic–Cretaceous Sevier orogeny using a distributed load system on a linear elastic plate. The crustal loads were approximated by rectangular blocks of density ρ_c, with their centers s situated at a distance x km, half-width a, and height above sea level h (Fig. 4.10). These crustal blocks float on a fluid mantle with density ρ_m. The deflection of each load block w_i is calculated using a solution of the universal flexure equation. The sum of the deflections from all of the rectangular crustal blocks gives the total deflection. Jordan (1981) moved the crustal blocks to represent different stages in the evolution of the Sevier

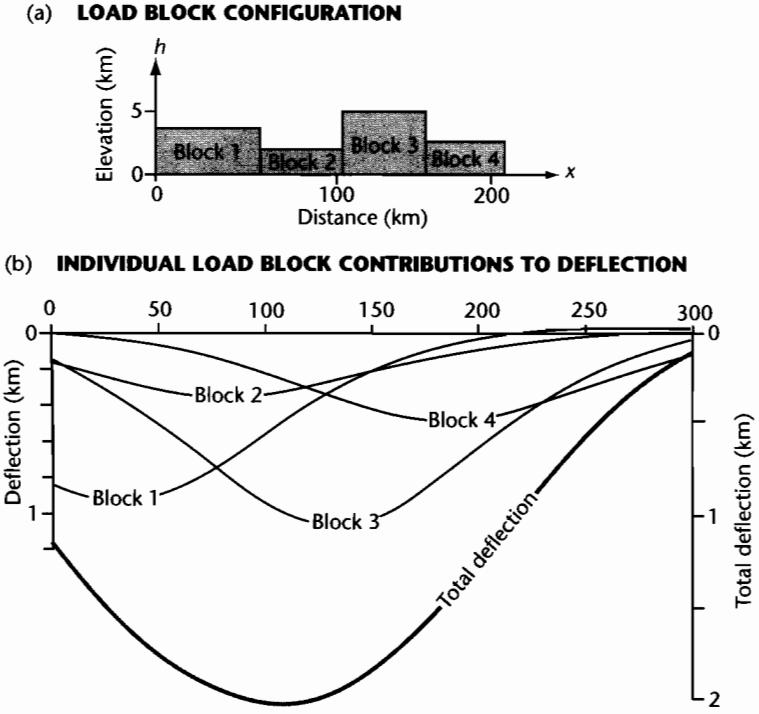

Fig. 4.11 Example of the individual deflections from a number of spatially distributed load blocks of crustal density (a), showing their mutual interference and total deflection (b). Flexural rigidity of $D = 10^{23}$ Nm.

orogen. For our purposes, we need only initially consider the static solution (Boxed text 4.1).

The deflections from a series of load blocks for a flexural rigidity of 10^{23} Nm is shown in Fig. 4.11. It is clear that the deflections of widely separated crustal blocks may destructively interfere.

The basins adjacent to eroding thrust belts are commonly filled with sediment. This sediment also acts as a vertically applied load on the continental lithosphere. The sedimentary infill of the basin can also be treated as a series of rectangular loads with height h_i and density ρ_i. The sum of the load profile $h(x)$ and the deflection profile $w(x)$ gives a topographic profile (Fig. 4.10). This type of 2-D modeling has been applied to the Tertiary Bermejo foreland basin of Argentina (Cardozo and Jordan 2001) and the Triassic Sichuan foreland basin of China (Yong et al. 2003).

A Matlab exercise to calculate the deflection caused by a distributed load can be found at www.erdw.ethz.ch/Allen.

4.3 FLEXURAL RIGIDITY OF OCEANIC AND CONTINENTAL LITHOSPHERE

4.3.1 Controls on the flexural rigidity of oceanic lithosphere

The lithosphere can be regarded as a thermal boundary layer losing heat to the atmosphere and oceans by conduction. The oceanic lithosphere thickens as a function of age, being ~6 km at ridge axes and thickening to about 100 km under the oldest (Jurassic) ocean floor (§2.2). Clearly, the ability of the oceanic lithosphere to support loads should also therefore be a function of its age. However, analysis of the flexure of the oceanic lithosphere at the Hawaiian–Emperor seamount chain (Watts 1978) suggested that equivalent elastic thicknesses were large at the old (75–80 Ma) end of the chain near the northernmost Emperor seamount, but low at the young (0–5 Ma) end near Hawaii, despite the fact that the age of the underlying oceanic crust (80–100 Ma) differs very

BOXED TEXT 4.1: Deflection under a Distributed Load

The deflection produced by each load i is given by the following set of equations (Heténi 1979; Jordan 1981).

If x is situated in the basin outboard from the load:

$$w_i = \frac{h}{2}\frac{\Delta\rho_1}{\Delta\rho_2}\left\{\begin{array}{l}\exp(-\lambda(x-s+a))\cos(\lambda(x-s+a)) \\ -\exp[-\lambda(x-s-a)]\cos[\lambda(x-s-a)]\end{array}\right\} \quad (4.13)$$

where

$\Delta\rho_1 = \rho_c - \rho_{air}$

$\Delta\rho_2 = \rho_m - \rho_{air}$

λ is an inverse flexural parameter ($1/\alpha$) (see equation 4.3), and $\Delta\rho$ is the density difference between mantle and air, and s is the position of the centre of the load, a is its half-width and h its height.

If x is under the load:

$$w_i = -\frac{h}{2}\frac{\Delta\rho_1}{\Delta\rho_2}\left\{\begin{array}{l}2-\exp[-\lambda(x-s+a)]\cos[\lambda(x-s+a)] \\ -\exp[-\lambda(-x+s+a)]\cos[\lambda(-x+s+a)]\end{array}\right\} \quad (4.14)$$

If x is situated behind (to the left of) the load block:

$$w_i = -\frac{h}{2}\frac{\Delta\rho_1}{\Delta\rho_2}\left\{\begin{array}{l}\exp[-\lambda(-x+s-a)]\cos[\lambda(-x+s-a)] \\ -\exp[-\lambda(-x+s+a)]\cos[\lambda(-x+s+a)]\end{array}\right\} \quad (4.15)$$

The total deflection resulting from the distributed load is found by summing the individual deflections w_i.

little along the length of the chain. In other words, volcanoes deflected oceanic lithosphere of different ages *at the time of loading*. A plot of 139 estimates of the elastic thickness of the oceanic lithosphere against age of the lithosphere at the time of loading (Fig. 4.12) (Watts 2001, p. 242) shows that oceanic flexural rigidity expressed as an equivalent elastic thickness (T_e) is approximated by the depth to the 300–600 °C isotherm. The lithosphere becomes stronger with the age of the lithosphere at the time of loading. This relationship is exponential with time, similar to that of the oceanic bathymetry using a cooling plate model such as that shown in Fig. 2.20 (Parsons and Sclater 1977). The evidence therefore suggests that the oceanic lithosphere can be treated as being elastic rather than viscoelastic (Watts et al. 1982) (§2.4.4) with a flexural rigidity dependent on its age at the time of loading. However, it is apparent from Fig. 4.13 that there is considerable scatter. Such variation may be due to viscoelastic effects in a multilayered oceanic lithosphere.

Although investigation of the oceanic lithosphere allows us to lay down some fundamental concepts in flexure, it is of little importance in basin analysis, since most sedimentary basins of interest to us are formed on continental lithosphere. It is therefore important to understand what controls the flexural rigidity of continental lithosphere.

4.3.2 Flexure of the continental lithosphere

4.3.2.1 Introduction

The continental elastic lithosphere responds differently to the oceanic elastic lithosphere on all scales of deformation. The continents appear to accumulate strains over long periods of geological time whereas the oceanic lithosphere remains relatively intact over its short lifetime of up to about 180 Myr. This is illustrated by the presence of narrow and well-defined plate boundaries in the oceans as opposed to the wide and diffuse zones in the continents such as the Himalayas and Tibet (reviewed in Molnar 1988). The continents are therefore exceedingly complex, particularly in their inherited fabric. In addition, strength profiles of the continental lithosphere show two high strength zones and two brittle–ductile transitions (§2.4.6). A four-layer lithosphere is unlikely to behave in a simple fashion when subjected to an applied load system. The flexure of continental lithosphere is therefore controversial. Some workers have proposed that there is a correlation in Eurasia between the equivalent elastic thickness of the continental lithosphere (derived from gravity anomalies and topography) and the thickness of the seismogenic crust (Maggi et al. 2000). However, this correlation is not substantiated elsewhere (e.g., Cardozo and Jordan

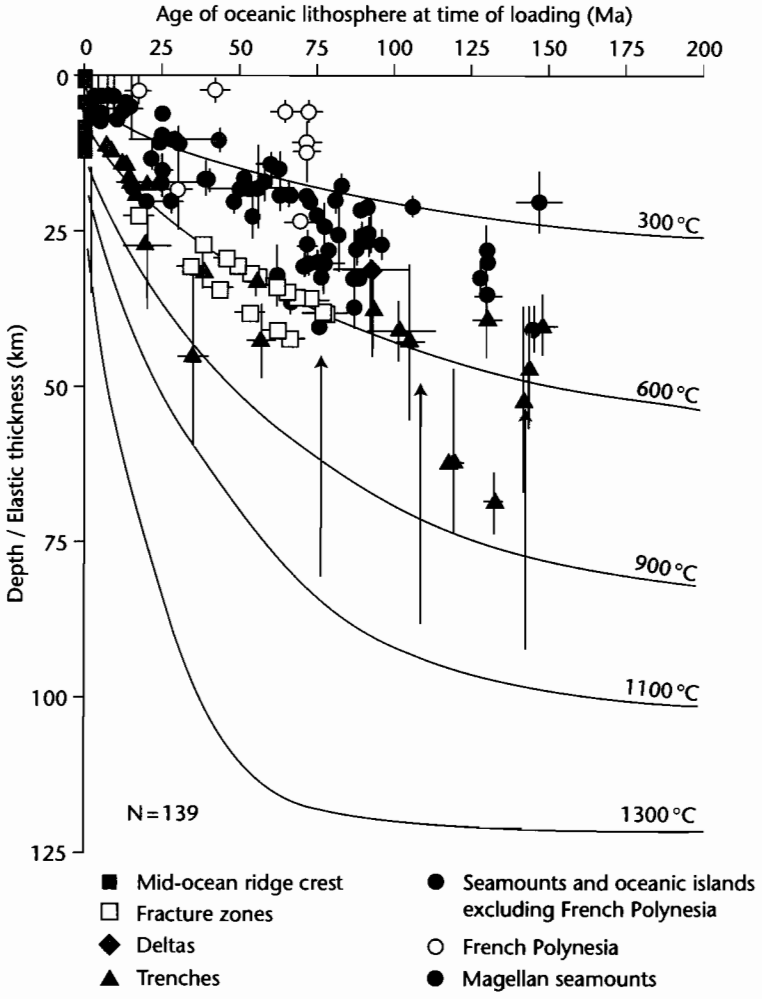

Fig. 4.12 Plot of the flexural rigidity of the oceanic lithosphere (expressed as equivalent elastic thickness *Te*), as a function of its age at the time of loading (after Watts et al. 1982, updated in Watts 2001). The equivalent elastic thickness estimates are shown for mid-ocean ridges and fracture zones, seamounts and oceanic islands, trenches and deltas. Isotherms are for a cooling plate model (Parsons and Sclater 1977), showing that most data fall within the 300 °C to 600 °C isotherms. The general relationship is that equivalent elastic thickness increases with the age of the oceanic lithosphere at the time of loading. Reproduced courtesy of Cambridge University Press.

2001) and there are no simple measurable parameters that can be confidently correlated with the observed flexural rigidity of the continental lithosphere (McNutt et al. 1988) (discussed below). The change through time ("secular evolution") of the flexural rigidity of continental lithosphere has in particular been widely discussed.

4.3.2.2 Controls on the flexural rigidity of the continental lithosphere

The elastic plate thicknesses (or flexural rigidities) for continental lithosphere have been calculated in a wide variety of tectonic settings. Flexural rigidities have been

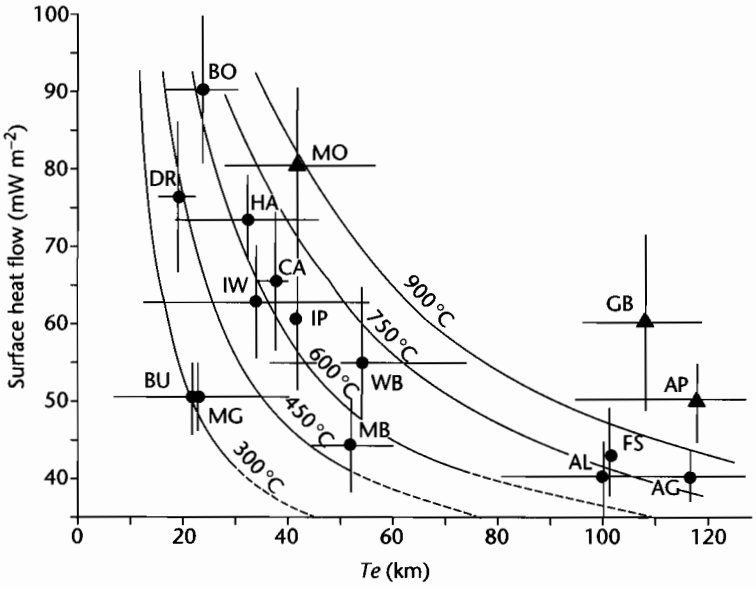

Fig. 4.13 Plot of the equivalent elastic thickness *Te* versus surface heat flow for a number of sites of flexure. The solid curves indicate depths to isotherms at a given surface heat flow for a steady state thermal model. The plot demonstrates the very wide range in temperature (300 °C to >900 °C) for the base of the elastic lithosphere. Flexure sites are as follows: AG, Lake Agassiz; AL, Lake Algonquin; FS, Fennoscandia; CA, Caribou Mountains; IP, Interior Plains; GB, Ganges Basin; IW, Idaho–Wyoming thrust belt; MB, Michigan Basin; BU, Boothnia Uplift; MG, Midcontinent gravity high: HA, Lake Hamilton; BO, Lake Bonneville; DR, North Great Dividing Range; AP, Appalachian Foreland Basin; MO, Molasse Basin; WB, Williston Basin (full details in Willett et al. 1985).

estimated from late glacial rebound, such as in Pleistocene Lake Bonneville (Crittenden 1963; Nakiboglu and Lambeck 1983), Lake Agassiz (Walcott 1970), and Fennoscandia (McConnell 1968). Estimates have also been obtained from regions of lithospheric extension such as the rifts of the East African Rift System (Banks and Swain 1978; Bechtel et al. 1987; Ebinger et al. 1991; Upcott et al. 1996), the North Sea (Kusznir et al. 1991) and Rhine Graben (Weissel and Karner 1989), and at passive continental margins, particularly that of the eastern seaboard of the USA–Canada (Watts 1988; Keen and Dehler 1997). By far the greatest data set, however, comes from the flexure of the continental lithosphere at foreland basins (Table 4.1).

Whereas, to a first approximation, the loading of oceanic and continental lithosphere can be modeled as a flexed elastic plate overlying a fluid substratum, laboratory-derived rock deformation data (Goetze 1978; Goetze and Evans 1979; Kirby 1983) show that the true rheology of the lithosphere is far more complex. Karner et al. (1983) applied a thermo-elastic rheologic model to the flexure of continental lithosphere and concluded that in terms of flexural rigidity, the results from oceanic and continental lithosphere were compatible. They believed that the long-term thermal behavior of the continental lithosphere is governed by a simple cooling plate model (plate thickness of 200–250 km), and that the effective elastic thickness for continental lithosphere corresponds with the depth to the 450 °C isotherm, and does not change following loading.

Others claim that there is no clear relation between thermal state and age of continental lithosphere, and that the effective elastic thickness does not correspond to the 450 °C isotherm, but rather spans a wide temperature range of 300 °C to >900 °C (Fig. 4.13). Willett et al. (1985) instead suggested a Maxwell viscoelastic heterogeneous lithosphere, i.e., a nonlinear thermally activated rheology (see §2.3.4), with viscous strain rates in the lithosphere determined by a power law ($n = 3$). In such a model, the deviatoric stress resulting from a supralithospheric load initially increases toward the base of the mechanical lithosphere, but immediately after loading,

Table 4.1 Equivalent elastic thickness (T_e) compiled by Watts (2001) for the continental lithosphere at sites of foreland basins. Particular foreland basins may appear more than once if estimates have been made by different authors. Sources given in Watts (2001, Table 6.2, pp.251–3).

Site	Age of plate (Ma)	Plate age error (Myr)	Age of load (ka)	Load age error (kyr)	*Te* (km)	*Te* error (km)
Idaho–Wyoming	2650	50	125	25	22.0	0.0
Alps East	350	50	110	0	50.0	10.0
Alps West	275	25	110	0	25.0	10.0
Appalachians	1050	50	375	75	105.0	25.0
Himalaya East	1200	500	52	2	90.0	10.0
Ganges	1500	500	52	2	86.5	25.0
Kunlun–Tarim	800	200	52	2	40.0	5.0
Apennines	300	50	5	0	11.5	6.5
Carpathians Southeast	1600	200	110	0	30.0	10.0
Bolivian Andes	950	350	60	0	45.0	20.0
Transverse Ranges S	100	0	50	0	10.0	10.0
Transverse Ranges N	100	0	50	0	50.0	0.0
Zagros	700	200	35	10	50.0	25.0
Ebro	275	25	40	5	18.6	6.9
Aquitaine	275	25	40	5	25.5	5.0
Colville	1900	100	140	20	65.0	5.0
Carpathians	1600	200	110	0	22.0	0.0
Calabria	300	50	2	2	18.7	4.7
Urals	1500	100	325	50	75.0	25.0
Apennines	300	50	5	0	20.0	5.0
Oman	700	200	85	10	13.0	3.0
Urals	1500	100	325	50	75.0	25.0
Verkhoyansk	1950	150	230	40	50.0	10.0
Pamir	300	100	52	2	15.0	5.0
Tien Shan Tarim	800	200	52	2	40.0	20.0
Sicily	275	25	25	0	6.0	4.0
Himalaya West	1200	500	52	2	34.0	6.0
Greater Caucasus	1600	200	100	0	45.0	5.0
Kilohigok	2575	75	1965	45	12.0	4.0
Thelon front	2575	75	2000	0	58.0	0.0
Grenville front	2700	100	1050	50	126.0	0.0
Labrador Trough	2575	75	1585	50	120.0	0.0
Cape Smith	2575	75	1800	50	74.0	0.0
New Guinea East	700	100	25	0	10.0	0.0
New Guinea West	700	100	25	0	75.0	25.0
Tarim	1800	50	900	50	55.0	5.0
Ebro	275	25	40	0	20.0	0.0
Dzhungarian	1800	50	900	50	12.5	12.5
Alps West	275	25	17	0	10.0	5.0
Po Basin	275	25	30	0	5.0	0.0
Apennines	300	50	5	0	6.3	2.2
Guadalquivir Betics	275	25	25	0	10.0	5.0
Apennines	300	50	5	0	20.0	0.0
Carpathians	1600	200	110	0	40.0	0.0
Hellenides	300	50	2	2	70.0	0.0
Himalayas	1200	500	52	2	80.0	0.0
East Alps	350	50	110	0	40.0	0.0
South Alps	300	50	110	0	20.0	0.0

Table 4.1 *Continued*

Site	Age of plate (Ma)	Plate age error (Myr)	Age of load (ka)	Load age error (kyr)	*Te* (km)	*Te* error (km)
West Alps	275	25	110	0	50.0	0.0
South Alps	300	50	110	0	15.0	0.0
Apennines	300	50	5	0	15.0	0.0
Oman	700	200	85	10	35.0	13.0
Apennines–Dinarides Plio–Quaternary	300	50	2	2	12.5	2.5
Apennines–Dinarides Eocene–Oligocene	300	50	40	5	7.5	2.5
Kopet Dag	1600	200	52	2	25.0	5.0
Karakorum India	1200	500	52	2	90.0	10.0
Karakorum Asia	1200	500	52	2	110.0	10.0
Andes Peru	950	350	60	0	39.0	16.0
Himalaya East	1200	500	52	2	90.0	0.0
Tarim	1800	50	900	50	40.0	0.0
Atlas East	300	50	25	0	20.0	1.0
Atlas West	300	50	25	0	9.0	1.0
Appalachians	1050	50	375	75	70.0	20.0
Alps East	350	50	110	0	25.0	10.0
Alps West	275	25	110	0	10.0	5.0
Carpathians Southeast	1600	200	110	0	12.0	8.0
Andes Colombia	950	350	80	0	45.0	40.0
Andes Equador	950	350	80	0	25.0	20.0
Andes North Peru	950	350	60	0	35.0	35.0
Andes Peru	950	350	60	0	25.0	20.0
Andes Peru–N. Chile	950	350	60	0	45.0	40.0
Andes Argentina	950	350	60	0	30.0	20.0
Ouachita	1050	50	375	75	50.0	10.0
E. Papua New Guinea	97	32	30	5	20.0	10.0
W. Papua New Guinea	387	132	30	5	75.0	5.0

viscous relaxation causes stresses to be progressively concentrated in the colder upper lithosphere. Any surface deflection should deepen and narrow with time since loading, but at long times after loading, the stress field and surface displacements do not change significantly, suggesting that there is a long-term asymptotic elastic thickness (see also Kusznir and Karner 1985). The orogenward migration of the flexural forebulge of the Appalachian foreland basin system has been interpreted as evidence for viscoelastic relaxation (Quinlan and Beaumont 1984; Tankard 1986).

A plot of flexural rigidity/elastic thickness of the continental lithosphere versus thermal age, or versus the age at the time of loading, using the most complete data set currently available (Watts 2001), shows no global relationship (Fig. 4.14). Values appear to range between <5 km and 110 km with no clear modes at particular depth ranges, although rift provinces tend to have values of T_e of <30 km. There clearly must be other factors contributing strongly to the value of the flexural strength of the lithosphere. One factor is the present day geothermal gradient, which is strongly influenced by the concentration of radiogenic heat-producing elements in the crust (Pinet et al. 1991). If continental T_e is determined by the depth to the 450 °C isotherm, variations in the continental geotherm would explain variations in the value of continental T_e. Estimates of T_e based on geothermal data in North America (Pinet et al. 1991) are supported by estimates of T_e from admittance and coherence studies (Bechtel et al. 1990).

Other mechanisms affecting the flexure of the continental lithosphere are the possible *decoupling* of a strong

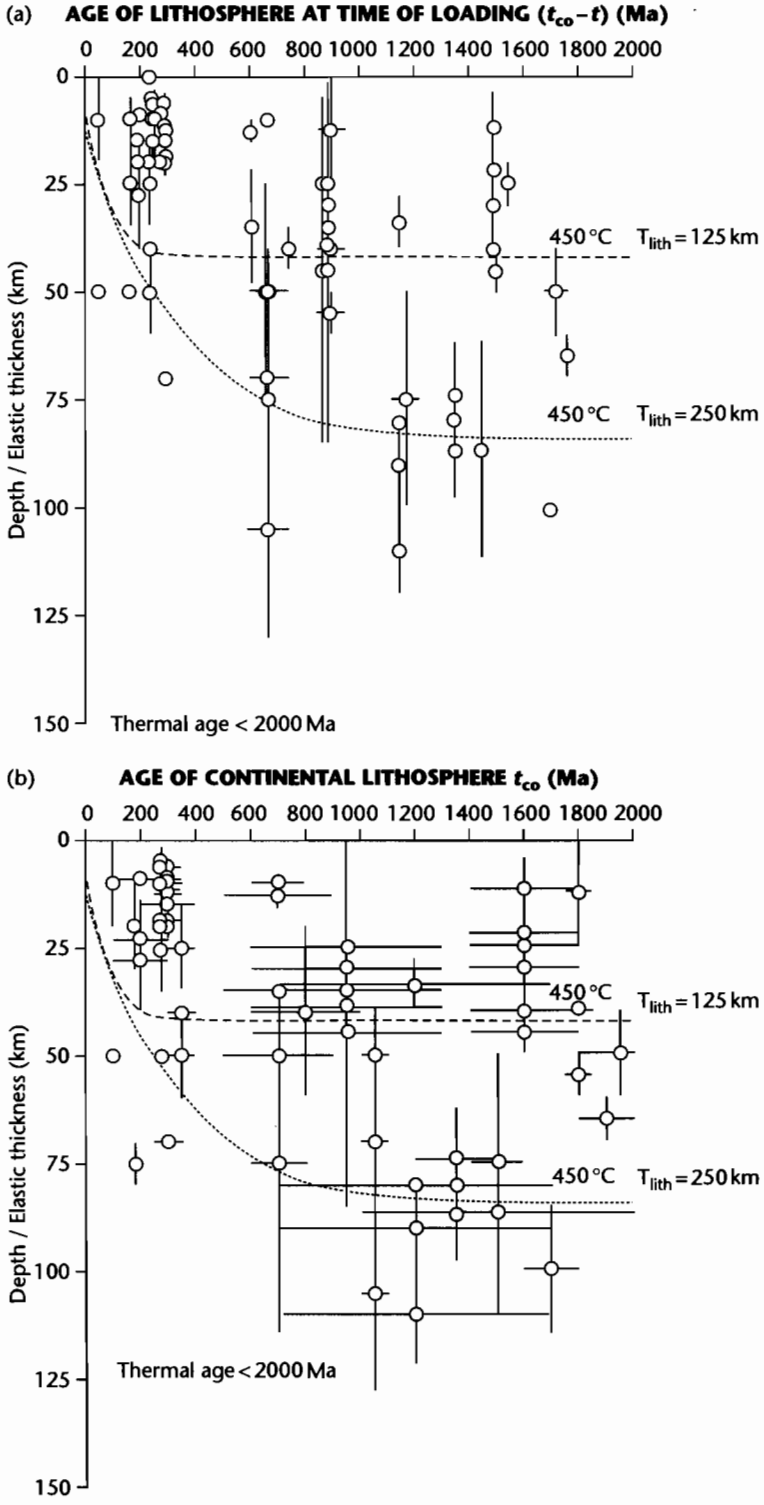

Fig. 4.14 Plots of flexural rigidity expressed as equivalent elastic thickness versus (a) age of the lithosphere at the time of loading and (b) age of the continental lithosphere, for 66 foreland basins and 6 late glacial rebound sites (after Watts 2001). Note that there is no correlation for this continental dataset. Reproduced courtesy of Cambridge University Press.

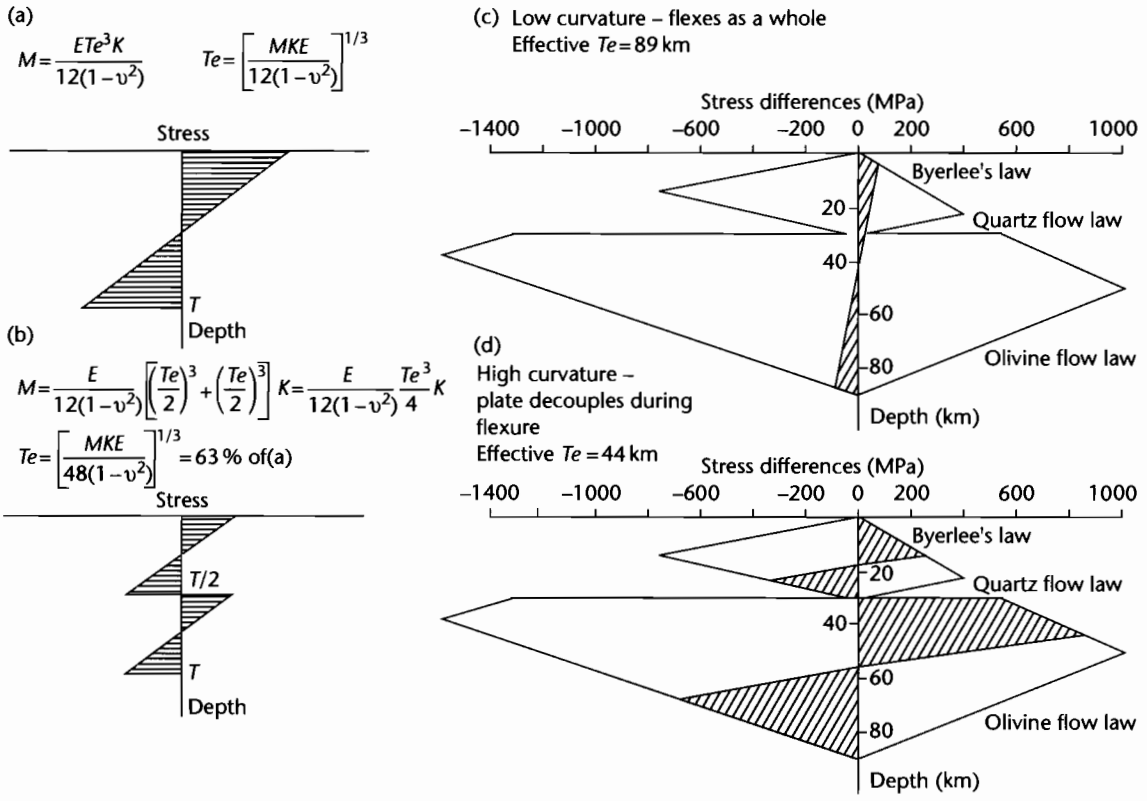

Fig. 4.15 The effects of decoupling at high curvatures illustrated by cross-sections of stress in the flexed lithosphere (after McNutt et al. 1988). (a) Distribution of fiber stresses in an elastic plate of thickness T showing extension in the upper half of the plate and compression in the lower half; (b) A purely elastic plate that is decoupled at $T/2$ so that the upper and lower portions flex independently with the same radius of curvature as in (a). The equivalent elastic thickness is 63% of that in (a). M is the bending moment, K the radius of curvature, E Young's modulus, υ Poisson's ratio; (c) and (d) Rheologically layered continental lithosphere showing the failure envelope under extension (positive stress) and compression (negative stress). The strength is limited by frictional sliding (Byerlee's law) in the upper crust and uppermost mantle and by ductile flow in the lower crust and lower lithosphere. The hatched areas represent the stress resulting from flexure superimposed on the failure envelope. In (c) the plate is flexed at a very low curvature. The fiber stresses rarely exceed the failure criterion of the plate (there is a small amount of yielding at the top and bottom) and the equivalent elastic thickness (89 km) is almost exactly the same as the thickness of the elastic plate. In (d) the plate is flexed to a high curvature. This leads to the failure criterion being exceeded and a decoupling zone forms in the lower crust. The equivalent elastic thickness calculated for the total bending moment sustained in both the crust and the mantle is just 44 km. Decoupling therefore has strong potential mechanical implications for flexure.

upper crust from a strong underlying mantle during plate bending (Fig. 4.15) (Burov and Diament 1995; Lavier and Steckler 1997). Where the lithosphere is young and hot, it is prone to decoupling, thereby explaining the low Te in regions such as the Apennines and Alps. Where the lithosphere is old and cold, the lithosphere does not decouple, which explains the high Te in regions such as the Himalayas. Lavier and Steckler (1997) stress the role of sediment blanketing in raising temperatures high enough to cause weakening, yielding, and therefore decoupling.

The concept of a yield strength envelope (§2.4.6) suggests that if stresses caused by loading exceed the strength of the lithosphere, it will *yield* rather than flex elastically

(Fig 4.15). The yielding of a flexed plate should be related to its curvature (Goetze and Evans 1979). Initially as curvature increases (beyond *c.* $10^{-7}\,m^{-1}$), the upper and lower parts of the plate should yield, thereby reducing its elastic thickness. Measurements at ocean trenches indicate curvatures from 1×10^{-6} to $8 \times 10^{-7}\,m^{-1}$, suggesting that some yielding should be taking place (McNutt 1984).

McNutt and Kogan (1987) believed there was a good correlation between the elastic plate thickness and the surface curvature in map view of the thrust belts of mountain ranges. Highly arcuate mountain belts are associated with low elastic thicknesses (Alps, Carpathians) whereas long linear belts tend to be supported by a strong plate (Urals, Appalachians). The highly arcuate belts are commonly associated with back arc extension (e.g., Pannonian Basin), itself related to the dip of the subducting slab (Uyeda and Kanamori 1979). McNutt and Kogan (1987) suggested that the plan view shape is related to the cross-sectional curvature of the flexed plate, steeply dipping highly curved plates appearing weaker, and shallowly dipping plates appearing stronger. This would imply that the equivalent elastic thickness is not so much related to a characteristic isotherm, but is more due to the extent to which the elastic lithosphere has flexed under high bending stresses.

McNutt et al. (1988) analyzed 15 mountain belts and concluded that there was no indication that older mountain belts had experienced viscoelastic relaxation causing their present flexural rigidities to be low. The age of the continental lithosphere at the time of loading appears to set an upper bound to the maximum possible equivalent elastic thickness that can be observed. However, many *Te* values fall well below this level, suggesting that some weakening has taken place, but regardless of plate age. As introduced above, this mechanism of weakening may be related to *decoupling* or to *yielding*, reducing the effective elastic thickness from the purely elastic case by a factor of up to 2.

It could be argued that the curvature of thrust belts is more strongly influenced by variations in the mechanical properties of the stratigraphy and shallow basement being deformed, rather than scaling on the rigidity of the underlying plate. Sinclair (1996) therefore plotted equivalent elastic thickness estimates versus the curvature of the foreland basin's outer margin using carefully screened examples (see discussion in Zweigel and Zweigel 1998). He found a linear relationship, supporting the idea that weak plates correlate with arcuate mountain belts and foreland basins (McNutt et al. 1988).

4.3.2.3 Spatial and secular variations in flexural rigidity

It was noted in §4.1 and §4.2 how gravity data can be used to constrain flexural models of the oceanic lithosphere at mid-plate seamount chains and deep-sea trenches. Gravity (Bouguer) anomalies have also been widely used to study the flexure resulting from continental collision (Karner and Watts 1983; Lyon-Caen and Molnar 1989; Stewart and Watts 1997). Commonly used techniques include the matching of observed Bouguer gravity measurements with predictions forward modeled for different values of flexural rigidity, and spectral methods using the coherence and admittance of the Bouguer gravity field with topography (see §2.3.3). Watts (2001) gives a detailed account.

Bouguer gravity data allow a comparison between the observed deflection and the topographic loads of mountain belts. For example, Bouguer gravity anomalies along profiles in the western Himalaya and Ganga Basin indicate a mass deficit over the basin and a mass excess in the Lesser Himalaya (Lyon-Caen and Molnar 1985) (Fig. 4.4). The Bouguer anomaly over the Ganga Basin is, however, smaller than expected from the topographic load of the Himalaya, suggesting that some additional force, acting upward on the deflected lithosphere, is necessary. In contrast, the topographic load of the Zagros Mountains is insufficient to cause the observed flexure of the Arabian Plate with the formation of the Mesopotamian Foredeep and Persian Gulf as the foreland basin (Snyder and Barazangi 1986). This leads to the requirement for an additional force flexing the Arabian Plate downwards. Snyder and Barazangi (1986) believe that this additional force may be horizontal compression. It is less likely to be subsurface density variations caused by overriding an initially thinned Arabian continental margin, since there is no associated positive Bouguer anomaly, unlike in the Alps and the Appalachians (Karner and Watts 1983; Stewart and Watts 1997).

Profiles transverse to the axis of mountain belts commonly reveal significant variations in the flexural rigidity of the lower plate. Based on Bouguer gravity profiles, the flexural rigidity of the Indian Plate being overridden by the western Himalayas varies considerably over even relatively small horizontal distances (Lyon-Caen and Molnar 1985). Between profiles 200 km apart, estimated flexural rigidities changed by a factor of 5–10 (between *c.* 10^{24} and 7×10^{24} Nm), corresponding to a variation of equivalent elastic thickness by a factor of 2 (from

c. 54km to 104km). The rapidity of the horizontal changes suggests that flexural rigidity variations are not a result purely of differences in convective heat supply or loss in the mantle, but may instead be a result of small temperature variations causing large changes in strength in a highly temperature-dependent lithosphere, or of compositional or thickness changes of the deflected lithosphere. It is necessary to infer a segment of the Indian Plate, now deeply buried beneath the lesser Himalaya, which is steeply dipping and considerably weaker than the segment under the Ganga Basin (*c.* $2–5 \times 10^{22}$ Nm). This turns out to be a common feature of collision zones, since a similar abrupt steepening of the Moho is found in the Carpathian, Apennine, Alpine, Andean, and Zagros mountain belts.

The Alpine chain of Europe also shows strong variations in the estimated flexural rigidity derived from Bouguer gravity modeling (Stewart and Watts 1997). In particular, flexural rigidities appear to be low in western Switzerland, in close proximity to the Rhine Graben. Stewart and Watts (1997) therefore invoked a reduction of lithospheric strength by the thermal weakening of the plate in the region of the Rhine Rift.

Spatial variations in the flexural rigidity of the foreland plate may affect its response to moving applied loads during their migration history. The most likely scenario involves the closure of an ocean basin, causing initially the loading of the attenuated continental margin prior to full collision, when normal thickness continental lithosphere is flexed (Stockmal et al. 1986). Stewart and Watts (1997) identified such a strike normal increase in flexural rigidity with distance from the Andean orogenic belt in Ecuador using the Bouguer gravity field. In such a situation, with continued convergence the upper plate should initially deflect a weak lower plate, and then a progressively stronger lower plate. Although this is conceptually reasonable, there is no evidence of an increase in flexural rigidity of the European foreland plate during Alpine orogenesis from the marine (Late Eocene–Early Oligocene "flysch" stage to the predominantly nonmarine (Late Oligocene–Miocene) "molasse" phase (Allen et al. 2001) (see also §8.3.1).

4.3.3 Effects of plate segmentation during subduction

We have so far considered the deflection of the lithosphere at collision zones to be perfectly cylindrical. That is, any 2-D transect would be representative of the flexure as a whole. However, in some instances, there are offsets in the positions of the depocenters marking distinct foredeep segments. The Apennines of Italy are a well-documented example (Royden et al. 1987). Four forebulge segments, each characterized by Bouguer gravity highs can be distinguished (Fig. 4.16). They are thought to be linked to four slab segments delimited by tears or lines of weakness in the subducted slab. Along transects within individual segments, the gravity data can be used to calculate the equivalent elastic thickness of the plate. (The topographic loads on the plate are thought to be insufficient to explain the deflection (Royden and Karner 1984) and substantial subsurface loads are invoked that are several times the magnitude of the surface load.) In all four segments, the equivalent elastic thickness is in the range 15–20km (Royden et al. 1987), suggesting a uniform but stepped response of the deflected lithosphere. The stepped deflection is thought to be due to segmentation of the lithosphere within the subduction zone. The model deflection using a semi-infinite elastic sheet is illustrated in Figure 4.17. Applied loads and bending moments applied to the segments of the subducted lithosphere produced a series of offset forebulges and foredeep basin compartments that match well with the Apenninic geology. The segmentation of the plate at depth is masked by a continuous zone underlying the foreland basin, the only evidence for the segmentation lying in the distribution of the swells and basins on the deflected plate.

Furthermore, the thrust belt appears to mimic the deeper segmentation. In the segment with a forebulge far to the northeast, the thrust belt has also advanced relatively far to the northeast. In contrast, the lesser-traveled thrust units are correlated with forebulges relatively to the southwest. Since subsurface loads (i.e., forces within a subduction zone) are thought to be much more important than surface loads in the Apennines, this implies that near-surface tectonics are also intimately related to lithospheric heterogeneity at depth.

4.4 LITHOSPHERIC BUCKLING

Long wavelength folding or *buckling* of the lithosphere has been suggested for the Indian Ocean and central Australia (Fleitout and Froideveaux 1982; Lambeck 1983), but the wide applicability to the continents has been in some doubt. Long wavelength folding of the continental lithosphere has now been suggested from several continents (central Australia, central Asia, Canada,

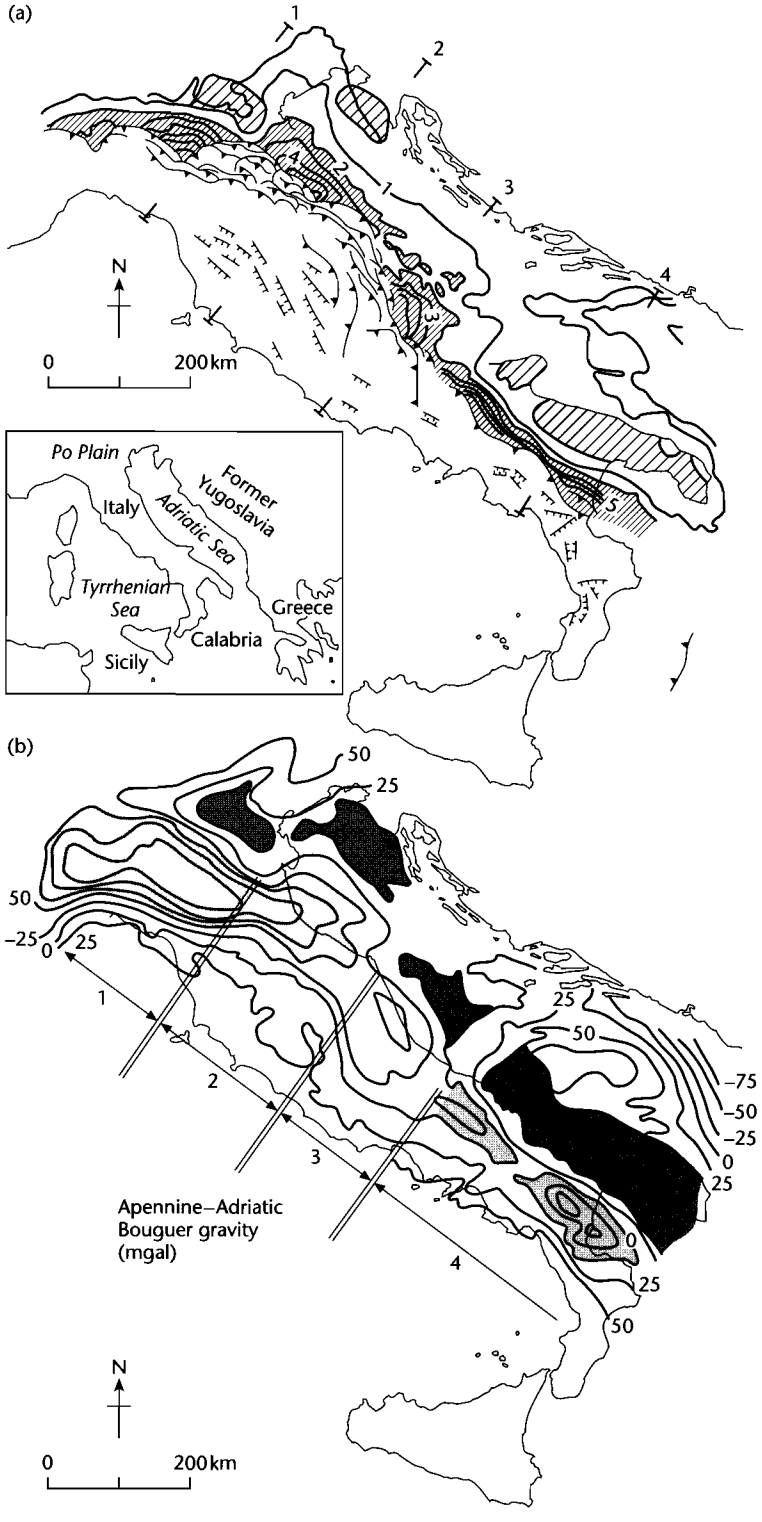
(a)
1
2
3
4
5
N
0
200 km
Po Plain
Italy
Former Yugoslavia
Adriatic Sea
Tyrrhenian Sea
Greece
Calabria
Sicily
(b)
50
25
0
−25
−50
−75
1
2
3
4
Apennine–Adriatic Bouguer gravity (mgal)
N
0
200 km

western Europe) (references and details in Cloetingh et al. 1999). The typical wavelengths observed are 50–600 km. If lithospheric buckling of significant amplitude takes place, it is important to recognize it and to discriminate it from the effects of lithospheric flexure due to the predominantly vertically applied loads in mountain belts. In this section, linear elastic theory is developed for the case of buckling of an elastic sheet embedded between an overlying ocean and an underlying fluid-like mantle (Boxed text 4.2). We then explore the inadequacies of this approach when applied to the case of the real continental lithosphere subjected to in-plane compressive stresses.

4.4.1 Theory: linear elasticity

We have previously seen that the lithosphere flexes under an applied system that may include vertically applied distributed loads, torques and horizontal loads (§2.1.4, §4.2). The question has not yet been addressed of whether the lithosphere is able to buckle under large horizontal, in-plane forces. We first approach this problem using an elastic beam under horizontal compression, and then extend the analysis to a lithosphere with an upward restoring force (see Boxed text 4.2).

We are now in a position to find out if the lithosphere should buckle under an in-plane stress. We take the following parameter values: Young's modulus $E = 70\,\text{GPa}$, Poisson's ratio $\nu = 0.25$, mantle density $\rho_m = 3300\,\text{kg m}^{-3}$, and ocean water density $\rho_w = 1000\,\text{kg m}^{-3}$, elastic plate thickness $h = 50\,\text{km}$. This gives a critical stress for buckling of 5.3 GPa, which is far too high for the brittle part of the lithosphere to withstand without faulting. If we reduce the elastic thickness and cover the elastic lithosphere by a sedimentary layer, thereby reducing the density difference $\Delta\rho$, the critical stress for buckling

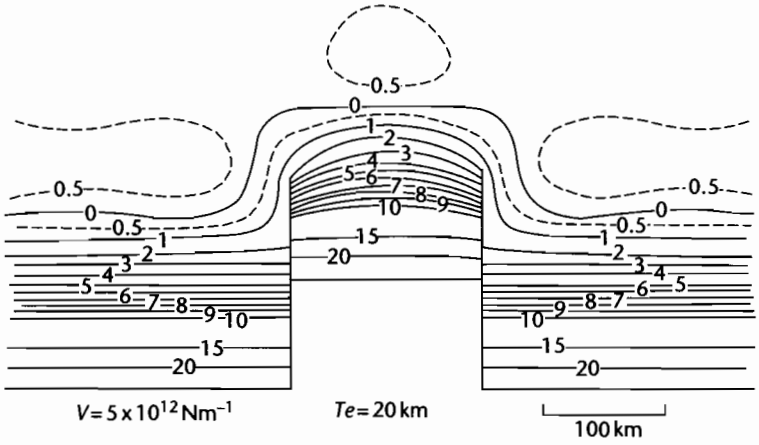

Fig. 4.17 Three-D model used by Royden et al. (1987) to simulate the flexure of segmented lithosphere. The lithosphere is assumed to be continuous in the foreland region but to be segmented by free boundaries or faults in the subduction zone. Vertical loads and/or bending moments are applied to the ends of the broken segments of the plate. The contours of the deflected surface, assuming the three slab segments to be initially at 1 km depth, are shown in km. A uniform equivalent elastic thickness of 20 km is assumed throughout and the vertical end load is $5 \times 10^{12}\,\text{Nm}^{-1}$. Note the offset of the outer rise segments and the 3-D pattern of the foreland basin depocenters.

Fig. 4.16 (a) General map of the Apennine system showing depth to the base of the Pliocene in the Adriatic and Po basins at a 1 km contour interval. There are four distinct outer rise/forebulge segments recognized in the basal Pliocene surface (shown in wide diagonal hatch). The narrow diagonal hatch shows the Apennine foreland basin and parts of the basal Pliocene surface that is below 2 km in depth; (b) Simplified map of the Bouguer anomaly gravity field (milligals). Contour interval is 25 mgal. The four morphological outer rises correspond to Bouguer gravity highs, suggesting that they are maintained by regional flexure. The shaded areas represent anomalies of greater than 0 mgal in sectors 1 to 3 and 50 mgal in sector 4: stipple shows gravity anomalies less than −50 mgal in sectors 1 to 3 and 0 mgal in sector 4. These sectors are believed to be bounded by major tears in the subducted plate, segmenting it at depth (after Royden et al. 1987, compiled from Ogniben et al. 1975, and Morelli et al. 1975).

BOXED TEXT 4.2: Buckling of an Elastic Beam

Initially, consider a beam fixed at its ends so that there are no applied torques (Fig. 4.18). The solution to the deflection of the beam under a horizontal load P is given by the general flexure equation (eqn 2.27). Integrating this equation twice with the boundary conditions that $w = 0$ at $x = 0$, $x = L$ and $d^2w/dx^2 = 0$ at $x = 0$ and $x = L$, gives

$$\lambda_c = 2\pi\left\{\frac{Eh^3}{12(1-\nu^2)(\rho_m-\rho_w)g}\right\}D\frac{d^2w}{dx^2}+Pw=0 \qquad (4.16)$$

This equation has the general solution

$$w = c_1 \sin\left(\frac{P}{D}\right)^{1/2} x + c_2 \cos\left(\frac{P}{D}\right)^{1/2} x \qquad (4.17)$$

where c_1 and c_2 are constants of integration. Equation 4.17 can be solved for the above boundary conditions to give

$$P = \frac{n^2\pi^2}{L^2}D \qquad (4.18)$$

where n is an integer multiple of π. The minimum horizontal load required to buckle the beam is when $n = 1$, in which case

$$P = P_c = \frac{\pi^2}{L^2}D \qquad (4.19)$$

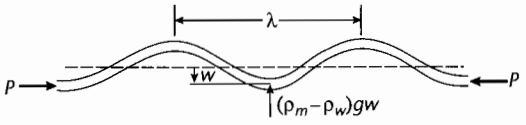

Fig. 4.18 Buckling of an infinitely long plate under an applied horizontal load with an upward restoring force (see Turcotte and Schubert 2002).

If P is smaller than the critical value P_c, the plate will not deflect under a horizontal load. If P is larger than P_c, the plate buckles, and its shape is half a sine curve of the form

$$w = c_1 \sin\left(\frac{P}{D}\right)^{1/2} x = c_1 \sin\frac{\pi x}{L} \qquad (4.20)$$

where c_1 is a constant relating the deflection to the horizontal force P.

This is not a realistic model of the lithosphere, since no restoring forces are exerted by underlying or overlying layers. The general flexure equation needs to be modified to incorporate the effects of an upward restoring force (eqn 2.28). The sinusoidal form of the deflection is of the form

$$D\left(\frac{2\pi}{\lambda}\right)^4 - P\left(\frac{2\pi}{\lambda}\right)^2 + (\rho_m-\rho_w)g = 0 \qquad (4.21)$$

where λ is the wavelength of the deflection and ρ_m and ρ_w are the mantle and water densities respectively. The solution (Turcotte and Schubert 2002, p. 124) is expressed in the form of the critical horizontal force to cause buckling as

$$P_c = \{4Dg(\rho_m-\rho_w)\}^{1/2} \qquad (4.22)$$

It is more convenient to express this critical horizontal force in terms of the critical horizontal stress and elastic plate thickness h, giving

$$\sigma_c = \left(\frac{Eh(\rho_m-\rho_w)g}{3(1-\nu^2)}\right)^{1/2}. \qquad (4.23)$$

The wavelength at the onset of buckling is

$$\lambda_c = 2\pi\left\{\frac{Eh^3}{12(1-\nu^2)(\rho_m-\rho_w)g}\right\} \qquad (4.24)$$

reduces (by about 75%) to slightly more realistic values. However, the wavelength at such reduced critical stresses is ≪50 km. This analysis suggests that although thin elastic layers embedded in surrounding rocks may deform by buckling, large scale, whole lithosphere folding should not occur in nature.

4.4.2 Lithospheric buckling in nature and in numerical experiments

The foregoing analysis highlights a problem. Unrealistically high stresses are required to initiate lithospheric buckling when it is treated using linear elasticity. Yet observations suggest that long wavelength buckles are common in the continental lithosphere, and develop early during phases of shortening in distant mountain belts. Sedimentary basins of central Australia, central Asia, the Himalayan perimeter, and Iberia have all been interpreted in terms of long wavelength lithospheric buckling. Basins with a previous extensional history are also believed to have been modified by in-plane stresses causing buckling (Ziegler et al. 1995).

Lithospheric folding is largely controlled by rheologic and thermal structure. The initial crustal thickness and thermal state of the lithosphere are therefore very important in determining the effectiveness of far-field compressive stresses (Cloetingh and Burov 1996). Consequently, different responses to compressive forces are expected in the relatively warm Alpine foreland of Europe compared to the relatively cold lithosphere of the Russian Platform because of their different strength profiles. In addition, buckling can be initiated at much lower compressive in-plane stresses with an elastic–ductile rheology than with a linear elastic rheology.

Cloetingh et al. (1999) recognized different types of long wavelength folding:

1 *Regular or periodic folding* is inferred from undulations of the "basement" imaged by seismic reflection and refraction, variations of Bouguer gravity anomalies and periodic vertical tectonic movements. Most cases of regular folding occur in young, weak lithosphere, which is strongly affected by horizontal loads. Long wavelength warping is occasionally detected by geomorphic observations such as the tilting of river terraces. Numerical experiments suggest a number of different behaviors based on the rheologic structure prior to folding. Where a strong upper crust overlies a weak lower crust and mantle, as in very young lithosphere, folds develop along the top and bottom of the upper crust monoharmonically (Fig. 4.19a). If the upper mantle is strong, the folds in the upper crust may develop independently from the folds at the top of the upper mantle, producing a decoupled, biharmonic pattern (Fig. 4.19b). The short wave-

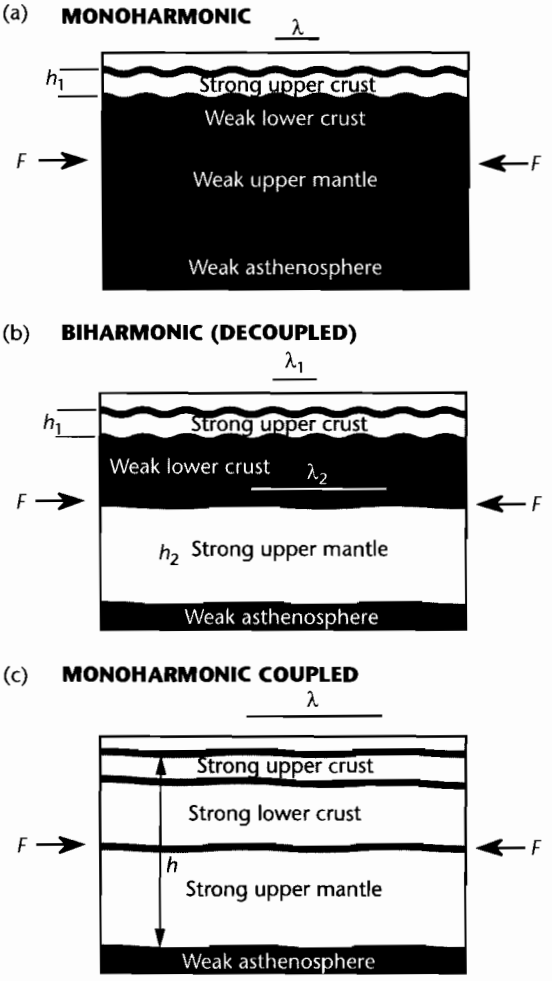

Fig. 4.19 Different styles of periodic buckling by a compressional force F; h_1 and h_2 are the thicknesses of the competent crust and mantle respectively, which fold with wavelengths λ_1 and λ_2. Where the lower crust is very weak, the upper crust and mantle lithosphere fold with different wavelengths ($\lambda_1 < \lambda_2$), producing decoupled or biharmonic folding (b). Where there is a single coherent layer of coupled crust and mantle, as in both young (<150 Ma) and very old (>1000 Ma) lithospheres, monoharmonic folding develops (a) and (c). After Burov et al. (1993) and Cloetingh et al. (1999).

length (30–60 km) corresponds to crustal folds, whereas the longer wavelength (200–350 km) corresponds to mantle folds. Where the combined crust and upper mantle are strong and mechanically welded, as in very old lithosphere, monoharmonic folds once again develop, but with a greater wavelength (>500 km) than in the "young lithosphere" case (Fig. 4.19c).

2 *Irregular or aperiodic folding* generally occurs in very young, weak lithosphere, where the deformation is strongly affected by such factors as erosion, lateral spreading of the sedimentary basin-fill, inhomogeneities in the crust (such as pre-existing sedimentary basins), and nonlinear rheologic behavior. Both wavelengths and amplitudes may vary unsystematically along the plate. They may also vary with progressive shortening.

Based on numerical plane strain models using nonlinear elastic–plastic (crust) and temperature-dependent power-law creep, Burg and Podladchikov (2000) predicted that lithospheric buckles, flanked by sedimentary basins, should spontaneously evolve into regions of asymmetric folding and thrusting. For example, the Kashmir and Peshawar basins either side of the Hazara–Kashmir syntaxis in northern Pakistan are thought to have been initiated by buckling. The Miocene to Recent central and south Adriatic basins, located between the Apennines and the Dinarides of southern Europe, are also thought to be due to lithospheric buckling of the Adriatic crust (Bertotti et al. 2001) (Fig. 4.20).

A persistent problem is how buckles are maintained over geological time scales, since in the absence of continuing compression, they should collapse because of the density contrasts between crust and mantle at the Moho. Only very strong crustal rheologies, expected in cold, strong cratons such as Australia or the Russian Platform, would be expected to withstand these pressure differences at the Moho for geological time scales of >20 Myr. In weak lithospheres, the buckles may collapse within 10 Myr.

Since basins due to lithospheric buckling are likely to be found in the foreland of continental collision zones, they may be difficult to discriminate from flexural basins driven by essentially vertically applied load systems in mountains belts. Despite some similarities in wavelength and amplitude, the main discriminating factors between the two types of basin are:

- Flexural foreland basins are very deep (< 10 km) close to the thrust front and taper strongly towards the foreland. Beyond the flexural forebulge in the backbulge region, amplitudes of the deflection are very small ($\ll$200 m). Migration of the orogenic wedge causes major stratigraphic onlap of the foreland plate through time;
- basins due to lithospheric buckling appear to form within a train of uplifts and depressions extending for $\gg$1000 km from the plate boundary. Depressions may be 10^2–10^3 m deep, with sediment derived from both margins, producing a symmetrical stratigraphic stacking.

Flexural foredeeps and basins due to lithospheric buckling should therefore not be confused. However, it may be very difficult to discriminate between some backbulge depositional zones and some basins representing synforms due to lithospheric buckling.

4.5 THE DYNAMICS OF OROGENIC WEDGES

4.5.1 Introduction

Foreland basins are dynamically linked to associated orogenic belts. The evolution of the orogenic wedge is important for basin development in a number of ways: (i) The wedge represents a supracrustal load on the foreland plate: its geometry and structure therefore influence the deflection of the foreland plate, (ii) the shortening and thickening of the wedge, or its extension and forward propagation, change the *configuration* of the load with respect to the deflected plate, i.e., its magnitude and distribution over the deflected plate, and thus change the shape of the deflection, and (iii) the unroofing by tectonic uplift and erosion of the orogenic wedge provides the detritus for deposition in the basin.

Here we concentrate on some of the broad processes of orogenic wedge evolution that have some bearing on the deflection of the foreland plate. Further information on foreland basin stratigraphy can be found in §8.6.2.

Three possible mechanisms for the driving forces responsible for crustal shortening have been proposed: (i) *gravity sliding*, (ii) *gravity spreading*, and (iii) *horizontal deviatoric push*. Gravity sliding requires a potential energy gradient for sliding under gravity alone. The gravitational force acting on the gradient must overcome the resistance to movement for gravity sliding to occur. Mathematical models suggest that the angle need only be small (a few degrees) where the effective normal stress on the inclined surface is reduced by the presence of high pore fluid pressures (Hubbert and Rubey 1959). However, field studies, particularly in the Rocky Mountains (e.g., Dahlstrom

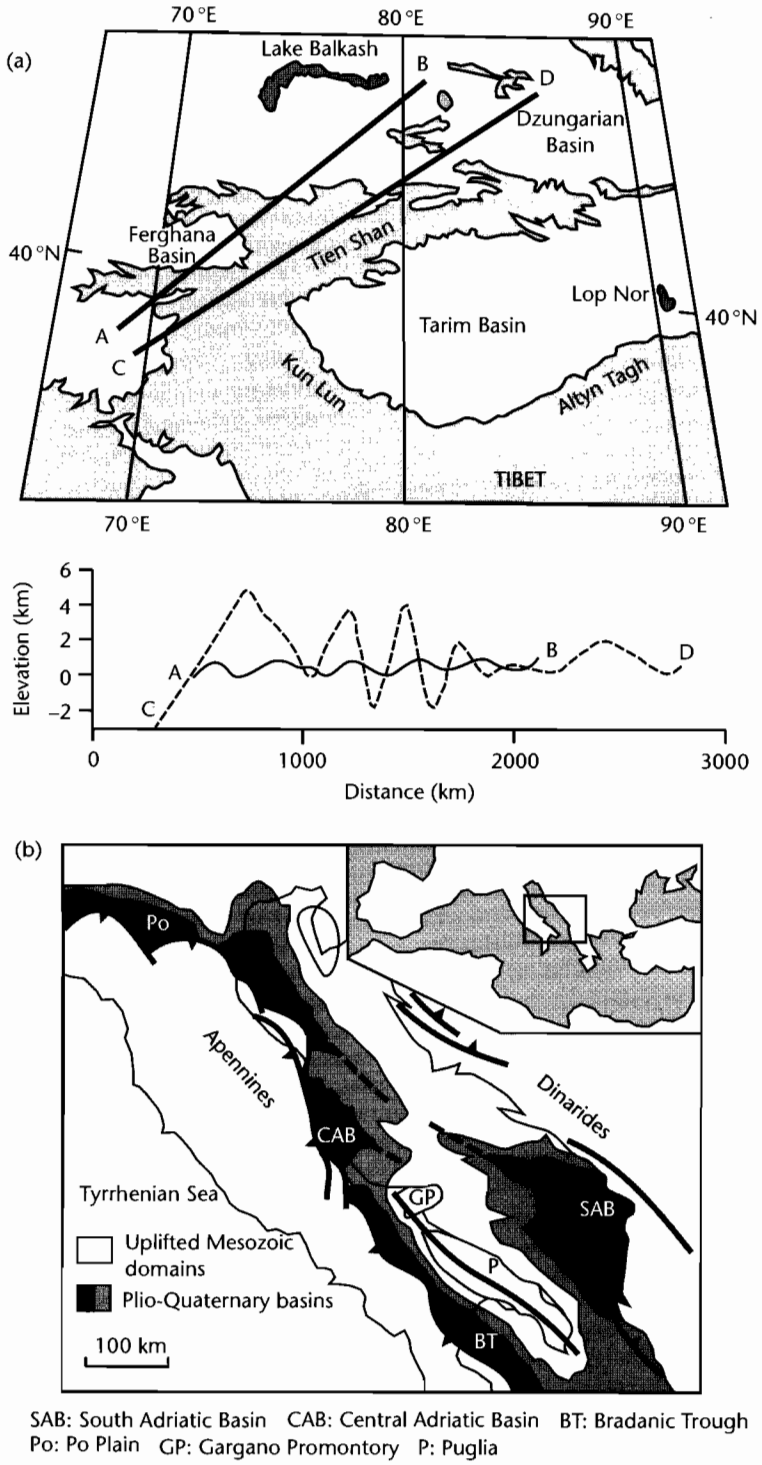

Fig. 4.20 Real-world examples of buckling from (a) central Asia (Cloetingh et al. 1999), showing elavation profiles for two transects A–B and C–D, and (b) Adriatic and eastern Italy (Bertotti et al. 2001), showing basins and highs oriented parallel to the strike of the Apennines and Dinarides. Reproduced courtesy of American Geophysical Union.

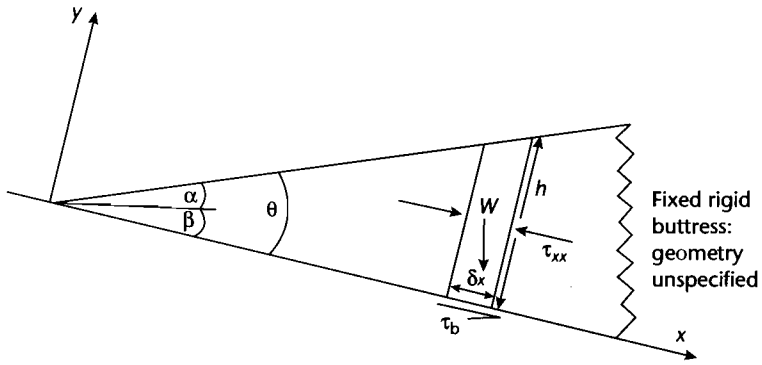

Fig. 4.21 Simplified model of an accretionary wedge (after Platt 1986). α is the surface slope, β is the basal slope and θ is the taper angle ($\alpha + \beta$). A small segment of the wedge of basal length δx and height h is subjected to a body force W, to a basal traction $\tau \delta x$, and to "push" forces from the rear, produced by the longitudinal deviatoric stresses τ_{xx}. The force balance is expressed in equation (4.26). Frontal accretion, underplating, erosion, and changes in basal shear stress (for examples by changes in the rate of convergence/subduction) place the wedge out of equilibrium. The wedge responds by shortening and thickening or by collapsing by extension.

1970) suggest that many thrusts dip in the opposite sense to the mass transport direction. Gravity sliding is therefore not likely to be the sole or dominant process in mountain belt tectonics. In the discussion that follows, we therefore concentrate on models involving horizontal deviatoric push and gravitational spreading. The most commonly used model involves a force balance in a tapered orogenic wedge.

4.5.2 Critical taper theory

Price (1973) believed that orogenic wedges behave as plastic entities as a result of the interfingering of a large number of thrust sheets into a mechanically interdependent system. Gravity acting on an orogenic "high" would provide the driving force for a spreading along thrust faults. The horizontal shear stress produced by gravity is given by (Elliott 1976)

$$\tau = \rho g h \alpha \qquad (4.25)$$

where ρ = density, g = gravitational acceleration, h = depth below surface, and α = surface slope of wedge. However, although this strain system is capable of producing local shortening, which must be compensated elsewhere by extension in order to maintain a constant angle of the wedge, it cannot explain the evidence of large scale net shortening in orogenic belts. Nor is any explanation given for the prior existence of a gravitational "high" at the onset of spreading.

Horizontal compressional forces (deviatoric "pushes") exerted along convergent plate boundaries may be primarily responsible for the dynamics of orogenic wedges. The convergent orogen can be regarded as a wedge-shaped prism resting on a rigid slab with a rigid buttress at the rear (Chapple 1978). The wedge behaves as a single mechanically continuous, dynamic unit, with the longitudinal force applied at the rear of the wedge counterbalanced by resistance to sliding on its base. The geometry attained is one of a wedge tapering along its length with a dynamic balance between the gravitational forces arising from the slope of the wedge, the push from the rear and the basal shear force or "traction." This balance can be expressed as follows (Platt 1986).

$$\tau_b = \rho g h \alpha + 2K\theta \qquad (4.26)$$

where the additional term on the right-hand side is due to the horizontal "push," K is the yield strength of the wedge, and θ is the angle at the front of the wedge (Fig. 4.21). Davis et al. (1983) also accounted for the internal strength and pore-fluid pressure of the wedge. They introduced the term "critical taper" to describe the surface slope that would produce a wedge in a state of yield throughout (Fig. 4.21). Davis et al. (1983) therefore expressed the basal shear stress in terms of the gravitational force and the material properties of the wedge as follows:

$$\tau_b = \rho g h \alpha + (1 - \lambda) K \rho g h \theta \quad (4.27)$$

where λ is the ratio of pore-fluid to lithostatic pressure, and the other terms are essentially the same as in equation (4.26).

Platt (1986) predicted patterns of deformation in the orogenic wedge resulting from externally imposed changes in its geometry. The most important change results from accretion. Two types are recognizable:

- *Frontal accretion* is the accumulation of material at the tip of the wedge, thereby lengthening the wedge. The response, if longitudinal deviatoric stresses are large enough, is internal shortening of the wedge. This may take the form of out-of-sequence thrusting or backthrusting;
- *underplating* of material to the underside of the wedge, causing the wedge to thicken and increase in surface slope. The wedge may respond by extension, lengthening the wedge, and lowering surface slopes.

Other factors influencing the shape of the orogenic wedge are: (i) *erosion* or removal of material from the top of the wedge, which encourages renewed shortening, and (ii) *changes in basal shear stress*: an increase in τ_b caused, for example, by an increase in the rate of subduction, leads to shortening and thickening; a decrease in τ_b may cause extension (Dahlen 1984). If subduction ceases, τ_b vanishes and the orogenic wedge should collapse by extension at the rear. Platt (1986) explains the uplift of high pressure rocks to surface positions in the rear of orogenic belts as due to this process of extension (Fig. 4.22).

The implications for basin development of this dynamic model are clear. Variations in rate of subduction, magnitude of deviatoric compression, or material properties of the wedge may cause large temporal variations in the load configuration and therefore in the deflection of the plate. In particular, lengthening and contraction of the wedge will have an impact on the position of the forebulge on the downgoing slab relative to the orogenic front (§4.6.2, §8.3.1).

4.5.2.1 The brittle–ductile transition in critically tapered wedges

The critical taper model is limited to cases of purely brittle-frictional (Coulomb) deformation. Many mountain belts, such as the Andes (Isaaks 1988) and Himalayas (Le Pichon et al. 1992), have a low-gradient toe area, and a steeper slope leading to a broad plateau region. These topographic features can best be explained by using a model including the effects of temperature-dependent ductile creep (Williams et al. 1994) (Fig. 4.23). The basal surface of the wedge, the decollement zone, may have different rheologic properties to the material within the wedge, because of the effects of dynamic crystallization (Rutter and Brodie 1988). This keeps deformation focused on the decollement. At the toe of the wedge, deformation within the wedge and in the basal decollement is dominated by frictional sliding and brittle failure, giving the classic tapered profile. However, at greater depths and higher temperatures the lower part of the wedge becomes ductile. This increases the ratio of applied basal shear stress to the strength of material in the lower part of the wedge, forcing an increase in the taper and a steeper surface slope. At even greater depths, the decollement zone itself may also become ductile, decreasing the ratio of applied basal shear stress to the strength of the lower part of the wedge and causing the surface profile to flatten into a plateau (Fig. 4.23b).

Abrupt changes in the wedge taper and the surface slope are brought about by abrupt changes in either the applied basal shear stress in the decollement zone or by the strength of the material in the lower part of the wedge. Such abrupt changes are most likely caused by a change in the deformational mechanism from brittle to ductile. A model using a brittle–ductile critical taper explains the east–west topographic profile across the Andes (near 20°S) from the Sub-Andean foothills to the steep slopes of the Eastern Cordillera and the high plateau of the Altiplano (Fig. 4.24).

The likelihood of orogenic wedges having brittle–ductile behavior depends on factors such as the thermal environment, material properties of the wedge and decollement materials, convergence rate, and elastic thickness of the lithosphere. Some wedges may be almost perfect frictional Coulomb wedges, such as in Taiwan, whereas others may exhibit significant ductile behavior.

4.5.3 Analogue models

Analogue experiments give insights into the mechanics of crustal deformation in orogenic wedges (Davy and Cobbold 1991). Analogue experiments are scaled to be representative of the lithosphere. Materials are therefore chosen to represent the rheologic layering and strength profile of the lithosphere. A simple system comprises a brittle upper sand layer simulating the crust, and a lower layer of high viscosity power-law silicone representing the lower crust, above a basal low viscosity fluid representing the mantle. This basal fluid layer allows the

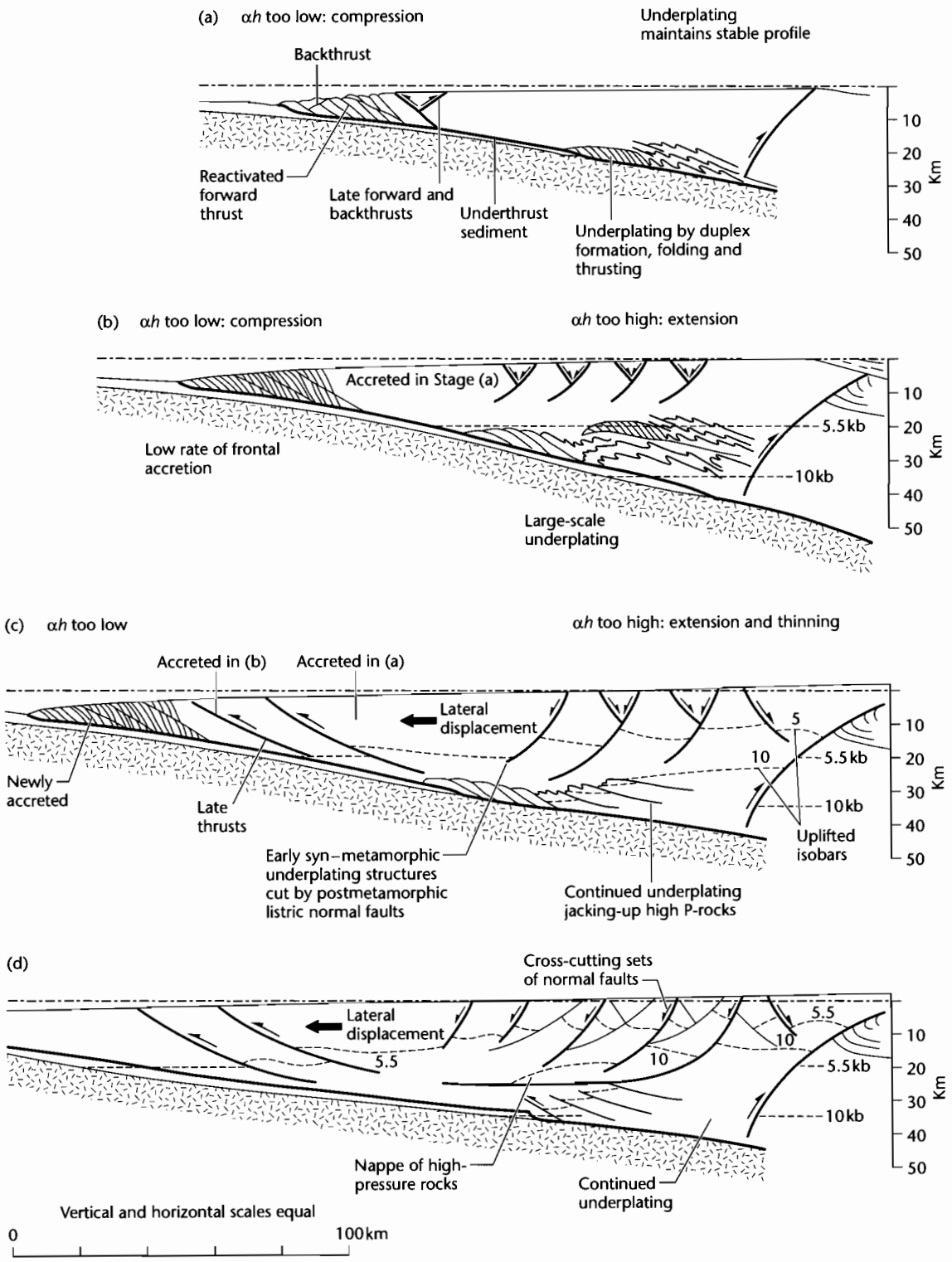
(a) αh too low: compression
Underplating maintains stable profile
Backthrust
Reactivated forward thrust
Late forward and backthrusts
Underthrust sediment
Underplating by duplex formation, folding and thrusting
10
20
30
40
50
Km
(b) αh too low: compression
αh too high: extension
Accreted in Stage (a)
Low rate of frontal accretion
5.5kb
10kb
Large-scale underplating
(c) αh too low
αh too high: extension and thinning
Accreted in (b)
Accreted in (a)
Lateral displacement
Newly accreted
Late thrusts
5
10
5.5kb
10kb
Uplifted isobars
Early syn-metamorphic underplating structures cut by postmetamorphic listric normal faults
Continued underplating jacking-up high P-rocks
(d)
Cross-cutting sets of normal faults
Lateral displacement
5.5
10
5.5kb
10kb
Nappe of high-pressure rocks
Continued underplating
Vertical and horizontal scales equal
0
100km

analogue experiment to be isostatically balanced. In a four-layer system, a brittle upper mantle lithosphere layer and ductile lower mantle lithosphere layer are constructed beneath a brittle upper crust and ductile lower crust.

Shortening in analogue experiments is normally produced by a piston and commonly results in buckling followed by bivergent thrusting (Cobbold et al. 1993; Burg et al. 1994b). The buckles have a wavelength controlled by the relative thicknesses of the brittle and ductile layers. Scaled up to the real world, such large buckles should be obvious as major crustal scale antiforms with a wavelength of *c.* 200 km, such as the Penninic culmination of the central Alps of Europe (Burg et al. 2002). The thrusts originate from the inflection points of the major buckles, and so are controlled in location and spacing by the presence of the early first-order buckles. Further shortening results in amplification of the thrusted buckles, giving rise to imbricated brittle wedges.

Indentation sand box models involve a rigid indenter

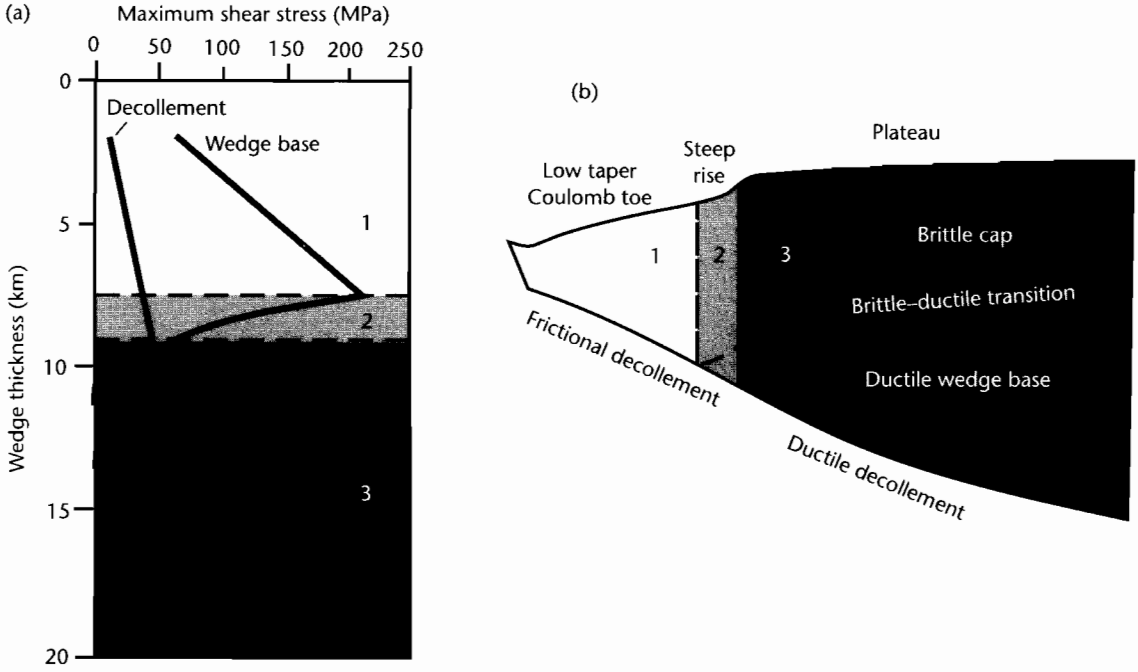

Fig. 4.23 Brittle–ductile critical taper model (after Williams et al. 1994). The wedge is divided into three regions: a narrow taper toe, where both the basal decollement and the wedge base behave in a brittle–frictional manner (Zone 1); a steep rise, where the decollement is still frictional but the wedge base region is ductile (Zone 2); and a flat plateau region, where both the wedge base and the decollement behave in a ductile manner (Zone 3). (a) The maximum shear stress (strength) of the wedge base and decollement; (b) The geometry of a critically tapered wedge corresponding to the strength profiles shown in (a). Reproduced courtesy of American Geophysical Union.

Fig. 4.22 Platt's (1986) evolutionary model of an accretionary wedge from youth to maturity. (a) Early stage with frontal accretion dominant. The gravitational effect of the surface slope (first term on right hand side of equation (4.27)) is too low in the frontal region, which therefore shortens and thickens internally; (b) Large scale underplating is the dominant mode of accretion, so that the rear of the wedge extends by extensional faulting and possibly by ductile flow near the base of the wedge. The deeper parts of the wedge may also undergo high pressure metamorphism; (c) Continued underplating and resultant extension has lifted the high pressure rocks towards the surface. Extension towards the rear of the wedge promotes some shortening (late thrusting) at the front; (d) In the mature stage underplating and extension have brought the high pressure rocks to levels accessible to erosion. The prism is now 300 km long, comparable to the Makran wedge of Pakistan.

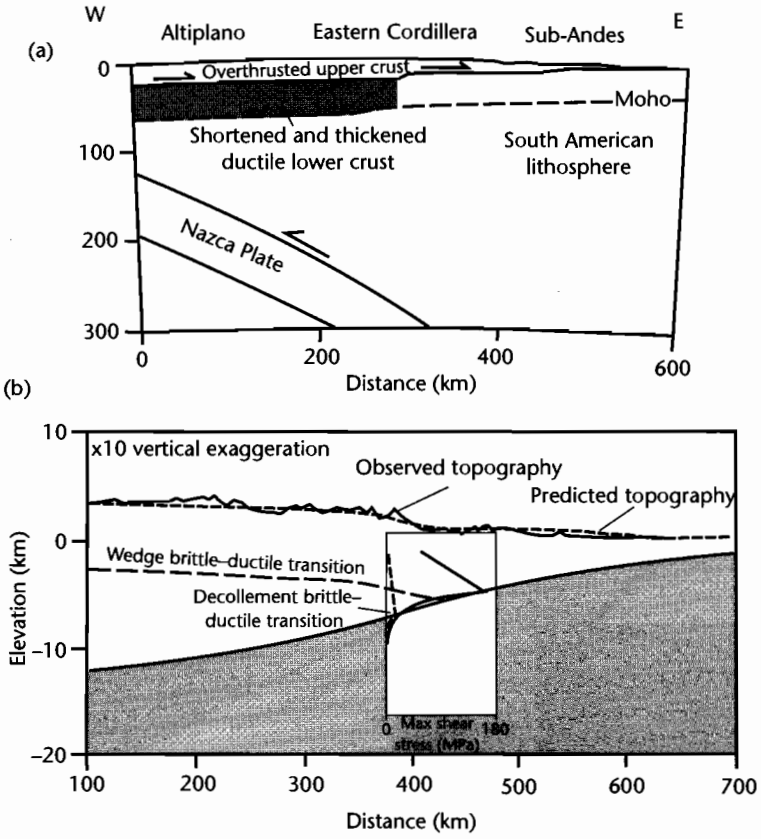

Fig. 4.24 Results of a brittle–ductile critical taper model applied to the Andes at 20 °S (after Williams et al. 1994). (a) Crustal model of the Andes along a transect at 20 °S (after Isacks 1988); (b) Observed and modeled topography using the geometry shown in cross-section, with the strength profile for wedge base (solid line) and decollement (dashed line) superimposed. The wedge base is significantly stronger than the decollement zone, except at where the decollement becomes ductile (*c.* 7.5 km below sea level). Reproduced courtesy of American Geophysical Union.

with the same height as the undisturbed sand (representing undeformed crust), which allows sand to spread laterally outwards over the indenting plate (Koons 1989, 1990). With progressive deformation, a doubly vergent wedge forms, with thrusts propagating away from the indenter to form an outboard wedge or retro-wedge, and towards and over the indenter as an inboard wedge or pro-wedge. The outboard wedge is decoupled along a low-friction Mylar sheet at the base, and thrusts rise from this surface. However, within the inboard wedge, thrusts propagate up through the wedge material itself at an angle corresponding to the angle of internal friction of the sand ϕ. Thrusts in the inboard wedge are therefore shallower than in the outboard wedge. Sand box experiments are also capable of reproducing the conditions of mantle subduction, where a sand cover is dragged by an underlying Mylar sheet (Malavieille 1984). Once again, a doubly vergent wedge is produced centered over the point of detachment, the majority of thrusts facing the subducting plate.

Analogue experiments are therefore good at allowing a visualization of the development of major crustal features such as thrusted antiforms and bivergent wedges. The tectonic wedges created in analogue experiments have geometries as predicted by critically tapered wedge mechanics (§4.5.2) and are very similar to the wedges produced in numerical simulations using the same boundary conditions (see §4.5.4 and §4.6.3). However, they have difficulty in simulating erosion at the surface of the wedge.

4.5.4 Numerical approaches to orogenic wedge development

There are three force systems that control deformation in the orogenic wedge:

- **F1**: The compressive force integrated over the thickness of the crust;
- **F2**: the gravitational force (or increased potential energy) due to crustal thickening;
- **F3**: the basal traction force integrated across the base of the deforming zone.

The tendency for the thickened crust to spread out laterally is given by the ratio **F2/F1**, which is known as the *Argand number* (see also §3.6.2) (England and McKenzie 1982). For a linear viscous material

$$Ar = \frac{\rho g h^2}{\mu V_p} \tag{4.28}$$

where ρ is the density, g is acceleration of gravity, μ is viscosity, h is the length scale (thickness) of the mechanical model, and V_p is the horizontal velocity at the base of the crust. For a typical crust with $\rho = 2800\,\mathrm{kg\,m^{-3}}$, $\mu = 10^{23}$ Pa s, $h = 35\,\mathrm{km}$, and $V_p = 0.05\,\mathrm{m\,yr^{-1}}$, the "viscous" Argand number is 5. For a Coulomb plastic material, the Argand number becomes (Willett 1999)

$$Ar = \frac{2}{\tan\phi} \tag{4.29}$$

where ϕ is the angle of internal friction, typically 15° for crustal rocks. Using this value, the "Coulomb" Argand number is 7.

If $Ar \gg 1$, even small increases in thickness are counteracted by gravity, redistributing the thickening away from the plate boundary and broadening the zone of deformation. If Ar is small, however, the crustal thickening is localized.

The ratio **F3/F1** is known as the *Ampferer number* (Ellis et al. 1995; Ellis 1996). It reflects the strength of the crust–mantle coupling. The length scale of deformation in subduction models scales on the Ampferer number. If Am is nearly 1, the model crust is strongly coupled to the underlying mantle, which means that the basal tractive forces are transmitted strongly into the crust, causing thickening. If Am is close to zero, there is weak coupling, and the basal tractive forces are inefficient at causing crustal thickening.

Numerical models of orogenic wedge development have been developed from two starting points (Fig. 4.25a):

1 *Indentation models* assume that forces are transmitted laterally from a rigid indenter into a less rigid continental plate approximated by a thin viscous sheet (England et al. 1985; England and Houseman 1986). As mimicked by plasticine analogue models (e.g., Peltzer and Tapponnier 1988), deformation of the viscous sheet spreads out over a strike-normal distance related to the width of the indenter. If λ is the length scale of the deformation and D is the strike-parallel width of the indenting body

$$\lambda = \frac{2D}{\pi\sqrt{n}} \tag{4.30}$$

where n is the power-law exponent of the viscous sheet. In this model, if D is 3000 km, which is the approximate scale of the India–Asia collision, and the rheology of the viscous sheet is linear ($n = 1$), the length scale of the deformation should be in the region of 2000 km. For $n = 2$ and n = 3, λ reduces to 1350 km and 1100 km respectively. In the indentation model, crust (and mantle lithosphere) is thickened in the relatively weak continental lithosphere against the boundary with the rigid indenter. Gravity acts on the thickened layer, which causes λ to increase as convergence continues. Eventually, very large regions of crustal uplift such as the Tibetan Plateau are produced. The forces on the thickened crust are quantified by the Argand number in indentation models.

2 *Mantle subduction* models invoke the transmission of forces from an underlying subducting mantle lithosphere to the base of the crust. These forces act across a crust–mantle boundary that must therefore undergo considerable subhorizontal shear. This zone of subhorizontal decoupling is termed a *detachment*. The width of the region of crustal thickening depends critically on the strength of the coupling along the detachment. This coupling is quantified by the Ampferer number. If the original thickness of the crust is h_0, the length scale of the deformation in mantle subduction models is given by

$$\lambda = \left(\frac{4}{nAm}\right)^{\frac{n}{n+1}} h_0 \tag{4.31}$$

If the crustal layer is initially 35 km thick, we adopt a linear viscous rheology ($n = 1$) and a very strong coupling between the crust and mantle ($Am = 1$), the width of deformation is just 70 km. If there is a very weak coupling between crust and mantle ($Am = 0.1$), λ becomes *c.* 220 km. Both of these estimates are considerably

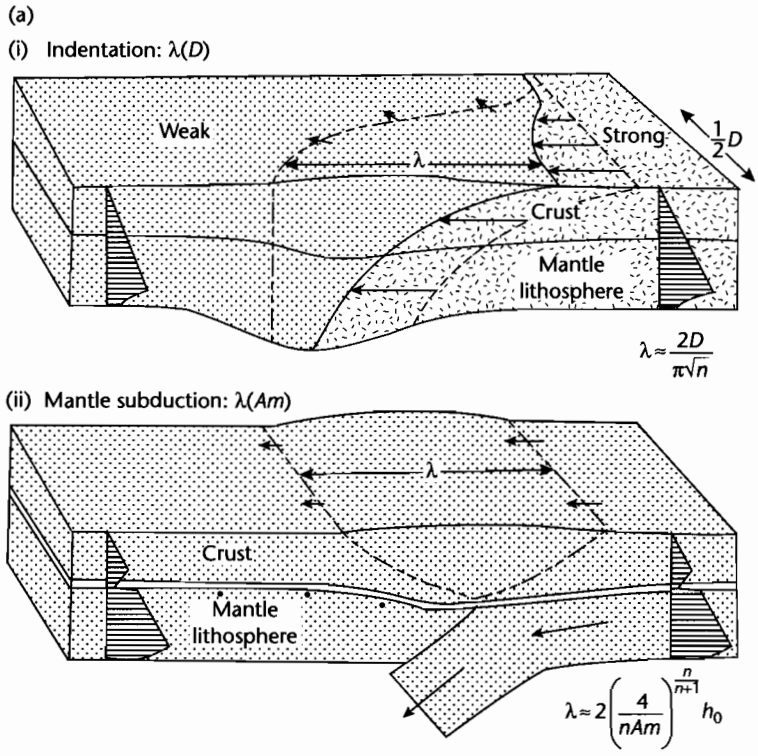

Fig. 4.25 (a) Schematic illustration of two end-member models of continental deformation resulting from convergent continent–continent tectonics (after Ellis 1996). In (i), indentation over a lateral length scale D causes thickening over a width λ. Half of the indenter is shown. Thickening occurs in the crust and mantle lithosphere in the relatively weak indented plate. (ii) Continental deformation is driven mostly by mantle subduction. Crust in both plates is weak, with a strength minimum at the Moho, which decouples crustal deformation from underlying mantle subduction. The width of deformation λ depends on the strength of the mantle–crust coupling, given by the Ampferer number Am; (b) Deformation width λ normalized by the initial crustal thickness h_0, versus the crust–mantle coupling Am. The normalized indenter lateral length scale is $D/h_0 = 25$. For a given indenter length scale, the combined model width of deformation width λ is controlled by indenter mechanics for weakly coupled (detached) systems ($Am = 0$), and by mantle subduction mechanics for strongly coupled ($Am \sim 1$) systems. Reproduced courtesy of Geological Society of America.

smaller than in the indentation model, suggesting that the length scale of deformation in an orogenic belt is an indicator of the underlying mechanics.

Comparing the indentation and mantle subduction models (Ellis 1996), the increase in the width of deformation increases with continued convergence, but at different rates. The value of λ is initially much lower in the mantle subduction case, but the growth of λ with convergence increases more rapidly than in the indentation model (Fig. 4.25b).

An orogenic model involving both indentation and mantle subduction processes suggests that there may be different evolutionary paths for orogenic belts:

1 For situations where the crust is strongly coupled to the mantle lithosphere (Am high) crustal thickening should initially be controlled by mantle subduction, especially where D is large. In the case of orthogonal relative plate motion, there will be very limited strike–slip or escape tectonics;
2 for situations where the crust is weakly coupled to the mantle lithosphere (Am low), mechanics will be dominated by indentation, especially for small indenter length scales (D). Even during orthogonal convergence, strike–slip tectonics and lateral escape should be widespread;
3 since λ grows faster for mantle subduction than for indentation, an orogen initially dominated by mantle

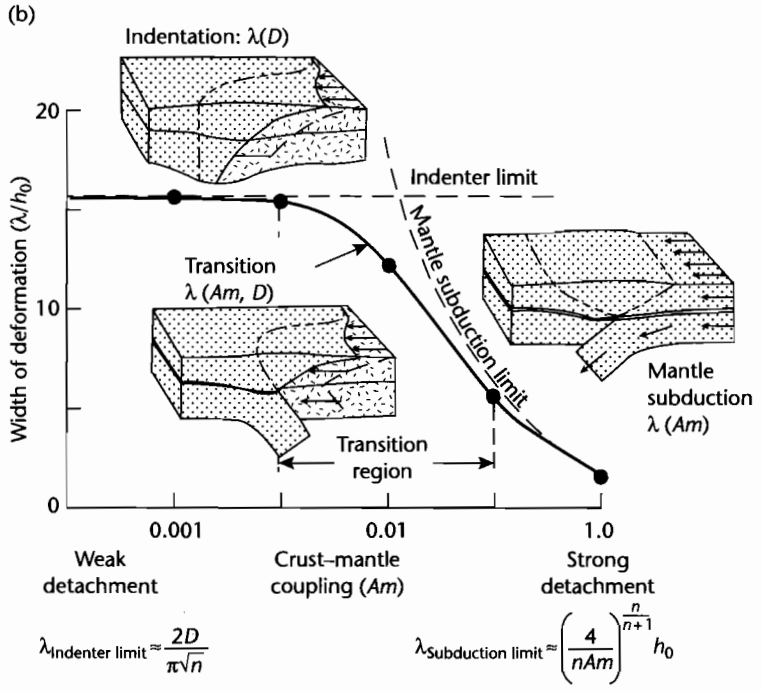

Fig. 4.25 *Continued*

subduction mechanics may, with continued convergence, evolve into an orogen dominated by indenter-style mechanics.

4.5.4.1 The mechanics of bivergent wedges

We have so far considered the mechanics of critically tapered orogenic wedges as a Coulomb model (Davis et al. 1983; Dahlen 1984; Platt 1986) and that the gross features of convergent orogens can be simulated from analogue experiments (Malavieille 1984). One of the conspicuous features of mountain belts and oceanic accretionary prisms is their doubly vergent nature. That is, thrust displacements are directed outwards from the core of the orogen on both flanks. Bivergent wedges can also be produced in numerical experiments involving the subduction of mantle lithosphere beneath a crustal layer with a Coulomb-plastic rheology (Willett 1992; Beaumont et al. 1996a). The basic model set up is a laterally uniform layer undergoing a plane strain deformation caused by coupling across a detachment to two underlying, converging rigid plates. One underlying plate slides (subducts) beneath the other at point *S*. At the base of the upper layer, the velocity field to the left of *S* is uniform and positive, acting from left to right (Fig. 4.26), whereas to the right of *S* the velocity is zero. The upper layer has a Coulomb yield strength with a coefficient of friction ϕ that is larger than the coefficient of friction in the weak detachment layer ϕ_a. Model runs show that deformation spreads upwards from *S*, initially as two conjugate shear zones, bounding a nearly triangular region of minimal internal deformation that is uplifted as a block (Fig. 4.27a). Subsequently, shear zones develop on the pro-wedge side of *S*, producing a long, tapered pro-wedge compared to the narrow retro-wedge (Fig. 4.27b). Finally, the retro-wedge is detached from its base and propagates strongly to the upper plate, producing a tapered retro-wedge (Fig. 4.27c). Whereas the pro-wedge grows by accretion at its toe and has the minimum taper angle for a critically tapered Coulomb wedge, the retro-wedge grows by material being added at the back, and has the maximum taper for a critically tapered Coulomb wedge. This is supported by the obviously different topographic slopes on the different flanks of mountains belts such as the Southern Alps of New Zealand and Alps of central–western Europe.

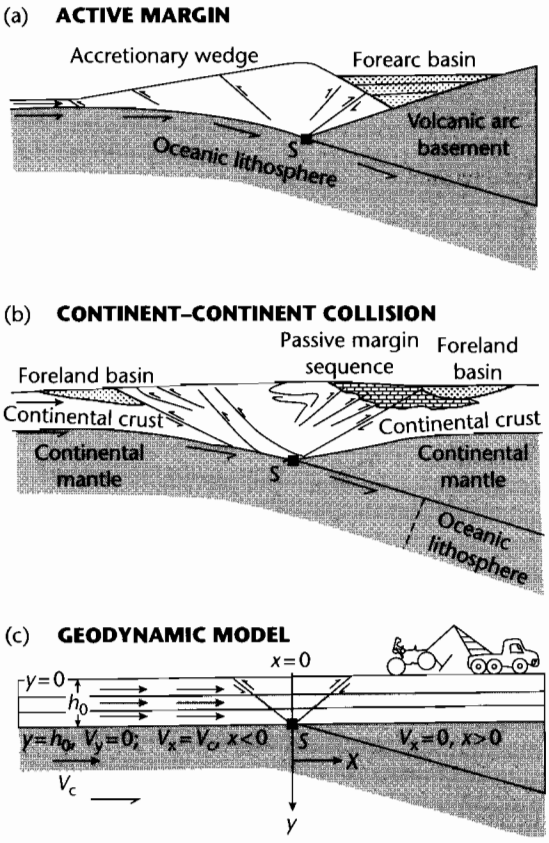

Fig. 4.26 (a) Active margin with bivergent wedge represented by an accretionary prism and a retro-basin represented by a forearc basin, and a pro-basin as an ocean trench; (b) Continent–continent collision zone with a pro-foreland and retro-foreland basin; (c) Geodynamic model, showing crustal deformation focused at a point S, where mantle of the plate on the left, moving with a constant tangential velocity V_p detaches and is underthrusted. Overlying crust has initial thickness h_0 to the left of S. The tangential velocity to the right of S is zero. There is no stress on the upper surface. There is no requirement for a "bulldozer" backstop in this geodynamic model. Modified from Willett et al. (1993). Reproduced courtesy of Geological Society of America.

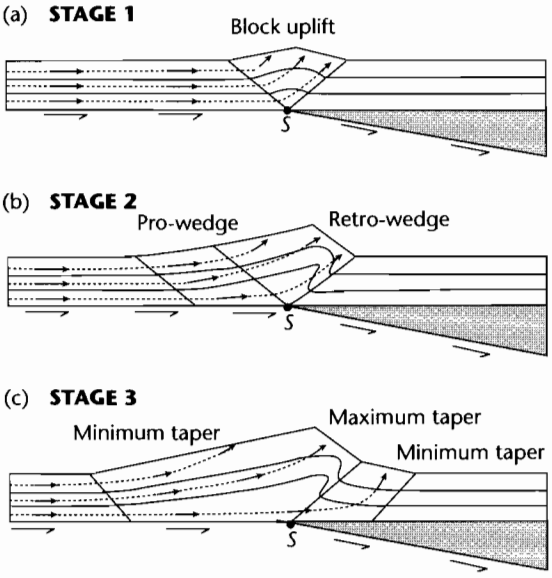

Fig. 4.27 Evolutionary development of a bivergent wedge (from Willett et al. 1993) from a block uplift bounded by two conjugate shear zones centered over S (a), to an asymmetrical bivergent wedge (b), and a tapered retro-wedge as deformation propagates strongly into the upper plate (c). Dashed lines are instantaneous flow lines with arrows proportional to velocity. Reproduced courtesy of Geological Society of America.

The thickened upper layer must be balanced isostatically, giving a crustal root. If the orogen is supported flexurally, flanking foreland basins will develop. As the root develops, however, heating may cause the rheology of crustal materials to change from a Coulomb-plastic flow to a thermally-activated power-law viscous flow (Fig. 4.28). This weakens support for the orogenic wedge, promoting the development of low surface slopes bounding a plateau. If heating continues, the orogen may collapse by extension in order to achieve a low taper angle. Orogenic collapse (Dewey 1988) drives material to the flanks, which continue to behave as Coulomb-plastic wedges. Consequently, extension in the rear of an orogen should be accompanied by contraction (thrusting) towards the flanks. The requirement of the wedge to alter its taper angle also depends on the convergence velocity. If the convergence velocity falls, the viscous-based orogen is required to achieve a new geometry with a lower taper, which can best be achieved by extension. If the convergence velocity stops, the wedge must extend until there is no surface slope. The removal of material from the surface of the wedge by erosion has a strong feedback to the generation of mass in the orogenic wedge caused by convergence. We should expect high rates of erosion to require high tectonic fluxes into the wedge to replace the material lost at the surface (Fig. 4.29). Consequently, erosion appears to "suck up" rocks from depth. This can be recognized in the exhumation patterns of mountain

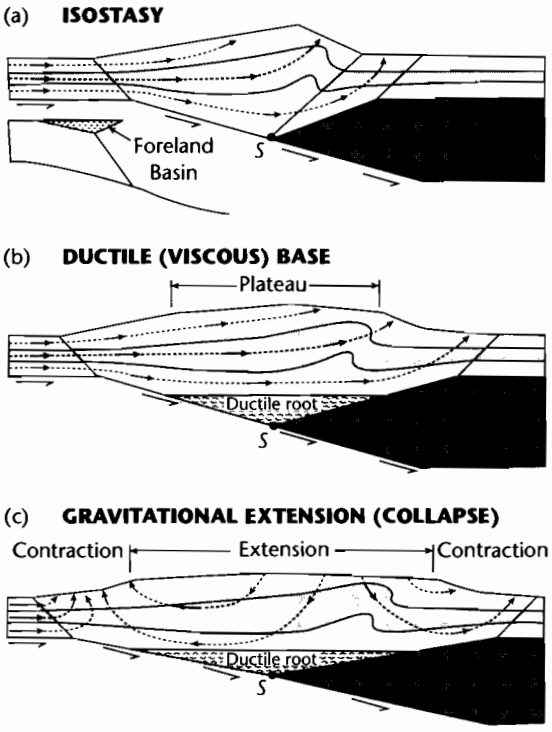

Fig. 4.28 The effects of isostasy and viscous (ductile) flow in the lower crust beneath a bivergent wedge (after Willett et al. 1993). In (a), isostasy causes the formation of flexural depressions (foreland basins); (b) Thickening of the bivergent wedge and increase in temperature decreases basal strength of the wedge and produces a ductile root. This promotes a reduction of surface slopes, resulting in a broad plateau. In (c), a further increase in lower crustal temperatures, or a decrease in the convergence rate causes the plateau to extend and increases contractional deformation in the bounding pro- and retro-wedges. Reproduced courtesy of Geological Society of America.

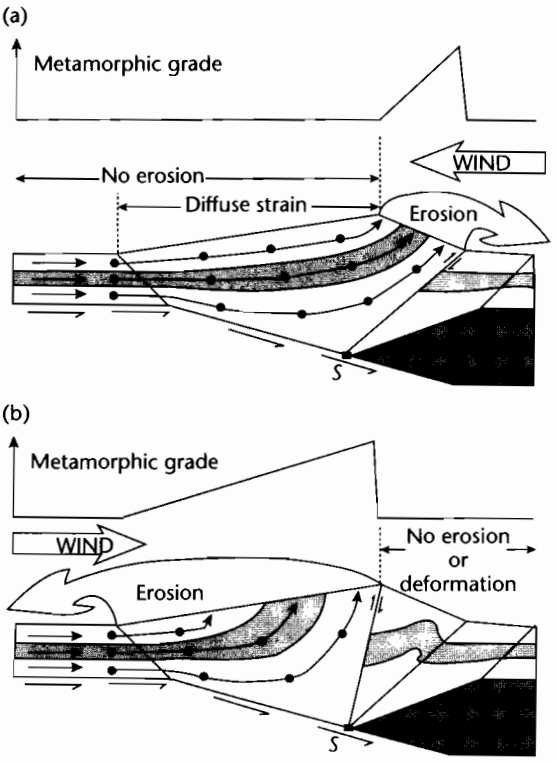

Fig. 4.29 Effects of erosion on a bivergent wedge (after Willett et al. 1993). Precipitation concentrated on the retro-wedge (a), and pro-wedge (b) increases erosion, causing an advection of high-grade metamorphic rocks from the middle and lower crust (and even mantle lithosphere) to the surface. Passive shaded layer shows middle crust. Lines are material trajectories and dots show progressive equal-time positions of points originally aligned vertically. Reproduced courtesy of Geological Society of America.

belts, which commonly have lower crustal (and even mantle) rocks exposed in their cores. If erosion is asymmetrical because of climatic differences on each side of the mountain belt, the wet, windward side of the orogen should be characterized by high exhumation rates of high grade metamorphic rocks, whereas the dry leeward side should continue to be draped by upper crustal rocks (Fig. 4.29). This pattern is seen well in the Southern Alps of New Zealand (Koons 1989; Norris et al. 1990), the central Himalaya (Fielding 2000), the European Alps (Beaumont et al. 1996a; Schlunegger and Willett 1999), and Taiwan (Lin 2000; Dadson et al. 2003).

We reconsider these scenarios posed by numerical models in relation to exhumation, sediment flux, and basin development in §4.6.3.

4.6 THE MODELING OF FORELAND BASINS

4.6.1 Basin evolution caused by a moving tectonic load

Deposition in foreland basin systems can be understood by investigating the effects of a moving load system on the deflection of an elastic foreland plate (Jordan 1981, and Schedl and Wiltschko 1984 for early treatments).

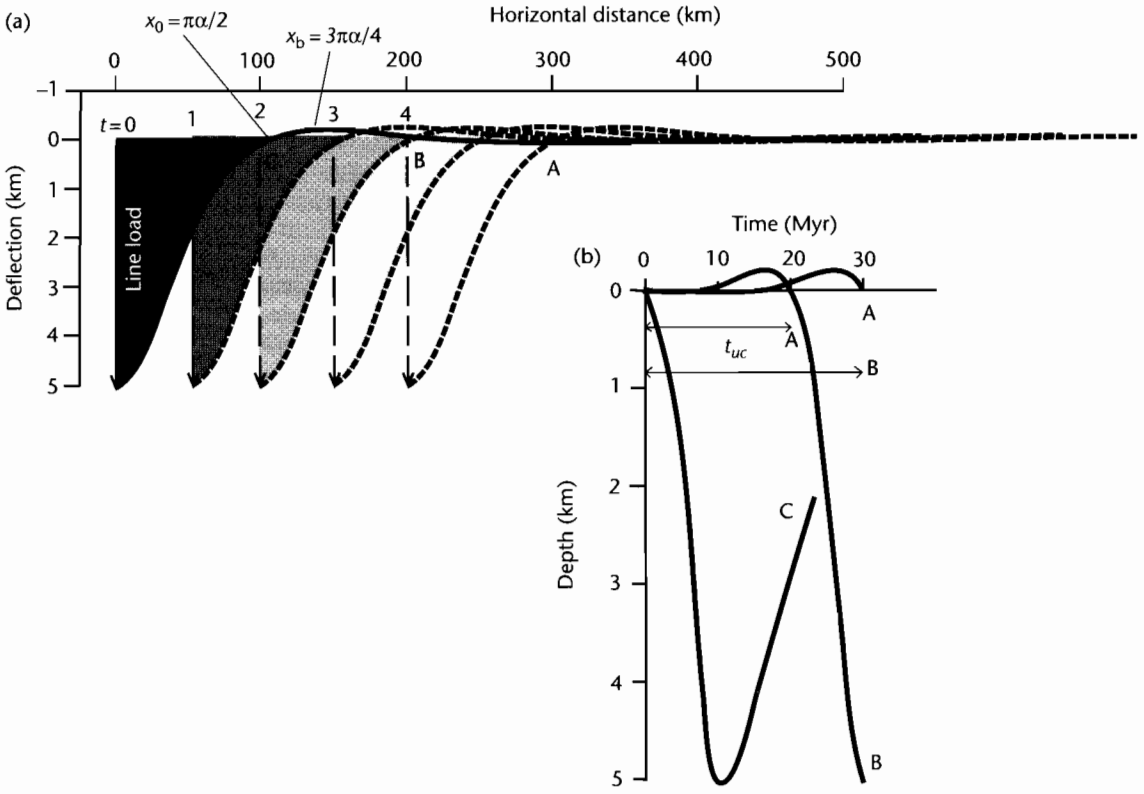

Fig. 4.30 Migration of a flexural wave under a moving load system. (a) Movement of the deflection across a foreland plate as a result of load migration; (b) Points A, B, and C experience different subsidence histories depending on their initial location with respect to the load. Point A spends 30 Myr in a backbulge or forebulge position. Point B is initially uplifted in the forebulge, then subsides in the foreland basin. Point C experiences basin subsidence, followed by uplift as it is incorporated into the thrust wedge.

The static deflection is described for continuous and broken plate models in §4.2. For a moving load system, the deflection simply moves as a wave through the foreland plate ahead of the load system. If the load system moves relative to the foreland plate, so does the deflection.

The shape of the deflection is an asymmetric "low" (foredeep) close to the load and a broad, low-amplitude, uplifted forebulge far from the load. Since the supracrustal load in a convergent mountain belt moves closer to a point fixed to the foreland plate through time, and since we know from the solution of the flexural equation (eqns 4.4 and 4.8 for continuous and broken plates) that the deflection increases towards the load, it follows that subsidence rates in the foreland basin should accelerate through time, until the same fixed point is overridden by the thrust wedge and sedimentation ceases. The original location of the point fixed to the foreland plate at the onset of flexure determines the precise subsidence history followed (Allen et al. 1991). Consider the following three locations (Fig. 4.30):

1 *Point A* is originally located beyond the flexural forebulge in the backbulge region (i.e., for a line load on the end of a broken plate, at $x/\alpha > 5$). It will initially experience negligible uplift/subsidence, but as convergence continues, will be "dragged" through the flexural forebulge, causing slow but prolonged rock uplift and erosion. The erosion will continue until $x = \pi\alpha/2$, producing an unconformity with a large chronostratigraphic gap of duration t_{uc};
2 *Point B* is originally situated within the forebulge region ($\pi\alpha/2 < x < 3\pi\alpha/2$). It will immediately experience

rock uplift and erosion. As convergence continues it will be dragged through the first node of the deflection where $w = 0$, and will then experience accelerating subsidence as the point becomes buried by foreland basin sediments. The chronostratigraphic gap should be smaller than for Point A;

3 *Point C* is originally located close to the orogenic wedge inboard from the first node and the flexural bulge. It will, from the outset, experience subsidence. The rate of subsidence will increase through time as the point becomes closer to the maximum deflection. Eventually, with continued convergence, the point is likely to become incorporated into the orogenic wedge itself so that the foreland basin stratigraphy can only be viewed in allochthonous thrust units. There should be a conformity at the basal surface of the foreland basin megasequence.

The key prediction for a foreland basin generated by a moving load is therefore that the basin-fill is underlain by an unconformity with a variable and predictable stratigraphic gap (Crampton and Allen 1995; Allen et al. 2001). This is a megasequence boundary caused by flexural forebulge uplift. Points located close to the load start subsiding earlier than distal points. At any one time slice, proximal locations subside faster than distal locations. The overall form of the subsidence rate at any one location is convex-up, indicating accelerating subsidence through time (e.g., Homewood et al. 1986). Further discussion is found in §8.3.1.

The plate tectonic scenario providing the context for the general evolution of foreland basins involves the inheritance of a passive margin, followed by an early convergent stage characterized by deep water conditions, and a later convergent stage during which a subaerial wedge is flanked with terrestrial or shallow marine foreland basins (see also §8.3.1) (Stockmal et al. 1986) (Fig. 4.31). Flexural forebulge unconformities are thought to be best developed during the early convergent stage, but may be buried beneath terrestrial sediments during the late convergent stage (Crampton and Allen 1995).

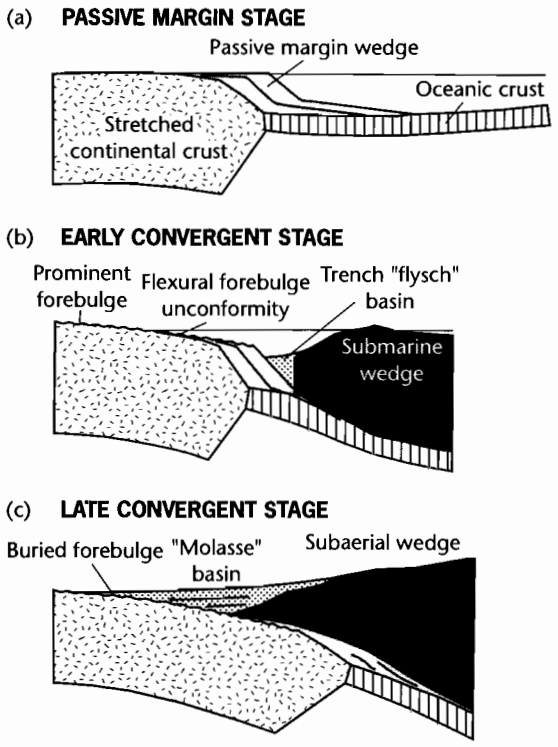

Fig. 4.31 Model involving orogenic loading of a previously stretched continental margin during the early stages of convergence (Stockmal et al. 1986; Watts 1992), modified by Allen et al. (1991). The first orogenic loads are emplaced on a weaker lithosphere at considerable water depths.

4.6.2 Diffusive models of erosion and deposition

The convergence of an orogenic thrust wedge over a foreland plate can be considered mechanically as a distributed vertical load system translating laterally over a flexed plate. Erosion of the thrust wedge and deposition in the foreland basin has been treated as a diffusional process (Flemings and Jordan 1989; Sinclair et al. 1991). In diffusional problems, the transport rate or flux is proportional to the topographic gradient and the rate of erosion or sedimentation is proportional to the curvature. The use of diffusion in modeling hillslope evolution is treated in more detail in §7.5.1.

Sinclair et al. (1991) proposed that the simplest model of mountain belt erosion and foreland basin sedimentation must be described by four parameters (Fig. 4.32): (i) the equivalent elastic thickness of the foreland plate, (ii) the rate of thrust front advance, (iii) the surface slope angle of the orogenic wedge, and (iv) the effective transport coefficient, representing the constant of proportionality between topographic slope and sediment transport rate. They modeled the orogenic wedge as a critically taped system (Davis et al. 1983; Platt 1986; Boyer 1995)

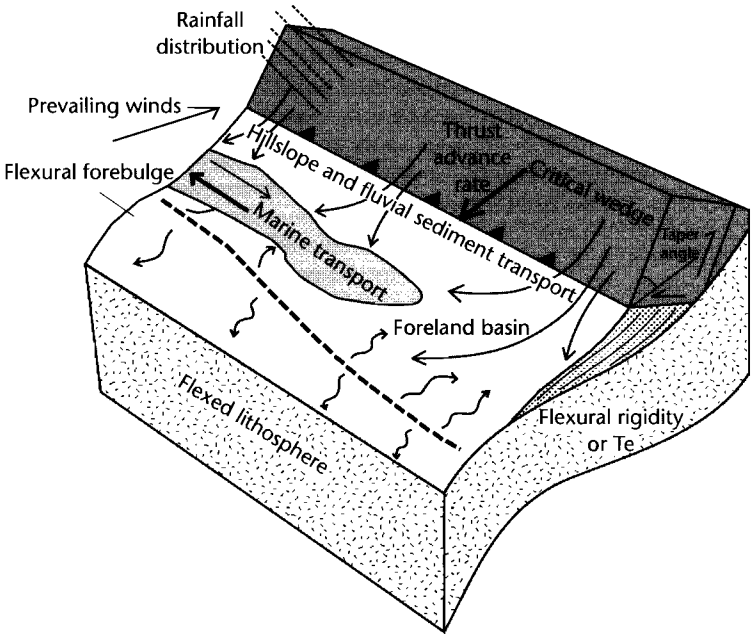

Fig. 4.32 Parameters necessary to describe a diffusive mountain belt system are the advance rate and taper of the orogenic wedge, flexural rigidity of the foreland plate, and sediment transport coefficients. The distinction between relatively local transport on hillslopes and far-field transport in river systems can either be tackled by attributing two different effective diffusivities to these geomorphic subsystems, or by treating the fluvial transport as advective (Johnson and Beaumont 1995).

migrating over an elastic plate that flexurally supports tectonic and sedimentary loads.

From the theory of diffusion, the rate of erosion in the mountain belt or rate of deposition in the basin is given by

$$\frac{\partial h}{\partial t} = K\frac{\partial^2 h}{\partial x^2} \tag{4.32}$$

where K is the effective transport coefficient or diffusivity. Deposition takes place (positive $\partial h/\partial t$) where the topographic curvature ($\partial^2 h/\partial x^2$) is positive. Erosion takes place (negative $\partial h/\partial t$) where topographic curvature ($\partial^2 h/\partial x^2$) is negative. In each increment of time, the thrust wedge moves over the foreland plate, so the total change in distributed load is made of two components

$$\Delta q(x) = \left(\frac{\partial h}{\partial t} + \frac{\partial T}{\partial t}\right)g\rho, \tag{4.33}$$

where the first partial derivative is the topographic change due to erosion or deposition, and the second partial derivative is the change in the tectonic load $T(x)$ in that time step. The new deflection is calculated using flexural isostasy (§2.3.3).

A sensitivity analysis of the four parameters shows that the flexural rigidity of the foreland plate is a first order control on the geometry of the flexed plate and foreland basin, as expected from line-load approximations (§4.2) (Fig. 4.33). However, a greater effect is caused by large variations in the transport coefficient K. For the same flexural rigidity, small transport coefficients ($100\,m^2\,yr^{-1}$) result in narrow, marine basins, whereas high transport coefficients ($800\,m^2\,yr^{-1}$) result in broad, terrestrial basins. The effect of large sediment loads is to force the flexural forebulge far from the orogenic wedge, perhaps even burying it in sediment derived from the orogenic wedge.

Diffusional models have been particularly informative in showing the stratigraphic consequences of changes in the load configuration. For example, a slowing of the advance rate of the orogenic wedge combined with an increase in its surface taper angle, was interpreted by Sinclair et al. (1991) as the cause of distal unconformi-

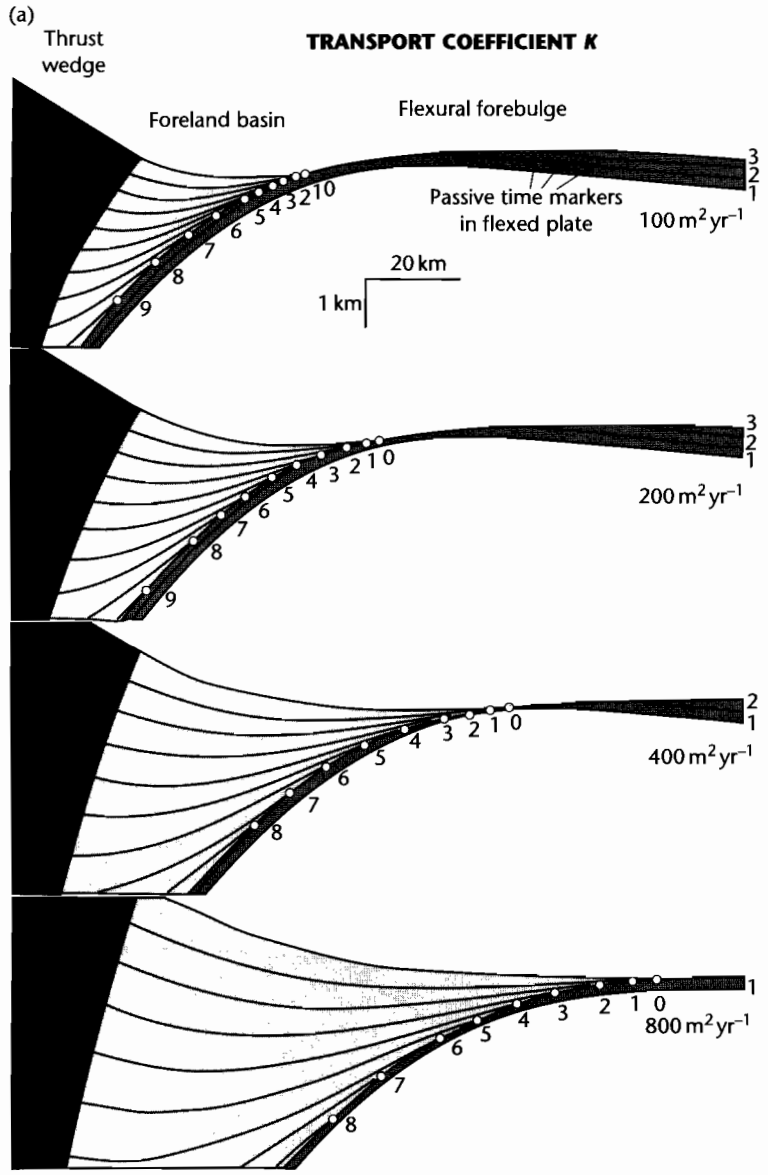

Fig. 4.33 Sensitivity tests of the parameters in Sinclair et al.'s (1991) diffusion model for mountain belt denudation and foreland basin evolution. The reference model involves a transport coefficient $K = 400\,m^2\,yr^{-1}$, slope angle = 1.5°, advance rate = $2.5\,mm\,yr^{-1}$, and equivalent elastic thickness of 20 km. In the sensitivity tests, one parameter is varied while the others are held constant at their reference values. Lines in basin are at equal time steps (chrons). Numbered positions on top of foreland plate are pinch-out (stratigraphic onlap) positions. Lines within foreland plate are passive markers to show extent of erosion of foreland plate in flexural forebulge. (a) Effect of variations in transport coefficient K, showing major impact on basin depth, basin width, and pinch-out migration rate; (b) Effect of variations in slope angle, showing major impact on basin depth, since sediment flux scales on slope; (c) Effect of variations in orogenic advance rate, showing major impact on pinch out migration rate; (d) Effect of variations in equivalent elastic thickness. Marine, underfilled basins are favored by low transport coefficients, low tapers, and fast advance rates, whereas continental overfilled basins are favored by high transport coefficients, high tapers, and slow advance rates, irrespective of flexural rigidity.

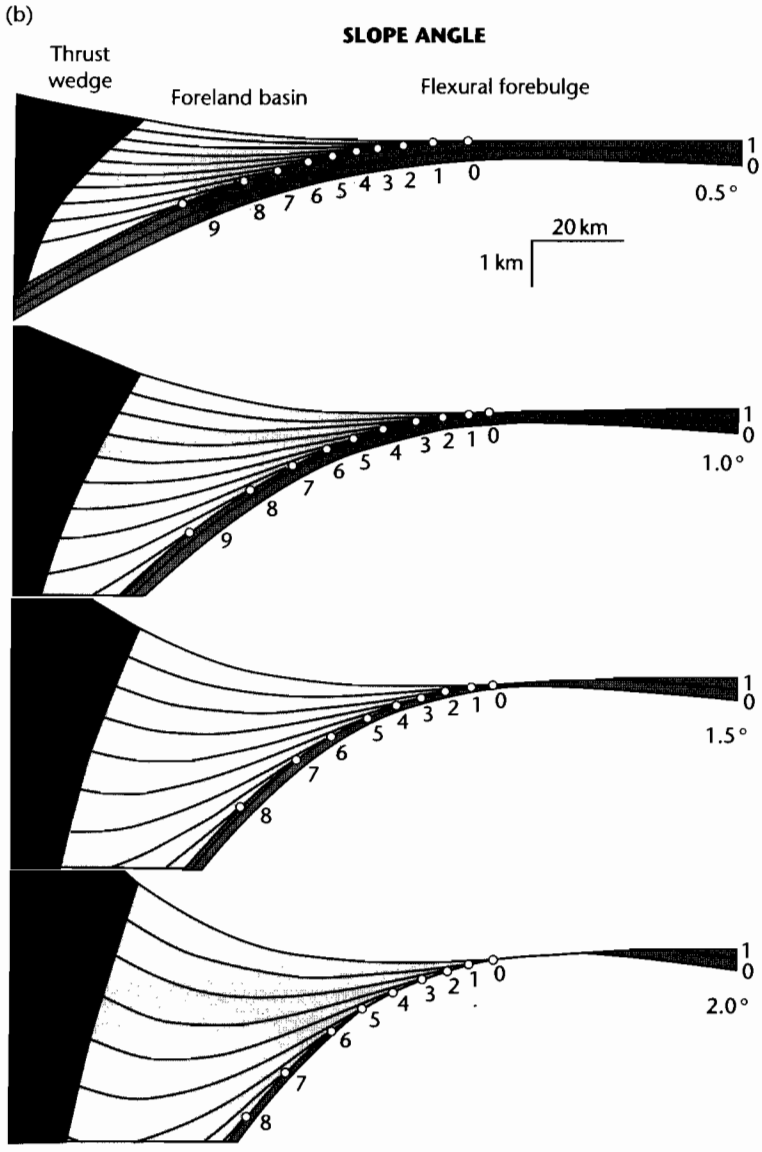

Fig. 4.33 *Continued*

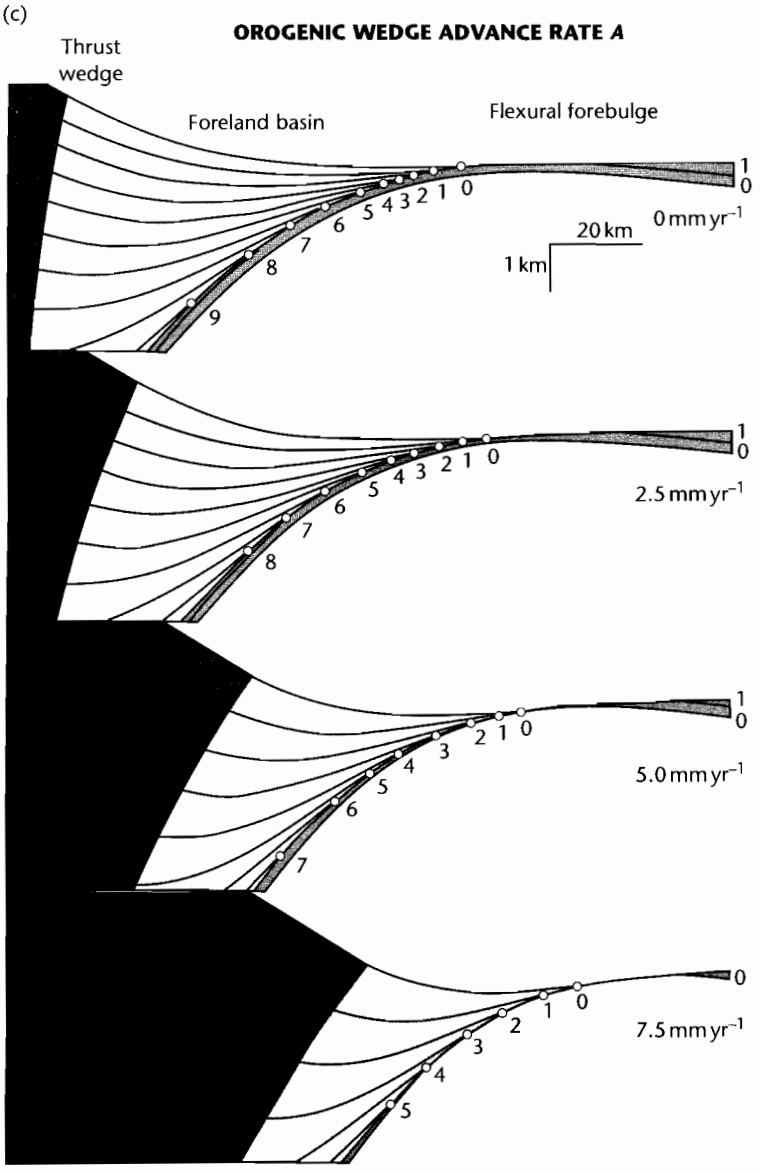

Fig. 4.33 *Continued*

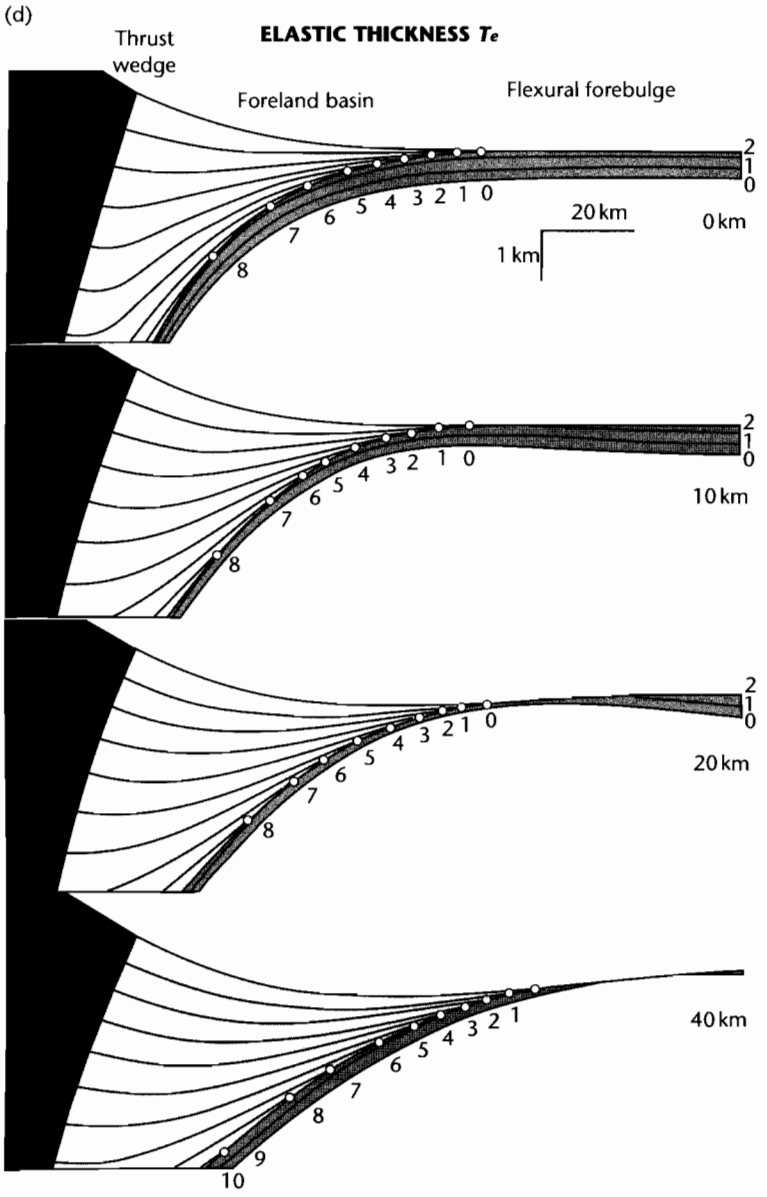

Fig. 4.33 *Continued*

ties in the North Alpine foreland basin of Switzerland, without the need to invoke viscoelastic relaxation of the lithosphere.

The effects of episodic thrusting have specifically been investigated (Flemings and Jordan 1989, 1990) using a model of a mountain belt as a fault-bend fold over a crustal scale ramp (Suppe 1983). Different transport coefficients were used for transport processes in rivers erosively incising the mountain belt and for alluvial rivers in the foreland basin. The change from quiescence to renewed thrusting was accompanied by a trapping of coarse sediment near the thrust front and the movement basinwards of the forebulge. Continued thrusting and sediment delivery to the basin forced the forebulge away from the orogen, causing stratigraphic onlap over an erosional unconformity. Other studies (Heller et al. 1988) suggest that during periods of tectonic activity, coarse clastic sediment wedges are trapped close to the thrust front, whereas during quiescence sediment is spread further from the thrust front, onlapping the basin margin (further discussion in §8.3). These different model results emphasize the importance of the fine detail of the different numerical models. Nevertheless, diffusional models have been helpful in enabling a link to be made between orogenic events and large-scale basin evolution.

4.6.3 Coupled tectonic-erosion dynamic models of bivergent wedges

Although a coupling between mountain belt denudation, exhumation, flexure, and deposition was made in the diffusional models discussed in §4.6.2, the coupling was through the arbitrary choice of an effective transport coefficient. This transport coefficient encapsulates all of the different factors influencing erosion, deposition, and sediment transport. In addition, tectonic fluxes have been crudely approximated (e.g., fault-bend fold over a crustal scale ramp) or left unspecified by use of a critical taper model. More recent models therefore have focused on: (i) a better treatment of the physical aspects of hillslope erosion, channel incision, and far field sediment transport, (ii) an investigation of the spatial variability of sediment routing systems and specifically the distribution of sediment entry points into the basin, and (iii) a coupling of realistic orogenic tectonic fluxes with exhumation patterns.

An early attempt to consider the mountain belt in planform and to incorporate the important geomorphic elements (hillslopes, channels) in the sediment routing system was the study by Koons (1989) of the Southern Alps of New Zealand. However, the channels were fixed and did not interact with the diffusive hillslopes in this early model. Subsequent models have incorporated the dynamics of stream incision, hillslope erosion, and sediment transport (see Chapter 7) on a deforming crustal template. A commonly used example at the orogenic scale is a 2-D plane strain thermomechanical model with a crust of thickness h with a strength profile determined by a brittle Coulomb-type upper layer and a temperature-dependent power-law lower layer (Willett 1992; Willett et al. 1993; Fullsack 1995). Below the crust are two mantle plates – one representing the subducting foreland lithosphere, and the other representing the overriding upper plate. Convergence between the two plates induces a shear force or traction on the base of the crustal layer, driving deformation. We have previously considered this type of model in terms of Argand number and Ampferer number (§4.5.4).

The tectonic development of the orogenic wedge, its isostatic compensation and its erosional unroofing, are clearly crucial to the analysis of foreland basins. On the basis of plane strain numerical models, we can consider the tectonic evolution of a convergent boundary such as the Alps of Europe as following three stages (Fig. 4.34) (Beaumont et al. 1996a):

1 Initially, tectonics are dominated by subduction of the pro-lithosphere due to the negative buoyancy of the downgoing slab (slab–pull effect). Subduction complexes form along a relatively thin shear zone above the subducting oceanic crust. Horizontal propagation of the accretionary prism is likely to be rapid, but the pro-foreland basin is likely to be underfilled with turbiditic "flysch."
2 In an intermediate stage, the subduction–collision transition, the subduction load decreases by the subduction of more buoyant continental lithosphere (or because of slab break-off), causing the pro-lithosphere to flexurally rebound. Parts of the pro-lithosphere detach and form part of a bivergent wedge instead of being subducted. Activity of a retro-shear should begin when the pro-lithosphere is no longer fully subducted during this transition phase.
3 In a final collision stage, when there is a negligible subduction load, well-defined pro- and retro-wedges form. The entire crustal pro-layer is incorporated into a critically tapered orogenic wedge. Denudation of the bivergent wedge should be particularly strong during this phase. Flexural basins (pro- and retro-

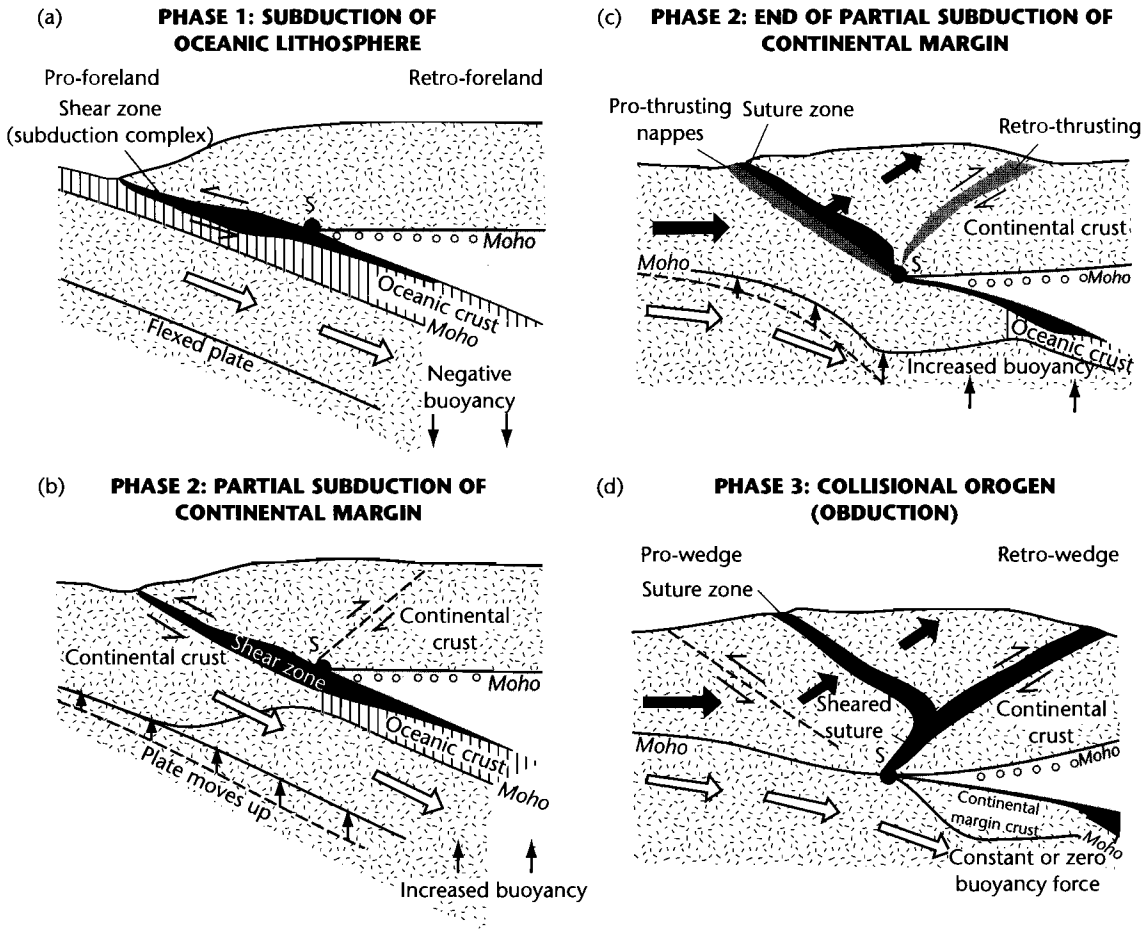

Fig. 4.34 Three-phase evolution of Beaumont et al.'s (1996a) plane strain finite element model from the subduction phase (phase 1) to the collision phase (phase 3). During phase 1 (a), the negative buoyancy of the lower plate is sufficient to fully subduct the entire plate. During phase 2 (b) and (c), the subduction load decreases because of continental lithosphere entering the subduction zone (and/or because of slab break-off). Progressively more of the lower plate detaches and a bivergent wedge begins to form. In phase 3 (d), all of the lower plate detaches to form a pro-wedge and continued propagation of deformation into the upper plate causes a retro-wedge to form. Convergence of pro-lithosphere with respect to stationary retro-lithosphere is shown by the white arrows. Black arrows show main transport direction of material in the pro-crust and wedge. Reproduced courtesy Geological Society of America.

foreland basins) are supplied with large amounts of basins, causing filling and overfilling in the "molasse" phase.

Since the tendency for thickened crust to spread laterally is strongly affected by the gravitational force, denudation of the orogen will hinder lateral tectonic progradation. If the rate of crustal thickening equals the rate of denudation, the orogen should not grow in size. We can refer to this as a *steady-state orogen*. The same idea applies to critically tapered Coulomb wedges (§4.5.2). If the wedge taper is reduced, for example by erosion, the Argand number falls, preventing lateral tectonic progradation. Only after internal deformation of the wedge has restored gravitational forces to a threshold level can the wedge continue to prograde laterally.

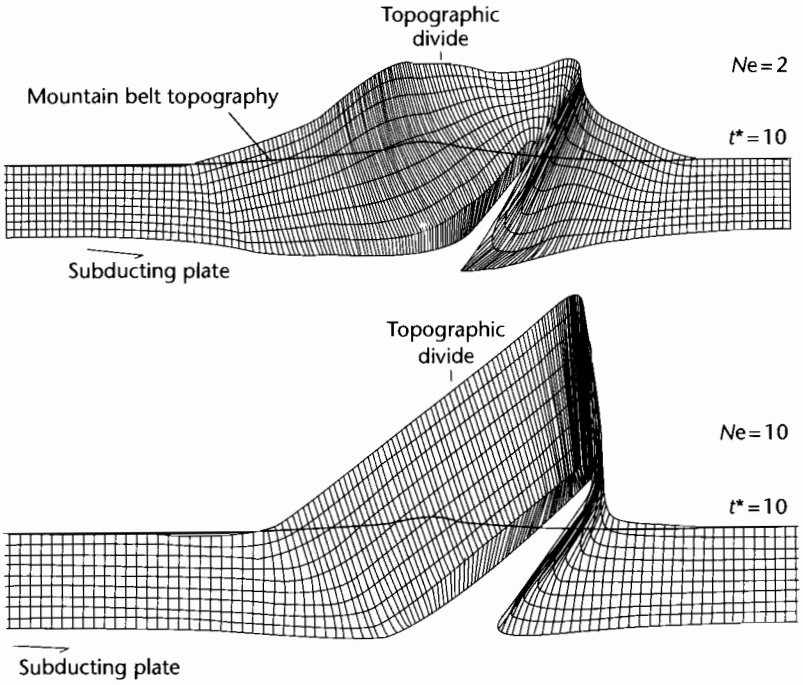

Fig. 4.35 Variations in coupled tectonic–erosion model for $Ne = 2$ and 10 for a dimensionless time of $t = 10$ ($t = tV_p/h$) (after Willett 1999). In both cases, elevation and exhumation have reached steady state. Note the greater amount of erosional removal of rock (exhumation) in the high erosion case. Reproduced courtesy of American Geophysical Union.

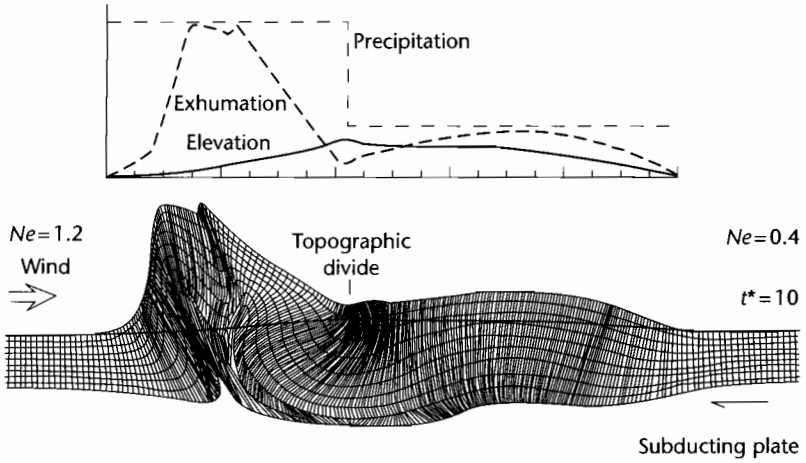

Fig. 4.36 Numcrical model of Willett (1999) with orographic focusing of precipitation such that the pro-wedge has an Erosion number Ne of 0.4 and the retro-wedge an Erosion number of 1.2, which closely reflects the precipitation patterns in the Southern Alps of New Zealand. Reproduced courtesy of American Geophysical Union.

Erosion at the surface can be modeled as either a function of elevation, relief or slope (Schlunegger and Willett 1999) or related to a set of geomorphic and climatic rules (Kooi and Beaumont 1994, 1996; Beaumont et al. 1996b; Willett 1999). As an example of the latter, erosion is commonly modeled through calculation of the rate of river incision, which is taken as proportional to stream power (Chapter 7). The efficiency of erosion versus tectonic uplift can be gauged from a dimensionless number, termed *Erosion number* by Willett (1999)

$$Ne = \frac{kL}{u} \tag{4.34}$$

where u is the rate of tectonic uplift, L is the half-width of the uplifting block of crust, and k is a coefficient proportional to the bedrock incision efficiency and precipitation rate with units time^{-1}. In the coupled tectonic-erosion model, Ne can be expressed in terms of the ratio between the accretion mass fluxes due to convergence (numerator) and the erosional mass flux through the upper surface (denominator), giving

$$Ne^* = \frac{4kL^2}{V_p h} \tag{4.35}$$

The Erosion number strongly controls the topographic profile and the exhumation pattern (Fig. 4.35). If Ne tends to infinity, erosion planes off the topography ruthlessly despite finite rates of tectonic uplift. The Erosion number Ne strongly controls the time taken for a mountain belt to achieve steady state and its maximum elevation. Coupled models therefore now allow specific precipitation patterns, such as wet orographic flanks (high Ne) and dry rain-shadow flanks (low Ne) to be investigated as mechanisms for particular patterns of exhumation and topography (Fig. 4.36).

CHAPTER 5

Effects of mantle dynamics

In Nature's infinite book of secrecy
A little I can read

(WILLIAM SHAKESPEARE, *ANTONY AND CLEOPATRA* (1606))

SUMMARY

Plate tectonics operates in the upper thermal boundary layer of an underlying mantle convection system. Flow within the mantle takes place at different spatial scales, including flows induced by the subduction of cold lithospheric slabs, incubation under continental lids, lower mantle megaplumes, and upper mantle hotspots. This flow and the consequent mass anomalies at depth result in a dynamic topography at the Earth's surface that may be important in basin analysis.

The fact that the mantle is convecting is supported by a number of lines of evidence. Consideration of the Rayleigh number for the upper mantle and lower mantle indicates that convection must be occurring. This slow convective flow is laminar. Numerical experiments demonstrate that simple heating from below produces a symmetrical system of upwellings and downwellings. Numerical models including internal radiogenic heating causes downwellings to be more numerous or vigorous than upwellings, a situation thought to pertain on Earth. Models using highly temperature-dependent viscosity structures in the mantle suggest that large aspect ratio convection cells are stable, such as must underlie the Pacific Plate. Detailed 3-D velocity models of the mantle (*seismic tomography*) also show mass anomalies that must be sustained by flow. These mass anomalies show that the effects of plate tectonics, such as mid-ocean ridges and subducting slabs, can be recognized deep into the Earth's interior.

Measurements of the Earth's gravity field reveal geoid height anomalies. Numerical experiments suggest that an underlying convecting system should produce variations in the height of the geoid over upwelling and downwelling limbs. At long wavelength, the observed geoid of the Earth shows major zones of positive and negative geoid anomaly. Viscous flow models of the mantle suggest that mass excesses in the upper mantle caused by the remnants of cold subducted slabs generate geoid lows, whereas hotspots and mid-ocean ridges are correlated with the presence of hot megaplumes in the lower mantle and are associated with geoid highs.

Dynamic topography is the elevation or depression of the Earth's surface as a result of flow in the mantle. Dynamic topography can be recognized, for example, by a *c.* 1000 km-wide and <500 m-deep depression of the plate surface behind ocean trenches, caused by subduction. The amplitude and wavelength of dynamic topography resulting from subduction is difficult to measure, but viscous flow models suggest that they depend on the age (thermal state) of the subducting plate, the velocity and angle of descent, the flexural rigidity of the plate as well as the viscosity structure of the upper mantle. The initiation of subduction, the flattening of slab dip, the accretion of terranes, and the closure of an ocean basin all have an impact on the dynamic topography, and therefore long wavelength tilting, of the continental surface. A series of subduction events around the edge of the North American Plate during the Phanerozoic may in large part be responsible for the stratigraphic supersequences and their bounding unconformities long recognized on the North American craton.

Numerical viscous flow models suggest that a large continental plate trapped between bounding downwellings may incubate the mantle. Heating of the mantle causes the supercontinent to move off the geoid high towards geoid lows situated over downwellings. If extensional deviatoric stresses are high enough, the supercontinent may fragment, with continental plates dispersing towards geoid lows. The flooding of continental plates

during their drift depends on the ratio between the geoid elevation and dynamic topography, known as *admittance*. Interactive models of mantle convection and supercontinental assembly and dispersal are illustrated by the assembly (*c.* 350 Ma) and break-up (*c.* 200 Ma) of Pangea.

Mantle convection at a smaller spatial scale (*c.* 10^3 km) is suggested by the distribution of hotspots and highspots. Hotspots are regions of elevated heat flows and volcanic activity and are classically developed in the oceans, causing bathymetric swells of 1 km height and <1000 km width above the adjacent seafloor. Highspots can be thought of as nonvolcanic hotspots. Hotspots and highspots are less easy to discern on the continents than in the ocean. The movement of plates with respect to a presumed stationary mantle reference frame produces hotspot tracks – 1000 km-wide zones of uplift and magmatic activity. Some regions of slow subsidence may be effectively coldspot basins. Some hotspots and coldspot basins that appear fixed to the continental plates for prolonged periods of time may reflect a small scale convection system "dragged" by the overlying plate.

5.1 FUNDAMENTALS AND OBSERVATIONS

5.1.1 Introduction: Mantle dynamics and plate tectonics

Although plate tectonics has been highly successful as an explanation of the relative motion of plates and the deformation at their boundaries, there is little integration of mantle dynamics into what is essentially a kinematic theory. For example, volcanic hotspots such as those of Hawaii and Iceland, which are related to the ascent of deeply rooted mantle plumes, do not fit into plate tectonic theory. Within the solar system, the operation of plate tectonics is unique to Earth, but plume volcanism occurs on Mars and Venus as well as on a number of moons. Whereas the surface of Mars appears to be a single plate acting as a "frozen lid," Venus has no "lid" at all and the tectonics is spatially continuous and unstable. On Earth therefore, we have a particular problem in understanding the interaction of internal thermal convection with an upper thermal boundary layer made of a discrete number of plates in relative motion.

The 3-D mapping of seismic velocity variations in the mantle (*seismic tomography*) now provides unprecedented detail on small but systematic density variations that reflect temperature (and/or chemical) heterogeneities. These heterogeneities reveal a picture of deep penetration of cold, subducted lithospheric slabs into the mantle, and of large, hot upwellings that seem to rise from a highly dynamic core–mantle boundary (Fig. 5.1). Subducted slabs of lithosphere both penetrate and pile up at the 670 km discontinuity. The residues of the subducted slabs that penetrate the discontinuity appear to descend to the core–mantle boundary, where they may be reheated for *c.* 10^9 years before being resurrected as a mantle plume. Mantle plumes travel upwards and impinge on the base of the lithosphere, spreading out like a mushroom, and uplifting the overlying plate. Extension of the lithosphere over the plume head may lead to continental splitting, the formation of new spreading centers and further subduction of lithosphere.

Convection systems in the mantle are the engines for the surface tangential motions of plates. Subducting slabs are cold downwellings, and spreading oceanic ridges are upwellings (Davies and Richards 1992), so the lithospheric plates must be regarded as an integral part of the convection system rather than being dragged passively by basal traction *over* the convection system. In other words, plate tectonics is the surface expression of convection.

Plate tectonic theory explains a wide range of geological and geophysical observations in the oceans and at plate boundaries. It has been far less successful in explaining the topography, seismicity, neotectonics, and subsidence history of the continental interiors. This is partly due to the complex rheology of the continental lithosphere, and partly due to the lack of integration of mantle dynamics into a satisfactory explanation of continental deformation and basin development. Stratigraphers have long recognized the supreme importance of vertical movements of the continents in generating the stratigraphic sequences of the world's cratons (Sloss 1963). In particular, the major transgressions of the continents that have taken place through geological time (e.g., Cambrian–Early Ordovician and Late Cretaceous, Bond 1979) cannot be explained purely by a eustatic sea level rise (Bond 1976, 1978) and must involve a major component of widespread subsidence most likely related to mantle processes.

It is increasingly recognized therefore that the near-surface motion of lithospheric plates needs to be understood by reference to the mantle convection system (Anderson 1982). In Chapter 5, we look briefly at the evidence for flow in the mantle, with the specific goal of understanding the significance of this flow for subsidence within continental sedimentary basins. The reader is

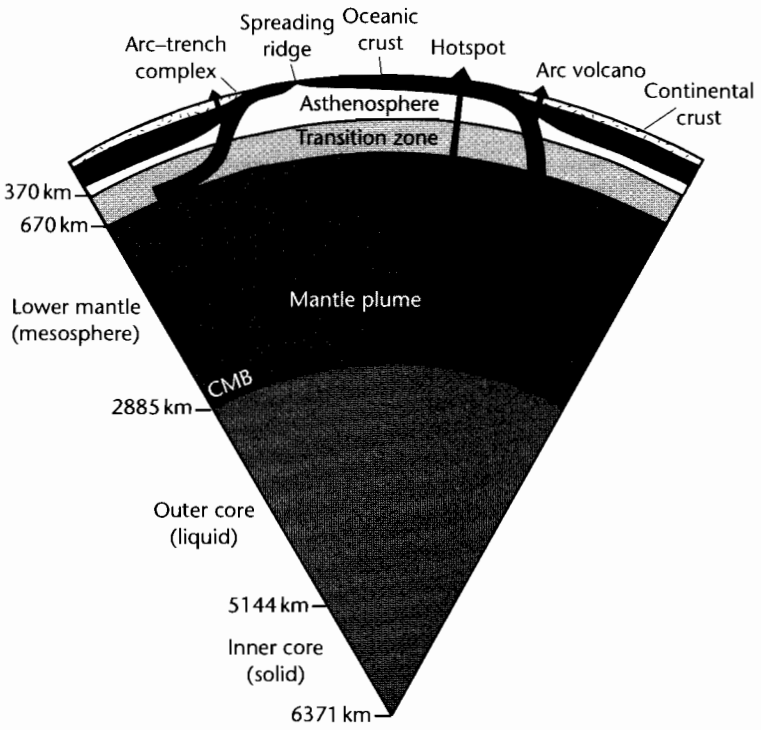

Fig. 5.1 Schematic section through a segment of the Earth showing the subduction of lithospheric slabs which are laid out along the 670 km discontinuity or penetrate to a graveyard above the core–mantle boundary (CMB). A mantle plume is shown rising from the CMB to produce a hotspot in the overlying oceanic plate. Modified from Stern (2002). Reproduced courtesy of American Geophysical Union.

referred to §2.3 for more information on gravity measurements and the geoid. He/she is also referred to §3.7 where the role of mantle plumes in continental extension and melt generation is discussed.

5.1.2 Convection in the mantle

The basic set-up for studying convection involves a thin fluid layer that, because it is heated from below, becomes gravitationally unstable and overturns. Studies of convection allow the conditions necessary for the onset of convection and the expected size of the convecting cells to be predicted. The convection cells have a width that scales on the thickness of the layer (Bercovici et al. 2000).

Accepting that the mantle is convecting in some way, it is possible to estimate whether the flow is laminar or turbulent. This is given by the *Reynolds number Re*

$$\mathrm{Re} = \frac{ud}{v} \tag{5.1}$$

where u is the velocity of the flow, d is the thickness of the layer, and v is the kinematic viscosity. The kinematic viscosity of the mantle is difficult to estimate, since it is dependent on the temperature, but let us take a value of $10^{17}\,\mathrm{m^2\,s^{-1}}$ as in the upper mantle calculations in the boxed text. The flow velocity can be estimated from flow laws for incompressible Newtonian fluids; let us take $u = 10^{-7}\,\mathrm{m\,s^{-1}}$ as an order of magnitude estimate ($1\,\mathrm{m\,yr^{-1}}$ is $3.17 \times 10^{-8}\,\mathrm{m\,s^{-1}}$, so u is about $3\,\mathrm{cm\,yr^{-1}}$ in this calculation). Using equation (5.3), *Re* is *c.* 7×10^{-19}. This is much smaller than the critical *Re* for turbulence, indicating that the convecting flow in the mantle is laminar.

Perhaps the most characteristic feature of simple convection where a constant-viscosity layer is heated from below and cooled at the top is that it is symmetrical, consisting of sinking cold currents with an equal and

BOXED TEXT 5.1: The Onset of Convection

The onset of convection is given by the *Rayleigh number*. It can be derived for different conditions of heating (Fig. 5.2). If we take the simple situation of heating from below, with no internal heating (Fig. 5.2a), and we keep the top and bottom temperatures isothermal, the vigor of convection resulting from a temperature difference between the top and bottom of the layer ΔT depends on the fluid density ρ, coefficient of thermal expansion α_v, viscosity μ, thermal diffusivity κ, gravitational acceleration g, and the layer thickness d. Increases in ρ, α_v, and g facilitate convection by allowing more buoyancy. However, increases in μ and κ impede convection by resisting motion and diffusing heat away faster. Combining these facilitating and impeding properties into a ratio, and introducing d^3 in the denominator to give units of temperature, we have

$$\frac{\mu\kappa}{\rho g \alpha_v d^3} = \frac{[ML^{-1}T^{-1}][L^2T^{-1}]}{[ML^{-3}][LT^{-2}][T^{-1}][L^3]} = [T] \qquad (5.2)$$

Equation (5.2) gives the temperature difference between the top and bottom boundaries that must be reached in order to cause convection. The Rayleigh number is the dimensionless ratio of these temperatures

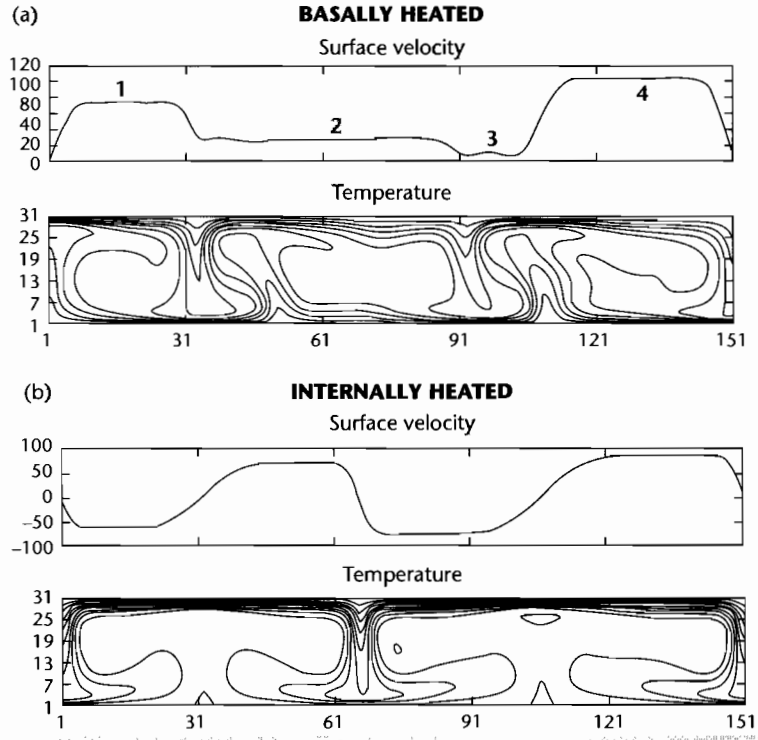

Fig. 5.2 2-D convection in a non-Newtonian power-law fluid at a Rayleigh number of 50,000 for the case of basal heating (a) and internal heating (b). Lower panels show a cross-section of the temperature field in the convecting layer. Upper panels show the horizontal velocity of the strong lithospheric layer. In (a) there are active upwellings and downwellings defining narrow divergent and convergent zones, and the surface lithospheric layer shows marked step changes in horizontal velocity, suggestive of plate formation. In (b) there are broad passive upwellings which cause the divergent zones to have smooth, wide and unplate-like changes in velocity. After Weinstein and Olson (1992) in Bercovici et al. (2000).

$$Ra = \frac{\rho g \alpha_v \Delta T d^3}{\mu \kappa} \quad (5.3)$$

The critical Rayleigh number for the onset of convection is in the region 600–2000, and can be taken as $\equiv 10^3$. For vigorous convection, *Ra* must be of the order of $>10^5$.

The Rayleigh number given above in equation (5.3) applies to the case of isothermal top and bottom boundaries and heating from below. Since Fourier's law gives the basal heat flux Q_m as proportional to the temperature gradient by the thermal conductivity k (eqn 2.29), we can substitute $Q_m d/k$ for ΔT in equation (5.3) giving

$$Ra = \frac{\rho g \alpha_v Q_m d^4}{k \mu \kappa} \quad (5.4)$$

We can also allow for some internal heating from radiogenic decay (Fig. 5.2b). If so, we make use of the equation for the geotherm where there is a basal heat flow Q_m and an internal heat generation A (eqn 2.46). Setting $y = y_c = d$, the temperature difference over the layer thickness d is $(d/k)(Q_m + Ad/2)$, so equation (5.3) becomes

$$Ra = \frac{\rho g \alpha_v \frac{d}{k}\left(Q_m + \frac{A}{2}d\right)d^3}{\mu \kappa} \quad (5.5)$$

which simplifies to

$$Ra = \frac{g \alpha_v d^4 \left(Q_m + \frac{A}{2}d\right)}{k \kappa \nu} \quad (5.6)$$

where α is the volumetric coefficient of thermal expansion, g is gravity, d is the thickness of the fluid layer, Q_m is the heat flow through the lower boundary, A is the internal heat generation, κ is the thermal diffusivity, k is the thermal conductivity, and ν is the kinematic viscosity (μ/ρ). For the upper mantle, let us initially put $A = 0$, $d = 700\,\text{km}$, $\alpha_v = 2 \times 10^{-5}\,°\text{C}^{-1}$, $\kappa = 10^{-6}\,\text{m}^2\text{s}^{-1}$, $\nu = 10^{17}\,\text{m}^2\text{s}^{-1}$, $k = 4\,\text{W m}^{-1}\,°\text{C}^{-1}$, $Q/k = 10^{-3}\,°\text{C}^{-1}\,\text{m}^{-1}$, and $g = 10\,\text{m s}^{-2}$, which gives a Rayleigh number of *c.* 5×10^5, indicating that even without radiogenic heating the upper mantle should be convecting. Substituting $d = 2000\,\text{km}$, $\nu = 10^{16}\,\text{m}^2\text{s}^{-1}$, and $Q/k = 10^{-4}\,°\text{C}^{-1}\,\text{m}^{-1}$ for the lower mantle gives $Ra = 3 \times 10^7$, again indicating that the lower mantle should be convecting. However, allowing an internal heat generation in the upper mantle of $A = 3.6 \times 10^{-8}\,\text{W m}^{-3}$, would raise the Rayleigh number for the upper mantle to *c.* 2×10^6. For the whole mantle, using $d = 2000\,\text{km}$ and $A = 3.6 \times 10^{-8}\,\text{W m}^{-3}$ and otherwise identical values to those in the upper mantle calculation, the Rayleigh number is 3.2×10^9. Despite the simplifications, this indicates that the mantle should be vigorously convecting.

opposite velocity and temperature to rising warm currents. In between the upper and lower thermal boundary layers, where temperature gradients are strong, is a well mixed fluid at the average temperature of the bottom and top boundaries. The Earth's lithospheric plates comprise this upper thermal boundary layer. If the layer convects more vigorously (*Ra* increases), more of the layer will have a homogeneous temperature, the thermal boundary layers will be thinner and the temperature gradients through them will be higher, driving larger heat fluxes through them. Fluid in the gravitationally unstable thermal boundary layers must eventually either rise or sink, producing upwellings or downwellings, which therefore must set up a flow of material in the thermal boundary layer from divergent zones above upwellings to convergent zones at downwellings. The thermal boundary layers must thicken in the direction of motion. For example, hot fluid arriving above an upwelling zone, travels towards a downwelling and cools to the surface as it does so, before becoming gravitationally unstable enough to sink. Simple theory of convection therefore explains many of the essential features of plate motion (§1.3).

The simplest type of convection is 2-D, with counter-rotating cylinders or rolls in the third dimension. The horizontal dimensions of the individual convecting cells in a fluid layer of vertical thickness d heated from below is approximately equal to d. This horizontal dimension is also the length of the horizontal currents in the thermal boundary layers. The length of the horizontal currents is determined by the amount of cooling necessary to induce gravitational instability and downwelling. Simplistically, if the upper mantle above the 670 km discontinuity is convecting in this simple manner, we should expect convection cells to have a lateral dimension of *c.* 700 km, and pairs of downwellings (or upwellings) to be approximately 1400 km apart. At higher *Ra* (*c.* $Ra = 10^5$) in fluids of constant viscosity, a 3-D pattern develops (Busse and Whitehead 1971), which may be bimodal

or spoke-like, with linear upwellings joining at a vertex. Fluids with temperature-dependent viscosity produce 3-D polyhedral patterns of squares, triangles, and hexagons.

5.1.2.1 Effects of internal heating

We saw that internal radiogenic heating affects the Rayleigh number of the mantle. We might therefore expect internal heating to affect the spatial pattern of convection as well as the vigor. The simplest situation of internal heating would be a uniform distribution of heat production with depth, an isothermal upper boundary, and a zero heat flux through the lower boundary. Because of the zero heat flux at the bottom boundary, no active upwellings occur, and instead a diffuse passive upward flow takes place to compensate for the active downwelling of cold material from the upper thermal boundary layer. If the bottom boundary is allowed to conduct a heat flux, and there is an internal heat generation, the upper boundary must conduct outwards both the basal heat as well as the internal heat. Consequently, the upper thermal boundary layer develops a greater temperature drop than the basal boundary. This causes the upper boundary to develop more numerous or more vigorous downwellings than upwellings rising from the lower boundary. Internal heating therefore breaks down the symmetry between upwellings and downwellings. Since the Earth is known to have very significant internal sources of heat relative to the basal heat flow from the core, we should expect downwellings of an upper thermal boundary layer to dominate the pattern of convection, and upwellings (plumes) should be relatively weaker (Bercovici et al. 2000). This is precisely the situation seen at the Earth's surface.

5.1.2.2 Effects of a temperature-dependent viscosity

The viscosity of mantle materials obeys a temperature-dependent Arrhenius-type law (eqn 9.43). Since the absolute temperature occurs in the denominator of the Arrhenius exponent, there are very large viscosity variations at lower temperatures. This is why the viscosity variation in the upper mantle may be extreme, from perhaps 10^{21} Pa s in its lower part to 10^{18} Pa s in the asthenosphere and 10^{25} Pa s in the lithosphere, representing a variation of viscosity of seven orders of magnitude in a depth range of just 200 km. This makes the lithosphere much stronger and potentially less mobile than the rest of the mantle. This in turn forces the underlying mantle to heat up, increasing the temperature contrast between the hot interior and the cold upper boundary. Since material in the upper thermal boundary layer must cool a great deal to become gravitationally unstable and sink relative to its cold, immobile surroundings, the horizontal extent of the convection cell may become elongated, as demonstrated in both laboratory and numerical experiments (Ratcliff et al. 1997). This would explain the very large lateral distance of the spreading ridge to the subducting margin of the Pacific Plate. Large aspect ratio (long wavelength) convection cells have also been imaged by seismic tomography (Su and Dziewonski 1992). With a stronger viscosity-temperature dependence, convection experiments show that the cold upper thermal boundary layer may form a stagnant, rigid lid over a convecting interior, as is believed occurs in the planet Mars.

Convection theory therefore goes some way towards explaining the occurrences of divergent and convergent boundaries in the lithosphere together with the long aspect ratio of plates required. Convection theory also predicts that there should be topographic variations at the surface due to upwellings (high topography) and downwellings (low topography). This topographic signal needs to be separated from the topographic effects of isostasy, caused by density and thickness variations in the lithosphere. The topography remaining after the removal of isostatic effects from the observed topography is referred to as *dynamic topography* (§5.2).

5.1.3 Seismic tomography

Very detailed velocity models of the mantle can be constructed using *seismic tomography*. Seismic tomography is a technique using many measurements of seismic wave arrivals at a network of recording stations to construct a best-fitting 3-D model of the **S** wave velocity structure of the upper mantle or the **P** wave velocity structure of the lower mantle (Dziewonski and Woodhouse 1987; Su et al. 1994; Kárason and van der Hilst 2000). By computing slices at different depth, it is possible to see how the velocity structure varies as a function of depth within the mantle. The velocity structure most likely reflects density differences, which in turn reflect temperature differences. Near the surface ($y = 50$ km), the velocity structure is dominated by the presence of the continental and oceanic plates, the continental shields being fast and the mid-ocean ridges being slow. The effects of the overlying plates are lost beneath a certain depth in the mantle, but

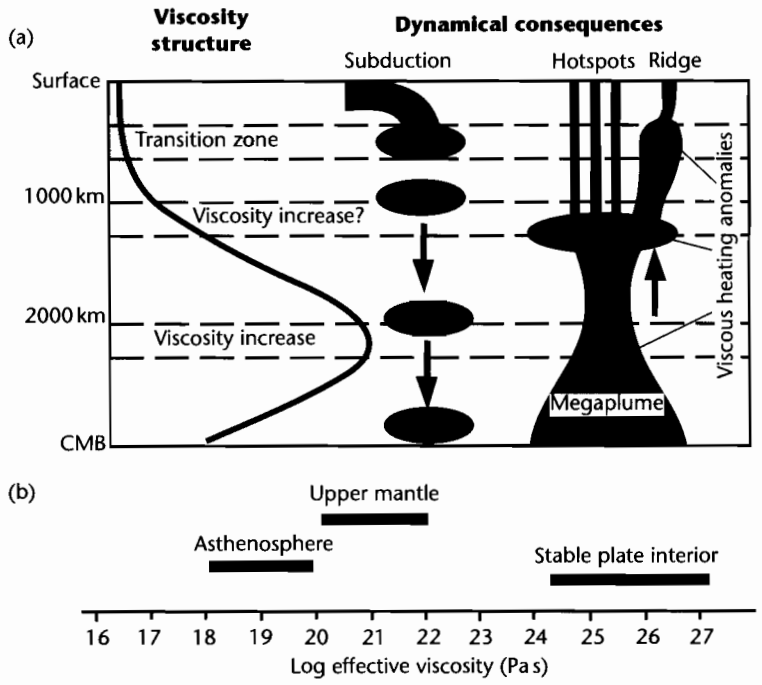

Fig. 5.3 (a) Schematic diagram showing the subduction of cold slabs and the development of megaplumes resulting in mid-ocean ridges and hotspots at the surface, based on seismic tomography of the mantle (adapted from Cadek et al. 1995); (b) Estimates of effective viscosities for stable plate interiors, upper mantle, and asthenosphere. Reproduced courtesy of Elsevier.

this depth is surprisingly large. A distinctive "slow" seismic structure can be related to overlying oceanic ridge systems down to at least 1000 km (Su et al. 1994; Cadek et al. 1995). The remnants of old lithospheric slabs have also been detected from their effect on seismic velocities down to more than 1000 km (Wen and Anderson 1995). The correlation with plate tectonics is lost at 1500–1700 km, but at about 2000 km the surface tectonic pattern can once again be weakly recognized from seismic tomography. In this region of the lower mantle, major mantle plumes and remnants of old lithosphere can be detected from seismic heterogeneities. This suggests that plumes originate close to the core–mantle boundary. It also suggests that this region is a graveyard for deeply subducted lithospheric remnants. Two "megaplume" structures can be detected in the lower mantle below 2000 km. These major upwellings in the lower mantle are correlated with an abundance of hotspots on the Earth's surface. The presence of lower mantle megaplumes, hotspots, mid-ocean ridges, subduction zones, and remnant lithospheric slabs have been explained as the dynamic consequences of a mantle with a strong viscosity stratification (Fig. 5.3).

5.1.4 The geoid

Measurements of the Earth's gravity field also provide much information about the dynamics of the mantle. Numerical simulations of convection in the upper mantle (McKenzie et al. 1980) show that upwellings and downwellings should be accompanied by variations in the sea surface (amplitude of up to 10 m) and in the gravity anomaly (amplitude of up to 20 mgal) (Fig. 5.4). The geoid is the gravitational equipotential surface around the Earth and has the form of an oblate spheroid (§2.3.1). Departures from the reference geoid due to the nonuniform distribution of mass within the Earth are called *geoid height anomalies*. Upwellings have positive gravity anomalies and an elevated sea surface (positive geoid

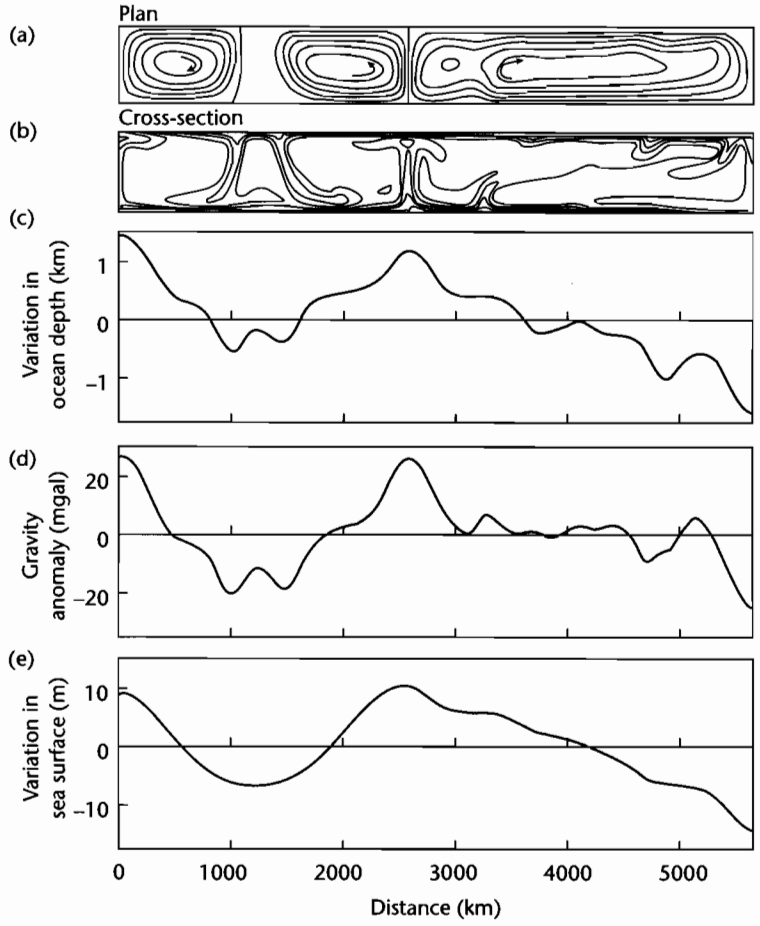

Fig. 5.4 Computer modeling of convection in an upper mantle with constant viscosity heated from below. (a) and (b) temperature field contoured at 100 °C intervals, showing three upwellings and two downwellings; (c) Variation in depth of the ocean floor; (d) Variation in the gravity anomaly and (e) Variation in the height of the sea surface (geoid height anomaly) resulting from the convection pattern in (a) and (b). From McKenzie et al. (1980). Reproduced courtesy of Macmillan Journals.

height anomaly), whereas the reverse is true of the downwellings. This is at first contradictory. We should expect a density excess at depth to cause a geoid high and a positive free-air anomaly, and a density deficit should produce a geoid low and a negative free-air anomaly. However, the free surface is deflected upwards over the rising limbs of the convection cells, and downwards over the descending limbs. This outweighs the effects of the density differences. The net result is that rising limbs are associated with geoid highs and positive free-air anomalies.

A global map of the geoid anomaly (Lemoine et al. 1998) shows maximum geoid anomalies of approximately 100 m, with highs in the southwestern Pacific (+80 m) and northern Atlantic (+60 m), and lows in the Indian Ocean (−100 m), Antarctica and Southern Ocean (−60 m), and the western Atlantic Ocean and adjoining American continent (−40 m) (Fig. 2.24). Although some of the geoid pattern is related to plate tectonic processes such as subduction (see below), many of the geoid height anomaly features cannot be explained in this way and reflect deeper processes in the mantle.

It was recognized at an early stage (e.g., Runcorn 1967) that zones of plate convergence are generally associated with highs in the observed long wavelength geoid. For example, the major subduction zones of the Earth all have geoid highs (Chase 1979). The long wavelength

(degree[1] <10) geoid anomalies are broadly comparable to those expected from the excess density of seismically active, cold subducted slabs. However, the geoid anomaly depends not only on the "driving" density contrasts at depth, but also on the viscosity structure of the mantle. This is because the density contrasts, such as due to chemical layering, set up flows causing a deformation of the boundaries of any density contrast, the amplitude of which depends on the viscosity structure. Incorporating dynamic effects, the presence of high-density material in the upper mantle (such as due to subducted lithosphere) should lead to long wavelength geoid highs. But the presence of dense material in the lowermost mantle should lead to long wavelength geoid lows. Consequently, long wavelength geoid highs can be associated with high-density material (old slabs) in the upper mantle and low-density material (megaplumes) in the lower mantle. Hager (1984) found that the geoid anomalies (at degree <10) associated with subduction could best be explained by a dynamic model in which the density effects of subducting slabs penetrated deep into the lower mantle (through the 670 km discontinuity) and in which the viscosity contrast between upper and lower mantle was of the order of 50–100.

Subtracting the estimated effects of subduction (the so-called "slab geoid") from the observed geoid reveals the *residual geoid* (Crough and Jurdy 1980; Hager 1984) (Fig. 5.5). It is noticeable that there is a residual geoid high along a nearly continuous E–W band, with a maximum in the Pacific Ocean and a secondary peak over Africa. This pattern may reflect megaplume activity in the lower mantle. The correlation of residual geoid highs with the location of hotspots supports this view.

In summary, the pattern of geoid anomalies is highly diagnostic of the processes of slab subduction and mantle convection. The challenge for us is how to make the connection between deep sublithospheric processes and basin development on the continents.

5.2 DYNAMIC TOPOGRAPHY

5.2.1 Introduction

The term *dynamic topography* is defined as "the vertical displacement of the Earth's surface generated in response to *flow* within the mantle" (Richards and Hager 1984). It is therefore distinct from *isostatic topography* generated by near-surface density contrasts such as crustal thickness changes.

When a viscous fluid is disturbed by the presence of a parcel of material with positive buoyancy, viscous stresses are set up that cause the free surface to move upward. The response time of the mantle to a disturbance is dependent on its viscosity (estimated from glacial rebound studies, see §2.2.7) and the wavelength of the parcel of positive buoyancy (Zhong et al. 1996). For mantle flow related to subduction (Fig. 5.6), with a wavelength of $1–3 \times 10^3$ km (Gurnis 1992, 1993; Burgess and Gurnis 1995) the time scale is 10^4 yr, and for larger wavelengths of anomaly ($>5 \times 10^3$ km), such as expected under insulating supercontinental assemblies (Anderson 1982; Gurnis 1988), the response time is $<10^5$ yr (Gurnis et al. 1996). The mantle can therefore be considered as responding effectively instantaneously to the disturbance by a positive buoyancy parcel.

The dynamic topography associated with the long-wavelength heterogeneities identified by seismic tomography should theoretically be large (>1000 m, Hager and Clayton 1989) in order to explain the undulations in the geoid. However, dynamic topography of this scale has not been detected (Le Stunff and Ricard 1995). A number of studies suggest that the global scale variations in dynamic topography, corrected for effects within the lithosphere are 300–500 m (e.g., Cazenave et al. 1989). However, variation in the degree-2 geoid is about 50 m (Hager et al. 1985). The ratio of geoid to dynamic topography is termed *admittance*. Although a continent may be located over a geoid high, which therefore has elevated water levels in the ocean, the greater dynamic topography in this region may cause subaerial emergence rather than flooding (Fig. 5.7). The admittance is therefore important in studying continental flooding histories (Gurnis 1990). For low admittance, flooding takes place preferentially over geoid lows. At high values of admittance, the continent may be flooded preferentially over a geoid high. The flooding history of the North American continent during the Phanerozoic (maximum of 30% of the continental surface) (Bond 1979) indicates that since the geoid should lie within the range 0–100 m, the amplitude of dynamic topography must be up to 150 ± 50 m.

5.2.2 Dynamic topography associated with subducting slabs

If dynamic topography results from thermal effects of flow in the mantle, we should be able to recognize

1 Wavelength is normally expressed in terms of spherical harmonic degree l. For degree l, there are l wavelengths in the circumference of the Earth. At degree 2, there are just two hemispherical highs and lows.

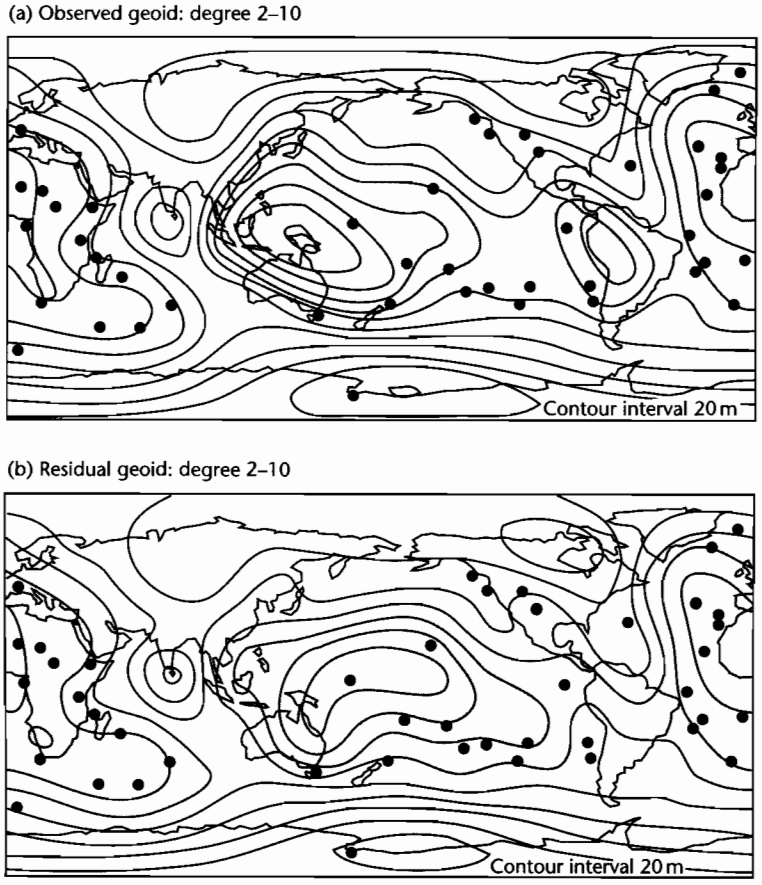

Fig. 5.5 Observed (a) and residual (b) long wavelength geoid at degree 2–10 (Lerch et al. 1983; Hager 1984), contoured at 20 m intervals. Geoid highs are shaded. The residual geoid is obtained by subtracting a dynamically consistent slab geoid from the observed geoid. The distribution of surface hotspots, sites of intraplate volcanism, and anomalous plate volcanism (black dots) shows a correlation with geoid highs. Reproduced courtesy of American Geophysical Union.

dynamic topography behind ocean trenches where cold lithospheric slabs disturb the mantle temperature field (Parsons and Daly 1983; Mitrovica and Jarvis 1985; Gurnis 1992) (Fig. 5.8). Although the amplitude of dynamic topography behind subduction zones is controversial, the wavelength is thought to extend 1000–2000 km from the ocean trench into the continental plate. Consequently, dynamic topography may be recognized as a realm of subsidence extending far beyond the location of retroarc foreland basins (Mitrovica et al. 1989; Catuneanu et al. 1997; Burgess and Moresi 1999) (Fig. 5.6).

Dynamic topography depressions of approximately 500 m are predicted by geoid models over subducting slabs (Hager and Clayton 1989). However, the measurement of dynamic topography behind trenches is problematic, since the dynamic topography must be separated from other forms of subsidence. One approach is to compare such regions with areas unaffected by slab-related dynamic topography. This can be done by a comparison of the distribution of topography (*hypsometry*) behind ocean trenches compared with a world average (Gurnis 1993). This suggests that regions within 1000 km of ocean trenches are depressed by 400–500 m in the

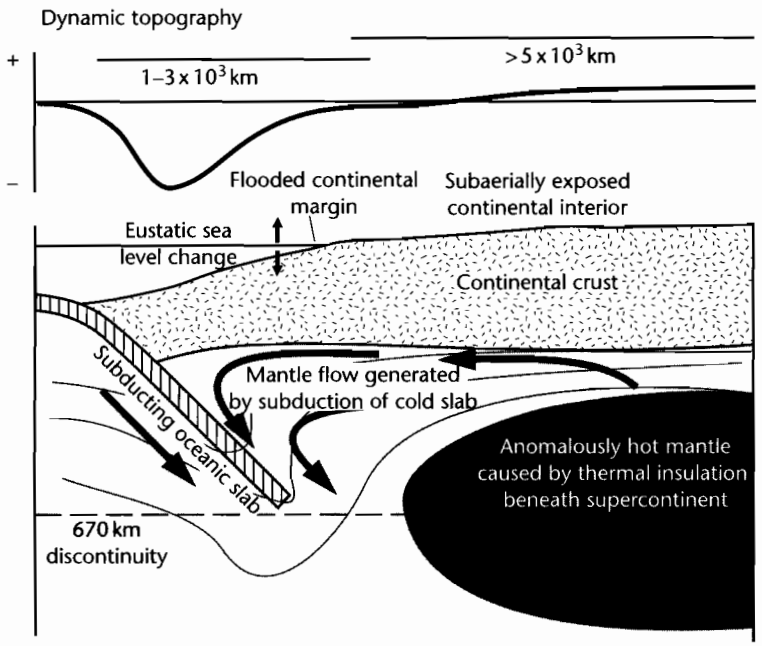

Fig. 5.6 Schematic diagram to show generation of dynamic topography from subduction of a cold oceanic slab (wavelength 1–3 $\times 10^3$ km) and from mantle insulation beneath a supercontinent (wavelength >5 $\times 10^3$ km) (after Burgess et al. 1997). Reproduced courtesy of Geological Society of America.

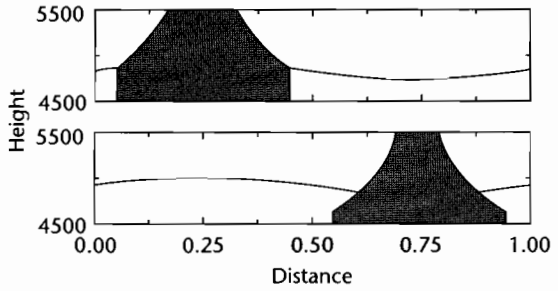

Fig. 5.7 Topography of continents and elevation of sea surface, showing degree of continental flooding when the continent is positioned over a geoid high (top), and geoid low (bottom). Admittance is 0.5, maximum geoid is 100 m. The topography of the continent is the result of isostasy, dynamic topography, and sea water loading. The continent experiences a greater amount of flooding when it is positioned over a geoid low. After Gurnis (1990). Reproduced courtesy of Macmillan Journals.

western Pacific (Gurnis 1993). A second approach is to remove the isostatic effects of lithospheric thickness changes and thermal subsidence. A study of backarc regions of the southwestern Pacific (Wheeler and White 2000) indicates a maximum of 300 m of negative long wavelength (*c.* 10^3 km) dynamic topography (Fig. 5.8).

Since there must be major uncertainties in the estimation of dynamic topography behind ancient subduction zones, a first approach to the modeling of dynamic topography in basin analysis is to use an expression for the geometric form of the dynamic topography by assuming that it is made of two components (Gurnis 1992; Coakley and Gurnis 1995; Burgess and Gurnis 1995): (i) an exponential component with an exponent λ and maximum deflection f_m, and (ii) a linear tilt with a maximum gradient α in m km^{-1} and a maximum distance from the trench at which tilting occurs η. Combining these components gives

$$f(x) = f_m(e^{-x/\lambda}) + \alpha(\eta - x) \tag{5.7}$$

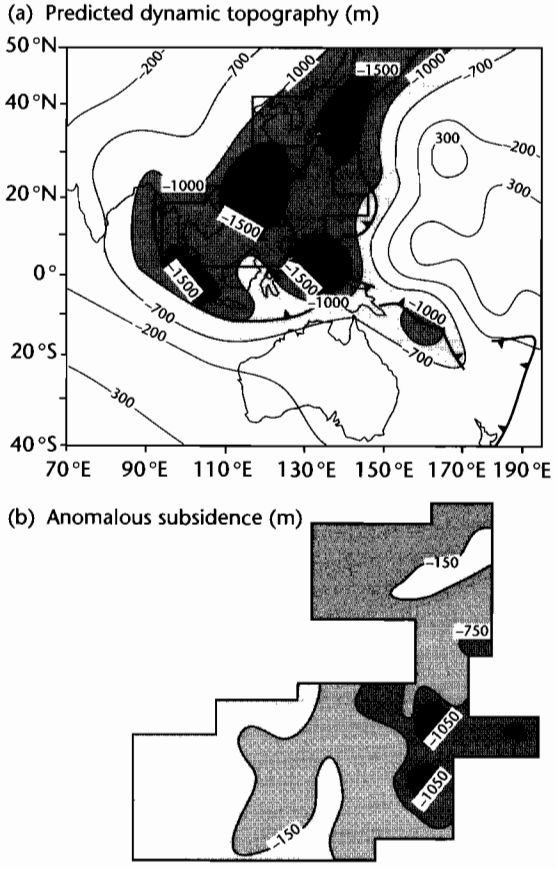

Fig. 5.8 (a) Predicted dynamic topography in Southeast Asia (Lithgow-Bertolloni and Gurnis 1997) using a history of subduction over the past 180 Myr and (b) the "anomalous" subsidence after removal of isostatic effects related to basin formation by Wheeler and White (2000), showing that the observed dynamic topography is far less than that predicted by slab models. Reproduced courtesy of Geological Society of America.

where x is the horizontal orthogonal distance from the trench.

With equation (5.7) we are able to calculate the dynamic topography as a function of distance from the trench axis. Let us initially take the following parameter values: $\lambda = 200\,\text{km}$, $f_m = 2000\,\text{m}$, $\alpha = 0.5\,\text{m km}^{-1}$, $\eta = 2000\,\text{km}$. If we superimpose on this distribution of dynamic topography $f(x)$ a realistic deflection due to flexure in the retroarc region $w(x)$, it is apparent that the dynamic topography is sufficient to exceed the effects of flexural forebulge uplift. Consequently, the backbulge and flexural forebulge regions are zones of (transient) subsidence (Fig. 5.9a), as envisaged by DeCelles and Giles (1996). The parameter values used are similar to those used to model the Phanerozoic evolution of the North American craton (Burgess and Gurnis 1995). If, however, we take parameter values that more closely reflect recent estimates of the amplitude of dynamic topography behind trenches ($\lambda = 200\,\text{km}$, $f_m = 500\,\text{m}$, $\alpha = 0.2\,\text{m km}^{-1}$, $\eta = 2000\,\text{km}$), the dynamic topography is insufficient to exceed the magnitude of forebulge uplift. Consequently, the flexural forebulge remains an erosional zone in the retroarc region (Fig. 5.9b). If we reduce the maximum distance of tilt to 1000 km, which might result from a steepening of slab dip (see below), the dynamic topography reduces to such low values that the backbulge region is most likely nondepositional while the forebulge is erosional (Fig. 5.9c). Clearly, the amplitude and wavelength of dynamic topography is extremely important to the preservation of forebulge and backbulge stratigraphy (see also Burgess and Moresi 1999).

Mitrovica et al. (1989) suggested that the horizontal distance into the upper plate affected by dynamic topography is controlled primarily by the *dip* of the subducting plate. The effects of variations in flexural rigidity of the continental plate and of variations in the initial temperature of the slab were thought to be relatively small (Fig. 5.10). Shallow subduction angles of <45° are required to produce deflections of the continental plate

Fig. 5.9 Combination of flexural subsidence and dynamic topography behind subduction zones. In all cases, the flexural subsidence is that due to a line load at $x = 300\,\text{km}$ on a continuous plate with flexural rigidity $5 \times 10^{23}\,\text{Nm}$ with a maximum deflection w_0 of 10 km. $\Delta\rho$ in the flexural parameter is $1300\,\text{kg m}^{-3}$. (a) Dynamic topography calculated using $f_m = 2000\,\text{m}$, $\lambda = 200\,\text{km}$, $\alpha = 0.5$, and $\eta = 2000\,\text{km}$. The dynamic subsidence is large enough to overwhelm flexural uplift in the flexural forebulge region; (b) Dynamic topography calculated using $f_m = 500\,\text{m}$, $\lambda = 200\,\text{km}$, $\alpha = 0.2$, and $\eta = 2000\,\text{km}$. Dynamic subsidence is sufficient to cause extensive backbulge deposition, but the flexural forebulge is erosional; (c) Dynamic topography calculated using $f_m = 500\,\text{m}$, $\lambda = 200\,\text{km}$, $\alpha = 0.2$, and $\eta = 1000\,\text{km}$. Dynamic subsidence is insufficient to offset the effects of flexural forebulge uplift and the backbulge region experiences such limited subsidence that it is likely to be nondepositional.

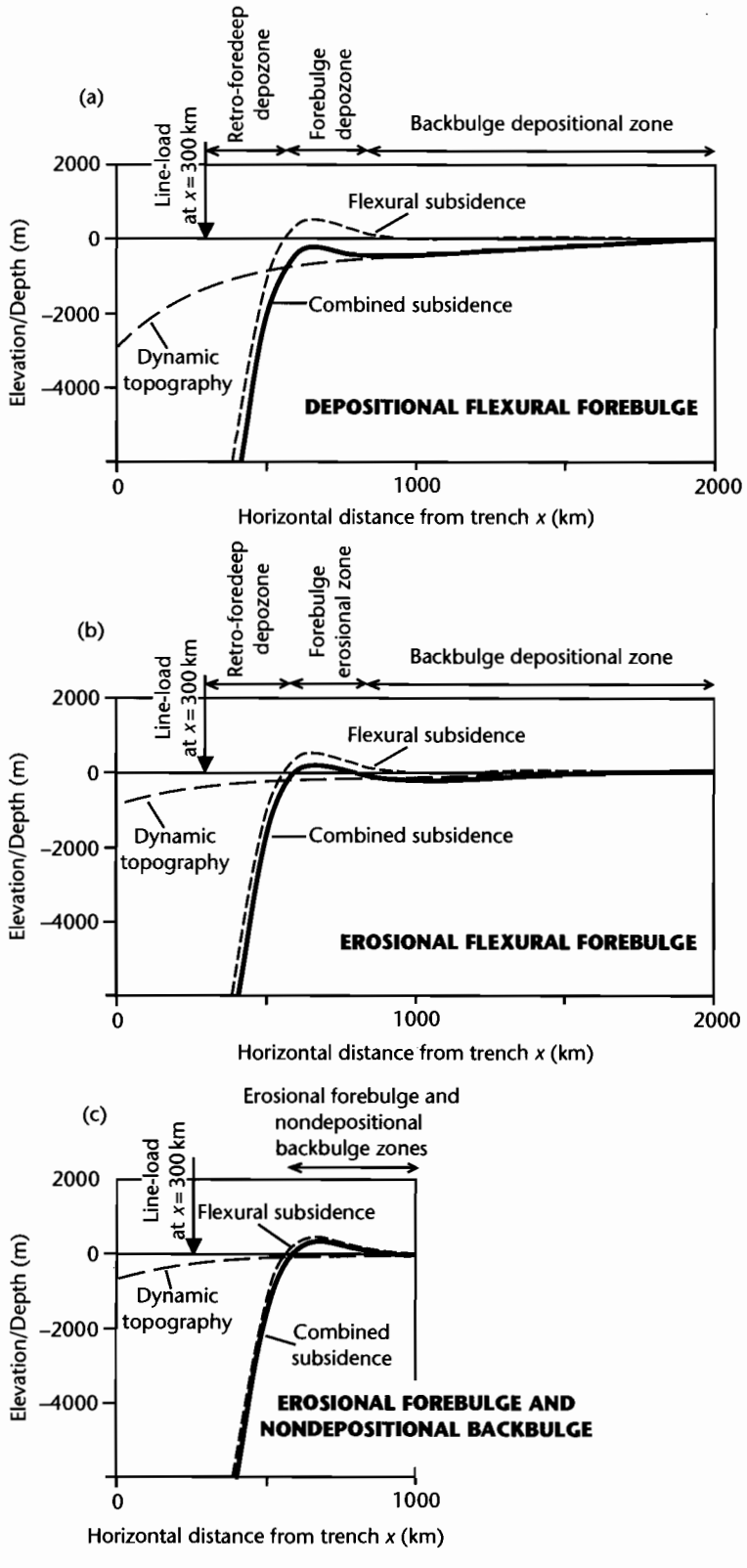
(a)
Retro-foredeep depozone
Forebulge depozone
Backbulge depositional zone
Line-load at x = 300 km
Flexural subsidence
Combined subsidence
Dynamic topography
DEPOSITIONAL FLEXURAL FOREBULGE
Elevation/Depth (m)
2000
0
-2000
-4000
0
1000
2000
Horizontal distance from trench x (km)
(b)
Retro-foredeep depozone
Forebulge erosional zone
Backbulge depositional zone
Line-load at x = 300 km
Flexural subsidence
Dynamic topography
Combined subsidence
EROSIONAL FLEXURAL FOREBULGE
Elevation/Depth (m)
2000
0
-2000
-4000
0
1000
2000
Horizontal distance from trench x (km)
(c)
Erosional forebulge and nondepositional backbulge zones
Line-load at x = 300 km
Flexural subsidence
Dynamic topography
Combined subsidence
EROSIONAL FOREBULGE AND NONDEPOSITIONAL BACKBULGE
Elevation/Depth (m)
2000
0
-2000
-4000
0
1000
Horizontal distance from trench x (km)

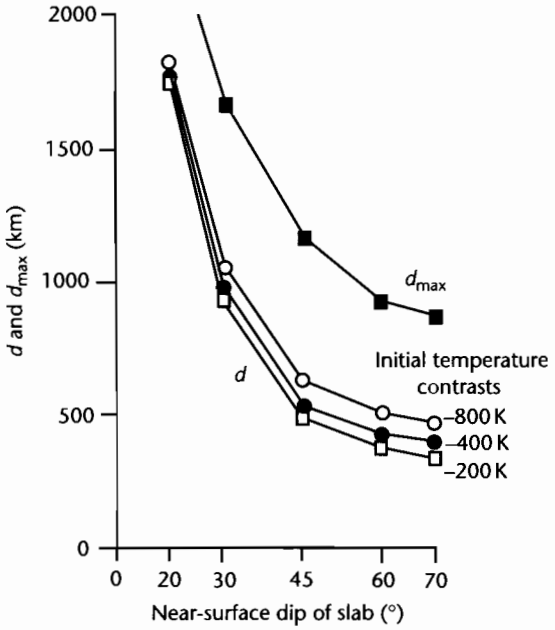

Fig. 5.10 Plot of the horizontal distance between the maximum dynamic topography and the point of zero deflection (d) versus the near-surface dip of the slab, using a model of the detachment (subduction) of blocks from the oceanic lithosphere (Freund et al. 1980) with initial temperature contrasts with the mantle ΔT of −200 K, −400 K, and −800 K. Flexural rigidity D is 5×10^{23} Nm. Also shown is the distance from the maximum dynamic topography to the point of maximum uplift d_{max}. Initial block temperature has little effect on d, whereas both d and d_{max} are strongly affected by changes in slab dip. After Mitrovica et al. (1989). Reproduced courtesy of American Geophysical Union.

>500 km from the ocean trench for a range of initial slab temperatures relative to the mantle of −200 K to −800 K. These initial temperature contrasts most likely reflect the age of the oceanic plate at the point of subduction. The vertical amount of dynamic topography, however, is determined by the temperature contrast between the slab and the surrounding mantle, the flexural rigidity of the lithosphere, as well as the slab dip (Mitrovica et al. 1989). On cessation of subduction, any transient dynamic topography should be removed, the time scale of the uplift depending only on the initial temperature contrast between the slab and the mantle (Fig. 5.11). 25 Myr is a typical recovery time for 95% of the uplift. There are therefore essentially two distinct modes of subduction, shallow and steep, that determine the dynamic subsidence of the continental interior behind ocean–continent boundaries, with secondary effects from plate age, rate of subduction, flexural rigidity, and viscosity structure of the upper mantle.

Since the dynamic topography in numerical models has a width dependent on the dip of the cold slab (Mitrovica et al. 1989) and an amplitude dependent on a number of parameters including the age (or temperature deficit) of the plate (Gurnis 1992), the evolution of dynamic topography through time may be complex (Figs 5.11, 5.12). This is because the age of the oceanic slab, the velocity of plate subduction, and the angle of subduction change through time. The dips of slabs soon after the initiation of subsidence are believed to be close to vertical (Gurnis and Hager 1988). Over a period of perhaps 50 Myr, the slab shallows as a horizontal pressure gradient in the upper mantle develops (Stevenson and Turner 1977). The two most steeply dipping subduction zones in the Pacific, the Mariana and Kermadec, corresponding to young oceanic lithosphere, are both nearly vertical, whereas the oldest slab, Japan, has a dip of just 45°. Shallow slab dips may also be due to the attempted subduction of relatively buoyant mid-ocean ridges and plateaus (e.g., Peru Trench).

One scenario is the subduction of progressively younger and more buoyant lithosphere as an ocean basin closes (Fig. 5.12). The model results illustrate three phases in the evolution of dynamic topography:

1 *0–10 Myr, the initiation of subduction*: a 160 Ma oceanic plate is subducted at a dip of 80°, producing a region of subsidence in the upper plate over 200 km across with a 25 m-high "forebulge" centered at 400 km from the trench. This is a dynamic topography forebulge caused by an upwelling related to the viscous mantle flow set up by subduction and should not be confused with a flexural forebulge;

2 *10–60 Myr, rapid shallowing of slab dip*: the development of horizontal pressure gradients in the upper mantle cause the slab dip to decrease (approaching 45°), which causes dynamic subsidence to extend farther into the continental interior. The dynamic topography bulge is also pushed cratonwards;

3 *60–c. 200 Ma, closure of ocean basin*: the subduction of progressively younger, more buoyant lithosphere causes long wavelength uplift of the continental interior. In the model run where the age of the subducting slab decreases

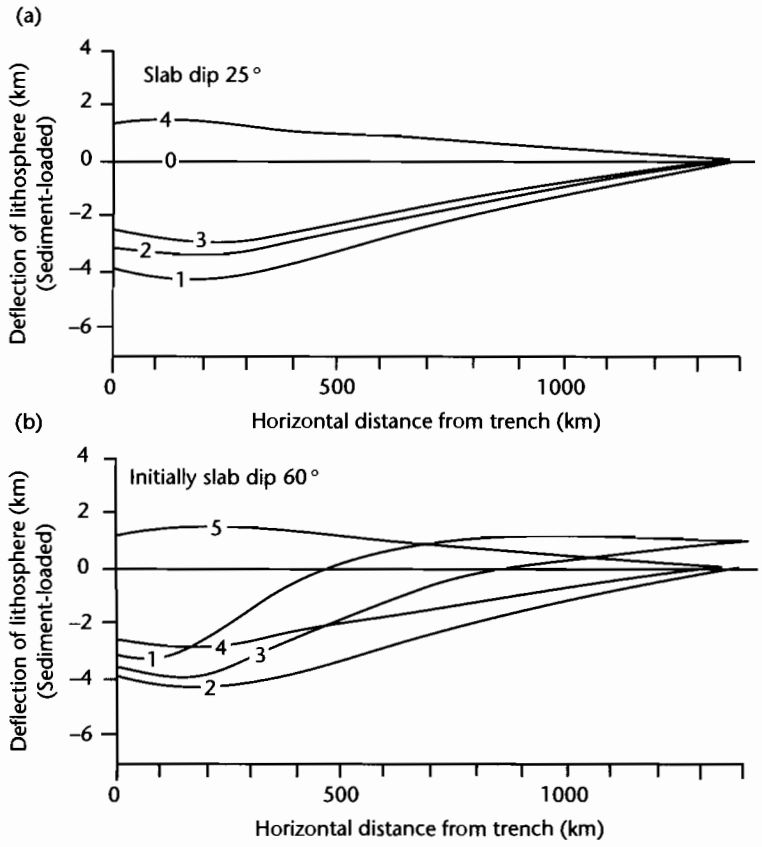

Fig. 5.11 Dynamic topography profiles generated by a model involving block subduction, with $\Delta T = -700$ K, $D = 10^{24}$ Nm, for slab dips of 25° (a) and initially 60° (b). (a) The sequence of profiles shows the maximum dynamic subsidence (1), then profiles 10 Myr (2) and 25 Myr (3) after the cessation of subduction. Assuming the dynamic subsidence is filled with sedimentary rocks (density 2300 kg m^{-3}), the surface potentially (no erosion) rebounds to profile (4); (b) Sequence of profiles shows the dynamic topography as the subduction geometry changes from 60° (1) to 25° (2) and back to 60° (3). The deflection 25 Myr after the cessation of subsidence is shown in (4), while the surface of the sedimentary basin, assuming the maximum deflection is filled with sedimentary rocks and no erosion, is shown as (5). Modified from Mitrovica et al. (1989). Reproduced courtesy of American Geophysical Union.

from 160 to 10 Ma, a plateau more than 1 km high and 800 km across is formed.

Some of these features can be identified in the subduction history of the Farallon Plate beneath North America. In the Tertiary, a very large tract of western USA was uplifted (e.g., Colorado Plateau) as the Farallon Plate shallowed in dip and decreased in age (Cross 1986), leading to high gravitational potential energy and extensional collapse (Jones et al. 1996). An alternative possibility for regional uplift of the upper plate is that accretion of island arc terranes may cause break-off of the oceanic slab, thereby weakening the upper mantle convective flow, causing uplift (Mitrovica et al. 1989). A similar model has recently been applied to the tilting of Laurentia in the Ordovician to explain subsidence in the Michigan Basin (Coakley and Gurnis 1995) and to the entire North American craton during the Phanerozoic in papers by Burgess and Gurnis (1995) and Burgess et al. (1997). Different timings of subduction, different slab angles and ages, and different locations of subduction, are capable of producing the alternate periods of uplift and subsidence demonstrated in the six transgres-

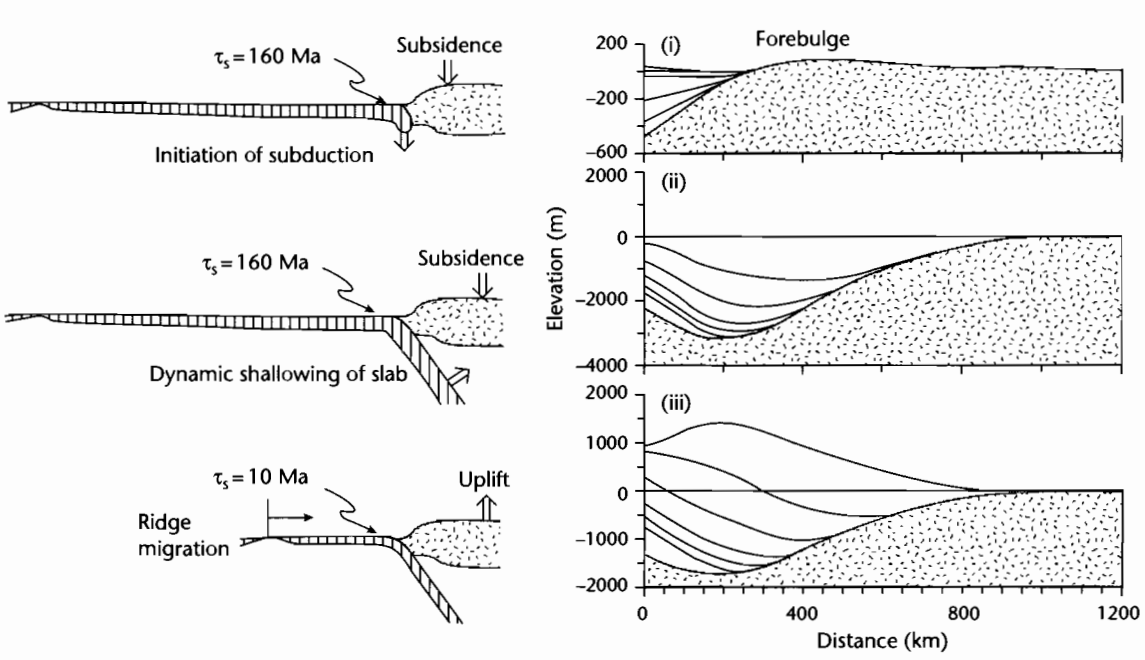

Fig. 5.12 Three stages in the evolution of dynamic topography over a subduction zone (a) and the associated chronostratigraphic surfaces in the region of the continental plate affected by dynamic topography (b). (i) An old (160 Ma) slab initially dips vertically, then penetrates the mantle by 100 km. The chronostratigraphic surfaces are separated by 2 Myr if the slab descent rate is 50 mm yr^{-1}. The slab then shallows in dip (ii). Chronostratigraphic surfaces are shown for each 10° decrease in slab dip. In (iii), the age of slab at ocean trench progressively decreases to 10 Ma, causing uplift (no erosion). After Gurnis (1992). Reproduced courtesy of American Association for the Advancement of Science.

sive/regressive sequences (supersequences) of Sloss (1963).

A point that is rarely addressed but which is of major importance is that dynamic subsidence is *transient* rather than permanent. When the flow responsible for dynamic topography is removed, the continental interior should rebound to its nondynamic position, at a rate determined by mantle viscosity. In the case of mantle plumes (§3.7), we saw that igneous underplating of the crust causes a permanent isostatic subsidence whereas dynamic uplift over the plume head is transient. Burgess and Gurnis (1995) correctly conclude that another mechanism must be present to allow long-term preservation of thick stratigraphic sequences in the continental interiors.

5.2.3 Dynamic topography associated with supercontinental assembly and dispersal

The history of continental migration is clearly marked by phases of continental aggregation into supercontinental assemblies, followed by break-up and dispersal before aggregation takes place once again (Anderson 1982; Kerr 1985). The time scale for this process (Wilson cycle) is of the order of hundreds of millions of years. Rodinia, Gondwana, and Pangea are all examples of supercontinental assemblies in the geological past. For example, the Laurentian (North American) Plate broke away from a Late Proterozoic Gondwanan supercontinent at about 575 Ma, then underwent accretions in the Late Devonian–Carboniferous (*c.* 360 Ma) marking the initial assembly of the Pangean supercontinent. By the Permian (*c.* 250 Ma) Pangea was a huge continental

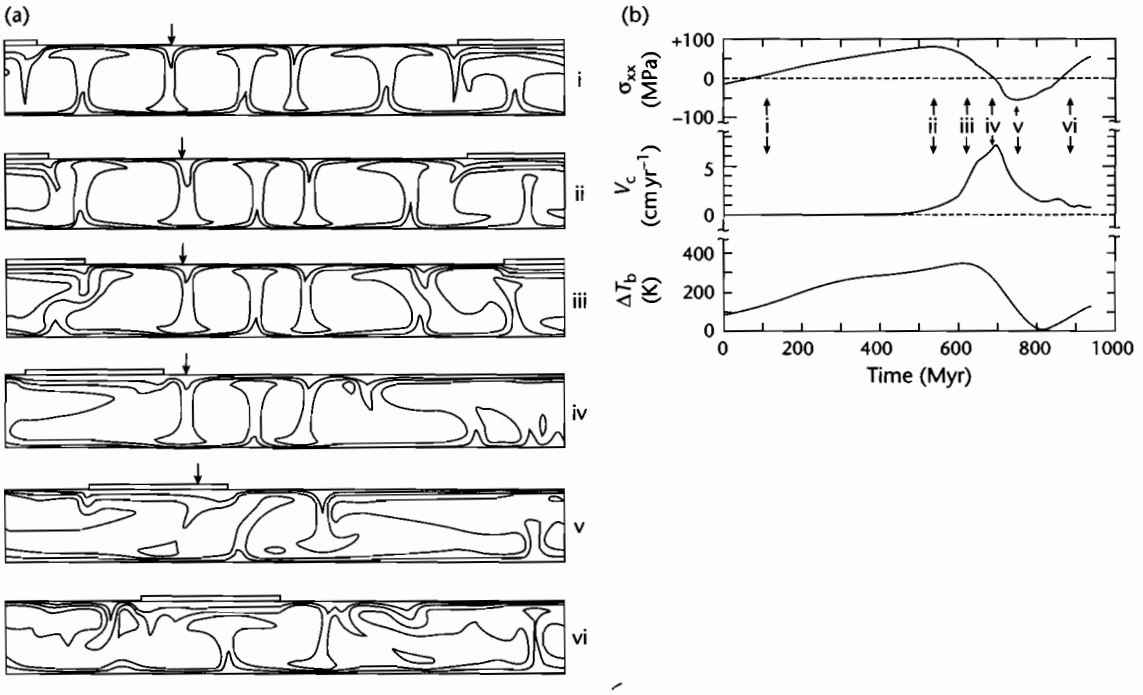

Fig. 5.13 Numerical experiments of convection beneath a single continental plate (after Gurnis 1988). (a) Numerical simulation at a Rayleigh number of 10^5 with a continental plate (shown as a rectangle above the fluid for illustration purposes only) within a convecting fluid, which moves towards the downwelling marked with a vertical arrow; (b) Average horizontal stress through the plate σ_{xx}, plate velocity V_c and the change in temperature beneath the plate ΔT_b for the single plate shown in (a). Details of model parameters and scalings in Gurnis (1988). Note that the temperature under the plate and the horizontal extensional stress through the plate rises over a period of 600 Myr, before relatively rapid migration towards a downwelling. Reproduced courtesy of Macmillan Journals.

mass. In the Triassic (*c.* 220 Ma) it started to split, with fragments dispersing rapidly in the Jurassic and Early Cretaceous. The time scale of the cycle above is of the order of 350 Myr. (It should not escape your attention that these aggregation–dispersal cycles roughly correspond with the first-order cycles of Vail et al. (1977a) and Haq et al. (1987), see Chapter 8.)

The movement of continental plates is tied to the dynamics of mantle convection, with downwellings acting as major forces driving plate motion. The residual core of Pangea is today represented by Africa, which is situated on a geoid high (§5.1.4). It is proposed that Pangea was also associated with a geoid high 200 Ma ago. Since we have drawn a connection between a long wavelength geoid high, hotspot locations and low seismic velocities in the lower mantle, it is likely that major geoid highs today and in the past overlie hotter than average mantle. Geoid lows are probably associated with cooler than average mantle.

Supercontinental assemblies are thought to act as insulators of the mantle, hindering it from losing heat as it does in the oceans. Over a period of time (approx. 100 Myr) subplate temperatures would rise as the positively buoyant supercontinent is trapped between two adjacent cold downwellings (Fig. 5.13). Eventually, the lateral spread of heat would allow the plate to rapidly move off the geoid high, causing a flooding of the continental surface, and to settle over a downwelling at a geoid low (Fig. 5.13). The accretion of continental fragments into a new supercontinent at a geoid low should also be associated with an increase in subsidence rates on the craton (e.g., North American Plate, Middle Devonian–Early Carboniferous, Kominz and Bond 1991).

Gurnis (1988) conducted numerical experiments on the feedbacks between supercontinental assembly and dispersal, the geoid and mantle convection. In experiments involving a single plate overlying a convecting mantle, a geodynamical cycle involves: (i) *phase of subplate heating over upwelling*: initially the plate is trapped between two downwellings and directly above an upwelling. At this stage the horizontal velocity of the plate is zero and the average horizontal stress is also zero. While the plate is stationary, the average temperature along its base rises (1 °C per 2.5 Myr for *c.* 450 Myr gives a temperature increase of 180 °C) and its topography rises; (ii) *plate migration*: as the subplate mantle is heated, the plate experiences significant tension. Its maximum topography corresponds to the time of maximum horizontal extensional stress. The adjacent downwellings are pushed laterally and the plate moves rapidly off the hot upwelling, relaxing the extensional stresses and reducing its surface topography as it does so; and (iii) *plate settling over downwelling*: the plate comes to rest over a downwelling and the average stress along its base becomes compressive. The topographic range experienced by the surface of the plate during this cycle is approximately 3 km. Gurnis (1988) also showed that a plate located over an upwelling could accumulate sufficient extensional stresses to break, the two continental fragments dispersing rapidly towards adjacent downwellings, and eventually (150 Myr after break-up) colliding with each other

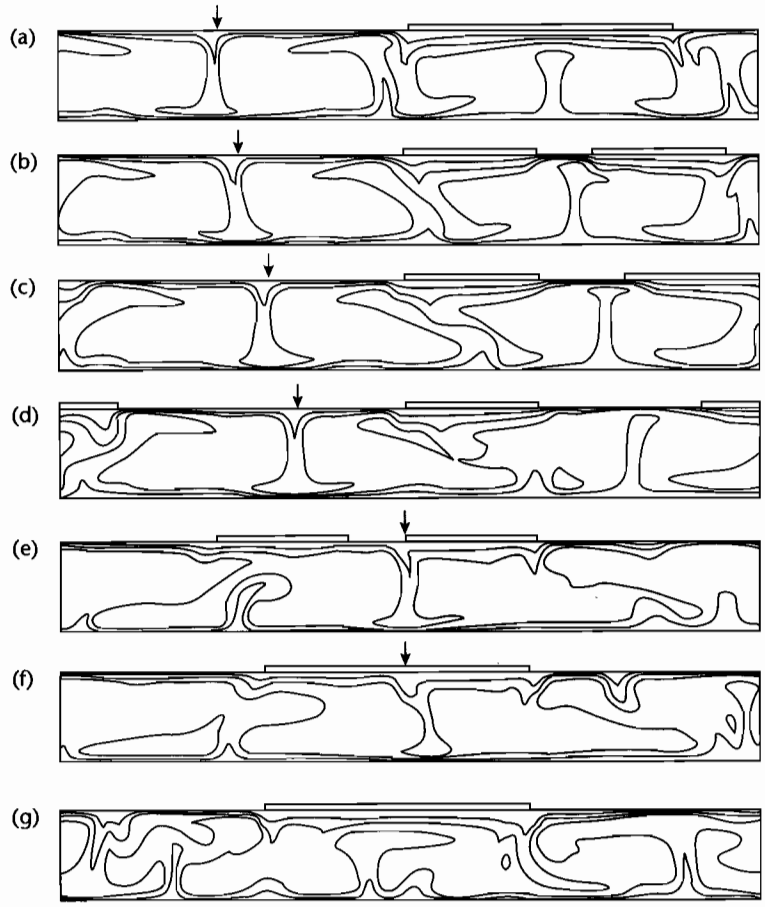

Fig. 5.14 Cross-sectional temperature field for a plate that breaks in two under a tensile yield stress of 70 MPa. The continental fragments migrate towards a cold downwelling (arrow) after break-up. The frame of reference is fixed with respect to the left corner of the original single plate. After Gurnis (1988). Reproduced courtesy of Macmillan Journals.

Table 5.1 World's major hotspots, with buoyancy flux, after Davies (1988) and Sleep (1990).

Hotspot	Flux (Sleep 1990) ($Mg\,s^{-1}$)	Reliability	Flux (Davies 1988) ($Mg\,s^{-1}$)
Afar	1.2	Good	–
Australia, East	0.9	Fair	–
Azores	1.1	Fair	–
Baja	0.3	Poor	–
Bermuda	1.1	Good	1.5
Bouvet	0.4	Fair	–
Bowie	0.3	Poor	0.8
Canary	1.0	Fair	–
Cape Verde	1.6	Good	0.5
Caroline	1.6	Poor	–
Crozet	0.5	Good	–
Discovery	0.5	Poor	0.4
Easter	3.3	Fair	–
Fernando	0.5	Poor	0.9
Galapagos	1.0	Fair	–
Great Meteor	0.5	Poor	0.4
Hawaii	8.7	Good	6.2
Hoggar	0.9	Fair	0.4
Iceland	1.4	Good	–
Juan de Fuca	0.3	Fair	–
Juan Fernandez	1.6	Poor	1.7
Kerguelen	0.5	Poor	0.2
Louisville	0.9	Poor	3.0
Macdonald	3.3	Fair	3.9
Marqueses	3.3	Fair	4.6
Martin	0.5	Poor	0.8
Meteor	0.5	Poor	0.4
Pitcam	3.3	Fair	1.7
Réunion	1.9	Good	0.9
St Helena	0.5	Poor	0.3
Samoa	1.6	Poor	–
San Felix	1.6	Poor	2.3
Tahiti	3.3	Fair	5.8
Tasman, Central	0.9	Poor	–
Tasman, East	0.9	Poor	–
Tristan	1.7	Fair	0.5
Yellowstone	1.5	Fair	–
Sum	54.9		

again to form a new supercontinent (Fig. 5.14). After *c.* 450 Myr, the supercontinent has insulated the mantle for long enough to develop a new upwelling under the plate. Assembly of continental fragments and incubation of the mantle beneath the supercontinent is therefore very slow, whereas break-up and dispersal are relatively fast.

5.2.4 Hotspots and coldspots

There is also a smaller wavelength of thermal activity in the mantle compared to the very long wavelength (degree 2–10) of the geoid. This shorter wavelength pattern is shown by the spatial distribution of hotspots (Fig. 5.5). Hotspots are at their most obvious in the ocean where

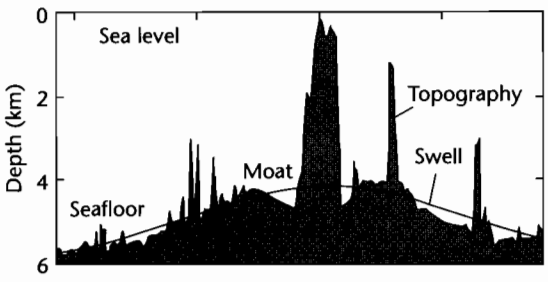

Fig. 5.15 Bathymetric profile of the Hawaiian Ridge at Oahu (after Watts 1978) showing that the hotspot swell is elevated about 2 km above the adjacent seafloor. Reproduced courtesy of American Geophysical Union.

they are associated both with volcanism and strongly elevated bathymetry. The Hawaiian Islands, Iceland, and Canaries are all excellent examples. The recognition of hotspots on the continents is far more problematic. A key feature of hotspots is that they are assumed (perhaps incorrectly) to be fixed relative to a stationary reference frame in the underlying mantle, so absolute plate motion causes a hotspot track to be formed on the moving plate (§3.7.1).

Initially, it is instructive to look at hotspot swells in the ocean (Table 5.1). Topographic uplifts over hotspots in the ocean are large, with swells elevated >1 km above the seafloor (Fig. 5.15). The topographic doming over a hotspot must be maintained by excess buoyancy. The buoyancy flux (Davies 1988; Sleep 1990) is given by

$$B = \Delta\rho W E v_p \tag{5.8}$$

where $\Delta\rho$ is the density contrast of the uplift, WE is the cross-sectional area of the swell, and v_p is the plate velocity. The buoyancy fluxes of the Earth's present-day hotspots (Table 5.1) range over a factor of 20 with Hawaii at 8.7 $Mg\,s^{-1}$ the largest. The average buoyancy flux for the 37 currently active hotspots is in the region of 1.35 $Mg\,s^{-1}$. It can immediately be appreciated that there is an inverse relationship between the cross-sectional area of the swell and the plate velocity for the same buoyancy flux from the mantle.

Hotspots should also produce swells on the continental lithosphere. Taking the globally "typical" hotspot (B = 1.35 $Mg\,s^{-1}$) and a continental plate ($\Delta\rho$ = 2700 $kg\,m^{-3}$) with a track velocity of 20 $mm\,yr^{-1}$, the cross-sectional area of an average topographic dome is about 800 km^2. For a dome elevated at 1 km above the regional elevation, we would expect a width of *c.* 1000 km. For a fast moving plate (say 100 $mm\,yr^{-1}$), the cross-sectional area reduces to just 160 km^2 for the same buoyancy flux. Since slow moving plates are likely to have better developed hotspot swells than fast moving plates, hotspot swells should be more significant and more easily recognized at times of continental assembly before rapid plate dispersal.

Fluid dynamical work (Griffiths and Campbell 1990; Hill 1991) suggests that low viscosity plumes may initiate from within the Earth and ascend as a spherical pocket of fluid (plume head) fed by a pipe-like conduit (plume tail) continuously supplying buoyant, hot material to the head region (Fig. 5.16). It is likely that enlargement of the plume occurs by the entrainment of material heated by the ascent of the plume from the core–mantle boundary. Flood basalt provinces have been interpreted as originating through the melting of the heads of newly started plumes, whereas oceanic island chains represent the tracks of the relatively long-lived plume tails as the plate migrates over the mantle.

Fluid dynamical experiments also suggest that the diameter of a new plume head varies according to the volume flux and temperature excess of the source material provided to the plume head, and the thermal and viscosity properties of the lower mantle into which the plume starts to ascend (Griffiths and Campbell 1990). The plume head then grows by entrainment as it ascends through the mantle, so that the plume head diameter grows as a function of the distance traveled. By the time the plume head has penetrated into the upper mantle it should have cooled to only 100–200 °C above the ambient temperature.

Upon nearing the surface of the Earth, the plume head spreads out into a disc of hot material with positive buoyancy (Fig. 5.16). This produces a dynamic surface uplift. The scaling of laboratory experiments suggests that the timing and magnitude of the surface uplift depend strongly on the viscosity of the upper mantle. The results from laboratory experiments in which a plume head is sourced from the core–mantle boundary with a buoyancy flux of $3 \times 10^4\,Ns^{-1}$ and a source temperature excess of 300 °C, lower mantle dynamic viscosity of 10^{22} Pa s (kinematic viscosity of $2.5 \times 10^{18}\,m^2s^{-1}$) ascending into an upper mantle with a viscosity of 3×10^{20} Pa s, is shown in Figure 5.16b. The surface is initially weakly uplifted while the plume head is entirely within the lower mantle (–25 Myr). When the plume head enters the low viscosity zone of the upper mantle (–3 Myr) the

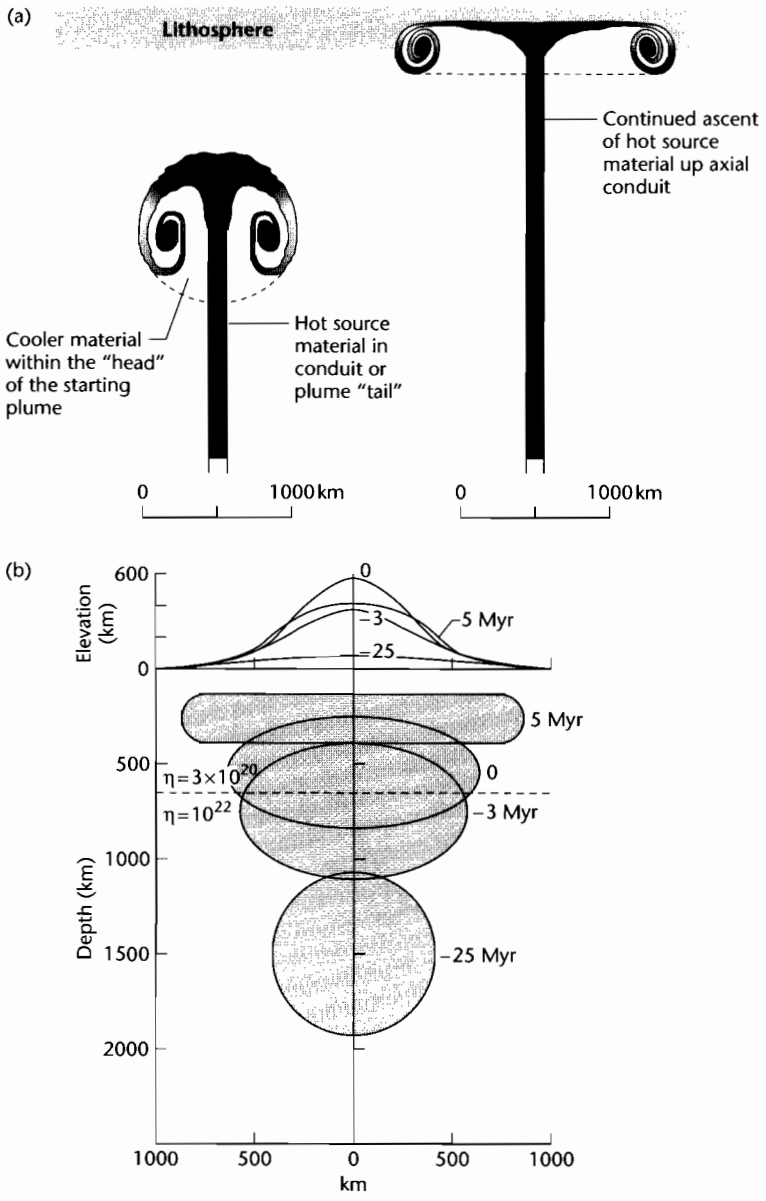

Fig. 5.16 (a) Schematic diagram of the ascent of a plume through the mantle and its mushrooming into a disc beneath the lithosphere, with darker shading indicating higher temperatures. After Hill, R.I. (1991); (b) The dimensions of a starting plume together with the predicted surface uplift, based on laboratory experiments. During the lateral spreading of the head the input of material from the source is discontinued, simulating the carrying away of the head from the source region by plate motion. After Griffiths and Campbell (1990).

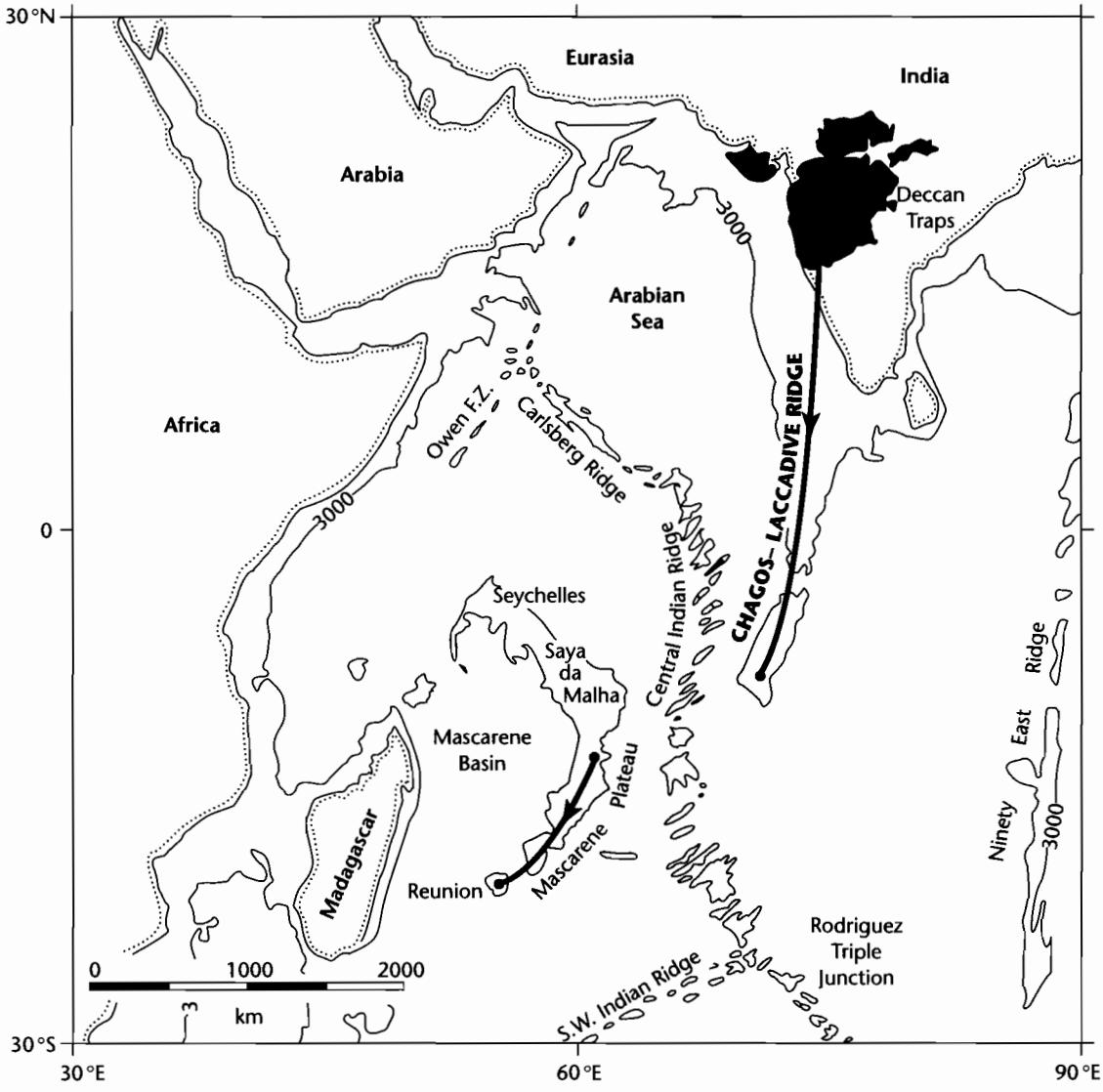

Fig. 5.17 The path of the Reunion hotspot track in the Indian Ocean and the Deccan flood basalt province (after White and McKenzie 1989). Reproduced courtesy of American Geophysical Union.

surface uplift takes place rapidly, reaching a maximum elevation of 600 m after further ascent to just beneath the lithosphere. At this stage the plume head has a diameter of 1300 km. A number of factors may increase the maximum elevation of the topographic dome: (i) penetration of the hot plume into the cold lithosphere, and (ii) a volume increase caused by melting. The release of large amounts of basalts by melting of the plume can only take place once the plume head has reached shallow depths. It should be noticed that this is only possible a number of millions of years after the maximum surface uplift. The development of smaller scale gravitational instabilities over the cap of the plume as cold, dense material is squeezed between the ascending plume head

and the Earth's surface may facilitate the last-stage ascent of the plume and produce the high surface uplifts seen today in locations such as East Africa, and the large outpourings of basalts in the geological past such as the Siberian and Deccan (India) Traps (Fig. 5.17).

Hotspots are related to upwellings of hot material through the mantle. If numerical experiments are informative, there should be a system of small scale convection with horizontal lengths that scale on the thickness of the convecting layer. If these small convection cells are restricted to the upper mantle, we should expect upwellings to be separated by approximately 10^3km. However, only a fraction of the total number of sublithospheric upwellings are likely to penetrate to the surface and produce volcanic activity. This will depend on the plate velocity, plate thickness, and rate of ascent of the lithosphere–asthenosphere boundary. If the plate is very thick, the time required for magma to penetrate to the surface will be longer than the time taken for the magma to cool and solidify, so there will be no hotspot at the surface, only a *highspot*, and plutonic activity at depth (Sahagian 1980).

Hotspot swells in the oceans are well documented. We might also expect topographic uplift of the continents over sublithospheric upwellings. Such uplifts are likely to be of the order of 1 km in height and perhaps 1000 km in width. The domes of Africa, such as the Hoggar, are good candidates for hotspot uplift (Fig. 3.6). Over geological time, all the continents must have passed over mantle upwellings, leaving hotspot tracks. Some parts of continents must have a veritable criss-cross pattern of hotspot tracks (Morgan 1983). Within a band of approximately 10^3km width, the continental surface should be transiently elevated, leading to erosion and the development of regional unconformities. Such unconformities would be recognizable long after the transient dynamic uplift has ceased. If we ignore flexural uplift due to mountain building (Chapter 4), and dynamic topography related to plate subduction (§5.2.2) and supercontinental assembly (§5.2.3), involvement in hotspot uplift may be a major cause for erosional unconformities in cratonic sedimentary sequences.

If there are upwellings beneath continents, we should also expect there to be downwellings, which would be cold and characterized by negative dynamic topography. The Congo Basin may be situated over one such downwelling (Fig. 3.6) (Hartley and Allen 1994). It is situated adjacent to the East African upwelling. The fact that many sedimentary basins have sedimentary sequences deposited over long periods of time raises the possibility that lithospheric plates may "drag" these small-scale convection systems beneath them. If so, these convection systems would have upwellings that do not move significantly relative to the plate, in contrast to the well-developed hotspot tracks caused by migration of a plate over a quasi-stationary system of mantle upwellings.

Hotspots and highspots should of course be important source areas of erosional detritus. Peripheral uplifts around a sedimentary basin may feed the basin with sediment and load the lithosphere. In this sense, some cratonic basins may be more passive receptacles for the erosional detritus of peripheral or annular uplifts than areas with strong mechanical subsidence (see Sahagian 1993 for a similar view).

CHAPTER 6

Basins associated with strike–slip deformation

On that day his feet will stand on the Mount of Olives, east of Jerusalem, and the Mount of Olives will be split in two from east to west, forming a great valley, with half of the mountain moving north and half moving south.

(ZECHARIAH 14:4, NEW INTERNATIONAL VERSION)

SUMMARY

Sedimentary basins generally form by localized extension along a strike–slip fault system which itself may be related to either divergent, convergent, or oblique relative plate motion. Less commonly, loading resulting from local crustal thickening may cause flexural subsidence. Although strike–slip basins form in a wide variety of geodynamical settings such as oceanic and continental transforms and arc and suture collisional boundaries, they are best known from intracontinental and continental margin environments.

In simple systems, the orientation of the strike–slip fault in relation to the plate slip vector is important in determining whether divergent (transtensile) or convergent (transpressive) strike–slip takes place. This guide breaks down, however, in complex regions of continental convergence such as Turkey.

Zones of strike–slip tectonics are characterized by active seismicity on strike–parallel and strongly oblique faults, with zones of infrequent, large earthquakes along locked segments, and frequent small earthquakes along unlocked segments. Some of the world's best known and most hazardous faults are strike–slip. Heat flows are generally low, suggesting that major strike–slip faults are weak and therefore generate little frictional heat. Geodetic surveys and paleomagnetic results show that small and large crustal blocks commonly rotate about a subvertical axis during strike–slip deformation. Characteristic geomorphic features result from the lateral displacement of adjacent terranes.

Sedimentary basins in zones of strike–slip deformation are diverse and complex. Some are clearly thin-skinned and related to extensional or contractional detachments in the weak lower crust. A number of different types of basin can be discriminated on the basis of kinematic setting, chief of which are fault bend basins, overstep basins, transrotational and transpressional basins.

The bulk of the shear strain is accommodated in a central *principal displacement zone* (PDZ) which may be linear to curvilinear in plan view and steeply inclined in section. The PDZ commonly branches upwards into a splaying system of faults producing a *flower structure*. Some fault zones, such as the Garlock Fault in California, penetrate to great depths, terminating in the middle crust, whereas others link at depth with relatively shallow low-angle detachments belonging to orogenic wedges. Strike–slip zones are characterized by *en echelon* arrangements of faults and folds that are orientated in a consistent pattern with respect to the strain ellipse. The most important fractures are termed *Riedel Shears*, but extension fractures are also formed. *En echelon* folds may form, with axes roughly at right angles to the extension fractures. The exact pattern of faults and folds produced in any particular fault zone depends on the local geological fabric and the youth or maturity of the fault system.

The precise structural pattern is controlled by a number of factors including: (i) the kinematics (convergent, divergent, parallel) of the fault system, (ii) the magnitude of the displacement, (iii) the material properties of the rocks and sedimentary infills in the deforming zone, and (iv) the configuration of pre-existing structures.

The PDZ is characteristically segmented. The individual segments may be linked, both in plan view and cross-sectional view, by *oversteps*. If the sense of an along-strike overstep is the same as the sense of fault slip, a *pull-apart basin* is formed: if the sense of the overstep is opposite to that of fault slip, a *push-up range* is formed. Pull-apart basins appear to develop in a continuous

evolutionary sequence at releasing bends with increasing offset, from narrow "spindle-shaped" basins to "lazy S" and "lazy Z" basins to "rhomboidal" basins and eventually into ocean-floored basins. However, the weakness of major strike–slip zones may cause transform-normal extension, producing markedly asymmetrical strike–slip basins. Numerical modeling of basins at stepovers using a basal forcing are successful at generating the broad features of pull-apart basins, such as the Dead Sea Basin.

Thermal and subsidence modeling is poorly developed in strike–slip basins, largely on account of their complex structural history. In basins involving lithospheric thinning, the uniform extension model has been applied with modifications for the lateral loss of heat through the basin walls during the extension. Other basins appear to form over zones of thin-skinned extension, with no mantle involvement. These basins, such as the Vienna Basin in the compressive Alpine–Carpathian system, are cool and lack a well-developed postextension thermal subsidence.

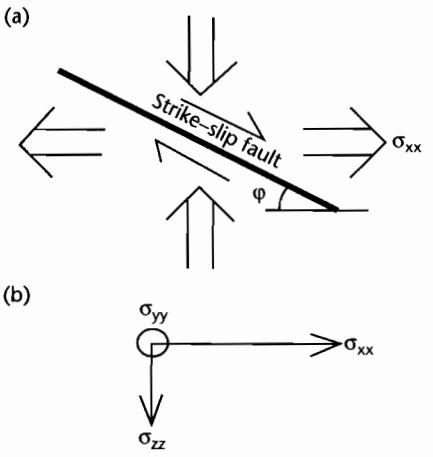

Fig. 6.1 Plane strain approximation for strike–slip faults. (a) Conjugate strike–slip faults at an angle φ to the principal stress σ_{xx}; (b) Principal stresses are related by $\sigma_{zz} > \sigma_{yy} > \sigma_{xx}$.

6.1 OVERVIEW

6.1.1 Geological and geophysical observations

Basins associated with strike–slip deformation are generally small and complex compared to cratonic sags, passive margins, and foreland basins. They are intimately linked to the detailed structural evolution of an area and mechanical models have been relatively slow to appear because of the extreme complexity of this history of deformation. Nevertheless, numerical 3-D models are available for basin development in particular structural settings within a zone of strike–slip deformation.

Strike–slip deformation occurs where principally lateral movement takes place between adjacent crustal or lithospheric blocks. In pure strike–slip, the displacement is purely horizontal, so there is no strain in the vertical dimension y. This is the situation of *plane strain*. The vertical stress in strike–slip faulting is the vertical lithostatic stress $\sigma_{yy} = \rho gh$. The horizontal stresses are the deviatoric stresses, one compressional, and the other extensional. The vertical stress is always the intermediate stress. Two conjugate strike–slip faults are anticipated from this state of stress, one right-lateral and the other left-lateral, inclined at an angle φ to the principal stress σ_{xx} (Fig. 6.1).

In reality, movement in strike–slip zones is rarely purely lateral, and displacements are commonly *oblique*, that is, involving a certain amount of normal or reverse dip–slip movement. Oblique slip may therefore characterize any strike–slip zone, but particular zones may experience a net contraction while others may suffer net extension. The stress regimes responsible for these two variants on pure strike–slip deformation are known as *transpressive* and *transtensile*.

Major strike–slip deformation and associated basin formation takes place in a wide range of geodynamic situations. Strike–slip zones may be associated with entire plate boundaries such as the San Andreas Fault system of California and the Alpine Fault system of New Zealand, microplate boundaries, intraplate deformations, or small fractures of limited displacement. Sylvester (1988), drawing considerably on Woodcock's (1986) genetic scheme (Fig. 6.2), proposed a classification of strike–slip faults into *interplate* and *intraplate* varieties (Table 6.1). He recommends use of the term "transform" fault for deep-seated interplate types and "transcurrent" fault for intraplate strike–slip faults confined to the crust. Of greatest importance to students of basin analysis are the strike–slip faults cutting continental lithosphere where uplifting and eroding source areas for sediment are available.

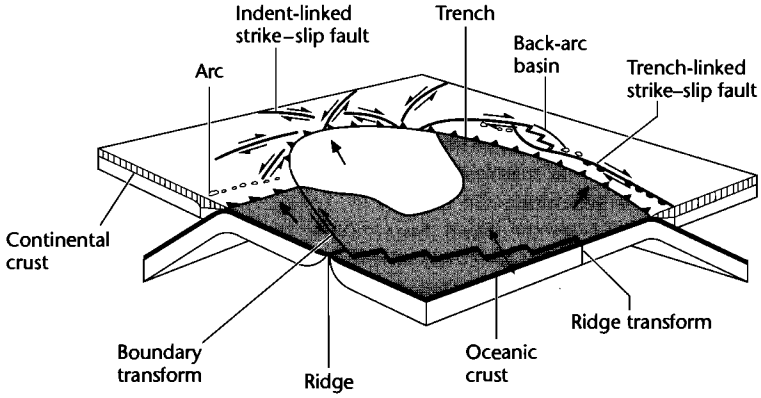

Fig. 6.2 Genetic classification of major classes of strike–slip fault according to plate tectonic setting (after Woodcock 1986). See also Table 6.1.

Table 6.1 Sylvester's (1988) classification of strike–slip faults.

1 **Interplate "transforms"** (deep-seated, delimiting plate)	2 **Intraplate "transcurrent" faults** (confined to crust)
1.1 *Ridge transform faults* Displace segments of oceanic crust with similar spreading vectors e.g., Romanche fracture zone (Atlantic Ocean)	2.1 *Indent-linked strike–slip faults* Bound continental blocks in collision zones e.g., North Anatolian (Turkey), Altyn Tagh, and Kunlun (Tibet)
1.2 *Boundary transform faults* Separate different plates parallel to the plate boundary e.g., San Andreas (California), Alpine Fault (New Zealand)	2.2 *Intracontinental strike–slip faults* Separate allochthons of different tectonic styles e.g., Garlock Fault (California)
1.3 *Trench-linked strike–slip faults* Accommodate horizontal component of oblique subduction e.g., Atacama Fault (Chile), Median Tectonic Line (Japan)	2.3 *Tear faults* Accommodate different displacement within a given allochthon or between the allochthon and adjacent structural units e.g., Asiak fold thrust belt (Canada)
	2.4 *Transfer faults* Linking overstepping or *en echelon* strike–slip faults e.g., Southern and Northern Diagonal Faults (eastern Sinai, Israel)

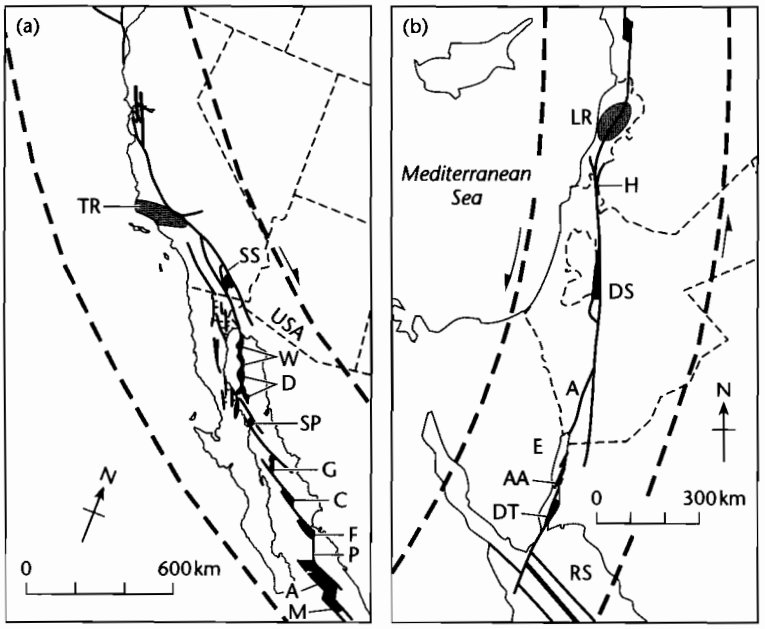

Fig. 6.3 Regions of compression and extension along strike–slip boundaries between rigid continental plates related to the orientation of the fault zone with respect to the plate slip vector (after Mann et al. 1983). (a) Pacific–North American Plate boundary. The dashed lines are theoretical interplate slip lines from Minster et al. (1974). The major zone of compression is the push-up block of the Transverse Ranges where the dextral San Andreas Fault Zone has a "convergent" orientation with respect to the interplate slip line. The prominent pull-apart basins, however, are situated relatively to the south where the fault zone has a "divergent" orientation with respect to the interplate slip line. TR, Transverse Ranges; SS, Salton Sea pull-apart as a right step between the San Andreas and Imperial Faults. Pull-aparts in the Gulf of California include: W, Wagner Basin; D, Delfin Basin; SP, San Pedro Martir Basin; G, Guaymas Basin; C, Carmen Basin; F, Farallon Basin; P, Pescadero Basin Complex; A, Alarcon Basin; M, Mazatlan Basin; (b) Arabia–Sinai (Levant) Plate boundary zone (Garfunkel 1981; Ben-Avraham et al. 1979). Theoretical interplate slip lines are from Le Pichon and Francheteau (1978). The prominent area of compression is the Lebanon Ranges push-up block where the sinistral Dead Sea Fault Zone is "convergent" with respect to the interplate slip lines. Most of the pull-apart basins are in the Dead Sea and Gulf of Aqaba regions where the fault zone is locally "divergent" with respect to the interplate slip lines. Pull-aparts include: H, Hula Basin; DS, Dead Sea Basin; A, Arava Fault Trough; E, Elat Basin in the northern Gulf of Aqaba; AA, Arnona–Aragonese Basin; DT, Dakar–Tiran Basin.

The development of regions of extension and shortening along strike–slip systems has been related to the relative orientation of the plate slip vectors and the major faults (Mann et al. 1983). In the case of the San Andreas and Dead Sea strike–slip systems, basins develop where the principal displacement zone is divergent with respect to the plate vector (Fig. 6.3). In contrast, uplifts or push-up blocks such as the Transverse Ranges, California and Lebanon Ranges, occur where the principal displacement zone is convergent with respect to the plate vector. This simple relationship is unlikely to apply where deformation takes place on many faults enclosing rotating crustal blocks. It is a very poor guide to patterns of uplift and subsidence in complex regions of continental convergence such as Turkey (Sengör et al. 1985).

Strike–slip zones are characterized by extreme structural complexity. Individual strike–slip faults are generally linear or curvilinear in plan view, steep (subvertical) in section and penetrate to considerable depths, perhaps decoupling crustal blocks at the base of the seismogenic crust (i.e., 10–15 km). In contrast to regions of pure extension or contraction, strike–slip zones possess promi-

nent *en echelon* faults and folds, and faults with normal and reverse slip commonly coexist. The vergence direction of folds and the mass transport indicators from thrusts associated with transpression are distinctively poorly clustered or apparently random.

Zones of major strike–slip tectonics are marked by important seismicity (Fig. 6.4). In California, the relative velocity between the Pacific and North American Plates is 47 mm yr^{-1}. Much of this displacement is taken up on the right-lateral (dextral) San Andreas Fault. However, like many other major translithospheric strike–slip faults, the San Andreas Fault occurs within a broader zone of faulting that may stretch laterally for 500 km. Much of the present day seismicity in the San Andreas system originates from faults oblique to the main fault zone (e.g., the NE-trending Garlock Fault and Big Pine Fault) (Nicholson et al. 1986). These oblique faults define crustal blocks that are rotating about a vertical axis. Seismicity dies out below about 15 km, indicating the brittle–ductile transition. Focal mechanism solutions in strike–slip zones are commonly highly variable, with mixtures of strike–slip, extension, and compression (e.g., North Anatolian Fault, Turkey, Taymaz et al. 1991), reflecting the complexities of deformation within a zone of overall strike–slip deformation.

Paleomagnetic studies support the idea that crustal blocks commonly undergo rotations about vertical axes (Fig. 6.5). The amount and scale of rotation varies greatly. The Western Transverse Ranges of southern California have experienced net clockwise rotations of 30°–90° for example, whereas in the Cajon Pass region there has been no significant rotation since 9.5 Ma. Small blocks can rotate rapidly, such as the Imperial Valley area, which has rotated by 35° in the last 0.9 Ma! The existence of such rotating blocks supports the view that the crustal blocks deform like a set of dominoes (Freund 1970). There is an obvious physical implication of the existence of rotating blocks, which is that the blocks must detach on their boundary faults at some level in the crust or upper mantle (Terres and Sylvester 1981; Dewey and Pindell 1985).

Pure strike–slip plate boundary faults should fall along a small circle drawn from the pole of rotation that defines the relative motion between the two plates. This is true for the San Andreas system along the boundary of the Pacific and North American Plates (Fig. 6.4). However, seismicity is distributed unevenly along the fault. In some regions there are very few historical earthquakes. The fault in these "locked" regions appears to accumulate strain and then release it in major earthquakes. The 1906 San Francisco moment magnitude 7.6 earthquake is an example. It produced a 4 m surface rupture all the way along a 200 km-long locked section from Redwood City to Cape Mendocino (Fig. 6.4). Elsewhere, small earthquakes are very abundant. In these "free" sections, frequent small earthquakes and aseismic creep release the accumulating strain.

The heat flow measured above major strike–slip faults, such as those of the San Andreas system, is low (Fig. 6.6) (Lachenbruch and Sass 1980, 1988). The heat flow associated with the Dead Sea transform is comparable to average continental values (Ben-Avraham et al. 1978). When slip on a fault occurs under a large stress, as given by Byerlee's law, significant frictional heating takes place. Repeated movements on a frictional strike–slip fault should generate large amounts of heat and contribute to elevated heat flows (Molnar 1992). The fact that observed heat flows are low suggests that major strike–slip faults are relatively weak structures set in a background of strong upper crust. Measurements of the principal stresses close to strike–slip faults in California also suggest that there is little shear stress resisting strike–slip fault motion (Zoback et al. 1987). Low heat flows also indicate that the localized extension along strike–slip zones does not in general involve significant mantle upwelling.

Whereas most of California has low to moderate surface heat flows, the Salton Trough–Imperial Valley in the extreme south has high surface heat flows (>2.5 HFU, Lachenbruch and Sass 1980) and known geothermal resource potential, as a northward continuation of the Gulf of California tectonic-thermal system (Figs. 6.6, 6.7). The region is active seismically, with right-lateral slip on the main Imperial Valley Fault. A seismic refraction and gravity study of the region (Fuis et al. 1984) shows that the Imperial Valley is a gravity high, despite the

Fig. 6.4 The San Andreas system, California. (a) Distribution of seismicity (stars). Solid arrows are relative plate velocities; open arrows are stress directions from focal mechanism studies; (b) Surface trace of the locked and unlocked sections of the San Andreas Fault. Dashed lines are small circles to the pole of rotation for the motion of the Pacific Plate relative to the North American Plate. Compiled from Jennings et al. (1975), Nicholson et al. (1986), and Turcotte and Schubert (2002). Reproduced courtesy of Cambridge University Press.

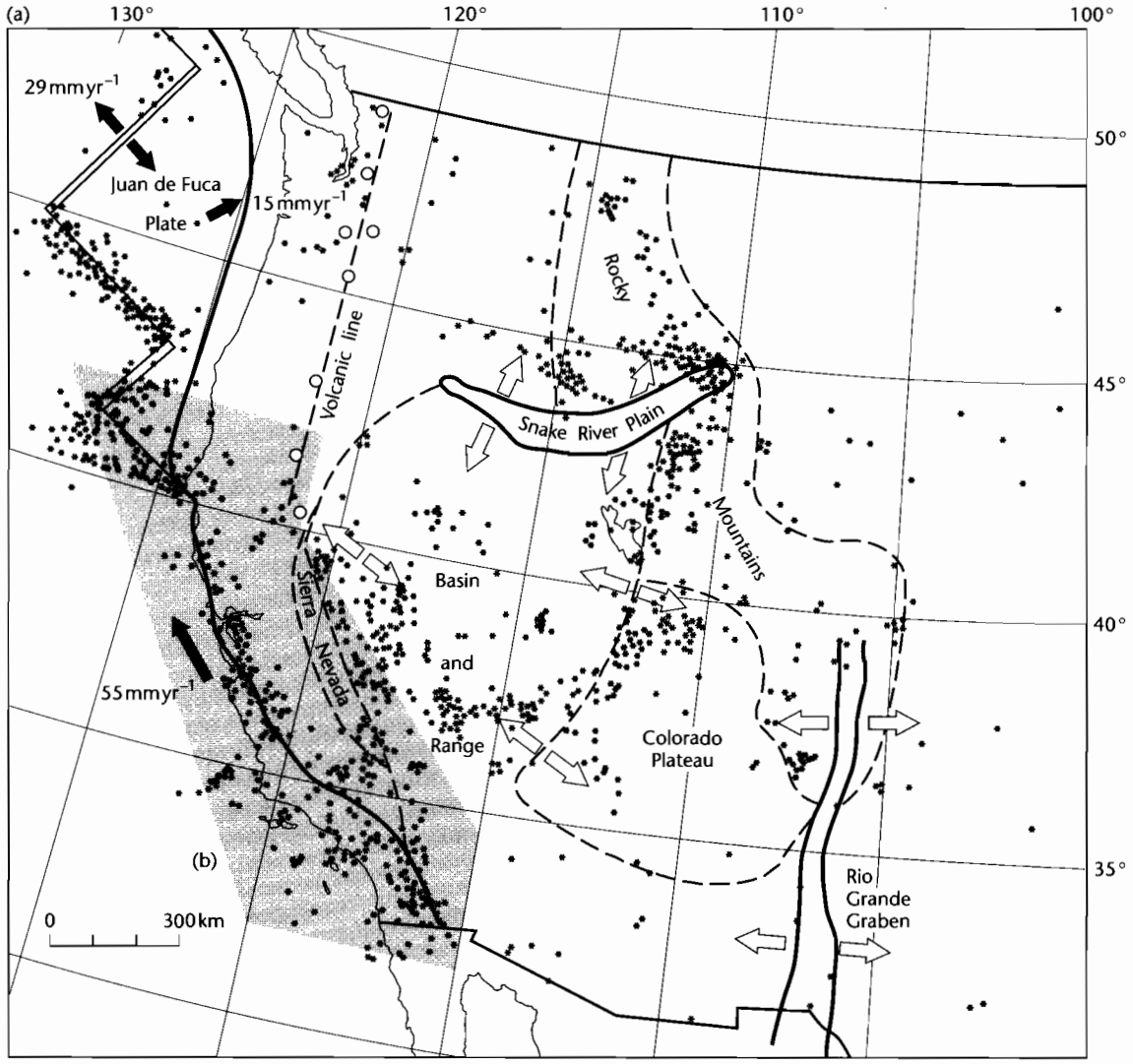
(a)
130°
120°
110°
100°
50°
45°
40°
35°
29 mm yr⁻¹
Juan de Fuca
Plate
15 mm yr⁻¹
Volcanic line
Rocky
Snake River Plain
Mountains
Basin
and
Range
Sierra Nevada
55 mm yr⁻¹
Colorado
Plateau
Rio
Grande
Graben
(b)
0
300 km

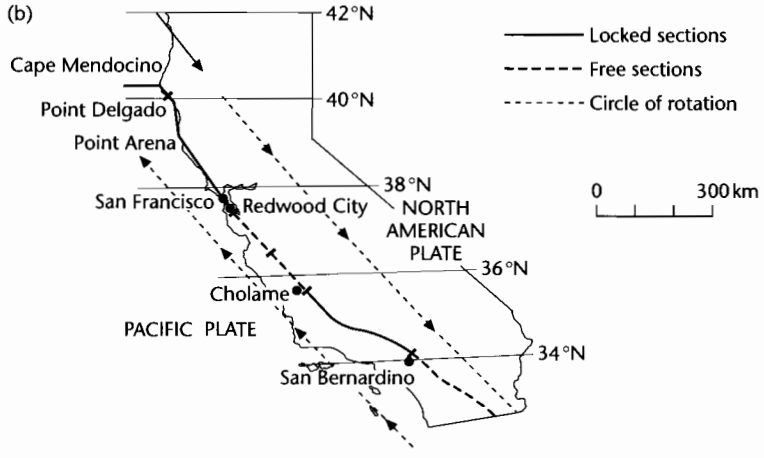
(b)
42°N
Cape Mendocino
40°N
Point Delgado
Point Arena
38°N
San Francisco
Redwood City
NORTH
AMERICAN
PLATE
36°N
Cholame
PACIFIC PLATE
34°N
San Bernardino
Locked sections
Free sections
Circle of rotation
0
300 km

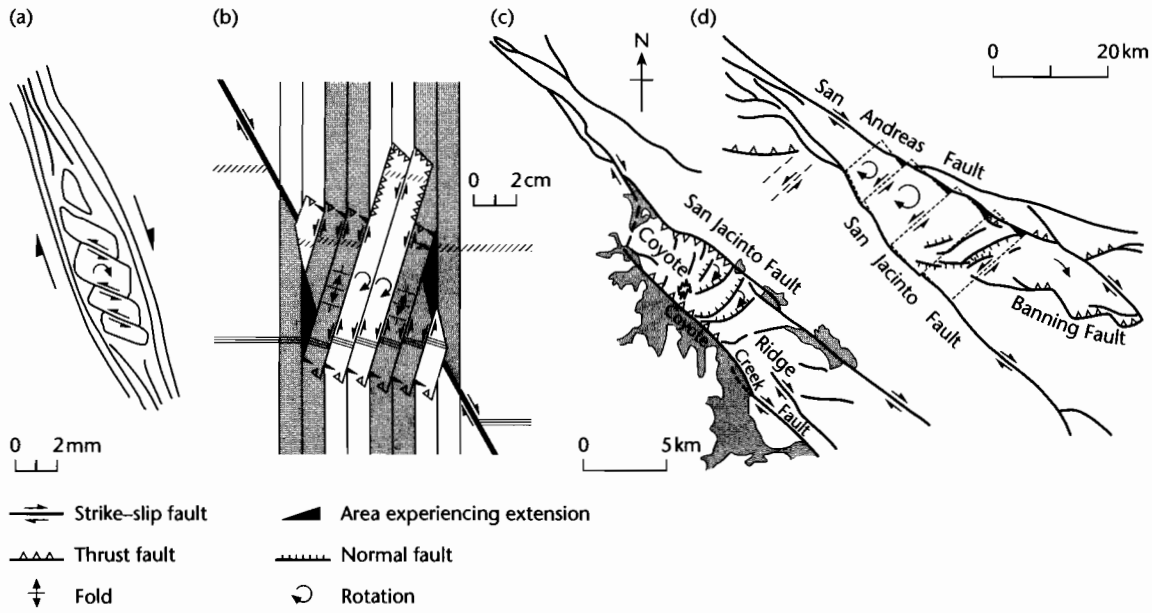

Fig. 6.5 Examples of block rotation by strike–slip faulting at scales from mm to km (after Nicholson et al. 1986). (a) Fracture and rotation of a felspar crystal along cleavage planes in a ductile matrix; (b) Rotation of a hard surface soil layer as a result of the Imperial Valley earthquake of 1979. The ruled lines are the evenly spaced furrows of a ploughed field; (c) Rotating blocks defined by secondary cross-faults between an overlapping right step from the Coyote Creek Fault to the San Jacinto Fault; (d) Block model for rotation near the intersection of the San Jacinto and San Andreas Faults inferred from geology and seismicity. Reproduced courtesy of American Geophysical Union.

presence of a 3.7–3.8 km thick sedimentary basin (Fig. 6.7). This is most likely due to the presence of intruded mafic basement domed up under the Imperial Valley where the extension is greatest.

Some of the world's best known and most hazardous faults, such as the San Andreas and North Anatolian Faults, are of the strike–slip variety. They commonly have startling geomorphic expression and stand out strongly in satellite images. The accumulation of individual slip events over long periods of time commonly results in a linear trough along the fault zone. Streams draining adjacent uplands and their interfluves are commonly offset laterally, demonstrating long-term strike–slip displacement. Since alluvial fans accumulate downstream of the range front, their apices may also be displaced laterally, and stream channels on the fan surface may thus become beheaded. Geomorphic evidence for strike–slip tectonics is classically displayed along the San Andreas system of California (Wesson et al. 1975; Keller et al. 1982) and along the Hexi Corridor of north-central China (Li and Yang 1998) (Fig. 6.8).

The evolution of some orogenic belts, notably the North American Cordillera, involves very large magnitude lateral displacements of terranes. Up to 1500 km of relative lateral motion is thought to have occurred in both the Mesozoic North American Cordillera and in the Tertiary India–Asia collision (Molnar and Tapponnier 1975). Clearly, strike–slip processes offer the possibility of immense lateral translations of crustal terranes.

6.1.2 Diversity of basins in strike–slip zones

Since the history of deformation is invariably complex in strike–slip zones, the associated sedimentary basins are correspondingly complex. They commonly form in areas of localized extension caused by the geometry and

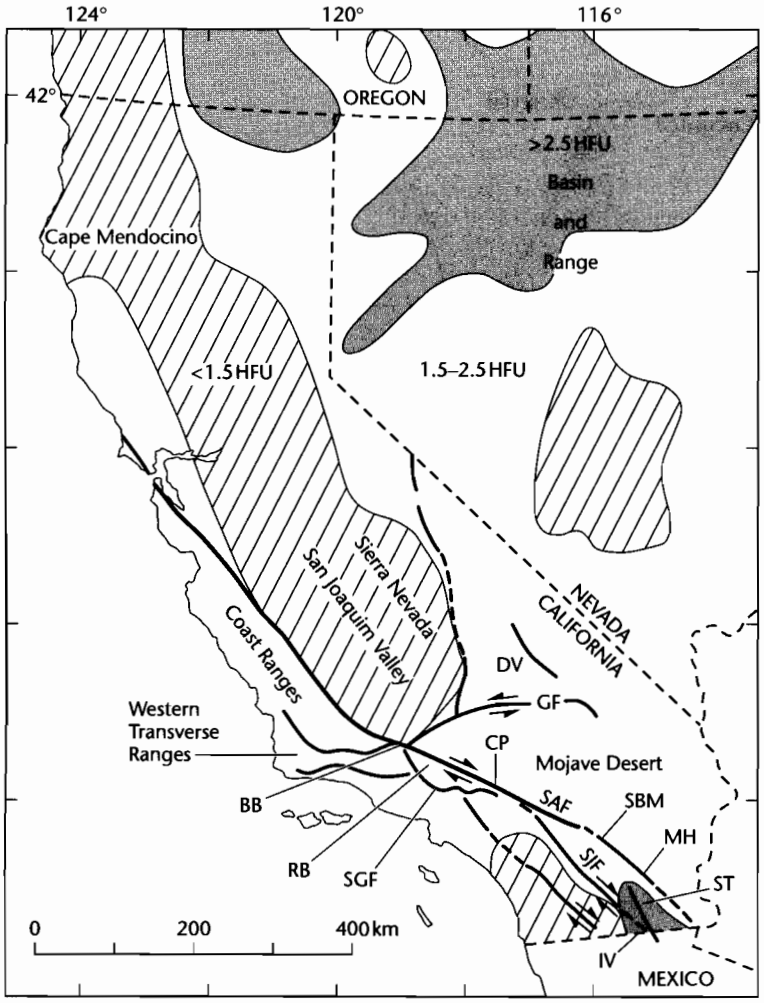

Fig. 6.6 Fault systems and heat flow provinces of California and adjacent regions (after Lachenbruch and Sass 1980). High heat flows are found in the extensional Basin and Range province and in the Salton Trough–Imperial Valley area close to the Mexican border. However, coastal California and most of southern California have low heat flows despite the presence of major strike–slip faults. BB, Big Bend; CP, Cajon Pass; DV, Death Valley; GF, Garlock Fault; IV, Imperial Valley; MH, Mecca Hills; RB, Ridge Basin; SAF, San Andreas Fault; SBM, San Bernardino Mountains; SGF, San Gabriel Fault; SJF, San Jacinto Fault; ST, Salton Trough.

kinematic history of the fault configuration, or in areas of net shortening, where flexural loading may drive subsidence. Characteristically, a basin experiences both extension and shortening during its life span (part of what Ingersoll (1988) calls the Reading cycle, after Reading (1980)), or one part of the basin may experience shortening while another part is undergoing extension.

Rift basins and foreland basins may undergo a phase of strike–slip deformation due to changes in the stress field set up by relative plate motion. Strike–slip basins are therefore emphatically syntectonic and there is little evidence of substantial thermally driven subsidence. This latter feature may be due at least in part to the small size of strike–slip basins. Their narrowness (usually less than

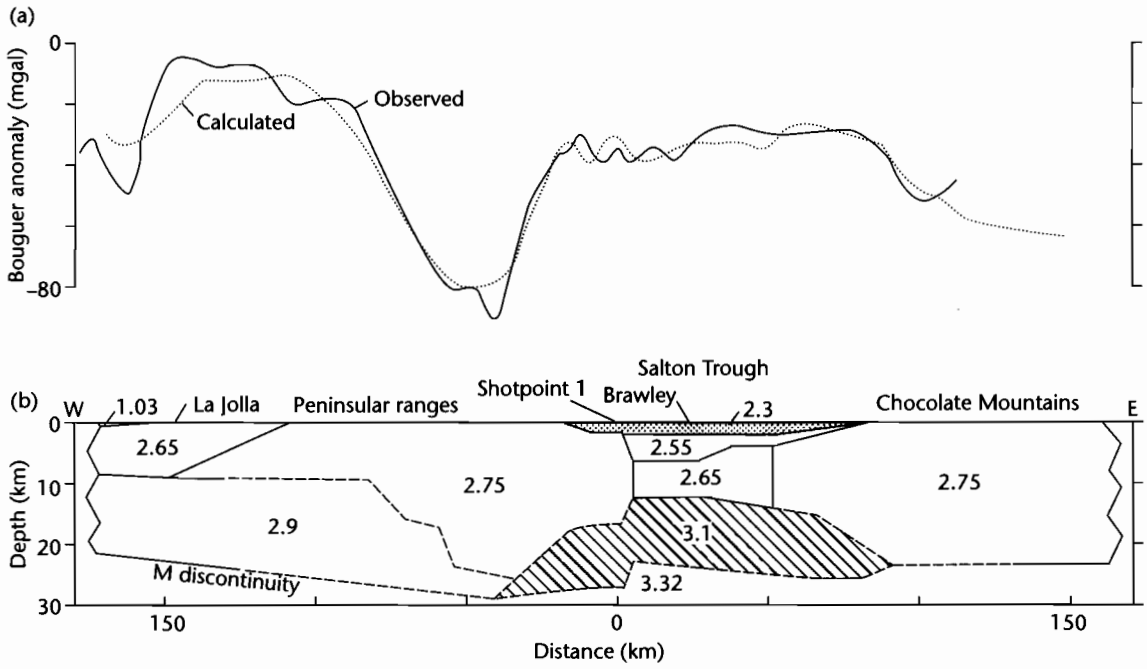

Fig. 6.7 Salton Trough–Imperial Valley region, southern California (after Fuis et al. 1982). (a) Gravity profile and (b) density model for a ENE cross-section of Imperial Valley from La Jolla to Chocolate Mountains. Solid lines on density model are derived from seismic refraction, whereas those that satisfy gravity data are shown dashed. A dense volume of sub-basement compensates gravitationally for the sedimentary rocks of the Salton Trough. Reproduced courtesy of United States Geological Survey.

50 km wide) causes extreme heat loss to the sides as well as vertical conduction to the overlying sea or atmosphere (§6.3.4).

A number of different types of basins form in strike–slip zones. General terms for these varied basins are "pull-apart basins" (Burchfiel and Stewart 1966) and "strike–slip basins" (Mann et al. 1983). The term "pull-apart basin" is also used for a subclass of basins formed in local transtensional settings (Ingersoll and Busby 1995).

We can identify two broad types of strike–slip basin in terms of thermal and subsidence history: (i) strike–slip basins with mantle involvement; these can be thought of as "hot" basins, and (ii) strike–slip basins that are relatively thin-skinned; they can be regarded as "cold" basins (Fig. 6.9).

A more detailed breakdown of basins in strike–slip zones on the basis of the kinematic setting and geometry of bounding faults has also been proposed. The advantage of such a scheme is that individual phases of basin evolution can potentially be discriminated, but the disadvantage is that many basins show characteristics of more than one type. A slightly modified version of the scheme proposed by Nilsen and Sylvester (1995) is as follows:

1 *Fault bend basins* commonly develop at bends in the main strike–slip fault where localized extension takes place. A type example is the Ridge Basin, California in the San Andreas system. The Vienna Basin, Austria is another basin developed at a releasing bend, but within a compressional orogenic setting;
2 *overstep basins* form between the ends of two subparallel strike–slip fault segments, which may merge at depth into one single master fault. A type example is the Dead Sea Basin along the Gulf of Aqaba–Dead Sea Transform, Middle East;
3 *transrotational basins* form as triangular gaps between crustal blocks undergoing rotation about a subvertical

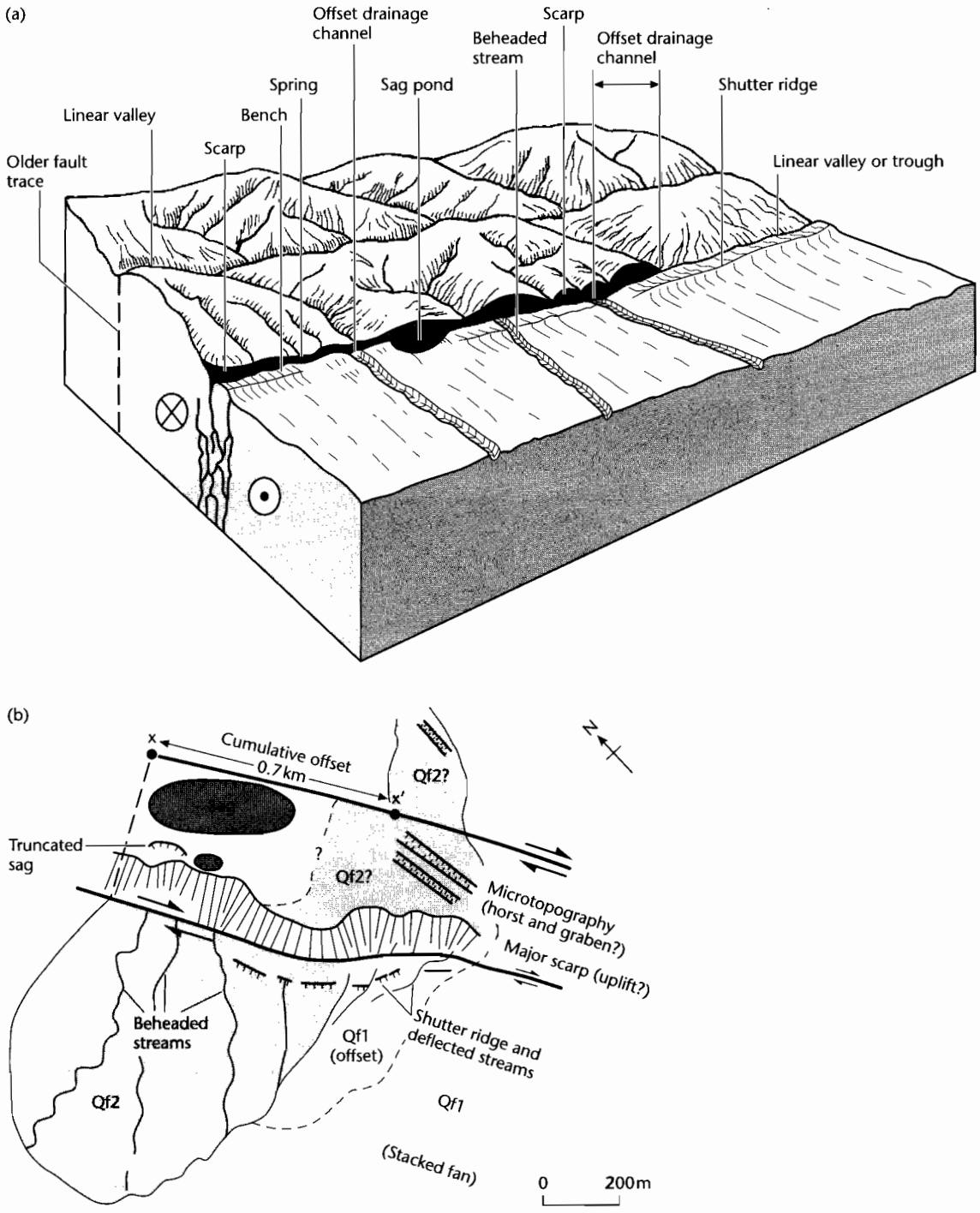

Fig. 6.8 Geomorphic features associated with strike–slip faults in the San Andreas system of California. (a) A linear trough along the fault, sag ponds, shutter ridges, offset ridges, and drainages, springs, scarps, and beheaded streams are typical geomorphic features indicative of strike–slip faulting. The older, abandoned fault trace displays analogous but erosionally degraded features. Modified from Wesson et al. (1975); (b) A large fan is offset from its catchment system, producing beheaded streams, shutter ridges, and extensional fault scarps. Modified from Keller et al. (1982). Reproduced courtesy of Blackwell Publishing Ltd.

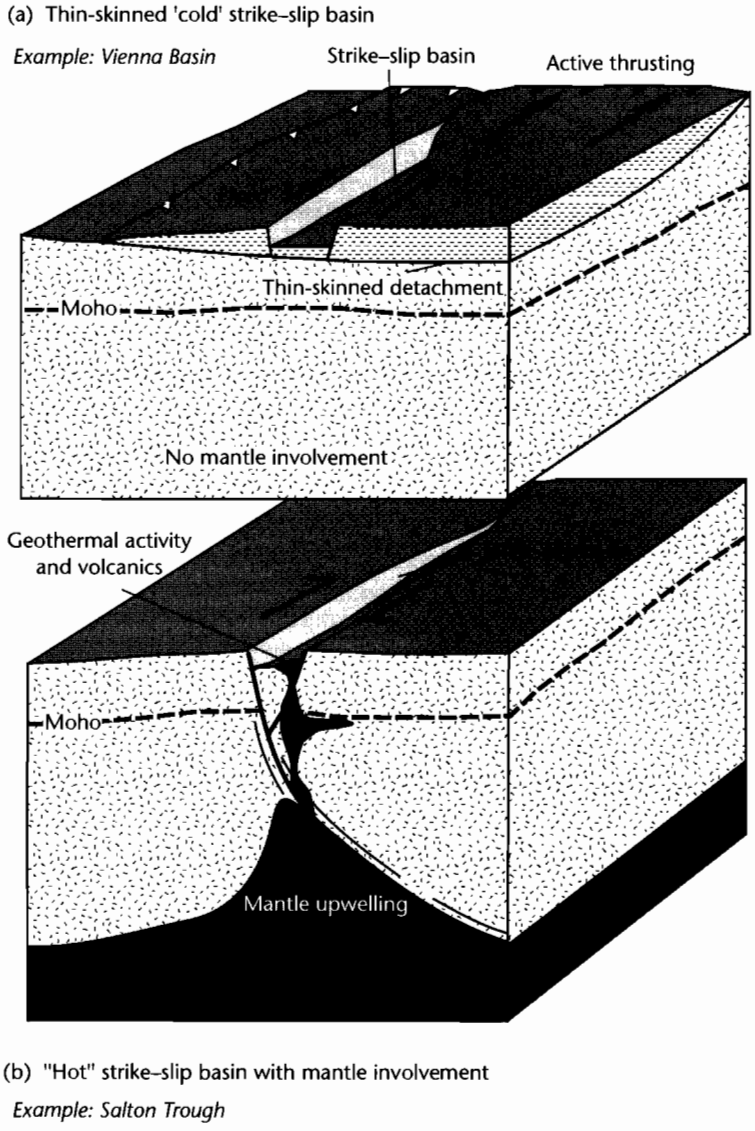

Fig. 6.9 Schematic diagram of broad classes of strike–slip basins. (a) Thin-skinned strike–slip basins, which are hypothermal; (b) Strike–slip basins with mantle involvement, which are hyperthermal.

axis. A type example is the Los Angeles Basin of southern California;

4 *transpressional basins* are elongate depressions parallel to the regional strike of folds and faults in zones of oblique convergence. These basins subside primarily by flexure caused by the supracrustal loads of compressional welts along the strike–slip zone. A type example is the Ventura Basin of California.

The sedimentary fill of strike–slip basins reflects their varied structural history, with highly asymmetrical longitudinal and transverse distribution of facies and abundant and complex unconformities. Subsidence rates

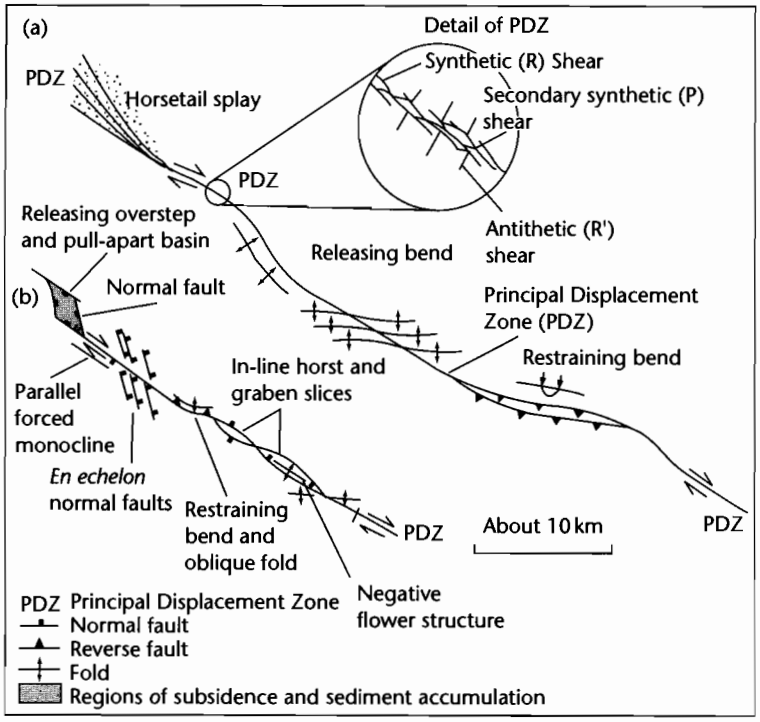

Fig. 6.10 (a) The plan view arrangement of structures associated with an idealized right-lateral (dextral) strike–slip fault; (b) Adaptation to a slightly divergent setting with the predominance of pull-aparts, *en echelon* normal faults, and graben slices within the PDZ.

are commonly extremely high, but subsidence may be relatively short-lived.

6.2 THE STRUCTURAL PATTERN OF STRIKE–SLIP FAULT SYSTEMS

6.2.1 Structural features of the principal displacement zone (PDZ)

Strike–slip faults are linear to curvilinear in plan view and generally possess a principal displacement zone (PDZ) along which the bulk of the shear strain is accommodated. However, changes in the orientation of the fault and/or the influences of the local geological fabric may cause deformation to extend beyond the PDZ into juxtaposed crustal blocks (Fig. 6.10). In cross-section, the principal displacement zones of large strike–slip faults are steeply inclined and commonly grade upwards from narrow, well-defined zones cutting igneous and metamorphic basement rocks at depth, to a braided, more diffuse deformation in the overlying sedimentary cover. This upward branching effect has led to the fault splays being christened "*flower structures*" or "*palm tree structures*" (Fig. 6.11). Some strike–slip faults link at depth with low-angle detachments, as occurs in foreland fold and thrust belts such as the Vienna Basin (Royden 1985) and in regions of regional extension such as the Basin and Range, USA (Cheadle et al. 1985). In the latter case, the Garlock Fault, a major strike–slip fault at a high angle to the San Andreas trend in California (Figs. 6.4, 6.6), appears to terminate downwards on a low angle surface situated in the middle crust (9–21 km depth) according to deep seismic reflection profiling (COCORP).

Figure 6.10 shows *en echelon* arrangements of faults and folds associated with strike–slip displacements. These structures are consistently arranged both in orientation and sense of strain with respect to the PDZ. They are

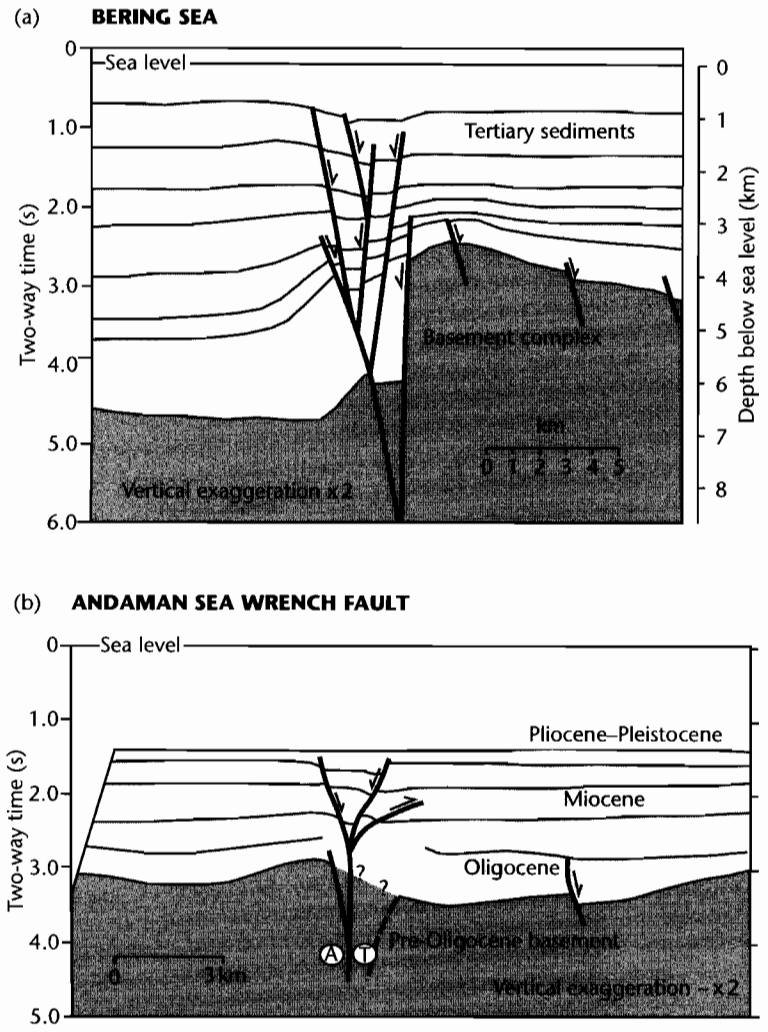

Fig. 6.11 The major characteristics in cross-sectional view of an idealized strike–slip fault. (a) Major fault zone in Bering Sea, (b) Andaman Sea wrench fault. Modified from Christie-Blick and Biddle (1985). A, displacement away from reader; T, displacement towards reader.

distinct from the *oversteps* between different segments of the principal displacement zone (§6.2.2). *En echelon* arrangements have been produced in model studies involving the deformation of clay, loose sand, or artificial materials (e.g., Riedel 1929; Cloos 1955; Harris and Cobbold 1984). Similar patterns have been observed in "natural" environments where alluvium has been affected by seismic disturbance, as in the 1975 earthquake in Imperial Valley, California (Sharp 1976). These experimental results and limited natural occurrences suggest that five sets of fractures are associated with a shear displacement (Fig. 6.12):

1 Synthetic strike–slip faults orientated at small angles to the regional shear couple. These are frequently termed *Riedel (R) shears*. The sense of offset is the same as that of the PDZ;
2 antithetic strike–slip faults orientated at high angles to the regional shear couple. These are termed *conjugate*

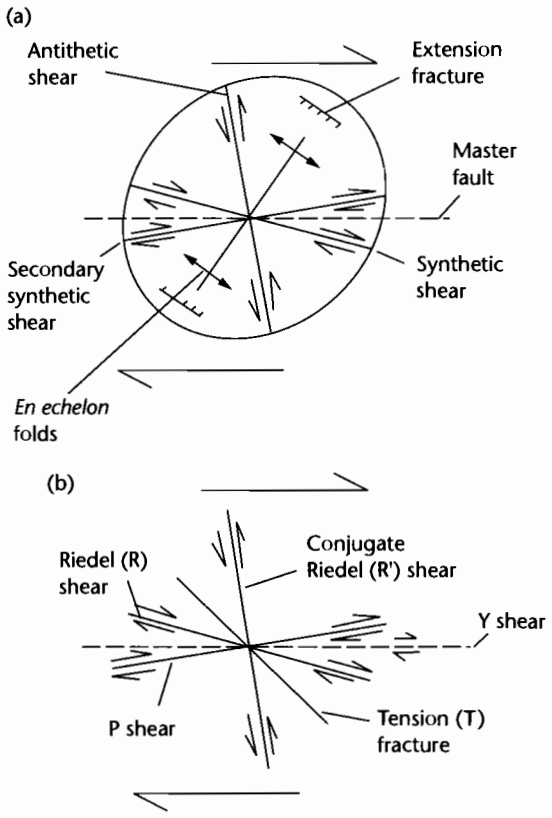

Fig. 6.12 The angular relations between structures that form in an idealized right-lateral simple shear, compiled from clay models and from geological examples (after Christie-Blick and Biddle 1985). (a) Fractures and folds superimposed on a strain ellipse for the overall deformation. Terminology of structures from Wilcox et al. (1973); (b) Riedel shear terminology modified from Tchalenko and Ambraseys (1970) and Bartlett et al. (1981).

Riedel shears or *R'*. The sense of offset is opposite to that of the PDZ;

3 secondary synthetic faults or *P-shears* with a sense of offset similar to that of the PDZ;
4 *tension fractures* related to extension in the strain ellipse;
5 faults parallel to the principal displacement zone and shear couple, or *Y-shears* of Bartlett et al. (1981).

En echelon folds develop with their axial traces parallel to the long axis of the strain ellipse, indicating shortening perpendicular to the extension demonstrated by the tension fractures (Fig. 6.12). Geological examples are invariably more complicated than the situation shown in figure 6.12, because the geological fabric influences fault orientations and also because faults and folds become rotated during progressive deformation so that the present fault configuration represents a cumulative picture over time. However, the idealized pattern is useful as a predictor of fault and fold occurrences if the regional shear direction is known, or, alternatively as a predictor of the latter where observations are possible on the resultant fracture and fold pattern.

The offset pattern on strike–slip faults in cross-section can be exceedingly complex. The sense of displacement may vary along one fault from horizon to horizon, and within a flower structure faults of opposite displacement occur together (Fig. 6.11). Additionally, a given fault in one cross-section may commonly switch in dip in another cross-section. These characteristics make strike–slip fault zones distinctive compared to regional extensional and contractional fault systems.

The precise structural pattern is controlled by a number of factors including (Christie-Blick and Biddle 1985): (i) convergent, divergent, or simple strike–slip (parallel) kinematics, (ii) magnitude of the displacement, (iii) material properties of the rocks and sedimentary infills in the deforming zone, and (iv) configuration of pre-existing structures giving a geological fabric.

(i) Convergent, divergent, and parallel kinematics

Convergent strike–slip causes the development of many reverse faults and *en echelon* folds. Depending on the obliquity of the strike–slip, this pattern may grade into a fold and thrust belt, as in the Western Transverse and Coast Ranges of California (Figs. 6.4, 6.6). Upward splaying flower structures have an overall antiformal structure caused by the net shortening. They are commonly known as *positive flower structures*. Folds are less well developed in divergent strike–slip settings, taking the form of flexures associated with extensional faulting. Flower structures take on an overall synformal structure in regions of net divergence, and are consequently known as *negative flower structures*. The Tekirdag Depression in the Marmara Sea, Turkey, situated along a restraining bend of the North Anatolian Fault, is situated in a broad negative flower structure (Okay et al. 1999) (Fig. 6.13).

The scale of the distribution of convergence or divergence varies from regional to local. For example, regional divergent strike–slip may take place where major fault

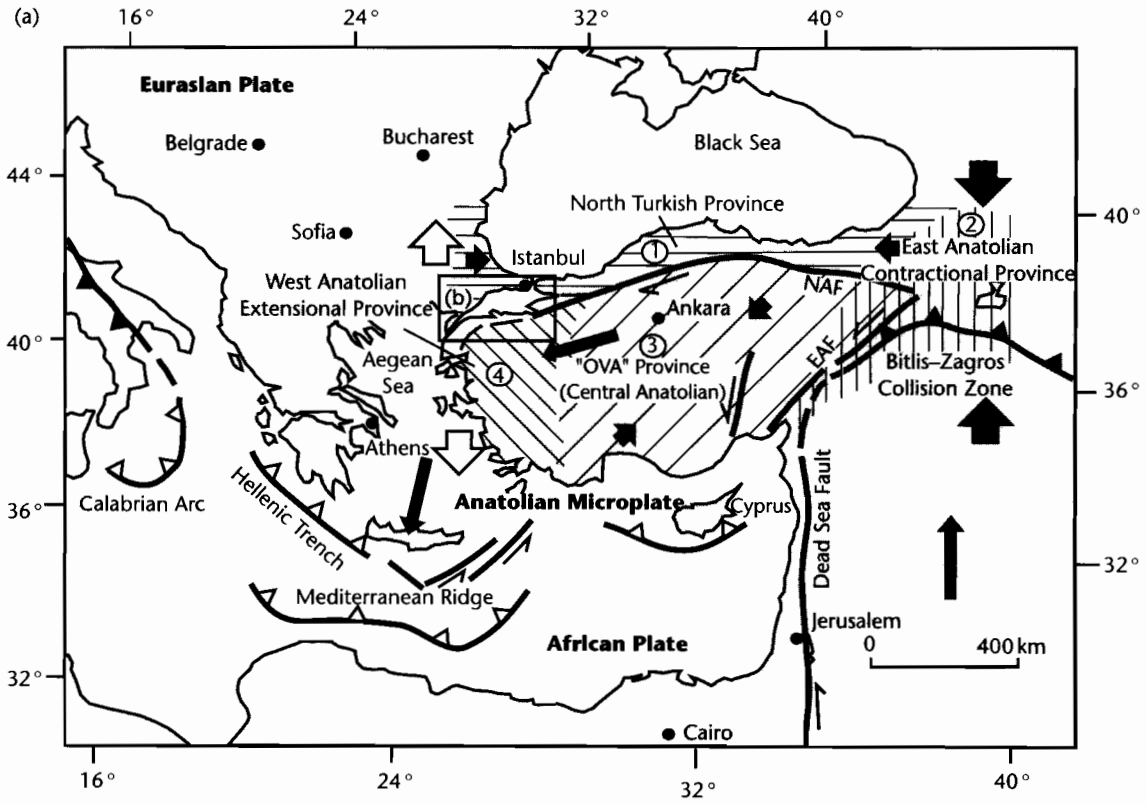
(a)
16°
24°
32°
40°
Eurasian Plate
Belgrade
Bucharest
Black Sea
44°
North Turkish Province
Sofia
Istanbul
East Anatolian
Contractional Province
West Anatolian
Extensional Province
(b)
NAF
Ankara
40°
Aegean
Sea
"OVA" Province
(Central Anatolian)
EAF
Bitlis–Zagros
Collision Zone
36°
Athens
Calabrian Arc
Hellenic Trench
Anatolian Microplate
Cyprus
Dead Sea Fault
32°
Mediterranean Ridge
Jerusalem
African Plate
0
400 km
Cairo
16°
24°
32°
40°

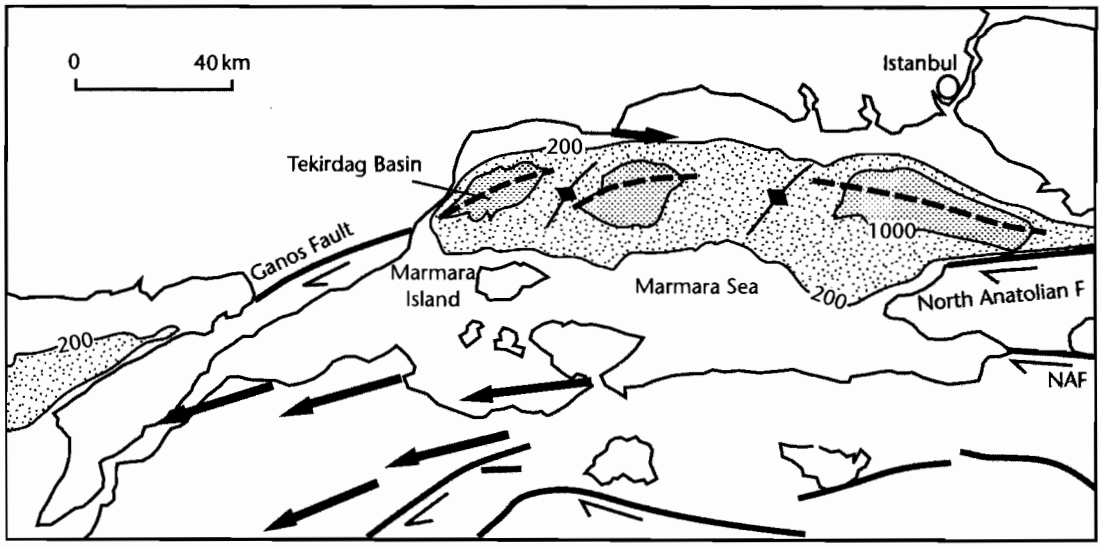
(b)
0
40 km
Istanbul
Tekirdag Basin
200
1000
Ganos Fault
Marmara
Island
Marmara Sea
200
North Anatolian F
200
NAF

strands are oblique to interplate slip vectors as in the Dead Sea Transform (Fig. 6.3). On a much more local scale, divergent strike–slip may take place at releasing fault oversteps and fault junctions. Divergent strike–slip faults also develop on a local scale where crustal blocks rotate between bounding wrench faults.

A detailed study of the rotations and oversteps associated with a strike–slip displacement following a recent earthquake was carried out by Terres and Sylvester (1981). The deformation of a recently ploughed carrot field in Imperial Valley following the earthquake of October 15, 1979 is shown in figure 6.5b. This very small-scale example shows many of the features predicted from model experiments with both extension and contraction occurring simultaneously. The topsoil broke up into elongate blocks along the furrows and these blocks moved relative to each other along conjugate Riedel shears (R') or antithetic shears. Extension occurred along the long axis of the strain ellipse and folding along the short axis. The elongate blocks delimited by shears, which Dewey (1982) has termed "*Riedel flakes*," show clockwise rotations in this example of right-lateral strike–slip. A much larger rotated block with dimensions of 20 km by 70 km, the Almacik flake along the North Anatolian Fault, Turkey, is also thought to be due to Riedel flaking (Sengör et al. 1985) (Fig. 6.14). Here, clockwise rotation of the tectonostratigraphic

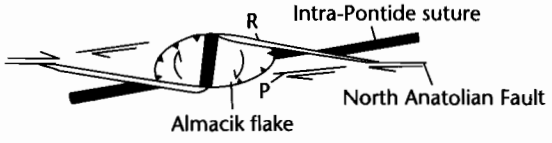

Fig. 6.14 Interpretation of the Almacik flake along the North Anatolian Fault in Turkey (Sengör et al. 1985), based on the idea of "Riedel flaking." R and P shears are shown.

domains of 110° has taken place since the initiation of faulting. The right-lateral strike–slip along the North Anatolian PDZ has produced families of thrusts, Riedel and P shears.

Rotations may also take place along straight segments of adjacent strike–slip faults, causing geometrical space problems. These space problems are resolved by gaps and overlaps occurring at fault block corners known as transrotational basins. Figure 6.15 (see also Fig. 6.5d) shows how regions of extension and contraction may alternate along the strike–slip fault.

(ii) Magnitude of the displacement

Laboratory experiments indicate that there is a sequential development of structural features in strike–slip zones (Tchalenko 1970 and Wilcox et al. 1973 for clay models, Bartlett et al. 1981 for rock samples under confining pressure). In the rock sample experiments, the zone of deformation first of all expands rapidly due to the development of folds and fractures. Weakening of the deforming zone soon, however, stabilizes the spread of the zone of deformation, and later structures are concentrated in a central core zone (Odonne and Vialon 1983). All early formed structures are rotated by later deformations, so their orientation is dependent on the magnitude of the displacement.

Some of the features observed in experiments can be found in natural occurrences, whereas other features are difficult to match. An increasing complexity from discontinuous faults and folds along low displacement boundaries to through-going PDZs along high displacement boundaries is commonly observed. Active fault systems that are accompanied by sedimentation may, however, be buried faster than they deform. In this way, the uppermost, younger sediments may record less deformation than the older stratigraphy.

Fig. 6.13 (a) Tectonics of the eastern Mediterranean. The four main tectonic regimes of Turkey (shown by numbers in circles) are caused by the post late Serravalian (*c.* 12 Ma) westward escape of the Anatolian block from the east Anatolian convergence zone onto the oceanic lithosphere of the eastern Mediterranean Sea (after Sengor et al. 1985). (1) Weakly active North Turkish province characterized by limited E–W shortening; (2) East Anatolian contractional province of N–S shortening, situated mostly to the east of the meeting point of the East Anatolian and North Anatolian strike–slip faults; (3) the Central Anatolian "Ova" province with NE–SW shortening and NW–SE extension, containing large, roughly equant-shaped complex basins termed "ovas"; (4) West Anatolian extensional province characterized by N–S extension. The arrows are roughly proportional to the magnitude of the total strain. EAF, East Anatolian Fault; NAF, North Anatolian Fault; (b) Detail of the Marmara Sea region along the North Anatolian Fault Zone (Okay et al. 1999), showing selected bathymetric contours. Fault plane solutions are from Taymaz et al. (1991). Arrows are displacement vectors derived from GPS using a fixed station at Istanbul (Straub and Kahle 1995). The Tekirdag Basin is located in a broad negative flower structure.

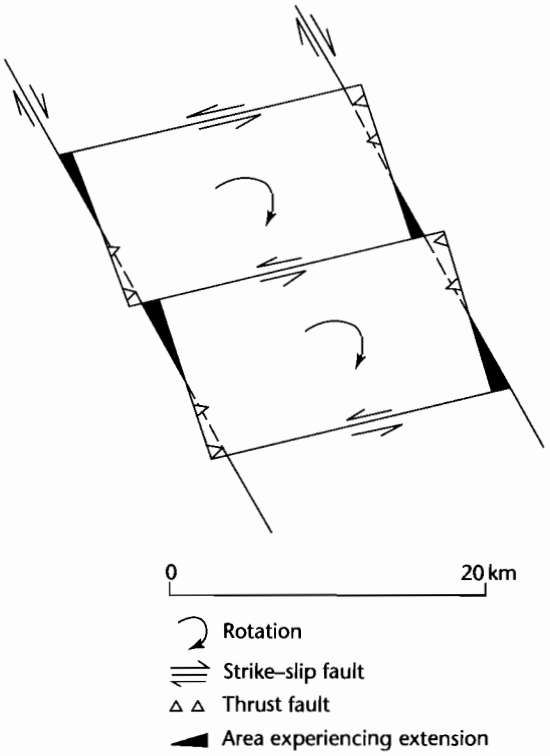

Fig. 6.15 Model of rotation of blocks near the intersection of the San Andreas and San Jacinto Faults, California, based on earthquake hypocentral locations and first motion studies (Dibblee 1977; Nicholson et al. 1985a, b). During a large earthquake, one of the bounding faults moves by right-lateral slip. Continued aseismic motion between the bounding faults is accommodated by clockwise rotations of small blocks and by minor left-lateral movements on faults defining these rotating blocks. Rotation causes overlaps (small reverse faults) and gaps (small normal faults) to form along the major bounding right-lateral faults. Viewed on a crustal scale, these rotating flakes would be detached from the underlying lower crust/mantle by thrust faults that would merge with the associated left-lateral strike–slip faults.

(iii) Material properties in the deforming zone

The lithologies of rocks in the strike–slip zone and the rates and pressure–temperature conditions of deformation all control the individual structural character of the fault zone. These factors vary from one strike–slip zone to another, but they also may vary in time within an individual strike–slip fault system. Deformation of different stratigraphic units, strain weakening, or strain hardening effects, uplift, and erosion or sedimentation and burial, or changes in heat flow related to crustal thinning and/or volcanism can all have significant effects on the evolution of the fault zone.

(iv) Pre-existing geological fabric

Continental strike–slip fault systems commonly intersect or make use of older heterogeneities. For example, the Great Basin, western USA underwent Laramide shortening (NE–SW trend), then two phases of extension, one related to backarc processes (axis of extension orientated NE–SW), the other to the development of a right-lateral megashear (change in extension direction to NW–SE). The right-lateral faults and, locally, conjugate left-lateral faults associated with this clockwise rotation in the extension direction may well be related to the existence of older crustal structures.

The Great Basin is an example of regional extension, so the strike–slip motion is taking place in a transtensile regime. The Rhine Graben of western Europe, however, originated in a background environment of continental collision north of the Alps in Late Eocene times. Early extensional faults in the Late Eocene–Oligocene were used as strike–slip faults in the Pliocene to Holocene (Illies 1977; Illies and Greiner 1978).

Pre-existing structures that significantly influence the location and orientation of folds and faults during strike–slip are termed "*essential*" structures. However, pre-existing structures that exert no control on later deformation are termed "*incidental*" (Christie-Blick and Biddle 1985, p.13).

6.2.2 Role of oversteps

In §6.1.2 the location of overstep basins between the tips of two subparallel strike–slip fault segments was introduced. An *overstep* or *stepover* is a structural discontinuity between two approximately parallel overlapping or underlapping faults. Oversteps are extremely important in determining the location of regions of subsidence and uplift along a strike–slip system. We consider a numerical model of basin development at an overstep in a later section (§6.3.3). There appear to be two basic types (Fig. 6.16):

- Oversteps along the strike of faults, that is, observed in plan view; faults are continuous in the down-dip direction;

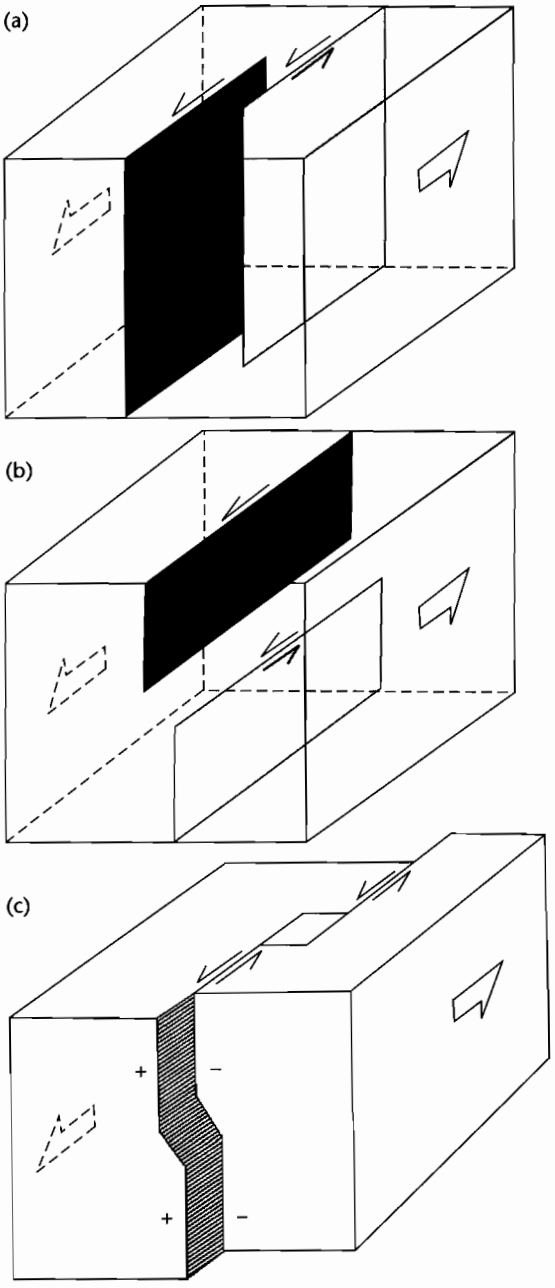

Fig. 6.16 Oversteps on strike–slip faults. (a) Along-strike oversteps in which faults are continuous in the down-dip direction; (b) Down-dip oversteps in which the faults are continuous in plan view; (c) Combination of along-strike and down-dip oversteps, with a pull-apart basin located at the along-strike overstep (after Aydin and Nur 1985).

- oversteps along the dip of faults, that is, observed in cross-section; faults are otherwise continuous in plan view.

Both types of overstep may occur along the same fault or fault zone. If the sense of an along-strike overstep is the same as the sense of fault slip, a *pull-apart basin* is formed (Aydin and Nur 1985). If, however, the sense of the overstep is opposite to that of fault slip, a *push-up range* is formed. Down-dip oversteps are probably as important as along-strike oversteps, but are more difficult to identify and map. Seismicity studies on active strike–slip faults such as the Calaveras Fault, California, show a distinct offset of the trends of hypocenters, breaking the fault into an upper segment (2–7 km depth) and a lower segment 2 km away (4–10 km depth). This suggests that a down-dip overstep is present (Reasenberg and Ellsworth 1982).

6.3 BASINS IN STRIKE–SLIP ZONES

In general, subsidence in strike–slip zones tends to occur where the deformation is accompanied by a component of divergence (Fig. 6.3), such as at bends and oversteps in the fault or in gaps between rotating flakes. Uplift, however, tends to occur where there is a component of convergence (Fig. 6.3), although flexure of an underlying block by an overriding block may cause subsidence. Uplift takes place at convergences of faults into a fault junction or at bends in fault traces. These zones of uplift provide sourcelands of detritus available to fill nearby basins. Bends, oversteps, and fault junctions associated predominantly with extension and subsidence are termed "*releasing*," whilst those associated with shortening and uplift are termed "*restraining*" (Crowell 1974). Parallel-sided basins in which oceanic crust occurs are termed *rhombo-chasms* (Carey 1976).

The causes of fault bends, oversteps, and junctions are varied. Some bends may result from pre-existing crustal heterogeneities, as in the case of strike–slip faults propagating along older extensional fractures. This appears to be the case in Jamaica (Mann et al. 1985), which lies entirely within a 200 km-wide seismic zone of left-lateral strike–slip deformation between the North American and Caribbean Plates. Extensional faults at the east of the Paleocene–Eocene Wagwater Rift Graben have been reactivated as reverse faults along a restraining bend in the Neogene strike–slip system. Other bends may be due to deformation of initially straight faults as a result of incompatible slip at a fault junction (e.g., the "big-bend"

of the San Andreas Fault, Figs. 6.4, 6.5), rotation of adjacent blocks (southern San Andreas Fault), or intersection of the fault with a zone of greater extensional strain (e.g., western end of North Anatolian Fault) or contractional strain (e.g., near junction of North Anatolian and East Anatolian Faults in eastern Turkey, Fig. 6.13).

Fault branching and oversteps may develop by a number of mechanisms including segmentation of curved fault traces, intersection of weak zones orientated obliquely to the direction of strike–slip and changes in stress fields caused by fault interaction. The precise reasons for the formation of oversteps and branches remains obscure (Aydin and Nur 1985).

Strike–slip basins may be *detached* and therefore thin-skinned. Examples are known from both areas of pronounced regional shortening such as the Vienna Basin and the St George Basin in the Bering Sea, Alaska, and in areas of regional extension such as the West Anatolian extensional province of Turkey and the Basin and Range of the USA.

6.3.1 Kinematic models for pull-apart basins

A number of kinematic models exist for the development of pull-apart basins (Fig. 6.17):

1 Overlap of side-stepping faults: The simplest model is based on pioneer field studies of active strike–slip basins such as the Dead Sea and the Hope Fault Zone in New Zealand. Discontinuous parallel fault segments which have a horizontal separation develop oversteps. As the master faults lengthen, producing more overlap, the basin lengthens while its width remains fixed by the original separation of the parallel master faults. This model has been widely applied to the San Andreas Fault system in the Gulf of California–Salton Trough area (Crowell 1974), and the Dead Sea Fault system (Garfunkel et al. 1981). This configuration of lengthening, parallel master faults has been used to simulate pull-apart development using elastic dislocation theory (Rodgers 1980) (see §6.3.3). This theory predicts that distinct changes occur in the strike–slip basin as the amount of overlap of the master faults increases. Specifically, when the overlap is about equal to the separation, the pull-apart develops two depocenters in regions of extension separated by a zone of secondary strike–slip faulting in the basement. As the overlap increases, the depocenters become more widely spaced and the intervening zone of strike–slip faulting broader. Although there are instances where field observations fit the theoretical elastic dislocation model rather well (e.g., Cariaco Basin, Venezuelan part of southern Caribbean, Schubert 1982), basins that are filled with sediment more rapidly than the upward propagation of faults from the basement may develop fault systems at strong variance to those predicted by elastic dislocation theory. The presence of two distinct depocenters associated with strain above each fault segment has rarely been observed.

2 Slip on divergent fault segments: Detailed field mapping of some active pull-aparts suggests that bounding strike–slip faults may be nonparallel (Freund 1971). If nonparallel, nonoverlapping faults are slightly divergent and connected by a short oblique segment, continued strike–slip may open up a basin along one side of the oblique fault and cause compression along the other side.

3 Nucleation on *en echelon* fractures or Riedel shears: Shear box experiments suggest that pull-apart basins may be structurally analogous to *en echelon* extensional fractures produced in clay materials. As deformation continues, the shear fractures join to form a pull-apart basin. A similar process of formation from rotated large scale tension gashes or Riedel shears has also been proposed.

4 Coalescence of adjacent pull-aparts into larger system: A worldwide compilation of the dimensions of a large number of pull-aparts suggests that there is a linear relation between the basin length (fault overlap) and the basin width (fault separation) (Aydin and Nur 1982). This scale dependence of pull-apart basins suggested that they are commonly three times as long as they are wide irrespective of their absolute size. This may be due to the coalescence of adjacent pull-aparts in a single larger basin with increasing offset, or to the formation of new fault strands parallel to existing ones.

5 Transform-normal extension: Markedly asymmetric, large strike–slip basins bounded by a transform segment on one side and subparallel normal faults on the other, may be due to transform–normal extension (Ben-Avraham and Zoback 1992). Examples of highly asymmetric basins are the Gulf of Elat (Dead Sea Transform) (Ben-Avraham 1985) and the Cariaco Basin (offshore Venezuela). In the Gulf of Elat (Fig. 6.18), the sense of asymmetry switches along the PDZ, the deeper side of

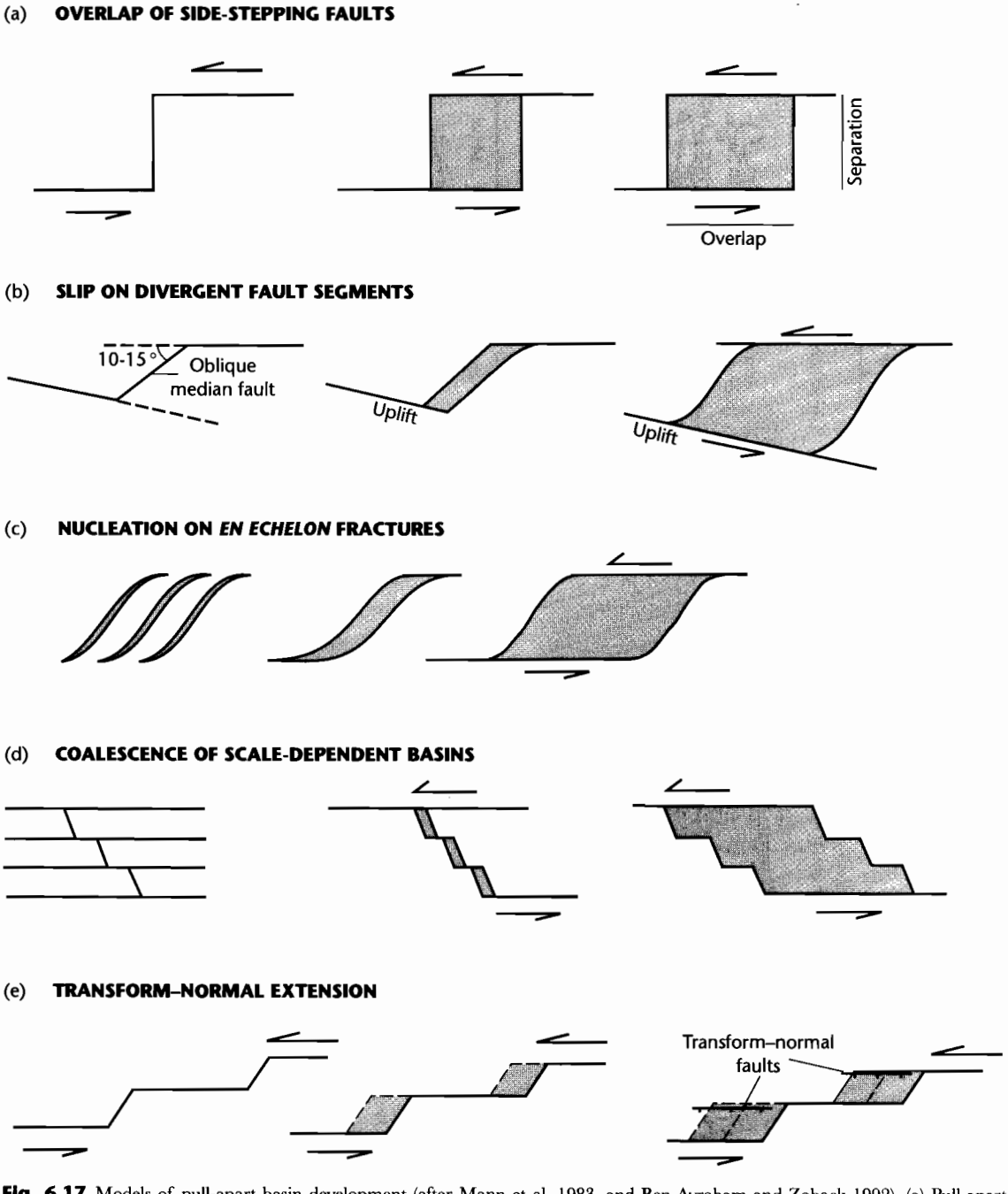

Fig. 6.17 Models of pull-apart basin development (after Mann et al. 1983, and Ben-Avraham and Zoback 1992). (a) Pull-apart opening between left-stepping and sinistral master strike–slip faults. Fault separation and basin width remain constant through time whereas fault overlap and basin length increase with the amount of strike–slip displacement. The elastic dislocation model of Rodgers (1980) applies to this kind of pull-apart mechanism; (b) Pull-apart opening across an oblique median fault and nonparallel master faults. Note that compression and uplift occur on one side of the pull-apart while an extensional "gap" develops on the other; (c) Pull-apart formation by nucleation from extensional fractures, based on shear box experiments (Koide and Bhattacharji 1977); (d) Pull-apart formation by coalescence of small scale-similar sub-basins, as suggested by Aydin and Nur (1982). This allows the widening of pull-aparts with increased offset, in contrast to (a); (e) Pull-apart basin formation caused by simultaneous strike–slip motion on a transform fault and transform–normal extension (after Ben-Avraham and Zoback 1992). The pull-aparts are markedly asymmetric towards the transform fault.

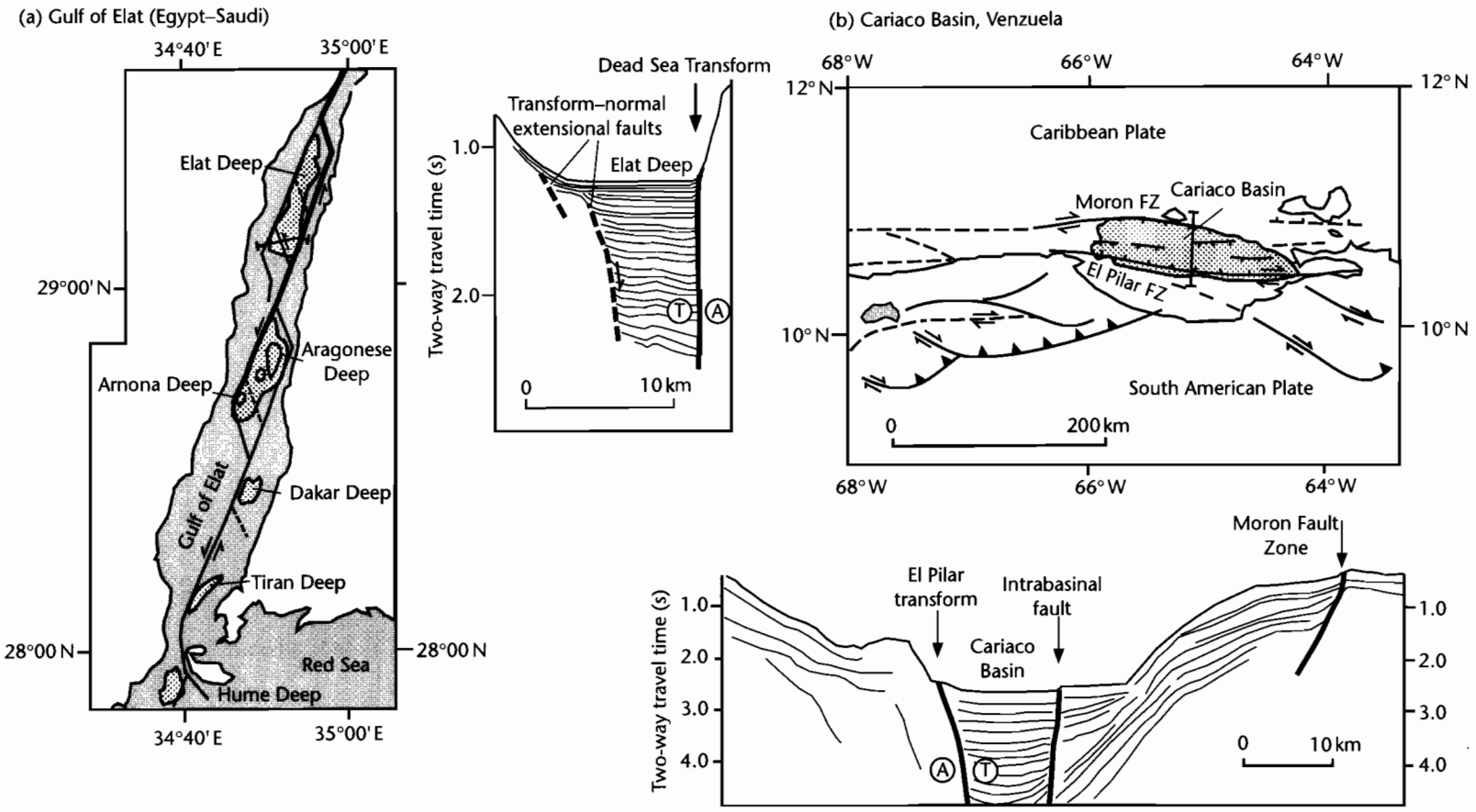

Fig. 6.18 (a) Bathymetry and structure of the Gulf of Elat showing segments of the Dead Sea Transform and location of main topographic depressions. Inset shows cross-sectional geometry across the Elat Deep derived from seismic reflection surveys. Asymmetry of the basin-fill is towards the transform fault; (b) Tectonic map and seismic profile across Cariaco Basin, northern Venezuela (Schubert 1982), showing basin asymmetry towards El Pilar Transform. A, displacement away from reader; T, displacement toward reader. Modified from Ben-Avraham and Zoback (1992).

the sub-basin always being located against the strike–slip Dead Sea Transform, with the shallower flank adjacent to normal faults. This suggests that subsidence occurs due to extension approximately normal to the transform at the same time as strike–slip displacement is taking place, in contrast with kinematic models of deformation in strike–slip zones where extension and compression directions are at 30–45° to the strike–slip fault plane (Fig. 6.12). This style of deformation may be due to the weakness of strike–slip faults (see also §6.3.3). A model of stress orientation close to weak transform faults embedded in a strong crust (Zoback et al. 1987) suggests that far-field transtensional stresses cause fault-normal extension, and transpressional stresses cause fault-normal compression.

6.3.2 Continuum development from a releasing bend: evolutionary sequence of a pull-apart basin

Analysis of neotectonic pull-apart basins in their embryonic stage suggests that they are associated with: (i) releasing bend geometries, in which master faults do not overlap but are connected by oblique median strike–slip faults, and (ii) nonparallel master faults (see also (1) and (2) above). Gentle restraining bends appear to produce narrow *spindle-shaped* pull-aparts like the Clonard Basin, Haiti at the left-step in the Enriquillo–Plantain Garden Fault Zone. In contrast, sharp restraining bends produce multiple, staggered pull-aparts as in the Salton Trough of California. Since embryonic pull-aparts appear to occur on releasing bends of through-going faults, they are unlikely to be analogous to the tension gashes or Riedel shears produced in shear box experiments (see (3) above).

Continued offset produces basin shapes known as "*lazy S*" (between sinistral faults) and "*lazy Z*" (between dextral faults) (Mann et al. 1983) (Fig. 6.19), representing a transitional stage between spindle-shaped basins between master faults with no overlap and rhomboidal basins between overlapping master faults. S- and Z-shaped pull-aparts are particularly common where the master faults are widely separated (>10 km) and their strikes are nonparallel. The Death Valley Basin, California has a pronounced Z-shape.

Lengthening of the S- or Z-shaped basins produces rhomb-shaped pull-aparts. Length to width ratios (overlap to separation) increase by this process because the separation remains fixed by the width of the releasing bend. Rhomboidal pull aparts are characterized by overlapping master faults and deep depocentres at the ends of the pull apart basin, separated by a shallow sill(s). The Cariaco Basin of the Venezuelan Borderlands is a good example, with two subcircular deeps in excess of 1400 m and a shallow sill at 900 m. Multiple deeps may be arranged diagonally across the rhomboidal pull-apart, as is the case in the Gulf of Aqaba in the northern Red Sea, the deepest segment of the sinistral Dead Sea Fault System (Ben-Avraham et al. 1979). The rapid subsidence between the overlapping master faults generally greatly exceeds sedimentation, leading to deep marine or lacustrine environments. The presence of prominent depocenters at the ends of rhomboidal pull-aparts does not support the mechanism of simple extension between overlapped master faults (see (1) above), but is predicted by the elastic dislocation model (Rodgers 1980). An alternative view is that the depocenters may in fact be smaller pull-aparts in the basin floor of the larger pull-apart, that is, the rhomboidal basin is in a coalesced stage of development (see (4) above).

With continued offset, rhomboidal pull aparts may develop into narrow oceanic basins where the length (overlap) greatly exceeds the basin width (separation). The Cayman Trough along the boundary between the Caribbean and North American Plates is a type example. The large length/width ratio suggests that coalescence is unimportant at this stage.

6.3.3 Numerical modeling of pull-apart basins

A number of quantitative approaches are possible to the formation of basins in strike–slip zones, involving a basal shear driving displacement on faults cutting the upper crust, or the transmission of far-field stress through the elastic upper crust. These two mechanisms of stress transfer may not be easily discriminated from surface displacement fields recognized in geomorphic and geodetic studies (Gomberg and Ellis 1994).

The *en echelon* faults typical of strike–slip zones can be modeled as surfaces of discontinuity that produce a neighboring displacement field using dislocation theory, but with no interaction between the faults (Rodgers 1980) (Fig. 6.20b). The faults can also be viewed as large-scale fractures that interact to produce a local stress field (Segall and Pollard 1980). Two-dimensional plane stress models for pull-apart basins such as the latter calculate the strain around two *en echelon* fault tips in an elastic

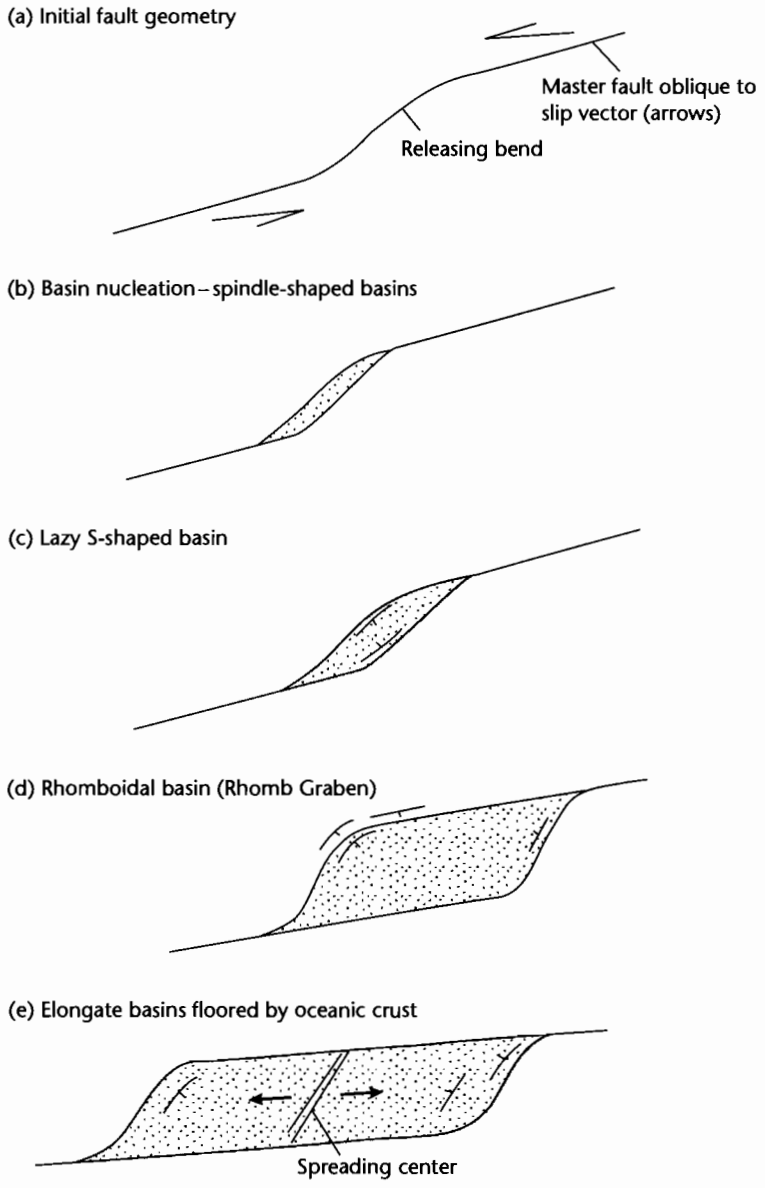

Fig. 6.19 Continuum model of pull-apart development, after Mann et al. (1983). (a) Pull-apart begins life on a releasing fault bend. The size of the bend controls the pull-apart basin width; (b) Spindle-shaped basin. Continued offset produces lazy S-shaped basin (c), then a rhomb-shaped basin (d), then finally a long, elongate trough floored with oceanic crust (e). Most pull-aparts do not reach the stage represented by (e). Instead they tend to be terminated after the basin length has reached about three times the original width of the releasing bend (or fault separation).

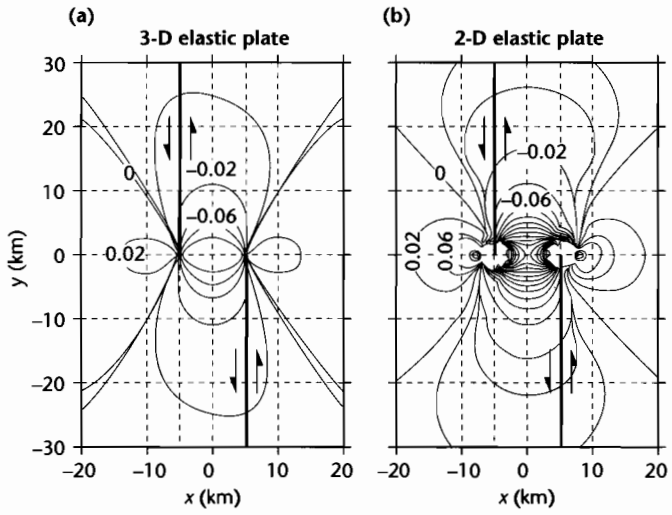

Fig. 6.20 Comparison between 2-D and 3-D plane stress models for pull-apart basins (after Katzman et al. 1995). A sinistral displacement discontinuity of 1 km is defined across two *en echelon* strike–slip faults. Vertical displacement is shown for (a) a 3-D elastic plate and (b) a 2-D thin elastic plate with elastic thicknesses of 15 km. Contour interval 0.02 km, Poisson's ratio 0.25 and Young's modulus 75 GPa. The 2-D plane stress model produces unrealistic deformation around the fault tips. Reproduced courtesy of American Geophysical Union.

medium. The 2-D plane stress model produces unrealistic, deep depocenters adjacent to the fault tips characterized by very high subsidence rates, together with unrealistic vertical uplifts above the fault tip. This results from the plane stress approximation, which does not allow stresses to develop in the vertical direction within the plate; consequently, stresses cannot resist deformation near the fault tips. The advantage of a 3-D model is that vertical stresses near the fault tips resist deformation, which dampens subsidence and uplift patterns in this region (Fig. 6.20a).

In the 3-D linear elastic model proposed by Katzman et al. (1995), the deformation is driven by a shear from below to simulate relative plate motion. The upper crust (*c.* 15 km) is penetrated fully by faults, that detach above the weak lower crust. Pull-apart basins develop close to two *en echelon* vertical faults 150 km long, spaced 10 km apart, with 0–20 km overlap (Fig. 6.21). The shear zone at the base of the plate is allowed to vary between 10 and 40 km. Two geometrical factors have important effects on pull-apart basin development:

1 *Shear zone width*: the basal shear causes slip to taper towards the fault tips, the rate of tapering decreasing with wider shear zones. As the shear zone width increases, the basin widens, lengthens and becomes shallower. Although the surface deformation varies strongly as a function of the shear zone width, the necking profiles in cross-section do not significantly vary.

2 *Fault overlap*: full graben develop between the overlapping faults over the entire overlap zone, becoming half-graben just outside the overlapping zone. Uplift decreases with the amount of overlap, reducing to zero at an overlap of *c.* 20 km. Less overlap causes greater rotation about a vertical axis.

The Dead Sea Basin is an ideal test for this 3-D numerical model. It is located along the left-lateral Dead Sea Transform at the plate boundary between the African and Arabian Plates (Garfunkel et al. 1981; Aydin and Nur 1982). The basin is narrow (*c.* 7–18 km), deep (*c.* 10 km), roughly symmetric, and extends along the strike of the bounding faults for 132 km (Fig. 6.22). Gravity and seismic reflection data (ten Brink and Ben-Avraham 1989) show that the Moho is not elevated beneath the basin. It is therefore thought to be uncompensated isostatically (as you would expect from the *c.* 10 km wavelength – see §2.3.3). The flanks of the basin are not topographically elevated compared to the regional

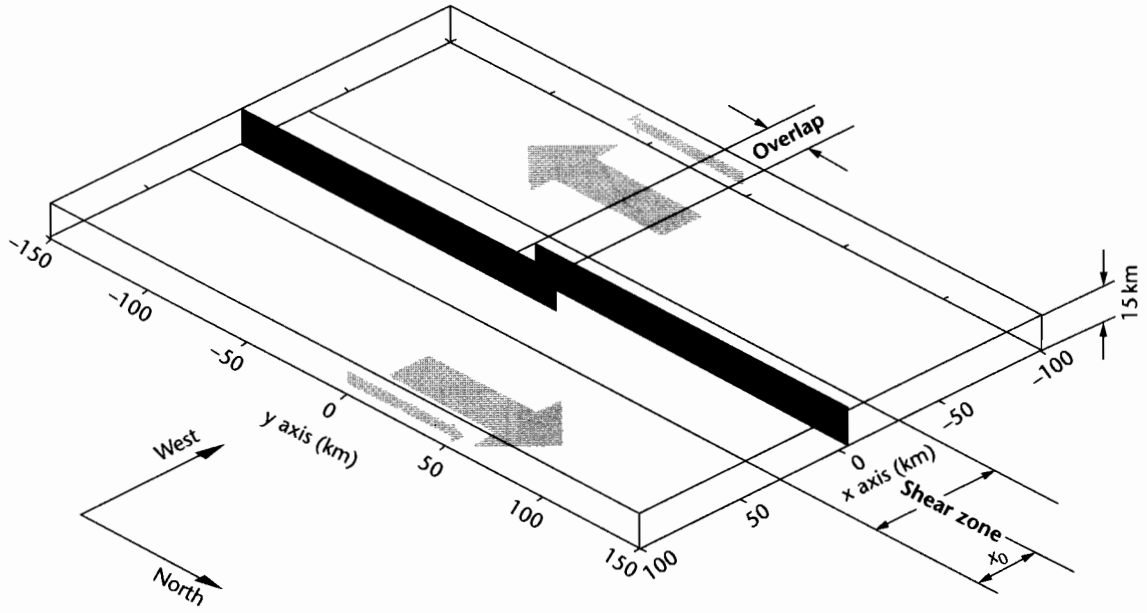

Fig. 6.21 Three-D block diagram showing the set up for the numerical pull-apart basin model (Katzman et al. 1995). Shaded planes define zones of weakness having zero shear strength (faults). Shaded arrows indicate the displacements defined as boundary conditions. The base of the model in the vicinity of the faults (within the shear zone) is stress free and thus freely deforming. The total width of the shear zone, $2x_0$, and the overlap distance between the fault segments, are varied in the model. Reproduced courtesy of American Geophysical Union.

elevation. The Dead Sea Basin is subsiding over a wide area, over several tens of kilometers in length. The extent of the basin subsidence is in harmony with the model predictions using 20–40 km-wide shear zones. However, the symmetric full-graben nature of the basin over a 50 km N–S distance, and the lack of topographic uplifts suggest that fault overlap must be greater than 20 km (twice the fault spacing). Katzman et al. (1995) suggested that the overlap distance increased during basin development.

6.3.4 Application of uniform extension model to pull-apart basins

The local extension in pull-apart basins causes very rapid subsidence and sediment accumulation, over 10 km of sediments accumulating in a period of less than 5 Myr in some examples such as the Miocene Ridge Basin of California (Link and Osborne 1978). The subsidence can be approximated by a model of lithospheric extension (McKenzie 1978a, §3.4.1), in which fault-controlled subsidence is followed by a thermal subsidence phase. Late Paleozoic pull-apart basins of eastern Canada (such as the 100 × 200 km Magdalen Basin, Gulf of St Lawrence area) are thought to have undergone a rift, then thermal subsidence history (Bradley 1983). However, the small size of pull-aparts implies that lateral temperature gradients must be large. Lateral heat conduction to the basin walls becomes an important source of heat loss, the narrower the basin the greater the cooling. The critical basin width below which lateral heat loss to the sides becomes important appears to be about 100 km (Steckler 1981) to 250 km (Cochran 1983). In comparison, most strike–slip basins are 10–20 km in width. Since narrow basins cool rapidly during extension, the subsidence is greater than predicted for the rift stage by the uniform extension model (§3.4.1). Rapid early subsidence related to lateral heat loss may help to explain the sediment starvation and deep bathymetries characteristic of the early

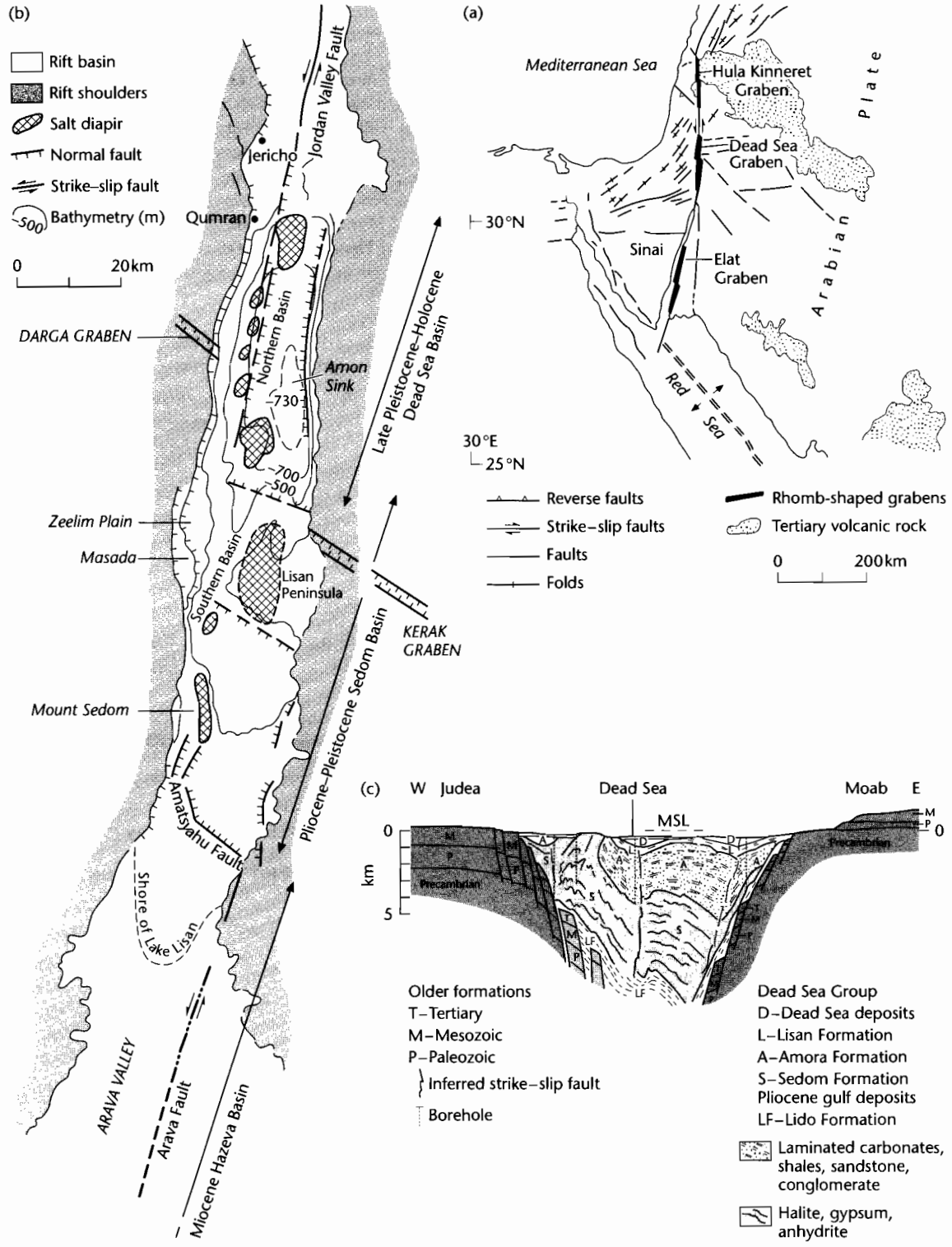

Fig. 6.22 (a) Location of Dead Sea Basin; (b) Structural interpretation, showing main faults, basins, and salt diapirs; (c) Cross-section of Dead Sea Basin between Mount Sedom and Moab. After ten Brink et al. (1993) and Katzman et al. (1995).

phases of pull-apart basin development. The subsequent postrift thermal subsidence should be correspondingly less.

Pitman and Andrews (1985) studied the subsidence history of small pull-aparts typical of the San Andreas zone of California. Here, thermal history and seismic data and geological studies (e.g., Atwater 1970) suggest an anomalously thin lithosphere in the mid to late Tertiary. In their model, the lithosphere was successively rifted then cooled over small time steps of 0.05 Myr to simulate the process of syn–rift heat loss (see also §3.5.3). For a basin filled with water only, the results of the model for a point in the center of the basin are shown in Figure 6.23a. The rapid initial subsidence is caused by faulting during crustal thinning combined with lateral heat loss to the basin walls. This steep curve flattens abruptly as extension terminates and the remaining subsidence is attributed to cooling only. Clearly, the initial basin width has a major influence on the subsidence history, the narrowest basins losing heat most rapidly to the sides and therefore subsiding both at a greater rate and with a greater magnitude than wider basins.

If the basin is kept at all times full to the brim, the subsidence must increase due to isostasy by a factor related to the different densities of water and infilling sediment $[(\rho_m - \rho_w)/(\rho_m - \rho_s)]$. Pitman and Andrews (1985) suggested that in the early stages of basin development, the sediment supply rate from uplifting and eroding catchments will not keep pace with tectonic subsidence, thereby explaining the starved youthful stages of many pull-apart basins. The basin should gradually fill as the subsidence rate slackens, eventually filling completely some 5 Myr after the start of rifting (Fig. 6.23b). The Tekirdag Depression along the North Anatolian Fault has been active in the Pliocene–Quaternary and has a basin

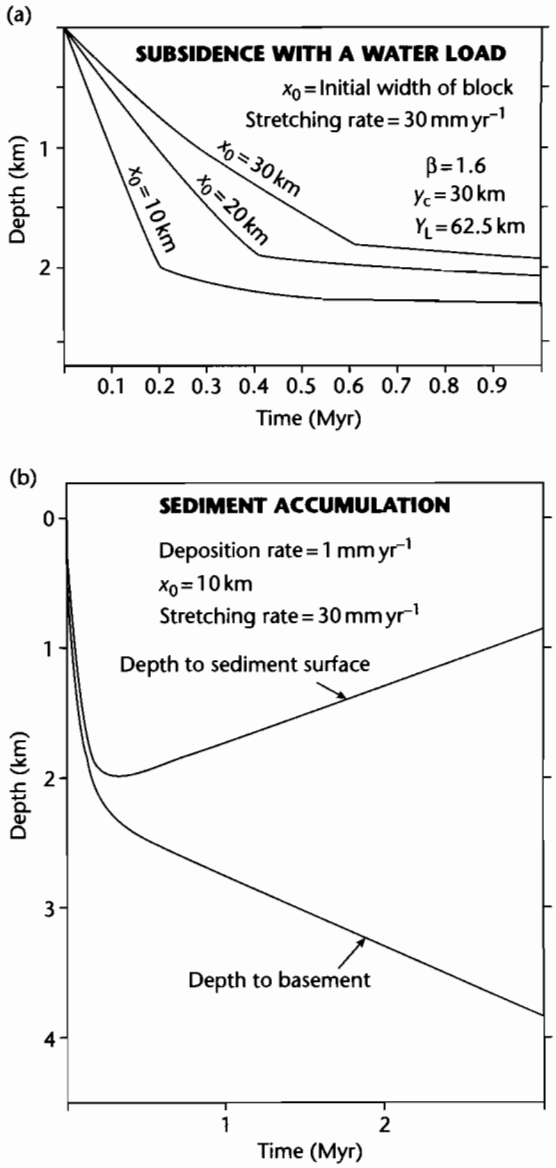

Fig. 6.23 (a) Subsidence as a function of time for basins experiencing lateral heat loss in addition to vertical conduction. Three subsidence curves are shown for three initial widths of zones of stretching (10, 20, and 30 km) for a point in the centre of the basin. The initial lithospheric thickness is 62.5 km. The infilling medium is assumed to be water. The crustal blocks are stretched at 30 mm yr^{-1} up to a stretch factor of 1.6. The curves comprise two segments. The initial steep segment represents subsidence due to lateral heat loss as well as crustal stretching. The flatter later segment represents subsidence due to the remaining thermal contraction. The total subsidence and the time history of subsidence are both influenced by the initial width of the zone of stretching between unstretched basin walls; (b) The depth to basement and the depth to the sediment surface in a narrow (initially 10 km-wide) basin characterized by lateral heat loss where the rate of sediment supply is restricted to 1 mm yr^{-1}. Local (Airy) isostasy is assumed throughout in compensating the depth to basement for the sediment load. The early history of the basin is marked by deep water sedimentation and several million years elapse before the sediment surface approaches sea level. Such a stratigraphic evolution is found, for example, in the Ridge Basin of California. After Pitman and Andrews (1985).

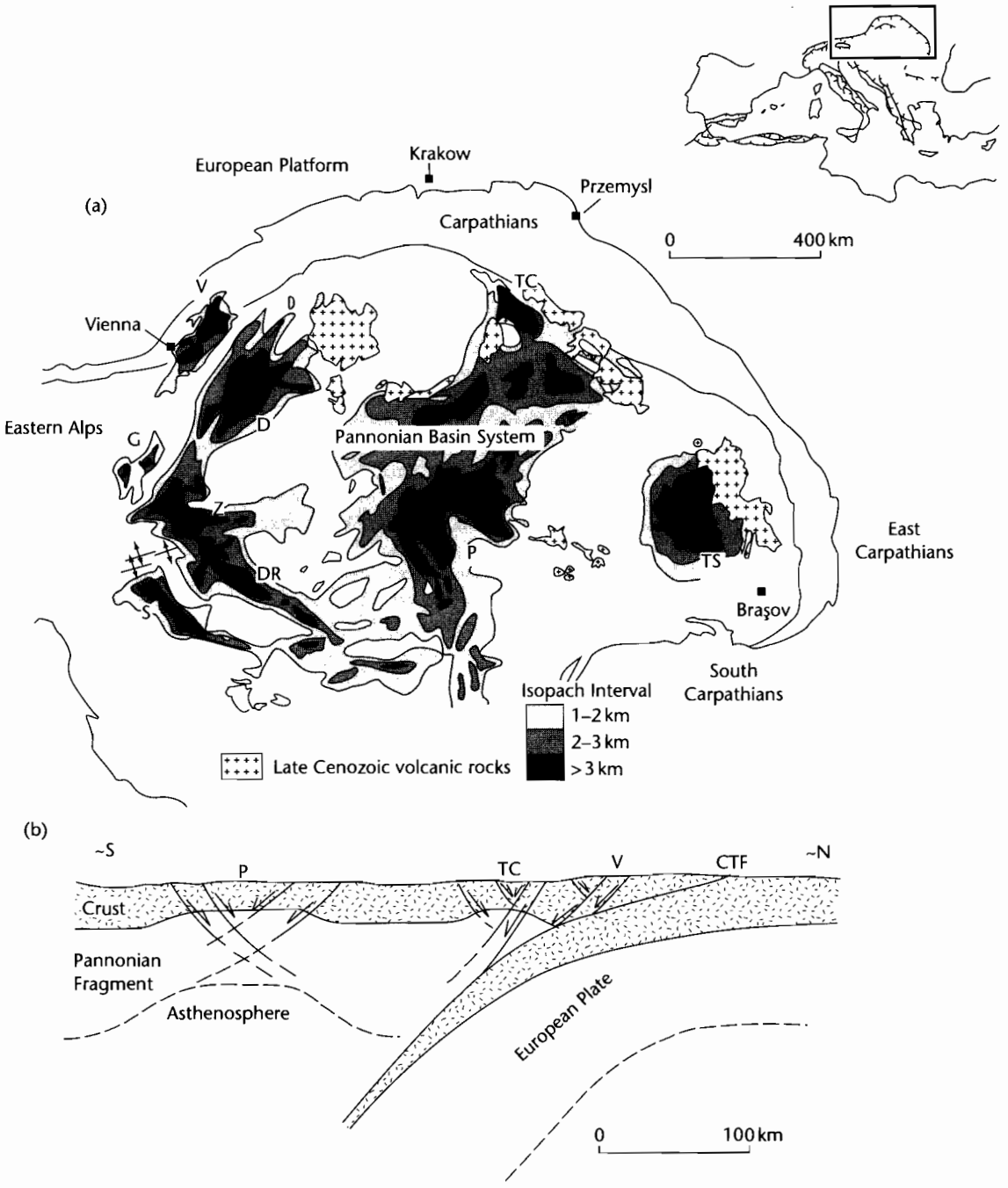

Fig. 6.24 Map (a) and schematic cross-section (b) to show the relationship between the Vienna Basin to other basins in the Carpathian–Pannonian system. The Vienna Basin is situated at a left step (releasing bend) in a sinistral strike–slip system accommodating relative movement between active and inactive nappes in the Alpine–Carpathian orogenic system. The Vienna and Transcarpathian Basins are located on the leading (thin) edge of the Pannonian lithosphere and above the deflected European Plate. The Pannonian Basin, however, is located entirely on the Pannonian lithosphere where it overlies asthenosphere. Extension in the Pannonian Basin therefore involves mantle and the basin is consequently "hot" compared to the "cool" Vienna Basin (Royden 1985). CTF, Carpathian Thrust Front; V, Vienna Basin; P, Pannonian Basin; TC, Transcarpathian Basin; TS, Transylvanian Basin; S, Sava Basin; DR, Drava Basin; D, Danube Basin; G, Graz Basin; Z, Zala Basin.

floor at maximum depths of 1150 m, suggesting that basin subsidence has far outstripped sediment supply for the last <4 Myr (Okay et al. 1999). The Ridge Basin of California was initiated in the Late Miocene and was initially occupied by a deep marine embayment before continental conditions prevailed in the Pliocene (Link and Osborne 1978). These two examples therefore support the idea of early underfilled stages in pull-apart basins caused by high subsidence rates.

6.3.5 Detached pull-apart basins in regions of lithospheric compression

It has previously been observed that the common block rotations in zones of strike–slip deformation require a detachment beneath the brittle upper crust. The stretching of the upper crust without associated mantle upwelling is suggested by the generally low heat flows of many strike–slip zones. The narrowness of strike–slip basins, and of the topographic features associated with strike–slip deformation, indicate that they are essentially uncompensated isostatically. We refer to such cases as thin-skinned strike–slip basins. Thin-skinned strike–slip basins should exhibit a distinctive subsidence and thermal history compared to basins involving mantle upwelling. Detachments beneath the upper crust may be related to lithospheric extension or to lithospheric convergence. The Vienna Basin of Austria is an example of the latter.

The 200 km by 60 km Vienna Basin contains up to 6 km of Miocene sedimentary rocks and formed adjacent to the coeval Carpathian thrust belt. The Vienna Basin is an excellent example of a rhombohedral pull-apart that developed on top of the allochthonous thrust terranes of the Alpine–Carpathian system in a background environment of lithospheric shortening (Fig. 6.24). The NE–SW trending major fault systems active during sedimentation in the Vienna Basin do not significantly disrupt the underlying autochthonous cover rocks of the European Plate and appear to pass into flat detachments using older thrust planes (Royden 1985).

An important observation in explaining the Vienna Basin is that the thrust sheets west of the Vienna Basin became fixed at the end of the early Miocene whilst thrusting continued east of the basin (Fig. 6.24). This relative displacement requires either: (i) sinistral bending of the thrust belt near the Vienna Basin, or the preferred case, (ii) left-slip along N or NE striking faults within the thrust belt. Thus, the Vienna Basin can be viewed as a result of diachronous thrusting in a region of oblique convergence.

If the Vienna Basin is essentially thin-skinned (<10 km), it has considerable implications for the subsidence and thermal history of this variety of pull apart basin. Since the extension is thin-skinned, the lower crust and mantle should be unaffected by the extension near the surface. This is supported by a number of lines of evidence: (i) the uniformly low heat flows of 45–60 $mW\,m^{-2}$ through the Vienna Basin and adjacent regions (Cermak 1979; Royden 1985), (ii) subsidence curves derived from boreholes show no recognizable thermal subsidence phase, and (iii) low thermal gradients and low levels of organic maturity. This contrasts strongly with strike–slip basins with involvement of the lower crust and mantle lithosphere. Such basins, like the neighboring Pannonian Basin (Fig. 6.24), have much higher geothermal gradients and correspondingly high levels of organic maturity.

Basins such as the Vienna Basin with shallow detachments may be typical of zones close to the thrust front. As the distance from the thrust front increases, extension may reach progressively greater depths, ultimately affecting the entire lithosphere. This may explain why the Pannonian Basin situated far to the south of the arcuate Carpathian suture involves mantle extension (Fig. 6.24) and elevated heat flows, whereas the Vienna Basin located within the Carpathian system is extremely thin-skinned and consequently cool, with no postextension thermal subsidence.

PART

3 *The sedimentary basin-fill*

CHAPTER 7

The sediment routing system

Earth felt the wound, and Nature from her seat Sighing through all her works gave signs of woe That all was lost.

(JOHN MILTON, *PARADISE LOST* (1667))

SUMMARY

The sediment routing system is the integrated geomorphic system involving sediment liberation, transport, and deposition. Understanding this complex system in terms of its physical laws and response times is important for the evaluation of sediment supply to sedimentary basins, which controls the stratigraphic architecture of the basin-fill (Chapter 8).

Pristine rock exposed at the Earth's surface is subject to physical and chemical weathering. The regolith is the weathering mantle between pristine bedrock and the land surface. The thickness of the regolith is principally dependent on two rate effects: the rate of bedrock weathering, and the rate of removal by erosion, both of which are strongly controlled by climatic and topographic factors. Regolith production rates are believed to decay exponentially with depth, and estimates from cosmogenic radionuclide analysis indicate bedrock to regolith conversion rates of $10–50 \times 10^{-6}\,m\,yr^{-1}$.

The flux connecting land and ocean reservoirs in the hydrological cycle is termed run-off. It varies strongly depending on climatic variables. Run-off transports sediment from source regions to sinks. The sediment yield is the total sediment discharge of the catchment, measured at the river mouth, divided by its area, and therefore has the units of a mass flux. Sediment yields can be estimated from the infilling rate of artificial reservoirs and lakes, and by calculating the volume of dated sediment in offshore depocenters. Global patterns of sediment yield show an arc of very high yields from Japan to the mouth of the Indus, where high rates of precipitation combined with young tectonic topography are found. There have been many attempts to identify the principal controls on sediment yield, such as rate of precipitation, or topographic variables such as elevation and relief. Recent analyses point to different controls in high relief, tectonically active regions *versus* low relief, tectonically inactive regions.

Chemical weathering also results in the release of ions in solution, which are transported away as a dissolved load, measured as total dissolved solids (TDS). The type of bedrock undergoing chemical weathering, and the climatic and topographic influences on precipitation, weathering, and evaporation, are crucial to understanding the amount and constituents of the dissolved load. The global average of solute load is roughly one-fifth of the global average of suspended particulate load, but the ratio varies strongly. Rivers in mountainous terrains have high particulate sediment yields, whereas lowland rivers tend to have high levels of dissolved load.

Measurements of erosion rates can also be made using a range of methods including thermochronologic techniques such as apatite fission track analysis and U–Th/He dating, and from analysis of cosmogenic radionuclides. Comparison of erosion rate estimates derived from different techniques with varying temporal resolution provides valuable insights into the functioning of the erosional system. In general, longer time scale and larger spatial scale "geological" estimates of erosion are strongly smoothed relative to the characteristics of individual erosive "geomorphic" events.

The engine for the sediment routing system is the coupled process systems of hillslopes and rivers, which degrade the topography produced by tectonics. In mountainous regions, rivers commonly cut down like cheese wires through regionally uplifting bedrock, and are supplied with the products of hillslope mass wasting. Landsliding dominates on hillslopes above a critical gradient.

Hillslope evolution can be modeled as a diffusive process, by making use of the sediment continuity equation and the assumption that the hillslope mass flux is proportional to the local topographic gradient. Hillslope profiles are therefore parabolic, but where channel incision rates are high, landsliding produces linear hillslope profiles. The spacing of transverse drainages and their maximum relief scales on the tectonic uplift rate of rock, as seen in the Southern Alps of New Zealand.

The products of hillslope erosion are transported away by rivers. The rate of incision of bedrock rivers can be estimated by different methods, but the most common approach is to approximate the incision rate by an area-slope or discharge-slope product. The increasing discharge downstream and the reducing slope downstream combine to produce maximum incision rates at a certain distance from the drainage divide. Deep incision by rivers causes an erosional unloading that may result in an isostatic uplift of mountain peaks. Such a process is likely to be responsible for the very high topography at the edges of major plateau regions such as Tibet.

Far-field sediment transport takes place in alluvial systems. The physics of long range sediment transport is complex. However, a common approach is to combine approximations and assumptions of uniform flow down an inclined plane, a flow resistance equation, conservation of discharge of water and the sediment continuity equation to derive a diffusive rule for alluvial systems. The transport coefficient can be regarded as varying smoothly in the downstream direction, or being constant for gravel ($0.01\,km^2\,yr^{-1}$) and sand ($0.1\,km^2\,yr^{-1}$), which successfully simulates the commonly observed "gravel front" in alluvial rivers. A two-diffusion numerical model shows the sensitivity of alluvial system behavior and alluvial stratigraphy to variations in forcing mechanisms such as sediment flux, subsidence rate, and gravel fraction. Tectonic–geomorphic systems have characteristic response times that may be long compared to the periodicity of any forcing. This implies that such systems may be frequently out of equilibrium with ambient forcing conditions, and that stratigraphic signals in basins are strongly smoothed by the buffering effect of large river systems.

A range of numerical landscape evolution models are currently available targeted at the understanding of coupled tectonic–geomorphic systems at a range of scales from extensional fault blocks and thrust-related folds to entire orogenic belts or passive margin mega-escarpments. Landscape evolution models are successful at simulating realistic landscapes, but are more important as a tool in investigating complex system behavior. A particularly fruitful line of research concerns the evolution of river drainage over evolving extensional fault arrays and contractional fold–thrust belts.

7.1 INTRODUCTION

The sedimentary character of basins is determined by the balance between tectonic subsidence causing long term accommodation and sediment influx. Sedimentary basins should not therefore be regarded as passive receptacles, but as dynamic entities occupied by complex physical and biologic process systems. This chapter concerns the geomorphologic and biogeochemical process systems or subsystems operating in the hinterlands of sedimentary basins. These hinterlands are source areas for particulate and dissolved river-borne mass fluxes. It is clearly important to be able to predict the long term mass flux from hinterlands to sedimentary basins and also the response time of the hinterland to changes in forcing variables such as climate and tectonics. Much research at present is targeted at understanding the coupling between erosion and tectonics at the medium to large spatial scales appropriate to sedimentary basins.

The structure of this chapter is to initially consider the global patterns of weathering and erosion. The transfer of mass from hillslope to basin will then be looked at in the context of sediment routing systems. We will be particularly concerned with how sediment routing systems function as physical systems. The development of landscape as a complex response to on-going tectonics is investigated in the contexts of tilted extensional fault blocks and thrust-related anticlines in fold–thrust belts. Having investigated the controls on and sensitivity of sediment transport systems, the reader is in a better position to appreciate the full set of parameters controlling stratigraphic architectures and variability of depositional style in the basin-fill in Chapter 8.

7.2 WEATHERING

Weathering is the decay and disintegration of rock *in situ* at the Earth's surface. A weathering mantle forms between pristine bedrock and the land surface, known as *regolith*. Water moves up and down in the regolith by capillary action and gravity respectively (Fig. 7.1). The presence of an enveloping and reactive moisture film is

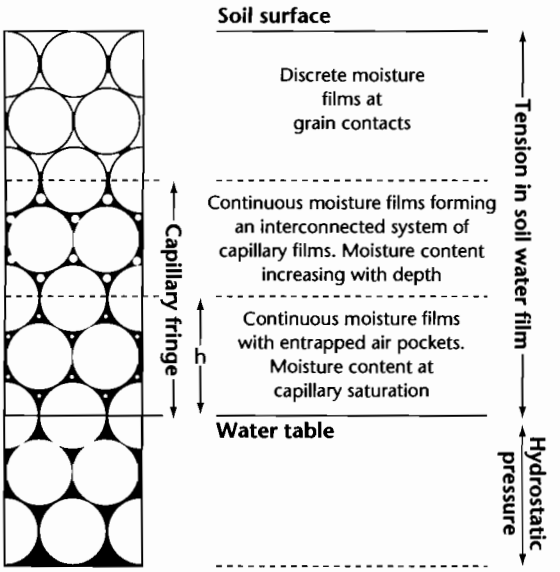

Fig. 7.1 The zones of moisture in the regolith, showing the extent of the capillary fringe (after Carson 1969).

critical to the weathering of bedrock and regolithic materials.

The processes and products of weathering have been treated exhaustively elsewhere. A useful treatment is found in the excellent text by Summerfield (1991) and is considered in a geochemical context in Andrews et al. (1995). An overview is given in Allen (1997). Weathering is conventionally divided into mechanical and chemical categories. Mechanical weathering involves: (i) processes causing a volumetric change in the rock mass, including exfoliation, insolation, and hydration weathering, and (ii) processes causing a volumetric change through the introduction of material, commonly water, but also salts, into pores, void spaces, and fissures in the rock mass, such as freeze–thaw processes and salt weathering. Although these processes of mechanical weathering may be locally dominant, chemical weathering is of greater global importance.

7.2.1 Chemical weathering processes

Chemical weathering involves the chemical breakdown of bedrock and the formation of new mineral products. The main chemical weathering processes are:

1 *Solution* involves the action of water as a solvent. The tendency of a mineral to dissolve in water is expressed by its *equilibrium solubility*. This is affected by the temperature and pH of the local environment. As an example, quartz (SiO_2) has a low solubility below a pH of 10, but is highly soluble in very alkaline waters above this value. Alumina (Al_2O_3) is only soluble in conditions seldom found in nature, below a pH of 4 and above a pH of 9. As a result, alumina accumulates as a residue during weathering, whereas silica may be slowly leached. Calcium carbonate ($CaCO_3$), in contrast, has a steadily decreasing solubility in alkaline waters. However, the low solubility of $CaCO_3$ in pure water is rarely applicable in the natural environment because dissolved CO_2 in water causes $CaCO_3$ to be replaced by calcium bicarbonate $Ca(HCO_3)_2$, which is highly soluble (see "Acid hydrolysis").
2 *Oxidation and reduction* involves the gain or loss of charge by the addition (reduction) or loss (oxidation) of negatively charged electrons. The oxygen dissolved in water is the most common oxidizing agent. Oxidation results in the formation of oxides and hydroxides, as in the oxidation of sulfides such as iron pyrite (FeS_2) under anaerobic conditions to produce sulfuric acid and iron hydroxide. The oxidation of organic matter in soils by bacteria produces CO_2 and therefore generates acidity. The acidity is then used in the hydrolysis of minerals (see "Acid hydrolysis"). The tendency for oxidation and reduction to take place is indicated by the *redox potential* (Eh), measured in millivolts.
3 *Hydration* involves the absorption of water into the crystal lattice, making it more porous and therefore more susceptible to weathering. A common example is the transformation of the iron oxide hematite to the hydrated iron hydroxide limonite.
4 *Acid hydrolysis* is the reaction of a mineral with acidic weathering agents, where the acidity is mainly derived from the dissociation of atmospheric CO_2 in rainwater and soil zones by respiration of plant roots and bacterial decomposition of plants, producing in both cases carbonic acid (H_2CO_3). Hydrolysis involves the replacement of metal cations in the crystal lattice such as K^+, Na^+, Ca^{2+}, and Mg^{2+} by the hydrogen or hydroxyl ions of water. The released cations combine with further hydroxyl ions, commonly to form *clay minerals*. Examples are the hydrolysis of albite (plagioclase felspar $NaAlSi_3O_8$) to *kaolinite* $(Al_4Si_4)O_{10}(OH)_8$, and the hydrolysis of orthoclase felspar ($KAlSi_3O_8$) to *illite* ($K_2Al_4(Si_6Al_2O_{20})(OH_4)$). Such reactions in general produce a clay mineral residue plus the release of

silica, metal cations, and bicarbonate ions in solution. Acid hydrolysis involving CO_2 is commonly termed *carbonation*. Carbonation dominates the weathering of limestones.

7.2.2 The regolith

The mineralogic composition of the regolith is determined not just by the type and intensity of chemical weathering processes, but also by the parent bedrock. There are considerable differences in the way basalts and granites weather under the same climatic regime. Clay minerals are particularly diagnostic of both weathering processes and parent material. A primary factor is the extent of leaching, which strips minerals of their metal cations and eventually of their silicon and iron, leading to a stable aluminum-rich residue (gibbsite).

A large throughput of water is necessary for advanced stages of leaching, leading to regoliths dominated by gibbsite, kaolinite, and aluminum oxides and hydroxides. This is only accomplished in regions of high precipitation rates such as the equatorial and humid tropical regions (Fig. 7.2). The process is commonly termed *laterization*. Where leaching is less intense, the cations released by the breakdown of bedrock promote the formation of cation-bearing clay minerals such as those of the illite and smectite groups. These zones of moderate leaching typify the temperate zones of Asia, Europe, and North America. In arid and semi-arid climates, there are very low rates of chemical weathering and little accumulation of weathering products except for carbonates and salts as hard crusts and concretions.

The clay mineral assemblage is not only a function of climate, but also of position within the regolith profile. This is because the flux of water generally decreases with depth in the regolith, caused by a downward reduction in permeability. Residual minerals such as kaolinite and gibbsite are consequently found at the top of weathering profiles, whereas smectite and illite may be found at deeper levels in the same regolith where leaching is less intense.

The thickness of the regolith depends on the trade-off of two rate effects:

1 Rate of bedrock weathering, which is strongly controlled by climatic factors;
2 rate of removal by denudation, which is controlled by climatic, tectonic, and topographic factors (§7.3).

Regoliths can only attain great thicknesses (over 100 m) in localities with humid, warm climates, and subdued topography. Even in these situations, regolith growth is self-limiting since the development of a thick weathered mantle decreases permeability and reduces the throughput of water to the weathering front in contact with pristine bedrock. Although studies suggest that weathering rates are higher under some finite thickness of regolith than on bare bedrock, the rate of regolith production is commonly assumed to decay exponentially with regolith thickness (Anderson and Humphrey 1990):

$$E_w = k_w \exp(-m_w R) \tag{7.1}$$

where E_W is the rate of descent of the bedrock–regolith weathering front, k_W is a coefficient representing the pristine bedrock weathering rate (units of LT^{-1}), m_W is a weathering rate decay constant (equal to $1/R_0$, where R_0 is the depth at which the weathering rate reduces to $1/e$ of its surface value k_W), and R is the regolith thickness. Under such circumstances of low bedrock weathering under thick regoliths, weathering activity may be restricted to intense leaching of the soil zone. The length scale R_0 is likely to be of the order of 1 m.

Regolith production rates are difficult to measure directly. New techniques in *cosmogenic radionuclide dating*, however, now allow more reliable estimates to be made. Cosmogenic radionuclides (such as ^{10}Be and ^{26}Al) are produced *in situ* by cosmic radiation, at a rate P_0 dependent on latitude and altitude (Lal 1991; Bierman 1994). The principle is that the production rate in a bare piece of bedrock P decays exponentially with depth below the surface y (Fig. 7.3), so that

$$P = P_0 \exp(-y/y^*) \tag{7.2}$$

where y^* is a rate constant equal to 0.5–0.7 m for most common lithologies (that is, the production rate decays downwards to P_0/e in a distance y^*). The rate of change of concentration with time is then the production rate $P(t)$ minus the rate of decay $\lambda\mathcal{N}$

$$\frac{\partial \mathcal{N}}{\partial t} = P(t) - \lambda\mathcal{N} \tag{7.3}$$

where $\mathcal{N}$ is the concentration of cosmogenic radionuclides per unit volume of rock and λ is a decay constant analogous to a half-life.

Regolith shields the underlying bedrock from bombardment by cosmic rays, reducing radionuclide production rates at the regolith–bedrock interface. If the thickness of regolith H at a site is constant over time

(losses at the surface balancing production of regolith from bedrock), the rock to regolith conversion rate is

$$E = \frac{\{P_0 \exp(-H/y^*)\}y^*}{\mathcal{N}} \quad (7.4)$$

where E is the bedrock lowering rate. Application of this technique, for example in the Wind River Range of USA (Small et al. 1999), showed that bedrock to regolith production rates were of the order of just 10×10^{-6} m yr^{-1}. This is much lower than typical erosion rates in tectonically active areas (§7.4).

In steep mountains with humid climates, although the rate of regolith production is high, it is removed by hillslope erosion. The combination of high regolith production caused by climatic factors and high topography

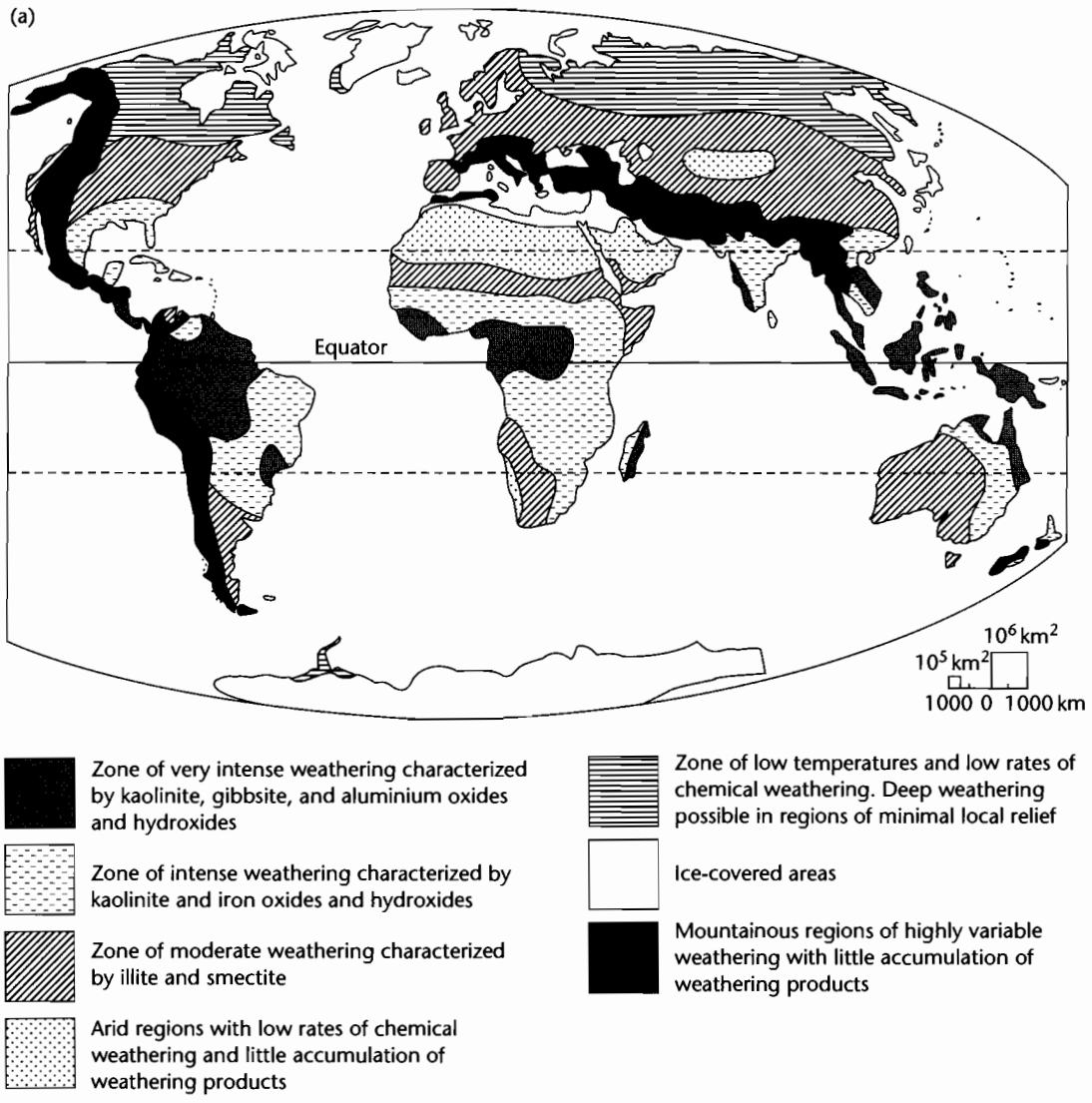

Fig. 7.2 The global pattern of weathering, modified from Strakhov (1967). (a) Map of major weathering zones, (b) latitudinal zonation showing regolith thickness and type.

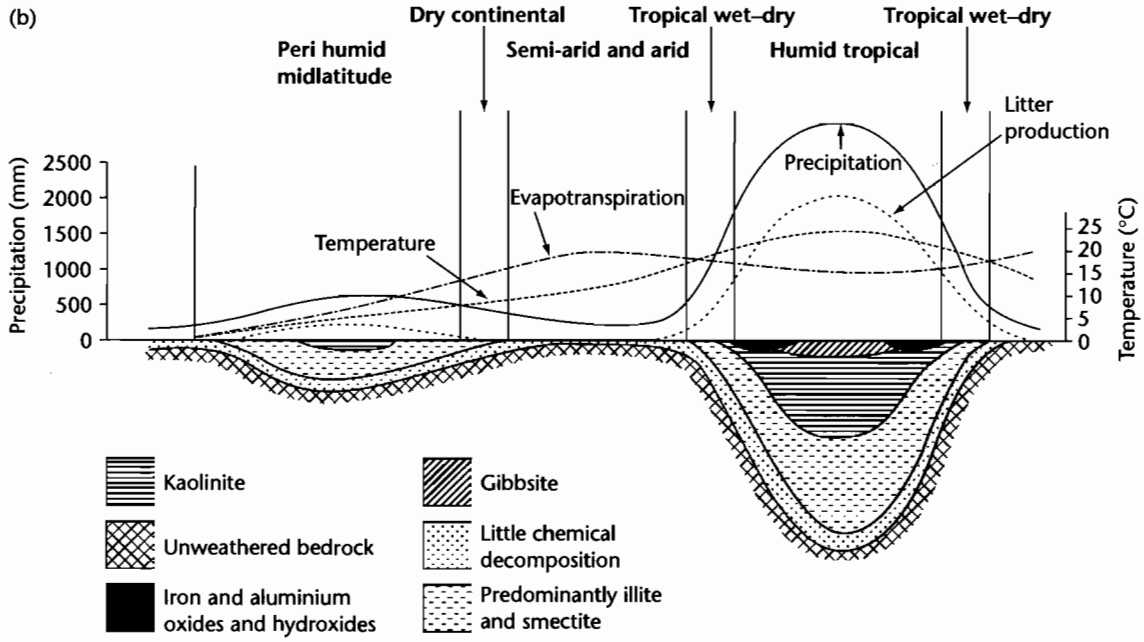

Fig. 7.2 *Continued*

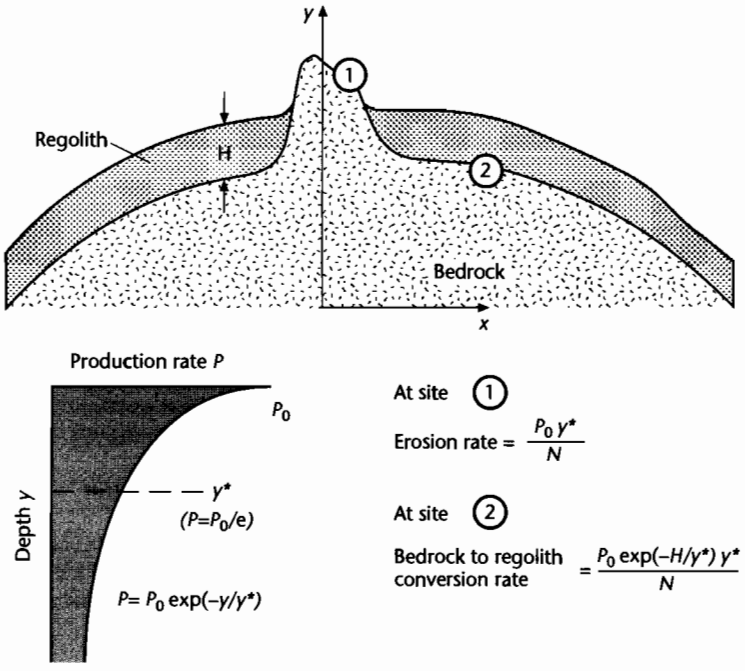

Fig. 7.3 Calculation of bedrock erosion and regolith production rates using cosmogenic radionuclides (after Burbank and Anderson 2001). At site 1, bedrock erosion rate depends on the production rate of the radionuclide at the sample site P_0, the depth rate constant y^*, and the concentration of radionuclides per unit volume of rock N. At site 2, bedrock is converted to regolith at a rate that is also affected by the thickness of the regolith H (see equations 7.2–7.4).

caused by tectonic factors produces optimum conditions for the erosional sediment efflux of the landscape.

In summary, there are a number of factors controlling the rate of chemical weathering:

- **Organic activity** in soils generates soil acidity (CO_2) through decomposition, aids the retention of water through the build-up of organic matter and biologic activity promotes permeability;
- **climate** controls weathering reactions through the effect on chemical kinetics of temperature, imparting a latitudinal gross pattern of chemical weathering rates (Fig. 7.2). Rainfall controls vegetation type, biologic activity in the soil and the activity of water as a solvent;
- **kinetics of mineral reactions;** chemical weathering requires pore waters to be undersaturated with respect to the mineral being weathered. Once saturation is achieved, an increase in the flow rate will not cause further reaction. Whereas the chemical weathering of evaporites is determined by the rate of removal of the saturated solution by flushing, in relatively insoluble minerals such as silicates the rate of chemical weathering is determined by the kinetics by which ions are detached from crystal surfaces;
- **bedrock composition** controls the stability of the mineral components to weathering through their degree of polymerization, as illustrated by the *Goldich series*. Monomer silicates like olivine are most easily weathered, and framework silicates such as quartz are most resistant;
- **topography** influences the rate of removal of regolith by erosion, which invigorates chemical weathering by subjecting new, fresh bedrock to weathering. Topography also controls drainage and therefore rates of flushing. Flow rates on mountainous slopes are high, but flat, poorly drained slopes have very low flow rates;
- **time** is required for chemical changes to take place. Weathering profiles are seldom in equilibrium with surface conditions.

Since chemical weathering depends on temperature (as well as the other factors noted above), it is commonly assumed that chemical weathering rates for silicates are approximated by an Arrhenius-type relationship (White and Blum 1995):

$$r_T = A\exp(-E_a/RT) \tag{7.5}$$

where r_T is the rate of chemical weathering (as a function of temperature), A is a prefactor that varies with the chemical species being weathered, E_a is the activation energy (in kJ mol^{-1}), R is the Universal gas constant, and T is absolute temperature (K). In gross terms this temperature dependence is shown by the latitudinal global pattern of weathering shown in Figure 7.2.

7.3 TERRESTRIAL SEDIMENT AND SOLUTE YIELDS

7.3.1 An introduction to continental run-off

The bulk of particulate and dissolved solids is transported from the continents by running water. This flux connecting land and ocean reservoirs of the hydrologic cycle is known as *run-off*. It can be viewed most simply in the context of a simple box model for the global water cycle. There is a net gain in the fluxes between the land and atmosphere (precipitation exceeds evaporation over the land areas), which is compensated by a run-off flux from the land to the ocean reservoirs. Although the quantity of water in the continental part of the hydrologic cycle is small compared to the ocean reservoir, the flux of water from land to ocean is considerable.

Rain is not simply channeled through rivers to the ocean. The surface water balance contains run-off as one component

$$P = E + T + \Delta S + \Delta G + R \tag{7.6}$$

where P is precipitation, E is evaporation, T is transpiration, ΔS is the change in storage of water in the soil, ΔG is the change in storage of water as groundwater, and R is run-off – the overland flow across the land surface as rills and gullies, streams, and rivers.

The relative importance of these parameters depends on climatic, topographic, and geological setting, with important regional variations. The ratio of streamflow measured from a river and the precipitation falling over the drainage basin is called the *run-off coefficient* C_r. The run-off coefficient varies strongly, principally according to climatic setting and the extent of human interference through irrigation and damming. The drainage basins listed in Table 7.1 provide some representative examples. The humid tropical (Amazon, Orinoco) and cold climate (Lena) drainage basins have high run-off coefficients compared to arid region catchments (Nile, Murray).

Major variations in run-off can be predicted by comparing global maps of precipitation versus evaporation:

- Mean annual precipitation is highest in the tropics where humid air rises because of convectional insta-

Table 7.1 Run-off of a selection of the world's major rivers.

River	Catchment area (km^2)	Annual precipitation ($mm\,yr^{-1}$)	Discharge at river mouth ($m^3\,s^{-1}$)	Run-off coefficient C_r
Amazon	6,150,000	1490	200,000	0.69
Nile	2,715,000	832	317	0.004
Lena (Russia)	2,430,000	355	16,200	0.59
Orinoco	945,000	1300	34,900	0.9
Murray (Australia)	910,000	582	698	0.04
Seine (France)	78,600	711	685	0.39

bility, in mountainous regions because of orographic cooling, and between 35° and 60°N and S associated with atmospheric instability causing storms;

- mean annual evaporation is highest where there is a heat source, a plentiful source of water, and low moisture contents in the air; these conditions are best satisfied in the subtropical oceans. Evaporation rates over dry continental areas are commonly much lower because of the scarcity of liquid water.

Precipitation exceeds evaporation in equatorial and high temperate to polar latitudes, whereas there is a net deficit in the subtropics. More than half of the global run-off occurs in South America, where it is concentrated in the equatorial regions. The Amazon River alone contributes 15% of the total annual global run-off.

7.3.2 Sediment yield

The erosion of the terrestrial surface results in a flux of sediment from source regions to depositional sinks. The closed system involving an erosional sector, a transport sector and a depositional sector is known as a *sediment routing system* (Allen 1997). The fluxes of sediment through the process subsystems of erosion, transport, and deposition are dependent not only on the processes operating within the subsystems, but also on the linking processes between the subsystems. This is particularly true of the transfer of sediment from the erosional zone to the transport zone. The functioning of sediment routing systems will be considered in §7.5. Here, we initially concentrate on a more descriptive approach to the global patterns of sediment production from erosional areas and its delivery to sedimentary basins.

The denudation of a drainage basin with area A_d results in a discharge of sediment and solute to the ocean or to lakes. If D is the total discharge of sediment and solutes at the exit of the drainage basin, and there is no change in the storage of sediment within the drainage basin over time, the long term average denudation of the drainage basin per unit area (Fig. 7.4) is simply

$$\frac{\partial h}{\partial t} = \frac{(1-\phi)}{\rho}\frac{D}{A_d} \tag{7.7}$$

where h is the elevation, ϕ is the porosity of rocks of density ρ in the catchment undergoing weathering and erosion, and the discharge D is measured as mass per unit time ($kg\,yr^{-1}$). Measurement of both the particulate and solute loads in rivers is required to calculate the total average denudation of the catchment. If D_s denotes the particulate sediment discharge, equation (7.7) can be rewritten as

$$\Upsilon = \frac{D_s}{A_d} \tag{7.8}$$

where Υ is termed the *sediment yield*, with units of $kg\,m^{-2}\,yr^{-1}$. Sediment yield therefore has the units of a *mass flux*. For example, the Amazon River at its mouth has a solid load of $1150\,Mt\,yr^{-1}$ and a solute load of $223\,Mt\,yr^{-1}$ (1 mega ton is 10^9 kg). The drainage area is $6{,}150{,}000\,km^2$. The sediment yield is therefore $187\,t\,km^{-2}\,yr^{-1}$, whereas the total average denudation rate is $223\,t\,km^{-2}\,yr^{-1}$. For a rock density of $2700\,kg\,m^{-3}$ and an average porosity of 5%, the catchment-wide average denudation rate (equation 7.7) is $79\,mm\,kyr^{-1}$. Although this figure is very low, it should be remembered that certain parts of the Amazon drainage basin in the Andes are experiencing very rapid denudation while large parts of the floodplain are undergoing no denudation at all.

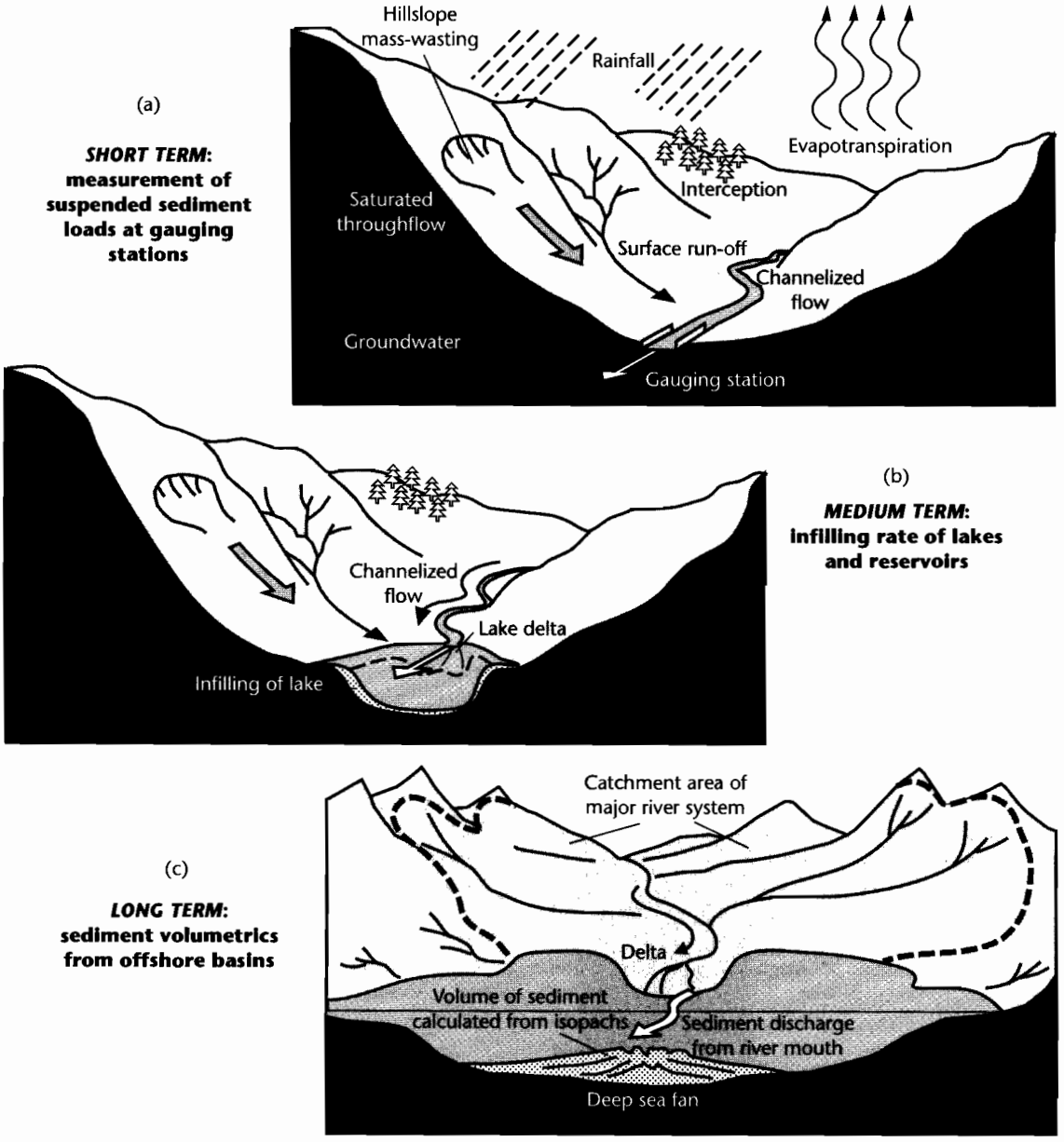

Fig. 7.4 Methods of estimating sediment yield. In (a), the short-term sediment yield is the discharge of sediment in $kg\,yr^{-1}$ measured at a gauging station divided by the contributing catchment area. In (b), the medium-term sediment yield is the infill rate of a lake basin or artificial reservoir divided by the contributing catchment area. In (c), the long term sediment yield is the solid sediment volume derived from sediment isopachs of dated intervals of the stratigraphy divided by the paleocatchment area.

There are two strategies for evaluating catchment-averaged sediment yields and mechanical denudation rates based on the sediment exported from the catchment: use of the rate of filling of artificial reservoirs and natural lakes, and calculation of the volume of sediment accumulated in sedimentary basins.

Einsele and Hinderer (1997) studied the filling of artificial reservoirs and lakes in order to estimate sediment yields in the contributing drainage basins. In open lakes and reservoirs the solutes are assumed to be flushed through, but the particulate load is mostly trapped, allowing a sediment budget to be calculated. For example, the Tarbela reservoir on the Indus River near Islamabad is an artificial lake extending 80 km upstream from the dam, covering an area of 625 km^2. It has a mean depth of 22 m, giving it an initial storage capacity of 13.9 km^3. The drainage area in the predominantly semi-arid northwestern Himalaya is 171,000 km^2. The rate of filling of the reservoir (about 2% per year) indicates that the average sediment yield is 1170 $t\,km^{-2}\,yr^{-1}$. The present-day mechanical denudation rate for the Indus catchment is therefore just over 400 $mm\,kyr^{-1}$.

The High Aswan reservoir in southern Egypt is 500 km long and covers an area of 5000 km^2, with a storage capacity of about 130 km^3. The drainage area feeding the reservoir is 1.839×10^6 km^2. After 25 years of operation the reservoir had collected 2800 to 3300×10^6 t of sediment. Three other reservoirs in SE Sudan upstream of the Aswan High Dam have accumulated about the same amount of sediment as the main Aswan reservoir, giving a total of about 6000×10^6 t. The annual accumulation rate is therefore $240 \times 10^6\,t\,yr^{-1}$. The sediment yield for the upper and middle reaches of the Nile River system is *c.* 130 $t\,km^{-2}\,yr^{-1}$, and the mechanical denudation rate (using $\rho = 2750\,kg\,m^{-3}$ and $\lambda = 0.05$) is 45 $mm\,kyr^{-1}$, an order of magnitude less than in the Himalayan Indus catchment.

An allied strategy is to estimate the volume of sediment in the depositional zone of the sediment routing system using isopachs and cross-sections derived from borehole and seismic reflection data. The average solid phase accumulation rate for Asian sedimentary basins since the beginning of the Tertiary has been calculated after correction of stratigraphic thicknesses for the effects of compaction (Métivier et al. 1999) (Fig. 7.5). The Bengal basin, for example, contains a vast amount of Upper Tertiary sediments (locally <21 km in thickness) deposited primarily from southwestward-prograding deltas feeding a large deep sea cone. The Bengal Basin has accumulated 12×10^6 km^3 solid volume during the Tertiary, with a rate of $0.45 \times 10^6\,km^3\,Myr^{-1}$ over the last 2 Myr. The Bengal basin has received sediment from the Ganges, Brahmaputra and the rivers of the eastern platform of India (Mahanadi, Krishna, and Godavari), which have a total drainage area of *c.* 2.266×10^6 km^2. The average mechanical denudation rate for these Indian Subcontinent catchments during the Quaternary is about 200 $mm\,kyr^{-1}$, with an average sediment yield of 546 $t\,km^{-2}\,yr^{-1}$ (using $\rho = 2750\,kg\,m^{-3}$). The Ganges, Brahmaputra, Mahanadi, Krishna, and Godavari rivers have a combined river mouth discharge of 0.49×10^6 $km^3\,Myr^{-1}$. This is in excellent agreement with the estimate derived from the volume of preserved stratigraphy, and indicates that present day discharges in large, buffered systems may be closely representative of longer term (geological) rates (Einsele et al. 1996; Métivier and Gaudemer 1999; Métivier et al. 1999).

7.3.3 Global patterns of sediment yield

The total amount of sediment discharged to the ocean is estimated to be *c.* $20 \times 10^9\,t\,yr^{-1}$ (Milliman and Syvitski 1992; Walling and Webb 1996). Since the land surface of the Earth is 1.48×10^8 km^2, the globally averaged sediment yield is 135 $t\,km^{-2}\,yr^{-1}$, but there is enormous variability around this globally averaged figure (Fig. 7.6). Some of the highest sediment yields come from rugged oceanic islands such as Java, New Guinea, Taiwan, and New Zealand (Table 7.2). Even higher values (>50,000 $t\,km^{-2}\,yr^{-1}$) come from Chinese rivers draining the easily erodible loess region. At the other extreme, there are some very large river systems with sediment yields of less than 1 $t\,km^{-2}\,yr^{-1}$, such as the Yenesei and Dneiper Basins of the former Soviet Union.

The main features to come out of the numerous published sediment yield maps (e.g., Milliman and Meade 1983; Walling and Webb 1983; Lvovich et al. 1991) (Fig. 7.6) are that sediment yields are highest in an arc around the Pacific and Indian Ocean margins from Pakistan to Japan. This area is characterized by Cenozoic mountain building, steep topography, and generally high annual rainfalls. Low sediment yields typify desert regions and the cold, formerly glaciated, low-relief regions of Eurasia and Canada. The key question is what controls this wide variability in sediment yield. If the answer to this question were known, it would assist the understanding of the likely mass fluxes to sedimentary basins in the geological past. Sediment yield models commonly use the sediment loads of rivers as an index of sediment yield (Milliman

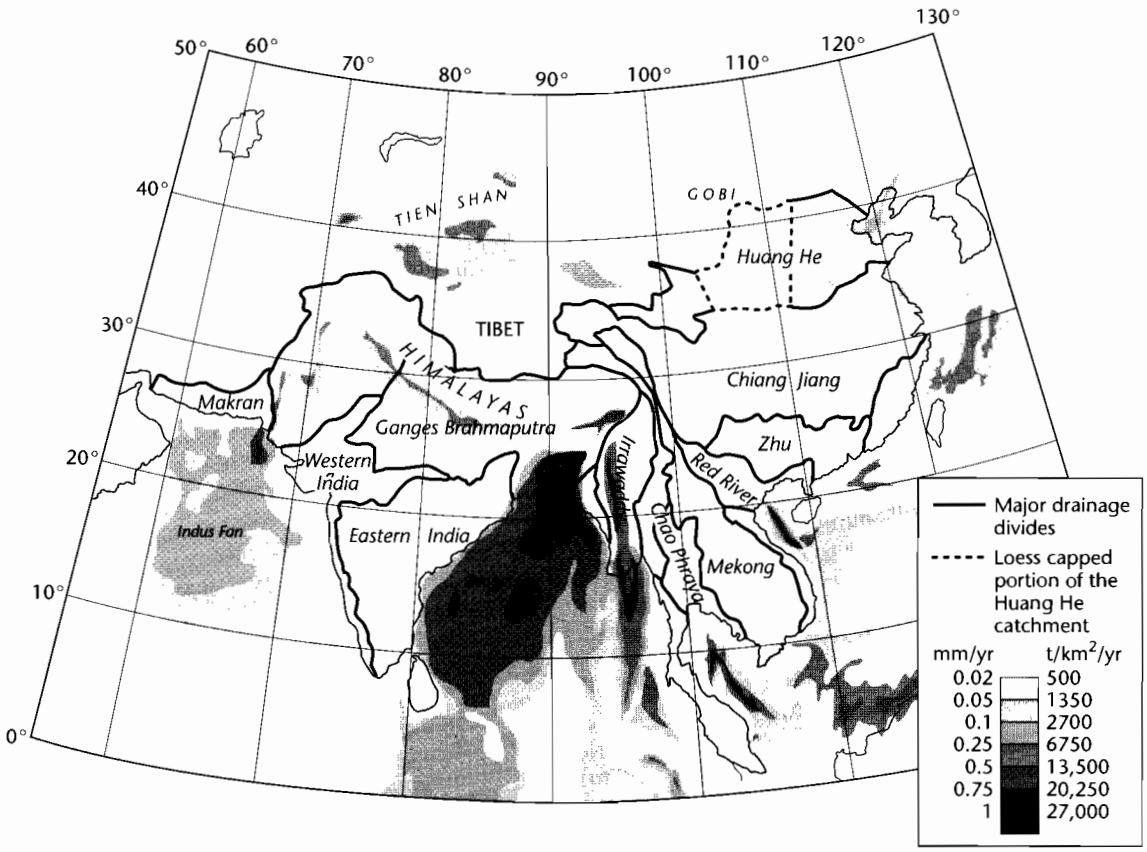

Fig. 7.5 Sediment mass accumulated in basins of south and southeastern Asia during the last 2 Myr, digitized from a large number of sources by Métivier et al. (1999). The sediment was delivered to the ocean by the river systems of Asia. Reproduced courtesy of Blackwell Publishing Ltd.

and Meade 1983; Summerfield and Hulton 1994; Hovius 1997; Hay 1998). These sediment load data are strongly biased towards measurements made at the mouths of the world's major rivers, although Milliman and Syvitski (1992) have emphasized the influence of small mountainous streams on the global sediment budget. The sediment loads at river mouths are affected by the extent to which sediment is stored in river floodplains. The extent of storage is likely to increase in larger drainage basins with substantial depositional and transportational components of the sediment routing system. This storage effect explains the well-established inverse relationship between drainage basin area and sediment yield (Fig. 7.7) (Milliman and Meade 1983; Milliman and Syvitski 1992). This inverse relationship has, however, been questioned as a fundamental property of natural drainage systems, and has been attributed at least in part to human impact (Walling and Webb 1996).

There are a large number of problems with the use of data on sediment loads measured at river mouths (Milliman and Meade 1983). The most obvious is that the effects of human activities, such as land use, dam con-

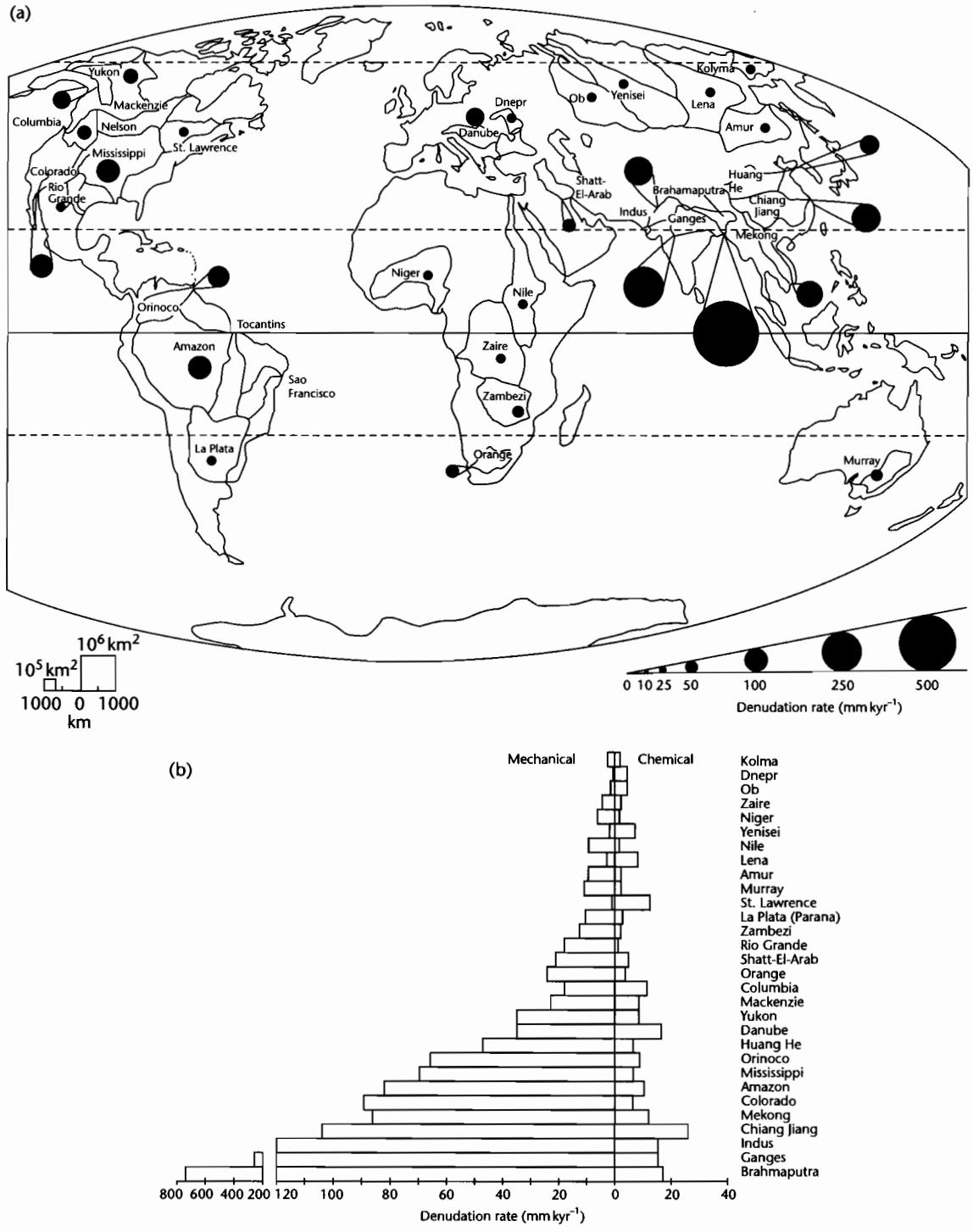

Fig. 7.6 (a) Estimated total denudation rates for major externally drained basins. Size of black circles is proportional to denudation rate; (b) Histogram comparing mechanical and chemical denudation rates for the world's major externally drained basins. After Summerfield and Hulton (1994). Reproduced courtesy of American Geophysical Union.

Table 7.2 Sediment and solute yields of the world's major rivers (after Summerfield and Hulton 1994, and sources cited therein).

River basin	Area 10^6 km^2	Sediment yield t km^{-2} yr^{-1} (equivalent mechanical denudation rate, mm kyr^{-1})	Solute yield t km^{-2} yr^{-1} (equivalent chemical denudation rate, mm kyr^{-1})	Chemical denudation as % of total
Amazon	5.98	221 (82)	29 (11)	11.6
Amur	2.04	28 (10)	6 (2)	17.6
Brahmaputra	0.64	1808 (670)	49 (18)	2.6
Chiang Jiang	1.73	281 (104)	72 (27)	20.4
Colorado	0.70	239 (89)	19 (7)	7.4
Columbia	0.67	48 (18)	32 (12)	40.0
Danube	0.79	94 (35)	45 (17)	32.4
Dnepr	0.54	2 (1)	12 (4)	85.7
Ganges	0.98	694 (257)	42 (16)	5.7
Huang He	0.79	127 (47)	18 (7)	12.4
Indus	0.93	323 (120)	42 (16)	11.5
Kolyma	0.65	9 (3)	4 (1)	30.8
La Plata (Parana)	2.86	30 (11)	9 (3)	23.1
Lena	2.45	7 (3)	22 (8)	75.9
Mackenzie	1.77	62 (23)	23 (9)	27.1
Mekong	0.76	232 (86)	36 (13)	13.4
Mississippi	3.20	189 (70)	20 (7)	9.6
Murray	1.14	30 (11)	6 (2)	9.7
Nelson	1.24	–	16 (6)	–
Niger	2.16	19 (7)	4 (1)	17.4
Nile	3.63	28 (10)	3 (1)	9.7
Ob	2.98	6 (2)	11 (4)	64.7
Orange	0.89	65 (24)	11 (4)	14.5
Orinoco	0.92	179 (66)	23 (9)	11.4
Rio Grande	0.63	48 (18)	4 (1)	7.7
Sao Francisco	0.62	11 (4)	–	–
Shatt-El-Arab	0.89	56 (21)	14 (5)	20.0
St Lawrence	1.05	2 (1)	34 (13)	94.4
Tocantins	0.76	–	–	–
Yenisei	2.55	5 (2)	18 (7)	78.3
Yukon	0.84	94 (35)	23 (9)	19.7
Zaire	3.63	14 (5)	6 (2)	30.0
Zambezi	1.41	34 (13)	6 (2)	15.0

struction and irrigation schemes, must be accounted for. In addition, measured sediment loads are invariably suspended load only, with the bedload contribution ignored. This is unlikely to be a problem in the downstream reaches of large rivers, but may introduce a significant error in short, steep, mountainous streams. Finally, the suspended load sediment data have been collected using different methods over protracted periods of time and are difficult to compare.

Glaciated terrains appear to have a different and more complex relation between sediment yield and catchment size than river basins (Hallet et al. 1996). Sediment delivery from the upland part of glaciated catchments may be particularly high when pluvial conditions promote the rapid evacuation of loose morainic material from a previously glaciated region. Some currently glaciated basins, such as the steep and wet catchments of Alaska and the Southern Alps of New

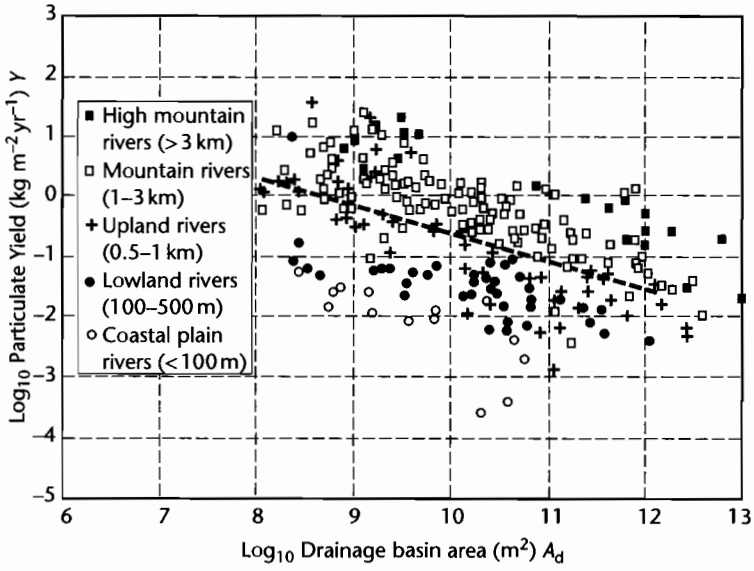

Fig. 7.7 Plot of drainage basin area versus particulate sediment yield for the elevation classes of rivers of Milliman and Syvitski (1992). The regression for all of the river data has the form $Y = \exp(9.18 - 0.46 \ln A_d)$. After Hay (1998). Reproduced courtesy of Elsevier.

Zealand, also have very high yields, in excess of most nonglaciated settings.

7.3.4 Controls on sediment yield

Numerous attempts have been made to correlate sediment yield with topographic and climatic factors. The resulting relationships invariably work reasonably well at restricted spatial scales, or in certain prescribed geomorphic settings, but involve a large amount of scatter at the global scale.

7.3.4.1 Rates of precipitation

A number of authors have investigated the link between sediment yield and mean annual precipitation, rainfall variability, and specific run-off (water discharge per square kilometer of drainage basin, in mm yr^{-1}). Any relationship between precipitation and run-off variables and sediment yield must be strongly mediated by the effects of vegetation (Leeder et al. 1998). There is some consensus that sediment yield reaches a maximum in semi-arid areas where vegetation cover is sparse, with a second maximum where mean annual precipitation exceeds 1000 mm. Since most hillslope processes are sensitive to the intensity of rainfall, however, the rainfall peakedness (ratio of average monthly precipitation and maximum monthly precipitation) may be more important in governing sediment yield (Fournier 1960). The effects of vegetation cover can be seen where catchments have been disturbed by human activities. Sediment yields from cleared, agricultural land is higher (by factors of up to 100) than from forested catchments. On steep, mountainous slopes, the magnification of sediment yield may be even higher.

7.3.4.2 Topographic effects

A number of workers have linked erosion rate to a variety of topographic parameters such as mean or maximum elevation, large-scale or local relief, slope and drainage basin area. Various correlations have been claimed for a range of different datasets. For example, these comprise the sediment discharges of 280 rivers, including small mountainous streams (Milliman and Syvitski 1992), a dataset of 285 drainage basins of varying size and climatic zone (Allen 1997, Hovius 1998), a subset of the world's largest 29 rivers (Summerfield and Hulton 1994), a compilation of sediment yields in central Europe (humid temperate climate) up to 1981 based on reservoir and lake studies (Schröder and Theune 1984), and a

selection of mid-latitude drainage basins (Ahnert 1970; Pazzaglia and Brandon 1996).

The bewildering range of correlations with topographic and climatic parameters claimed by different authors suggests that erosion rate data cannot be compressed onto one simple plot. A multivariate analysis of sediment yield data reveals that a combination of environmental and topographic factors only explains about half of the variance in global sediment yield data (Hovius 1997, 1998). However, when plotted against a proxy for tectonic uplift rate (Fig. 7.8), tectonically inactive and tectonically active settings are clearly discriminated. For example, tectonically inactive cratonic settings are characterized by very low sediment yields of $<100\,t\,km^{-2}\,yr^{-1}$, whereas currently or recently tectonically active contractional mountain belts have sediment yields of 100–$10\,000\,t\,km^{-2}\,yr^{-1}$. Pinet and Souriou (1988) similarly noted different relationships for young, tectonically active orogens and old, tectonically inactive landscapes. This suggests that physical insights based on the different sets of processes dominating in low relief and high relief areas must be included in the analysis.

Montgomery and Brandon (2002) suggested a non-linear regional-scale relation between erosion and mean slope derived from a digital elevation model (DEM):

$$E = E_0 + \frac{KS}{\left[1-(S/S_c)^2\right]} \tag{7.9}$$

where E is the erosion rate, E_0 is a background erosion rate due to chemical weathering (*c.* $0.01\,mm\,yr^{-1}$ based on the mean chemical denudation rate for the world's 35 largest drainage basins, Summerfield 1991), S is the mean slope, S_c is a limiting hillslope gradient for landsliding, and K is a rate constant. Here, mean slope is derived from the range of values within a 10 km diameter analysis window around points spaced every 2 km, using a 10 m-resolution DEM. In the Olympic Mountains of Washington, USA, $E_0 = 0.016$–$0.059\,mm\,yr^{-1}$, $K = 0.6\,mm$

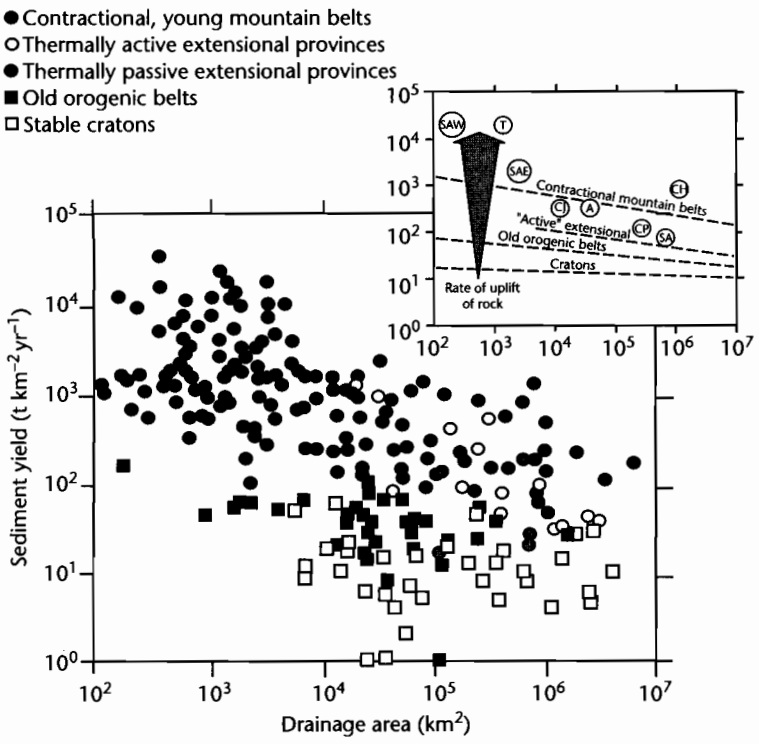

Fig. 7.8 Plot of sediment yield versus drainage basin area for five categories of tectonic setting, derived from Hovius (1995) using the sediment yield data of Milliman and Syvitski (1992). SAW, Southern Alps New Zealand western flank; SAE, Southern Alps New Zealand eastern flank; T, Taiwan; CJ, Central Japan; A, Alps; CP, Colorado Plateau; SA, Southern Africa; CH, Central Himalaya.

yr^{-1}, and $S_c = 40°$. Equation (7.9) can be expressed in terms of a mean local relief, derived from the same 10 m-resolution DEM with a 10 km-diameter analysis window, giving

$$E = E_0 + \frac{KR_z}{\left[1-(R_z/R_c)^2\right]} \tag{7.10}$$

where R_z is the mean local relief, and R_c is the limiting local relief. Data from low relief, tectonically inactive areas show a linear relation between erosion and mean local relief, as previously suggested by Ahnert (1970). However, this linear relation does not hold for high relief, tectonically active areas. In such cases, equation (7.10) gives a good fit with $E_0 = 0.01\,mm\,yr^{-1}$, $R_c = 1500\,m$, and $K = 2.5 \times 10^{-4}\,mm\,yr^{-1}$ (Fig. 7.9). The mean local relief R_z appears to reach a maximum of *c.* 1500 m ($R_c = 1500\,m$), and is very rarely >2000 m, suggesting that rock strength may control the maximum relief attainable in a mountain belt.

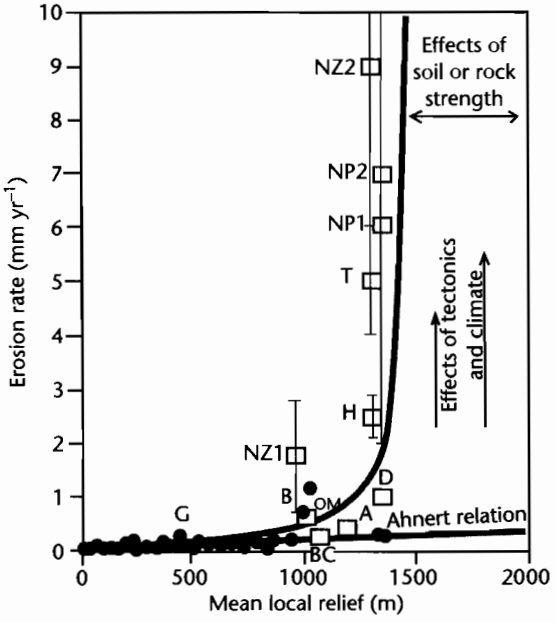

Fig. 7.9 Plot of erosion rate versus mean local relief using data compiled from Ahnert (1970), Summerfield and Hulton (1994) and Pazzaglia and Brandon (1996). Solid line is model fit using equation (7.10) with $E_0 = 0.01\,mm\,yr^{-1}$, $R_c = 1500\,m$, and $K = 2.5 \times 10^{-4}\,mm\,yr^{-1}$. Squares are from tectonically active regions; NZ1 and NZ2, Southern Alps of New Zealand: H, central Himalaya: NP1 and NP2, the Himalayan portion of the Indus River Basin; BC, British Columbia Coast Range; OM, Olympic Mountains; D, Denali portion of the Alaska Range; A, European Alps. Ganges (G) and Brahmaputra (B) also shown for reference. After Montgomery and Brandon (2002). Reproduced courtesy of Elsevier.

There are therefore essentially two different sorts of landscape in terms of erosion rate. In *low relief landscapes*, such as low-lying shield areas and alluvial floodplains, thick regoliths may develop. The rate of removal of regolith is determined mainly by the erosivity of the transport processes, rather than by the availability of loose, easily transportable material. This may also be the case in regions of extreme aridity where streamflow processes are negligible. In these *transport-limited* circumstances, parameters such as mean annual rainfall and specific run-off may offer the best correlation with sediment yield. Where the removal of loose material by streams is efficient, the rate of removal of sediment may, however, be limited by the rate at which loose material is supplied by hillslope weathering. These circumstances are therefore *weathering-limited*, and hillslope erosion processes determine the erosion rate, which depends linearly on mean slope or local relief. These conditions may be typical of low relief, mid-latitude, temperate zone landscapes. In *high relief landscapes*, however, physical transport processes of hillslope erosion by landsliding and channelized flow are almost always capable of removing regolith above a critical rate of rock uplift. Erosion rates then stabilize at a certain mean local relief determined by rock and soil strength. It is estimated that rock uplift rates of $1\,mm\,yr^{-1}$ are required to sustain combined potential chemical and physical erosion in mountainous areas (Koons 1995). In high relief landscapes therefore, the key process is the landsliding of critically steep hillslopes and efficient removal of debris by streams.

7.3.5 Transport of dissolved loads

Chemical weathering results in the release of ions in solution. Precipitation must infiltrate to deep levels in the regolith in order to promote chemical breakdown and the flushing of solutes into the groundwater system. This process of infiltration and flushing depends on climate and topography. In semi-arid regions, water is drawn to the surface during dry periods, leading to reprecipitation of solutes, and chemical weathering is retarded. On steep slopes, water runs off hillslopes quickly and does not spend long periods in contact with bedrock and regolith. In low-lying, gently sloping areas, the regolith is poorly

drained, so flushing rates are low. Chemical fluxes are highest on gentle upland slopes, where both infiltration and flushing are moderately high. Although particulate sediment yields are far higher than solute yields in mountainous areas, solute yields are relatively higher in lowland regions.

The groundwater system delivers solutes to rivers. The solute discharge of rivers may be modified by nondenudational inputs such as precipitation, wind-blown dust, salt aerosols (particularly close to the ocean), mineralization of organic matter, plant metabolism, and human pollution. Outputs include those of evaporation and losses to groundwater and soils. Consequently, the dissolved loads of rivers cannot be simply or directly linked to rates of chemical denudation.

The chemistry of water in the hydrologic cycle strongly reflects the reactions taking place with soil, with plants and with decomposing organic matter, through dilution or concentration caused by additions of precipitation and losses by evaporation, and particularly through the weathering of rock. Waters from calcareous catchments contain high amounts of *total dissolved solids* (TDS), particularly Ca^{2+} and HCO_3^-, but small particulate loads. Waters draining varied igneous, metamorphic, and sedimentary rock types have a varied chemical composition and higher TDS.

It is customary to plot river and lake water on a graph with axes of TDS ($mg\,l^{-1}$) and the cationic ratio (Fig. 7.10)

$$\frac{Na^+}{Na^+ + Ca^{2+}}$$

or the anionic ratio

$$\frac{Cl^-}{Cl^- + HCO_3^-}$$

Waters are consequently classified in terms of the source of the solute load (Gibbs 1970):

1 Dominated by *atmospheric precipitation*, with low salt concentrations because of dilution (20–30 $mg\,l^{-1}$), and a chemistry dominated by Na^{2+}, so the cationic ratio is nearly 1. This class of water characterizes rivers draining areas of low relief with well-weathered bedrock and plentiful rainfall, such as the tropical rivers of Africa and South America.
2 Dominated by *weathering reactions* in rock and soil, with higher TDS and a wide spread of cationic ratio depending on the reactions involved. There is a low ratio in limestone terrains where waters are dominated by calcium bicarbonate. In the Amazon Basin, 85% of the solute load is derived from a relatively small area of intense chemical weathering in the Andes, whereas in the lowland part of the catchment the control is by precipitation.
3 Dominated by *evaporation* and subsequent precipitation, with high salt concentrations (TDS 1000–2000 $mg\,l^{-1}$), reflecting the precipitation of $CaCO_3$ and the relative concentration of Na^+ and Cl^- through evaporative losses. This is common in the rivers of hot and arid climates such as the Jordan River of the Near East. These typical river compositions evolve to the composition of sea water.

The chemistry of river input to the ocean therefore varies from continent to continent and from region to region in response to variations in the control of precipitation, weathering and evaporation superimposed on the signature provided by bedrock type (see below). Rivers in arid Kazakhstan have solute concentrations of 6000–7000 $mg\,l^{-1}$, compared to 10 $mg\,l^{-1}$ for rivers in the humid Amazon Basin, where solutes are diluted by large amounts of run-off.

The measurement of the solute concentration or "salinity" of a water sample is conventionally in units of $mg\,l^{-1}$. That is, the solutes are measured as a concentration. Consequently, the transport rate of solutes is the product of the water discharge ($m^3\,yr^{-1}$) and the solute concentration expressed as TDS ($mg\,l^{-1}$). The solute discharge from the world's rivers, and the solute flux from river catchments, reflect the competing effects of concentration and run-off.

7.3.6 Effects of bedrock weathering on solutes

Study of unpolluted catchments composed on one bedrock lithology illuminates, after correction for atmospheric salts, the typical solute loads of rivers draining known rock types (Meybeck 1987) (Fig. 7.11). The solute loads of rivers draining large multilithologic catchments (such as the Amazon; Stallard and Edmond 1983), or even the entire land surface of the Earth (Holland 1981), can therefore be estimated with knowledge of the percentage of each rock type comprising the region being investigated. The calculated global value for solute discharge to the ocean can then be compared with the measured average composition of rivers (Livingstone 1963; Meybeck 1979). More than 80% of the total dis-

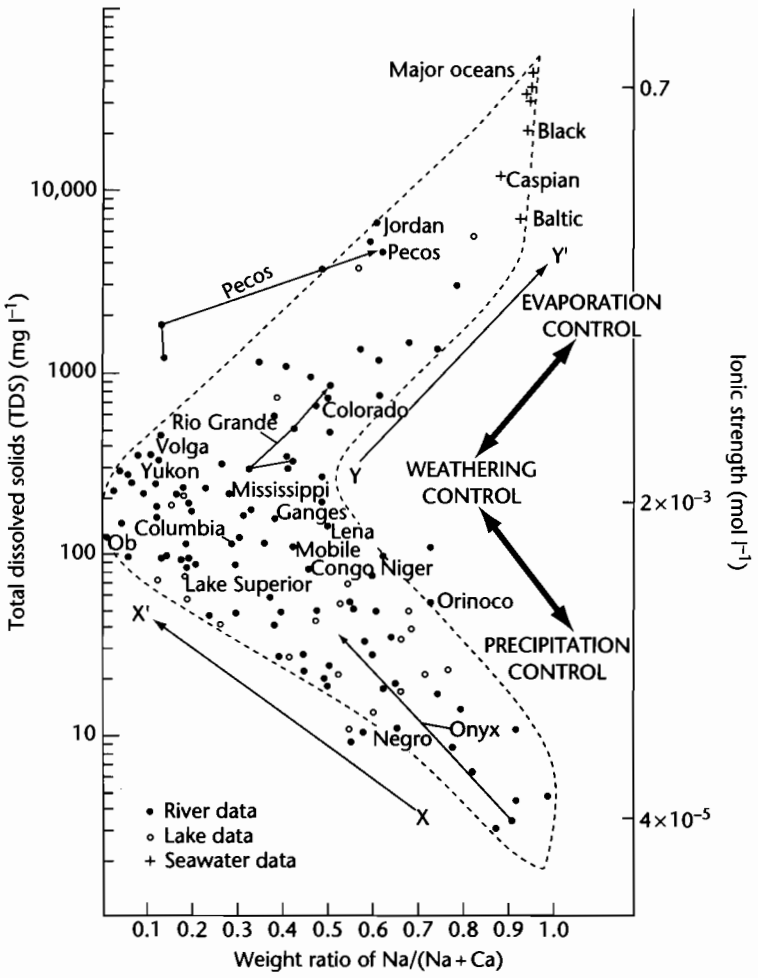

Fig. 7.10 Gibbs's (1970) scheme for global water chemistry, wherein the total dissolved solids (TDS) and ionic strength of surface waters are plotted against the cationic weight ratio of Na/(Na + Ca). The arrows connecting data points show the geochemical evolution of river waters from source downstream. Rivers plotting along the trend from X–X', such as the McKenzie (Arctic Canada) and Ganges (India), occur in regions with highly active weathering processes. Rivers falling along the trend from Y–Y', such as the Jordan (Middle East), Rio Grande and Colorado (arid southwestern North America) occur in areas experiencing high amounts of evaporation, and evolve towards the composition of sea water.

solved load of the world's rivers is made of four ions: HCO_3^-, SO_4^{2-}, Ca^{2+}, and SiO_2.

The geographic origin of river-borne material has an important impact on the total dissolved solids and suspended loads, expressed as percentages of the total input to the oceans (Table 7.3). The dissolved and suspended loads from cold, temperate, tropical, and arid regions shows that the tropical zone dominates the world's run-off. It is therefore the major source of silica and organic carbon. The dissolved silica reflects the high rates of chemical weathering in tropical regions. Despite occupying 17% of the Earth's surface, the arid regions contribute a minute amount of run-off. However, the total ions, though small, are 4 to 5 times the volume of run-off, indicating higher ionic concentrations in arid region rivers. Cold regions, despite occupying 23% of the

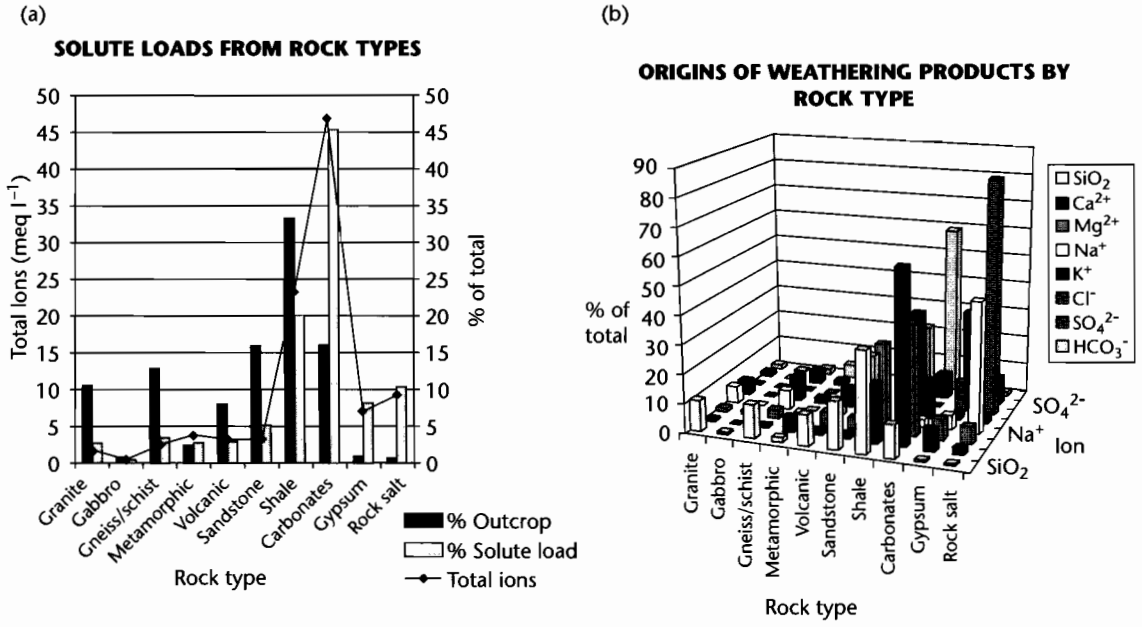

Fig. 7.11 (a) Solute loads ($meq l^{-1}$) from a range of common rock types compared to their outcrop area; (b) Distribution of eight major ions according to rock type, expressed as a percentage of the total solute load. Data from Meybeck (1987).

Table 7.3 Dissolved and suspended loads of rivers in different climatic regions. TOC is total organic carbon.

Geographic region	Area (%)	Run-off (%)	Dissolved SiO_2 (%)	Ions (%)	TOC (%)	Suspended matter (%)
Cold regions	23.4	14.7	5.4	15.5	17.5	2.7
Temperate	22.4	27.5	19.9	39.9	28.5	56.5
Tropical	37.0	57.2	73.6	41.8	52.0	34.2
Arid	17.2	0.65	1.0	2.8	1.3	6.6

Earth's surface, contribute less than 3% of the suspended matter to the ocean.

7.3.7 The composition of waters draining different rock types

The surface of the Earth is covered with different rock types (Table 7.4). The weathering of these rock types produces distinct chemistries of solutes in the run-off. (Atmospheric contribution of salts must be accounted for if necessary and care must be taken to exclude all anthropogenically affected waters.) If we combine the typical water analyses of major rock types with their relative abundance on the surface of the continents, we get a global picture of the solute delivery to the ocean from rivers (corrected for atmospheric salts). The solutes derived from different rock types is shown in Figure 7.11a.

Taking *granite* as a standard, the chemical weathering rates of the world's major rock types (Table 7.5) shows that evaporites and carbonates weather most rapidly. Volcanic and noncrystalline metamorphic rocks and shales weather at moderate rates, while granites, gneisses, gabbros, and sandstones have low rates of weathering. Chemical sediments, such as carbonates and evaporites (which have high yields of solutes), and shales (which are very extensive) therefore dominate the solute fluxes of

Table 7.4 Rock types at the Earth's surface by percentage.

Class	Rock type	Percentage (by area)
Plutonic	Granite	10.4
	Gabbro and ultrabasics	0.6
Metamorphic	Marble	0.4
	Amphibolite	1.9
	Mica–schist	1.5
	Gneiss	10.4
	Quartzite	0.8
Volcanic	Basalt	4.15
	Andesite	3.0
	Rhyolite	0.75
Sedimentary	Quartz-arenite	12.6
	Arkose (felspathic arenite)	0.8
	Greywacke (lithic, argillaceous arenite)	2.4
	Shale	33.1
	Limestone and dolomite	15.9
	Evaporite (gypsum and halite)	1.3

Table 7.5 Weathering rates of major rock types, relative to granite.

Rock type	Weathering rate
Granite	1
Gneiss/schist	1
Gabbro	1.3
Sandstones	1.3
Volcanics	1.5
Shales	2.5
Other metamorphic	5
Carbonates	12
Gypsum	40
Rock salt	80

rivers draining to the ocean. Crystalline rocks have a minor contribution to global weathering in terms of solutes.

In terms of individual elements (Fig. 7.11b), *silica* and *potassium* originate mostly by weathering of silicates. *Sodium* is derived mostly from the weathering of the salt halite (NaCl), the remainder coming from the weathering of silicates. *Magnesium* originates from both dolomites, silicates and to a lesser extent Mg-rich evaporites. *Calcium* is mainly derived from the weathering of carbonates. *Chloride* is complicated by the contamination from the atmosphere, but is strongly controlled by the dissolution of halite. *Sulfate* comes from the weathering of pyrite, evaporitic sulfate, and organic sulfur compounds. *Bicarbonate* is derived from atmospheric and soil CO_2 as well as from the dissolution of carbonate rocks.

7.3.8 Relation between solute and suspended load

The global average of solute load is roughly one-fifth of the global average of suspended load, but the ratio varies from continent to continent and from drainage basin to drainage basin. A key determinant is the topographic setting of the river. In mountainous regions, the particulate sediment yield is much higher than the solute yield, whereas in lowland regions the two are roughly in balance (Fig. 7.12).

The relationship between suspended and solute load (Table 7.6) can be appreciated by completing the practical exercise available at www.erdw.ethz.ch/Allen.

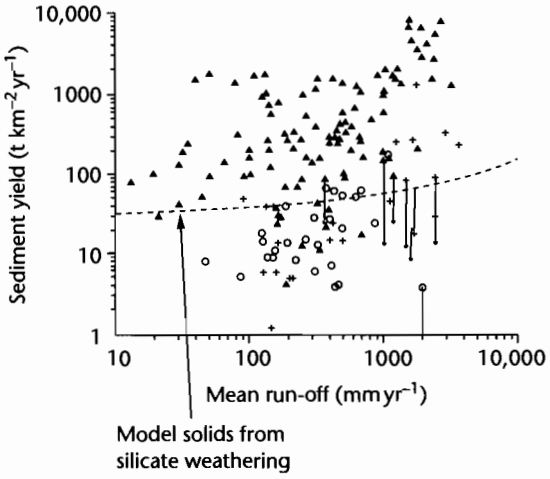

Fig. 7.12 Relation between mean run-off and sediment yield for rivers throughout the world. Open circles, coastal plain (0–100 m at headwaters) and lowland (100–500 m); crosses, upland rivers (500–1000 m); solid triangles, mountain (1–3 km) and high mountain (>3 km). Model curve is prediction for solids derived by silicate weathering (after Stallard 1995), showing that mountainous catchments provide high solid yields for a given run-off, whereas lowland rivers provide low solid yields for the same run-off.

Table 7.6 Water discharge, suspended and solute loads, and mean elevation of world's major rivers.

River	Water discharge (m^3s^{-1})	Suspended load ($Mtyr^{-1}$)	Solute load ($Mtyr^{-1}$)	Mean elevation (m)
Amazon	200,000	1150	223	426
Brahmaputra	19,300	520	61	2734
Columbia	7930	15	35	1329
Colville	492	520	6	469
Danube	6660	70	60	501
Dnepr	1650	2.1	11	152
Fraser	3550	20	11	1140
Ganges	11,600	524	75	890
Indus	7610	250	41	1855
Irrawaddy	13,600	260	92	758
Jana	920	3	1	703
Lena	16,200	12	88	602
Mackenzie	9830	125	64	634
Magdalena	6980	220	28	1203
Mekong	14,900	160	60	1062
Mississippi	18,400	400	125	656
Murray	698	30	9	266
Niger	6020	32	10	429
Nile	317	125	18	662
Ob	12,200	16	50	301
Orange	2890	91	12	1241
Orinoco	34,900	150	39	456
Parana	18,000	112	56	564
Po	1490	18	10	793
Rio Grande	95	30	2	1279
Shatt al Arab	1460	103	18	669
St. Lawrence	14,300	4	59	265
Xi Jiang	9510	80	132	670
Yangtze	28,500	480	226	1688
Yellow (Huang He)	1550	120	22	1885
Yenisei	17,800	13	65	749
Yukon	6180	60	34	741
Zaire	40,900	32.8	36	740
Zambezi	6980	48	15	1033

7.4 MEASUREMENTS OF EROSION RATES

7.4.1 Rock uplift, exhumation, and surface elevation change

There is considerable confusion in the literature regarding the terminology for various rates involved in tectonics and denudation (for discussion see England and Molnar 1990). A given point on the Earth's surface experiences vertical changes in its position relative to some reference datum such as the centre of the Earth caused by: (i) the uplift of underlying crustal rocks caused by tectonic or isostatic processes, (ii) denudation or deposition at the surface of the Earth, and (iii) compaction of the underlying sediment pile. All of these factors may contribute to a surface elevation change. Neglecting compaction and deposition in upland areas, surface elevation change is normally the net result of rock uplift and denudation.

Now consider a crustal section through a mountain range with an average elevation h and a crustal thickness h_c, shown in Figure 7.13a. If we instantaneously erode this crustal section and do not thicken the crust tectonically to compensate for the loss of crust by erosion, it will

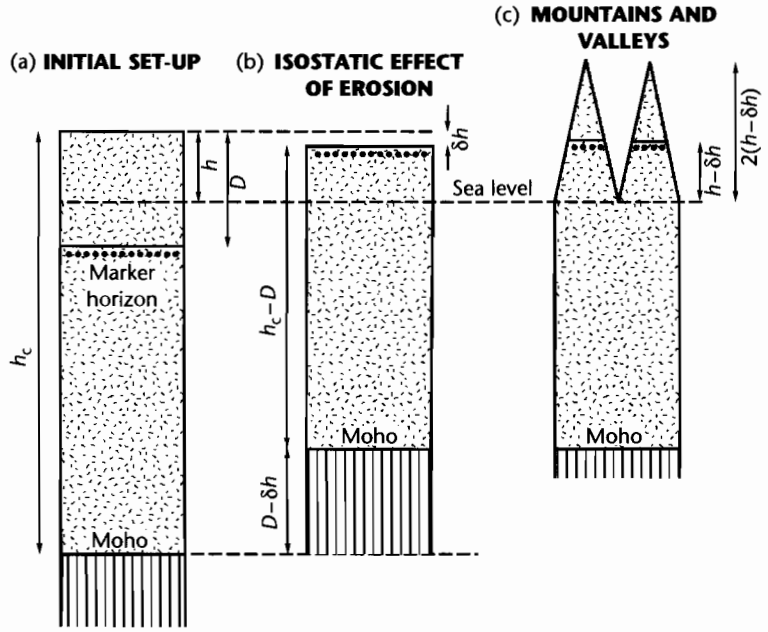

Fig. 7.13 Schematic crustal cross-sections to illustrate the possible isostatic effects of erosion on the elevation of mountain peaks and valleys, modified from Molnar and England (1990). The initial set-up in (a) shows a surface elevation of h and a marker horizon at a depth D. Erosion of amount D in (b) brings the marker horizon to the surface, resulting in a change in surface elevation Δh. In (c), rivers excavate deep valleys to sea level, which results in an uplift of the mountain peaks to an elevation $2(h - \Delta h)$, while the marker horizon remains at an elevation of $h - \Delta h$. Airy isostasy is assumed throughout.

respond isostatically to the unloading by erosion as shown in Figure 7.13b. The line with circles below it is a reference horizon in the crust. Note that it has been uplifted between (a) and (b). This is the *uplift of rock*. Note also that all of the crust above the reference horizon has been eroded between (a) and (b). This is the *exhumation* or *denudation* D. As a result of the erosion and the isostatic adjustment, there is a change in the mean elevation of the surface Δh. In this case it is a surface lowering, so the surface uplift is negative. It is essential to recognize the differences between the uplift of rock, the denudation and the surface uplift.

Now imagine that the Earth's surface is carved into mountains and valleys (as shown in Figure 7.13c). In this case the mean elevation is the same as in Figure 7.13b, but the highest mountain peaks are considerably higher than the mean elevation initially. In this sense, erosion builds mountains. The isostatic balance for the situation described above is as follows. The pressure at depth h_c in (a) is simply $\rho_c h_c g$. The pressure at the same depth after erosion (b) is $\rho_c(h_c - D)g + \rho_m(D - \Delta h)g$. Equating the two pressures and simplifying slightly, we obtain

$$\Delta h = D\frac{(\rho_m - \rho_c)}{\rho_m} \tag{7.11}$$

If $\rho_c = 2800\,\mathrm{kg\,m^{-3}}$ and $\rho_m = 3300\,\mathrm{kg\,m^{-3}}$, the elevation change is only 15% of the total denudation.

In Figure 7.13c valleys are carved down to sea level, and the highest peak is therefore at an elevation of $2(h - \Delta h)$. If the denudation is 4 km, the elevation change from equation (7.11) is 0.454 km. If the mountain range is initially at an elevation of 3 km, the highest peak will now be at 5 km, with deep valleys incised to sea level. Although this concept has been successfully applied to the Laramide uplifts of the Rocky Mountain region and Sierra Nevada, USA (Small and Anderson 1995, 1998) and the Himalayas (Molnar and England 1990; Burbank 1992), it probably exaggerates the uplift of the mountain peaks as an isostatic result of surface erosion.

It is also important to discriminate between local rates and regional rates of surface uplift and denudation. Whereas a local rate is measured at a point, and may be influenced by very specific tectonic and geomorphic processes such as slip on a fault or the occurrence of a

landslide, isostatic responses depend on regional rates of denudation.

7.4.2 Point-wise erosion rates from isotopic studies and other thermochronometers

There is a wide range of techniques used to estimate erosion rates at a point. Any individual technique is useful for a particular time range, using particular materials. A large number of techniques are applicable only to Quaternary materials (see Noller et al. 2000 for an excellent compilation). For example, dendrochronology (tree rings) can only be used up to about 10 ka, and radiocarbon dating (^{14}C) has a useful time range of only up to 35 ka. U–Th radioisotopic dating, amino acid racemization, thermoluminescence and optically stimulated luminescence all have upper age limits of *c.* 300 ka. All of these techniques therefore are restricted to Quaternary materials and are routinely used in geomorphologic studies. The time range is significantly extended by the use of *in situ* cosmogenic radionuclides (e.g., ^{10}Be and ^{26}Al), and even further by the use of thermochronometric methods such as He diffusion during U–Th decay and apatite/zircon fission track analysis. Dating techniques making use of radiometric clocks with higher closure temperatures and longer half-lives, such as ^{87}Rb–^{87}Sr (half-life 1.4×10^9 yr), ^{40}K–^{40}Ar (half-life 4.89×10^9 yr), ^{235}U–^{207}Pb (half-life 7.04×10^8 yr) and ^{147}Sm–^{143}Nd (half-life of 1.06×10^{11} yr), provide estimates of very long term (10^6–10^7 Myr) erosion rates. It needs to be stressed that the numerical values for erosion rate derived from different techniques with different temporal sensitivities cannot be directly compared (but see §7.4.4).

Since this book concerns basin analysis, we are mostly focused on the techniques providing "geological" rather than "geomorphological" rates of erosion. Use of a number of radiometric clocks with different closure temperatures (Table 7.7) allows cooling histories to be estimated. Combined with assumed or estimated geothermal gradients, these cooling histories can be used to calculate denudation rates over geological time periods. As an example, a cooling curve based on several different thermochronometers is shown for the Central Alps of Switzerland (Hurford 1986; Hurford et al. 1989) (Fig. 7.14). More recent studies across a major extensional shear zone in the Central Alps (Mancktelow and

Table 7.7 Closure temperatures of some common isotopic systems.

Mineral and dating technique	Closure temperature (°C)
Hornblende (K–Ar)	525 ± 25
Monazite (U–Pb)	525 ± 25
Muscovite (Rb–Sr)	500 ± 25
Muscovite (K–Ar)	325 ± 25
Zircon (fission track)	300 ± 55
Biotite (K–Ar)	300 ± 25
Biotite (Rb–Sr)	275 ± 25
K-Felspar (K–Ar)	200 ± 25
Apatite (fission track)	110 ± 20
Apatite (U–Th/He)	70 ± 10

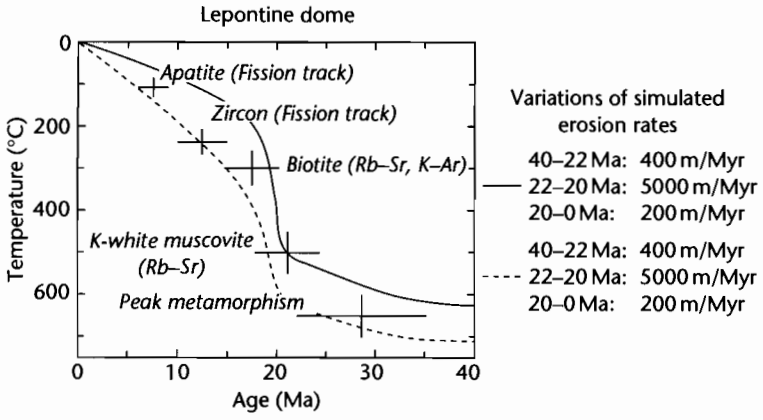

Fig. 7.14 Example of the use of a range of radiometric and thermochronometric techniques from the Lepontine dome, Central Alps, to constrain thermal (cooling) history (Schlunegger and Willett 1999). Solid and dashed lines are alternative model curves based on erosion data shown to right. Reproduced courtesy of Geological Society of London.

Grasemann 1997) show the different thermal evolution of the footwall and hangingwall blocks using multiple thermochronometers.

Conversion of a cooling history to a denudation history is not necessarily straightforward. The geothermal gradient is rarely well-constrained, though a value of 25–30 °C km^{-1} is often assumed. This geothermal gradient may be affected by changes in the basal heat flow, the internal radiogenic heat production, the advection of heat from magmas and hot fluids, and the bending of isotherms by the upward exhumation of rock towards an erosional surface of high relief. This latter effect is especially important to account for with low temperature chronometers (Fig. 7.15). Rapid erosion rates (>5 mm yr^{-1}) may cause very high geothermal gradients (60–100 °C km^{-1}) to exist in the exhuming rock body (Stüwe et al. 1994; Mancktelow and Grasemann 1997), and geothermal gradients may be very different between mountain peaks and valley floors (Fig. 7.15).

Further details on the use of apatite fission tracks and the (U–Th)/He method are found in §9.7.3.

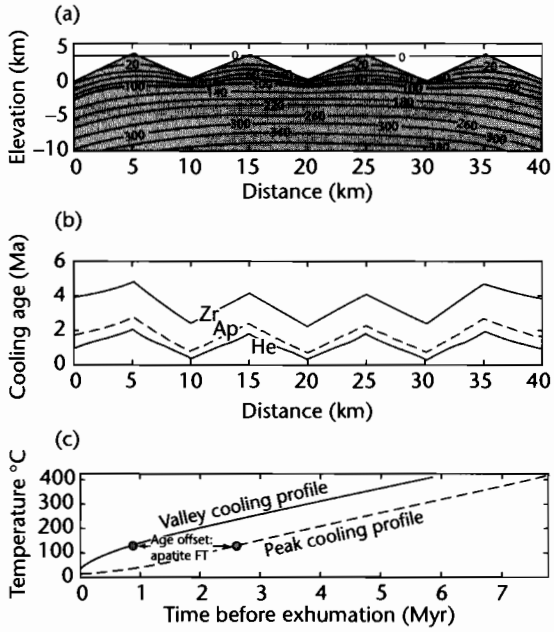

Fig. 7.15 Thermal effect of 2-D V-shaped topography (10 km wavelength, 4 km relief) on three thermochronometers with different closure/annealing temperatures; zircon fission track (Zi, 220 °C), apatite fission track (Ap, 110 °C) and U–Th/He (He, 60 °C), from Burbank and Anderson (2001). Atmospheric lapse rate is 6.5 °C km^{-1}, erosion rate is spatially uniform at 2 mm yr^{-1}, implying steady state. Note the warping of isotherms near the surface in (a), giving different geothermal gradients between the ridges and the valleys; (b) shows the expected spatial pattern of cooling ages, showing higher cooling ages for all 3 thermochronometers under the ridges; (c) shows the offset of the temperature paths of rocks exhumed in the central valley (solid) and the central peak (dashed). The apatite fission track age is offset by nearly 2 Myr. The relative effect on the cooling age is greatest for the low temperature thermochronometers, especially U–Th/He. Reproduced courtesy of Blackwell Publishing Ltd.

7.4.3 Catchment-scale erosion rates from cosmogenic nuclides

We have previously learnt that the accumulation of cosmogenic nuclides in rocks at the Earth's surface depends on latitude, altitude, and depth below the surface. If a rock is brought closer to the surface by erosion, it experiences a greater amount of cosmic-ray bombardment. The cosmogenic nuclide abundance is therefore partly a function of the rate of erosion. If samples are taken of many detrital quartz grains derived from the catchment, it is possible to estimate a catchment-wide mean erosion rate (Brown et al. 1995; Granger et al. 1996). However, since altitude and topographic shielding affect the cosmic flux, the best results come from catchments with little (less than a few hundred meters) relief. The distribution of quartz-bearing lithologies should also be relatively uniformly distributed throughout the area of the catchment. Different erosional processes (bedrock landsliding through to soil creep) also affect cosmogenic dosages. This effect can be accounted for by considering the abundance of cosmogenic nuclides in different size classes of the total detrital sediment load. Using this technique, a 3 km^2 catchment in Puerto Rico was found to have a catchment-wide average denudation rate of 40 mm kyr^{-1} using the concentrations of ^{10}Be (Brown et al. 1995). On a larger scale, Schaller et al. (2001) used ^{10}Be concentrations in quartz grains in river terraces and bedload from a number of European river basins to estimate catchment-wide denudation rates of 20–100 mm kyr^{-1} over the last *c.* 10^4 years.

Erosion rates may also be calculated by measuring the isotopic signatures of river water or sediment loads, in comparison to the isotopic composition of different source lithologies in the catchment. A spatially uniform erosion of the catchment would yield isotopic signatures in water or sediment that reflected the isotopic ratio of

the parent lithology and the area (as a percentage) of the catchment occupied by this lithology. Departures from this uniform model should reflect different erosion rates in the catchment. The total denudation rate for the whole catchment can then be obtained by summing the effects of the source areas with different lithologies. The isotopic ratios of Sr and Nd in detrital clay minerals from Nepalese catchments in the Himalayas have been used in this way (Galy et al. 1996).

7.4.4 Erosion rates at different temporal and spatial scales

It is clear from the discussion above that erosion rates can be estimated at different temporal resolutions. Consequently, an erosion rate estimate derived for a very short time resolution provides very different information to the erosion rate derived for a long time resolution. For example, the rate of bedrock lowering caused by a single debris flow in an upland channel gives a local erosion rate over a time period of minutes to hours. At the other extreme, cooling histories obtained from apatite fission track studies provide estimates of erosion rates at the time scale of millions of years.

There is considerable value in compiling the variation of erosion rates derived from methods with different temporal resolution (Dadson et al. 2003). The Taiwan orogen has rock uplift rates of 5–7 mm yr^{-1}, mean annual precipitation of 2.5 m yr^{-1}, and common strong earthquake activity, which together promote rapid rates of landsliding, debris flows, and fluvial bedrock incision (Hovius et al. 2000). Erosion rates at the decadal time scale have been calculated from the suspended sediment discharges of Taiwanese rivers at 130 gauging stations, from the rate of filling of 12 major reservoirs, and from the annual discharge of sediment into the ocean by rivers. The 30-year annual average erosion rate of Taiwan is 3.9 mm yr^{-1} using suspended load data, with significant regional differences (up to 60 mm yr^{-1} in the tectonically active SW Taiwan). Discharges of sediment into the ocean (average of 384 Mt yr^{-1} for the period 1970–2000) support the gauging station data. Erosion rates for the Holocene (<10 ka) have been derived from dated river terraces cut into bedrock using ^{14}C in wood or plant fragments in the alluvial veneer. Incision rates were calculated by dividing the radiocarbon age by the elevation of the bedrock terrace above the present-day river. Holocene erosion rates range from 1.5 mm yr^{-1} to 15 mm yr^{-1}, with broadly the same pattern as the rates obtained from sediment discharges. Long term erosion rates derived from low temperature thermochronometry (apatite fission track) are 3.0–6.0 mm yr^{-1} and 1.5–2.5 mm yr^{-1} in the metamorphic core of the mountain belt and in the fold–thrust belt of SW Taiwan respectively. A comparison of these erosion rates suggests that despite the difference in temporal resolution, the metamorphic core of the Central Range of Taiwan has consistent values of 3–6 mm yr^{-1} across the temporal scales considered. However, large variations in Holocene rates are thought to reflect the more localized impact of growing tectonic structures (e.g., in the fold and thrust belt of SW Taiwan). At decadal scales, individual major earthquakes are responsible for major spatial and temporal variations in erosion rate.

We saw in §7.3.2 that erosion rates can be estimated from the sediment volumes in neighboring sedimentary basins. This enables sediment volumes of known age to be used to calculate erosion rates at the temporal resolution of the stratigraphy. The spatially and temporally variable sediment effluxes of channel–hillslope systems in individual catchments are smoothed as the sediment is transported through major fluvial systems with large storage capacities in floodplains, channel bars, and lakes. Consequently, erosion rates (sediment yields) derived from the sediment discharge at the mouths of large river systems such as the Ganges–Brahmaputra are a buffered record of the contributing inputs (Métivier et al. 1999). In addition, the sediment preserved as marine stratigraphy is a time-integrated record of the sediment discharge from the land area over the time periods resolvable from stratigraphic dating tools. In general, therefore, longer time scale and larger spatial scale "geological" estimates of erosion rate are strongly smoothed relative to the characteristics of the individually erosive geomorphic events.

7.5 THE FUNCTIONING OF SEDIMENT ROUTING SYSTEMS

The engine for the sediment routing system, termed the *clastic factory* by Leeder (1999), is the coupled process systems of hillslopes and rivers. The topography generated by tectonics is degraded through the action of this coupled system. Rivers typically become entrenched in position, cutting down like cheese wires through the regionally uplifting bedrock (Burbank et al. 1996). The intervening hillslope system provides erosional material by soil creep, overland flow, gullying, debris flows, landslides, and rockfalls. If the rate of hillslope erosion is slower than the rate of valley lowering, hillslopes steepen

and eventually become susceptible to landsliding involving bedrock. The amplitude of hillslopes is therefore set by the effect of rock strength on landsliding. The fluvial system transports away material derived from hillslope erosion through its channel networks. This evacuation of valley bottoms is particularly rapid where the stream is incising into bedrock. Evacuation may be significantly delayed where high magnitude trigger events such as earthquakes cause an instantaneous discharge from hillslopes, blocking valleys with landslide and debris flow dams. The efflux of the hillslope–bedrock channel system sets a boundary condition for far-field sediment dispersal.

In mountain ranges, landslide activity, triggered by rainstorms and coseismic shaking (Densmore and Hovius 2000), is critical to the clearing of hillslopes (Densmore et al. 1997). A number of rapidly uplifting mountain belts (Southern Alps of New Zealand, Karakorum of the western Himalayas) are believed to exhibit a steady-state topography where the tectonic rate of uplift of rock is balanced by the landslide-dominated erosional sediment efflux. In the Southern Alps of New Zealand, the flux of material due to landsliding estimated over a 60 year period (several mm yr^{-1}) is roughly equivalent to the sediment output of the main rivers draining the region (Hovius et al. 1997).

In the sections that follow, we present a physically based but necessarily incomplete account of the processes operating in hillslope–channel systems. These processes fashion landscapes and deliver sediment to basins. Rather than attempt a comprehensive review of such a rapidly growing field of study, we highlight some basic modeling approaches to the evolution of hillslopes (§7.5.1), the incision of bedrock rivers (§7.5.2) and the far-field transport of sediment in alluvial rivers (§7.5.3). In doing so, the reader will appreciate the common methodologies used. We especially wish to emphasize that geomorphic systems have characteristic length scales and, importantly, characteristic response times. A fundamental concern is whether a step or cyclical change in a forcing parameter results in a system response that is short or long compared with the frequency of the forcing process. This will strongly impact on our ability to "invert" stratigraphic signals to interpret forcing mechanisms. Finally, we introduce some additional concepts in numerical landscape models as a way of integrating many of the ideas found in the preceding sections.

7.5.1 Modeling hillslopes

The evolution of hillslopes can be modeled as a diffusive process, in a manner similar to the 1-D conduction of heat (Chapter 2). Sediment diffusion models are based on two first-order assumptions: (i) the *sediment continuity equation*, which states that the spatial variation in the sediment transport rate is proportional to the vertical erosion or aggradation rate of the substrate, assuming there to be no changes in the concentration of suspended sediment (see Allen 1997, pp.180–1) (Boxed text 7.1), and (ii) that the flux is proportional to the local gradient, which is a basic notion underpinning all diffusional problems.

BOXED TEXT 7.1: The Sediment Continuity Equation

We derive the sediment continuity equation by the conservation of mass in an alluvial channel, and then apply it to the topographic evolution of hillslopes.

Consider an area of stream bed with unit width normal to the flow and length parallel to the flow of dx with a height of h above some reference datum (Fig. 7.16). The area of this piece of stream bed is therefore dx. A fluid flow with suspended sediment volume concentration C has a sediment transport rate (per unit width of stream bed) at the upstream end of the reference area $(q_s)_1$ and at the downstream end of the reference area $(q_s)_2$. We can denote the difference in the transport rate at the upstream and downstream ends of the reference area as dq_s. Any change in the bed elevation due to either erosion or deposition must be reflected in a downstream change in the sediment transport rate as long as the sediment concentration C does not change. The amount of sediment deposited over the reference area associated with a downstream decrease in the sediment transport rate is simply the product of the difference between the upstream and downstream sediment transport rates (dq_s) and the time interval dt. This sediment produces a layer of thickness dh with a porosity λ over an area dx. Expressed mathematically

$$dh\,dx = -\frac{1}{1-\lambda} dq_s\,dt \qquad (7.12)$$

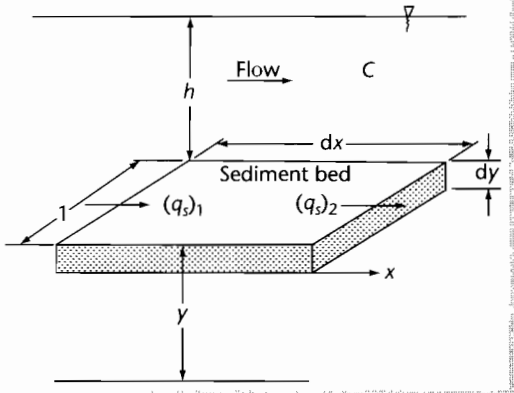

Fig. 7.16 Set-up and notation for the derivation of the sediment continuity equation. Notation explained in text.

A change in bed elevation may also result from a temporal change in the volume concentration of suspended sediment throughout the flow. For example, if the suspended sediment concentration throughout the flow is decreasing, the bed must be accreting irrespective of downstream variations in the sediment transport rate. The bed elevation change due to this effect in a flow of depth h is

$$dh\,dx = -\frac{1}{1-\lambda}(dC.h)dx \tag{7.13}$$

The net change in bed elevation over a time interval dt is therefore

$$\frac{dh}{dt} = -\frac{1}{1-\lambda}\left(\frac{dq_s}{dx} + h\frac{dC}{dt}\right) \tag{7.14}$$

In other words, the change of bed elevation in time (erosion or deposition) is related to the downstream change of the sediment transport rate and to the change of the suspended sediment concentration in time. If the suspended sediment concentration does not vary in time, that is, $dC/dt = 0$, or if the suspended sediment concentration is zero, then the sediment continuity equation simplifies to

$$\frac{dh}{dt} = -\frac{1}{1-\lambda}\frac{dq_s}{dx} \tag{7.15}$$

The change in the bed elevation is affected by the subsidence (or uplift) of the alluvial basin. If $\sigma(x)$ is the subsidence rate as a function of the downstream distance x, the sediment continuity equation becomes

$$\sigma(x) + \frac{dh}{dt} = -\frac{1}{1-\lambda}\frac{dq_s}{dx} \tag{7.16}$$

The sediment continuity equation (7.15) can easily be modified for the case of the topography of a hillslope:

$$\frac{\partial q}{\partial x} = -\rho_b \frac{\partial y}{\partial t} \tag{7.17}$$

where q is the discharge of mass per unit width of hillslope, ρ_b is the bulk density of the mobile regolith, x is the horizontal distance from the ridge crest, y is the vertical coordinate, and t is time (Fig. 7.17). The mass discharge per unit width is assumed to be proportional to the local topographic slope by a transport coefficient k, encompassing all of the geomorphic processes acting on the hillslope such as rainsplash, soil creep, bioturbation, overland flow, rilling, and gullying:

$$q = -k\frac{\partial y}{\partial x} \tag{7.18}$$

The discharge of sediment per unit width is given by equation (7.18) as long as the regolith production rate by weathering (§7.2.2) is sufficiently large. Combining (7.17) and (7.18) gives the familiar diffusion equation

$$\frac{\partial y}{\partial t} = \kappa\frac{\partial^2 y}{\partial x^2} \tag{7.19}$$

where the *diffusivity* $\kappa = k/\rho_b$. This states the familiar result that the erosion or deposition scales on the topographic curvature. The form of a hillslope profile therefore depends on the diffusivity, but the amplitude of the profile is set by the rate of channel incision. Let the incision rate be $\dot{e}$, and the length of the hillslope from ridge crest to valley bottom L. The steady state profile of the hillslope is obtained by integrating the diffusion equation twice:

$$y = \frac{\dot{e}}{2\kappa}(L^2 - x^2) \tag{7.20}$$

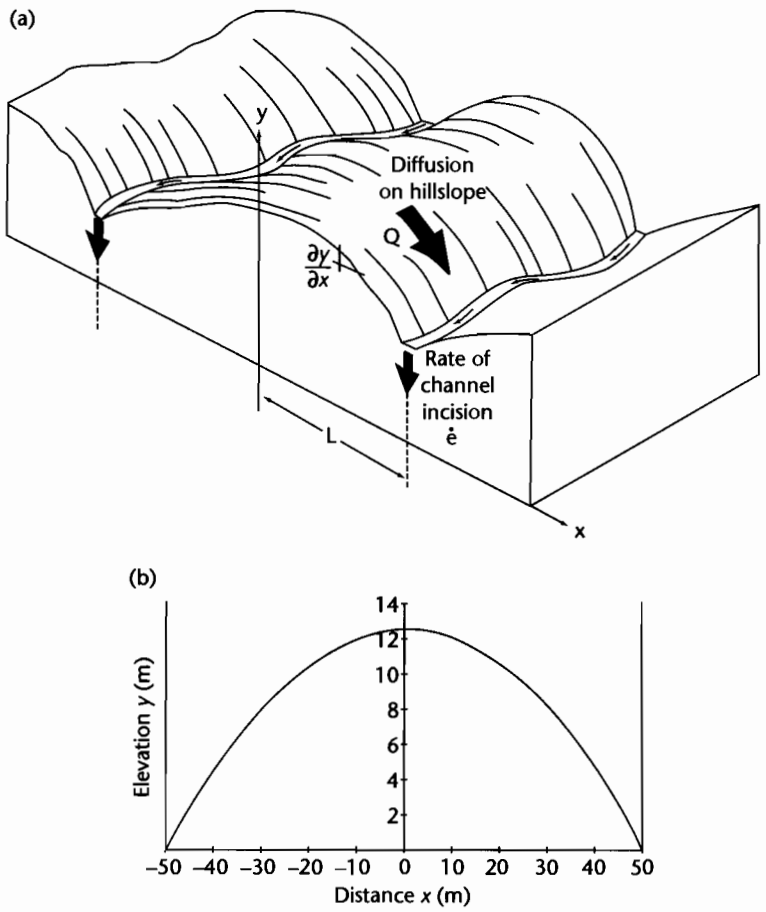

Fig. 7.17 (a) Schematic showing hillslopes and bedrock channels, with notation; (b) Solution (parabolic) for the hillslope profile using the parameter values given in the text.

which shows that the hillslope profile is parabolic. The slope of the hillslope at the ridge crest is zero, and the maximum slope is at the boundary with the river channel (at $x = L$), where it has the value

$$\left|\frac{\partial y}{\partial x}\right|_{\max} = \frac{\dot{e}L}{\kappa} \tag{7.21}$$

The time constant for the hillslope system is given by

$$\tau = \frac{L^2}{\kappa} \tag{7.22}$$

We can use these relationships to predict the hillslope landforms under a range of parameter values (Fig. 7.17b). If two channels located 100 m apart ($L = 50$ m) incise at a rate of 0.5 mm yr^{-1}, typical of tectonic uplift rates, and a diffusion coefficient applicable to the slow processes of rainsplash and soil creep is 50×10^{-3} m^2 yr^{-1}, the maximum gradient of the hillslope as given by equation (7.21) is 0.5 ($\tan^{-1}$ 0.5 is 27°). The time constant from equation (7.22) is 50 kyr.

Diffusional theory such as presented above can also be used to study the degradation of fault scarps (Hanks et al. 1984), river terraces (Avouac 1993), or independently dated wave-cut lake margin scarps, such as those of Pleistocene Lake Bonneville, Utah. The scarp profile evolves over time by an erosional smoothing of the upper portion and a depositional smoothing of the lower portion. The slope of the midpoint of the scarp decays as the square

root of time, exactly as in the thermal evolution of a piece of newly created oceanic crust (§2.2.4). Diffusivities in the present-day arid landscapes of the American west were estimated as $5–100\,m^2 \times 10^{-3}\,yr^{-1}$ (Burbank and Anderson 2001). However, a large number of studies suggest that we cannot always assume that the diffusivity κ is constant and independent of x on hillslopes and scarps of various origin. Furthermore, the upper parts of hillslope profiles may be strongly affected by the regolith production rate (§7.2.2), so that they are weathering-limited and therefore not strictly determined by linear diffusion (Rosenbloom and Anderson 1994).

If the channel incision rate is large compared to the diffusive mass wasting of the hillslope, a critical slope will be reached after which landsliding takes place. This is why mountains with high channel incision rates such as the Southern Alps of New Zealand and the Finisterre Range of Papua New Guinea have hillslopes dominated by landsliding. Landslide-dominated hillslopes are straight rather than parabolic (Anderson 1994; Densmore et al. 1997; Densmore and Hovius 2000). The critical slope for the onset of landsliding depends on bedrock strength, vegetation cover, and fluid pressures in the regolith and bedrock. It is likely to vary between *c.* 30° and 60°. For example, Ellis et al. (1999) found a critical slope for landsliding of just 34°. For the hillslope system above, this critical slope would be achieved at a channel incision rate of $1.2\,mm\,yr^{-1}$. For effective diffusivities in the range 10 to $100 \times 10^{-3}\,m^2\,yr^{-1}$, the channel incision rates required to initiate landsliding at critical slopes between 40° and 60° is between $0.2–3.5\,mm\,yr^{-1}$. This range covers the tectonic uplift rates of recent mountain belts. The rates of rock uplift along the Alpine Fault in the Southern Alps of New Zealand is over 5 mm yr^{-1}, with rates of $1\,mm\,yr^{-1}$ along the main drainage divide of the Southern Alps (Koons 1989). The Central Range of Taiwan and the Finisterre Range, Papua New Guinea, have similar tectonic rates of rock uplift.

The flanks of mountain belts are commonly sculpted into transverse valleys and interfluve ridges with a characteristic spacing (Hovius 1996). The transverse river systems draining linear mountain belts appear to maintain a near constant aspect ratio (Fig. 7.18; Table 7.8)

$$\frac{L_x}{L_z} \approx 2.2 \tag{7.23}$$

where L_x is the length of the main transverse trunk stream and L_z is the width of the catchment or outlet

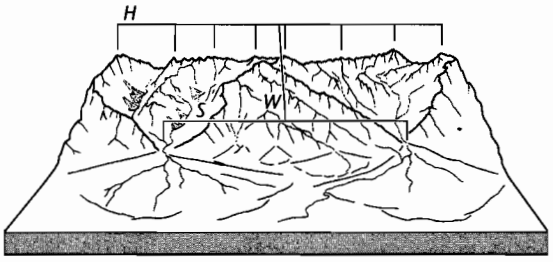

Fig. 7.18 Schematic illustration of two river catchments in a mountainous area with an average elevation of the axial ridge H and half-width W. The catchments have a transverse spacing S at the mountain front, as seen from the locations of the apices of the alluvial fans. Table 7.8 gives data from Hovius (2000).

spacing. In the Southern Alps of New Zealand, the transverse landslide-dominated catchments on the wet western flank have transverse spacings of 5–10 km and catchment lengths of 20–25 km. Maximum hillslope relief is about 1500 m. What controls this geomorphologic sculpture?

The diffusion equation can be modified to include an advective term to account for the vertical uplift rate of rock:

$$\frac{\partial y}{\partial t} = \kappa\left(\frac{\partial^2 y}{\partial x^2}\right) + V(x) \tag{7.24}$$

where $V(x)$ is the vertical tectonic uplift rate of rock. This diffusion–advection equation can be integrated twice to obtain the height of the hillslopes. We first assume that the landscape is in steady state, so $\partial y/\partial t \rightarrow 0$. Consequently equation (7.24) becomes

$$\kappa\frac{\partial^2 y}{\partial x^2} = -V(x) \tag{7.25}$$

which when integrated is

$$\frac{\partial y}{\partial x} = -\frac{Vx}{\kappa} + c_1 \tag{7.26}$$

Since $\partial y/\partial x = 0$ at $x = 0$, $c_1 = 0$. Integrating (7.26) once again we obtain

$$y = -\frac{Vx^2}{2\kappa} + c_2 \tag{7.27}$$

Table 7.8 Mountain belt geometry and drainage spacing (after Hovius 2000).

Mountain belt	H (m)	W (km)	a (m km^{-1})	L (km)	n	S (km)	R
Southern Alps	2653	21.1	123	198	19	10.99	1.92
Finisterre Range	3640	25.5	137	187	15	13.36	1.91
Maoke Range	4038	36.4	108	298	19	16.56	2.20
Barisan Range	1914	28.0	66	439	33	13.72	2.04
Central Range	3292	25.0	124	243	20	12.29	1.95
Kirgizskiy Khrebet	4101	34.7	92	202	14	15.52	2.23
Northern Tien Shan	4950	38.1	84	269	15	19.18	1.99
Apennines	1949	39.2	48	547	33	17.65	2.22
Sierra Nevada	3192	84.0	36	422	12	38.36	2.19
Peruvian Andes	5797	81.9	70	1000	25	40.00	2.05
Central Himalayas	7822	158	49	1610	12	139.2	1.17

Note: H, mean height of the culminations of the drainage divide: W, average half-width of the mountain belt, measured from the main drainage divide to the mountain front: a, mean gradient of the enveloping slope of the range flank: L, length of section over which spacing of drainage outlets was measured: n, number of streams draining section measured: R, aspect ratio of transverse drainages for the section ($R = W/S$). Note that the value of R in the central Himalayas is markedly different to the tight clustering of R around 2 for the other mountain belts. Anticlines in the Himalayan foothills cause drainage deflection and capture, which amalgamates transverse streams into larger catchments with a wider spacing.

The constant of integration can be found by applying the boundary condition that $y = 0$ at $x = L$. Consequently, $c_2 = VL^2/2\kappa$. Equation (7.27) therefore becomes

$$y = \frac{V}{2\kappa}(L^2 - x^2) \tag{7.28}$$

The maximum height of the hillslope y_{max} is the height at $x = 0$ minus the height at $x = L$. Consequently,

$$y_{\max} = \frac{VL^2}{2\kappa} \tag{7.29}$$

It is now possible to return to the western flank of the Southern Alps of New Zealand (Koons 1989) (Fig. 7.19) where $L = 3000$ m, $y_{max} = 1500$ m and V is approximately 5 mm yr^{-1}. The effective erosional hillslope diffusivity must be 15 m^2 yr^{-1}. It is considerably higher than the value of 0.01 m^2 yr^{-1} estimated for the semi-arid to arid hillslopes in the western United States (Rosenbloom and Anderson 1994). The effective erosional hillslope diffusivity encompasses a whole range of geomorphologic processes acting on the hillslope, and therefore may lump together the effects of mean annual precipitation (over 12 m yr^{-1}) and rainfall intensity, rock strength, vegetation, and temperature-dependent weathering. The value calculated here reflects the high activity of rapid mass wasting events. The mean gradient of the hillslopes from the diffusion model is y_{max}/L, which for the Southern Alps examples is 0.5, or 27°. This corresponds closely with measured mean values. Inspection of equation (7.29) shows that the transverse spacing of hillslopes must always be small in order to balance high rates of tectonic uplift of rock in a steady state landscape. On the drier eastern flank of the Southern Alps (<1 m yr^{-1} mean annual precipitation) the tectonic uplift rates reduce from 1 mm yr^{-1} at the main divide to zero at the east coast of South Island. On this flank, braided river valleys are broadly spaced and less deeply entrenched into bedrock.

From equation (7.29), the aspect ratio of y_{max}/L can also be written as $VL/2\kappa$. This is a dimensionless ratio of a flow rate of rock across a section of the transverse drainage versus an effective erosional diffusivity. It has the form of a *Peclet number*. If the *erosional Peclet number* is greater than about 0.6, it is unlikely that erosional processes can keep pace with tectonic uplift rates to produce a steady state landscape. The erosional Peclet number for the wet western flank of the Southern Alps using the parameter values above is 0.5.

7.5.2 River incision

The products of hillslope erosion are transported away by channelized flows (rivers). Channelized flow takes place wherever a stream power threshold is locally exceeded (Montgomery and Dietrich 1988). There is a fundamental distinction, however, between rivers incised into bedrock (this section) and alluvial rivers with beds and banks of sediment (§7.5.3). Bedrock rivers are those that lack a coherent bed of active alluvium (Howard

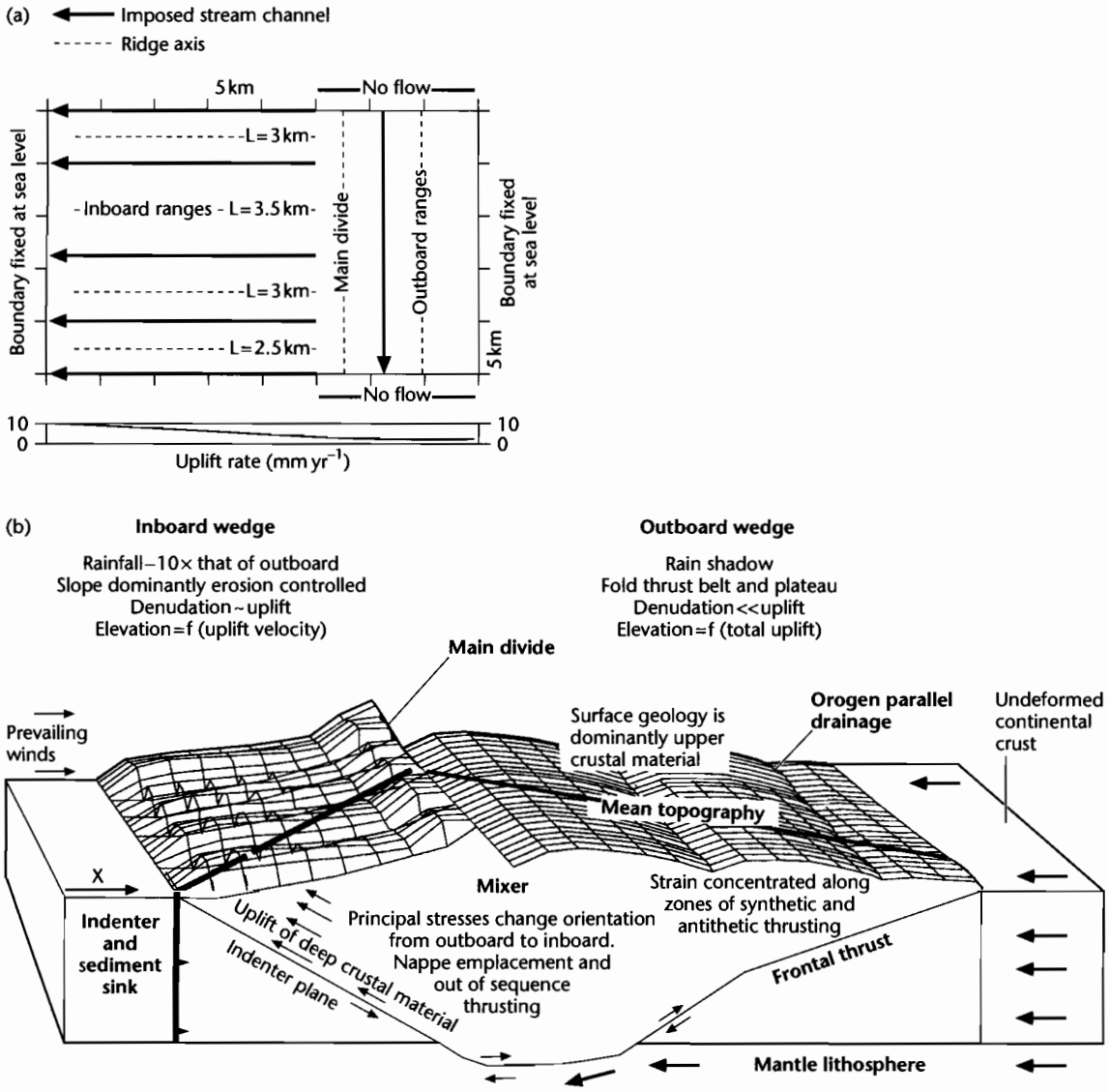

Fig. 7.19 The doubly vergent orogenic wedge of the Southern Alps has deeply etched, narrowly spaced, transverse drainages on the wet, western flank where tectonic uplift rates are high. On the drier eastern flank, rivers are much less deeply entrenched and are broadly spaced. (a) Boundary and initial conditions for the numerical model in Koons (1989); (b) Plate velocities outside the wedge, tectonic transport directions within the wedge, and surface topography for a doubly vergent wedge with precipitation from the left. The marked asymmetry in denudation promotes a strong asymmetry in rock uplift within the wedge. Modified from Koons (1989).

1987). Consequently, bedrock rivers have a transport capacity that is larger than that required to transport all of the available sediment. They incise by abrasion by the sediment load, plucking of blocks from the bed and cavitation (Hancock et al. 1998). Bedrock rivers are the dominant channel type in mountainous topography.

There are a number of interrelated ways of approximating the rate of bedrock incision. A common approach makes use of the idea that bedrock incision is controlled by an area-slope or discharge-slope product. This is often termed the *stream power rule* (Boxed text 7.2). A related view (Howard 1994) is that the rate of bedrock

BOXED TEXT 7.2: Use of the Stream Power Rule

Consider a volume V of water, density ρ_w, in a river that moves downstream changing its elevation by dy over a lateral distance dx in a time period dt. There is a change in potential energy caused by this downstream motion. If we assume that the mass of water ($V\rho_w$) does not change, this change in potential energy is $V\rho_w g dy$. The rate of change of energy loss, or power, is simply $V\rho_w g dy/dt$. Now the volume of water moving through the river per interval of time dt is Q_w/dt, where Q_w is the water discharge. Consequently, the stream power per length of stream channel dx is given by

$$P/dx = kQ_w \frac{dy}{dx} \tag{7.30}$$

where the coefficient $k = \rho_w g$. The stream power (per length of stream channel) is therefore proportional to a discharge-slope product. The rate of bedrock incision is conventionally assumed to have the form of a power law version of equation (7.30)

$$\frac{\partial y}{\partial t} = -c_b Q_w^m S^n \tag{7.31}$$

where Q_w is the total discharge of water, S is the slope, m and n are empirical coefficients and c_b is a bedrock incision coefficient. The parameters contributing to the value of the bedrock erosion coefficient c_b remains debatable. In the simplest case, let us assume that it is a constant determined by lithology, ranging from 7×10^{-3} for mudstones to 6×10^{-6} for granite and basalt (Stock and Montgomery 1999).

The discharge of water in the channel depends on the drainage area upstream of the stream channel A, the average precipitation over the area P, and a run-off coefficient C_r that accounts for transmission losses through the hillslope-channel system (§7.3) ($Q_w = C_r AP$). If the long-term effective discharge varies linearly with drainage area, then $m = n = 1$ and the incision rate is then linearly proportional to stream power (Seidl and Dietrich 1992).

The drainage area upstream of a particular point in the channel increases with distance down the channel, and on the basis of empirical results (Montgomery and Dietrich 1992) is well described by

$$A = \frac{x^2}{3} \tag{7.32}$$

Consequently, the rate of channel incision can be expressed as

$$\frac{\partial y}{\partial t} = -c_1 x^2 S \tag{7.33}$$

where c_1 is a coefficient equal to $c_b P C_r/3$. It can be seen therefore that in a bedrock valley where the width of the stream does not change significantly in the downstream direction, the rate of bedrock incision varies by the square of the distance from the drainage divide x and the single power of the slope S. These two effects are traded off against each other. The result is that the rate of valley incision increases to a maximum at a certain distance from the drainage divide.

However, theory and empirical data suggest that m/n is ~0.5, and analysis of the topography of the Zagros fold and thrust belt (Tucker 1996) indicates that m and n are 1/3 and 2/3 respectively. In such a case, the rate of bedrock channel incision becomes

$$\frac{\partial y}{\partial t} = -c_2 x^{2/3} S^{2/3} \tag{7.34}$$

where c_2 is equal to $c_b (PC_r/3)^{1/3}$.

It is also possible that the bedrock erosion coefficient is a more complex function of hydrological variables, including the flow resistance of the bed. The channel incision rate can also be expressed in terms of an "*erosional velocity*" c_v (units of $m\,s^{-1}$), so that

$$\frac{\partial y}{\partial t} = -c_v \left(\frac{Q_w}{Q_*} \right)^m S^n \tag{7.35}$$

where Q^* is a characteristic channel discharge (equal to the total area of the catchment times the average precipitation rate, Tucker and Slingerland 1996).

incision is proportional to the shear stress on the bed. Alternatively, the rate of incision could be related to the excess stream power available to erode bedrock in the channel bed above that required for sediment transport (Seidl and Dietrich 1992). For simplicity we illustrate the modeling of bedrock incision using the area-slope or discharge-slope product in Boxed text 7.2.

Hillslopes and bedrock channels are dynamically linked, but they have different response times. The hillslope response time is L^2/κ (eqn 7.22). The response time of the channel system must be influenced by the length of the channel and the average velocity of the knickpoints generated when the channel adjusts to its new base level. Such knickpoints migrate headwards, but slow down in their upstream velocity as the stream power decreases due to a reduction in the contributing drainage area. Anderson (1994) calculated channel system response times assuming the stream power rule as typically 10^3–>10^4 yr. This is significantly longer than the response time for landslides, but is comparable to the hillslope response time. This suggests that hillslopes characterized by the high effective diffusivities produced by landslides are always in equilibrium with the incising channels. Less steep hillslopes dominated by slow diffusion, however, may not be in equilibrium with channel incision and may display transient rather than steady state morphologies.

We saw in §7.4.1 that deep incision by rivers causes a removal of mass from the area undergoing erosion, which drives an isostatic compensation (Molnar and England 1990). Consequently, the high mountain peaks fringing deeply incised valleys may experience a surface uplift. We can now restate this possibility in terms of a bedrock river incision rule. Assuming the isostatic uplift to be due to a local (Airy) compensation rather than to a regional flexure (Chapter 4), the rate of uplift of the mountain peaks is

$$\frac{\partial y_p}{\partial t} = \frac{1}{2}\left(\frac{\rho_c}{\rho_m}\right) c_1 x^2 S \tag{7.36}$$

where ρ_c and ρ_m are the crustal and mantle densities respectively. Using $c_1 = 0.5\,\mathrm{m^{-1}\,Myr^{-1}}$, profiles along the Arun and Karnali Rivers in the Nepalese Himalaya show the elevation of mountain peaks some distance downstream from the drainage divides in the Tibetan Plateau (Montgomery 1994) (Figs. 7.20, 7.21). The greatest relief is on the edge of the Himalayan Plateau, where the Karnali River has incised 4500 m below the surrounding peaks. As much as 20–30% of the present elevation of the Himalayan peaks can be explained by isostatic compensation.

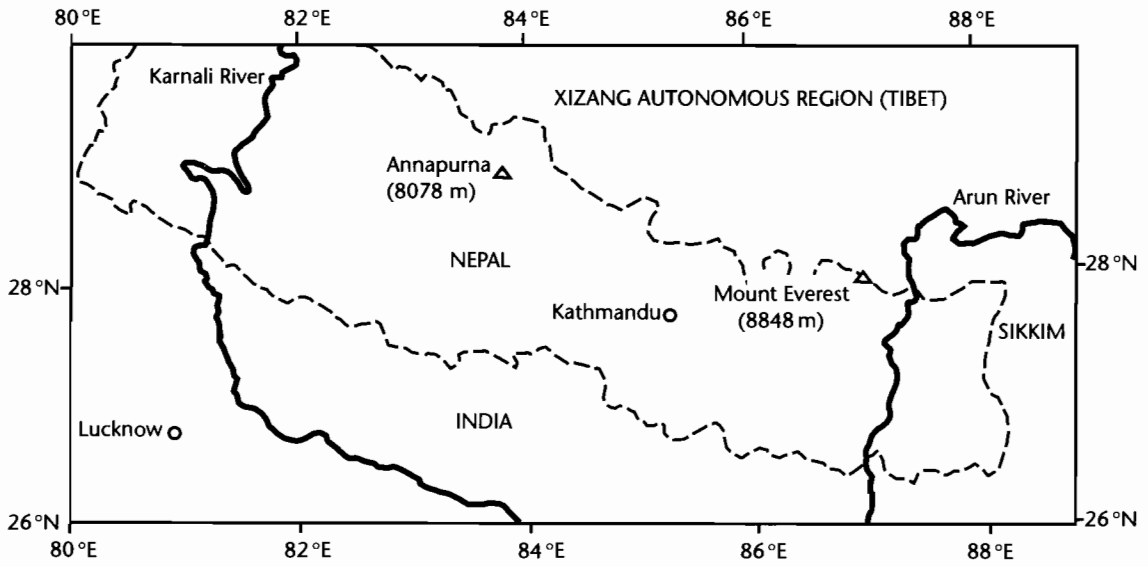

Fig. 7.20 The Himalayas and Tibetan Plateau, with location of Arun and Karnali Rivers.

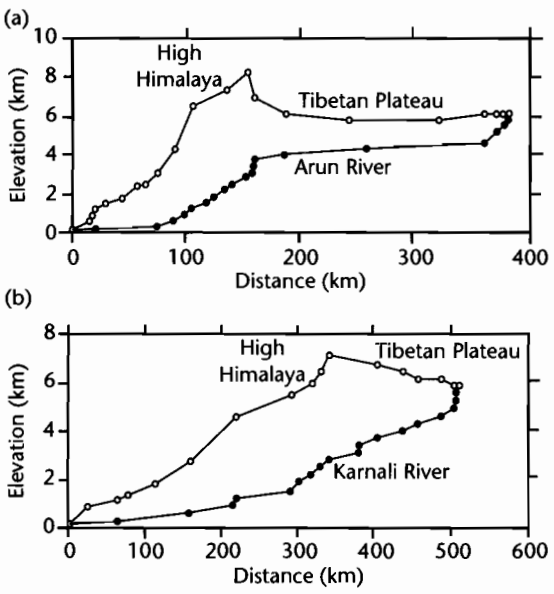

Fig. 7.21 Long profiles of the mountain peaks and valley bottoms along the Arun (a) and Karnali (b) rivers, showing the high elevation of the summits *c.* $x = 200$ km from the headwater regions, suggesting that bedrock river incision rates produce an isostatic uplift of the peaks. After Montgomery (1994). Reproduced courtesy of American Geophysical Union.

7.5.3 Long range fluvial transport

A fundamental characteristic of alluvial channels is that they have sufficient sediment to equal or exceed the transport capacity. The transport of sediment in river systems has been the subject of modeling by a generation of civil engineers, geomorphologists, and latterly, geologists. Our purpose here is not to attempt a full description of long range sediment transport by rivers. For more comprehensive treatments the reader is referred to Parker (1978a, b), Paola et al. (1992) and Dade and Friend (1998).

Various forms of diffusion equation of the type given in equation (7.24) have been applied to long range fluvial transport. Here we concentrate on an assessment of long range fluvial transport of a mixture of gravel and sand. The quantitative development of this group of models can be found in Paola et al. (1992) and Marr et al. (2000). It is well known in modern mixed gravel–sand fluvial systems that there is a relatively steep gravelly proximal zone with an abrupt change to a lower gradient sandy zone (Sambrook-Smith and Ferguson 1995). To be able to predict the movement of the "gravel front," or "gravel–sand transition" would be of considerable benefit in basin analysis.

Most models of sediment transport in rivers make the same set of assumptions.

1 First, it is assumed that the long term flow of water in a river approximates that of a steady uniform flow down an inclined plane. For a flow of depth h and density ρ on a slope $\delta y/\delta x$, the downslope component of the fluid weight on a unit area of the river bed is $\rho g h \delta y/\delta x$. This downslope acting force must be opposed by an equal and opposite drag force exerted on the fluid by the unit area of bed – this is the shear stress τ_0 (Fig. 7.22a). Consequently, the force balance gives

$$\tau_0 = -\rho g h \frac{\partial y}{\partial x} \tag{7.37}$$

Rivers are anything but steady and uniform. However, equation (7.37) can be used as an approximation for long-term river behavior. It works best for shallow high-gradient streams and worst for deep, low-gradient streams. If the flow depth is large compared to the channel width, h should be replaced by the *hydraulic radius* R in equation (7.37) (Fig. 7.22b).

2 Second, we make use of an equation that expresses the resistance to flow in the channel. A fluid moving over its bed and banks experiences frictional losses of energy known as *flow resistance*. Where the bed of the river is rough, as is always the case in natural rivers, the energy losses should in some way be related to the length scale of the roughness of the bed. This roughness can be expressed in a number of ways. A common method is to use the *Darcy–Weisbach friction factor* f

$$f = \frac{8\tau_0}{\rho_f u^2} \tag{7.38}$$

where u is the flow velocity. The friction factor (or similar forms such as the Chézy coefficient C and Manning's n) varies strongly according to the grain size of the sediment on the river bed and is especially affected by the presence of bedforms such as ripples and dunes and of macroforms such as bars, chutes, and pools.

3 Third, we conserve the discharge of water through the system. Consider a slice of width B of an alluvial basin of length L, which has active channels on its surface with

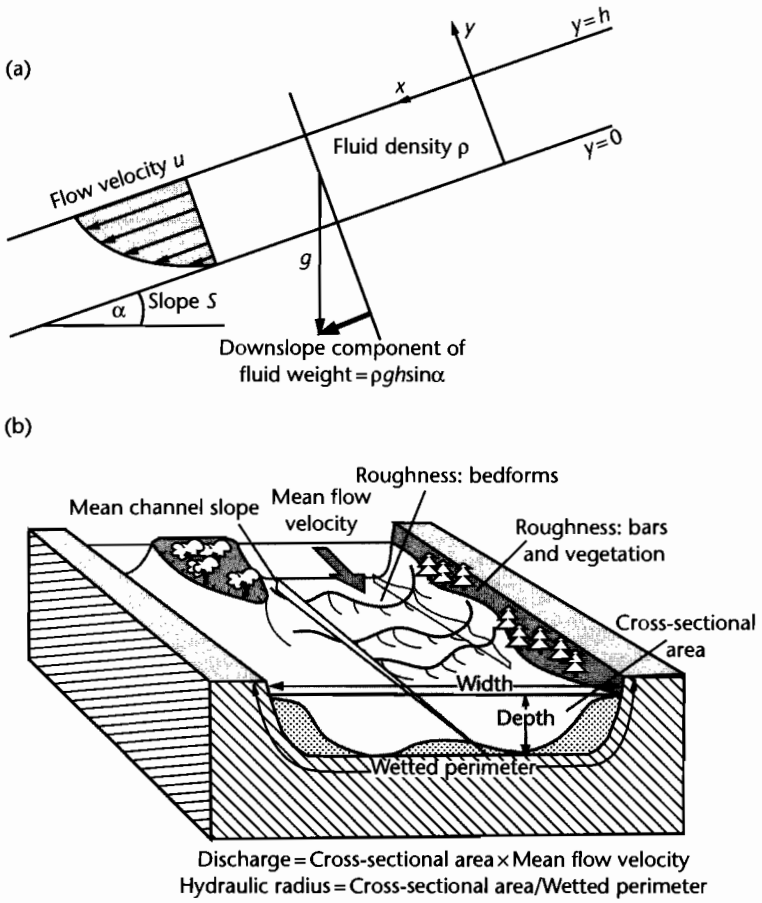

Fig. 7.22 (a) Notation for steady uniform flow down an inclined plane of slope sin α; (b) The wetted perimeter and hydraulic radius of a river. The presence of bar forms, pools, dunes and ripples, vegetation, and pebbles all contribute to the friction factor of the river.

cumulative width b, of flow depth h and containing flows of velocity u (Fig. 7.23). Let β be the fraction of the section width B occupied by channels, so $\beta = b/B$. The discharge of water Q_w in the channels occupying the width of floodplain B is bhu, or averaged across the floodplain is βhu. Consequently,

$$\beta = \frac{Q_w}{hu} \tag{7.39}$$

4 Finally, we make use of the sediment continuity equation (7.16), modified by the use of a dimensionless shear stress τ_*, as given by Shields

$$\tau_* = \frac{\tau_0}{(\rho_s - \rho_f)gD} \tag{7.40}$$

where D is the median grain size and ρ_s and ρ_f are the sediment and fluid densities respectively. There appear to be strong limits on the value of the dimensionless shear stress, so that it can be treated as a constant, at about 1.4 times the critical shear stress at the threshold of particle motion in coarse-grained braided rivers, and between 1 and 2 in alluvial sand-bed rivers (Paola and Seal 1995; Dade and Friend 1998; Parker et al. 1998). It is probably a constant because if it is too high, the stream erodes its banks and widens its bed, thereby reducing the shear

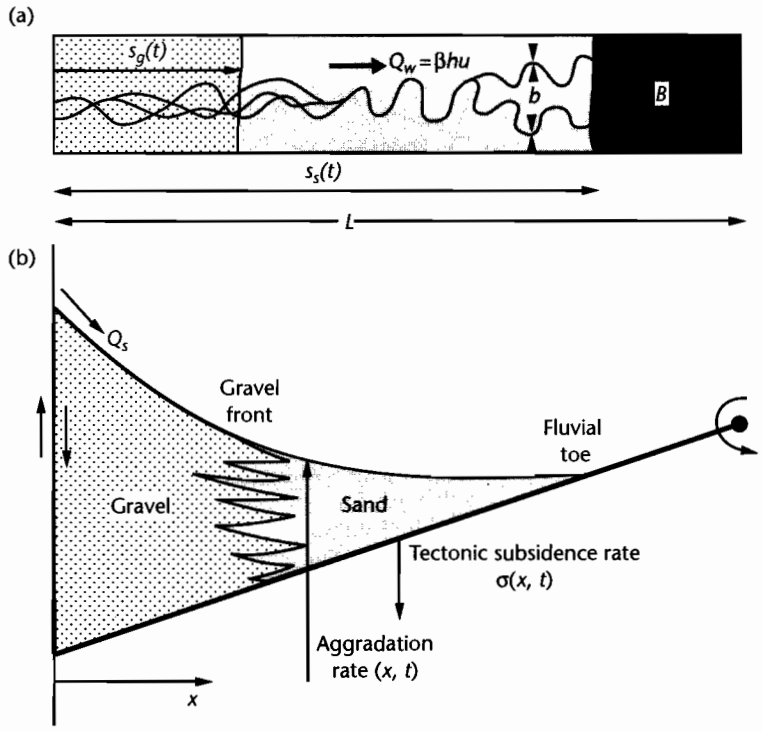

Fig. 7.23 Map view and cross-section of a slice of alluvial basin of length L, width B, containing channels with cumulative width b undergoing tectonic subsidence $\sigma(x)$ approximated by a linear tilt from a distant hinge. Note the break in slope at the gravel front and the position of the fluvial toe. After Marr et al. (2000). Reproduced courtesy of Blackwell Publishing Ltd.

stress per unit area of stream bed (Parker 1978a, b). There is a sharp jump in τ_* at the gravel–sand transition or "gravel front" in many rivers. The modified sediment continuity equation therefore has the form

$$\frac{\partial y}{\partial t} = \frac{\partial}{\partial x}\left(\kappa \frac{\partial y}{\partial x}\right) - \sigma(x) \tag{7.41}$$

where the effective diffusivity or transport coefficient κ of the alluvial system is dependent principally on the discharge of water, a friction (flow resistance) factor, a dimensionless sediment transport rate, and the dimensionless shear stress. The transport coefficient is constant within the gravel and sand regimes, but changes by a factor of about 10 at the boundary. Typical values for κ used by Marr et al. (2000) are $0.01\,\mathrm{km^2\,yr^{-1}}$ in the gravel regime and $0.1\,\mathrm{km^2\,yr^{-1}}$ in the sand regime.

The simplest approximation of the time required for equilibrium to be achieved with a set of forcing conditions, or *basin response time* T_{eq}, is L^2/κ, where L is the basin length, as in the diffusional problems previously encountered. In a two-diffusion model, the gravel and sand regimes may have their own response times. For a basin length of 100 km and κ for gravel of $0.01\,\mathrm{km^2\,yr^{-1}}$, the response time is 10^6 yr, whereas with κ for sand, we have a response time of 10^5 yr. An important parameter should be the period of the forcing T compared to the basin response time T_{eq}. Marr et al. (2000) considered cross-sections of basin stratigraphy under different conditions of forcing, using the total sediment flux Q_s, the water discharge Q_w, the gravel fraction f_g, and the rate of tectonic subsidence σ. When the forcing variable has a rapid sinusoidal change (for example, in sediment supply), $T << T_{eq}$, the time for equilibrium to be re-established is almost constant for a fixed gravel fraction, suggesting that the basin response time is controlled by the fluvial system rather than the frequency of the forcing. The value of this *intrinsic* response time is determined by the gravel fraction (fast – $<10^5$ yr – with low gravel fractions and

slow – 10^5–10^6 yr – for high gravel fractions). In the simulations found in Figures 7.24 and 7.25, slow forcing is $T = 10^7$ yr, whereas fast forcing is $T = 10^5$ yr. The important aspects for basin analysis are as follows.

With *slow forcing* (Fig. 7.24):

1 The movements of the sand toe and gravel front are in phase with variations in sediment flux, with proximal and distal accumulation of sediment both occurring at the time of high sediment flux. Retreat of the fluvial toe at times of low sediment flux produces distal unconformities.
2 During periods of increased subsidence, sediment is trapped in proximal regions and distal areas are starved, causing a retreat of both the gravel front and the fluvial toe and the creation of distal unconformities. During periods of reduced subsidence rate, the gravel front and fluvial toe prograde since accommodation is reduced. Both proximal and distal accumulation are therefore out of phase with subsidence rate.
3 The position of the gravel front moves outwards when the gravel percentage (for a constant sediment flux) increases, producing a coarsening up in a vertical section.

For *rapid forcing* (Fig. 7.25):

1 Rapid changes in sediment flux produce gravel and sand regions with markedly different slopes, and the position of the gravel front is out of phase with the forcing. Reduced sediment supply causes a reduction in proximal slopes, the cutting of proximal unconformities and the progradation of the gravel front. In contrast, reduced sediment supply causes the fluvial toe to retreat. During periods of increased sediment supply, proximal slopes increase, which causes the gravel front to retreat, while the fluvial toe progrades slightly.
2 Rapid variations in subsidence rate have little effect on the gravel front.
3 The position of the gravel front and proximal accumulation are in phase with the percentage gravel fraction.

It is clear therefore that the stratigraphy of an alluvial system exhibits a complex response to the various forcing mechanisms. The response of the system depends on the time scale of the forcing compared to the basin response time T/T_{eq}. Proximal and distal unconformities, variations in proximal and distal accumulation and movements of the gravel front and fluvial toe may be in phase or out of phase with external forcing.

The response times of alluvial systems have also been approximated from measurements of the sediment discharge leaving the catchment. River basins may have extensive floodplain areas in their downstream portions, which act as buffers to changes in any forcing variables, such as base level change at a river mouth, or changes in sediment flux near their headwaters, and therefore may have long response times. If the system is assumed to be diffusive in character, and the discharge of water varies systematically with floodplain width W, the mass effective diffusivity κ of the channel–floodplain system is

$$\kappa = \frac{Q_s}{W\left\langle \frac{\partial y}{\partial x} \right\rangle} \tag{7.42}$$

where Q_s is the sediment discharge and $< >$ denotes the spatial average of the slope. If L is the downstream length of the river–floodplain system and H the maximum relief between its upstream and downstream ends, the response time becomes

$$\tau = \frac{L^2}{\kappa} = \frac{L^2 W \langle \partial y/\partial x \rangle}{Q_s} = \frac{LWH}{Q_s} \tag{7.43}$$

The large river systems of Asia have typical values of $L \sim 10^6$ m, $W \sim 10^5$ m, $H \sim 1$–2×10^2 m (slopes of 10^{-3} to 10^{-4}), and sediment discharges Q_s of 10^{7-8} m^3 yr^{-1} (Métivier and Gaudemer 1999). The characteristic response time is therefore in the region of 10^5 to 10^6 years. Castelltort and Van Den Driessche (2003) carried out a similar analysis on 93 of the world's major rivers, and found that response times varied between 10^4 yr to more than 10^6 yr. (Fig. 7.26). The response time depends on the scale of the channel–floodplain system. As we saw in the forward modeling of alluvial stratigraphy above, large alluvial systems therefore strongly buffer any variations in sediment supply with frequencies of less than 10^{5-6} years. This has strong implications for the detection of high frequency driving mechanisms in the stratigraphy of sedimentary basins.

7.5.4 Some aspects of numerical landscape evolution models

The numerical modeling of landscapes has developed over the last couple of decades. The significance of numerical landscape evolution for basin analysis is that such models allow the sediment supply to basins to be simulated in terms of tectonic, climatic, and geomorphic sets of rules. The incorporation into a physically realistic numerical model of feedbacks between the various processes that shape a landscape also allows system behavior, such as the response time to a change in a

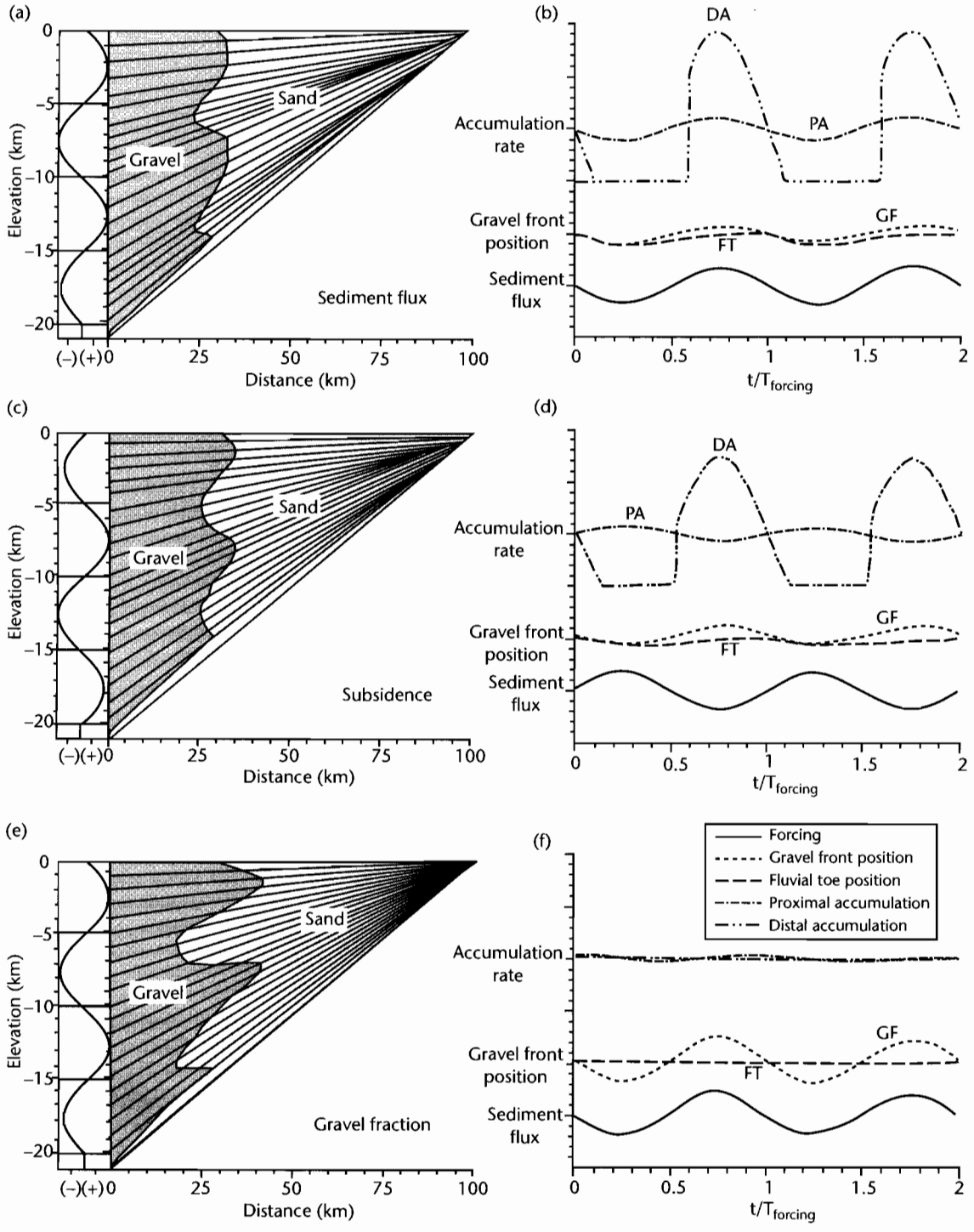

Fig. 7.24 Cross-sections of alluvial stratigraphy under slow sinusoidal forcing ($T > T_{eq}$) of sediment flux (a), tectonic subsidence (c) and gravel fraction (e). Diagrams on right (b, d, f) show time variation of the position of the gravel front and fluvial toe, proximal and distal accumulation and the forcing variable. Further details can be found in Marr et al. (2000). GF, gravel front; FT, fluvial toe; DA, distal accumulation; PA, proximal accumulation. Reproduced courtesy of Blackwell Publishing Ltd.

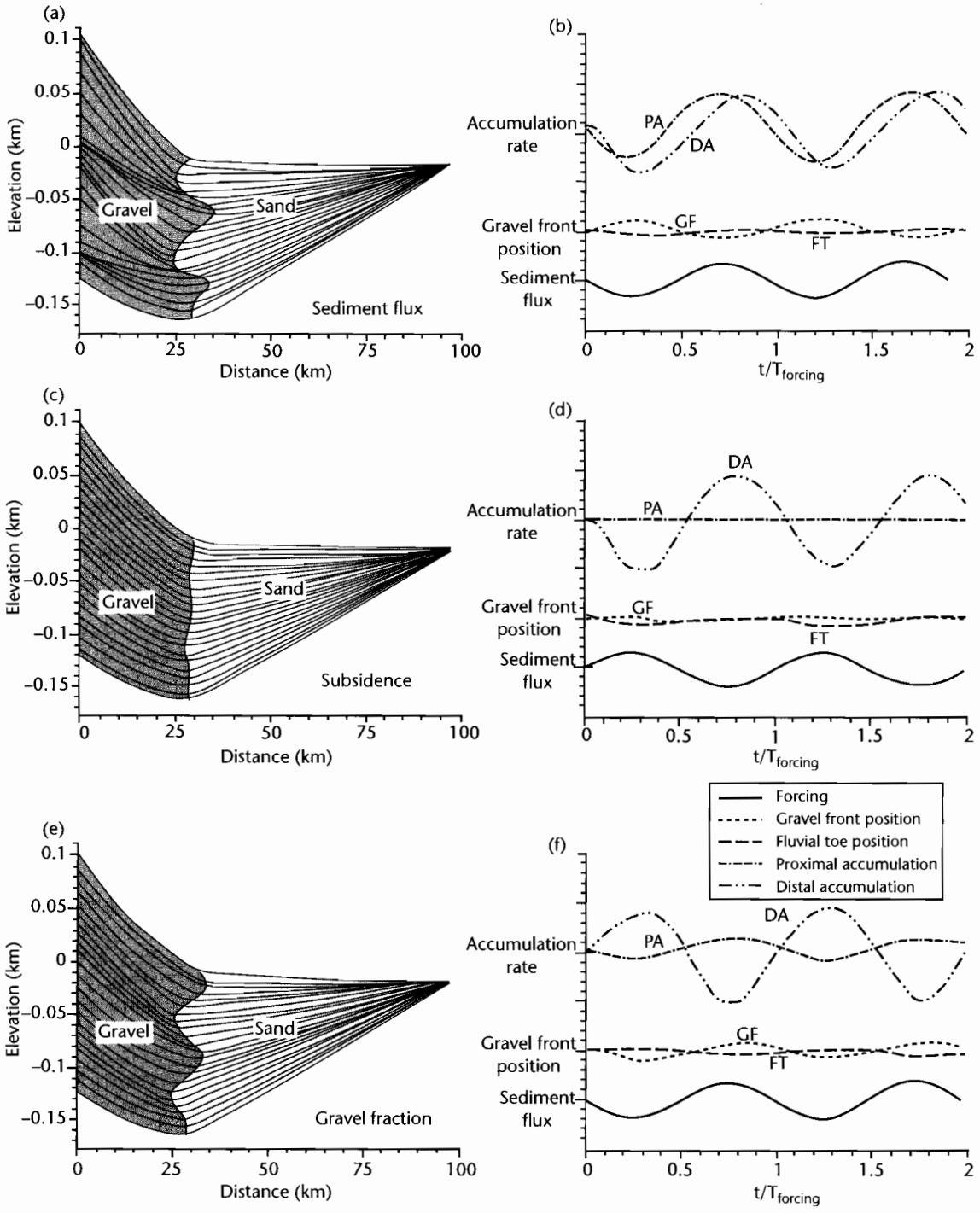

Fig. 7.25 Cross-sections of alluvial stratigraphy under fast sinusoidal forcing ($T < T_{eq}$) of sediment flux (a), tectonic subsidence (c), and gravel fraction (e). Diagrams on right (b, d, f) show time variation of the position of the gravel front and fluvial toe, proximal and distal accumulation and the forcing variable. Further details can be found in Marr et al. (2000). Reproduced courtesy of Blackwell Publishing Ltd.

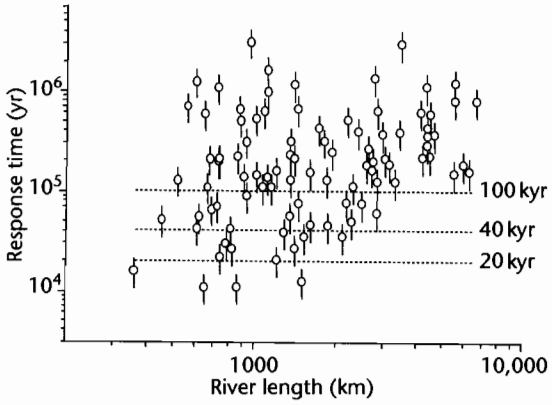

Fig. 7.26 Response times of some modern drainage basins, from a dataset compiled by Castelltort and Van Den Driessche (2003) using the relations given in equations (7.42) and (7.43). Hydrologic and geomorphologic data from Hovius (1998). Response time is plotted against river length. Vertical bars show uncertainties based on the unknown bedload sediment transport rates of the rivers shown. Note that the majority of response times are $>10^5$ yr, and some are $>10^6$ yr. Reproduced courtesy of Elsevier.

driving mechanism or forcing variable, to be studied. Numerical landscape models range in their spatial and temporal scales, from whole contractional orogens and passive margin mega-escarpments (length scales of *c.* 100 km and time scales of *c.* 10^7 yr) to individual extensional fault blocks or thrust-related anticlines (length scales of *c.* 10 km, time scales of *c.* 10^6 yr), and even to the fault scarps generated by single seismic events (length scale of *c.* 100 m, time scales of 10^3–10^5 yr). The resolution (of the elevation of topography) required by the landscape evolution model varies accordingly, from cm in the case of a degrading fault scarp, to *c.* 100 m for an orogen. The spatial and temporal scale and topographic resolution commonly affect the way in which tectonic and geomorphic processes are dealt with in the numerical model. Burbank and Anderson (2001) provide a useful summary. Many of the algorithms used in numerical landscape models are identical to or similar to those given in §7.5.1–§7.5.3. We concentrate here on the intermediate scale of extensional fault blocks and anticlinal folds in fold–thrust belts.

7.5.4.1 Tilted extensional fault blocks and thrust-related anticlines

Early attempts to model the evolution of simple fault-bounded ranges used a single planar fault with uniform slip, diffusional modification of the tectonically generated topography using a single, constant value of κ, and flexural compensation (King et al. 1988; Stein et al. 1988). Later models incorporated channels and hillslopes that strongly interacted (§7.5.1 and §7.5.2), with transport rules for the disposal of sediment derived from hillslope erosion, and hillslopes were allowed to fail by landsliding (Densmore et al. 1998; Ellis et al. 1999). Such models not only simulated very realistic landscapes in the Basin and Range Province of SW USA, but also allowed system behavior to be better evaluated. These tectonic–geomorphic systems involve steep transverse drainage systems over uplifting footwall blocks, with fans in the neighboring hangingwall basins (Whipple and Trayler 1996; Allen and Hovius 1998). The area of the catchment acting as a source terrain for sediment A_1, relative to that of the hangingwall fan A_2, is an indicator of how this relatively simple tectonic–geomorphic system functions (Fig. 7.27).

We introduce a dimensionless proportionality coefficient V, following Allen and Hovius (1998), which incorporates all the various processes resulting in the transport of sediment eroded from the catchment, routed to the fan head and then distributed across the fan with a spatially averaged deposition rate $\dot{y}$:

$$\phi = \frac{1}{\dot{y}} V \frac{(1-\lambda_r)}{(1-\lambda_s)} e_s e_f \tag{7.44}$$

and

$$A_1 = \phi A_2 \tag{7.45}$$

where V is the sediment efflux of the catchment, λ_r and λ_s are the porosities of rocks in the catchment and sediments on the fan respectively, e_s is an efficiency factor accounting for temporary storage of sediment within the catchment, and e_f is an efficiency factor allowing for escape of some sediment from the fan into down-fan sabkhas, lakes, or axial river systems. In the simplified case of complete evacuation of the catchment with no storage ($e_s = 1$) and a closed system for sediment delivery to the fan ($e_f = 1$), and assuming that rock and sediment porosities are comparable ($\lambda_r \equiv \lambda_s$), equations (7.44) and (7.45) simply illustrate that ϕ depends strongly on the rate at which the fan aggrades, which is controlled fundamentally by the rate of tectonically created accommodation. Consequently, tectonics play a major role in the creation of uplifting footwalls as source regions for sediment, in determining the spatial pattern and rate of hangingwall subsidence, and thereby in controlling fan

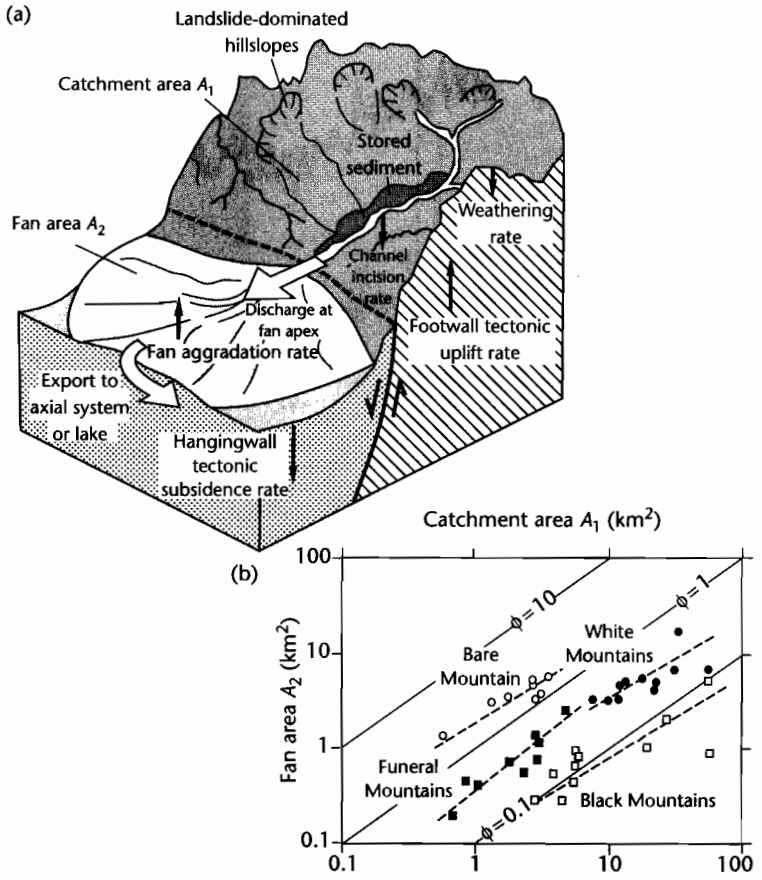

Fig. 7.27 (a) Schematic illustration of a catchment–fan system associated with a tilted extensional fault block (after Allen and Hovius 1998, Allen and Densmore 2000); (b) shows plot of catchment area A_1 versus fan area A_2 for catchment–fan systems in the arid southwestern US, showing that individual regions with particular slip rates are discriminated in terms of their value of ϕ.

thickness and fan progradation distance. Not surprisingly, plots of fan area versus catchment area from examples in the arid SW USA (Allen and Hovius 1998) show that areas with high fault displacement rates and areas with low fault displacement rates are discriminated by their value of ϕ (Fig. 7.27b). This implies that coarse-grained fan bodies are stacked against active range-bounding faults, whereas fans coalesce and prograde basinwards where fault displacement rates are smaller.

Using the landscape evolution model developed by Densmore et al. (1998), Allen and Densmore (2000) showed that abrupt changes in the rate of slip on range-bounding extensional faults could be recognized by changes in mean catchment erosion rate and mean fan deposition rate (Fig. 7.28), but that there was a delay in the achievement of a new steady state under the new fault slip rate conditions. This response time was *c.* 50 kyr for the catchment–fan systems in the Death Valley region of eastern California, regardless of climatic conditions. In other words, changes in the tectonic boundary conditions at a frequency of less than 50 kyr will be difficult to recognize in the stratigraphic record.

The deforming crustal template in regions of extension strongly interacts with erosion and drainage development. As footwalls emerge, river systems are etched into their flanks either side of a catchment divide. Individual *en echelon* fault segments interact at their tips in a variety of geometrical arrangements, most important of which is the *relay zone* (Larsen 1988). These relay zones are thought to have an important role in focusing

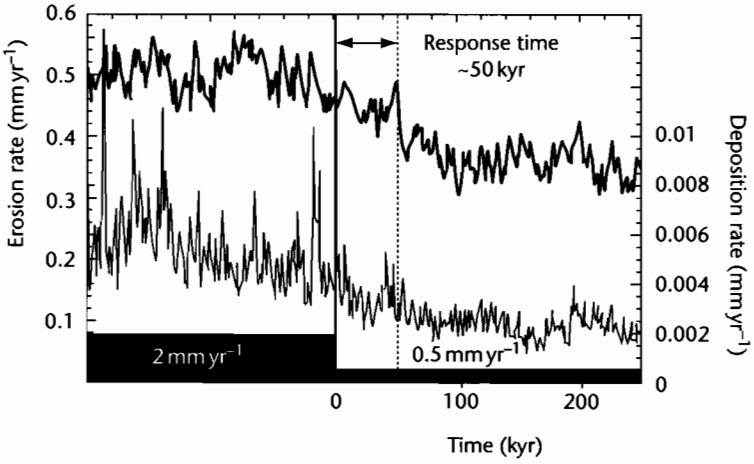

Fig. 7.28 Mean catchment-averaged erosion rate (heavy line) and mean fan deposition rate (thin line) before and after a step change in fault slip rate from $2\,mm\,yr^{-1}$ to $0.5\,mm\,yr^{-1}$. Note the progressive decrease in erosion and deposition rates to new equilibrium values. The response times (the time required for each rate to fall to $1/e$ of its initial value) are 56 kyr for erosion rate and 48 kyr for deposition rate. After Allen and Densmore (2000). Reproduced courtesy of Blackwell Publishing Ltd.

sediment delivery to hangingwall basins from larger-than-normal catchments and are therefore thought to be associated with fan and fan–delta development (Leeder and Gawthorpe 1987; Gupta et al. 1999) (Fig. 7.29). Such sedimentary bodies adjacent to relay zones are potentially important as hydrocarbon reservoirs in rift provinces (§10.4). However, numerical landscape evolution models of fault systems under different histories of growth and linkage failed to produce large catchments and fans at relay zones (Densmore et al. 2003). This suggests that large catchment–fan systems at relay zones may be related to antecedent drainage rather than to local fault growth. Whereas the Basin and Range is typified by hydrologically closed footwall catchment systems, in which we do not expect to find large catchment–fan systems at relay zones, other extensional provinces may possess regional, antecedent drainages that deposit large fans at relay zone entry points into hangingwall depocenters, such as the southern Afar Rift, Gulf of Suez, and central Greece.

At a similar wavelength to the extensional fault blocks of the Basin and Range are the thrust-related folds of contractional tectonic provinces such as the Zagros of Iran and western Pakistan (Mann and Vita-Finzi 1988). Folds are *c.* 10 km in wavelength and 2–3 km in amplitude. There are a number of issues that are especially relevant to this tectonic situation: as hangingwall rocks are transported up the thrust ramp, how is the topographic profile and river drainage development related to the tectonic paths of hangingwall rocks? What is the effect of progressively unroofing rocks with markedly different erodibilities (or values of c_b or c_v)? And what effects do the contractional tectonics have on antecedent rivers?

In areas with high rates of tectonic uplift of rocks, the topographic relief is essentially controlled by the ratio U/c_v, where U is the tectonic uplift rate of rock and c_v is the efficiency of bedrock incision expressed as a velocity (eqn 7.35). Streams are known to change their gradients markedly over substrates of different erodibility (Hack 1973). Tucker and Slingerland (1996) estimated bedrock erodibilities c_v to vary from $0.02\,m\,yr^{-1}$ to $0.2\,m\,yr^{-1}$ in the arid landscapes of the Zagros. Using a numerical landscape evolution model, they successfully simulated the progressive unroofing of stratigraphy with strongly varying erodibility related to the growth of a series of tectonic folds. Sediment flux from the fold–thrust belt reflects both tectonic growth of the fold structures but also the extent of exposure of resistant versus weak lithologies. For a landscape dominated by bedrock channels, the time required to reach equilibrium (90% of equilibrium sediment flux) with a given rate of tectonic uplift is proportional to the rock erodibility c_v, the rock uplift rate U, and the spatial scale (width) of the uplifting rock region L,

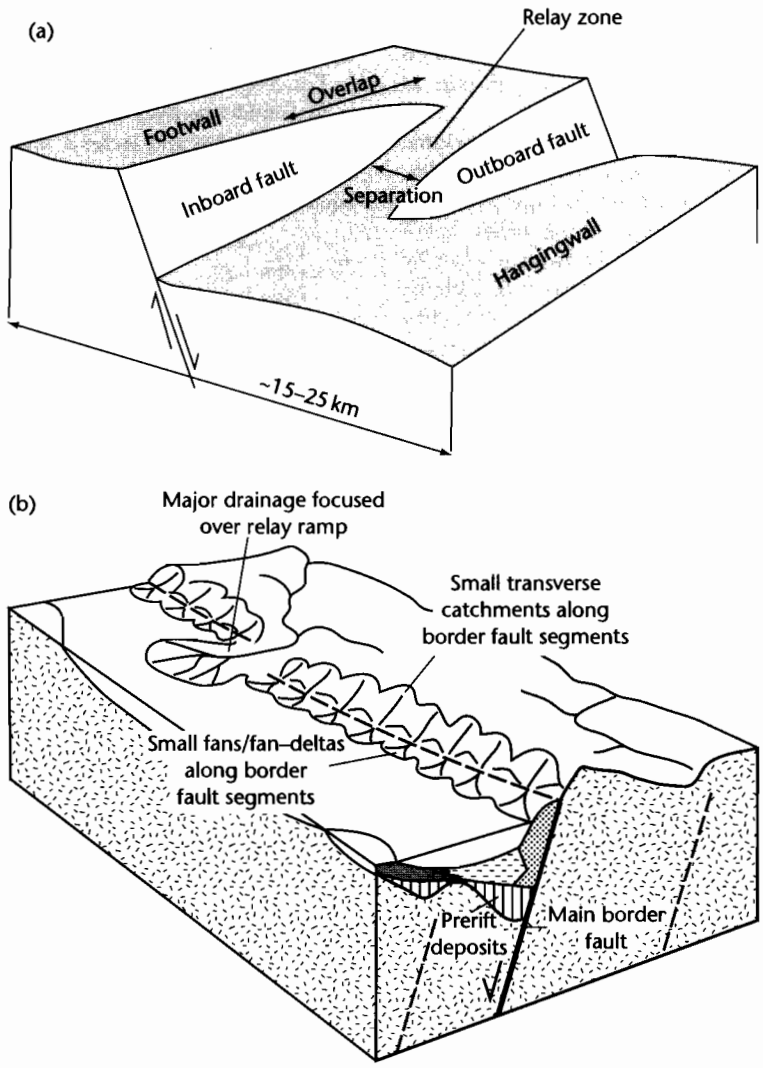

Fig. 7.29 (a) Perspective view of a soft-linked extensional relay zone; (b) Conventional view of relay zones as sites of large fan systems, whereas the main border faults have small transverse catchments and small fans/fan deltas.

$$\tau = k\frac{U^{\left(\frac{1}{n}-1\right)}L}{c_v^{1/n}} \tag{7.46}$$

where n is the exponent for slope in equation (7.35), commonly assumed to be 2/3. Calibrated against model output from a landscape evolution model used to simulate the topography of the Zagros (using $c_v = 0.02$ to $0.2\,\mathrm{m\,yr^{-1}}$, $L = 40\,\mathrm{km}$, and $U = 1\,\mathrm{mm\,yr^{-1}}$), the coefficient of proportionality k in (7.47) is 7–10. The geomorphic response time τ for sediment flux is between *c.* 0.1 Myr and 4 Myr for the weak and resistant lithologies respectively. For the resistant lithologies, the geomorphic response time is very long (>1 Myr). In this case, it is most likely that periods of different thrust displacement rate in the fold–thrust belt would not be discernible in the stratigraphic record of neighboring foreland and thrust-sheet-top basins. However, small thrust-related anticlines

composed of weak lithologies should respond quickly to changes in tectonic boundary conditions, and produce a recognizable pulse of sediment in the basin. Figure 7.30 shows the evolution of sediment flux through time as rocks with different erodibility are unroofed.

It is apparent from a casual inspection of topographic maps that some streams cut transversely through folds, whereas others are deflected around their tips (Fig. 7.31). For example, in the Marche region of the Italian Apennines, a series of rivers drain to the Adriatic coast by cutting straight through the points of maximum tectonic uplift in NW–SE oriented folds (Alvarez 1999). The impact of growing tectonic structures on drainage patterns has been discussed by a number of authors (Jolley et al. 1990; Burbank and Vergés 1994; Talling et al. 1995; Burbank et al. 1996; Gupta 1997). One of the major impacts for basin analysis is that sediment entry points into basins may be shifted by growing tectonic structures.

The simplest approach to understanding this problem is to consider a river that is in equilibrium between channel incision and tectonic uplift rates. For bedrock streams, we can modify equation (7.35) for the case of equilibrium to give

$$\frac{U}{c_v} = \left(\frac{Q_w}{Q_*}\right)^m S^n \tag{7.47}$$

If the uplift rate of rocks in the fold crest region is high ($U = 0.01\,\mathrm{m\,yr^{-1}}$) and the stratigraphy is strongly resistant ($c_v = 0.025\,\mathrm{m\,yr^{-1}}$), the dimensionless ratio U/c_v is high

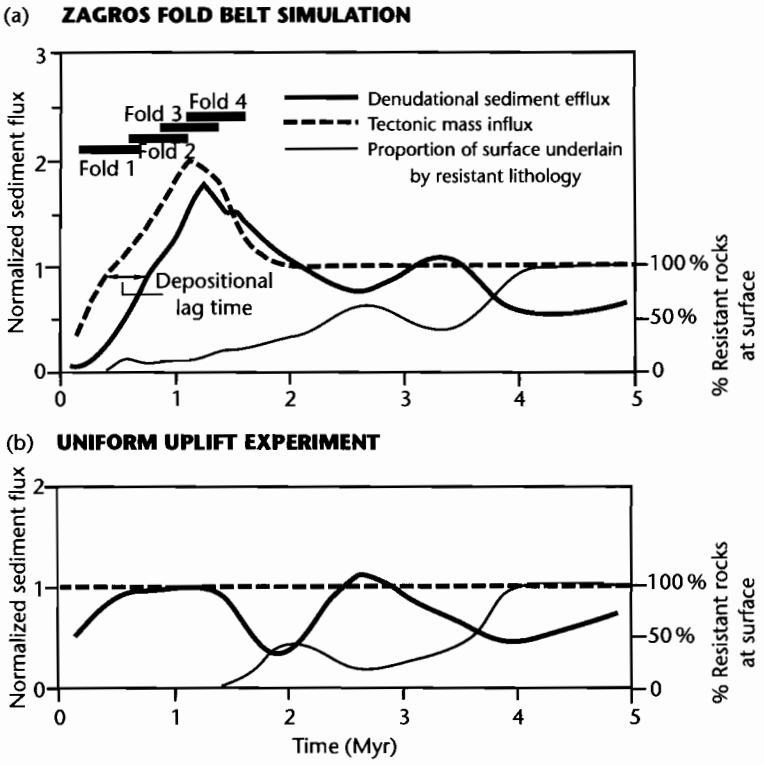

Fig. 7.30 Landscape evolution model results of the unroofing of folds in the Zagros fold–thrust belt. (a) Tectonic influx from uplift of rock (dashed line) and sediment efflux out of the model grid (solid line) versus time. In this simulation, four anticlinal folds grow progressively in time. Note the lag time between tectonic influx and depositional response of <0.5 Myr during the growth phase of the folds. The thin solid line shows the percentage of resistant rocks exposed at the land surface as a function of time. Note that the decrease then increase of sediment efflux is due to this variation in erodibility of outcropping rocks; (b) Sediment efflux in which the variations are solely due to lithological variations in the stratigraphy being unroofed. Tectonic influx is spatially and temporally uniform. After Tucker and Slingerland (1996). Reproduced courtesy of Blackwell Publishing Ltd.

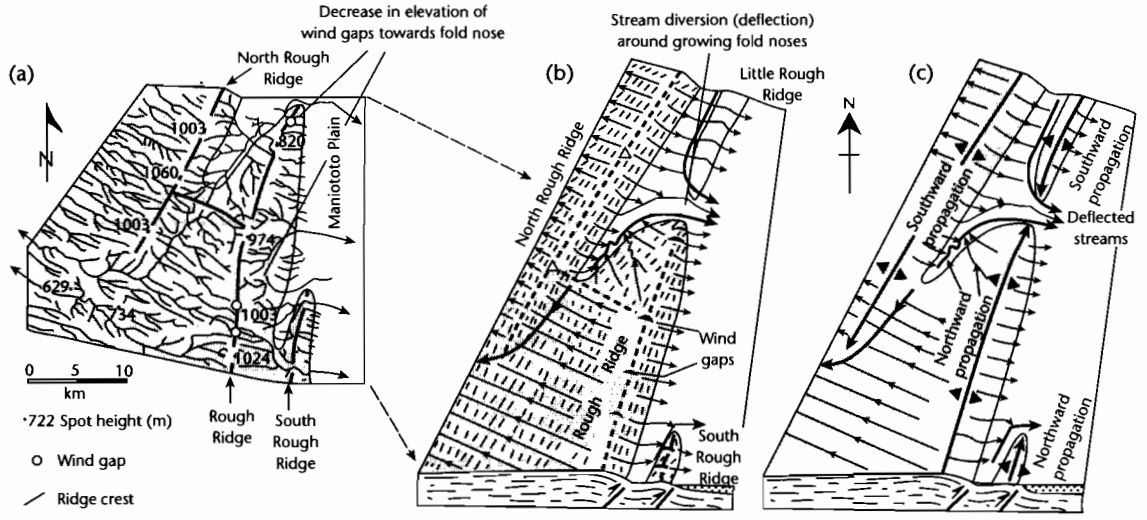

Fig. 7.31 Evolution of landscape in the face of growing folds, exemplified by the Southern Alps of central Otago, New Zealand (after Jackson et al. 1996). (a) Drainage network, fold crests, plunging fold noses, water gaps, wind gaps, and their elevations in the vicinity of Rough Ridge. Note the decrease in elevation of the wind gaps towards the fold nose; (b) Schematic diagram of drainage pattern, showing clear diversion of drainages around the nose of each growing fold; (c) Interpretation of fold propagation of same region of Rough Ridge and the resultant drainage development. Reproduced courtesy of Pergamon Press, Oxford.

(0.4), indicating that a stream is likely to be deflected. If, however, the uplift rate of rocks in the fold crest region is low ($U = 0.001\,\mathrm{m\,yr^{-1}}$) and the rocks are weakly resistant to erosion ($c_v = 0.25\,\mathrm{m\,yr^{-1}}$), U/c_v is low (0.004), indicating that the discharge–slope product of the stream may be sufficient to cut through the growing anticline. As a growing fold emerges, the width of the fold should increase. Field studies (e.g., Burbank et al. 1996; Jackson et al. 1996) suggest that if the elevation of the entrance and exit of the fold are fixed, the widening of the fold may cause a decrease in stream gradient and stream power, leading to defeat of the stream by the growing structure (see eqn 7.47). Alternatively, aggradation upstream of the entrance to the fold may cause avulsion of the stream to a lower position of the floodplain, effectively diverting the stream away from the growing fold. Deflected (defeated) streams are commonly captured by adjacent streams, which increases their discharge, allowing them to incise through the growing fold. The interaction of river drainage, erosion, topography and tectonic displacements is currently a rich area of research.

Coupled tectonic–erosion models at the scale of whole orogens, discussed in §4.6 and §4.7, involve the description of the tectonic deformation of the lithosphere in zones of convergence, coupled with a surface landscape of hillslopes and active channels and depositional basins (Beaumont et al. 1992, 1996b; Willett et al. 1993; Kooi and Beaumont 1994, 1996). As we have seen (§4.7), orogenic wedges with an asymmetry of climate (precipitation) on windward and leeward flanks are associated with an asymmetry of exhumation of deep crustal rocks. A structurally much simpler situation at a similar spatial and temporal scale is provided by the classic mega-escarpments found along segments of passive margins (Gilchrist and Summerfield 1990). The high escarpments of southern India (Western Ghats) (Gunnell 1998), Namibia–South Africa (Gallagher and Brown 1999), and SE Australia (Seidl et al. 1996) are good examples. Landscape evolution models of passive margin mega-escarpments are found in Kooi and Beaumont (1994) and Braun and Sambridge (1997).

CHAPTER 8

Basin stratigraphy

Earth and Ocean seem
To sleep in one another's arms and dream
Of waves, flowers, clouds, woods, rocks and all that we
Read in their smiles, and call reality.

(PERCY BYSSHE SHELLEY, *EPIPSYCHIDION* (1821))

SUMMARY

The stratigraphy in a sedimentary basin is the result of the interplay of the generation of space or accommodation and the influx of sediment. Stratigraphic geometries and gross depositional environments are therefore determined by the tectonic mechanisms causing subsidence, local patterns of faulting, the nature of sediment routing systems, and sea-level change.

Stratigraphic cycles can be modeled from first principles using expressions for accommodation and sediment supply. A fundamental parameter is the magnitude of the eustatic change compared to the subsidence rate. Increasing importance of tectonic subsidence causes stratigraphic cycles to become asymmetrical and retrogradational. Typical glacio-eustatic cycles have a high enough frequency and amplitude to generate unconformities, even at high tectonic subsidence rates. Lower frequency/amplitude "nonglacial" cycles are easily overwhelmed by tectonic subsidence to produce monotonically rising relative sea levels. Key stratigraphic surfaces are commonly diachronous, with a phase shift of up to one-quarter of a eustatic period. The evolution of water depth through a set of stratigraphic cycles depends on relative sea level and sediment supply. The magnitude of the sediment supply determines whether accommodation is underfilled or overfilled. In the case of the latter, sediment is bypassed *via* a nondepositional surface. Even small variations in sediment supply can have major impact on depositional facies, water depth, and movement of the coast. Stratigraphy may be either accommodation-limited, where cycles and facies are determined by accommodation and sediment supply is always adequate: or sediment supply-limited, where depositional space is always great enough to accommodate the sediment supply.

Stratigraphy is packaged into large and small genetic units, from megasequences (or supersequences) to depositional sequences and then parasequences (or higher order genetic units). Depositional sequences are bounded by unconformities or lateral conformities, but may be better recognized by their maximum flooding surfaces.

The widely used Vail–Haq curve of "global" sea-level change relies on a global correlation of synchronous stratigraphic boundaries. However, it is unlikely that sequence boundaries are truly synchronous, partly because of the variations of tectonic subsidence rate in co-existing sedimentary basins, and partly because the different response times of sediment routing systems to base level change produces different sediment inputs in coeval basins. The search for perfect synchrony is therefore futile.

Depositional sequences can be subdivided into *systems tracts* deposited at particular intervals on the relative sea level curve. *Lowstand systems tracts* consist of basin-floor fans, slope fans, and wedges accreting onto the continental slope, at the shelf edge or as a series of regressive wedges on continental ramps. During relative sea-level lowstands, the continental shelf may become exposed, karstified, or incised by river drainage networks. During rapid relative sea-level rise, *transgressive systems tracts* backstep onto the basin margin. After the period of maximum flooding of the basin margin, *highstand systems tracts* prograde into the basin producing marked clinoform geometries over basal downlap surfaces. Smaller genetic stratigraphic units or parasequences are recognized ubiquitously in core, electric logs, and at outcrop. The boundaries of shallow marine, shallowing-up

parasequences are commonly marked by a flooding surface accompanied by a marked facies dislocation. In both carbonate and siliciclastic systems, parasequences may be driven by orbital mechanisms in the Milankovitch band or may be unforced (autocyclic).

The driving mechanisms for stratigraphic patterns fall into two major categories: tectonic and eustatic. Tectonic mechanisms include flexure under sediment loads during phases of thermal subsidence in failed rift and passive margin basins, flexure by moving tectonic loads in foreland basins, and accommodation generation during the evolution of fault arrays in extensional and contractional settings. Changes in regional in-plane stress fields caused by major plate boundary reorganizations can also cause vertical movements that are large enough to have an impact on basin stratigraphy.

Absolute changes in sea level (*eustatic* changes) may be caused by changes in the volume of ocean water or changes in the volume of ocean basins. Additions of juvenile water from the continuing differentiation of the lithosphere are probably compensated by losses due to hydrothermal alteration of new ocean crust. Sediment influx to ocean basins is potentially able to cause slow sea-level rises but the process is counteracted by sediment removal at subduction zones. Volume changes in the ocean ridge system caused by variations in spreading rate are thought to be responsible for long-term changes in global sea level, involving a maximum sea level during the Late Cretaceous and falling with varying severity through the Cenozoic to the present. Thermal expansion and contraction of the oceanic reservoir causes small changes in absolute sea level. Glaciations and deglaciations are very rapid processes changing the volume of water in the ocean system and are responsible for the familiar sea level variations of the Quaternary. Climate change also affects the functioning of sedimentary systems, principally through the effect on vegetation, weathering and erosion, and far-field sediment transport to basins.

The last decade has seen the growth of numerical approaches to the simulation of stratigraphy. Numerical models for carbonates rely on a carbonate productivity versus depth function combined with rules for the surface transport of sediment. Siliciclastic models require a linkage between catchment processes, fluvial transport, and sediment distribution in the basin. Numerical schemes are successful at simulating the geometries observed in stratigraphy and in furthering our understanding of the complexity of catchment–basin systems.

The depositional systems of sedimentary basins are highly variable. Continental systems include fluvial, desert, lacustrine, and glacial systems. Coastal and nearshore systems include siliciclastic shorelines and carbonate–evaporite shorelines. Continental shelf systems include siliciclastic systems as well as carbonate shelves and reefs. Deep sea depositional systems include slope aprons, submarine fans, deep-water sediment drifts and basins plains, and the predominantly biochemical sediments of the pelagic realm.

Basins of different type have different assemblages of depositional styles. The sedimentary systems of *intracratonic* sags are commonly continental and endorheic. Whereas the Chad Basin, Africa is predominantly composed of siliciclastic fluviatile, lacustrine and aeolian deposits, the Michigan Basin, USA is dominated by shallow marine carbonates and evaporites. *Continental rift basins* have tectonically controlled syn–rift fills that are commonly lacustrine and fluviatile in the early stages and may become shallow marine and even deep marine in later stages. Vulcanism accompanies rift sedimentation. The nature of the sedimentary fill depends on its climatic zone – the East African Rift system illustrates this phenomenon, with alkaline shallow lakes in the semi-arid north and deep, freshwater lakes in the wetter south. Supply of clastics to rift lakes is determined by the geometry of tilted fault blocks producing half-graben. *Failed rifts* such as the Benue Trough, Africa or North Sea pass from the syn–rift stage into a period of thermal subsidence characterized by marginal and open marine, commonly deltaic, sedimentation. Continued stretching leads to *proto-oceanic troughs* with evaporites, sapropels, and pelagic sediments. *Passive margins* are characterized by sediment derived from the continent, building thick seaward-prograding, principally shallow marine clastic wedges. Other margins are typified by thick carbonate banks. Deeply buried evaporites are commonly remobilized during the passive margin phase.

In convergent settings, sediment accumulates in foredeep and thrust-sheet-top basins in the flexural downwarp (*foreland basin*) ahead of orogenic wedges. Early deposits are commonly turbiditic and the basin underfilled. Later deposits are shallow marine or continental as the basin reaches steady-state or overfilled status. Retroarc foreland basins differ in having a composition of the sedimentary fill that reflects the large amounts of plutonic and volcanic rocks in the orogenic belt.

Ocean trenches, *accretionary basins*, and *forearc basins* are found at convergent ocean–ocean or ocean–continent boundaries. The sedimentary fills are typically strongly

tectonized and their compositions are dominated by detritus from adjacent ocean crust and arc. Sediments are generally deep water and commonly turbiditic, although some accretionary complexes are above sea level, as in the Makran of Pakistan. *Backarc basins* on oceanic crust are dominated by deep marine sedimentation of pelagic oozes with marginal shallow water or alluvial fringes. There are some examples of backarc spreading on continental crust, such as the Pannonian Basin of central Europe.

Strike–slip basins have complex sedimentary fills indicating rapid subsidence, and major lateral facies changes from active fault scarps with breccias and conglomerates to centrally located finer grained zones. The Ridge Basin California and the Dead Sea are classic examples on land whereas the California Borderland basins represent deep marine equivalents.

The previous chapters have provided some insights into the possible physical causes of the main classes of sedimentary basin. The long-term response of the depositional surface in sedimentary basins is prolonged subsidence, but the detailed interplay of subsidence and sediment supply in time and place gives rise to the stratigraphy of a basin. In this chapter we examine how large scale factors and their interaction give rise to distinct basin stratigraphies.

8.1 A PRIMER ON PROCESS STRATIGRAPHY

8.1.1 Introduction

In this book, we define *Process Stratigraphy* as the science of the recognition and interpretation of the genetic structure of stratigraphy. *Genetic Stratigraphy* (Galloway 1989; Homewood et al. 1992) and *Dynamic Stratigraphy* (Matthews 1974; Cross 1990) are equally appropriate terms, and *Time Stratigraphy* (Wheeler 1964) is an allied concept. However, we avoid the term *Sequence Stratigraphy* since this implies a restriction of concern to the level of the depositional sequence. Process stratigraphy makes use of systematic branches of stratigraphy (biostratigraphy, magnetostratigraphy, chemostratigraphy, lithostratigraphy) but is not itself a taxonomic exercise. The fundamental aim of process stratigraphy is to understand the driving mechanisms for the range of stratigraphic architectures found in sedimentary basins. The science of process stratigraphy has revolutionized sedimentary geology by replacing simple but potentially erroneous lithological correlations with the beginnings of a process understanding of the distribution of stratigraphic elements within time–space. In common with other rapidly developing enterprises, process stratigraphy has become heavily jargonized and vulnerable to overgeneralized, totalitarian world views (see discussion in Miall and Miall 2001). However, it represents an extremely valuable methodological and interpretational tool for the dynamic understanding of the stratigraphy of sedimentary basins.

A number of texts provide a modern understanding of process stratigraphy, often from the utilitarian point of view of a hydrocarbon industry explorationist, such as Emery and Meyers (1996) and Homewood et al. (1992, 2000). Many texts provide sections on process stratigraphy as part of a wider mission, such as Reading (1996), Leeder (1999), and Miall (2000). High resolution sequence stratigraphy, which focuses on the structure of stratigraphy below the level of the depositional sequence, is colorfully examined by van Wagoner et al. (1990). The application of sequence stratigraphy to carbonate reefs and platforms is treated by Schlager (1992) and Sarg (1988).

The history of process stratigraphy dates back to the mid-1900s when stratigraphy was recognized to be divisible into packages of sedimentary rock separated by unconformities of inter-regional extent (Sloss 1950, 1963). A major breakthrough, however, was the use of seismic reflection surveys in the 1960s and 1970s carried out for hydrocarbon exploration (Payton 1977). An analysis of the geometry of stratigraphic units deduced from their seismic reflection character led industry Earth scientists to believe that eustatic changes of sea level were the primary control on the development of stratigraphic packages. In 1987 a "global" sea-level chart was published (Haq et al. 1987) on the basis of the apparent recognition of distinctive stratigraphic boundaries (unconformities and correlative conformities) in widely separated locations. The volume edited by Wilgus et al. (1988) represented a second wave of sequence stratigraphic thinking by introducing ideas on accommodation (see below) in sedimentary basins and on the relationship between stratigraphic packaging and cycles of relative sea level. Since the late 1980s there has been substantial criticism of some of the new stratigraphic terminology, of its reliance on eustasy as its overwhelming driving mechanism and on the presumed global synchroneity of key stratigraphic surfaces such as sequence boundaries (see Miall 1991, 1992 for a trenchant view).

More recently, numerical modeling (Harbaugh et al. 1999; Burgess et al. 2002) has been directed at examining in detail some of the controls and feedbacks involved in the generation of stratigraphic packages.

The key idea of process stratigraphy is that space is made available for sediment to accumulate, termed *accommodation*. Sediment fluxes cause an underfilling, filling, or overfilling of this available space. Accommodation generation and sediment supply vary strongly in space and in time, causing a complex 4-D packaging of stratigraphic units.

8.1.2 Relative sea-level change and accommodation: definitions

Eustasy is global sea level measured from the sea surface to a fixed datum, such as the center of the Earth. The controls on eustatic sea level are discussed in §8.3.

Relative sea level is sea level measured relative to a moving datum, often a distinctive horizon such as a horizon within a sediment pile, or the lower contact with basement. Relative sea level is therefore affected by processes such as tectonic uplift and subsidence, compaction and eustasy.

Water depth is of course the vertical distance between the sea surface and the seabed. Although water depth commonly changes during a relative sea-level change, it may also be influenced by the sediment input into a sedimentary basin with no relative sea-level change. Eustasy, relative sea level, and water depth are all distinctive concepts (Fig. 8.1).

Accommodation – the space made available for sediment to accumulate – is controlled by *base level*, since sediment can only accumulate long term up to base level. Base level may be a graded stream profile on land, or a graded shelf profile on the continental shelf.

We can write a change in accommodation ΔA as

$$\Delta A = \Delta E + \Delta S + \Delta C \tag{8.1}$$

where A is accommodation, E is eustasy, S is subsidence, and C is compaction. A change in water depth ΔW can also be written

$$\Delta W = \Delta A - \Delta D = (\Delta E + \Delta S + \Delta C) - \Delta D \tag{8.2}$$

where ΔD is the amount of sediment deposited.

8.1.3 Forward modeling of stratigraphic cycles from first principles

Sloss (1962) argued some time ago that transgressions and regressions of the shoreline were controlled (at least in part) by the relative magnitudes of the rate of sea-level change and rate of subsidence. Pitman (1978) developed an early model of a slowly subsiding continental margin with a more rapidly changing sea level and by treating the problem quantitatively was able to create a synthetic stratigraphy that could be compared with seismic reflection results. The papers by Read et al. (1986) and Grotzinger (1986a, b) were early attempts to forward

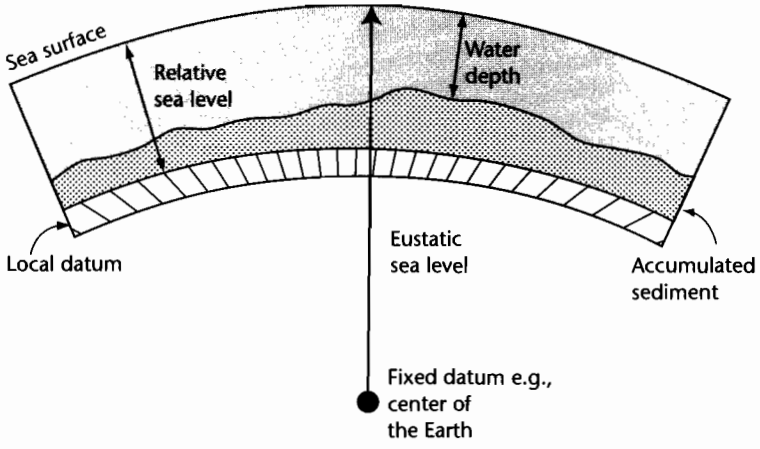

Fig. 8.1 Definitions of terms used in process stratigraphy (after Jervey 1988; Emery and Meyers 1996): eustatic sea level, relative sea level, and water depth.

model cyclical, high-resolution, shallow marine carbonate platform stratigraphy.

Any forward model must make use of the relationship among the key parameters in equation (8.2). For example, Turcotte and Willeman (1983), Turcotte and Kenyon (1984), and Turcotte and Bernthal (1984) modeled eustatic sea level in terms of two end-member types: (i) a rapid rise followed by a slow fall, and (ii) slow rise in sea level followed by a rapid fall. In initial forward modeling studies and conceptual exercises such as the early offerings of the Exxon group (Vail et al. 1977a, b) sediment supply was considered to be constant through the cycle of relative sea-level change.

In the discussion that follows, we build an analytical method for considering the stratigraphic cycles generated under a sinusoidal eustatic variation in a basin with a background tectonic subsidence rate and with a sediment supply coupled to the relative sea-level variation. We ignore compaction and the isostatic response to water and sediment loads. Although the assumptions and algorithms are undoubtedly a crude simplification of the complexities of nature, a simple 1-D forward model is the prerequisite for all process stratigraphic thinking. A Matlab program is provided at www.erdw.ethz.ch/Allen.

We therefore initially consider the variation of relative sea level through a cycle of eustatic change with wavelength λ and amplitude h_0 in a basin with a linear tectonic subsidence rate a (Fig. 8.2). The elevation in sea level caused by a sinusoidal eustatic fluctuation is

$$h = h_0 \sin\left(\frac{2\pi t}{\lambda}\right) \tag{8.3}$$

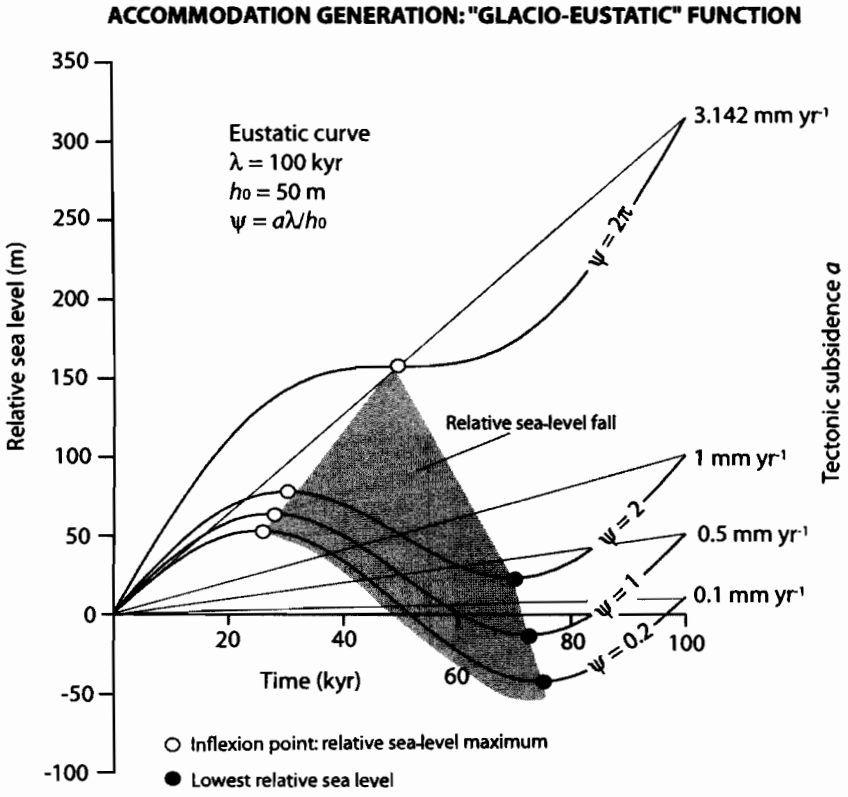

Fig. 8.2 Variation in relative sea level through a cycle of eustatic change with wavelength λ and amplitude h_0 in a basin with a linear tectonic subsidence rate a. The dimensionless parameter Ψ varies from 0.2 to 2π, corresponding to tectonic subsidence rates from 0.1 to πmm yr^{-1} (grey area). Increasing values of Ψ cause the relative sea-level maximum (open circle) to be delayed in the cycle. For the "glacial" eustatic parameters used, tectonic subsidence must be $> \pi$mm yr^{-1} in order for the relative sea-level fall to disappear.

Adding the tectonic subsidence rate, assumed linear, to obtain the relative sea level h_{rel}, we have

$$h_{rel} = h_0 \sin\left(\frac{2\pi t}{\lambda}\right) + at \tag{8.4}$$

where t is time. A number of different relative sea-level scenarios result from the magnitude of the eustatic change compared to the subsidence rate. This can be expressed in terms of the dimensionless parameter $\Psi = a\lambda/h_0$. If the amplitude of the sinusoidal eustatic change far exceeds the change in tectonic subsidence (Ψ is small), the relative sea-level variation is also near-sinusoidal and the maximum relative sea level is very close to the eustatic peak (Fig. 8.2). As the tectonic subsidence rate increases relative to the amplitude of eustatic change (Ψ increases), the relative sea-level curve becomes more asymmetrical and the peak of relative sea level becomes delayed in the eustatic cycle. At a critical tectonic subsidence rate (Ψ is large), there is no relative sea-level fall, but instead an inflexion point in relative sea level significantly following the eustatic peak. In Figure 8.2, relative sea level is equivalent to accommodation since the curves begin at zero water depth rather than at some point on a graded profile.

The point at which the inflexion point in relative sea level occurs is at $dh_{rel}/dt = 0$. Differentiating (8.4) gives

$$\frac{dh_{rel}}{dt} = h_0 \frac{2\pi}{\lambda} \cos\left(\frac{2\pi t}{\lambda}\right) + a \tag{8.5}$$

Setting $dh_{rel}/dt = 0$ gives the solution

$$t = \frac{\lambda}{2\pi} \cos^{-1}\left(-\frac{\lambda}{2\pi}\frac{a}{h_0}\right) \tag{8.6}$$

Equation (8.6) shows that for a given eustatic period λ, the time period to the relative sea-level inflexion point decreases with increasing values of the dimensionless parameter $\Psi = a\lambda/h_0$.

At what critical value of a does relative sea level increase monotonically, that is, dh_{rel}/dt is always positive? This is when

$$a > h_0 \frac{2\pi}{\lambda} \cos\left(\frac{2\pi t}{\lambda}\right) \tag{8.7}$$

for all t, which is when $\lambda a/2\pi h_0 > 1$, or $\Psi/2\pi > 1$.

Eustatic sea-level change takes place at a wide range of periods and amplitudes. The dominant signal for the glacial–interglacial variations of the Pleistocene is a period of 100 kyr and amplitude of 50 m (variation in height of 100 m). Let us call this a typical "glacio-eustatic cycle." On the other hand, cycles of eustatic change inferred from stratigraphy (e.g., mid–late Eocene cycles in the Nummulitic Limestone of Switzerland, Allen et al. (2001), and from the Oligocene stratigraphy of the New Jersey coastal plain, Kominz and Pekar 2001) imply cycles of longer duration (*c.* 0.5–2 Myr) and lower amplitude (10–20 m). The fact that these cycles exist in stratigraphy deposited during climatic conditions when there was limited ice suggests that mechanisms other than glacio-eustasy were responsible. Let us call these variations "nonglacial cycles." In unforced cycles (§8.3.6) no eustatic change is required and the facies and water depth changes are produced by internal dynamics driving variations in sediment transport.

Substitution of parameter values in equation (8.7) shows that the critical tectonic subsidence rate for a monotonic rise in relative sea-level ($h_0 = 50$ m, $\lambda = 100$ kyr) is 3.14 mm yr^{-1}. Such rates of tectonic subsidence are rare, which implies that eustatic cycles of this type are likely to always produce relative sea-level falls. If relative sea-level falls are accompanied by erosion, we should expect to find erosional unconformities in stratigraphy formed under the influence of "glacio-eustatic" cycles. If, however, the eustatic variation is 20 m amplitude with a wavelength of 400 kyr, the critical tectonic subsidence rate becomes 0.3 mm yr^{-1}, and if the amplitude and wavelength are 10 m and 1 Myr, the critical tectonic subsidence rate becomes 0.06 mm yr^{-1}. These values are similar to or below the rate of subsidence experienced in most sedimentary basins. In situations of slow "nonglacial" eustatic change, relative sea level may monotonically rise under a background tectonic subsidence.

It can also be seen from Figure 8.2 that the triangular field of relative sea-level fall narrows to a point at $t =$ 50,000 yr on the curve $a_{crit} = 3.14$ mm yr^{-1}. Clearly, when correlating different locations in a basin with spatially variable tectonic subsidence rate, we should expect significant diachroneity of the onset of erosion due to relative sea-level fall and of flooding during relative sea-level rise. The delay in the onset of erosion is a quarter of a eustatic wavelength or $\lambda/4$. The difference in the timing of flooding is also $\lambda/4$. Since diachroneity of key stratigraphic surfaces is to be expected from a globally synchronous eustatic change, it is curious that the inference of stratigraphic synchroneity is seen as an acid test for a eustatic control (see also Miall 1991, 1994).

We now add the effects of sediment supply. Sediment supply controls how much of the accommodation is filled (Fig. 8.3). In the simplest scenario, the sediment supply rate s could be considered a constant velocity, in which case water depth as a function of time $w(t)$ is given by

$$w(t) = h_0 \sin\left(\frac{2\pi t}{\lambda}\right) + at - st \tag{8.8}$$

However, it is reasonable to assume that sediment supply rate is coupled in some way to the rate of change of relative sea level. If sediment supply rate $s(t)$ peaks at the maximum rate of relative sea-level fall, and is zero at the maximum rate of relative sea-level rise, we can write

$$s(t) = \frac{1}{2} s_0 \{1 + \sin(2\pi t/\lambda)\} \tag{8.9}$$

It would also be simple to formulate sediment supply as coupled to the rate of relative sea-level variation but with a certain time lag to account for the response time of sediment delivery systems to any base level change (§7.5). However, to obtain the sediment accumulated S at any point within a relative sea-level cycle simply using eqn (8.9), we integrate it to give

$$S(t) = \frac{1}{2} s_0 \left\{ t - \frac{\lambda}{2\pi} \cos\left(\frac{2\pi t}{\lambda}\right) \right\} + c \tag{8.10}$$

Since the total accumulated sediment is zero at $t = 0$, c must be $\frac{1}{2} s_0 \frac{\lambda}{2\pi}$. The thickness of *potential* accumulated sediment is

$$S(t) = \frac{1}{2} s_0 \frac{\lambda}{2\pi} \left\{ \frac{2\pi t}{\lambda} - \cos\left(\frac{2\pi t}{\lambda}\right) + 1 \right\} \tag{8.11}$$

and the water depth is therefore

$$w(t) = h_0 \sin\left(\frac{2\pi t}{\lambda}\right) + at - \frac{1}{2} s_0 \frac{\lambda}{2\pi} \left\{ \frac{2\pi t}{\lambda} - \cos\left(\frac{2\pi t}{\lambda}\right) + 1 \right\} \tag{8.12}$$

where the first term is the eustatic effect, the second the tectonic subsidence effect and the third the sediment supply effect. The evolution of water depth through a relative sea-level cycle with different rates of sediment supply and tectonic subsidence rate is sketched in Figure 8.3.

For high rates of sediment supply relative to the rate of relative sea-level change, water depths initially increase, then decrease as sediment fills the available accommodation. Shortly after the peak of relative sea level, sediment supply exceeds accommodation, causing bypassing of excess sediment and the cutting of a disconformity or unconformity as relative sea level continues to fall. At intermediate sediment supply rates, water depths increase for a significant part of the relative sea-level cycle, then gradually decrease until accommodation is filled. The onset of bypassing and erosion is delayed in the cycle of relative sea-level change compared to the high sediment supply case. As relative sea-level rises, sediment again starts to accumulate in unfilled accommodation under initially increasing water depths. In the case of low sediment supply rates, water depth increases initially, and decreases during relative sea-level fall, but accommodation is never completely filled during a cycle of relative sea-level change. Clearly, the variation in water depth through a stratigraphic cycle, the thickness of sediment preserved, the nature of flooding surfaces and disconformities and their time span, are all related to the interplay of eustatic variation, tectonic subsidence rate and sediment supply rate. This is a fundamental reason why stratigraphic cycles are so variable. Synthetic stratigraphic cycles are shown in Figure 8.4 to illustrate the variations in thickness and water depth in "glacio-eustatic" cycles with varying sediment supply rates.

Some selective conclusions from this quantitative analysis of cycle development are as follows:

8.1.3.1 Cycle thickness

If previously deposited sediment is easily eroded during a relative sea level fall, stratigraphic cycle thicknesses depend on two factors: (i) where sediment supply rates are high, cycle thickness depends on the tectonic subsidence over the period of time between the onset of the cycle and the time of relative sea level lowstand. (ii) where sediment supply rates are low compared to the tectonic subsidence rate, cycle thickness depends only on the sediment accumulated over the duration of the eustatic cycle. We can therefore get similar stratigraphic cycle thicknesses under two contrasting scenarios – by erosion during a relative sea-level fall, and by underfilling of the available accommodation. The first is obviously a case of *accommodation-limited* stratigraphy. The latter is a case of *sediment supply-limited* stratigraphy.

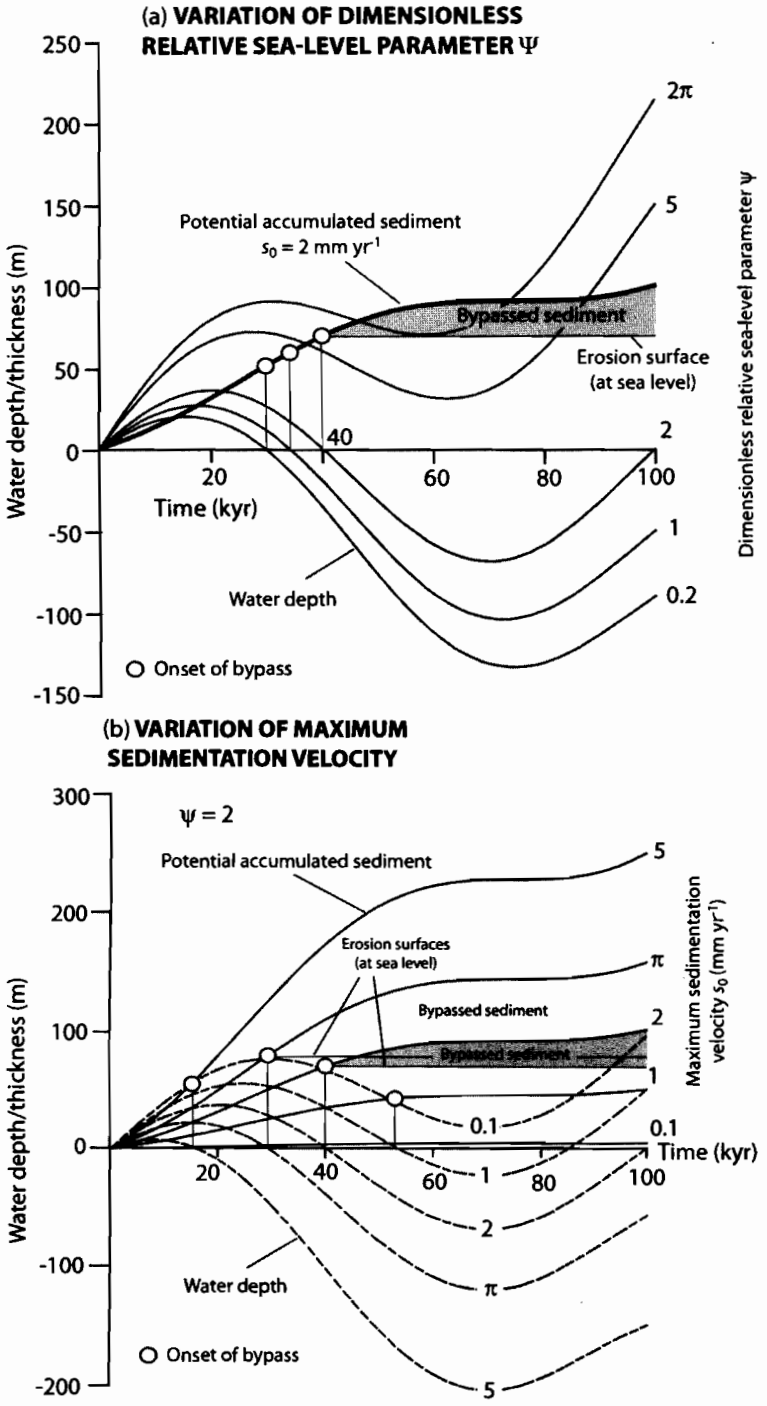

Fig. 8.3 Water depth and potential sediment accumulation during a cycle of relative sea-level change with variable tectonic subsidence rate and sediment supply, using the glacio-eustatic function. (a) Variation in water depth as a function of the dimensionless relative sea-level parameter ψ with a constant maximum sedimentation parameter $s_0 = 2\,\text{mm yr}^{-1}$. When accommodation is filled, sediment starts to bypass the depositional site (illustrated for the case of $\psi = 2$). The onset of bypass occurs progressively later as tectonic subsidence increases (ψ increases). At $\psi = 2$, the basin remains water-filled until 40 kyr, after which erosion and sediment bypass take place until the beginning of the next glacio-eustatic cycle. (b) Variation in water depth and potential accumulated sediment as a function of the sedimentation velocity s_0, with a constant dimensionless relative sea-level parameter ψ of 2, corresponding to a tectonic subsidence rate a of 1 mm yr^{-1}. High sediment supply rates cause the available accommodation to be filled early during the cycle of relative sea-level change, after which sediment is bypassed and eroded (two illustrations at $s_0 = 2$ and $\pi\,\text{mm yr}^{-1}$), whereas at low supply rates ($s_0 = 0.1\,\text{mm yr}^{-1}$), the accommodation remains unfilled. The evolution of water depth during a cycle of relative sea level, sedimentary facies, and the occurrence of erosional bypass surfaces are all critically dependent on the sediment supply.

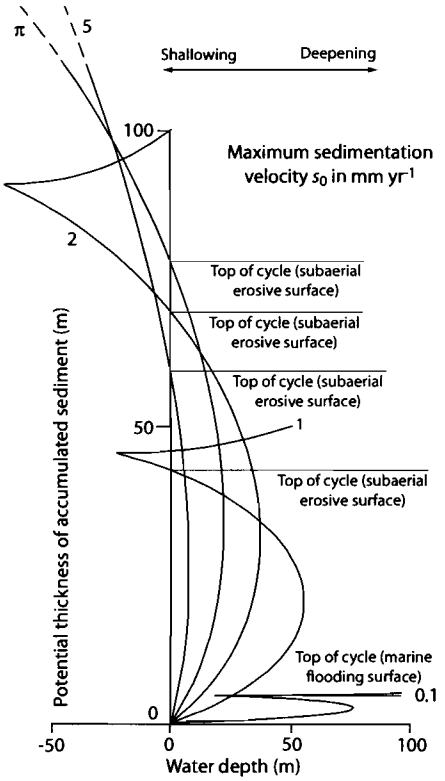

Fig. 8.4 Stratigraphic cycles generated using the algorithms in the text for a glacio-eustatic cycle ($\Psi = 2$) using different values of the maximum sedimentation velocity s_0, from 0.1 to 5 mm yr^{-1}. Cycle thicknesses and water depth trends vary strongly from the thin, sediment starved, deep water case ($s_0 = 0.1$ mm yr^{-1}) with a nonerosional flooding surface as an upper boundary, to the thicker, top-truncated shallow-water cycles at higher values of s_0.

8.1.3.2 Sedimentary facies and water depth variation

For simplicity, we assume that sedimentary facies are dependent on water depth. A common feature of model output is that stratigraphic cycles have thick deepening-up portions. This is because in the case of high sediment supply, relative sea-level fall causes erosion and therefore the removal of the upper, shallow-water part of the stratigraphic cycle. In the case of low sediment supply, accommodation generation outstrips sediment accumulation, causing a temporal increase in water depth. How then do we generate the common *shallowing-up* cycles of the stratigraphic record?

If we believe that eustatic change is important, the most straightforward answer is that the preservation of the shallow-water upper portion of a stratigraphic cycle must be due to the predominance of relative sea-level cycles possessing inflexion points, but insignificant relative sea-level falls. We know from equation (8.7) that inflexion points in the relative sea-level curve occur at $a/h_0 = 2\pi/\lambda$. If $\Psi = a\lambda/h_0$ falls below 2π there is an increasing risk of erosion of the upper part of the stratigraphic cycle as long as the sediment supply is adequate to fill the accommodation space. As base-level, or the graded profile is reached, excess sediment is bypassed into deeper water. In many continental and shallow marine environments, sediment supply is easily capable of filling accommodation. The generation of shallowing-upward cycles therefore depends critically on the value of Ψ, rather than on the sediment supply rate.

Alternatively, if there is no eustatic change, and the cycles are unforced, the common pattern of shallowing-up cyclicity may be due to variations in flooding and progradation driven by internal dynamics of the sedimentary system under a background tectonic subsidence.

Sediment cannot accumulate for long periods of time above the graded profile. Consequently, within a relative sea-level cycle, sediment may be bypassed downstream or into deeper water. High sediment supply in a basin with adequate accommodation will cause sedimentary facies belts to *aggrade*. If sediment supply is less than the accommodation, facies belts will *retrograde*. If sediment supply exceeds accommodation, facies belts will *prograde*. We illustrate the effects of a variable sediment supply on progradation and retrogradation as follows. Consider a sedimentary basin undergoing a uniform and steady rate of tectonic subsidence a with a sinusoidal sediment supply expressed as a vertical velocity of sedimentation as given in equation (8.9).

Choosing realistic parameter values, it is simple to produce (mathematically) stratigraphic cycles involving shallowing and deepening of water depth. Since "negative" water depths may result in erosion, and deepening may be associated with *transgressive ravinement*, some cycles will be bounded by unconformities and flooding surfaces. The balance between the rate of accommodation generation by tectonic subsidence and the long-term sediment accumulation rate determines whether a succession of cycles is retrogradational or progradational. These markedly different stratigraphic styles are very sensitive to this balance (Fig. 8.5). Cycles are retrogradational with

$s_0 = 2\,\text{mm yr}^{-1}$ and $\psi = 2.2$ ($a = 1.1\,\text{mm yr}^{-1}$), but become aggradational if the tectonic subsidence rate is reduced to $a = 1.0\,\text{mm yr}^{-1}$ ($\psi = 2.0$) and progradational at $a = 0.9\,\text{mm yr}^{-1}$ ($\psi = 1.8$). A 20% change in tectonic subsidence rate can therefore cause major changes in cycle stacking patterns. Consequently, sediment supply variations, caused by climate change or internal dynamics, are potentially extremely important in influencing stratigraphic packaging, without recourse to eustatic change.

Consider Figure 8.3b where the low sediment supply causes a low sediment accumulation rate compared to relative sea level. Sediment accumulation can be said to be *sediment supply-limited*. In this case, new water depth is generated with every cycle of relative sea level. After several cycles of relative sea level, marine shorelines will be strongly retrogradational or transgressive, and basinal locations should be dominated by deep-water shale deposition. Where sediment supply is moderate, an initially marine basin is filled to sea level, coastal plain sediments accumulated up to the graded stream profile (base level), followed by erosion and incision as relative sea level falls. Excess sediment is bypassed and delivered to other places in the basin where accommodation may be higher. If sediment supply is high, the shoreline regresses immediately, causing the progradation of deltaic and coastal plain sediments. In this case, sediment accumulation is *accommodation-limited*.

The depositional architecture is therefore very sensitive to the interplay between sediment supply and accommodation generation. We can envisage a continuum of geometrical possibilities where the sediment supply rate varies in relation to the accommodation. For example, for a morphology involving low gradient topsets and steeper gradient clinoforms (Fig. 8.6), the increase in topset accommodate ΔV_{ta} (as a volume) is the product of the relative sea-level change and the topset area. If the sediment supply is greater than ΔV_{ta}, the clinoforms will prograde, the *offlap break* migrating strongly offshore. However, if the sediment supply is progressively reduced, the offlap break first climbs, then becomes near-vertical, and then migrates landward when sediment supply is less than ΔV_{ta}.

8.2 STRATIGRAPHIC CYCLES: DEFINITION AND RECOGNITION

Although the cyclical nature of stratigraphy at a range of scales has been recognized for many decades, a significant advance was made by the recognition of the packaging of stratigraphic units from seismic reflection data. Vail et al. (1977a) claimed to recognize a hierarchy of cycles of relative sea-level change largely on the basis of the depositional limits of onlap and toplap within the coastal facies of marine sediments.

8.2.1 Supersequences and megasequences

Sloss (1988) traced the history of ideas on sequence stratigraphy over the second half of the last century. The importance of rock-stratigraphic units traceable over wide areas of the North American continent and bounded by unconformities of "interregional scope" has long been recognized (Sloss 1950, 1963). Six such *supersequences* (termed "sequences" by Sloss) occupying the Phanerozoic were defined, with a duration of 50–120 Myr (Fig. 8.7). Each supersequence is thinner and represents a shorter period of deposition at the center of the craton compared to its margin, so that the bounding unconformities increase in duration from the craton edge (10 Myr gap) to the craton center (150 Myr gap). Burgess and Gurnis (1995) and Burgess et al. (1997) interpreted the supersequences as due to the effects of cycles of subduction around the edges of the North American Plate (Chapter 5).

Hubbard et al. (1985), using primarily a subsurface seismic reflection database, introduced a similar concept of *megasequences*, representing the stratigraphic packages deposited during distinct phases of plate motion. Consequently, a megasequence may correspond to a period of continental extension with synrift and postrift components, or to a period of convergent plate motion characterized by flexure of the continental lithosphere. Megasequences are also bounded by extensive but not global major unconformities. Since sedimentary basins are deformations of the lithosphere under a set of plate-scale driving forces, the concept of the megasequence is of primary importance in basin analysis.

8.2.2 Depositional sequences

The primary meso-scale units of stratigraphy are termed *depositional sequences*. They are coherent packets of strata that are genetically related and which can be traced for considerable distances across a basin. Depositional

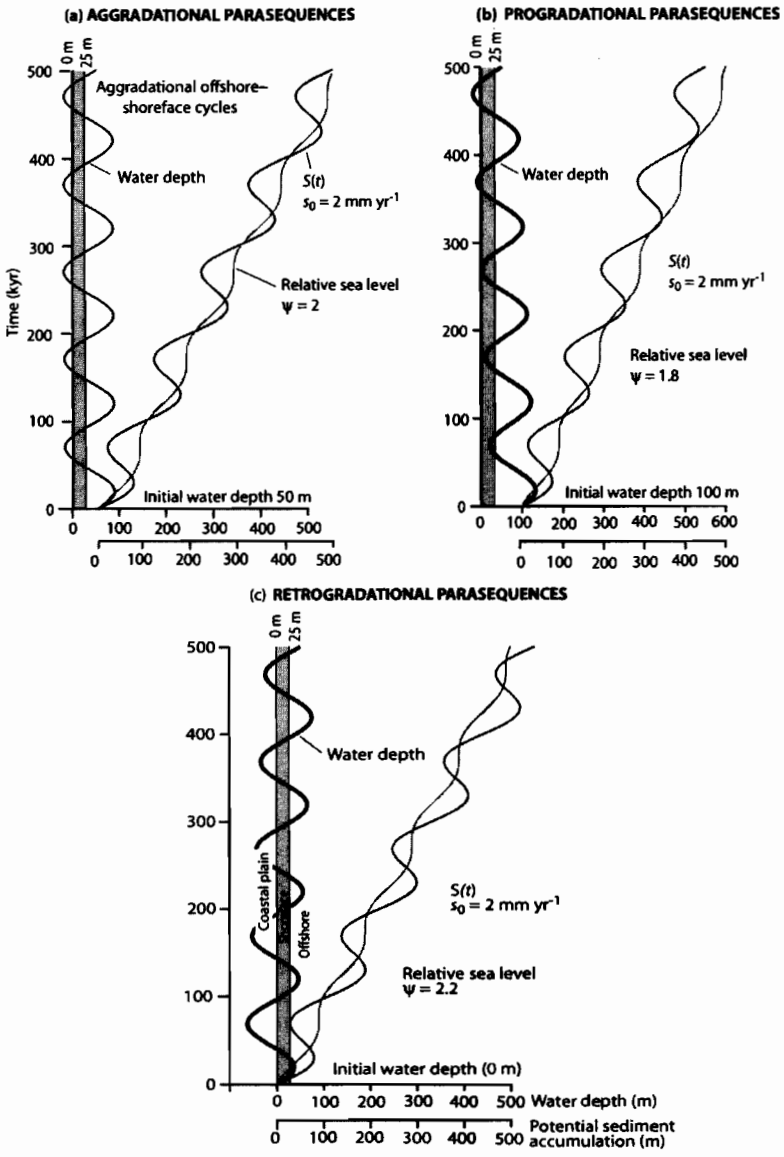

Fig. 8.5 Sensitivity of retrogradational *versus* progradational cycles resulting from variations in tectonic subsidence rate a, with a constant maximum sedimentation velocity of $s_0 = 2\,\text{mm yr}^{-1}$. (a) Aggradational cycles (parasequences) containing offshore, shoreface (0–25 m) and potentially thin coastal plain deposits are produced at $\psi = 2$ ($a = 1\,\text{mm yr}^{-1}$), using an initial water depth of 50 m. Relative sea level and sediment supply are in balance. (b) Progradational cycles produced by a small decrease in ψ to 1.8 ($a = 0.9\,\text{mm yr}^{-1}$), with an initial water depth of 100 m, showing that younger cycles contain progressively lesser amounts of offshore deposits and more shoreface deposits. (c) Retrogradational cycles produced by a small increase in ψ to 2.2 ($a = 1.1\,\text{mm yr}^{-1}$), with an initial water depth of zero, showing that coastal plain–shoreface cycles are progressively replaced by shoreface–offshore cycles with time. Small variations in tectonic subsidence rate (relative to the sediment supply) therefore cause major variations in the stacking patterns of cycles.

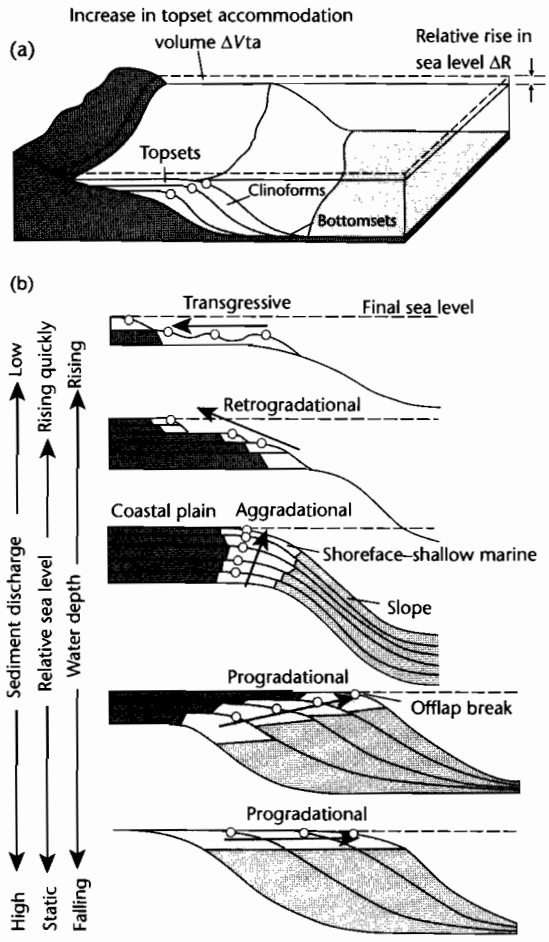

Fig. 8.6 Large scale architecture of depositional units in relation to accommodation and sediment supply (after Galloway 1989). (a) A rise in relative sea level causes an increase in topset accommodation volume ΔV_{ta}, equal to the product of the relative sea-level rise and the topset area; (b) Stratigraphic patterns change from transgressive to retrogradational, aggradational, and progradational as the sediment supply increases relative to the topset accommodation. White circles approximate position of beach (or offlap break).

sequences can be recognized in the subsurface using seismic stratigraphic methods, the tops and bases being marked by bounding unconformities or laterally correlatable conformities (Mitchum et al. 1977) (Fig. 8.8). Within a depositional sequence, individual strata can exhibit a variety of geometrical relationships to the depositional boundary (Dunbar and Rogers 1957) (Fig. 8.9). Widespread recognition of these geometric relationships was only possible with the availability of high-quality seismic reflection data. As well as helping to define a depositional sequence boundary, these types of discordant relationship also furnish clues as to the origin of the unconformity. Onlap, downlap, and toplap indicate nondepositional hiatuses, whereas truncation indicates an erosional hiatus or it may be the result of structural disruption (Vail et al. 1977a).

The minimum stratigraphic unit that can be called a depositional sequence must have a significance in the basin either in terms of thickness or in terms of geological time. Depositional sequences have a chronostratigraphic significance because they were deposited during a time interval limited by the ages of the sequence boundaries where they are conformities. Where unconformities mark the boundaries, the age range is reduced. The total time interval during which a sequence is deposited is called a *sechron*.

It has been claimed that many genetic depositional sequences are better recognized not by their erosional sequence boundaries, but by their *maximum flooding surfaces* (Frazier 1974; Galloway 1989) (Fig. 8.10). Maximum flooding surfaces represent the period of greatest inundation of the basin margin. Although the depositional sequence boundary (Mitchum et al. 1977) can be easily recognized on seismic reflection sections by a downward shift in the position of coastal onlap (see below), it is commonly difficult to recognize in log, core, and outcrops. The maximum flooding surface, which is also easily recognized on seismic reflection sections as the reflector with most landward penetration, is also easily recognized in electrical logs, cores, and outcrop, since it is commonly associated with the deepest water or condensed sedimentary facies (Loutit et al. 1988). The position of the maximum flooding surface within depositional sequences is strongly determined by the minima in sediment supply. The use of maximum flooding surfaces as a tool in subsurface mapping is well illustrated by the case study of Partington et al. (1993) in the North Sea basin.

The algebra expressing the variation between eustasy, tectonic subsidence, and sediment supply in §8.1 demonstrates that the period of greatest increase in new space available is at the *inflection point* of the *rising limb* of the curve of rate of relative sea-level change, and the period of greatest decrease in new space available is at the inflection point of the *falling limb* of the curve of rate of relative sea level. Since the inflection points on the falling

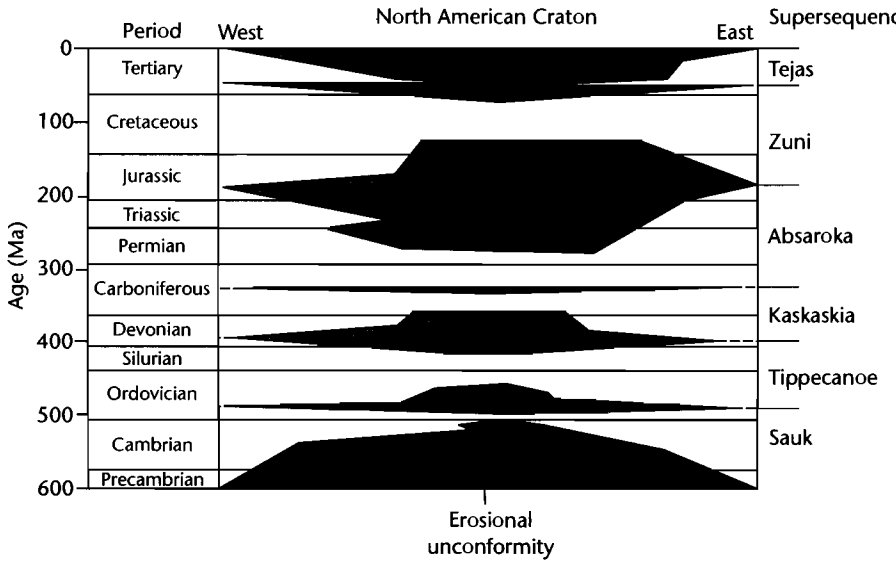

Fig. 8.7 The supersequences of the North American craton of Sloss (1963).

limb of the rate of relative sea-level curve mark times of least available new space, sedimentation commonly shifts to the basin plain and the shelf is subjected to erosion. An unconformity is produced and is accompanied by a basinward shift in coastal onlap and a cessation of fluvial deposition. If the rate of relative sea-level fall is rapid, streams are rejuvenated and incise into the former shelf giving *Type 1 unconformities* (Fig. 8.11). However, if the rate of relative sea-level lowering is slow, there is a gradual but widespread denudation without substantial river incision, giving *Type 2 unconformities*.

Using seismic reflection results, a team of geologists and biostratigraphers from Exxon constructed a chart of relative sea level through time (Vail et al. 1977b), updated and improved by Haq et al. (1987, 1988). These charts, colloquially known as the Vail and Haq curves, are based on the concept of depositional sequences and the kinds of baselap and toplap at sequence boundaries. The Vail–Haq curves are composed of *cycles of relative change of sea level*. In essence, the Haq et al. (1987) curve is presented as having two components: (i) a *long-term* eustatic curve defining "first order cycles" or "megacycles" of period >100 Myr; it is probably equivalent to the sea-level change resulting from changes in mid-ocean ridge volumes of from the dynamic topography associated with subduction (see §8.3, §5.2), and (ii) a *short-term* eustatic curve, composed of higher frequencies defining "second order cycles" or "supercycles" of duration 8–10 Myr and "third order cycles" or "cycles" of duration 1–5 Myr.

The chronostratigraphic basis for the global sea-level chart of Haq et al. (1987) is a combination of radiometric dates, magnetostratigraphy (geomagnetic polarity reversals), and biostratigraphy, but there is a limit to the time resolution of stratigraphic boundaries, which makes the question of their global synchroneity problematic (Miall 1991, 1994). The Vail–Haq global sea-level chart remains controversial. It is evident from our consideration of process stratigraphy that the timing of depositional sequence boundaries is determined by the interacting rate effects of sediment accumulation, tectonic subsidence and eustatic change. For example, we know (§7.5) that large river catchments are strongly buffered systems that have long response times to a base-level change such as eustatic rise or fall. Since different catchments have different response times (10^4–10^6 yr), a *synchronous* base-level change should result in a *diachronous* stratigraphic response. An eustatic change at a point in time should only produce a *partial* or *apparent* synchroneity in basins with different tectonic and sediment supply

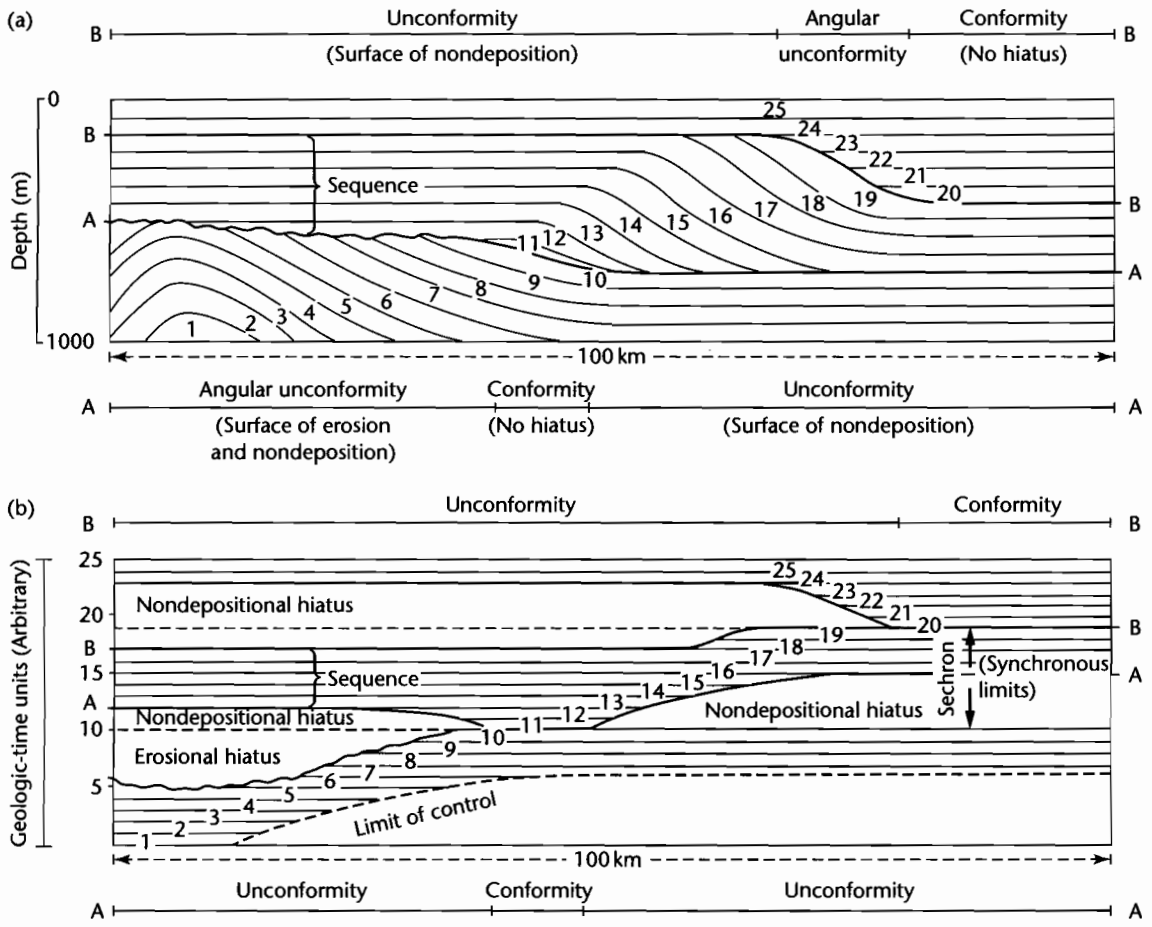

Fig. 8.8 The basic concept of the depositional sequence as outlined by Vail et al. (1977a). (a) Generalized stratigraphic section of a depositional sequence. A sequence boundary A changes from an angular unconformity in the left half of the diagram to a conformity in the centre and to a nondepositional unconformity on the right. The sequence boundary B passes from a nondepositional unconformity on the left to an angular unconformity in the centre and a lateral conformity on the right. Unconformities are dated at the points where they have become conformable. Units 1–25 represent strata deposited during successive time intervals; (b) Generalized chronostratigraphic section of the same stratigraphic sequence as in (a). The depositional sequence between surface A and B ranges in age from the beginning of 11 until the end of 19. Chronostratigraphic charts of this type are sometimes termed "Wheeler diagrams" following Wheeler (1958).

histories (see also Parkinson and Summerhayes 1985 for a thought experiment along these lines). The search for global synchroneity is therefore fundamentally futile. There is also some doubt as to whether 2nd, 3rd, 4th.... *n*th order cycles can actually be discriminated, and it is possible that stratigraphic cyclicity exists in a broad continuum of frequency (Wilkinson et al. 1998).

In summary, we believe that the Haq et al. (1987) curve is a "noisy" accumulation of a wide range of sea-level signals, and should not be used as a global benchmark.

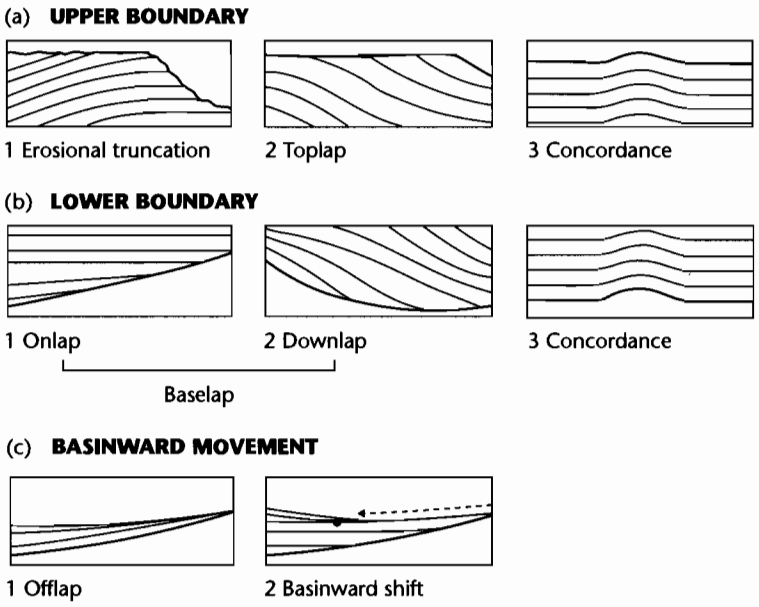

Fig. 8.9 The geometrical relationships of strata to a depositional sequence boundary or to any other surface within a depositional sequence. (a) Relations to upper surface, involving (1) erosional truncation, (2) toplap (commonly nondepositional rather than erosional), and (3) concordance; (b) Relations to lower surface involving (1) onlap where the overlying strata are near-horizontal and the surface is inclined, (2) downlap where the overlying strata are inclined, and (3) concordance; (c) Additional geometrical patterns of (1) offlap, where there is a progressive basinward migration of the stratigraphic units, and (2) basinward shifts, where the basinward movement is discrete rather than progressive.

It should never be used as a chronostratigraphic tool by assuming *a priori* that a certain stratigraphic boundary has a globally synchronous and precise age, which it is therefore safe to extrapolate into a basin with poor age control.

8.2.3 Systems tracts

Depositional sequences can be subdivided into smaller units of stratigraphy that have distinct stacking patterns of chronostratigraphic increments. These smaller units are termed *systems tracts* (Van Wagoner et al. 1988), and they are themselves composed of *parasequences*, or *paracycles*. The tracts of depositional systems (Brown and Fisher 1977) have been related to specific intervals of cycles of relative sea level (Posamentier et al. 1988; Posamentier and Vail 1988; Van Wagoner et al. 1988). Although systems tracts were defined as the stratigraphic response of a system to the competing effects of rate of relative sea-level change and rate of tectonic subsidence, they are clearly sensitive to variations in sediment supply. In the description that follows, it should be remembered that sediment supply variations may complicate and even override the effects of rate of relative sea-level change on systems tract behavior.

Systems tracts are broadly divided into the following classes according to their relationship to specific segments of the relative sea-level change curve (Fig. 8.12):

1 *Lowstand systems tract*: When relative sea-level fall is rapid, no space is available for further sedimentation, the former shelf is incised by streams (producing incised valley systems) and sedimentation is transferred to the basin floor and slope. Base-of-slope fans (*lowstand fans*) are nourished by sediment bypassed through the shelf and slope by valleys and canyons. *Slope fans* result from deposition on the middle or base of the continental slope and may be coeval with the basin-floor fan. *Lowstand wedges* are characterized by onlap onto the slope and at the same

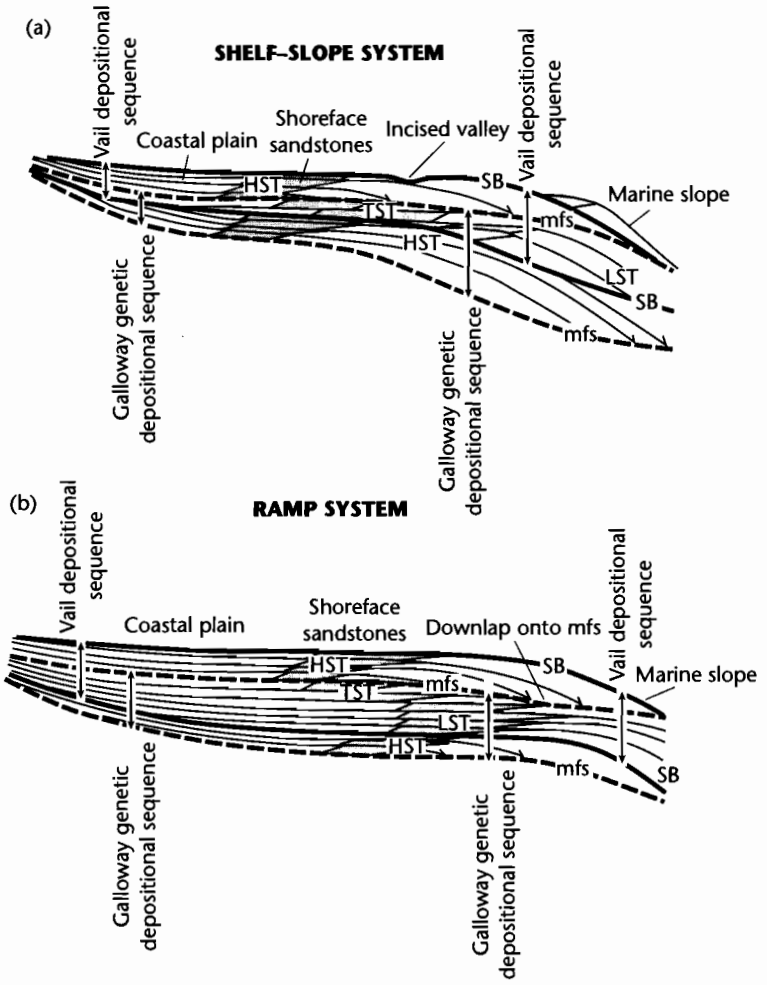

Fig. 8.10 Recognition of depositional sequences and genetic stratigraphic units using their bounding unconformities and maximum flooding surfaces respectively. A Vail-type depositional sequence is bounded by erosional unconformities or their correlative conformities, whereas a Galloway-type genetic depositional sequence is bounded by maximum flooding surfaces. HST, Highland systems tract; LST, Lowland systems tract; TST, Transgressive systems tract; SB, Sequence boundary; mfs, maximum flooding surface.

time by progradation and downlap onto the previous basin floor or slope fans. They are deposited at times of low but very slowly changing sea level, particularly during a slow relative rise. Lowstand fans, slope fans, and lowstand wedges are all associated with underlying Type I sequence boundaries. When the relative sea-level fall is gradual, sedimentation may be progressively shifted basinwards to the shelf edge where both onlap in a landward direction and downlap in a basinward direction takes place. The base of the *shelf margin* systems tract is therefore a Type 2 sequence boundary. On a ramp margin rather than a shelf-break margin, slopes are too low to allow for significant submarine canyon formation and turbidite deposition (Van Wagoner et al. 1988). Since there is little bypass of sediment to the basin floor, falling relative sea level may cause the deposition of a set of downstepping prograding wedges, known as *forced regressive wedges* (Posamentier et al. 1992) in a *forced regressive*

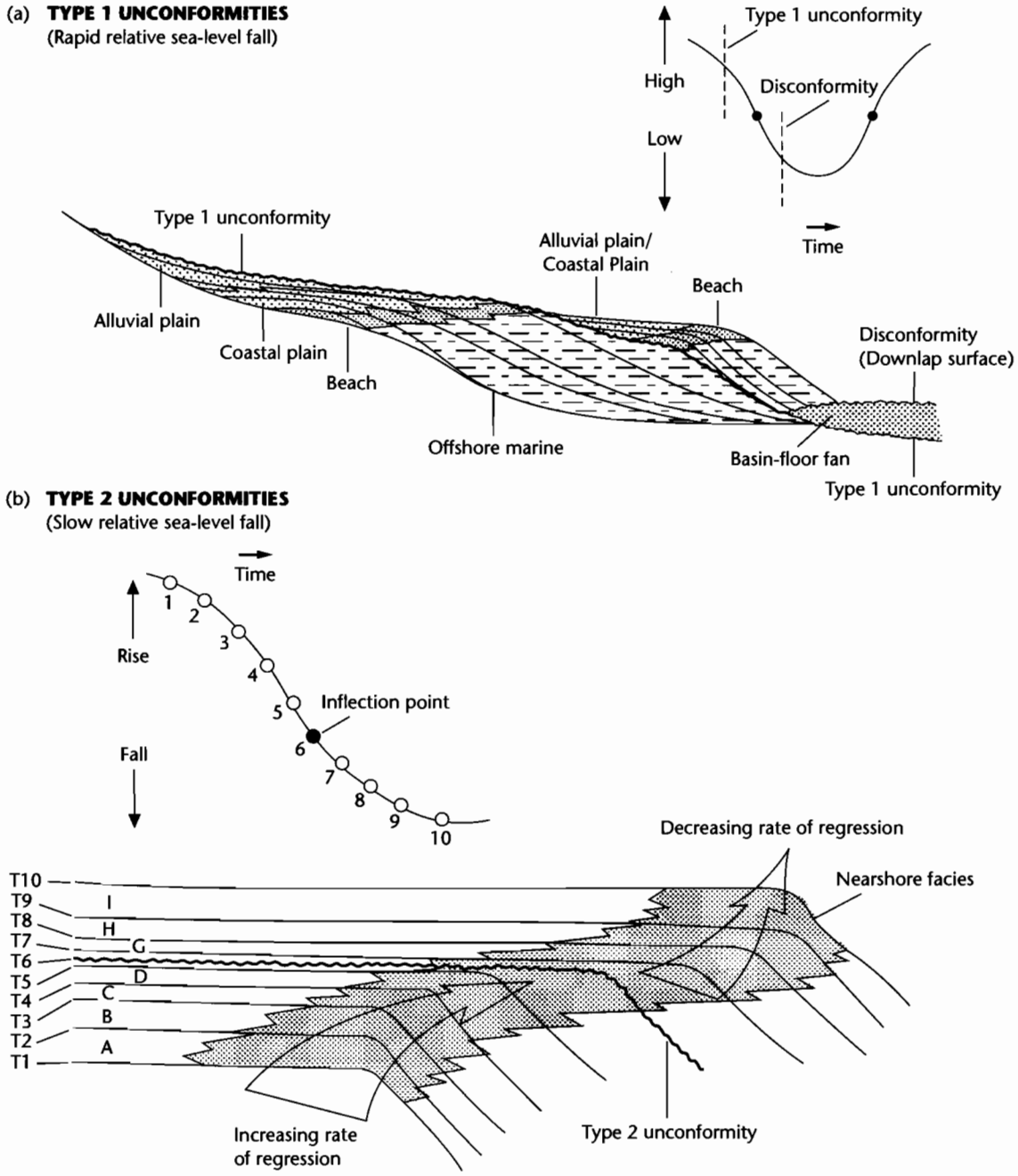

Fig. 8.11 Type 1 and Type 2 unconformities (after Posamentier et al. 1988). Type 1 unconformities (a) erode into older shelf sediments and may underlie basin-floor fans. They are believed to be formed during a rapid lowering of relative sea level. The sediments of the second depositional sequence downlap onto a disconformity or onlap the Type 1 unconformity. Type 2 unconformities (b) do not strongly erode the underlying depositional sequence, but signal a change from prominent progradation to aggradation as the rate of regression slows. Overlying sediments may onlap the Type 2 boundary landward of the shelf edge, although it is not illustrated above. Type 2 unconformities are interpreted to form at the inflection point of a slow relative sea-level fall.

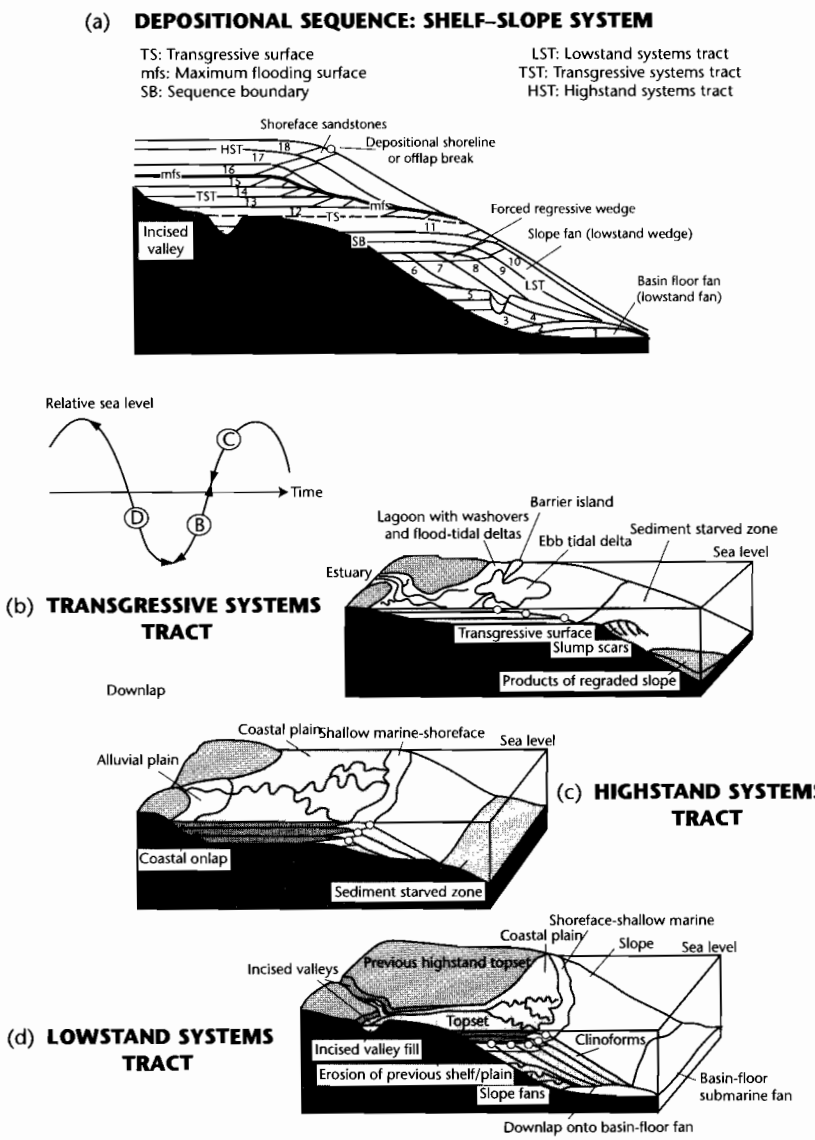

Fig. 8.12 Characteristic systems tracts and their relation to the relative sea-level curve, according to the Exxon group (Posamentier et al. 1988), modified by Emery and Myers (1996). These block diagrams are extremely idealized and have a strong vertical exaggeration. (a) Arrangement of systems tracts within a depositional sequence in a coastal plain–continental shelf-slope system. Numbers are relative ages of chrons; (b), (c) and (d) show transgressive, highstand, and lowstand systems tracts respectively. Open circles are depositional shoreline or offlap break. Reproduced courtesy of Blackwell Publishing Ltd.

systems tract (Hunt and Tucker 1992; Posamentier and James 1993).

2 *Transgressive systems tract*: During a rapid relative sea-level rise, the underlying lowstand or shelf margin system tracts are transgressed (the *transgressive surface*). Where the transgressive surface is erosional, it is called a *ravinement surface*. Sets of parasequences making up the transgressive system tract are commonly retrogradational (Fig. 8.13), that is, they back-step onto the basin margin, with strong onlap in a landward direction and downlap onto the transgressive surface in a basinward direction. As the rate of relative sea-level change slows down, the sets of parasequences change from being retrogradational to being aggradational, the surface at which this occurs being that of the *maximum flooding*. *Condensed sections* occur in the basin during times of transgression.

3 *Highstand systems tract:* After the maximum flooding, the relative sea-level rise slows and sets of aggradational parasequences are succeeded by progradational parasequences with clinoform geometries (Fig. 8.13). These highstand systems tract parasequences onlap onto the underlying sequence boundary in a landward direction and downlap onto the top of the transgressive systems tract or lowstand systems tract in a basinward direction, so that there is a prominent *downlap surface* below a highstand system tract. Marine condensed sequences occur during the early stages of a highstand systems tract before major progradation takes place (Loutit et al. 1988). Highstands offer the possibility of thick subaerial deposition of fluviatile sediments.

The methodology of systems tract recognition has been extended to carbonate-dominated systems (e.g.,

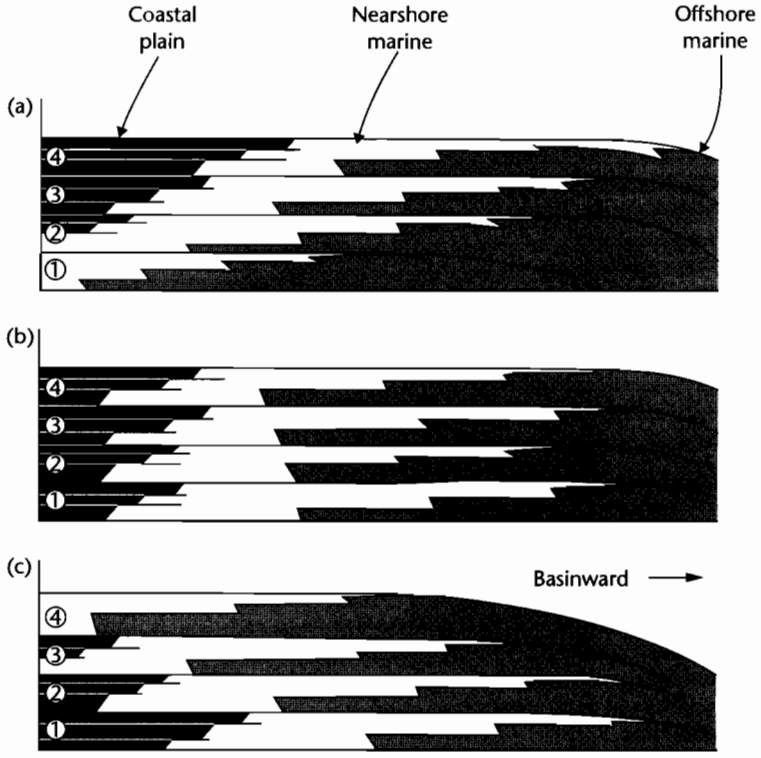

Fig. 8.13 Stacking patterns of parasequence sets (after Van Wagoner et al. 1988) are indicative of the trend in time of sediment supply and relative sea-level change or accommodation. (a) Progradational parasequence set with a basinward migration of the shoreline, characteristic of the highstand systems tract and lowstand prograding wedge; (b) Aggradational parasequence set showing no movement of the shoreline, characteristic of the shelf-margin systems tract; (c) Retrogradational parasequence set, with a landwards migration of the shoreline, characteristic of the transgressive systems tract. Reproduced courtesy of Society for Sedimentary Geology.

Sarg 1988; Schlager 1992). Although there are significant differences between siliciclastic and carbonate systems, the underlying principles are similar.

8.2.4 Smaller genetic stratigraphic units

The resolution of most seismic reflection sections generally allows only depositional sequences and megasequences to be recognized. However, log, core and outcrop data show that stratigraphy is marked by variability at higher resolution. The larger stratal geometries of depositional sequences can be linked at high resolution with their typical facies assemblages (Van Wagoner et al. 1990; Posamentier and Chamberlain 1993).

The typical small-scale cycles seen in core and at outcrop consist of an upward-shallowing trend followed by an abrupt deepening. These cycles are known as *parasequences* (Van Wagoner et al. 1990), who defined them as relatively conformable units of genetically related beds or bed-sets bounded by marine flooding surfaces or their correlative surfaces (Fig. 8.14). The boundaries of parasequences, as in depositional sequence boundaries, are thought to be synchronous surfaces. Parasquences thus defined are placed at a lower level than depositional sequences, but there is no further implication of hierarchical level (3rd, 4th, 5th order etc.). They have long been recognized in a variety of paleoenvironmental settings ranging from fluvial to deep marine, and in both siliciclastic- and carbonate-dominated systems. Parasequences are small scale but fundamental building blocks of stratigraphy, generally a few meters to <15 m in thickness. Their lateral extent varies according to the uniformity of basin tectonic subsidence and the nature of the external or internal forcing. In the Proterozoic Rocknest Platform of northwest Canada (Grotzinger 1986a) 140 to 160 progradational shallowing-up cycles can be traced for enormous distances (>100 km) both perpendicular and parallel to strike, whereas other field studies suggest that parasequences are commonly laterally impersistent.

The glacially forced sea-level changes of the Late Quaternary (§8.3.4) have a similar frequency to those required to explain some parasequences. The time scale of the fluctuation is also reminiscent of the frequency of climatic change attributed to eccentricities in the orbital motion of the Earth (Hays et al. 1976; Imbrie 1982). These variations are commonly termed *Milankovitch* cycles (see also §8.3.4). Time-series analysis of the

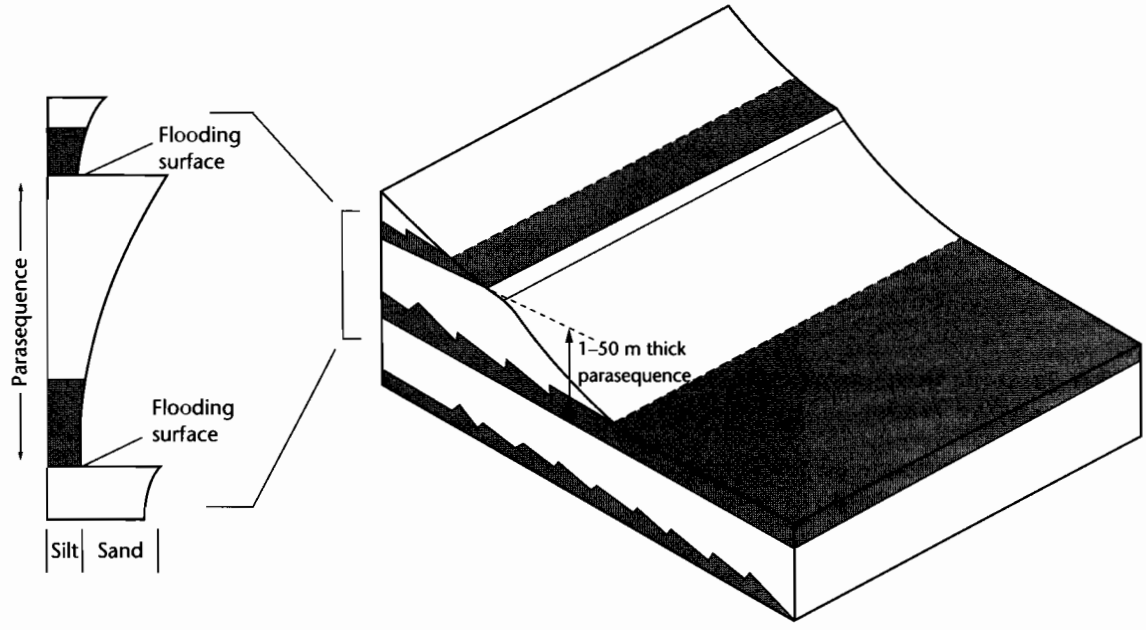

Fig. 8.14 A shallow marine parasequence involving upward coarsening, representing a shallowing of water depth over time. The parasequence is bounded by flooding surfaces. After Emery and Myers (1996). Reproduced courtesy of Blackwell Publishing Ltd.

periodicity of stratigraphic cycles, such as in the Alpine Triassic, have led to different claims about the identification of Milankovitch-type forcing (e.g., Goldhammer et al. 1990), and some cycles may be entirely unforced (Burgess et al. 2001).

Parasequences deposited at greenhouse periods, when glacio-eustatic changes are expected to have been minimal, may be unforced, or forced at a longer frequency than typical icehouse Milankovitch cycles. For example, cycles of relative sea-level change interpreted in Eocene "greenhouse" stratigraphy in the Swiss Alps appear to have a frequency of *c.* 0.4–1 Myr (Allen et al. 2001). The Oligocene stratigraphy of the New Jersey coastal plain exhibits cycles of *c.* 0.5–2 Myr duration (Kominz and Pekar 2001). Clearly, on identifying parasequences, it is not a safe assumption that they were deposited within the Milankovitch wave band.

8.3 DRIVING MECHANISMS FOR STRATIGRAPHIC PATTERNS

In Chapters 3–6 we introduced the main mechanisms for the formation and development of sedimentary basins. In this section we consider in more detail some of the mechanisms responsible for stratigraphic patterns in the basin-fill. They can be divided into tectonic mechanisms that control the spatial and temporal pattern of subsidence and the evolution of sediment routing systems, and eustatic mechanisms that essentially control accommodation and set base level. We then briefly examine the other effects of climate change, principally through sediment yield, and consider cyclicity that is unforced by external controls and which originates from the internal complexity of sediment routing systems. An overview of the depositional styles of basins in a wide variety of tectonic settings is found in §8.5.

8.3.1 Tectonic mechanisms: Flexure under applied loads

8.3.1.1 Effects of flexure on stratigraphy in basins due to stretching

The mechanisms of subsidence in stretched basins comprise: (i) a fault-controlled initial subsidence caused by mechanical stretching of the upper brittle layer of the lithosphere, and (ii) a thermal subsidence caused by the cooling and contraction of the upwelled asthenosphere (Chapter 3). These mechanisms are amplified by sediment and water loading (Chapter 9). In the period of active stretching or rifting, the lithosphere is generally viewed as being in a state of purely local (Airy) isostasy. That is, the lithosphere behaves as a very weak support for any superimposed loads in the active rift. However, the presence of gently dipping postrift sediments suggests that a broadly distributed subsidence characterizes the postrift stage. The way in which the lithosphere distributes loads in the postrift stage is by flexure. Whereas the stretching event determines the first-order depth and size of the basin, the subtleties of the flexural response of the lithosphere have a profound influence on depositional sequences in the postrift stage.

If the lithosphere behaves *elastically* over geological time periods, flexural rigidity should depend on its thermal age (§4.3.2). Basin stratigraphy should reflect this increase in flexural rigidity with time, by a progressive overstepping of younger strata at the margin of the basin. If the lithosphere behaves *viscoelastically* (and the time constant of the viscous relaxation is long), stresses are relaxed by a viscous flow, causing the flexural rigidity to decrease with time. For the same tectonic (cooling plate) driving mechanism, this different basement response produces a pattern of stratigraphic offlap, with the youngest sediments restricted to the basin center. The widths of the basins produced on elastic and viscoelastic lithosphere are therefore markedly different (Fig. 8.15). For the elastic lithosphere, the postrift sediments strongly overstep the synrift sediments giving a *steer's-head* geometry. In contrast, on a viscoelastic plate, the overstep of the postrift sediments is absent because of stress relaxation with time.

The pattern of stratigraphic onlap has been modeled in detail for the passive margin of eastern North America (Watts 1982). Sedimentation is assumed to keep pace with subsidence, maintaining a constant bathymetric profile through time. Figure 8.16 shows the initial strong onlap of sediments onto the basement at the transition from fault-controlled Airy-type subsidence to flexural-controlled subsidence. However, lateral heat flow causes thermal uplift on the coastal plain, abruptly terminating onlap. By about 16 Myr after rifting, flexural subsidence outstrips thermal uplift and the sediments again progressively onlap basement.

8.3.1.2 Role of flexure in generating foreland basin stratigraphy

The typical large-scale geometry of foreland basin stratigraphy is of wedge shaped units, thick close to the

orogenic load and thinning onto the foreland into a "feather-edge." This is a reflection of the lateral gradient in subsidence rate from the center of the load to the peripheral bulge. Superimposed on this is commonly a spatial translation (with respect to the underlying plate) of stratigraphic units ahead of a moving load, a consequence of continued convergence being accommodated in the orogenic belt. This effect causes a general onlap of successively younger stratigraphy onto the foreland (Fig. 8.17). Numerous case studies exist that demonstrate this simple geometric style, such as the Magallanes Basin of southern South America (Fig. 8.18).

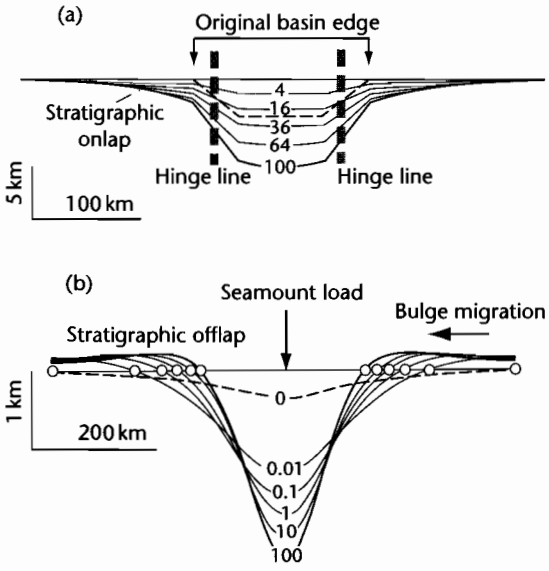

Fig. 8.15 Contrast of elastic and viscoelastic behaviors. (a) Stratigraphy of a model stretched basin with $\beta = 2.0$, overlying an elastic lithosphere where the equivalent elastic thickness is the depth to the 450 °C isotherm. T_e increases with thermal age, causing stratigraphic onlap (steer's head geometry); (b) Response of a visocoelastic lithosphere with a viscous relaxation time of 10^4 yr to seamount loading. The lithosphere weakens rapidly following loading, causing stratigraphic offlap and a gradually narrowing basin. Vertical exaggeration of × 10. Numbers are time in Myr since rifting. After Watts et al. (1982).

The deflection of a foreland plate must depend on the flexural rigidity of the flexed lithosphere, the nature of the distributed loads (topographic/thrust loads, subsurface loads, horizontal end forces, bending moments, sediment and water loads) and the presence of pre-existing heterogeneities. As a consequence, it is vital in considering foreland basin stratigraphy to consider the previous geological history of the lithosphere. The most common scenario is the *Wilson cycle* (§1.3).

The Wilson cycle implies that during continental collision, the overriding plate flexes an inherited passive margin structure in the underlying plate. Two points immediately stand out: (i) since the lithosphere has been previously heated and stretched (§3.1) it will possess a flexural rigidity or equivalent elastic thickness that reflects this history, the "memory" diminishing with time since rifting, (ii) the first loads will be emplaced on a pre-existing continental margin bathymetry rather than on an imaginary flat surface representing the regional elevation.

Stockmal et al. (1986), using a depth-dependent plate rheology, proposed four end-member models to account for the transition from passive margin to foreland basin (Table 8.1). Whereas at early stages the thermal age of the passive margin is an important, even dominant control on basin development, this effect becomes less important as the overthrust wedge is progressively emplaced on stronger unstretched lithosphere. At this stage, the thickness of the overthrust load is of greatest importance. The maximum foreland basin depths prior to postdeformational erosion vary from ~3 km for a low

Table 8.1 Four end-members of foreland basins superimposed on passive margins (Stockmal et al. 1986).

	High topographic profile* (e.g., Himalayas) Frontal slope ~3°	***Low topographic profile* (e.g., Zagros) Frontal slope ~0.5°†**
Thermally young (~10 Myr) continental margin	Young–high	Young–low
Thermally old (~120 Myr) continental margin	Old–high	Old–low

Notes:
* Seeber, Armbruster and Quittmeyer (1981);
† Chapple (1978).

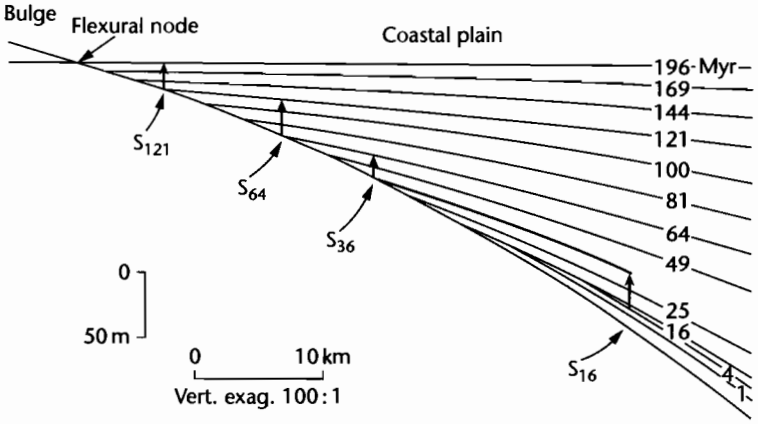

Fig. 8.16 Coastal plain and shelf stratigraphy using a model of a passive margin in which the tectonic subsidence is due to thermal contraction following stretching. Sediments rapidly infill the continental shelf, keeping a near-constant bathymetry with time. The sedimentary load flexes a cooling plate that increases in rigidity with time since heating. The initial lithospheric thickness y_L is 125 km, initial crustal thickness y_c 31.2 km, coefficient of thermal expansion α, 3.4×10^{-5} °C $^{-1}$, mantle temperature 1333 °C, initial densities of 2800 and 3300 kg m^{-3} for crust and mantle lithosphere respectively, and the uniform density of the infilling material is 2500 kg m^{-3}. The stretch factor is 3.0 and the equivalent elastic thickness is given by the depth to the 450 °C isotherm. Solid boundaries are stratigraphic units with ages in Myr since the end of rifting. Effects of compaction have been ignored. The arrowed lines show the amounts of coastal aggradation at given time periods. After Watts (1982).

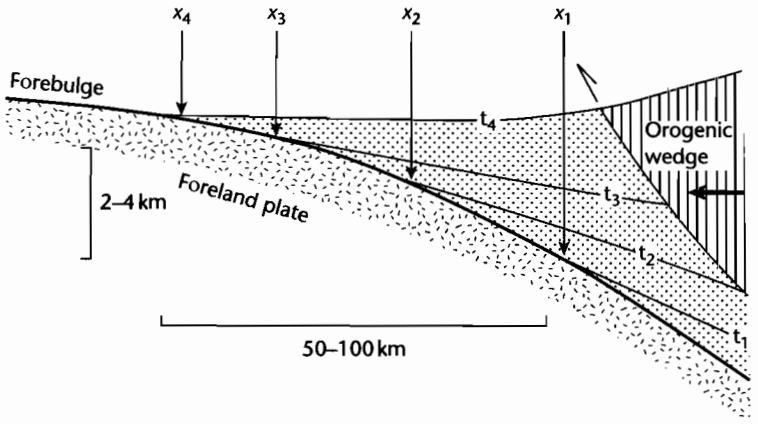

Fig. 8.17 Diagrammatic illustration of a foreland basin showing stratigraphic onlap. Locations x_1 to x_4 show the successive positions of pinch-outs corresponding to the chronostratigraphic lines t_1 to t_4.

topography (e.g., Zagros) to ~16 km for a high topography (e.g., Himalayas). Postdeformation erosion and tectonic thinning (extension) can cause massive unroofing of up to 40 km, bringing high grade metamorphic rocks to the surface. Very thick overthrust wedges can develop with little topographic expression if they are emplaced on a deep oceanic bathymetry. Further information on the development of orogenic wedges and their numerical modeling is found in §4.5 and §4.6.

8.3.1.3 The flexural forebulge unconformity

Passage of the flexural forebulge can cause a complex arrangement of unconformities (Price and Hatcher

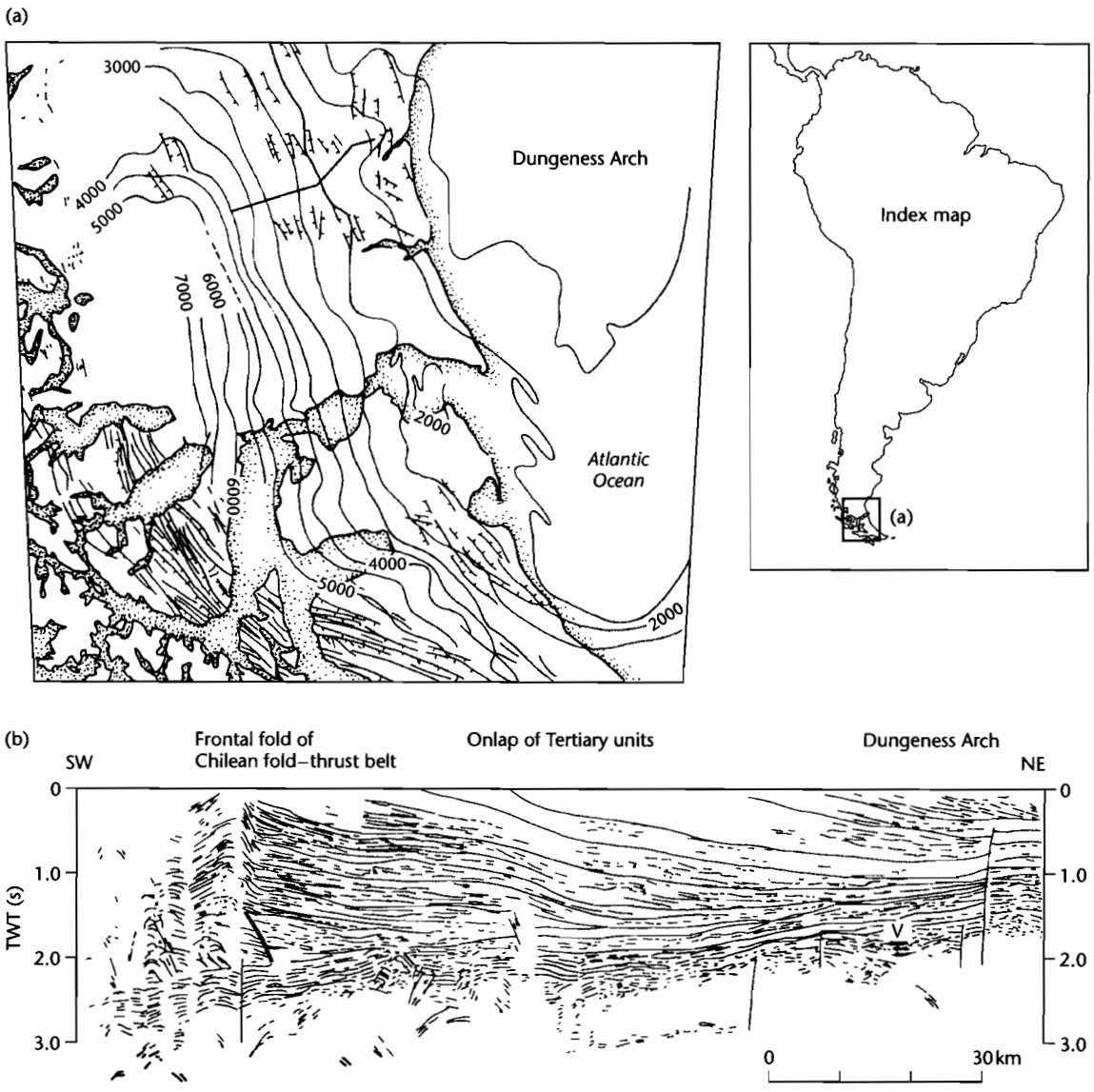

Fig. 8.18 The Magallanes Basin, southern South America (after Biddle et al. 1986). (a) Isopachs (in m) of sedimentary fill of Magallanes Basin above the level of the Tobifera volcanics, representing the last stages of rifting prior to foreland basin flexure (Bruhn et al. 1978; Gust et al. 1985). Isopachs show a clear thinning onto the Dungeness Arch; (b) Line drawing interpretation of seismic reflection record from the frontal folds of the Chilean fold–thrust belt to the flank of the Dungeness Arch. Stratigraphic units show strong onlap above the Tobifera volcanics (V). The clinoforms are thought to be fan deltas derived from the Andean mountain belt that prograded into deep marine shales.

1983). Initial uplift in the forebulge region is followed by subsidence as the bulge moves onto the craton. The unconformities should migrate in a time-transgressive manner onto the craton (Crampton and Allen 1995).

Consider a flexural forebulge unconformity generated by an orogenic load moving across a linear elastic foreland plate of flexural rigidity D. If the advance of the orogen is steady, the stratigraphic gap is dependent on:

(i) the time-average erosion rate on the forebulge, and (ii) the duration of uplift in the forebulge region, given by

$$\tau = \frac{x_2 - x_1}{V} \tag{8.13}$$

where x_1 and x_2 are the first node and second node of the deflection respectively, which is equivalent to the width of the forebulge, and V is the advance rate of the orogenic system. The width of the forebulge on a continuous elastic plate scales on the flexural parameter α (equation 4.4), with $x_2 = 7\pi\alpha/4$ and $x_1 = 3\pi\alpha/4$. Hence

$$\tau = \frac{x_2 - x_1}{V} = \frac{\pi x}{V} \tag{8.14}$$

where

$$\alpha = \left\{\frac{4D}{\Delta\rho g}\right\}^{1/4}$$

as given by equation (4.3), D is the flexural rigidity and $\Delta\rho$ is the difference in density between the mantle and the material filling the deflection. The model stratigraphic gap should increase from zero at the point of conformity corresponding to the initial position of the first node of the deflection, to a maximum at a distance corresponding to the initial position of the second node of the deflection (Fig. 8.19). In other words, this zone of increasing stratigraphic gap is equivalent to the initial width of the forebulge. In the case of inherited bathymetry from the passive margin stage, the zone of increasing stratigraphic gap is telescoped because the initial uplift of the forebulge takes place below sea level. The model prediction of Crampton and Allen (1995) compares favorably with the observed spatial distribution of stratigraphic gap at the base of the Tertiary foreland basin megasequence in the Alps of Switzerland (Fig 8.20).

In some cases, such as the Devonian (Acadian) peripheral bulge to the Appalachian orogen, the forebulge unconformity system shows an orogenward migration

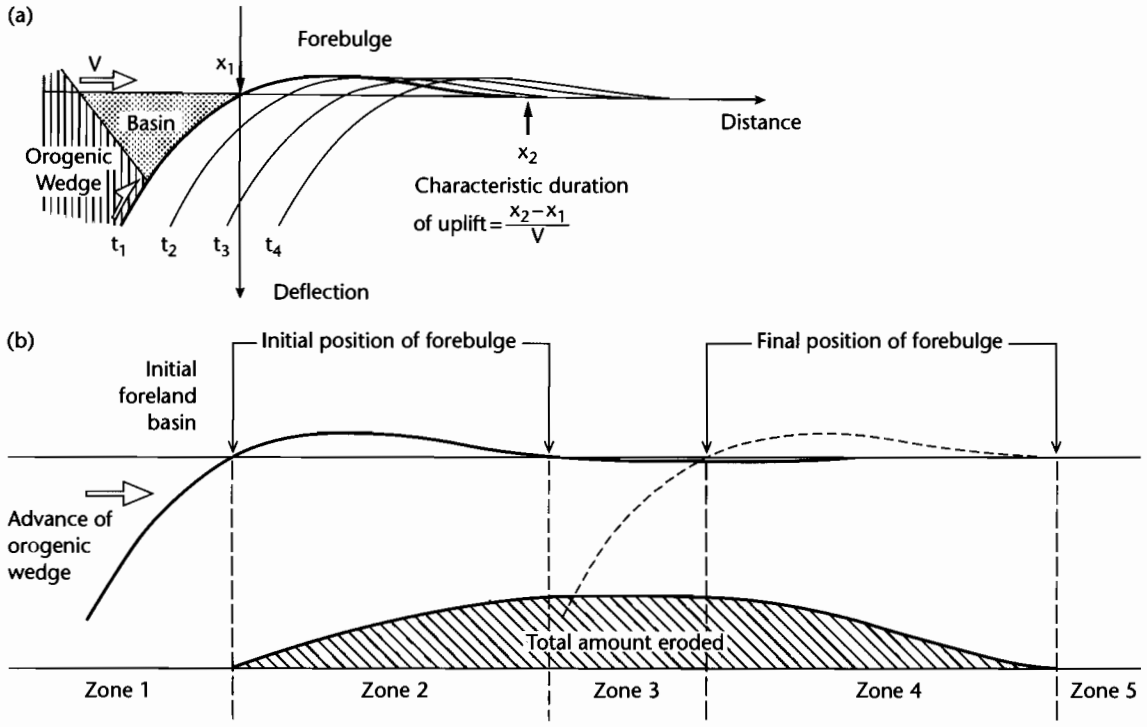

Fig. 8.19 (a) Flexural profiles at times t_1 to t_4, to show the duration of uplift in the flexural forebulge region, using a broken elastic plate; (b) Geometry of the flexural forebulge unconformity. The existence of inherited bathymetry causes zones 1 and 2 to be translated farther onto the foreland plate and zone 2 becomes narrower. After Crampton and Allen (1995). Reproduced courtesy of American Association of Petroleum Geologists.

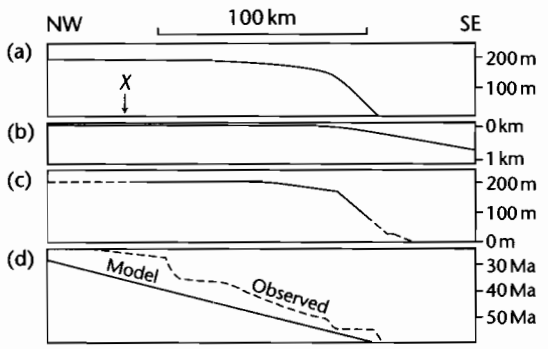

Fig. 8.20 Fit between model predictions for the forebulge unconformity and observations in eastern Switzerland, using the linear elastic model of Crampton and Allen (1995). (a) The modeled total erosion at the forebulge unconformity *versus* distance from the initial position of the orogenic wedge, with $T_e = 10$ km, orogenic advance rate 8 mm yr^{-1} and erosion proportional to elevation with coefficient 0.02. Point X is initially 200 km from the orogenic front. Note the rapid increase in erosional gap from 0 to 200 m across the zone of inherited shelf bathymetry shown in (b); (c) The observed erosion *versus* approximate restored distance from the orogen (based on Herb 1988), showing close similarity to the modeled erosion; (d) As a test, the modeled onlap of sedimentary rocks overlying the unconformity are compared with the observed onlap along a restored section (based on Herb 1988; Sinclair et al. 1991). Reproduced courtesy of American Association of Petroleum Geologists.

that has been attributed to viscoelastic relaxation of the lithosphere (Tankard 1986). A series of splaying unconformities that overstep systematically toward the orogen indicates contemporaneous uplift and orogenward movement of the forebulge at this time.

The location and geometry of a flexural forebulge may also be strongly influenced by pre-existing lithospheric heterogeneities (Waschbusch and Royden 1992). The flexural forebulge may position itself over weak zones in the lithosphere, and then episodically migrate to another weak zone, instead of migrating steadily. Reactivation of old faults may also strongly disrupt the uplift, subsidence and migration history of the forebulge region. Extensional reactivation of normal basement faults by outer arc bending stresses (Bradley and Kidd 1991) or inversion of normal basement faults by the compressional stresses generated during orogeny (Meyers et al. 1992; Ussami et al. 1999; Gupta and Allen 2000) have both been described.

8.3.1.4 Foreland basin isopachs and pinch-outs

The migration of depocenters and of feather-edge pinch-outs of stratigraphy gives an impression of the mobility of the distributed loads and/or variations in the lithospheric response. An early modeling exercise was carried out on the Cretaceous retro-foreland basin in the western United States (Jordan 1981). The progressive eastward shift of depocenters through time in the Idaho–Wyoming region (Fig. 8.21) was predicted using the palinspastically restored thrust load configuration during the Sevier orogeny. Careful matching of predicted with observed stratigraphy allowed a flexural rigidity of about 10^{23} Nm to be estimated for the Cretaceous lithosphere. There was no necessity to invoke a changing flexural rigidity with time, suggesting that the lithosphere behaved elastically over the modeled 70 Myr time span and that lateral variations in rigidity were also insignificant. Similar modeling exercises have been carried out in the Neogene Argentinian foreland of South America (Cardozo and Jordan 2001) and in the Triassic Longmen Shan foreland basin of Sichuan, China (Yong et al. 2003).

Some of the Alpine foreland basins of Europe also show a clear relationship between load mobility and depocenter migration. In the North Alpine foreland basin of western Switzerland, a classical peripheral foreland basin, pinch-outs and depocenters of stratigraphic units migrated onto the European craton during the Oligo–Miocene, corresponding to the main collisional phase of Alpine orogenesis. A palinspastic restoration of thrust units over the same time period coupled with a time-bracketing technique for dating thrust movements allowed fault tip propagation and shortening rates to be estimated (Homewood et al. 1986; Sinclair and Allen 1992). There was a close correspondence between the rates of depocenter and pinch-out migration and of thrust-related shortening in western Switzerland. This feature initially suggests, as in the Cretaceous Sevier belt, that the lithospheric response is constant through time.

If the pinch-out migration rate far exceeds the rate at which the mountain belt advances, the foreland basin should progressively widen with time (Fig. 8.22). This might result from a number of processes. For example, it would be expected if the mountain belt loaded a progressively stronger elastic lithosphere as it overrode first the passive margin, then the unstretched craton. It might also result from the forelandward shift of the center of gravity of the load by erosion and deposition of sediment

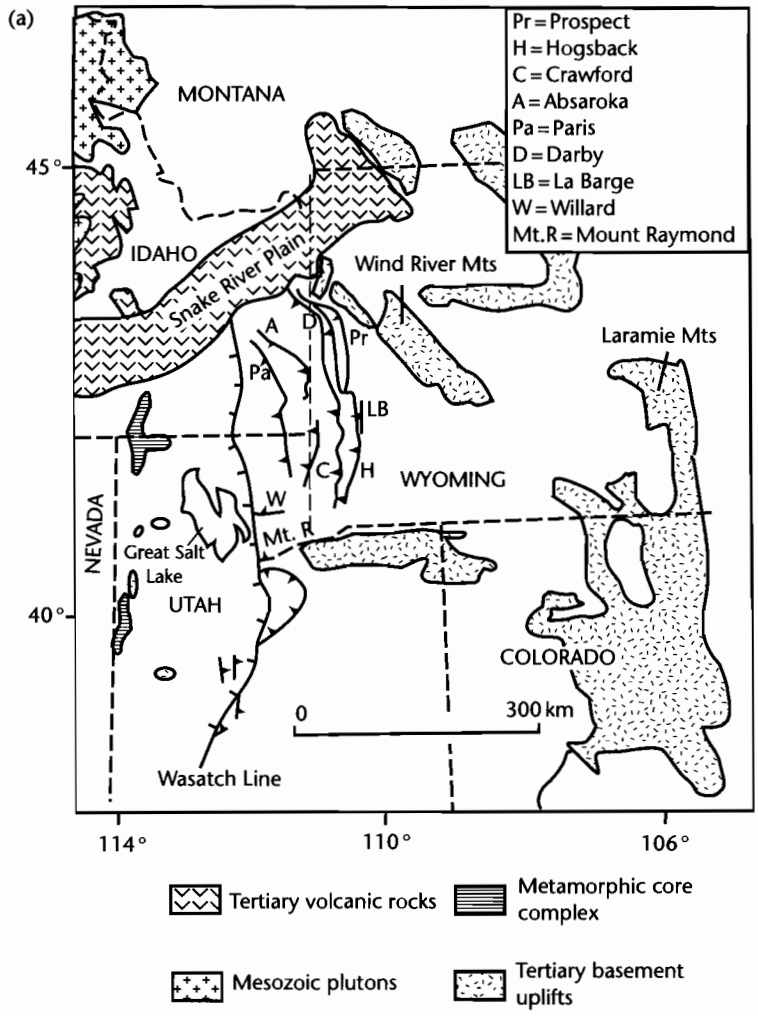

Fig. 8.21 (a) Location of Jurassic–Tertiary Sevier thrust belt in western USA. Volcanic rocks, basement uplifts, and the extensional Wasatch Line are all younger than the thrusting; (b) Plot of age versus distance (relative to the present day trace of the easternmost major thrust) showing the eastward displacement of basin depocenters through time, which is mirrored by an eastward migration of active thrusting. After Jordan (1981). Reproduced courtesy of American Association of Petroleum Geologists.

in the basin (see below). On the other hand, if the pinch-out migration rate slows relative to the rate of advance of the mountain belt or if the forebulge is dragged inwards toward a stationary mountain front, the foreland basin should narrow (Fig. 8.22). Although this kind of offlapping relationship has been interpreted to result from stress relaxation in a viscoelastic lithosphere (Quinlan and Beaumont 1984; Tankard 1986), a similar effect can be produced by thickening of the adjacent orogenic wedge loading an elastic plate (Flemings and Jordan 1989; Sinclair et al. 1991).

8.3.1.5 Underfilling and overfilling

The topography caused by thrusting in mountain belts is eroded to provide detritus to fill the foreland basin.

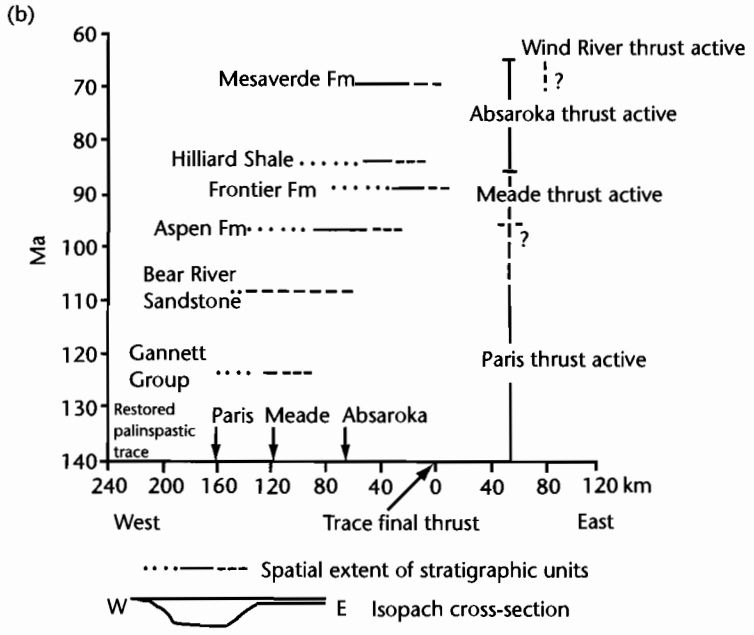

Fig. 8.21 *Continued*

Moretti and Turcotte (1985) first applied a diffusion equation to this process and Flemings and Jordan (1989) and Sinclair et al. (1991) have specifically applied 2-D diffusion modeling to the stratigraphy of foreland basins. The coupling between orogenic wedge development and basin filling has been extended to 3-D by Johnson and Beaumont (1995) and the doctoral theses of Peper (1993) and Clevis (2003) provide further valuable details.

The 2-D diffusion model provides a starting point for considering the controls on foreland basin stratigraphy. Sinclair et al. (1990) modeled the stratigraphy of the North Alpine Foreland Basin in the central Alps using a diffusion model for erosion, a thrust-wedge model based on the concept of a critical taper (§4.5 for details), and a rheology of a linear elastic plate for the flexed European lithosphere. The amount of sediment transported to the foreland basin is proportional to the slope, the transport coefficient (K) varying over several orders of magnitude according to climatic and hydrologic setting (§7.5 for details). Flemings and Jordan (1989), for example, suggest that K for fluvial transport is *c.* $10^4 m^2 yr^{-1}$ whereas it is only $10^{-2} m^2 yr^{-1}$ for the decay of isolated hillslopes. The values obtained from a study of the modern sub-Andean foreland were of the order $10^4 m^2 yr^{-1}$ (Flemings and Jordan 1989). Marr et al. (2000) estimated the transport coefficient to be $10^4 m^2 yr^{-1}$ and $10^5 m^2 yr^{-1}$ for gravel and sand respectively (§7.5.3). The magnitude of the rate of transport of sediment into the basin clearly determines whether, for a given flexural response, it is *underfilled* or *overfilled* (Covey 1986).

Sinclair et al. (1991) simulated movement of the forebulge, both vertically and horizontally, and the attendant unconformities produced in the basin-filling stratigraphy purely by varying the rate of thrust belt propagation and wedge thickening coupled with diffusive erosion (Fig. 4.34). It was not necessary to vary the flexural rigidity of the European plate through time, nor to invoke a nonelastic rheology for the flexed plate. Subtle unconformities ('sequence boundaries") associated with abrupt basinward shifts or progressive offlap could be produced by thickening the load and slowing its propagation rate. Erosion of the load then caused onlap as the center of gravity of the load migrated forelandwards through redistribution of sediment from wedge to basin. Rapid advance of the thrust tip encouraged underfilling of the basin, whereas lower values of thrust belt migration rate promoted overfilling, the sedimentation keeping pace with the creation of new space in the basin.

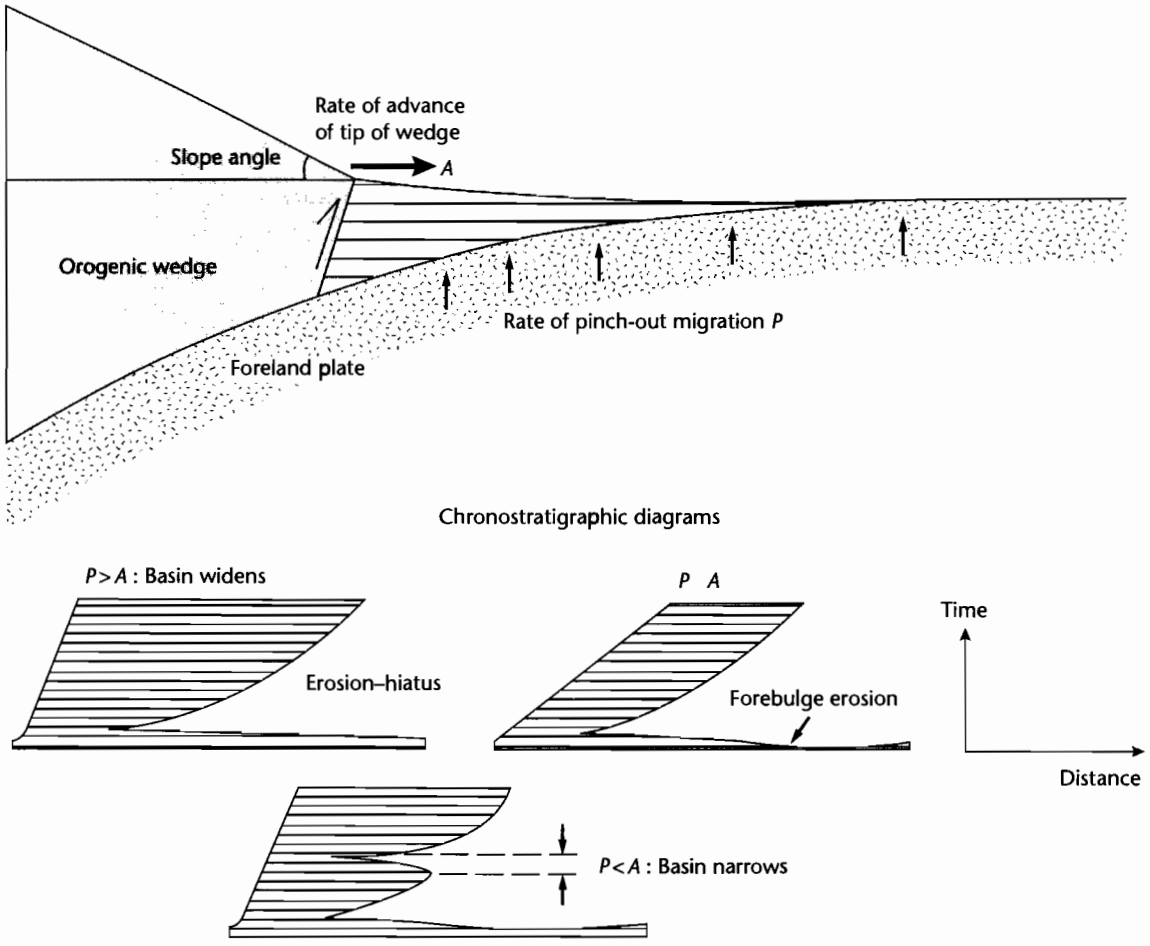

Fig. 8.22 Influence of the rates of advance of the tip of the orogenic wedge and of pinch-out migration on the foreland basin width. Note that onlap onto the foreland plate takes place even in the case of a time-constant basin width. A narrowing of the basin has been interpreted as due to viscoelastic relaxation, but can also result from reorganization of the orogenic load on an elastic plate.

8.3.2 Tectonic mechanisms: fault array evolution

Sediment deposited in rift basins does not simply fill a passive receptacle. The extending crust has an important impact on sedimentary thicknesses, stratigraphic packaging and gross depositional environments in the synrift phase of extensional basins (summarized in Gawthorpe and Leeder 2000). The extension of the crust produces an array of predominantly normal, dip–slip faults. On each fault, a slip event generates hangingwall subsidence and footwall uplift. Accommodation is therefore generated in the hangingwall, while a source of sediment is provided in the footwall. The time–space characteristics of accommodation generation are therefore closely linked to the evolution of normal fault arrays.

Crustal scale normal faults are not simple planar structures with uniform displacements along their length. Instead, they form parts of complex arrays of fault segments with cumulative displacements that vary systematically along the length of the fault segment, and which mutually interfere (Cowie et al. 2000). A single fault segment, whose length is commonly between 10 and

100 km, has a maximum cumulative displacement *d*-length *L* relationship (Schlische 1991; Dawers and Anders 1995).

$$d \approx kL \tag{8.15}$$

where k is a constant of proportionality that varies between 0.01 and 0.05 for many fault systems (Fig. 8.23). The cumulative displacement and the displacement rate are highest near the center of the fault segment, and decrease to zero at the tip. However, fault segments form part of an interacting array, so that some fault segments "grow" at the expense of other fault segments (Fig. 8.24). Faults that are able to link at an early stage with a neighboring fault may therefore continue to grow into major crustal features with large displacement, whereas other faults may quickly become dormant. Large depocenters develop adjacent to major rift faults. Eventually, the full array may become linked, with basin subsidence taking place almost exclusively along a long, linked border fault. Studies of such evolving fault arrays during the Jurassic synrift phase of the North Sea Basin suggest that linkage takes place rapidly, perhaps over 3–4 Myr (McLeod et al. 2000).

The stratigraphic patterns of rift basins reflect this underlying pattern of fault array evolution. Scenarios for fault array evolution in continental and coastal/marine settings are given in Gawthorpe and Leeder (2000) and summarized in Figure 8.25. The common evolution from small, disconnected faults to full linkage produces a stratigraphic theme of isolated continental, hydrologically closed basins with lakes evolving into open rifts connected to the ocean containing shallow marine or deep marine sediments fringed by fan-deltas. The Miocene evolution of the Gulf of Suez is a classically documented example of such a rift evolution (Garfunkel and Bartov 1977; Evans 1988; Sharp et al. 2000). It is impossible to ignore the profound effects of tectonic uplift and

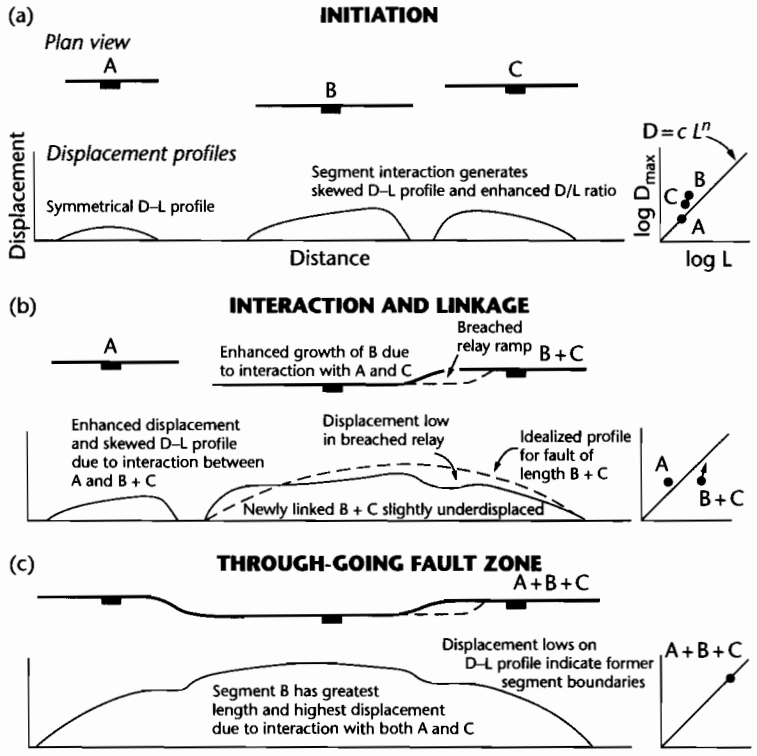

Fig. 8.23 Displacement–length relationship of normal faults. Fault segments grow from an initiation stage (a) with individualized displacement–length relationships, to interaction and linkage (b), and then to a through-going fault zone (c), where there is one displacement–length profile that may contain remnant information of the original fault segments. From Gawthorpe and Leeder (2000). Reproduced courtesy of Blackwell Publishing Ltd.

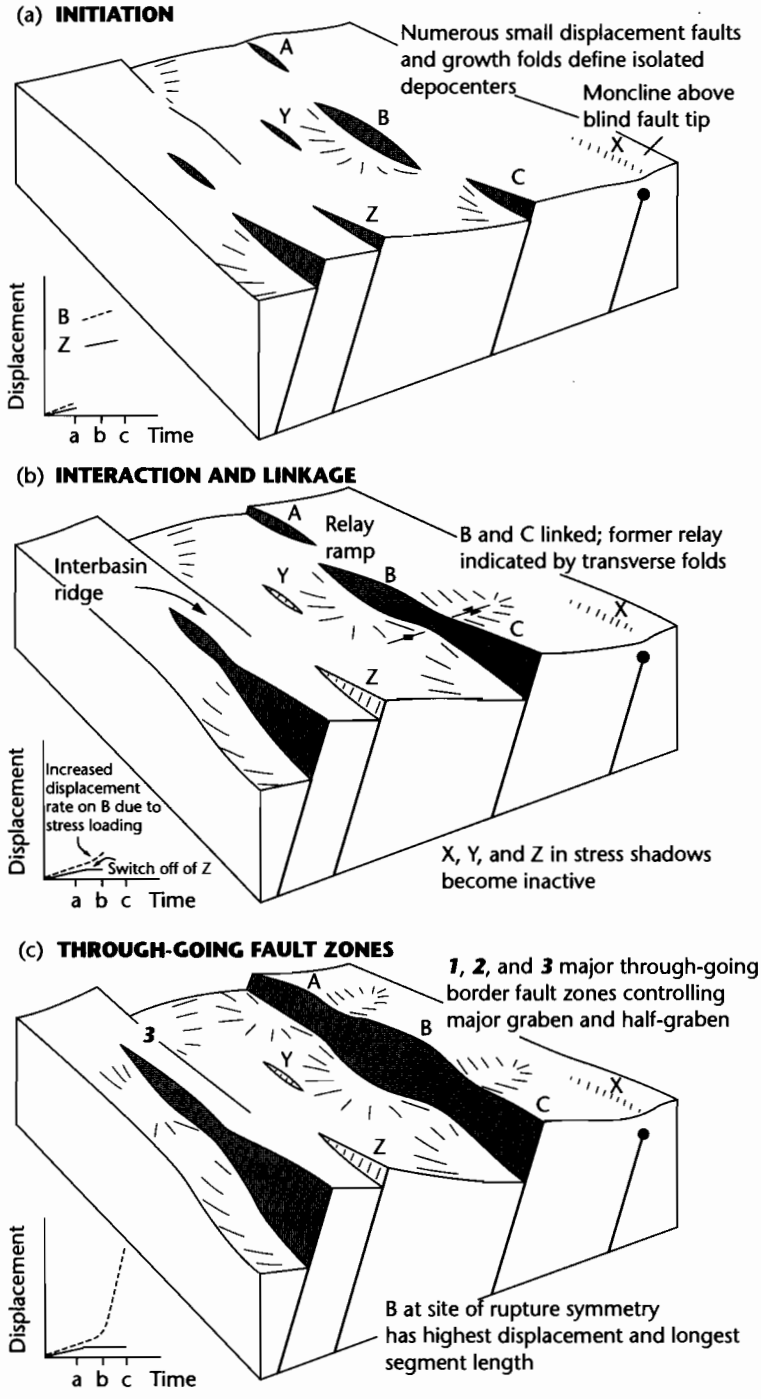

Fig. 8.24 Model of fault interaction and growth from initiation (a), interaction and linkage (b), to a through-going fault zone (c). From Gawthorpe and Leeder (2000). Reproduced courtesy of Blackwell Publishing Ltd.

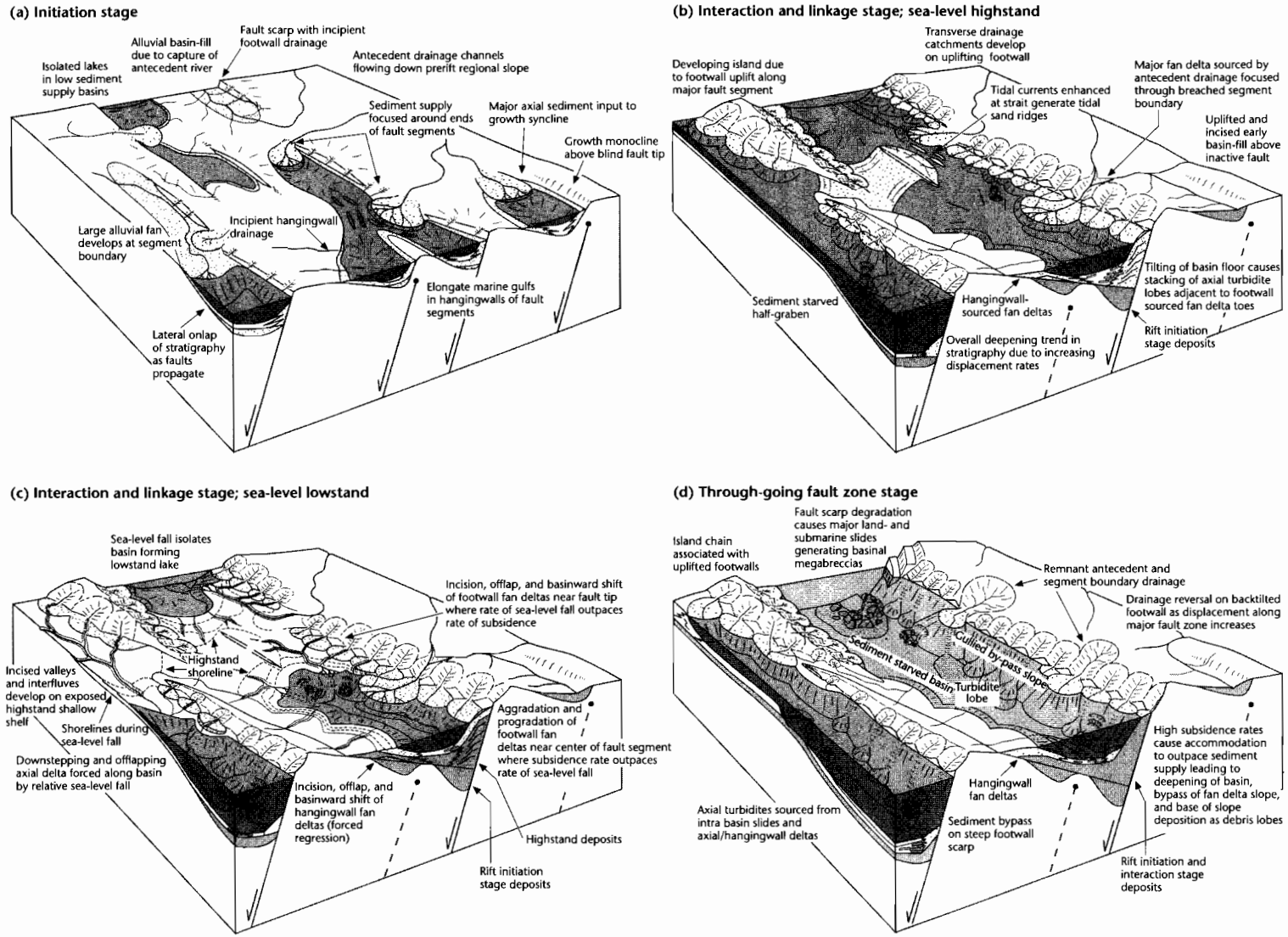

Fig. 8.25 Schematic diagrams of depositional systems related to fault growth and linkage for coastal/marine environments, after Gawthorpe and Leeder (2000). Reproduced courtesy of Blackwell Publishing Ltd.

subsidence in generating sequence boundaries and systems tracts in active rifts. For example, Underhill (1991) found from subsurface data in the Inner Moray Firth Basin, UK, that the main sequence boundaries were produced by fault activity during the synrift phase of the North Sea Basin.

Similar concepts of fault array evolution and associated folding can be applied to contractional terrains such as fold–thrust belts (Tucker and Slingerland 1996) (§7.5.4).

8.3.3 Changes of in-plane stress

Variations in regional stress fields acting within inhomogeneous lithospheric plates may cause vertical movements large enough to have a major impact on stratigraphy. The horizontal in-plane forces that might be responsible for these vertical movements include ridge push forces from spreading centers and deviatoric compression originating from sites of continental collision. Although the horizontal (in-plane) stress required to buckle an undeformed elastic plate is enormous (§4.4), in-plane stresses acting on a deflected plate may enhance or reduce the curvature of the deflection. In-plane forces may also produce long wavelength lithospheric buckles where the plate is rheologically layered, with a weak lower crust.

An early examination of the possible effects of changing horizontal stresses on a passive continental margin with an overlying sedimentary load and an age-dependent elastic thickness (Cloetingh et al. 1985) showed that the application of an in-plane force causes a modification of the deflection of the continental lithosphere. For example, changing from an in-plane tensional stress of $5 \times 10^{12}\,\mathrm{Nm}^{-1}$ (2.3 Kbar) to a compressional stress of the same magnitude on a lithosphere with an equivalent elastic thickness appropriate for an age of 30 Myr, produces a net uplift on the edge of the basin of about 100 m. The effectiveness of the in-plane force in producing large changes in the deflection increases with increasing thickness of sediment load, but decreases with the increasing age of the lithosphere. As a consequence, it was suggested that in-plane forces are particularly important on young, rapidly loaded margins. Changes in horizontal stresses also have effects towards the basin center, but because the total subsidence is large in these areas, the contribution of in-plane stresses to the deflection is masked.

Karner (1986) applied the concept of in-plane stresses to a lithospheric structure where the flexural rigidity varied not only in time (cooling effect) but also in space as a result of basin formation. He showed that the effect of a tensile in-plane stress was to reduce the curvature of the plate, and that of a compressive in-plane stress to increase the curvature. The impact of an in-plane stress change is affected by the geometry of inhomogeneities in the lithosphere, such as the basement–sedimentary basin interface and the Moho. Their effects are likely to be amplified in foreland basins; in-plane compression generates additional basinal subsidence and marginal uplift, whereas in-plane tension generates basin uplift and marginal subsidence.

According to Karner (1986) the application of a compressive ($12.5 \times 10^{12}\,\mathrm{Nm}^{-1}$ or 4 Kbar) stress on a typical extensional basin margin would cause the basin margin to uplift, producing an unconformity recognized by a sharp drop in the amount of stratigraphic onlap. In contrast, an identical tensile in-plane stress would cause a major transgression as the basin margin is depressed (Fig. 8.26). The resulting patterns of stratigraphic offlap and onlap might erroneously be attributed to eustatic sea-level change.

Later investigations of the importance of in-plane stresses have focused on the possibility of the buckling of a layered lithosphere (§4.4). Large-scale lithospheric folding is found, for example, in the oceanic lithosphere of the Indian Ocean (Stein et al. 1989) and in the continental lithosphere of central Australia (Lambeck 1983). Lithospheric buckles have been interpreted in compressional regimes such as the Himalayan syntaxes (Burg and Podladchikov 2000) and the Alpine foreland of Europe (Ziegler et al. 1995). Buckling has been interpreted as a component in the deformation of some of the major extensional basins of Europe such as the North Sea, Pannonian Basin, the south Adriatic, and the Paris Basin (Horvath and Cloetingh 1996; Lefort and Agarwal 1996; van Balen et al. 1998; Bertotti et al. 2001).

Accepting that large-wavelength lithospheric folds exist, the critical question is therefore whether in-plane stresses of significant magnitude change in sign over a sufficiently short time period to significantly influence stratigraphic packaging, and whether any such changes can be recognized in the sedimentary record of basins. Vertical motions due to changes of in-plane stress combined with the effects of dynamic topography may be highly influential in controlling the stratigraphic packaging of many of the world's cratons.

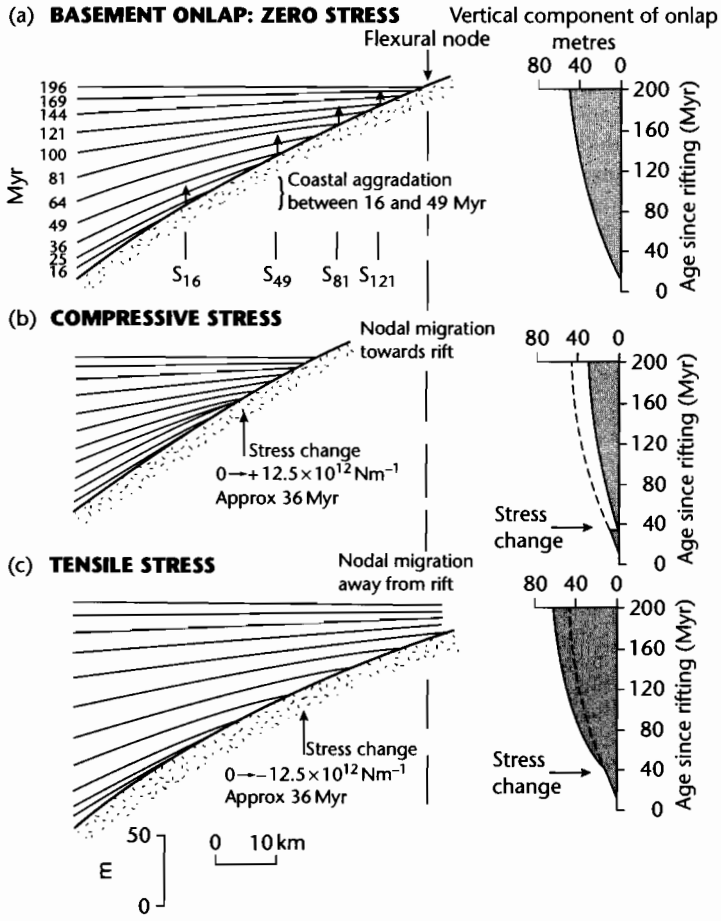

Fig. 8.26 Stratigraphic patterns in a stretched basin based on the numerical experiments of Karner (1986). Diagrams at right show the amount of coastal aggradation as a function of time, which serves as a proxy for apparent relative sea-level change. (a) Stratigraphic onlap caused by the cooling of the lithosphere following rifting; (b) Effects of applying a *compressive* in-plane force of $12.5 \times 10^{12}\,\mathrm{Nm^{-1}}$ at 36 Myr after the end of rifting, at which point the equivalent elastic thickness is 32 km. This produces basin margin uplift and a basinward shift in coastal onlap; (c) An increase in the rate of coastal onlap is produced by the application of a *tensile* in-plane force of $12.5 \times 10^{12}\,\mathrm{Nm^{-1}}$ at 36 Myr after rifting.

8.3.4 Eustatic mechanisms

In Chapters 3–5 we considered changes in basement height relative to a datum (sea level or "regional") in terms of large-scale mechanisms such as lithospheric thickness changes, flexure, and mantle dynamics. The elevation changes caused by these tectonic mechanisms may be extremely widespread, being determined by mantle convection processes, flexural response of the lithosphere or plate boundary forces, but they are not global. Global sea-level changes (absolute changes relative to the center of the Earth) result either from changes in the amount of water in the oceans or from changes in the volume of the ocean basins.

In considering absolute sea-level change, it is important to incorporate the effects of isostasy (§2.1.1). An increase in water depth in the ocean basins causes a sub-

sidence of the ocean floor due to the excess weight of the water at the new sea level. A decrease in water depth causes uplift of the ocean floor due to the removal of part of the water column. The displacement of the oceanic basement relative to the center of the Earth by changes in the water load would be found throughout the oceans, although the effect would only be observed at places such as oceanic islands. These regions would experience the same displacement as the oceanic basement, and would therefore act as a "dipstick," indicating the sea-level change.

Consider an ocean basin of depth h_1 which deepens to a depth h_2 (Fig. 8.27). The greater depth of the ocean is made up of two components: the subsidence of the ocean floor S, and the sea level rise Δ_{SL}. If rocks comprising the ocean crust have a density (ρ_m) of 3300 kg m^{-3} and the water a density (ρ_w) of 1000 kg m^{-3}, the isostatic subsidence of the ocean floor is approximately 0.4 of the sea-level change. Expressed slightly differently, the sea-level change is 0.7 of the increase in the water depth of the ocean ($h_2 - h_1$) (see also §9.3.2). These figures represent approximate upper bounds on the water loading of the oceanic lithosphere since they result from a purely local (vertical) isostasy. A flexural response of the lithosphere (§2.3.3) would reduce the water-loaded subsidence. However, the approximation is reasonable, since the wavelength of the water load (the ocean) is very large compared to lithospheric thickness.

We can examine global sea-level change in terms of five possible causes:

1 *Continuing differentiation of lithospheric material as a result of plate tectonic processes*: The volume of water in the oceans may be added to by contributions from mid-ocean ridge and island arc volcanism. Counteracting this, water may be removed by hydrothermal alteration of new crust and at subduction zones. These processes are probably roughly balanced. There is no evidence for appreciable, long-term changes in the chemical composition of the oceans during the past 1500 Myr, suggesting that the volume of sea water has not greatly increased as a result of Phanerozoic volcanism.

2 *Changes in the volumetric capacity of the ocean basins caused by sediment influx or removal*: The total sediment discharged to the oceans is *c.* 20×10^9 tons yr^{-1} (Milliman and Syvitski 1992; Walling and Webb 1996). If we ignore the volume of sediment produced autochthonously in the oceans, and the oceans have an area of 3.2×10^8 km^2, the average accumulation rate of terrestrially derived sediment is 25 mm per 1000 yr (assuming a sediment density of 2500 kg m^{-3}). This would cause a sea-level rise of 6 mm per 1000 yr (derivation in Figure 8.28). However, sediment in the ocean is removed by tectonic accretion and subduction at active margins and continued spreading creates new ocean floor. It is uncertain how much sediment is removed at subduction zones and eventually melted to contribute to arc volcanism, and how much is tectonically accreted to the edge of the overriding plate. It is likely that the balance between influx and removal of sediment, when averaged over long

$$\rho_w h_1 + \rho_m C_1 = h_2 \rho_w + \rho_m (C_1 - S)$$
$$\rho_m S = \rho_w (h_2 - h_1)$$
$$\rho_m S = \rho_w (S + \Delta_{SL})$$
$$S \left(\frac{\rho_m - \rho_w}{\rho_w}\right) = \Delta_{SL}$$

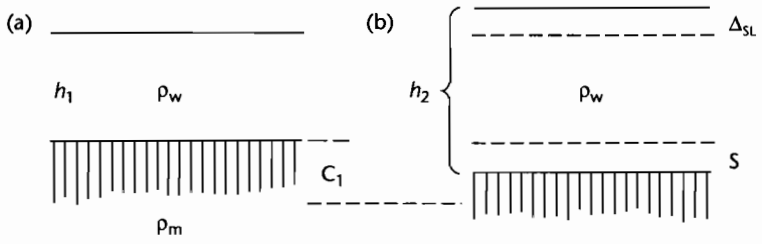

Fig. 8.27 Isostatic effect of a change in water depth in the ocean. Since the wavelength of the water load is very large, the compensation can be regarded as local (Airy). (a) Initial ocean of depth h_1; (b) An increase in water depth h_2 results in an increase in sea level of Δ_{SL}.

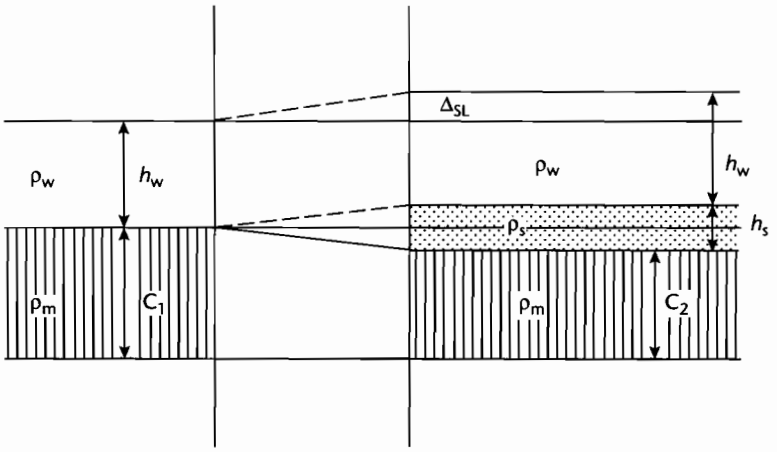

$$\rho_m C_1 + h_w \rho_w = \rho_m C_2 + \rho_s h_s + h_w \rho_w$$
$$\rho_m(C_1 - C_2) = \rho_s h_s$$
Since $C_1 - C_2 = h_s - \Delta_{SL}$,
$$\rho_m(h_s - \Delta_{SL}) = \rho_s h_s$$
$$\therefore \Delta_{SL} = h_s(1 - \rho_s/\rho_m)$$

Fig. 8.28 Derivation of the sea-level change resulting from the deposition of sediment in the ocean. If the density of mantle is 3300 kg m^{-3} and the density of ocean sediment is 2500 kg m^{-3}, the sea-level change is 0.24 of the sediment thickness h_s. Consequently, if 25 mm of sediment is deposited every 1000 yr, the sea-level change is 6 mm per 1000 yr.

periods of time, is insufficient to cause rates of sea-level change of more than *c.* 1 mm per 1000 yr (Pitman 1979).

3 *Changes in the volumetric capacity of the ocean basins caused by volume changes in the mid-ocean ridge system*: That changes in the volume of the mid-ocean ridge systems could be responsible for major sea-level changes has been argued for some time (Hallam 1963; Menard 1964; Russell 1968; Valentine and Moores 1970; Hays and Pitman 1973). This is based on the observation that the volume of the present world ridge system (*c.* 1.6×10^8 km^3) is a significant proportion, over 10%, of the volume of ocean water (*c.* 1.35×10^9 km^3). Because the bathymetry of the ocean is dependent on age, variations in spreading rates cause major changes in ridge volumes, the faster spreading ridges being hotter and therefore more voluminous. A second way of modifying the world ridge volume is through changes in the total length of spreading axes. Hallam (1977) believed that at certain geological times, the latter mechanism was the more important of the two. Bearing in mind that a change in ocean depth of magnitude Δh produces a change in sea level relative to the center of the Earth of magnitude $\Delta_{SL} = 0.7\Delta h$, the sea-level fluctuations resulting from mid-ocean ridge volume changes can be estimated if the shape of the ocean basins is known (Pitman 1979). The latter can be gauged from the *hypsometric curve*. Sea-level changes track changes in mid-ocean ridge volumes, with maximum rates of change of 4 mm per 1000 yr for the spreading history illustrated in Figure 8.29. The "first-order" or "long term" (225–300 Myr) eustatic curves of Vail et al. (1977a) and Haq et al. (1987) may be driven by variations in mid-ocean ridge volumes (Larson and Pitman 1972). The postulated sea-level changes as a result of ocean ridge volume fluctuations (Fig. 8.30) show a maximum sea level in the latest Cretaceous (Maastrichtian) when it was elevated some 350 m above present, and a fall of varying severity through the Cenozoic to the present. The Late Cretaceous maximum of 350 m above present sea level is, however, in disagreement with estimates from continental margin stratigraphy (Watts and Steckler 1979), from estimates of the flooding of continents using individual hypsometric curves (Bond 1978) and from estimates of the amount of crustal generation through time

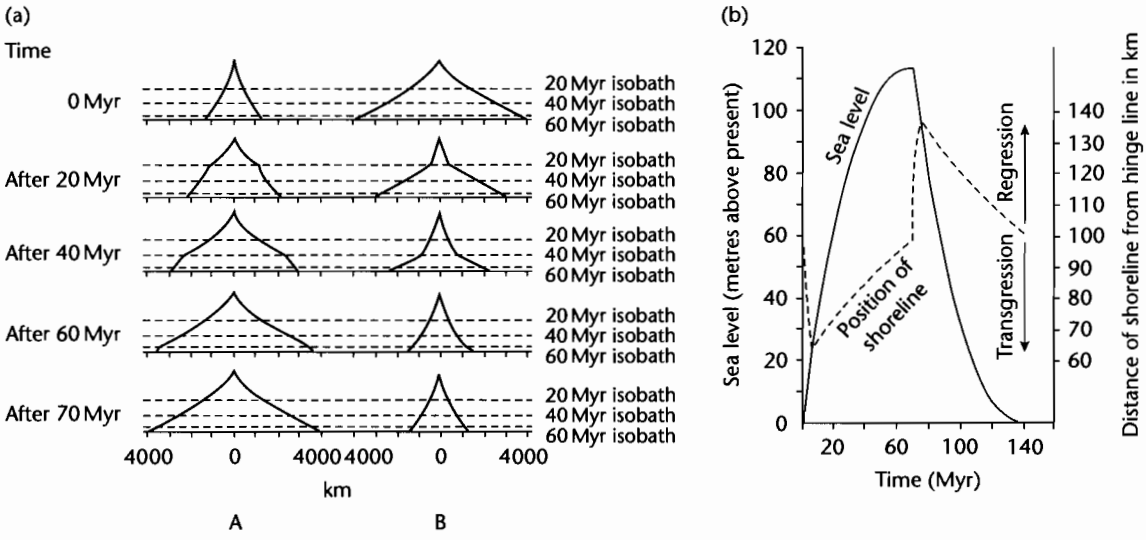

Fig. 8.29 Volume changes of spreading ridges as a function of the spreading rate (after Pitman 1979). (a) Sequence A shows a ridge that has been spreading at 20 mm yr^{-1} for 70 Myr. At 0 Myr the spreading rate changes to 60 mm yr^{-1}. Subsequent diagrams show the sequential changes in the ridge cross-section. Sequence B shows the reverse evolution: a ridge that has been spreading at 60 mm yr^{-1} for 70 Myr slows at 0 Myr to 20 mm yr^{-1}. The cross-sectional areas of equilibrium ridge profiles (after 70 Myr of spreading at the new rate) change by a factor of 3 in both cases; (b) Change in sea level resulting from the changes in spreading rates shown in sequence A of (a). The maximum rate of sea-level change occurs immediately after the change in the spreading rate.

(Parsons 1982), which all suggest a Late Cretaceous maximum of smaller magnitude (<100 to 150 m above present) (Fig. 8.30).

4 *Thermal expansion and contraction of the oceanic water reservoir*: Changes in the average temperature of the oceanic reservoir, caused by climate change, should cause changes in its volume by thermal expansion and contraction. The importance of this effect can be easily estimated by considering the volumetric coefficient of thermal expansion of water (α_v), which varies between $7.81 \times 10^{-5} K^{-1}$ at 2.5 °C and $34.13 \times 10^{-5} K^{-1}$ at 30 °C. The oceanic water reservoir is $1{,}400{,}000 \times 10^{15}$ kg, or $1{,}400{,}000 \times 10^{12} m^3$, its average depth is 3794 m and the area of the oceans excluding the continental shelves is $3.1 \times 10^{14} m^2$. The mean temperature of the ocean reservoir at the present day is about 4 °C. Taking $\alpha_v = 10 \times 10^{-5} K^{-1}$, a 1 K increase in temperature of the present-day oceanic reservoir therefore causes an increase in volume of water of $14 \times 10^{13} m^3$, which causes an increase in depth of 0.45 m. Climate change of course does not cause a uniform change in temperature of the oceanic reservoir because of the intricasies of the operation of the thermohaline system. However, the calculation above shows that the effects of thermal expansion and contraction during a climatic cycle while significant, are relatively small compared to the water depth changes caused by growth and melting of ice caps (see below).

5 *Changes of available water by abstraction in and melting of polar ice caps and glaciers*: Large sea-level changes can be caused by abstraction of water from the oceans into land-based ice-sheets, and of course, the subsequent release on melting. Ice shelves are unimportant since the floating ice displaces its own mass of water. These changes can be called *glacio-eustatic* (Fairbridge 1961; Donovan and Jones 1979). Total melting of the Antarctic land ice, some 2 to $3 \times 10^7 km^3$, would result in an increase in water depth of between 60 and 75 m. Melting of the much smaller Greenland ice cap would probably cause an additional 5 m increase in water depth. Allowing for the water-loaded depression of the ocean floor discussed above (Fig. 8.27), the actual sea-level rise associated with the complete melting of today's land-based ice sheets is expected to be in the region of 50 m. Calculations of former ice sheet volumes are speculative. Assuming that

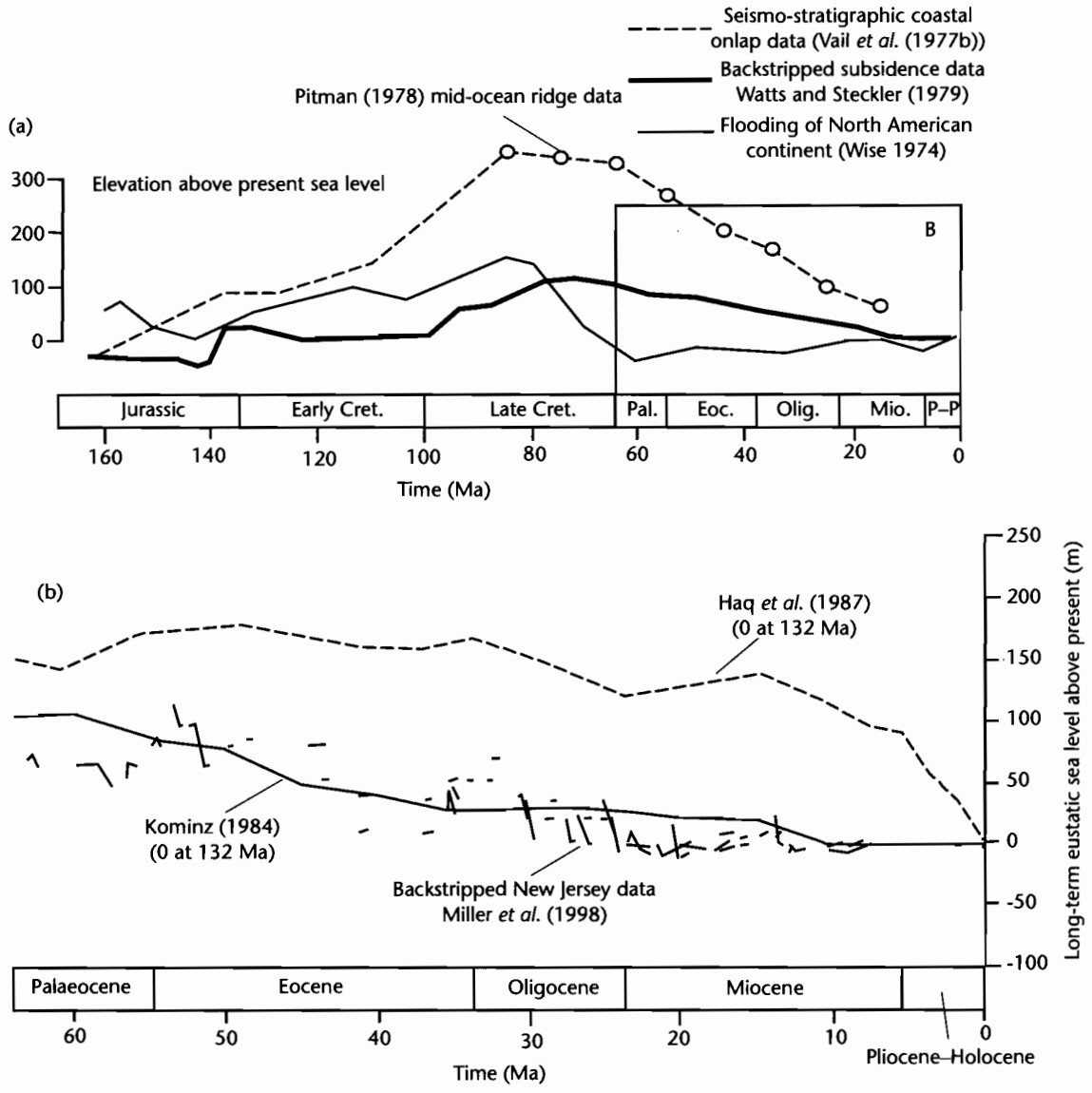

Fig. 8.30 (a) A comparison of estimates of sea-level changes in the last 160 Myr. The heavy solid line is based on the subsidence history of boreholes from the continental margins of eastern North America (Watts and Steckler 1979). The dashed line is the estimate of Vail et al. (1977b) based on patterns of coastal onlap recognized on seismic reflection lines, calibrated by the data of Pitman (1978) (circles) based on changes in the rates of spreading of mid-ocean ridges. The fine solid line is from estimates of the amount of flooding of the continental area of North America (Wise 1974); (b) The Cenozoic section of the sea-level history, showing the data obtained from backstripping of wells drilled in the New Jersey coastal plain (Miller et al. 1998), which are fitted well by the eustatic curve of Kominz (1984). The Haq et al. (1987) curve appears to significantly over-predict long-term eustatic sea level. Both curves are normalized to pass through a eustatic sea level of 0 m at 132 Ma.

former ice sheets reached an equilibrium maximum thickness, and delineating their maximum limits from Quaternary geology, the sea-level fall resulting from locking up of water in Pleistocene ice sheets is thought to have been about 100 m. The total change in sea level corresponding to the removal of Pleistocene-scale ice sheets is therefore about 150 m and liable to have major impacts on basin stratigraphy. In geological terms, the formation and melting of ice caps is a rapid process (*c.* 10 mm yr^{-1}) (Hays et al. 1976; Imbrie 1982) – about three orders of magnitude greater than those expected to result from changes in ocean ridge system volumes.

The lithosphere also responds to changes in water and ice loads; these *glacio-isostatic* adjustments (Clark et al. 1978; Peltier 1980) operate at a rate dependent on mantle viscosity. At any high latitude locality close to the former ice front, there is therefore a competition in the history of deglaciation between isostatic rebound rates and rates of eustatic sea-level rise (Belknap et al. 1987 for an example from the Late Quaternary of Maine).

Late Quaternary and Holocene sea-level fluctuations following the Pleistocene glaciation are relatively well understood compared to more ancient sea-level changes (Fig. 8.31). Sea-level curves derived from oxygen isotopes from benthonic foraminifera recovered in deep sea cores (Shackleton and Opdyke 1973; Shackleton 1977) and tropical coral terraces and related fauna (Fairbanks and Matthews 1978; Aharon 1983) show a high frequency fluctuation, with 8 sea-level maxima (and 8 minima) in the last 120,000 years. These sea-level changes vary from 20 m to 180 m in total height. They have a long primary period of about 10^5 yr, and shorter secondary periods of about 40,000 and 20,000 years.

The Serbian physicist Milankovitch first suggested that periodic variations in solar forcing might be caused primarily by orbital fluctuations of the Earth. For example, changes in the shape of the elliptical path of the Earth's orbit around the Sun (or *eccentricity*) have a periodicity of approximately 100 kyr, and may be responsible for the glacial cycles characteristic of the Pleistocene. The Earth also wobbles in its spin about its axis of rotation (*precession*), with the axis of rotation varying in its inclination with a periodicity of *c.* 21 kyr. The axis of rotation also leans with respect to the plane of the Earth's orbit around the Sun (*obliquity* of the ecliptic), the angle of lean varying on a period of *c.* 41 kyr. These three different frequencies interact to produce a complex signal that may act as a pacemaker for climate change, causing eustatic variations responsible for stratigraphic parasequences. Unfortunately, the precision of dating ancient sequences is generally too poor to allow comparison of parasequence durations with Milankovitch frequencies.

It has been shown that the Mediterranean Basin dried out during the late Miocene (Hsu et al. 1973) as it became isolated from the world's oceans. The Messinian desiccation event appears at first sight to correlate with a sea-level fall at 6.6 Ma on the global cycle chart of Haq et al. (1987). However, detailed work on ODP and DSDP cores and onshore studies in Sicily suggest that the desiccation event postdates the Tortonian–Messinian boundary (now placed at 6.5 Ma) by 0.5 Myr, so that the correlation is inexact. Perhaps more importantly, desiccating the Mediterranean by land-locking is likely to have caused a sea-level *rise* (perhaps 12 m) in the remaining oceans by reducing the volume of the ocean basins. This scale of sea-level change is considerably smaller than the variations caused by glaciations, although the rates of change of sea level would be rapid and similar to those estimated for glaciations (*c.* 10 mm yr^{-1}) (Donovan and Jones 1979).

8.3.5 Other climatic mechanisms for stratigraphic cyclicity

The influence of climate on depositional systems and depositional products is the staple diet of a number of texts in sedimentary geology and will not be repeated here. The influence of climate on weathering and erosion is also a central theme of a number of geomorphology texts (e.g., Summerfield 1991). From the point of view of basin analysis and stratigraphic cyclicity, however, the overriding importance of climate is in its influence on the sediment discharge to sedimentary basins. Climate affects vegetation and soils, precipitation and the distribution of precipitation (storminess, large floods), weathering, hillslope processes and mass wasting, the balance of solute and particulate loads, and the sediment yield from catchments. Because of its pervasive influence on such a wide set of processes, the detailed linkage between climate change, depositional processes, and stratigraphic products is poorly understood.

A very wide range of features are influenced by variations in sediment supply to the sediment routing system. Depositional water depths, cycle development, parasequence stacking patterns, formation of unconformities and ravinement surfaces, position of the maximum flood-

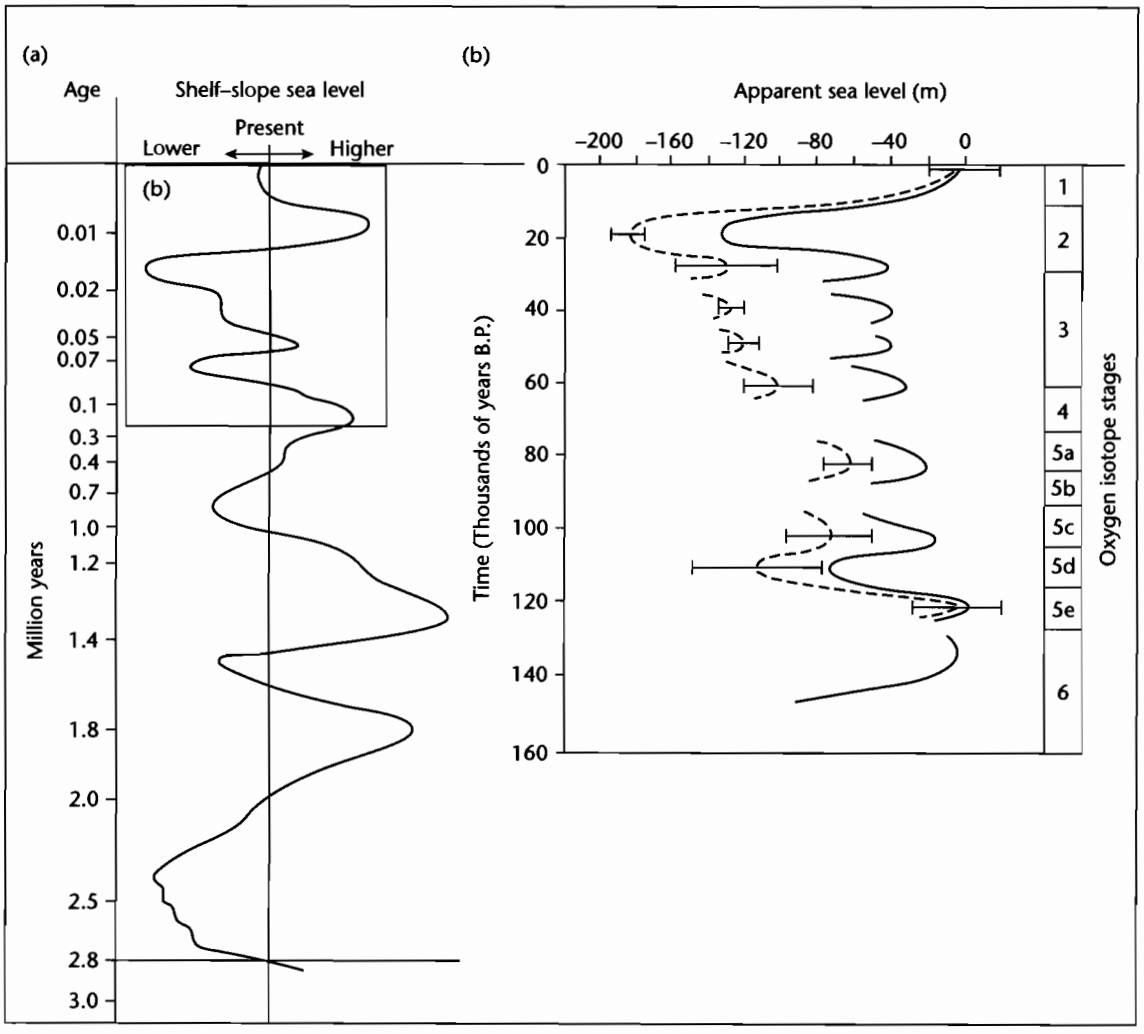

Fig. 8.31 (a) Inferred Pleistocene sea-level fluctuations in the northwestern Gulf of Mexico since 3 Ma (after Morton and Price 1987), derived by Smith (1965) from interpreted water depth and paleotemperatures, and modified by Beard et al. (1982). Note non-linear scale for age; (b) Detailed glacio-eustatic record (dashed line, Moore 1982) and oxygen isotope record based on deep sea benthic foraminifera (solid line, Williams 1984) for the last 130 000 yr (after Suter et al. 1987).

ing surface, are all strongly affected by sediment supply. The reader is referred to §7.3 for information on the effect of climate change on sediment yield, to §7.5.3 for the effects of variations in sediment flux in building stratigraphy in alluvial basins, and to §8.1.3 for a quantitative analysis of the role of sediment supply in stratigraphic packaging.

8.3.6 Unforced cyclicity

A large number of authors favor the formation of parasequences by allocyclic mechanisms such as eustatic sea-level change, commonly assumed to be driven by Milankovitch orbital forcing (e.g., Goldhammer et al.

1990; Osleger 1990). A convincing demonstration of orbital forcing should include a spectral analysis of the cyclicity. However, such statistical analyses sometimes show that apparently ordered patterns of cycles are indistinguishable from patterns produced by random depositional processes (Drummond and Wilkinson 1993; Wilkinson et al. 1996, 1997). It is possible therefore that many high frequency cycles may be produced by an unforced autocyclicity.

An early theory for the generation of shallowing up cycles in peritidal carbonates envisaged a subtidal carbonate factory, with landward transport to produce progradational supratidal and intertidal facies belts (Ginsburg 1971). Progradation was thought to reduce the area of subtidal carbonate production. Continued tectonic subsidence would therefore eventually outpace sediment production, leading to flooding. Two-dimensional (Demicco and Spencer 1989; Hardie et al. 1991; Goldhammer et al. 1993) and 3-D (Burgess et al. 2001) numerical models successfully simulate stacked autocyclic parasequences in peritidal carbonates. The internal dynamics of the numerical model developed by Burgess et al. (2001) involves an advective landward transport of sediment from subtidal areas driven by prevailing winds leading to accretion of carbonate on the seaward flanks of the islands, causing them to prograde (Fig. 8.32). A less important seaward sediment transport takes place by a gradient-dependent diffusive transport. Laterally impersistent, peritidal cycles (<2.5 m thick) are produced by the landward nucleation, detachment, and seaward migration of intertidal–supratidal islands, leaving new subtidal zones in their rear. Such cycles resemble the thin, laterally impersistent, shallowing-up peritidal cycles commonly reported from field studies (Hardie and Shinn 1986; Pratt and James 1986; Shinn 1986; Adams and Grotzinger 1996).

It is likely that external forcing and internal dynamics both take place to varying degree, and that the separation of any external signal from a system with its own internal dynamics may be difficult to achieve.

8.4 NUMERICAL SIMULATION OF STRATIGRAPHY

Numerical approaches to the simulation of stratigraphy blossomed in the last decade of the twentieth century. However, the groundwork for many numerical stratigraphic models was provided by Sloss (1962) who identified the four main variables affecting stratigraphic geometries: the quantity of sediment supply from the basin margins, the rate of subsidence in the basin relative to base level, the dispersal of sediment by various transport processes, and the composition and texture of the sediment. It is regrettable that much early sequence stratigraphic literature ignored this groundwork, and instead focused on eustatic change as the exclusive control on stratigraphic geometries. A number of approaches to quantitative modeling of the basin-fill have simultaneously developed (review in Paola 2000). This section can give a mere snapshot of the wide diversity and complexity of the modeling approaches to stratigraphy. We do so by reviewing some of the fundamental and commonly used principles upon which more sophisticated approaches are based.

8.4.1 Carbonate stratigraphy

The building of carbonate stratigraphy is fundamentally based on a notion of carbonate productivity as a function of water depth. This water-depth dependence is caused by the attenuation of light with depth, but the effects of turbidity and temperature may also be important (Lerche et al. 1987). Pomar (2001) suggested that the depth–productivity curve is also strongly affected by the type of biota. Euphotic biota produce a strong depth-dependence, with a maximum productivity in very shallow waters; oligotrophic biota produce a mid-water depth maximum, and photo-independent biota produce a weak depth-dependence (Fig. 8.33). Armed with a carbonate productivity–depth curve (e.g., Bice 1991; Bosscher and Schlager 1992; Demicco 1998), the modeler can readily simulate carbonate sedimentation in 1-D. Two-dimensional models must account for physical transport of carbonate sediment. A strong depth dependence of carbonate productivity should produce steep-edged carbonate platforms, whereas a less strong dependence on depth, or vigorous offshore transport, should flatten the carbonate platform slope into that of a ramp (Fig. 8.34). Euphotic organisms such as corals and green algae should produce steep-edged platforms, whereas oligophotic organisms such as the larger foraminifera and red algae should produce ramps. Carbonate depositional systems commonly possess clinoforms whose shape depends on the effects of lateral sediment transport, carbonate productivity, eustatic variation and accommodation generation by tectonic subsidence (Lawrence et al. 1990). Continued subsidence of clinoform geometries produced by a strongly depth-

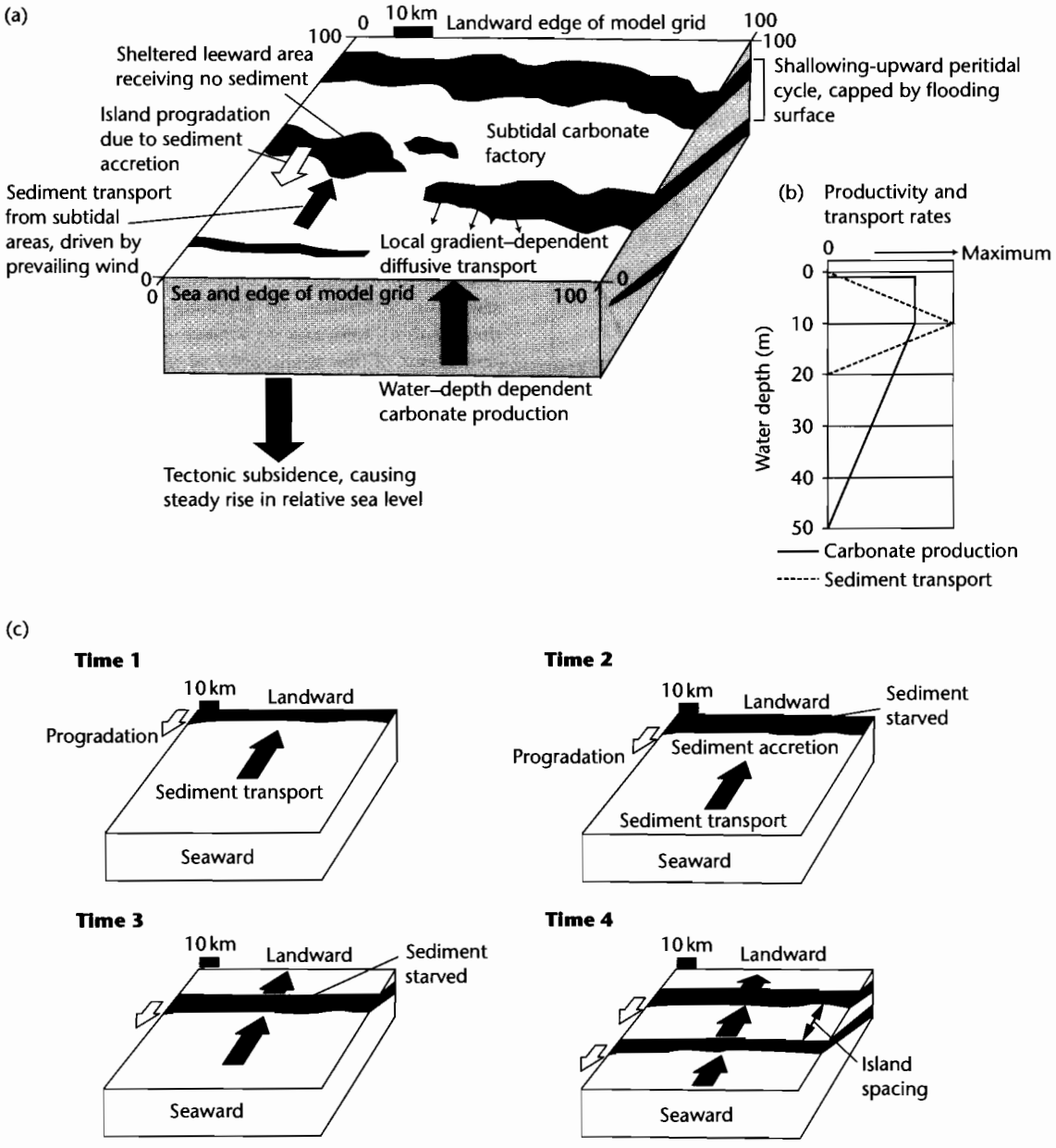

Fig. 8.32 Model for the generation of unforced high resolution cyclicity in peritidal carbonates, after Burgess et al. (2001). (a) Illustration of different processes involved in generating prograding inter- and supratidal islands and autocyclic shallowing-upward cycles; (b) Depth-dependent carbonate productivity relationship and sediment transport rate; (c) Different stages in the evolution of prograding islands. Time 1: landward transport of sediment causes accretion of inter- and supratidal flat. Time 2: Continued accretion drives inter- and supratidal flat progradation, which causes a sediment starved leeward side to develop. Time 3: Sediment starved lee subsides and prograding island forms, allowing a new subtidal carbonate factory to develop. Time 4: A second island system develops as the entire process is repeated. Reproduced courtesy of Blackwell Publishing Ltd.

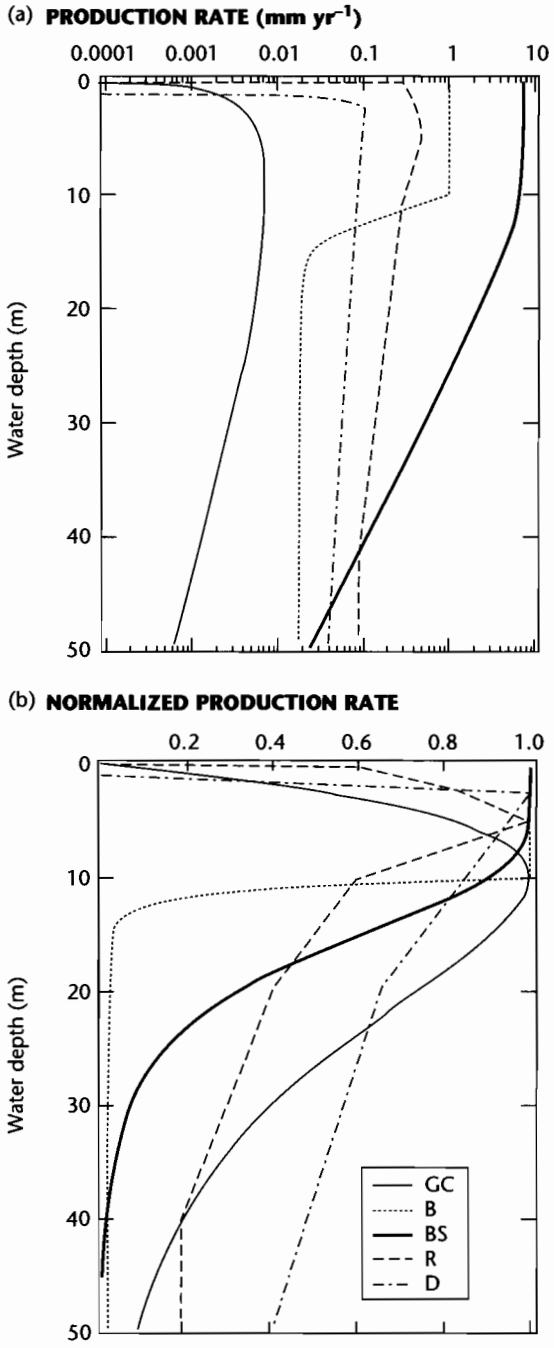

Fig. 8.33 Carbonate productivity versus depth from various authors (a), normalized by the maximum production rate in (b), after Paola (2000). GC, Gildner and Cisne (1990); B, Bice (1991); BS, Bosscher and Schlager (1992); R, Read et al. (1991); D, Demicco (1998). Reproduced courtesy of Blackwell Publishing Ltd.

dependent productivity curve may cause drowning of the platform/ramp (Schlager 1981). This may occur spontaneously, without external forcing, or during a eustatic rise superimposed on the background tectonic subsidence (Dorobek 1995; Galewsky 1998; Allen et al. 2001).

Two-dimensional geometrical models rely on sediment filling available accommodation on a template subject to tectonic subsidence. The geometrical model of Aigner et al. (1989, 1990), Lawrence et al. (1990) and Shuster and Aigner (1994) is a good example of an industry-based (Shell) model capable of dealing with both carbonate and siliciclastic sediments. By adjusting parameter values, these authors were able to achieve remarkably realistic simulations of the stratigraphy of the Paris Basin, for example. Mixed carbonate–siliciclastic sedimentation was also modeled in the model known as SEDPAK (Kendall et al. 1991a, b) and tested against the clinoform-dominated stratigraphy of the Great Bahama Bank.

More dynamic treatments of carbonate systems, such as the 3-D model of Burgess et al. (2001), combine physical processes of sediment transport (diffusion, advection) with a carbonate productivity–depth relationship to produce a dynamic mosaic of carbonate depositional environments. As we saw in §8.3.6, this model is capable of simulating the common small-scale cycles typical of peritidal sequences. Dynamic models involving the transport of carbonate sediments inevitably share much in common with models designed for siliciclastic systems.

8.4.2 Siliciclastic stratigraphy

Since the accumulation of siliciclastic sediment is not a straightforward function of depth, early simulations of siliciclastic stratigraphy were 2-D geometrical models in which the sediment filled available space up to an equilibrium profile. This was the graded stream profile on land, the shoreface profile, and the graded continental shelf (e.g., Jervey 1988; Ross et al. 1995; Burgess and Allen 1996). Commonly these models are a combination of a dynamic treatment of thermal subsidence and flexural response to sediment loads, but a geometrical treatment of the physical processes of sediment transport (Fig. 8.35) (Burgess and Allen 1996; Steckler 1999). Within this spectrum, some models (Ross et al. 1995) consider the grain size distribution of the sediment by partitioning sand and mud deposition within different depositional environments. Others (Kendall et al. 1991a, b) include the effects of sediment compaction, or incorporate a viscous relaxation time in calculations of isostatic support (Steckler 1999). However, the physical laws of erosion,

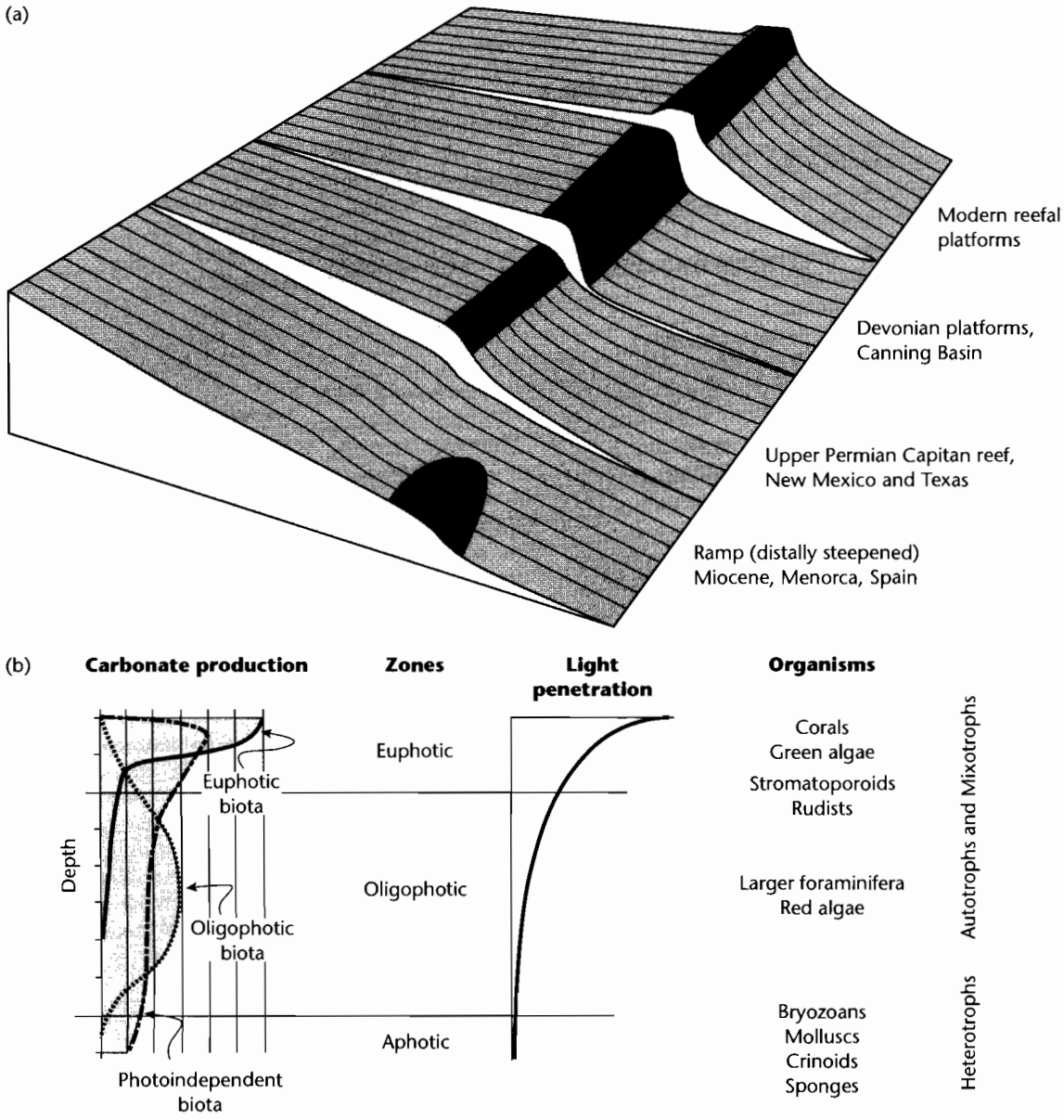

Fig. 8.34 Carbonate depositional geometries, modified after Pomar (2001). (a) Range of morphologies from ramps to rimmed platforms; (b) Carbonate productivity in relation to the type of biota. Variations in the dominant biota control the water depth range of maximum productivity. Ramps may be distally steepened where oligophotic organisms dominate. Reproduced courtesy of Blackwell Publishing Ltd.

sediment transport, and deposition are not explicitly treated in these geometric models.

We have investigated in other sections (§7.5) some of the governing laws for hillslope transport and long range fluvial transport. Other transport laws govern particle motion on the shoreface and shelf. The first dynamical models were applied to fluvial systems, which were treated as diffusive. When combined with tectonic subsi-

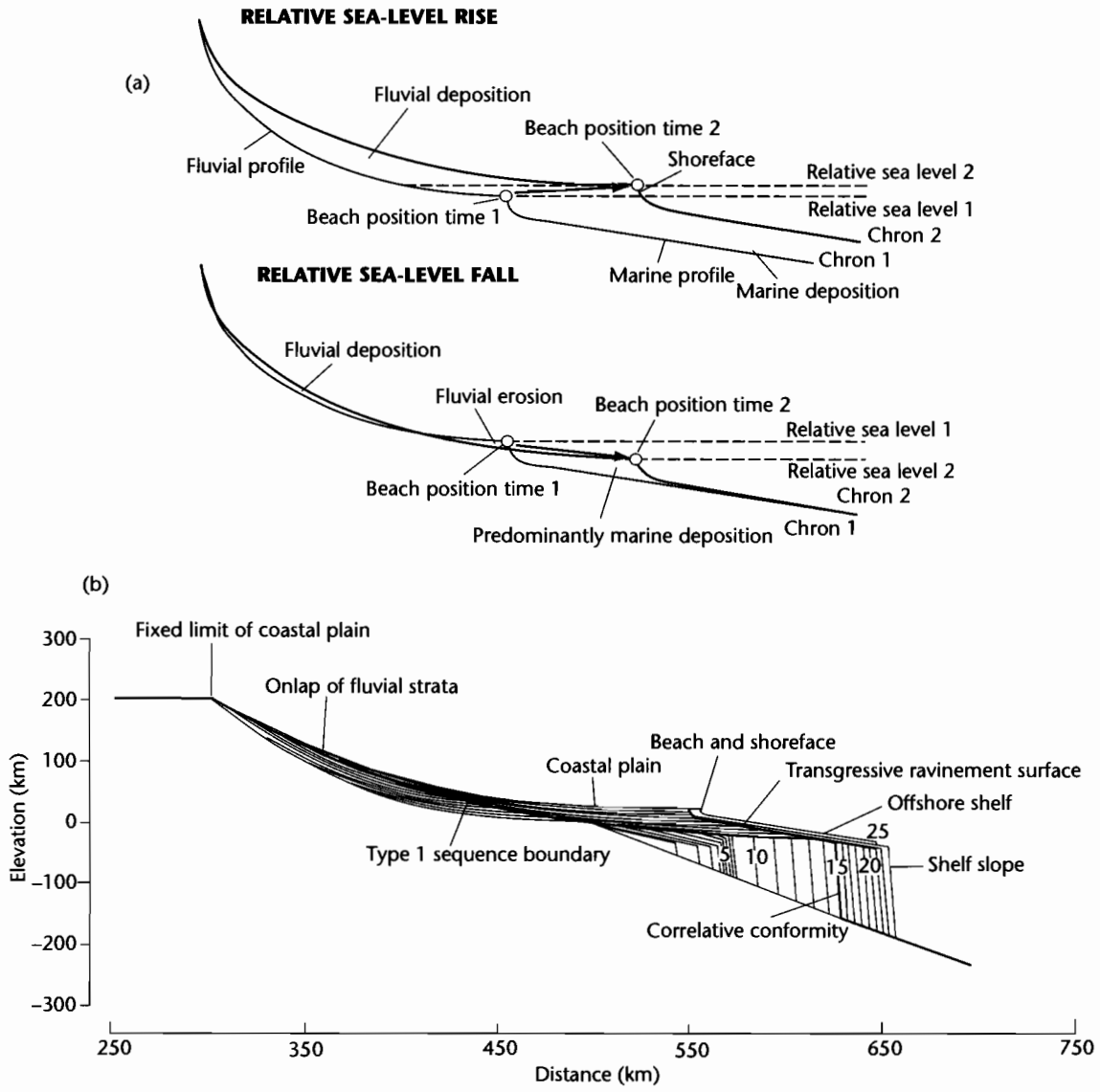

Fig. 8.35 Example of a geometrical 2-D model for stratigraphy at a passive margin (after Burgess and Allen 1996), showing how depositional sequences and bounding unconformities can be simulated. (a) Movement of the fluvial and marine profile during relative sea-level rise and fall; (b) Computer-generated stratigraphy with a Type 1 sequence boundary and its distal marine conformity and a transgressive ravinement surface generated during relative sea-level rise. Details in Burgess and Allen (1994). Small numbers are chrons. Reproduced courtesy of Geological Society of London.

dence, stratigraphy can be simulated as a function of the diffusive sediment transport coefficient as well as tectonic parameters controlling accommodation and source-area erosion (Flemings and Jordan 1989; Sinclair et al. 1991; Paola et al. 1992). Paola (2000) reviewed and justified the use of diffusive models in fluvial systems. Assuming that they can legitimately be treated diffusively, a key problem is the formulation of the diffusive transport coefficient.

Paola (2000) suggested that it depends on a number of hydrological and sediment transport parameters (§7.5.3). Interestingly, the dimensionless shear stress appears to be roughly constant (*c.* 0.05) for gravel bed rivers and a different constant (1 to 2) for sand bed rivers, implying different transport coefficients in these two regimes. Within these two regimes of gravel and sand bed rivers, the downstream variation in grain size is controlled by the size distribution of the sediment supply instead of the hydraulics.

While retaining the essential diffusive character of sediment transport, a number of approaches have been developed to deal with the problem of the transport coefficient (see also §7.5). The two-diffusion model of Marr et al. (2000) used separate transport coefficients for gravel and sand that were different by a factor of 10, whereas Rivenaes (1992, 1997) assigned transport coefficient values across a continuum according to the percentages of sand and mud, and Granjeon and Joseph (1999) invoked multiple grain size classes. These latter approaches may be more valid for the continental shelf than for fluvial systems. Kaufman et al. (1991) used a depth-dependent diffusivity for the continental shelf, which accounted for the decrease of wave energy with depth. A more dynamic approach considers the details of individual sediment transport events summed over time (Niedoroda et al. 1995). Although individual transport events may be advective, the aggregate effect may be broadly diffusive. As in fluvial systems, evaluating the net diffusive sediment transport coefficients as a function of meteorologic and oceanographic conditions is problematical. Numerical code needs to be adapted in moving from a storm-dominated continental shelf (Niedoroda et al. 1995) to a tidally dominated continental shelf (Ericksen and Slingerland 1990).

Dynamic forward models are successful in simulating many of the high resolution features seen in stratigraphy at outcrop and in borehole records, including the sand : shale ratio in the deposited layers. The evolution of the sand : shale ratio and stratigraphic geometry through a cycle of progradation and retrogradation for a fluvial-dominated delta is shown as an example in Figure 8.36 (Cross et al. 1993; Granjeon and Joseph 1999). During progradation, sand is concentrated in a high energy, narrow upper shoreface, whereas during retrogradation driven by a relative sea-level rise, sand is distributed more widely due to erosional ravinement of the underlying deltaic deposits. The same model can be used to produce a 3-D simulation at the basin-scale.

Fully coupled models do not assume that sediment supply is determined by some empirical formula related to elevation, slope or relief, nor that it is always available in sufficient quantity to fill accommodation, but instead incorporate surface process laws into a sediment routing model on a tectonically active template (e.g., Johnson and Beaumont 1995). These models provide powerful insights into the linkage between catchment development, sediment routing and depositional geometries in a fully coupled system containing geodynamic representations of tectonic uplift and basin subsidence. Models developed by different research groups may in due course be integrated into a "community" model.

8.5 DEPOSITIONAL SYSTEMS

8.5.1 Depositional systems and facies models

Depositional systems are sets of depositional environments linked by the process of sediment routing. They are responsible for large stratigraphic thicknesses, and environmental changes in one part of the system can generally be recognized in the stratigraphy of another part of the system, however distant. Depositional systems and their sedimentary products reflect the integration of autogenic (internal) and allogenic (external) controls. Sedimentary basins with different driving mechanisms (Chapters 3–6) have distinctive assemblages of depositional systems and facies. We give an overview of this linkage of tectonic environment and sedimentary character in §8.6. In this section, the main depositional systems are briefly summarized.

A hierarchy of depositional products based on scale exists from facies/beds to assemblages of facies in parasequences, to the tracts of depositional systems and finally depositional sequences. As the scale of the product increases, the cause of its deposition also changes from short-term, local and often autogenic causes at one extreme, to long-term, large scale causes involving lithospheric and climatic allogenic processes at the other extreme. In practice it may be very difficult to discriminate allogenic from autogenic causes.

The processes acting in particular depositional environments give rise to a suite of relatively small-scale characteristics of the resultant sedimentary deposits. The sum total of these small scale attributes that make a particular rock unit distinctive are embodied in the term *facies*. The term was introduced by Steno in 1669, but its

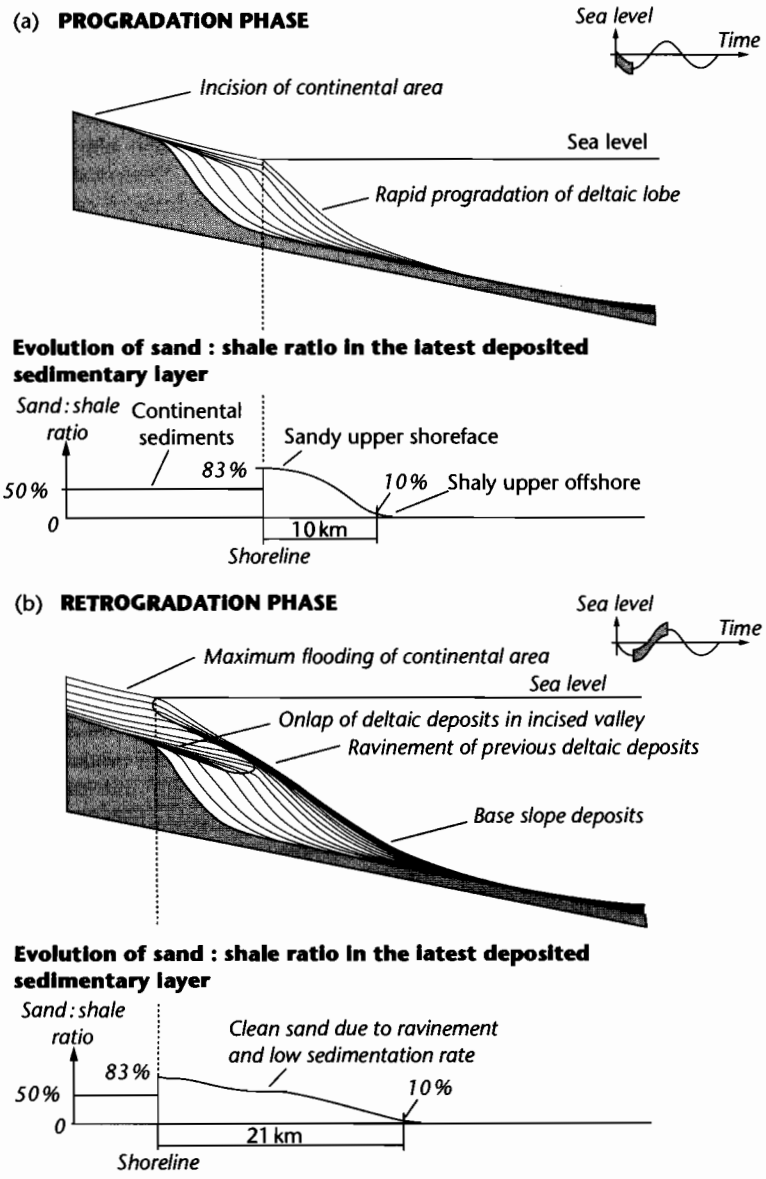

Fig. 8.36 Computer-generated 2-D transects through a fluvial-dominated delta, showing the sand:shale ratio in the preserved sediment during the progradational phase (a) and retrogradational stage (b). After Granjeon and Joseph (1999). Reproduced courtesy of Society for Sedimentary Geology.

modern usage follows Gressly (1838) who used the term to imply the full assemblage of lithological and paleontologic features of a rock unit (Cross and Homewood 1997). The term "facies" has been used subsequently in a number of ways, both purely descriptively and in terms of interpreted process of deposition (Middleton 1978; Reading 1986). A *facies model* is an interpretive device used to explain the association of facies. Facies models generally achieve this explanatory function by linking observations on modern processes and ancient deposits

into a coherent synthesis. The summary that the facies model provides should be usable in a number of different ways. It should incorporate large volumes of data into a form that generalizes sedimentary processes. It should be a stimulant for further investigations and should act as a predictor in new geological situations. Finally, it should help to give insights into the dynamic interpretation of the sediment unit (Walker 1984).

The art of facies modeling is, however, subject to its own problems. Most facies models depend on studies of *modern environments*: it is therefore necessary to assume that the present is an accurate reflection of the past. The time scale of the observations is critical, and we are often left asking the question of how typical are the last 100 years of the geological past, and what is the effect of the infrequent or catastrophic "event" on the geological record? (Dott 1983). Second, it is difficult to assess the true preservation potential of modern sedimentary sequences, and studies of present-day and sub-Recent deposits may be strongly biased compared to the ancient record.

The *vertical sequence* has played a very important role in the development of facies models. Stratigraphy is invariably cyclic at high frequency. However, the vertical profile is clearly an inadequate and sometimes misleading representation of the sedimentary evolution of a succession. Two-dimensional panels, constructed from well-exposed surface outcrops or from high quality seismic reflection lines, are now a standard tool in stratigraphic and facies analysis. Three-dimensional geometries can often be interpreted from a series of differently orientated 2-D sections. The mapping of very high resolution seismic reflection data derived from 3-D surveys also reveals remarkable detail of the geometric properties of sediment bodies and the "texture" of stratigraphic surfaces. For example, 3-D seismic mapping reveals dendritic drainage patterns etched into Type 1 sequence boundaries representing incised, subaerial continental shelves (e.g., Underhill 2001). Sedimentary geometries have been mapped digitally in the field using differential GPS and laser ranging techniques (Adams et al. 2001).

The variability of depositional units, both vertically (in time) and laterally, contribute to its *heterogeneity* (see also §10.4.2). The 2- and 3-D study of sediment geometry has given rise to the concept of "*architecture*," that is, the way in which individual sediment bodies are stacked in time and space. There are now a very large number of studies of architecture. Initially, much progress was made in alluvial and aeolian sedimentary systems. More recently, the focus has shifted to deep marine siliciclastic systems.

In the sections that follow, we outline some of the main depositional systems filling continental and marine sedimentary basins. Vast amounts of information can be found in a large number of authoritative sedimentological texts covering the entire range of depositional systems, environments, and facies. Examples are Reineck and Singh (1980), Walker (1984), Reading (1996), Leeder (1999), Einsele (2000), and Miall (2000).

8.5.2 Continental depositional systems

Terrestrial depositional systems may include the deposits of alluvial fans and fan deltas, rivers, deserts, lakes, slope wastage, and ice sheets and glaciers. Continental basins have a basic two-fold subdivision. Basins with *through drainage* are dominated by well-established river systems and perennial lakes, whereas basins with *internal drainage* are characterized by ephemeral river systems, generally shallow and short-lived lakes, continental sabkhas and deserts.

8.5.2.1 Fluvial systems

A number of specialized volumes provide a wealth of detail on *fluvial systems* and their deposits, including Collinson and Lewin (1983), Ethridge et al. (1987), Shanley and McCabe (1998), Marzo and Puigdefabregas (1993), and Miall (1997). Fluvial style is a complex response to a number of autocyclic and allocyclic controls. The primary allocyclic controls include: (i) climate, which controls run-off (discharge) and the weathering of parent rocks, and (ii) tectonics, which controls basin slopes and relief of hinterlands in the drainage basin. This interplay results in a distinctive set of characters of the river system (e.g., sediment load, discharge, slope, vegetation) which in turn determine channel patterns (braided, meandering, anastomosing), avulsion rates, and floodplain accretion rates. All of these factors control the architecture of alluvial basin-fills (Leeder 1978; Bridge and Leeder 1979; Leeder 1993; Mackey and Bridge 1995).

Alluvial basin types may be dominated by transverse (e.g., Atlantic coastal plain of North America) or longitudinal (e.g., Po system in northern Italy, Ganges of northern India) drainage systems (Fig. 8.37). Alluvial basins can also be classified according to the nature of proximal, medial, and distal elements. Tectonically active basin margins commonly have alluvial fans as proximal elements. Medial elements include braidplains and high-

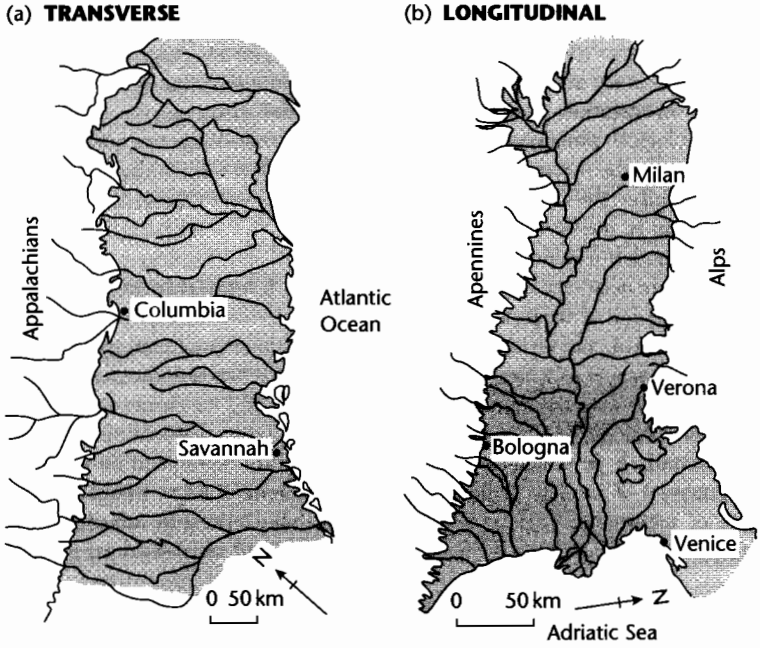

Fig. 8.37 Transverse and longitudinal river drainage patterns. (a) The Atlantic coastal plain of North and South Carolina and Georgia; (b) The Po Basin of northern Italy (after Miall 1984).

sinuosity alluvial systems of transverse or longitudinal type. Distal elements may be lake margins, terminal fans and sabkhas, deltas, and estuaries.

Alluvial fans form where rivers emerge from valleys onto an unconfined plain or major trunk valley, building semi-conical depositional landforms (Bull 1977; Blair and McPherson 1994). They are sensitive indicators of the erosional unroofing of hinterland terrains and of the accommodation generation in the neighboring basin (Whipple and Trayler 1996; Allen and Hovius 1998; Allen and Densmore 2000). Fans vary greatly in area. The classical arid-region fans of the American southwest, such as those of Death Valley, California, have radial distances of 1–7 km, slopes of 2–7° and are dominated by debris-flow processes. Other depositional systems are low-gradient, fluvial megafans with radial distances of over 100 km, such as that of the Kosi River in the Himalayan foreland (Gupta 1997). Megafans depend on an amalgamation of catchments in the mountainous hinterland to supply large quantities of sediment and water. Where fans enter a deep marine, fjord, or lake basin, its surface processes may be dominated by subaqueous mass flows and turbidity currents (Nemec and Steel 1988; Collella and Prior 1990).

Fluvial systems respond rapidly to environmental change, and the effects of tectonic activity can be assessed on-land in neotectonically active regions (Alexander and Leeder 1987) (Fig. 8.38). They therefore serve as sensitive barometers of allocyclic processes. The effects of tectonic tilting on alluvial processes can be seen in channel avulsion patterns, the preservation of asymmetrical meander loops and the interconnectedness of sandstone channel belts (Mike 1975; Alexander and Leeder 1987; Leeder and Alexander 1987; Peakall et al. 2000). River channel processes in regions of growing tectonic structures can be particularly well seen in the Canyonlands region of SW USA (Trudgill 2002). The effects of cycles of base level change at the river mouth can be recognized in systems of terraces and incisions in the river valley, as demonstrated classically by Fisk (1947) in the Mississippi Valley and later by Blum (1993) from the Colorado River of USA.

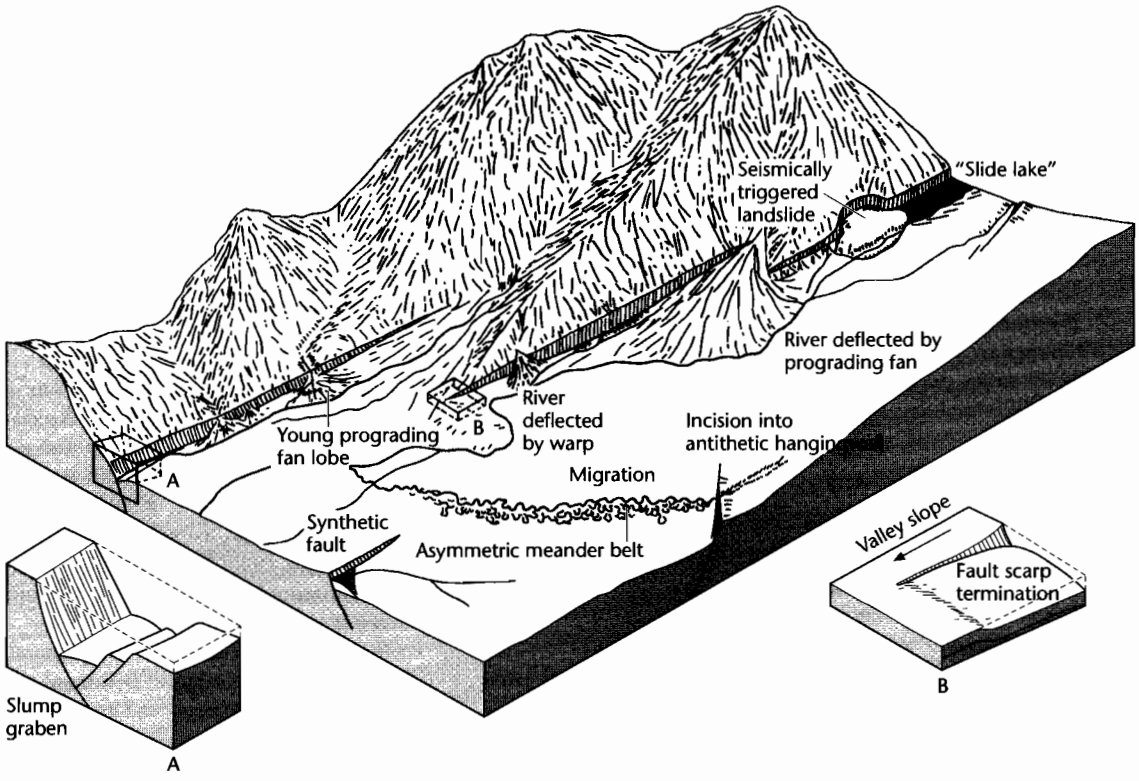

Fig. 8.38 An idealized alluvial half-graben based on studies of the Basin and Range province of western USA, showing some of the common geomorphologic features resulting from extensional neotectonics (from Alexander and Leeder 1987).

8.5.2.2 Desert systems

Deserts include a variety of environments of deposition from the giant sand seas (ergs) to stony wastelands, interdune sabkhas with temporary lakes, and dried up river courses. Deserts occur in both Arctic areas, where sediment is derived from wasting glaciers, and tropical zones where ergs are concentrated. Areas of low rainfall occur as two discontinuous belts around latitudes of 20–30° and are associated with persistently high atmospheric pressures. Deserts also occur in the centers of large continental masses. The occurrence of aeolian deposits in the stratigraphic record is therefore to a large extent a reflection of an ancient climatic zone.

Sediment transport by wind is responsible for large sand dune fields called *ergs*, accumulations of silt and clay termed *loess*, and for transport of dust into the deep sea. The largest present-day ergs occur in topographic basins in cratonic positions, such as the Saharan examples (Rub al Khali erg in Saudi Arabia is 560,000 km^2 in area), the Taklimakan and Gobi deserts of the Asian interior and those of central Australia. The average thickness of the erg may exceed 100 m with bedform (draa) heights of several tens of meters to over 200 m. Ancient examples such as the Permian Rotliegend Sandstone of northern Europe similarly occupy large continental sags. The Permian–Jurassic stratigraphy of the Utah–Arizona–Colorado region is the best-documented ancient desert succession (Peterson 1988). It contains the Lower Jurassic Navajo Sandstone, which alone is 700 m thick.

Aeolian systems can be classified as "dry" or "wet" systems. In dry systems, the water table has no effect, so there are no stabilizing factors restricting sediment transport. Erosion, transport, and deposition are controlled by aerodynamic factors. In wet systems, the water table or capillary fringe intersects the accumulation surface,

leading to stabilization. Wet interdune areas and sabkhas are preserved in the aeolian stratigraphy of wet systems, such as the Entrada Formation of western USA (Kocurek 1981a,b). Wet interdune, sabkha, and lake sediments and extremely important in contributing to the heterogeneity of aeolian reservoirs.

Distinct trends have been identified in transects from erg center to erg margin (Fig. 8.39). Such erg fringes may merge with ephemeral fluvial systems, playa lakes, or marine environments. These erg margin environments are characterized by a complex interaction of sedimentary processes (Porter 1987; Clemmensen and Blakey 1989; Langford 1989; Langford and Chan 1989), and models of *aeolian–fluviatile interaction* and *aeolian–lacustrine interaction* have been developed.

8.5.2.3 Lacustrine systems

Lacustrine depositional systems are also highly sensitive to climate. There is a great diversity of lake basins and lake waters. They can be divided into lakes that have an outlet and are hydrologically open and those that lack an outlet and are hydrologically closed (Fig. 8.40) (Allen and Collinson 1986; Talbot and Allen 1996). Their hydrological status determines lakewater chemistry and therefore the terrigeneous clastic *versus* chemical and biochemical sedimentation in the lake. Hydrologically closed lakes commonly form in the centers of endorheic (internal drainage) regions such as the Chad Basin, north-central Africa. They are characterized by a dominance of chemical and biochemical sediments and evaporites are common. Through-flowing lakes typify many continental rift systems such as in East Africa and the Baikal Rift of central Asia. They are dominated by terrigenous clastic input and, where river input is negligible, by alkaline earth carbonates. Apart from the hydrologic status of the lake, the most important controls on lacustrine depositional systems are the slope of the nearshore zone, lake bathymetry, stratification of the water column, size and shape of the lake as well as the overriding importance of climate.

Lacustrine depositional systems may change in character rapidly as a result of climatic fluctuations. A large number of present-day lakes are shrunken, saline remnants of much larger and more dilute ancestors that existed during the pluvial period coinciding with the last glacial maximum (Flint 1971). Examples are the Dead Sea and precursor Lake Lisan, Great Salt Lake, USA and precursor Lake Bonneville, and Lake Eyre, Australia and precursor Lake Dieri. The expanded lakes, such as Lake Lisan, typically accumulated alkaline earth carbonates with an abundant flora of diatoms, whereas the present-day remnant has a lake floor covered with gypsum and halite. An analysis of Holocene/Quaternary lake levels and salinities suggests that minima and maxima recur at a frequency that is most likely a result of orbital eccentricities of the Earth around the Sun. The lake level variations therefore appear to be a complex response to Milankovitch forcing.

8.5.2.4 Glacial systems

About 10% of the present Earth's surface is covered with ice and a further 20% is affected by permafrost. During some periods of Earth history, such as the Ordovician, Permo-Carboniferous and Late Cenozoic, ice and permafrost cover was much more extensive (Hambrey 1994), and during the Neoproterozoic it is thought that the Earth repeatedly froze over completely or near-completely (Hoffman et al. 1998). The assembly of plates into supercontinental assemblies appears to be a major factor in the onset of major glaciations.

Glacial environments are complex and laterally extremely variable. Moving ice is found in a number of settings, principally as polar ice sheets and as coastal ice shelves, and as valley glaciers and their marine outlets (tidewater glaciers). Glacial sedimentary facies reflect the various processes involved in ice movement and melting (Eyles et al. 1985; Ehlers 1996) (Fig. 8.41). On land, sediment is deposited by direct deposition or lodgment under active ice, some from reworking by later sediment gravity flows at the ice terminus, and some is deposited by subglacial streams or as deltas at their exit points. Sediment is also dumped from ice at its contact with lakes and in the ocean as glacilacustrine and glacimarine sediment. Rain-out diamictites are caused by the melting of sediment-loaded floating ice, which distributes a wide grain size range of sediment, including large *dropstones*, over the lake or seabed. Such dropstone-bearing rain-out diamictites are a common feature of many Neoproterozoic glacial successions.

8.5.3 Coastal and nearshore depositional systems

8.5.3.1 Siliciclastic shoreline systems

The geomorphology and oceanography of the Earth's siliciclastic coastlines reveals an exceedingly complex

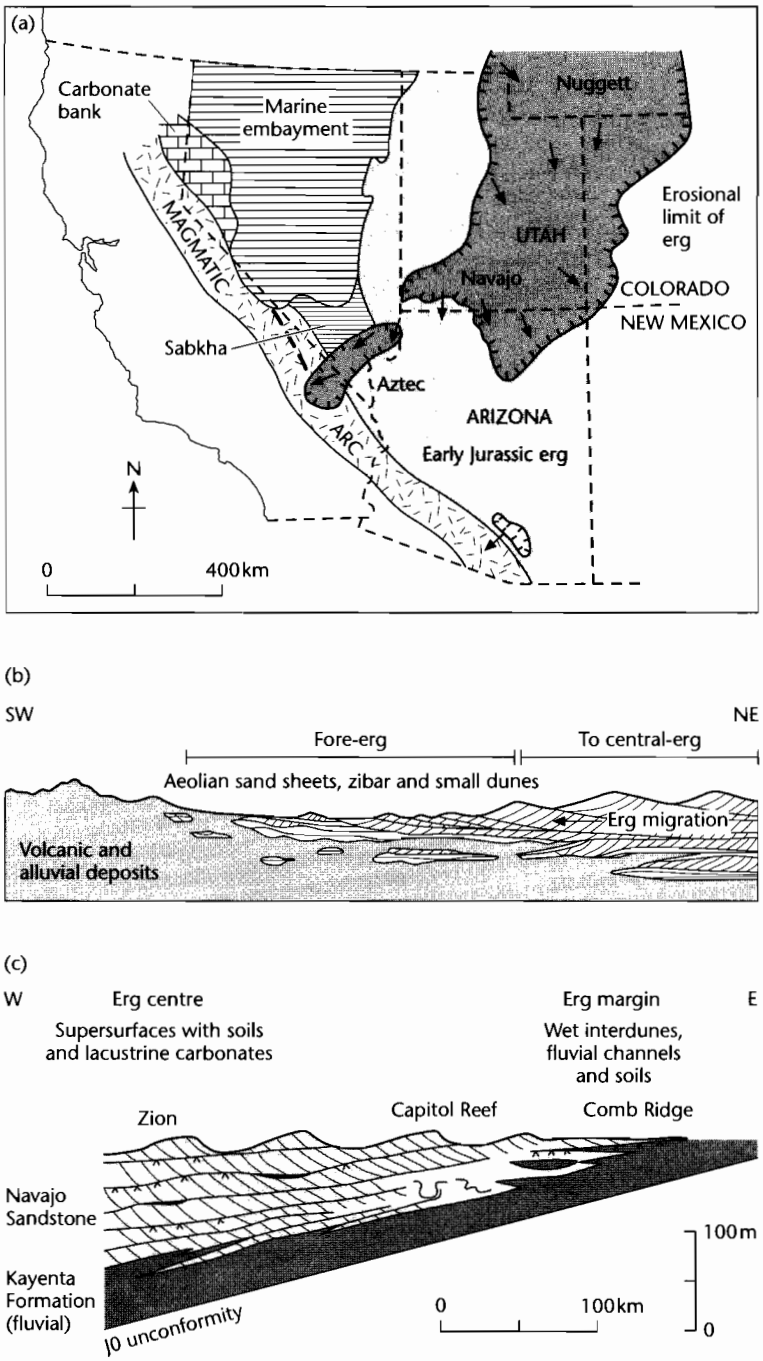

Fig. 8.39 Eolian erg centre to erg margin transect from the Lower Jurassic stratigraphy of southwestern USA (after Porter 1987; Blakey et al. 1988). (a) Generalized Early Jurassic paleogeography; (b) Schematic section across erg margin in southwest (Aztec Sandstone); (c) Cross-section of the Navajo erg showing a depositional erg margin in the east which now corresponds closely to its erosion limit. Supersurfaces show soils and locally carbonate ponds.

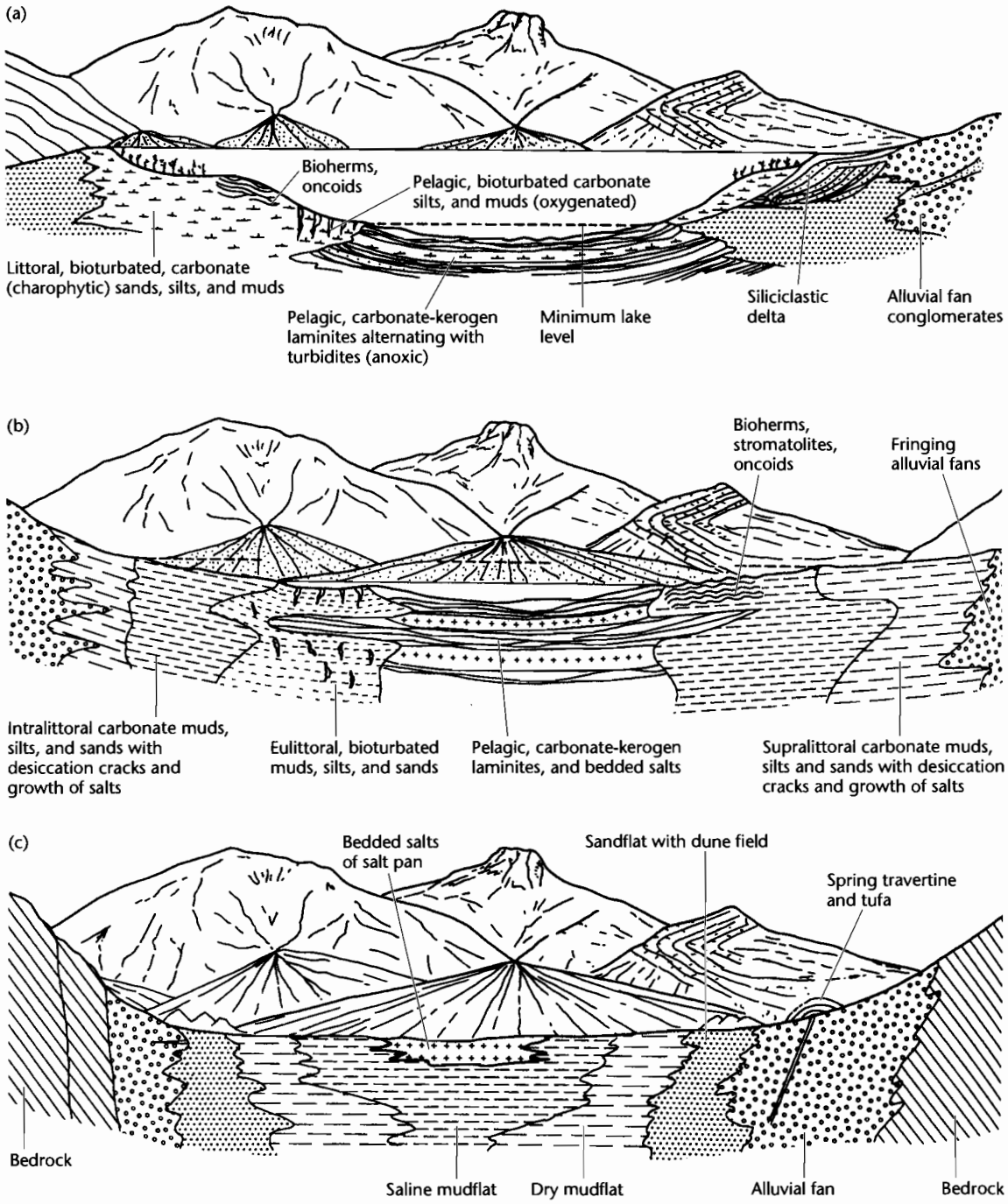

Fig. 8.40 Idealized depositional environments and facies in lacustrine systems. (a) Open freshwater lake with through drainage; (b) Hydrologically closed perennial salt lake; (c) Hydrologically closed ephemeral salt pan. After Eugster and Kelts (1983), modified from Allen and Collinson (1986).

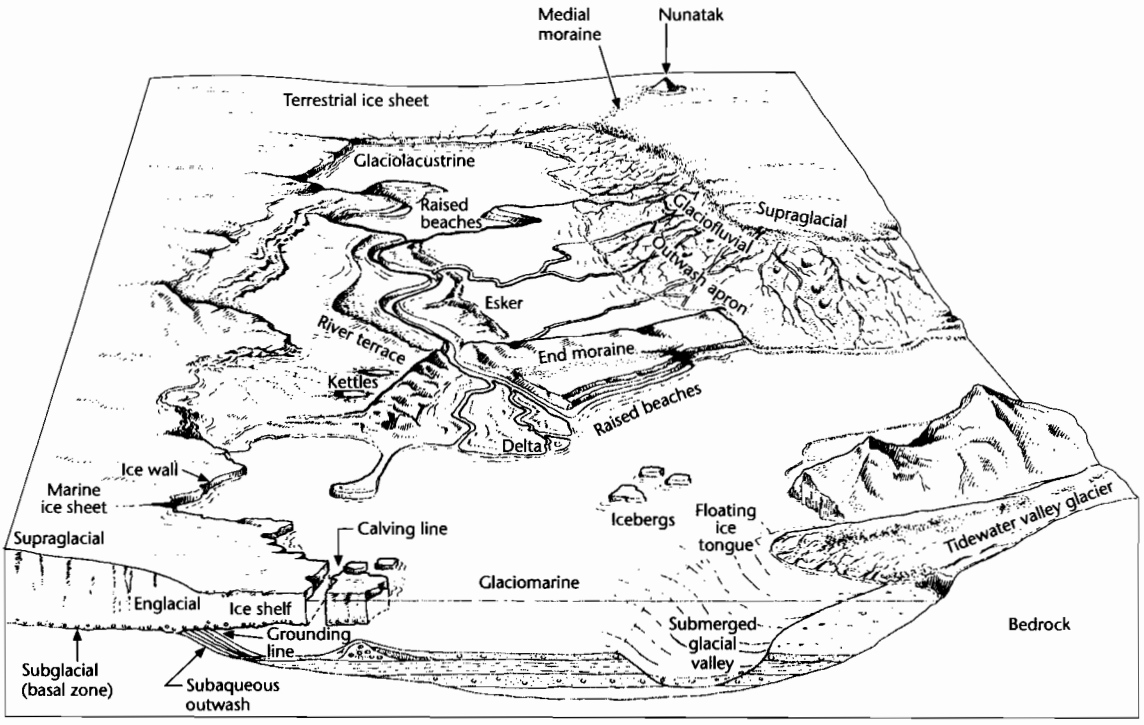

Fig. 8.41 The main depositional environments and facies at an ice margin (after Edwards 1986). Reproduced courtesy of Blackwell Publishing Ltd.

interplay between fluvial input on the one hand, and basinal parameters such as wave energy, tidal range, and storm regime on the other. The two main types of coastal depositional system are *deltaic* and *nondeltaic*. Deltaic coasts are strongly influenced by the dynamics of the outflowing river water. Nondeltaic coastal systems may be: (i) *wave-dominated*, containing beaches, microtidal barrier islands, and cheniers, (ii) *mixed wave-tide influenced*, consisting of mesotidal barrier islands with tidal inlets and ebb- and flood-tidal deltas, and (iii) *tide-dominated*, made up of tidal flats and estuaries (Hayes 1979).

Deltas develop where river systems debouch into the ocean, inland seas, and lakes. Their form is controlled by a number of factors, chief of which is the relative effectiveness of river discharge compared with the tidal and wave energies of the receiving basin (Galloway 1975; Postma 1990) (Fig. 8.42). Where tidal and wave energies are low, distributary channels are able to build out into the sea unhindered by coastal erosion producing a typical "birdsfoot" pattern, as shown by the Mississippi Delta, USA. Where wave energies are strong compared to the river inflows and tides, the sediment delivered to the sea is molded into curved ridges at the delta's front and some is redistributed along the shore as beaches and spits. Deltas of this type, such as the Senegal (West Africa) or the Grijalva (Gulf of Mexico) are roughly arc-shaped and prograde slowly because of the destructive nature of approaching waves. Deltas strongly affected by tides have tidal channels cutting deep into the coastline with associated tidal sand ridges or shoals elongated in the same direction as the tidal current pathways, such as the Ganga–Brahmaputra delta in the Bay of Bengal, and the Mahakam delta, Indonesia.

Depositional patterns at river mouths can also be studied in relation to the dynamics of outflow dispersion (Wright and Coleman 1974; Wright 1977), an extension of the original concept proposed by Forel (1892) from his studies of the delta of the Rhône River in Lake Geneva. The dispersion of the outflow into the receiving water body falls into three categories: inertia-dominated jets, friction-dominated jets, and buoyancy-dominated outflows. The dynamics of the outflow control the transport

1 Mississippi
2 Po
3 Danube
4 Ebro
5 Nile
6 Rhône
7 São Francisco
8 Senegal
9 Burdekin
10 Niger
11 Orinoco
12 Mekong
13 Copper
14 Ganges-Brahmaputra
15 Gulf of Papua
16 Mahakam

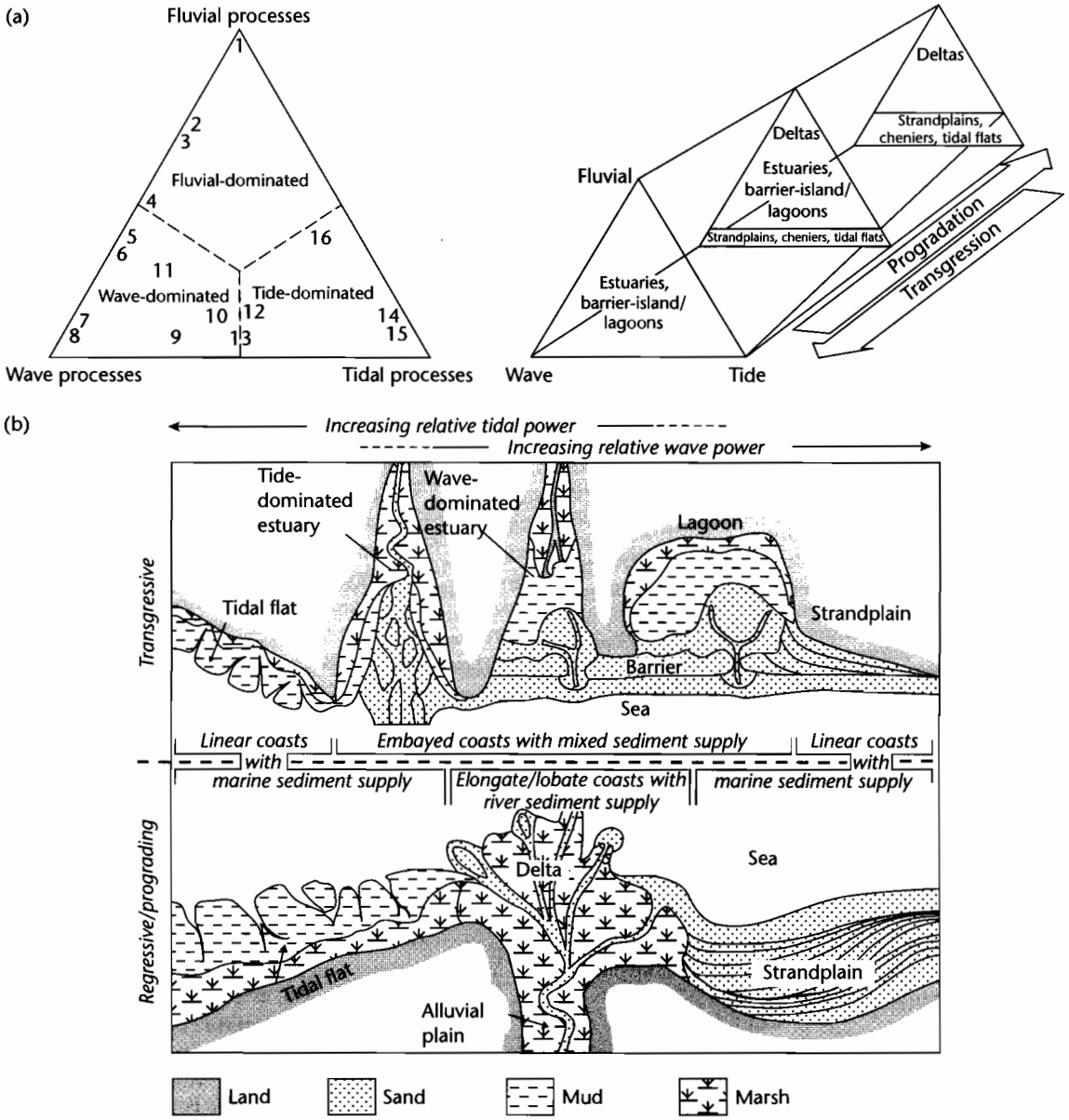

Fig. 8.42 Delta classification according to fluvial discharge, wave power and tidal range, following Galloway (1975), Postma (1990), Reading and Collinson (1996). (a) Ternary diagram and its modification into a Swiss *Toblerone*, to account for the different morphological features found during progradation and transgression of the coast. Reproduced courtesy of Society for Sedimentary Geology. (b) Plan views of trangressive/retrogradational and regressive/progradational coasts under varying conditions of wave power, tidal range, and marine and fluvial sediment supply (based on Heward 1981 and Boyd et al. 1992). Reproduced courtesy of Blackwell Publishing.

distance of particulates of different size in the estuary, lake, or ocean.

Wave-dominated shorelines may occur on delta fronts or on nondeltaic coasts. They are dominated by beaches (directly attached to the land) and barrier islands separated from the land by a shallow lagoon. Cheniers are sandy or shelly beach ridges isolated in coastal mudflats. The beachface subenvironments are controlled largely by wave approach, and vary from high energy to low energy settings. Barrier islands on wave-dominated coasts share much in common with beaches. They are found particularly in coastal environments that have a low gradient continental shelf adjacent to a low relief coastal plain, an abundant sediment supply and moderate to low tidal ranges (Glaeser 1978). An excellent example of a barrier is Galveston Island in the Gulf of Mexico (Bernard et al. 1962; McCubbin 1982). Tidal inlets are few and short-lived on wave-dominated barrier islands. Because of the limited connection to the open sea, the lagoons behind such barriers are prone to abnormal salinities (e.g., Padre Lagoon, Gulf of Mexico). Storms are capable of breaching the barrier, however, producing washover channels and fans.

Wave- and tide-influenced shorelines comprise barrier islands highly dissected by tidal inlets and associated tidal deltas. Wave-influenced tidal inlets are highly mobile, migrating in the direction of net longshore sediment transport. They therefore progressively replace the wave-built barrier with coalesced tidal inlet sequences. When tidal range is large (mesotidal to macrotidal, 2 to >4 m) estuaries dominate the coastal geomorphology (Dalrymple et al. 1992). Fine-grained sediments fringe the estuary in the form of intertidal and supratidal flats, whereas sands dominate the central zone. Tidal flats dissected by highly sinuous tidal creeks can be extremely extensive on some low wave-energy mesotidal to macrotidal coasts. Progradation of estuarine depositional systems should give rise to a fining upward sequence as subtidal and low intertidal sandflats are replaced by high intertidal and supratidal mudflats.

8.5.3.2 Carbonate and evaporite shoreline systems

Carbonate sediments are produced in great abundance in shallow, warm waters where the biological and physicochemical conditions are optimal for carbonate precipitation and fixation. Arid shorelines with low terrigenous input are characterized by deposition of carbonates and evaporites. The Trucial coast, Persian Gulf is an example of a modern carbonate-rich marginal marine *sabkha* (Fig. 8.43). A wide variety of coastal geomorphological elements are present, including beaches, barrier islands, tidal channels, and associated tidal deltas, intertidal and supratidal flats and aeolian dunes. The beaches, tidal deltas, and bars are commonly composed of oolitic-skeletal grainstones, whereas the back-barrier lagoons accumulate pelletal muds and, where predation is restricted, stromatolites. The upper intertidal zone is dominated by algal mats, constituting the lowest part of the sabkha *sensu stricto*. The supratidal zone is the main part of the sabkha and is the site of the precipitation of evaporitic minerals in the sediment column, as surface encrustations and in small ponds. Detrital carbonate grains are transported onto the sabkha by marine flooding.

Arid shorelines may also be dominated by siliciclastic sedimentation, as in Baja California, the Gulf of Elat and some parts of the Arabian Gulf. Here the sabkhas are composed of siliceous sands and muds with a possible admixture of carbonate grains. In many ways siliciclastic sabkhas are similar to their carbonate-rich counterparts. During progradation of the sabkha, normal marine sediments are first overlain by intertidal deposits, then supratidal sabkha evaporites, giving a vertical sequence indicative of increasing salinity. In some sabkhas, however, the deposits are arranged in a "bullseye" pattern, suggesting the progressive infilling of water bodies rather than shoreline progradation.

8.5.4 Continental shelf depositional systems

8.5.4.1 Siliciclastic shelf systems

Continental shelf systems are extremely complex and are highly sensitive to sea level fluctuations. *Modern siliciclastic shelves* contain sedimentary facies associations based on the physical processes operating in the nearshore-inner shelf zone, the rate of sea-level fluctuation and the nature and rate of sediment supply (Curray 1964, 1965). Some sediment on the shelf (perhaps 50% of the Earth's shelf area) is *relict*, that is, it is remnant from an earlier environment and is now out of equilibrium with the new conditions. Other sediments are termed *palimpsest*, which means that they are reworked and therefore possess aspects of both their present and former environments. Finally, some sediment is *modern* and is supplied from outside the shelf area.

Modern continental shelves can therefore be classified according to the nature of the sediment (relict, palimpsest, modern) and the hydraulic regime (wave-, tide-, storm-, or oceanic current-dominated) (Swift 1974;

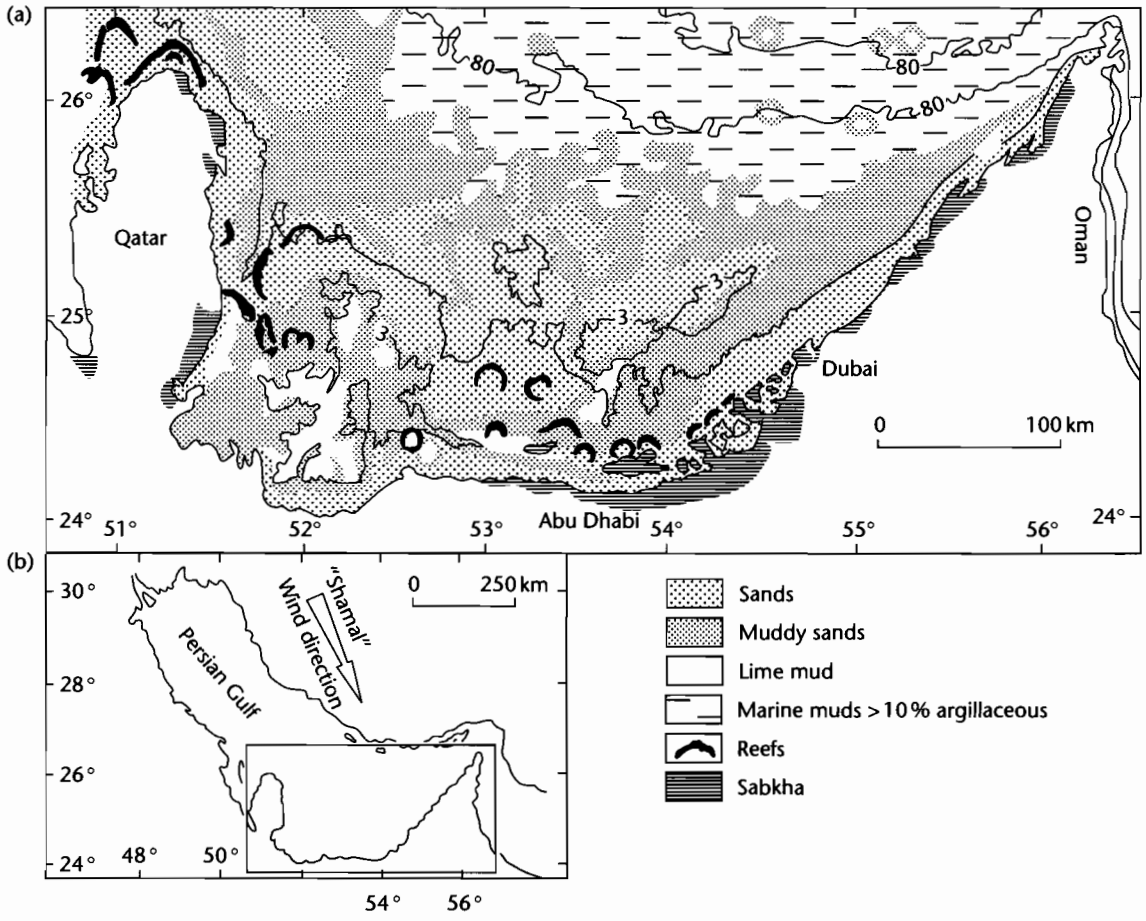

Fig. 8.43 Depositional environments of the open shelf and arid carbonate shoreline of the Trucial Coast, Persian Gulf. The Persian Gulf is an example of an open shelf, unprotected by a rim or reefs. (a) Bathymetry and facies on part of the southern shelf of the Persian Gulf (after Wagner and van der Togt 1973). Classical supratidal sabkhas are found in the Abu Dhabi area. Sediment transport on the shelf is influenced by the predominant "Shamal" wind from the NNW, shown in (b).

Johnson and Baldwin 1986) (Fig. 8.44). Classifying shelves according to the dominant shelf currents (Swift et al. 1986), tide-dominated shelves occupy 17% of the present-day shelf area, storm-dominated 80%, and shelves dominated by intruding ocean currents a very small percentage.

8.5.4.2 Carbonate shelf systems and reefs

Much of the continental shelf between the latitudes of 30°S and 30°N is an area of high organic productivity and is covered not by river-derived or relict siliciclastic sediments, but by organic carbonate material. There are two major categories of *subtropical carbonate shelf* (Ginsburg and James 1974). (i) *Rimmed shelves* sheltering protected shelf lagoons (Fig. 8.45). Their margins often fall precipitously into the abyssal depths. Some rimmed shelves are attached to continental areas as in the Great Barrier Reef of Australia. Others are now *isolated platforms* as in the Bahamas, and (ii) *open shelves* on the other hand, such as Yucatan, western Florida and northern Australia, slope gently towards the continental edge and are termed

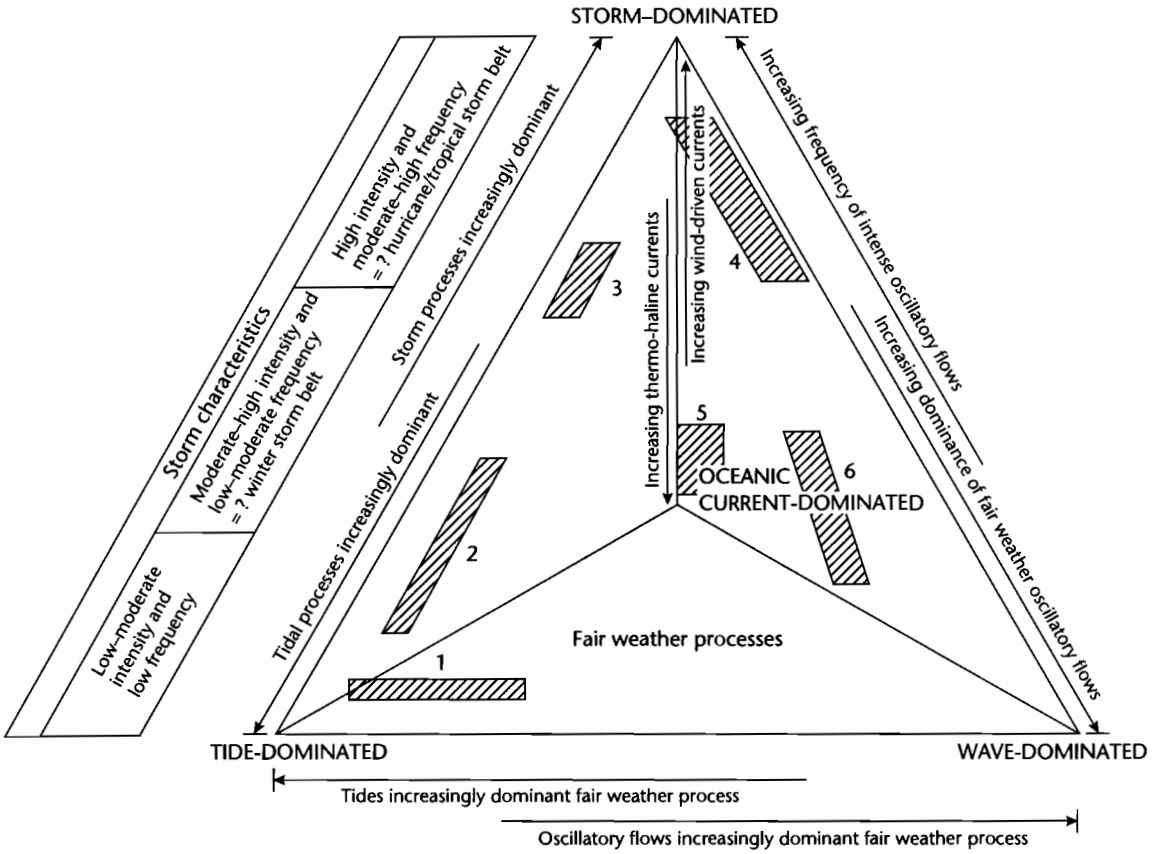

Fig. 8.44 The main types of hydraulic regime on modern shelves (modified from Johnson and Baldwin 1986). Modern shelves may be tide-dominated, ocean current-dominated or wave-dominated, where fairweather processes are of greatest importance, or storm-dominated where fairweather processes are of lesser importance. Shelf currents capable of transporting large amounts of sediment occur on shelves dominated by storms, tides, or intruding ocean currents. (1) Macrotidal and mesotidal embayments and estuaries (e.g., Bay of Fundy, Nova Scotia; Chesapeake Bay, USA; German Bight, North Sea) (2) Tidal straits and seas (e.g., English Channel, Malacca Strait, Taiwan Strait, North Sea, Yellow Sea). (3) Winter storm and tide-influenced shelf of the NW Atlantic, off eastern North America. (4) Storm-dominated shelves (e.g., Oregon–Washington and Californian shelves; SE Bering Sea; Gulf of Mexico. (5) Ocean current-swept shelves (e.g., SE Africa, Moroccan Shelf, NW Africa). (6) Low-energy embayments and shelves (e.g., Amazon–Orinoco Shelf; Niger Shelf; Baltic Sea; Hudson Bay).

ramps. Because of the lack of a protective rim, they are strongly affected by storm waves and tidal currents.

Reefs are *biogenic* constructions on the seafloor and reef facies models must successfully integrate sedimentologic and paleontologic observations. Reefs can generally be divided into: (i) a reef core comprising skeletons of reef-building organisms and a lime-mud matrix, (ii) reef flank of bedded reef debris, and (iii) inter-reef of subtidal shallow marine carbonates (or siliciclastics). Where reefs form a natural breakwater on the windward sides of shelves or islands, however, they protect a back-reef environment from wave attack. The types of reef building organisms has changed from the Precambrian through the Phanerozoic (James 1983).

8.5.5 Deep sea depositional systems

There are four fundamentally different environments of deposition of clastic sediments in the deep sea (Fig. 8.46):

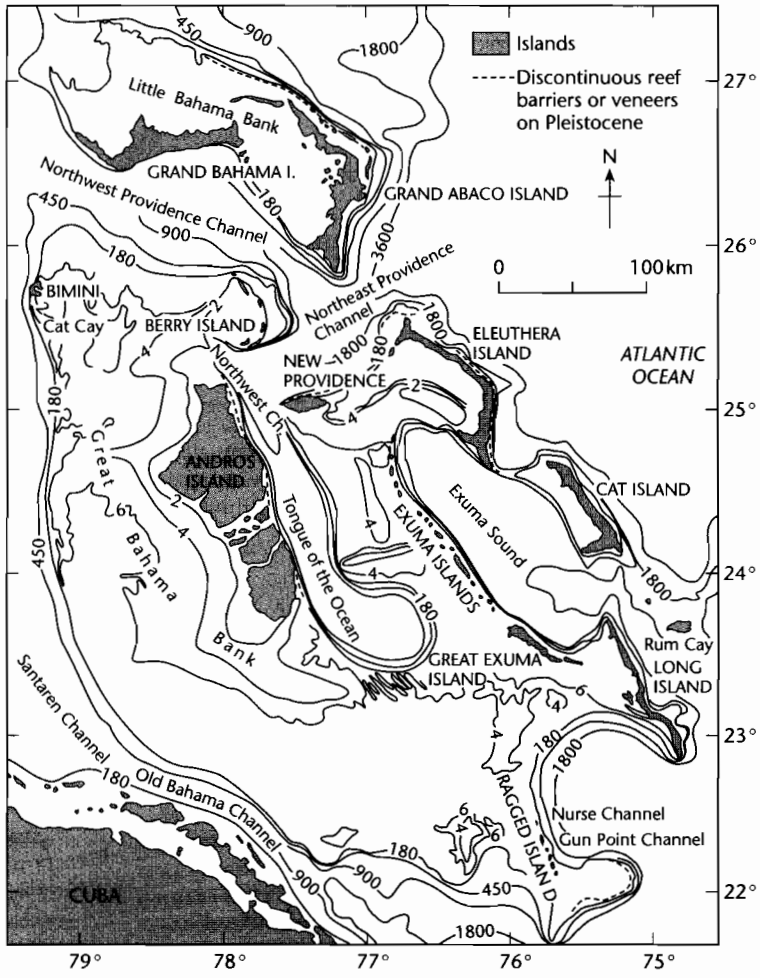

Fig. 8.45 General bathymetry of the Bahamian–Florida area, showing depths in m (after Multer 1971; Bathurst 1971, modified from Sellwood 1986). The area is a recently flooded rimmed shelf. The trace of the 6 m contour gives an impression of the former extent of the subaerial portion of the shelf prior to *c.* 7000 yr BP.

1 *Slope aprons*, which accumulate between the shelf and basin floor, vary in width from <1 km to >200 km. Normal siliciclastic slope aprons have a smooth convex–concave profile built by slope progradation. Faulted slope aprons typically have a highly stepped profile with perched basins alternating with steeply dipping slope segments. Carbonate slope aprons may form against reef edges or carbonate shoal margins. Where such margins are steep, sediment largely bypasses the slope apron so that it is dominated by calcirudite talus wedges. Where the margins are gentle, the slope apron is more actively depositional and more like its siliciclastic counterpart.

2 *Submarine fans* are constructional bodies that build oceanward at the base of the shelf slope. They receive sediment from river mouths or from alternative feeder systems such as submarine canyons. Fans vary greatly in scale and geometry, but there appear to be two end members, radial and elongate (Stow 1985). Radial fans develop concentrically around a single feeder canyon or channel (e.g., La Jolla and Navy fans off California). Elongate fans often have two or more feeder channels and extend for considerable distances from the supply margin. Examples are the enormous Bengal (off the Ganga delta), Amazon, and Laurentian (eastern North

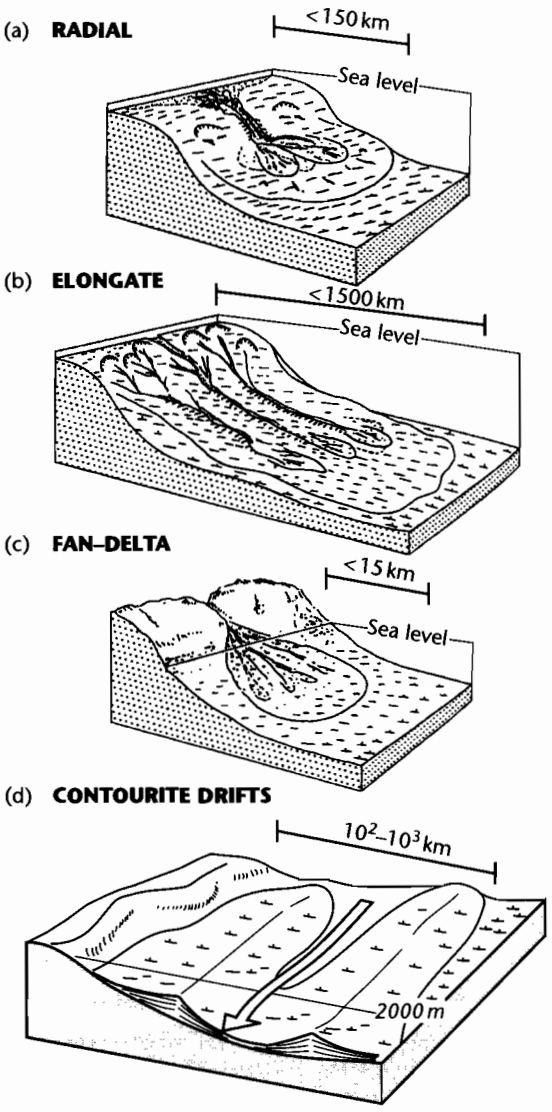

Fig. 8.46 Main types of deep sea depositional environment for siliciclastics. All diagrams are vertically exaggerated.

America) fans. Some large elongate fans, such as the Amazon, are covered with extensive debris flow deposits as well as channel-levee complexes with remarkable sinuous channels extending to beyond 4000 m depth (Cramp et al. 1995).

3 *Deep water sediment drifts* are formed by the relatively slow (generally <20 mm yr^{-1}) deep thermohaline circulation of the oceans, and to a lesser extent by wind-driven circulations where they impinge on the seabed, such as the Gulf Stream gyres of the North Atlantic. The more vigorous bottom currents may suspend diffuse clouds of sediment and organic material as *nepheloid layers*, as is found along the western margin of the North and South Atlantic (Biscaye and Eittreim 1977). Bottom currents also locally erode the seafloor, or deposit large sediment drifts composed of fine-grained *contourites*. Contourite drifts are particularly common at the edges of deep bottom water pathways (McCave and Tucholke 1986).

4 *Basin plains* are flat, relatively deep areas that act as the ultimate sediment traps for clastic sediments eroded from the continents and from submarine highs. Facies types and distributions are controlled primarily by basin geometry, tectonics, and source area (Pilkey et al. 1980). Abyssal plains are extensive and elongated parallel to the adjacent continental margin (e.g., Hatteras Abyssal Plain on the western North Atlantic). Marginal seas also have basin plains, fed from widely varied sources with a centripetal pattern (e.g., Sigsbee Basin Plain, Gulf of Mexico, Davies 1968). Deep sea trenches may consist wholly or in part of basin plains. In this case the plain parallels the highly elongate to arcuate trench orientation, and the dispersal of sediment by turbidity currents is also generally longitudinal. Strike–slip basins or borderland basins may also contain small, relatively confined basin plains.

The facies models of deep sea sedimentation of sands and gravels have been dominated by the concept of sediment gravity flows in general and turbidity currents in particular. Turbidity currents are responsible for the transport of large quantities of sand and mud into the deep sea. Turbidite beds can be recognized by their sharp, often erosive bases ornamented with sole marks, upward grading of grain size, and a vertical sequence of sedimentary structures. The greatest volume of modern turbidites accumulates in submarine fans and this depositional system has received strong emphasis in geological studies.

The seabed off northwest Africa provides an informative example of an integrated system of slope and deep marine processes and products (Weaver et al. 1992; Masson 1996) (Fig. 8.47). Catastrophic collapse of volcanic islands in the Canaries has repeatedly produced debris avalanches that load the adjacent seabed and trigger large debris flows. Some of these debris flows may have yielded turbidity currents that traveled downslope to the Madeira abyssal plain at water depths of over 5000 m.

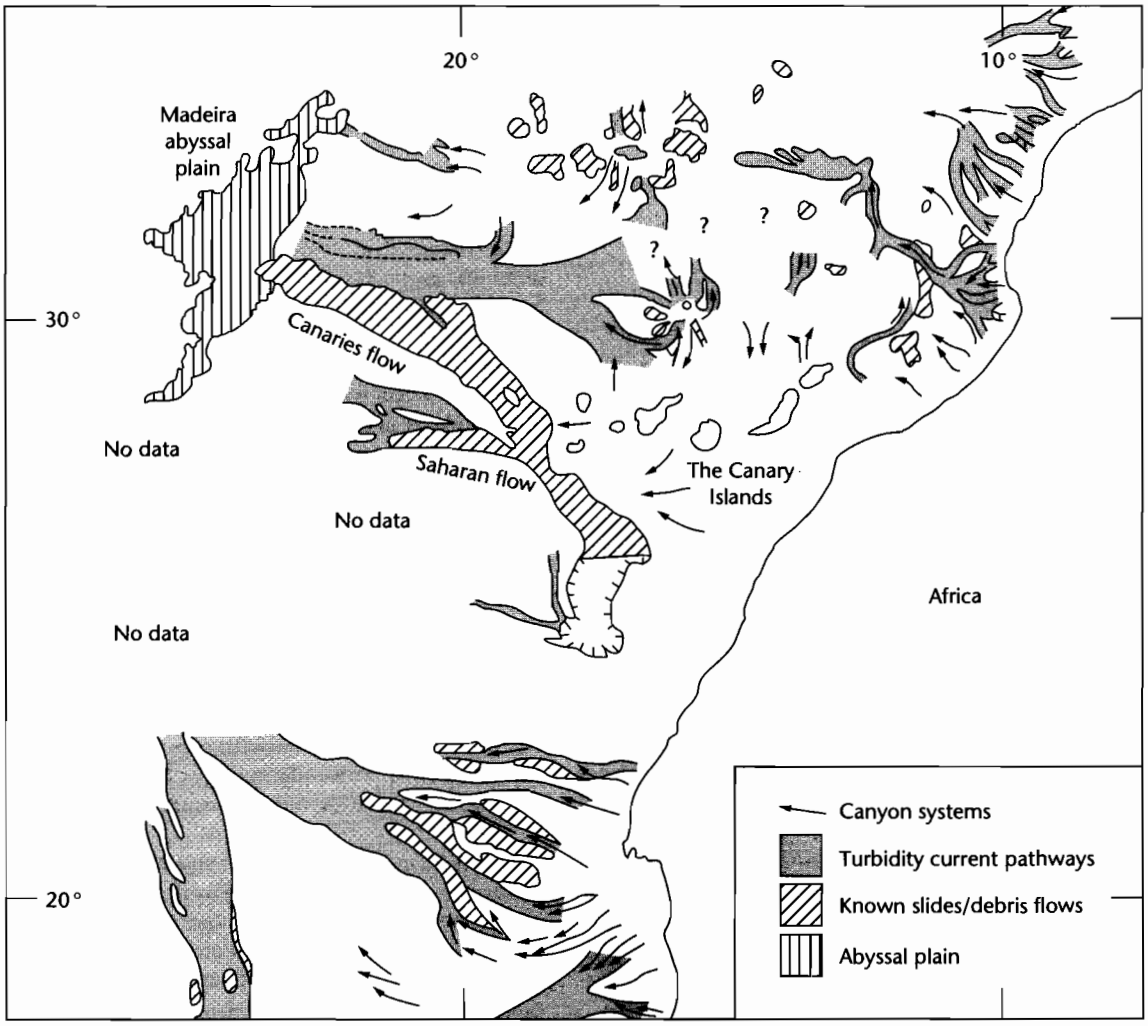

Fig. 8.47 Sediment routing systems offshore NW Africa, showing the transport paths of turbidity currents and giant debris flows. The Canaries debris flow originated by the loading of the sea bed by a rock avalanche caused by the catastrophic collapse of a nearby volcanic seamount. The Saharan debris flow, however, was due to slope failure of the continental margin. After Weaver et al. (1992).

Elongate but narrow troughs are commonly filled by turbidites deposited by longitudinal currents. The confinement of the basin, often as a result of tectonic activity, causes the turbidity currents to pond, deflect, and reflect off the basin flanks. Excellent examples are found in structurally confined basins perched at the thrust front of orogenic belts, as in the Tertiary Gres d'Annot Basins of southeastern France (Sinclair 1994) and the Tertiary Betic Sorbas Basin of southeastern Spain (Haughton 2001). In these cases traditional fan models are unlikely to closely resemble the observed facies associations.

8.5.5.1 Pelagic systems

Sedimentation in the open sea beyond the influence of the continental land masses is controlled by two major factors: the fertility of the surface water and the presence of the *calcite compensation depth* (CCD) below which carbonate

from the skeletons of marine organisms is dissolved. The biologic productivity of the oceans is highly concentrated in near-surface waters where light allows photosynthesis of phytoplankton. A small percentage (1%) of the carbon fixed by photosynthesis accumulates in dead organic tissues on the ocean bed. In low oxygen conditions, this organic matter is converted into black, laminated, organic-rich shales known as *sapropels*. Highest productivity is where there is an ample supply of nutrients, as in upwelling zones. Nutrient supply may also be strongly influenced by climate change, with increased productivity during glacial periods when nutrients such as iron are blown into the ocean from expanded desert regions.

Above the CCD, calcareous oozes derived from microorganisms such as formanifera predominate. Below this, the silica skeletons of radiolaria and diatoms produce siliceous oozes. There are also regions of seafloor dominated by red and brown clays derived from volcanoes, meteorites and dust blown from continents. The CCD has varied in its depth in the ocean during geological time, commonly as a result of variations in temperature and productivity, as at the Eocene–Oligocene boundary (Kennett and Shackleton 1976).

8.6 RELATION OF DEPOSITIONAL STYLE TO BASIN SETTING

Sedimentary basins form by deformation of the lithosphere (stretching, cooling, bending) and their gross stratigraphic patterns primarily reflect the various allogenic processes, principally climate and tectonics, causing base-level or relative sea-level change. It follows therefore that basins of a similar genetic type may show a consistent pattern in their sedimentary evolution, whereas basins of different type show correspondingly different sedimentary styles. Knowing the formative mechanism of a basin consequently has predictive power in assessing the basin-fill. In the following sections some characteristic sedimentary histories of various basin types will be sketched out. However, this should not be done in isolation from the particular "basin-specific" tectonic and burial history. The examples and generalizations that follow are a snap-shot of a subject area with an almost limitless bibliography. Further details can be found in Allen and Allen (1990), Ingersoll and Busby (1995), Leeder (1999), Einsele (2000), and Miall (2000), and in the various contributions of Bill Dickinson, who pioneered the linkage between tectonics and sedimentary geology (e.g., Dickinson 1974, 1976, 1993).

8.6.1 Basins related to divergent plate motion

Some basins on continental lithosphere appear to be purely sags with no obvious rifted basement. Others are clearly fault-bounded rift valley basins and yet others are rift basins that have since undergone a widespread subsidence unrelated to active tectonics (failed rifts or aulacogens). Large amounts of stretching lead to the formation of proto-oceanic troughs and passive margins. The underlying process that unites these various basin styles is lithospheric thinning and associated thermal disturbances. In this section we overview the typical kinds of sedimentary infillings of these basins formed on continental lithosphere.

8.6.1.1 Intracratonic sags

Intracratonic sags are characterized by prolonged but slow subsidence and a lack of strong syn-sedimentary structural activity. The sedimentary systems filling intracratonic sags are most commonly terrestrial, often in the form of rivers draining into centrally located, shallow lakes. Such endorheic systems are found in the Chad Basin of north central Africa and the Eyre Basin of southern Australia. In other intracontinental sags, shallow seas are able to enter the basin, as in the Paleozoic Hudson Bay Basin and Michigan Basin of North America.

There are a number of plausible mechanisms for the development of intracratonic sags, some of which may act in combination: subsidence as a response to recovery of the lithosphere following a thermal disturbance; subsidence driven by phase changes in the underlying mantle; subsidence related to the dynamic topography associated with subduction of oceanic slabs around the plate margin; subsidence over a mantle downwelling; long wavelength buckling of a layered lithosphere. Whatever the primary mechanism, the subsidence of intracratonic sags is strongly amplified by the effects of water and sediment loading. Fringing uplifts may act as an annulus that simultaneously serves as a source region for sediment and a topographic load on the lithosphere.

The *Chad Basin* is situated deep in the African interior >500 km from the nearest sea. The watershed bounds a roughly square area with sides of about 1200 km. The shallow (<10 m) centrally located lake occupies at present a relatively small area (30,000 km^2) compared to the extent of its late Pleistocene precursor Lake Mega-Chad (almost 1.5×10^6 km^2, Grove and Warren 1968). Most of the subsidence of the Chad Basin has taken place in the

Neogene and it has been concentrated in the zone within the confines of the beach ridges represented by the maximum limit of Lake Mega-Chad (Fig. 8.48). Sediment supply is thought to have been from fringing uplifts that acted as a dynamically supported annulus around the basin (Burke 1976). The intracratonic sag overlies an Early Cretaceous rift system, but cannot simply be due to thermal relaxation following stretching, because sedimentation in the modern basin is Neogene to present. Hartley and Allen (1994) suggested that the Chad Basin might be situated over an asthenospheric downwelling, which causes slow basin subsidence.

The *Michigan Basin* of northern USA (Wilson and Burke 1972; Burke and Dewey 1973) (Fig. 8.49) has undergone subsidence at varying rates for 500 Myr, yet the greatest thickness of basin-fill, found in the basin center, is still only 4 km. The Cambrian to Jurassic sediments are largely unaffected by structural activity, but the strong positive Bouguer gravity anomaly trending NW–SE across the basin and the sedimentary rocks penetrated by a deep borehole (Sleep and Sloss 1978) suggest the existence of a turbidite-filled Precambrian rift (~1100 Ma) underlying the basin (Hinze et al. 1975; Fowler and Kuenzi 1978).

Subsidence probably started in the Cambrian (Catacosinos 1973; Haxby et al. 1976) and continued through the Paleozoic with episodes of erosion producing continent-wide unconformities (Sloss 1963; Sloss and Speed 1974) (Fig. 8.49). Although the Cambrian contains extensive shallow marine sheet sandstones, the bulk of the Middle Ordovician to Devonian succession is made of carbonates, shales, and evaporites. The limestones, which are also found in the Illinois Basin to the south, are well known for their build-up complexes. In the Silurian, barrier complexes grew around the perimeter of the Michigan Basin, whilst so-called "pinnacle reefs" developed closer to the basin center where biogenic construction kept pace with the greater rate of subsidence (Wilson 1975 for synthesis) (Fig. 8.50). Evaporites are interfingered with and overlie the carbonate build-ups. Whereas the origin of the carbonate build-ups is undisputed, the evaporites are controversial. Deep water, shallow water, and supratidal environments have all been suggested. Since both the shelf carbonate reefs and the more basinal pinnacle reefs show signs of subaerial exposure (calcretes, dolomitization, travertine cements, karstic erosion, and solution features), and the associated evaporites possess a range of shallow water or supratidal features, it is believed that the entire shelf region became periodically desiccated, attesting to the very low depositional slopes typical of intracratonic basins.

More details on intracratonic basins, such as the Williston and Illinois Basins in North America and the Baltic and Siberian Basins of northern Eurasia, can be found in the volume edited by Leighton et al. (1990).

8.6.1.2 Continental rift basins

The location of continental rifts is sometimes determined by the existence of old fundamental weaknesses in the lithosphere. A number of examples of this phenomenon are the opening of the modern Atlantic Ocean along the Paleozoic Iapetus suture (Wilson 1966), the Cretaceous separation of southeastern Africa from Antarctica along a Paleozoic failed rift (Natal Embayment) (Tankard et al. 1982) and Cenozoic rifting in the East African Rift system, which follows Precambrian structural trends (McConnell 1977, 1980).

Continental rifting is the initial stage of a sequence leading to complete splitting and ocean floor generation (Veevers 1981). The duration of the rift phase is highly variable (§3.2.1, §3.6) and a series of rift events may be interspersed with relatively quiescent periods, as in the East Greenland Rift Basins (Surlyk et al. 1981) and North Sea (Glennie 1986). Nevertheless, within individual rift phases, the evolution of fault arrays may be rapid, with initial rifting developing into full linkage within a small number of millions of years (§8.3.2).

The nature of the sedimentary fill of a rift basin depends on its climatic zone, uplift pattern of the rift shoulders or arches acting as sediment sources or barriers, subsidence rate of central rift valleys determining alluvial base levels and lake water depths, and tectonic evolution of linked extensional fault systems. We can view the sedimentary fill on two scales – firstly the large scale features traceable along an entire rift, perhaps over some hundreds of kilometers, and secondly, the more detailed response of sedimentary facies to subsidence and uplift in rift compartments or in individual graben or half-graben. The broad features of the initial deposits of rifts are that they are predominantly nonmarine, comprising arkosic, commonly volcaniclastic fluviatile deposits, lacustrine (freshwater or evaporitic), and aeolian deposits. Fault-controlled subsidence commonly outpaces sedimentation at later stages of rift development, encouraging marine incursions in the rift climax phase (Prosser 1993) (Fig. 8.51), as seen in the Miocene of the Gulf of Suez (Gupta et al. 1999; Young et al. 2000). Shallow marine sediments may be overlain by deeper marine sediments as the rift evolves towards a site of seafloor spreading, as in the Mesozoic rifts of East Greenland (Surlyk 1990).

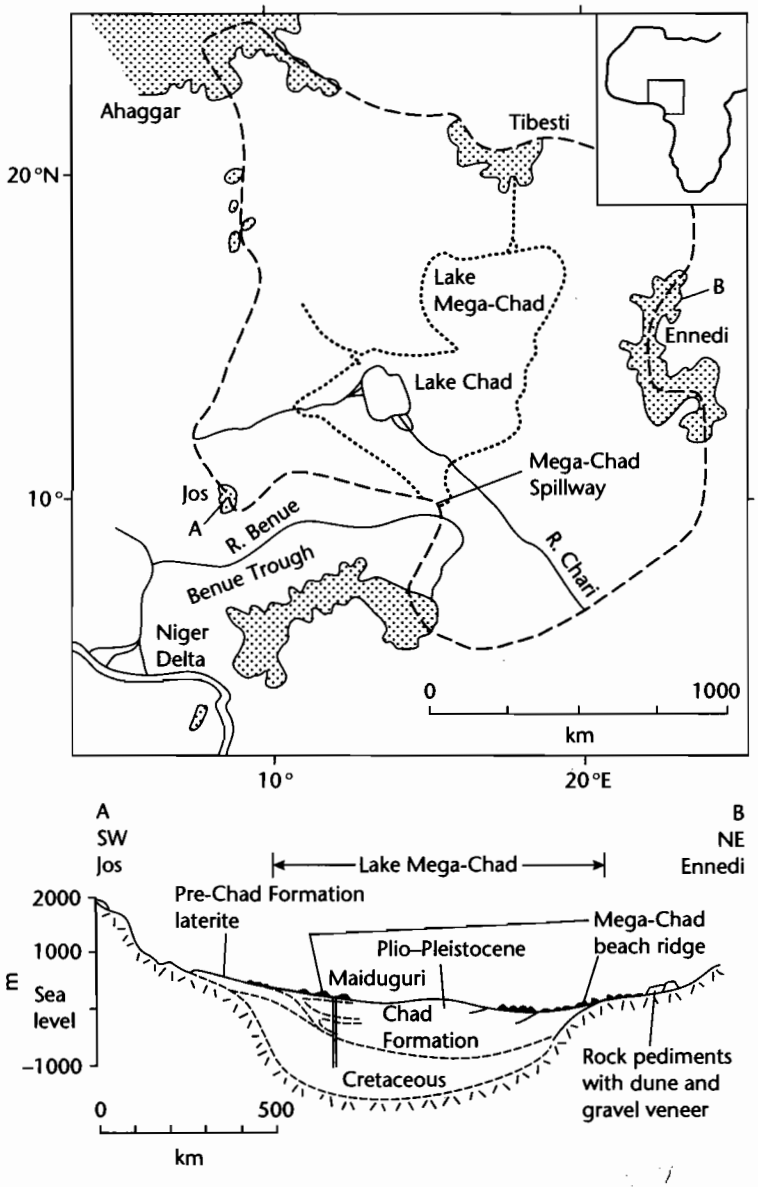

Fig. 8.48 The Chad Basin of the southern Sahara, showing the basin watershed (dashed line) enclosing an area of about 20×10^6 km, and the extent of Lake Mega-Chad (dotted line). This expanded lake spilled over to the Atlantic *via* the River Benue. Areas higher than 1 km above sea level represent peripheral uplifts (stippled). Cross-section along A–B shows that Quaternary sediments are restricted to the limits of ancient Lake Mega-Chad. This depositional area is fringed by a wide annular area of pediment and high ground. A borehole at Maidiguri penetrated 600 m of Quaternary Chad Formation (after Burke 1976).

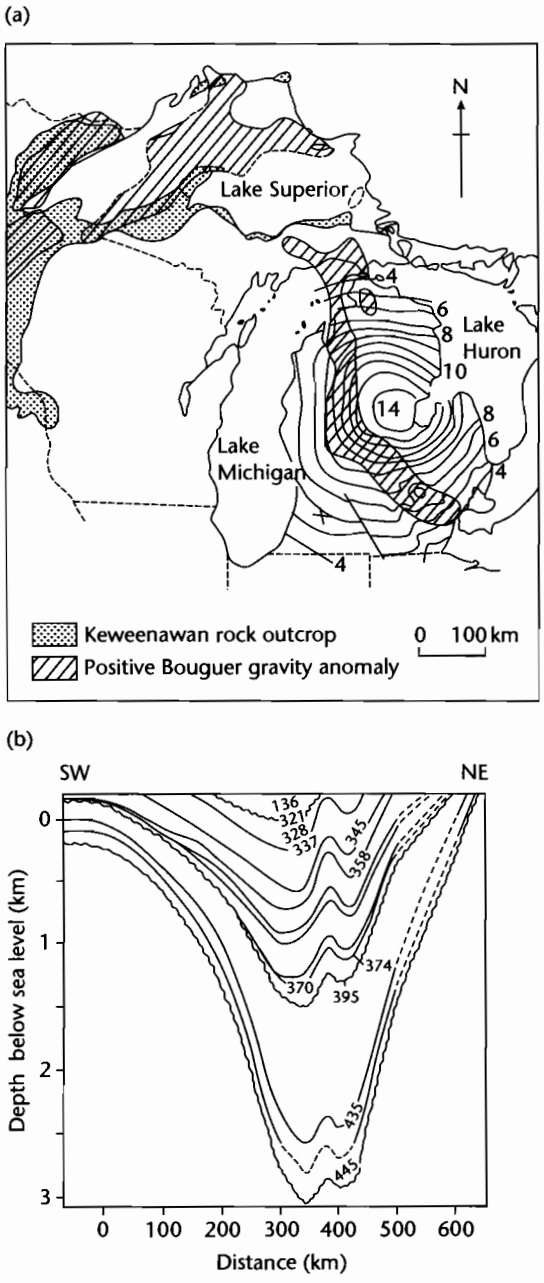

The Neogene East African Rift System demonstrates some typical stratigraphic and sedimentologic responses to continental rifting. The Neogene rift valleys of East Africa are located within broad plateaux rising as high as 4.5 km above a background mean elevation of about 0.5 km. Rift valleys split the plateaux centrally, as in Ethiopia, or occur on the flanks of individual arches as in the Central Plateau of Tanzania, Kenya and Uganda (Fig. 3.1). There are also rift divergence zones where well-developed single rift valleys pass into zones of diffuse extension composed of tilted fault blocks (as in northeast Tanzania). Seismic investigations of some rift valleys such as that of Lake Tanganyika (Rosendahl et al. 1986; Morley 2001) suggest that they are composed of a linked, alternating arrangement of arcuate half-graben (Fig. 8.52). Individual half-graben are separated by interbasinal ridges, trending oblique to the rift axis, which serve as barriers to sediment spillover between the various rift compartments (Contreras and Scholz 2001). The structural template implies that the amounts of subsidence and extension and sediment infill are all dependent on location within the rift valley zone. Sedimentary facies within the Lake Tanganyika Basin result from an interplay of river input of clastics and input of fanglomerates along border fault scarps and background "rain" of biogenic sediment from lake waters. The entry points of clastics into the Lake Tanganyika basin are: (i) the axial flowing River Ruzizi entering the lake in the north, (ii) rivers flowing over platforms, e.g., Malagarasi River entering the lake from the east, (iii) as conglomerates and breccias derived from slope wastage along border faults, and (iv) rivers entering over the shoaling sides of half-graben (Fig. 8.52).

Climatic variations cause major oscillations of lake level and therefore strongly control stratigraphic architectures (Scholz et al. 1998). Major climate-driven

Fig. 8.49 (a) Location of the Michigan Basin, USA and structural contours on the Precambrian basement surface in thousands of feet (after Hinze and Merritt 1969; Fowler and Kuenzi 1978). The basement depth increases gradually into the centre of the basin, which is almost perfectly circular in plan view. A buried Precambrian Keeweenawan rift, recognized by a positive Bouguer gravity anomaly, is thought to underlie the basin; (b) Cross-section of the Michigan Basin from Middle Ordovician to Jurassic (after Sleep and Snell 1976). Major unconformities are from Sloss (1963). Youngest units are found in the center of the basin, and some unconformities (e.g., at 395 Ma) are associated with a basinward shift in onlap. The anticline in centre right is due to Paleozoic tectonics.

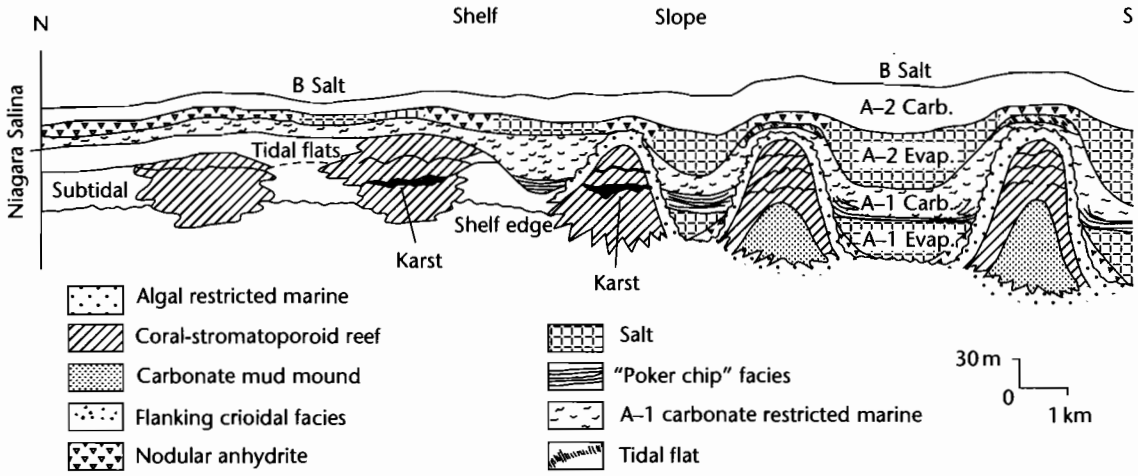

Fig. 8.50 Reconstruction of the facies and stratigraphy of the evaporite-dominated Upper Silurian of the northern part of the Michigan Basin (after Sears and Lucia 1979, 1980).

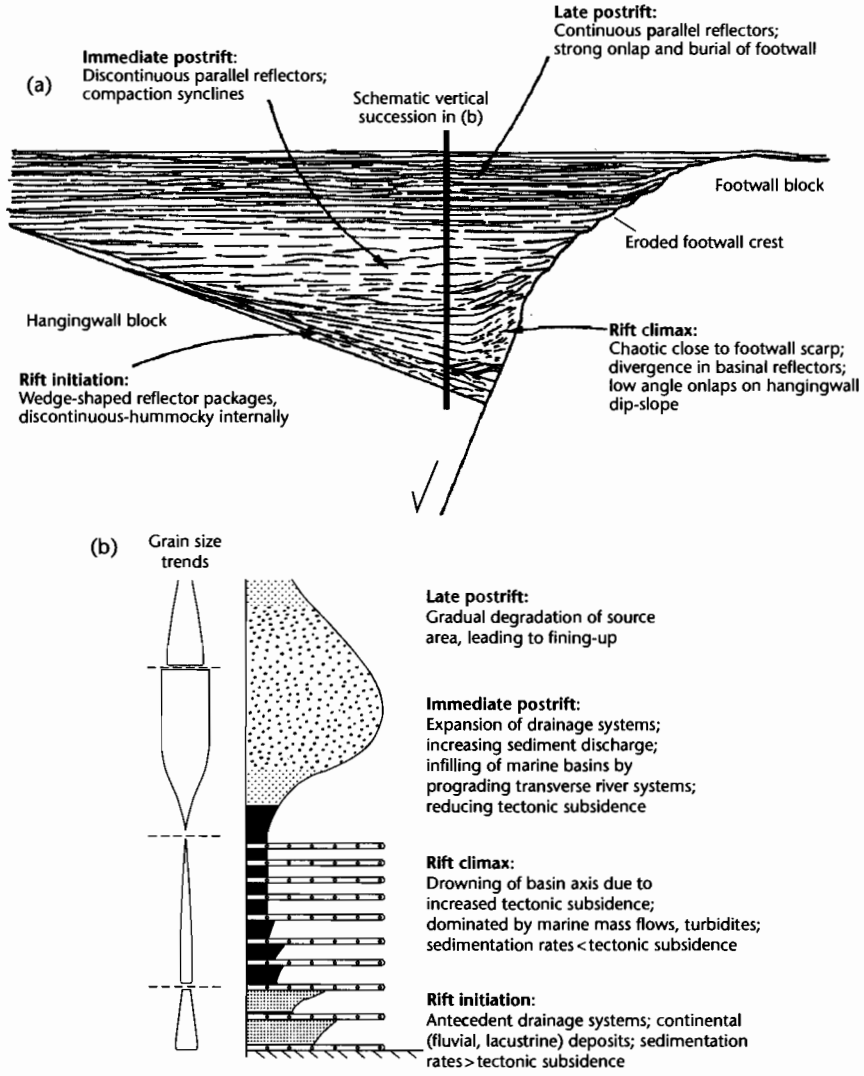

Fig. 8.51 Cross-section (a) and stratigraphic column (b) for an extensional basin evolving from rift initiation through rift climax to the postrift stage, based primarily on seismic stratigraphic data (modified from Prosser 1993). Reproduced courtesy of Geological Society of London.

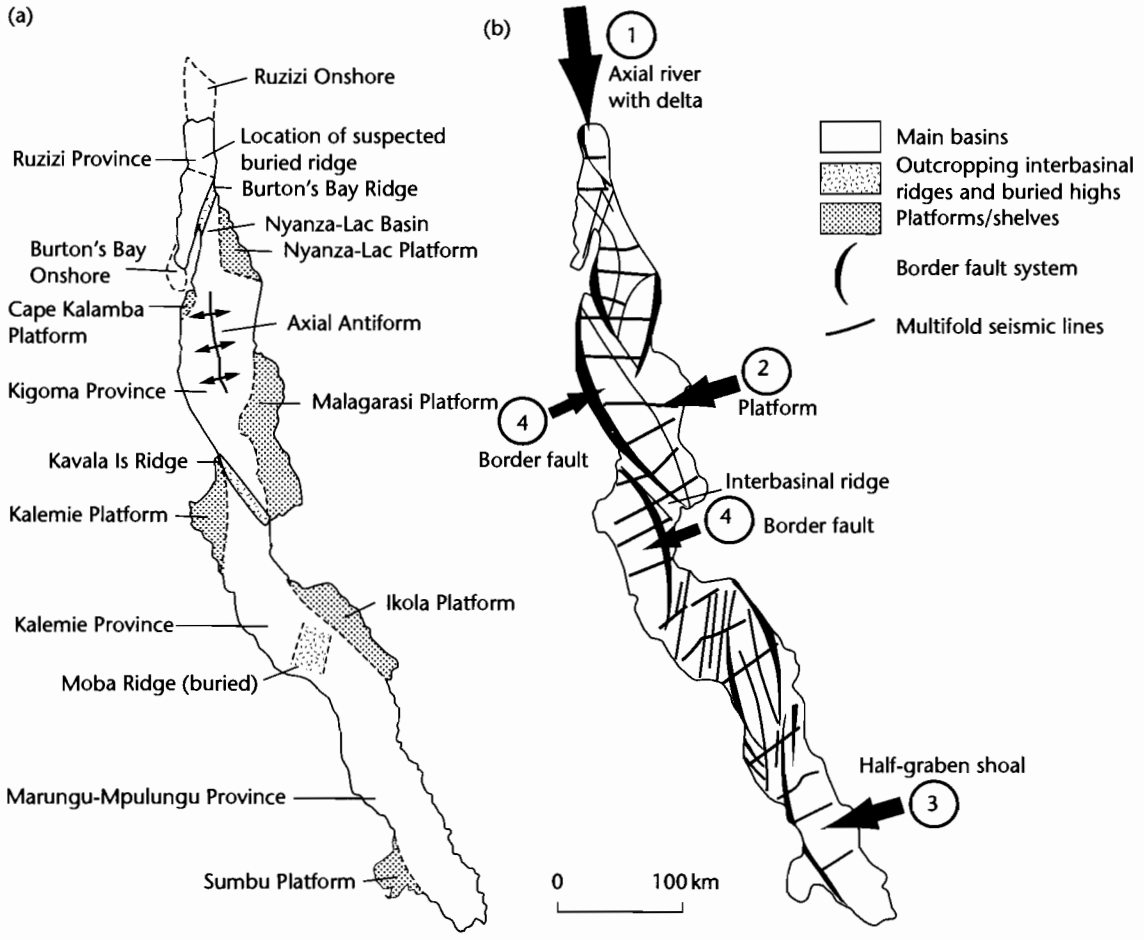

Fig. 8.52 Structural geometry, basin compartments, and sediment entry points into the Lake Tanganyika rift system (after Rosendahl et al. 1986; Contreras and Scholz 2001).

oscillations in lake level are particularly important in low-latitude lakes, such as those of the East African Rift system. Lake level variations may be rapid and high in amplitude (>100 m over 10^2 yr, >350 m over 10^{3-5} yr, Owen et al. 1990) because of the dominance of evaporation in the hydrological cycle. (In contrast, high-latitude lakes, such as Lake Baikal, do not experience severe lake level fluctuations.) Sequence architectures are dominated by these climate-driven lake level changes. Lake drawdown, enhanced by tectonic tilting, produces sequence bounding unconformities and basinward shifts of progradational deltas. Subsequent lake level rise encases the delta bodies in deep marine shales. During the rift initiation stage, individual half-graben sub-basins are fed with sediment from flexural margins and axial rivers. During the rift climax, however, the deeply subsiding sub-basins are walled off by major border faults, and sediment input is concentrated at accommodation (transfer or relay) zones and at axial deltas. Today, much of the East African Rift system is in a semi-arid climatic zone. Consequently, river deltas are markedly ephemeral in their discharges, perhaps flowing for only a few hours each year (Frostick and Reid 1986). Only a few deltas are fed by large perennial streams (e.g., River Omo, Lake Turkana). Some lakes, especially in the north of the rift system have internal drainage and, under a negative water budget, precipitate evaporites.

Volcanic activity has a major influence on rift sedimentation, as exemplified by the eastern rift of Kenya and the Rio Grande Rift of southwestern USA (Mack

and Seager 1990). Volcanism exerts this influence by the intercalation of subaerial and subaqueous lava flows within the terrestrial and lacustrine stratigraphy, by diversion or damming of surface drainage by volcanic eruptions, and by overloading of streams with volcanic, especially pyroclastic, detritus. Leaching of volcanic material leads to alkaline to hyperalkaline groundwaters and hot springs that then influence lake chemistry, as in Lake Magadi, Kenya. Inorganic cherts and Na-Al-Si gels, the precursors of zeolites, have been described from the lake (Eugster 1967). The chief mineral precipitating today is the evaporite mineral trona, which is interbedded with thin beds of wind-blown volcaniclastic sand and silt and black anoxic muds. The centrally located salt pan and fringing mudflats, ephemeral streams and springs provide an arid-region closed rift-lake model that can be identified in the stratigraphic record, such as in the Eocene Green River Formation of eastern USA (Eugster and Hardie 1975).

8.6.1.3 Failed rifts

Failed rifts are those basins in which rifting has been aborted before the onset of seafloor spreading and passive margin development. Their rift phase is identical to that outlined in the previous paragraphs. During cooling, failed rifts widen and postrift sedimentary rocks onlap the previous rift shoulders, producing a steer's-head geometry. A sedimentary evolution from nonmarine to shallow marine in the synrift phase and deeper marine in the postrift phase seems to be typical.

The Benue Trough of central-western Africa and the North Sea are two excellent examples of aborted rifting. The Benue Trough is 1000 km long, 100 km wide, and is filled with <5 km of fluvial, deltaic, and marine Cretaceous sedimentary rocks. At the southwestern end of the failed rift, the Tertiary Niger delta has built a wedge of fluvial, deltaic, and submarine fan deposits 12 km thick.

In the northern North Sea a major period of rifting took place in the Middle Jurassic. At this time sediment was dispersed longitudinally along the graben. In the N–S oriented Viking Graben, fluviatile deposits pass northwards into deltaic and shallow marine deposits of the Brent Group (Morton et al. 1992). The mid-Cretaceous saw the end of the rift phase and sediment onlapped the graben shoulders onto the East Shetland Platform in the west and the Norwegian Platform in the east. Thick deposits of Cretaceous chalks, Paleogene submarine fan sandstones and basinal shales, and Neogene mudstones typify this postrift phase. In the southern part of the North Sea, the basin was filled by major sediment supplies from rivers draining the European mainland, producing megaclinoforms due to westward delta progradation (Huuse and Clausen 2001; Overeem et al. 2001) (Fig. 8.53). The southern-central North Sea therefore shows the tendency for basin filling during the later stages of the thermal subsidence phase of failed rifts.

8.6.1.4 Proto-oceanic rifts

At high amounts of stretching, continental rifts, or backarc basins may evolve into new oceanic basins through a stage known as a proto-oceanic trough. The transition can be seen in northeastern Africa and Arabia. The southern Red Sea contains young (<5 Ma) oceanic crust along its 50 km-wide axial zone, with flanking shelves underlain by stretched continental lithosphere. To the south the Red Sea undergoes a transition to the continental Afar Rift, and to the north into the continental Gulf of Suez Rift. The sedimentary evolution of the Red Sea area involves Oligo-Miocene synrift sedimentation of basin margin fans and fan-deltas and shallow marine carbonates and silicilastics. As stretching continued through the Miocene, thick evaporites formed in the periodically isolated proto-oceanic trough. During the Pliocene to Holocene, the Red Sea has accumulated pelagic foraminferal-pteropod oozes in deep water.

At the transition from rift basin to youthful ocean basin subsidence commonly outpaces sediment supply, leading to the deposition of a number of distinctive facies associations indicative of sediment starvation:

- *Evaporites*: The intermittent connection of developing rifts with the sea during the incipient stage provides ideal conditions for the formation of thick evaporites. Such evaporites occur along the margins of the Atlantic Ocean (Emery 1977; Rona 1982) and under the Red Sea (Lowell and Genik 1972);
- *black organic-rich shale:* High organic productivity and restricted marine circulation may allow the preservation of organic-rich shales. Such conditions are likely to prevail where youthful ocean basins contain submarine sills restricting the throughput of water;
- *pelagic carbonates*: In new ocean basins with little clastic supply, deep water pelagic carbonate facies may directly overlie the foundered prerift "basement" or newly created seafloor. The faulted basement topography controls the type of deposit, with uplifted fault block edges and seamounts accumulating shallow water carbonates, and intervening troughs being the sites of fine-grained pelagic sedimentation. This pattern of sedimentation related to fault block shoulders

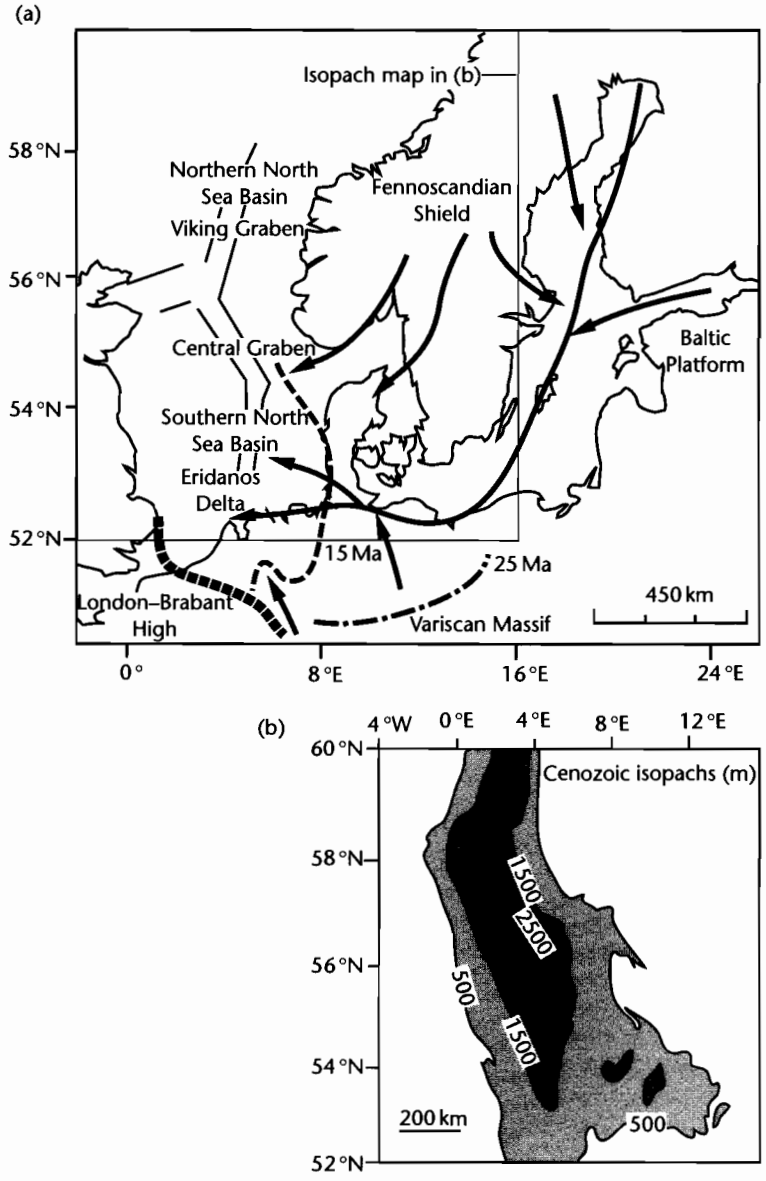

Fig. 8.53 Postrift stratigraphy in the southern North Sea is dominated by megaclinoforms produced by delta progradation related to major river systems draining Europe, such as the Eridanos delta (after Overeem et al. 2001). (a) Drainage system for the Eridanos delta, with the shoreline shown at 25 Ma and 15 Ma; (b) Cenozoic isopachs (excluding Danian) in the North Sea (after Huuse and Clausen 2001). Reproduced courtesy of Blackwell Publishing Ltd.

and troughs has been interpreted from the Triassic–Jurassic of the Tethyan realm of southern Europe. By the Late Jurassic, most of the fault blocks had been buried beneath radiolarites, red marls, and fine-grained pelagic white limestones (Bernoulli and Jenkyns 1974).

8.6.1.5 Passive margins

The formation of juvenile oceanic spreading centers, as in the 20 Myr-old Red Sea–Gulf of Aden, and then mature (<40 Myr) ocean basins is accompanied by the development of passive margins on the adjacent stretched continental lithosphere (Fig. 8.54) (review in Bond et al. 1995). Fully developed passive margins, such as those bordering the Atlantic Ocean, are characterized by extensional faulting, large-scale gravitational tectonics (slumps, slides, glide-sheets) and salt tectonics (§3.2.2). Extensional faulting dies out in the postrift phase with only minor reactivation of older normal faults. Growth faults are common in areas of high sedimentation rate (e.g., off the Niger delta, African coast). Gravitational mass movements, from small slumps to gigantic slides, are very important during the postrift drifting phase. The continental slope and rise off southwestern and southern Africa was subject to major slope instability during the Cretaceous and again in the Tertiary (Dingle 1980). The slide units are over 250 m thick and can be traced for 700 km along strike and for nearly 50 km down paleoslope. The recent 3500 km^3 Storegga slide (8150 yr BP) off the Norwegian margin (Bondevik et al. 1997) is a reminder of the on-going gravitational instability of continental margins.

Deep seismic reflection images of continental margins show a strongly elevated Moho, tilted extensional fault blocks with wedges of syn-rift sedimentary rocks, and an overlying, onlapping postrift stratigraphy. The Atlantic margin of Iberia shows all of these features (e.g., Pickup et al. 1996). The sediment supply to the passive margin prism comes principally by erosion of the continent by rivers, but significant quantities of sediment may be accreted to the lower continental slope by thermohaline current-driven drifts. Major river systems build out large embankments and submarine fans that may extend directly onto oceanic crust, as in the case of the Amazon fan.

Evaporites typify the closed lake basins of the rift stage and the first marine incursions during the incipient ocean phase of the proto-oceanic trough. When buried under an overburden of passive margin sediments these evaporites become mobile, producing diapirs. The Brazilian continental margin and the western Grand Banks, Newfoundland show examples of major diapiric activity (Fig. 8.54).

The Atlantic margin shows great variety in the nature of the passive margin prograding wedge (Fig. 8.54). The Senegal margin of western Africa contains a thick carbonate bank extending over the stretched continental crust. Further to the SE the Niger has built a thick deltaic clastic wedge, provoking growth faulting and mud diapirism. Further south off Gabon and remote from the Niger delta, oceanic muds overlie thick diapirs of evaporite. Off the coast of southwestern Africa a "normal" siliciclastic margin exists with seaward prograding clinoforms reaching far out into the basin and overlying the oceanic crust. This latter type is also common to the highly sediment-nourished North American Atlantic margin, where a well-developed coastal plain and continental shelf extend to 200 m water depth, with a continental slope descending to the abyssal plain of the Atlantic Ocean at water depths in excess of 4 km.

8.6.2 Basins related to convergent plate motion

8.6.2.1 Morphological and tectonic elements at arc-related margins

The main components of convergent arc-related systems are, from overriden oceanic plate to overriding plate (Dickinson and Seely 1979) (Fig. 8.55),

- An *outer rise* on the oceanic plate recognized as an arch in the abyssal plain. This is the flexural forebulge of the descending oceanic plate (§3.1);
- a *trench* or deep trough, commonly >10 km deep situated oceanward of the arc (review in Underwood and Moore 1995). The sediments of trenches are dominated by fine-grained turbidites and pelagic deposits. The bathymetric expression of the trench much depends on the sediment supply into it and, associated with this, the rate of encroachment from the arc of the accretionary wedge. The trench is the bathymetric expression of the deflected (flexed) oceanic plate (§3.1);
- a *subduction complex* composed of tectonic stacks of fragments of oceanic crust, its pelagic cover and arc-derived turbiditic sediments, together with *perched* or *accretionary basins* ponded on top of the accretionary wedge. The subduction complex makes up the inner slope of the trench. Where accretion rates are high, the

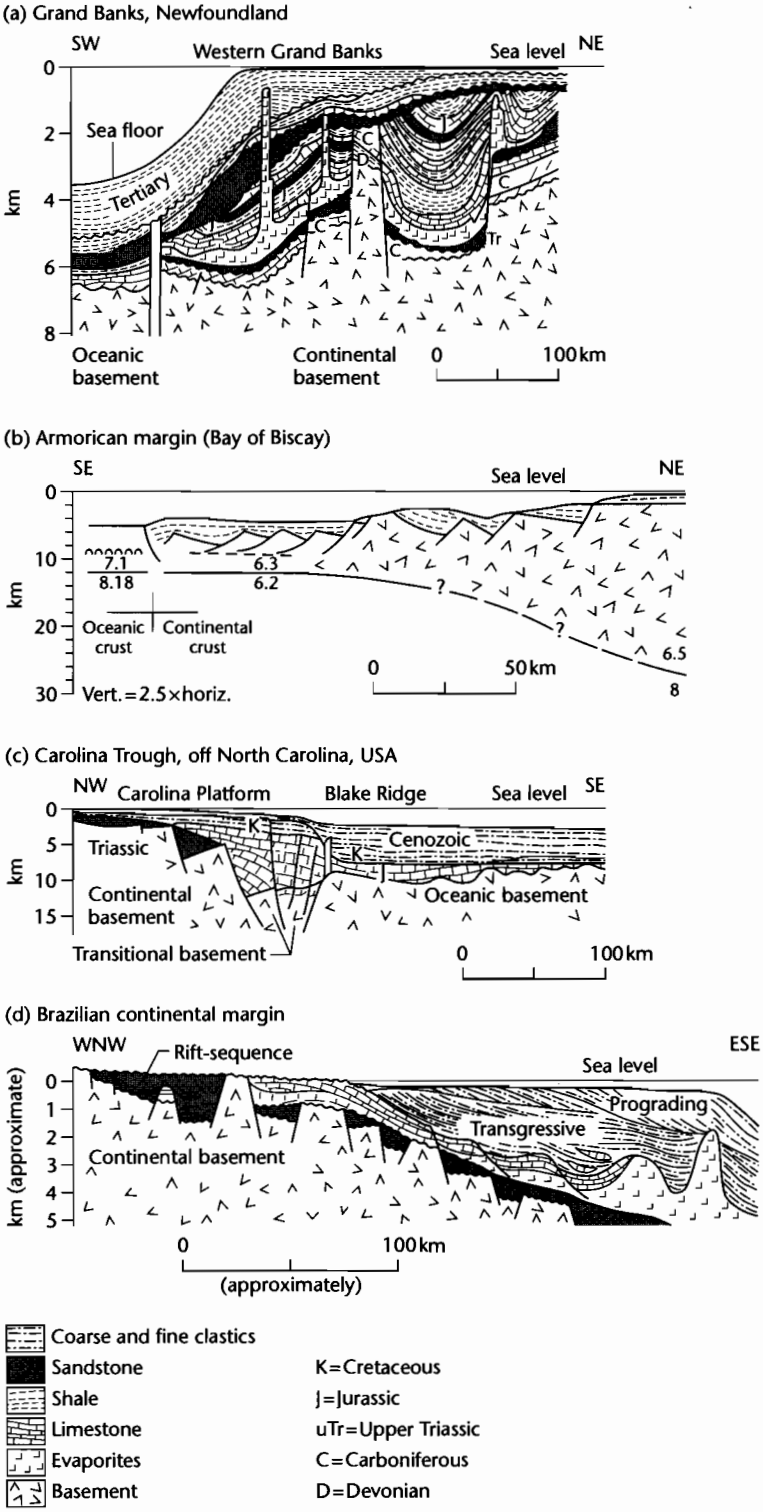

Fig. 8.54 Types of passive margin stratigraphy around the Atlantic Ocean. (a) The sediment-nourished margin of Grand Banks, Newfoundland shows complex unconformities and salt diapirism originating from the Jurassic; (b) The sediment-starved Armorican margin (Bay of Biscay) retains deep water depths; (c) Carolina Trough, eastern US seaboard has a thick Jurassic carbonate bank extending onto oceanic basement; (d) Brazilian continental margin shows salt diapirism originating in the Lower Cretaceous and prograding clastic wedges. Modified after Miall (1984).

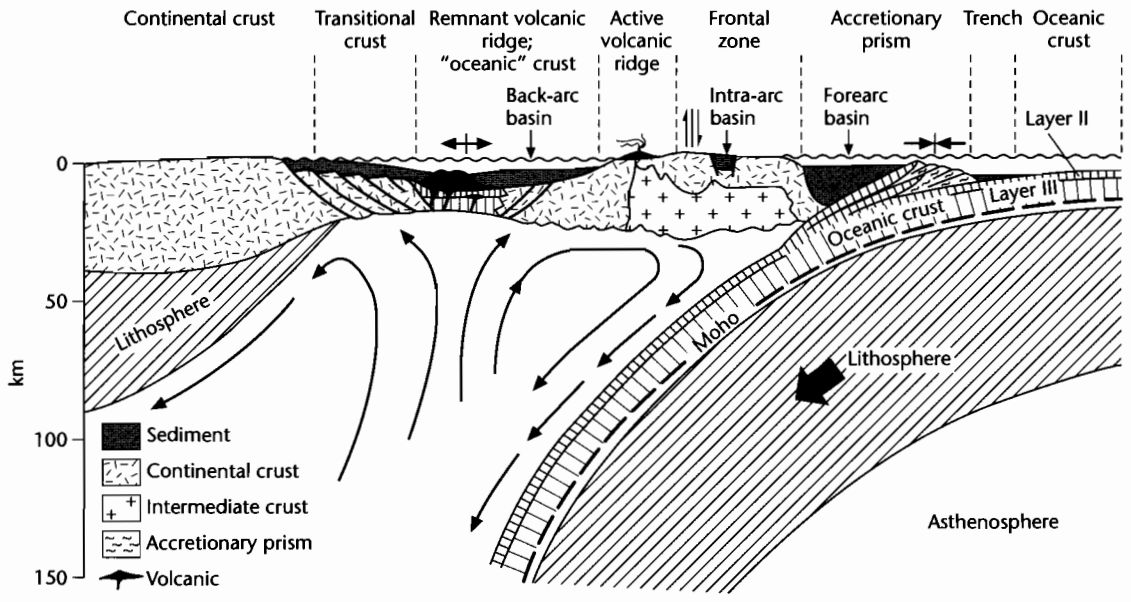

Fig. 8.55 A convergent ocean–arc boundary showing the location of the trench, accretionary wedge, forearc basin, intra-arc and backarc basins. Modified from Dickinson and Seeley (1979). The intra-arc or intra-massif basin and the forearc basin both contain deep marine to nonmarine sediments. The accretionary basin on the subduction complex contains tectonic slices of abyssal plain, slope and trench deposits together with ophiolites and metamorphics.

subduction complex may rise to shelf depths or even become emergent;

- a *forearc basin* between the ridge or terrace formed by the subduction complex and the volcanic arc (review in Dickinson 1995);
- the *magmatic* arc caused by partial melting of the overriding plate and possibly subducted plate when the latter reaches between 100 and 150 km depth. The volcanism is predominantly andesitic. Small intra-arc basins may form by extensional or strike–slip tectonics or in collapsed calderas (Smith and Landis 1995);
- the *backarc* region floored by oceanic or continental lithosphere (review in Marsaglia 1995). Where the lithosphere is oceanic, the backarc region typically undergoes extension. Backarc basins are some of the most rapidly extending regions of the Earth's crust today, a prime example being the Aegean Sea of the eastern Mediterranean. Where the lithosphere is continental, as in Andean-type margins, the backarc (or retroarc) region is typically a zone of flexural subsidence related to major fold–thrust tectonics along the arc boundary. These retroarc basins are therefore discussed in the section below on foreland basins.

8.6.2.2 Brief outline of ideas on kinematics of arcs

Molnar and Atwater (1978) first attempted to answer the question of why some convergent margins consist of oceanic arcs and extensional backarcs and some consist of magmatic arcs on continental crust with active backarc compression (Cordilleran-type). These two possibilities are exemplified by the western and eastern margins of the Pacific Ocean respectively (Tamaki and Honza 1991) (Fig. 8.56).

In the western Pacific the convergent margins are generally subducting oceanic lithosphere of Mesozoic age (i.e., ~100 Ma) and backarc extension is widespread. In the eastern Pacific the subducting lithosphere is much younger (<50 Ma). Here the arcs are located on the overriding continental plates, with fold–thrust belts and retroarc foreland basins in the backarc region. Since oceanic lithosphere cools and thickens with age, the older Mesozoic lithosphere of the western Pacific should be more gravitationally unstable than the <50 Ma lithosphere of the eastern Pacific. The older lithosphere should therefore subduct more rapidly and may exceed

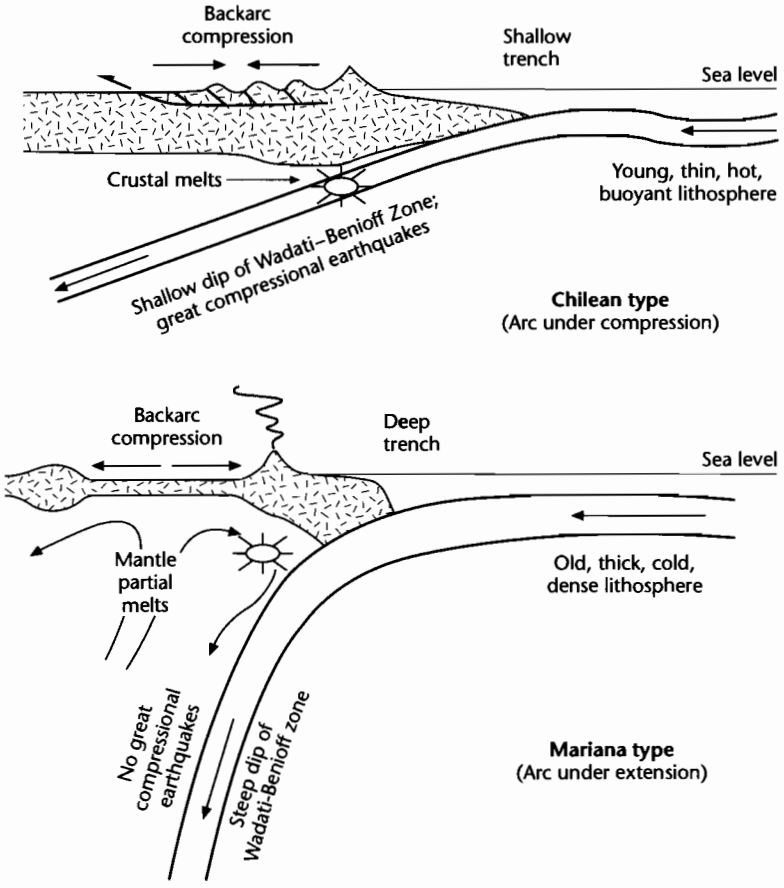

Fig. 8.56 End-member types of subduction zones, based on the age of the lithosphere being subducted, after Uyeda and Kanamori (1979) and Stern (2002). Reproduced courtesy of American Geophysical Union.

the convergence rates of the plates. This should cause an oceanward migration of the subducting hinge together with the forearc elements. This process has been called *roll-back* (e.g., Dewey 1980). It leads to extension in the region behind the rolled-back forearc, that is, backarc spreading. Others believe that backarc extension is related to secondary mantle convection above the subducted oceanic plate (Fig. 8.55) (Toksöz and Bird 1977; McKenzie 1978b).

Dewey (1980) suggested that there are three families of arc-systems. (i) *Extensional arcs* where the velocity of roll-back exceeds the oceanward velocity of the overriding plate, producing backarc extensional basins. As the arc migrates oceanward the forearc region becomes isolated from continental sediment sources and consequently is starved of major sediment supply. Examples are the Mariana and Tonga arcs, eastern Indonesia, (ii) *neutral arcs* where there is a balance between the rates of roll-back and oceanward movement of the overriding plate, producing well-developed subduction complexes but no backarc extension. Examples are the Alaska–Aleutian and Sumatran (western Indonesia) arcs, and (iii) *compressional arcs* where the subducting crust is young and the velocity of roll-back is low. This places the forearc region in compression, causing thrusting in both overriden oceanic and overriding continental crust. Examples are the Canadian–western USA Cordillera and the Peruvian Andes.

Arc behavior may change through time as the age of the subducted oceanic lithosphere changes. If the age of the subducted oceanic lithosphere gets progressively older for example, backarc basins may form, then be

closed and margins change from western Pacific type to Cordilleran type.

8.6.2.3 Continental collision – basic scenarios

Suturing of two continental plates produces a complex amalgam of intense structural deformation, regional metamorphism, plutonism, and basin formation (see summaries in Dewey 1977; Hsu 1983; chapters in Ingersoll and Busby 1995). The ocean closing process may involve a number of variations in the manner of continent–continent docking: (i) the continental plate may initially collide with an arc–backarc system before continent–continent suturing, causing inversion of extensional backarc basins, and choking of subduction complexes with continental fragments, (ii) the continental plates may compress a number of microplates in the collision zone, and (iii) the collision may be highly irregular or oblique, triggering diachronous orogenic activity and major strike–slip displacements. The lithospheric shortening, thickening, metamorphism, and plutonism involved in continental collision is accompanied by the formation of sedimentary basins in a number of settings. Foreland basins form both in front of (pro- or peripheral foreland basins) and behind (retro-foreland basins) the overriding plate. Intermontane basins are found within the megasuture. Extensional and strike–slip basins are located in shear zones produced by "escape tectonics" from the collision.

8.6.2.4 Foreland basins (peripheral and retroarc types)

In the simplest terms foreland basins develop at the front of active thrust belts where the bulk transport direction is towards the evolving basin. Because the thrust load is inherently mobile the foreland basin itself becomes involved in the deformation. To what extent the basin becomes dissected or becomes completely detached depends on a number of variables including the propagation rate of the thrust tips, availability of subsurface easy-slip horizons underlying the basin, and the angle of convergence. The foreland basin system (DeCelles and Giles 1996) contains four depositional zones (Fig. 8.57):

- Basins that rest on moving thrust sheets as a *thrust-sheet top* (Ori and Friend 1984) or *piggy-back basin*, which receives sediment from the eroding orogenic wedge (Fig. 8.58);
- a basin ahead of the active thrust system in a *foredeep*, which is supplied with sediment from both the continental foreland and the orogenic wedge (Fig. 8.58);
- sediment may also accumulate on the flexural forebulge if accommodation is available, for example because the foreland lithosphere is submerged below sea level as a result of negative dynamic topography (§5.2)
- a shallow, broad backbulge basin filled with shallow marine and continental sediments; ongoing convergence should cause the backbulge depozone to be uplifted and eroded in the flexural forebulge.

Individual foreland basins may contain examples of these four depozones, but foredeep and thrust-sheet-top basin-fills are by far the most common. In the North Alpine Foreland Basin of Switzerland (Allen et al. 1991; Sinclair 1997) the first clastic wedges (Early Oligocene), composed essentially of turbidites, were shed partly into ponded basins located on top of thrust sheets and partly overspilled into foredeeps. As the foreland basin evolved through the Oligocene, thrust-sheet-top basins became far less conspicuous features of the inner margin of the basin. Postdepositional tectonics (Late Miocene–Pliocene) detached the entire basin in western Switzerland, using Triassic salt as an easy slip horizon, as deformation progressed into the Jura province (Homewood et al. 1986).

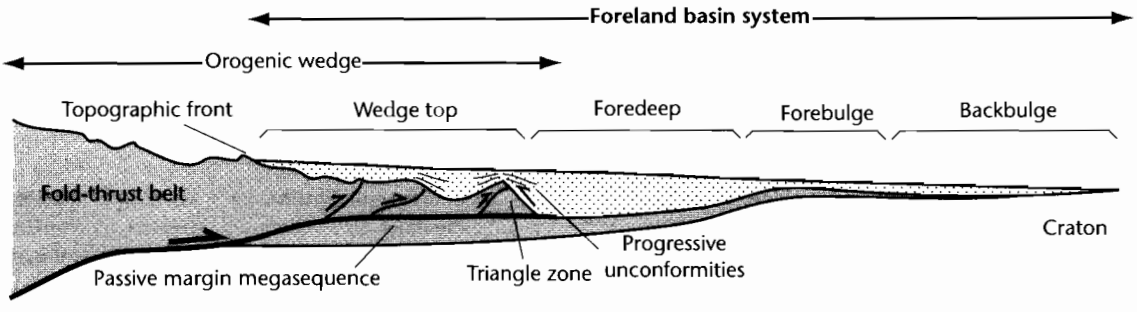

Fig. 8.57 The four depositional zones of a foreland basin system as envisaged by DeCelles and Giles (1996).

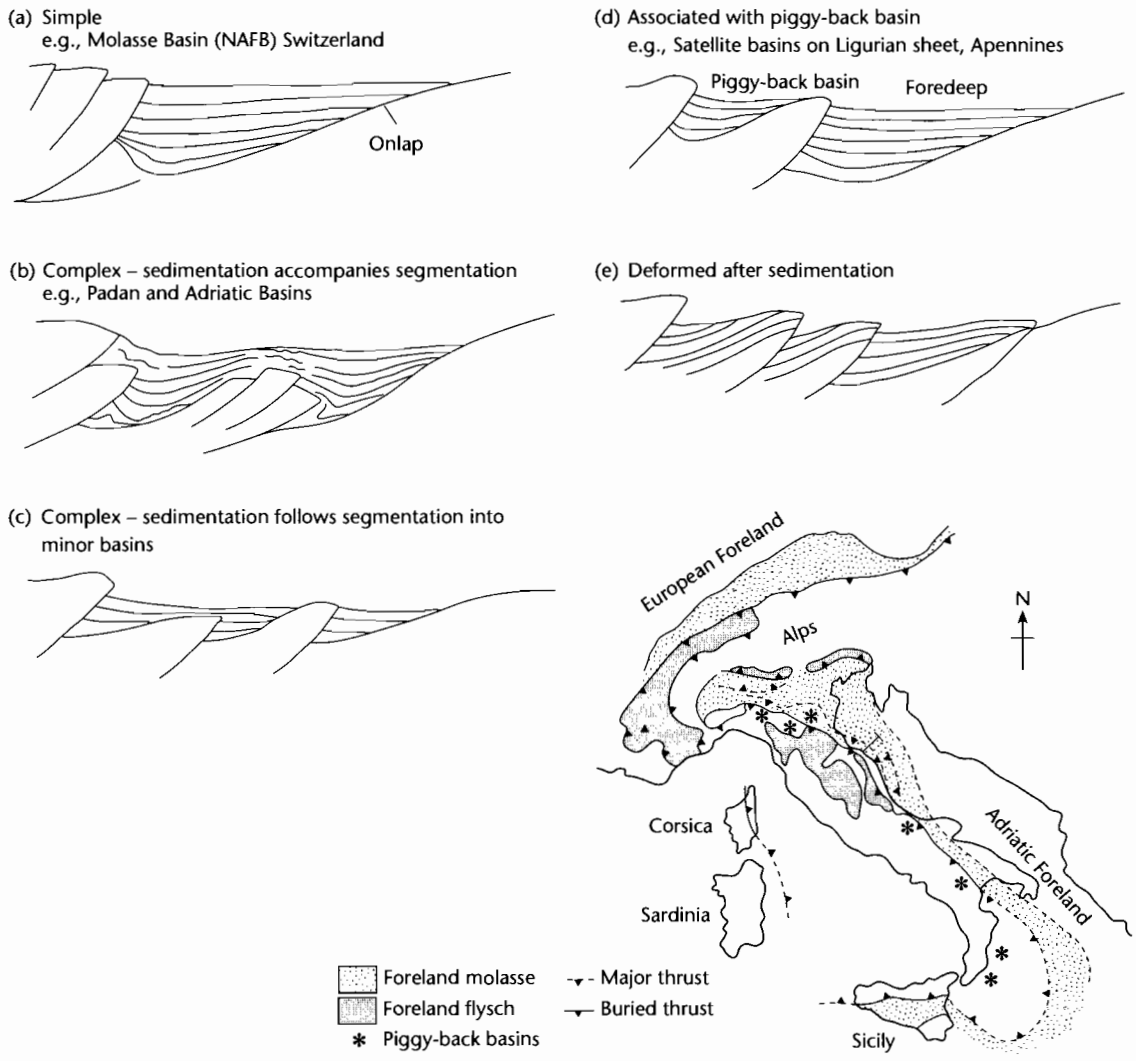

Fig. 8.58 Foreland basin–thrust belt interactions, based mainly on seismic records from the Apennines and forcland of Italy (after Ricci-Lucchi 1986). Basins may bc *simple*, asymmetrical wedges with stratigraphic onlap onto the foreland plate (a). Basins may be *complex* as a result of segmentation during thrusting. Some complex basins were segmented contemporancously with sedimentation (b), whereas others were dcformed and then passively draped with sediment over the thrusted basement topography (c). The minor basins may be subequal or of markedly different size and shape. Foredeeps may be associated with distinct thrust-sheet-top or piggy-back basins (d). Forcland basins may also bc deformed after sedimentation, leading to erosion of part of the foreland basin successions (e). Inset shows location of main foreland basin depocenters and satellite basins in Italy and thc Adriatic.

A lucid picture of a linked system of inner thrust-sheet-top basins and outer foredeeps is provided by the Apenninic chain of Italy (Ricci Lucchi 1986 for synthesis). The entire system of basins migrated eastwards onto the foreland. Scdimentation was initially dominated by turbidites and some hemipelagics. As deformation continued, the inner thrust-sheet-top basins became uplifted at the end of the Miocene and cannibalized to provide erosional detritus for the foredeep. Sediments range from continental coarse clastics to shelfal mixed carbonate-

siliciclastics and turbiditic deep-water sandstones. The Apenninic foreland basin depocenter has now extended into the Adriatic Sea where penecontemporaneous thrust deformations have produced submarine structural culminations. These seafloor highs have been subsequently denuded by slope failure and submarine erosion (Ori et al. 1986). Three depositional seismic units have been recognized in the Plio-Pleistocene of the Adriatic section of the foreland basin comprising initially turbiditic and hemipelagic deposits and subsequently deltaic deposits shed from the Apennines and Southern Alps.

Tectonics have a primary influence on sediment dispersal patterns. Uplifting thrust fronts may not act as major sediment suppliers but may instead form barriers to basinward sediment transport. This is well illustrated in the Miocene of the Southern Pyrenees. Alluvial dispersal patterns in the foreland basin south of the Pyrenees are controlled by the position of the frontal and lateral ramps of the thrust front (Fig. 8.59). The apices of major fluviatile systems are located at structural lows or re-entrants in the thrust front, whereas small, locally developed fans with highly restricted drainage basins typify the structural salients in the thrust front (Hirst and Nichols 1986). This same bimodal picture of small, locally sourced fans coexisting with large megafans sourced from deep within the orogen is also found in the Andes (Horton and DeCelles 1997) and Himalayas (Gupta 1997).

Structural re-entrants are commonly provided by lateral or oblique ramps or through-going strike–slip faults unrelated to the boundaries of thrust sheets. They act as conduits for the removal of erosional detritus from the orogenic belt to the foreland basin, and if they traverse the basin itself can be responsible for large thickness variations in the sedimentary fill. Transverse faults, such as the Sillaro Line and Forli Line had a strong influence on sedimentation in the Apennines. The Sis paleovalley is an example from the Southern Pyrenees (Vincent 2001).

Foreland basins contain a gross stratigraphic evolution related to the geodynamical controls on subsidence and sediment supply. The oldest deposits of foreland basins are commonly predominantly fine-grained, often turbiditic sediments that accumulated in sub-shelf water depths, which pass distally into shallow water carbonates deposited close to the flexural forebulge (Dorobek 1995; Sinclair 1997; Allen et al. 2001). The later deposits of foreland basins are, in contrast, predominantly shallow-water or continental and typify the term "Molasse." This kind of vertical megasequence is found in the North Alpine Foreland Basin (NAFB) of Switzerland (Matter et al. 1980; Sinclair et al. 1991; Allen et al. 1991; Schlunegger et al. 1997a, b) (Fig. 8.60) in the form of a basal deepening-up trend, followed by two shallowing-upwards megasequences. The shoreline unit at the top of the Lower Marine Molasse (Fig. 8.60) can be thought of as the pivot point between an early *underfilled* stage (Covey 1986) and a later steady-state stage (see §8.3.1). During the underfilled stage the topography of the orogenic wedge was most likely relatively subdued, sediment delivery rates were low and the orogenic advance rate relatively high, which collectively caused deep-water conditions in the foreland basin (Sinclair and Allen 1992). After the mountain belt had grown to a steady state, rapid erosion counterbalanced tectonic uplift, the advance rate was slow, and the basin was filled to the spill point with detritus. During this phase any excess sediment was exported from the foreland basin by fluvial and/or shallow marine processes.

Retroarc foreland basins such as the Cretaceous Rocky Mountains foreland basin in western USA and the series of basins east of the Andes do not fundamentally differ from peripheral foreland basins. Their main distinguishing characteristic is that they commonly evolve from regions of backarc extension, and the composition of the sedimentary fill reflects the large amounts of plutonic and volcanic rocks in the orogenic belt. Excellent examples are the Magallanes Basin of Argentina (Biddle et al. 1986), the basins of the northern Argentinian Precordillera, such as the Bermejo Basin (Cardozo and Jordan 2001) and the Central Andean foreland basin system of eastern Bolivia, northernmost Argentina, Paraguay and southwestern Brazil (Horton and DeCelles 1997).

Key processes in the foreland that affect sedimentation are the reactivation of crystalline basement uplifts, such as the Laramide structures in the Rocky Mountain area of North America (Beck et al. 1988) and the Sierras Pampeanas of Argentina (Jordan and Allmendinger 1986). Basement grabens in the foreland plate may be inverted during compression, such as the Birmingham Graben during the Lower Paleozoic Appalachian orogeny (Bayona and Thomas 2003), or the foreland plate may be faulted by the outer arc extensional stresses caused by flexure (Bradley and Kidd 1991). These are examples of important effects superimposed on the larger wavelength first-order signature of flexure.

8.6.2.5 Ocean trenches and accretionary basins

Ocean trenches are one of a series of sedimentary basin types found at convergent arc-related or ocean–continent

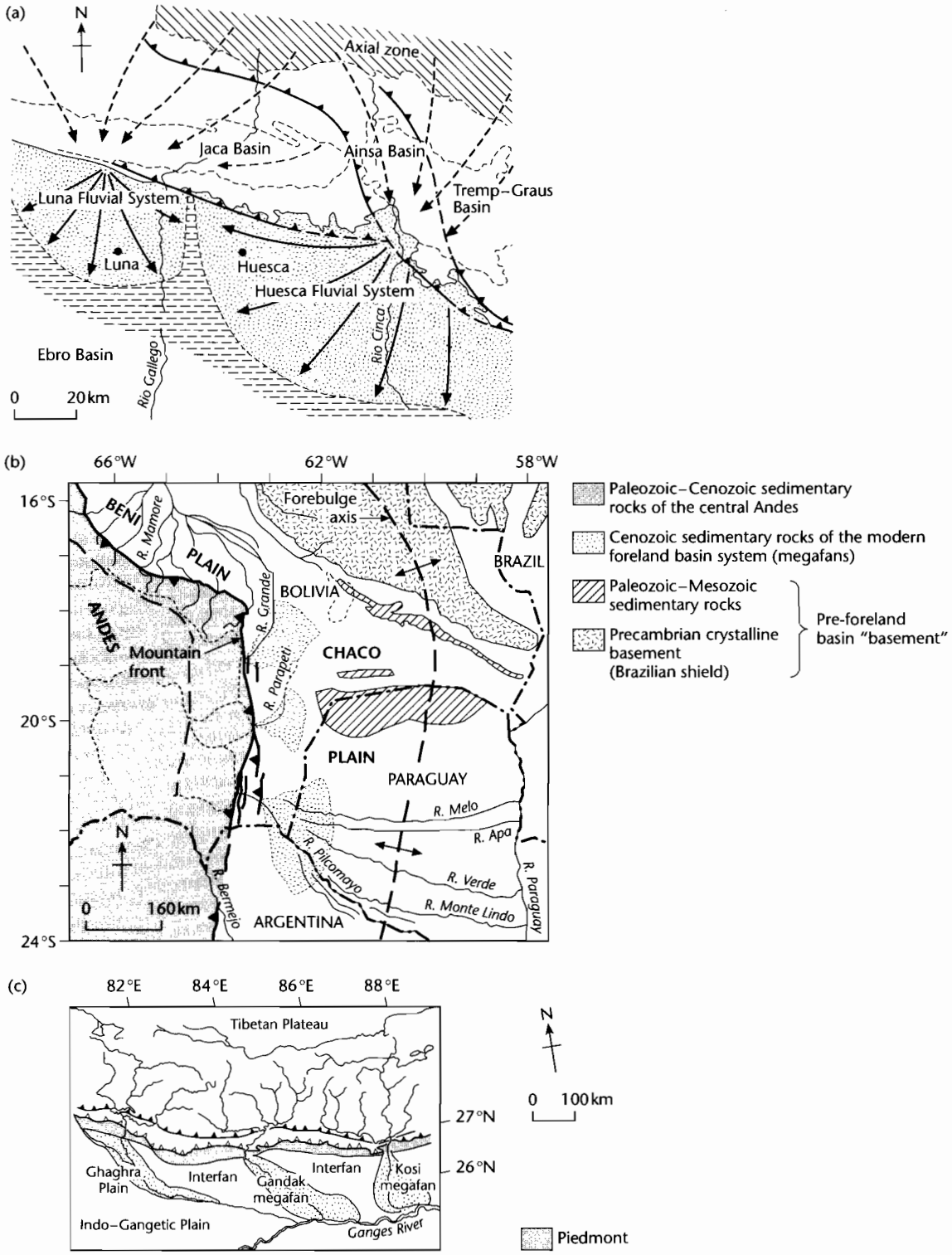

Fig. 8.59 Sediment dispersal patterns by rivers at mountain fronts. Large systems draining deep into the axial zones of orogenic belts break through the mountain front at re-entrants, producing large, low-gradient fans and megafans. Between the megafans are small, catchment–fan systems with local catchments. (a) Southern Pyrenees (Hirst and Nichols 1986), (b) Andes (Horton and DeCelles 1997), and (c) Himalayas (Gupta 1997). Note large variations in scale. (b), (c) Reproduced courtesy of Geological Society of America.

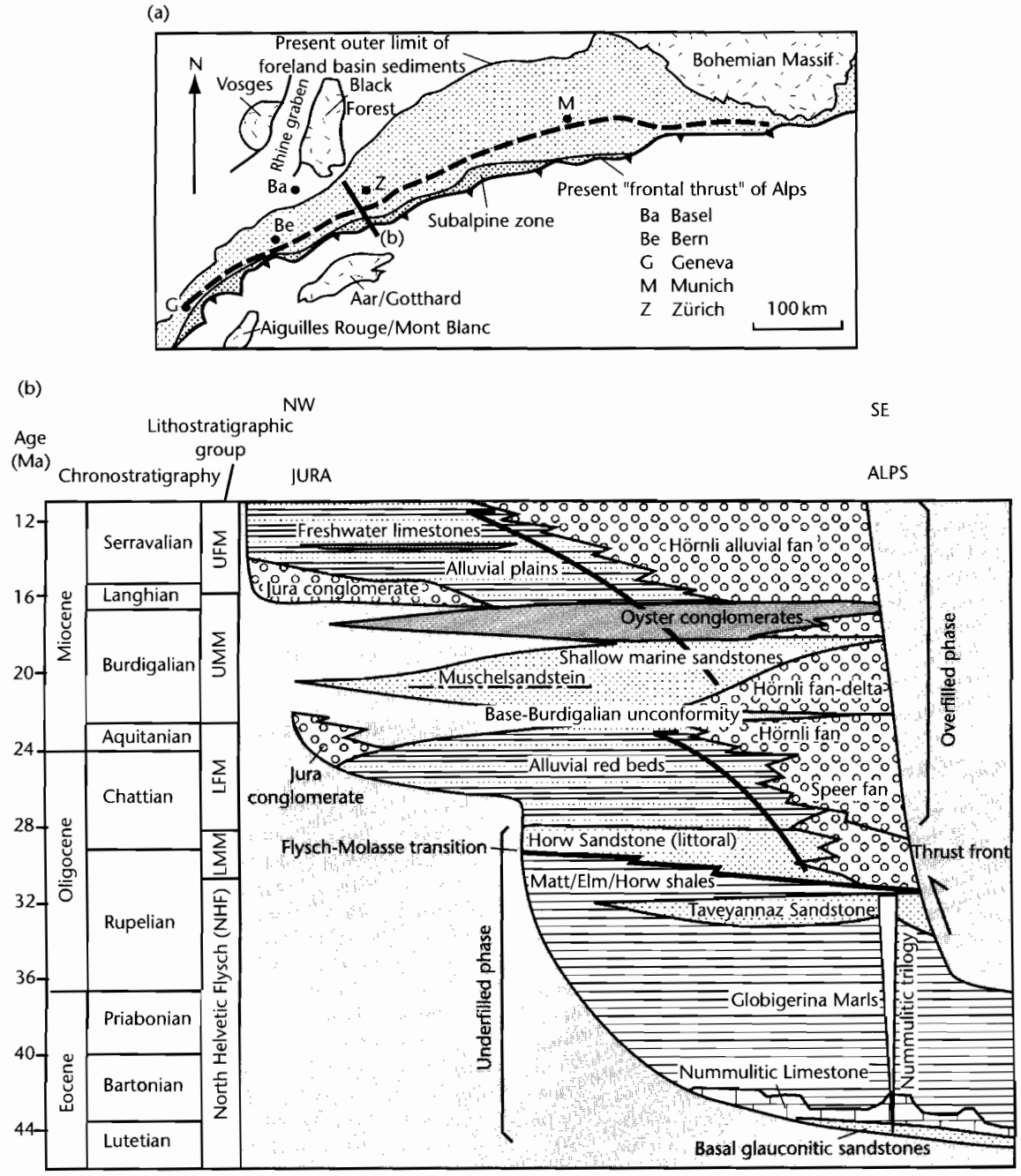

Fig. 8.60 The stratigraphy of the North Alpine Foreland Basin along a transect passing through Zürich, Switzerland (modified from Sinclair et al. 1991). The stratigraphy is made of a basal deepening-up sequence from shallow water Nummulitic Limestones to hemipelagic marls and turbidites derived from the Alpine orogen (the Nummulitic trilogy), followed by two grand shallowing-up and coarsening-up cycles. Coarse clastic wedges fringe the Alpine thrust front, whereas the feather-edge of the basin along the Jura margin was relatively passive, with the exception of some local pockets of conglomerate.

boundaries. Here we draw the distinction between: (i) *trenches* situated on the downbent oceanic lithosphere, (ii) *accretionary basins* perched on the accretionary subduction complex, (iii) *forearc basins* located between the arc and the subduction complex, and (iv) *backarc basins* found on the landward side of the arc (Fig. 8.55).

The association of *trench* and *accretionary basins* perched on the subduction complex of accreted slices of oceanic basement and cover is mechanically analogous to the foredeeps and thrust-sheet-top basins of continental collision zones. Although the mechanics may be similar between the two cases, the sedimentary fills are markedly different.

The longitudinal supply of sediment from the Bengal Fan in the north has produced marked differences in the nature of the trench and subduction complex around the Sunda arc. In Java, remote from the sediment source, the trench is 7 km deep and the accretionary subduction complex is under 1–3 km of water. Off northern Sumatra the trench is at 4 km depth and the subduction complex is partly emergent (Hamilton 1979). High sedimentation rates therefore appear to favor the growth of submarine fans or accretionary wedges completely across the trench, whereas sediment-starved margins have deep trenches with well-developed bathymetric profiles. Some active accretionary complexes can accumulate sediment in shelf and coastal environments, such as off the Alaskan arc, in the Makran, Pakistan, and Hawke Bay, New Zealand.

8.6.2.6 Forearc and backarc basins

Three types of sedimentary basin occur in the forearc region: (i) the accretionary basins located on subduction complexes mentioned in the previous section, (ii) intra-arc or intra-massif extensional basins, common where a broad forearc region has developed over continental crust, as in the Andes. These elongate basins typically follow volcanic lines or fundamental tectonic lineaments and are filled mainly with nonmarine fluviatile and lacustrine sediments dominated by volcanic constituents, and (iii) large basins located between the subduction complex and the magmatic arc, comprising "*residual*" basins with a basement of stretched continental crust or obducted oceanic crust, and "*constructed*" basins underlain by the landward portion of the subduction complex.

The oldest sediments of "residual" forearc basins are generally deep-water pelagic deposits, whereas those of "constructed" types may be shallower. Submarine fans build into the basins transversely from the magmatic arc. Intra-oceanic forearcs tend to be sediment-starved and remain deep marine, whereas sediment-nourished examples near major continental catchments may rapidly become shallow marine.

Depositional environments in *backarc basins* on oceanic crust are also deep marine, except along their margins where fluviatile, coastal, and shallow marine depositional environments may exist. Karig and Moore (1975) presented a model for the evolution of backarc basins based on the western Pacific examples. Initially, volcaniclastic wedges shed from the arc interfinger with a background of pelagic clays. As subsidence continues and outstrips sediment supply, the seafloor commonly descends below the *carbonate compensation depth* (CCD), so that the more evolved basin accumulates siliceous rather than calcareous clays. The adjacent continent may contribute clastic wedges into the landward edge of the basin.

Backarc extension is less common on continental crust because the arc commonly becomes compressional. However, some continental areas behind convergent ocean–continent boundaries are undergoing or have undergone widespread extension. The Basin and Range province of western USA is an example. The area has been substantially uplifted to a regional elevation of 2 to 3 km and half-graben and graben contain up to 3 km of nonmarine sediment. The Pannonian Basin, located to the south of the Carpathians (Burchfiel and Royden 1982), may also be due to backarc spreading.

8.6.3 Strike–slip basins

The tectonic style and evolutionary sequence of strike–slip (especially pull-apart) basins were discussed in Chapter 6. The sedimentary fills of strike–slip basins have a number of features in common (Miall 2000). Basin geometries are deep but relatively narrow, with high syndepositional relief causing conglomerates and breccias to be banked up against faulted basin margins. Sedimentation rates are rapid. Lateral facies changes are also rapid, so that marginal breccias may pass laterally directly into lacustrine mudstones. Fault movements cause syndepositional unconformities to form in individual basins and different stratigraphies to develop in closely adjacent basins, making correlation difficult. Basin sediments are commonly offset from their source, as may be proved by a mismatching between size of depositional system and drainage area, or between sediment petrography and hinterland geology. In modern basins there may be offsets of geomorphological features such as rivers, alluvial fans, or submarine canyons.

The best known intracontinental transform is the San Andreas system, and one of the best documented pull-

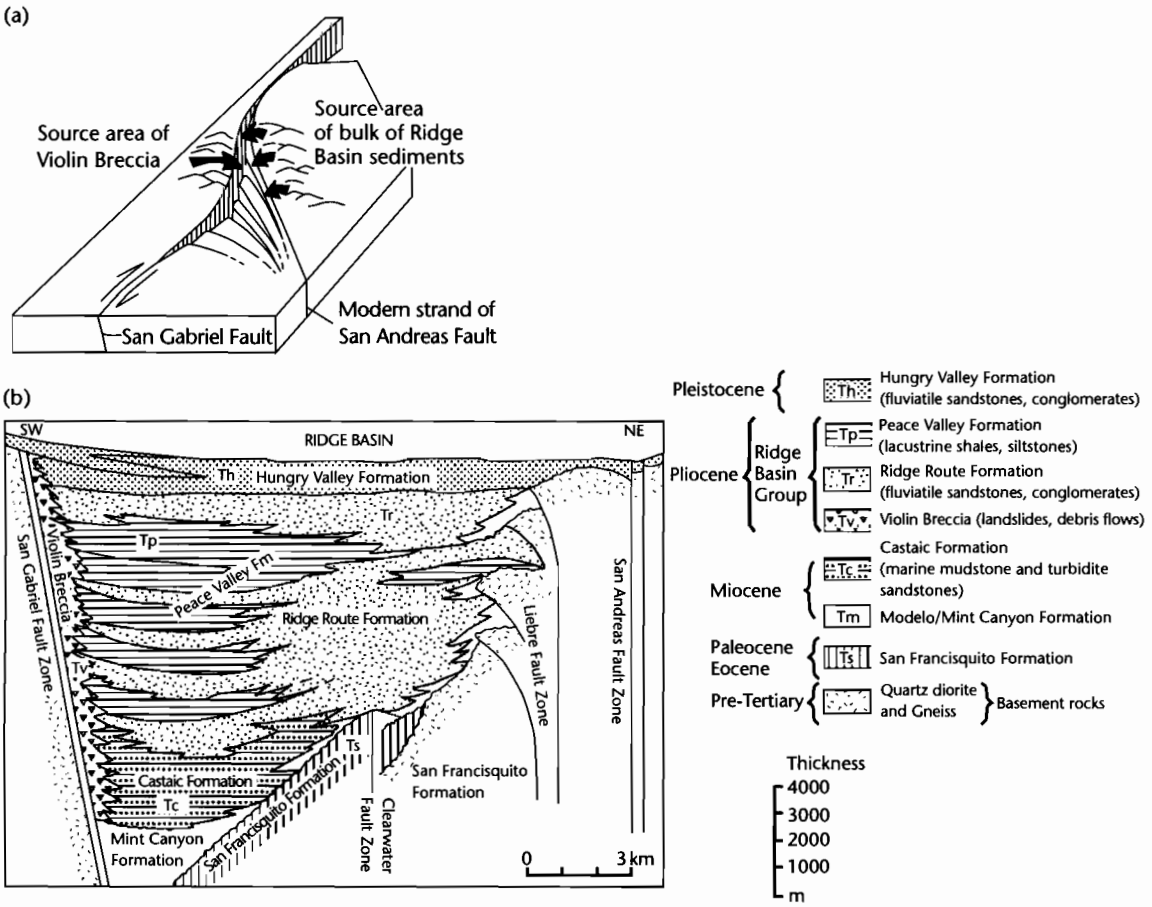

Fig. 8.61 Ridge Basin, California. (a) General tectonic and depositional setting for the Ridge Basin as a pull-apart on the releasing bend of the San Gabriel Fault (Crowell 1974); (b) Generalized cross-section showing the sedimentary facies and principal faults. The fine grained lacustrine depocenters (Peace Valley) and landslide-debris flow breccias (Violin Breccia) occur close to the San Gabriel Fault Zone (after Link and Osborne 1978; Crowell and Link 1982).

apart basins in this system is *Ridge Basin*, California. It shows many of the elements indicated above. The basin was initiated in the Miocene and continued to accumulate sediment during the Pliocene, after which it was uplifted. It contains over 13.5 km of sediment deposited at an estimated rate of 3 mm yr^{-1}, and is located between the San Andreas and San Gabriel Faults (Fig. 8.61). During the Late Miocene the San Gabriel Fault was a major active strand of the San Andreas system. The Ridge Basin formed to the east of a releasing bend in the fault. During the late Miocene–Pliocene over 60 km dextral strike–slip took place along the San Gabriel Fault, but in the Pleistocene slip was transferred to the San Andreas Fault along the northeastern flank of the basin.

The sedimentary fill of the basin (Crowell and Link 1982, Link 1982) is made up of a basal nonmarine unit (Mint Canyon) overlain by the 2.2 km thick, upper Miocene Castaic Formation, consisting of marine mudstones and turbidites. The Castaic Formation is overlain by the 9–11 km thick, mostly nonmarine Ridge Basin Group, with marine deposits in the lowermost 600 m. The Ridge Basin Group comprises marginal breccias along the active western fault scarp (Violin Breccia), central lacustrine deposits, chiefly mudstones (8 km), of the Peace Valley Formation, fluviatile clastic wedges of the Ridge Route Formation (9 km) along the eastern margin of the basin, and a basin-wide, final basin filling of alluvial sands and gravels (1.1 km) of the Hungry

Valley Formation. The marginal alluvial cones and talus of the Violin Breccia were derived from the SW and pass very rapidly (within 1.5 km) into lacustrine shales and siltstones of the Peace Valley Formation, or sandstones of the Ridge Route Formation. The thick clastic wedges of the Ridge Route Formation were shed from source areas to the NE of the basin, but the younger Hungry Valley Formation was derived from the N, NW, and W. This demonstrates the complexity of sourceland switching in strike–slip basins. Dextral strike–slip along the San Gabriel Fault displaced the source region for the Violin Breccia northwestwards with time. As a result, the successive alluvial fans that form the Violin Breccia become younger northwestward, and form an overlapping or shingled pattern. Within the axial part of the basin, sediments were transported southeastward down the axis of the basin concurrently with northwestward migration of the depocenter.

The Ridge Basin has been compared, in terms of its structural and sedimentological development, with the larger Hornelen Basin, Norway, and the smaller Little Sulphur Creek group of basins, southern California (Nilsen and McLaughlin 1985). Each basin is characterized by marginal fans located tight up against the active strike–slip fault, axial lacustrine facies, and stream-flow-dominated fans along the opposite margin. These

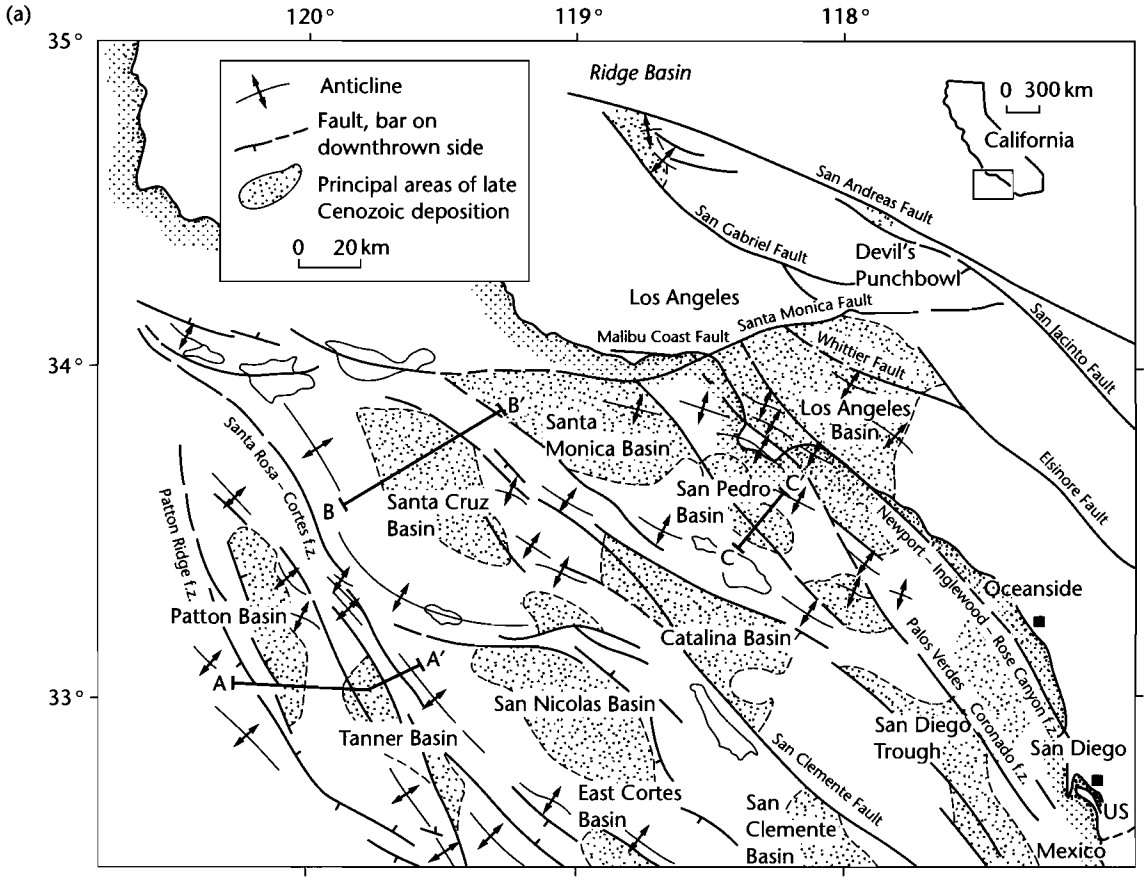

Fig. 8.62 Strike–slip basins of the California Borderland (Moore 1969; Junder 1976). (a) Map view; (b) Interpretations of seismic reflection profiles (Howell et al. 1980). Q, Pleistocene and Holocene sediments: Tp, middle and late Pliocene sediments; Tpm, Miocene and early Pliocene sediments; Tm, early to middle Miocene sediments; Tmo, cherty, calcareous and siliceous shale of upper Oligocene to middle Miocene; Tmv, Miocene volcanics; Kl-To, Upper Cretaceous to Oligocene sediments; TKJ, acoustic basement, probably equivalent to the Franciscan.

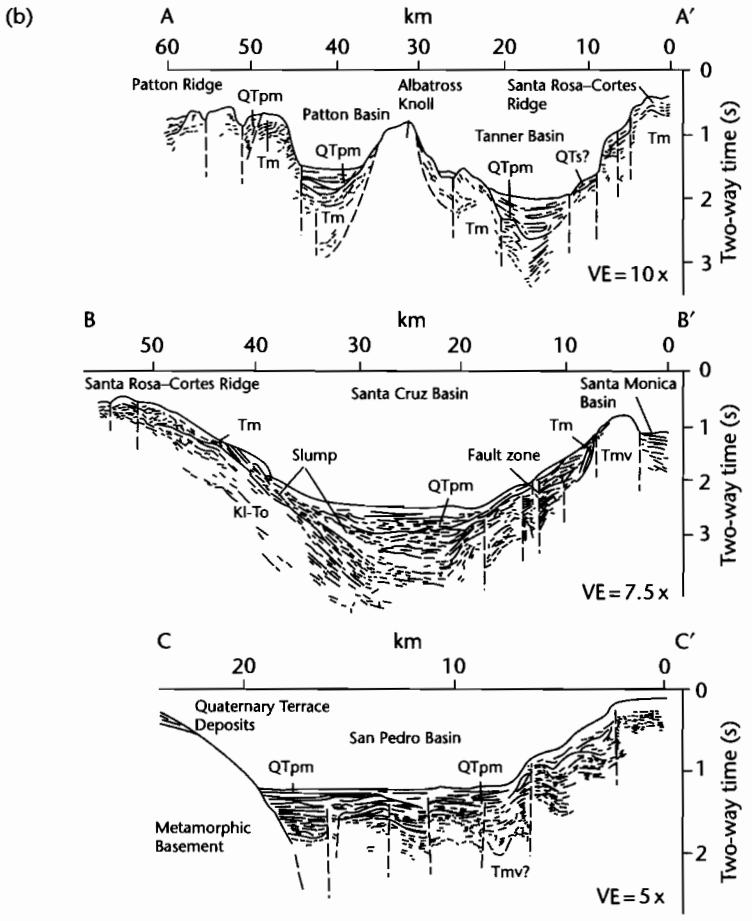

Fig. 8.62 *Continued*

streamflow-dominated fans contribute most of the sediment to the basin, sometimes filling the basin completely and spreading alluvial deposits across to the active fault scarp to interfinger with the talus fans. Rates of deformation, catchment, and fan development are commonly highly asymmetrical in basins of this type (Allen and Hovius 1998).

The present-day submarine equivalents of the Ridge Basin are found in the California Borderland Basins. This area, to the west of the San Andreas Fault, is underlain by an arc complex formed during subduction of the Pacific Plate in the Mesozoic to Early Cenozoic (Howell and Vedder 1981). A large number of small basins filled with submarine fans formed during the Paleogene, and Oligocene dextral strike–slip faulting fragmented the region into *en echelon* ridges and rhomboidal basins (Fig. 8.62). Sedimentation is dominated by turbidites fed from the nearby American coast into a background environment of fall-out of fine-grained terrigenous and pelagic material. The region has several well-studied deep sea fans (e.g., La Jolla, Navy) characterized by important submarine slides (e.g., Sur Submarine slide on Monterey fan, described by Normark and Gutmacher 1988). Sedimentation rates increase towards the coast, so that the Los Angeles and Ventura Basins located close to the continental source contain as much as 8 km of Neogene sediment, whereas the more offshore basins such as the Tanner and Patton Basins (Fig. 8.62) have much reduced sedimentary thicknesses (Howell et al. 1980).

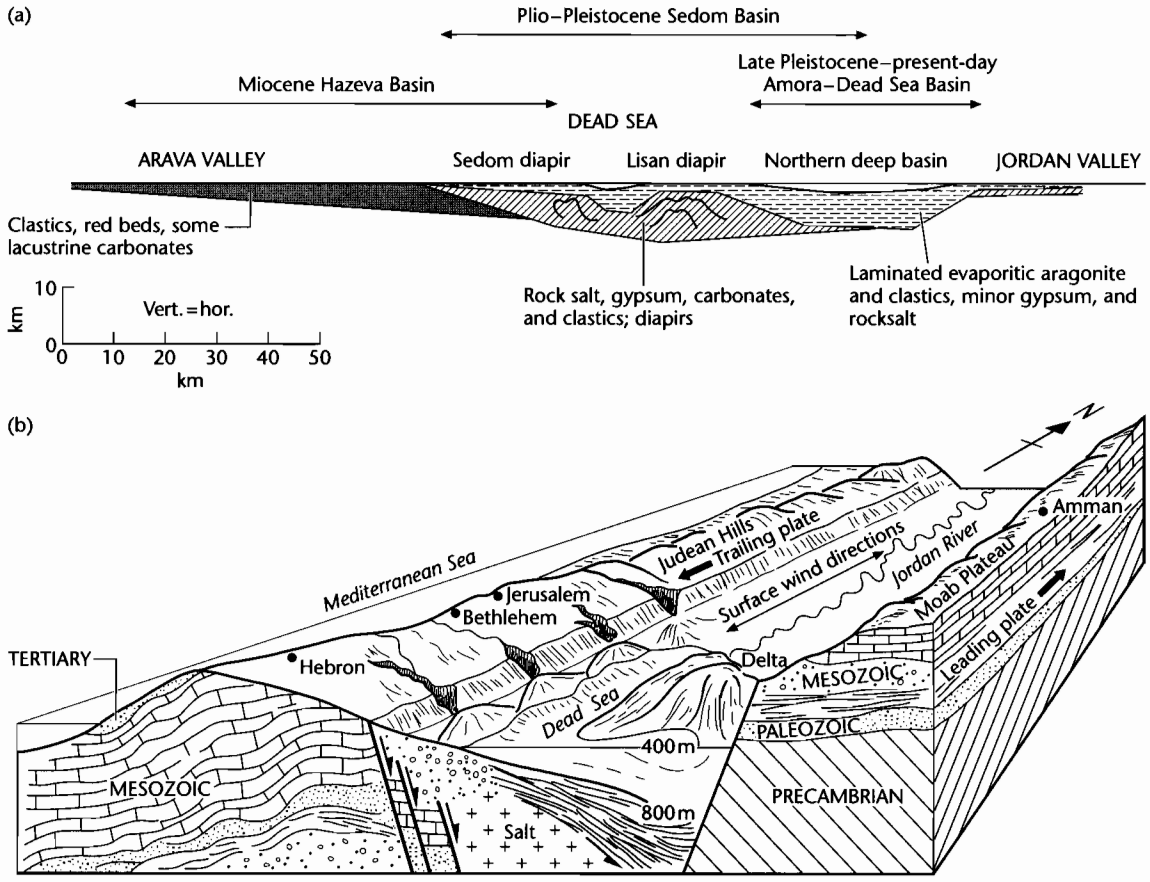

Fig. 8.63 Cross-section (a) and 3-D view (b) of the Dead Sea–Arava depression. (a) shows the northward migration of the basin depocenters. Early Miocene (25–14 Ma) strike–slip of about 60–65 km opened up the Arava Basin, which was filled with about 2 km of red beds during a pause in the strike–slip displacement. Later movement in the last 4.5 Myr has allowed the deposition of >4 km of marine to lacustrine rock salt of the Sedom Formation, followed by 3.5 km of lacustrine evaporitic carbonates and clastics (after Zak and Freund 1981); (b) Today, sediment enters the northern Basin *via* high discharge ephemeral streams feeding fan deltas along the semi-arid western edge of the basin (Judean Hills), and the perennial, axial-flowing Jordan River. The Jordan has a drainage area in a humid region, and deposits a fine-grained delta at its mouth. Autochthonous supply to the lake is of aragonite and gypsum precipitates (Manspeizer 1985).

The sedimentation in a classic pull-apart in an arid climate is well illustrated by the Dead Sea. Movement along the Dead Sea Fault commenced in the Miocene in response to the opening of the Red Sea. It has continued to move up to the present day. The basin contains over 10 km of fluvial clastics, lacustrine limestones, and evaporites. Like the Ridge Basin, depocenters have moved considerably, producing a highly diachronous fill. The Miocene Hazeva Formation consists of continental clastics and some lacustrine carbonates and is found in the Arava Valley in the south. The Pliocene–lower Pleistocene Sedom Formation consists mainly of lacustrine salts, gypsum, carbonates, and some clastics and occurs in the central section. The Pleistocene to Recent Amora and younger formations consist of laminated evaporitic (gypsum) and aragonite sediments which are accumulating today in the modern Dead Sea in the northern sector of the basin (Fig. 8.63) (Zak and Freund 1981).

CHAPTER 9

Subsidence and thermal history

Accuse not Nature, she hath done her part;
Do thou but thine.

(JOHN MILTON, *PARADISE LOST* (1667))

SUMMARY

The burial of sedimentary layers in a basin causes porosity loss, which may be due to mechanical compaction, physicochemical changes such as pressure solution, and cementation. Most procedures used in the study of subsidence in sedimentary basins assume that there is no change in the solid volume during burial, so that mechanical compaction of framework grains due to increasing compression from the overlying sediment-water column solely drives porosity reduction. Despite the fact that this is manifestly not true, quantitative incorporation of the effects of cementation and pressure solution are still in their infancy.

Present-day stratigraphic thicknesses are a product of cumulative changes in rock volume through time. A quantitative analysis of subsidence rates through time, sometimes called *geohistory analysis*, relies primarily on the decompaction of stratigraphic units to their correct thickness at the time of interest. Two other corrections must also be made in order to plot subsidence relative to a fixed datum such as present sea level. These are: (i) corrections for the variations in depositional water depth through time, and (ii) corrections for absolute fluctuations of sea level (eustasy) relative to the present sea-level datum.

The decompaction of stratigraphic units requires the variation of porosity with depth to be known. Some sedimentary formations exhibit a linear relation between porosity and depth but, self-evidently, a linear relationship cannot hold at large depths since porosities would become negative. Estimates of porosity from borehole logs (such as the sonic log) for a wide range of different lithologies suggest that normally pressured sediments exhibit an exponential relationship of the form $\phi = \phi_0 e^{-cy}$, where ϕ is the porosity at any depth y, ϕ_0 is the surface porosity, and c is a coefficient that is dependent on lithology and describes the rate at which the exponential decrease in porosity takes place with depth. There are a number of different formulations of this exponential relationship, with different pre-exponential factors and exponents. The driving force for compaction is the effective stress acting at grain–grain contacts. Since the total lithostatic stress is the sum of the effective stress and the pore fluid pressure, overpressuring of pore fluids trapped in a formation has the effect of inhibiting compaction. This causes strong deviations from the expected porosity–depth curve in the overpressured units. Overpressuring can be predicted from a dimensionless parameter representing the ratio of hydraulic conductivity to rate of sediment accumulation.

Information on changing paleobathymetry through time may come from sedimentary facies and distinctive geochemical signatures, but principally from micropaleontological studies. Benthic microfossils are especially useful. Eustatic corrections are hazardous to apply and a simple transferral from the Vail–Haq curve is not recommended. Correction for the widely accepted long-term eustatic variation of sea level is, however, justified.

The sediment deposited in a marine basin replaces water, and so drives further subsidence of the basement. The exercise of partitioning the subsidence due to tectonics and that due to sediment loading is termed *backstripping*. If the lithosphere is in local Airy isostasy, the decompacted subsidence, corrected for paleobathymetric and eustatic variations, can be simply used to calculate

the tectonic component. This requires the average bulk density of the sediment column as a function of time to be calculated. However, if the lithosphere supports the sediment load by a regional flexure, the separation of the tectonic and sediment contributions is more complex. The flexural loading of the sedimentary basin can be accounted for if both the flexural rigidity and spatial distribution of the sediment load are known.

Subsidence in sedimentary basins causes thermal maturation in the progressively buried sedimentary layers. Indicators of the thermal history include organic, geochemical, mineralogical, and thermochronometric parameters. The most important factors in the maturation of organic matter are temperature and time, pressure being relatively unimportant. This temperature and time dependency is described by the *Arrhenius equation*, which states that the reaction rate increases exponentially with temperature; the rate of the increase, however, slows with increasing temperature because the materials undergoing thermal maturation are used up. The cumulative effect of increasing temperature over time can be evaluated by integrating the reaction rate over time. This is called the *maturation integral*. It can be related directly to measurable indices of burial.

Paleotemperatures are controlled by the basal heat flow history of the basin (which in turn reflects the lithospheric mechanics), but also by internal factors such as variations in thermal conductivities, heat generation from radioactive sources in the continental crust and within the sedimentary basin-fill, regional water flow through aquifers, and surface temperature variation. Thermal conductivity models of the basin-fill can be developed from knowledge of framework mineralogy and porosity. The effect of a heterogeneous basin-fill, assuming a constant heat flow, is an irregular rather than linear geotherm. Radiogenic heat production is greatest where the underlying basement is granitic, and where the basin-fill contains "hot" shales. Radiogenic heat production is particularly important in deep, long-lived basins. Advection of fluids has profound consequences for heat flow in basins and can locally override basal heat flow contributions. Advective heat transport depends on the temperature of the pore fluids but also on rock porosity. Although compactionally driven fluid movement is slow and thermally relatively ineffective, gravitationally driven flow through aquifers is very important. Recharge areas of water in topographically elevated areas around the basin margin, such as in foreland basins and intracratonic sags, displaces basinal brines and strongly affects the temperature history of basin sediments. Major climatic changes of long frequency cause temperature changes to be propagated through the upper part of the basin-fill that may affect thermal indicators.

Formation temperatures can be estimated from borehole measurements, with a correction applied to account for the cooling that takes place during the circulation of drilling fluids. These corrected formation temperatures allow geothermal gradients to be calculated.

Vitrinite reflectance is the most widely used organic indicator of thermal maturity. Other organic and mineralogical indicators are also used. Apatite fission track analysis is now a well-established thermochronological tool, but the diffusion of helium during U–Th decay is a promising emerging technique. Both thermochronometers allow the timing of thermal events as well as the maximum paleotemperature to be assessed.

Vitrinite reflectance measurements plotted against depth – termed R_o profiles – provide useful information on the thermal history of the basin. The "normal" pattern is a sublinear relationship between log R_o and depth, indicating a continuous, time-invariant geothermal gradient. R_o profiles with distinct kinks between two linear segments (doglegs) indicate two periods of different geothermal gradient separated by a thermal event. R_o profiles with a sharp break or jump (offsets) indicate the existence of an unconformity with a large stratigraphic gap. The R_o profile in basins that have undergone continuous subsidence intersect the surface at values of 0.2–0.4% R_o. Inverted basins that have lost the upper part of the basin-fill by crustal uplift and erosion have profiles intersecting the surface at higher values of R_o. The offset of the R_o profile from the "normal" profile can be used to estimate the amount of denudation, but care needs to be taken with the possible effects of thermal conductivity variations in the basin and the correct choice of surface temperature at the time of maximum paleotemperature of the basin-fill.

Studies of present-day heat flows and ancient geothermal gradients suggest that thermal regime closely reflects tectonic history. In particular, *hypothermal* (cooler than average) basins include ocean trenches and outer forearcs and foreland basins. *Hyperthermal* (hotter than average) basins include oceanic and continental rifts, some strike–slip basins with mantle involvement, and magmatic arcs in collisional settings. Mature passive margins that are old compared with the thermal time constant of the lithosphere tend to have near-average heat flows and geothermal gradients.

9.1 INTRODUCTION TO GEOHISTORY ANALYSIS

Improvements in the dating of stratigraphic units and in estimates of paleobathymetry, largely brought about by advances in micropaleontology, have allowed the development of quantitative techniques in geological analysis of sedimentary basins. Van Hinte (1978) termed this quantitative approach *geohistory analysis*. The first qualitative attempts at plotting subsidence/uplift and paleowater depth as a function of time date back at least to Lemoine's *Géologie du Bassin de Paris* published in 1911. Quantitative geohistory analysis was developed in the 1970s, principally in response to a vastly improved commercial paleontological data base.

Geohistory analysis aims at producing a curve for the subsidence and sediment accumulation rates through time. In order to do this, three corrections to the present stratigraphic thicknesses need to be carried out:

- *Decompaction*: present-day stratigraphic thicknesses must be corrected to account for the progressive loss of porosity with depth of burial;
- *paleobathymetry*: the water depth at the time of deposition determines its position relative to a datum (such as present-day sea level);
- *absolute sea level fluctuations*: changes in the paleosea level relative to today's also needs to be considered (see §8.3.4).

Having made these corrections, comparisons between boreholes or other sections are readily made possible. In addition, the subsidence curves give an immediate visual impression of the nature of the driving force responsible for basin formation and development (§9.3.5).

The time–depth history of any sediment layer can be evaluated therefore if the three corrections above can be applied. Such a time-depth history can also be tested from independent methods. These fall into the main classes of organic thermal indicators (§9.7.2), thermochronometric indicators (§9.7.3–9.7.4) and mineralogical thermal indicators (§9.7.5).

The addition of a sediment load to a sedimentary basin causes additional subsidence of the basement. This is a simple consequence of the replacement of water ($\rho = 1000\,\mathrm{kg\,m^{-3}}$), or less commonly air, by sediment ($\rho \sim 2500\,\mathrm{kg\,m^{-3}}$). The total subsidence is therefore partitioned into that caused by the tectonic driving force and that due to the sediment load. The way in which this partitioning operates depends on the isostatic response of the lithosphere (§2.3.2–§2.3.3). The simplest assumption is that any vertical column of load is compensated locally (Airy isostasy). This implies that the lithosphere has no strength to support the load. Alternatively, the lithosphere may transmit stresses and deformations laterally by a regional flexure. The same load will therefore cause a smaller subsidence in the case of a lithosphere with a strength sufficient to cause flexure. The technique whereby the effects of the sediment load are removed from the total subsidence to obtain the tectonic contribution is called *backstripping*. Backstripped subsidence curves are useful in investigating the basin-forming mechanisms (§9.3.5).

Burial history and thermal history can be used to determine the oil and gas potential of a basin and to estimate reservoir porosities. Burial history curves from a number of locations can also be used to construct paleostructure maps at specific time slices. Combined with information on thermal maturity, this can be a powerful tool in evaluating the timing of oil migration and likely migration pathways in relation to the development of suitable traps (see Chapter 10 for fuller discussion).

9.2 POROSITY LOSS DURING BASIN SUBSIDENCE

9.2.1 Porosity loss: mechanical compaction, physicochemical compaction, and cementation

Progressive burial of sediment by overlying layers during basin evolution causes a number of physical and chemical changes to the basin-fill. In this chapter we are primarily concerned with the loss of porosity, increase in bulk density and decrease in stratigraphic thickness that accompany burial, and in the changes resulting from thermal maturation. The implications of basin subsidence for petroleum systems, particularly the generation of petroleum fluids and reservoir quality, are dealt with in Chapter 10.

It is initially important to define some terminology. *Compaction* is the change in dimensions of a volume of sediment as a result of loading, which commonly takes the form of the gravitational load of an overlying column of water-saturated sediment. Compaction is therefore a strain. *Porosity loss* refers to the loss of pore volume that commonly accompanies burial, and may or may not be related to volumetric strains. For example, cementation of a sandstone may result in a loss of porosity but may not affect the volume occupied by the sedimentary rock,

and therefore involves no strain. Compaction and porosity loss are affected by three sets of interrelated processes (Giles 1997):

1 Mechanical compaction, which is the mechanical rearrangement and compression of grains in response to loading;
2 physicochemical compaction due to processes such as pressure solution, which is particularly important in carbonates;
3 cementation, which involves the filling of pore space by chemical precipitation, which is related to temperature rather than to loading.

For a given lithology, observations show that there is a general exponential porosity reduction and increase in bulk density with depth. The following sections therefore aim to explain this trend and to highlight important consequences for basin analysis.

The total volume of a sedimentary rock is made of a solid volume V_s and pore volume V_f. During burial the total volumetric strain is therefore made of a change in pore volume and a change in volume of the solid phase. Compaction causes a major reduction in the pore fluid volume accompanied by a small reduction of the solid volume due to compression, whereas cementation increases the solid volume at the expense of the pore fluid volume. Changes in the solid volume during mineral transformation and cementation are commonplace. For example, the transformation of aragonite to calcite causes an increase in 8% by volume, but the dehydration of gypsum to anhydrite causes a reduction of 37.5% in volume, and dehydration reactions in shales such as the illitization of K-feldspar and kaolinite causes a volume decrease of 9.6%. This means that the common starting point to the study of the loss of porosity during burial, the assumption that the solid volume remains constant (since the compressibilities of many rock-forming minerals are small) (Schneider et al. 1993) is prone to error.

9.2.2 The idea of effective stress

General relationships for the burial of sedimentary layers can be obtained using basic principles of soil mechanics. For a water-saturated clay for example, the overlying weight on a layer of sediment is supported jointly by the fluid pressure in the pores and the grain to grain mechanical strength of the clay aggregates:

$$\text{Effective stress } \sigma = \text{vertical compressive stress s} - \text{fluid pressure } p \tag{9.1}$$

This well-known relationship is known as *Terzaghi's law* (Terzaghi 1936; Terzaghi and Peck 1948). As the amount of gravitational compaction increases, the effective stress also increases. Since the vertical compressive stress s is determined by the weight of the overlying water-saturated sediment column,

$$s = \bar{\rho}_b g y \tag{9.2}$$

(where $\bar{\rho}_b$ is average water-saturated bulk density, g is acceleration due to gravity, and y is depth), this increasing vertical load must be divided between p and σ.

If the ratio of fluid pressure to overburden pressure $p/s = \lambda$, it must vary between zero where the fluid pressure is nonexistent, to 1 where the sediment layer is effectively "floating" on the highly pressured pore-filling fluid. We can therefore write

$$p = \lambda s = \lambda \bar{\rho}_b g y \tag{9.3}$$

and

$$\sigma = (1 - \lambda)\bar{\rho}_b g y \tag{9.4}$$

As the sediment load is increased, the extra vertical stress is taken up initially by an increase in pore fluid pressure so that both p and λ increase. With time, however, water is expelled from the pores, reducing fluid pressures but increasing effective stresses. The increase in σ results in compaction of the grains supporting the stresses, reducing porosity. The lowest pressure that the pore fluid can attain is that due to the hydrostatic column, that is

$$p = \rho_w g y \tag{9.5}$$

in which case

$$\lambda = \frac{\rho_w}{\bar{\rho}_b} \tag{9.6}$$

This is called the normal pressure since the pore fluids are at a pressure equivalent to the head of a static body of water and the grain–grain contacts are supporting the formation. If $\lambda > \rho_w/\bar{\rho}_b$, the pore fluids are at a higher pressure than hydrostatic.

Assuming that water is free to be expelled from the sediment pore space and is not trapped, increasing burial

should lead to the equilibrium state where p is hydrostatic. If this is the case, from (9.4) and (9.6)

$$\sigma = (\bar{\rho}_b - \rho_w)gy \tag{9.7}$$

which states that the magnitude of the stress causing compaction is a function of depth and the difference between the water-saturated sediment and water densities.

It is commonly assumed that the effective stress is a function of the porosity. Drawing on soil mechanics literature (Burland 1990), Audet and McConnell (1992) related the effective stress to a void ratio e equal to $\phi/(1-\phi)$ where ϕ is the porosity:

$$\sigma = \sigma_1 \exp\left(\frac{e_1 - e}{C/\ln(10)}\right) \tag{9.8}$$

where σ_1 is an effective stress at some reference void ratio e_1, and C is a constant known as the *compression index* reflecting sediment strength. Both σ_1 and C can be determined from compression tests and are typically 1.62 and 0.5 MPa respectively.

The Terzhagi law is a statement of the importance of fluid pressures, but it is not an explanation of the physical processes leading to normally pressured and overpressured sediments. Audet and McConnell (1992, 1994) proposed a dimensionless sedimentation parameter α given by

$$\alpha = \frac{\kappa_1}{V_0}\left(\frac{\rho_s}{\rho_f} - 1\right) \tag{9.9}$$

where κ_1 is the hydraulic conductivity of the sediments (typical values of 10^{-7} to 10^{-9} mm s^{-1}, Olsen 1960), which is dependent on permeability, fluid viscosity, and density as well as clay mineralogy, V_0 is the time-averaged sedimentation rate (typical values of 0.1 to 1 mm yr^{-1}), and ρ_s and ρ_f are the sediment and pore fluid densities respectively (typically 2700 and 1050 kg m^{-3}). The sedimentation parameter is the ratio of the rate at which pore fluid moves through the sediments *versus* the rate at which new sediment accumulates as an overburden at the depositional surface. Consequently, if $\alpha >> 1$, fluid is expelled from the compacting sediment relatively fast, leading to normally pressured pore fluids. In contrast, if $\alpha << 1$, pore fluid is retained in the compacting sediment, probably caused by fast sediment accumulation rates, leading to overpressured pore fluid.

9.2.3 Measuring porosity in the subsurface

As a prerequisite for a discussion of compaction and porosity loss during burial, it is important to have some understanding of how porosity can be estimated in the subsurface. Porosity can be directly measured on core and sidewall cores recovered from a borehole, but such direct measurements tend to be concentrated on zones of known economic interest, such as reservoir intervals (see below, Fig. 9.1a). The distribution of porosity with depth in a borehole must therefore be obtained by remote methods, principally from the interpretation of downhole electrical logs. For example, sonic, neutron, and density logs are sensitive to formation lithology and porosity.

The *sonic log* is a recording of the time taken (interval transit time, Δ_t) for a compressional sound wave emitted from a sonic sonde to travel across 1 foot (*c.* 25 cm) of formation to a receiver. The interval transit time is the inverse of velocity, which is a function of lithology and porosity. When lithology is known from other data such as a drill cuttings log, Δ_t may be used to calculate porosity from the *Wyllie time-average equation*:

$$\Delta_t = \Delta_{t\,ma}(1-\phi) + \phi(\Delta_{t\,f}) \tag{9.10}$$

where $\Delta_{t\,ma}$ is the transit time through the solid rock matrix (51.3–55.5 μs ft^{-1} for sandstones, 43.5–47.6 μs ft^{-1} for limestones), and $\Delta_{t\,f}$ is the transit time through the pore space fluid (dependent on fluid salinity, 189 μs ft^{-1} for fresh water). Rearranging equation (9.10), a solution is obtained for porosity:

$$\phi = \frac{\Delta_t - \Delta_{t\,ma}}{\Delta_t - \Delta_{t\,f}} \tag{9.11}$$

Instead of using equation (9.11) for each porosity determination, it may be more convenient to use a chart such as those provided by Schlumberger (1974). It has been found that in uncompacted, geologically young sands, the Wyllie time-average equation needs to be corrected by a compaction factor.

The principle of the *density log* is that gamma rays are emitted by a radioactive source in the logging tool, and are scattered and lose energy as a result of collisions with electrons in the formation. The number of scattered gamma rays recorded at a detector, also on the logging tool, depends on the density of electrons in the forma-

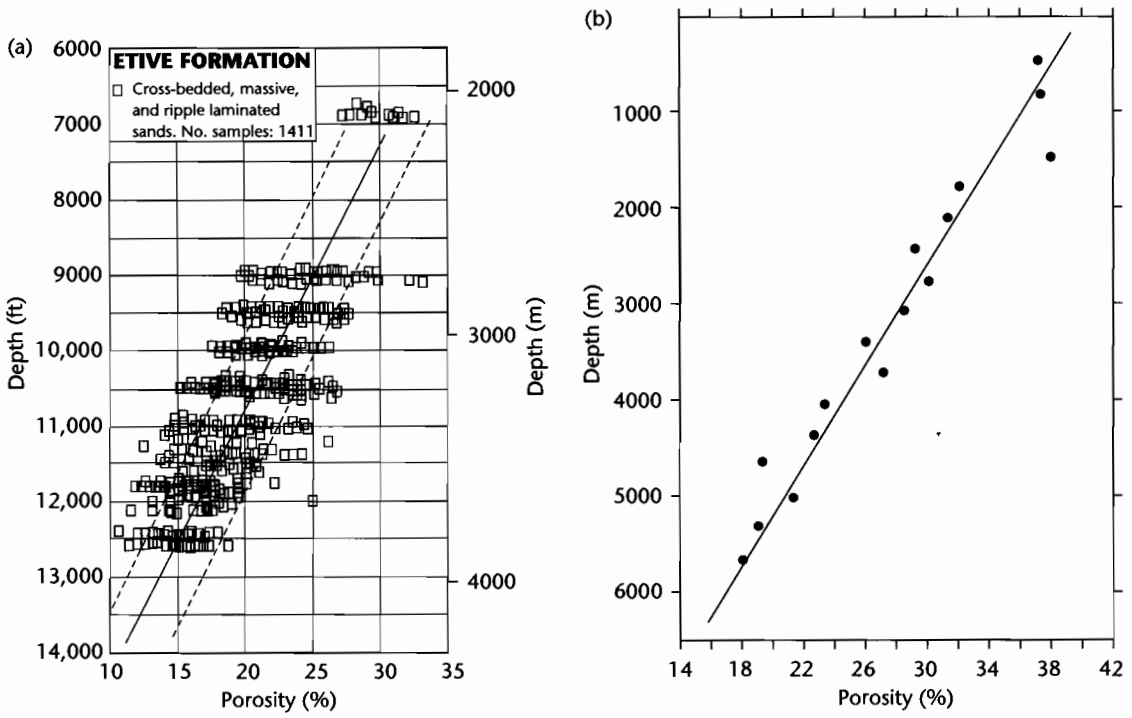

Fig. 9.1 Examples of a linear relationship between porosity and depth. (a) Cross-bedded, massive, and ripple-laminated sandstones from the Jurassic Etive Formation, Brent Group of the North Sea, from Giles (1997). Dashed lines give the 90% confidence interval for porosity about the regression line. Plot is based on 1411 samples; (b) Tertiary sands, southern Louisiana, based on over 17,000 cores, averaged every 1000 ft (*c.* 300 m), after Blatt (1979). The reduction in sand porosity with depth is thought to be due to the compaction of ductile rock fragments. Reproduced courtesy of Springer.

tion. This electron density is virtually the same as the formation bulk density for most common minerals, although for some evaporite minerals such as rock salt and sylvite (KCl), and coal, there is a significant difference.

The *Formation Density* (FDC) sonde is normally calibrated in fresh-water filled limestone formations, so that the log reads the actual bulk density for limestone and for fresh water. The bulk density ρ_b is a function of the average density of the substances making up the formation, that is, both the rock matrix and fluid-filled pores, and the relative volumes occupied, as shown by the equation

$$\rho_b = \phi\rho_f + (1-\phi)\rho_{ma} \tag{9.12}$$

where ρ_f is the average density of the fluid occupying the pore space, which is a function of temperature, pressure and salinity, and ρ_{ma} is the average density of the rock matrix. By rearranging equation (9.12) we very easily arrive at a means to determine porosity:

$$\phi = \frac{\rho_{ma} - \rho_b}{\rho_{ma} - \rho_f} \tag{9.13}$$

ρ_{ma} may itself be decomposed into its constituent parts. When clay minerals are present, a correction that accounts for the density and amount of clay may be needed in order to avoid inaccurate porosity determination,

$$\rho_b = \phi\rho_f + V_{clay}\cdot\rho_{clay} + (1-\phi-V_{clay})\rho_{ma} \tag{9.14}$$

where ρ_{clay} is the average density of the clay and V_{clay} is the fraction of the total rock occupied by clay. The clay correction is substantial when ρ_{ma} and ρ_{clay} are very dif-

ferent. This is usually at shallow depths where the clay is particularly uncompacted. Hydrocarbons may also lower the density log recording. Generally, the presence of oil in the invaded zone pore space has a negligible effect on the density log, but residual gas has a considerable effect that must be corrected for.

The principle of the *neutron log* is that neutrons emitted from a radioactive source collide with formation nuclei and are captured. A detector, or detectors, counts the returning neutrons. Because neutrons lose most energy when they collide with a hydrogen nucleus in the formation, the neutron log gives a measure of the hydrogen content, that is, the liquid-filled content of the formation. It can be used, therefore, to determine porosity. The most commonly used neutron tool is the *Compensated Neutron Log* (CNL). The CNL is calibrated to read true porosity in clean limestone formations. Its unit of measurement, as presented on the log, is therefore the "limestone porosity unit." When measuring in lithologies other than limestone, for example in a quartzose sandstone, a correction needs to be made.

The neutron log responds to *all* the hydrogen present in the formation, including the water bound up in clay minerals. As a result, it is very sensitive to clay content. In shales, the neutron log normally shows a very high reading, and needs correction. Although oil has a hydrogen content close to water and has only a small effect on the CNL, the hydrogen content of gas is considerably lower. As a result, the neutron response is low in formations that contain gas within the depth of investigation of the tool (generally <30 cm).

Of all the porosity tools, the sonic log is most widely used (e.g., Magara 1976; Ware and Turner 2002). This is largely because the neutron and density logs are normally only run in the deeper zones of hydrocarbon interest in a borehole, and the sonic log may therefore be the only porosity log available in the shallow sections of the borehole. Porosity from the sonic log can be determined if the lithology is known. The most common method of obtaining porosity from the density and neutron logs is to cross-plot them. The techniques and corrections necessary are given in manuals such as Schlumberger (1974) or Rider (1996).

Precise porosity determinations can be made on samples of the formation penetrated by a borehole. During a logging run, small sidewall cores can be obtained by firing a sleeved bullet into the formation. Intervals of reservoirs that are cored provide more promising material for porosity and permeability determination. Samples are drilled out of the slabbed core and analysed in the laboratory. Porosity trends with depth can then be obtained from a particular geological province if the same reservoir is cored at a wide range of different depths.

9.2.4 Porosity–depth relationships

Observations on the porosity–depth relationship of sedimentary rocks come from rock deformation experiments and from measurements from natural subsurface settings.

Rock deformation tests show that compaction rate is a strong function of mineralogy, with a linear relationship between log porosity and effective stress. Clays compact easily and quartz-rich lithologies compact relatively slowly. There are important deviations from this behavior. For example, sandstones with ductile lithic clasts compact more quickly than the linear relationship between log porosity and effective stress.

Direct measurements on core material and remote measurements from downhole logging devices provide an enormous database on the relation between present depth and porosity (Fig. 9.1). A number of factors affect the porosity–depth relationship, chief of which are: (i) gross lithology, shales compacting quickly compared to sandstones, (ii) depositional facies, which controls grain size, sorting and clay content and therefore initial (surface) porosity, (iii) composition of framework grains: for example, pure quartz arenites differ from lithic arenites containing ductile fragments, (iv) temperature strongly affects chemical diagenesis, such as quartz cementation, clay mineral growth, and pressure solution, and (v) time: porosity loss may require sufficiently long periods of time. The simplest trend recognized between porosity and depth is a linear trend of the form

$$\phi = \phi_0 - ay \tag{9.15}$$

where ϕ and ϕ_0 are the porosity at depth y and the initial porosity respectively, and a is an empirically derived coefficient. This linear relationship appears to fit data carefully chosen from specific sedimentary facies within a certain formation of given geological age from one basin, for example, cross-stratified, massive, and ripple cross-laminated sandstones of the Jurassic Etive Formation of the North Sea (Fig. 9.1a). In this example, the slope of the linear regression gives $a = 0.09\,\text{km}^{-1}$. However, a linear relationship self-evidently cannot apply at large depths, since porosities would have to become negative. A more widely used porosity–depth relation therefore has

the form of a negative exponential (Athy 1930; Hedberg 1936), which produces an asymptotic low porosity with increasing depth. For normally pressured sediments, the variation of porosity ϕ with depth y is given by

$$\phi = \phi_0 e^{-cy} \tag{9.16}$$

where c is a coefficient determining the slope of the ϕ-depth curve, y is the depth, and ϕ_0 is the porosity at the surface. In other words, the surface porosity declines to $1/e$ of its original surface value at a depth of $1/c$ km (Fig. 9.2). On a depth versus log porosity graph, the value of c is the inverse of the rate of change of porosity with depth. The coefficient c can therefore be estimated if a number of porosity measurements can be made, for example from a sonic log from a representative borehole in the basin. This relationship has been applied to a range of different lithologies, each with its own value of c (Sclater and Christie 1980; Halley and Schmoker 1983) (Table 9.1) (Fig. 9.3).

Substituting (9.7) into (9.16) to eliminate depth y,

$$\phi = \phi_0 \exp\left[-\left\{\frac{c}{(\bar{\rho}_b - \rho_w)g}\right\}\sigma_{eff}\right] \tag{9.17}$$

where σ_{eff} is the vertical effective stress, equal to the overburden stress minus the pore pressure. This equation expresses a fundamental relation between the effective stress on sediment grains and the resultant porosity. However, it is difficult to solve since the bulk density of the water-saturated sediment column $\bar{\rho}_b$ is itself a function of the porosity ϕ. If we simply state that the effective stress driving compaction is a linear function of depth, equation (9.16) simplifies to

$$\phi = \phi_0 \exp[-c_2\sigma_{eff}] \tag{9.18}$$

where c_2 is a composition- and temperature-dependent coefficient derived for each lithology or facies under consideration. In normally pressured basins at depths of >1 km, where the lithostatic (overburden) and pore

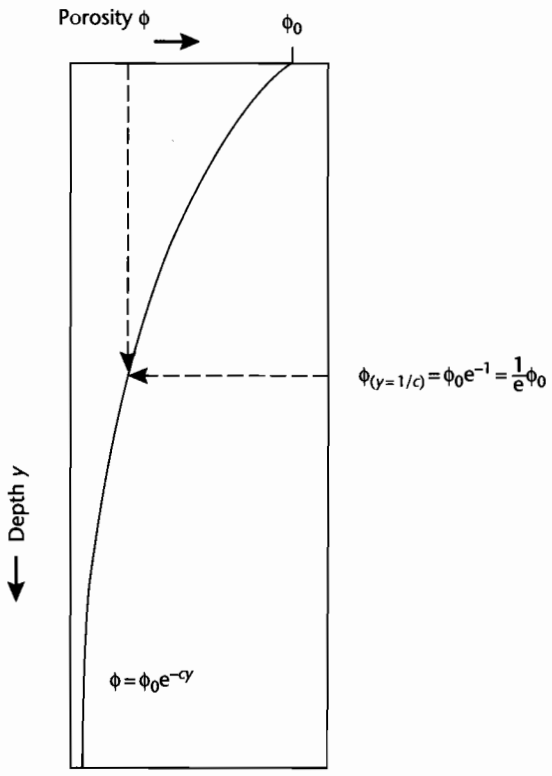

Fig. 9.2 Schematic diagram illustrating the use of the porosity–depth coefficient c. If a porosity–depth curve is known and it is exponential, c can be found by determining the depth at which the porosity ϕ has decreased to 1/e of its surface value ϕ_0. This should be repeated for all lithologies.

Table 9.1 Exponents used by Sclater and Christie (1980) for different lithologies in the subsurface of the North Sea.

Lithology	Surface porosity ϕ_0	Porosity–depth coefficient c (km^{-1})	Sediment grain density ρ_{sg} (kg m^{-3})
Shale	0.63	0.51	2720
Sandstone	0.49	0.27	2650
Chalk	0.70	0.71	2710
Shaly sandstone	0.56	0.39	2680

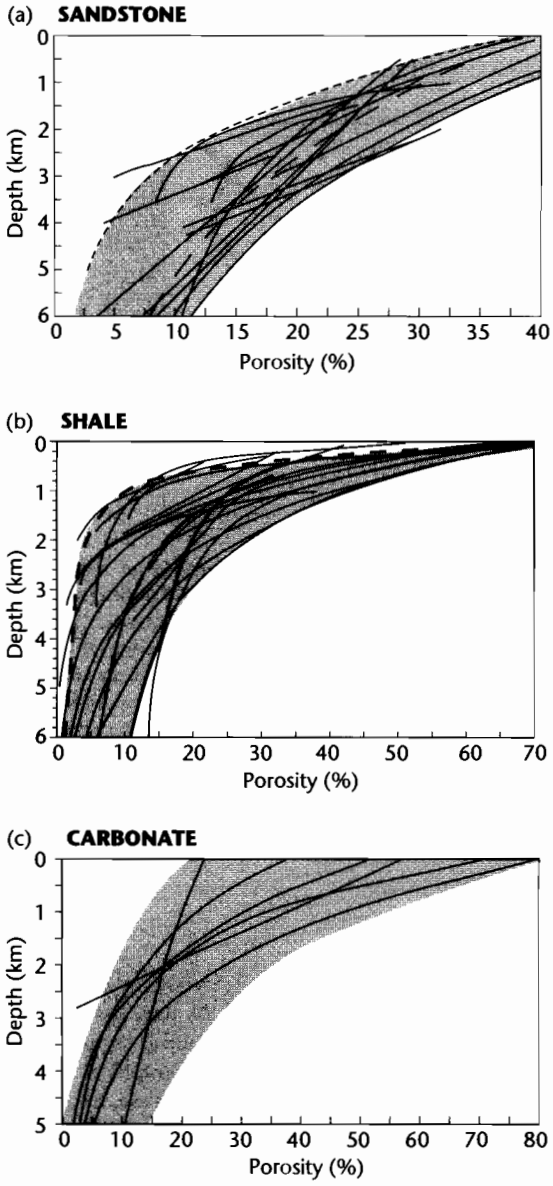

Fig. 9.3 Compilation of porosity–depth curves for sandstones (a), shales (b), and carbonates (c). Sources of datasets in Giles (1997). Note that shales compact early compared to sandstones. The porosity–depth relation for carbonates varies according to grain types and amount of cementation. Reproduced courtesy of Springer.

fluid pressure gradients are roughly constant, the porosity can be expressed

$$\phi = \phi_0 \exp\{-c_2(s-p)y\} \tag{9.19}$$

It has been argued that the exponential porosity–depth relationship does not fit shallower depth data particularly well (Falvey and Middleton 1981; Falvey and Deighton 1982). An alternative general porosity–depth function is based on the assumption that an incremental change in porosity is proportional to the change in the load and the ratio of void space to skeletal (grain) volume. This relationship is given by

$$1/\theta = 1/\theta_0 + c_3 y \tag{9.20}$$

where c_3 is a coefficient again related to lithology.

Baldwin and Butler (1985) expressed the porosity loss with depth in terms of the solid rock volume S, equivalent to $1-\phi$:

$$S = 1-\phi = 1-a\exp(-by) \tag{9.21}$$

where a and b are coefficients equal to 0.49 and 0.27 for sandstones and y is measured in kilometers. It can immediately be seen that this is the familiar exponential porosity–depth relation proposed by Athy (1930). For mudstones, Baldwin and Butler (1985) suggest an expression that can be modified to

$$\phi = 1-S = 1-ay^b \tag{9.22}$$

where a and b are 0.75 and 0.16 respectively for mudstones <200 m thick, which are thought to be normally pressured, and 0.71 and 0.125 for thicker mudstone sections that may develop overpressures.

In overpressured sections the effective stress–porosity equation can be modified by use of the ratio between fluid pressure and overburden pressure λ. This gives

$$\phi = \phi_0 \exp\left[-c\left\{\frac{\overline{\rho}_b(1-\lambda)y}{(\overline{\rho}_b-\rho_w)}\right\}\right] \tag{9.23}$$

The example from a North Sea borehole shown in Figure 9.4 illustrates the effect of overpressuring on the porosity–depth curve.

The evolution of porosity with depth can also be investigated in a physically more meaningful way by using Audet and McConnell's (1992, 1994) sedimentation parameter α. Numerical solution of the equation governing the evolution of porosity as a function of depth below the depositional surface d and time t, as a function of the sedimentation parameter, shows that clay strength (compressibility) and permeability (hydraulic conductivity) strongly affect overpressure and the evolution of porosity in a sedimentary basin. The curve of porosity versus depth is strongly affected by the sedimentation parameter (Fig. 9.5). As α varies from 1 to 10, the sediment becomes more compacted at a given depth d. This is because at $\alpha = 10$ pore fluid is easily expelled, leading to near hydrostatic pore fluid pressures and significant compaction, whereas when $\alpha = 1$ pore fluid motion is inhibited, causing reduced porosity loss in the sediment.

Some porosity–depth relationships are entirely based on the statistical analysis of large numbers of samples derived from different depths and known or "normal" geothermal gradients (Dzevanshir et al. 1986; Scherer 1987). Although potentially useful, these multivariate regressions lack any underlying physical principles.

In summary, there is a proliferation of porosity–depth relations, each based on a similar principle of porosity destruction under the increasing effective stresses experienced during burial, but differing in detail. It seems likely that each "standard" porosity–depth curve may be valuable if carefully calibrated and then used only within the region of calibration. For example, coefficients in the expressions should be evaluated for carefully selected porosity data in which grain size/sorting, composition, geothermal gradient and geological age are constrained.

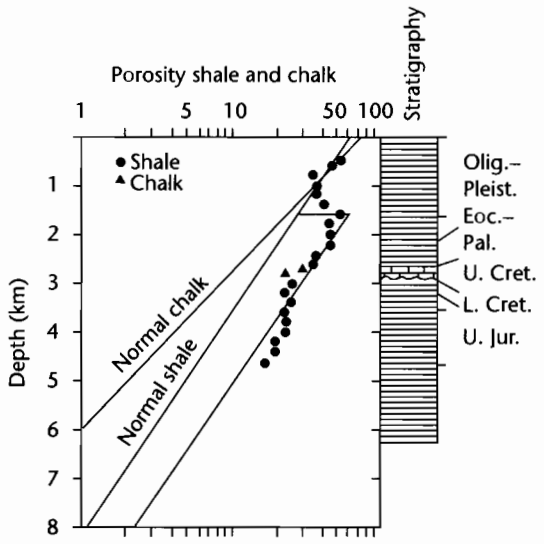

Fig. 9.4 Estimated porosity versus depth for an overpressured borehole in the Central Graben of the North Sea (Amoco 2/11-1). The increase in estimated porosity between 1500 and 2000 m is thought to be due to overpressuring. It causes a marked offset of the exponential segments of the porosity–depth curves (after Sclater and Christie 1980). The porosity–depth curves were calculated assuming total sealing occurred at the end of the Eocene, with overpressured units below and normally pressured above. The wavy line in the stratigraphic column represents the Albian–Aptian unconformity.

9.2.5 Decompacted thicknesses

To calculate the thickness of a sediment layer at any time in the past, it is necessary to move the layer up the appropriate porosity–depth curve: this is equivalent to sequentially removing overlying sediment layers and allowing the layer of interest to decompact. In so doing, we keep mass constant and consider the changes in volumes and therefore thicknesses (Boxed text 9.1).

Alternative porosity–depth relationships can be used as the basis for decompaction exercises. For example, Falvey and Middleton's (1981) formulation is used to calculate decompacted thicknesses in Allen and Allen (1990, p.270).

Equation (9.30) calculates the thickness of a sediment layer at any time from the point of deposition to the present day. A decompacted subsidence curve can therefore be plotted. The sources of the data points of the subsidence curve are the stratigraphical boundaries of presumed known age defining stratigraphical units of known present-day thickness. All depths are, however, in relation to a present-day datum, normally taken as mean sea level. Consequently it is necessary to correct the decompacted subsidence curve for firstly the difference in height between the depositional surface and the regional datum (*paleobathymetric correction*), and secondly, for past variations in the ambient sea level compared to today's (*eustatic correction*). Finally, the sediment weight drives basement subsidence. In order to calculate the true tectonic subsidence, it is necessary to remove the effects of the excess weight of the sediment compared to water. This is known as *backstripping* (§9.3).

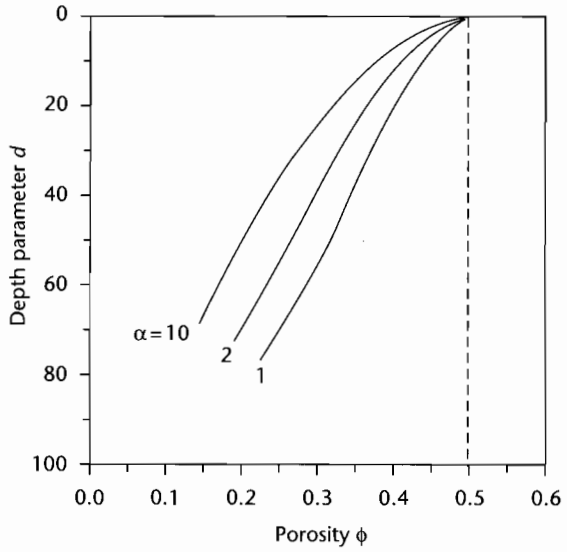

Fig. 9.5 Effect of the sedimentation parameter α on the porosity–depth curve. Porosity is shown versus a dimensionless depth for a time corresponding to 20 Myr after the start of gravitational compaction. For the parameter values used to calculate the porosity–depth curves, $d = 10$ corresponds to *c.* 1 km burial depth, and maximum burial depths are 7–8 km. Note that at high values of the sedimentation parameter α, the curve is "normal" or hydrostatic, with increasing effects of overpressuring at lower values of α. The initial porosity ϕ_0 is 0.5. After Audet and McConnell (1992). Reproduced courtesy of Blackwell Publishing Ltd.

9.3 SUBSIDENCE HISTORY AND BACKSTRIPPING

In the previous section we saw how it was possible to account for the progressive compaction of a sedimentary column during burial in a sedimentary basin. The decompacted sediment thicknesses allow a graph of *sediment accumulation rate* versus time to be constructed. However, this sediment accumulation rate graph is not the same as the subsidence rate of a chosen geological horizon relative to a constant datum. Nor does it directly give us the magnitude of the tectonic driving force as a function of time. To gain insights into subsidence rate and tectonic driving force we need to make a number of modifications or "corrections" to the sediment accumulation rate curve derived by decompaction of the stratigraphic column. In this section we perform these modifications on a 1-D stratigraphic column. In §9.4 we briefly consider the use of 2-D and 3-D models.

9.3.1 Paleobathymetric corrections

The estimation of water depth for a given stratigraphic horizon is generally far from easy, yet it is essential in order to accurately study subsidence history. As an example of the potential problems, consider two sedimentary basins (a) and (b) (Fig. 9.7). In basin (a) the water depth is 5 km. If the basement subsides tectonically by 1 km over a certain time period and during this time sediment is supplied to the basin such that it becomes filled to the brim, local isostasy shows that

BOXED TEXT 9.1: Decompaction

Consider a sediment layer at present depths of y_1 and y_2 which is to be moved vertically to new shallower depths y'_1, and y'_2 (Fig. 9.6). From equation (9.16) the amount of water-filled pore space V_w between depths y_1 and y_2 is simply the porosity integrated over the depth interval,

$$V_w = \int_{y_1}^{y_2} \phi_0 e^{-cy} dy \qquad (9.24)$$

which on integration gives

$$V_w = \frac{\phi_0}{c}\{\exp(-cy_1) - \exp(-cy_2)\} \qquad (9.25)$$

Since the total volume of the sediment layer (V_t) is the volume due to pore-filling water (V_w) and the volume of the sediment grains (V_s),

$$V_s = V_t - V_w \qquad (9.26)$$

and from (9.25), considering a unit cross-sectional area,

Continued

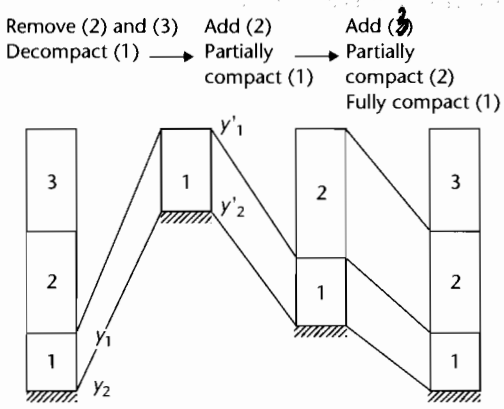

Fig. 9.6 Concept of the successive stages in a decompaction exercise.

$$y_s = y_2 - y_1 - \frac{\phi_0}{c}\{\exp(-cy_1) - \exp(-cy_2)\} \qquad (9.27)$$

On decompaction the sediment volume remains the same, only the volume of water expanding. The height of the water in a unit area sedimentary column lying between depths y'_1, and y'_2 is from (9.25)

$$y'_w = \frac{\phi_0}{c}\{\exp(-cy'_1) - \exp(-cy'_2)\} \qquad (9.28)$$

The new decompacted thickness of the sediment layer is the sum of the thickness due to the sediment grains (9.27) and that due to the water (9.28). That is,

$$y'_2 - y'_1 = y_s + y'_w \qquad (9.29)$$

which becomes

$$y'_2 - y'_1 = y_2 - y_1 - \frac{\phi_0}{c}\{\exp(-cy_1) - \exp(-cy_2)\} + \frac{\phi_0}{c}\{\exp(-cy'_1) - \exp(-cy'_2)\} \qquad (9.30)$$

This is the general decompaction equation. It represents mathematically the exercise of sliding the sediment layer up the exponential porosity–depth curve. Its solution is by numerical iteration, which makes it ideal for solving by computer. A Matlab decompaction program is provided on the web site www.erdw.ethz.ch/Allen.

about 15 km of sediment will have accumulated at the end of the time period. In basin (a), therefore, a stratigraphic thickness of 15 km reflects a very small (1 km) driving subsidence. In basin (b), however, a tectonic subsidence of 1 km takes place in a basin that has its depositional surface already at sea level. The resultant sediment thickness is barely 3 km at the end of the same time period. Clearly, for the same rate of tectonic subsidence, enormously different stratigraphic thicknesses can result depending on the initial and ensuing paleobathymetry.

Information on paleobathymetry comes from a number of sources, chief of which are benthic microfossils, other faunal and floral assemblages, sedimentary facies, and distinctive geochemical signatures. Without paleontology, it is very difficult to constrain paleobathymetry. A recent compilation of papers illustrating the use of micropaleontological data in assessing sea-level change and stratigraphic architectures is found in Olson and Leckie (2003).

Although some organisms inhabit a particular depth range as an adaptation to hydrostatic pressure, most paleodepth estimates are indirectly obtained. For example, qualitative estimates can be obtained by a comparison with the modern occurrences of certain species or assemblages and by recognition of the ecological trends of benthonic and planktonic organisms through time. Estimates can also be obtained by quantitative methods, using ratios of, for example, plankton/benthos, arenaceous/calcareous foraminifers, percent radiolarians or ostracods, or alternatively using species dominance and diversity, morphological characters and so on. These many techniques allow the paleontologist to make meaningful interpretations of environmental factors such as the chemical environment (salinity, pH, oxygen and CO_2 contents, nutrient availability), the physical environment (temperature, light, energy level, type of substrate, turbidity), and the biological environment. As much information as possible needs to be synthesized to produce a reliable depth estimate. An early example given in Figure 9.8 shows the type of depth information that can be obtained paleontologically, together with the ranges over which the estimate may span.

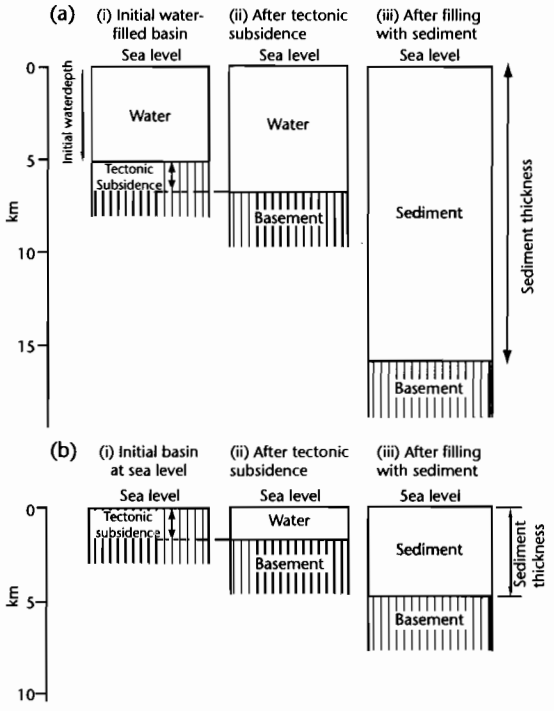

Fig. 9.7 Schematic illustration of the effects of initial water depth on sediment thickness. (a) Sedimentary basin with an initial water depth of 5 km (i) undergoes 1 km of tectonic subsidence (ii) and is filled with sediment to a depth of 15 km (iii); (b) Sedimentary basin initially at sea level (i) undergoes 1 km of tectonic subsidence (ii) and accumulates *c.* 3 km of sediment (iii).

Sedimentary and geochemical data are, by comparison, far less useful. Sedimentary facies reflect supply and process and are not therefore particularly diagnostic of depth. Although some structures, such as wave ripple marks, are restricted to particular depth ranges (<200 m), the sedimentary facies more likely will provide a back-up to the paleontological observations in marine sediments. In continental environments the potential for using sedimentary facies is greater. If shoreline facies can be identified for example, the calculation of floodplain slopes from fluviatile sediments can give valuable information on heights above sea level (Fasel 1986; Homewood et al. 1986). The most obvious geochemical data relate to the depth of carbonate dissolution (CCD) below which calcareous material is dissolved. Because most of this material is in the form of calcareous microfossils, it falls within the realm of the paleontologist. Some mineral species such as glaucony and phosphates may provide useful information on paleowater depth, but estimates are likely to be far from precise.

9.3.2 Eustatic corrections

The concept of sea-level change relative to a reference datum is known as *eustasy*, and the absolute, global sea-level variation relative to this reference datum is a eustatic change. We saw in §8.3.4 that any increase (or decrease) of water in the ocean must be compensated isostatically. If an ocean with initial water depth h_1 is filled with water to a new depth h_2, the sea-level rise Δ_{SL} compensated for isostatic depression of the ocean floor is

$$\Delta_{SL} = \left(\frac{\rho_m - \rho_w}{\rho_m}\right)(h_2 - h_1) \tag{9.31}$$

The new elevation of sea level relative to a sea level datum, caused by an increase in the water column h, termed *freeboard*, is therefore simply

$$f = \frac{(\rho_m - \rho_w)h}{\rho_m} \tag{9.32}$$

Inserting reasonable values for the density terms for an oceanic basin ($\rho_m = 3300\,\mathrm{kg\,m^{-3}}$ and $\rho_w = 1030\,\mathrm{kg\,m^{-3}}$) gives $f = 0.69h$.

At present, there is no consensus on a global eustatic curve that could be used to make corrections of decompacted subsidence data in order to extract the tectonic subsidence. Backstripping is required to remove the effects of sediment loading from observed basin subsidence (see §9.3.3). To extract the eustatic signal from the backstripped subsidence curve, the component due to tectonics must be identified and removed. However, this is not known and must be inferred or modeled. Detailed analysis of a number of borehole records from the Atlantic coastal plain in northeastern USA and the adjacent continental slope has used a tectonic model of slow cooling following rifting, to isolate the eustatic component (Miller et al. 1998). The long-term eustatic curves for the Cenozoic, which show a long term lowering of 150–200 m since 65 Ma, are similar to the estimates

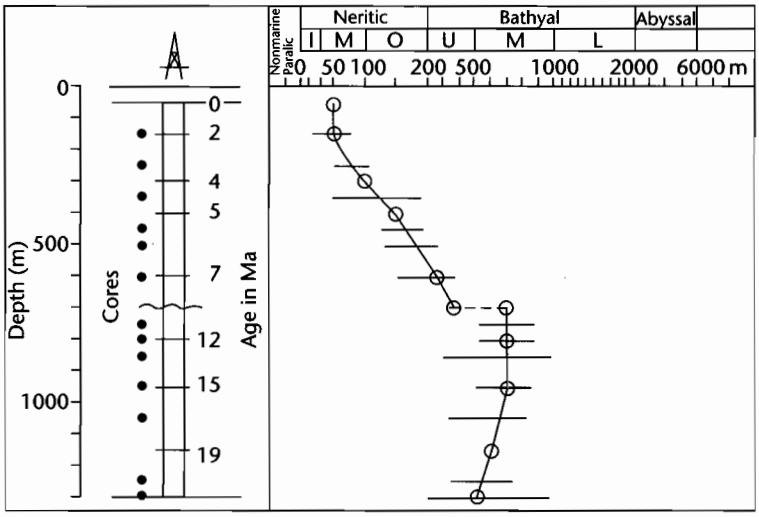

Fig. 9.8 An early example of the use of micropaleontological data to estimate paleobathymetric changes through time (after van Hinte 1978). Dots indicate core data, from which paleobathymetric estimates are made. As much paleontological information as possible is used to guide the choice of the position of the paleobathymetric curve through the depth ranges indicated by the horizontal lines. The midpoints of the ranges need not be used.

based on ocean ridge volume changes (Pitman 1978; Kominz 1984), but substantially less than the Haq et al. (1987) estimate of a *c.* 300 m lowering (Fig. 8.31). Shorter term eustatic changes are more difficult to extract. Short-term eustatic height changes are <50 m – similar to those derived from oxygen isotope records (Miller et al. 1991) but once again somewhat lower than the *c.*50–100 m estimates of Haq et al. (1987).

Bearing in mind these uncertainties, it is advisable firstly to decompact ignoring any possible global sea-level fluctuations. Following this, the sea level changes associated with first-order (long-term) cycles can be included, following Kominz (1984), Kominz et al. (1998) and Miller et al. (1998). The amplitudes of long-term eustatic change in Haq et al. (1987) are too high by a factor of about 2. It is not advisable to *a priori* invoke the short term eustatic excursions proposed by Haq et al. (1987).

9.3.3 Backstripping the sediment load

The sediment and water load above a horizon of interest in a sedimentary basin causes an isostatic effect so that the total subsidence observed is made of a tectonic driving force component and a sediment/water load component. Watts and Ryan (1976) were the first to propose the isolation of the tectonic driving force by removal of the isostatic effects of the sediment load and called the technique *backstripping*. Backstripping using Airy isostasy is shown in Boxed text 9.2.

9.3.4 Flexural support for sediment loads

Since the lithosphere underlying sedimentary basins has flexural strength, it is likely that sediment loads of appropriate wavelength are compensated flexurally rather than in a local Airy fashion. In order to understand the principle of flexural backstripping we return to the problem of the deflection of the lithosphere under a periodic load found in §2.3.3. The degree of compensation for a periodic load (eqn 2.84) is determined principally by the flexural rigidity D and the wave number $2\pi/\lambda$. The relationship between degree of compensation and wave number is shown in Figure 2.27. Taking the fill of a sedimentary basin 200 km wide ($\lambda/2 = 200$ km) with a

BOXED TEXT 9.2: Backstripping

At its simplest, the influence of the sediment load can be evaluated as follows. The porosity of the sediment layer at its new depth is

$$\phi = \frac{\phi_0}{c} \cdot \frac{\exp(-cy_1') - \exp(-cy_2')}{y_2' - y_1'} \tag{9.33}$$

Since the bulk density of the new sediment layer (ρ_b) depends on the porosity and the density of the sediment grains (ρ_{sg})

$$\rho_b = \phi\rho_w + (1-\phi)\rho_{sg} \tag{9.34}$$

the bulk density of the entire sedimentary column ($\bar{\rho}_b$) made up of i layers is

$$\bar{\rho}_b = \sum_i \left\{ \frac{\bar{\phi}_i\rho_w + (1-\bar{\phi}_i)\rho_{sgi}}{S} \right\} y_i' \tag{9.35}$$

where $\bar{\phi}_i$ is the mean porosity of the ith layer, ρ_{sgi} is the sediment grain density of the same layer, y_i' is the thickness of the ith sediment layer, and S is the total thickness of the column corrected for compaction.

The loading effect of the sediment can then be treated as a problem of a local (Airy) isostatic balance. Where sediment is replacing a column of water,

$$Y = S\left(\frac{\rho_m - \bar{\rho}_b}{\rho_m - \rho_w}\right) \tag{9.36}$$

where Y is the depth of the basement corrected for sediment load and ρ_m, $\bar{\rho}_b$, ρ_w are mantle, mean sediment column, and water densities.

Incorporating the various effects of paleobathymetry, eustatic sea-level change, and sediment loading gives the Airy compensated tectonic subsidence

$$Y = S\left(\frac{\rho_m - \bar{\rho}_b}{\rho_m - \rho_w}\right) - \Delta_{SL}\left(\frac{\rho_w}{\rho_m - \rho_w}\right) + (W_d - \Delta_{SL}) \tag{9.37}$$

where Δ_{SL} is the paleosea level relative to the present, and W_d is the paleowater depth (Bond and Kominz 1984). This is the subsidence relative to a stationary datum (today's sea level) that would have occurred in an entirely water-filled basin. An example of a decompacted, corrected, and backstripped subsidence history is given in Fig. 9.9.

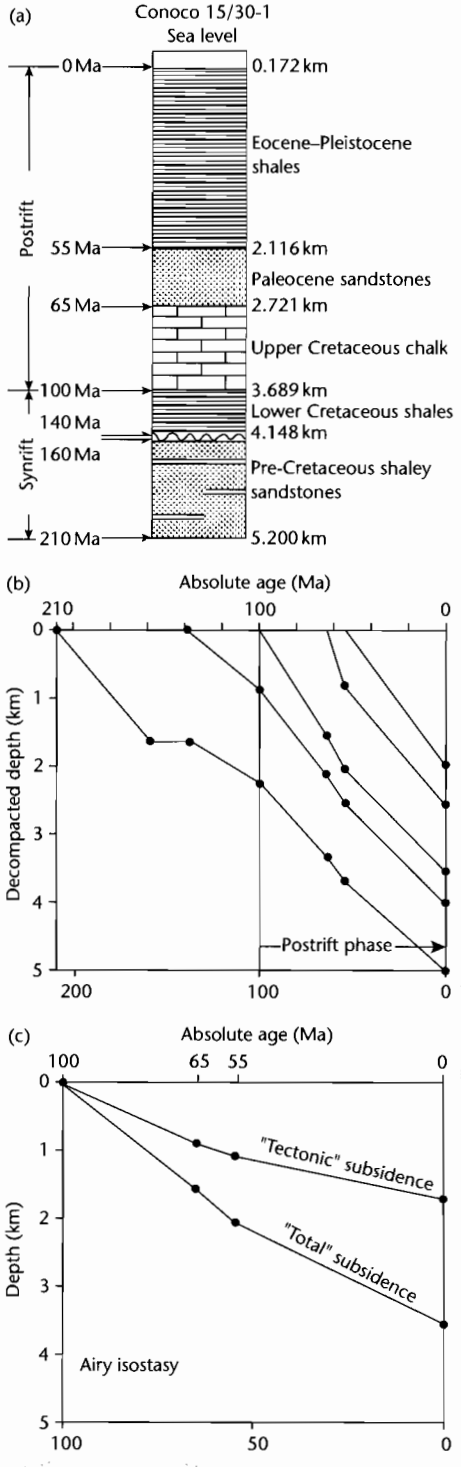

Fig. 9.9 Example of a decompaction and backstripping of the stratigraphy penetrated in a North Sea borehole, Conoco 15/30-1. (a) Summary stratigraphic column, (b) decompacted depth versus time, (c) backstripped subsidence for the postrift phase, using an Airy isostatic model and eustatic and paleobathymetric corrections at 100 Ma, 65 Ma, 55 Ma, and 0 Ma. Full dataset and Matlab exercise is provided at www.erdw.ethz.ch/Allen

sinusoidal sediment load and an underlying lithosphere of flexural rigidity 10^{24} Nm, $(\rho_m - \rho_s) = 800\,\mathrm{kg\,m^{-3}}$, the degree of compensation C is about 0.12. This suggests that the lithosphere behaves very rigidly to this kind of wavelength of load. Changing the wavelength of the load such that $l/2$, the width of the basin, is now 400 km, C = 0.68, indicating that the sediment load is only weakly supported. In this case of large compensation, Airy-type isostasy is approached.

Flexural backstripping can therefore only be carried out if there is knowledge of the flexural rigidity of the underlying lithosphere and of the spatial distribution of the sediment load. The procedure is normally carried out sequentially on a number of sediment layers where the isopachs of each layer are known from seismic reflection data. The flexure is then given by

$$\mathbf{Y}(k) = \frac{(\rho_s - \rho_w)\mathbf{S}(k)}{(\rho_m - \rho_s)}\mathbf{\Phi}(k) \tag{9.38}$$

where $\mathbf{Y}(k)$ is the frequency domain equivalent of the flexure, $\mathbf{S}(k)$ is the frequency domain equivalent of the sediment thickness, and $\mathbf{\Phi}(k)$ is a wave number function equivalent to the compensation C outlined above.

Flexural backstripping can be extended to three dimensions by replacing the wave number by a 3-D wave number

$$k = \sqrt{(k_x^2 + k_z^2)} \tag{9.39}$$

where k_x is the wave number in the x direction and k_z is the wave number in the z direction.

An example of the use of flexural backstripping from the Valencia Trough of the western Mediterranean is given in Figure 9.10.

9.3.5 Tectonic subsidence signatures

One of the benefits of a complete decompaction and backstripping procedure is that the subsidence history of basins can be compared without the complications of different paleobathymetric, eustatic, compactional, and isostatic effects. This enables the tectonic driving force for subsidence, for example, the stretch factor β, to be evaluated at different positions within a single basin, and for the same tectonic mechanism to be compared between different basins. It also enables the tectonic subsidence history of sedimentary basins to be discriminated and compared with theoretical curves.

Stretching of the continental lithosphere and flexure of the lithosphere are by far the most important mechanisms for prolonged and widespread subsidence. Stretching and flexure produce entirely different subsidence profiles:

1 Stretching of the continental lithosphere produces a rapid synrift subsidence followed by an exponentially decreasing postrift subsidence due to thermal relaxation. Although a range of subsidence history possibilities arise from the duration of the stretching, 3-D heat flow, induced convection in the zone of upwelled asthenosphere, maintenance or removal of a hot source in the mantle, lateral relay during simple shear, and depth-dependent stretching, nevertheless the diagnostic signature of continental stretching is an early, rapid, fault-controlled phase of subsidence followed by a "concave-up" phase as the lithosphere cools. The amount of synrift and postrift subsidence depends essentially on the amount of stretching β.

2 Flexure of the lithosphere under a moving load, such as an orogenic wedge, typically produces an accelerating subsidence through time. This is the simple result of the propagation of a flexural wave with a maximum deflection under the load across the lithosphere. Consequently, locations on the foreland plate distant from the load are initially uplifted in a forebulge region, producing an unconformity, and then subside at an increasing pace as they become involved in foredeep subsidence. The magnitude and geometry of the flexural subsidence depend on the flexural rigidity of the underlying plate and the magnitude and spatial distribution of the applied load.

The typical subsidence signatures of stretched basins and foreland basins are compared in Figure 9.11(a, b). A first-order conclusion from such a comparison is that: (i) stretched basins contain rift to postrift megasequences with a duration of $10^1 - >10^2$ Myr, with synrift tectonic subsidence rates of typically $<0.2\,\mathrm{mm\,yr^{-1}}$ and exponentially decreasing postrift tectonic subsidence rates of $<0.05\,\mathrm{mm\,yr^{-1}}$, and (ii) foreland basin megasequences are typically 20–40 Myr in duration and involve convex-up subsidence signatures with maximum tectonic subsidence rates of 0.2–0.5 $\mathrm{mm\,yr^{-1}}$. Thicknesses of foreland

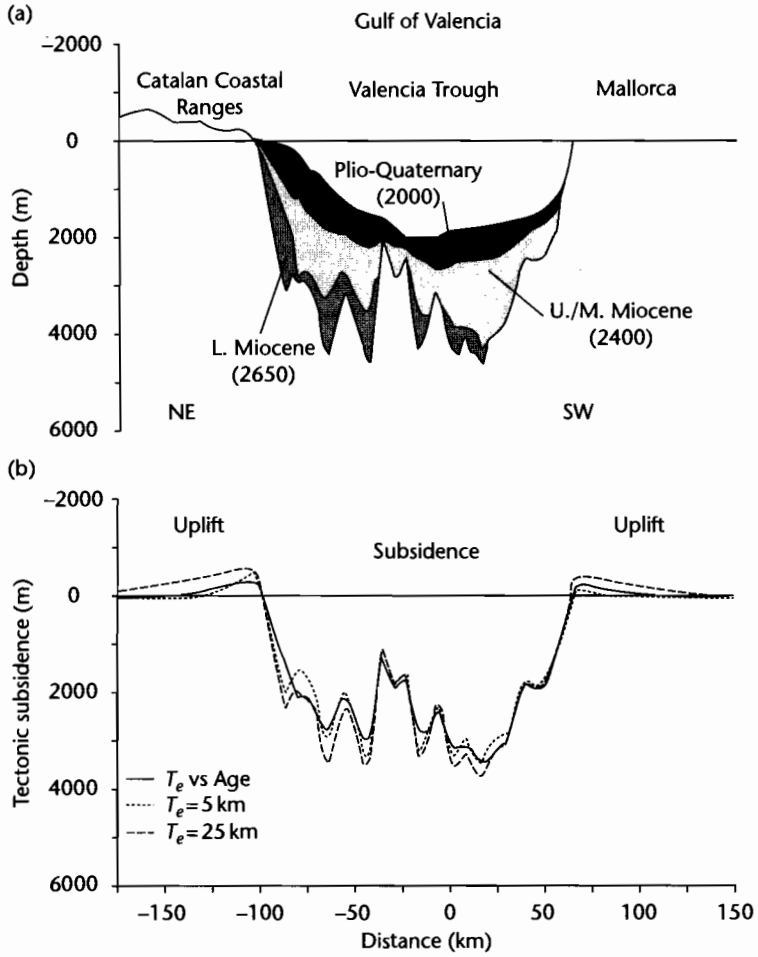

Fig. 9.10 Application of flexural backstripping technique to the Valencia Trough, a young rift basin in the western Mediterranean between the Spanish mainland and the Balearic Islands, that extended in the early Miocene. (a) Stratigraphic cross-section with estimated densities (in $kg\,m^{-3}$) of the Plio-Quaternary, upper/middle Miocene and lower Miocene; (b) Backstripped tectonic subsidence using three models for the equivalent elastic thickness. After Watts and Torné (1992b). Reproduced courtesy of American Geophysical Union.

basin stratigraphy range up to 10 km. Cratonic basins are typified by very long periods ($>10^2$ Myr) of slow subsidence interrupted by regional unconformities, with tectonic subsidence rates of $0.01–0.04\,mm\,yr^{-1}$. Strike–slip basins may be particularly difficult to discriminate on the basis of tectonic subsidence signature, since basins in strike–slip zones are strongly related to the kinematics of border fault movement. Basins may have components of thermal relaxation, lateral heat loss, and flexure from nearby push-up ranges contributing to the tectonic subsidence signature. Tectonic subsidence rates are commonly very high compared to all other basin types ($>0.5\,mm\,yr^{-1}$), but strike–slip megasequences may be short in duration (*c.* 10 Myr) due to the complexities of deformation within the Principal Displacement Zone.

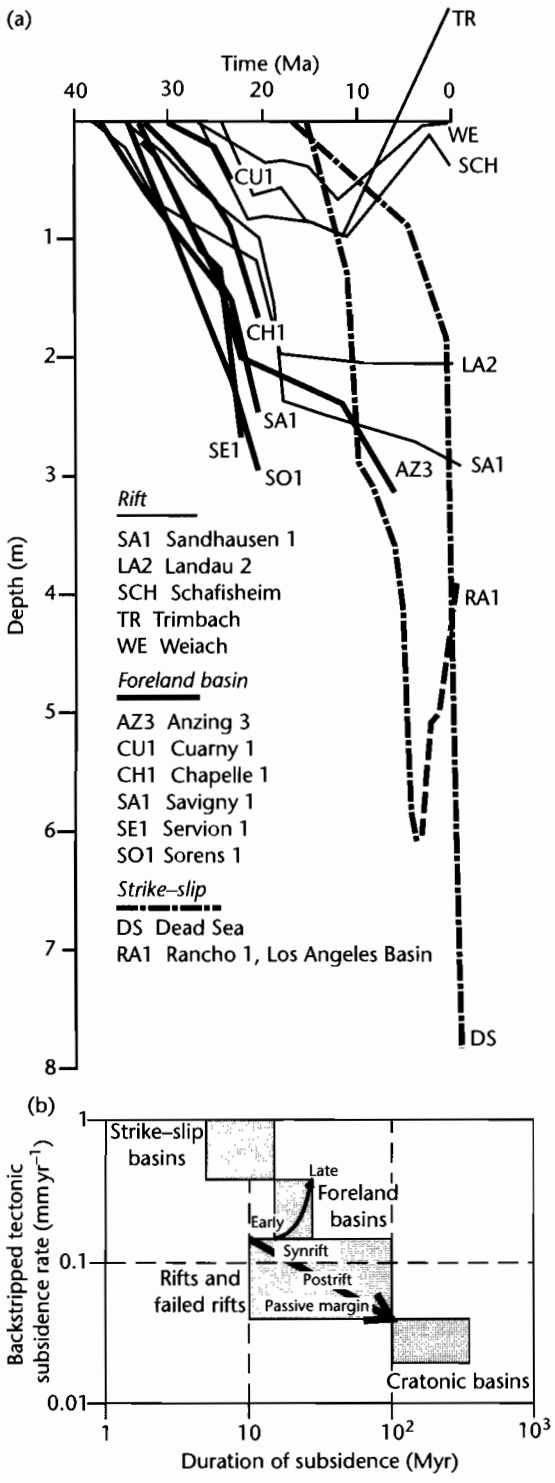

In many basins more than one subsidence mechanism may operate. This may be particularly the case in the retro-foreland regions of major ocean–continent convergence zones. In these regions flexural subsidence due to loading in retro fold and thrust belts may be added to by dynamic subsidence associated with subduction of cold oceanic slabs. Allen et al. (2000), for example, recognized two convex-up flexural events superimposed on a very long-term, linear to slightly concave-up subsidence curve in the Mesozoic of the Colorado Plateau area, USA. The addition of an in-plane stress related to continental collision to the postrift history of stretched basins may also be recognized by "anomalous" increases in subsidence rate. This combination of mechanisms has been invoked, for example, in the Late Cenozoic history of the North Sea failed rift (van Wees and Cloetingh 1996).

9.4 INTRODUCTION TO THERMAL HISTORY

Subsidence in sedimentary basins causes material initially deposited at low temperatures and pressures to be subjected to higher temperatures and pressures. Sediments may pass through diagenetic, then metamorphic regimes and may contain indices of their new pressure–temperature conditions. Thermal indices are generally obtained from either dispersed organic matter, temperature-dependent chronometers such as apatite fission tracks or from mineralogical trends. A great deal of effort has been spent in attempting to find an analytical technique capable of unambiguously describing thermal maturity, and an equal amount of effort attempting to correlate the resulting proliferation of indicators.

Numerical values of the organic geochemical parameters are dependent on time, thermal energy, and type

Fig. 9.11 Comparison of the typical subsidence histories of foreland basins, rift and strike–slip basins, using decompacted subsidence curves (a). Thick solid curves are boreholes in the flexural North Alpine foreland basin of Switzerland and southern Germany. Thin solid curves are the Tertiary rift phase of boreholes in the Rhine rift and its southerly continuation in northern Switzerland. The Swiss boreholes (TR, WE and SCH) have experienced Neogene uplift. Dash-dot lines are two strike–slip basins; (b) Plot of duration of subsidence versus typical tectonic subsidence rate, allowing foreland basins, rift, failed rift, passive margin and strike–slip basins to be discriminated.

of organic matter (e.g., Weber and Maximov 1976 for an early contribution). The evolution of clays and other minerals is controlled by temperature and by chemical and petrological properties. The scale of maturation to which a given organic or mineralogical phase can be calibrated is that of *coal rank*. Any analytical technique must be able to make use of very small amounts of dispersed organic matter in order to be valuable in basin analysis. Vitrinite reflectance and elemental analyzes enable coal rank to be related to hydrocarbon generation stages. Thermochronological tools such as apatite fission track analysis and the diffusion of He during U–Th decay offer the important advantage of providing information on thermal evolution instead of solely on maximum paleotemperature.

The objective in the remainder of this chapter is to describe the use of a number of thermal indicators in constraining and calibrating the thermal evolution of the basin-fill. The implications for the generation of hydrocarbons and for the diagenesis of reservoir rocks is developed in Chapter 10.

9.5 THEORY: THE ARRHENIUS EQUATION AND MATURATION INDICES

It is now believed that the effects of depth *per se* on the maturation of organic matter are of minor importance, the most important factors being *temperature* and *time*. Pressure is relatively unimportant. Philippi (1965) assessed the effect of pressure by studying hydrocarbons in two Californian basins. In the Los Angeles Basin, hydrocarbons were generated at about 8000 ft (~2.4 km) whereas in the Ventura Basin, generation did not take place until about 12,500 ft (3.8 km) of burial. Since pressure is directly related to depth of burial ($\sigma = \rho gh$) this suggests that pressure does not play a major part in hydrocarbon generation. However, the generation of hydrocarbons in the two basins took place at the same temperature, strongly suggesting that subsurface temperature was the overriding control.

The relationship between temperature and the rate of chemical reactions is given by the *Arrhenius equation*:

$$K = A\exp(-E_a/RT) \tag{9.40}$$

where K is the reaction rate, A is a constant sometimes termed the *frequency factor* (it is the maximum value that can be reached by K when given an infinite temperature), E_a is the activation energy, R is the Universal Gas Constant, and T is the absolute temperature in Kelvin. The constants in the Arrhenius equation can be estimated from compilations of organic metamorphism (e.g., Hood et al. 1975; Shibaoka and Bennett 1977). The activation energies of each individual reaction involved in organic maturation are not known, but for each organic matter type a distribution of activation energies may be established from laboratory and field studies. For example, a distribution of activation energies for the maturation of vitrinite from 159 to 310 kJ mol^{-1}, centered on 226 kJ mol^{-1}, was suggested by Burnham and Sweeney (1989).

The Arrhenius equation suggests that reaction rates should increase exponentially with temperature, so that a 10 °C rise in temperature causes the reaction rate to double. This result is widely known, but it is less widely realized that the rate of increase in reaction rate slows down with increasing temperature, so at 200 °C the reaction rate increases by a factor of 1.4 for a 10 °C rise in temperature (Robert 1988). Clearly, both time and temperature influence organic maturation, a view supported by the occurrence of shallower oil generation thresholds as the sediments containing the organic matter become older (Dow 1977) (Fig. 9.12). Connan (1974) believed that the threshold of the principal zone of oil generation was related to the logarithm of the age of the formation, further supporting a time–temperature dependence obeying the laws of chemical kinetics.

The cumulative effect of increasing temperature can be evaluated from the *maturation integral*, the reaction rate integrated over time,

$$C = A\int_0^t \exp(-E_a/RT) + C_0 \tag{9.41}$$

where C_0 is the original level of maturation of the organic material at the time of deposition ($t = 0$). The maturation integral for any nominated horizon can be calculated if the decompacted burial history, heat flow through time and thermal conductivities of the sediments and basement are known or can be assumed. For the less mathematically inclined, equation (9.41) shows that when paleotemperatures are plotted on an exponential scale, the area under the curve from deposition to a given time is proportional to the maturation integral at that time at the nominated horizon (plus the value of C_0) (see §9.6). Some authors believe that the maturation integral is related to measurable values of vitrinite reflectance (see §9.7.2, 9.8) (Royden et al. 1980; Falvey and Middleton 1981).

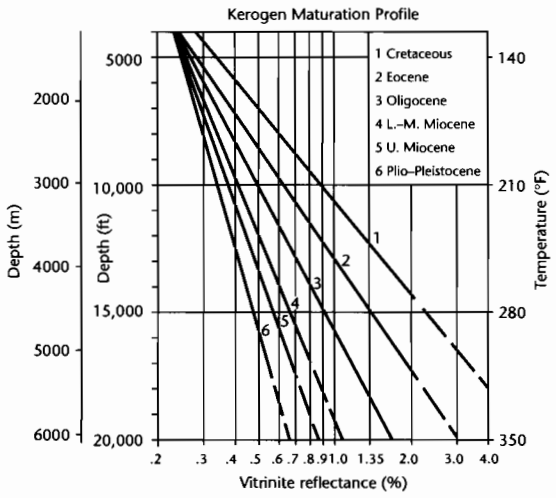

Fig. 9.12 Plot of depth versus an index of thermal maturation (vitrinite reflectance) for kerogens of various ages (after Dow 1977). For the same depth of burial (and therefore for the same temperature at a constant geothermal gradient), older kerogens are significantly more mature than younger kerogens.

Hood et al. (1975) devised an artificial maturation parameter, the *Level of Organic Metamorphism* (LOM), based on a rank progression of coals, from lignites to meta-anthracites. Hood's diagram shows the relationship between the "effective heating time" and the maximum temperature attained. The effective heating time is defined as the length of time the temperature remains within a 15 °C range of the maximum temperature. This method, although not stated explicitly by Hood et al. (1975), is based on the first-order chemical kinetics outlined above.

Another application of the Arrhenius relationship is the *Time–Temperature Index* (TTI) (Lopatin 1971; Waples 1980). This index is based on the view that the reaction rate doubles for every 10 °C rise in temperature over the entire range from 50 °C to 250 °C. Since the method assumes that the reaction rate continues to double over 10 °C intervals over the entire temperature range to 250 °C, it tends to overestimate maturity. The reaction cannot continue indefinitely because the materials undergoing thermal maturation are used up.

Other techniques, such as those of Tissot (1969), Tissot and Espitalié (1975), and Mackenzie and Quigley (1988), have been developed that enable masses of petroleum generated during thermal maturation of organic matter to be calculated. The Mackenzie and Quigley model is described in relation to petroleum source rocks in §10.3.2.2.

9.6 FACTORS INFLUENCING TEMPERATURES AND PALEOTEMPERATURES IN SEDIMENTARY BASINS

Chapter 2 contains some basic concepts about heat flow, and the specific problem of 1-D (vertical) heat flow in basins due to stretching is addressed in Chapter 3. Here, we are concerned with the various "internal" factors that influence the temperatures within sedimentary basins: (i) variations in thermal conductivity, (ii) internal heat generation, (iii) convective/advective heat transfer within sediments, and (iv) surface temperature changes.

9.6.1 Effects of thermal conductivity

The distribution of temperature with depth (geotherm) in the continents is primarily determined by conductive heat transport. We know the relation between heat flux and temperature gradient as given by Fourier's law (eqn 2.29). This law states that conductive heat flux is related to the temperature gradient by a coefficient, K, known as the coefficient of *thermal conductivity*. If two measurements of temperature are known, one T_y, at depth y and another T_0 at the surface ($y = 0$), Fourier's law can be restated as

$$q = -K(T_y - T_0)y \tag{9.42}$$

which by rearrangement becomes

$$T_y = T_0 + \left(\frac{-qy}{K}\right) \tag{9.43}$$

where q is the heat flux (negative for y increasing downwards). We are here initially ignoring internal heat production within the sedimentary pile (see §9.6.2).

Ignoring for the moment lithological variations, thermal conductivities of sediments vary as a function of depth because of their porosity loss with burial (§9.2).

Equation (9.43) can be modified to account for the different thermal conductivities of the sedimentary layers,

$$T_y = T_0 + (-q)\left\{\frac{l_1}{K_1} + \frac{l_2}{K_2} + \frac{l_3}{K_3} + \ldots\right\} \quad (9.44)$$

where l_1 to l_n are the thicknesses of the layers with thermal conductivities K_1 to K_n, and $l_1 + l_2 + l_3 \ldots$ must of course be equal to y.

Falvey and Middleton (1981) recommended the use of a function that assumed an exponental relation between porosity and depth

$$K = K_d - \{(K_d - K_0)\exp(-\gamma y)\} \quad (9.45)$$

where K_d is the thermal conductivity deep in the sedimentary section, K_0 that at the sediment surface, and γ is a constant for a given section. Since K varies with depth, temperature gradients must also vary with depth in order to maintain a constant heat flow. If present-day heat flow can be calculated from a borehole by measurement of conductivities and surface and bottom hole temperatures (§9.7.1), equations (9.43) and (9.45) can be used to find the temperature at any depth. If paleoheat flow is then assumed to be constant with depth, the temperature history of any chosen stratigraphic level can be estimated. The assumption of a constant heat flow with depth is a condition of any 1-D steady-state heat conduction model. Measurements in some sedimentary basins such as the North Sea failed rift (Andrews-Speed et al. 1984), however, suggest that this is not a good assumption, deep circulation of water most likely being responsible for the departure from the steady-state assumption (see §9.6.3).

A fundamental requirement in the estimation of geotherms, temperatures, and paleotemperatures in sedimentary basins is therefore the bulk thermal conductivity of the different sedimentary layers making up the basin-fill. Thermal conductivities can be measured in the laboratory (Carslaw and Jaeger 1959; Sass et al. 1971) and *in situ* (Beck et al. 1971). The bulk thermal conductivity of most sedimentary rocks ranges between 1.5 $Wm^{-1}K^{-1}$ (shales) and 4.5 $Wm^{-1}K^{-1}$ (sandstones) (Table 9.2). These estimates depend mostly on the mineralogy of the framework grains, the type and amount of material in the matrix (commonly clay minerals), and the porosity and fluid content (commonly water) (Brigaud and Vasseur 1989). The individual conductivities of framework, matrix, and pore-fluid are also dependent on temperature. The general trend is that nonargillaceous rocks have higher conductivities than argillaceous rocks, and that conductivity increases with increasing porosity. If measurements of the thermal conductivities of the different components in a rock can be made, the bulk thermal conductivity of the sedimentary layer can be estimated. The overall thermal conductivity structure of the basin-fill can then be estimated from a knowledge of the mineralogy, porosity, and fluid content of the stratigraphy filling the basin. The availability of large "continuous" subsurface datasets from hydrocarbon exploration boreholes has revolutionized the ability to make such estimates.

The *effective thermal conductivity* of a clean quartzose sandstone with pore-filling water should decrease with increasing porosity, since the pore fluid is insulating. However, the effective thermal conductivity of a clean quartzose sandstone with depth may be almost invariant (Fig. 9.13b). This is because of the decrease in conductivity of the framework quartz grains with increasing temperature, which offsets the increase in conductivity due to compaction (porosity loss) (Palciauskas 1986).

The effects of clays in a sandstone, for example as pore-filling authigenic cements, is to decrease the bulk thermal conductivity of the argillaceous sandstone, since clays have an insulating effect (Fig. 9.13a). Felspar and most clays do not show a marked effect of temperature on thermal conductivity, so the effect of compaction commonly dominates. A clay–water mixture (shales) increases in conductivity rapidly with depth because of compaction (§9.2), whereas a feldspar–water mixture, because it compacts similarly to a sand, increases in conductivity much more slowly with depth (Fig. 9.13c).

The bulk conductivity of a sediment layer can therefore be thought of as being made up of the contributions of the pore-fluid and the grain conductivities. Assuming a geometric mean model for the two-phase media of solid and fluid (Woodside and Messmer 1961), the bulk conductivity is

$$K_{bulk} = K_s^{(1-\phi)} K_w^{\phi} \quad (9.46)$$

where K_s and K_w are the thermal conductivities of sediment grains and water respectively and ϕ is the porosity, assumed to be filled with water. An alternative method, termed the *effective medium* theory calculates an effective bulk thermal conductivity for a randomly inhomogeneous medium made of constituents with volume fractions V_i and thermal conductivities K_i. The basic result of the theory is

Table 9.2 Density and thermal properties of some common minerals and rock types.

Rock type	Density ($kg\,m^{-3}$)	Thermal conductivity K^* ($Wm^{-1}K^{-1}$)	Volumetric coefficient of thermal expansion α_v ($10^{-5}K^{-1}$)
Minerals common in sediments and sedimentary rocks			
Water (pore-fluid)	1000	0.6	–
Quartz	2650	7.7	–
Calcite	2710	3.3	–
Dolomite	2870	5.3	–
Anhydrite	2960	6.3	–
Kaolinite	2630	2.6	–
Chlorite	2780	3.3	–
Illite/smectite	2660	1.9	–
Sedimentary rocks			
Shale	2100–2700	1.2–3.0	–
Sandstone	1900–2500	1.5–4.2	3
Limestone	1600–2700	2.0–3.4	2.4
Dolomite	2700–2850	3.2–3.5	–
Metamorphic			
Gneiss	2600–2850	2.1–4.2	–
Amphibolite	2800–3150	2.1–3.8	–
Igneous			
Basalt	2950	1.3–2.9	–
Granite	2650	2.4–3.8	2.4
Gabbro	2950	1.9–4.0	1.6
Peridotite	3250	3.0–4.5	2.4

Note:
* Thermal conductivities at surface temperatures (in part from Brigaud and Vasseur 1989).

$$K^{-1} = \sum_{i=1}^{n} 3V_i(2K + K_i)^{-1} \tag{9.47}$$

This expression is particularly useful where mixed components are present in the sediment layer. For example, for the water–quartz mixture mentioned above, if the quartz framework ($K_q = 5.4\ Wm^{-1}°C^{-1}$ at $T = 100°C$) occupies 0.7 of the rock volume and water ($K_w = 0.7\,W\,m^{-1}°C^{-1}$ at $T = 100°C$) occupies 0.3 of the rock volume, the bulk conductivity from effective medium theory (9.47) is approximately $3.3\,Wm^{-1}°C^{-1}$. From the general result in (9.46), the bulk conductivity is approximately $2.9\,Wm^{-1}°C^{-1}$.

A fundamental result of maintaining a constant heat flux through a heterogeneous basin fill is that the geothermal gradient must vary with depth. As an example, consider the thermal conductivity structure derived from the borehole shown in Figure 9.14a. Keeping the basal heat flux at $63\,mW\,m^{-2}$, the geotherm varies as in Figure 9.14b. Clearly, the presence of a heterogeneous basin-fill negates the assumption of a linear conduction geotherm. The implications for the interpretation of maturity profiles are discussed in §9.8.

9.6.2 Effects of internal heat generation in sediments

Heat generation by radioactive decay in sediments may significantly affect the heat flow in sedimentary basins (Rybach 1986). Although all naturally occurring radioactive isotopes generate heat, the only significant contributions come from the decay series of uranium and thorium and from ^{40}K (Table 9.3). As a result, heat

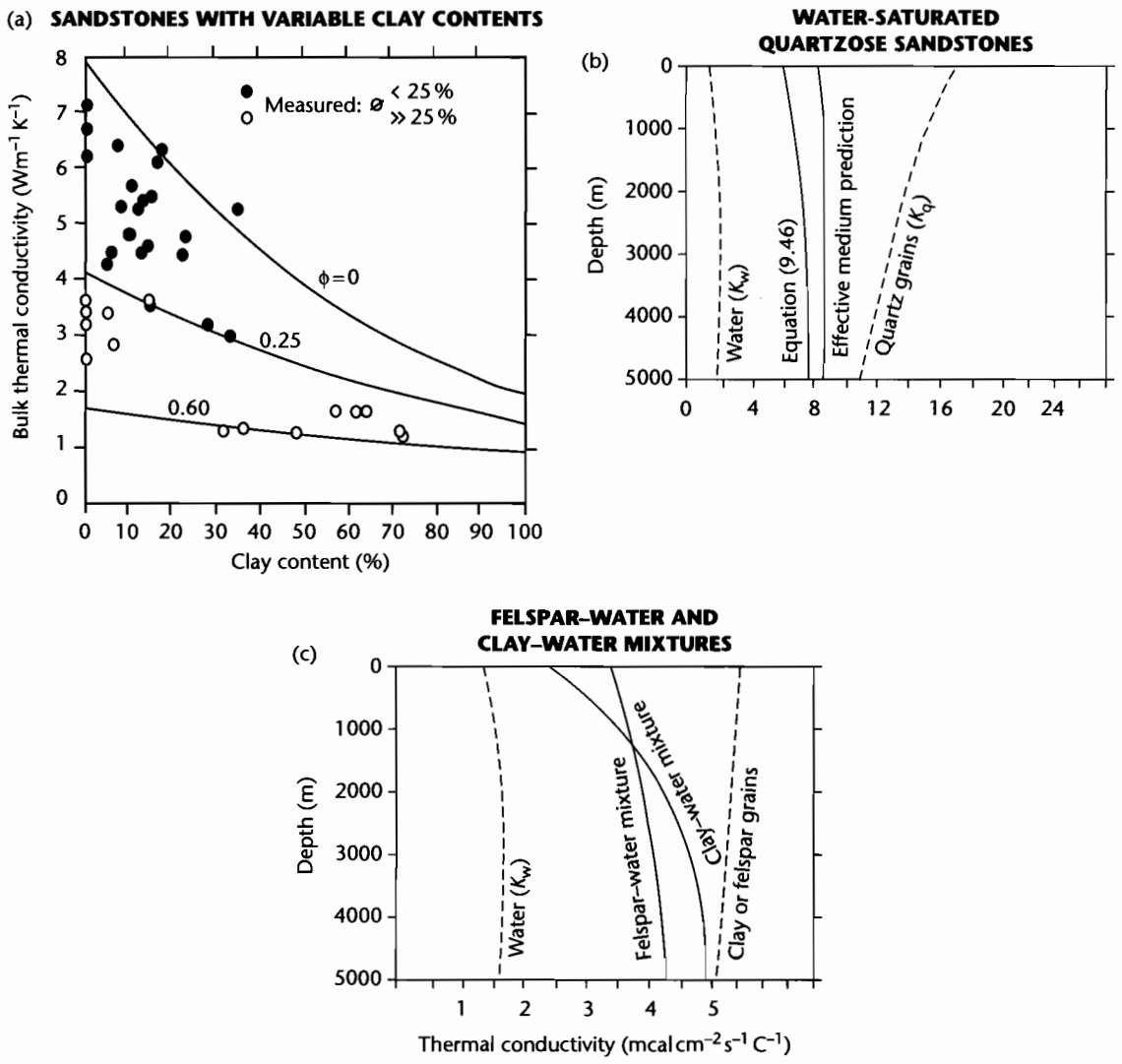

Fig. 9.13 The thermal conductivities of sedimentary rocks. (a) Influence of mineralogy on thermal conductivity of water saturated sandstones with a variable clay content, using thermal conductivities of $7.7\,W\,m^{-1}\,K^{-1}$, $2.0\,W\,m^{-1}\,K^{-1}$, and $0.6\,W\,m^{-1}\,K^{-1}$ for quartz, clay, and water respectively (after Brigaud and Vasseur 1989); (b) Thermal conductivity of water-saturated quartzose sandstone as a function of depth. The effective medium prediction and the empirical relation closely agree, demonstrating a negligible increase in thermal conductivity with depth, despite the fact that the quartz grains decrease in thermal conductivity considerably with depth; (c) Felspar–water and clay–water mixtures, showing that the thermal conductivities increase markedly with depth, especially for clay-rich sediments. This is principally due to the effects of compaction. In (b) and (c) the temperature gradient is $30\,°C\,km^{-1}$ and the surface temperature 20 °C. After Palciauskas (1986).

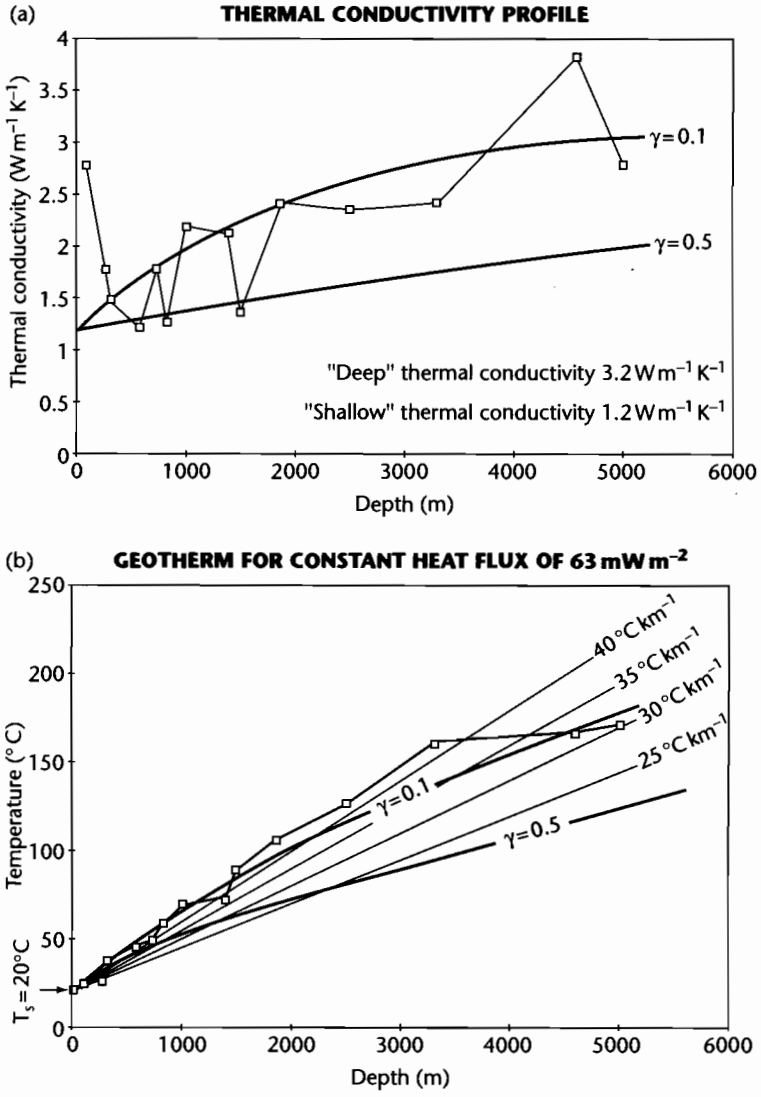

Fig. 9.14 (a) Thermal conductivity structure of stratigraphy penetrated by borehole 14/20-1 close to Wexford, southeastern Ireland. Two curves represent exponential distribution of thermal conductivity with depth with a depth constant γ of 0.1 and 0.5. The thermal conductivity in the deep section is *c.* 3.2 W m^{-1} K^{-1}, and *c.* 1.2 W m^{-1} K^{-1} in the shallow, near-surface section; (b) Geotherm using the thermal conductivity structure in (a) and a constant basal heat flow of 63 mW m^{-2}. Linear geotherms between 25 and 40 °C km^{-1} are shown for comparison.

production varies with lithology, generally being lowest in evaporites and carbonates, low to medium in sandstones, higher in shales and siltstones and very high in black shales (Haack 1982; Rybach and Cermak 1982; Rybach 1986).

In the continents, crustal radioactivity may account for a large proportion (20–60%) of the surface heat flow (Chapter 2). For a purely conductive, 1-D (vertical) heat flow, the temperature at any depth y is determined by the surface temperature T_0, the basal heat flow q_b, the

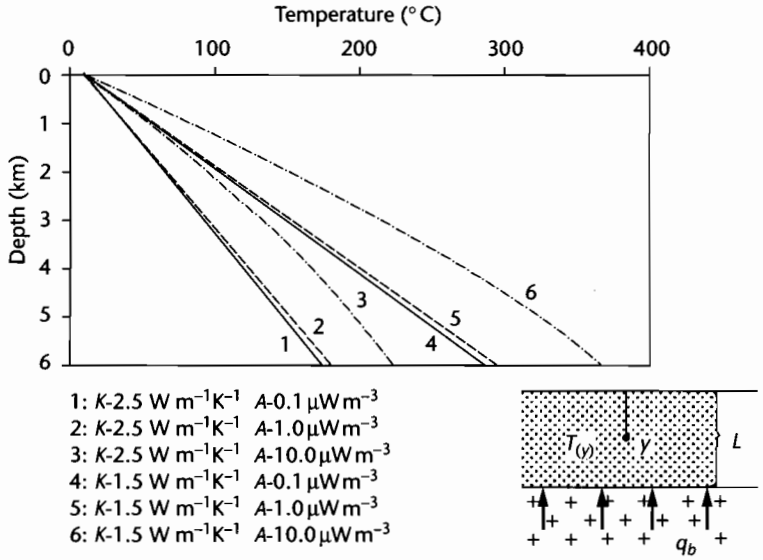

Fig. 9.15 The influence of internal heat generation per unit volume in the sedimentary column A and the thermal conductivity K on the distribution of temperature with depth $T(y)$. The different curves were calculated by Rybach (1986) for a thickness of the heat-producing zone of 6 km, a basal heat flux q_b of 70 mW m^{-2} and a surface temperature T_0 of 20 °C.

Table 9.3 Typical concentrations of heat-producing elements in various rock types.

Rock type	U (ppm)	Th (ppm)	K (%)
Granite	4.7	20	4.2
Shale	3.7	12	2.7
Average continental crust	1.42	3.6	1.43
Reference mantle	0.031	0.124	0.031
Chondritic meteorite	0.008	0.029	0.056

average thermal conductivity of the sediments K and the internal heat production A (estimated from natural gamma ray logs) (eqn 2.46). The effect of the internal heat generation is greatest at large depths, as can be seen from the third term in equation (2.46) (Fig. 9.15). The temperature increase after a time t as a result of the internal heat generation depends on the value of A, but the net temperature change also depends on the rate of conductive heat loss. Over geological time scales of >10 Myr the temperature rise may be considerable (Rybach 1986, p.317). Internal heat generation in sediments may therefore strongly affect the temperature field in the basin if it is deep (>5 km) or long-lived (>10 Myr).

The presence of a thick cover of sedimentary rocks with high radiogenic heat production has the effect of "blanketing" the underlying crust and deeper parts of the sedimentary basin (Karner 1991; Wangen 1995). This blanketing effect may be important in terms of the temperature-dependent rheology of rocks underlying the basin, but more importantly in the present context in elevating paleotemperatures in the basin-fill.

9.6.3 Effects of water flow

The temperatures in sedimentary basins may also be affected by the advective flow of heat through regional aquifers. Such processes may cause anomalously low surface heat flows at regions of recharge, and anomalously high surface heat flows in regions of discharge. The heat flow distributions of the Great Plains, USA (Gosnold and Fischer 1986) and the Alberta Basin (Majorowicz and Jessop 1981; Majorowicz et al. 1984) have been explained in this way.

It is important to know the relative contributions of conduction from the interior of the Earth, internal heat production from radiogenic deacy (and chemical reactions), and advective transport of fluids through pore space. We perform this heat balance in Boxed Text 9.3

BOXED TEXT 9.3: Advective Heat Transport by Fluids

Consider a subsiding and compacting volume of porous rock with a cross-sectional area a and thickness δy (Fig. 9.16). The total heat gain or loss across this volume of porous rock of thickness δy is made of three components: a change in conductive heat flow q_c, an internal heat generation A, and a change in advective heat flow q_a

$$(a\partial y)\frac{\partial q_c}{\partial y}+(a\partial y)A+(a\partial y)\frac{\partial q_a}{\partial y} \tag{9.48}$$

The mass of the rock volume is $\rho_r a\delta y$ where ρ_r is the density of the porous rock. The heat stored in this rock volume is therefore the product of the specific heat c_r and its mass, $c_r\rho_r a\delta y$. If this rock volume undergoes a temperature change δT over a short time period δt, the rate of heat loss or gain is $c_r\rho_r a\delta y\delta T/\delta t$. Consequently,

$$c_r\rho_r a\partial y\frac{\partial T}{\partial t}=(a\partial y)\frac{\partial q_c}{\partial y}+(a\partial y)A+(a\partial y)\frac{\partial q_a}{\partial y} \tag{9.49}$$

The mass of fluid occupying the pore space is $(a\delta y\rho_f\phi)$. Its heat content is therefore $(a\delta y\rho_f\phi)c_f T$, and the advective heat flow is

$$q_a=(a\partial y)\rho_f\phi c_f v_f T \tag{9.50}$$

Substituting (9.50) into (9.49), making use of Fourier's law (eqn 2.29), simplifying and rearranging, equation (9.49) can be written

$$\frac{\partial T}{\partial t}=\frac{1}{c_r\rho_r}\left\{K_r\frac{\partial^2 T}{\partial y^2}+A+c_f\rho_f\phi v_f\frac{\partial T}{\partial y}\right\} \tag{9.51}$$

where K_r is the thermal conductivity of the rock volume, and it is assumed that the pore fluid velocity v_f does not vary with depth in the rock volume.

Clearly, one of the most important parameters in an analysis of the temperature changes caused by advection of pore waters is the flow velocity of the moving groundwater. Flow velocities of groundwater vary greatly, from very high velocities in shallow unconfined aquifers (>10^3 m yr^{-1}, equivalent to *c.* >10^{-4} m s^{-1}), lower values in common producing aquifers (10^{-1} to 10^2 m yr^{-1}, equivalent to *c.* >10^{-5} to 10^{-8} m s^{-1}), and very low velocities of compactionally driven flow (10^{-6} to 10^{-2} m yr^{-1}, equivalent to *c.* >10^{-13} to 10^{-9} m s^{-1}) (Fig. 9.17). Using the parameter values for a volume of rock deeply buried in a sedimentary basin (Table 9.4)

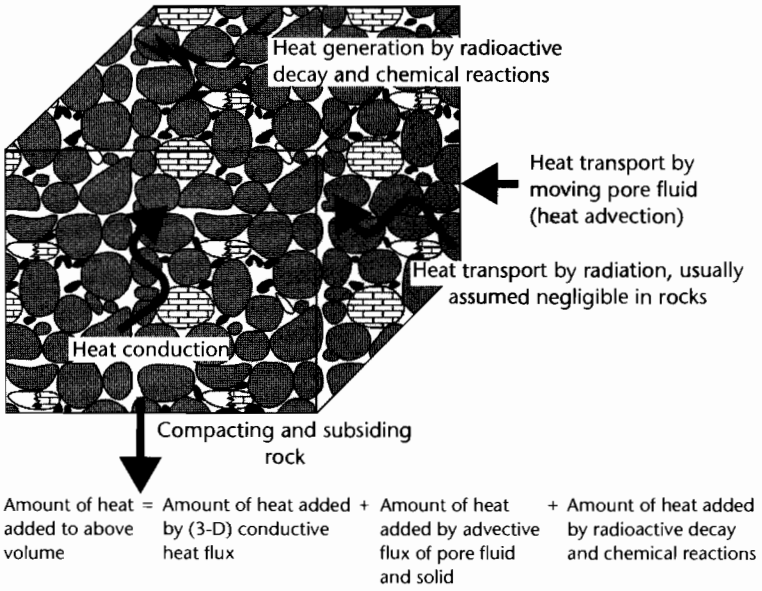

Fig. 9.16 Schematic representation of a cube of subsiding and compacting sedimentary rock as a basis for a heat balance (after Giles 1997). Reproduced courtesy of Springer.

Table 9.4 Typical parameter values for a porous sedimentary unit deeply buried in a sedimentary basin.

Parameter	Notation	Typical value	Units
Rock volume density	ρ_r	2500	$kg\,m^{-3}$
Rock volume bulk thermal conductivity	K_r	3	$Wm^{-1}K^{-1}$
Rock volume heat capacity	c_r	1×10^3	$J\,kg^{-1}K^{-1}$
Pore fluid density	ρ_f	1000	$kg\,m^{-3}$
Pore fluid heat capacity	c_f	4.185×10^3	$J\,kg^{-1}K^{-1}$
Pore fluid velocity*	v_f	10^{-13}–10^{-9}	$m\,s^{-1}$
Rock volume porosity	ϕ	0.1	
Internal heat generation	A	1.25×10^{-6}	Wm^{-3}
Formation and pore fluid temperature	T	373	K

Note:
* Typical of compactionally driven flow (see Giles 1997, p. 278, Fig. 12.3).

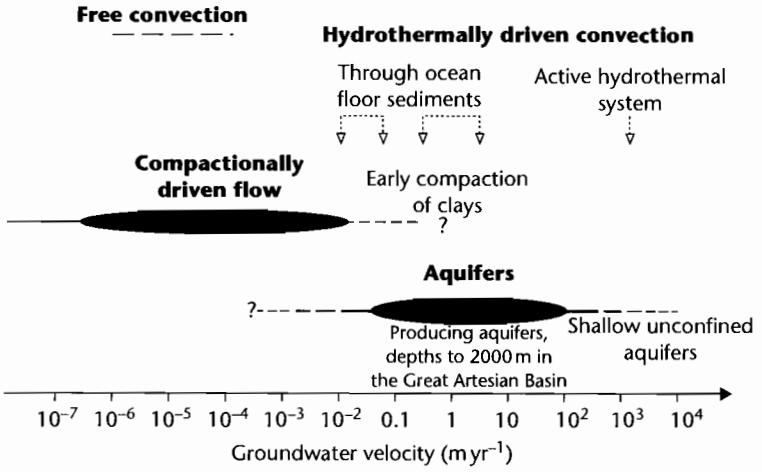

Fig. 9.17 Typical measured pore fluid velocities associated with compactionally driven flow, confined and unconfined aquifers and hydrothermally driven convection, after Giles (1997). Reproduced courtesy of Springer.

equation (9.50) gives an advective heat flow of 16 mW m^{-2} for a pore fluid velocity of 10^{-10} m s^{-1} and 2 mW m^{-2} for a pore fluid velocity of 10^{-11} m s^{-1}, typical of compaction-driven flow (Giles 1997, p. 278). Advective heat flows are therefore likely to be important in porous sedimentary rocks (such as uncemented eolian sandstones) with compaction-driven groundwater velocities, and to dominate in aquifers with high groundwater velocities (10^{-6} to 10^{-7} m s^{-1}).

Flow velocity can be estimated from the *Darcy equation*

$$U = K\frac{\partial P}{\partial x} \tag{9.52}$$

where K is the permeability and $\delta P/\delta x$ is the pressure gradient. Flow velocities are therefore strongly dependent on lithology. With compaction during burial, sedimentary units become less permeable and therefore less able to transmit fluids.

and, taking reasonable parameter values for a deeply buried rock in a sedimentary basin, calculate the role of advection in controlling the heat flow.

The likely impact of fluids on the thermal history of the basin-fill is linked to the tectonic evolution of the basin. For example, uplift of rift shoulders during stretching of the continental lithosphere may cause meteoric-derived groundwater flows driven by the topographic elevation of the basin flanks. The meteoric fluxes in this case must displace brines filling pore space within the basin-fill. If the density of pore-filling brine is $1028\,kg\,m^{-3}$ and the density of meteoric water is $1000\,kg\,m^{-2}$, a simple pressure balance indicates that the extent of downward penetration of meteoric water is nearly 40 times the topographic elevation of its influx (Bjorlykke 1983). This implies that for even low topographic basin margin uplifts, meteoric gravitationally driven water is able to displace basinal brines from the entire depth of the sedimentary basin. At the other extreme, fluid movement caused by progressive compaction of basin sediments is slow, with vertical rates of $<10\,mm\,yr^{-1}$, with lower values still as the permeability reduces during compaction (Giles 1987) (Fig. 9.17).

Smith and Chapman (1983) provide a review of the effects of fluid flow on heat flow in regional scale systems. Luheshi and Jackson (1986) have applied the theory of Smith and Chapman (1983) to the Alberta Basin. Using a permeability and thermal conductivity structure for the basin, they were able to explain the raised temperatures at discharge points of fluid flow and lowered temperatures at the recharge areas in the fringing hills (Fig. 9.18). The model results suggest that the temperature distribution is dominated by convection above the Paleozoic succession, while the heat flows within the Precambrian section can be explained simply by conduction. Andrews-Speed et al. (1984) similarly found that heat flow measurements strongly suggested a deep water circulation, possible controlled by the configuration of faults, in the North Sea failed rift. The implications of detailed studies such as this are that simple 1-D conductive heat flow models may be very poor predictors of actual heat flows in some sedimentary basins. The most strongly affected basins are likely to be continental basins with marginal uplifts, such as foreland basins and some intracratonic rifts and sags.

9.6.4 Effects of surface temperature changes

The possible effects of surface temperature changes on the maturation of thermal indicators have been relatively neglected, although the effects of, for example, glacial retreat on near-surface temperatures has been evaluated (Beck 1977). The likelihood of a surface temperature change penetrating an underlying basin-fill is essentially a question of heat diffusion (§2.2.4), and the problem can therefore be approached in a similar way to the cooling of the oceanic lithosphere. The amount of time necessary for a temperature change to propagate a distance l in a medium with thermal diffusivity κ is

$$\tau = \frac{l^2}{\kappa} \tag{9.53}$$

and the characteristic distance (or thermal diffusion distance) over which a temperature change is felt is

$$L = \sqrt{\kappa t} \tag{9.54}$$

Taking a thermal diffusivity of $\kappa = 10^{-6}\,m^2\,s^{-1}$, appropriate for the sandstones of a basin-fill, a surface temperature disturbance would be registered at 1 km depth in just over 30 kyr. Expressed differently, the surface temperature change would propagate to a depth of 5.6 km in 1 Myr. We should therefore expect a surface temperature change to rapidly propagate through the upper part of the basin-fill. O'Sullivan and Brown (1998) for example, suggested that the effects of a surface temperature change of *c.* 17 °C during the Miocene on the North Slope of Alaska could be recognized in apatite fission tracks in borehole samples. If geotherms derived from apatite fission track analysis were used to calculate denudation in this example, estimates would be significantly in error.

A key point in this argument is that for thermal indicators to be affected by a surface temperature change, the surface temperature change must be sustained for a prolonged period of time. Yet, climatically induced surface temperature changes tend to be cyclic. What would be the effect of a periodic variation in surface temperature on the geotherm? Temperatures must vary cyclically within a surface zone of the Earth whose thickness is determined by the thermal properties of the crust or basin-fill and the period of the temperature fluctuation. If the temperature variation is described by

$$\omega = \frac{2\pi}{f} \tag{9.55}$$

where f is the period of the temperature variation, we can define a *skin depth* L at which the amplitude of the temperature variation is 1/e of that at the surface of the Earth

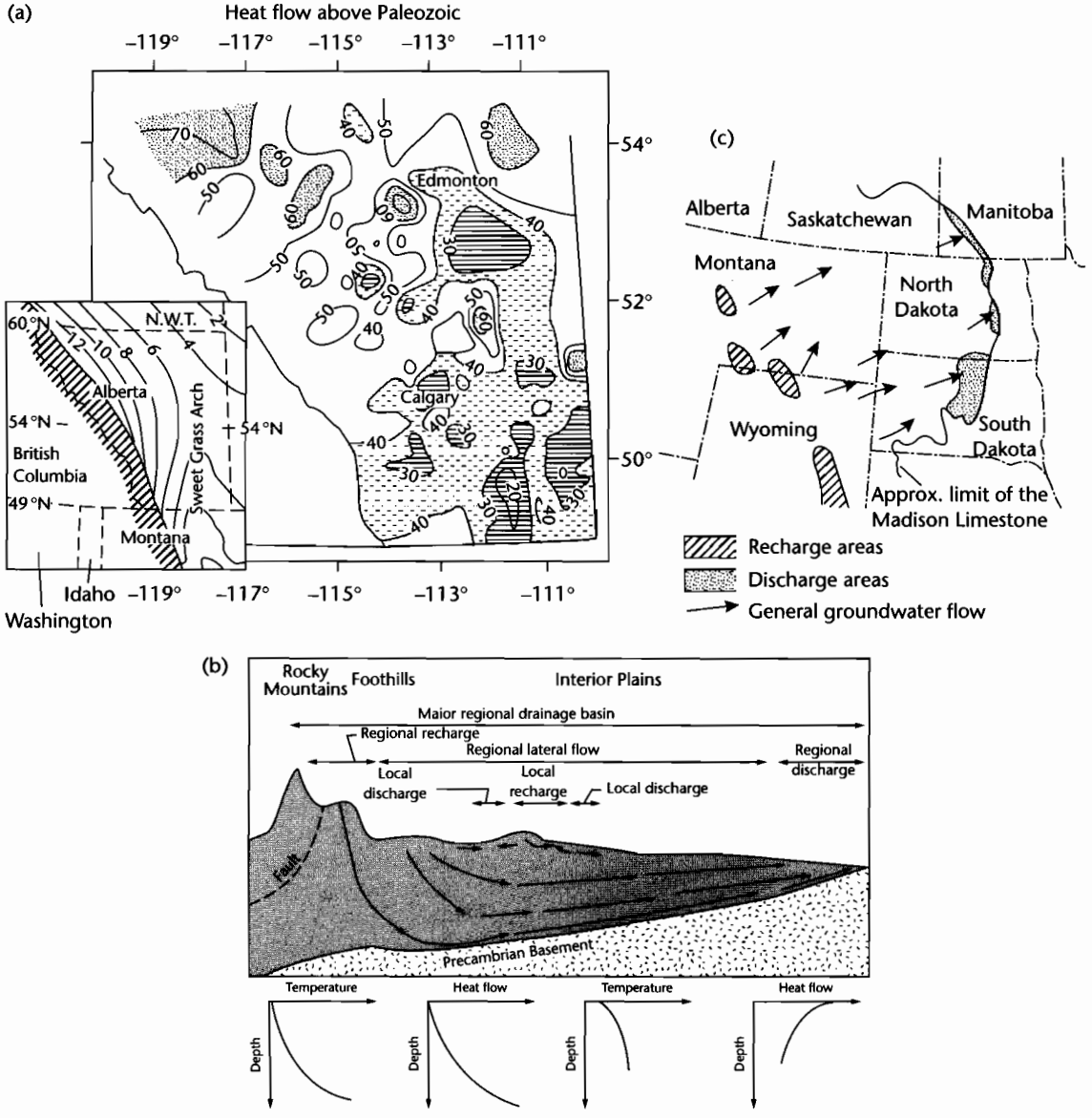

Fig. 9.18 Effects of groundwater flow on surface heat flows in sedimentary basins. (a) Heat flow map of southern and central Alberta, Canada based on estimated heat flow values (in $mW m^{-2}$) above the top of the Paleozoic, based on 33,653 bottom hole temperature data from 18,711 wells (Majorowicz et al. 1984). The heat flows are strongly influenced by groundwater flow from recharge areas in structurally high regions, such as the Sweet Grass Arch (inset), to discharge areas; (b) Pattern of recharge and discharge in a cross-section from the Rocky Mountains to the Great Plains (after Majorowicz et al. 1984), and (c) plan view of groundwater flow in the Mississippian (Lower Carboniferous) Madison Limestone aquifer (after Downey 1984).

$$L = \sqrt{\frac{2\kappa}{\omega}} \tag{9.56}$$

Using $\kappa = 8 \times 10^{-6}\,m^2 s^{-1}$, it is clear that the skin depth for daily temperature variations ($\omega = 7.27 \times 10^{-5}\,s^{-1}$) is less than 20 cm, but for Pleistocene climate change variations of frequency 10^5 yr ($\omega = 1.99 \times 10^{-12}\,s^{-1}$), the skin depth is 1 km. This means that long period variations in surface temperature may be felt deep within the sedimentary basin-fill.

9.7 MEASUREMENTS OF THERMAL MATURITY IN SEDIMENTARY BASINS

Approaches to understanding the mechanisms of subsidence and uplift in sedimentary basins invariably involve model predictions for burial history, heat flow, and paleotemperature that can be compared with reality. But what direct observations are possible in a sedimentary basin that provide information on thermal history and thereby allow a test and calibration of these models? A wide range of techniques are currently available, making use of the changes with temperature of organic particles, clay minerals, geochemical markers, and of the annealing and diffusion histories of certain minerals such as apatite. Most of these techniques generate data on the *maximum* temperature reached by a particle within the basin-fill. This is because thermal reactions are irreversible. Only thermochronological techniques such as apatite fission track analysis and U–Th/He diffusion analysis provide any information on thermal evolution. Each technique has its advantages and drawbacks. Taken together, a range of diverse techniques may provide important information on the thermal history of the basin-fill. This information is critically important not only in understanding the driving mechanisms for basin formation, but also in the evaluation of hydrocarbon prospectivity (Tissot and Welte 1978) (Chapter 10).

In the following sections, a number of techniques are presented in outline. For further information and detailed applications, the reader is referred to the references cited. Useful summaries are found in Héroux et al. (1979), Gallagher et al. (1998) and Giles (1997).

9.7.1 Estimation of formation temperature from borehole measurements

Formation temperatures from boreholes are used in thermal modeling studies to calculate the geothermal gradient and basal heat flow to the sedimentary section. The temperature in the borehole is recorded on each logging run, using a suite of maximum recording thermometers. Because the circulation of drilling fluid tends to cool the formation, it is necessary to analyze the rate at which temperature restores itself to its original true formation value using temperatures recorded on each successive logging run within a suite of logs. These temperatures may be plotted on a "Horner"-type plot, as described by Dowdle and Cobb (1975).

The form of the temperature build-up plot is shown in an example from the Gulf Coast in Figure 9.19. Temperature measured on each logging run is plotted against

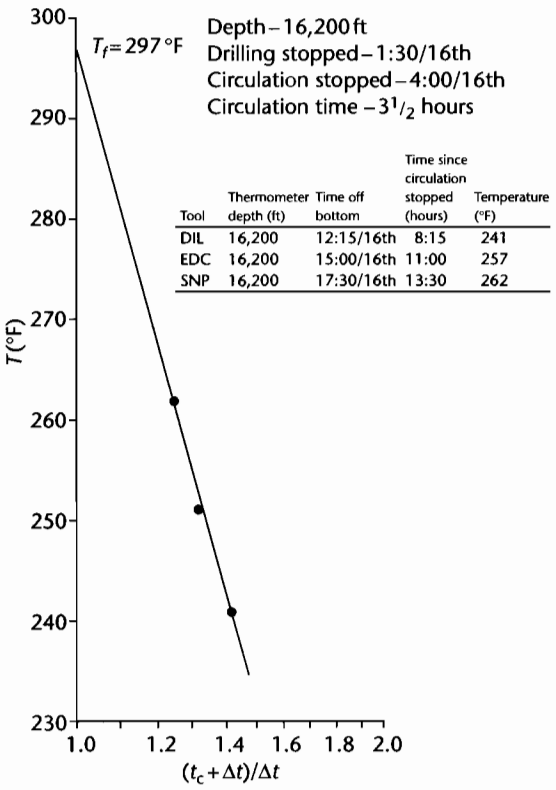

Fig. 9.19 The determination of true formation temperature from a Horner plot (after Dowdle and Cobb 1975). This example is from a high temperature well in the Gulf Coast, USA. The depth at which measurements were taken was 16,200 ft (*c.* 5 km). Temperature increased from 241 °F measured at 8 h 15 min after circulation of mud stopped, to 262 °F taken 13 h 30 min after circulation stopped. The estimated formation temperature T_f is 297 °F.

a dimensionless time factor, $(t_c + \Delta t)/\Delta t$, where t_c is the cooling time (the duration of mud circulation from the time the formation opposite the thermometer was drilled to the time circulation of the drilling mud stopped), Δt is the thermal recovery time (time since mud circulation stopped to the time the logging sonde is in position at the bottom of the borehole). A fully recovered or stabilized formation temperature T_f is obtained by extrapolation to the ordinate, where $(t_c + \Delta t)/\Delta t = 1$. Serra (1984, 1986) discusses the calculation of heat flow from borehole temperature measurements.

9.7.2 Organic indicators

The progressive maturation of organic materials has long been understood in terms of *coal rank*. The coalification process changes peat to anthracite through the intermediate steps of brown coal (lignite and sub-bituminous coal) and bituminous coal. During coalification, the percentage of carbon increases whereas moisture and volatiles are gradually eliminated (Fig. 9.20). Of much greater importance to basin analysis is the quantitative measurement of maturity through the reflectance of the vitrinite maceral, and to a lesser extent the structural changes in distinctive organic molecules known as biomarkers, and the semi-quantitative assessment of spore color.

9.7.2.1 Vitrinite reflectance

Vitrinite reflectance is the most widely used indicator of maturity of organic materials. It is an optical parameter and is denoted by VR or R_o (reflectance in oil). Standard procedures for the measurement of vitrinite reflectance are given in Bostick and Alpern (1977), Bostick (1979), Hunt (1979), Dow and O'Connor (1982), Stach et al. (1982), van Gijzel (1982), and Tissot and Welte (1984). Section 10.3.1.3 provides more details. The reflectance of the vitrinite group of macerals appears to vary smoothly and predictably with temperature (Lopatin 1971; Burnham and Sweeney 1989; Sweeney and Burnham 1990).

Drawbacks in the use of vitrinite reflectance measurements are outlined by Héroux et al. (1979), Kübler et al. (1979) and Durand et al. (1986). These arise from a number of problems. Reflectance measurements taken from maceral types other than vitrinite (especially in lacustrine and marine sediments), and even from different macerals within the vitrinite group, may significantly differ (Bensley and Crelling 1994). Other drawbacks are the possibility of reworking of organic material (especially in sandstones), and the lack of higher plants yielding vitrinite in pre-Devonian strata. Vitrinite reflectance tends to be unreliable at low levels of thermal maturity (R_o less than 0.7 or 0.8%). At high temperatures equivalent to depths of >4 km the vitrinite maceral is increasingly anisostropic, making accurate measurement problematical. Nevertheless, with care, reflectance values are a good indicator of maximum paleotemperature within the approximate depth range of 1–4 km (Whelan and Thompson-Rizer 1993).

Unfortunately, the distribution of activation energies and value of the frequency factor (see eqn 9.40) for the maturation of vitrinite are not convincingly known (Lerche et al. 1984; Burnham and Sweeney 1989; Lakshmanan et al. 1991), and a wide range of values have been proposed. The most reliable estimates give a value of E_a in the range 200–300 kJ mol^{-1}, and of A from 2.5×10^{10} to 7.48×10^{18} s^{-1}. It must be emphasized therefore that the uncertainties in knowledge of the parameters in the Arrhenius equation make the use of vitrinite reflectance data useful but inexact, and VR measurements should always be compared with paleotemperature estimates from other indices.

Vitrinite reflectance measurements from samples recovered at different depths allows a plot of vitrinite reflectance *versus* depth to be made (e.g., Corcoran and Clayton 2001). These plots are known as VR or R_o profiles. Examples of their interpretation are given in §9.8. A compilation of VR data from 28 extensional basins shows a relatively well-defined trend (Fig. 9.21), with a surface intercept at 0.2–0.4% R_o, and a gradient of $0.15 \pm 0.09\%$ R_o km^{-1} at depths of <4 km.

The Anadarko Basin in western Oklahoma has some of the deepest exploratory wells in the world, penetrating to more than 7900 m (~26,000 ft), and is therefore an excellent case study for thermal maturation. Vitrinite reflectance contours (*isoreflectance lines*) on the Upper Devonian–Lower Mississippian *Woodford Shale* have been constructed from 28 boreholes (Fig. 9.22) (Cardott and Lambert 1985). Isoreflectance maps are useful in combination with structural contours, since cross-cutting relationships give an indication of local thermal anomalies superimposed on the burial-related maturation.

Since vitrinite reflectance in a nonreversible thermal indicator, it is important to know whether the distribution of vitrinite reflectance with depth in a sedimentary basin allows a geotherm at a particular time in basin history to be constructed. For example, is it possible that

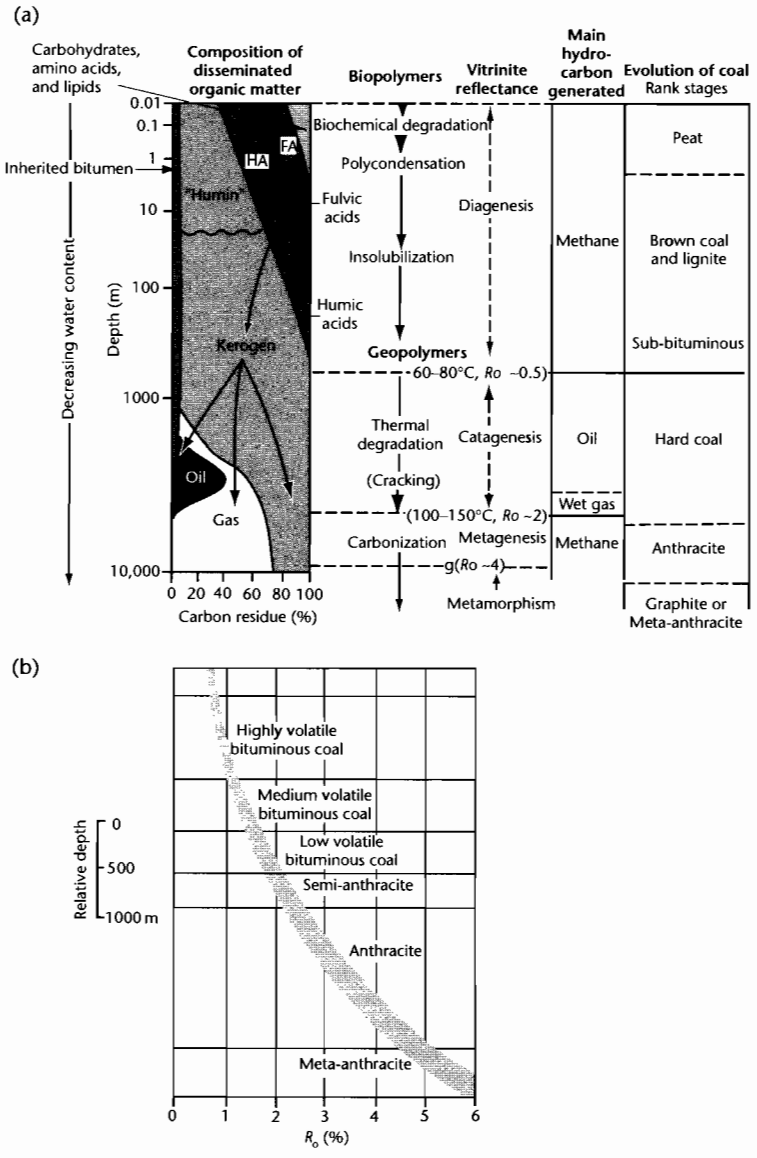

Fig. 9.20 (a) Evolution of organic matter from organic-rich sediment or peat through the various ranks of coal to meta-anthracite and the main hydrocarbons generated, correlated with vitrinite reflectance values. After Tissot and Welte (1984). Coal ranks from Stach et al. (1982). Reproduced courtesy of Springer; (b) Correlation of coal rank with vitrinite reflectance R_0 (%). Reproduced courtesy of Gebrüder Borntträger, Berlin.

the maximum temperature at different depths in the basin was reached at different times? If so, a R_o profile would not represent a single geotherm. This problem can be approached from a forward model of paleotemperature and vitrinite reflectance in a basin with a time-dependent basal heat flow. The heat flow and temperature algorithms are based on the uniform stretching model, but with an additional heat flow originating from the internal heat generation of crustal rocks and sediments due to radioactive decay. The time–temperature

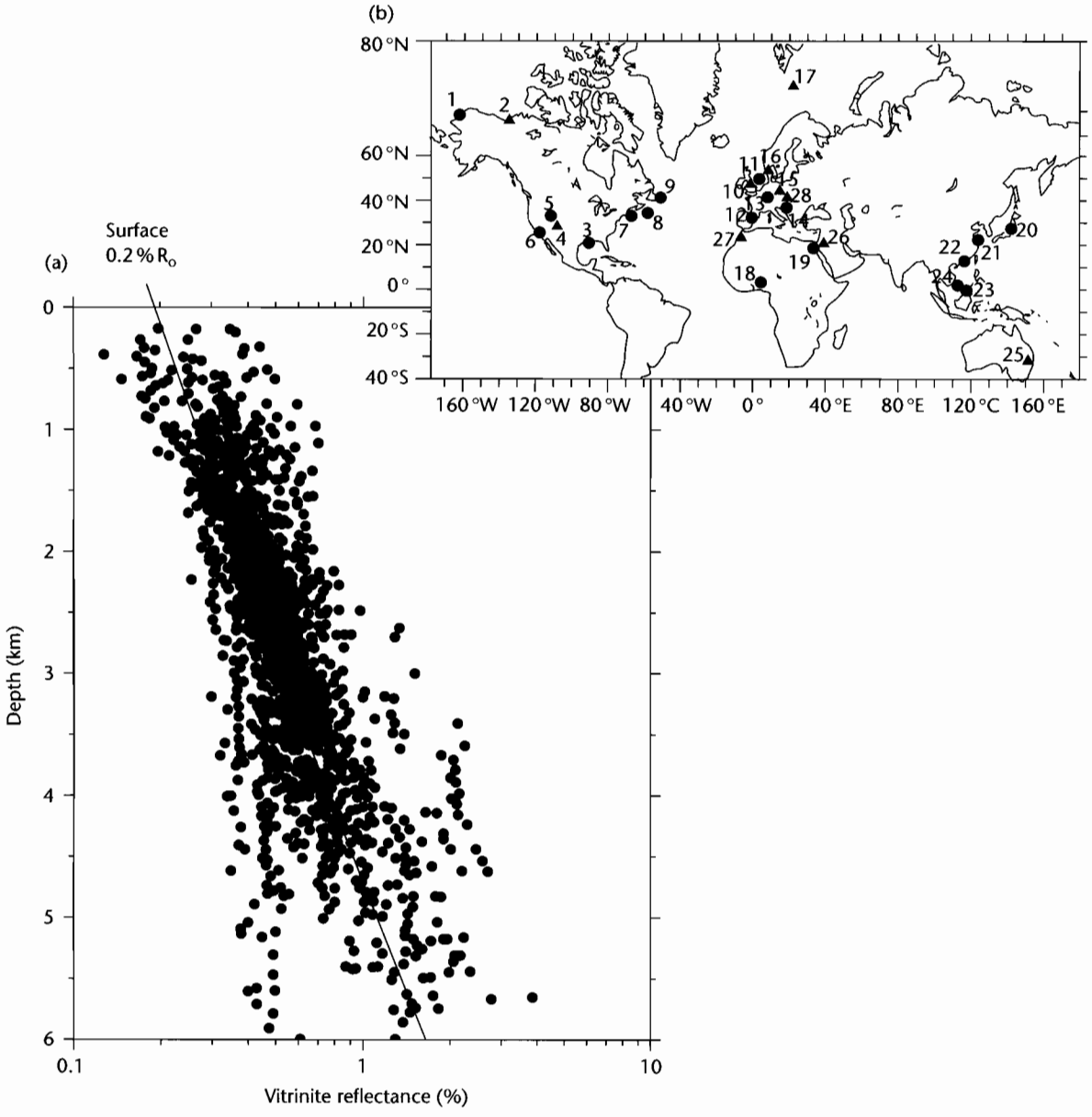

Fig. 9.21 Vitrinite reflectance (logarithmic scale) *versus* depth for a wide range of selected extensional sedimentary basins (marked on world map) with predictable subsidence histories, after Rowley and White (*pers. comm.*).

history of a number of horizons within a borehole can then be calculated based on the thermal model and the subsidence history derived from the stratigraphy penetrated by the borehole (see §9.3). Paleotemperatures can be converted to vitrinite reflectance using empirical relationships (Barker and Pawliewicz 1986; Burnham and Sweeney 1989; Sweeney and Burnham 1990) to create a synthetic VR profile. Two interacting effects control the paleotemperature and vitrinite reflectance of the basin-fill. On the one hand, the basal heat flux decreases

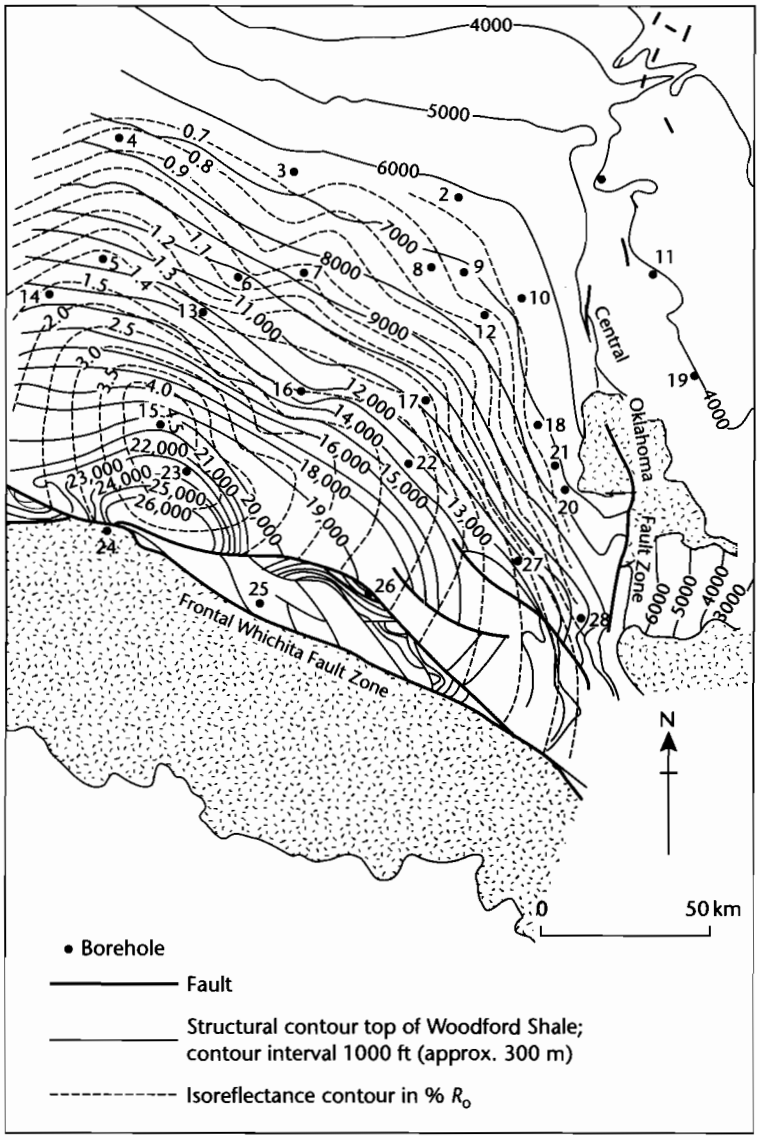

Fig. 9.22 Combined isoreflectance and structure map of the Woodford Shale of the Anardarko Basin of Oklahoma (Cardott and Lambert 1985). Vitrinite reflectance values in general increase with depth of burial, but strong cross-cutting relationships of the isoreflectance and structure contours suggest that there may have been local thermal disturbances superimposed on the burial-related maturation.

through time due to thermal relaxation following stretching, causing cooling. On the other hand, subsidence causes a reference horizon to descend to increasing depths over time, causing heating. Figure 9.23 shows that for low to moderate values of stretching in a basin undergoing continuous subsidence, the present-day temperatures represent the maximum temperatures reached by all but the deepest horizons within the basin-fill. Consequently, the vitrinite reflectance profile can be used to estimate the geotherm. However, model results suggest

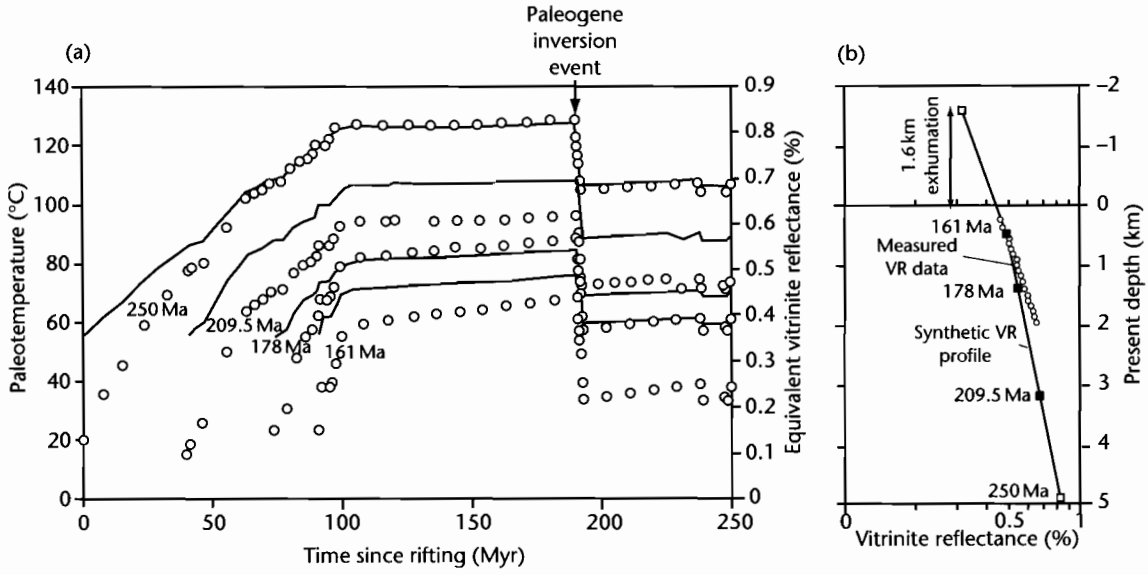

Fig. 9.23 (a) Paleotemperature and equivalent vitrinite reflectance *versus* time for 4 different horizons in well 42/21-1 in the extensional Irish Sea Basin ($\beta = 1.5$ at 250 Ma) with internal heat generation ($H_s = 9.6 \times 10^{-10}$ W kg^{-1}; $h_r = 10$ km) and the thermal conductivity structure shown in Fig. 9.14. Open circles are data points derived by forward modeling temperature from the borehole subsidence history. Solid lines are equivalent vitrinite reflectance; (b) The forward modeled R_0 profile is compared with measured values. Extrapolation of the profile upwards gives an estimate of 1.6 km of denudation since the VR values were set at the maximum temperature at *c.* 60 Ma (*c.* 190 Myr since rifting).

that in highly stretched basins and for old (especially synrift) stratigraphy, VR values may represent maximum paleotemperatures attained early in basin history and not subsequently exceeded. Consequently, measured VR profiles may not reflect closely the distribution of temperature with depth at any particular instant in time.

The use of R_o profiles in estimating the amount of section removed as a result of basin inversion events is discussed in §9.8.2.

Although vitrinite reflectance has become pre-eminent in its use in basin studies, it is not the only index of thermal maturity (§10.3.1.3). Other optical parameters derived from organic material include sporinite microspectrofluorescence and spore, pollen, and conodont coloration scales. Fluorescence and reflectance studies are complementary, fluorescence intensity and reflectance being inversely proportional.

9.7.2.2 Biomarkers

Certain organic molecules (*biomarkers*) undergo transformations with increasing temperature. For example, single *isomers* in biological material are progressively converted to mixtures of isomers with increasing temperature (Abbott et al. 1990). *Aromatization* reactions can also be used, such as the conversion on mono-aromatic to tri-aromatic steroids (Mackenzie and McKenzie 1983). Biomarker transformations take place at rates approximated by the Arrhenius equation.

9.7.3 Thermochronology: Apatite fission track analysis

Fission track analysis is a relatively modern (since the 1960s) thermochronological technique based on the atomic damage caused to minerals by their spontaneous decay, almost exclusively by the fission of ^{238}U. The fission of ^{238}U produces a trail of damage to the lattice known as a *fission track*. Fission tracks become visible when the crystal is chemically etched and viewed at high magnification.

It is safe to assume that statistically fission takes place at a constant rate. The concentration of the parent isotope ^{238}U in minerals such as apatite ($Ca_5(PO_4)_3(F,Cl,OH)$), zircon ($ZrSiO_4$) and sphene

($CaTiO(SiO_4)$) is high enough to produce plenty of tracks, but low enough so that the crystal is not completely criss-crossed by tracks, making measurement difficult.

A *fission track age* (Hurford and Carter 1991) can be determined in a similar way to other radiometric methods, that is, through knowledge of the relative abundance of the parent and daughter products. In the case of fission track dating, the abundance of the parent is the original number of ^{238}U atoms – this can be estimated by irradiating the sample in a nuclear reactor. The abundance of the daughter product is proportional to the number of spontaneous fission tracks per unit volume of the apatite crystal.

There are a number of ways in which fission tracks can be measured and analyzed. The most common is to measure the lengths of between 50 and 150 individual horizontal tracks that have been etched just below the surface of the polished section of the crystal. These are known as *confined tracks*. The data are normally shown as a histogram of track length with a mean and standard deviation. Importantly, fission tracks are metastable features that fade or *anneal*, which causes track lengths to shorten. Annealing is mostly controlled by temperature (and also time), so track length distributions reveal information about thermal history. The higher the temperature experienced by the apatite crystal, the greater the annealing.

Individual minerals have a closure temperature below which fission tracks are preserved. For *apatite*, the closure temperature is 110 °C ± 10 °C, but at geological time scales there is a range of temperature of at least 60 °C below the closure temperature where significant annealing takes place: this is termed the *Partial Annealing Zone* (PAZ). Some annealing may even take place at room temperature, but it is generally regarded as negligible at these temperatures. For *zircon*, the PAZ is between 200 and 350 °C, but the annealing behavior of zircon is not as well known as for apatite. Because of the different closure temperatures of apatite and zircon, apatite fission track analysis is particularly useful in thermal studies of the upper few km of the crust, whereas zircon fission track analysis is more informative for deeper levels of burial.

In summary, fission tracks are continuously formed at all temperatures, but are only preserved for geological time scales below the closure temperature. Their abundance therefore gives a fission track age. The track length distribution gives a record of the annealing history, which can be related to the time–temperature trajectory of the crystal.

The fission track ages and track length distributions for four different thermal histories are shown in Figure 9.24. These are illustrative of the way in which apatite fission tracks are sensitive to different tectonic histories.

- **Linear heating** produces a tightly clustered, unimodal, symmetrical histogram of track length with a short mean track length (MTL); all tracks experience the same maximum temperature; the fission track age bears no relation to any specific or thermal event. Linear heating is likely to take place during progressive subsidence in a sedimentary basin;
- **linear cooling** causes tracks to experience different maximum temperature, causing the track length histogram to be negatively skewed; the MTL is longer and the standard deviation larger than in the case for linear heating; once again the fission track age bears no relation to any specific thermal or tectonic event. Linear cooling may result from prolonged, slow basin inversion;
- **rapid cooling** causes most tracks to have been produced after the early cooling episode at temperatures below those of the PAZ; track lengths are long; the fission track age gives a good indication of the date of the cooling event. Rapid cooling may result from tectonic processes driving rapid exhumation, for example on a rift flank or in an orogenic belt;
- **heating–cooling** scenario; old tracks formed during the heating phase have a similar length with a short MTL; newer tracks experience different maximum temperatures during the cooling phase, causing the histogram to be bimodal, with a high standard deviation; the fission track age does not accurately reflect the onset of uplift. Heating–cooling is typical of basin development followed by inversion.

Apatite fission track analysis is routinely used in the quantification of denudation in a wide range of tectonic situations including convergent mountain belts, rift flanks, and passive margin escarpments (useful summary in Gallagher et al. 1998). The rate of cooling derived from fission track thermochonometry is very valuable in estimations of long term sediment effluxes from erosional hinterlands, and in the timing of distinct tectonic exhumation events. For example, the onset of rapid exhumation in the Central Alaska Range was dated as 6 Ma on the basis of the recognition of two distinct populations of fission tracks (Fitzgerald et al. 1995). Some highly annealed tracks formed during a period of slow cooling, whereas other relatively unannealed tracks formed during a rapid exhumation event.

AFT analysis has also been extensively applied to the thermal history of sedimentary basins (Naeser 1979).

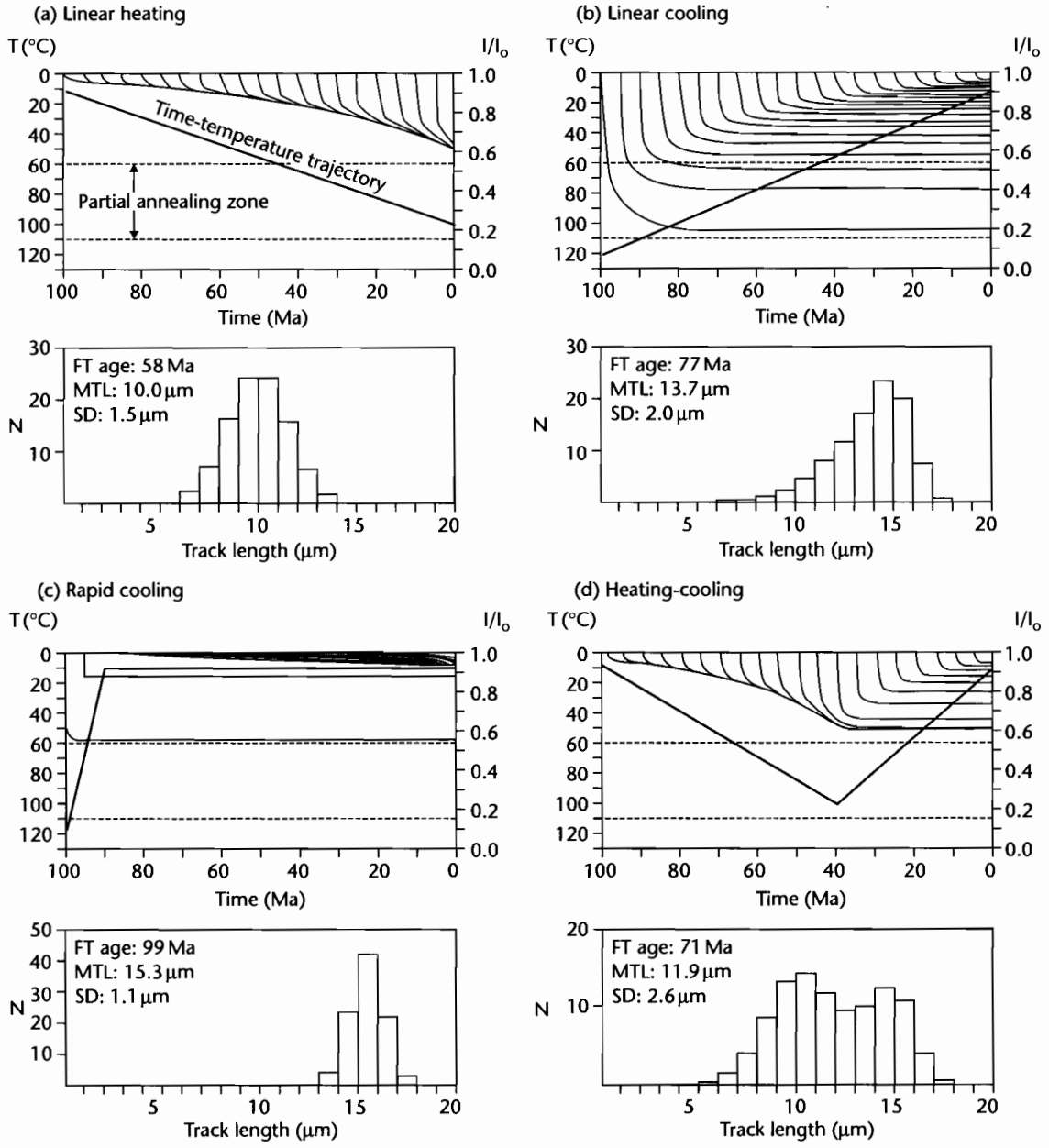

Fig. 9.24 Simple thermal histories and the predicted fission track length parameters using Durango apatite and the annealing model of Laslett et al. (1987), after Gallagher et al. (1998). Each model simulation has 20 tracks formed at equal time increments over the total duration of the thermal history. Track length reduction (annealing) is shown by the ratio l/l_0, where l is the track length and l_0 is the initial track length. (a) Linear heating, giving a symmetrical, unimodal track length distribution and a short mean track length. Note that the fission track age does not relate to any distinct tectonic or thermal event; (b) Linear cooling, with a negatively skewed track length distribution, since each track experiences a different maximum temperature. The fission track age does not correspond with any distinct tectonic or thermal event; (c) Rapid cooling, with long tracks caused by rapid exhumation through the Partial Annealing Zone. The fission track age gives a good indication of the age of the cooling event; (d) Heating–cooling trajectory gives a bimodal track length distribution, and the fission track age does not correspond to any distinct tectonic or thermal event. Reproduced courtesy of Annual Reviews, Palo Alto.

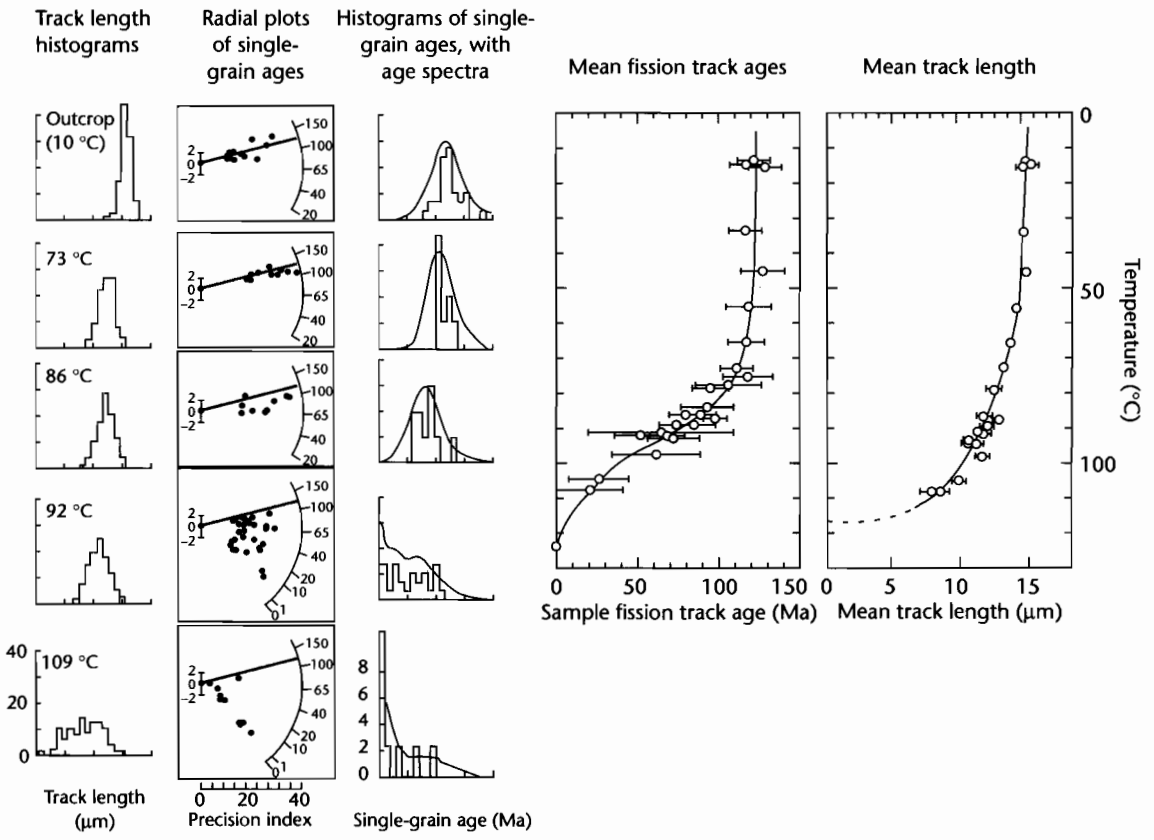

Fig. 9.25 Apatite fission track data from the Otway Basin, southeast Australia (Gleadow and Duddy 1981). The stratigraphic age of the samples is *c.* 120 Ma (shown on the radial plots as a grey band). Note the progressive annealing of fission tracks and reduction of fission track ages of single grains with depth of burial. Reproduced courtesy of Annual Reviews, Palo Alto.

This is because the temperature range over which apatite fission track analysis is sensitive (*c.* 50–120 °C) is also the temperature range over which hydrocarbons are generated (Gleadow et al. 1983). The fission track data from the Otway Basin of Australia (Gleadow and Duddy 1981) illustrate the important principles (Fig. 9.25). At shallow depths above the PAZ, the fission track lengths are tightly clustered and long (*c.* 14 μm), indicating minimal annealing. The fission track age is more or less equivalent to the stratigraphic age of the samples (120 Ma). With greater depth, fission track length histograms show a wider distribution and a shorter mean track length. The fission track ages decrease due to the greater amount of annealing at elevated temperatures, reaching 0 Ma at a temperature of 120 °C (Fig. 9.25).

Apatite fission track analysis of a number of samples at different depths in a sedimentary basin has been used to calculate geothermal gradients. We have seen in §9.6 that there is a number of factors that may affect the distribution of temperature with depth, including variations in thermal conductivity, effects of fluids, and internal heat generation. Consequently, calculation of geothermal gradients from apatite fission track data alone are likely to be significantly in error. Combination of paleothermal data from apatite fission track, vitrinite reflectance, and any other available techniques is therefore always advised.

9.7.4 Thermochronology: U–Th/He method

The accumulation of ^{4}He from the decay of U and Th can also be used as a thermochronological tool (Wolf et al. 1996). The basis for U–Th/He dating is that ^{4}He nuclei (α particles) are produced by the decay of ^{238}U, ^{235}U and ^{232}Th. The helium produced diffuses from the crystal over time, escaping through its surface faces. The rate of diffusion scales on temperature with an Arrhenius-type relationship (eqn 9.40).

$$\frac{\kappa}{a^2} = \frac{\kappa_\infty}{a^2} \exp(-E_a/RT) \tag{9.57}$$

where κ is the diffusivity, κ_∞ is the diffusivity at an infinite temperature, and a is the diffusion domain radius, which may be the physical grain dimension. Diffusivities are measured in the laboratory for certain minerals with different chemical compositions, grain size, and shape. He diffusivity is best understood in apatite. Laboratory data suggest that the closure temperature for the retention of helium is *c.* 80 °C in apatite (Zeitler et al. 1987), so U–Th/He methods extend the temperature range of sensitivity to lower temperatures compared to apatite fission track analysis. This gives additional data on the thermal evolution of the upper 1–2 km of the crust or sedimentary basin-fill.

However, the diffusivity behavior in natural settings is more problematic. One method of investigating this is to study the He age distribution in boreholes where the temperature distribution with depth is known. He ages are predicted to decrease rapidly downhole, because of the effect of temperature on diffusion rates (Wolf et al. 1998). Consequently, there is a Helium Partial Retention Zone (HePRZ), which extends from approximately 40 °C to 80 °C. This is conceptually similar to the Partial Annealing Zone (PAZ) in fission track analysis. The existence of a HePRZ was confirmed by Stöckli et al. (2000) who found a HePRZ overlying an apatite PAZ in samples taken from the White Mountains of California.

Cooling ages from (U–Th)/He diffusion are most simply related to the time of cooling of a sample through its closure temperature. Rapid cooling of samples during exhumation may reveal a fossil or paleo-HePRZ, as we have seen with apatite fission track analysis. Stöckli et al. (2000) recognized a distinct break in slope at 12 Ma when apparent He ages were plotted against depth, signifying the onset of rapid exhumation caused by extensional faulting in the White Mountains of eastern California (Fig. 9.26). This event is barely recognizable from the distribution of apatite fission track apparent ages.

The use of the U–Th/He technique is still in its infancy, and it remains to be discovered where the technique works best and where it suffers from insurmountable problems. In combination with apatite fission track analysis, and thermochronometry using different host minerals such as zircon and titanite, it appears to offer major benefits in evaluating thermal histories within the upper few km of the Earth (Reiners 2002). At present, its application to the thermal history of sedimentary basins is strongly outweighed by its application to exhumation histories.

9.7.5 Mineralogical indices

Mineralogical parameters are controlled by the temperature and chemical properties of the diagenetic environment of the sediment (Fig. 9.27). A number of diagenetic models now exist (e.g., Frey et al. 1980; Burley et al. 1985; Worden and Morad 2003) that allow an interpretation of the sequence of authigenic minerals in terms of their relationship to their depositional environment or surface chemistry (*eogenesis*), the burial or subsurface conditions (*mesogenesis*), and the weathering or re-exposure to surface conditions (*telogenesis*). The reader is referred to §10.4.3 on sandstone reservoirs for further details.

Since eogenetic changes are strongly related to depositional environment, climate, and associated pore-water chemistry, they are of limited use in thermal modeling. However, mesogenesis marks the removal of the sediment from the predominant influence of surface agents in the interstitial pore water. A number of temperature dependent reactions commonly take place in siliciclastic rocks. Kaolinite transforms to dickite, smectites transform to illite via a process of interlayering, and chloritization takes place. Physical processes accompany these chemical changes during burial diagenesis. The most important result is *compaction* due to the weight of the overlying sediments (§9.2). In sandstones, compaction brings about a number of porosity-reducing adjustments including initial mechanical compaction, which simply compresses grains together, rotation, grain slippage, brittle grain deformation and fracturing and plastic deformation of ductile grains.

The best-documented mineral transformations of use in evaluating thermal maturity are from shaly mudstones, where the clay mineral assemblages, the position of the (001) reflection of smectite, the percentage of illite layers in the mixed layer illite 2:1 expandable, and the illite

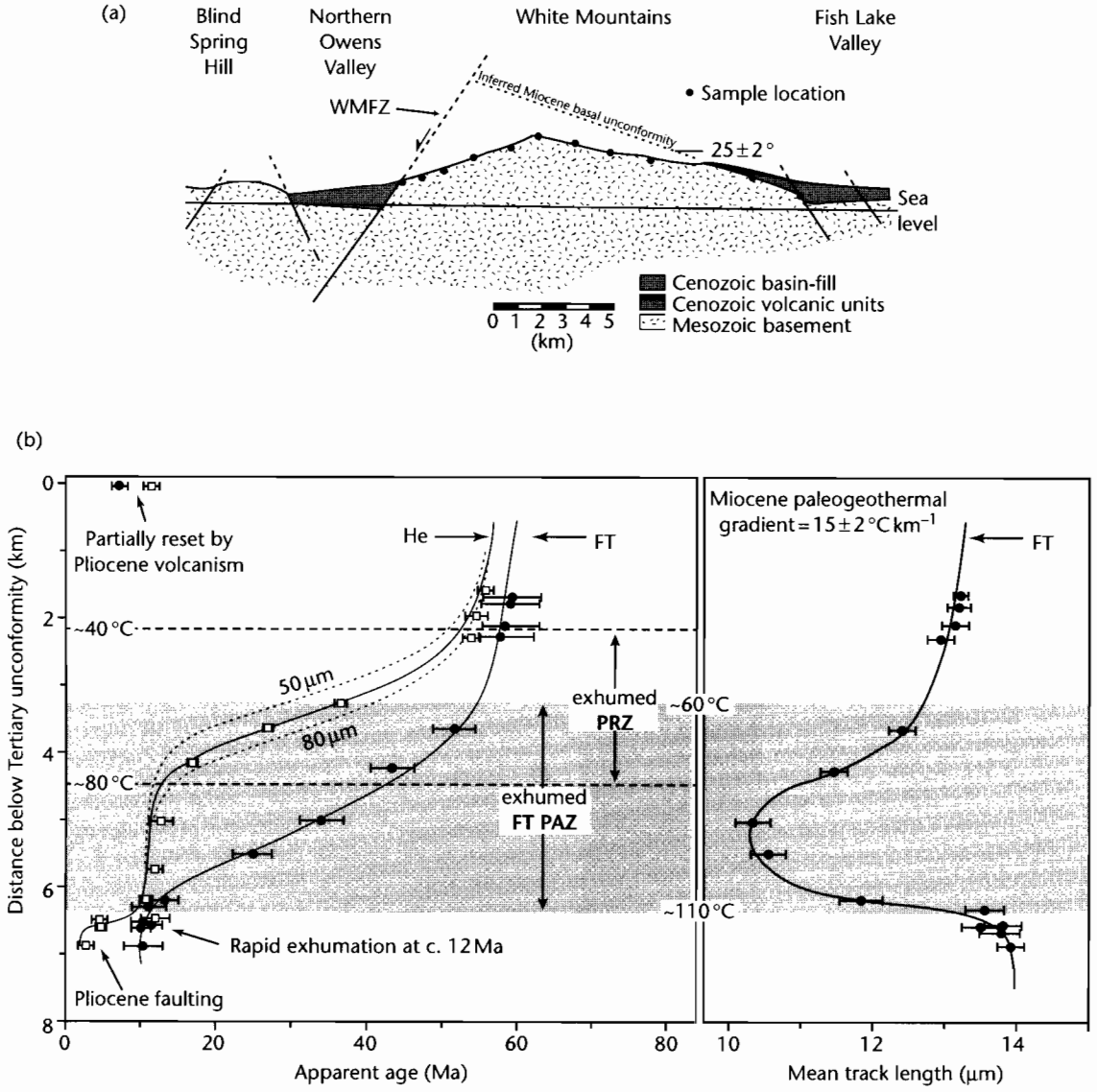

Fig. 9.26 (a) Cross-section of the northern White Mountains, east-central California and west-central Nevada, showing the tilted fault block geometry. The main border fault (White Mountains Fault Zone, WMFZ) has a total of 8–9 km normal displacement, resulting in a 25° eastward tilt recorded by Tertiary volcanic rocks; (b) Integrated apatite fission track and U–Th/He data showing an exhumed partial annealing zone for apatite fission tracks and an exhumed partial retention zone for U–Th/He. Samples from below the exhumed PRZ are invariant with age and directly date the time of inception of footwall cooling caused by extensional faulting. After Stöckli et al. (2000). Reproduced courtesy of Geological Society of America.

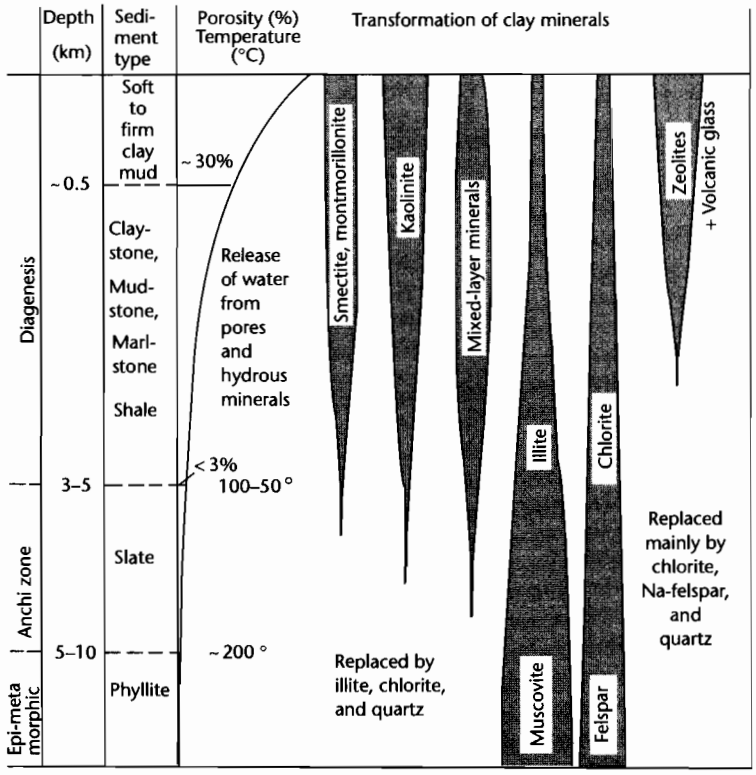

Fig. 9.27 Diagenesis of clay-rich sediments as a function of depth and temperature, showing the most important mineral transformations (after Frey et al. 1980). Reproduced courtesy of Springer.

crystallinity index are used. The approximate relationship between mineralogical changes of this type and organic maturity indices has been attempted (Fig. 9.28). One of the fundamental problems is the need for quantitative indices with which to correlate temperature-driven changes. Kübler et al. (1979) for example, proposed a quantitative measure of the crystallinity of illite using the width of the illite peak on an X-ray diffractogram measured at half of the peak height. The beginning of oil generation ($R_o = 0.5\%$) has been correlated with the disappearance of smectite (e.g., Powell et al. 1978; Kübler et al. 1979).

Quartz cementation and consequent porosity loss is also a temperature-related process acting in sandstones buried to temperatures above 60 °C (Walderhaug 1996). At about the same temperature of 60 °C, smectite clay starts to react with K-felspar to form illite (Hower et al. 1976; Nadeau and Reynolds 1981). At higher temperatures of 100–120 °C, illite precipitates at the expense of kaolinite and K-felspar (Bjorlykke et al. 1986). This can be seen in the percentage of illite in the clay fraction of sandstones penetrated by wells on the Norwegian continental shelf (Fig. 9.29). Quartz cementation and illite precipitation are both temperature dependent, with activation energies of *c.* 15 kcal mol^{-1} and 20 kcal mol^{-1} respectively. The combined temperature-driven effects of quartz cementation and illite precipitation makes sandstones that have experienced temperatures above 120 °C unattractive as potential reservoirs and aquifers (§10.4).

The K content of diagenetic illites allows the age of illite growth to be calculated using the ^{40}K–^{40}Ar radiometric technique. K–Ar ages from samples obtained from different depths can then be used to plot age-depth relationships (Hamilton et al. 1989). The K–Ar age should, for a continuously subsiding basin, increase with depth, since the deeper horizons should reach the critical tem-

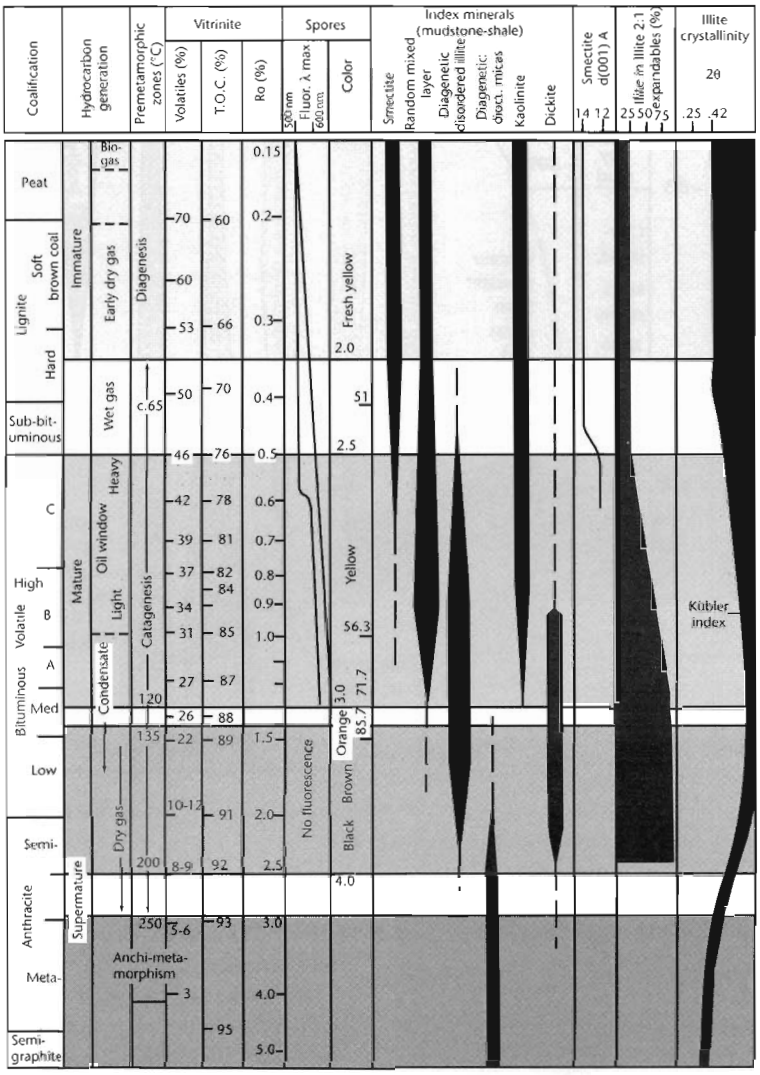

Fig. 9.28 Comparison of a range of thermal indices, modified from Héroux et al. (1979). Thermal indices shown are coal rank, vitrinite total organic carbon and % volatiles, vitrinite reflectance, spore fluorescence and coloration, typical clay mineral distributions, position of the (001) reflection of smectite, % illite in the mixed layer illite 2 : 1 expandable, and illite crystallinity (Kübler index). These indices are correlated with temperature and hydrocarbon products generated.

perature for illite cementation first. A study of sandstone reservoir rocks from the Brent province of the North Sea showed that illite growth began at temperatures of 100–110 °C (corresponding to a vitrinite reflectance in overlying shales of 0.62%), but that there was considerable scatter in the K–Ar age/depth relationship (Hamilton et al. 1992).

9.7.6 Other burial indices

9.7.6.1 Sonic logs

Some indices result from the loss of porosity with increasing burial (§9.2), which is driven by the effective stress on framework grains. Although porosity estimates can be

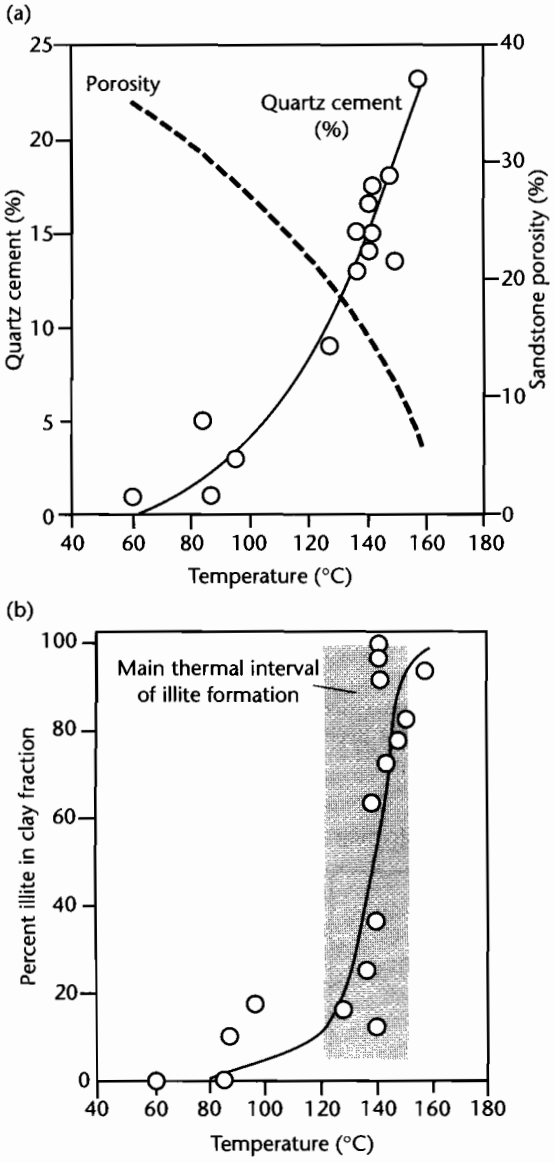

Fig. 9.29 (a) Plot of temperature versus quartz cement content and porosity for wells from the Norwegian continental shelf (Bjorkum and Nadeau 1998), showing an exponential increase in amount of quartz cement with depth; (b) Plot of temperature versus diagenetic illite content measured by X-ray diffraction. Increasing illite content severely reduces permeability. The main thermal interval for illite formation is 120–150 °C.

obtained from a number of downhole logging devices (§9.2.3), the most widely used is the sonic log (Bulat and Stoker 1987; Menpes and Hillis 1995). For a given lithology, such as shales, the curve of sonic interval transit time versus depth reflects the maximum depth (or minimum porosity) attained by a given interval. The curve commonly has an exponential form, so porosity variations at great depth are small.

Two effects are important in the interpretation of sonic log porosity curves. (i) If a sedimentary basin is overpressured, the pore fluid reduces the effective stress on framework grains and impedes compaction. Consequently, overpressured sections have offset porosity–depth curves compared to the "normal" curve. (ii) Uplift and erosion of the basin-fill causes strongly compacted sedimentary rocks to occur at shallower depths. The amount of uplift can be estimated from the offset of the sonic porosity–depth curve of the uplifted section (Fig. 9.30) (Giles and Indrelid 1998; Ware and Turner 2002).

9.8 APPLICATION OF THERMAL MATURITY MEASUREMENTS

9.8.1 Vitrinite reflectance (R_o) profiles

Vitrinite reflectance measurements can be plotted as a function of depth to give R_o profiles. The slope of the R_o curves gives an indication of the geothermal gradients in the history of the basin. Although many profile shapes are possible (Fig. 9.31), they generally indicate an exponential evolution of the organic matter with time (Dow 1977), as expected from the kinetics described in §9.5. In basins largely unaffected by major unconformities, young dip-slip faulting and localized igneous activity, there should therefore be a linear relationship between depth and log R_o. Plots of large numbers of reflectance measurements from many sedimentary basins worldwide (Rowley and White 1998) or from many locations within a basin system (Corcoran and Clayton 2001) show a strong clustering along a roughly linear trend in depth–log R_o space, with an intercept at a depth of zero of 0.2–0.4% (Fig. 9.21).

Individual R_o profiles follow a number of different trends, each of which is diagnostic of a particular thermal history. An example of a simple, sublinear profile is the Terrebonne Parish Well in Louisiana (Heling and Teichmilller 1974) (Fig. 9.32a). R_o is 0.5% at 3 km and 1% at 5 km. It indicates a normal and constant geother-

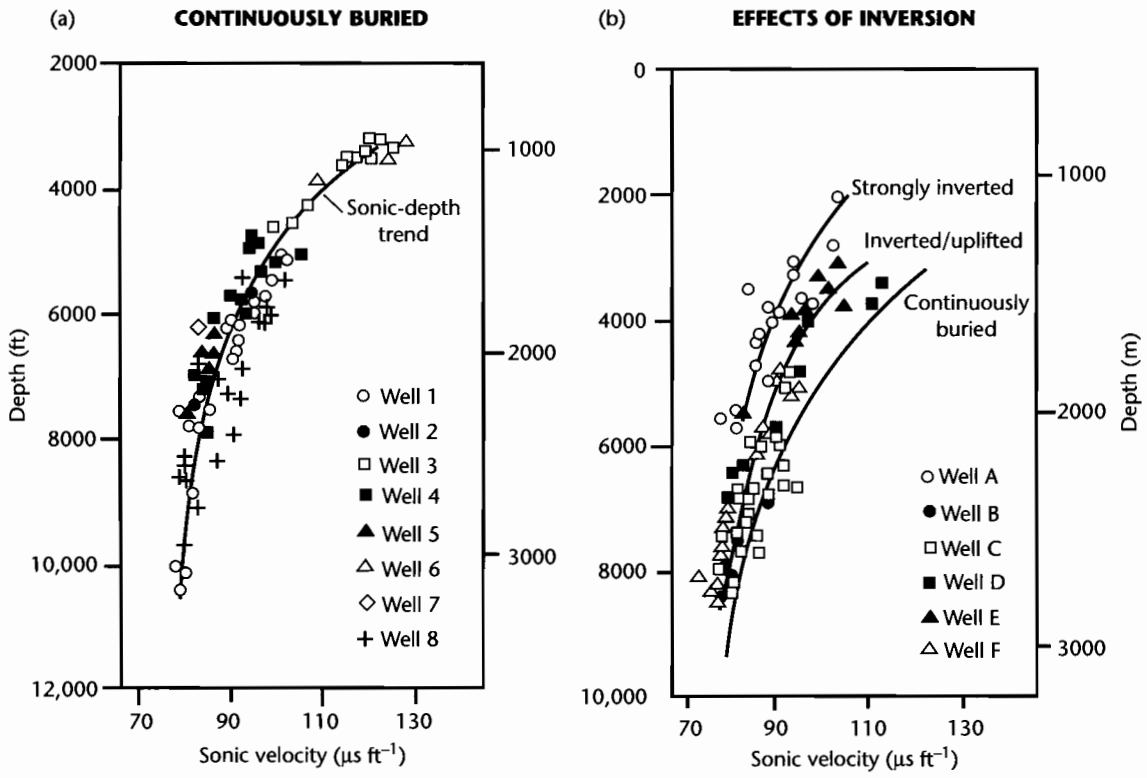

Fig. 9.30 (a) Sonic transit time versus depth for a continuously buried sedimentary succession; (b) Offset of sonic transit time versus depth trends for wells penetrating successions that have been uplifted (after Giles 1997). Reproduced courtesy of Springer.

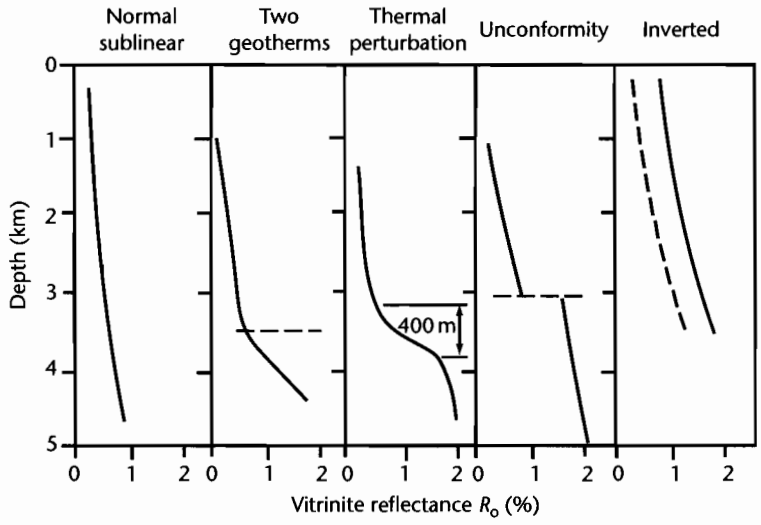

Fig. 9.31 The main types of R_o profile. 1, normal sublinear (constant geothermal gradient); 2, dogleg, two periods with different geothermal gradient; 3, strong thermal perturbation, returning to normal; 4, jump in R_o profile due to unconformity; 5, offset R_o profile in inverted basin.

mal gradient through time. The Woodford Shale of the Anardarko Basin is another example of a sublinear R_o profile with a surface intercept at $R_o = 0.2\%$, indicating the amount of maturation that the vitrinite had undergone prior to deposition (Fig. 9.32b).

Other R_o profiles are more complex. A dogleg pattern of two linear segments of different slope indicates that two periods of different geothermal gradient have occurred. This may result from a thermal "event" occurring at the time presented by the break in slope. Such an interpretation is plausible for the R_o profiles from boreholes in the Rhine Graben (Teichmüller 1970, 1982; Robert 1988) (Fig. 9.33).

R_o profiles may consist of two sublinear segments offset by a sharp break or jump in R_o values. The jump may correspond to an unconformity with a large stratigraphic gap. This is well illustrated in the Mazères 2 borehole in the Lacq area of the Aquitaine Basin, France (Fig. 9.34), where R_o values jump from *c.* 0.8% to *c.* 2.4% at the level of an unconformity separating Aptian–Albian rocks from underlying Kimmeridgian.

If there is a known (logarithmic) relationship of R_o with depth and the subsidence history of a sedimentary basin is known, the R_o values give an indication of the variation of the geothermal gradient through time. This then allows different tectonic histories to be tested (Middleton 1982).

9.8.2 Estimation of denudation from R_o profiles

R_o profiles can be used to estimate the amount of denudation resulting from a period of basin inversion, since the vitrinite locks in information about the maximum paleotemperature experienced. The technique has been used extensively, particularly in the region of the British Isles where an important crustal uplift event took place in the Early Tertiary (Rowley and White 1998). This uplift event, which was most likely related to the thermal, isostatic, and dynamic effects of the Icelandic plume (White 1988; Brodie and White 1994), caused an unconformity that cuts down variably into Mesozoic rocks. The paleotemperature profiles from areas such as the Irish Sea Basin system are linear and subparallel to the present-day geotherm (Duncan et al. 1998), suggesting that heating was caused primarily by burial rather than by basal heat flow variations or local magmatic and fluid flow effects. However, most of the R_o values in boreholes in the British–Irish area have elevated

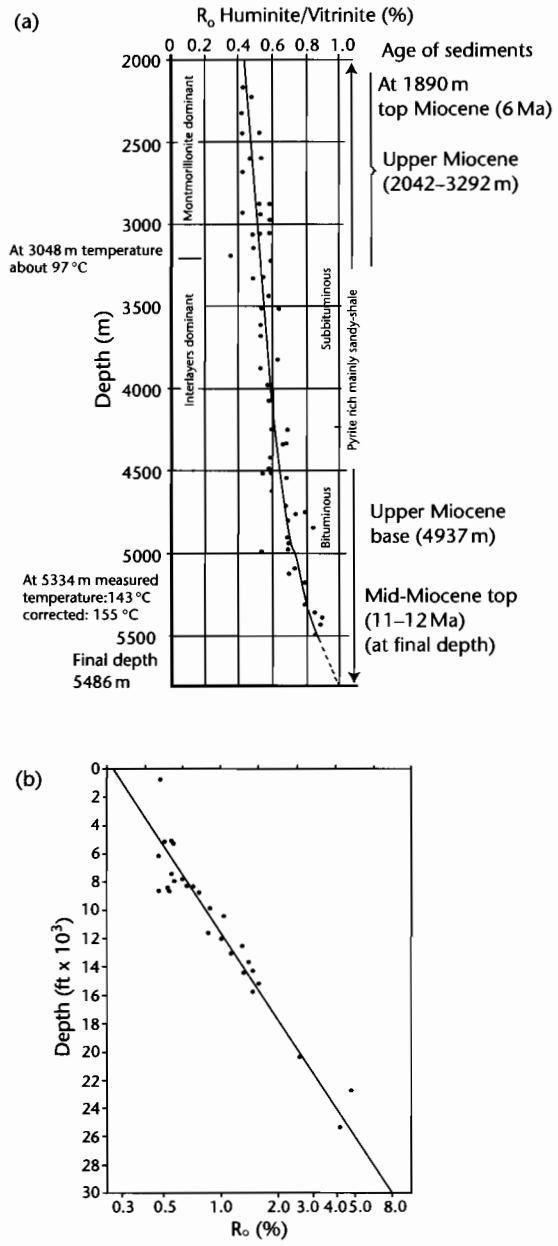

Fig. 9.32 (a) Vitrinite reflectance profile for Terrebonne Parish, Pont au Fer well in Louisiana. The profile is sublinear and continuous, suggesting a near-constant geothermal gradient through time (after Heling and Teichmüller 1974); (b) Woodford Shale of the Anadarko Basin also shows a good sublinear trend (Cardott and Lambert 1985). Note logarithmic scale.

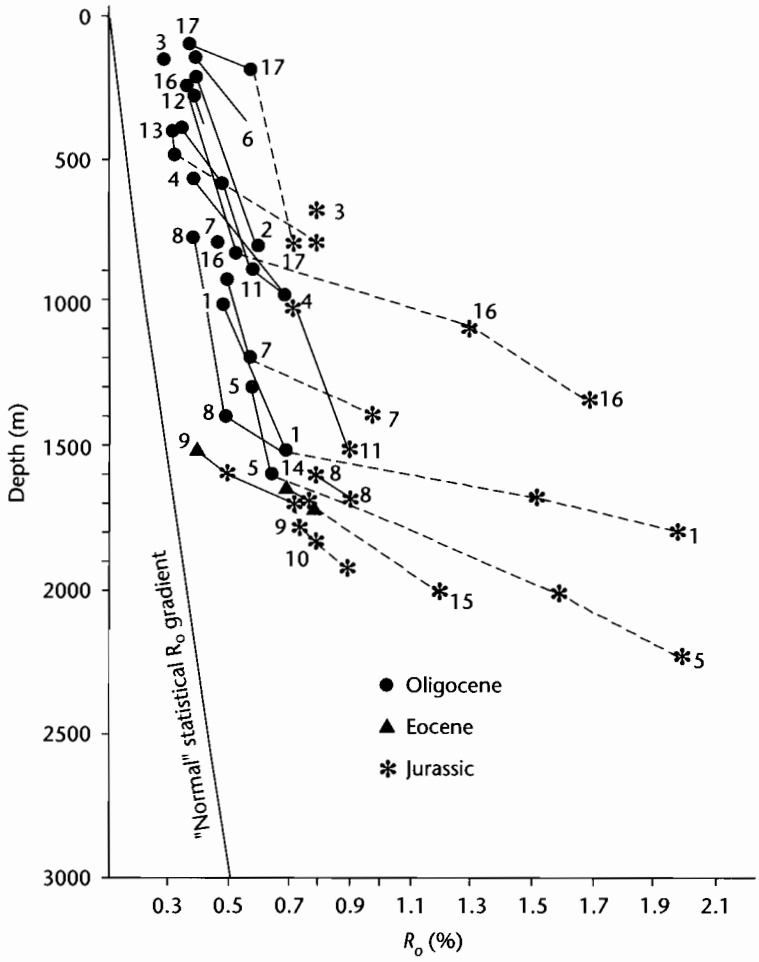

Fig. 9.33 Reflectance profiles from a number of wells in the Alsace region of the Rhine Graben (after Teichmüller 1970). In general, there are pronounced doglegs in the R_o profiles at about the age of the Oligocene–Eocene boundary. The post-Eocene history shows a "normal" gradient, whereas the pre-Oligocene sedimentary rocks have high reflectance values in relation to their depth of burial. This suggests that rifting in the late Eocene caused higher than normal maturity in the older rocks of the basin-fill.

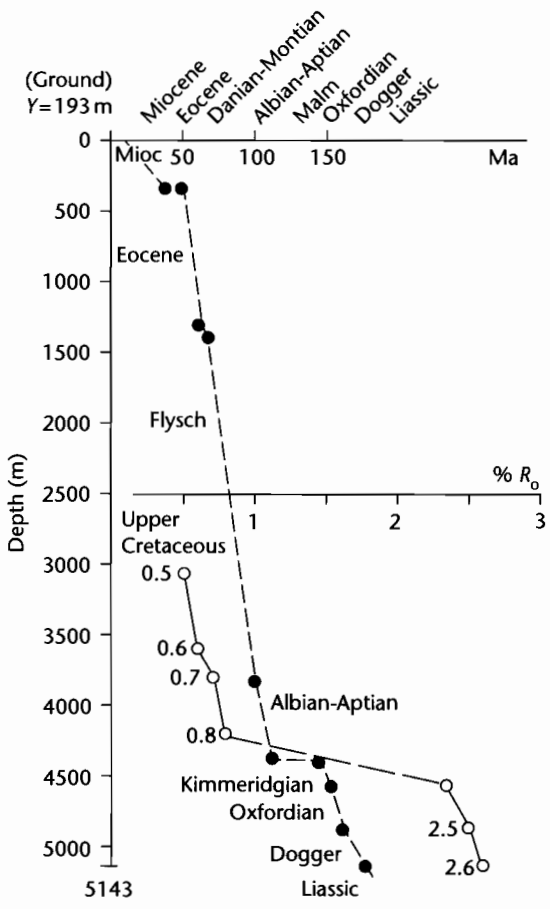

Fig. 9.34 Stratigraphic depth and vitrinite reflectance profiles for the Mazères 2 borehole in the Lacq region of southern France. The sharp increase in R_o marks an unconformity between the Lower Cretaceous and the Upper Jurassic (after Robert 1988).

values compared to the global dataset of noninverted basins (Fig. 9.35) (Corcoran and Clayton 2001). Calculations of the amount of denudation from the R_o profile can be performed using a number of different methods:

1 The curve of log R_o versus depth is extrapolated linearly upwards to a value of approximately 0.2% R_o (Dow 1977; Corcoran and Clayton 2001). The displacement of the depth axis is the amount of denudation. Although this method has been very widely applied, it makes the erroneous assumption that the geothermal gradient is linear. This is a particularly poor assumption in the shallow parts of basins where thermal conductivities vary strongly. It is more likely that the geotherm is convex near the surface (Figs. 9.14, 9.15). Secondly, large errors may result from the incorrect choice of surface temperature (and therefore R_o at $y = 0$) at the time of maximum paleotemperatures.

2 Maximum depths of burial can be estimated from VR values from empirical relations such as (Barker and Pawlewicz 1986)

$$\ln R_0 = 0.0096T - 1.4 \tag{9.58}$$

where T is the temperature, which must be converted to depth using a geothermal gradient. The empirically derived depth can be compared with the present-day depth of the sample. However, there are large uncertainties in the accuracy of the R_o–T relationship, and geotherms may be unknown.

3 Vitrinite reflectance can be calculated from a forward thermal model using the kinetic approaches described in §9.5 (e.g., Middleton 1982). A comparison of observed VR values with the results of a number of forward models allows the most likely parameter values and amount of denudation to be estimated. Alternatively, the amount of denudation can be estimated by inverse methods using the same chemical kinetics.

Increasingly, vitrinite reflectance data are interpreted alongside other thermal indicators, such as apatite fission track thermochronometry. Both techniques require a conversion to temperature. It is estimated that total fission track annealing in apatites (closure temperature) with typical Cl content corresponds to a vitrinite reflectance value of 0.7%. This in turn corresponds to a temperature of 110–120 °C.

9.9 GEOTHERMAL AND PALEOGEOTHERMAL SIGNATURES OF BASIN TYPES

We have previously seen that vitrinite reflectance measurements and apatite fission track and (U–Th)/He analysis can be used to constrain paleotemperatures and paleogeothermal gradients. This then helps to determine the formative mechanism of the basin. Robert

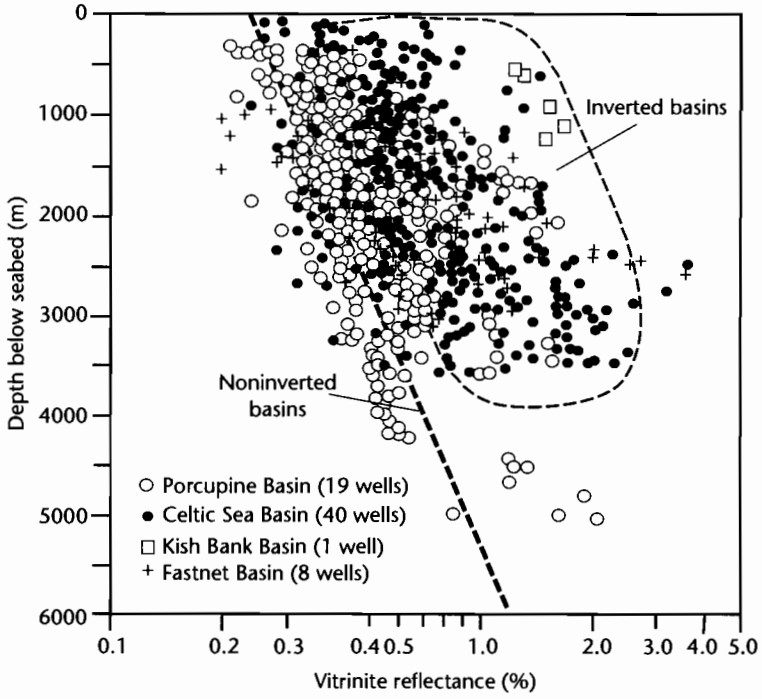

Fig. 9.35 Vitrinite reflectance versus depth for Mesozoic and Cenozoic successions penetrated in boreholes in a number of basins offshore Ireland (Corcoran and Clayton 2001). Basins such as the Porcupine Basin show a "normal" R_o profile indicative of continual subsidence, whereas those basins that have experienced tectonic uplift and exhumation (such as the Celtic Sea, Kish Bank, and Fastnet Basins) have displaced R_o profiles indicating higher thermal maturity than expected from the present depth of burial.

(1988) suggested three main types of paleogeothermal history: (i) basins with normal or near-normal paleogeothermal history, (ii) cooler than normal basins, and (iii) hotter than normal basins.

(i) Basins with normal or near-normal paleogeothermal history

Old passive margins have present-day geothermal gradients of *c.* 25–30 °C km^{-1} (Congo 27 °C km^{-1}, Gabon 25 °C km^{-1}, Gulf Coast USA 25 °C km^{-1}). The Terrebonne Parish Well (Fig. 9.32a) shows a vitrinite reflectance of about 0.5% at a depth of 3 km and the shape of the curve is sublinear. Mature passive margins therefore have near-normal geothermal gradients.

(ii) Cooler than normal (*hypothermal*) basins

Hypothermal basins include oceanic trenches, outer forearc and foreland basins. Ocean trenches are cold, with surface heat flows often less than 1 HFU (42 mW m^{-2}). In the Japanese archipelago Eocene–Miocene coals occur in two regions: one in Hokkaido in the north along a branch of the present-day Japan trench, and the other in Kyushu in the south is situated in a volcanic arc position relative to the Ryu-Kyu trench (Fig. 9.36). Figure 9.37 shows the R_o profiles for the two different regions. The Hokkaido region is cold with poorly evolved coals (sub-bituminous coals with R_o = 0.5% still occurring at a depth of 5 km) whereas the volcanic arc in Kyushu is hot, containing anthracites (>2% R_o). The Mariana Trench, which is a southward continuation of the Japan Trench, and its forearc region are also cold, with surface heat flows of less than 1 HFU (42 mW m^{-2}).

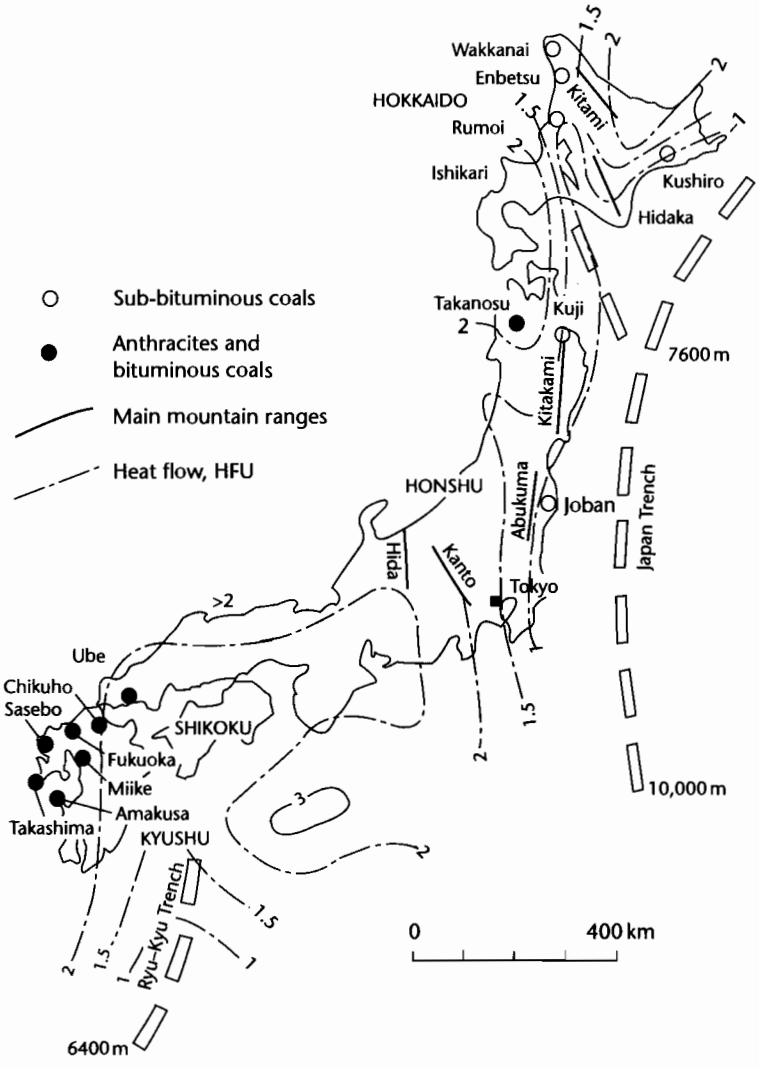

Fig. 9.36 The deposits of Tertiary coals in Japan and the surface heat flows in HFU (Aihara 1980). Note that anthracites and bituminous coals are found in Kyushu and the extreme southwest of Honshu, whereas sub-bituminous coals are found in the north of Honshu and on Hokkaido.

Foreland basins are also characterized by low present-day geothermal gradients, 22 °C km^{-1} to 24 °C km^{-1} being typical of the North Alpine Foreland Basin in southern Germany (Teichmüller and Teichmüller 1975; Jacob and Kuckelhorn 1977). The Anzing 3 well near Munich penetrates the autochthonous Molasse, undisturbed by Alpine tectonic events. At the base of the Tertiary at 2630 m depth the R_o is still only 0.51%. The Miesbach 1 well cuts through about 2 km of thrust sheets of the frontal thrust zone of the Alps (the subalpine zone), before penetrating the autochthonous sediments to a depth of 5738 m (Fig. 9.38). Even at this great depth, the R_o is still only 0.6%, indicating an abnormally low geothermal gradient during the Tertiary. The greater subsidence rate at Miesbach 1 (nearly 0.3 mm yr^{-1}) compared with Anzing 1 (0.1 mm yr^{-1}) may have been responsible

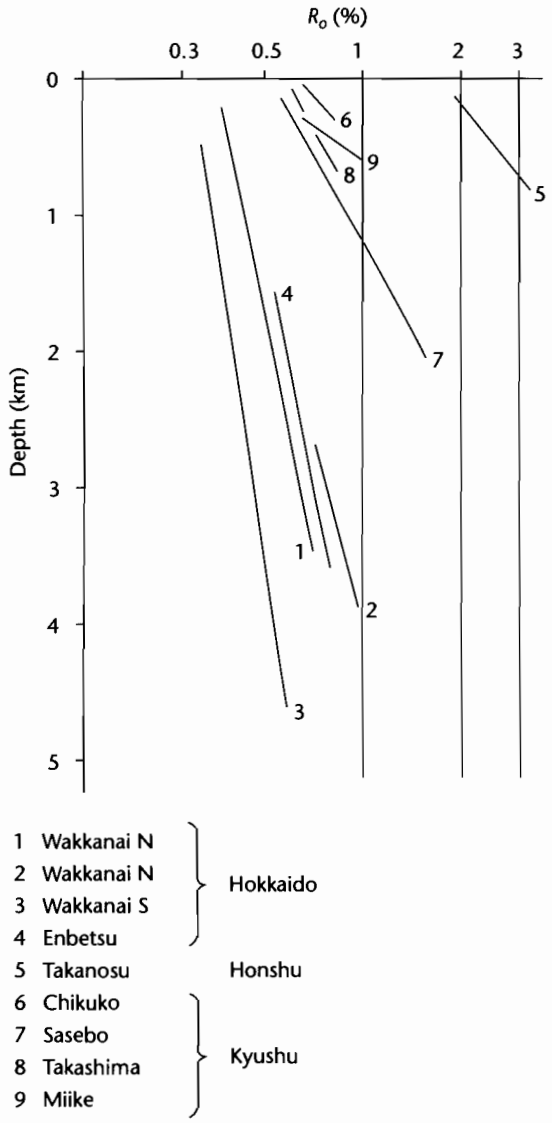

Fig. 9.37 Vitrinite reflectance profiles for the locations shown in Fig. 9.36. The first set of locations (1–4) belong to a branch of the oceanic Japan trench system running along the east of Japan; they are characterized by low reflectances and are associated with low present-day heat flows. The second group of locations (6–9) corresponds to the internal arc relative to the Ryu-Kyu trench. These locations are highly evolved at shallow depths of burial and are associated with high present-day heat flows. The single location 5 from the NW of Honshu occurs in the present volcanic arc area where the heat flows exceed 2 HFU, and the vitrinite reflectance is very high. There is thus a clear relationship between tectonic environment and geothermy. After Robert (1988).

for the very low geothermal gradient in the former. The low present-day geothermal gradients (Anzing 3, 22.8 °C km^{-1}, Miesbach 1, 23.5 °C km^{-1}) may have been even lower in the past during the phase of rapid subsidence related to continental collision and flexure.

(iii) Hotter than normal (*hyperthermal*) basins

Hyperthermal basins are found in regions of lithospheric extension such as backarc basins, oceanic and continental rift systems, some strike–slip basins, and the internal arcs of zones of B-type subduction. This follows from the mechanics of basin formation in stretched regions, involving the raising towards the surface of isotherms.

Oceanic rifts are zones of very high heat flows, 3–4 HFU (120–170 mW m^{-2}) being typical and values occasionally reaching 5–6 HFU (200–250 mW m^{-2}). Some Californian *strike–slip basins* have very high geothermal gradients (*c.* 200 °C km^{-1} in Imperial Valley), so that very young sediments can be highly mature. Continental rifts have high present-day geothermal gradients (>50 °C km^{-1} in the Red Sea, up to 100 °C km^{-1} in the Upper Rhine Valley) and ancient continental rifts have high organic maturities in their basin sediments.

Oceanic measurements and deep boreholes in the *Red Sea* (Girdler 1970) suggest that high surface heat flows (generally >3 HFU, >125 mW m^{-2}) occur in a broad band at least 300 km wide centered on the axis of the rift. The organic maturation shown by R_o profiles and the occurrence of oil, gas, and condensate fields suggests that the highest maturity is found in the south of the Red Sea, intermediate values are found in the north of the Red Sea, and the lowest occur in the Gulf of Suez. This can be correlated with different amounts of extension, the largest amount being in the south of the Suez–Red Sea system. The former elevated heat flows in the Oligo–Miocene of the Gulf of Suez have now diminished to near-normal values, while the southern Red Sea, which is still actively rifting, still has very high heat flows.

There are many other examples of high organic maturation in ancient continental rift basins: 2–3% R_o in the Lower Cretaceous of the Congo; 3.3% R_o in the Upper Cretaceous of Cameroon; 3.5% R_o in the Coniacian of the Benue Trough, Nigeria; 5% R_o in the Permian of the Cooper Basin, Australia.

Internal arc heat flows are elevated because of magmatic activity. The Tertiary anthracites of Honshu, Japan (see

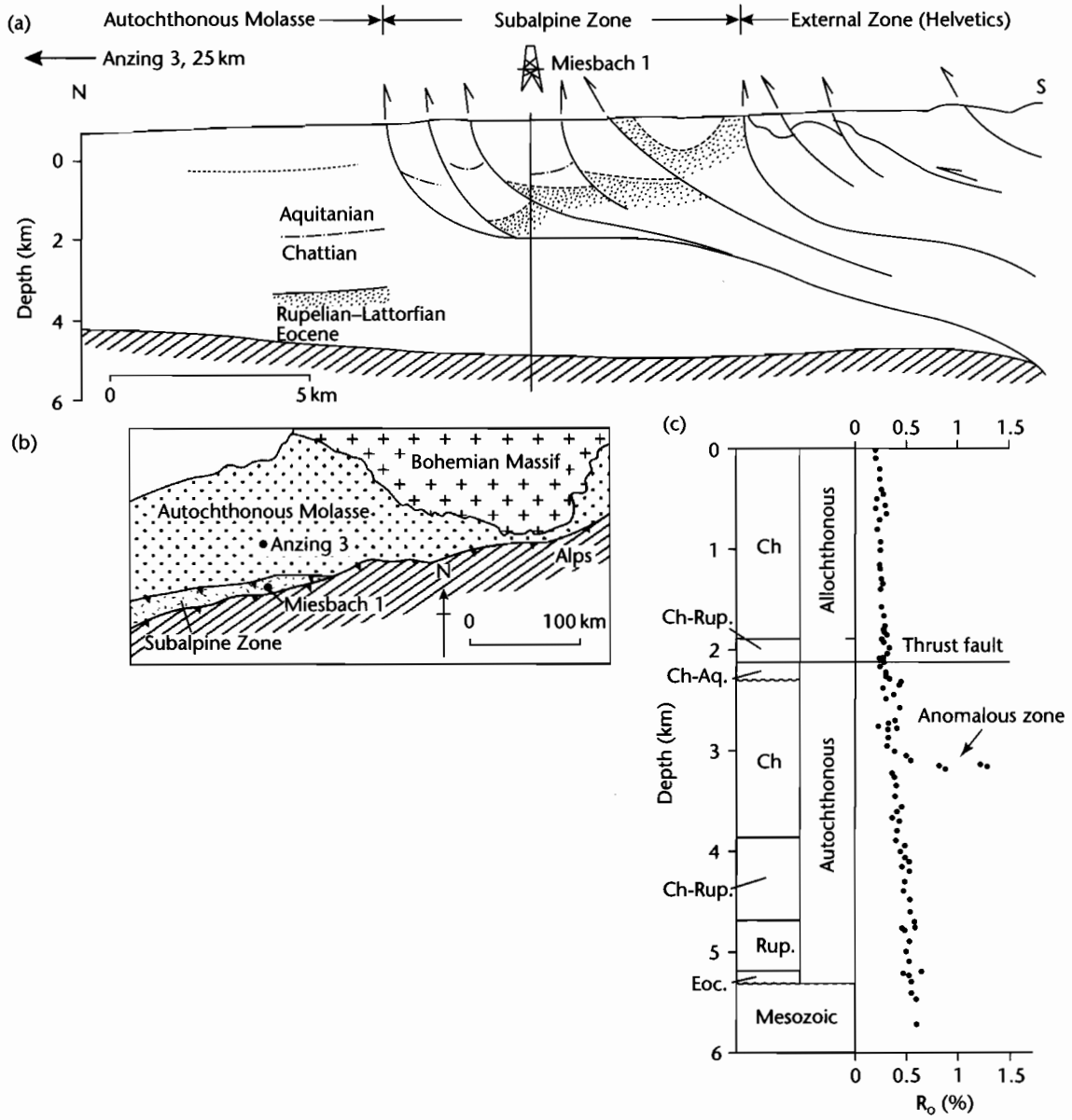

Fig. 9.38 (a) Location of the Bavarian part of the North Alpine foreland basin in southern Germany. Anzing 3, near Munich, and Miesbach 1, are boreholes discussed in the text; (b) Cross-section of the southernmost part of the Bavarian section of the North Alpine foreland basin, showing the location of Miesbach 1 in the tectonically imbricated subalpine zone (after Teichmüller and Teichmülller 1975); (c) The R_o profile at Miesbach 1 (Jacob and Kuckelhorn 1977) shows that the autochthonous "Molasse" under the basal subalpine thrust is poorly evolved, not exceeding 0.6% even at 5738 m depth. This is indicative of a very low geothermal gradient during the period of rapid sedimentation in the Oligocene.

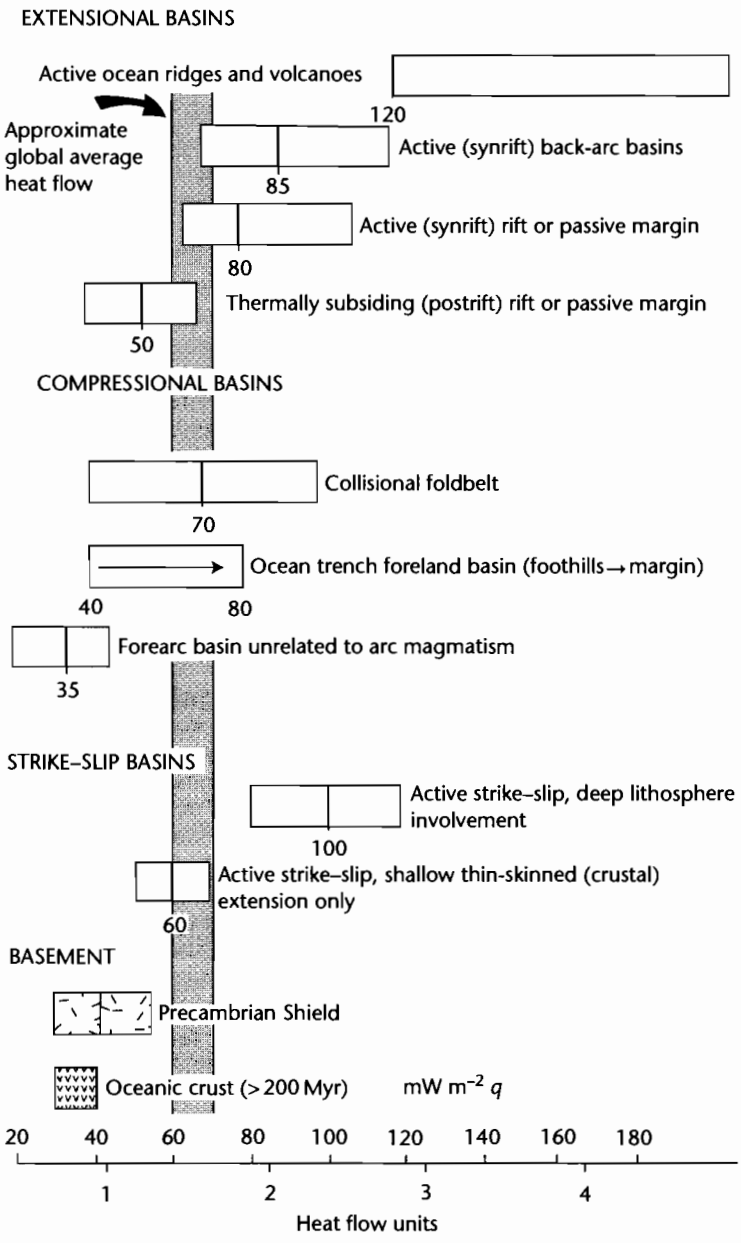

Fig. 9.39 Summary of the typical heat flows associated with sedimentary basins of various types.

above) (2–3% R_o) are an example. Similar patterns are found in ocean–continental collision zones such as the Andean Cordillera, and hyperthermal events may also affect parts of continent–continent collision zones such as the Alps: the "Black Earths" of southeastern France have R_o values of over 4%, but the precise origin of the thermal event is unknown (Robert 1988, p. 261).

The heat flows of the main genetic classes of sedimentary basin are summarized in Figure 9.39.

PART

4 *Application to petroleum play assessment*

CHAPTER 10 *The petroleum play*

Ah! Vanitas vanitatum! Which of us is happy in this world? Which of us has his desire? or, having it, is satisfied? – Come, children, let us shut up the box and the puppets, for our play is played out.

(WILLIAM MAKEPEACE THACKERAY, *VANITY FAIR* (1848))

SUMMARY

A play is a perception or model of how a producible reservoir, petroleum charge system, regional topseal, and traps may combine to produce petroleum accumulations at a specific stratigraphic level. Prediction of source rocks, reservoirs, topseals, and traps requires an understanding of the structural and stratigraphic evolution of the depositional sequences within a basin. This understanding can be achieved through basin analysis, which serves as the platform for the assessment of petroleum plays. Correct identification and interpretation of the fundamental tectonic and thermal processes controlling basin formation, and the geometry and sedimentary facies contained in the basin-fill, is the first and most important step towards building the geological models that underpin play assessment.

The basic unit of petroleum resource assessment is the play, but the "petroleum system" concept is also a useful way for the practicing petroleum geologist to organize his/her investigations. A petroleum system comprises a pod of mature source rock and all of the migration paths, reservoir rocks, caprocks, and traps that can be charged by that source rock to produce oil and gas accumulations. Petroleum systems may be classified to help describe and predict the abundance, geographic location, and habitat of petroleum occurrences in a basin. This may be particularly useful in the ranking of relatively immature exploration provinces.

The first requirement for a play is that there is a *petroleum charge*. The petroleum charge system comprises source rocks, which must be capable of generating and expelling petroleum, and a migration pathway into the reservoir unit. Source rocks are sediments rich in organic matter derived from photosynthesizing marine or lacustrine algae and land plants which contain chemical compounds known as lipids. Lipids are preserved when sediments are deposited under anoxic conditions. Lakes, deltas, and marine basins are the main depositional settings of source beds.

Organic matter buried in sediments is in an insoluble form known as kerogen. Petroleum is generated when kerogen is chemically broken down as a result of rising temperature. For typical rates of heating, a stage of oil generation at approximately 100–150 °C is followed by a stage of oil cracking to gas (150–180 °C) and finally by dry gas generation (150–220 °C). Petroleum expulsion probably occurs as a result of the build-up of overpressure in the source rock as a consequence of hydrocarbon generation. For lean (i.e., organic poor) source rocks, petroleum expulsion is probably very inefficient. Secondary migration carries expelled petroleum towards sites of accumulation, and is driven by the buoyancy of petroleum fluids relative to formation pore waters. Migration stops when the capillary pressure of small pore systems exceeds the upward-directed buoyancy force.

A further requirement for a play is a porous and permeable *reservoir rock*. Pore space enables the reservoir to act as a tank of hydrocarbons, and permeability provides the plumbing system by which the reservoir may be drained of its hydrocarbon content. In both carbonates and sandstones, reservoir quality depends on depositional environment and paleoclimate but is very strongly affected by diagenetic pathway. The nature of near-surface diagenesis is predictable from the position of the reservoir in a depositional sequence or parasequence. A number of scales of heterogeneity exist, from kilometer scale to microscopic, that affect the distribution of porosity and permeability in the gross reservoir unit. Particu-

lar basin tectonic settings have associated with them particular types of reservoir geometry and composition.

A *regional topseal* or caprock is needed to seal petroleum in the gross reservoir unit. The mechanics of sealing are the same as those that control secondary migration. The ideal caprock is of a fine-grained lithology, and is ductile and laterally persistent. Thickness and depth of burial do not appear to be critical. Two of the most successful reservoir–caprock associations are where marine shales transgress over gently sloping clastic shelves, and where sabkha evaporites regress over shallow-marine carbonate shelves.

The final requirement for the operation of a petroleum play is the presence of *traps*. Traps are local subsurface concentrations of petroleum and may be classified into structural, stratigraphic, and hydrodynamic traps. Structural traps represent the habitat of most of the world's already discovered petroleum, and are formed by tectonic, diapiric, and gravitational processes. Stratigraphic traps are those inherited from the original depositional morphology of, or discontinuities in, the basin-fill, or from subsequent diagenetic effects. Large volumes of undiscovered petroleum probably reside in stratigraphic traps, and owing to difficulties in detection, may remain so.

10.1 FROM BASIN ANALYSIS TO PLAY CONCEPT

Basin analysis is a platform for assessment of the undiscovered petroleum potential of an area. Assessments of this kind guide the exploration programs of the petroleum industry. An understanding of the distribution and evolution of depositional sequences and facies allows rational and realistic predictions to be made of petroleum source rocks, reservoir rocks, and caprocks – the building-blocks of a petroleum play. The associated structural development of the basin is primarily responsible for the formation of petroleum traps.

The bulk of subsurface information in a sedimentary basin is obtained from seismic reflection surveying and well log interpretation. These are both technologically fast-moving fields that are documented elsewhere. The reader is referred to Badley (1985) for a thorough description of seismic interpretation, and to Bacon et al. (2003) and Brown (1999) for 3-D methods. Rider (1996) provides a summary of well log interpretation.

Play concepts are founded on an understanding of the stratigraphic and structural evolution of the basin. The geological models upon which predictions of source, reservoir, and caprocks, and their evolution through time are based, are outcomes of this understanding. The validity of these models, and therefore of the plays that are generated from them, is dependent on a correct interpretation of the boundaries and overall *geometry* of the genetic stratigraphic units, systems tracts, and depositional sequences involved in the play, and on a correct interpretation of the *sedimentary facies* within these stratigraphic units. Basin analysis provides the means of making these interpretations.

The previous chapters of this book have shown that the location and overall form of megasequences and depositional sequences may be understood in terms of the mechanical processes of basin formation. Thus basins due to lithospheric stretching, flexure, mantle dynamics, and strike–slip deformation each exhibit characteristic locations, geometries, and evolutions that may be understood in terms of the controlling broad plate tectonic and mantle processes. Knowledge of the underlying basin-forming process also implies a particular tectonic and thermal development for the basin, which is an important input to the thermal modeling of potential source rock intervals.

Correct identification and interpretation of the megasequences present in a province is the first step towards building the geological models for play assessment. Each megasequence can be broken down into a series of depositional sequences and systems tracts representing discrete phases of the basin infill (§8.2). This information forms the basis for the prediction of source, reservoir, and caprocks.

The type, amount, and quality of data available will limit the confidence held in any stratigraphic interpretation. The goal is to achieve a reliable *chronostratigraphic* interpretation of a basin-fill, so that the distribution and nature of sedimentary facies may be understood in terms of geological processes operating at a specific time. The chronostratigraphic interpretation must, however, be built up from interpretations of lithostratigraphy, biostratigraphy, and seismic stratigraphy. Each of these on their own are potentially unreliable.

Lithostratigraphy is dependent on outcrop and well information. Lithostratigraphic boundaries tend to be diachronous, and may cause serious chronostratigraphic miscorrelations. Reliability is limited by low outcrop exposure, sparse well control, and our general inability to reliably determine lithology from seismic data. *Biostratigraphy* is again restricted to outcrop and well data. Environmental conditions at the time of deposition may

strongly influence the existence and likelihood of preservation of sensitive fossil groups, and diagenesis/metamorphism may destroy important biostratigraphic information. Both lithostratigraphy and biostratigraphy provide important stratigraphic "fence-posts." It is only *seismic stratigraphy*, however, that provides the inter-well and inter-outcrop information that forms the "fences" of the stratigraphic interpretation. As a result, seismic stratigraphy has had an enormous impact on the interpretation of basin stratigraphy.

Miscorrelation of information, and misinterpretation of sedimentary facies, is a serious danger unless lithostratigraphic and seismostratigraphic interpretations are integrated. The confidence held in a stratigraphic interpretation may be assessed by considering the adequacy of each of the required data types – outcrop, well, and seismic data – in terms of both quantity and quality. Deficiencies in the data base must be recognized. Normally, more than one interpretation fits the observable data, each with different implications for petroleum plays. Each geological model carries an associated risk of not being valid. This is called *model risk*.

A *chronostratigraphic diagram* is a useful way of illustrating the relationships between sedimentary facies in a depositional sequence (Fig. 10.1). Combined with a sequence isopach map, the chronostratigraphic diagram may be used to make sedimentary facies predictions for the entire sequence. Given these sedimentary facies, the next step is to make predictions of potential source, reservoir, and caprocks. The thermal maturity of the source rock (Chapter 9, §10.3), and the presence and timing of traps must also be addressed (§10.6). There is a risk that these elements of the petroleum play do not exist, even though the geological model is valid. This additional element of risk is termed *conditional play risk*.

10.2 THE PETROLEUM SYSTEM AND PLAY CONCEPT

10.2.1 Play definition

A play may initially be defined as a perception or model in the mind of the geologist of how a number of geological factors might combine to produce petroleum accumulations at a specific stratigraphic level in a basin. These geological factors must be capable of providing the essential ingredients of the petroleum play, namely:

- A *reservoir unit*, capable of storing the petroleum fluids and yielding them to the well bore at commercial rates;
- a *petroleum charge system*, comprising thermally mature petroleum source rocks capable of expelling petroleum fluids into porous and permeable carrier beds, which transport them towards sites of accumulation (traps) in the gross reservoir unit;
- a *regional topseal* or *caprock* to the reservoir unit, which contains the petroleum fluids at the stratigraphic level of the reservoir;
- petroleum *traps*, which concentrate the petroleum in specific locations, allowing commercial exploitation;
- *the timely relationship* of the above four ingredients so that, for example, traps are available at the time of petroleum charge.

Thus, a play may further be defined as a family of undrilled prospects and discovered pools of petroleum that are believed to share a common gross reservoir, regional topseal, and petroleum charge system. A brief description of a play might be:

"Mid-Jurassic submarine fan sandstone reservoirs in Late Jurassic fault blocks, sealed by Lower Cretaceous marine mudstones, and charged during the Early Tertiary from Upper Jurassic marine source rocks (Fig. 10.2).

The geographical area over which the play is believed to extend is the *play fairway*. The extent of the fairway is determined initially by the depositional or erosional limits of the gross reservoir unit, but may also be limited by the known absence of any of the other factors. The mapping-out of the play fairway is discussed in §10.2.3.

A play may be considered *proven* if petroleum accumulations (pools or fields) are known to have resulted from the operation of the geological factors that define the play. These geological requirements are thus known to be present in the area under investigation, and the play may be said to be "working." In *unproven* plays, there is some doubt as to whether the geological factors actually do combine to produce a petroleum accumulation. One of the objectives of play assessment is to estimate the probability of the play working; this is known as *play chance*. Play chance combines model risk and conditional play risk into one factor.

10.2.2 The petroleum system

The basic unit of petroleum resource assessment is the play, but the "*petroleum system*" concept is also a useful way for the practising petroleum geologist to organize his/her investigations. The original work that gave birth to the

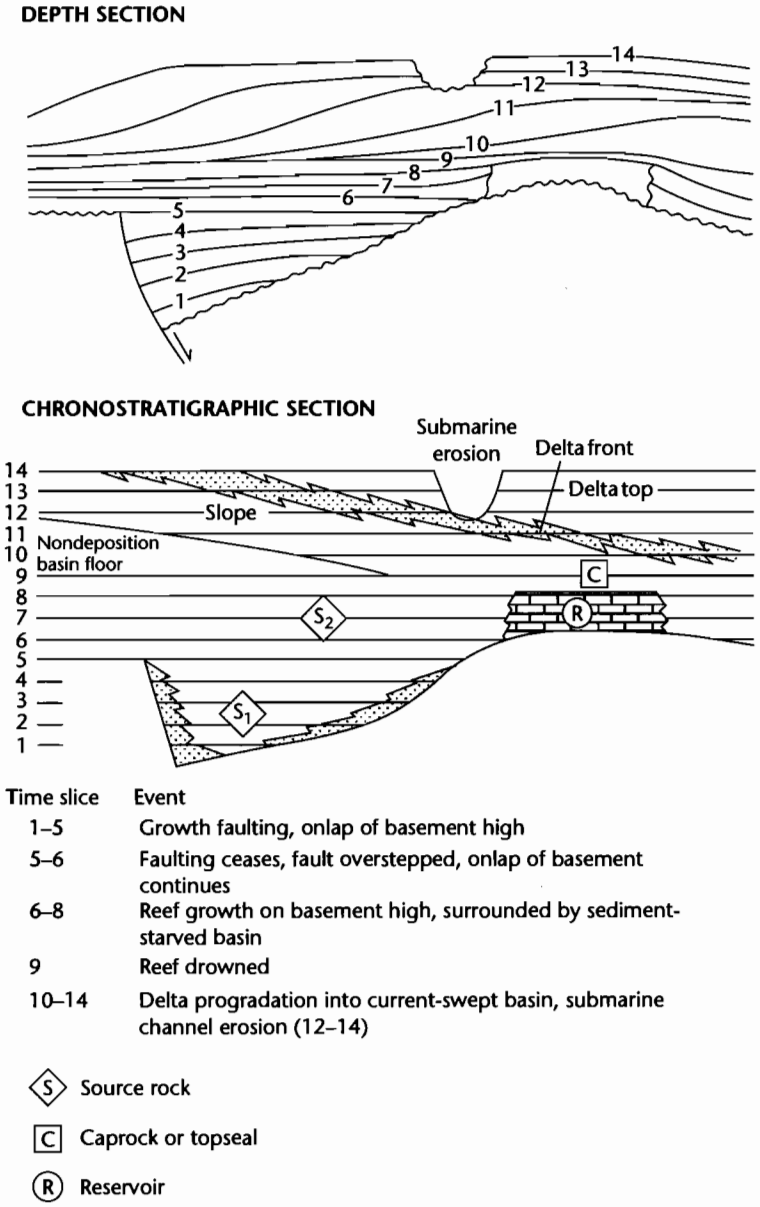

Time slice	Event
1–5	Growth faulting, onlap of basement high
5–6	Faulting ceases, fault overstepped, onlap of basement continues
6–8	Reef growth on basement high, surrounded by sediment-starved basin
9	Reef drowned
10–14	Delta progradation into current-swept basin, submarine channel erosion (12–14)

◇S Source rock

C Caprock or topseal

(R) Reservoir

Fig. 10.1 Schematic chronostratigraphic diagram, showing the relationships between sedimentary facies in a depositional sequence and the overall development of the basin.

petroleum system concept was carried out in the Williston basin of the USA (Dow and Momper 1972). Related concepts were subsequently described by Demaison (1984) (the *generative basin concept*), Meissner et al. (1984) (the *hydrocarbon machine*) and Ulmishek (1986) (the *independent petroliferous system*). The concept was subsequently defined more rigorously in Magoon and Dow (1994).

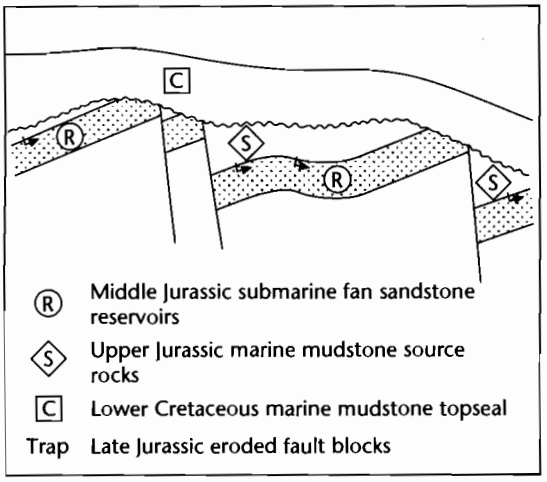

Fig. 10.2 Schematic illustration of a petroleum play. Plays must be carefully defined in terms of their reservoir, charge system, and regional topseal.

A petroleum system comprises a pod of mature source rock and all of the migration paths, reservoir rocks, caprocks, and traps that can be charged by that source rock to produce oil and gas accumulations. The concept, which has seen widespread practical application in the petroleum exploration industry since the mid-1990s, places the source rock as the first and foremost element of the geological system required to produce a petroleum play. When adopting this concept, the practising petroleum geologist goes through an assessment process that reflects the geological process of hydrocarbon generation, migration, and entrapment. By starting with the source rock, the petroleum system concept encourages the petroleum geologist to consider all the journeys and destinations of hydrocarbons generated and expelled from a source rock, and is more likely to stimulate ideas on new plays than an exploration approach strongly focused on one or two reservoirs that are already proven in the basin.

The petroleum system should be defined in terms of:

1 Its *stratigraphic* extent: in the system proposed by Magoon and Dow (1994), it takes its name from the source rock, qualified by the main reservoir rock that it charges. This linkage, between source and reservoir, may be: (i) *known* if the petroleum can be conclusively related to the source rock through oil-source or gas-source geochemical correlation, (ii) *hypothetical* if geochemical evidence indicates a source rock but a firm correlation has not been made, and (iii) *speculative* if based only on geological or geophysical evidence. An example is the Mandal–Ekofisk petroleum system of the North Sea described by Cornford (1994). The stratigraphic extent of the petroleum system should also reference the other essential elements, namely the carrier bed and caprock, and be illustrated by a cross-section drawn at the *critical moment* (defined in (3) below).

2 Its *geographic* extent, shown by a petroleum system map. This map shows the pod of active source rock, together with the associated discoveries, seeps, and shows, at the *critical moment* for the system. As part of the petroleum system documentation, a table of the discovered accumulations and their field sizes should be included.

3 Its *temporal* extent, illustrated by a burial history chart and events chart that shows the critical moment. The *critical moment* is the time at which most of the hydrocarbons were generated, migrated, and accumulated in the primary trap type. The events chart shows the time of deposition of the stratigraphic components of the system, and timing of key processes (trap formation, generation-migration, and entrapment) and the period over which trapped hydrocarbons are preserved, modified or destroyed.

A genetic classification of petroleum systems has been developed by Demaison and Huizinga (1994) to help describe and predict the abundance, geographic location and habitat of petroleum occurrences in a basin. This may be particularly useful in the ranking of relatively immature exploration provinces. This classification is based on three key factors that can be deduced from basin analysis and geochemical data (Fig. 10.3):

1 *Charge factor*: reflects the initial richness and volume of mature source rock, and is therefore a guide to the regional charge potential of the petroleum system. The Source Potential Index (SPI) combines source rock richness and source rock thickness into a single parameter that is known to be positively correlated (in well-explored petroleum provinces) with discovered petroleum reserves. Systems may be categorized into supercharged, normally charged, and undercharged. Charge factor is the single most important control on the petroleum richness of a system.

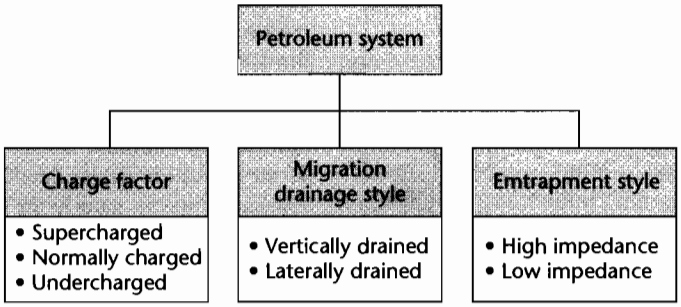

Fig. 10.3 Demaison and Huizinga's (1994) genetic classification of petroleum systems.

2 *Migration drainage style*: a reflection of the structure and stratigraphy of the basin-fill. Migration drainage style may be either dominantly vertical or dominantly lateral. A *vertical migration style* is assisted by faults and fractures that penetrate regional seals, or by reservoir and carrier beds that interconnect vertically over large distances, and is most common in rifted basins, sandy deltaic sequences, and in highly fractured fold and thrust belts. Examples are the North Sea and Gulf of Suez failed rifts, passive margin basins such as the Lower Congo Basin of Angola, the Campos Basin of Brazil, and the Barrow–Dampier Basin of NW Australia, and the Tertiary deltas of Nigeria and the US Gulf of Mexico. Traps ideally need to be located vertically above the mature pod of source rock in order to be charged. In supercharged, vertically drained petroleum systems, abundant surface seepage may occur, as in the San Joaquin Basin of California, the US Gulf Coast salt dome province, the Zagros fold–thrust belt of Iran, and the Magdalena Valley of Colombia. A *lateral migration style* is dominant in basins with extensive reservoir-seal couplets in tectonically stable settings, for example in foreland basins. Migration may be focused into arches or noses that plunge into the basin. Traps located along these focused migration routes may collect the charge from much of the source kitchen, while other areas are starved. Petroleum occurrences may be located long distances (several hundred km) away from the mature source pod. Excellent examples are the Oriente/Maranon Basin of Peru/Ecuador and the North Slope of Alaska. In supercharged, laterally drained petroleum systems, very large petroleum volumes may migrate as far as the shallow edges of the basin, as in the heavy oil provinces of western Canada (Athabasca) and eastern Venezuela (Orinoco).

3 *Entrapment style*: reflects the degree to which hydrocarbons are dispersed in moving from source rock to trap. Thermodynamic principles suggest that over geological time, natural geological processes work to ultimately disperse and destroy petroleum in sedimentary rocks. As petroleum migrates from source rock to its ultimate fate of destruction at the Earth's surface, local geological factors (trapping mechanisms) may resist this wholesale process, at least temporarily, and give rise to petroleum accumulations. Physical resistance to petroleum dispersion, or *impedance*, is largely a function of structural and stratigraphic complexity. A *low impedance entrapment style* indicates a tendency for hydrocarbons to flow efficiently along major migration routes with little resistance or dispersion, and occurs where good quality carrier beds and regional seals are continuous over large distances. Very large volumes of petroleum may be focused into relatively few ultimate sites of accumulation. A *high impedance entrapment style* is one in which hydrocarbon migration is dispersed by stratigraphic complexity or structural deformation into many different routes and sites of entrapment, at both the macro and micro scale. Large volumes of petroleum may be lost from commercial exploitation.

10.2.3 Definition and mapping of the play fairway

Play fairway maps show the geographical distribution of the key geological controls on the play fairway. These geological controls determine the presence of an effective reservoir, a petroleum charge into the reservoir, a regional topseal to the reservoir, the presence of traps, and the timely relationship of the above factors (§10.2.1).

A suite of maps showing the distribution of potential reservoir, source, and caprock facies can be drawn. Caprocks and sources may be external to the sequence containing the reservoir. As discussed in §10.2.2, a single source rock horizon may charge a number of separate reservoir-defined plays. A single reservoir-defined play may also be charged from a variety of separate source rock intervals. The objective of play assessment is to anticipate all of the possible combinations of potential reservoirs, sources and caprocks that may produce petroleum plays in the basin. For each reservoir-defined play, a single map can be produced that shows the distribution of the potential reservoir facies, the source "kitchen(s)" needed to charge the reservoir, and the potential caprock facies.

Demaison (1984) introduced the "generative basin concept," and described how petroleum generative kitchens could be mapped out. White (1988) extended this concept by including the reservoir, topseal, and trapping controls on the play.

Plays are essentially reservoir-defined. Hence, fairways at different stratigraphic levels in a basin may be stacked vertically. Within a single play, all prospects and discovered fields share a common geological mechanism for petroleum occurrence. Petroleum accumulations, discovered or undiscovered, within a single play fairway, can be considered to constitute a naturally occurring population or family of geological phenomena. Thus, each play can have a characteristic field size distribution and drilling success ratio.

In assessing an unproven play, the probability of the play working (play chance) should be estimated as part of the resource assessment process. Owing to the interplay of the critical geological factors over the extent of the fairway, it is normal for play chance to vary spatially. This variation in play chance may be due to hard evidence of adverse geology in different parts of the fairway (determined, for example, from well or seismic data), or to variations in the quantity or quality of the data base, which allows greater or lesser confidence in the interpretations made. As a result, an unproven fairway may be subdivided into a mosaic of segments (*common-risk segments*) – play chance may vary for each segment, but within a segment it is constant.

The fairway can also be subdivided into segments if there are strong reasons for believing field sizes are likely to be significantly different (for example, as a result of differing structural development in different parts of the fairway), or drilling success ratios are likely to vary significantly. Thus, the three factors that define fairway segments are variations in: (i) play chance, (ii) expected field sizes, or (iii) expected drilling success ratios. In this way, reservoir-defined plays are sometimes subdivided by trap type. Examples are the Kapuni Overthrust segment and the Kapuni Inversion segment of the Eocene Kapuni Coal Measures play of the Taranaki Basin, New Zealand.

The following items of geological information are contained on a play map (Fig. 10.4):

1 The depositional or erosional limits of the reservoir unit;
2 the distribution of reservoir facies within the gross reservoir unit;
3 the areas where a source rock is present;
4 the area where it is mature (the kitchen);
5 a migration zone around the kitchen; together with (4) it represents the area receiving a petroleum charge;
6 areas where there is an effective regional seal;
7 areas where traps are present (structural or stratigraphic);
8 oil and gas fields, dry holes, and untested prospects, leads and notional prospects;
9 drilling success ratios for specific parts of the fairway.

The drilling success ratio is the ratio of the number of *technical successes* to the number of *valid tests* of the fairway. A *technical success* is an exploration well that flows petroleum to surface or in which the presence of petroleum in drill-stem or wireline formation tests convincingly demonstrates the presence of a pool of recoverable petroleum. It carries no implication of commerciality. A *commercial success* is a well that discovers a petroleum accumulation that can be economically developed. A *valid test* is a well that penetrated the play fairway, and intended to test an exploration target in the play fairway. In basins with vertically stacked fairways, there may be many more penetrations of a fairway than there are valid tests. Valid tests are not only those wells that tested valid traps in the fairway.

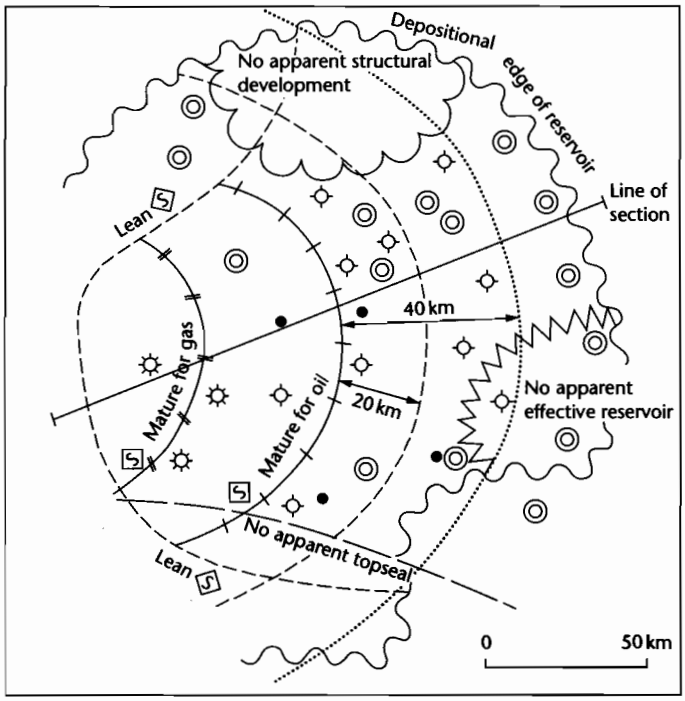

X section

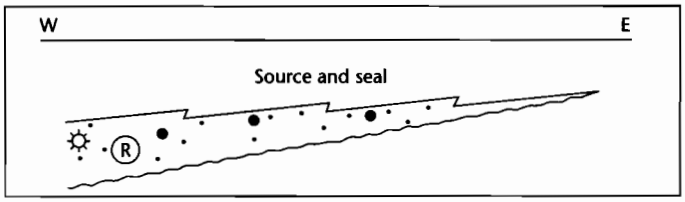

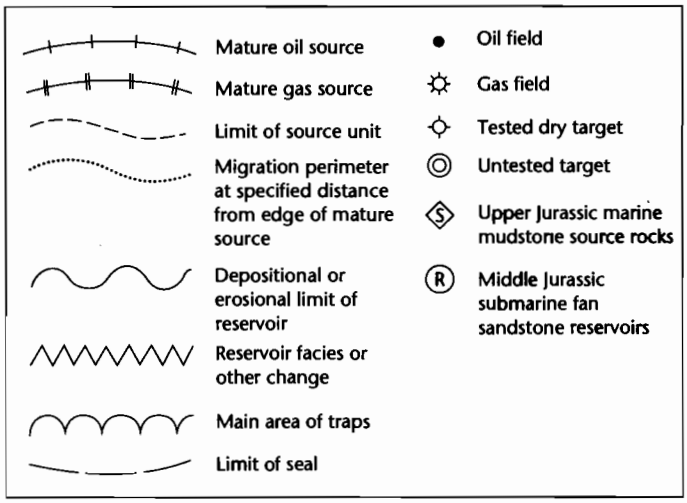

Fig. 10.4 Example of a play map (after White 1988). The play map should show all the important geological factors likely to control hydrocarbon accumulation in the fairway. The fairway is initially reservoir-defined, then the extent of the charge, topseal, and likely trap development are added.

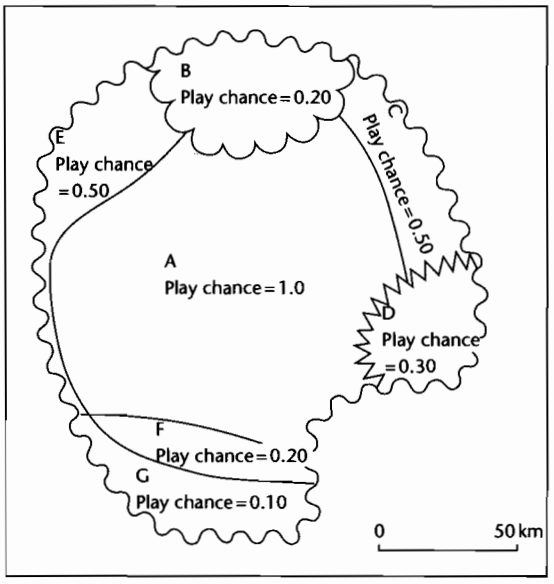

Fig. 10.5 Subdivision of the play fairway into common-risk segments. These are controlled by the distribution of reservoir charge, topseal, and likely trap development shown in Fig. 10.4. A play chance is assessed for each common-risk segment. In this illustration, segment A is considered already proven (play chance is 1.0).

There are normally far more dry holes than technical successes in a play. Within a proven play, dry holes are caused by local geological variations, such as the absence of a lateral seal in a faulted prospect, the existence of a migration shadow, or local diagenetic destruction of reservoir porosity. These factors contribute to *prospect-specific risk.*

In Figure 10.4, an area of mature source in the west of the area has experienced the highest drilling success ratio (75%). As we move outwards, firstly a migration distance of 20 km, and then a migration distance of 40 km, the success ratios drop to 28% and then 20%. This is interpreted to be caused by more and more prospects failing to lie on migration routes as the distance from the kitchen increases. Despite these variations in success ratio, however, the play is effectively proven in these areas. Beyond the 40 km migration perimeter, there are no existing discoveries and the play is unproven.

Common risk segment A is considered already proven (play chance of 1.0). The unproven part of the fairway is divided into the following common risk segments (Fig. 10.5):

- B: an area of no apparent structural development in the north (no traps). The seismic grid, however, is coarse and there may be stratigraphic traps, so the possibility of traps cannot be ruled out (play chance assessed at 0.20);
- C: an area beyond the 40 km migration perimeter in the east. Although unlikely, a very focused migration path could charge a prospect in this segment (play chance is assessed at 0.50);
- D: an area beyond the 40 km migration perimeter where reservoir effectiveness may be destroyed by diagenesis (play chance assessed at 0.30);
- E: an area in the northwest, up-dip from a lean source. However, the geochemical database is in fact quite poor and source rock interpretations unreliable (play chance is assessed at 0.50);
- F: an area in the south with no apparent topseal (play chance assessed at 0.20);
- G: an area in the south up-dip from a lean source and also with no apparent regional topseal (play chance assessed at 0.10).

Beyond the depositional or structurally controlled limits of the gross reservoir unit, there is no play at all. This is the outer limit of the fairway.

10.2.4 A note on resource assessment

Quantitative estimates of the undiscovered potential of plays are required by petroleum exploration companies in order to evaluate exploration investment opportunities and guide long-term strategic plans. Estimates of the likely size and timing of future discoveries, and hence future petroleum supply, also form an important element in the planning studies of government organizations.

A range of geological, geochemical, and statistical techniques has been developed over the years to estimate undiscovered resources. We have shown how play fairway maps indicate the key geological controls on the play. Further stages in resource assessment – estimation of the number and sizes of undiscovered fields, assessment of risk, and calculation of resource assessment curves – are not covered in this volume but are discussed in Allen and Allen (1990, Ch. 11). Oil and gas exploration companies and government agencies are likely to have their own methodologies and protocols that govern this task, and it is a specialized topic best researched through industry literature.

10.3 THE PETROLEUM CHARGE SYSTEM

10.3.1 Source rocks

Summary

There is now a wealth of geochemical evidence that petroleum is sourced from biologically derived organic matter buried in sedimentary rocks. Organic-rich rocks capable of expelling petroleum compounds are known as *source rocks*. In order to understand and predict the distribution and type of petroleum source rocks in space and time, it is necessary to consider the biological origin of petroleum. Source beds form when a very small proportion of the organic carbon circulating in the Earth's carbon cycle is buried in sedimentary environments where oxidation is inhibited.

In the world oceans, simple photosynthesizing algae (phytoplankton) are the main primary organic carbon producers. Their productivity is controlled primarily by sunlight and nutrient supply. The zones of highest productivity are in the surface waters (euphotic zone) of continental shelves (rather than open ocean) in equatorial and midlatitudes, and in areas of oceanic upwelling or large river input. The productivity of land plants is controlled primarily by climate, particularly rainfall. Coals have formed in the geological past, predominantly in the equatorial zone and in the cool wet temperate zone centred at about 55° latitude (N and S).

All living organic matter is made up of varying proportions of four main groups of chemical compounds – *carbohydrates*, *proteins*, *lipids*, and *lignin*. Only lipids and lignin are normally resistant enough to be successfully incorporated into sediment and buried. Lipids are present in both marine organisms and certain parts of land plants, and are chemically and volumetrically capable of sourcing the bulk of the world's oil. Lignin is found only in land plants and cannot source significant amounts of oil, but is an important source of gas. Geochemical studies of coal macerals have shown a very significant oil potential in the exinite group, comprising material derived from algae, pollen and spores, resins, and epidermal tissue.

The organic compounds provided to sea-bottom sediments by primitive aquatic organisms have probably not changed dramatically over geological time. In contrast, important evolutionary changes have taken place in land plant floras. As a result, a distinction can be made between the generally gas-prone Paleozoic coals, and the coals of the Jurassic, Cretaceous, and Tertiary, which may have an important oil-prone component.

Anoxic conditions (depleted in oxygen) are required for the preservation of organic matter in depositional environments, because they limit the activities of aerobic bacteria and scavenging and bioturbating organisms which otherwise result in the destruction of organic matter. Anoxic conditions develop where oxygen demand exceeds oxygen supply. Oxygen is consumed primarily by the degradation of dead organic matter; hence, oxygen demand is high in areas of high organic productivity. In aquatic environments, oxygen supply is controlled mainly by the circulation of oxygenated water, and is diminished where stagnant bottom waters exist. The transit time of organic matter in the water column from euphotic zone to seafloor, sediment grain size, and sedimentation rate also affect source bed deposition.

The three main *depositional settings* of source beds are lakes, deltas, and marine basins.

Lakes are the most important setting for source bed deposition in continental sequences. Favorable conditions may exist in deep lakes, where bottom waters are not disturbed by surface wind stress, and at low latitudes, where there is little seasonal overturn of the water column and a temperature–density stratification may develop. In arid climates, a salinity stratification may develop as a result of high surface evaporation losses. Source bed thickness and quality is improved in geologically long-lasting lakes with minimal clastic input. Organic matter on lake floors may be autochthonous, derived from freshwater algae and bacteria, which tends to be oil-prone and waxy, or allochthonous, derived from land plants swept in from the lake drainage area, which may be either gas-prone or oil-prone and waxy. The Eocene Green River Formation of the western USA, and the Paleogene Pematang Rift sequences of central Sumatra, Indonesia are examples of rich, lacustrine source rock sequences.

Deltas may be important settings for source bed deposition. Organic matter may be derived from freshwater algae and bacteria in swamps and lakes on the delta-top, from marine phytoplankton and bacteria in the delta-front and marine prodelta shales, and, probably most importantly, from terrigenous land plants growing on the delta plain. On post-Jurassic deltas in tropical latitudes, the land plant material may include a high proportion of oil-prone, waxy epidermal tissue. Mangrove material may be an important constituent. Examples of deltaic source rocks include the Upper Cretaceous to Eocene Latrobe Group coals of the Gippsland Basin, Australia.

Much of the world's oil has been sourced from *marine* source rocks. Source beds may develop in *enclosed basins* with restricted water circulation (reducing oxygen supply), or on open shelves and slopes as a result of *upwelling* or impingement of the *oceanic midwater oxygen-minimum layer*. Examples of modern enclosed marine basins include the Black Sea and Lake Maracaibo (Venezuela). Source bed deposition is favored by a positive water balance, where the main water movement is a strong outflow of relatively fresh surface water, leaving denser bottom-waters undisturbed. The Upper Jurassic Kimmeridge Clay Formation of the North Sea, and the Jurassic Kingak and Aptian–Albian HRZ Formations of the North Slope, Alaska, are examples of source rocks deposited in restricted basins on marine shelves.

The upwelling of nutrient-rich oceanic waters may give rise to exceptionally high organic productivity. Oxygen depletion may occur in the underlying bottom waters as oxygen supply is overwhelmed by the demand created by degradation of dead organic matter. Upwelling coastlines tend to be arid, and the organic matter in upwelling deposits is almost entirely of marine origin and strongly oil-prone. Upwelling may have played a part in the formation of source rocks such as the Permian Phosphoria Formation of the western USA, the Triassic Shublick Formation of the North Slope, the Cretaceous La Luna Formation of Venezuela and Colombia, and the Miocene Monterey Formation of California.

In open oceans whose floors are swept by cold, dense currents originating in the polar regions, an oxygen-deficient layer develops at depths of 100–1000 m. At times in the geological past, during periods of warmer climate and higher sea level, this layer may have intensified and impinged on large areas of the continental shelves and slope. The "global anoxic events" of the Mid-Cretaceous may have resulted from this process. The Toarcian source rocks of western Europe may also be an example.

The organic matter buried in sediments is in a form known as kerogen. *Geochemical measurements* may be used to determine the presence, richness, and stage of thermal maturity of a petroleum source rock, as well as the range of compounds likely to be generated and expelled. The richness or petroleum-generating potential of a source rock can be determined by measurements of Total Organic Carbon (TOC) and pyrolysis yield. Rocks with pyrolysis yields of greater than approximately 5 kg tonne^{-1} have the potential to be effective source rocks. More sophisticated geochemical techniques, such as gas chromatography and isotope studies, can be used to determine likely petroleum products, and in a range of other applications, including the correlation of source rocks with oils. Visual (optical) descriptions of kerogen may also give a useful guide to petroleum potential and petroleum type. From microscopic examination in reflected light, kerogen may be classified into the *exinite*, *vitrinite*, and *inertinite* groups. The exinite group comprises macerals with significant oil potential, whereas the vitrinite group is gas-prone. Inertinites have no petroleum-generating potential. Measurements of the reflectance of vitrinite are used as an index of thermal maturity (§9.7.2).

10.3.1.1 The biological origin of petroleum

Since the discovery by Treils in 1934 of a porphyrin "biological marker" compound in rock material, a wealth of geochemical evidence has accumulated to show that petroleum is sourced from biologically derived organic material buried in sediments. In order to understand the distribution in space and time of source rocks for oil and gas, it is necessary to first consider the characteristics of the biomass from which the organic material is originally derived. This section briefly discusses a number of topics: source bed deposition in the context of the overall carbon cycle; the main components of the biomass; geographical variations in organic productivity in the world's environments at the present day, and the main factors controlling these variations; changes in the composition of the biomass through geological time; the chemical composition of living organic matter and its likely hydrocarbon products.

THE CARBON CYCLE

The carbon cycle is initiated by photosynthesizing land plants and marine algae that convert carbon dioxide present in the atmosphere and seawater into carbon and oxygen using energy from sunlight (Fig. 10.6). Carbon dioxide is recycled back in many ways, the most important of which are back to the atmosphere by animal and plant respiration, by bacterial decay and natural oxidation of dead organic matter, and by combustion of fossil fuels – both natural and by humans. However, the importance of the carbon cycle to the petroleum geologist is that a small proportion of carbon escapes from the cycle as a result of deposition in environments where oxidation to carbon dioxide cannot occur. These environments are generally depleted in oxygen (for example, some restricted marine basins and deep lakes), or toxic for bacteria (swamps).

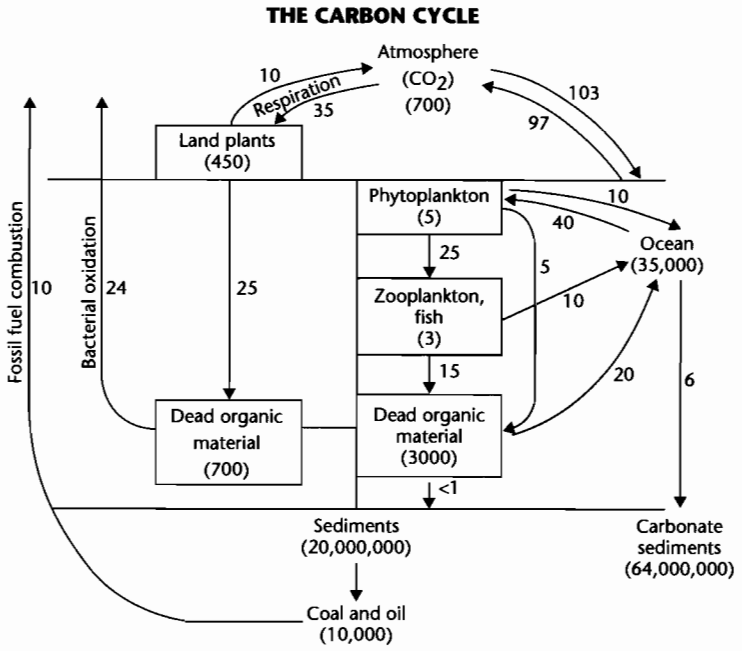

Fig. 10.6 The main elements of the carbon cycle. Numbers represent quantities in billions of metric tons (10^9 t). Numbers in parentheses represent stored quantities, numbers without parentheses are yearly fluxes. A relatively small amount of organic carbon escapes the carbon cycle to form organic-rich sediments, the source rocks for oil and gas. Data from Waples (1981).

The proportion of organic material buried in sediments in this way, relative to that originally produced, is very small (<1%), but over geological time is significant. Because it is preferentially concentrated in specific environments, it results in commercially significant petroleum source bed development. Petroleum is sourced therefore from organic carbon that has dropped out of the carbon cycle, at least temporarily. It rejoins the cycle when extracted by humans and combusted.

Organic production

The nature of organic production is quite different in continental and marine ecosystems. Continental ecosystems are dominated by land plants in low-lying coastal plain environments and by freshwater algae in lakes. Marine ecosystems are overwhelmingly dominated by phytoplankton.

Marine ecosystems

Figure 10.7 illustrates the fate of the 26.6×10^9 tonnes supply of organic carbon per year. Only a small percentage (0.4% according to Romankevich 1984) of the net carbon production in the world's seas and oceans is transferred to and preserved in sea bottom sediment.

Simple photosynthesizing algae are the primary organic carbon producers in the world's oceans, and are the start of a complex food chain. Phytoplankton are responsible for over 90% of the supply of organic matter in the world's oceans. The phytoplankton group includes the diatoms, dinoflagellates, blue green algae, and nannoplankton. Apart from phytoplankton, other organisms such as zooplankton, benthos, bacteria, and fish may also be important elements of the biomass. In the Black Sea (Romankevich 1984), annual bacteria production far exceeds even the phytoplankton. The main function of bacteria is to break down dead organic matter, but the

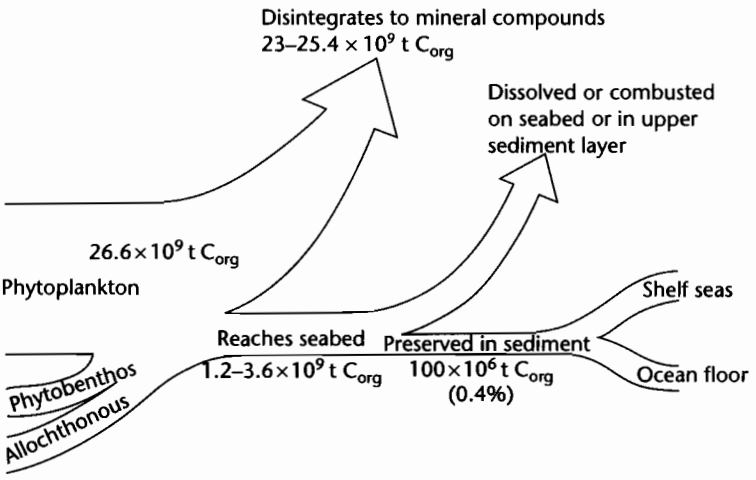

Fig. 10.7 Fate of the 26.6×10^9 tons of annual organic carbon (C_{org}) production in the world's oceans. In the order of 0.4% is preserved in the bottom sediments of shelf seas and ocean floors.

Table 10.1 Global net primary production (Woodwell et al. 1978; Nienhuis 1981).

Ecosystem type	Area 10^6 km^2	Total net primary production		Total plant mass of carbon 10^9 t C_{org}
		10^9 t C_{org} yr^{-1}	g C_{org} m^{-2} yr^{-1}	
Marine ecosystems including:	361.0	24.7	68.7	1.74
Algal bed and reef	0.6	0.7	1166.7	0.54
Estuaries	1.4	1.0	714.3	0.63
Upwelling zones	0.4	0.1	250.0	0.004
Continental shelf	26.6	4.3	161.6	0.12
Open ocean	332.0	18.7	56.3	0.45

bacteria may themselves also contribute to the organic content of the sediment.

Geographical variations in phytoplankton production in the world's marine environments are shown in Table 10.1 and Figure 10.8. Although the open ocean accounts for a large percentage of the organic carbon produced, the concentration of organic carbon per square meter in open ocean water is relatively low, which explains why the red pelagic oozes of the deep ocean basins are typically very lean in organic content. In contrast, the continental shelves are very rich, particularly in some specific environments of enhanced organic activity such as the algally dominated intertidal zone and in reefs and estuaries. Upwelling zones, such as those off the Peruvian coast at the present day, are also areas of relatively high organic productivity.

At a global scale, several trends in organic productivity may be recognized. Primary productivity decreases from coastal/marine shelf into open ocean. Mid-latitude humid and equatorial latitudes are more productive than tropical latitudes. Lowest productivity is in polar and tropical areas. The factors controlling organic productivity include:

- *Sunlight*: The zone of highest productivity is the top 200 m of the world seas, especially the upper 60–80 m. This is the *photic zone*;

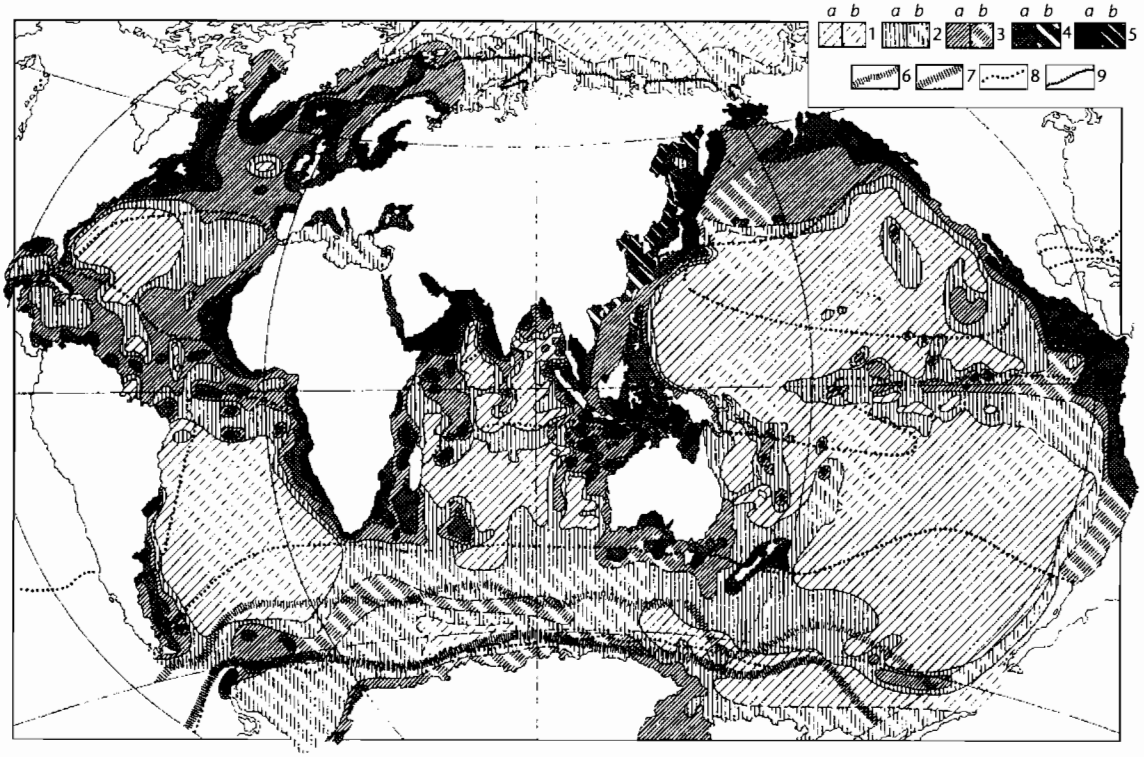

Fig. 10.8 Distribution of phytoplankton production in the ocean in units of mg C m^{-2} day^{-1}: 1=<100, 2=100–150, 3=150–250, 4=250–500; 5=>500. *a*, direct measurements; *b*, indirect data; 6, Antarctic convergence; 7, Antarctic divergence; 8, boundaries of climatic zones; 9, line with teeth, ice boundary in the Arctic. The highest phytoplankton productivities are in shelf areas rather than in oceans, particularly in algally-dominated intertidal zones, reefs, estuaries, and upwelling zones. (Reproduced with permission from Romankevich 1984.)

- *nutrient supply*: Nutrients, particularly nitrates and phosphates, are required to sustain high organic productivity. These are supplied by water circulation. Stagnant seas are not very productive. Ocean bottom currents set up by the sinking of very cold water in the polar regions may cause upwelling along the western coasts of continents in tropical latitudes. The best known examples are offshore Peru and west Africa. A rich nutrient supply is provided, and organic productivity is very high. Nutrient supply is also locally increased in areas of large river input and coastal abrasion;
- *turbidity*: Productivity is limited in areas with turbid coastal waters;
- *salinity*: Extremes of salinity (high or low) reduce the diversity of species present, though productivity of certain groups may still be very high;
- *temperature*: Temperature also influences the composition of the phytoplankton population, rather than net productivity. Dinoflagellates for example, require high water temperatures of >25 °C. Diatoms and radiolarians prefer 5–15 °C.

Figure 10.9 illustrates the concentration of organic carbon in sea-bottom sediment, and shows that a large proportion is in continental shelf environments. Organic productivity in surface waters is an important, but not sole factor controlling the concentration of organic matter in bottom sediments. Indeed, Demaison and Moore (1980) were unable to find a convincing systematic correlation between these two factors at the present day.

The critical factors for source bed development are the *deposition* and *preservation* of organic matter in significant

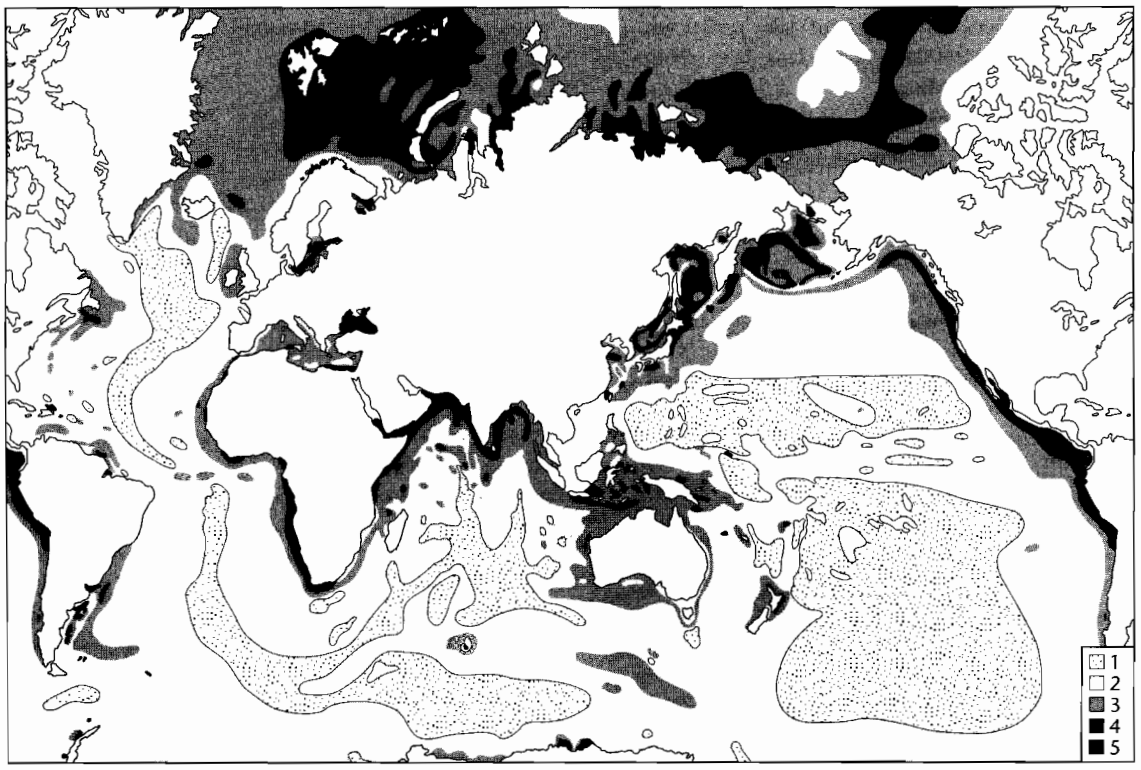

Fig. 10.9 Distribution pattern of organic carbon in the upper sedimentary layer (0–5 cm) beneath the world's oceans, in percentages on a dry weight basis. 1, <0.25; 2, 0.25–0.50; 3, 0.51–1.00; 4, 1.01–2.00; 5, >2.00. The highest organic carbon concentrations in bottom sediments are also in shelf areas. Organic productivity is a major controlling factor. (Reproduced with permission from Romankevich 1984.)

quantities in sediments, rather than organic productivity *per se*. Factors affecting the deposition and preservation of organic matter in sediment are discussed in §10.3.1.2.

Continental ecosystems

Organic productivity in continental ecosystems is dominated by land plants and freshwater algae.

The productivity of land plant material is controlled primarily by climate. Land plant material may be swept by rivers into lakes and adjoining marine areas, constituting an allochthonous organic supply. The most important allochthonous land plant deposit is peat, which forms below the water table in swamps or stagnant lakes where a wet climate allows luxuriant plant growth and topography causes poor drainage. A balance is necessary between the rate of accumulation of dead plant matter and the rate of subsidence. Accumulated peat may be preserved where bacterial decay of the dead organic matter is inhibited by anoxic or toxic conditions and where net subsidence takes place. Peat swamps form in the lower delta plain environment, typically in the lagoonal areas behind coastal spits and barriers, and in bays between vertically accreting distributary channels.

Ancient coal occurrences can be predicted using paleoclimatic maps such as those of Parrish et al. (1982). Paleolatitude studies show that coals ranging in age from Early Triassic to mid-Miocene are concentrated in the equatorial zone and in the cool wet temperate zone centred on about 55° N and S.

Freshwater algae make an important contribution to the organic matter supply in lakes. An example is the

present day alga, *Botryococcus*. Ancestors of *Botryococcus* have been identified in ancient lake sediments, and derived geochemical compounds have been recognized in many lake-sourced oils.

CHEMICAL COMPOSITION OF LIVING ORGANIC MATTER

The chemical compounds that make up all living organic matter fall into four groups. These are: (i) carbohydrates, (ii) proteins, (iii) lipids, and (iv) lignin.

Carbohydrates are compounds that function as sources of energy and as supporting tissue in plants and some animals. Examples are sugar, such as glucose and fructose, starch, cellulose, and chitin. Cellulose is an important supporting tissue in land plants, while chitin is the material manufactured by crustaceans to form a hard protective exoskeleton.

Proteins are organic compounds made up of amino acids, and perform a variety of biochemical functions vital to life processes. Examples are enzymes, hemoglobins, and antibodies. Proteins also make up most of the organic matter in shells and substances such as hair and nails.

Lipids are a range of organic substances that are insoluble in water, and include animal fats, vegetable oils, and waxes. They are similar in chemical composition to petroleum. Lipids are abundant in marine plankton, and are present in the seeds, fruit, spores, leaf coatings, and barks of land plants. A range of lipid-like substances, for example sterols, are important biological markers in crude oils.

Lignin and *tannins* are compounds common in higher plants. Lignin is the substance that gives strength to plant tissue, for example in trees, providing a much firmer support than cellulose. Tannins are found in some tree barks, seed coats, nut shells, algae, and fungi.

Other important organic compounds are *resins* and *essential oils*. Resins are found in the wood and leaf coatings of trees, and are particularly resistant to chemical and biological attack.

The relative amounts of these groups of organic compounds in living organisms varies enormously (Table 10.2). Factors such as food supply and overcrowding are also known to affect lipid content. Of the four groups of compounds, proteins and carbohydrates are very susceptible to degradation, and tend to be dissolved, oxidized, or bacterially degraded, without being incorporated in sediment beyond its surface layers. In contrast, lipids and lignin are much more resistant to mechanical, chemical, and biochemical breakdown, and under the conditions to be discussed later, will be buried successfully in sediment. Lipids are closest in chemical composition to petroleum. A relatively small number of chemical changes are involved in transforming lipids into petroleum, and more petroleum can be produced from lipids than from any of the other substances. The lipid content

Table 10.2 Composition of living matter (Hunt 1980).

	% Weight (ash-free basis)			
	Proteins	**Carbohydrates**	**Lignin**	**Lipids**
Plants				
Land plants				
Spruce wood	1	66	29	4
Oak leaves	5	44	32	4
Scots-pine needles	7	41	15	24
Diatoms	29	63	0	8
Lycopodium spores	8	42	0	50
Animals				
Zooplankton	53	5	0	15
Copepods	65	22	0	8
Higher invertebrates	70	20	0	10

of organic matter buried in sediments is probably sufficient to source all of the world's known oil.

If the biological precursors of petroleum can be microscopically identified, we can go a long way towards predicting the kind of hydrocarbons that are likely to be generated. Marine organic matter in sediments tends to be amorphous, but much of our understanding of the generating potential of land plant source rocks is derived from coal petrography. A large number of coal macerals have been identified. The three main groups are listed below. Kelley et al. (1985) have geochemically analyzed the generating potential of some macerals:

- *Vitrinite* is derived from the lignin and cellulose component of plant tissues. It is normally the largest constituent of the so-called *humic coals*, and generates predominantly gas;
- *inertinite* is also derived from the lignin and cellulose of plants, but has been oxidized, charred, or biologically attacked. The consensus is that it has negligible hydrocarbon generating potential. What potential it has is for gas. Dispersed inertinite has, however, been proposed as one of the sources of the liquid hydrocarbons in the Permian Gidgealpa Group of the Australian Cooper Basin;
- *exinite* is a diverse group of macerals: (i) *Alginite* is derived from algae, and when abundant forms a *boghead* or *cannel coal*. It is the main constituent of the torbanites of Scotland. This type of coal is quite rare, being most common in the Permo-Carboniferous. The algae responsible for these alginites are similar to the modern freshwater alga *Botryococcus*. Alginite is strongly oil prone. (ii) *Sporinite* is derived from the spores and pollen of plants, and may be abundant in coals from the Devonian through to the present day. The sporinite in Paleozoic coals is derived mainly from spores, whereas in Mesozoic and Tertiary sporinite, pollen predominates. Spores and pollen are extremely lipid-rich (50%) and may give rise to excellent oil-prone source rocks. Since spores and pollen are often transported large distances by wind or water, oxidation before burial in sediment often occurs. The best source rocks are therefore those in which the spores and pollen are autochthonous to the depositional environment, as for example in a coal swamp. (iii) *Resinite* is derived from the resins and essential oils of land plants. It is a prolific source of napthenic and aromatic hydrocarbons. (iv) *Cutinite* is derived from the protective surface coating or cuticle of higher plants. The cuticle occurs on the outside of the epidermal tissue. It is rich in hydrocarbon waxes, and is thus an important oil source. Poor preservation may result in a gas-prone cutinite, with very little remaining oil potential.

Thus, all of the exinite macerals have oil generating potential. Preservation of the maceral is, however, critical. This is a function of the transport route and distance, and the depositional environment The oil generating potential of sporinite and cutinite is particularly strongly affected by poor conditions for preservation.

Of the four groups of compounds found in living organic matter therefore, only lipids and lignins are likely to be substantially incorporated into sediment beyond the surface layer. Lipids are present in both marine organisms and parts of land plants, are chemically suited to sourcing petroleum, and could account for all of the world's known oil. Lignin is found only in land plants. It is unlikely to source oil, but is an important source of gas.

CHANGES IN THE COMPOSITION OF THE BIOMASS THROUGH GEOLOGICAL TIME

The ancestors of the primitive aquatic organisms that comprise phytoplankton, zooplankton, and bacteria may be traced back into the Precambrian with little apparent evolutionary change. The kind of aquatic organic matter buried in marine sediment has therefore probably changed very little over geological time. For land plants, however, important floral changes have taken place since their appearance in the Late Silurian–Devonian that have had a major impact on the hydrocarbon generating characteristics of the source rocks in which they are buried (Fig. 10.10).

The Carboniferous coals of the northern hemisphere and the Permian coals of the southern hemisphere contain floras dominated by early plant groups (mostly lycopods) without extensive foliage. The resulting coal macerals are gas-prone vitrinite and its oxidation product inertinite, with minor amounts or local concentrations of sporinite, resinite, cutinite, and alginite. Paleozoic coals, therefore, tend on the whole to be gas-prone.

Important evolutionary changes took place in floras in the Jurassic and Cretaceous. Conifers became dominant in the Jurassic, and angiosperms (flowering plants) appeared in the Cretaceous. Both these plant groups are rich in waxy epidermal tissue and resin, and have significant oil generating potential. Large volumes of gas are also generated from coals of this type, since vitrinite is normally still abundant. Most of Australia's waxy oils have been sourced from coals of this type, most notably the Gippsland Basin oils from the Early Tertiary Latrobe

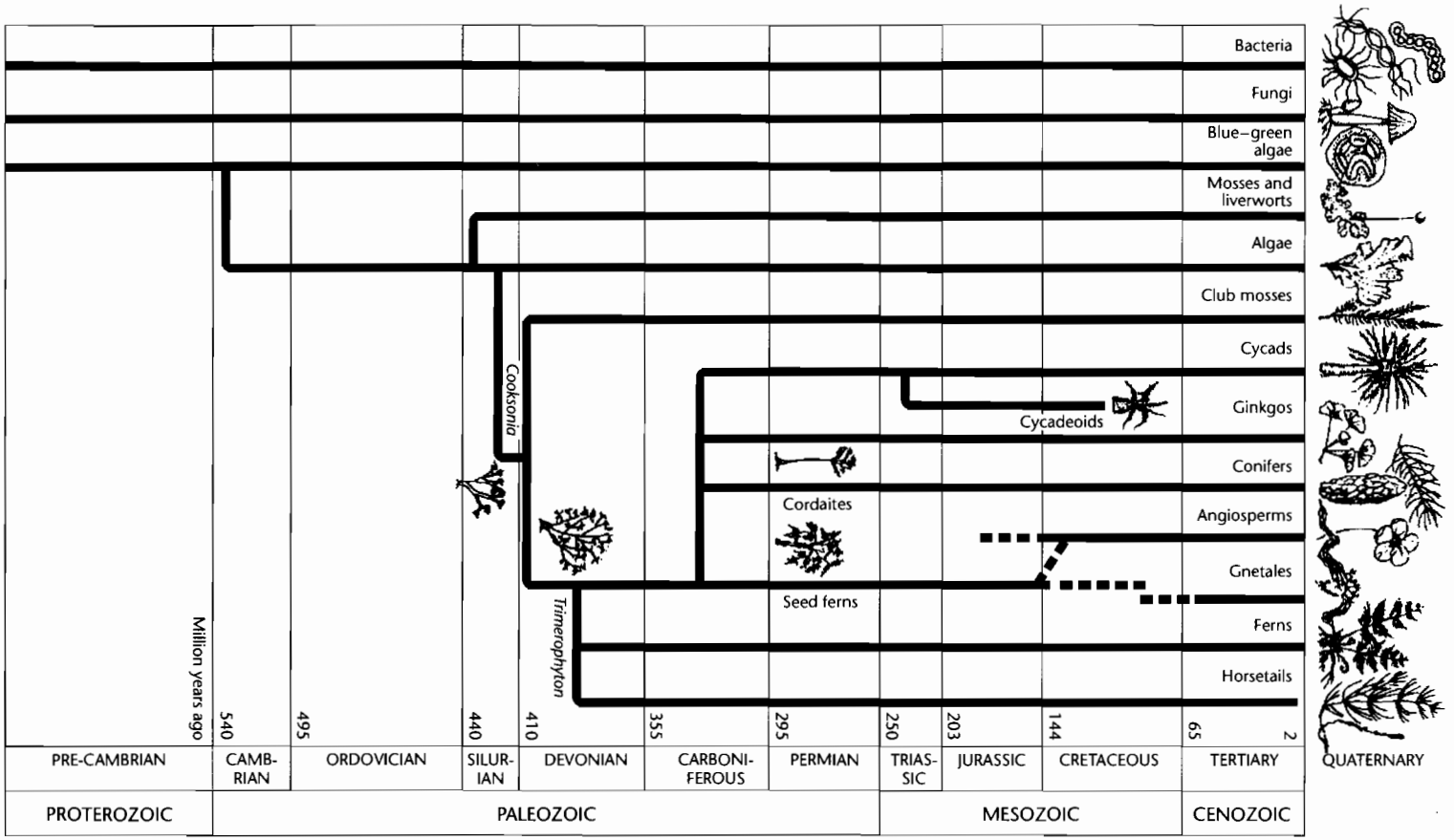

Fig. 10.10. Plant evolution over the last 600 Myr. The first land plants (primitive vascular varieties) such as Cooksonia appeared in the Silurian. A large number of new groups evolved in the Devonian. Important changes in land plant floras have taken place since the Silurian which have affected their hydrocarbon-generating characteristics. Only Mesozoic and Tertiary land plants have significant oil-generating potential. Today, two main groups dominate the land; the *conifers*, which cover over more than $10 \times 10^6 \text{km}^2$ of the Earth's surface, mainly in the cooler, drier areas, and *flowering plants* (angiosperms), which occur everywhere. The conifers may date back as far as the Carboniferous. The oldest definite flowering plants in the geological record are Barremian (Early Cretaceous), but some authors place their origin in the Late Jurassic. In the sea, organisms adapted to life in water, such as the algae, have undergone their own evolution.

Group, and the Eromanga and Surat Basin oils from the Jurassic (Thomas 1982).

Thus, evolutionary changes in land plant floras through geological time are responsible for the oil-prone component of Mesozoic and Tertiary coals, while Paleozoic sediments are more typically sources solely for gas.

10.3.1.2 Source rock prediction

INTRODUCTION: ANOXIA

Anoxic conditions are critical to the preservation of organic matter in sediments. Source rock prediction is therefore concerned primarily with predicting where and when in the geological past anoxic conditions are likely to have existed. Questions addressed in this section are: "What causes anoxic conditions?" and "In what geological environments are anoxic conditions likely to develop?"

"Anoxic" means "devoid of oxygen," but the term is frequently used in the sense of "depleted in oxygen" – *dysaerobic*. "Anaerobic" means that insufficient oxygen is available for aerobic biological processes. This critical oxygen concentration is different for different organisms. Below 1.0 milliliters of oxygen per liter of water there is a serious reduction in biomass, but deposit-feeding organisms (those responsible for bioturbation of the sediment) can persist down to concentrations of $0.3\,ml\,l^{-1}$. As a general guide, $0.5\,ml\,l^{-1}$ may be taken as the oxic/anoxic threshold. Anoxic conditions are critical for source bed deposition because they prevent the scavenging of dead organic matter and bioturbation of the surface sediment by benthic fauna and degradation of organic matter by bacteria, which would otherwise destroy the organic matter prior to burial. Anoxic conditions develop where *oxygen demand* exceeds *oxygen supply*.

Oxygen demand is caused primarily by the degradation of dead organic matter. Large amounts of organic matter are supplied to the seafloor in areas of high surface organic productivity (photosynthesizing algae in the euphotic zones of seas and lakes) and/or where there is a large terrigenous supply of organic matter. Oxygen is consumed as the dead organic matter is degraded.

Oxygen supply is controlled by the circulation of oxygenated water. This may be a downward movement of oxygen-saturated surface waters as a result of mixing by waves, or a movement of cold, oxygen-bearing ocean bottom currents. Cold water can dissolve more oxygen than warm water. A feature of the world's oceans at the present day is that cold, dense water carrying large amounts of oxygen descends in the polar regions and moves over the ocean floor towards the equator, bringing oxygenated conditions to almost all parts of the oceans. It is reasonable to expect, however, that there were times in the past when such a circulation was less well developed. This has important implications for source bed deposition.

A sea or lake floor, therefore, is prone to anoxic conditions primarily under the following two sets of circumstances: (i) when organic productivity in the overlying water column is very high and the system becomes overloaded with organic matter, and (ii) when stagnant bottom water conditions exist, causing a restriction in the supply of oxygen. These factors largely determine the geological settings in which source beds are deposited.

Source beds may, under exceptional circumstances, be deposited under oxic conditions. This sometimes occurs when sedimentation rate is very high. A special case is when mass gravity flows deposit an anoxic sediment almost instantaneously into oxic waters. As a rule, however, a source rock is not expected to be developed under oxic conditions.

The factors that affect the development of anoxia are discussed in more detail in the next section.

FACTORS AFFECTING SOURCE BED DEPOSITION

An understanding of anoxic environments and their importance in petroleum exploration has rapidly developed since the 1980s (e.g., Demaison and Moore 1980). We have seen that anoxic conditions are a prerequisite for source bed deposition primarily because they prevent the bacterial degradation of dead organic matter and the scavenging and bioturbation of the surface sediment by benthic fauna. These and other factors will now be discussed in greater detail.

Bacterial degradation

Degradation of organic matter by bacteria takes place in both the water column and in sediment pore waters, under both aerobic and anaerobic conditions (Fig. 10.11). Organic matter is oxidized by aerobic bacteria using the available oxygen in the environment until there is no more organic matter to oxidize or there is no more oxygen. If the latter, the environment becomes anoxic. Anaerobic bacteria derive oxygen first of all from nitrates, and then from sulfates. It is thought that they

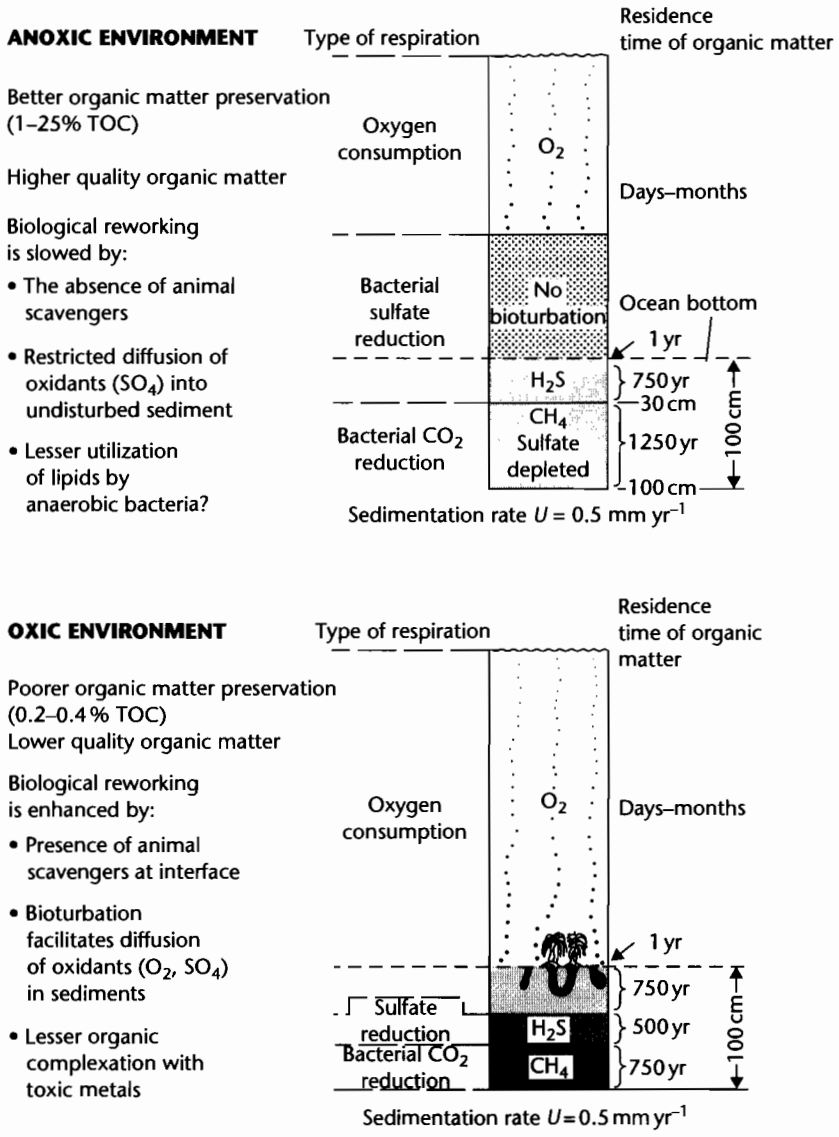

Fig. 10.11 Degradation of organic matter under anoxic and oxic conditions (after Demaison and Moore 1980). Anoxic environments are the primary sites of organic matter preservation because scavenging and bioturbation by benthic fauna and aerobic bacterial degradation are inhibited.

can degrade organic matter just as fast as aerobic bacteria. An important difference, however, is that anaerobic degradation appears to result in a greater preservation of lipid-rich, oil-prone material. Furthermore, under anoxic conditions, the bacteria population itself may contribute significantly to the preserved organic matter.

Scavenging and reworking by benthic fauna

The role of benthic metazoans such as worms, bivalves, and holothurians is critical to the preservation of organic matter. Their activity is important in two respects. First,

they consume particulate organic matter in the water just above the sea or lake floor and in the surface sediment itself. Second, burrowing metazoans churn up the sediment to a depth of 5–30 cm, allowing the penetration of oxygen and sulfates into the sediment column, thus promoting bacterial degradation.

Bioturbation seems to take place at all water depths under oxic water columns. Below oxygen concentrations of 0.3 ml l^{-1} this activity is virtually eliminated, and sediments remain laminated and organic-rich. Even the activity of anaerobic sulfate-reducing bacteria is limited because oxidants cannot easily penetrate the surface. The occurrence of unbioturbated laminated muds in the Gulf of California is closely correlated with low oxygen concentrations in bottom waters (Fig. 10.12). For these reasons, organic matter stands a much better chance of being preserved in the absence of benthic fauna, that is, in anoxic environments.

Transit time of organic matter in the water column

Almost all marine organic matter is formed by photosynthesis in the euphotic zone. Before it can accumulate on the seabed it has to fall through a water column of up to 6 km (in deep ocean areas). The smallest particles take the longest to fall, faecal pellets falling the fastest. Organic matter is scavenged by fauna during its transit through the water column. Preservation of organic matter is therefore favored by shallow water depths and large organic particle size. Scavenging in the water column is probably one of the factors that contributes to the general lack of source bed deposition in deep ocean areas. Another factor is low organic productivity due to remoteness from nutrient supply.

Sediment grain size

The low permeability of fine-grained sediments inhibits the diffusion of oxidants from the water column into the sediment, and, as a result, bacterial activity is lower than in coarse-grained sediment. Coarse-grained sediment is usually associated with high energy environments that are in any case likely to be well oxygenated.

Sedimentation rate

Under oxic conditions, high sedimentation rates favor source bed deposition because they reduce the period during which organic matter is subject to metazoan grazing, bioturbation, and aerobic bacterial attack. Sufficient organic matter may be preserved even under oxic

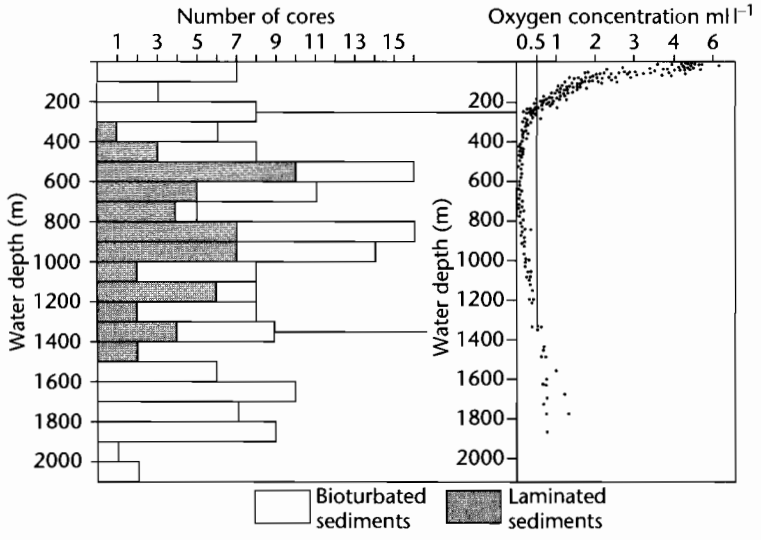

Fig. 10.12 The correlation of laminated sediments with low oxygen concentrations in the bottom waters of the Gulf of California demonstrates that bioturbation is limited by oxygen concentrations of less than 0.5 ml l^{-1}.

conditions to form a source bed. The organic matter becomes diluted, however, by the large amount of mineral matter in the sediment and the resulting source rock usually has a low organic matter concentration. It may not be capable of generating sufficient liquid hydrocarbons to saturate the source rock and expel oil. Hydrocarbons may instead be expelled at high maturity as gas. Rapidly deposited successions such as thick, muddy prodeltas, therefore, rarely contain good oil sources. Under anoxic conditions, high sedimentation rates are likely to have only an adverse diluting effect on organic content. Deposition of rich source beds is therefore favored by low sedimentation rates.

The ideal conditions for oil source bed deposition are therefore: (i) anoxic conditions with high organic productivity and restricted oxygen supply (poor water circulation), (ii) shallow water depths, and (iii) fine-grained sediment. Under oxic conditions, moderate sedimentation rates favor source bed deposition.

DEPOSITIONAL SETTINGS OF SOURCE BEDS

The main depositional settings of source beds are lakes, deltas, and marine basins. There are a number of other less important settings, including freshwater swamps, non-deltaic shorelines, and continental slopes and rises, which appear to have sourced a relatively small proportion of the world's oil and, in terms of source prediction, provide only a relatively low probability of source bed presence.

Lakes

Lakes are the most important depositional setting for source beds in continental stratigraphy (§8.5.2). In order to form volumetrically significant source beds, lakes must be geologically long-lasting. Anoxic conditions develop in "permanent" lakes when the water column becomes stratified. This is most likely to occur in the following circumstances (Allen and Collinson 1986 for summary):

- *In deep lakes*: Whereas wind stress causes the mixing of the whole water column in shallow lakes, causing oxygenation of bottom waters and sediments, deep lakes commonly have anoxic hypolimnia. The 1500 m-deep Lake Tanganyika in the East African rift system is anoxic below 150 m. TOCs (total organic carbon) of 7–11% have been recorded from bottom sediment in the anoxic part of the lake. In contrast, the shallower Lake Mobutu (Albert) and Lake Victoria are oxic;
- *at low latitudes*: Wide seasonal variations in weather cause overturn of the water column, and cold, dense river waters carrying large amounts of dissolved oxygen sink to the bottom of temperate lakes, causing oxygenation. Consequently, all temperate lakes at the present day, even the 1620 m-deep Lake Baikal, are oxygenated for at least part of the year. In warm, tropical, equable climates river water is less dense, does not have a tendency to form high-density underflows, and carries less oxygen. These conditions favor the development of anoxic conditions. In addition, the temperature–density behavior of water (Ragotzkie 1978) means that more work is required to mix two layered water masses at elevated temperatures (e.g., 29 °C and 30 °C) than at low temperatures (e.g., 4 °C and 5 °C), so tropical lakes tend to stratify easily. On the other hand, the slightest cooling in a tropical lake may initiate convection currents which may eventually affect the entire water body, causing mixing and oxygenation of bottom waters;
- *abundant water supply*: a wet climate ensures that the lake is kept filled with water, whereas in arid climates lakes may intermittently dry up, resulting in oxidation of its surface sediment. Provided this does not happen, however, high evaporation losses may encourage anoxia, by producing a *salinity stratification*. Salinity stratified lakes may form important source environments in low latitudes. Ancient examples are the Devonian Orcadian basin of the UK (review in Allen and Collinson 1986) and the Eocene Green River Formation of western USA (Eugster and Hardie 1975).

Hydrothermal solutions in areas of volcanic activity, and run-off over peralkaline volcanic products, may produce alkaline lakes. Strongly reducing conditions may develop at the lake floor. Distinctive mineral assemblages are characteristic of alkaline lakes. The Lakes Magadi and Natron of East Africa are today precipitating trona, and the Wilkins Peak Member of the Eocene Green River Formation of Colorado and Utah has a similar evaporite mineralogy.

Source beds will be richer and thicker and more likely to develop if a deep lake can be maintained for a long time with the minimum of particulate input. Clastic input is a complex function of topographic, climatic, and bedrock variables in the catchment area of the lake (see Chapter 7). Hilly or mountainous relief in tectonically active regions commonly causes rapid erosion and the rapid infilling of a lake basin by coarse detritus. Small lakes are prone to be swamped with clastic input, whereas the centres of large lakes may see little terrigenous influence. If the hinterland is an area of carbonate outcrop,

however, much of the weathering is chemical rather than mechanical, and the suspended particulate input to the lake is small. Chemical weathering is dominant in humid climates, rocks quickly breaking down under the combination of high temperatures and abundant water. Lush vegetation, particularly grasses, in the drainage area will tend to reduce the amount of surface erosion, and hence the particulate input to the lake.

Organic matter input to lakes is of two types:

- *Produced within the lake itself (autochthonous)*, comprising algae and bacteria. It produces strongly oil-prone kerogen. Ancestors of the present day alga *Botryococcus braunii* have been identified in ancient lake sediments, and its biomarker compound Botryococcane has been recognized in many lake-sourced oils. An example is the oil of the Minas field in central Sumatra (Williams et al. 1985);
- *swept into the lake from the drainage area (allochthonous)*, comprising organic matter from higher plants. Much of the allochthonous supply is lignin, which is gas-prone, but there may also be a contribution of oil-prone waxy epidermal tissues, spores or pollen. As discussed previously, these oil-prone components are only likely to be important in tropical areas since the Jurassic. Terrigenous organic matter is likely to dominate a small lake. In large lakes, it may be concentrated around the margins (particularly around river mouths) leaving the centre the site of algal and bacterial organic matter deposition.

Lake sediments may source oil, gas-condensate, or gas, depending on the factors discussed above. Lacustrine oils tend to be very variable in density, low in sulfur, and have a very variable wax content, ranging up to 40%. Wax is derived from land plant cuticles and from wax-secreting freshwater algae.

The lacustrine oil shales of the *Eocene Green River Formation* of Utah, Wyoming, and Colorado accumulated in paleolakes Uinta and Gosiute, now preserved in the Uinta and Piceance Creek sub-basins (Lake Uinta) and the Green River and Washakie sub-basins (Lake Gosiute) (Smoot 1983; Dubiel 2003). A range of lacustrine environments are represented by the members of the Green River Formation. Some of the most important oil source rock units (e.g., Laney Shale, Mahogany Oil Shale) were deposited in deep, anoxic, density-stratified, generally saline lakes, while *hypersaline* shallow lakes (Wilkins Peak and Parachute Creek members) and their fringes were also sites of significant organic matter accumulation. Hypersalinity and lack of sulfate inhibited bacterial oxidation of the organic matter. Arid conditions precluded significant land plant input to the lake systems; organic matter is, as a result, autochthonous and oil-prone.

In contrast to the saline and hypersaline units of the Green River Formation, the Pematang lake sediments of the *Paleogene Rifted Basins of Central Sumatra, Indonesia*, are deposits of low salinity lakes (Williams et al. 1985). The Pematang reaches up to 1800 m in thickness and was deposited in structurally controlled half-grabens, under humid tropical conditions. The most important oil source rock unit is the Brown Shale Formation, which represents the deposits of deep lakes formed by rapid synrift subsidence. These are well-laminated, reddish brown to black noncalcareous mudstones. Geochemical correlations demonstrate a convincing match between Brown Shale algal source rocks and crude oils, including those of the giant Minas and Duri fields. In contrast to the deep-lake oil-prone Brown Shale Formation, gas condensate-prone land plant source rocks predominate in the shallow lake sequences of the Coal Zone Formation.

Albian–Turonian lacustrine source rocks have been described from the *Songliao Basin of eastern China*. These represent the deposits of deep thermally stratified freshwater lakes. Small-scale examples of rich oil-prone lacustrine source rocks have been described from the Tertiary Mae Sot and Mae Tip Basins of northwest Thailand (Gibling 1985a, b). They were deposited in shallow fresh to brackish lakes.

Deltas

Deltas may be an important setting for source rock deposition (§8.5.3). In SE Asia and Australasia, deltas appear to have sourced a large proportion of the discovered oil. Constructive deltas (fluvial or tide dominated) are characterized by persistent low-energy environments on the delta top which favor source bed deposition. Destructive or static deltas (wave dominated) generally provide less favorable environments for source bed deposition. Migration of shoreline bars tends to rework the sediments in the lower delta plain, and organic matter is usually degraded to an inert state.

Organic matter in deltaic stratigraphy may be of three types:

- *Freshwater algae (phytoplankton) and bacteria* present in lakes, swamps, and abandoned channels on the delta top. This material is oil-prone. It will only be preserved if anoxic conditions exist at the sediment surface. Fluvial channel migration results in the infilling of lakes in deltaic environments. Lakes are most likely to

persist, therefore, in the upper part of the delta plain. High subsidence rates on the lower delta plain may allow lakes to persist despite rapid sedimentation rates, as occurs on the Niger and Nile deltas at the present day;

- *marine phytoplankton and bacteria* in the delta front and prodelta areas. Abundant nutrients provided by river input frequently stimulate high organic productivity in the marine basin into which the delta debouches, but conditions for preservation are generally poor. Preservation requires anoxicity in the marine basin. The delta front is normally a high-energy, oxic environment. High accumulation rates allow the preservation of some organic matter, but it is strongly diluted with mineral matter, and source rocks are usually lean with potential to expel only gas;
- *terrigenous land plant material.* Vegetation growing on the delta plain contributes a large amount of organic matter to depositional environments. On tropical deltas since the Jurassic, the land plant material is likely to comprise both oil-prone (waxy epidermal tissues, resins, spores) and gas-prone (lignin) material. Pre-Jurassic and temperate land plants are predominantly gas-prone. The most prolific sites of accumulation are the interdistributary peat swamps, where *in situ* coals may form. Terrigenous organic matter may, however, be dispersed across the entire delta top, and into the prodelta environment where preservation will largely depend on high sedimentation rate. In peat swamps, the high accumulation rates, highly acidic conditions, and presence of bactericidal phenol compounds released from lignin, enhance the preservation of organic material. In the upper part of the delta plain, freshwater swamps dominate. On the lower delta plain, where waters are brackish to saline as a result of some marine influence, mangrove swamps dominate. Mangroves trap plant material drifted in from the freshwater upper delta plain. Terrigenous organic matter may also be reworked onto low energy tidal flats.

Mangrove-dominated shorelines may be important source depositional environments. A modern example is Missionary Bay, north Queensland, Australia (Risk and Rhodes 1985). Mangrove litter originating on intertidal mudflats is swept into the adjoining anoxic bay bottom sediments, providing organic matter with a very high lipid content. The mangrove swamps are sites of prolific organic productivity. A thin intertidal strip of mangrove swamp may produce a vast quantity of lipid-rich organic matter and spread it over a large offshore area. The high oxygen demand caused by the abundant influx of mangrove detritus may cause anoxia in the surrounding depositional environments. Mangrove material is also relatively resistant to degradation, both physical and chemical. Under fungal and bacterial attack, the waxy lipid-rich cuticle that coats mangrove epidermal tissue appears to be preferentially preserved. Mangrove material is likely to source oils that have a high wax content.

Reworking of upper delta plain plant material in brackish conditions appears to result in a selective bacterial (or fungal) degradation of cellulose and lignin (to humic acids), leaving a relative enrichment in oil-prone waxy and resin components (Thomas 1982).

The Upper Cretaceous–Eocene *Latrobe Group* of the Gippsland Basin of SE Australia (Shanmugam 1985) have sourced about 3000 million barrels of oil. The coals are dominantly vitrinitic but contain up to 15% exinite macerals, comprising cutinite, sporinite, and resin. These components are derived from the cones, bark, seeds, leaves, and resin bodies originating in the adjacent coniferous forests. The climate was temperate and wet. Oils have been geochemically matched with these coals, and have typical coal source characteristics, including high wax content (<27%).

Marine basins

Marine source rocks may form in enclosed, silled basins such as the Black Sea, Baltic Sea, and Lake Maracaibo, or on open marine shelves and continental slopes. The mechanisms for source bed development in each of these settings are quite different. Enclosed basins are typified by water stratification, which reduces oxygen supply. Open shelves and slopes are characterized by oceanic upwelling causing high organic productivity and hence high oxygen demand. Impingement of the oceanic mid-water oxygen minimum layer may also reduce oxygen supply.

(a) Enclosed basins

These marine basins are physically restricted to some extent, by land or by chains of islands, but retain some connection with the open sea. Water exchange is limited, however, and the basin is prone to water stratification and hence anoxic conditions. The nature of the water exchange with the open sea is important, since not all enclosed basins become anoxic.

A *positive water balance* is where the outflow of freshwater (as a surface layer) exceeds the relatively small inflow of deeper saline water. Most of the water movement takes place in the surface layers, allowing stratification of

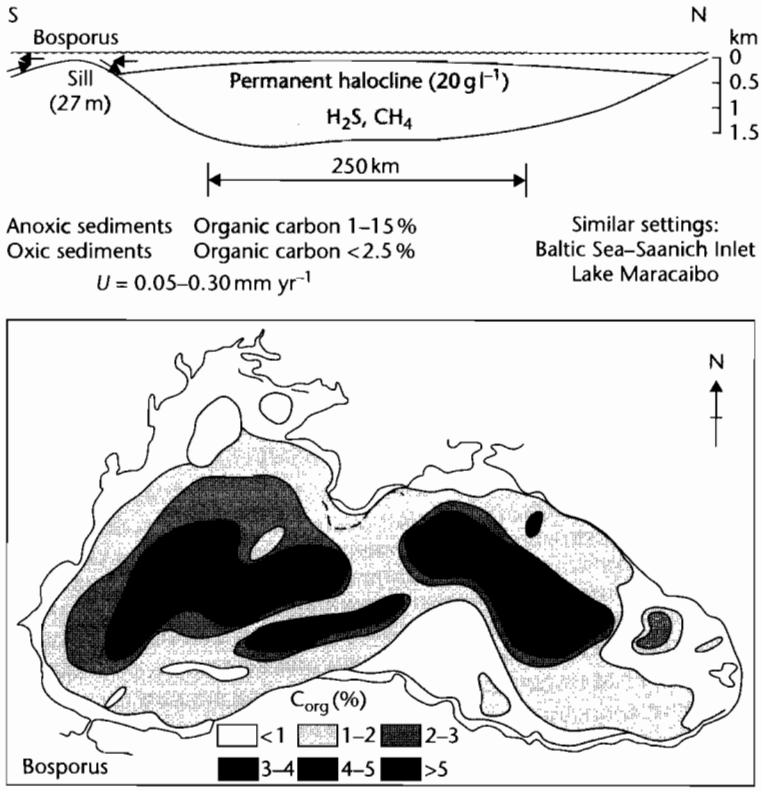

Fig. 10.13 Geometry and total organic carbon concentrations in modern sediments of the Black Sea. This is an example of a silled marine basin with a positive water balance. Organic carbon concentrations are locally up to 15% in the deeper parts of the basin (after Demaison and Moore 1980).

deeper waters. This process occurs in the Black Sea, Baltic Sea, and Lake Maracaibo. The Black Sea is one of the best-documented anoxic silled marine basins (Fig. 10.13). Total organic carbon is <15% in sediment 7000–3000 years old. At the present day, it is anoxic below 150–250 m water depths. In contrast, a *negative water balance* is where the inflow of oceanic water dominates over a relatively meager freshwater input. This often develops in arid climates where high evaporation losses at the surface cause the sinking of oxygenated waters (Fig. 10.14). Examples of oxic enclosed basins include the Red Sea, Mediterranean Sea, and Persian Gulf. The Mediterranean is the world's largest silled marine basin, but it is well oxygenated and organic contents in bottom sediment are very low.

Size and depth of enclosed basins do not appear to be critical. Lake Maracaibo, for example, is only 30 m deep.

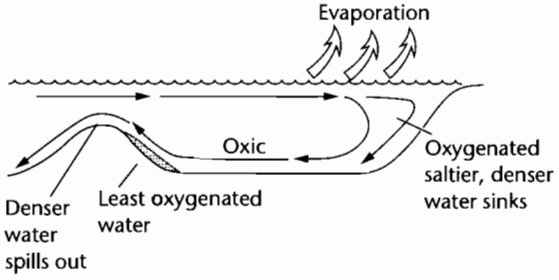

Fig. 10.14 Model for a silled marine basin with a negative water balance (after Demaison and Moore 1980). Oceanic inflow dominates over freshwater fluvial input, a situation that commonly develops in arid climates. Dense, salty, oxygenated waters resulting from surface evaporation may sink and sweep the basin floor, preventing anoxia.

The danger of water mixing by wind-generated waves, however, renders shallow basins less favorable source bed environments. Enclosed basins may range in size up to the South Atlantic Ocean during the Aptian. Small basins tend to be short-lived, particularly when there is high clastic input.

Organic matter type in enclosed marine basins depends on the amount of terrigenous land plant material brought into the basin by rivers. Wet climates imply a positive water balance and hence a tendency to water stratification. However, high terrigenous organic input may produce gas-prone source rocks. In arid climates, the organic matter is made up largely of marine phytoplankton and, when source beds are developed (often in association with carbonates and evaporites), they are predominantly oil-prone. The Devonian of the western Canada basin is believed to be an example. Source bed deposition is sensitive to changes in the water balance of the basin, and tends to be periodic and of varying lateral extent. Deep, big, enclosed marine basins in areas of wet paleoclimate offer the highest probability of source bed occurrence.

Examples of source rocks deposited in restricted marine basins probably include the Upper Jurassic Kimmeridge Clay Formation of the North Sea, and the Jurassic Kingak and Aptian–Albian HRZ Formation of the North Slope, Alaska.

(b) Open marine shelves

Upwelling occurs along coastlines where wind-driven currents flowing parallel to the coast are deflected offshore by the Earth's rotational (Coriolis) force. It is most common on the east side of oceans. Upwelling occurs today along the coasts of Peru–Chile, California, Namibia, and Morocco. The deep ocean water drawn into the upwelling cell to replace the offshore moving surface water is rich in nutrients such as phosphates and nitrates, and can give rise to exceptionally high organic productivity in the near-surface photic zone. Degradation of dead organic matter creates a high demand for oxygen, and anoxicity may develop in the underlying waters. Underneath the Benguela current offshore Namibia, for example, there is a 340 km by 50 km oxygen depleted zone. Under this zone, the sediment contains 5–26% total organic carbon (Fig. 10.15) (Demaison and Moore 1980). The organic matter is almost entirely made up of marine plankton. There is very little terrestrial input from the arid hinterland, a feature of many upwelling coastlines at the present-day.

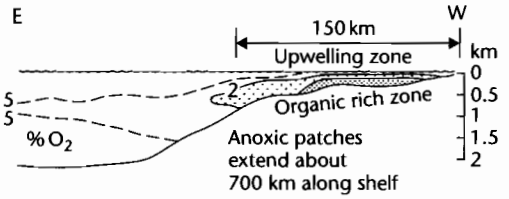

Anoxic sediments Organic carbon 3–26% Similar setting:
Oxic sediments Organic carbon < 3% Peru

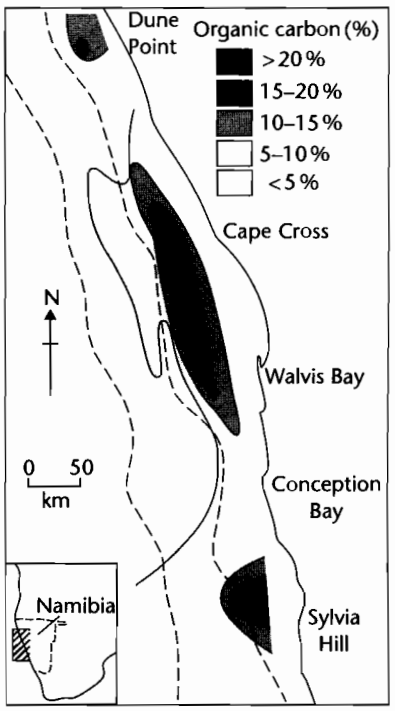

Fig. 10.15 Upwelling zone, offshore Namibia, showing oxygen-depleted zone, and total organic carbon concentrations of up to 26% (after Demaison and Moore 1980). Upwelling causes high phytoplankton productivity in surface waters. The sea bottom sediments are anoxic under the highly productive waters.

Not all upwelling zones develop anoxic conditions. Oxic examples include off SE Brazil, the northern Pacific, and bordering Antarctica. The most likely reason for the lack of anoxicity is that the upwelling is only seasonal.

A diagnostic feature of sediments deposited under upwelling currents is a distinctive mineral assemblage

including phosphorites and uranium minerals, as in the Neogene deposits of the Californian basins.

Prediction of ancient upwelling zones depends on the accurate reconstruction of atmospheric circulation and paleogeography. Occurrence of upwelling means significantly improved chances of source bed presence. Examples of source beds thought to have been deposited as a result of upwelling include the Permian Phosphoria Formation of western USA, the Triassic Shublick Formation of the North Slope, Alaska, the Cretaceous La Luna Formation of Venezuela/Colombia, the Upper Cretaceous Brown Limestone of Egypt, and the Miocene Monterey Formation of California.

The oceanic midwater oxygen minimum layer occurs in the world's oceans at depths of *c.* 100–1000 m. It is caused by the degradation of organic matter that has fallen from the overlying highly productive photic zone. Below this midwater zone, oxygen contents rise again because of the influence of cold, dense currents that originate in the polar regions and sweep along the ocean floors towards tropical latitudes. These currents supply oxygen that prevents the midwater oxygen minimum layer becoming anoxic, except in rare examples. The present-day Atlantic Ocean is well oxygenated because there is virtually no obstruction to the passage of cold polar waters from both its northern and southern ends. In contrast, in the eastern Pacific and northern Indian Oceans (Fig. 10.16), oxygen levels drop to less than 0.5 ml l^{-1}. Ocean floor currents reaching these areas have lost much of their oxygen, and the midwater oxygen minimum layer is free to intensify. TOCs in these areas range up to 11%.

The presence of strong ocean currents derived from the poles is a relatively recent feature of the world's oceans. At the present day, the Earth is in an interglacial phase. At times in the past, for example during most of the Mesozoic (particularly during the Late Jurassic and Mid-Cretaceous), the global climate was warmer, and the shape of the world's oceans was quite different from that of today. At this time, oceanic circulation may have been much more sluggish, and an intense midwater oxygen minimum zone may have developed. The Mid-Cretaceous "global anoxic events" probably occurred under such circumstances.

During times of high sea level, the midwater oxygen minimum zone may impinge on the continental shelf over wide areas. As a result, source beds are deposited on the continental shelf in association with reservoir and carrier beds, and a hydrocarbon play may be produced. Oxygen deficiency could be reinforced in bathymetric depressions in the broad epicontinental seas produced at this time. Sediments deposited in midwater anoxic zones

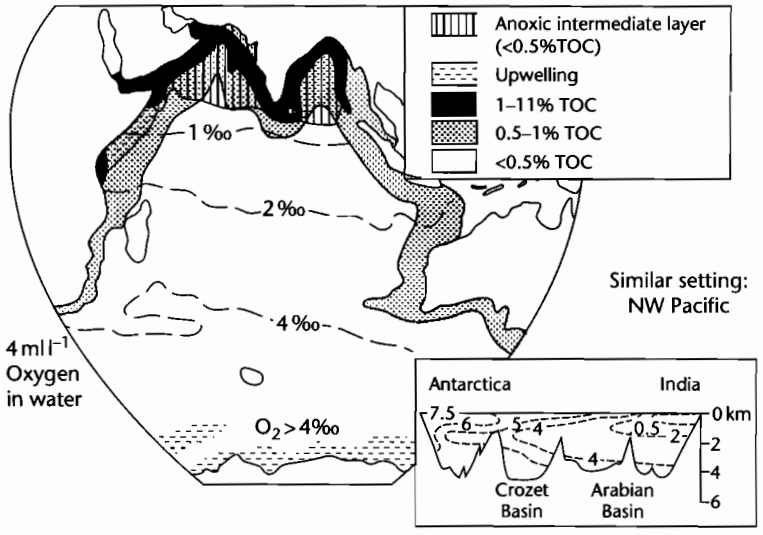

Fig. 10.16 Midwater oxygen concentrations and total organic carbon (TOC) concentrations in the Indian Ocean. TOCs are the highest around the Indian coastline where oxygen levels in the midwater layer fall to less than 0.5 ml l^{-1} and impinge on the continental slope and shelf.

may be finely laminated, nonbioturbated, organic-rich, diatomaceous mudstones (Gulf of California) or olive grey muds (northern Indian Ocean). Examples of source rocks thought to have been deposited as a result of impingement of the midwater oxygen minimum zone on the continental shelf include the Toarcian source rocks of western Europe.

The optimum conditions for marine source bed deposition occur when one of the mechanisms is reinforced by another. For example, a silled geometry may combine with the midwater oxygen minimum zone, or the midwater oxygen minimum may be intensified by upwelling.

The gas- or oil-proneness of a marine source rock depends primarily on the presence or absence of gas-prone terrigenous plant material. Enclosed marine basins close to a major clastic source may be gas-prone. Oil-prone organic matter of truly marine origin occurs in upwelling zones offshore from arid land areas.

10.3.1.3 Detection and measurement of source rocks

A range of geochemical techniques has been developed to identify and measure source rocks and petroleum fluids. These techniques may be used initially to establish simply whether a source rock exists in the sediments being sampled, but a series of other important questions about the petroleum charge system operating in an area may also be addressed. The richness of a source rock and the petroleum type or composition likely to be expelled may be determined. The thermal maturity may also be measured. Source rocks and fluids may be correlated geochemically, so that migration routes can be interpreted. Detection and measurement of source rocks is therefore necessary for efficient exploitation of most known plays, and for the recognition of new conceptual plays.

Attempts have been made to identify mature source rock horizons on petrophysical wireline logs, such as the gamma ray, sonic, and resistivity logs. Detection generally depends on the occurrence of nonconductive petroleum in the pore space of the mature source rock, which makes it abnormally resistive, or on the overpressure that tends to be created by actively generating source rocks, which causes abnormally long sonic transit times. Source rocks have also been known to be abnormally radioactive compared to surrounding nonsource shales, and may therefore be detected on gamma ray logs. The Kimmeridgian "hot" shale of the North Sea is an example. There are numerous pitfalls, however, in the identification of source rocks on wireline logs, and potential source horizons should always be confirmed where possible by correlation with geochemical indicators.

Before outlining some routine geochemical and visual microscopic measurements on source rocks, it is necessary to understand the nature of the petroleum-bearing matter contained in source rocks, and the nature of petroleum itself. We have seen that petroleum is derived mainly from lipid-rich organic material buried in sediments. Most of this organic matter is in a form known as *kerogen*. *Kerogen* is that part of the organic matter in a rock that is insoluble in common organic solvents. It owes its insolubility to its large molecular size. Different types of kerogen can be identified, each with different concentrations of the five primary elements, carbon, hydrogen, oxygen, nitrogen and sulfur, and each with a different potential for generating petroleum.

The organic content of a rock that is extractable with organic solvents is known as *bitumen*. It normally forms a small proportion of the total organic carbon in a rock. Bitumen forms largely as a result of the breaking of chemical bonds in kerogen as temperature rises.

Petroleum is the organic substance recovered from wells and found in natural seepages. Bitumen becomes petroleum at some point during migration. Important chemical differences often exist between source rock extracts (bitumen) and crude oils (petroleum).

Crude oil is naturally occurring petroleum in a liquid form. The term black oil is sometimes used to indicate petroleum that is liquid at both reservoir and surface temperatures and pressures.

Natural gas is petroleum occurring in the gaseous phase. *Wet gas* is differentiated from *dry gas* in that it yields significant volumes of liquid (*condensate*) on changing from reservoir to surface conditions. When the condensate yield is potentially high, the fluid is called a *gas condensate*.

Under conditions of very low temperature and high pressure, *gas hydrates* may form. These are solid crystalline structures, usually containing methane. Methane hydrates may be found in arctic permafrost regions but also under the deep seafloor even in tropical latitudes.

Natural gas resulting from the thermal breakdown of kerogen is known as *thermogenic*. *Biogenic gas*, however, is a natural gas formed solely as a result of bacterial activity in the early stages of diagenesis (<60–70 °C). It normally occurs at shallow depths, and is always very dry.

TOTAL ORGANIC CARBON (TOC)

TOC is a measure of the carbon present in a rock in the form of both kerogen and bitumen. Typical values of TOC for different lithologies are shown in Table 10.3.

Shales tend to be more rich in organic matter than carbonates. TOC values in source rocks may be quite low, and are frequently <2%. Coals, however, may have TOCs of over 50%. 0.5% TOC is frequently taken as the minimum organic content for a shale source rock; a slightly lower value applies for carbonates. Below 0.5% TOC, not enough petroleum can possibly be generated to saturate the source rock; saturation must take place before expulsion can occur. Rocks with greater than 0.5% TOC are not, however, guaranteed as source rocks. If the organic carbon is inert, no amount of it will form a source rock.

Amount of soluble extract (bitumen)

The soluble extract of source rocks reflects oil content, and hence varies strongly with maturity. Figure 10.17 shows its variation with maturity for source rocks in four different basins; in each case it is strongly correlated with the onset of oil generation.

Rock pyrolysis

Espitalié developed a standard procedure for the pyrolysis of rock samples, known as Rock-Eval pyrolysis. About 100 mg of finely ground rock sample is placed into a furnace at 250 °C in an inert atmosphere and then raised to a temperature of 550 °C. The amount of hydrocarbon products evolved is recorded by a flame ionization detector (FID) as a function of time. Three peaks are typically recorded, known as the S_1, S_2, and S_3 peaks (Fig. 10.18). The S_1 peak represents hydrocarbons evolved at low temperatures – these represent free or adsorbed hydrocarbons (bitumen) that were already present in the rock before pyrolysis. The S_2 peak is produced at higher temperatures by the thermal breakdown of kerogen. Oxygen-bearing volatile compounds (carbon dioxide and water) are passed to a separate (thermal conductivity) detector, which produces an S_3 response. S_1, S_2, and S_3 are expressed as milligrams per gram of original rock ($mg\,g^{-1}$) or kilograms per tonne ($kg\,t^{-1}$).

Table 10.3 Average values of hydrocarbons, nonhydrocarbon bitumen, and organic carbon in ancient nonreservoir sediments (from Tissot and Welte 1978).

Origin	Type of rock	Number of samples	Extractable bitumen (ppm) HC	Extractable bitumen (ppm) non HC	Organic carbon (%)	Average HC Ave. org. C ($mg\,g^{-1}$)	Author
200 formations from 60 sedimentary basins	shales	791	300	600	1.65	18	Hunt (1961)
	carbonates	281	340	400	0.18	151	Hunt (1961)
Rocks of various origins	shales	very large	180		0.9	20	Vassoevich et al. (1967)
	silts		90		0.45	20	Vassoevich et al. (1967)
	carbonates		100		0.2	50	Vassoevich et al. (1967)
Source rocks from 18 sedimentary basins	all types	668	860	780	1.82	47	Institut Francais du Pétrole (unpublished)
	shales and silts	418	930	810	2.16	43	
	calcareous shales	97	1260	1220	1.90	66	
	carbonates	118	335	440	0.67	50	
9 source rocks	not specified	not specified	267–2360		0.53–3.67	34–101	Philippi (1965)

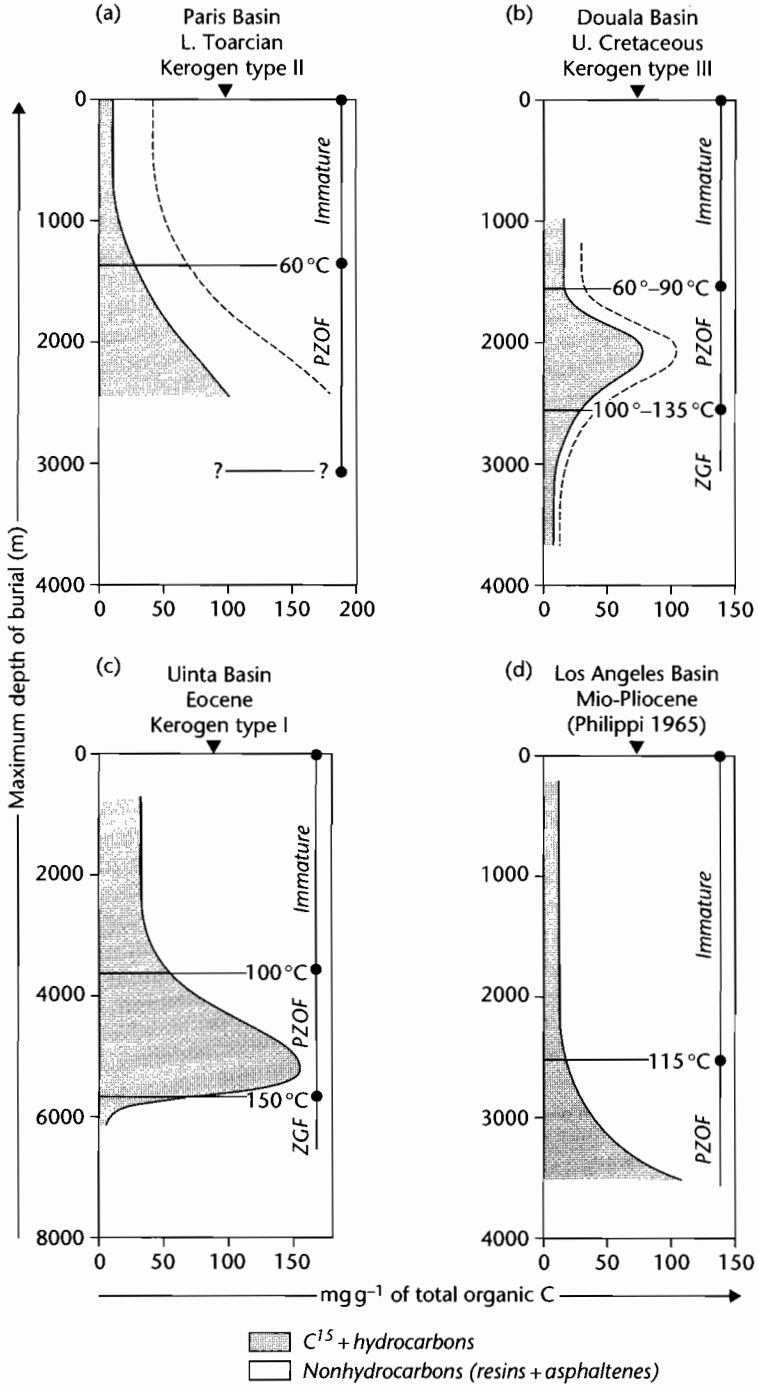

Fig. 10.17 Formation of hydrocarbons and nonhydrocarbons (resins and asphaltenes containing N, S, O) as a function of burial depth in different basins. For each basin, the temperatures that mark the upper and lower limits of the main oil generation zone (PZOF) are marked. Bitumen content clearly rises as the oil generation zone is entered, and diminishes as the underlying gas zone (ZGF) is approached. Bitumen content represents the oil content that can be dissolved from a rock, and this shows a strong correlation with its thermal maturity.

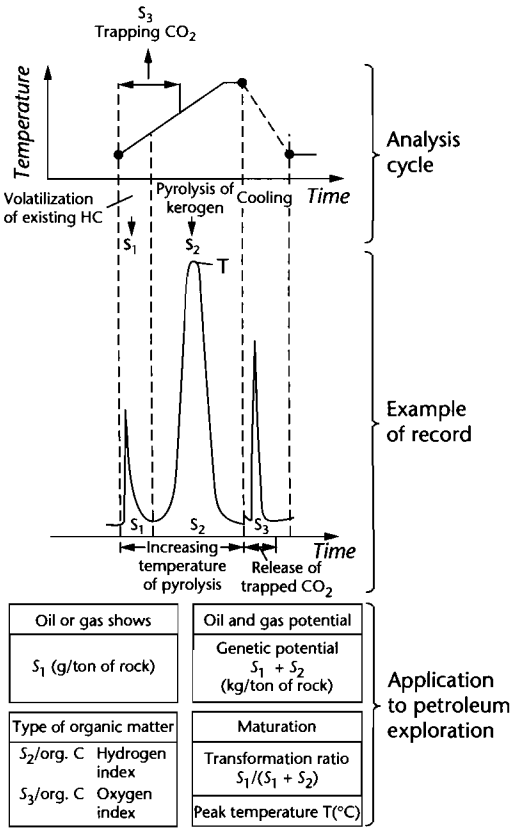

Fig. 10.18 Cycle of analysis and example of record obtained by the pyrolysis method of Espitalié et al. (1977) (after Tissot and Welte 1978). Three peaks are normally observed. The S_1 peak represents already existing bitumen. S_2 represents hydrocarbons generated from the thermal breakdown of kerogen. The S_3 response is produced by oxygen-bearing compounds released at high temperature. S_1 and S_2 can be used to assess oil-generating potential, whereas S_2 and S_3 can be used to calculate *hydrogen index* and *oxygen index*, which indicate kerogen type. The temperature corresponding to the S_2 peak, and the $S_1/(S_1+S_2)$ ratio indicate the level of thermal maturation.

The temperature at which the S_2 generation peak occurs is also recorded, and is an indicator of source maturity.

Rocks with (S_1+S_2) values of less than $2\,kg\,t^{-1}$ are considered as insignificant source rocks. Between $2\,kg\,t^{-1}$ and $5\,kg\,t^{-1}$ a significant amount of petroleum may be generated in the source rock but it may be too small to result in expulsion. If the source rock is raised to higher maturity, generated oil may be cracked to gas and expelled in the gas phase. Source rocks with values of $5–10\,kg\,t^{-1}$ have the potential to expel a proportion of their generated oil. Source rocks with greater than $10\,kg\,t^{-1}$ are considered rich; oil generated will almost certainly be in sufficient quantities to ensure expulsion. Exceptionally, yields of several hundred $kg\,t^{-1}$ are measured; these are usually from coals or oil shales.

The type of kerogen in the source rock is indicated by the *hydrogen index*, which combines the S_2 pyrolysis peak with TOC:

$$\text{Hydrogen index} = \frac{S_2}{TOC} \times 100 \text{ mg g}^{-1}\,^{\circ}\text{C}^{-1} \qquad (10.1)$$

It expresses the "usable" or pyrolysable fraction of the organic content. What is left is inert carbon, which is incapable of sourcing petroleum.

Hydrogen indices of <50 imply that the kerogen is made up predominantly of inert kerogen. Values of >200 suggest the presence of significant amounts of hydrogen-rich (oil-prone) kerogen. The hydrogen index may be as high as 900 in strongly oil-prone oil shales. The ratio of S_3 to TOC is known as the *oxygen index*. Tissot and Welte (1978) cross-plot hydrogen index and oxygen index in order to classify source rocks into three types, I, II, and III (Fig. 10.19), each of which has different petroleum generating characteristics.

Gas chromatography

Gas chromatography is a technique that separates the individual petroleum compounds in a petroleum mixture, according to increasing carbon number (Fig. 10.20). Gas chromatography can be performed on the products from pyrolysis (pyrolysates), on soluble extracts or on crude oil samples. From pyrolysis gas chromatography (PGC), the broadest application is in estimating the oil versus gas proneness of the kerogen. This can be determined by dividing the pyrolysate into gas (C_1–C_5) and liquid (C_{6+}) fractions. At a greater level of refinement, the gas chromatogram determines the detailed composition of the fluid for use in rock–rock, rock–oil, and oil–oil correlations.

Visual kerogen descriptions

The size, shape, structure, and color of kerogen fragments, once isolated from the rock, can be microscopically examined in *transmitted light*. Kerogen containing weakly translucent to opaque, structured fragments

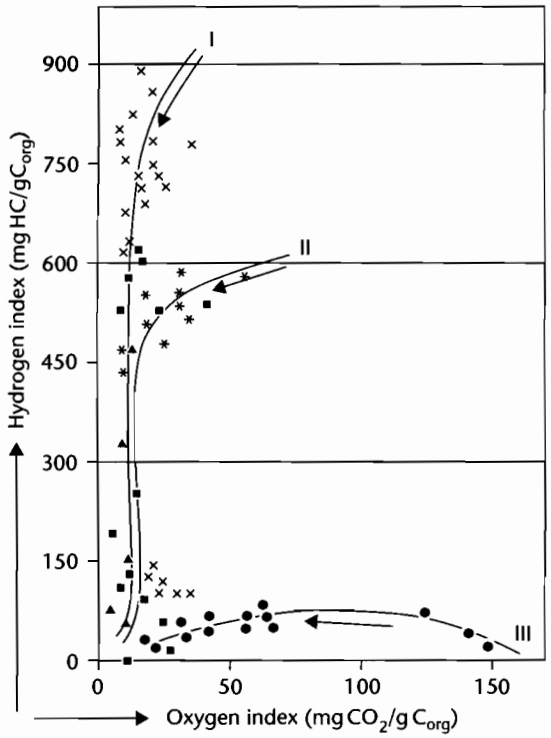

Fig. 10.19 Classification of kerogen types using hydrogen and oxygen indices. The diagram is readily comparable with the van Krevelen diagram plotted from elemental analyses of kerogen (Espitalié et al. 1977). Each kerogen type has different hydrocarbon-generating characteristics. Type I is the most oil prone whereas Type III produces mostly gas (after Tissot and Welte 1978).

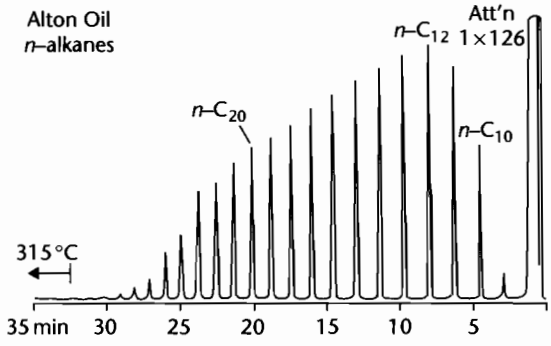

Fig. 10.20 Gas chromatogram of *n*-alkanes of an Australian crude oil. Each *n*-alkane compound in the oil is identified by a peak in the gas chromatogram.

recognizable as higher plants is sometimes referred to as *humic*, whereas translucent amorphous kerogen is called *sapropelic*. Translucent algae, spores, cuticles, pollen, and resin bodies may also be recognized on the basis of internal structure, shape, and color. The color of spores, pollen, and other microfossils has been found to be broadly related to thermal maturity: spore color changes from yellow, through orange to brown, and eventually black, as thermal maturity increases. Humic kerogen was formerly equated with gas-prone source rocks, and sapropelic kerogen with oil-prone source rocks, but this correlation is now known to be exceedingly unreliable. Certainly, not all sapropelic material is oil-prone.

Examination of kerogen particles in *reflected light* allows the definition of three major groups. In order of increasing reflectance, these are the *exinite* group, the *vitrinite* group and the *inertinite* group (§10.3.1.1). Figure 10.21 shows reflectance measurements on the organic particles in a mid-Liassic shale, illustrating the differing reflectances of the three main maceral groups.

The *fluorescence* of organic particles under ultraviolet light allows the identification of the liptinite group, which fluoresce strongly. The vitrinite and inertinite groups do not usually fluoresce.

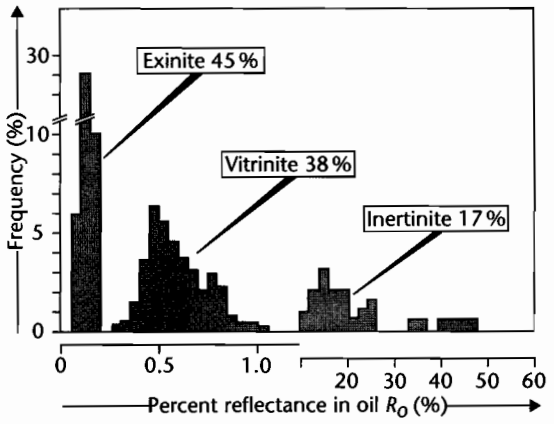

Fig. 10.21 Histograms showing reflectance measurements on different groups of kerogen particles. The exinite, vitrinite, and inertinite groups each have different ranges of reflectance. The reflectance of vitrinite is used as an index of thermal maturity (Ch. 9). Middle Liassic shale, Luxembourg, modified by Tissot and Welte (1978) from Hagemann (1974).

VITRINITE REFLECTANCE MEASUREMENTS

Vitrinite reflectance (§9.7.2) is the most widely used indicator of source rock maturity. Values measured on the different vitrinite particles present in a sample tend to vary widely (Fig. 10.21). To ensure reliable results, a reasonably large number of determinations (e.g., 20) need to be carried out on the same sample, and the mean calculated. Where a distribution of vitrinite reflectances is strongly bimodal, reworking of the higher reflectance group has probably taken place.

The vitrinite reflectance scale has been calibrated by other maturity parameters (§9.7.2) and by field studies in oil and gas provinces, so that R_o can be correlated with the main zones and thresholds of petroleum generation as follows:

$R_o < 0.55$	Immature
$0.55 < R_o < 0.80$	Oil and gas generation
$0.80 < R_o < 1.0$	Cracking of oil to gas (gas condensate zone)
$1.0 < R_o < 2.5$	Dry gas generation

Vitrinite reflectance is a very good maturity indicator above about 0.7 or 0.8% R_o. An important use of vitrinite reflectance measurements in basin analysis is in calibrating thermal and burial history models with present-day maturity data (§9.7.2, §9.8.1).

10.3.2 The petroleum charge

Summary

A petroleum charge occurs when petroleum is generated in a source rock, is expelled, and migrates through a carrier bed to a trap.

Petroleum is chemically a mixture of saturated and aromatic hydrocarbons and NSO (nitrogen-sulfur-oxygen) compounds. A wide range of geochemical analyzes can be carried out on petroleum and source rock extracts that aim to relate the petroleum back to its original source rock and depositional environment. Important physical properties of petroleum are its density, formation volume factors, and boiling points; these influence secondary migration processes, subsurface volume changes, and phase behavior.

Petroleum generation takes place as a result of the chemical breakdown of kerogen with rising temperature. As hydrocarbons are released, the remaining kerogen evolves towards a carbon residue. Temperature and time are the most important factors affecting the breakdown of kerogen. The rate of breakdown can be calculated from the Arrhenius equation given in §9.5. The reactive fraction of kerogen can be subdivided into a labile portion, which yields chiefly oil, and a refractory portion, which yields mainly gas. Labile kerogen breaks down over approximately the 100–150 °C range, followed by refractory kerogen from 150–220 °C. Over the 150 to 180 °C range, oil is rapidly cracked to gas. Thus a stage of oil generation is succeeded by a stage of wet gas/gas-condensate generation, and finally by a stage of dry gas generation.

Petroleum expulsion is probably caused by microfracturing of the source rock after overpressure has built up as a result of hydrocarbon generation. Lean source rocks may not generate sufficient oil to cause expulsion. If raised to higher maturity, generated oil may be cracked to gas that will be efficiently expelled. For rich source rocks (>5 kg t^{-1}) efficiency of oil expulsion may be quite high (60–90%).

Secondary migration carries petroleum from the site of expulsion through porous and permeable carrier beds to sites of accumulation (traps) or seepage. The main driving force behind secondary migration is buoyancy, caused by the density difference between oil (or gas) and formation pore waters. The main restricting force is capillary pressure, which increases as pore sizes become smaller. During secondary migration, petroleum flows as slugs through the interconnected network of largest pores in the carrier bed, rather than sweeping its whole volume. Movement is stopped when a smaller pore system is encountered whose capillary pressure exceeds the upward-directed buoyancy of the petroleum column. This pore system constitutes a seal. The maximum petroleum column height that can be supported by a seal can be calculated.

Petroleum will tend to move in the true dip direction of the top of the carrier bed. Thus structural contour maps can be used to model migration pathways. During long distance migration, for example in some foreland basins, petroleum flow may be strongly focused along regional highs. Losses of petroleum during secondary migration are difficult to quantify.

Petroleum may be physically and chemically altered while it is in the trap by the processes of biodegradation, water-washing, deasphalting, and thermal alteration.

10.3.2.1 Some chemical and physical properties of petroleum

In order to understand petroleum generation, expulsion and migration, and the chemical changes that may take

place in the trap, we need to know a little more about the chemical and physical properties of petroleum. Tissot and Welte (1978), Hunt (1979), and Kinghorn (1983) provide further details.

Hydrocarbons are compounds made up solely of hydrogen and carbon. Petroleum is usually a mixture of hydrocarbon compounds and other compounds containing additional substantial amounts of nitrogen, sulfur and oxygen, and other minor elements. There are three main groups of compounds found in petroleum (Fig. 10.22, Table 10.4):

- *Saturated hydrocarbons* are compounds in which each carbon atom is completely saturated with respect to hydrogen. Structures include simple straight chains of

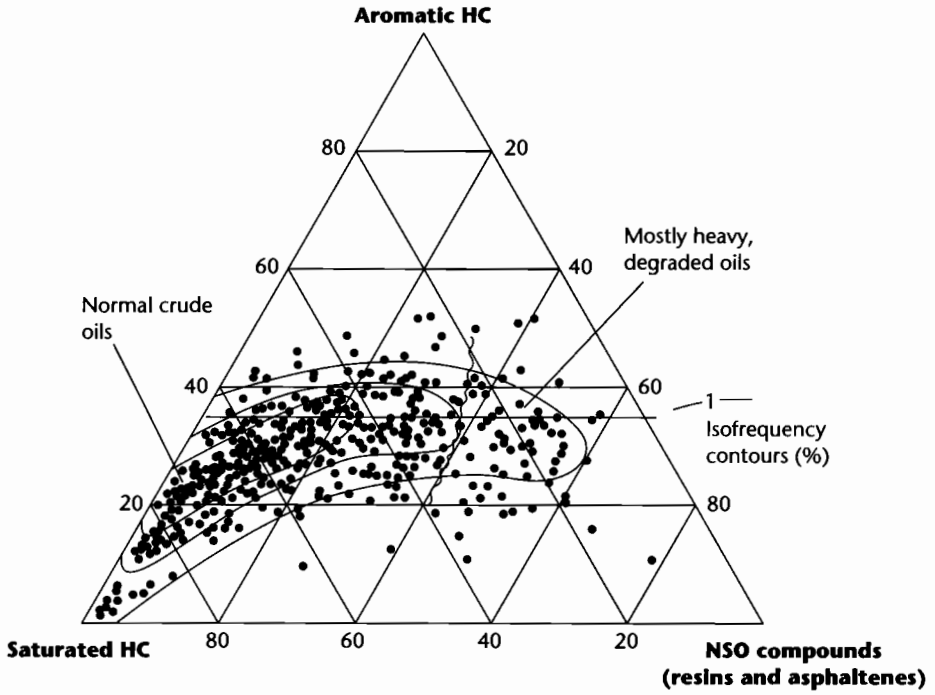

Fig. 10.22 Gross composition of 636 crude oils (from Tissot and Welte 1978) in terms of the three main groups of compounds found in petroleum – saturates, aromatics and NSO compounds. Normal (nondegraded) crudes typically contain 60–80% saturates, and less than 20% NSO compounds.

Table 10.4 Average composition of hydrocarbons (weight %) for a large number of crude oils (number of samples in brackets) (Tissot and Welte 1978, p. 342).

	Normal producible crude oils (517)	All crude oils including tars (141)	Disseminated bitumen (668)
n + iso-alkanes	33.3	31.7	27.7
Cyclo-alkanes	31.9	32.1	29.3
Aromatics	34.5	36.2	43.0
Saturated/aromatics	2.8	2.7	1.8
Alkanes/saturated	0.49	0.48	0.47

carbon atoms (the normal paraffins or normal alkanes), branched chains (the isoalkanes), and rings (cyclic hydrocarbons). Methane and ethane are examples of simple normal alkanes, and are commonly referred to as C_1 and C_2. For all normal alkanes, the subscript after the C refers to the number of carbon atoms in the molecule;

- *aromatic hydrocarbons* are a group of unsaturated hydrocarbons with cyclic structures, and include several important biomarker compounds that allow oils and source rocks to be correlated;
- *NSO compounds (resins and asphaltenes)* contain atoms other than carbon and hydrogen, predominantly nitrogen (N), sulfur (S), and oxygen (O). They are known as heterocompounds and are subdivided into the *resins* and the *asphaltenes*.

The composition of source rock bitumens tends to be different from crude oils – they contain fewer aromatic and saturated hydrocarbons and more resins and asphaltenes. These differences are probably due to important chemical changes that take place during migration.

Biomarkers are compounds found in crude oils and source rock extracts that can be unmistakably traced back to living organisms (Mackenzie 1984). The nature of the biological input to a sediment, and the chemistry of the depositional environment, give source rock extracts and expelled oils a characteristic "fingerprint," which is superimposed by the effects of diagenesis and maturation. These fingerprints may be geochemically recognized. Biomarker compounds may be used to assess thermal maturity (at low levels), and to correlate oils with source rock extracts.

Carbon isotope ($\delta^{13}C$) values (Fig. 10.23) of crude oils and source rock extracts may be used to distinguish marine from freshwater/terrestrial sources, and biogenic from thermogenic gases.

Crude oils may be classified to enable specific oil types to be directly related back to their source rocks. Such classification schemes use parameters such as oil density,

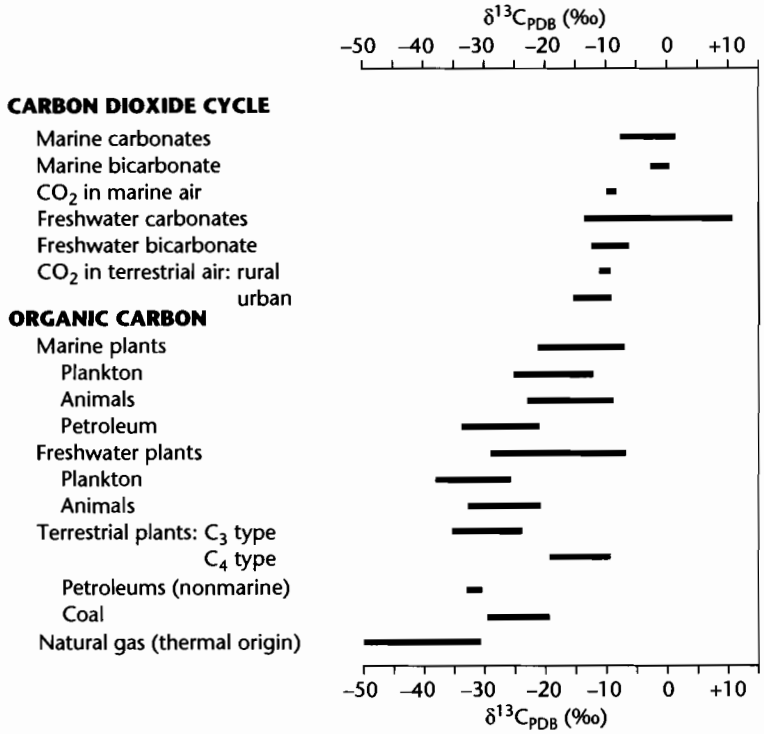

Fig. 10.23 Ranges of $\delta^{13}C$ values for various sources of organic and inorganic carbon *versus* PDB standard (after Waples 1981). Carbon isotope values can be used to distinguish marine from freshwater/terrestrial sources, and biogenic from thermogenic gas.

sulfur content, metals content, wax content, carbon isotope value, and pristane/phytane ratio. High sulfur contents (>1%) indicate marine sources, high wax content indicates land plant or freshwater algae sources, and high pristane/phytane ratios (>3) indicate land plant material as the source.

Oil density is normally quoted as an API (American Petroleum Institute) gravity

$$°API = \frac{141.5}{SG_{60}} - 131.5 \tag{10.2}$$

where SG_{60} is the specific gravity at 60 °F (15.6 °C). From equation (10.2), a fluid with a specific gravity of 1.0 has an API gravity of 10°. *Heavy oils* are those with API gravities of less than 20 (SG_{60}>0.93). These oils have frequently suffered chemical alteration as a result of microbial attack (biodegradation) and other effects. Not only are heavy oils less valuable commercially, but they are considerably more difficult to extract. API gravities of 20–40° (SG_{60} 0.83–0.93) indicate *normal oils*. Oils of API gravity >40° (SG_{60}<0.83) are *light*.

At surface conditions, normal oils are clearly less dense than water (SG<1). However, under subsurface conditions, this density difference is much greater. Oil has a great capacity to contain dissolved gas at elevated temperatures. As a result, subsurface oil densities are typically in the 0.5–0.9 g cm^{-3} range. Subsurface pore water densities, in contrast, are typically 1.0–1.2 g cm^{-3}, and largely dependent on salinity. This density difference is the main driving force behind the secondary migration of petroleum.

Gas densities vary markedly between surface and subsurface conditions. At atmospheric pressure, the density of methane (C_1) is only 0.0003 g cm^{-3}, but at subsurface pressures of 5000 psi (1 MPa = 10 bars = 145 lb in^{-2} (psi)), equivalent to depths of 3–4 km, typical natural gas mixtures have densities of approximately 0.2–0.4 g cm^{-3}. In the subsurface, therefore, oils and gases take on more similar physical properties. Methane is the lightest of the hydrocarbon gases, and is normally the most abundant. Dry gases typically have methane concentrations of over 95%.

Formation volume factors relate the subsurface volumes of oil or gas to the volumes occupied at surface under standard conditions of temperature and pressure (60 °F and 14.7 psi). These factors must be estimated in order to calculate the potential recoverable reserves of an exploration prospect. Gas expands enormously on release of subsurface pressure, and may occupy several hundred times its subsurface volume at surface. The relationship between subsurface and surface volumes is given by

$$\text{Gas expansion factor} = \frac{P_r T_s Z}{T_r P_s} \tag{10.3}$$

where P_r and P_s are the pressures at reservoir (subsurface) and standard (surface) conditions respectively (psi), T_r and T_s are the temperatures at reservoir and standard conditions respectively (°Rankine = °F + 460) (the Rankine scale begins at absolute zero but has units equal to the Fahrenheit scale), and Z is termed the *gas deviation factor* (frequently close to 1.0).

Oil shrinks on movement to the surface, owing to the release of dissolved gas. Oil shrinkage factors vary from nearly 1.0 for shallow oils with almost no dissolved gas, to 2.0 or more for extremely gassy oil in deep reservoirs.

The boiling point of a petroleum compound is the temperature above which it is in a vapor state. At temperatures below its boiling point, the compound is in a liquid state. C_1 (methane) to C_4 (butane) are the only hydrocarbon compounds that are gases (vapors) at surface temperature and pressure. The other compounds are liquids.

Phase changes may take place in the subsurface during the processes of hydrocarbon generation, migration, and entrapment. These may be important in prospect and play assessment. Liquids may condense out of a petroleum vapor as it migrates through a carrier bed into areas of lower pressure. These valuable liquids may be lost as a residual oil saturation in the pores of the carrier bed. If an oil accumulation is uplifted as a result of, for example, inversion tectonics or thrust tectonics, large quantities of gas may be exsolved from the oil. This may cause displacement of oil from the trap.

10.3.2.2 Petroleum generation

CHEMICAL CHANGES TO KEROGEN DURING SOURCE ROCK MATURATION

At shallow depths of burial of only a few hundred meters kerogen remains relatively stable. At greater depths of burial, however, under conditions of higher temperature and pressure, it becomes unstable and rearrangements take place in its structure in order to maintain thermodynamic equilibrium. Structures that prevent the parallel arrangement of cyclic nuclei are progressively eliminated. By this process, a wide range of compounds are generated (heteroatomic compounds, hydrocarbons, carbon dioxide, water, hydrogen sulfide, etc.), as the

kerogen evolves towards a highly ordered graphite structure. Petroleum generation is, therefore, a natural consequence of the adjustment of kerogen to conditions of increased temperature and pressure.

Kerogen is a complex macromolecule composed of nuclei linked by heteroatomic bonds or carbon chains that are successively broken as temperature increases. As breakdown occurs, the first products released are heavy heteroatomic compounds, carbon dioxide, and water. These are followed by progressively smaller molecules, including hydrocarbons. The kerogen left behind becomes progressively more aromatic and evolves towards a carbon residue.

Mackenzie and Quigley (1988) classify kerogen into *reactive kerogen* and *inert kerogen* (Fig. 10.24). Reactive kerogen is transformed into petroleum at elevated temperatures, whereas inert kerogen rearranges towards graphite-like structures without the generation of petroleum. Reactive kerogen is subdivided into a labile portion which is transformed into petroleum that is chiefly oil at surface, and a refractory portion that generates chiefly gas.

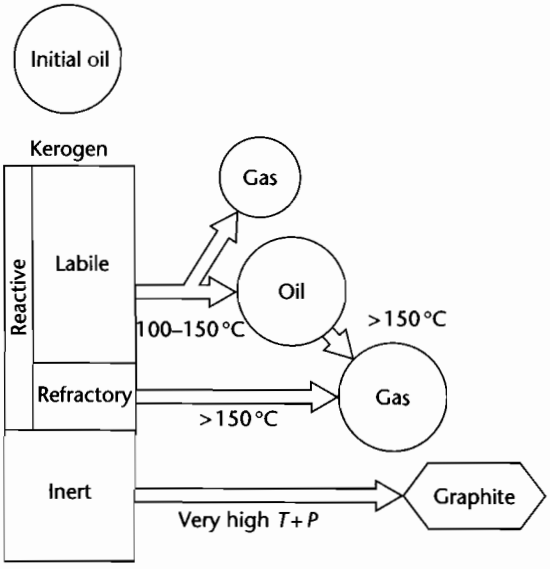

Fig. 10.24 Classification and fate of organic matter in source rocks. Kerogen is divided into reactive and inert portions. Inert kerogen rearranges towards graphite-like structures at very high temperatures (T) and pressures (P) without generating petroleum. Reactive kerogen is subdivided into a refractory part that yields mainly gas, and a labile portion that is transformed into petroleum, which is chiefly oil at the surface. Initial oil corresponds to bitumen normally present in immature source rocks. Relative amounts of initial oil, labile, refractory, and inert kerogen are determined by the nature of the precursory organisms and the depositional setting of the host source rock (after Mackenzie and Quigley 1988).

KINETIC MODELS OF KEROGEN BREAKDOWN

We have seen in §9.5 that temperature and time are the most important factors in controlling the maturation of organic matter. The complex series of consecutive reactions that cause kerogen breakdown proceed at varying rates, governed primarily by temperature and the activation energy of the particular reaction, and expressed in the *Arrhenius equation* (equation 9.40). If the constants in the Arrhenius equation are known for a particular petroleum-forming reaction, the rate at which it will proceed may be determined as a function of temperature, and the temperature range over which the bulk of the reaction will take place (before the raw material is used up) can be calculated. Masses of petroleum generated as a result of kerogen breakdown can also be calculated as a function of temperature, and hence, if the subsidence and thermal history of an area are known, as a function of geological time.

The activation energies of each individual reaction are not exactly known, but for each kerogen type a distribution of activation energies can be established from laboratory and field studies. These distributions, together with the other parameters in the Arrhenius equation, can be used to model kerogen breakdown and the associated generation of petroleum products for each kerogen type.

The kinetic model of Mackenzie and Quigley (1988) shows that kerogen concentrations diminish with increasing temperature for a range of heating rates (Fig. 10.25). Separate sets of curves are shown for labile and refractory kerogen. The heating rate parameter incorporates the time factor in source rock maturation, which is known to be important from the occurrence of generally shallower oil generation thresholds in older basins (Dow 1977). Depending on heating rate, kerogen breakdown into petroleum takes place largely over the 100–150 °C range for labile kerogen. For refractory kerogen, the range is approximately 150–220 °C.

Any oil left in a source rock from the breakdown of labile kerogen will be cracked to gas if temperatures continue to rise above 150 °C, and most cracking reactions take place over the 150–180 °C range (Mackenzie and Quigley 1988). The time required to crack half the

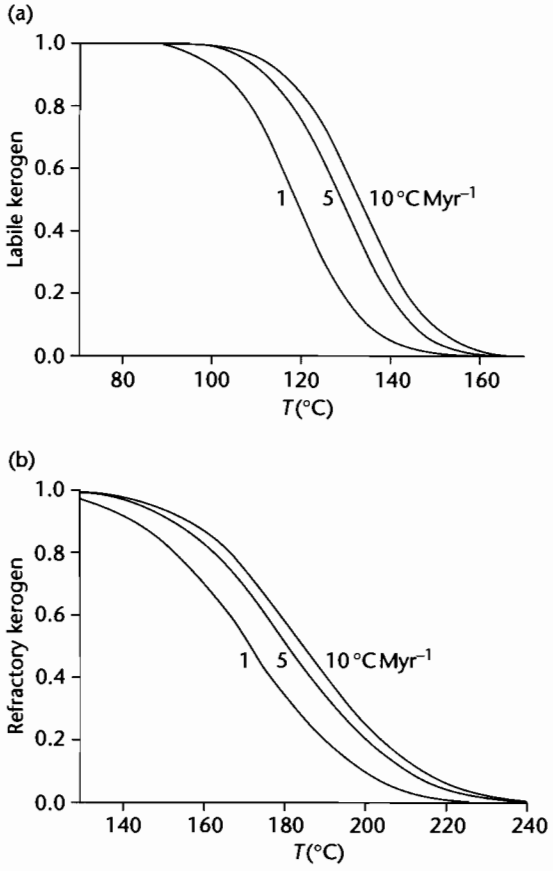

Fig. 10.25 Calculated concentrations of reactive labile (a) and refractory (b) kerogens, relative to initial amount of reactive kerogen, as a function of maximum temperature for the range of heating rates shown. Mean heating rates of about 0.5°C Myr^{-1} occur in old stretched basins. Mean heating rates of about 10°C to 50°C Myr^{-1} occur in young (<25 Myr) stretched basins. Labile kerogen breaks down generally over the 100–150°C range. Refractory kerogen, however, breaks down at much higher temperatures, from about 150–200°C. After Mackenzie and Quigley (1988).

mass of oil to gas (the "half-life" of oil), if held at a constant temperature of 180 °C, is less than a million years. Consequently, at temperatures above 160 °C, oil would not be expected to exist for geological periods of time. The cracking process applies, of course, to oil accumulations as well as to oil remaining in source rocks. As a result, oil fields will not exist at depths greater than those corresponding approximately to the 160 °C isotherm.

The kinetic model predicts that a number of stages of petroleum formation succeed each other without significant overlap (Figs 10.26, 10.27). The immature stage precedes petroleum generation (the *diagenesis stage* of Tissot and Welte 1978). It is followed by a stage of oil and gas generation from labile kerogen containing lipid material (exinitic macerals), and a stage of wet gas/gas condensate generation resulting from the cracking of previously generated oil, together making up the *catagenesis* stage. Finally, there is a stage of dry gas generation from refractory (vitrinitic) kerogen, called the *metagenesis stage*. Methane is the main petroleum product.

Some heavy heteroatomic (NSO) compounds, together with carbon dioxide and water, are generated in the immature (diagenesis) stage of kerogen evolution, but there is effectively no hydrocarbon generation. Hydrocarbons present in rocks of this maturity are inherited from their precursor organisms (biomarkers, or geochemical fossils) and have not been generated from kerogen. During the main zone of oil formation, hydrocarbon compounds (normal and iso-alkanes, cycloalkanes, and aromatics) are generated; the proportions of each depends on kerogen type. As maturity increases, low molecular weight hydrocarbons become most abundant, until only methane is present.

10.3.2.3 Expulsion from the source rock

Mechanics

Expulsion is also known as *primary migration*.

As a result of the compaction of source rocks during burial, pore sizes may become smaller than the size of some petroleum molecules (Fig. 10.28). This presents a difficulty in explaining how petroleum migrates out of the source rock. Of all the possible mechanisms of primary migration debated in the geological literature, the most likely appears to be as a discrete phase through microfractures caused by the release of overpressure. The cause of the overpressure in the source rock may be a combination of oil or gas generation, fluid expansion on temperature increase, compaction of sealed source rock units, or release of water on clay mineral dehydration.

The conversion of kerogen to petroleum results in a significant volume increase. This causes a pore pressure build-up in the source rock. The pressure build-up is sometimes large enough to result in microfracturing. This

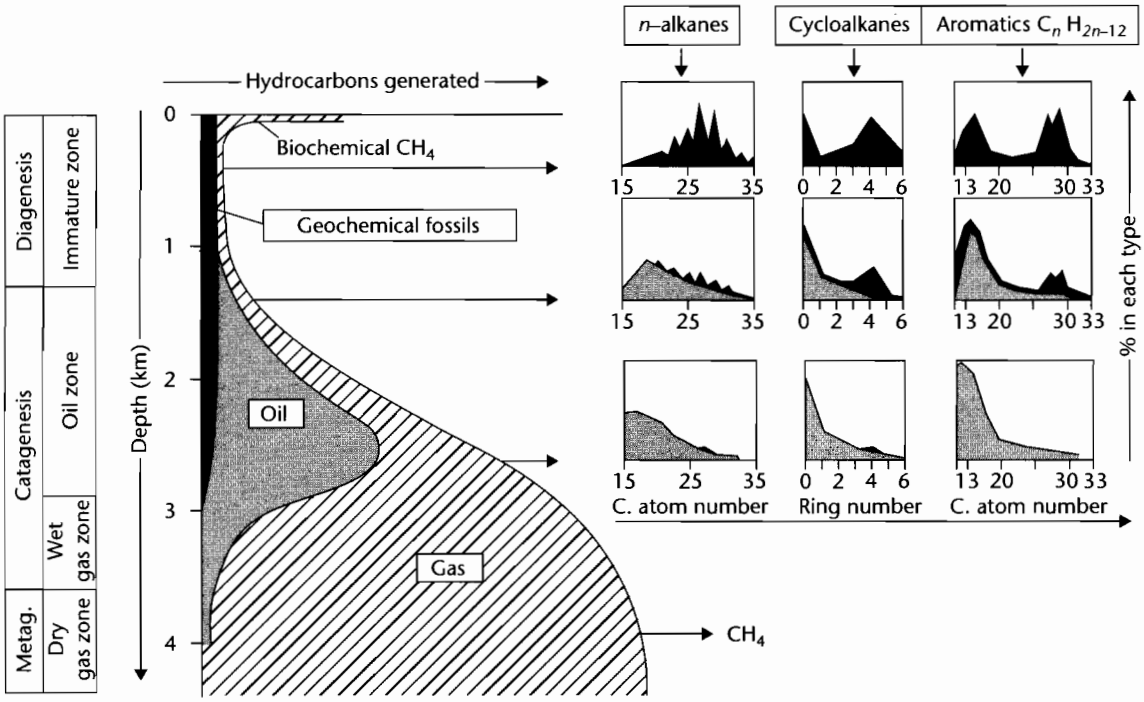

Fig. 10.26 General scheme of hydrocarbon formation as a function of burial of the source rock, according to Tissot and Welte (1978). As formation temperature rises on progressive burial, an immature stage is succeeded by stages of oil generation, oil cracking (wet gas stage), and finally dry gas generation. Typical distributions of *n*-alkanes, cycloalkanes, and aromatics at three points in this general evolution are shown.

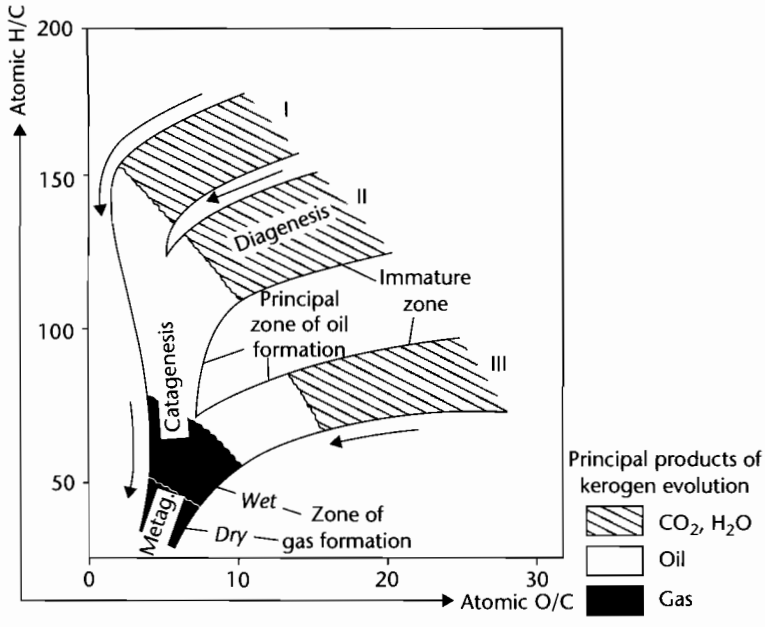

Fig. 10.27 General scheme of kerogen evolution presented on van Krevelen's diagram. The diagenesis, catagenesis, and metagenesis stages are indicated and the principal products generated during that time are shown (after Tissot 1973).

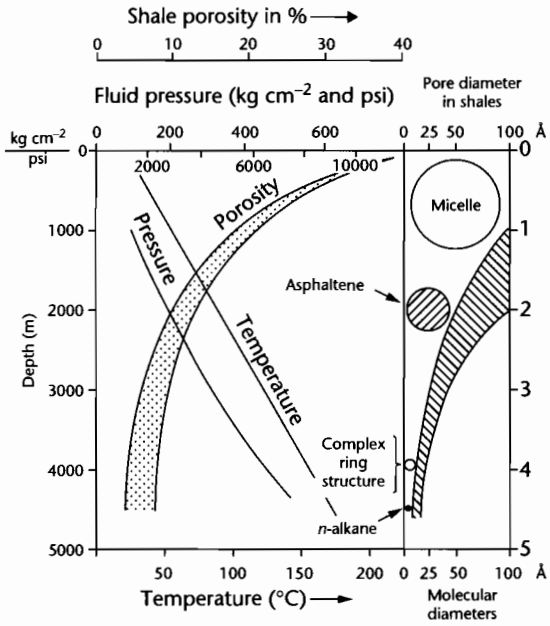

Fig. 10.28 Interrelationship of various physical parameters with increasing depth of burial for shale-type sediments, showing shale pore diameters in relation to the molecular diameters of the petroleum. At moderate depths of burial, shale pore diameters typically become very small in relation to the larger petroleum molecules.

releases pressure, and allows the migration of petroleum out of the source rock and into adjoining carrier beds, from which point secondary migration processes take over. Cycles of petroleum generation, pressure build-up, microfracturing, petroleum migration, and pressure release continue until the source rock is exhausted. The implication of this theory is that mature source rocks will always expel petroleum as long as they are rich enough. In this sense, primary migration is not a major concern for the practicing petroleum geologist. Primary migration clearly takes place both upwards and/or downwards out of the source beds, as governed by local pressure gradients.

A large volume expansion takes place when petroleum liquids are cracked to gas within the source rock. A lean oil-prone source rock may not generate sufficient hydrocarbons to cause microfracturing. As a result, no expulsion will occur. If raised to higher maturity, however, the oil that has remained in the source rock will be cracked to gas. The resulting volume increase and overpressure may allow expulsion to occur. Thus, lean oil-prone source rocks tend to expel gas condensate once they are raised to sufficiently high maturity.

Efficiency of expulsion

How much of the generated (plus initial) petroleum is likely to be expelled from the source rock? Cooles et al. (1986) have shown that, between 120 and 150 °C, petroleum expulsion efficiency is strongly dependent on the original richness of the source rock. In some rich source rocks (potential >5 kg ton^{-1}, TOC > 1.5%) oil expulsion may be very efficient, with 60–90% of the total petroleum generated being expelled. There is a lag, however, between petroleum generation and petroleum expulsion. It appears that a certain minimum petroleum saturation (probably about 4%) in the source rock is required before efficient expulsion takes place. In leaner source rocks (<5 kg ton^{-1}, <1.5% TOC) expulsion efficiency is much lower, and most of the oil generated remains in the source rock. As we have seen, if raised to higher maturity, it may be cracked to gas and expelled. Expulsion appears to be very efficient for gas or gas condensate, irrespective of original source richness.

Mackenzie and Quigley (1988) have classified source rocks into three end-member classes on the basis of initial kerogen concentration and kerogen type (Fig. 10.29). These parameters determine the timing and composition of the petroleum expelled. The *Petroleum Generation Index* (PGI) is the fraction of petroleum-prone organic matter that has been transformed into petroleum, and is thus a measure of source maturity. *Petroleum Expulsion Efficiency* (PEE) is the fraction of petroleum fluids formed in the source rock that has been expelled.

A *Class 1* source rock has predominantly labile kerogen at concentrations of >10 kg ton^{-1}. Generation starts at about 100 °C as the labile kerogen generates an oil-rich fluid. This rapidly saturates the source rock, and between 120 and 150 °C, 60–90% of the petroleum is expelled as oil with dissolved gas. The remaining fluid is cracked to gas at higher temperatures and expelled as a gas phase initially rich in dissolved condensate. Examples of Class 1 source rocks are the North Sea Kimmeridge Clay, and the Bakken Shale of the Williston Basin, Canada–USA.

Class 2 source rocks are a leaner version of Class 1, with initial kerogen concentrations of <5 kg ton^{-1}. Expulsion is very inefficient up to 150 °C because insufficient oil-rich petroleum is generated. Petroleum is expelled mainly as gas condensate formed by cracking above 150 °C, followed by some dry gas.

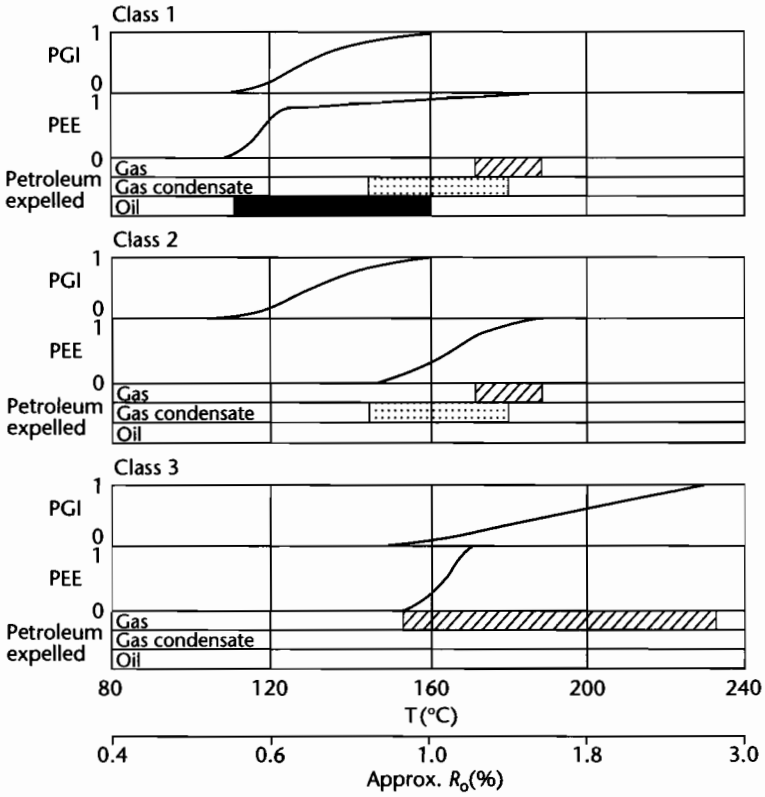

Fig. 10.29 Petroleum Generation Index (PGI) and Petroleum Expulsion Efficiency (PEE) as a function of maximum temperature for three classes of source rock, according to Mackenzie and Quigley (1988). Principal petroleum phases expelled over relevant temperature ranges are shown. Curves were constructed assuming a mean heating rate of 5°C Myr^{-1}. PGI is the fraction of petroleum-prone organic matter that has been transformed into petroleum. PEE is the fraction of petroleum fluids generated in the source rock that have been expelled. Class I are rich source rocks containing mainly labile kerogen. Class II are lean source rocks comprising labile kerogen. Class III source rocks contain mostly refractory kerogen.

Class 3 source rocks contain mostly refractory kerogen. Generation and expulsion takes place only above 150 °C, and the petroleum fluid is a relatively dry gas.

Some formations contain mixtures of different source rock classes.

10.3.2.4 Secondary migration: through carrier bed to trap

Introduction

Secondary migration concentrates subsurface petroleum into specific sites (traps) where it may be commercially extracted. The main difference between primary migration (out of the source rock) and secondary migration (through the carrier bed) is the porosity, permeability, and pore size distribution of the rock through which migration takes place. These parameters are all much higher for carrier beds. As a result, the mechanics of migration may be quite different. The end points of secondary migration are the trap or seepage at surface. If a trap is disrupted at some time in its history, its accumulated petroleum may re-migrate either into other traps, or leak to the surface. The same processes of secondary migration apply to the re-migration as to the original migration into the trap.

A knowledge of the mechanics of secondary migration is important in the general understanding of active

charge systems, but specifically in tracing and predicting migration pathways (hence in defining areas receiving a petroleum charge), in interpreting the significance of subsurface petroleum shows and surface seepages, and in estimating seal capacity in both structural and stratigraphic traps.

The mechanics of secondary migration are now well studied and well understood (Hubbert 1953; Gussow 1954; Berg 1975; Schowalter 1976). In the following section we describe secondary migration in terms of the main driving forces and the main restricting forces. The main driving forces are *buoyancy*, caused by the density difference between oil (or gas) and the pore waters of carrier beds, and *pore pressure gradients*, which attempt to move all pore fluids (both water and petroleum) to areas of lower pressure. The latter is known as a *hydrodynamic* condition. The main restricting force to secondary migration is *capillary pressure*, which increases as pore sizes become smaller. When capillary pressure exceeds the driving forces, entrapment occurs.

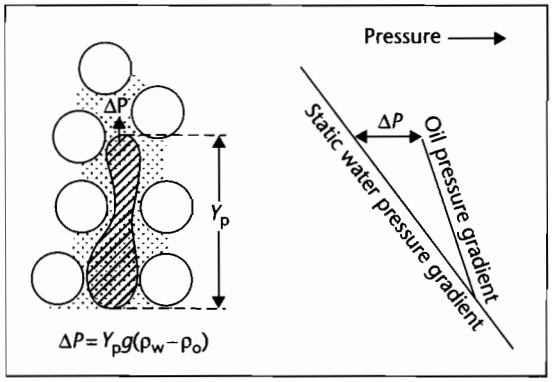

Fig. 10.30 Buoyancy as a driving force in secondary migration. Buoyancy is the pressure difference between a point in the petroleum column and the surrounding pore water. It is a function of the petroleum/water density difference and the height of the petroleum column. A large buoyancy pressure may develop at the tops of large, low-density (gas) petroleum columns. Pressure measurements at points throughout the petroleum column define a petroleum pressure gradient; this intersects the hydrostatic gradient at the petroleum–water contact.

Driving forces in secondary migration

Buoyancy is a vertically directed force caused by the difference in pressure between some point in a continuous petroleum column and the adjacent pore water. It is a function of the density difference between the petroleum and the pore water, and the height of the petroleum column (Fig. 10.30):

$$\Delta P = Y_p g(\rho_w - \rho_p) \tag{10.4}$$

where ΔP is the buoyant force, Y_p is the height of petroleum column, g is acceleration due to gravity, and ρ_w and ρ_p are the subsurface densities of water and petroleum respectively. Under *hydrostatic conditions*, buoyancy is the only driving force in secondary migration. Under *hydrodynamic conditions* (that is, when water flows through a carrier bed), however, the driving force is modified. Hydrodynamics may either assist or inhibit secondary migration, depending on whether it acts with or against the buoyancy force. Hydrodynamics may be important in a number of respects: (i) by affecting the directions and rates of secondary migration, (ii) by increasing or decreasing the driving pressures against vertical or lateral seals, thus reducing or increasing the heights of the petroleum columns that the seals can withstand, and (iii) by tilting petroleum water contacts and displacing petroleum accumulations (for example, off the crests of structural closures).

The effect of hydrodynamics on rates and directions of secondary migration may be safely ignored except in basins where there is good evidence of hydrodynamics operating at the present-day. Without this evidence, it is difficult to support a strong argument for hydrodynamics having operated during secondary migration. Geologically long-lasting hydrodynamic conditions are most likely to have existed in foreland basins (see §9.6.3).

Restricting forces in secondary migration

When a petroleum globule or slug moves through the pores of a rock, work has to be done to distort the globule and squeeze it through the pore throats (Fig. 10.31). The force required is called capillary pressure (or displacement, or injection pressure), and it is a function of the size (radius) of the pore throat, the interfacial surface tension between the water and the petroleum, and the wettability of the petroleum–water–rock system:

$$\text{Displacement pressure} = \frac{2\gamma \cos\Theta}{R} \tag{10.5}$$

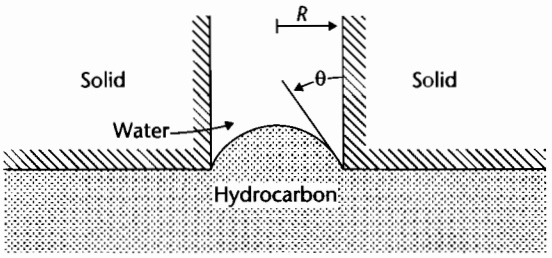

$$p_d = \frac{2\gamma \cos \theta}{R}$$

where p_d = Displacement pressure
γ = Oil–water interfacial tension
θ = Contact angle of oil and water against the solid
R = Radius of the pore throat

As γ increases p_d increases
As θ decreases p_d increases
As R decreases p_d increases

Fig. 10.31 Resistant forces in secondary hydrocarbon migration. Higher pressures are needed to force petroleum globules through smaller pores (after Purcell 1949 in Schowalter 1976).

where γ is the interfacial tension between petroleum and water (dyne cm^{-1}), Θ is the wettability, expressed as the contact angle of the petroleum–water interface against the rock surface (degrees), and R is the radius of the pore (cm). Higher pressures are needed to force petroleum globules through smaller pores.

Interfacial tension depends on the properties of the petroleum and water, and is independent of the rock characteristics. It is a function primarily of the composition of the petroleum (it is smaller for light, low viscosity oils), and temperature (interfacial tension generally decreases with increasing temperature). The effects of pressure and water chemistry are less important. For a given petroleum composition, therefore, interfacial tension may be considered effectively constant over large parts of the migration pathway, unless considerable vertical migration takes place. Gas–water interfacial tensions are in fact generally higher than those for oil–water. This means that, for the same rock, displacement pressures are higher for gas than for oil. The buoyancy pressures, however, are normally greater for gas.

Wettability is a function of the petroleum, water, and rock. Most rock surfaces are "water-wet" and Θ may be taken to be zero. In carrier beds along secondary migration routes, and in lateral and vertical seals to petroleum accumulations, the $\cos\Theta$ term in equation (10.5) can be ignored so that:

$$\text{Displacement pressure} = \frac{2\gamma}{R} \qquad (10.6)$$

Some of the grains of oil-filled reservoir rocks may be oil-wet, and organic-rich source rocks may also be partly oil-wet. Displacement pressures in these cases could, as a result, be considerably smaller than in water-wet rocks. This would assist oil migration.

Pore sizes are the most important control on secondary migration and entrapment. Pore sizes can be estimated visually (in thin section, or by scanning electron microscope, for example) in reservoir/carrier bed lithologies. Ideally, displacement pressure can be measured directly by mercury injection techniques for both reservoir and potential sealing lithologies. The principle of this technique is that a nonwetting fluid (mercury) is injected into a core plug and its saturation as a percentage of pore volume (cumulative volume of mercury injected) is recorded as a function of steadily increasing injection pressure (Fig. 10.32). The pressure at which mercury first begins to saturate the pores of the rock is the displacement pressure. This takes place when the *largest* pores are invaded. Thereafter, at higher pressures, the smaller pores are successively invaded. Mercury injection pressure can be easily converted to petroleum–water displacement pressure.

Once the displacement pressure has been overcome, and a connected petroleum slug is established in the largest pores of the rock, secondary migration may take place. One of the interpretations made from mercury capillary test data is that the petroleum saturation required to produce this connected petroleum slug is surprisingly small. In a series of experiments reported by Schowalter (1976), this critical saturation for a range of rock types varied from 4.5 to 17%, and averaged 10%. Active secondary migration pathways may therefore be characterized by petroleum saturations of only about 10%. Such low saturations provide weak shows that frequently go undetected or are considered of no significance.

Since it is the network of largest pores that controls displacement pressure (and hence secondary migration and seal potential), care should be taken that the rock material analyzed is representative of the carrier bed or potential seal as a whole. If larger pore systems exist in the carrier bed or potential seal than were analyzed in the injection tests, displacement pressures may be seriously overestimated.

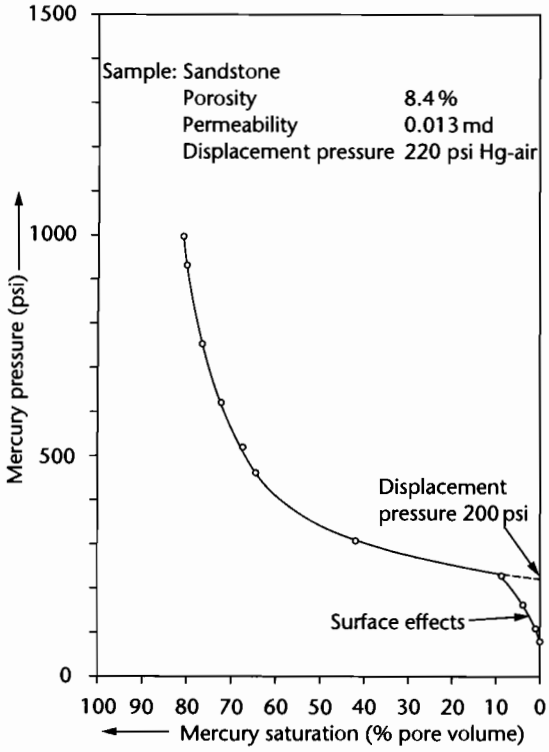

Fig. 10.32 Typical mercury capillary pressure curve. Mercury first begins to saturate the pores of the rock when the largest pores are invaded (the displacement pressure). A relatively small further increase in pressure commonly results in rapid saturation of the pore space and the establishment of a connected petroleum slug that may migrate through the rock. As little as 10% oil saturation may be required before secondary migration takes place (after Schowalter 1976).

So far we have considered only the entry of petroleum into a pore network from an infinite body (Fig. 10.31). Within the pore network of a rock, the pore throat radii at both upper and lower ends of the oil globule need to be considered (Fig. 10.33), and the capillary pressure equation is modified to:

$$\text{Capillary pressure} = 2\gamma\left(\frac{1}{r_t} - \frac{1}{r_b}\right) \qquad (10.7)$$

where r_t is the radius of upper pore throat and r_b is the underlying pore radius.

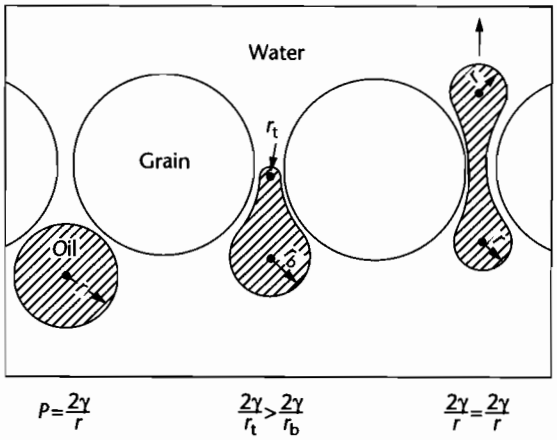

Fig. 10.33 Transport of an oil globule through pore throats in a water-wet subsurface environment. Capillary pressure opposes the buoyant force until the radius of curvature inside the distorted oil globule is equal at its lower and upper ends. The oil globule may then pass through the pore throat. After Berg (1975) in Tissot and Welte (1978).

PETROLEUM COLUMN HEIGHTS AND SEAL POTENTIAL

Once a petroleum slug has entered a pore system of a constant size it will continue to move. Its rate of movement is governed by the driving forces and the permeability of the rock. When a smaller pore system is encountered, the driving forces may not be sufficient to overcome the increased capillary pressure. In this case, movement into the smaller pore network will not take place. The slug will either migrate away laterally (in a dipping carrier bed), using the larger pore system, or remain trapped. If joined by a large number of other petroleum slugs, a sufficient vertical column of petroleum may build up to provide a large, buoyant force that is enough to cause invasion of the finer pore network. Thus, a seal may be effective only up to a *critical petroleum column height*, at which point it leaks.

The critical petroleum column height (Y_{pc}) is given by

$$Y_{pc} = \frac{2\gamma\left(\frac{1}{r_t} - \frac{1}{r_b}\right)}{g(\rho_w - \rho_p)} \qquad (10.8)$$

When the pore size of a sandstone reservoir r_b is very large in relation to the very small pore throat size r_t of a

shale caprock, the $1/r_b$ term becomes relatively very small and equation (10.8) can be simplified to:

$$\gamma_{pc} = \frac{2\gamma}{r_t g(\rho_w - \rho_p)} \tag{10.9}$$

Since the subsurface density of gas is less than that of oil, it is clear that seals can support much larger oil columns than gas columns. This has important implications for migration and entrapment. For example, it may prevent the formation of gas caps overlying oil columns. It also suggests that gas should migrate vertically more successfully than oil.

In order to calculate seal potential, we need to know the pore radius that is relevant to leakage. This should be the smallest pore throat in a network of large pores that, if penetrated, would allow an interconnected petroleum slug to be established. This is clearly not the largest pore throat, nor the smallest, but somewhere in between! It may be approximated by a mean hydraulic radius, r_h, where

$$r_h = 2.8(K/\phi) \tag{10.10}$$

where K is permeability and ϕ is porosity. The difficulty of estimating the critical pore radius of the caprock renders seal capacity calculations subject to wide ranges of error. They may frequently give only order of magnitude estimates.

Faults and fractures

Fault zones can act as both conduits and barriers to secondary migration (Jones et al. 1998). The material crushed by the frictional movement of the fault, the fault gouge, is frequently impermeable and does not allow the passage of petroleum. Clay smeared along fault planes, as in the growth faults of the Niger delta (Weber et al. 1978) and in the Louisiana Gulf Coast region (Smith 1980; Lopez 1990), also blocks petroleum migration. Fractures formed in either the footwall or hangingwall, if they remain open, may form effective vertical migration pathways. This is unlikely except at shallow depths, but may occur in the uplifted hangingwalls of contractional (thrust) faults on release of compressive stresses. Tensional fractures in the crestal zones of anticlinal structures may also allow migration of petroleum. Lateral migration will tend to be inhibited by the presence of faults, since they interrupt the lateral continuity of the carrier bed.

The sealing qualities of fault zones are discussed further in §10.6 on petroleum traps.

Migration pathways

Since the driving force behind secondary migration (in the absence of hydrodynamics) is buoyancy, it is clear that petroleum will tend to move in a homogeneous carrier bed in the direction of steepest slope. This is perpendicular to its structural contours, that is, in the true dip direction. Lines drawn at right angles to the structural contours of the top carrier bed/base seal horizon are known as *orthocontours*. Orthocontour maps illustrate the focusing and de-focusing effects of structural features in prospect drainage areas (Fig. 10.34). When lateral migration is long distance, as for example in foreland basins, where prospects may be remote from areas of mature source rock (source kitchens), these effects may strongly influence the pattern of hydrocarbon charge. It is important in play assessment to recognize those parts of the fairway that are located on petroleum migration routes. A petroleum flow may be split when encountering a low, and concentrated along regional highs. The geometry of the kitchen also affects petroleum charge volumes; prospects located close to the ends of strongly elongate source kitchens will receive relatively little charge.

It is important that orthocontour maps are constructed for the actual time of secondary migration. Present-day structure maps may be used to model present-day migration. Isopaching (or 3-D decompaction, see §9.3) allows the production of paleostructure maps for use in modeling paleomigration routes. For example, an isopach of the base Upper Cretaceous to base Miocene interval will allow the modeling of migration routes in a carrier bed situated at the base of the Upper Cretaceous sequence at the beginning of Miocene time.

Other factors that should also be considered in evaluating migration pathways include the presence of sealing faults, which may deflect petroleum flow laterally, and nonsealing faults, which allow petroleum to flow across the fault plane into juxtaposed permeable units at a different stratigraphic level. From this point a different structure map needs to be used for migration modeling. Communication between carrier beds caused by lateral stratigraphic changes (e.g., by the sanding-out of a shale seal) also needs to be considered. The orthocontour map should be constructed only as far as a seal persists. These factors affect the likelihood of petroleum charge into specific segments of the play fairway, and into specific prospects within them.

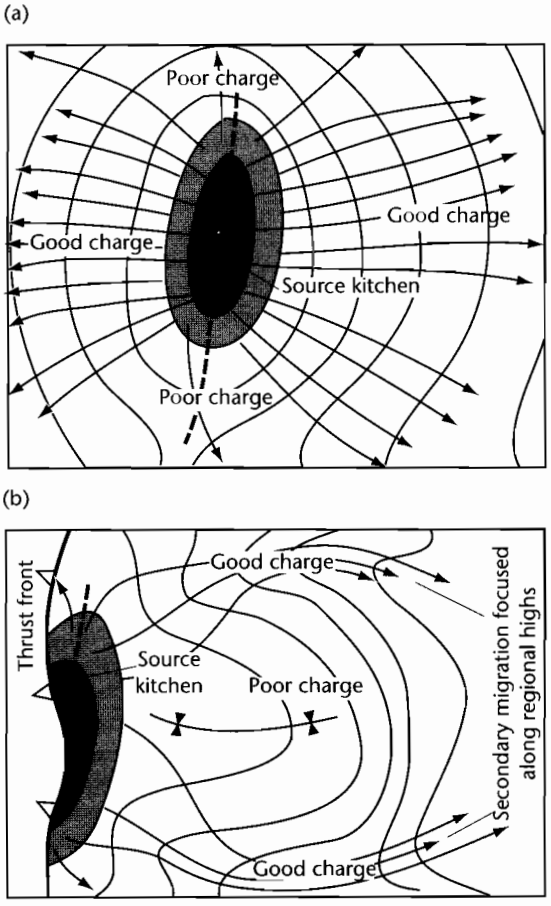

Fig. 10.34 Orthocontours illustrating secondary migration routes. (a) Effect of an elongate kitchen on migration directions. Areas along the long axis of the kitchen may receive a relatively poor charge; (b) Migration is focused along regional highs in the basin drainage area, and may penetrate large distances away from the source kitchens. Some foreland basins show examples of this type of migration.

SECONDARY MIGRATION LOSSES

Volume losses occur along secondary migration pathways. These losses are in two distinct habitats:

- In miniature traps – dead-ends along the migration route – produced by faulted and dip-closed geometries, and by stratigraphic changes. The traps may be observable but of no commercial interest, or they may not be observable at all, for example, if they are below the resolution of the seismic tool;
- as a residual petroleum saturation in the pores of the carrier rock, trapped by capillary forces in dead-end pores and absorbed onto rock surfaces. This may represent up to 30% of the pore volume through which the petroleum migrates (and a greater percentage of the hydrocarbon saturation achieved during active migration), so major losses may occur in this way. Losses are minimized when petroleum flows through a relatively small volume of carrier rock. This is achieved in high permeability strata where migration is rapid and takes place without large petroleum columns building up.

The petroleum volumes expelled, lost and trapped can be related by

$$V_{\text{expelled}} = V_{\text{lost}} + V_{\text{trapped}} \tag{10.11}$$

The aim of play assessment and prospect evaluation is to estimate V_{trapped}. Volumes expelled can be calculated after geochemical source rock evaluation, taking into account source rock richnesses, thicknesses, source rock kitchen sizes and maturities, and expulsion efficiencies. However, at the basin or play scale, volumes lost are almost impossible to quantify. Moreover, they are likely to be very large in relation to volumes trapped. As a result, it is very difficult to estimate the volumes trapped in a play fairway through geochemical source rock volumetrics.

It is conceivable that a prospect may lie beyond the "migration front" of oil generated from a source kitchen. It will not receive a charge, since all of the oil expelled into the carrier bed is lost as a residual saturation (and in small traps) in the carrier bed. In order to determine the position of the migration front, accurate calculations of the volumes of petroleum expelled from the kitchen and the rate of loss in the carrier bed need to be made. The errors involved are huge and it would be most unwise for a prospect lying just beyond the calculated migration front to be severely downgraded for this reason. The calculations may, however, give useful order-of-magnitude estimates that assist risk estimation.

The focusing of oil migration into specific flow routes, which sweep through only a very small volume of carrier rock, is probably a very important contributing factor in enabling huge oil volumes to migrate very large distances (several hundred km) in some foreland basins. These have been previously described in §10.2.2 as petroleum systems with low-impedance entrapment style and a lateral migration style. The heavy oil/asphalt

belts on the gentle flanks of these basins (e.g., western Canada) have formed at enormous distances from their source kitchens.

10.3.2.5 Alteration of petroleum

Trapped petroleum is not in equilibrium with its environment. Changes may take place in the physical and chemical properties of petroleum while it is in the trap. The longer that petroleum sits in the trap, the more likely it is that physical, chemical, and biological processes will significantly alter its original composition. These changes may have an important impact on the recoverable fraction and commercial value of an oil accumulation.

Source rock characteristics are the greatest influence on oil composition prior to trapping. Pressure-volume-temperature (PVT) conditions are the main influence on the original composition of reservoired oil. Secondary alteration processes are considered under the following four main headings.

1 Biodegradation

Biodegradation is the bacterial alteration of crude oils. Bacteria use any dissolved oxygen present in formation pore waters, or derive oxygen from sulfate ions, in order to selectively oxidize hydrocarbons. Firstly, the light normal-alkanes are removed, followed by branched (iso) alkanes, cycloalkanes, and finally the aromatics. The physical effect of biodegradation is to increase the density and viscosity of the oil.

Biodegradation appears to take place only at temperatures of less than 60–70 °C. It also appears to require a supply of meteoric water containing dissolved oxygen and nutrients (primarily nitrates and phosphates). These conditions are frequently met in foreland basins, where meteoric water enters the carrier bed/reservoir system in the bordering uplifted thrust belts. Biodegradation may take place in both the thrust belt and in the gentle foreland flank. An example of the former is the Napo Basin, Ecuador; the Athabaska Tar Sands of Canada are an example of the latter. Biodegradation may also occur at the oil–water contacts of petroleum accumulations, resulting in the formation of tar mats, as in the Burgan field of Kuwait.

2 Water washing

Water washing commonly accompanies biodegradation. Hydrocarbon-undersaturated meteoric waters may dissolve some hydrocarbons from a reservoired petroleum mixture. Light alkanes and low boiling point aromatics (e.g., benzene, toluene, and zylene) are the most soluble and preferentially removed. The net result is a change in composition similar to that caused by biodegradation. Water washing takes place at temperatures greater than 70 °C. The only requirement is a continued flow of meteoric water.

An example of the profound effects of water washing on petroleum volumes and composition is the northern Bonaparte Basin of Australia (Newell 1999). Long columns of residual oil occurring beneath many of the 11 discovered oil fields had been previously attributed to failure of fault seals. However, aspects of the geochemical composition of the very light oils found in this basin, most importantly the almost complete absence of the highly water-soluble light aromatics benzene and toluene, indicate alteration by water washing. Remarkably, in the order of 70% of the original oil volume in the reservoir has been lost by this process. Subsurface pressure data collected during exploration drilling operations indicate a water flow from the northwest, which can probably be explained by the dewatering of sediments overthrusted by a terrane forming the island of Timor during the last 7 Myr.

In assessing the chances of encountering biodegraded or water washed petroleum in a prospect or play, it is necessary to consider the history of fluid movement in the basin since the time of migration through to the present day. Although *present-day* reservoir temperatures may be >70 °C, this is not a guarantee that biodegradation has not taken place. The effects of strong convective meteoric water flow on geothermal gradients must also be taken into account when reconstructing the thermal history of the petroleum.

3 Deasphalting

Deasphalting is a process whereby the precipitation of the heavy asphaltene compounds in a crude oil takes place as a result of the injection of light C_1–C_6 hydrocarbons. This may occur when an oil accumulation experiences a later gas charge as its source kitchen becomes highly mature. It may also occur as a result of oil cracking in the reservoir rock. Deasphalting leads to the formation of light oil and a solid residue rich in asphaltenes. The tar mat in the Norwegian Oseberg field may have been produced by deasphalting processes (Dahl and Speers 1986).

4 THERMAL ALTERATION

The variations in petroleum composition that take place with increasing thermal maturity of the source rock were described in §10.3.2.2. Similar compositional changes take place in a reservoired petroleum with rising temperature. This normally occurs when trapped oil is heated through continued burial. Heavy compounds are replaced by progressively lighter ones, until only methane and a solid residue (pyrobitumen) is present. At high temperatures (>160°C), oil cracking reactions proceed so rapidly that an oil accumulation may be destroyed within a geologically short period of time.

In addition to the four processes described above, oil composition may also be altered as a result of *gravity segregation* and *dysmigration*. Gravity segregation may take place over long periods of time as heavier molecules sink under gravity toward the base of a hydrocarbon column. Leakage through a caprock (dysmigration) may result from faulting or micro-fracturing that alters the PVT conditions in the reservoir. A gas phase may form as a result of the pressure drop, and leak through the fractured caprock, leaving a heavier oil accumulation in place.

It is important when assessing exploration plays to block out parts of the fairway that are considered to be susceptible to the petroleum alteration processes described above.

10.4 THE RESERVOIR

Summary

A petroleum play is defined initially by the depositional or erosional limit of its gross reservoir unit. A reservoir rock must be porous enough to constitute a "tank" of petroleum within the trap, and its pores must be sufficiently interconnected to allow the contained petroleum fluids to flow through the rock towards the well-bore. Thus, the primary considerations in the assessment of reservoir potential are the likely reservoir *porosity* and *permeability*.

Reservoir porosity affects the reserves of a prospect or play. Reservoir permeability affects the rate at which petroleum fluids may be drawn off from the reservoir during production. Both of these parameters have a large impact on the commercial attractiveness of an exploration or field development opportunity. Reservoir rocks may result from deposition in a very wide range of environments. Particularly favorable reservoir rocks occur in specific depositional environments and in specific positions within the stratigraphic architecture. There is a strong depositional control on reservoir quality but also a very strong overprint from diagenetic changes.

The pore systems of carbonate rocks are complex, partly due to the varied biological origin of the carbonate grains, but also because their chemical reactivity makes them susceptible to major changes after deposition. Diagenetic changes, such as dolomitization, fracturing, dissolution and recrystallization and cementation are therefore a key element in the development of carbonate reservoirs. Diagenetic changes in the near-surface zone (eogenesis) can be related to depositional environment, climate, and relative sea level. Some of the most important carbonate reservoirs result from dolomitization of carbonate sediments from brines originating in evaporative marginal marine sabkhas and extensive shelf lagoons. Other carbonate reservoirs have been strongly influenced by meteoric waters flushing through the carbonate sediment at relative sea-level lowstands. Burial diagenesis (mesogenesis) of carbonate rocks is dominated by rock–water interaction and mixing with basin-derived fluids. Dedolomitization is a process causing an improvement in permeability that takes place during mesogenesis.

Sandstone reservoirs have a depositional porosity and permeability controlled by grain size, sorting, and packing of the particulate sediment. Diagenetic changes include the formation of clay minerals in the pore space. The formation of kaolinite, "green clay minerals" and smectites is extremely important in the eogenetic zone. As in carbonate reservoirs, the particular diagenetic products are related to depositional environment, climate and relative sea level. Subaerial exposure of the shelf at lowstands promotes kaolinite cementation, whereas transgression favors "green clay minerals" such as glauconite and berthierine formation. Burial diagenesis causes mineral transformations to dickite, illite, and chlorite as a function of temperature. Uplift and erosion (telogenesis) favors dissolution and kaolinite cementation.

Reservoirs are heterogeneous on a number of scales from the km-scale first-order heterogeneities of stratigraphic packages to the microscopic grain scale. Reservoir heterogeneity is the main concern of the development geologist, and constitutes essential input into numerical simulation models of the flow of fluids through the reservoir.

10.4.1 Porosity and permeability

The pore volume of a sediment can be expressed either as an absolute porosity ϕ_a given by

$$\phi_a = \left(\frac{V_b - V_s}{V_b}\right)100 \tag{10.12}$$

where V_b and V_s are the bulk and solid volumes respectively, or, as an *effective porosity*

$$\phi_e = \left(\frac{V_i}{V_b}\right)100 \tag{10.13}$$

where V_i is the interconnected pore volume. Effective porosity is normally measured in studies of reservoirs. Different rock types possess different pore geometries, carbonate rocks (§10.4.2) being very different to siliciclastic rocks (§10.4.3) in this respect. As described in §9.2.3, porosity can be estimated from a number of downhole wireline logs.

Permeability K or hydraulic conductivity measures the ability of a medium to transmit fluids and is defined according to the Darcy equation which states

$$Q = KA(\mathrm{d}P/\mathrm{d}l) \tag{10.14}$$

where Q is the volume of transmitted flow per unit time (flow rate), A is the cross-sectional area and $\mathrm{d}P/\mathrm{d}l$ is the pressure gradient over distance l, or hydraulic gradient. The value of permeability depends not only on rock properties, but also on the medium being transmitted. The *specific permeability*, k, is defined as

$$Q = \frac{kA\gamma}{\mu}\left(\frac{\mathrm{d}P}{\mathrm{d}l}\right) \tag{10.15}$$

where γ is the specific weight of the fluid and μ is its absolute viscosity.

Permeability can be measured by (i) well testing (measurement of the flow rate of a fluid to the well bore from the reservoir), which provides an average measurement of permeability across a certain reservoir interval, (ii) downhole wireline logs (reviewed by Ahmed et al. 1991), and (iii) core analysis (sidewall cores, core plugs, and whole core) which allows direct measurement of porosity and permeability under controlled laboratory conditions.

The porosity and permeability therefore describe the "plumbing" of the reservoir. Porosity and permeability are not, however, simply or directly related. Complex pore geometries may present highly tortuous paths for transmitted fluids with many dead-ends. This will lower permeability while porosity may be largely unaffected. Similarly, particular pore-filling mineral habits may have different effects on porosity and permeability.

10.4.2 Carbonate reservoirs

Carbonate rocks are particularly amenable to the study of the relationship between pore geometry and permeability (e.g., Jardine and Wilshart 1987). Carbonate reservoirs are characterized by extremely heterogeneous porosity and permeability on a number of scales. The main reasons for such heterogeneity are the biological origin of the carbonate grains and their strong chemical reactivity. The types of heterogeneity are therefore dependent on the original grain types and, most importantly, on the subsequent diagenetic alteration of the sedimentary fabric.

Carbonate porosity classification

A number of carbonate porosity classifications have been suggested (see Moore 2001 for review). Choquette and Pray (1970) presented a genetic classification that emphasized the importance of depositional and diagenetic fabrics in controlling pore systems (Fig. 10.35a). If porosity is determined by fabric elements, it is said to be *fabric-selective*. Five types of primary fabric-selective porosity were identified: interparticle, intraparticle, fenestral, shelter, and growth framework. Two types of secondary fabric-selective porosity, intercrystal and moldic, were also recognized. Some porosity types are not determined by the fabric of the sediment, such as fracture porosity, channel, vug, and cavern types. Other porosity types may be either fabric-selective or not, such as breccia, boring, burrow, and shrinkage types. Each of these porosity types may be associated with a particular depositional environment, diagenetic history, and position within a cycle of relative sea-level change.

Lucia (1983, 1995, 1999) placed emphasis on the petrophysical aspects of carbonate pore systems, suggesting that there are two major types of carbonate porosity. The pore space between grains is termed interparticle pore space and all other pore space is termed vuggy, subdivided into separate vugs connected only through the

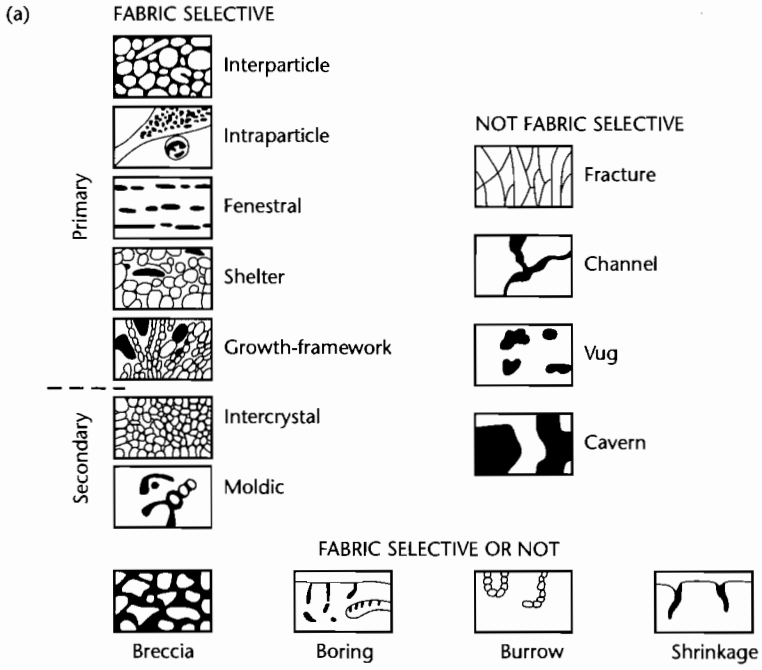

(b)

VUGGY PORE SPACE		
Separate-vug pores (vug-to-matrix-to-vug connection)		Touching-vug pores (vug-to-vug connection)
Grain-dominated fabric	Mud-dominated fabric	Grain- and mud-dominated fabrics
Moldic pores	Moldic pores	Cavernous
Composite moldic pores	Intrafossil pores	Breccia
Intrafossil pores	Shelter pores	Fractures
Intragranular microporosity		Solution-enlarged fractures
		Fenestral

Fig. 10.35 Classification of carbonate porosity: (a) based on the fabric-selective and the non fabric-selective criteria of Choquette and Pray (1970), (b) based on the petrophysical classification of vuggy pore space and vug interconnection of Lucia (1995). Reproduced courtesy of American Association of Petroleum Geologists.

interparticle pore network, and touching vugs that form part of an interconnected pore system (Fig. 10.35b). These three types have different porosity–permeability characteristics and are therefore distinct petrophysically.

DIAGENESIS OF CARBONATES

Although depositional environment and grain types are important in determining the primary porosity of a carbonate sediment, the postdepositional evolution of porosity is often the key element in the formation of carbonate reservoirs. Dissolution during burial of a carbonate sediment dominates the formation of secondary porosity. Initially, secondary porosity is fabric-selective in the so-called *eogenetic* zone. Later during burial, in the *mesogenetic* (beyond the influence of surficial processes) and *telogenetic* (exhumation back to the region of surficial processes) zones, porosity generation is generally not fabric-selective. One of the most important processes during diagenesis of carbonate rocks is *dolomitization.* Dolomitization may result in cementation because of a net import of CO_3 (Lucia and Major 1994), or if CO_3 is locally sourced, may result in net production of porosity (Moore 1989; Purser et al. 1994). Dissolution by ingress of fresh meteoric water during periods of exposure is perhaps the most important process enhancing porosity during dolomitization.

Secondary porosity associated with breccias can result from evaporite solution collapse, limestone solution collapse, faulting, and soil formation (Blount and Moore 1969). For example, solution collapse breccias produced during periods of influx of fresh meteoric waters at times of subaerial emergence contribute significantly to the porosity of the Ordovician Ellenburger carbonate reservoir in Puckett field, west Texas (Loucks and Anderson 1985). Major karstic dissolution associated with major unconformities is responsible for a number of important carbonate reservoirs, such as the Mississippian Northwest Lisbon field, Utah (Miller 1985) and the Permian Yates field, west Texas (Craig 1988). Intense fracturing commonly enhances porosity in carbonate rocks. A good example is the Oligocene Asmari Limestone of Iran. Despite a matrix porosity of just 9%, the reservoir produces up to 80,000 barrels of oil per day from a fractured reservoir (McQuillan 1985).

EOGENESIS AND RELATIVE SEA-LEVEL CHANGE

The methodology of process stratigraphy (§8.1–§8.2) facilitates an explanatory approach to the occurrence of carbonate reservoirs. A number of common stratigraphic contexts (Fig. 10.36) can be linked to the occurrence of productive carbonate reservoirs (Saller et al. 1994; Harris et al. 1999; Moore 2001):

Sea-level lowstand (lowstand systems tract, LST)

On carbonate ramps and rimmed carbonate shelves, lowstands of sea level are important because in humid climates chemically unstable marine sediments are potentially subjected to flushing by large volumes of undersaturated meteoric waters. This modifies the porosity and permeability of the host sediment. Marine carbonate sediments commonly are exposed and develop *karst systems* that enhance vertical conductivity of fluids. Gravity-driven meteoric water may move towards the coastline, mixing with marine water, and causing dissolution, secondary porosity, and some dolomitization. On isolated carbonate platforms (such as atolls), there is no active gravity-driven flow beneath the platform, leaving a platform-wide meteoric lens floating on marine water at a sea-level lowstand. Cementation may take place along the water table, negatively impacting porosity, but cavernous, karstic porosity may develop along the periphery of the platform. The core of the platform is pervasively dolomitized in a mixing zone between the meteoric lens and marine water drawn into the platform.

Sea-level rise (transgressive systems tract, TST)

Diagenesis during sea-level rise is dominated by marine water. During sea-level rise on a ramp, deposition of transgressive deposits seals a confined, gravity-driven flow in the highstand deposits of the underlying depositional sequence, often associated with porosity gain in the up-dip recharge area, and porosity loss by cementation in the down-flow area. On rimmed carbonate shelves, reef growth typifies the shelf margin during relative sea-level rise, giving good framework porosity, but marine cementation may reduce porosity along the shelf margin. The interiors of isolated carbonate platforms are generally open to marine waters during a sea-level rise and there is little meteoric water influence. Reefs may track sea-level rise, particularly on the windward side. Minor dolomitization of platform margins by marine waters driven by thermal convection, or reflux from the interior of the platform during arid periods, results in porosity loss by cementation.

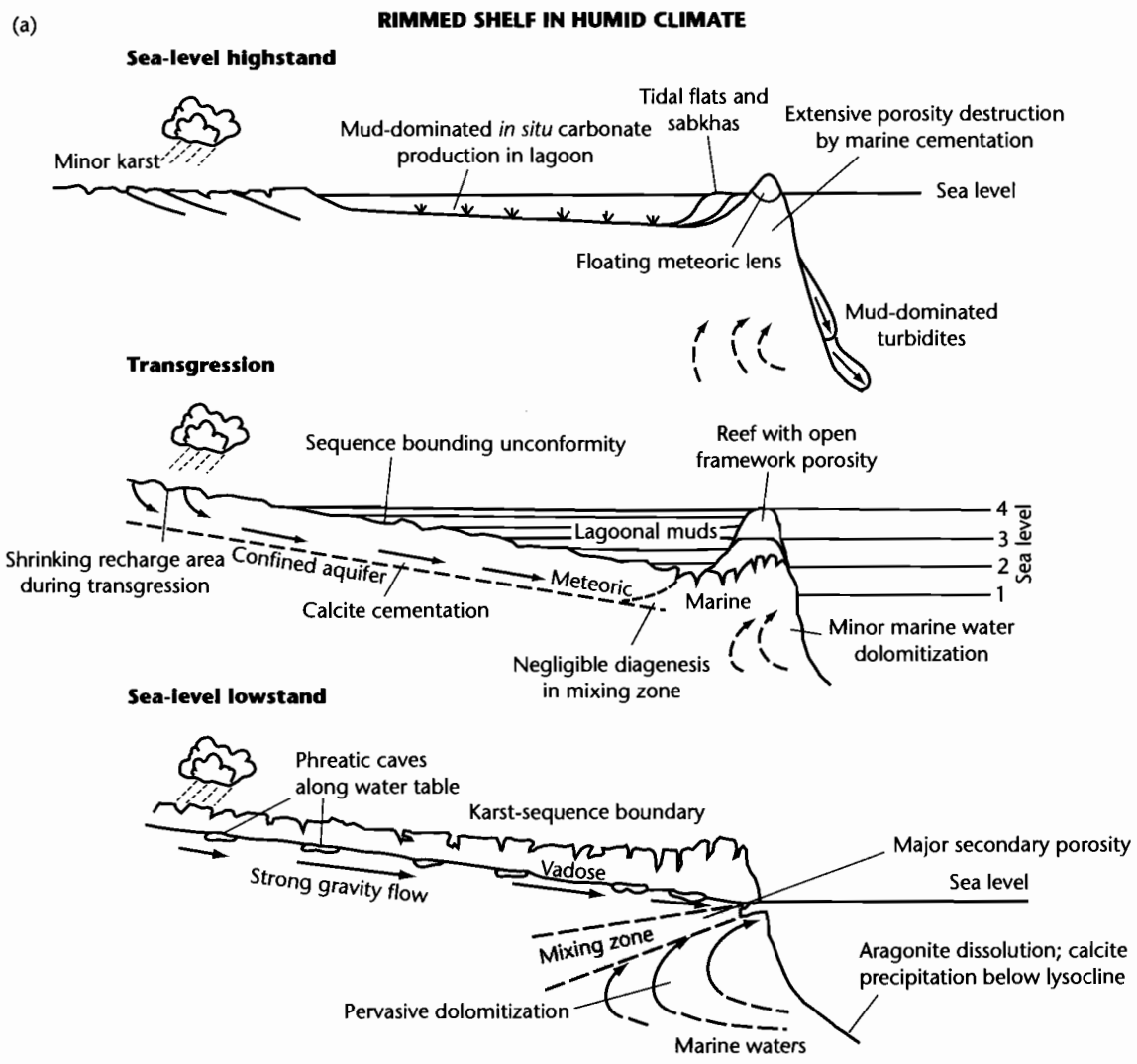

Fig. 10.36 Effects of relative sea level, depositional environment, and climate on the eogenetic changes in carbonate sediments, using a rimmed shelf system as an example (after Moore 2001). (a) Eogenetic processes during relative sea-level lowstand, transgression and highstand for a rimmed shelf in a humid climate; (b) The equivalent processes in an arid climate.

Sea-level highstand (highstand systems tract, HST)

Ramps strongly prograde and shelf and platform margins slowly accrete during the late highstand as accommodation generation reduces. At a time close to the maximum flooding, the slope and basin offshore ramps receive minimal sediment input, allowing deep-water microbial *mud mounds* to form. The progradational carbonate shoreline of the ramp contains freshwater lenses during humid periods, but during arid intervals, short-lived meteoric lenses are isolated by saline ponds. Heavy brines reflux downwards through underlying coastal zone sediments causing significant

(b)

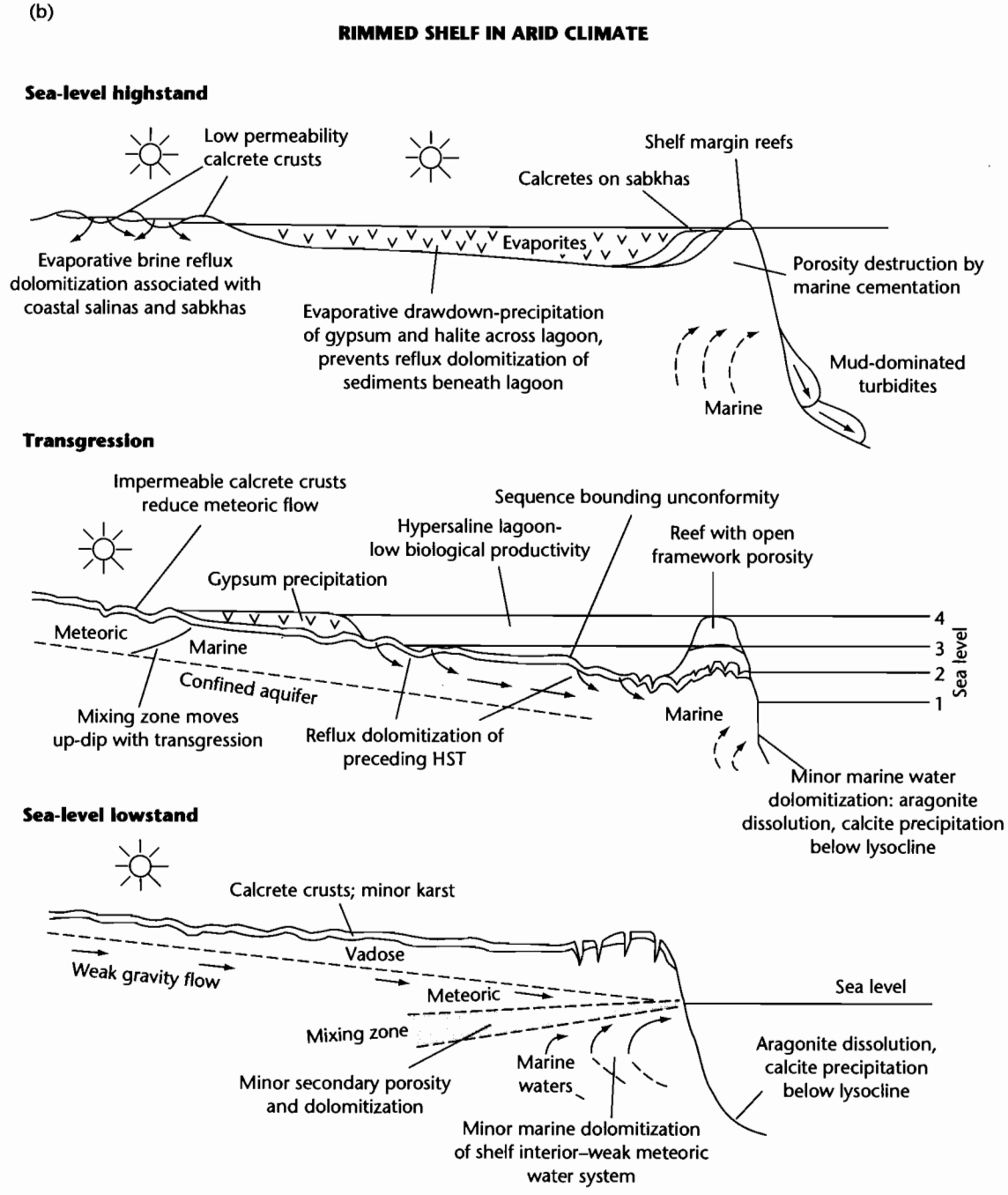

Fig. 10.36 *Continued*

dolomitization. If evaporites are precipitated in the salinas above, the brines are deficient in the Ca and CO_3 necessary for dolomitization, so the underlying carbonates are dissolved during dolomitization, which enhances secondary porosity. On rimmed shelves and isolated platforms, reefs easily keep up with sea level and shelter mud-dominated aggradational and progradational coastal tidal flats, while turbidites are shed into deep water. Reef bodies, if leached by meteoric water, or dolomitized in a marine–meteoric mixing zone, may have good reservoir properties, but otherwise, may suffer extensive porosity-reducing marine cementation.

The depositional and diagenetic histories of individual carbonate reservoirs are therefore complex and unique. Some of the most important carbonate reservoirs result from dolomitization from brines originating in evaporative marginal marine sabkhas and shelf lagoons. The Permian Capitan reef complex of the Guadalupe Mountains of west Texas and New Mexico evolved from a progradational build-up on a ramp to a steep fronted shelf margin reef and eventually into patch reefs (Kirkland et al. 1998). The reef carbonates have a good primary framework porosity. The shelf margin carbonates of the Capitan pass laterally into extensive Upper Permian shelfal carbonates and evaporites of the Artesia Group, representing deposition in a large evaporative shelf lagoon (Sarg 1981). Dense brines moved from this evaporative lagoon and dolomitized associated carbonate facies, to produce the most prolific oil-producing reservoirs in west Texas (Silver and Todd 1969). The Upper Jurassic Smackover Formation of east Texas, which accumulated as ooidal grainstones on high energy platforms in a late highstand systems tract, has been extensively dolomitized by reflux from overlying evaporites deposited during a lowstand in the overlying depositional sequence (Moore and Heydari 1993). One of the most prolific hydrocarbon systems in the world is found in the Upper Jurassic of the Persian Gulf and Saudi Arabia (Droste 1990) (Fig. 10.37). The Arab Formation carbonates and Hith anhydrite form part of a highstand systems tract. The dolomitization of Arab D reservoirs, including the world's largest field at Ghawar, is due to refluxing brines from the overlying Arab D evaporative lagoon, as in the case of the Smackover Formation.

Flushing with freshwater has also been identified as an important factor in the development of carbonate reservoirs (Fig. 10.36). The Pennsylvanian carbonate reservoirs of the Aneth Field of the Paradox basin, USA (Grammer et al. 1996) are carbonate mud mounds that have experienced secondary meteoric dissolution during

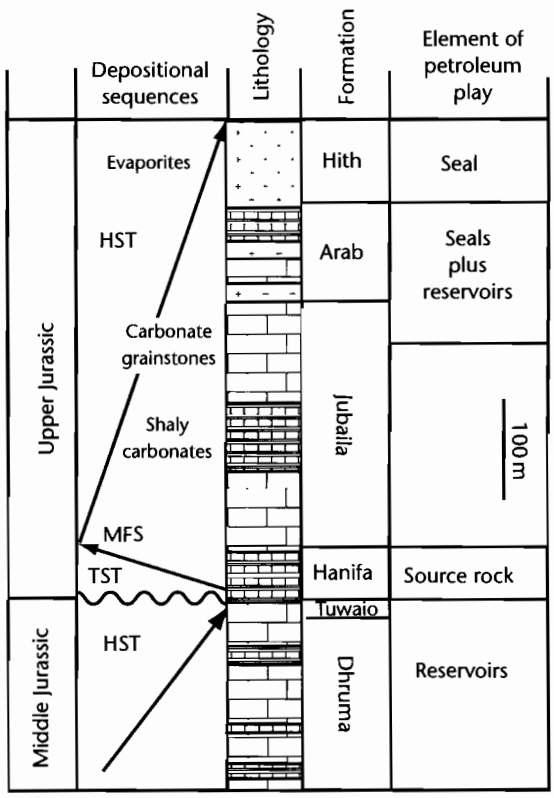

Fig. 10.37 Stratigraphic column of the Middle and Upper Jurassic of Saudi and the Persian Gulf, modified after Droste (1990). The Hith Formation constitutes an excellent regional topseal. Arab carbonate reservoirs are sealed by Arab evaporitic beds. The Hanifa Formation is an important source rock. Reproduced courtesy of Elsevier.

sea-level lowstands. The Ordovician Red River reservoirs of the Williston Basin, USA–Canada (Ruzyla and Friedman 1985) are dolomitized sabkha carbonates associated with evaporites, but secondary porosity is strongly influenced by freshwater flushing. The Ordovician Ellenburger Formation of west Texas consists of shallow marine shelf to marginal marine supratidal–intertidal deposits that have experienced freshwater flushing during lowstands. The Puckett Field has produced >2.6 tcf gas from dolomites produced by reflux of evaporative brines from adjacent sabkhas (Loucks and Anderson 1985), but secondary porosity has been strongly enhanced by solution collapse breccias related to subaerial exposure. Freshwater flushing of a prograding highstand shoreline succession has been invoked to explain diagenesis in the

Jurassic Oaks Field, Louisiana (Moore and Heydari 1993).

Burial diagenesis

The depositional fabrics and early diagenetic changes outlined above are invariably part of an evolutionary pathway leading to deep burial diagenesis or mesogenesis (Fig. 10.38). In the burial environment, sediments are beyond the reach of surface-related processes. Pressures and temperatures increase, and fluids are cut off from free exchange with the atmosphere. Chemical changes are therefore dominated by rock–water interaction and mixing with basin-derived fluids. The hydrology of deep basins depends on their large-scale tectonics (Fig. 10.39). For example, passive margin wedges (e.g., Northern Gulf of Mexico) have a high velocity, near surface, gravity-driven flow towards the distal basin, and a deep, moderate velocity, compaction-driven flow moving from deep

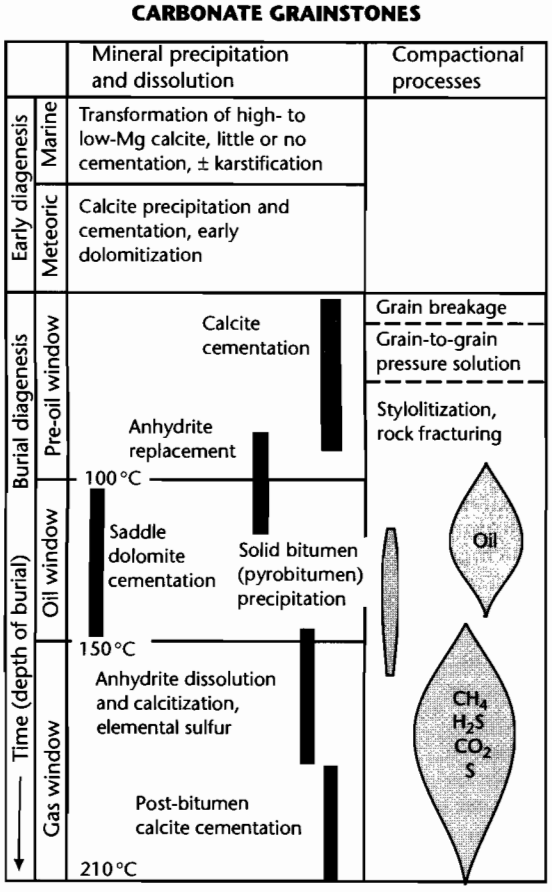

Fig. 10.38 Relationship between early (eogenesis) and deep burial diagenesis of carbonate grainstones, and the maturation of organic matter. After Heydari (1997). Reproduced courtesy of Springer.

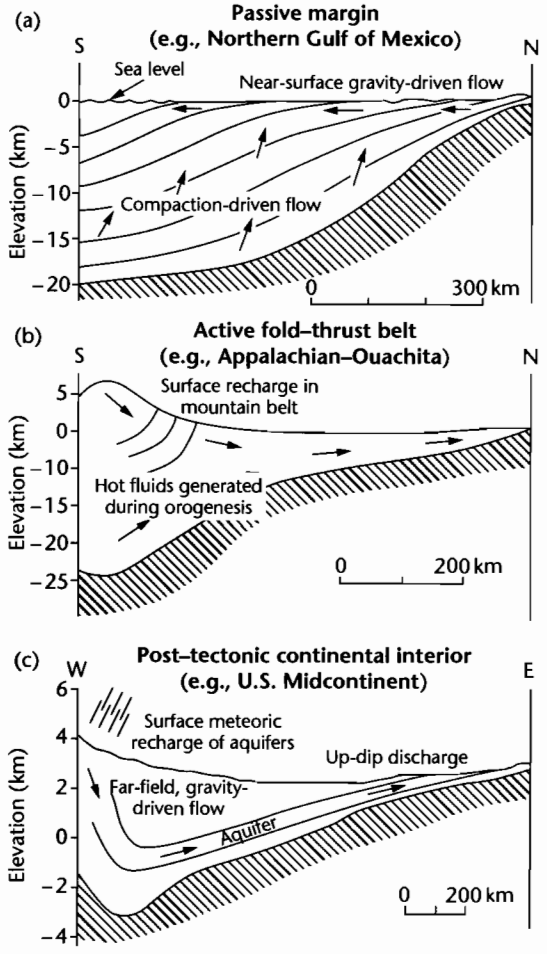

Fig. 10.39 Models of basin-scale fluid movement (after Moore 2001). (a) Passive margin, with near-surface gravity-driven flow and slow upward movement driven by compaction of the deep sedimentary column; (b) Active fold–thrust belt causes the up-dip migration of hot fluids; (c) Post-tectonic environment, characterized by long distance fluid transport in regional aquifers, driven by gravity acting on recharged water in the upland. Reproduced courtesy of Elsevier.

to shallow levels (Harrison and Summa 1991). Mechanical and chemical compaction dominate porosity changes, and cementation is relatively unimportant. The major source of $CaCO_3$ for cementation is pressure solution, but the volumes involved are limited. Other sources are dissolution caused by the action of aggressive pore fluids produced during organic diagenesis. Active fold–thrust belt and foreland basin settings (e.g., Lower Paleozoic Ouachita–Appalachians) have focused hot fluid flows caused by tectonic loading. The hot fluids react strongly with the rocks forming conduits for migration, causing recrystallization of early-formed calcite and dolomite, replacement dolomitization, dissolution of evaporites and precipitation up-dip. The Upper Knox Group carbonates (Lower Ordovician) of the southern Appalachians, USA have been strongly affected by a regional burial replacement dolomitization (Montanez 1994). In less active settings (Rocky Mountains of western USA–Canada), meteoritic waters recharge aquifers exposed in the mountain belt, setting up a far-field gravity-driven flow into the basin. Such meteoric recharge has negligible effects on carbonate porosity unless evaporites are dissolved. If so, the dissolution of gypsum promotes the dissolution of dolomite and precipitation of calcite (*dedolomitization*), thereby enhancing porosity. The Mississippian Madison aquifer of the mid-continent, USA (§9.6.3) is thought to show this down-flow path trend of dolomite dissolution and calcite precipitation (Plummer et al. 1990). The Madison is the reservoir for a number of fields, including the giant (>1 tcf gas), super-deep (23,000 ft, 7000 m) gas field at Madden Field, Wind River Basin, Wyoming, USA.

10.4.3 Sandstone reservoirs

POROSITY AND PERMEABILITY OF SANDSTONE RESERVOIRS

The primary porosity and permeability of sandstones are dependent on the grain size, sorting, and packing of the particulate sediment (see summary in Pettijohn 1975, pp. 72–79) and are therefore easier to predict than in carbonate reservoirs. The porosity of artificially packed natural sand is independent of grain size for sand of the same sorting, but porosity varies strongly with sorting. Average wet-packed porosity for a range of sorting groups varies between 28% for very poorly sorted sand to over 42% for extremely well-sorted sand.

In siliciclastic rocks, permeability is related to the pore throat size and the number of interconnected pores. However, the geological factors controlling these parameters may be complex. In unconsolidated sands, the most important factors are grain size and sorting. Sands with coarser grains have large pore throats and therefore a higher permeability. Consequently, permeability may vary over several orders of magnitude between very fine and coarse sand. For example, Hogg et al. (1996) measured permeability and porosity on samples obtained while drilling from the Triassic Sherwood Sandstone of Wytch Farm field, Dorset, UK (Fig. 10.40). The intercept of the regression on the permeability axis, representing the notional permeability at a zero porosity ranges from *c.* 0.001 mD for very fine grained sandstones to >1 mD for coarse grained sandstones.

Sands with poorer sorting have smaller mean pore throat diameters and therefore lower permeability than better sorted sediments with the same mean grain size. For wet-packed samples, permeability varies over more than an order of magnitude between extremely well sorted sands and very poorly sorted sands. The dual effects of sorting (expressed as standard deviation of grain size) and grain size (expressed as mean) on permeability is shown in Figure 10.41. The probable effect of low sphericity (grain shape) and high angularity (grain roundness) is to increase porosity and permeability of unconsolidated sand.

Apart from textural properties of the sand, the presence of ductile clay intraclasts (Gluyas and Cade 1997), which may compact to form pseudomatrix, and infiltrated clays both serve to reduce porosity and permeability. Further porosity and permability losses occur during burial, when compaction reduces pore throat size and eventually blocks them completely. Although the evolution of porosity with depth in sedimentary rocks of different lithology is beginning to be understood (§9.2), the impact on permeability is less well known (see Ethier and King 1991). Different clay mineral cements can have different effects on permeability because they occupy different positions in the pore space (e.g., Howard 1992). Tangential grain coatings have a much smaller effect on permeability than clays growing perpendicularly to grain surfaces or lying within pore throats (Pallatt et al. 1984; Kantorowicz 1990). Discrete aggregates, though reducing porosity, may have little effect on permeability, unless they occur as a pseudomatrix, which on compaction severely reduces porosity and permeability.

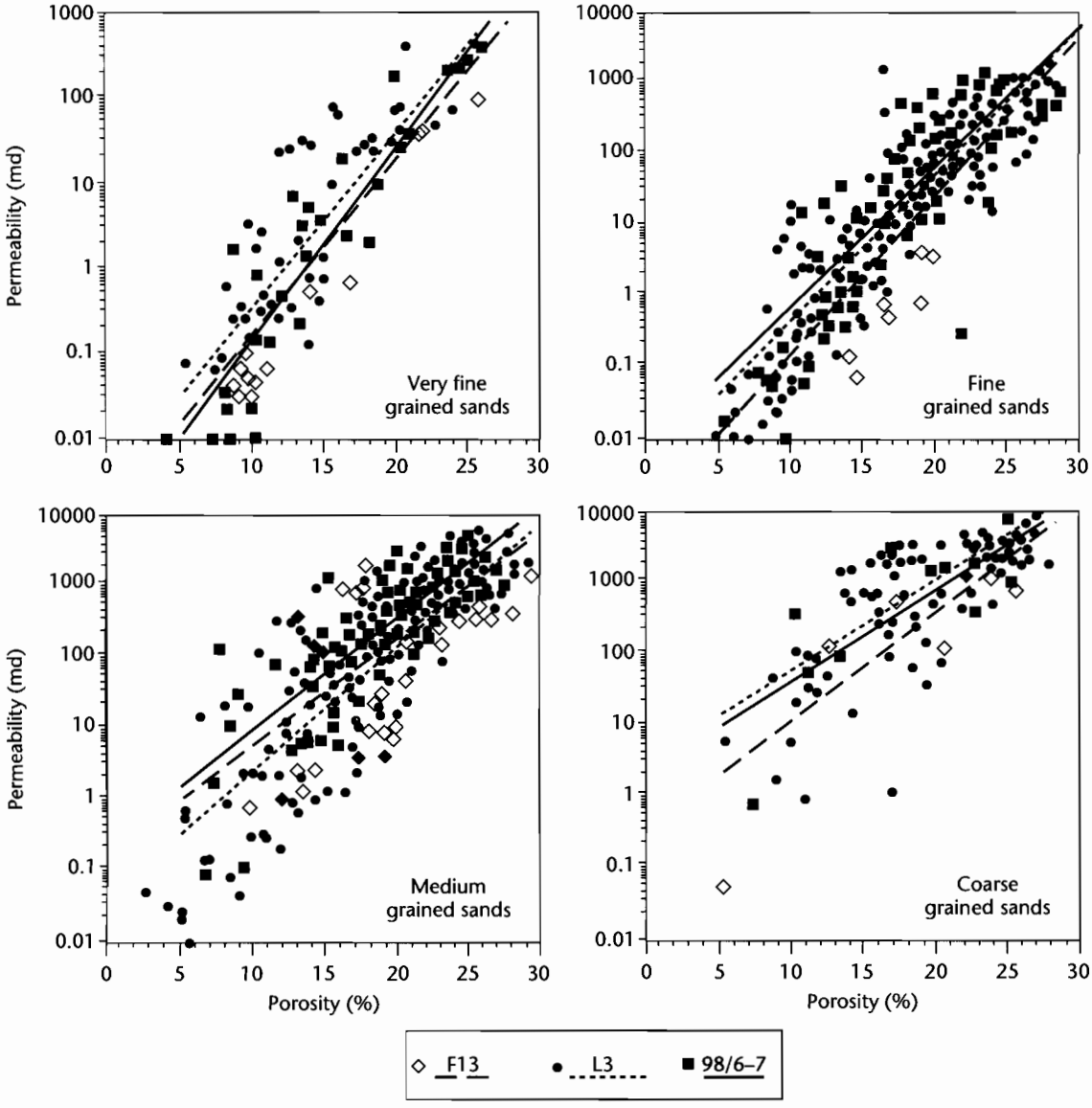

Fig. 10.40 Relationship of permeability with horizontal core plug porosity for four grain size classes in the Triassic Sherwood Sandstone reservoir in three wells in the Wytch Farm field, Dorset, UK. After Hogg et al. (1996). Reproduced courtesy of Geological Society of London.

Porosity and permeability can also be affected positively by early clay mineral growth. For example, chlorite rims on grains can inhibit later quartz cementation and pressure dissolution. Early introduction of oil into pore space stops or slows clay diagenesis in sandstones, thereby improving porosity and permeability relative to sandstones receiving a late hydrocarbon charge.

The major factors controlling permeability in sandstones are therefore grain size, sorting, percentage of

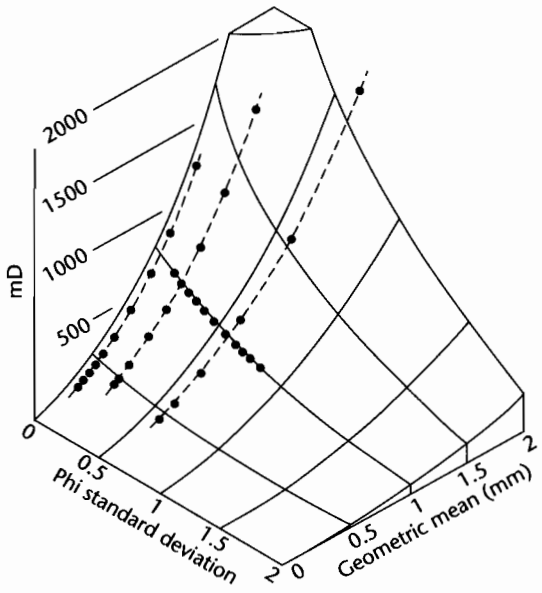

Fig. 10.41 Relation of permeability to grain size and sorting (after Krumbein and Monk 1942). The vertical axis is the permeability in milliDarcys. The grid lines on the "permeability surface" are parabolas parallel to the Darcy-size plane, and negative exponentials parallel to the Darcy-standard deviation plane.

ductile clasts, early clay infiltration, compaction, and cementation (Cade et al. 1994).

CLAY MINERAL DIAGENESIS, DEPOSITIONAL ENVIRONMENT, AND RELATIVE SEA-LEVEL CHANGE

There is now an impressive literature on the formation of clay minerals in sandstones during burial (Haszeldine et al. 2000; Morad et al. 2000; Ketzer et al. 2003; Worden and Morad 2003). The distribution of clay minerals formed in the *eogenetic* regime (<70 °C, <2 km burial) is closely related to depositional facies, climate, and stratigraphic surfaces (Fig. 10.42). Consequently, knowledge of the stratigraphic architecture of a basin is valuable for prediction of diagenetic trends and therefore sandstone reservoir quality.

The main eogenetic clay minerals can be grouped under the following headings: (i) kaolinite, (i) green clay minerals (glauconite, berthierines, verdine), and (iii) smectite, mixed layer illite/smectite, mixed layer chlorite/smectite and Mg-clay minerals (e.g., palygorskite). The formation of diagenetic clay minerals in near-surface sandstones and during shallow burial is controlled by depositional environment, detrital composition, and climatic conditions:

- Eogenetic *kaolinite* has a vermicular and book-like habit and forms under humid climatic conditions in continental sediments (Emery et al. 1990). It commonly forms during relative sea-level lowstand and relative sea-level fall (forced regression), when large areas of marine sediment are subaerially exposed and subjected to flushing by meteoric water. High rates of flushing are promoted by humid climatic conditions and high permeabilities, as in channel or shoreface sands;
- *green clay minerals*: berthierine and verdine occur as small (<5 μm) lath-shaped grain coatings and crystals, as coats, pellets, ooids, and void-fillings, or as replacements of detrital grains, commonly below the sediment–water interface in deltaic–estuarine deposits, primarily in tropical to subtropical seas. Berthierine is favored under reducing conditions in volcanogenic sediments in estuarine–coastal plain environments (Jeans et al. 2000), whereas verdine forms in mildly reducing conditions in continental shelf sediment off river deltas (<200 m water depths) under low sedimentation rates (Kronen and Glenn 2000). Glauconite forms exclusively in open marine sediments (Odin and Matter 1981) decimeters to meters below the seabed;
- *smectite* and mixed layer illite/smectite forms as grain-hugging flakes in semi-arid climates, whereas Mg-smectites and palygorskite form fibers or fiber bundles during near-surface diagenesis of lacustrine, fluvial, and eolian sediments under evaporative conditions. These minerals therefore commonly form eodiagenetically in arid continental environments.

Ketzer et al. (2003) and Worden and Morad (2003) provide summaries of the association of eogenetic clay minerals and systems tracts (Fig. 10.43). These associations can be summarized as:

1 Lowstand systems tract (LST): sediments on the subaerially exposed continental shelf are subjected to kaolinite eogenesis under humid climatic conditions and formation of Mg-rich clay minerals such as palygorskite under evaporitic arid conditions. Paleosols may form on interfluves between the main incised channels.
2 Transgressive systems tract (TST): berthierine may form in the upper part of incised valley fills at they are flooded during transgression. The transgressive surface may be lined with high amounts of glauconite

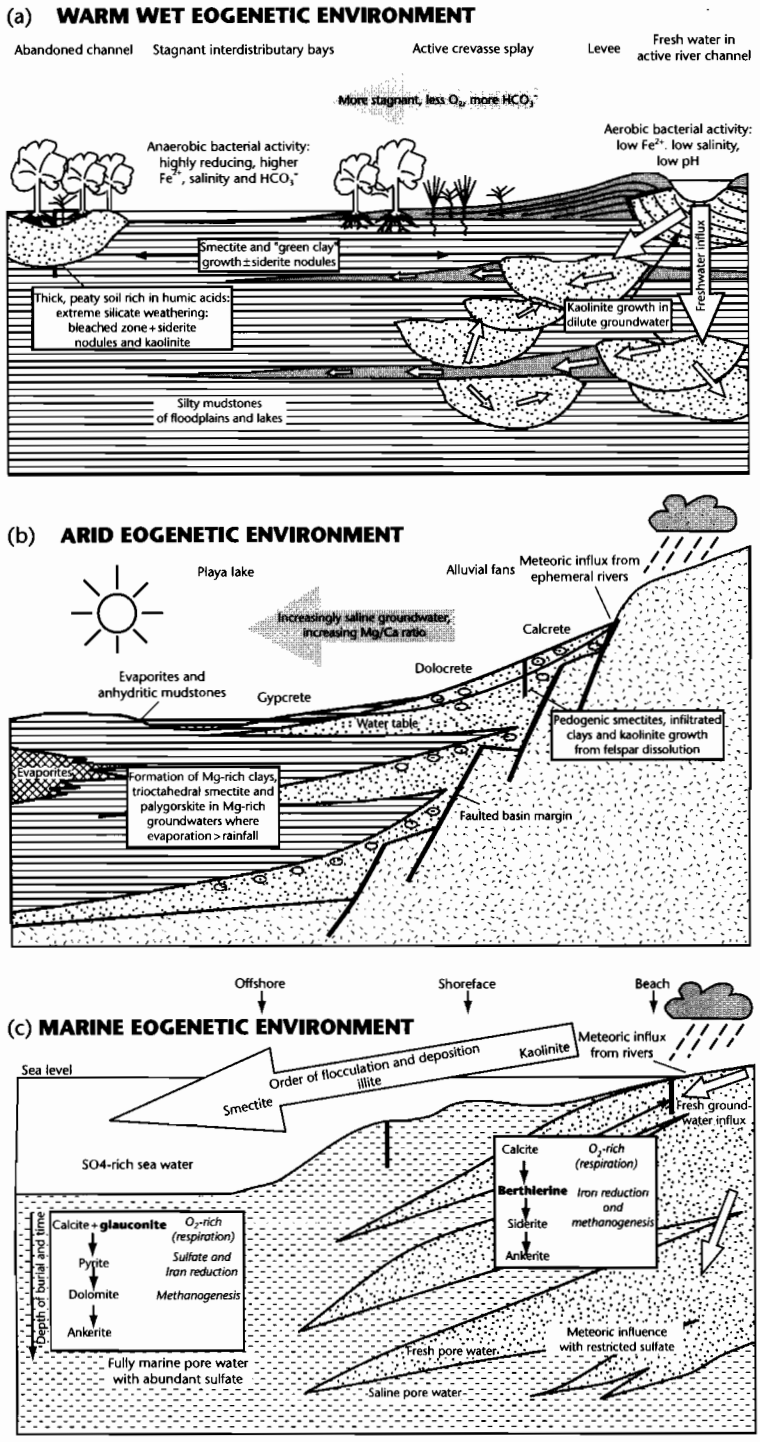

Fig. 10.42 Relation of clay mineral formation to depositional environment. (a) Warm, wet eogenetic environment of river channels, crevasse splays, and interdistributary bays; (b) Arid eogenetic environment of basin margin fans and evaporitic playas; (c) Marine eogenetic environment offshore from river entry points. For more details see Worden and Morad (2003). Reproduced courtesy of Blackwell Publishing Ltd.

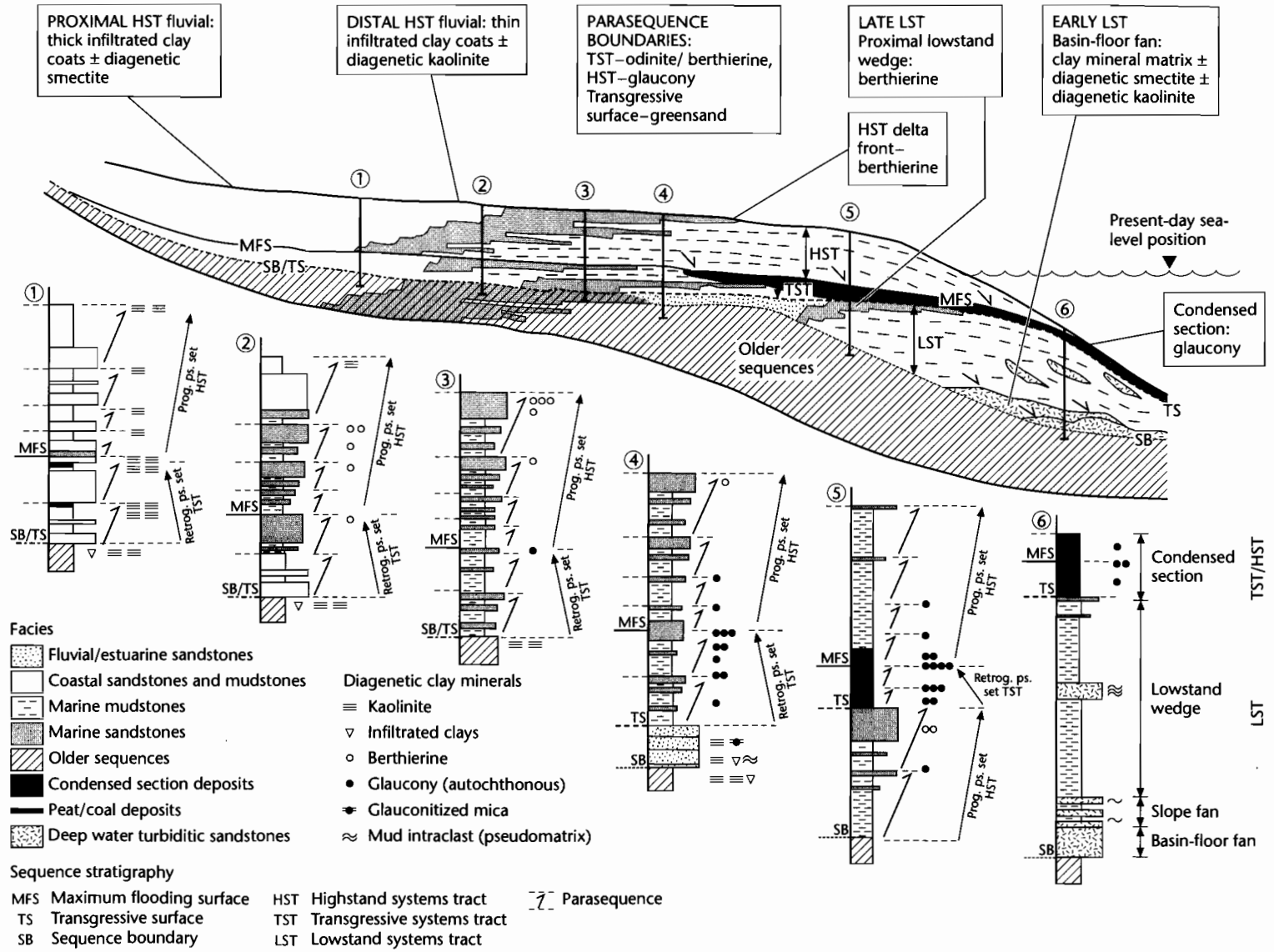

Fig. 10.43 Distribution of diagenetic clay minerals within a depositional sequence, modified after Ketzer et al. (2003). Sequence architecture from Van Wagoner et al. (1990). Diagenetic clay mineral types are shown in their typical positions within successions 1 to 6. Reproduced courtesy of Blackwell Publishing Ltd.

and verdine intraclasts, giving "greensands" overlying coastal plain sediments. As water depths deepen and the shelf becomes starved of coarse sediment, authigenic glauconite and verdine forms, with maximum concentrations along the maximum flooding surface, while berthierine forms in estuarine and shallow marine environments in front of deltas.

3 Highstand systems tract (HST): as highstand progradation takes place, the amounts of glauconite and verdine decreases and authigenic berthierine increases. The landward end of the HST may be composed of fluviatile sandstones subjected to kaolinitization under humid conditions, pedogenesis, or the formation of Mg-rich clay minerals in arid conditions.

MESOGENESIS AND TELOGENESIS OF SANDSTONES

In the burial diagenesis (mesogenesis) zone, temperature is the most important control on the formation of clay minerals. Eogenetic kaolinite, berthierine, and smectite are replaced by mesogenetic dickite, illite, and chlorite. Vermicular (worm-like) and book-like stacks of kaolinite crystals are progressively replaced by dickite above 70–90 °C (2–3 km burial depth), with a loss of the typical eogenetic kaolinite stacking pattern with increasing temperature and transformation to dickite (Beaufort et al. 1998). Transformation is aided by high permeabilities, so cannot be used as a simple paleothermometer. With burial and heating smectites pass progressively through interlayered forms to illite. Kaolinite also transforms to illite at temperatures above 70 °C, but especially above 130 °C. K-felspar and kaolinite react to produce illite and quartz, the quartz byproduct commonly forming discrete crystals or overgrowths. Dickite also transforms to illite at high temperatures. Finally, mesogenesis is typified by chloritization. Chlorite grain replacements may form as a result of breakdown of volcaniclastic grains, by transformation of smectite, or by alteration of previous "green mineral" grain coatings. Chloritization of kalonite can also occur at burial depths of 3500–4500 m (165–200 °C) (Boles and Franks 1979).

Burial diagenetic changes are well illustrated by the intensively studied Jurassic sandstone reservoirs of the Brent Group, North Sea. Reservoirs that have experienced only shallow burial have partially dissolved felspars and authigenic kaolinite. Deeper (>4 km) Brent reservoirs, however, have extensive illite, quartz, and ferroan carbonate cements, severely impairing reservoir quality (Bjorlykke et al. 1992; Giles et al. 1992). Felspars are essentially absent in these deep reservoirs (Glasmann 1992).

Based on a wide survey of diagenetic histories of sandstones (Primmer et al. 1997), there appear to be five distinct diagenetic styles that are related to original depositional environment, detrital composition and burial history:

- *Quartz*, commonly with smaller quantities of neoformed clays (kaolinite and/or illite) and late-diagenetic ferroan carbonate. This is the most common diagenetic style and is most likely to occur in mineralogically mature sandstones, deposited in high energy eolian, deltaic, and shallow marine environments. Quartz cements are temperature dependent and occur in large volumes at temperatures >75 °C;
- *clay minerals* (illite or kaolinite) with smaller quantities of quartz or zeolite and late-diagenetic carbonate. Illite rarely forms below 100 °C (Robinson et al. 1993). Kaolinite is very common and occurs in more mineralogically mature sandstones. Chlorite is very common in immature sandstones, and smectite only occurs in immature sandstones, such as deep marine deposits;
- *early diagenetic (low temperature) grain coating clay mineral cements* such as chlorite, which may inhibit quartz cementation during later burial;
- *early diagenetic carbonate or evaporite cement*, often localized, which severely reduces porosity at very shallow burial depths. Siderite is a common early carbonate cement in mature sandstones, typically fluviatile and shallow marine, whereas late diagenetic ferroan dolomite and calcite cements are most common in mineralogically immature sandstones;
- *zeolites*, which occur over a wide range of burial temperature, in association with abundant clay minerals (usually smectite or chlorite) and late diagenetic nonferroan carbonates. This style is also likely to occur in mineralogically immature sandstones. Zeolites are common in deep marine sandstones and especially sandstones derived from volcanogenic terrains.

Telogenetic changes related to uplift and erosion leave a distinctive fingerprint on sandstone reservoirs. Meteoric water fluxes, especially along basin margins and uplifted fault blocks, are commonly dilute, oxidizing, saturated with CO_2 and therefore acidic. Felspars rapidly alter to clay minerals, reduced iron-bearing cements are oxidized, and calcite, dolomite, and sulfate cements are dissolved. The occurrence of kaolinite in the Jurassic Brent Group reservoirs of the North Sea is thought to be due to telogenesis.

HETEROGENEITY OF SANDSTONE RESERVOIRS

So far we have emphasized the factors influencing porosity and permeability on the grain to microscopic scale. All sedimentary deposits, however, have an inhomogeneity caused by the distribution in time and space of sedimentary facies ("architecture"), and by compaction, deformation, cementation, and the nature of pore-filling fluids. A classification system of reservoir heterogeneities can be based on their size, origin, and influence on fluid flow (early examples are Pettijohn et al. 1973; Weber 1986, p. 489) (Fig. 10.44). One of the major factors in any classification is the size of the heterogeneities, as illuminated in the scheme that follows:

- *First-order heterogeneities* (1–10 km scale), including the presence of sealing faults and the boundaries of major genetic units of sediment such as fluviatile channelbelts;
- *second-order heterogeneities* (cm to tens of m scale) which represent variation in permeability within the larger genetic units. The interbedding of shales at channel margins, or the permeability contrasts caused by the coarse–fine stratification of a point bar are examples;
- *third-order heterogeneities* (mm to m scale) result from the geometrical arrangements of individual depositional units such as bedforms producing cross-stratification. The inclined foresets of cross-sets also produce a finer scale alternation of moderate and high permeabilities, whereas the toesets of bedforms introduce essentially horizontal low permeability "breaks" or "baffles" into the reservoir (Weber 1987). *Fractures* and *stylolites* also fall within this physical scale of heterogeneity;
- *fourth-order heterogeneities* (μm to mm scale) are represented by variations in grain size and sorting, and *microscopic heterogeneities* caused by the way in which pores are interconnected or blocked.

Large scale heterogeneities of well-spacing size can often be analyzed on the basis of detailed well log correlations and by the use of sedimentological models derived from core descriptions. For smaller scale heterogeneities, cores are indispensable, since they provide information on bed thickness, style of cross-stratification, grain size, and microscopic features. The correct identification of the environment of deposition of the sediment greatly helps in an assessment of heterogeneity.

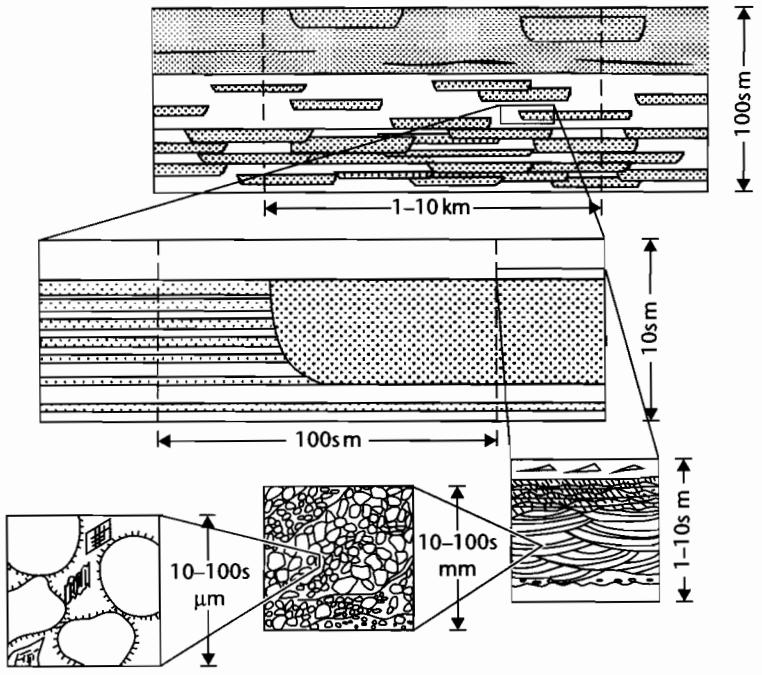

Fig. 10.44 Example of various levels of heterogeneity in a fluviatile reservoir from the km scale down to the microscopic scale.

A thorough study of the various scales of heterogeneity is essential to the efficient recovery of hydrocarbons from a reservoir but is of less direct concern to the basin analyst. A major objective of the production geologist is to supply engineers with information on the porosity and permeability structure of a reservoir rock. This is commonly done by assigning porosity and permeability values to individual cells in a numerical model of the reservoir. The petroleum engineer then performs a simulation of the flow of fluids, including hydrocarbons, through the reservoir. Where geological information on heterogeneity is poor, it is useful to use scaling relationships between bed thickness, bed width, and bed volume derived from field studies as a guide. Turbidite successions have in particular been analyzed very promisingly in this way (Rothman et al. 1994; Malinverno 1997; Talling 2001; Sinclair and Cowie 2003).

PROVENANCE OF RESERVOIR SEDIMENT

Investigations of the source area for a sediment are called provenance studies. Provenance studies classically developed as an analysis of the mineralogy of the light fraction of siliciclastic sediments in the form of ternary diagrams of quartz (Q), felspars (F), and lithics or rock fragments (L) (e.g., Dickinson 1980; Dickinson and Suczek 1979; Ingersoll and Suczek 1979; Dickinson and Valloni 1980; Lash 1987). Variations on the standard QFL diagram are used by distinguishing between, for example, polycrystalline and other forms of quartz, or sedimentary versus volcanic rock fragments. These ternary diagrams are divided into fields representing distinct plate tectonic settings for the sandstone sample, but overlapping of some of the fields severely limits their uses. Although these techniques continue to be used, they have been supplemented by other methods including heavy mineral analysis (Mange and Maurer 1993), fission track thermochronology of detrital apatites and zircons, and isotopic studies such as U–Pb dating of detrital zircons and Sm–Nd analysis of basin sedimentary rocks. All of these techniques are directed towards understanding the mineralogy, geochronology, and thermal evolution of the source regions providing basin sediment.

The effects of *transport* of sediment on the resulting composition of a sandstone is critical to the correct interpretation of provenance. Transport in terrestrial systems invariably modifies the composition of the sand, but the effects differ markedly according to climatic zone and type of river system. Franzinelli and Potter (1983) provide an elegant study of the Amazon drainage system in this respect. Large river systems in humid and hot climates are optimal for the chemical weathering of unstable grains such as lithic fragments. As a result, the sand at the mouth of the Amazon is dominated by quartz, despite the fact that considerable proportions of lithic grains were contributed to the drainage system at the source. Other smaller or cold climate terrestrial systems on the South American continent produce relatively immature sands (Potter 1978, 1984). The marine sedimentary record is increasingly used to interpret climate change or changes in sediment routing systems in the source regions. Well-documented examples from the Indian Ocean are provided by Einsele et al. (1996), Prins and Weltje (1999), and Clift and Gaedicke (2002).

The likelihood of the presence of reservoir units of adequate quality in different basin types can therefore be broadly assessed from a knowledge of the hinterland geology and sediment dispersal systems (Kingston et al. 1983a, b). In broad outline, continental sags typically contain extensive shallow marine, fluviatile, eolian, and lacustrine reservoirs. Rifts may contain early spatially restricted and volcanic-rich reservoir units of poor quality, and younger, more extensive, fluviatile, deltaic, and marine good quality reservoirs. Passive margins have very extensive shallow marine and deltaic sands or thick carbonate reservoirs, and deep water turbiditic reservoirs. Strike–slip basins have a composition of sedimentary infill determined by the nature of the adjacent plates. Ocean–ocean boundaries generally provide poor reservoirs because of contamination by pelagic and volcanogenic material; continent–ocean and continent–continent zones have more chance of providing sources of sand. Forearc and trench sediments contain large amounts of volcanogenic material, and porosity and permeability are severely reduced during diagenesis. It must be emphasized, however, that these are broad generalizations and the practicing basin analyst should in some sense treat every basin on its own merits after a collation of all available data.

10.5 THE REGIONAL TOPSEAL

Summary

The existence of a petroleum play depends on the presence of an effective regional caprock or topseal.

The basic physical principles governing the effectiveness of petroleum caprocks are the same as those that

control secondary migration of petroleum. A caprock is effective if its capillary or displacement pressure exceeds the upward buoyancy pressure exerted by an underlying hydrocarbon column. The capillary pressure of the caprock is largely a function of its pore size. This may be laterally very variable.

The buoyancy pressure is determined by the density of the hydrocarbons and the hydrocarbon column height. A caprock of extremely small pore size is required to prevent the buoyant rise of a tall underlying gas column. Hydrodynamics also affect caprock effectiveness. Loss of gas through caprocks may take place through the process of diffusion.

A worldwide survey of caprocks indicates that the most effective caprock lithologies are fine-grained siliciclastics and evaporites. Ductility is also an important requirement, particularly in tectonically disturbed areas. Salt and anhydrite are the most ductile, followed by organic-rich shales. Caprocks do not need to be thick to be effective, as long as they are laterally persistent. Similarly, depth of burial does not appear to be critical – seals may be effective at all depths. A good example of a regional caprock is the Upper Jurassic Hith Anhydrite in the Arabian Gulf area, which seals in excess of 100 billion barrels of oil in the underlying Arab reservoirs.

The conditions required for the development of regionally extensive, effective caprocks in association with reservoir rocks are frequently met in two particular depositional settings. One of these is where marine shales transgress over gently sloping siliciclastic shelves, as in the Miocene Telisa Formation shales of the Central Sumatra Basin. The other is where evaporites in regressive sabkhas regress over shallow marine carbonate reservoirs, as in the case of the Hith anhydrite of the Arabian Gulf.

10.5.1 Introduction

The regional caprock or topseal is one of the three essential ingredients of the petroleum play. The nature of the caprock determines not only the efficiency of the subsurface trapping system, but influences the migration routes taken by petroleum fluids on leaving the petroleum source rock. The continuity of the regional topseal largely determines whether the basin has a laterally or vertically focused migration system. Compared to the enormous literature devoted to reservoir rocks, and the massive effort devoted to understanding the geochemistry of source rocks, relatively little has been written on caprocks. Downey (1984) and Grunau (1987), however, provide important reviews.

10.5.2 The mechanics of sealing

The basic physical principles governing the effectiveness of petroleum caprocks are the same as those controlling secondary migration (§10.3.2.4). The physical principles themselves are relatively well understood (Schowalter 1976), though much has still to be learned about seals in general.

In §10.3.2.4, we divided the forces that control secondary migration into those that drive secondary migration, and those that restrict it. The main driving force is *buoyancy*, caused by the fact that petroleum fluids are generally less dense than formation pore waters. The main restricting force to the movement of a globule or slug of petroleum through a porous rock is its *capillary* or *displacement pressure*. This depends primarily on the size (radius) of the pore throats. A rock will seal an underlying petroleum accumulation if the displacement pressure of its *largest* pore throats equals or exceeds the upwardly directed buoyancy pressure of the petroleum column (Fig. 10.45). The seal potential or capacity of a caprock can be expressed as the maximum petroleum column height that it will support without leakage. Owing to subsurface density differences of oil and gas, caprocks can support much larger oil columns than gas columns, other things being equal.

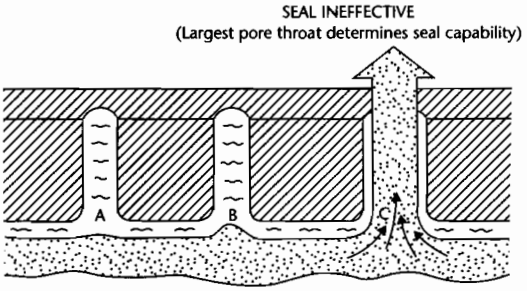

Fig. 10.45 Diagrammatic illustration of the effect of the largest pore throat size on sealing capacity of caprocks (modified from Downey 1984).

The displacement pressure of a piece of caprock can be measured directly in the laboratory by mercury-injection techniques, or can be estimated from the rock porosity and permeability. These data are useful in evaluating seals, but a very severe limitation is caused by the doubtful representativeness of the analyzed sample with respect to the entire sealing surface of the trap. Pore sizes are likely to vary considerably over the lateral extent of the caprock, so a core sample tells us little about the sealing capacity of the caprock as a whole. The existence of large pore networks is critical; these represent the weakest points of the seal. As a result of these difficulties, seal capacity calculations are subject to wide ranges of error.

10.5.2.1 The effect of hydrodynamics and overpressured caprock

Under hydrodynamic conditions, the driving forces for migration or leakage are modified. Hydrodynamic flow may either increase or decrease the driving pressure against seals, thus modifying the petroleum column heights the seal can support. When the hydrodynamic force has an upward vector, it acts in support of buoyancy; when it is downward it diminishes the effect of buoyancy on the seal. Hydrodynamic effects on seal capacity may, however, for all practical purposes, be ignored except in those basins with clear evidence of hydrodynamic conditions operating at the present day. In the Powder River Basin of Wyoming, Berg (1975) has shown that hydrodynamic down-dip flow has assisted the lateral sealing of the Recluse Muddy and Kitty Muddy fields.

The existence of overpressure in a shale caprock may create a local pore pressure gradient that greatly assists its capacity to seal adjacent normally pressured reservoirs. Studies in the Niger delta (Weber et al. 1978) and Gulf Coast (Stuart 1970) provide field examples.

10.5.2.2 Loss of petroleum through caprocks by diffusion

Gas may diffuse through water-filled caprocks over geological time scales (Leythaeuser et al. 1982). In a study of the 68 billion cubic feet Harlingen gas field in Holland, it is estimated that half of the accumulation would be lost by diffusion through the 400 m thick shale caprock in 4.5 Myr. Thus, gas fields overlain by water-saturated shale caprocks are likely to be ephemeral phenomena unless continuously topped up by active generation in the area. If losses by diffusion are as severe as Leythaeuser et al. (1982) suggest, there are some difficulties in explaining the existence of gas fields charged and reservoired in very old sequences, such as the Lower Paleozoic.

10.5.3 Factors affecting caprock effectiveness

The effectiveness of caprocks worldwide may be examined in terms of their lithology, ductility, thickness, lateral continuity, and burial depth.

10.5.3.1 Lithology

Nederlof and Mohler (1981), in a statistical analysis of 160 reservoirs/seals, found that caprock lithology was of considerable importance in influencing seal capacity. Caprocks need small pore sizes, so the vast majority of caprocks are fine-grained siliciclastics (clays, shales), evaporites (anhydrite, gypsum, halite) and organic-rich rocks. Other lithologies such as argillaceous limestones, tight sandstones and conglomerates, cherts and volcanics may also seal, but they are globally far less important, are frequently of poor quality, and geographically of limited extent.

Grunau (1987) compiled information on the caprock lithologies of the world's 25 largest oil and 25 largest gas fields. There was a roughly equal split between shales (13) and evaporites (12) for the 25 oil fields. For the gas fields, shales (16) predominated over evaporites (9).

About 40% of the ultimately recoverable oil reserves from the world's giant oil fields are capped by evaporites, and 60% by shales (Grunau 1987). For gas, the corresponding percentages are 34% for evaporite caprocks and 66% for shales. The majority of giant oilfields with evaporite caprocks are located in the Middle East and North Africa, while shale caprocks to giant *oil fields* are more ubiquitous, and include Alaska, western Canada, California, the Gulf Coast, Mexico, Venezuela, the North Sea, the Soviet Union, Indonesia, and Brunei. Evaporite caprocks to giant *gas fields* are geographically more widely distributed, and apart from the Middle East and North Africa, include the Soviet Union, Netherlands/southern North Sea, and Brazil.

10.5.3.2 Caprock ductility

Ductile caprock lithologies are less prone to faulting and fracturing than brittle lithologies. Caprocks are placed

under substantial stress during periods of structural deformation, including the deformation responsible for trap formation. During the formation of a simple anticline, for example, tensional fractures may occur in brittle caprocks in the crestal parts of the fold. Ductility is, therefore, a particularly important requirement of caprocks in strongly deformed areas such as fold and thrust belts.

The most ductile lithologies are evaporites, and the least ductile cherts (Table 10.5). This may explain the extraordinary success of evaporites as caprocks. A high kerogen content appears to enhance the ductility of shale caprocks. Many source rocks, therefore, also serve as seals. Ductility is also a function of temperature and pressure. Evaporites may be brittle at shallow depths, but very ductile at depths of over 1 km.

10.5.3.3 Caprock thickness

A small thickness of fine-grained caprock may have sufficient displacement pressure to support a large hydrocarbon column. Thin caprocks, however, tend to be laterally inpersistent; thus a thick caprock substantially improves the chances of maintaining a seal over the entire prospect, or even over the entire play fairway or basin. Typical caprock thicknesses range from 10s of m to 100s of m (Grunau 1987). Very large volumes of petroleum may be sealed by relatively modest thicknesses of caprock. For example, the 3 m-thick Ahmadi shales seal the 74 billion barrel Burgan field in Kuwait; the 20 m-thick Arab C-D anhydrite seals the Arab D-Jubaila main reservoir of the Ghawar field in Saudi Arabia, the world's largest oil field (approx 80 billion barrels); the 33 m-thick Cap-Rock anhydrite seals the Asmari oilfields of the Iranian Zagros Fold Belt. For gas reservoirs, a thick caprock reduces the risk of substantial losses by diffusion.

Table 10.5 Ductility of caprocks (Downey 1984).

Caprock lithology	Ductility
Salt	Most ductile
Anhydrite	↑
Organic-rich shales	↑
Shales	↑
Silty shales	↑
Calcareous mudstones	↑
Cherts	Least ductile

10.5.3.4 Lateral seal continuity

In order to provide good regional seals, caprocks need to maintain stable lithological character (and hence capillary pressure and ductility characteristics) and thickness over broad areas. Most prolific petroleum provinces contain at least one of these regional seals. The search for petroleum in these basins may be focused on the base of the regional seal, rather than on any particular reservoir horizon. The lateral variability of the regional seal may be studied using wireline log information and seismostratigraphic analysis.

Some depositional environments and basin settings are more conducive to the establishment of thick and effective regional caprocks than others. Two of these will be discussed in §10.5.4. Of particular importance are the distinctive depositional environments that give rise to evaporite deposition (§8.5).

10.5.3.5 Burial depth of caprocks

The present burial depth of caprocks does not appear to be an important factor in influencing seal effectiveness. Grunau (1987) presents histograms showing the seal depths of the world's giant oil and gas fields. Almost half of the ultimately recoverable reserves of oil occurs in the 1000–2000 m depth range, and 31% in the 2000–3000 m range. The world totals are, of course, strongly influenced by the Middle East. There are, however, important regional variations. The most striking variations are North America, where over half of the ultimately recoverable oil reserves in giant fields are at depths of <1000 m, and the Far East and Australasia, where, in contrast, 72% is at depths >3000 m. For giant gas fields, the depth distribution is similar at the world level, and regional variations are slightly less strong. As Grunau (1987) points out, deep gas is probably much more abundant in nature than the statistics indicate, but in many cases it is uneconomic to explore for or to develop.

The overall impression, therefore, is that seals may be effective at all depths. The requirement always is that a unit of high displacement pressure and ductility is present over wide areas. This has got little to do with *present-day* depth of occurrence. However, we know that shale pore diameters do decrease with burial, particularly over the first 2 km (see §9.2). The *maximum attained depth of burial* of shale caprocks is, therefore, likely to have an influence on sealing capability. Many shallow oil accumulations occur in structures that have undergone significant uplift, bringing well-compacted caprocks close to

the surface. Provided these caprocks retain their ductility and avoid brittle deformation through the uplift period, there is no reason why they should not be effective caprocks. In the *Duri* field (3.9×10^9 barrels recoverable) of the Central Sumatra Basin, Indonesia, the oil-bearing lower Miocene Bekasap Formation sands occur at depths of only 100 m below ground surface over the crest of the structure, sealed above by lower to mid-Miocene Telisa Formation shales. Furthermore, the overlying Duri Formation reservoirs in the field occur at depths of less than 30 m. The *Minas* field (4.3×10^9 barrels recoverable) in the same basin is deeper, with the lower Miocene Sihapas A-1 sand at approximately 700 m. This reservoir is sealed from younger water-bearing sands in the Upper Telisa by 70 m of Telisa Formation shales.

10.5.3.6 Case study: the Hith anhydrite regional topseal of the central Arabian Gulf

A classic example of the importance of regional seals on the location of oil and gas is provided by the Middle East (Murris 1980) (Fig. 10.46). The two main regional caprocks are the Tithonian Hith anhydrite and the Albian Nahr Umr Shale. The Hith anhydrite is the regional topseal to the prolific Upper Jurassic Arab reservoirs, sealing well in excess of 100×10^9 (billion) barrels of recoverable oil reserves. Not only do prolific accumulations in the underlying Arab reservoirs demonstrate the effectiveness of the Hith anhydrite as a seal, but so also does the general *lack* of accumulations in the overlying Lower Cretaceous where the Hith is present. The Hith is occasionally breached by faulting, allowing upward migration of oil from the Upper Oxfordian–lower Kimmeridgian Hanifa source rock (for example, at Idd el Shargi in Qatar). Oils in Arab reservoirs have been confidently traced back to Hanifa source rocks, using a broad range of geochemical parameters. In the east of the central Gulf area, where, at and beyond the Upper Jurassic shelf edge the Hith is depositionally absent, hydrocarbons generated in the Hanifa have penetrated upwards into Lower Cretaceous reservoirs. Figure 10.47 shows the areal distribution of Upper Jurassic and Lower

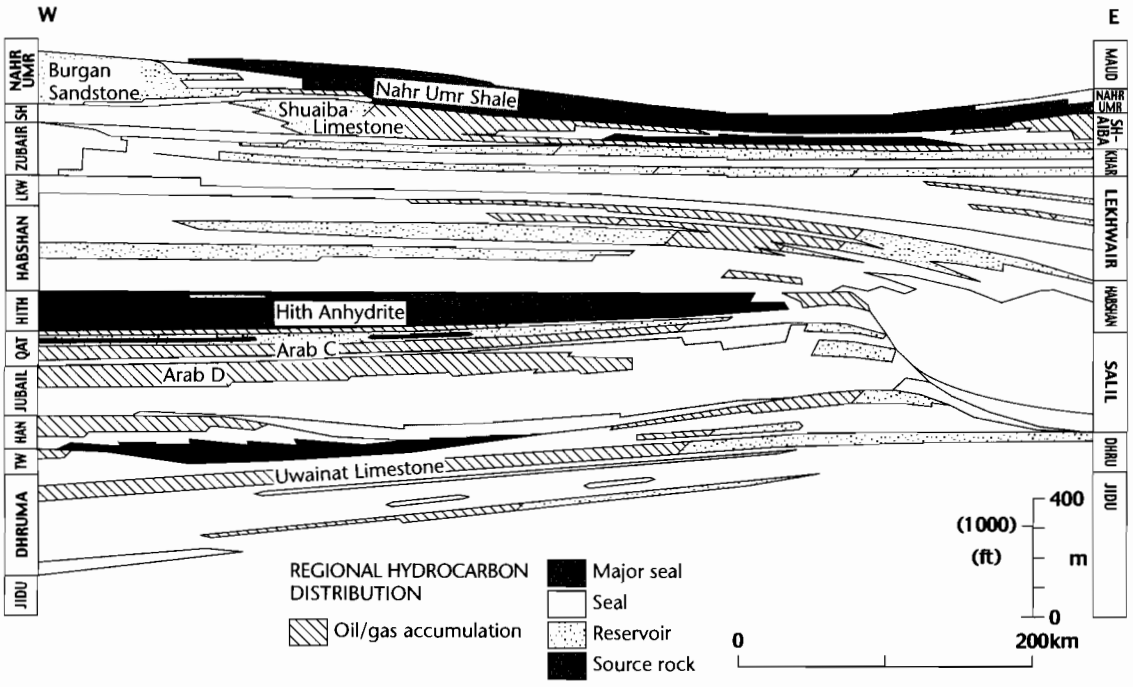

Fig. 10.46 Relationship of oil and gas accumulations to the regional topseals in the Middle Jurassic to Albian sequences, central Gulf area, Middle East (after Murris 1980). The Upper Jurassic Hith Anhydrite seals the prolific underlying Arab reservoirs, which contain over 100×10^9 (billion) barrels of recoverable oil reserves. The Hith anhydrite terminates by facies change towards the Upper Jurassic shelf edge in the east of the area. The oil has been sourced from the Upper Jurassic Hanifa. (Reproduced with permission from Murris 1980.)

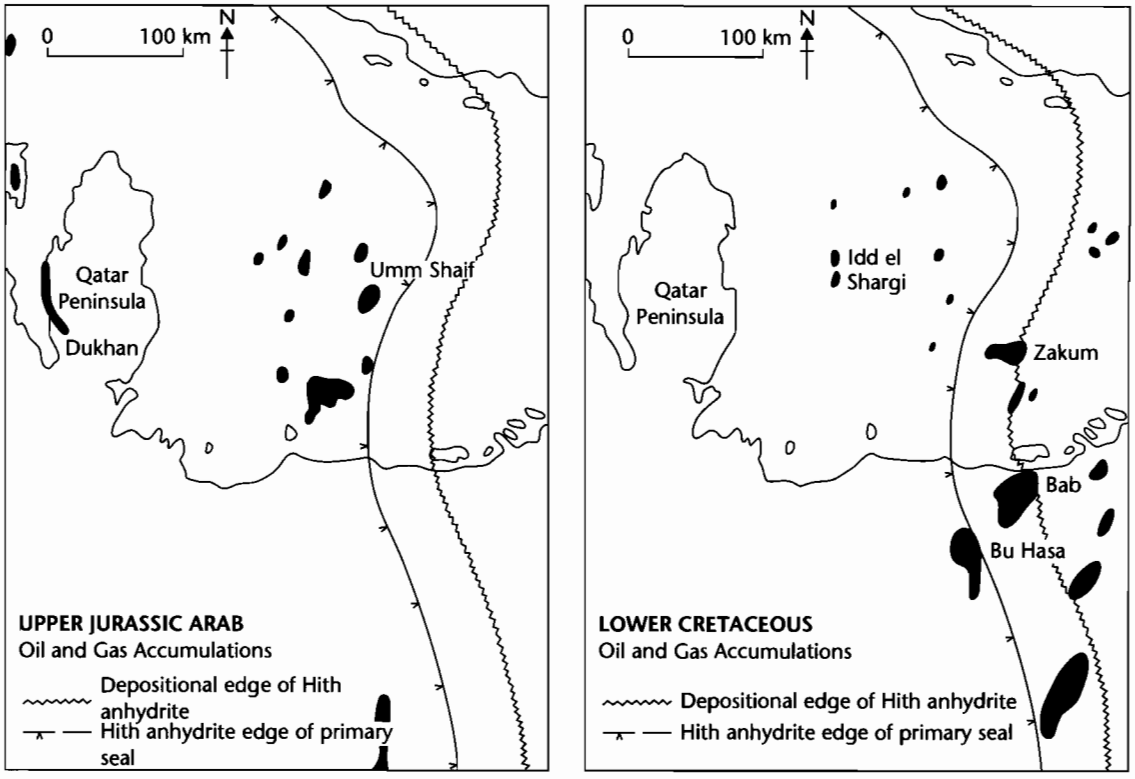

Fig. 10.47 Areal distribution of oil and gas accumulations in the central Gulf area in relation to the Hith anhydrite caprock (adapted from Mums 1980). Arab accumulations are closely related to the occurrence of the Upper Jurassic Hith topseal. Lower Cretaceous accumulations also occur above the Hith where it is locally breached.

Cretaceous accumulations in the central Gulf area, in relation to the main seal edge and depositional edge of the Hith anhydrite. An unknown but probably high proportion of the Lower Cretaceous reservoired oil in the east of the area has been sourced, however, from the Shuaiba source rock, which is mature only in this eastern area. This contribution, therefore, is quite independent of the presence or absence of the Hith anhydrite.

10.5.4 The depositional settings of caprocks

We have seen in the previous pages that the requirements for good regional caprocks are the maintenance of stable lithology and ductility over broad areas. A stratigraphic unit is not a caprock unless it seals an underlying reservoir; thus the ideal regional caprock maintains its sealing characteristics over wide areas but also occurs in stratigraphic association with reservoirs. These conditions are liable to be met particularly in the following two types of depositional setting.

1 *As transgressive marine shales on gently sloping siliciclastic shelves*: these regionally extensive shales may form an excellent seal to basal transgressive sandstone reservoirs. This petroleum play, occurring in the *wedge-base position* of the depositional sequence, as described by White (1980), is a very successful one throughout the world (Fig. 10.48a). The marine transgression may flood wide areas of low-lying coastal flats, and isolate the marine shelf from supplies of coarse clastics. Thus the *transgressive systems tract* (§8.2.3), extending from the time at which the paleoshelf begins to be onlapped, to the time of sea-level

highstand, is frequently an ideal location for the development of regional caprocks. However, sandy transgressive systems tracts, which line the lower depositional sequence boundary, may act as "thief-zones", allowing the migration up-dip of petroleum. The correct prediction of shales in the transgressive systems tract is therefore essential. An example of an excellent and extensive transgressive marine shale caprock is the lower-mid Miocene Telisa Formation of the highly productive Central Sumatra Basin, Indonesia. Over 12×10^9 barrels of recoverable oil reserves have been discovered in this basin, much of it as a result of the development of the Telisa shale regional topseal. The Telisa is a marine shelf unit deposited as a result of the flooding of lower Miocene sand-rich deltas (for example, the Bekasap-Duri and Sihapas deltas). In this way, a prolific reservoir-topseal doublet was formed.

2 *As evaporitic deposits on regressive supratidal sabkhas and in evaporitic interior basins*: in siliciclastic systems, the regressive wedge-top deposits (*sensu* White 1980) (Fig. 10.48b), or the late highstand systems tract or shelf margin wedge systems tract (see §8.2.3) are of generally poor seal quality, comprising shallow marine and coastal sands and

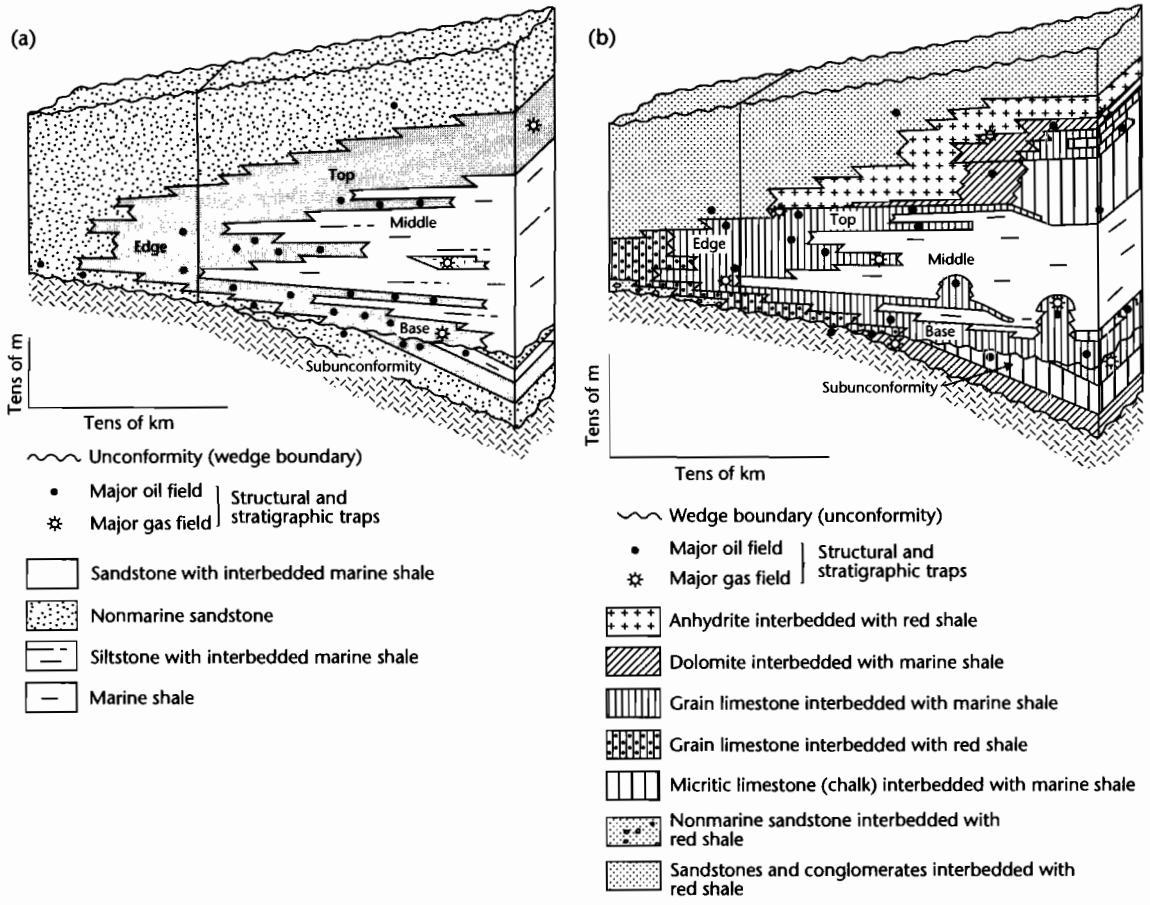

Fig. 10.48 (a) Distribution of facies in the sand–shale wedge of White (1980), corresponding to a continental to marine siliciclastic depositional sequence. Wedge-base, wedge-edge, wedge-middle, wedge-top, and subunconformity positions may be identified; (b) Distribution of facies in the carbonate-shale wedge of White (1980), corresponding to an arid continental-peritidal to shallow marine carbonate-evaporite depositional sequence. A prominent feature is the thick evaporite unit in the wedge top, which may form an excellent regional topseal.

nonmarine deposits. These may form excellent reservoirs, but they do not make good seals. In carbonate systems, however, extensive evaporitic sabkhas may gently prograde across flat marine carbonate platforms, providing extensive and excellent quality seals. The Tithonian Hith anhydrite of the Arabian Gulf is a good example (Murris 1980). As the climate became arid in the Tithonian, the shallow carbonate platform in which the prolific Arab reservoirs were deposited was replaced by an extensive sabkha (§10.4.2).

Evaporites develop through the interaction of paleoclimate and paleogeography. They may develop on supratidal sabkhas (§8.5.3), in evaporitic continental interior basins (§8.5.2) or in wide rifted basins during the early stages of seafloor spreading (§8.5.2) (e.g., the Albian salt of the South Atlantic). Clear paleoclimatic and paleogeographic controls can normally be determined. Shale caprocks may be deposited in a wider range of depositional environments, ranging from lacustrine (§8.5.2) through marine shelf (§8.5.4) to bathyal (§8.5.5).

10.6 THE TRAP

Summary

The final requirement for the operation of an effective petroleum play is the presence of traps within the play fairway. A trap represents the location of a subsurface obstacle to the migration of petroleum towards the Earth's surface, which causes its local concentration. The petroleum exploration industry is primarily concerned with the recognition of these sites of petroleum accumulation.

Traps are classified into structural, stratigraphic, and hydrodynamic traps.

Structural traps are those caused by tectonic, diapiric, gravitational, and compactional processes, and represent the habitat of the bulk of the world's already discovered petroleum resources. The development of most structural traps can be understood in terms of basin-forming mechanics and the ensuing burial history of the basin-fill. Examples are the contractional folds of the Zagros fold belt of Iran and the Wyoming–Idaho fold–thrust belt, the inversion anticlines of Sumatra, the extensional tilted fault blocks of the North Sea, the extensional rollovers and fault traps of the Niger Delta and US Gulf Coast, the compactional drape anticlines of the North Sea, and the salt domes and related diapiric structures of the Gulf Coast. The majority of the world's giant oil fields have so far been found in anticlinal structural traps.

Stratigraphic traps are a diverse group in which the trap geometry is essentially inherited from the original depositional morphology of, or discontinuities in, the basin-fill, or from subsequent diagenetic effects. Large volumes of *undiscovered* petroleum may reside in stratigraphic traps, and their discovery will require a very high level of geological expertise. Examples of stratigraphic traps are the fluvial channels and barrier bars in the Cretaceous basins lying along the east flank of the Rockies, the Tertiary submarine fans of the North Sea; the carbonate reefs of the western Canadian Devonian, southern Mexico and Arabian Gulf; the subunconformity truncation traps exemplified by the Prudhoe Bay (Alaska) and East Texas fields; and the subunconformity paleotopographic traps of the Gulf of Valencia, Spain. Diagenetic traps include those formed by mineral diagenesis, petroleum tar mat formation, and permafrost and gas hydrate formation.

Hydrodynamic traps are those formed by the movement of interstitial fluids through basins and, in a worldwide context, tend to be relatively uncommon. Hydrodynamic effects, however, are important in some foreland basins.

Not only must a sealed trap geometry be present for the existence of a petroleum trap, but the timing of its development must also be considered. The geometry must be present prior to the petroleum charge in order to trap petroleum. Thus, an understanding of the history of individual trap growth, together with the burial and thermal history of the basin, is essential to the evaluation of petroleum prospects.

10.6.1 The formation of traps for petroleum: introduction

The final requirement for the operation of an effective petroleum play is the presence of traps within the play fairway. A trap exists where subsurface conditions cause the concentration and accumulation of petroleum. After petroleum is generated and expelled from source rocks, it will move from sites of high potential energy to sites of low potential energy. This process ultimately leads to the loss of the petroleum at the Earth's surface. Subsurface traps *en route* may be considered local (and temporary) potential energy minima. In these places, the migration route of petroleum is obstructed.

The commercial exploitation of petroleum resources depends on the concentration and accumulation of petroleum in traps. The petroleum industry has been

dominated by exploration for specific subsurface geometries that are diagnostic of the presence of a trap. The recognition of these geometries, frequently on seismic sections, has been the goal of explorers for decades. The same basic physical principles apply to trapping as to secondary migration and seals. A trap is formed where the capillary displacement pressure of a seal exceeds the upward-directed buoyancy pressure of petroleum in the adjoining porous and permeable reservoir rock (§10.3.2.4 and §10.5.2).

Both oil and gas may occur in a trap; the gas lies above the oil because it is less dense. If a trap is charged first with oil, and then with gas (for example, as a result of increasing source rock maturity), the expanding gas cap may displace oil downwards past the spill point(s) of the trap. The oil may then migrate up-dip to the next available trap. Thus, traps may contain greater proportions of oil relative to gas as the distance from the source kitchen increases. This is the so-called *Gussow principle.*

Figure 10.49 shows some terms commonly used in the description of traps. Note that the trap illustrated is not full-to-spill. A *gas cap* overlies an *oil leg*, but the (structural) spill point is some distance below the *oil–water* contact.

10.6.2 Trap types

The main purpose of trap classification is to allow comparison between one prospect, or one play, and another. A particular trap type in a basin may be characterized by a distinctive field size distribution and drilling success ratio. Trap classification (Table 10.6) more readily allows the drawing of geological analogies which may be useful in estimation of prospect and play petroleum volumes and risk. The main subdivision is between *structural traps*, in which the majority of the world's petroleum resources have been found, and *stratigraphic traps*. The classification is based essentially on the *process* causing the formation of the trap, rather than its geometry. If the geological processes operating in a basin are known, therefore, a particular suite of traps may be predicted. Particular structural traps, for example, can be related to tectonic setting and basin-forming mechanics (Chapters 3–6). The detection of stratigraphic traps, on the other hand, is dependent on a good understanding of basin evolution and the stratigraphy of the basin-fill (Chapters 7–9).

Table 10.6 Classification of trap types based on the process causing trap formation, rather than trap geometry.

Structural	Tectonic	Extensional
		Contractional
	Compactional	Drape structures
	Diapiric	Salt movement
		Mud movement
	Gravitational	
Stratigraphic	Depositional	Reefs
		Pinch-outs
		Channels
		Bars
	Unconformity	Truncation
		Onlap
	Diagenetic	Mineral
		Tar mats
		Gas hydrates
		Permafrost
Hydrodynamic		

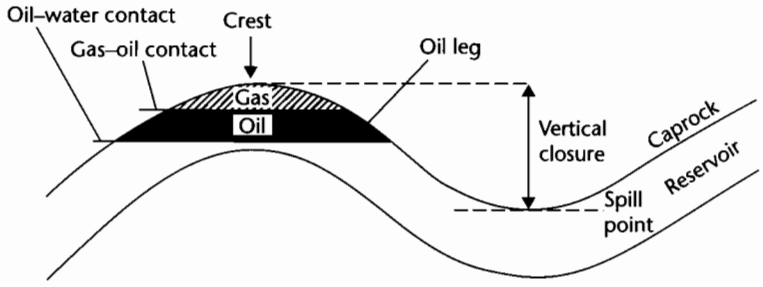

Fig. 10.49 Terms commonly used in the description of traps. A gas cap overlies an oil leg, and the trap in this case is not filled down to its structural spill point.

Structural traps are those caused by tectonic, diapiric, gravitational, and compactional processes. The essential point is that movement has occurred in the basin-fill some time after its deposition. *Stratigraphic traps* are those in which the trap geometry is inherited from the original depositional morphology of the basin-fill, or from diagenetic changes that took place subsequently. The best-known stratigraphic traps are caused by facies change or related to unconformities, but we have also included here traps sealed by the up-dip clogging of pore-space by biodegraded oil, gas hydrates or permafrost. *Hydrodynamic traps* are caused by the flow of water through a reservoir/carrier bed. They may be important in some basins, but are generally rare. More than one process may contribute towards the formation of a trap. Examples are hydrodynamic closures developed on structural noses, onlap, and pinch-out traps combined with structural deformation, and channel sands developed on unconformity surfaces. Furthermore, different trap types may be genetically related. A reef, for example, may be overlain by a compactional (drape) anticline.

10.6.2.1 Structural traps

STRUCTURAL TRAPS FORMED BY TECTONIC PROCESSES

Contractional folds and thrust-fault structures

Contractional folds occur in areas undergoing tectonic compression, and are generally associated with convergent plate boundaries, particularly where continent–continent collision has taken place (Chapter 4). They may also develop where transpression occurs along strike-slip boundaries (Chapter 5).

From a petroleum viewpoint, the most prolific zone of contractional folding is the external zone of the *Zagros Mountains in Iran* (Falcon 1958; Hull and Warman 1970) (Fig. 10.50). The main producing reservoir is the lower Miocene Asmari Limestone, which owes its prolific productivity to tectonically induced fracturing. The brittle limestone reservoir is overlain by the ductile evaporite caprocks of the Miocene Lower Fars Group. The folds

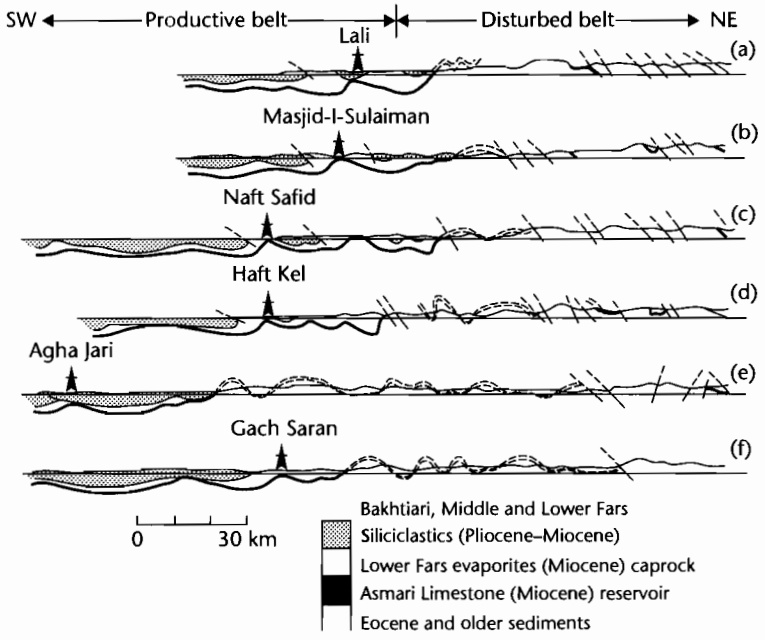

Fig. 10.50 Cross-sections across the Zagros foldbelt of Iran (after Falcon 1958). The folds are large and, at surface, relatively simple. The main producing reservoir is the lower Miocene Asmari Limestone; it has been tectonically fractured, and is sealed by the ductile Lower Fars Group evaporites.

are up to 60 km long and relatively simple where dramatically exposed in outcrop. At depth, however, they are considered to be tighter and associated with thrust faults which sole out onto a basal detachment (Fig. 10.51), possibly in the Hormuz Salt.

Another example of an area of productive contractional fold structures is the *Wyoming Thrust belt*, USA. The Painter reservoir field (Lamb 1980), discovered in 1977, is a large overturned anticline developed in the hanging wall of the Absaroka Thrust (Fig. 10.52). The producing reservoir is the Triassic–Jurassic Nugget Sandstone, which has been thrust over the Cretaceous. The field was found in a seismically defined structure along trend and 16 km south of the previously discovered Ryckman Creek field, which also produces from the Nugget. As can be seen from Figure 10.52, the Painter structure has no surface expression because it is overlain by the Bridger Hill detachment and a Cretaceous unconformity. It owes its discovery to an improvement in seismic processing techniques in the mid-1970s, which allowed subsurface closure to be detected.

Surface outcrop lithology and terrain have a large influence on the quality of seismic data in fold–thrust belts. Subsurface accumulations may be very difficult to find in those areas where surface structure bears little or no relation to subsurface structure, and where surface or subsurface conditions (karstified limestone, volcanics, rugged terrain) prevent the acquisition of good-quality seismic data.

Anticlines may also develop in areas of local contraction along strike–slip systems. The Wilmington field in the Los Angeles Basin, California, is such an example (Mayuga 1970). It is developed along the San Andreas Fault system. Transpressional anticlines are arranged *en echelon* and are very strongly faulted: they depend on the presence of thick caprocks to seal reservoirs across fault planes. Other examples of highly complicated faulted anticlines that have developed along predominantly strike–slip fault systems are probably the large Seria and Champion fields of Brunei. These fields are located on the relatively proximal part of the Miocene–Recent Baram Delta, and are not only subdivided into a large number of fault compartments but also contain numerous stacked deltaic reservoirs. Some component of shale diapirism is present in the development of Champion.

Some contractional anticlines have developed as a result of the reversal of movement along old extensional faults (see Cooper and Williams 1989). These are known as *inversion anticlines*. The evidence for the earlier extensional history is usually the thickening of sediments towards the fault plane during its period of growth. Good examples are the so-called "Sunda" folds of some Indonesian basins, for example, central Sumatra. Inversions tend to occur in areas where relatively subtle

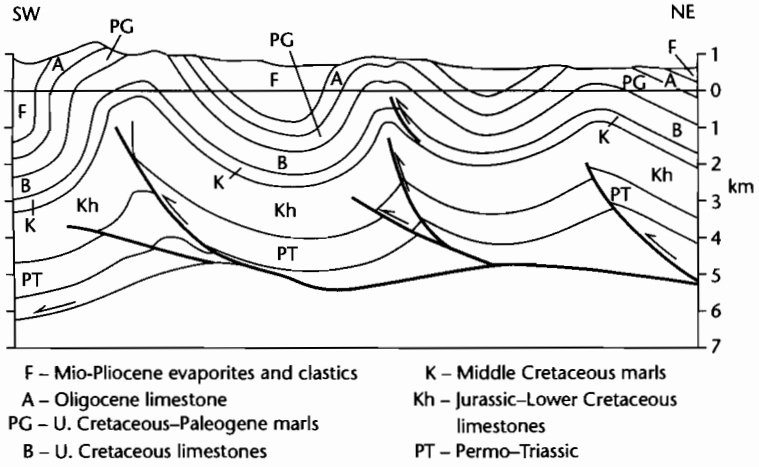

Fig. 10.51 Interpretation of the relationship of Zagros folds to structure at depth, showing the soling out of the thrust faults onto a basal detachment (after Bailey and Stoneley 1981). Similar listric fault styles typify the thrust belts of the western United States (e.g., Idaho–Wyoming) and the Canadian Rockies of Alberta and British Columbia.

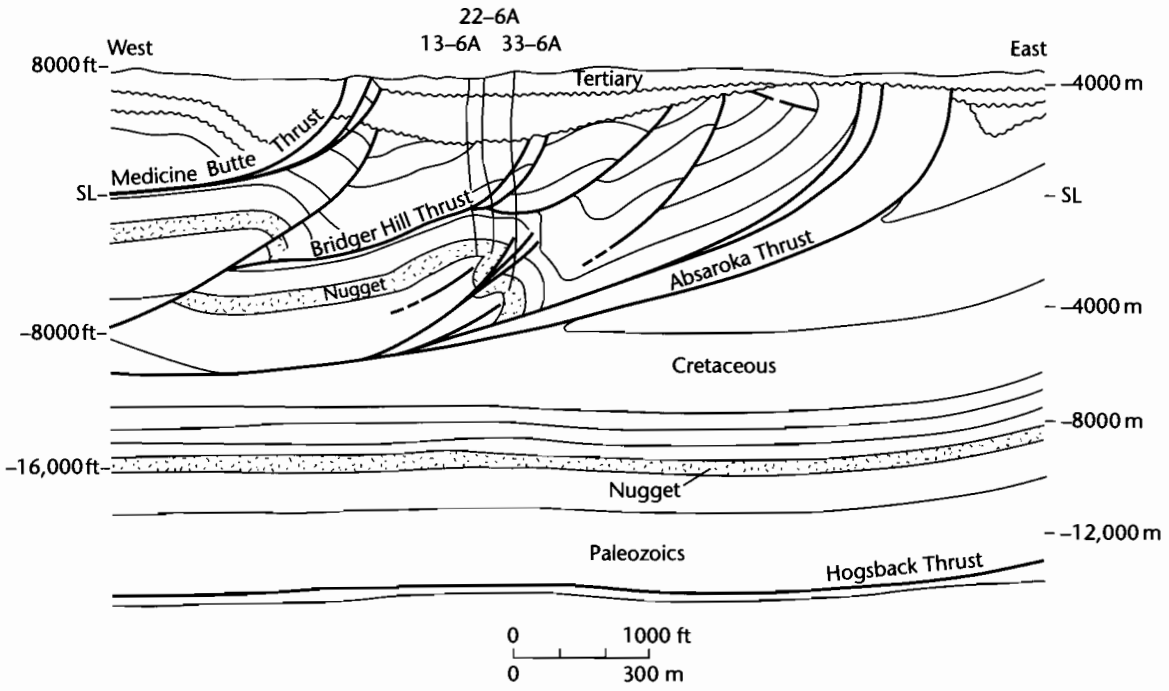

Fig. 10.52 Interpretation of the structure of the Painter Reservoir Field, Idaho–Wyoming thrust belt. The Painter structure has no surface expression, but was identifiable from seismic data. The producing reservoir is the Triassic–Jurassic Nugget Sandstone.

changes in the regional stress field cause reversal of movement along faults, and are therefore frequently associated with fault systems that have a strong strike–slip component. Petroleum charge into inversion anticlines may be a problem if a closure did not exist at the time of extension. Migration will tend to be away from the site of the inversion anticline during the extensional phase, and inversion of the basin tends to stop further petroleum generation. Charge may result from the postinversion remigration of petroleum.

Traps may develop along contractional faults without any element of folding (Fig. 10.53). These may be in the hangingwall or footwall of the fault, and depend for closure on the juxtaposition of sealing lithologies, or on the sealing of the fault zone itself, for example as a result of a finely powdered fault gouge or cemented zone. To complete the trap, closure is also needed in the third dimension, i.e., into the plane of the paper in Figure 10.53. This is frequently produced by slight curvature or angularity in the map view of the fault plane, or by the intersection by further faults.

The footwall has sometimes provided an exploration target in thrust belts. These traps are very difficult to define, mainly due to velocity variations caused by the presence of the overthrust sheet, which make seismic interpretation very difficult. Many dry holes have been drilled on velocity "pull-ups" in subthrust positions – mere illusions of the presence of a trap.

Extensional structures

Extensional structures form a very important group of traps, being responsible for many of the fields discovered in basins that have experienced a phase of rifting in their geological history (Chapter 3). We will deal in this section only with structural traps resulting from extension of the basement, that is, in stretched rift basins. The extensional structures occurring, for example, in delta sequences that developed in the postrift stage on passive margins are covered in the section on gravitational structures.

Rollover anticlines may develop in association with basement-controlled growth faults. The Vicksburg flexure

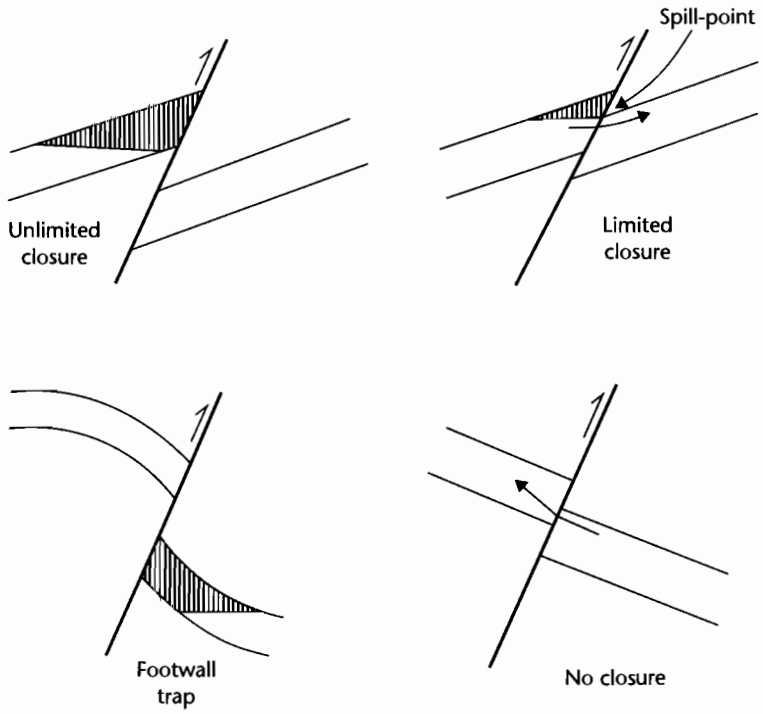

Fig. 10.53 Traps formed by high-angle reverse (contractional) faults. Juxtaposition of permeable bed limits closure. For maximum closure, fault throw needs to be large in relation to reservoir thickness. All of the illustrated trap types also require closure in the third dimension, that is, into the plane of the paper. After Bailey and Stoneley (1981).

in south Texas is an example. Very large sediment thickness changes occur across the fault zone, particularly in the Oligocene section. Large quantities of oil and gas are trapped in rollover anticlines, fault traps, and stratigraphic pinch-outs.

The most prolific play in the East Shetland Basin of the North Sea province occurs in extensional *tilted fault blocks*. The giant Statfjord field (*c.* 3 billion barrels recoverable), the largest in the North Sea, contains Lower Jurassic Statfjord Formation sandstone reservoirs in a large, westward tilted fault block that has been eroded at its crest to produce a series of Late Jurassic so-called "Kimmerian" unconformities (Kirk 1980) (Fig. 10.54). Block faulting is responsible for the uplift and erosion of the east flank of Statfjord. The fault block is onlapped by Upper Jurassic Kimmeridgian source rocks, which, together with Lower Cretaceous shales, form the caprocks to the field. The source rocks were deposited in a restricted basin to the west that was bounded to the east by the uplifted Statfjord block, and to the west by the Hutton/Murchison block.

The main down-to-the-east bounding fault on the east flank of Statfjord has a total displacement of over 1800 m at Statfjord Formation level, and also controls the location of the giant Brent field, only 20 km and on trend to the south. The Statfjord field has a total areal extent of 81 km^2. The trap is a result of truncation of the Brent reservoir at the unconformity surface, and could be considered as stratigraphic. The Statfjord reservoir, however, relies on fault closure. The field is therefore a huge combination structural–stratigraphic trap.

The Ninian field to the southwest is another of the many examples in the East Shetland Basin of this style of trap – the eroded rotated fault block (Albright et al. 1980). As in the Brent Formation reservoir in the Statfjord field, the trap at Ninian is produced primarily by the truncation of Mid-Jurassic reservoirs at Upper Jurassic and Cretaceous unconformities (Fig. 10.55).

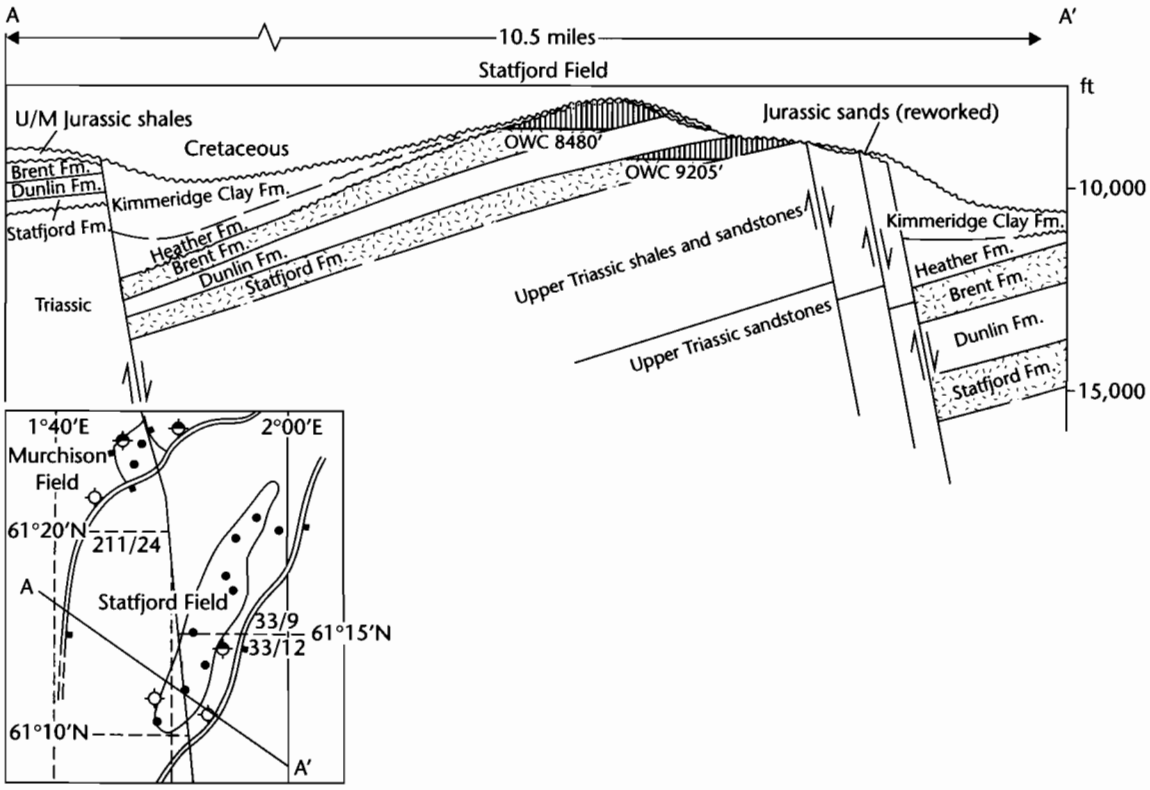

Fig. 10.54 Schematic structural cross-section across the Statfjord Field, North Sea (after Kirk 1980). Statfjord is a large westward-tilted fault block that has been strongly eroded at its crest. The trap at Brent Formation level is formed by seal at the erosional unconformity, but the deeper Statfjord Formation reservoir depends on fault closure.

Several varieties of extensional fault trap are shown diagramatically in Figure 10.56; closure is dependent on the juxtaposed lithology. It is clearly advantageous for the throw of the fault to exceed the gross reservoir thickness. The sealing or nonsealing properties of the fault plane itself are discussed in the section on gravitational structures. It is important to consider the juxtaposed lithology over the whole length of the fault trap. An "Allan" fault plane map (Allan 1980) shows the intersection of both footwall and hangingwall lithostratigraphic units onto the fault plane. In Figure 10.57, the intersection of the spill point of the footwall reservoir onto the hangingwall is at 1720 m; closure might have been mapped down to 1740 m had the geometry of the hangingwall been ignored, resulting in an overestimation of the size of the trap. A more complicated schematic is shown in Figure 10.58; petroleum migrates several times across the fault plane to higher structural levels.

Gravitational structures

The most important gravitational structure that forms petroleum traps is the rollover anticline into listric growth faults, occurring particularly in delta sequences. These structures are not caused by extension in the basement, but are due to instability in the sedimentary cover and its movement under gravity. They are most prone to form where a level of undercompacted (overpressured) clays or ductile salt occurs at depth, into which the growth faults sole out, and which is overlain by a thick succession of more competent sedimentary rocks. These conditions are commonly created in thick, progradational delta sequences, as in the Gulf of Mexico and Niger Delta (Fig. 10.59).

The roll-over anticline is the least risky trap for petroleum. Growth faulting may also give rise to *fault traps*. The integrity of the trap depends on the juxtaposition of a

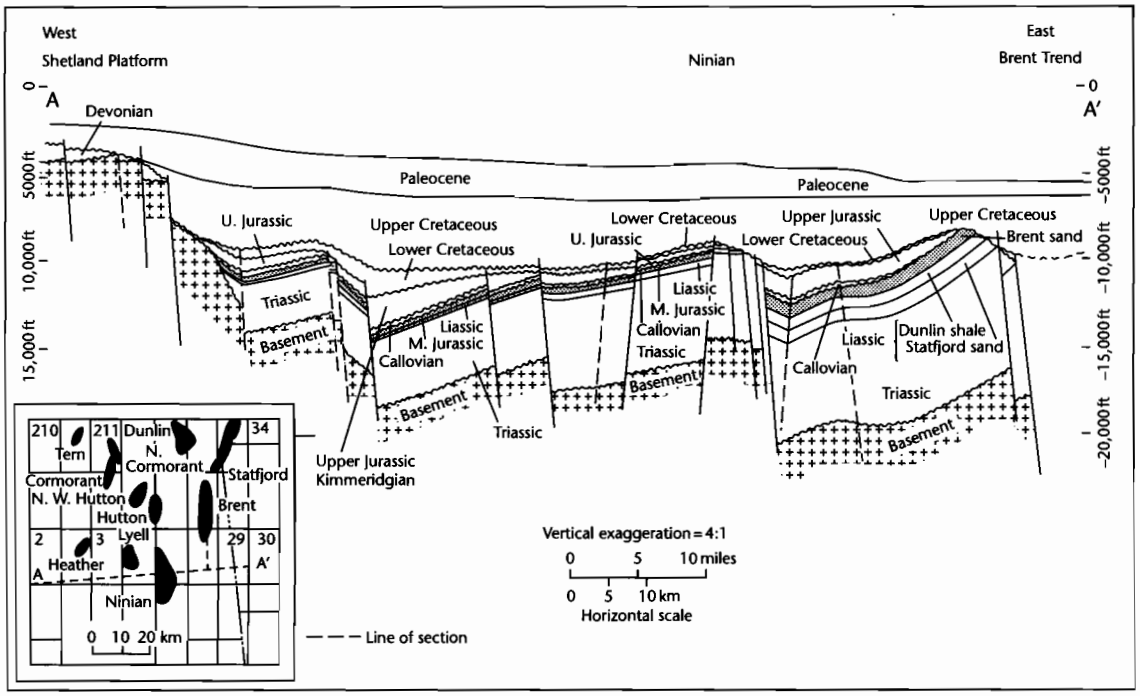

Fig. 10.55 Structural cross-section across the eroded, tilted fault blocks of the Ninian area, East Shetland Basin, North Sea (after Albright et al. 1980). This is a common and successful trap type in the North Sea.

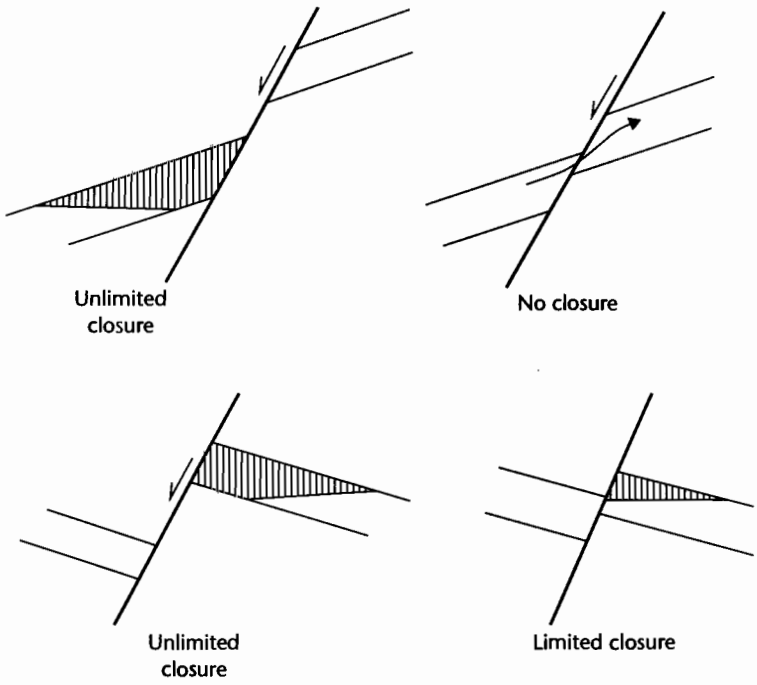

Fig. 10.56 Traps formed by extensional faults (after Bailey and Stoneley 1981). Seal depends on the lithologies juxtaposed against the reservoir across the fault plane. Ideally, fault throw should exceed gross reservoir thickness.

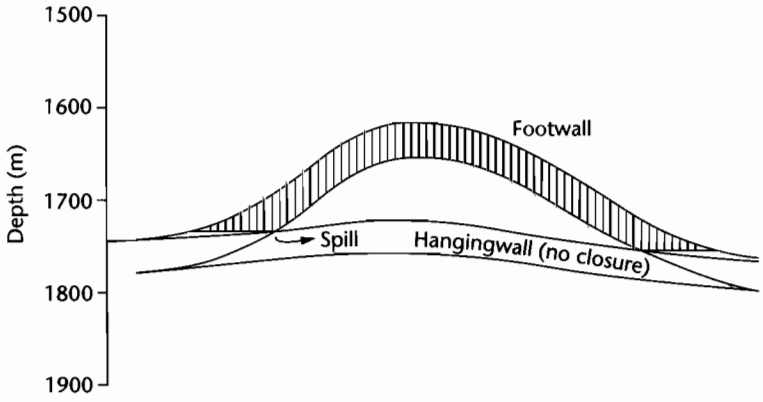

Fig. 10.57 Simple "Allan" fault plane map showing intersection of permeable lithological units in footwall and hangingwall onto fault plane. The actual spill point may lie at a position above the mapped closure in the footwall, and is controlled by the geometry of the hangingwall.

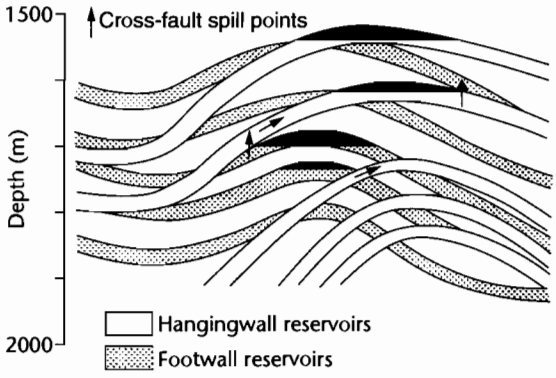

Fig. 10.58 "Allan" fault plane map showing intersection of reservoir strata in footwall and hangingwall to the fault plane. These intersections determine the spill points at each reservoir level. Petroleum may migrate several times across the fault plane, each time moving to higher structural levels.

shale seal across the fault plane, so these traps tend to be effective on those parts of the delta where the sand/shale ratio is relatively low (say, less than 50%). Even here, many of the sands may be water-bearing owing to cross-fault leakage; production may be obtained from relatively few sands, interspersed with the water-bearing zones, and distributed over a large gross vertical interval.

The fault zone itself may or may not seal. Slivers of sand tend to get caught up in the fault zones on the Niger Delta, allowing vertical leakage of petroleum (Weber et al. 1978). Although destroying fault traps at deeper levels, this leakage may allow a petroleum charge into shallower reservoirs. Other faults off the Niger Delta are sealing because of clay smears along the fault plane (Weber et al. 1978). Smith (1980) has investigated fault seal in the Louisiana Gulf Coast, and found that some faults seal even when sandstones are juxtaposed across the fault zone, as long as the sands are of different ages. This is due to the presence of fault-zone material that has formed as a result of mechanical or chemical processes directly or indirectly related to the faulting. Where parts of the *same* sandstone are juxtaposed, the fault tends *not* to seal. Where sand is juxtaposed against shale, a seal is produced.

At shallow depths (a few hundred m), extensional faults may form open conduits for petroleum; at greater depths, they are likely to be forced closed by overburden pressure. It is reasonable to expect that the likelihood of a fault zone providing a high permeability conduit for petroleum leakage is enhanced: (i) at shallow depths, (ii) in tensional settings, (iii) during periods of fault movement, and (iv) where reservoirs are overpressured. At depth and in active compressional settings, fault zones are very unlikely to provide a pathway for petroleum migration. In the absence of well-understood local circumstances, it is best for the practicing petroleum geologist to evaluate a fault trap on the basis of the juxtaposed lithology alone, that is, assuming the fault zone allows lateral but not vertical migration.

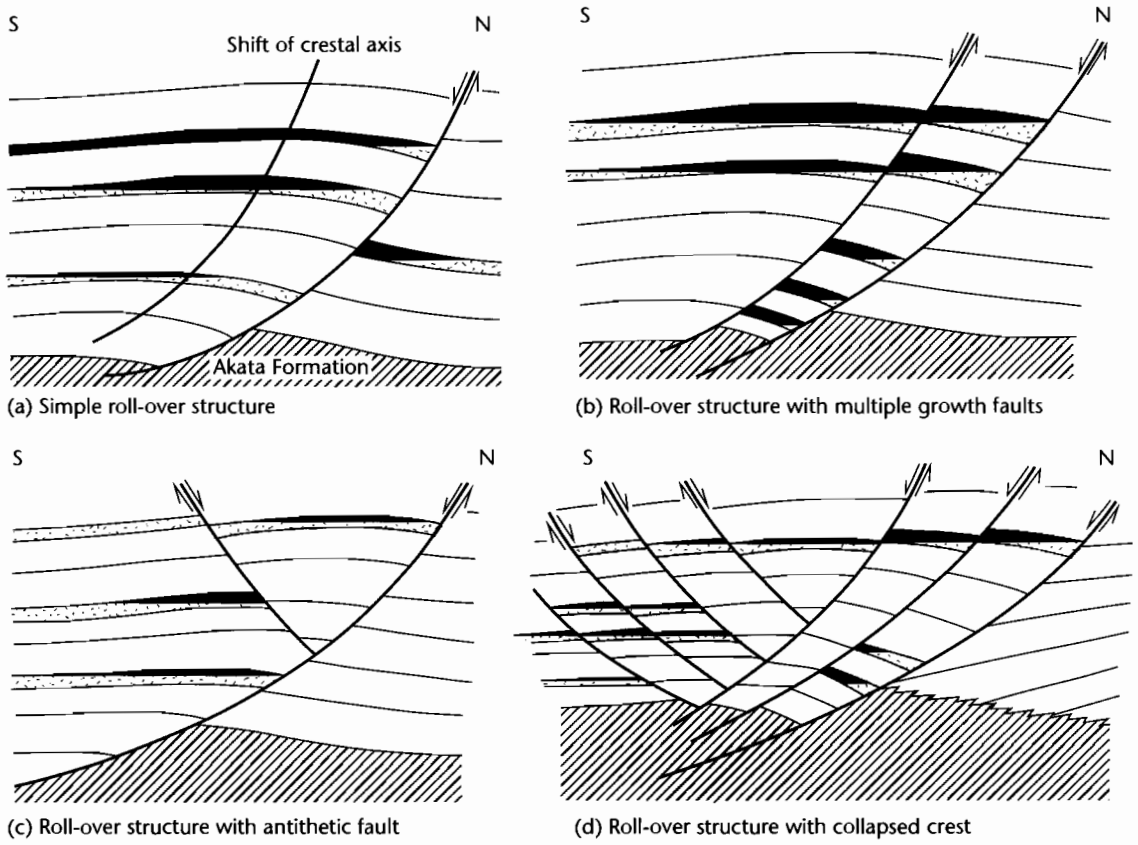

Fig. 10.59 Varieties of roll-over structure forming petroleum traps in the Niger Delta area (after Weber et al. 1978). Only a few reservoir sands are shown in the schematic sections and the sand thickness has been enlarged.

A further trap that may form as a result of gravitational processes is the *ramp anticline* at the front of *gravitational thrust sheets*. When sheets of detached sediment slide downslope, they may pile up at local obstructions, forming contractional anticlinal features. These occur particularly on deep water delta slopes.

Compactional structures

The most important trap type formed by compactional processes is the drape anticline (Fig. 10.60), caused by differential compaction. The presence of a basement horst (effectively noncompactible) causes significant thickness variations in the overlying highly compactible sediments. As these compact, drape features are formed because the absolute amount of compaction is greatest where the sediment is thickest.

If the area above the horst remains elevated relative to surrounding areas, shallower water sedimentary facies may develop that are less compactible than the surrounding muds. This will exaggerate the differential compaction. The sedimentary facies and diagenetic history of the reservoir unit may be quite different over the crest of the drape anticline than off its flanks.

Drape anticlines form a very successful trap type. They are frequently simple features formed without tectonic disturbance (unless basement faults are reactivated) and frequently persist over a long period of geological time, from shortly after the time of reservoir deposition through to the present-day. They are therefore available

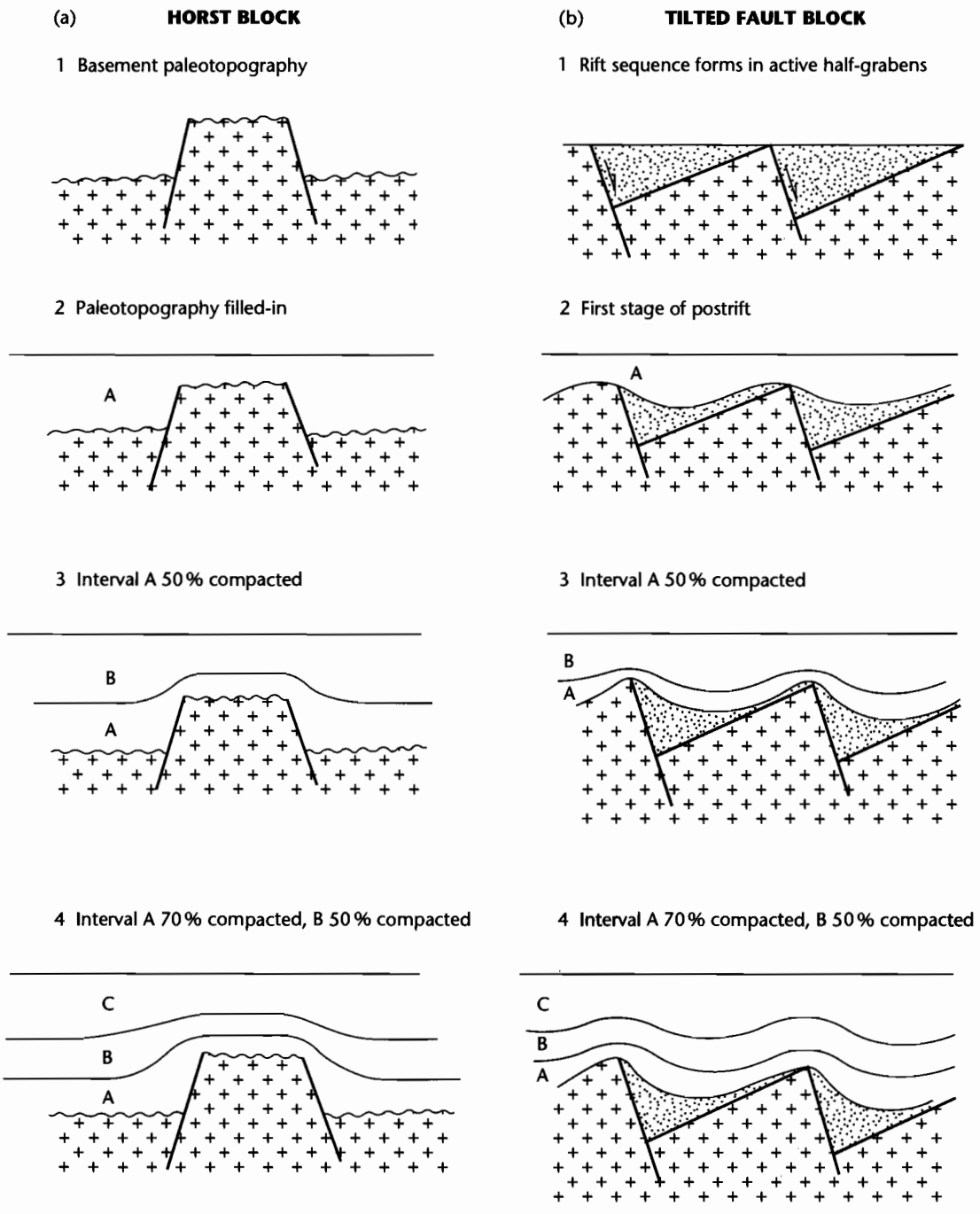

Fig. 10.60 Formation of drape anticline by differential compaction. Relief of anticline increases with depth. Basement topography causes thickness variations in the compactible sediment column. As these sediments compact, drape anticlines are formed.

to trap a petroleum charge over a long time span, and are very forgiving of inaccuracy in estimation of charge timing.

Owing to dependence on the existence of basement topography, drape anticlines commonly form in the passive sedimentary cover to rifted megasequences, particularly over the relatively elevated parts of tilted fault blocks in the prerift (Fig. 10.60b). In these settings, a petroleum charge is frequently needed from synrift or very early postrift source rocks, since the later postrift is commonly devoid of a source. Communication of the reservoir with the source is often, therefore, the critical factor for this play. A second critical factor may also be the presence of a reservoir in the postrift. Since a considerable amount of crustal thinning is the cause of the basement topography that forms the drape anticline, these areas commonly subside rapidly due to thermal contraction, leading to deep water conditions. The only reservoirs present may be deep-sea fans, as in the Lower Tertiary submarine fans of the North Sea.

Examples of drape anticlines are the Forties and Montrose fields of the North Sea, which occur within very large (90 km^2 and 181 km^2 respectively) low relief domal closures at Paleocene level formed by drape over deeper fault blocks. In the Frigg gas field, the present-day closure on the Eocene submarine fan reservoir is due not only to compaction processes but also to the rejuvenation of Jurassic faults controlling the deeper structure, and to original depositional topography on top of the fan (Blair 1975).

Diapiric traps

Diapiric traps result from the movement of salt or overpressured clay. At depths in excess of 600–1000 m, salt is less dense than its overburden, and liable to upward movement through buoyancy. Salt can flow at surprisingly low temperatures and over long periods of geological time. Once a density inversion is present, heterogeneities in either the mother layer of salt or clay, or in the overburden, are sufficient to trigger upward movement. Examples of heterogeneities are lateral changes in thickness, density, viscosity, or temperature. These changes may be essentially depositional or may be imposed as a result of faulting or folding. In extensional faulted zones, diapirs tend to form through buoyancy where overburden load is most reduced in the footwall. The salt rollers of the US Gulf Coast are examples of this triggering mechanism (Fig. 10.61). Faulting may be basement-involved, or thin-skinned, usually soling out in the ductile layer. This layer may also provide a zone of detachment in contractional areas. Differential loading of a salt layer by thick overlying sediments is a powerful triggering mechanism of diapirism in young shallow delta sequences (Fig. 10.62).

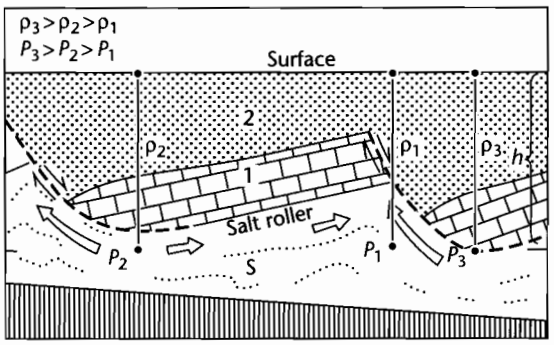

Fig. 10.61 The formation of a salt roller by extensional faulting may trigger the buoyant rise of salt (after Jackson and Galloway 1984). ρ_1, ρ_2 and ρ_3 are sediment column densities, P_1, P_2, and P_3 are pressures at three locations, h is the maximum overburden height (in the hangingwall of the fault) on the top of the salt (S). Overburden pressure is relaxed in the footwall (position P_1) as a result of the extension.

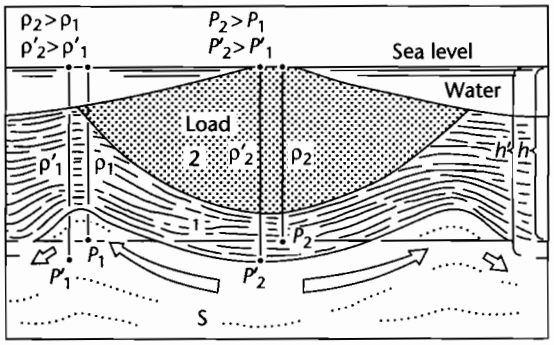

Fig. 10.62 Triggering of salt movement as a result of differential loading by a body of dense sediment. ρ_1, and ρ_2 are the sediment densities prior to movement, exerting pressures P_1 and P_2 at the flank and at the centre of the load respectively. Increased pressure on the salt under the load (P'_2) relative to the pressure at the flank (P'_1) causes lateral and upward displacement towards the lateral diapirs. h and h' are the initial and subsequent depths at which pressures are considered. These conditions commonly occur in young delta sequences (after Jackson and Galloway 1984).

Stages in the growth of salt structures

Salt structures pass through three stages of growth (Fig. 10.63):

- *The pillow stage*, characterized by the thinning of sediments over the crest of the pillow, and thickening into the adjacent *primary peripheral sink*. No piercement or intrusion of the overlying sediments has taken place. Depositional facies are affected by pillow growth, with higher energy facies, perhaps reefs, developing over the crest. Traps formed at this stage are typically broad domes, while sediments that have been channeled into the topographically low peripheral sink may pinch out pillow-wards, forming stratigraphic traps;
- *the diapir stage*, when the salt body pierces the overburden. These structures are known as salt piercement structures. As the pillow withdraws to form the diapir, *secondary peripheral sinks* may develop close to the diapir, and inside the earlier primary peripheral sinks of the pillow stage. *Turtle structures*, representing thick lenses of sediment that accumulated in the primary sinks subsequently tilted during diapir growth may form petroleum traps. Thick clastics may again pinch out onto the flanks of the diapir, forming stratigraphic traps;
- *the postdiapir stage*. As the diapir grows, a point is reached where the underlying reservoir of salt is depleted, and it can only continue to rise by thinning of its lower trunk or by complete detachment from the mother salt. Overhangs commonly develop. The geometry of the salt diapir and surrounding strata beneath an overhang is generally poorly known. This is due to the fact that the area is in a seismic shadow, and is relatively in-

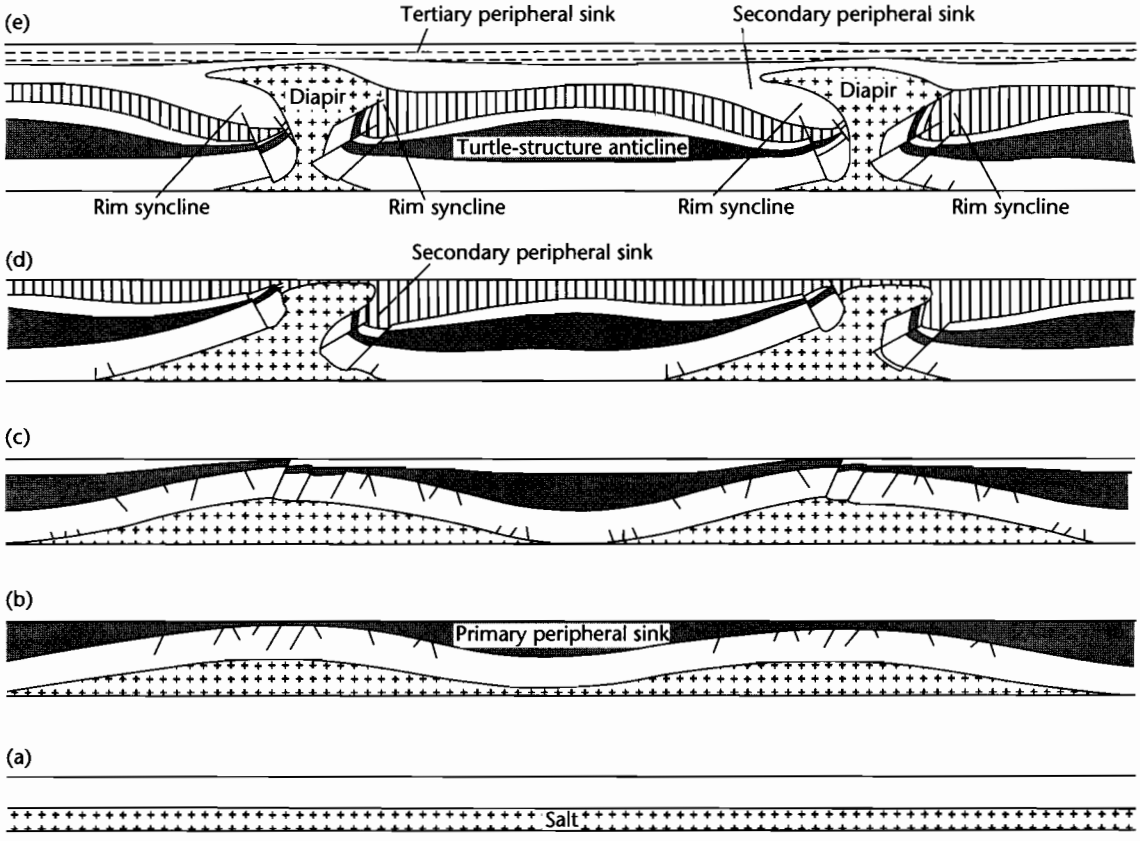

Fig. 10.63 Evolution of salt structures through pillow stage (b) and (c), diapir stage (d), and postdiapir stage (e). Note the lateral migration of peripheral sinks with each stage (from Seni and Jackson 1984). Turtle structures represent the preserved fill of the peripheral sink.

frequently drilled. The typical thickness of a diapir stem is largely unknown. Piercement of salt may take place through to the surface, forming salt domes that are particularly noticeable on Landsat images and aerial photographs, as in north-central Oman.

Trapping potential

Our understanding of the petroleum entrapment possibilities of salt pillows and diapirs has been developed largely through exploration of the Gulf Coast area of the USA. After the Spindletop discovery in 1901, traps associated with salt diapirs became one of the most important and prolific plays in this outstandingly successful hydrocarbon province. The piercement salt diapirs of the Houston Salt Basin were formed by the loading of Jurassic salt with a thick sequence of Mesozoic and Tertiary sediments. Most of the diapirs have intruded to shallow depths, and have created complexly faulted structures. Radial fault patterns are common over the diapir flanks. Reservoirs are commonly broken into a very large number of separate fault compartments. Syndepositional diapir growth caused substantial thickness and facies changes, as well as local erosion. Stratigraphic pinch-out and unconformity traps were formed, and local reef limestone reservoirs developed.

Most production comes from Eocene to Pliocene age sediments overlying and surrounding the salt, and from the diagenetic salt-dome caprock, which directly overlies and is in contact with the salt. The Cap Rock is a calcite deposit with zones of gypsum and anhydrite, formed by the solution of anhydrite-bearing salt by ground waters. Secondary porosity may be very high (>40%), but may be irregularly distributed. The Spindletop (Fig. 10.64) and Sour Lake diapirs have produced 60 to 81 million barrels respectively from Cap Rock reservoirs.

The petroleum trapping possibilities in sediments above and around a mature diapir deposited during its postdiapir stage are shown schematically in Figure 10.65. A variety of further traps, mainly stratigraphic, may develop in the diapir- and pillow-stage sediments (Fig. 10.65). These include structural and combined structural-stratigraphic traps on the crests of turtle structures. A variety of other fault, pinch-out, and unconformity traps are also shown.

In summary, diapiric structures may give rise to a very wide range of petroleum traps of both structural and stratigraphic origin. Although the detection of diapirs on

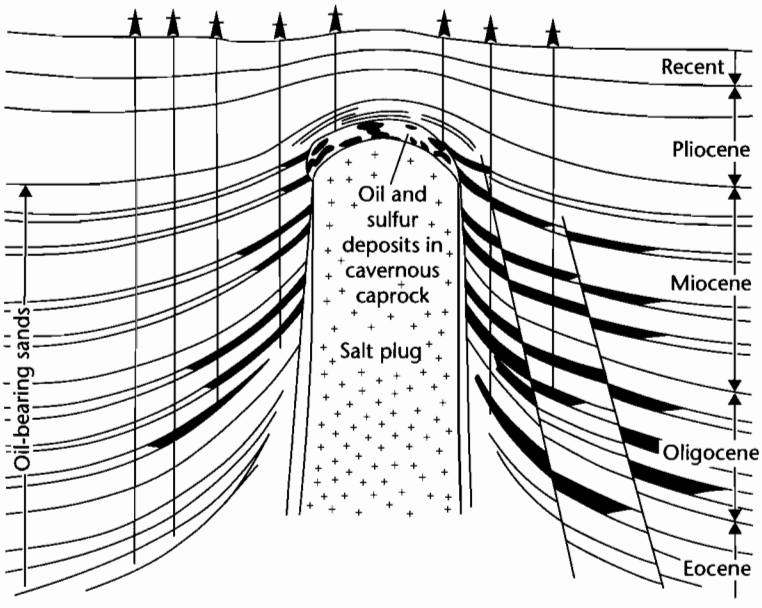

Fig. 10.64 Schematic cross-section through the Spindletop Dome, Texas, showing the distribution of oil reservoirs in both the caprock and on the flanks of the salt plug (after Halbouty 1979).

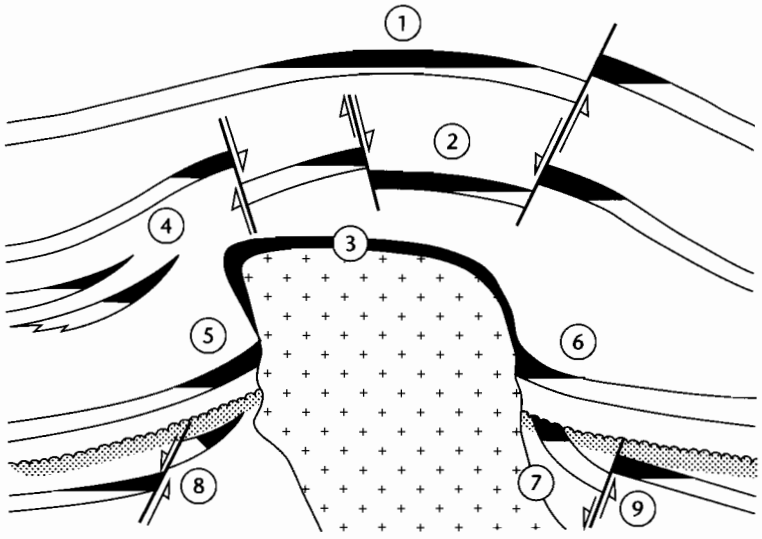

Fig. 10.65 Potential petroleum traps associated with salt diapirs (after Halbouty 1979). A wide variety of stratigraphic and structural traps may develop above and around the diapir, and in its diagenetic caprock. 1, Simple domal trap above the diapir with relatively simple or no associated faulting; 2, Domal trap faulted into graben structures; 3, Diapir caprock reservoir; 4, Stratigraphic up-dip pinch-out caused by facies change into the peripheral sink; 5 and 6, Reservoirs sealed against the diapir wall; 5 is beneath an overhang. 7, Unconformity trap formed by erosion towards the diapir crest; 8 and 9, Fault traps in the flanking area.

seismic sections is not difficult, trap development above and around the diapir is frequently very complex, and individual reservoir units may be quite small, owing to rapid lateral facies changes and complex faulting.

Salt diapirism is likely to occur in quite distinct geological settings. Thick salt deposits may develop in enclosed basins subject to cycles of flooding and desiccation. These may occur in the rift and early postrift stages of continental margin development. Examples are the Jurassic salt of the Gulf Coast and Albian salt of the South Atlantic. The occurrence of salt substantially enhances the petroleum resource potential of these provinces.

Mud diapirism

Mud diapirism is most likely to develop in prodelta clay sequences underneath the thick, rapidly deposited regressive sandy sequences of modern and Tertiary deltas. Examples are the Baram (Borneo), Niger (West Africa), Mississippi (USA), and Mackenzie (Arctic Canada) deltas. Excess pore pressure builds up in these clay sequences because low permeability prevents the expulsion of sufficient pore fluids as the sediment undergoes compaction (§9.2). The overpressure lowers the strength of the sediment and promotes ductile flow.

Although traps associated with salt diapirs have been better studied, the indications are that mud diapir structures offer broadly similar trapping possibilities. Structures may be very complexly faulted, with reservoirs broken into a multitude of separate units. Mud diapirs can be distinguished from salt diapirs on seismic sections on the basis of seismic velocity. Salt has a much higher velocity than overpressured shale. Furthermore, mud diapirs tend to lack the well-developed rim synclines that typically surround salt diapirs. Factors may be the shorter lived process of mud diapirism, and the smaller volume from which mud withdrawal appears to take place (Harding and Lowell 1979).

10.6.2.2 Stratigraphic traps

A stratigraphic trap is primarily caused by some variation in the stratigraphy of the basin-fill. This variation

may be essentially inherited from the original depositional characteristics of the fill, or may result from subsequent diagenetic changes to it. The detailed stratigraphic trap classification of Rittenhouse (1972) (modified slightly in Allen and Allen 1990, p. 390) emphasizes the tremendous diversity present amongst stratigraphic traps. Stratigraphic traps may be classified as either *depositional* (in which the trap geometry is related to sedimentary facies changes), related to *unconformity* surfaces (either above or below), or *diagenetic*. Among the diagenetic traps, there are not only those caused by mineral diagenesis such as dolomitization, but also biodegradation of petroleum (tar mats) and phase changes to petroleum gas (gas hydrates) and interstitial water (permafrost).

A large number and wide range of stratigraphic traps have been discovered by over a century of exploration, since the drilling of the first exploration well by Colonel Drake at Titusville, Pennsylvania in 1857. Many of these stratigraphic discoveries, however, have been made by complete accident or at least by incorrect geological reasoning (Halbouty 1982). The giant East Texas field for example, a 5×10^9 barrel unconformity trap, was drilled as an anticlinal trap. The detection of stratigraphic traps requires a high level of geological expertise. Great emphasis must be placed on an understanding of the stratigraphic evolution of the basin, through a detailed sequence-by-sequence analysis. Of particular importance is the understanding of paleogeography and sedimentary facies for each depositional sequence and parasequence.

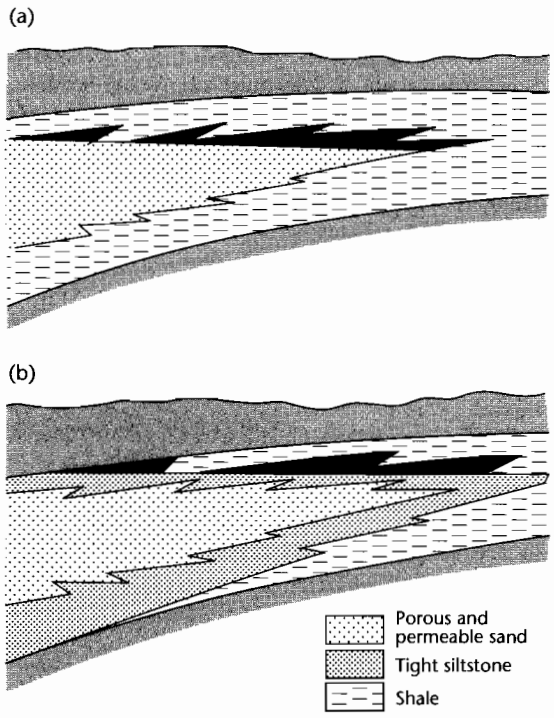

Fig. 10.66 Location of petroleum accumulation in facies change traps. When the change is abrupt (a), the petroleum is trapped in good quality reservoir rock. When the change is gradual (b), the petroleum is trapped in an up-dip "waste zone" of nonreservoir rock (after Downey 1984).

PINCH-OUTS

Whatever the geometry and origin of the entire reservoir unit, any porous facies may pinch out laterally, and, when combined with regional structural dip, may give rise to a stratigraphic pinch-out trap. Such traps were previously described on the flanks of salt diapirs. Pinch-out traps may be extensive and of very low dip. When the depositional pinch-out is gradational, an up-dip transitional "waste-zone" of very poor quality reservoir rock may be present (Fig. 10.66). Much or all of the petroleum charge may leak into the poorly producible waste-zone, forming a noncommercial accumulation. Ideally, the up-dip facies change should be rapid and complete in order for an effective lateral seal to be produced (Downey 1984).

DEPOSITIONAL TRAPS

Traps may develop in a wide range of depositional environments, ranging from eolian dune to submarine fan (§8.5). The selection of just three of the more common depositional traps discussed below are representative of the variability and complexity of depositional traps.

Fluvial channel traps have been described from the Cretaceous basins along the eastern flanks of the Rockies (Selley 1985). An example is the South Glenrock field of the Powder River Basin, Wyoming (Curry and Curry 1972), which clearly shows the meandering channel geometry of the productive sand. The South Glenrock example illustrates two important features of many channel traps: that reservoir sand thicknesses are typically small, limiting the reserves of these accumulations, and that the channel-fill may not be reservoir rock but clay. The geometry of the trap clearly depends on the

geometry of the channel. Braided, meandering, anastomosing, delta distributary, and tidal channels would have different geometries. Channels may sometimes be detected as a result of differential compaction relative to the surrounding shales. Some degree of structural closure may be needed to produce the trap (for example, a regional tilt or structural nose). Owing to the isolated nature of channel sands, they may not receive a petroleum charge. It is important, therefore, that source rocks are developed within the same depositional sequence. The effectiveness of a channel trap clearly depends on the lithology into which the channel is incised. Thus, although the channel itself may have a very distinct, sharp, lateral boundary, leakage may occur into the adjoining fluvial sediments.

Clay-filled channels may provide a lateral seal to reservoir sands in the adjacent incised sequence. Examples are present in the Sacramento Valley of California (Garcia 1981), and the Pennsylvanian Minnelusa sandstones of the Powder River Basin, Wyoming (Van West 1972).

Submarine fans may be developed on a very much larger scale, and give rise to large petroleum accumulations. An understanding of the sediment transport system is required for accurate prediction of submarine fans; a sequence-by-sequence basin analysis is particularly critical. We have previously seen that submarine fans tend to be developed at particular stages (lowstands) and locations (base of slope) in the depositional sequence (see especially §8.2).

The Tertiary of the North Sea provides numerous examples of submarine fan reservoirs. The Balder oilfield of the Norwegian sector (Sarg and Skjold 1982) for example is a series of Paleocene-age sand-rich suprafan lobes, with the trap geometry provided by depositional topography and subsequent submarine erosion. A hemipelagic shale caprock seals the suprafan complex. The discovery well was drilled by Esso in 1967 as a test of a structural prospect. The area was reinterpreted in the 1970s using seismostratigraphic principles and the field found to be a stratigraphic lowstand systems tract trap.

Reefs (§8.5.4) may provide high-relief stratigraphic traps. Isolated pinnacle reefs may be completely encased in younger marine shale. Barrier reefs on carbonate shelves generally need to be sealed up-dip by tight back-reef facies. As noted for pinch-out traps, there is a risk that the back-reef facies will constitute a waste zone of nonproductive reservoir rock. Although the relief on many reef traps may be considerable, the size of the accumulation is dependent on the presence or absence of permeable strata that terminate against the reef body. Careful seismostratigraphic analysis may be required to detect these zones of leakage. The distribution of reservoir units within reef complexes may be variable and unpredictable, not only owing to depositional facies changes but also to the effects of diagenesis. Reefs have formed very successful petroleum traps around the world, including in the Devonian of the Western Canada Basin, in the Sirte Basin of Libya, in the Tertiary of the Salawati and North Sumatra Basins of Indonesia, in the Miocene of Sarawak, in the Permian Basin of west Texas, and in southern Mexico and the Arabian Gulf. Sophisticated exploration techniques, primarily in geophysical data acquisition, processing and interpretation, may be needed to explore successfully for reefs in mature provinces. The remaining, smaller reefs in these provinces are extremely subtle features, their detection requiring a very high level of geological and geophysical expertise.

UNCONFORMITY TRAPS

A variety of traps may develop at unconformities, both immediately above and immediately below the unconformity surface. Many of the depositional stratigraphic traps previously described may also develop on unconformities. An example is a pinch-out trap. Overstepping marine shales frequently provide a topseal to shallow shelf or shoreline sands. These traps develop on margins undergoing marine onlap, and transgression, typically in the transgressive systems tract.

Supra-unconformity sands may be localized by topography on the unconformity surface. Thus, incised valleys and channels on the Type 1 unconformity surface formed at a relative lowstand may become sand-filled during rising sea level. Valleys developed along the strike of the outcropping preunconformity strata may be the location of the first postunconformity fluvial sediment. In both cases, a stratigraphic trap at the unconformity surface may be formed, particularly if regional structural dip is in a suitable direction.

Traps developed beneath an unconformity by *truncation* of reservoir beds may give rise to giant fields. Examples have been previously described of eroded extensional fault blocks in the East Shetland Basin of the North Sea (e.g., the Brent reservoir in the Statfjord field, Fig. 10.54). A further example is the Fortescue–Halibut field of the Gippsland Basin, Australia. There may be several elements to the closure developed in subunconformity traps, including the topography present at the

erosional unconformity, and the structural geometry of the preunconformity beds. Cross-faulting, for example, may provide closure in the strike direction. Topography on the unconformity may have been provided in the first instance by fault scarps.

The lithology of postunconformity sediments is critical to the effectiveness of subunconformity truncation traps. If, for example, a thin marine basal transgressive sand is present above the unconformity, leakage may occur. This sand may be so thin as to be below seismic resolution. Careful seismostratigraphic interpretation and basin analysis is required in order to understand the causes of the unconformity and the evolution of the sequences above and below it, before accurate predictions may be made of sedimentary facies impinging on the unconformity surface. Ideal conditions are created where the unconformity subsides rapidly into deep water depths, perhaps as a result of rapid initial fault-controlled or thermal subsidence, and the topography is passively infilled by deep marine muds. Traps developed at unconformities that have been onlapped by shelf, shoreline, or nonmarine sequences may not be effectively sealed (cf. §10.5.4).

When the subunconformity strata are carbonates, exposure at the surface may have very important implications for reservoir development in the subunconformity trap. The Casablanca field in the Gulf of Valencia, offshore southern Spain, was formed by Miocene faulting, erosion and leaching of a Mesozoic sequence of tight, dense limestones (Watson 1981). The faulting formed the paleotopography and fractured the brittle carbonates, allowing the penetration of meteoric waters and the development of secondary porosity to depths of up to 150 m. The eroded, elongate limestone ridge is overlain by mid-Miocene Alcanar Formation organic-rich marls, which charge and cap the accumulation. A similar example is the Angila field in the Sirte Basin of Libya (Fig. 10.67); in this case it is weathered granite that forms the reservoir in the unconformity trap (Williams 1968).

Probably the two best-known North American examples of unconformity traps are the Prudhoe Bay field in Alaska, and the East Texas field.

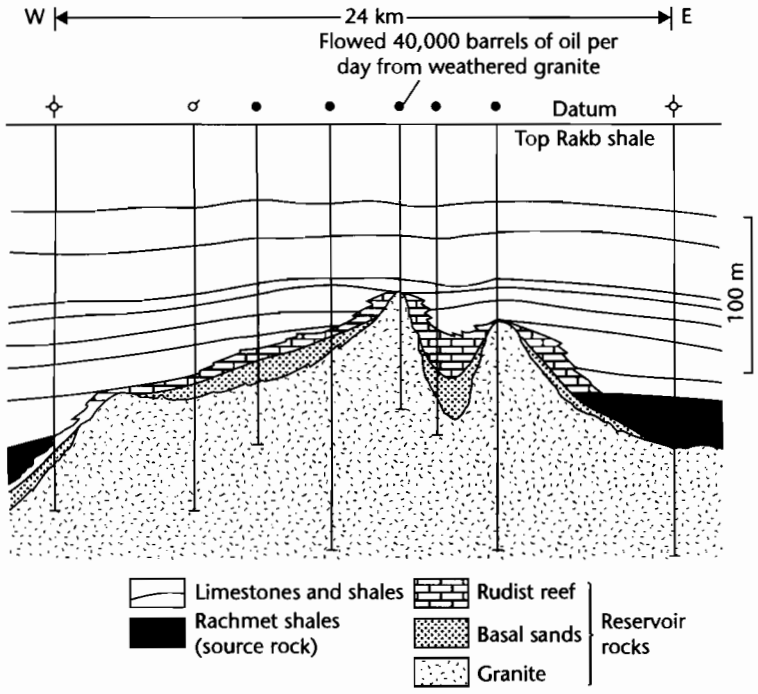

Fig. 10.67 Cross-section through the subunconformity trap of the Angila Field, Libya. Some of the production is from fractured and weathered subunconformity granitic basement (after Williams 1968).

DIAGENETIC TRAPS

There are a number of traps in which diagenesis has played a significant part. Examples are where cementation (e.g., of dolomite or calcite) has provided an up-dip seal to an accumulation, or where leaching has produced a local reservoir in an otherwise impermeable sequence. These trapping mechanisms are usually established after the main phase of oil generation, and have relatively low predictive importance.

An interesting form of diagenetic trap is where cementation has taken place below the oil–water contact of an existing accumulation (diagenesis is frequently inhibited by the presence of petroleum in the pore space). This may seal in the accumulation despite the subsequent removal of the original trapping mechanism, for example by tectonic activity.

At temperatures of less than about 70 °C, and in the presence of meteoric water, we have seen that bacterial degradation of oil may take place (§10.3.2.5). This can form an impermeable up-dip tar mat that seals subsequently migrated oil. Examples have been quoted from the Californian San Joaquin Valley (Wilhelm 1945) and Russian Volga–Ural region (Vinogradov et al. 1983). Similarly, a change of phase from gas or liquid to solid may also provide an unusual kind of trap. At high latitudes, permafrost may provide an up-dip seal to petroleum accumulations. At particular pressure–temperature conditions (low temperature, high pressure) petroleum gases may form *solid hydrates*. These are solid crystalline precipitates of gas and water. Not only is gas trapped in the hydrates themselves, but may accumulate in reservoirs underlying the zone of hydrate formation (Downey 1984). Hydrates are most likely to form in shallow onshore reservoirs in permafrost areas (examples have been quoted at depths of up to 200 m in Siberia), and in cold, deep sea areas (the Glomar Challenger cored gas hydrates at subsea depths of 600 m on the Blake Plateau).

10.6.2.3 Hydrodynamic traps

Hydrodynamics was briefly introduced in §10.3.2.4 in the context of the movement of petroleum fluids through basins. There are relatively few basins worldwide where hydrodynamics is known to have a significant impact on the entrapment of petroleum. These are typically foreland basins where porous and permeable carrier beds have been uplifted and exposed in adjoining fold–thrust belts, allowing the influx of meteoric water (see §9.6.3). If an outlet for the water is available elsewhere in the "plumbing system" of the basin, hydrodynamic flow of the basin fluids may take place (Hubbert 1953). Once the necessary conditions are known to be established at the basin scale, individual exploration prospects can be evaluated with a view to hydrodynamic effects.

Under conditions of strong hydrodynamic flow, petroleum–water contacts may be inclined rather than horizontal, petroleum may be completely flushed from structural or stratigraphic closures, or hydrodynamic closures may be produced (for example, on structural noses) where there is no other form of closure present. Each prospect needs to be evaluated individually, since prospectivity will depend on a host of regional and local factors that may be difficult to assess.

Clearly, an understanding of the structural and stratigraphic evolution of the basin is required for an assessment of the impact, if any, of hydrodynamic conditions on petroleum entrapment. Generally, however, hydrodynamic traps and hydrodynamic effects appear to be relatively rare.

10.6.3 Timing of trap formation

An understanding of the mechanism of trap formation, and therefore the timing of trap formation, is essential to prospect evaluation. A trap that developed too late to receive a petroleum charge will be filled with pore water. Each of the structural, stratigraphic, and hydrodynamic trap types discussed in this section has implications for trap timing that are obvious. Depositional and unconformity traps are very early, dating from the time the sealing units became effective. Thus these traps are ready to receive a charge from a very early stage. Some structural traps, however, are very late in relation to petroleum charge. Each trap needs to be individually evaluated.

The timing problem is perhaps best illustrated by considering a currently active fold–thrust belt. The fold–thrust belt forms as a result of shortening, at least in the sedimentary cover, which results in uplift. Uplift results in cooling of the overthrust sheets, which switches off petroleum generation. Thus, a timing problem may exist, unless generation is maintained in subthrust positions by loading of the allochthonous sheet, or unless earlier trapped petroleum remigrates into the new fold structures. A similar problem exists for inversion structures. Prior to inversion, migration is usually directed

away from the site of the future trap. Inversion may switch off new generation, thus the charge into the inversion trap must be from remigrated oil.

Structures formed in areas of continuous subsidence also need careful evaluation, so that the growth of the structure may be closely related to the timing and volume of petroleum charge. The sedimentary section may need to be backstripped (§9.3) to the time of first trap formation, and the charge system geochemically modeled.

References

Abbott, G.D., Wang, G.Y., Eglington, T.I. and Petch, G.S. (1990) The kinetics of sterane biological marker release and degradation during the hydrous pyrolysis of vitrinite kerogen. *Geochimica et Cosmochimica Acta*, **54**, 2451–2461.

Adams, E.W., Schroeder, S., Grotzinger, J.P., McCormick, D.S., Amthor, J.E., Al-Hashimi, R., Al-Jaidi, O., Al-Siyabi, M. and Smith, D.W. (2001) Digital mapping of the geometry and stratal patterns of microbial reefs, terminal Neoproterozoic Nama Group, Namibia. *Geological Society of America, Abstracts with Programs*, **33**.

Adams, R.D. and Grotzinger, J.P. (1996) Lateral continuity of facies and parasequences in Middle Cambrian platform carbonate, Carrara Formation, southeastern California, USA. *Journal of Sedimentary Research*, **66**, 1079–1090.

Aharon, P. (1983) 140 000 yr isotope climatic record from raised coral reef in New Guinea. *Nature*, **304**, 720–723.

Ahmed, U., Crary, S.F. and Coates, G.R. (1991) Permeability estimation: the various sources and their interrelationships. *Journal of Petroleum Technology*, **42**, 578–587.

Ahnert, F. (1970) Functional relationships between denudation, relief and uplift in large mid-latitude drainage basins. *American Journal of Science*, **270**, 243–263.

Aigner, T., Brandenburg, A., van Vliet, A., Doyle, M., Lawrence, D. and Westrich, J. (1990) Stratigraphic modelling of epicontinental basins: two applications. *Sedimentary Geology*, **69**, 167–190.

Aigner, T., Doyle, M., Lawrence, D., Epting, M. and van Vliet, A. (1989) Quantitative modeling of carbonate platforms: some examples. In: *Controls on Carbonate Platform and Basin Development* (eds. P.D. Crevello et al.), *Special Publication Society of Economic Paleontologists and Mineralogists*, **44**, 323–338.

Aihara, A. (1980) Formation and organic metamorphism of the Palaeogene coal deposits in the Japanese islands. *Congres géologique international (Paris 1980), Industrie Minerale: les Techniques.* 6–80, Suppl. June 1980, 307–314.

Albright, W.A., Turner, W.L. and Williamson, K.R. (1980) Ninian field, UK sector, North Sea. In: *Giant Oil and Gas Fields of the Decade 1968–1978* (ed. by M.T. Halbouty), *American Association of Petroleum Geologists Memoir*, **30**, 173–194.

Alexander, J. and Leeder, M.R. (1987) Active tectonic control on alluvial architecture. In: *Recent Developments in Fluvial Sedimentology* (eds. F.G. Ethridge, R.M. Flores and M.D. Harvey), *Special Publication Society of Economic Paleontologists and Mineralogists*, **39**, 243–252.

Allan, U.S. (1980) A model for the migration and entrapment of hydrocarbons. *American Association of Petroleum Geologists Research Conference on Seals for Hydrocarbons*, Keystone, Colorado, Sept. 14–17, 1980, unpublished book of abstracts.

Allen, P.A. (1997) *Earth Surface Processes.* Blackwell Scientific Publications, Oxford.

Allen, P.A. and Allen, J.R. (1990) *Basin Analysis: Principles and Applications.* Blackwell Scientific Publications, Oxford.

Allen, P.A. and Collinson, J.D. (1986) Lakes. In: *Sedimentary Environments and Facies* (ed. by H.G. Reading), 63–94, Blackwell Scientific, Oxford.

Allen, P.A. and Densmore, A.L. (2000) Sediment flux from an uplifting fault block. *Basin Research*, **12**, 367–380.

Allen, P.A. and Hovius, N. (1998) Sediment supply from landslide-dominated catchments: implications for basin-margin fans. *Basin Research*, **10**, 19–35.

Allen, P.A., Burgess, P.M., Galewsky, J. and Sinclair, H.D. (2001) Flexural-eustatic numerical model for drowning of the Eocene perialpine carbonate ramp and implications for Alpine geodynamics. *Bulletin Geological Society of America*, **113**, 1052–1066.

Allen, P.A., Crampton, S. and Sinclair, H.D. (1991) Inception and early evolution of the North Alpine Foreland Basin, Switzerland. *Basin Research*, **3**, 143–163.

Allen, P.A., Verlander, J.E., Burgess, P.M. and Audet, D.M. (2000) Jurassic giant erg deposits, flexure of the United States continental interior, and timing of the onset of Cordilleran shortening. *Geology*, **28**, 159–162.

Allenby, R.A. and Schnetzler, C.C. (1983) United States crustal thickness. *Tectonophysics*, **93**, 13–31.

Alvarez, W. (1999) Drainage on evolving fold-thrust belts: a study of transverse canyons in the Apennines. *Basin Research*, **11**, 267–284.

Anderson, R.S. (1982) Hotspots, polar wander, Mesozoic convection and the geoid. *Nature*, **297**, 391–393.

Anderson, R.S. (1994) Evolution of the Santa Cruz Mountains, California, through tectonic growth and geomorphic decay. *Journal of Geophysical Research*, **99**, 20161–20179.

Anderson, R.S. and Humphrey, N.F. (1990) Interaction of weathering and transport processes in the evolution of arid landscapes. In: *Quantitative Dynamic Stratigraphy* (ed. by T.A. Cross), Englewood Cliff, NJ, Prentice Hall., 349–361.

Andrews, J.E., Brimblecombe, P., Jickells, T.D. and Liss, P.S. (1995) *An Introduction to Environmental Chemistry.* Blackwell Science, Oxford.

Andrews-Speed, C.P., Oxburgh, E.R. and Cooper, B.A. (1984) Temperatures and depth-dependent heat flow in western North Sea. *Bulletin American Association of Petroleum Geologists*, **68**, 1764–1781.

Ashby, M.F. and Verall, R.A. (1977) Micromechanisms of flow and fracture and their relevance to the rheology of the upper mantle. *Phil. Trans. R. Society London*, **A288**, 59–95.

Athy, L.F. (1930) Density, porosity and compaction of sedimentary rocks. *Bulletin American Association of Petroleum Geologists*, **14**, 1–24.

Atkinson, B.K. (1987) *Fracture Mechanics of Rock.* New York, Academic Press.

Atwater, T. (1970) Implications of plate tectonics for the Cenozoic tectonic evolution of western North America. *Bulletin Geological Society of America*, **81**, 3513–3536.

Aubouin, J. (1965) *Geosynclines. Developments in Geotectonics*, Elsevier, Amsterdam.

Audet, D.M. and McConnell, J.D.C. (1992) Forward modelling of porosity and pore pressure evolution in sedimentary basins. *Basin Research*, **4**, 147–162.

Audet, D.M. and McConnell, J.D.C. (1994) Establishing resolution limits for tectonic subsidence curves by forward basin modelling. *Marine and Petroleum Geology*, **11**, 400–411.

Avouac, J.P. (1993) Analysis of scarp profiles: evaluation of errors in morphologic dating. *Journal of Geophysical Research*, **98**, 6745–6754.

Aydin, A. and Nur, A. (1982) Evolution of pull-apart basins and their scale independence. *Tectonics*, **1**, 91–105.

Aydin, A. and Nur, A. (1985) The types and roles of stepovers in strike-slip tectonics. In: *Strike-Slip Deformation, Basin Formation and Sedimentation* (eds. K.T. Biddle and N. Christie-Blick), *Special Publication Society of Economic Paleontologists and Mineralogists*, **37**, 35–44.

Bacon, M., Simm, R. and Redshaw, T. (2003) *3-D Seismic Interpretation.* Cambridge University Press.

Badley, M.E. (1985) *Practical Seismic Interpretation.* Prentice Hall.

Badley, M.E., Price, J.D., Rambech Dahl, C. and Agdestein, T. (1988) The structural evolution and the northern Viking Graben and its bearing upon extensional modes of basin formation. *Journal of Geological Society of London*, **145**, 455–472.

Bailey, R.J. and Stoneley, R. (1981) Petroleum: entrapment and conclusions. In: *Economic Geology and Geotectonics* (ed. by D.H. Tarling), 73–97, Blackwell Scientific, Oxford.

Baker, B.H., Mohr, P.A. and Williams, L.A.J. (1972) Geology of the Eastern Rift System of Africa. *Special Paper Geological Society of America*, **136**.

Baker, B.H. and Wohlenberg, J. (1971) Structure and evolution of the Kenya Rift Valley, *Nature* **229**, 538–542.

Baldwin, B. and Butler, C.O. (1985) Compaction curves. *American Association of Petroleum Geologists Bulletin*, **69**, 622–626.

Bally, A.W. (1975) A geodynamic scenario for hydrocarbon occurrences. *Proceedings 9th World Petroleum Congr., Tokyo*, 33–44, Vol. 2 (Geology). Applied Science Publishers, Barking.

Bally, A.W. and Snelson, S. (1980) Realms of subsidence. In: *Facts and Principles of World Petroleum Occurrence* (ed. by A.D. Miall), *Canadian Society Petroleum Geologists Memoir*, **6**, 9–75.

Bamford, D. (1979) Seismic constraints on the deep geology of the Caledonides of northern Britain. In: *The Caledonides of the British Isles – Reviewed* (eds. A. Harris, C.H. Holland and B.E. Leake), *Special Publication Geological Society of London*, **8**, 93–96.

Banks, R.J. and Swain, C. (1978) The isostatic compensation of East Africa. *Proceedings R. astr. Society*, **A364**, 331–352.

Barazangi, M. and Dorman, J. (1969) World seismicity map compiled from ESSA Coast and Geodetic Survey epicentre data, 1961–1967. *Bulletin Seismology Society America*, **59**, 369–380.

Barker, C.E. and Pawlewicz, M.J. (1986) The correlation of vitrinite reflectance with maximum temperature in humic organic matter. In: *Lecture notes* (eds. G. Buntebarth and L. Stegena), *Earth Sciences*, **5.** Palaeogeothermics. Springer-Verlag, Berlin, 79–93.

Bartlett, W.L., Friedman, M. and Logan, J.M. (1981) Experimental folding and faulting of rocks under confining pressure. Part IX. Wrench faults in limestone layers. *Tectonophysics*, **79**, 255–277.

Barton, P.J. (1986) Comparison of deep reflection and refraction structures in the North Sea. *Reflection Seismology: A Global Perspective* (eds. M. Barganzi and L. Brown), *American Geophysical Union Series*, **13**, 297–300.

Bassi, G. (1991) Factors controlling the style of continental rifting: insights from numerical examples. *Earth and Planetary Science Letters*, **105**, 430–452.

Bathurst, R.G.C. (1971) Carbonate Sediments and their Diagenesis. *Developments in Sedimentology*, **12**, Elsevier, Amsterdam, 620 pp.

Bayona, G. and Thomas, W.A. (2003) Distinguishing fault reactivation from flexural deformation in the distal stratigraphy of the Peripheral Blountain Foreland Basin, southern Appalachians, USA. *Basin Research*, **15**, 503–526.

Beard, J.H., Sangree, J.B. and Smith, L.A. (1982) Quaternary chronology, palaeoclimate, depositional sequences, and eustatic cycles. *Bulletin American Association of Petroleum Geologists*, **66**, 158–169.

Beaufort, D., Cassagnabere, A., Petit, S. et al. (1998) Kaolinite-to-dickite reaction in sandstone reservoirs. *Clay Minerals*, **33**, 297–316.

Beaumont, C. (1981) Foreland basins. *Geophysical Journal of the Royal Astronomical Society*, **65**, 291–329.

Beaumont, C., Ellis, S., Hamilton, J. and Fullsack, P. (1996a). Mechanical model for subduction-collision: tectonics of Alpine-type compressional orogens. *Geology*, **24**, 675–678.

Beaumont, C., Fullsack, P. and Hamilton, J. (1992) Erosional control of active compressional orogens. In: *Thrust Tectonics* (ed. by K.R. McClay), London, Champman and Hall, 1–18.

Beaumont, C., Kamp, P.J.J., Hamilton, J. and Fullsack, P. (1996b) The continental collision zone, South Island, New Zealand; comparison of geodynamic models and observations. *Journal of Geophysical Research*, **101**, 3333–3359.

Beaumont, C., Keen, C.E. and Boutilier, R. (1982) On the evolution of rifted continental margins; comparison of models and observations for Nova Scotian margin. *Geophysical Journal of R. astr. Society*, **70**, 667–715.

Bechtel, T., Forsyth, D. and Swain, C. (1987) Mechanisms of isostatic compensation in the vicinity of the East African rift, Kenya. *Geophysical Journal of R. astr. Society*, **90**, 445–465.

Bechtel, T.D., Forsyth, D.W., Sharpton, V.L. and Grieve, R.A.F. (1990) Variations in effective elastic thickness of the North American lithosphere. *Nature*, **343**, 636–638.

Beck, A.E. (1977) Climatically perturbed temperature gradients and their effect on regional and continental heat flow means. *Tectonophysics*, **41**, 17–39.

Beck, A.E., Anglin, F.M. and Sass, J.H. (1971) Analysis of heat flow data – *in situ* thermal conductivity measurements. *Canadian Journal of Earth Sciences*, **8**, 1–19.

Beck, R.A., Vondra, C.G., Filkinds, J.E. and Olander, J.D. (1988) Syntectonic sedimentation and Laramide basement thrusting, Cordilleran foreland: Timing of defomation. In: *Interaction of the Rocky Mountain Foreland and the Cordilleran Thrust Belt* (eds. C.A. Schmidt and W.J. Jr Perry), *Memoir Geological Society of America*, **171**, 465–487.

Belknap, D.F. et al. (1987) Late Quaternary sea level changes in Maine. In: *Sea Level Fluctuation and Costal Evolution* (eds. D. Nummedal, O.H. Pilkey and J.D. Howard), *Special Publication Society of Economic Paleontologists and Mineralogists*, **41**, 71–85.

Ben-Avraham, Z. (1985) Structural framework of the Gulf of Elat (Aqaba), northern Red Sea. *Journal of Geophysical Research*, **90**, 703–726.

Ben-Avraham, Z. and Zoback, M.D. (1992) Transform-normal extension and asymmetric basins: An alternative to pull-apart models. *Geology*, **20**, 423–426.

Ben-Avraham, Z., Almagor, G. and Garfunkel, Z. (1979) Sediments and structure of the Gulf of Elat (Aqaba) – northern Red Sea. *Sedimentary Geology*, **23**, 239–267.

Ben-Avraham, Z., Hanel, R. and Villinger, H. (1978) Heat flow through the Dead Sea rift. *Geology*, **28**, 253–269.

Bennett, R.A., Wernicke, B.P., Davis, J.L., Elösegui, P., Snow, J.K., Abolins, M.J., House, M.A., Stirewalt, G.L. and Ferrill, D.A. (1997) Global Positioning System constraints on fault slip rates in the Death Valley region, California and Nevada. *Geophysical Research Letters*, **24**, 3073–3076.

Bensley, D.F. and Crelling, J.C. (1994) The inherent heterogeneity within the vitrinite maceral group. *Fuel*, **73**, 1306–1316.

Bercovici, D., Ricard, Y. and Richards, M.A. (2000) The relation between mantle dynamics and plate tectonics: A primer. In: *The History and Dynamics of Global Plate Motions* (eds. M.A. Richards, R.G. Gordon and R.D. van der Hilst), *American Geophysical Union, Geophysical Monograph*, **121**, 5–46.

Berg, R.R. (1975) Capillary pressures in stratigraphic traps. *Bulletin American Association of Petroleum Geologists*, **59**, 939–956.

Berggren, W.A., Kent, D.V., Swisher, C.C. and Aubry, M.P. (1995) A revised Cenozoic geochronology and chronostratigraphy. In: *Geochronology, Time Scales and Global Stratigraphic Correlation* (eds. W.A. Berggren et al.). *Special Publication Society for Sedimentary Geology*, **54**, 129–212.

Bernard, H.A., LeBlanc, R.J. and Major, C.F. Jr (1962) Recent and Pleistocene geology of southeast Texas. In: *Geology of Gulf Coast and Central Texas and Guidebook of Excursion*. Geological Society, Houston, 175–225.

Bernoulli, D. and Jenkyns, H.C. (1974) Alpine, Mediterranean and Central Atlantic Mesozoic facies in relation to the early evolution of the Tethys. In: *Modern and Ancient Geosynclinal Sedimentation* (eds. R.H. Dott and R.H. Shaver), 129–160, *Special Publication Society of Economic Paleontologists and Mineralogists*, **19**.

Bertotti, G., Picotti, V., Chilovi, C., Fantoni, R., Merlini, S. and Mosconi, A. (2001) Neogene to Quaternary sedimentary basins in the south Adriatic (Central Mediterranean): foredeeps and lithospheric buckling. *Tectonics*, **20**, 771–787.

Bice, D.M. (1991) Computer simulation of carbonate platform and basin systems. In: *Sedimentary Modeling: Computer Simulations and Methods for Improved Parameter Definition* (eds. E.K. Franseen, W.L. Watney, C.G.S.C. Kendall and W. Ross), *Kansas Geological Survey Bulletin*, **233**, 431–447.

Biddle, K.T., Uliana, M.A., Mitchum, R.M. Jr, Fitzgerald, M.G. and Wright, R.C. (1986) The stratigraphic and structural evolution of the central and eastern Magallanes Basin, southern South America. In: *Foreland Basins* (eds. P.A. Allen and P. Homewood), *Special Publication International Association of Sedimentology*, **8**, 41–61.

Bierman, P.R. (1994) Using *in situ* produced cosmogenic isotopes to estimate rates of landscape evolution. A review from the geomorphic perspective. *Journal of Geophysical Research*, **99**; 13885–13896.

Bilham, R., Larson, K., Freymüller, J. and Project Idylhim members (1997) GPS measurements of present-day convergence across the Nepal Himalaya. *Nature*, **386**, 61–64.

Bird, J.M. (1980) *Plate Tectonics* (Second Edition). American Geophysical Union, Washington D.C.

Biscaye, P.E. and Eittreim, S.L. (1977) Suspended particulate loads and transports in the nepheloid layer of the abyssal Atlantic Ocean. *Marine Geology*, **23**, 1–2.

Bjorkum, P.A. and Nadeau, P.H. (1998) Temperature controlled porosity/permeability reduction, fluid migration, and petroleum exploration in sediment basins. *APPEA Journal*, pp. 453–465.

Bjorlykke, K. (1983) Diagenetic reactions in sandstones. In: *Sediment Diagenesis* (eds. A. Parker and B.W. Sellwood), Reidel, 169–213.

Bjorlykke, K., Aagaard, P.A., Dypvik. H., Hastings, D.S. and Harper, A.S. (1986) Diagenesis and reservoir properties of Jurassic sandstones from the Haltenbanken area, offshore mid-Norway. In: *Habitat of Hydrocarbons on the Norwegian Continental Shelf* (ed. by A.M. Spencer), The Norwegian Petroleum Society, London, Graham and Trotman, 275–286.

Bjorlykke, K., Nedkvitne, T., Ramm, M. and Saigal, G.C. (1992) Diagenetic processes in the Brent Group (Middle Jurassic)

reservoirs of the North Sea: An overview. In: *Geology of the Brent Group* (eds. A.C. Morton, R.S. Haszeldine, M.R. Giles and S. Brown), *Geological Society of London Special Publication*, **61**, 263–287.

Blair, D.G. (1975) Structural styles in North Sea oil and gas fields. In: *Petroleum and the Continental Shelf of NW Europe*, Vol. 1 (ed. by A.W. Woodland), 327–338, Applied Science Publishers, Barking.

Blair, T.C. and McPherson, J.G. (1994) Alluvial fan processes and forms. In: *Geomorphology of Desert Environments* (eds. A.D. Abrahams and A.J. Parsons), pp. 354–402. Chapman & Hall, London.

Blakeley, R.J., Jachens, R.C., Calzia, J.P. and Langenheim, V.E. (1999) Cenozoic basins of the Death Valley extended terrane as reflected in regional-scale gravity anomalies. In: *Cenozoic Basins of the Death Valley Region* (eds. L. Wright and B. Troxel), pp. 381, 1–16.

Blakey, R.C., Peterson, F. and Kocurek, G. (1988) Syntheses of late Paleozoic and Mesozoic eolian deposits of the Western Interior of the United States. In: *Late Paleozoic and Mesozoic Eolian Deposits of the Western Interior of the United States* (ed. G. Kocurek). *Sedimentary Geology*, **56**, 3–125.

Blasband, B., White, S., Brooijmans, P., de Boorder, H. and Viser, W. (2000) Late Proterozoic extensional collapse in the Arabian-Nubian Shield. *Journal of the Geological Society of London*, **157**, 615–628.

Blatt, H. (1979) Diagenetic process in sandstones. In: *Aspects of Diagenesis* (eds. P.A. Scholle and P.R. Schluger), 141–157, *Special Publication Society of Economic Paleontologists and Mineralogists*, **26**.

Blount, D. and Moore, C.H. (1969) Depositional and non-depositional carbonate breccias, Chiantla Quadrangle, Guatemala. *Geological Society of America Bulletin*, **80**, 429–442.

Blum, M.D. (1993) Genesis and architecture of incised valley fill sequences: A Late Quaternary example from the Colorado River, Gulf Coastal Plain of Texas. In: *Siliciclastic Sequence Stratigraphy: Recent Developments and Applications* (eds. P. Weimer and H.W. Posamentier), *Memoir American Association of Petroleum Geologists*, **58**, 259–283.

Boles, J.R. and Franks, S.G. (1979) Clay diagenesis in Wilcox sandstones of southwest Texas: Implications of smectite diagenesis on sandstone cementation. *Journal of Sedimentary Petrol.*, **49**, 55–70.

Bond, G. (1976) Evidence for continental subsidence in North America during the Late Cretaceous global submergence. *Geology*, **4**, 557–560.

Bond, G. (1978) Speculations on relative sea level changes and vertical motions of continents at selected times in the Cretaceous and Tertiary periods. *Geology*, **6**, 247–250.

Bond, G. (1979) Evidence for some uplifts of large magnitudes in continental platforms. *Tectonophysics*, **61**, 285–305.

Bond, G.C. and Kominz, M.A. (1984) Construction of tectonic subsidence curves for the early Paleozoic miogeocline, southern Canadian Rocky Mountains: implications for subsidence mechanisms, age of breakup, and crustal thinning. *Bulletin Geological Society of America*, **95**, 155–173.

Bond, G., Kominz, M.A. and Sheridan, R.E. (1995) Continental terraces and rises. In: *Tectonics of Sedimentary Basins* (eds. C. Busby and R. Ingersoll), Blackwell Science, Oxford, 149–178.

Bondevik, S., Svendson, J.I., Johnsen, G., Mangerud, J. and Kaland, P.E. (1997) The Storegga tsunami along the Norwegian coast, its age and run-up. *Boreas*, **26**, 29–53.

Bosscher, H. and Schlager, W. (1992) Computer simulation of reef growth. *Sedimentology*, **39**, 503–512.

Bostick, N.H. (1979) Microscopic measurement of the level of catagenesis of solid organic matter in sedimentary rocks to aid exploration for petroleum and to determine former burial temperatures – a review. In: *Aspects of Diagenesis* (eds. P.A. Scholle and P.R. Schluger), *Special Publication Society of Economic Paleontologists and Mineralogists*, **26**, 17–43.

Bostick, N.H. and Alpern, B. (1977) Principles of sampling, preparation and constituent selection for microphotometry in measurement of maturation of sedimentary organic matter. *Journal of Microscopy*, **109**, 41–47.

Bott, M.H.P. (1982) *The Interior of the Earth: its Structure, Constitution and Evolution*, 2nd edition. Elsevier, Amsterdam.

Bott, M.H.P. (1992) Modelling the loading stresses associated with active continental rift systems. *Tectonophysics*, **215**, 99–115.

Boyd, R., Dalrymple, R.W. and Zaitlin, B.A. (1992) Classification of clastic coastal depositional environments. *Sedimentary Geology*, **80**, 139–150.

Boyer, S.E. (1995) Sedimentary basin taper as a factor controlling the geometry and advance of thrust belts. *American Journal of Science*, **295**, 1220–1254.

Brace, W.F. and Kohlstedt, D.L. (1980) Limits on lithospheric stress imposed by laboratory experiments. *Journal of Geophysical Research*, **85**, 6248–52.

Bradley, D.C. (1983) Tectonics of the Acadian orogeny in New England and adjacent Canada. *Journal of Geology*, **91**, 381–400.

Bradley, D.C. and Kidd, W.S.F. (1991) Flexural extension of the upper continental crust in collisional foredeeps. *Geological Society of America Bulletin*, **103**, 1416–1438.

Braun, J. and Beaumont, C. (1987) Styles of continental rifting: Results from dynamic models of lithospheric extension. In: *Sedimentary Basins and Basin-Forming Mechanisms* (eds. C. Beaumont and A.J. Tankard), *Calgary, Canadian Society of Petroleum Geologists*, **12**, 241–258.

Braun, J. and Beaumont, C. (1989) A physical explanation of the relationship between flank uplifts and the break-up unconformity at rifted continental margins. *Geology*, **17**, 760–764.

Braun, J. and Sambridge, M. (1997) Modelling landscape evolution on geological time scales: A new method based on irregular spatial discretization. *Basin Research*, **9**, 27–52.

Bridge, J.S. and Leeder, M.R. (1979) A simulation model of alluvial stratigraphy. *Sedimentology*, **26**, 617–644.

Brigaud, F. and Vasseur, G. (1989) Mineralogy, porosity and fluid control on thermal conductivity of sedimentary rocks. *Geophysical Journal*, **98**, 525–542.

Brodie, J. and White, N. (1994) Sedimentary basin inversion caused by igneous underplating: Northwest European continental shelf. *Geology*, **22**, 147–150.

Brown, A.R. (1999) *Interpretation of 3-dimensional Seismic Data.* Memoir 42, Geological Society Publishing House.

Brown, E.T., Stallard, R.F., Larsen, M.C., Raisbeck, G.M. and Yiou, F. (1995) Denudation rates determined from the accumulation of *in situ*-produced ^{10}Be in the Luquillo experimental forest, Puerto Rico. *Earth and Planetary Science Letters*, **129**, 193–202.

Brown, L.F. and Fisher, W.L. (1977) Seismic-stratigraphic interpretation of depositional systems. In: *Seismic Stratigraphy – Applications to Hydrocarbon Exploration* (ed. by C.E. Payton), *American Association Petroleum Geologists Memoir*, **26**, 213–248.

Bruhn, R.L., Stern, C.R. and De Wit, M.J. (1978) Field and geochemical data bearing on the development of a Mesozoic volcano-tectonic rift zone and back-arc basin in southernmost South America. *Earth and Planetary Science Letters*, **41**, 32–46.

Brun, J.P. (1999) Narrow rifts versus wide rifts: inferences for the mechanics of rifting from laboratory experiments. *Philosophical Transactions of the Royal Society, London*, **A357**, 695–712.

Buck, W.R. (1984) *Small–scale convection and the evolution of the lithosphere.* Unpublished PhD thesis, MIT.

Buck, W.R. (1986) Small scale convection induced by passive rifting: the cause for uplift of rift shoulders. *Earth and Planetary Science Letters*, **77**, 362–372.

Buck, W.R. Steckler, M.S. and Cochran, J.R. (1988) Thermal consequences of lithospheric extension: pure and simple. *Tectonics*, **7**, 213–234.

Bulat, J. and Stoker, S.J. (1987) Uplift determination from interval velocity studies. In: *Petroleum Geology of North West Europe* (eds. J. Brooks and K. Glennie), Graham and Trotman, London, 293–305.

Bull, W.B. (1977) The alluvial fan environment. *United States Geological Survey Professional Paper*, **353-E**, 89–129.

Burbank, D.W. (1992) Causes of recent Himalayan uplift deduced from depositional patterns in the Ganges basin. *Nature*, **357**, 680–682.

Burbank, D.W. and Anderson, R.S. (2001) *Tectonic Geomorphology.* Blackwell Science, Oxford.

Burbank, D.W. and Vergés, J. (1994) Reconstruction of topography and related depositional systems during active thrusting. *Journal of Geophysical Research*, **99**, 20281–20297.

Burbank, D.W., Beck, R.A. and Mulder, T. (1996) The Himalayan foreland basin. In: *The Tectonic Evolution of Asia* (eds. A. Yin and T.M. Harrison), 149–188, Cambridge University Press, Cambridge.

Burchfiel, B.C. and Royden, L. (1982) Carpathian foreland fold and thrust belt and its relation to Pannonian and other basins. *Bulletin American Association of Petroleum Geologists*, **66**, 1179–1195.

Burchfiel, B.C. and Stewart, J.H. (1966) "Pull-apart" origin for the central segment of Death Valley, California. *Geological Society of America Bulletin*, **77**, 439–441.

Burg, J.-P. and Podladchikov, Y. (2000) From buckling to asymmetric folding of the continental lithosphere: numerical modelling and application to the Himalayan syntaxes. In: *Tectonics of the Nanga Parbat Syntaxis and the Western Himalaya* (eds. M.A. Khan, P.J. Treloar, M.P. Searle and M.Q. Jan), *Special Publication Geological Society of London*, **170**, 219–236.

Burg, J.P., Davy, P. and Martinod, J. (1994b) Shortening of analogue models of the continental lithosphere: New hypothesis for the formation of the Tibetan plateau. *Tectonics*, **13**, 475–483.

Burg, J.P., Guiraud, M., Chen, G.M. and Li, G.C. (1984) Himalayan metamorphism and deformations in the North Himalayan Belt (southern Tibet, China). *Earth and Planetary Science Letters*, **69**, 391–400.

Burg, J.-P., Sokoutis, D. and Bonini, M. (2002) Model-inspired interpretation of seismic structures in the Central Alps: Crustal wedging and buckling at mature stage of collision. *Geology*, **30**, 643–646.

Burg, J.-P., Van Den Driessche, J. and Brun, J.-P. (1994a) Syn- to post-thickening extension in the Variscan Belt of Western Europe: mode and structural consequences. *Géologie de la France*, **3**, 33–51.

Burgess, P.M. and Allen, P.A. (1996) A forward modelling analysis of the controls on sequence stratigraphic geometries. *Sequence Stratigraphy in British Geology* (eds. S.P. Hesselbo and W. Parkinson), *Special Publication Geological Society of London*, **103**, 9–24.

Burgess, P.M. and Gurnis, M. (1995) Mechanisms for the formation of cratonic stratigraphic sequences. *Earth and Planetary Science Letters*, **136**, 647–663.

Burgess, P.M. and Moresi, L.N. (1999) Modelling rates and distribution of subsidence due to dynamic topography over subducting slabs: is it possible to identify dynamic topography from ancient strata? *Basin Research*, **11**, 305–314.

Burgess, P.M., Gurnis, M. and Moresi, L. (1997) Formation of sequences in the cratonic interior of North America by interaction between mantle, eustatic, and stratigraphic processes. *Bulletin Geological Society of America*, **108**, 1515–1535.

Burgess, P.M., Paola, C. and Mountney, N. (eds.) (2002) Numerical and Physical Experimental Modelling of Stratigraphy, *Basin Research* Thematic Set, **14**.

Burgess, P.M., Wright, V.P. and Emery, D. (2001) Numerical forward modelling of peritidal carbonate parasequence development: Implications for outcrop interpretation. *Basin Research*, **13**, 1–16.

Burke, K. (1976) The Chad Basin: an active intracontinental basin. *Tectonophysics*, **36**, 197–206.

Burke, K. (1977) Aulacogens and continental breakup. *Annual Review of Earth and Planetary Sciences*, **5**, 371–396.

Burke, K. and Dewey, J.F. (1973) Plume generated triple junctions: key indicators in applying plate tectonics to old rocks. *Journal of Geology*, **81**, 406–433.

Burland, J.B. (1990) On the compressibility and shear strength of natural clays. *Géotechnique*, **40**, 329–378.

Burley, S.D., Kantorowicz, J.D. and Waugh, B. (1985) Clastic diagenesis. In: *Sedimentology: Recent Developments and Applied Aspects* (eds. P.J. Brenchley and B.P.J. Williams), *Special Publication Geological Society of London*, **18**, 189–226.

Burnham, A.K. and Sweeney, J.J. (1989) A chemical kinetic model of vitrinite reflectance maturation. *Geochimica et Cosmochimica Acta*, **53**, 2649–2657.

Burov, E.B. and Diament, M. (1995) The effective elastic thickness (T_e) of continental lithosphere: What does it really mean? *Journal of Geophysical Research*, **100**, 3905–3927.

Burov, E.B., Lobkovsky, L.I., Cloetingh, S. and Nikishin, A.M. (1993) Continental lithosphere folding in Central Asia (part 2): Constraints from gravity and topography, *Tectonophysics*, **226**, 73–87.

Busby, C.J. and Ingersoll, R.V. (1995) *Tectonics of Sedimentary Basins*. Blackwell Science, Oxford.

Busse, F.H. and Whitehead, J.A. (1971) Instabilities of convection rolls in high Prandtl number fluid. *Journal Fluid Mechanics*, **47**, 305–320.

Byerlee, J. (1977) A review of rock mechanics studies in the United States pertinent to earthquake prediction. *In*: Proceedings of Conference II; experimental studies of rock friction with application to earthquake prediction. *U. S. Geology Surv., Off. Earthquake Stud.. Menlo Park, Calif.*, 559–590.

Byerlee, J.D. (1978) Friction of rocks. *Pure and Applied Geophysics*, **116**, 615–626.

Cade, C.A., Evans, J. and Bryant, S.L. (1994) Analysis of permeability controls: A new approach. *Clay Minerals*, **29**, 491–501.

Cadek, O., Kyvalova, H. and Yuen, D.A. (1995) Geodynamical implications from the correlation of surface geology and seismic tomographic structure. *Earth and Planetary Science Letters*, **136**, 615–627.

Caldwell, J.G., Haxby, W.F., Karig, D.E. and Turcotte, D.L. (1976) On the applicability of a universal elastic trench profile. *Earth and Planetary Science Letters*, **31**, 239–246.

Cardott, B.J. and Lambert, M.W. (1985) Thermal maturation by vitrinite reflectance of Woodford Shale, Anadarko Basin, Oklahoma. *Bulletin American Association of Petroleum Geologists*, **69**, 1982–1998.

Cardozo, N. and Jordan, T. (2001) Causes of spatially variable tectonic subsidence in the Miocene Bermejo Foreland Basin, Argentina. *Basin Research*, **13**, 335–358.

Carey, S.W. (1976) *The Expanding Earth. Developments in Geotectonics*, **10**, Elsevier, Amsterdam.

Carslaw, H.S. and Jaeger, J.C. (1959) *Conduction of Heat in Solids* (2nd Edition). Oxford University Press, Oxford.

Carson, R.J. (1969) *Water, Earth and Man*. Methuen, London.

Castelltort, S. and Van Den Driessche, J. (2003) How plausible are high-frequency sediment supply-driven cycles in the stratigraphic record? *Sedimentary Geology*, **157**, 3–13.

Catacosinos, P.A. (1973) Cambrian lithostratigraphy of the Michigan Basin. *Bulletin American Association of Petroleum Geologists*, **57**, 2404–2418.

Cathles, L.M. (1975) *The Viscosity of the Earth's Mantle*. Princeton University Press.

Catuneanu, O., Beaumont, C. and Waschbusch, P. (1997) Interplay of static loads and subduction dynamics in foreland basins: Reciprocal stratigraphies and the "missing" peripheral bulge. *Geology*, **25**, 1087–1090.

Cazenave, A., Souriau, A. and Dominh, K. (1989) Global coupling of the Earth surface topography with hotspots, geoid and mantle heterogeneity. *Nature*, **340**, 54–57.

Cermak, V. (1979) Review of heat flow measurements in Czechoslovakia. In: *Terrestrial Heat Flow in Europe* (eds. V. Cermak and L. Rybach), New York, Springer-Verlag, 152–160.

Chapple, W.M. (1978) Mechanics of thin-skinned fold-and-thrust belts. *Bulletin Geological Society of America*, **89**, 1189–1198.

Chase, C.G. (1979) Subduction, the geoid, and lower mantle convection. *Nature*, **282**, 464–468.

Chase, T.E., Menard, H.W. and Mammerickx, J. (1970) *Bathymetry of the North Pacific*, Chart 8 of 10, Scripps Institution of Oceanography and Institute of Marine Resources.

Cheadle, M.J., Czuchra, B.L., Byrne, T., Ando, C.J., Oliver, J.E., Brown, L.D., Kaufman, S., Malin, P.E. and Phinney, R.A. (1985) The deep crustal structure of the Mojave Desert, California, from COCORP seismic reflection data. *Tectonics*, **5**, 293–320.

Chen, W.-P. and Molnar, P. (1983) Focal depths of intracontinental and interplate earthquakes and their implications for the thermal and mechanical properties of the lithosphere. *Journal of Geophysical Research*, **88**, 4183–4214.

Choquette, P.A. and Pray, L.C. (1970) Geologic nomenclature and classification of porosity in sedimentary carbonates. *Bulletin American Association of Petroleum Geologists*, **54**, 207–250.

Christiansson, P., Faleide, J.I. and Berge, A.M. (2000) Crustal structure in the northern North Sea: An integrated geophysical study. In: *Dynamics of the Norwegian Margin* (ed. by A. Nottvedt), *Special Publication Geological Society of London*, **167**, 15–40.

Christie-Blick, N. and Biddle, K.T. (1985) Deformation and basin formation along strike-slip faults. In: *Strike-slip Deformation, Basin Formation and Sedimentation* (eds. K.T. Biddle and N. Christie-Blick), *Special Publication Society of Economic Paleontologists and Mineralogists*, **37**, 1–34.

Clark, J.A., Farrell, W.E. and Peltier, W.R. (1978) Global changes of post-glacial sea level: a numerical calculation. *Quaternary Research*, **9**, 265–287.

Clarke, P.J., Davies, R.R., England, P.C. et al. (1998) Crustal strain in central Greece from repeated GPS measurements in the interval 1989–1997. *Geophysical Journal International* **135**, 195–214.

Clemmensen, L.B. and Blakey, R.C. (1989) Erg deposits in the Lower Jurassic Wingate Sandstone, northeastern Arizona: oblique dune sedimentation. *Sedimentology*, **36**, 449–470.

Clevis, Q. (2003) *Three-dimensional Modelling of Thrust-Controlled Foreland Basin Stratigraphy*. Geologica Ultraiectina, Mededelingen van de Faculteit Aardwetenschappen Universiteit Utrecht, **226**.

Clift, P. and Gaedicke, P. (2002) Accelerated mass flux to the Arabian Sea during the middle to late Miocene. *Geology*, **30**, 207–210.

Cloetingh, S. and Burov, E. (1996) Thermomechanical structure of European continental lithosphere: Constraints from rheological profiles and EET estimates. *Geophysical Journal International*, **124**, 695–723.

Cloetingh, S., Burov, E. and Poliakov, A. (1999) Lithospheric folding: Primary response to compression? (From Central Asia to Paris Basin). *Tectonics*, **18**, 1064–1083.

Cloetingh, S., McQueen, H. and Lambeck, K. (1985) On a tectonic mechanism for regional sea level variations. *Earth and Planetary Science Letters*, **75**, 157–166.

Cloetingh, S., Van Balen, R.T., Ter Voorde, M., Zoetemeijer, B.P. and Den Bezemer, T. (1997) Mechanical aspects of sedimentary basin formation: Development of integrated models for lithosperic and surface processes. *Geologische Rundschau*, **86**, 226–240.

Cloetingh, S., Van Wees, J.D., Van der Beck, P.A. and Spadini, G. (1995) Role of pre-rift rheology in kinematics of basin formation: Constraints from thermo-mechanical modelling of Mediterranean basins and intracratonic rifts. *Journal Marine and Petroleum Geology*, **12**, 793–808.

Cloos, E. (1955) Experimental analysis of fracture patterns. *Bulletin Geological Society of America*, **66**, 241–256.

Coakley, B.C. and Gurnis, M. (1995) Far field tilting of Laurentia during the Ordovician and constraints on the evolution of a slab under an ancient continent. *Journal of Geophysical Research*, **100**, 6313–6327.

Cobbold, P.R., Davy, P., Gapais, D., Rossello, E.A., Sadybakasov, E., Thomas, J.C., Tondji Biyo, J.J. and de Urreiztieta, M. (1993) Sedimentary basins and crustal thickening. *Sedimentary Geology*, **86**, 77–89.

Cochran, J.R. (1983) Effects of finite extension times on the development of sedimentary basins. *Earth and Planetary Science Letters*, **66**, 289–302.

Collella, A. and Prior, D.B. (eds.) (1990) *Coarse Grained Deltas. Special Publication International Association of Sedimentologists*, **10**.

Collinson, J.D. and Lewin, J. (eds.) (1983) *Modern and Ancient Fluvial Systems. Special Publication International Association of Sedimentologists* **6**. Blackwell Scientific Publications, Oxford.

Connan, J. (1974) Time-temperature relation in oil genesis. *Bulletin American Association of Petroleum Geologists*, **58**, 2516–2521.

Contreras, J. and Scholz, C.H. (2001) Evolution of stratigraphic sequences in multisegmented continental rift basins; comparison of computer models with the basins of the East African rift system. *American Association of Petroleum Geologists Bulletin*, **85**, 1565–1581.

Cooles, G.P., Mackenzie, A.S. and Quigley, T.M. (1986) Calculations of masses of petroleum generated and expelled from source rocks. In: *Advances in Organic Geochemistry* (eds. D. Leythaeuser and J. Rullkotter), 235–246, Pergamon Press, Oxford.

Cooper, M.A. and Williams, G.D. (1989) *Inversion Tectonics. Special Publication Geological Society of London*, **44**.

Corcoran, D.V. and Clayton, G. (2001) Interpretation of vitrinite reflectance profiles in sedimentary basins, onshore and offshore Ireland. In: *The Petroleum Exploration of Ireland's Offshore Basins* (eds. P.M. Shannon, P.D.W. Haughton and D.V. Corcoran), *Special Publication Geological Society of London*, **188**, 61–90.

Cornford, C. (1994) Mandal-Ekofisk Petroleum System in the Central Graben of the North Sea. In: *The Petroleum System – From Source To Trap* (eds. L.B. Magoon and W.G. Dow). *American Association of Petroleum Geologists Memoir*, **60**.

Courtney, R.C. and White, R.S. (1986) Anomalous heat flow and geoid across the Cape Verde Rise: Evidence for dynamic support from a thermal plume in the mantle. *Geophysical Journal of Royal Astronomical Society*, **87**, 815–867.

Covey, M. (1986) The evolution of foreland basins to steady state: evidence from the western Taiwan foreland basin. In: *Foreland Basins* (eds. P.A. Allen and P. Homewood), 77–90, *Special Publication International Association of Sedimentology*, **8**, Blackwell Scientific, Oxford.

Coward, M.P. (1986) Heterogeneous stretching, simple shear and basin development. *Earth and Planetary Science Letters*, **80**, 325–336.

Cowie, P.A., Gupta, S. and Dawers, N.H. (2000) Implications of fault array evolution for synrift depocentre development: Insights from a numerical fault growth model. *Basin Research*, **12**, 241–261.

Cox, A. (ed.) (1973) *Plate Tectonics and Geomagnetic Reversals*. W.H. Freeman, San Francisco.

Cox, A. and Hart, R.B. (1986) *Plate Tectonics: How it Works*. Blackwell Scientific Publications, Palo Alto, California.

Cox, K.G. (1989) The role of mantle plumes in the development of continental drainage patterns. *Nature*, **342**, 873–877.

Craig, D.H. (1988) Caves and other features of Permian karst in San Andres Dolomite, Yates field reservoir, west Texas. In: *Paleokarst* (eds. N.P. James and P.W. Choquette). Springer-Verlag, New York, 342–363.

Cramp, A., Maslin, M., Long, D. and the Shipboard Scientific Party Leg (1995) The Amazon submarine fan: Sedimentary processes and climate change: Initial results from ODP Leg 155. *Geoscientist*, **5**, 23–25.

Crampton, S.E. and Allen P.A. (1995) Recognition of forebulge unconformities associated with early stage foreland basin development: example from the North Alpine Foreland Basin. *Bulletin American Association of Petroleum Geologists*, **79**, 1495–1514.

Crittenden, M.D. Jr. (1963) Effective viscosity of the Earth derived from isostatic loading of Pleistocene Lake Bonneville. *Journal of Geophysical Research*, **68**, 5517–5530.

Cross, T.A. (1986) Tectonic controls of foreland basin subsidence and Laramide style deformation, western United States. In: *Foreland Basins* (eds. P.A. Allen and P. Homewood), *Special Publication International Association Sedimentologists*, **8**, 15–39.

Cross, T.A. (ed.) (1990) *Quantitative Dynamic Stratigraphy*. Prentice–Hall, New Jersey.

Cross, T.A. and Homewood, P. (1997) Amanz Gressly's role in founding modern stratigraphy. *Geological Society of America Bulletin*, **109**, 1617–1630.

Cross, T.A. et al. (1993) Applications of high resolution sequence stratigraphy to reservoir analysis. In: *Subsurface reservoir characterization from outcrop observations* (eds. R. Eschard and B. Doligez). Editions Technip, Paris, 11–33.

Crough, S.T. and Jurdy, D.M. (1980) Subducted lithosphere, hotspots and the geoid. *Earth and Planetary Science Letters*, **48**, 15–22.

Crough, S.T. (1978) Thermal origin of mid-plate hot-spot swells. *Geophysical Journal of Royal Astronomical Society*, **55**, 451–469.

Crowell, J.C. (1974) Origin of late Cenozoic basins in southern California. In: *Tectonics and Sedimentation* (ed. by W.R. Dickinson), *Special Publication Society of Economic Paleontologists and Mineralologists*, **22**, 190–204.

Crowell, J.C. and Link, M.H. (1982) Ridge Basin, Southern California. In: *Geologic History of Ridge Basin, Southern California* (eds. J.C. Crowell and M.H. Link), 1–4, *Society of Economic Paleontologists and Mineralogists, Pacific Section.*

Curray, J.R. (1964) Transgressions and regressions. In: *Papers in Marine Geology* (ed. by R.L. Miller), 175–203, Macmillan, New York.

Curray, J.R. (1965) Late Quaternary history, continental shelves of the United States. In: *The Quaternary of the United States* (eds. H.E. Wright and D.G. Frey), 723–735, Princeton University Press, New Jersey.

Curry, W.H. and Curry, W.H. III (1972) South Glennock oilfield, Wyoming: a pre-discovery thinking and post-discovery description. In: *Stratigraphic Oil and Gas Fields* (ed. by R.E. King), *American Association Petroleum Geologists Memoir* **16**, 415–427.

Dade, W.B. and Friend, P.F. (1998) Grain size, sediment-transport regime and channel slope in alluvial rivers. *Journal of Geology*, **106**, 661–675.

Dadson, S.J., Hovius, N. and 10 others (2003) Erosion of the Taiwan orogen. *Nature*, **426**, 648–651.

Dahl, B. and Speers, G.C. (1986) Geochemical characterization of a tar mat in the Oseberg Field, Norwegian Sector, North Sea. In: *Advances in Organic Geochemistry, 1985; Part I, Petroleum Geochemistry* (eds. D. Leythaeuser and J. Ruellkotter). *Organic Geochemistry*, **10**, 547–558.

Dahlen, F.A. (1984) Non-cohesive critical Coulomb wedges: an exact solution. *Journal of Geophysical Research*, **89**, 10125–10133.

Dahlstrom, C.D.A. (1970) Structural geology in the eastern margin of the Canadian Rocky Mountains. *Bulletin Canadian Society of Petroleum Geologists*, **18**, 332–406.

Dalrymple, R.W., Zaitlin, B.A. and Boyd, R. (1992) Estuarine facies models: Conceptual basis and stratigraphic implications. *Journal of Sedimentary Petrol.*, **62**, 1130–1146.

Davies, D.K. (1968) Carbonate turbidites, Gulf of Mexico. *Journal of Sedimentary Petrol.*, **38**, 1100–1109.

Davies, G.F. (1988) Ocean bathymetry and mantle convection, 1, large-scale flow and hotspots. *Journal of Geophysical Research*, **93**, 10467–10480.

Davies, G.F. and Richards, M.A. (1992) Mantle convection. *Journal of Geology*, **100**, 151–206.

Davis, D., Suppe, J. and Dahlen, F.A. (1983) Mechanics of fold-and-thrust belts and accretionary wedges. *Journal of Geophysical Research*, **88**, 1153–1172.

Davy, P. and Cobbold, P.R. (1991) Experiments on shortening of a 4-layer model of the continental lithosphere. *Tectonophysics*, **188**, 1–25.

Dawers, N.H. and Anders, M.H. (1995) Displacement-length scaling and fault linkage. *Journal of Structural Geology*, **17**, 607–614.

DeCelles, P.G. and Giles, K.A. (1996) Foreland basin systems. *Basin Research*, **8**, 105–124.

DeCelles, P.G., Gehrels, G.E., Quade, J., Ojha, T.P., Kapp, P.A. and Upreti, B.N. (1998) Neogene foreland basin deposits, erosional unroofing, and the kinematic history of the Himalayan fold-thrust belt, western Nepal. *Geology Society of American Bulletin*, **110**, 2–21.

Demaison, G. (1984) The generative basin concept. In: *Petroleum Geochemistry and Basin Evaluation* (eds. G. Demaison and R.J. Murris). *American Association of Petroleum Geologists Memoir*, **35**, 1–14.

Demaison, G. and Huizinga, B.J. (1994) Genetic classification of petroleum systems using three factors: Charge, migration and entrapment. In: *The Petroleum System – From Source To Trap* (eds. L.B. Magoon and W.G. Dow), *American Association of Petroleum Geologists Memoir*, **60**.

Demaison, G.J. and Moore, G.T. (1980) Anoxic environments and oil source bed genesis. *Bulletin American Association of Petroleum Geologists*, **64**, 1178–1209.

Demicco, R.V. (1998) CYCOPATH 2D – A two-dimensional forward model of cyclic sedimentation on carbonate platforms. *Computers and Geosciences*, **24**, 405–423.

Demicco, R.V. and Spencer, R.J. (1989) Maps – A basic program to model accumulation of platform sediments. *Computers and Geosciences*, **15**, 95–105.

Densmore, A.L. and Hovius, N. (2000) Topographic fingerprints of bedrock landslides. *Geology*, **28**, 371–374.

Densmore, A.L., Anderson, R.S., McAdoo, B.G. and Ellis, M.A. (1997) Hillslope evolution by bedrock landslides. *Science*, **275**, 369–372.

Densmore, A.L., Dawers, N.H., Gupta, S., Allen, P.A. and Gilpin, R. (2003) Landscape evolution at extensional relay zones. *Journal of Geophysical Research*, **108**, No. B5, 2273, doi: 10.1029/2001JB001741, 2003.

Densmore, A.L., Ellis, M.A. and Anderson, R.S. (1998) Landsliding and the evolution of normal-fault-bounded mountains. *Journal of Geophysical Research*, **103**, 15203–15219.

Dewey, J.F. (1977) Suture zone complexities: a review. *Tectonophysics*, **40**, 53–67.

Dewey, J.F. (1980) Episodicity, sequence, and style at convergent plate boundaries. In: *The Continental Crust and its Mineral Deposits* (ed. by D.W. Strangeway), *Special Paper Geology Association of Canada*, **20**, 553–573.

Dewey, J.F. (1982) Plate tectonics and the evolution of the British Isles. *Journal of Geological Society of London*, **139**, 371–414.

Dewey, J.F. and Bird, J.M. (1970) Mountain belts and the new global tectonics. *Journal of Geophysical Research*, **75**, 2625–2647.

Dewey, J.F. and Pindell, J.L. (1985) Neogene block tectonics of eastern Turkey and northern South America: continental applications of the finite difference method. *Tectonics*, **4**, 71–83.

Dewey, J.F.D. (1988) Extensional collapse of orogens. *Tectonics*, **7**, 1123–1139.

Dibblee, T.W. Jr (1977) Strike-slip tectonics of the San Andreas fault and its role in Cenozoic basin development. In: *Late*

Mesozoic and Cenozoic Sedimentation and Tectonics in California, San Joaquin Geological Society Short Course, 26–38.

Dickinson, W.R. (1974) Plate tectonics and sedimentation. In: *Tectonics and Sedimentation* (ed. by W.R. Dickinson), 1–27, *Special Publication Society of Economic Paleontologists and Mineralogists*, **22**, Tulsa, Oklahoma.

Dickinson, W.R. (1976) *Plate tectonic evolution of sedimentary basins.* American Association of Petroleum Geologists Continuing Education Course Notes Series 1, 62 p.

Dickinson, W.R. (1980) Plate tectonics and key petrologic associations. In: *The Continental Crust and its Mineral Deposits* (ed. by D.W. Strangeway), 341–360, *Special Paper Geological Association of Canada*, **20**, J.T. Wilson Volume.

Dickinson, W.R. (1993) Basin geodynamics. *Basin Research*, **5**, 195–196.

Dickinson, W.R. (1995) Forearc basins. In: *Tectonics of Sedimentary Basins* (eds. C. Busby and R. Ingersoll), Blackwell Science, Oxford, 221–262.

Dickinson, W.R. and Seely, D.R. (1979) Structure and stratigraphy of forearc regions. *Bulletin American Association of Petroleum Geologists*, **63**, 2–31.

Dickinson, W.R. and Suczek, C.A. (1979) Plate tectonics and sandstone compositions. *Bulletin American Association of Petroleum Geologists*, **63**, 2164–2182.

Dickinson, W.R. and Valloni, R. (1980) Plate tectonics and provenance of sands in modern ocean basins. *Geology*, **8**, 82–86.

Dietz, R.S. (1963) Collapsing continental rises, an actualistic concept of geosynclines and mountain building. *Journal of Geology*, **71**, 314–333.

Dingle, R.V. (1980) Large allochthonous sediment masses and their role in the construction of the continental slope and rise off southwestern Africa. *Marine Geology*, **37**, 333–354.

Doglioni, C., Mongelli, F. and Pialli, G. (1998) Boudinage of the Alpine Belt in the Apenninic back-arc. In: *Results of the CROP03 Deep Seismic Reflection Profile* (eds. G. Pialli, M. Barchi and G. Minelli), *Memorie della Societa Geologica Italiana*, **52**, 457–468.

Donovan, D.T. and Jones, E.J.W. (1979) Causes of world-wide changes in sea level. *Journal of Geological Society of London*, **136**, 187–192.

Doré, A.G., Cartwright, J.A., Stoker, M.S., Turner, J.P. and White, N. (2002) *Exhumation of the North Atlantic Margin: Timing, Mechanisms and Implications for Petroleum Exploration.* Geological Society London Special Publication, **196**.

Dorman, L.M. and Lewis, B.T.R. (1972) Experimental isostasy. 3. Inversion of the isostatic Green's function and lateral density changes. *Journal of Geophysical Research* **77**, 3068–3077.

Dorobek, S.L. (1995) Synorogenic carbonate platforms and reefs in foreland basins: Controls on stratigraphic evolution and platform/reef morphology. In: *Stratigraphic Evolution of Foreland Basins* (eds. S.L. Dorobek and G.M. Ross), *SEPM (Society for Sedimentary Geology) Special Publication*, **52**, 127–147.

Dott, R.H. Jr (1983) Episodic sedimentation: how normal is average? How rare is rare? Does it matter? *Journal of Sedimentary Petrol.*, **53**, 5–23.

Dow, W.G. (1977) Kerogen studies and geological interpretations. *Journal of Geochemical Exploration*, **7**, 79–99.

Dow, W.G. and Momper, J. (1972) The application of oil correlation and source rock data to exploration in the Williston Basin. *Bulletin of the American Association of Petroleum Geologists*, **56**, 615.

Dow, W.G. and O'Connor, D.I. (1982) Kerogen maturity and type by reflected light microscopy applied to petroleum exploration. In: *How to Assess Maturation and Paleotemperatures. Society of Economic Paleontologists and Mineralogists Short Course Notes*, **7**, 133–157.

Dowdle, W.L. and Cobb, W.M. (1975) Static formation temperature from well logs – an empirical method. *Journal of Petroleum Technology*, Nov. 1975, 1326.

Downey, J.S. (1984) Geohydrology of the Madison and associated aquifers in parts of Montana, North Dakota, South Dakota, and Wyoming. *Prof. Paper U.S. Geology Survey*, **1273–G**.

Droste, H. (1990) Depositional cycles and source rock development in an epeiric intra-platform basin: The Hanifa Formation of the Arabian peninsula. *Sedimentary Geology*, **69**, 281–296.

Drummond, C.N. and Wilkinson, B.H. (1993) Aperiodic accumulation of cyclic peritidal carbonate. *Geology*, **21**, 1023–1026.

Dubiel, R.F. (2003) Geology, depositional models, and oil and gas assessment of the Green River total petroleum system, Uinta-Piceance Province, eastern Utah and western Colorado. In: *Petroleum Systems and Geologic Assessment of Oil and Gas in the Uinta-Piceance Province, Utah and Colorado. U.S. Geological Survey, Denver, Colorado.* DD3–0069–B.

Dunbar, C.O. and Rogers, J. (1957) *Principles of Stratigraphy.* Wiley, New York.

Dunbar, J.A. and Sawyer, D.S. (1989) How pre-existing weaknesses control the style of continental breakup. *Journal of Geophysical Research*, **94**, 7278–7292.

Duncan, W.I., Green, P.F. and Duddy, I.R. (1998) Source rock burial history and seal effectiveness: Key facets to understanding hydrocarbon exploration potential in the East and Central Irish Sea Basins. *American Association Petroleum Geologists Bulletin*, **82**, 1401–1415.

Durand, B., Alpern, B., Pittion, J.L. and Pradier, B. (1986) Reflectance of vitrinite as a control of thermal history of sediments. In: *Thermal Modeling in Sedimentary Basins* (ed. by J. Burrus), 441–474, *1st IFP Exploration Research Conference, Carcans, France, June 3–7, 1985.* Editions Technip, Paris.

Dzevanshir, R.D., Buryakovskiy, L.A. and Chilingarian, G.V. (1986) Simple quantitative evaluation of porosity of argillaceous sediments at various depths of burial. *Sedimentary Geology*, **46**, 169–173.

Dziewonski, A.M. and Woodhouse, J.H. (1987) Global images of the Earth's interior. *Science*, **236**, 37–48.

Ebinger, C.J., Bechtel, T.D., Forsyth, D.W. and Bowin, C.O. (1989) Effective elastic plate thickness beneath the East African and Afar plateaus and dynamic compensation of the uplifts. *Journal of Geophysical Research*, **94**, 2883–2901.

Ebinger, C.J., Karner, G.D. and Weissel, J.K. (1991) Mechanical strength of extended continental lithosphere. Constraints from the Western Rift System, *Tectonics*, **10**, 1239–1256.

Edwards, M. (1986) Glacial environments. In: *Sedimentary Environments and Facies, 2nd Edition* (ed. by H.C. Reading), Blackwell Scientific Publications, pp. 445–470.

Ehlers, J. (1996) *Quaternary and Glacial Geology*, Wiley, Chichester.

Einsele, G. (2000) *Sedimentary Basins: Evolution, Facies and Sediment Budget* (Second Edition). Springer, Berlin.

Einsele, G. and Hinderer, M. (1997) Terrestrial sediment yield and the lifetimes of reservoirs, lakes and larger basins. *Geologische Rundschau*, **86**, 288–310.

Einsele, G., Ratschbacher, L. and Wetzel, A. (1996) The Himalaya-Bengal fan denudation-accumulation system during the past 20 Ma. *Journal of Geology*, **104**, 163–184.

Elliott, D. (1976) The motion of thrust sheets. *Journal of Geophysical Research*, **81**, 949–963.

Ellis, M.A., Densmore, A.L. and Anderson, R.S. (1999) Evolution of mountainous topography in the Basin and Range Province. *Basin Research*, **11**, 21–42.

Ellis, S. (1996) Forces driving continental collision: Reconciling indentation and mantle subduction tectonics. *Geology*, **24**, 699–702.

Ellis, S., Fullsack, P. and Beaumont, C. (1995) Oblique convergence of the crust driven by basal forcing: Implications for length-scales of deformation and strain partitioning in orogens. *Geophysical Journal International*, **120**, 24–44.

Emery D. and Meyers, K.J. (1996) *Sequence Stratigraphy*. Blackwell Science, Oxford.

Emery, D., Myers, R.J. and Young, R. (1990) Ancient subaerial exposure and freshwater leaching in sandstones. *Geology*, **18**, 1178–1181.

Emery, K.O. (1977) Structure and stratigraphy of divergent continental margins. In: *Geology of Continental Margins* (eds. H. Yarborough et al.), *American Association of Petroleum Geologists Continuing Education Course Notes Series*, **5**, B1–B20, Washington, D.C.

Emter, D. (1971) *Ergebnisse seismischer Untersuchungen der Erdkruste und des obersten Erdmantels in Südwestdeutschland*. Dissertation, Universität Stuttgart, 108 pp.

England, P. and Houseman, G. (1986) Finite strain calculations of continental deformations, 2, Comparison with the India-Asia collision. *Journal of Geophysical Research*, **91**, 3664–3676.

England, P., Houseman, G. and Sonder, L. (1985) Length scales for continental deformation in convergent, divergent and strike-slip environments: Analytical and approximate solutions for a thin viscous sheet model. *Journal of Geophysical Research*, **90**, 4797–4810.

England, P.C. (1983) Constraints on extension of continental lithosphere. *Journal of Geophysical Research*, **88**, 1145–1152.

England, P.C. (1987) Diffuse continental deformation – length scales, rates and metamorphic evolution. *Philosophical Transactions Royal Society London*, **A321**, 1557, 3–22.

England, P.C. and Houseman, G. (1989) Extension during continental convergence, with application to the Tibetan Plateau. *Journal of Geophysical Research*, **94**, 17561–17579.

England, P.C. and Houseman, G.A. (1988) Uplift and extension of the Tibetan plateau. *Journal of Geophysical Research*, **326**, 301–320.

England, P.C. and McKenzie, D.P. (1982) A thin viscous sheet model for continental deformation. *Geophysical Journal of the Royal Astronomical Society*, **70**, 295–322.

England, P.C. and McKenzie, D.P. (1983) Correction to a thin viscous sheet model for continental deformation. *Geophysical Journal of the Royal Astronomical Society*, **73**, 523–532.

England, P.C. and Molnar, P. (1990) Surface uplift, uplift of rocks, and exhumation of rocks. *Geology*, **18**, 1173–1177.

Ericksen, M.C. and Slingerland, R. (1990) Numerical simulations of tidal and wind-driven circulation in the Cretaceous Interior Seaway of North America. *Geology Society of America Bulletin*, **102**, 1499–1516.

Espitalié, J., Laporte, J.L., Madec, M., Marquis, F., Leplat, P., Paulet, J. and Boutefeu, A. (1977) Méthode rapide de caractérisation des roches mères, de leur potentiel pétrolier et de leur degré d'évolution. *Revue de l'Institut Francais du Petrole et Annales des Combustibles Liquides*, **32**, 23–42.

Ethier, V.G. and King, H.R. (1991) Reservoir quality evaluation from visual attributes on rock surfaces: Methods of estimation and classification from drill cuttings or cores. *Bulletin of Canadian Petroleum Geologists*, **39**, 233–251.

Ethridge, F.G., Flores, R.M. and Harvey, M.D. (1987) Recent Developments in Fluvial Sedimentology. *Special Publication Society of Economic Paleontologists and Mineralogists*, **39**.

Eugster, H.P. (1967) Hydrous sodium silicates from Lake Magadi, Kenya: precursors of bedded chert. *Science*, **157**, 1177–1180.

Eugster, H.P. and Hardie, L.A. (1975) Sedimentation in an ancient playa-lake complex: the Wilkins Peak member of the Green River formation of Wyoming. *Bulletin Geological Society of America*, **86**, 319–334.

Eugster, H.P. and Kelts, K. (1983) Lacustrine chemical sediments. In: *Chemical Sediments and Geomorphology* (eds. A.S. Goudie and K. Pye), 321–368, Academic Press, London.

Evans, A.E. (1988) Neogene tectonic and stratigraphic events in the Gulf of Suez area, Egypt. *Tectonophysics*, **153**, 235–247.

Eyles, C.H., Eyles, N. and Miall, A.D. (1985) Models of glaciomarine sedimentation and their application to the interpretation of ancient glacial sequences. *Palneogeography, Palaeoclimatology, Palaeoecology*, **51**, 15–84.

Fairbanks, R.G. and Matthews, R.R. (1978) The marine oxygen isotope record in Pleistocene corals, Barbados, West Indies. *Quaternary Research*, **10**, 181–196.

Fairbridge, R.W. (1961) Eustatic changes in sea level. In: *Physics and Chemistry of the Earth* (ed. by L.H. Ahrens), **4**, 99–185, Pergamon Press, London.

Falcon, N.L. (1958) Position of oil fields of southwest Iran with respect to relevant sedimentary basins. In: *Habitat of Oil* (ed. by L.G. Weeks), 1279–1293, Symposium Volume, *American Association of Petroleum Geologists*, Tulsa.

Falvey, D.A. (1974) The development of continental margins in plate tectonic theory. *Journal of Australian Petroleum Exploration Association*, **14**, 95–106.

Falvey, D.A. and Deighton, I. (1982) Recent advances in burial and thermal geohistory analysis. *Journal of Australian Petroleum Exploration Association*, **22**, 65–81.

Falvey, D.A. and Middleton, M.F. (1981) Passive continental margins: evidence for a pre-breakup deep crustal metamorphic subsidence mechanism. In: *Colloquium on Geology of Continental Margins* (C3, Paris, 7–17 July 1980), *Oceanologica Acta*, **4** (Supplement), 103–114.

Fasel, J.-M. (1986) *Sédimentologie de la Molasse d'Eau Douce Subalpine entre Le Léman et la Gruyère*. Unpubl. PhD thesis, University of Fribourg (Switzerland).

Fernandez, M. and Ranalli, G. (1997) The role of rheology in extensional basin formation modelling. *Tectonophysics*, **282**, 129–145.

Fielding, E.J. (2000) Morphotectonic evolution of the Himalayas and Tibetan Plateau. In: *Geomorphology and Global Tectonics* (ed. by M.A. Summerfield), Wiley, 201–222.

Fischer, A.G. (1975) Origin and growth of basins. In: *Petroleum and Global Tectonics* (eds. A.G. Fischer and S. Judson). Princeton University Press.

Fisk, H.N. (1947) *Fine Grained Alluvial Deposits and their Effects on Mississippi River Activity*. Mississippi River Commission, Vicksburg, Miss.

Fitzgerald, P.G., Sorkhabi, R.B., Redfield, T.F. and Stump, E. (1995) Uplift and denudation of the central Alaska Range: A case-study in the use of apatite fission track thermochronology to determine absolute uplift parameters. *Journal of Geophysical Research*, **100**, 21075–21091.

Fleitout, L. and Froideveaux, C. (1982) Tectonic stresses in the lithosphere. *Tectonics*, **2**, 315–324.

Flemings, P.B. and Jordan, T.E. (1989) A synthetic stratigraphic model of foreland basin development. *Journal of Geophysical Research*, **94**, B3851–B3866.

Flemings, P.B. and Jordan, T.E. (1990) Stratigraphic modelling of foreland basins: interpreting thrust deformation and lithospheric rheology. *Geology*, **18**, 430–434.

Flint, R.F. (1971) *Glacial and Quaternary Geology*. Wiley, New York.

Forel, F.A. (1892) *Le Léman: Monographie Limnologique*, Vol. 1, Géographie, Hydrographie, Géologie, Climatologie, Hydrologie. F. Rouge, Lausanne.

Forsyth, D.W. (1985) Subsurface loading and estimates of the flexural rigidity of continental lithosphere. *Journal of Geophysical Research*, **90**, 38–47.

Fountain, D.M. and Salisbury, M.H. (1981) Exposed cross-sections through the continental crust: implications for crustal structure, petrology and evolution. *Earth and Planetary Science Letters*, **56**, 263–277.

Fournier, F. (1960) *Climat et érosion; la relation entre erosion du sol par l'eau et les precipitations atmosphériques*. Presses Universitaires de France, Paris.

Fowler, C.M.R. (1990) *The Solid Earth: An Introduction to Global Geophysics*. Cambridge University Press.

Fowler, J.H. and Kuenzi, W.D. (1978) Keweenawan turbidites in Michigan (deep borehole red beds): a foundered basin sequence developed during evolution of a proto-oceanic rift system. *Journal of Geophysical Research*, **83**, 5833–5843.

Franzinelli, E. and Potter, P.E. (1983) Petrology, chemistry and texture of modern river sands, Amazon River system. *Journal of Geology*, **91**, 23–39.

Frazier, D.E. (1974) Depositional episodes: their relationship to the Quaternary stratigraphic framework in the northwestern portion of the Gulf Basin. *University of Texas at Austin, Bureau of Economic Geology, Geological Circular* **4**(1).

Freund, R. (1970) Rotation of strike slip faults in Sitan, southeast Iran. *Journal of Geology*, **78**, 188–200.

Freund, R. (1971) The Hope Fault, a strike-slip fault in New Zealand. *Bulletin N.Z. Geology Survey*, **86**, 1–49.

Frey, M., Teichmüller, M., Teichmüller, R., Mullis, J., Kunzi, B., Breitschmid, A., Gruner U. and Schwizer, B. (1980) Very low grade metamorphism in the external parts of the Central Alps: Illite crystallinity, coal rank and fluid inclusion data. *Eclogae geologicae Helvetiae*, **73**, 173–203.

Friedmann, S.J. and Burbank, D.W. (1995) Rift basins and supradetachment basins: Intracontinental extensional endmembers. *Basin Research*, **7**, 109–127.

Frisch, W., Dunkl, I., Kuhlemann, J. (2000) Post-collisional orogen-parallel large-scale extension in the Eastern Alps. *Tectonophysics*, **327**, 239–265.

Frostick, L.E. and Reid, I. (1986) Evolution and sedimentary character of lake deltas fed by ephemeral rivers in the Turkana basin, northern Kenya. In: *Sedimentation in the African Rifts* (eds. L.E. Frostrick et al.), *Special Publication Geological Society of London*, **25**, 113–125.

Fuis, G.S., Mooney, W.D., Healey, J.H., McMechan, G.A. and Lutter, W.J. (1982) Crustal structure of the Imperial Valley region. *U.S. Geology Survey Prof. Pap.*, **1254**, 145–154.

Fuis, G.S., Mooney, W.D., Healy, J.H., McMechan, G.A. and Lutter, W.J. (1984) A seismic refraction survey of the Imperial Valley region, California. *Journal of Geophysical Research*, B, **89**, 1165–1189.

Fullsack, P. (1995) An arbitrary Langrangian-Eulerian formulation for creeping flows and its application to tectonic models. *Geophysical Journal International*, **120**, 1–23.

Galewsky, J. (1998) The dynamics of foreland basin carbonate platforms: tectonic and eustatic controls. *Basin Research*, **10**, 409–416.

Gallagher, K. and Brown, R. (1999) Denudation and uplift at passive margins: The record on the Atlantic Margin of southern Africa. *Philosophical Transactions Royal Society London*, **357**, 835–859.

Gallagher, K., Brown, R. and Johnson, C. (1998) Fission track analysis and its application to geological problems. *Annual Reviews of Earth & Planetary Sciences*, **26**, 519–572.

Galloway, W.E. (1975) Process framework for describing the morphologic and stratigraphic evolution of deltaic depositional systems. In: *Deltas, Models for Exploration* (ed. by M.L. Broussard), 87–98, Houston Geological Society, Houston.

Galloway, W.E. (1989) Genetic stratgraphic sequences in basin analysis: Architecture and genesis of flooding surface bounded depositional units. *American Association of Petroleum Geologists Bulletin*, **73**, 125–142.

Galy, A., France-Lanord, C., Hutrez, J.E. and Lucazeau, F. (1996) Mass transfer during Himalayan erosion during the monsoon: Mineralogical and geochemical constraints. *EOS (Transactions of the American Geophysical Union)*, **77**, 236.

Garcia, R. (1981) Depositional systems and their relation to gas accumulation in Sacramento Valley, California. *Bulletin American Association of Petroleum Geologists*, **65**, 653–673.

Garfunkel, Z. (1981) Internal structure of the Dead Sea leaky transform (rift) in relation to plate kinematics. *Tectonophysics*, **80**, 81–108.

Garfunkel, Z. and Bartov, Y. (1977) The tectonics of the Suez rift. *Bull Geology Survey Israel*, **71**, 44 pp.

Garfunkel, Z., Zak, I. and Freund, R. (1981) Active faulting in the Dead Sea Rift. *Tectonophysics*, **80**, 1–26.

Gawthorpe, R.L. and Hurst, J.M. (1993) Transfer zones in extensional basins: their structural style and influence on drainage development and stratigraphy. *Journal of Geological Society London*, **150**, 1137–1152.

Gawthorpe, R.L. and Leeder, M.R. (2000) Tectono-sedimentary evolution of active extensional basins. *Basin Research*, **12**, 195–218.

Gibbs, R.J. (1970) Mechanisms controlling world water chemistry. *Science*, **170**, 1088–1090.

Gibling, M.R., Charn Tantisukrit, Wutti Utamo, Theerapongs Thanasuthipitak and Mungkorn Haraluck (1985a) Oil shale sedimentology and geochemistry in Cenozoic Mae Sot basin, Thailand. *Bulletin American Association of Petroleum Geologists*, **69**, 767–780.

Gibling, M.R., Yongyut Ukakimaphan and Suthep Srisuk (1985b) Oil shale and coal in intermontane basins of Thailand. *Bulletin American Association of Petroleum Geologists*, **69**, 760–766.

Gilchrist, A.R. and Summerfield, M.A. (1990) Differential denudation and flexural isostasy in formation of rifted-margin upwarps. *Nature*, **346**, 739–742.

Gildner, R.F. and Cisne, J.L. (1990) Quantitative modelling of carbonate stratigraphy and water-depth history using depth-dependent sediment accumulation function. In: *Quantitative Dynamic Stratigraphy* (ed. by T.A. Cross), pp. 417–432. Prentice Hall, Englewood Cliffs, New Jersey.

Giles, M.R. (1987) Mass transfer and the problems of secondary porosity creation in deeply buried hydrocarbon reservoirs. *Marine and Petroleum Geology*, **4**, 188–204.

Giles, M.R. (1997) *Diagenesis: A Quantitative Perspective. Implications for Basin Modeling and Rock Property Prediction*. Kluwer Academic Publishers, Dordrecht.

Giles, M.R. and Indrelid, S.L. (1998) Divining burial and thermal histories from indicator data: application and limitations. In: *Advances in Fission Track Geochronology* (eds. P. van den Haute and F. De Corte), Kluwer Academic Publishers, Dordrecht, 115–150.

Giles, M.R., Stevenson, S., Martin, S.V., Cannon, S.J.C., Hamilton, P.J., Marshall, J.D. and Samways, G.M. (1992) The reservoir properties and diagenesis of the Brent Group: A regional perspective. In: *Geology of the Brent Group* (eds. A.C. Morton, R.S. Haszeldine, M.R. Giles and S. Brown), *Geological Society, London. Special Publication*, **61**, 289–327.

Giltner, J.P. (1987) Application of extensional models to the northern Viking graben. *Norsk Geologisk Tidsskrift*, **67**, 339–352.

Ginsburg, R.N. (1971) Landward movement of carbonate mud: new model for regressive cycles in carbonates. *American Association Petroleum Geologists Annual Meeting, Abstracts with Programs*, **55**, 340.

Ginsburg, R.N. and James, N.P. (1974) Holocene carbonate sediments of continental margins. In: *The Geology of Continental Margins* (eds. C.A. Burke and C.L. Drake), Springer-Verlag, New York, 137–155.

Girdler, R.W. (1970) A review of Red Sea heat flow. *Philosophical Transactions Royal Society London*, **A267**, 191–203.

Glaeser, J.D. (1978) Global distribution of barrier islands in terms of tectonic setting. *Journal of Geology*, **86**, 283–297.

Glasmann, J.R. (1992) The fate of feldspar in Brent Group reservoirs, North Sea: A regional synthesis of diagenesis in shallow, intermediate, and deep burial environments. In: *Geology of the Brent Group* (eds. A.C. Morton, R.S. Haszeldine, M.R. Giles and S. Brown), *Geological Society London Special Publication*, **61**, 329–350.

Gleadow, A.J.W. and Duddy, I.R. (1981) A natural long term annealing experiment for apatite. *Nuclear Tracks*, **5**, 169–174.

Gleadow, A.J.W., Duddy, I.R. and Lovering, J.F. (1983) Apatite fission track analysis as a paleotemperature indicator for hydrocarbon exploration. *Journal of Australian Petroleum Exploration Society*, **23**, 93–102.

Glennie K.W. (1986) *Introduction to the Petroleum Geology of the North Sea, 2nd Edition*, Blackwell Scientific Publications.

Gluyas, J. and Cade, C.A. (1997) Prediction of Porosity in Compacted Sands. In: *Reservoir Quality Prediction in Sandstones and Carbonates* (eds. J.A. Kupecz, J. Gluays and S. Bloch), *American Association Petroleum Geologists Memoir*, **69**, 19–28.

Goetze, C. (1978) The mechanisms of creep in olivine. *Philosophical Transactions Royal Society London*, **A288**, 99–119.

Goetze, C. and Evans, B. (1979) Stress and temperature in the bending lithosphere as constrained by experimental rock mechanics. *Geophysical Journal of Royal Astronomical Society*, **59**, 463–478.

Goldhammer, R.K., Dunn, P.A. and Hardie, L.A. (1990) Depositional cycles, composite sea level changes, cycle stacking patterns, and the hierarchy of stratigraphic forcing: examples from Alpine Triassic platform carbonates. *Bulletin Geological Society America*, **102**, 535–562.

Goldhammer, R.K., Lehmann, P.J. and Dunn, P.A. (1993) The origin of high-frequency platform carbonate cycles and third-order sequences (Lower Ordovician El Paso Group, West Texas): Constraints from outcrop data and stratigraphic modelling. *Journal of Sedimentary Petrology*, **63**, 318–359.

Gomberg, J. and Ellis, M. (1994) Topography and tectonics of the central New Madrid Seismic Zone: results of numerical experiments using a 3-Dimensional boundary element program. *Journal of Geophysical Research*, **99**, 20299–20310.

Gordon, M.B. and Hempton M.R. (1986) Collision-induced rifting: the Grenville orogeny and the Keweenawan rift of North America. *Tectonophysics*, **127**, 1–25.

Gosnold, W.D. and Fischer, D.W. (1986) Heat flow studies in sedimentary basins. In: *Thermal Modeling in Sedimentary Basins* (ed. by J. Burrus), 199–218, *1st IFP Exploration Research Conference, Carcans, France, June 3–7*, 1985. Editions Technip, Paris.

Gould, S.J. (1989) *Wonderful Life: The Burgess Shale and the Nature of History*. W.W. Norton & Co., New York.

Grammer, G.M., Eberli, G.R., Van Buchem, F.S.P., Stegvenson, G.M. and Homewood, P. (1996) Application of high-resolution sequence stratigraphy to evaluate lateral variability in outcrop and subsurface-Desert Creek and Ismay intervals, Paradox Basin. In: *Paleozoic Systems of the Rocky Mountain Region* (eds. M.W. Longman and M.D. Sonnenfeld). *Rocky Mountain Section of the Society Economic Paleontologists and Mineralogists*, 235–266.

Granger, D.E., Kirchner, J.W. and Finkel, R. (1996) Spatially averaged long-term erosion rates measured from *in situ*-produced cosmogenic nuclides in alluvial sediments. *Journal of Geology*, **104**, 249–257.

Granjeon, D. and Joseph, P. (1999) Concepts and applications of a 3-D multiple lithology, diffusive model in stratigraphic modeling. In: *Numerical Advances in Stratigraphy: Recent Advances in Stratigraphic and Sedimentologic Simulations* (eds. J.W. Harbaugh et al.), 197–210. *Special Publication Society for Sedimentary Geology*, **62**, Tulsa, Oklahoma.

Gressly, A. (1838) Observations géologiques sur le Jura Soleurois. *Neue Denkschr. allg. schweiz. Ges. ges. Naturw.*, **2**, 1–112.

Griffiths, R.W. and Campbell, I.H. (1990) Interaction of mantle plume heads with the Earth's surface and onset of small-scale convection. *Journal of Geophysical Reasearch*, **96**, 18295–18310.

Griggs, D.T., Turner, F.J. and Heard, H.C. (1960) Deformation of rocks at 500 to 800 °C. In: *Rock Deformation* (eds. D.T. Griggs and J. Handin), 21–37, *Geology Society America Memoir*, **79**.

Grocott, J. and Watterson, J. (1980) Strain profile of a boundary within a large ductile shear zone. *Journal of Structural Geology*, **2**, 111–117.

Grotzinger, J.P. (1986a) Cyclicity and paleoenvironmental dynamics, Rocknest platform, northwest Canada. *Bulletin Geological Society of America*, **97**, 1208–1231.

Grotzinger, J.P. (1986b) Upward-shallowing platform cycles: a response to 2.2 billion years of low-amplitude, high-frequency (Milankovitch band) sea level oscillations. *Paleoceanography*, **1**, 403–416.

Grove, A.T. and Warren, A. (1968) Quaternary landforms and climate on the south side of the Sahara. *Geographical Journal of London*, **134**, 194–208.

Grow, J.A. and Bowin, C. (1975) Evidence for high-density crust and mantle beneath the Chile Trench due to the descending lithosphere. *Journal of Geophysical Research*, **80**, 1449–1458.

Grow, J.A., Mattick, R.E. and Schlee, J.S. (1979) Multichannel seismic depth sections and interval velocities over outer continental shelf and upper slope between Cape Hatteras and Cape Cod. In: *Geological Investigations of Continental Margins* (eds. J.S. Watkins, L. Montadert and P.W. Dickerson), *American Association of Petroleum Geologists Memoir*, **29**, 65–83.

Grunau, H.R. (1987) A worldwide look at the caprock problem. *Journal of Petroleum Geology*, **10**, 245–266.

Gunnell, Y. (1998) The interaction between geological structure and global tectonics in multistoreyed landscape development: A denudation chronology of the South Indian shield. *Basin Research*, **10**, 281–310.

Gupta (1997) Himalayan drainage patterns and the origin of fluvial megafans in the Ganges foreland basins. *Geology*, **25**, 11–14.

Gupta, S. and Allen, P.A. (2000) Implications of foreland paleotopography for stratigraphic development in the Eocene distal Alpine foreland basin. *Bulletin Geological Society of America*, **112**, 515–530.

Gupta, S. and Cowie, P. (ed.) (2000) Processes and Controls in the Stratigraphic Development of Extensional Basins. *Thematic set, Basin Research*, **12**, 185–448.

Gupta, S., Underhill, J.R., Sharp, I.R. and Gawthorpe, R.L. (1999) Role of fault interactions in controlling synrift sediment dispersal patterns; Miocene, Abu Alaqa Group, Suez Rift, Sinai, Egypt. *Basin Research*, **11**, 167–189.

Gurnis, M. (1988) Large-scale mantle convection and the aggregation and dispersal of continents. *Nature*, **332**, 695–699.

Gurnis, M. (1992) Rapid continental subsidence following the initiation and evolution of subduction. *Science*, **255**, 1556–1558.

Gurnis, M. (1993) Depressed continental hypsometry behind ocean trenches: a clue to subduction controls on sea-level change. *Geology*, **21**, 29–32.

Gurnis, M. and Hager, B.H. (1988) Controls of the structure of subducted slabs. *Nature (London)*, **335**, 317–321.

Gurnis, M. (1990) Bounds on global dynamic topography from Phanerozoic flooding of continental platforms. *Nature*, **344**, 754–756.

Gurnis, M., Eloy, C. and Zhong, S. (1996) Free-surface formulation of mantle convection; II, Implication for subduction-zone observables. *Geophysical Journal International.*, **127**, 719–727.

Gussow, W.C. (1954) Differential entrapment of oil and gas: a fundamental principle. *Bulletin American Association of Petroleum Geologists*, **38**, 816–853.

Gust, D.A., Biddle, K.T., Phelps, D.W. and Uliana, M.A. (1985) Associated Middle to Late Jurassic volcanism and extension in southern South America. *Tectonophysics*, **116**, 223–253.

Haack, U. (1982) Radioactivity of rocks. In: *Physical Properties of Rocks* (ed. by G. Angenheister), 433–481, Vol. 1b, Springer-Verlag, Berlin.

Hack, J.T. (1973) Drainage adjustment in the Appalachians. In: *Fluvial Geomorphology* (ed. by M. Morisawa), 51–69. SUNY Publications in Geomorphology, Binghampton, N.Y.

Hagemann, H.W. (1974) Petrographische und Palynologische Untersuchung der organischen Substanz (Kerogen) in den Liassischen Sedimenten Luxemburgs. In: *Advances in Organic Geochemistry* (eds. B. Tissot and F. Bienner), 29–37, Technip, Paris.

Hager, B.H. (1984) Subducted slabs and the geoid: constraints on mantle rheology and flow. *Journal of Geophysical Research*, **89**, B7, 6003–6015.

Hager, B.H., Clayton, R.W., Richards, M.A., Comer, R.P. and Dziewonski, A.M. (1985) Lower mantle heterogeneity, dynamic topography and the geoid. *Nature (London)*, **313**, 541–545.

Hager, B.H. and Clayton, R.W. (1989) Constraints on the structure of mantle convection using seismic observations, flow models, and the geoid. In: *Mantle Convection* (ed. by R.W. Peltier), Gordon and Breach, New York, 657–763.

Halbouty, M.T. (1979) *Salt Domes, Gulf Region, United States and Mexico, 2nd Edition*. Gulf Publishing, Houston, Texas.

Halbouty, M.T. (1982) The time is now for all explorationists to purposely search for the subtle trap. In: *The Deliberate Search for the Subtle Trap* (ed. by M.T. Halbouty), 1–10, *American Association of Petroleum Geologists Memoir*, **32**.

Halbouty, M.T., King, R.E., Klemme, H.D. Dott, R.H. and Meyerhoff, A.A. (1970) World's giant oil and gas fields, geologic factors affecting their formation, and basin classification, part II, Factors affecting formation of giant oil and gas fields, and basin classification. In: *Geology of Giant Petroleum Fields* (ed. by M.T. Halbouty), *American Association of Petroleum Geologists Memoir*, **14**, 528–555.

Hall, T. and Al-Haddad, F.M. (1976) Seismic velocities in the Lewisian metamorphic complex, north-west Britain – *in situ* measurements. *Scot. Journal of Geology*, **12**, 305–314.

Hallam, A. (1963) Major epeirogenic and eustatic changes since the Cretaceous and their possible relationship to crustal structure. *American Journal of Science*, **261**, 397–423.

Hallam, A. (1977) Secular changes in marine inundation of USSR and North America through the Phanerozoic. *Nature*, **269**, 769–772.

Hallet, B., Hunter, L. and Bogen, J. (1996) Rates of erosion and sediment evacuation by glaciers. A review of field data and their implications. *Global and Planetary Change*, **12**, 213–235.

Halley, R.B. and Schmoker, J.W. (1983) High-porosity Cenozoic carbonate rocks of South Florida: Progressive loss of porosity with depth. *Bulletin American Association of Petroleum Geologists*, **67**, 1191–1200.

Hambrey, M.J. (1994) *Glacial Environments*. UCL Press, London.

Hamilton, P.J., Giles, M.R. and Ainsworth, P. (1992) K-Ar dating of illites in Brent Group reservoirs: A regional perspective. In: *Geology of the Brent Group* (eds. A.C. Morton, R.S. Haszeldine, M.R. Giles and S. Brown), *Geological Society London Special Publication*, **61**, 377–400.

Hamilton, P.J., Kelley, S. and Fallick, A.E. (1989) K-Ar dating of illite in hydrocarbon reservoirs. *Clay Minerals*, **24**, 215–231.

Hamilton, W. (1979) Tectonics of the Indonesian region. *Prof. Paper U.S. Geology Survey*, **1078**.

Hancock, G.S., Anderson, R.S., Whipple, K.X. and Wohl, E.E. (1998) Beyond power: Bedrock river incision process and form. *Rivers over rock, fluvial processes in bedrock channels. Geophysical Monograph*, **107**, 35–60.

Hanks, T.C. (1971) The Kuril trench–Hokkaido rise system: large shallow earthquakes and simple models of deformation. *Geophysical Journal of the Royal Astronomical Society*, **23**, 173–189.

Hanks, T.C., Bucknam, R.C., LaJoie, K.R. and Wallace, R.E. (1984) Modification of wave-cut and faulting controlled landforms. *Journal of Geophysical Research*, **89**, 5771–5790.

Haq, B.U., Hardenbol, J. and Vail, P.R. (1987) Chronology of fluctuating sea levels since the Triassic (250 Myr ago to present). *Science*, **235**, 1156–1167.

Haq, B.U., Hardenbol, J. and Vail, P.R. (1988) Mesozoic and Cenozoic chronostratigraphy and cycles of sea-level change. In: *Sea-level Changes: An Integrated Approach* (eds. C.K. Wilgus, B.S. Hastings, C.G. St. Kendall, H.W. Posamentier, C.A. Ross and J.C. Van Wagoner), *Special Publication, Society of Economic Paleontologists and Mineralogists*, Tulsa, **42**, 40–45.

Harbaugh, J.W., Watney, L., Rankey, G., Slingerland, R., Goldstein, R. and Franseen, E. (eds.) (1999) *Numerical Experiments in Stratigraphy. Recent Advances in Stratigraphic and Sedimentologic Computer Simulations. Society for Sedimentary Geology Special Publication*, **62**, Tulsa, Oklohama.

Hardie, L.A. and Shinn, E.A. (1986) Carbonate depositional environments, modern and ancient – 3, tidal flats. *Quarterly Journal of Colorado School of Mines*, **81**.

Hardie, L.A., Dunn, P.A. and Goldhammer, R.K. (1991) Field and modelling studies of Cambrian cycles, Virginia Appalachians – Discussion. *Journal of Sedimentary Petrology*, **61**, 636–646.

Harding, T.P. and Lowell, J.D. (1979) Structural styles, their plate tectonic habitats and hydrocarbon traps in petroleum provinces. *Bulletin American Association of Petroleum Geologists*, **63**, 1016–1058.

Harris, L.B. and Cobbold, P.R. (1984) Development of conjugate shear bands during simple shearing. *Journal of Structural Geology*, **7**, 37–44.

Harris, P.M., Saller, A.H. and Simo, J.A. (1999) Introduction. In: *Advances in Carbonate Sequence Stratigraphy: Applications to Reservoirs, Outcrops and Models* (eds. P.M. Harris, A.H. Saller and J.A. Simo), *Society of Economic Paleontologists and Mineralogists* Tulsa, Oklahoma, 1–10.

Harrison, W.J. and Summa, L.L. (1991) Paleohydrology of the Gulf of Mexico Basin. *American Journal of Science*, **291**, 109–176.

Hartley, R.W. and Allen, P.A. (1994) Interior cratonic basins of Africa: relation to continental break-up and role of mantle convection. *Basin Research*, **6**, 95–113.

Haszeldine, R.S., Macaulay, C.I., Marchands, A. et al. (2000) Sandstone cementation and fluids in hydrocarbon basins. *Journal of Geochemical Exploration*, **69–70**, 195–200.

Haughton, P. (2001) Contained turbidites used to track sea bed deformation and basin migration, Sorbas basin, south-east Spain. *Basin Research*, **13**, 117–140.

Haxby, W.F. Turcotte, D.L. and Bird, J.M. (1976) Thermal and mechanical evolution of the Michigan Basin. *Tectonophysics*, **36**, 57–75.

Hay, W.W. (1998) Detrital sediment fluxes from continents to oceans. *Chemical Geology*, **145**, 287–323.

Hayes, M.O. (1979) Barrier island morphology as a function of tidal and wave regime. In: *Barrier Islands from the Gulf of St. Lawrence to the Gulf of Mexico* (ed. S.P. Leatherman), 1–27, Academic Press, New York.

Hays, J.D. and Pitman, W.C. (1973) Lithospheric plate motion, sea level changes, and climatic and ecological consequences. *Nature*, **246**, 18–22.

Hays, J.D. Imbrie, J. and Shackleton, N.J. (1976) Variations in the Earth's orbit: pacemaker of the ice ages. *Science*, **194**, 2212–2232.

Heard, H.C. (1960) Transition from brittle fracture to ductile flow in Solenhofen limestone as a function of temperature, confining pressure, and interstitial fluid pressure. In: *Rock Deformation* (eds. D.T. Griggs and J. Handin), 193–226, *Geological Society of America Memoir*, **79**.

Hedberg, H.D. (1936) Gravitational compaction of clays and shales. *American Journal of Science*, **31**, 241–287.

Heling, D. and Teichmüller, M. (1974) Die Grenze Montmorillonit/Mixed Layer Minerale und ihre Beziehung zur Inkohlung in der grauen Schichtenfolge des Oligozäns im Oberrheingraben. *Fortschritte in der Geologie von Rheinland und Westfalen, Krefeld*, **24**, 113–128.

Heller, P.L., Angevine, C.L. and Winslow, N.S. (1988) Two-phase stratigraphic model of foreland basin sequences. *Geology*, **16**, 501–504.

Hellinger, S.J. and Sclater, J.G. (1983) Some comments on two-layer extensional models for the evolution of sedimentary basins. *Journal of Geophysical Research*, **88**, 8251–8270.

Herb, R. (1988) Eocaene palaeogeographie and palaeotektonic des Helvetikums. *Eclogae Geologicae Helvetiae*, **81**, 611–657.

Héroux, Y., Chagnon, A. and Bertrand, R. (1979) Compilation and correlation of major thermal maturation indicators. *Bulletin American Association of Petroleum Geologists*, **63**, 2128–2144.

Hetényi, M. (1979) *Beams on Elastic Foundations*. Ann Arbor, Michigan, University of Michigan Press.

Heward, A.P. (1981) A review of wave-dominated clastic shoreline deposits. *Earth Science Reviews*, **17**, 223–276.

Heydari, E. (1997) Hydrotectonic models of burial diagenesis in platform carbonates based on formation water geochemistry in North American sedimentary basins. *Special Publication Society for Sedimentary Geology. Tulsa, OK, United States*, **57**, 53–79.

Hill, K.C. (1991) Structure of the Papuan Fold Belt, Papua New Guinea. *Bulletin American Association of Petroleum Geologists*, **75**, 857–872.

Hill, R.I. (1991) Starting plumes and continental break-up. *Earth & Planetary Science Letters*, **104**, 398–416.

Hinze, W.J. and Merritt, D.W. (1969) Basement rocks of the Michigan Basin. In: *1969 Annual Field Excursion* (ed. by H.B. Stonehouse), 28–59, Michigan Basin Geological Society, Lansing, Michigan, USA.

Hinze, W.J., Kellog, R.L. and O'Hara, N.W. (1975) Geophysical studies of basement geology of the southern peninsula of Michigan. *Bulletin American Association of Petroleum Geologists*, **59**, 1562–1584.

Hirn, A. (1976) Sondages sismiques profonds en France. *Bulletin Society Géol. France*, **23**, 1065–1071.

Hirn, A. and Perrier, G. (1974) Deep seismic sounding in the Limagne graben. In: *Approaches to Taphrogenesis* (eds. J.H. Illies and K. Fuchs), Stuttgart, E. Schweizerbartsche Verlagsbuchhandlung, 329–340.

Hirst, J.P.P. and Nichols, G.J. (1986) Thrust tectonic controls on Miocene alluvial distribution patterns, southern Pyrenees. In: *Foreland Basins* (eds. P.A. Allen and P. Homewood), 247–258, *Special Publication International Association of Sedimentology*, **8**, Blackwell Scientific, Oxford.

Hoffman, P.E., Kaufman, A.J., Halverson, G.P. and Schrag, D.P. (1998) A Neoproterozoic snowball Earth. *Science*, **281**, 1342–1346.

Hogg, A.J.C., Mitchell, A.W. and Young, S. (1996) Predicting well productivity from grain-size analysis and logging while drilling. *Petroleum Geoscience*, **2**, 1–15.

Holland, H.D. (1981) River transport to the oceans. In: *The Sea*, (ed. by C. Emiliani), **7**, *The Oceanic Lithosphere, Wiley*, 763–800.

Homewood, P., Allen, P.A. and Williams, G.D. (1986) Dynamics of the Molasse Basin of western Switzerland. In: *Foreland Basins* (eds. P.A. Allen and P. Homewood), 199–217, *Special Publication International Association of Sedimentology*, **8**, Blackwell Scientific, Oxford.

Homewood, P.W., Guillocheau, F., Eschard, R. and Cross, T.A. (1992) Corrélations haute résolution et stratigraphie génétique: Une démarche intégrée. *Bulletin Cent. Rech. Explor.-Prod. Elf Aquitaine*, **16**, 357–381.

Homewood, P.W., Mauriaud, P. and Lafont, F. (2000) *Best Practices in Sequence Stratigraphy*. ELF EP Edition, Mémoire **25**, p. 81.

Hood, A., Gutjahr, C.C.M. and Heacock, R.L. (1975) Organic metamorphism and the generation of petroleum. *Bulletin American Association of Petroleum Geologists*, **59**, 986–996.

Horton, B.K. and DeCelles, P.G. (1997) The modern foreland basin system adjacent to the central Andes. *Geology*, **25**, 895–898.

Horton, B.K., Hampton, B.A. and Waanders, G.L. (2001) Paleogene synorogenic sedimentation in the Altiplano plateau and implications for initial mountain building in the central Andes. *Geological Society of America Bulletin*, **113**, 1387–1400.

Horvath, F. and Cloetingh, S. (1996) Stress-induced late-stage subsidence anomalies in the Pannonian Basin. *Tectonophysics*, **266**, 287–300.

Houseman, G. and England, P.C. (1986) A dynamical model of lithosphere extension and sedimentary basin formation. *Journal of Geophysical Research*, **91**, 719–729.

Hovius, N. (1995) *Macro scale process systems of mountain belt erosion and sediment delivery to basins*. Unpublished DPhil. thesis, University of Oxford.

Hovius, N. (1996) Regular spacing of drainage outlets from linear mountain belts. *Basin Research*, **8**, 29–44.

Hovius, N. (1998) Controls on sediment supply by large rivers. In: *Relative Role of Eustasy, Climate and Tectonics in Continental Rocks* (eds. K.W. Shanley and P.J. McCabe), *Society of Economic Paleontologists and Mineralogists Special Publication*, **59**, 3–16.

Hovius, N. (2000) Macroscale process systems of mountain belt erosion. In: *Geomorphology and Global Tectonics* (ed. by M.A.

Summerfield). John Wiley & Sons. Chichester, United Kingdom. 77–105.

Hovius, N. and Leeder, M.R. (1998) Clastic sediment supply to basins. *Basin Research*, **10**, 1–5.

Hovius, N., Stark, C.P. and Allen, P.A. (1997) Sediment flux from a mountain belt derived by landslide mapping. *Geology*, **25**, 231–234.

Hovius, N., Stark, C.P., Chu, H.T. and Lin, J.C. (2000) Supply and removal of sediment in a landslide-dominated mountain belt: Central Range, Taiwan. *Journal of Geology*, **108**, 73–89.

Howard, A.D. (1987) Modelling fluvial systems: Rock-, gravel- and sandbed channels. In: *River Channels* (ed. by K. Richards), Basil Blackwell, New York, 69–94.

Howard, A.D. (1994) A detachment limited model of drainage basin evolution. *Water Resources Research*, **30**, 739–752.

Howard, J.J. (1992) Influence of authigenic clay minerals on permeability. In: *Origin, Diagenesis, and Petrophysics of Clay Minerals in Sandstones* (eds. D.W. Houseknecht and E.D. Pittman), *Special Publication of the Society of Economic Paleontologists and Mineralogists*, Tulsa, Oklahoma, **47**, 257–264.

Howell, D.G. and Vedder, J. (1981) Structural implications of stratigraphic discontinuities across the southern California borderland. *Journal of Sedimentary Petrol.*, **49**, 517–540.

Howell, D.G., Crouch, J.K., Greene, H.G., McCulloch, D.S. and Vedder, J.G. (1980) Basin development along the late Mesozoic and Cainozoic California margin: a plate tectonic margin of subduction, oblique subduction and transform tectonics. In: *Sedimentation in Oblique Slip Mobile Zones* (eds. P.F. Ballance and H.G. Reading), 43–62, *Special Publication International Association of Sedimentology*, **4**, Blackwell Scientific, Oxford.

Hower, J., Eslinger, E.V., Hower, M. and Perry, E.A. (1976) Mechanism of burial metamorphism in argillaceous sediments. I. Mineralogical and chemical evidence. *Geological Society of America Bulletin*, **87**, 725–737.

Hsu, K.J. (ed.) (1983) *Mountain Building Processes*. Academic Press, Orlando, Florida.

Hsu, K.J., Ryan, W.B.F. and Cita, M.B. (1973) Late Miocene desiccation of the Mediterranean. *Nature*, **242**, 240–244.

Hubbard, R.J., Pape, J. and Roberts, D.G. (1985) Depositional sequence mapping as a technique to establish tectonic and stratigraphic framework and evaluate hydrocarbon potential on a passive continental margin. In: *Seismic Stratigraphy II: An Integrated Approach* (eds. O.R. Berg and D. Woolverton), *American Association Petroleum Geologists Memoir*, **39**, 79–91.

Hubbert, M.K. (1953) Entrapment of petroleum under hydrodynamic conditions. *Bulletin American Association of Petroleum Geologists*, **37**, 1954–2026.

Hubbert, M.K. and Rubey, W.W. (1959) Role of fluid pressure in mechanics of overthrust faulting. *Bulletin Geological Society of America*, **70**, 115–166.

Huff, K.F. (1978) Frontiers of world oil exploration. *Oil and Gas Journal*, **76**, No. 40, 214–220.

Hull, C.E. and Warman, H.R. (1970) Asmari oil fields of Iran. In: *Geology of Giant Petroleum Fields, American Association Petroleum Geologists Memoir*, **14**, 428–437.

Hunt, D. and Tucker, M.E. (1992) Stranded parasequences and the forced regressive wedge systems tract: deposition during base level fall. *Sedimentary Geology*, **81**, 1–9.

Hunt, J.M. (1961) Distribution of hydrocarbons in sedimentary rocks. *Geochimica et Cosmochimica Acta*, **22**, 37–49.

Hunt, J.M. (1979) *Petroleum Geochemistry and Geology*. W.H. Freeman, San Francisco.

Hunt, J.M. (1980) Application of Geochemistry to Petroleum Exploration. *Proceedings American Association of Petroleum Geologists Fall Education Conference, Houston, Texas.*

Hurford, A.J. (1986) Cooling and uplift patterns in the Lepontine Alps, south-central Switzerland, and an age of vertical movement on the Insubric fault line. *Contributions to Mineralogy and Petrology*, **92**, 413–427.

Hurford, A.J. and Carter, A. (1991) The role of fission track dating in discrimination of provenance. In: *Developments in Sedimentary Provenance Studies* (eds. A. Morton, S.P. Todd and P.D.W. Haughton), *Geological Society of London Special Publication*, **57**, 67–78.

Hurford, A.J., Flisch, M. and Jäger, E. (1989) Unravelling the thermo-tectonic evolution of the Alps: a contribution from fission track analysis and mica dating. In: *Alpine Tectonics* (eds. M.P. Coward, D. Dietrich and R.G. Park), *Geological Society of London Special Publication*, **45**, 369–398.

Huuse, M. and Clausen, O.R. (2001) Morphology and origin of major Cenozoic sequence boundaries in the eastern North Sea Basin: Top Eocene, near-top Oligocene and the mid-Miocene unconformity. *Basin Research*, **13**, 17–41.

Illies, J.H. (1977) Ancient and recent rifting in the Rhine graben. *Geologie en Mijnbouw*, **56**, 4, 329–350.

Illies, J.H. and Greiner, G. (1978) Rhine graben and the Alpine system. *Bulletin Geological Society of America*, **89**, 770–782.

Imbrie, J. (1982) Astronomical theory of the Pleistocene ice ages: a brief historical review. *Icarus*, **50**, 408–422.

Ingersoll, R.V. (1988) Tectonics of sedimentary basins. *Bulletin Geological Society of America*, **100**, 1704–1719.

Ingersoll, R.V. and Busby, C.J. (1995) Tectonics of sedimentary basins. In: *Tectonics of Sedimentary Basins* (eds. C.J. Busby and R.V. Ingersoll), 1–52, Blackwell Science, Oxford.

Ingersoll, R.V. and Suczek, C.A. (1979) Petrology and provenance of Neogene sand from Nicobar and Bengal fans, DSDP 211 and 218. *Journal of Sedimentary Petrol.*, **49**, 1217–1228.

Isaaks, B.L. (1988) Uplift of the central Andean plateau and bending of the Bolivian orocline. *Journal of Geophysical Research*, **93**, 3211–3231.

Isacks, B. and Molnar, P. (1971) Distribution of stresses in the descending lithosphere from a global survey of focal-mechanism solutions of mantle earthquakes. *Reviews of Geophysics and Space Physics*, **9**, 103–174.

Isacks, B., Oliver, J. and Sykes, L. (1969) Seismology and the new global tectonics. *Journal of Geophysical Research*, **73**, 5855–5899.

Isacks, B.L. and Barazangi, M. (1977) Geometry of Benioff zones: Lateral segmentation and downward bending of the subducted lithosphere. In: *Island Arcs, Deep Sea Trenches and*

Back-arc Basins (eds. M. Talwani and W.C. III Pitman). 99–114.

Jackson, M.P.A. and Galloway, W.E. (1984) Structural and depositional styles of Gulf Coast Tertiary continental margins: application to hydrocarbon exploration. *American Association of Petroleum Geologists, Continuing Education Course Notes Series*, **25**.

Jackson, J., Norris, R. and Youngson, J. (1996) The structural evolution of active fault and fold systems in central Otago, New Zealand: evidence revealed by drainage patterns. *Journal of Structural Geology*, **18**, 217–234.

Jacob, H. and Kuckelhorn, K. (1977) Das Inkohlungsprofil der Bohrung Miesbach 1 und seine erdölgeologische Interpretation. *Erdöl-Erdgas Z.*, **4**, 115–124.

James, N.P. (1983) Reef environment. In: *Carbonate Depositional Environments* (eds. P.A. Scholle, D.G. Bebout and C.H. Moore), *American Association of Petroleum Geologists Memoir*, **33**, 346–440.

Jansa, L.F. and Wade, J.A. (1975) Geology of the continental margin off Nova Scotia and Newfoundland. In: *Offshore Geology of Eastern Canada* (eds. W.J.M. Van der Linden and J.A. Wade) 74–30, Paper – Geological Survey of Canada **2**, 51–105.

Jardine, D. and Wilshart, J.W. (1987) Carbonate reservoir description. In: *Reservoir Sedimentology* (eds. R.W. Tillman and W.J. Weber), *Special Publication Society of Economic Paleontologists and Mineralogists*, **40**, 129–152.

Jarvis, G.T. and McKenzie, D.P. (1980) The development of sedimentary basins with finite extension rates. *Earth and Planetary Science Letters*, **48**, 42–52.

Jeans, C.V., Wray, D.S., Merriman, R.J. and Fisher, M.J. (2000) Volcanogenic clays in Jurassic and Cretaceous strata of England and the North Sea basin. In: *Mineral Diagenesis and Reservoir Quality, the Way Forward* (eds. D.C. Bain, P.L. Hall, H.F. Shaw and D.A. Spears), *Clay Minerals*, **35**, 25–55.

Jennings, C.W., compiler (1975) Preliminary fault and geologic map of southern California. In: *San Andreas Fault in Southern California* (ed. by J.E. Crowell), *California Division of Mines and Geology Special Report*, **118**, Scale 1:750,000.

Jervey, M.T. (1988) Quantitative geological modeling of siliciclastic rock sequences and their seismic expressions. In: *Sea Level Changes: An Integrated Approach* (eds. C.K. Wilgus et al.), *Special Publication Society of Economic Paleontologists and Mineralogists*, **42**, 47–69.

Jessop, A.M. and Lewis, T. (1978) Heat flow and heat generation in the Superior Province of the Canadian Shield. *Tectonophys*, **50**, 55–77.

Johnson, D.D. and Beaumont, C. (1995) Preliminary results from a planform kinematic model of orogen evolution, surface processes and the development of clastic foreland basin stratigraphy. In: *Stratigraphic Evolution of Foreland Basins* (eds. S.L. Dorobek and G.M. Ross), *Special Publication Society of Economic Paleontologists and Mineralogists*, **52**, 3–24.

Johnson, H.D. and Baldwin, C.T. (1986) Shallow siliciclastic seas. In: *Sedimentary Facies and Environments* (ed. by H.G. Reading), 229–282, Blackwell Scientific, Oxford.

Jolley, E.T., Turner, P., Williams, G.D., Hartley, A.J. and Flint, S. (1990) Sedimentological response of an alluvial system to Neogene thrust tectonics, Atacama Desert, northern Chile. *Journal of the Geological Society of London*, **147**, 769–784.

Jones, C.H., Unruh, J.R. and Sonder, L.J. (1996) The role of gravitational potential energy in active deformation in the southeastern United States. *Nature*, **381** (6577), 37–41.

Jones, G., Fisher, G.J. and Knipe, R.J. (eds). (1998) *Faulting, Fault Sealing and Fluid Flow in Hydrocarbon Reservoirs. Special Publication Geological Society London*, **147**.

Jordan, T.E. (1981) Thrust loads and foreland basin evolution, Cretaceous, western United States. *Bulletin American Association of Petroleum Geologists*, **65**, 2506–2520.

Jordan, T.E. and Allmendinger, R.W. (1986) The Sierras Pampeanas of Argentina; a modern analogue of Rocky Mountain foreland deformation. *American Journal of Science*, **286**, 737–764.

Junger, A. (1976) Tectonics of the southern California borderlands. In: *Aspects of the geol. hist. of the California Continental Borderland Miscellaneous Publication*, **24** (ed. D.G. Howell), 486–498. *American Association of Petroleum Geologists*, Pacific Section, Bakersfield, CA, United States.

Kantorowicz, J.D. (1990) The influence of variations in illite morphology on the permeability of Middle Jurassic Brent Group sandstones, Cormorant Field, UK North Sea. *Marine and Petroleum Geology*, **7**, 66–74.

Karason, H. and van der Hilst, R.D. (2000) Constraints on mantle convection from seismic tomography. In: *The History and Dynamics of Global Plate Motions* (eds. M.A. Richards, R.G. Gordon and R.D. van der Hilst), American Geophysical Union, Geophysical Monograph, **121**, 277–288.

Karig, D.E. and Moore, G.F. (1975) Tectonically controlled sedimentation in marginal basins. *Earth and Planetary Science Letters*, **26**, 233–238.

Karner, G. (1991) Sediment blanketing and the flexural strength of the extended continental lithosphere. *Basin Research*, **3**, 177–185.

Karner, G.D. (1986) Effects of lithospheric in-plane stress on sedimentary basin stratigraphy. *Tectonics*, **5**, 573–588.

Karner, G.D. and Watts, A.B. (1983) Gravity anomalies and flexure of the lithosphere at mountain ranges. *Journal of Geophysical Research*, **88**, 10449–10477.

Karner, G.D. Steckler, M.S. and Thorne, J.A. (1983) Long-term thermo-mechanical properties of the lithosphere. *Nature*, **304**, 250–252.

Katzman, R., ten Brink, U.S. and Lin, J. (1995) Three-dimensional modeling of pull-apart basins: implications for the tectonics of the Dead Sea Basin. *Journal of Geophysical Research*, **100**, B4, 6295–6312.

Kaufman, P., Grotzinger, J.P. and McCormick, D.S. (1991) Depth-dependent diffusion algorithm for simulation of sedimentation in shallow marine depositional systems. In: *Sedimentary Modeling: Computer Simulations and Methods for Improved Parameter Definition* (eds. E.K. Franseen, W.L. Watney, C.G.S.C. Kendall and W. Ross), *Kansas Geology Survey Bulletin*, **233**, 489–508.

Kay, M. (1947) Geosynclinal nomenclature and the craton. *Bulletin American Association of Petroleum Geologists*, **31**, 1289–1293.

Kay, M. (1951) North American Geosynclines. *Geological Society of America Memoir*, **48**.

Kearey, P. and Vine, F.J. (1996) *Global Tectonics* (Second Edition), Blackwell Science, Oxford.

Keen, C.E. (1985) The dynamics of rifting: deformation of the lithosphere by active and passive driving forces. *Geophysical Journal of the Royal Astronomical Society*, **80**, 95–120.

Keen, C.E. (1987) Some important consequences of lithospheric extension. In: *Continental Extensional Tectonics* (eds. M.P. Coward, J.F. Dewey and P.L. Hancock), *Geological Society Special Publication*, **28**, 67–73.

Keen, C.E. and Dehler, S.A. (1997) Extensional styles and gravity anomalies at rifted continental margins. Some North Atlantic examples. *Tectonics*, **16**, 744–754.

Keen, C.E., Stockmal, G.S., Welsink, H., Quinlan, G. and Mudford, B. (1987) Deep crustal structure and evolution of the rifted margin northeast of Newfoundland. Results from Lithoprobe East. *Canadian Journal of Earth Sciences*, **24**, 1537–1550.

Keller, E.A., Bonkowski, M.S., Korsch, R.J. and Shlemon, R.J. (1982) Tectonic geomorphology of the San Andreas fault zone in the southern Indio Hills, Coachella Valley, California. *Geological Society of America Bulletin*, **93**, 46–56.

Kelley, P.A., Bissada, K.K., Burda, B.H., Elrod, L.W. and Pheifer, R.N. (1985) Petroleum generation potential of coals and organic-rich deposits: significance in Tertiary coal rich basins. *Proceedings Indonesian Petroleum Association, 14th Annual Convention*, 1985.

Kendall, C.G.S.C., Moore, P., Strobel, J., Cannon, R., Perlmutter, M., Bezdek, J. and Biswas, G. (1991a). Simulation of the sedimentary fill of basins: In: *Sedimentary Modeling: Computer Simulations and Methods for Improved Parameter Definition* (eds. E.K. Franseen, W.L. Watney, C.G.S.C. Kendall and W. Ross), *Kansas Geological Survey Bulletin*, **233**, 489–508.

Kendall, C.G.S.C., Strobel, J., Cannon, R., Bezdek, J. and Biswas, G. (1991b). The simulation of the sedimentary fill of basins. *Journal of Geophysical Research*, **96**, 6911–6929.

Kennett, J.P. and Shackleton, N.J. (1976) Critical development in evolution of deep-sea waters 38 m.y. ago; oxygen isotopic evidence from deep-sea sediments. *Eos, Transactions, American Geophysical Union*, **57**, 256.

Kerr, R.A. (1985) Plate tectonics goes back 2 billion years. *Science*, **230**, 1364–1367.

Ketzer, J.M., Morad, S. and Amorosi, A. (2003) Predictive diagenetic clay-mineral distribution in siliciclastic rocks within a sequence stratigraphic framework. In: *Clay Mineral Cements in Sandstones* (eds. R.H. Wordon and S. Morad), Blackwell Publishing. *International Association of Sedimentologists, Special Publication*, **34**, 43–61.

Khain, V.Y. (1992) The role of rifting in the evolution of the Earth's crust. *Tectonophysics*, **215**, 1–7.

King, B.C. and Williams, L.A.J. (1976) The East African rift system. In: *Geodynamics; Progress and Prospects* (ed. by C.L. Drake), American Geophysical Union, Washington D.C., 63–74.

King, G.C.P., Stein, R.S. and Rundle, J.B. (1988) The growth of geological structure by repeated earthquakes. 1. Conceptual framework. *Journal of Geophysical Research*, **93**, 13307–13318.

Kinghorn, R.R.F. (1983) *An Introduction to the Physics and Chemistry of Petroleum*. Wiley, Chichester, United Kingdom.

Kingston, D.R., Dishroon, C.P. and Williams, P.A. (1983a) Global basin classification. *Bulletin American Association of Petroleum Geologists*, **67**, 2175–2193.

Kingston, D.R., Dishroon, C.P. and Williams, P.A. (1983b) Hydrocarbon plays and global basin classification. *Bulletin American Association of Petroleum Geologists*, **67**, 2194–2198.

Kinsman, D.J.J. (1975) Rift valley basins and sedimentary history of trailing continental margins. In: *Petroleum and Global Tectonics* (eds. A.G. Fischer and S. Judson), Princeton University Press, 83–126.

Kirby, S.H. (1983) Rheology of the lithosphere. *Reviews Geophysics and Space Physics*, **21**, 1458–1487.

Kirk, R.H. (1980) Statfjord field: a North Sea giant. In: *Giant Oil and Gas Fields of the Decade 1968–1978* (ed. by M.T. Halbouty), 95–116, *American Association Petroleum Geologists Memoir*, **30**.

Kirkland, B.L., Dickson, J.A.D., Wood, R.A. and Land, L.S. (1998) Microbialite and microstratigraphy: The origin of encrustations in the middle and upper Capitan Formation, Guadalupe Mountains, Texas and New Mexico. *Journal of Sedimentary Research*, **68**, 956–969.

Kite, G.W. (1972) An engineering study of crustal movement around the Great Lakes. *Inland Waters Directorate, Dept Environment, Technical Bulletin*, **63**, Ottawa.

Klemme, H.D. (1980) Petroleum basins: classification and characteristics. *Journal of Petroleum Geology*, **3**, 187–207.

Klemperer, S.L. (1988) Crustal thinning and nature of extension in the northern North Sea from deep seismic reflection profiling. *Tectonics*, **7**, 803–821.

Kocurek, G. (1981a) Significance of interdune deposits and bounding surfaces in aeolian dune sands. *Sedimentology*, **28**, 753–780.

Kocurek, G. (1981b) Erg reconstruction: the Entrada Sandstone (Jurassic) of northern Utah and Colorado. *Palaeogeography, Palaeoclimatology, Palaeoecology*, **36**, 125–153.

Kohlstedt, D.L., Evans, B. and Mackwell, S.J. (1995) Strength of the lithosphere; constraints imposed by laboratory experiments. *Journal of Geophysical Research*, **100**, 17587–17602.

Koide, H. and Bhattacharji, S. (1977) Geometric patterns of active strike-slip faults and their significance as indicators for areas of energy release. In: *Energetics of Geological Processes* (ed. by S.K. Saxena), 46–66, Springer-Verlag, New York.

Kominz, M.A. (1984) Oceanic ridge volumes and sea level change: an error analysis. In: J. Schlee (ed.) *Interregional Unconformities and Hydrocarbon Accumulation: American Association of Petroleum Geologists Memoir*, **36**, 109–127.

Kominz, M.A. and Bond, G.C. (1991) Unusually large subsidence and sea-level events during middle Paleozoic time; new

evidence supporting mantle convection models for supercontinent assembly. *Geology*, **19**, 56–60.

Kominz, M.A. and Pekar, St.F. (2001) Oligocene eustasy from two-dimensional sequence stratigraphic backstripping. *Geological Society of America Bullein*, **113**, 291–304.

Kominz, M.A., Miller, K.G. and Browning, J.V. (1998) Long-term and short-term global Cenozoic sea-level estimates. *Geology*, **26**, 311–314.

Kooi, H. and Beaumont, C. (1994) Escarpment retreat on high-elevation rifted continental margins: Insights derived from a surface-processes model that combines diffusion, reaction and advection. *Journal of Geophysical Research*, **99,** 12191–12209.

Kooi, H. and Beaumont, D. (1996) Large-scale geomorphology: Classical concepts reconciled and integrated with contemporary ideas via a surface processes model. *Journal of Geophysical Research*, **101**, 3361–3386.

Kooi, H., Cloetingh, S. and Burrus, J. (1992) Lithospheric necking and regional isostasy at extensional basins; 1. Subsidence and gravity modeling with an application to the Gulf of Lions margin (SE France). *Journal of Geophysical Research*, **97**, 17553–17571.

Koons, P.O. (1989) The topographic evolution of collisional mountain belts: a numerical look at the Southern Alps, New Zealand. *American Journal of Science*, **289**, 1041–1069.

Koons, P.O. (1990) Two-sided orogen: Collision and erosion from the sandbox to the Southern Alps, New Zealand. *Geology*, **18**, 679–682.

Koons, P.O. (1995) Modelling the topographic evolution of collisional belts. *Annual Reviews of Earth and Planetary Sciences*, **23**, 375–408.

Kronen, J.D.Jr. and Glenn, C.R. (2000) Pristine to reworked verdine: Keys to sequence stratigraphy in mixed carbonate-siliciclastic forereef sediments (Great Barrier Reef). In: (eds. C.R. Glenn, J. Lucas and L. Lucas) *Marine Authigenesis: From Global to Microbial. Special Publication Society of Economic Paleontologists and Mineralogists*, Tulsa, Oklahoma, **65**, 387–403.

Krumbein, W.C. and Monk, G.D. (1942) Permeability as a function of the size parameters of unconsolidated sand. *American Institute of Mining, Metallurgical and Petroleum Engineers, Technical Publication*, **1492**, 11 pp.

Kübler, B., Pittion, J.-L., Héroux, Y., Charolais, J. and Weidmann, M. (1979) Sur le pouvoir réflecteur de la vitrinite dans quelques roches du Jura, de la Molasse et des Nappes préalpines, helvétiques et penniques (Suisse occidentale, Haute Savoie). *Eclogae geologicae Helvetiae.*, **72**, 347–373.

Kusznir, N.J. (1982) Lithosphere response to externally and internally derived stresses: A viscoelastic stress guide with amplification. *Geophysical Journal of the Royal Astronomical Society*, **70**, 399–414.

Kusznir, N.J. and Egan, S.S. (1990) Simple-shear and pure-shear models of extensional sedimentary basin formation: Application to the Jeanne d'Arc Basin, Grand Banks of Newfoundland. In: *Extensional Tectonics of the North Atlantic Margins* (eds. A.J. Tankard and H.R. Balkwill), *American Association of Petroleum Geologists Memoir*, **46**, 305–322.

Kusznir, N.J. and Karner, G.D. (1985) Dependence of the flexural rigidity of the continental lithosphere on rheology and temperature. *Nature*, **316**, 138–142.

Kusznir, N.J. and Morley, C. (1990) The Lake Tanganyika rift, East Africa. Application of the flexural cantilever model of continental extension. *Geophysical Journal International*, **101**, 275.

Kusznir, N.J. and Park, R.G. (1987) The extensional strength of the continental lithosphere: its dependence on geothermal gradient, and crustal composition and thickness. In: *Continental Extensional Tectonics* (eds. M.P. Coward, J.F. Dewey and P.L. Hancock), *Special Publication Geological Society of London* **28**, 35–52.

Kusznir, N.J. and Ziegler, P.A. (1992) The mechanics of continental extension and sedimentary basin formation; a simple-shear/ pure-shear flexural cantilever model. *Tectonophysics*, **215**, 117–131.

Kusznir, N.J., Karner, G.D. and Egan, S. (1987) Geometric, thermal and isostatic consequences of detachments in continental lithosphere during extension and basin formation. In: *Sedimentary Basins and Basin-Forming Mechanisms* (eds. C. Beaumont and A.J. Tankard), 185–203, *Canadian Society Petroleum Geologists Memoir* **12**.

Kusznir, N.J., Marsden, G. and Egan, S.S. (1991) A flexural-cantilever simple-shear/ pure-shear model of continental lithosphere extension: Applications to the Jeanne d'Arc Basin, Grand Banks and Viking Graben, North Sea. In: *The Geometry of Normal Faults. Special Publication Geological Society*, **56**, 41–60.

Lachenbruch, A.H. and Sass, J.H. (1978) Models of extending lithosphere and heat flow in the Basin and Range province. In: *Cenozoic Tectonics and Regional Geophysics of the Western Cordillera, Geological Society of America Memoir*, **152,** 209–250.

Lachenbruch, A.H. and Sass, J.H. (1980) Heat flow and energetics of the San Andreas fault zone. *Journal of Geophysical Research*, **85**, 6185–6222.

Lachenbruch, A.H. and Sass, J.H. (1988) The stress-heat flow paradox and preliminary thermal results from Cajon Pass. *Geophysical Research Letters*, **15**, 981–984.

Lakshmanan, C.C., Bennett, M.L. and White, N. (1991) Implications of multiplicity in kinetic parameters to petroleum exploration; distributed activation energy models. *Energy and Fuels*, **5**, 110–117.

Lal, D. (1991) Cosmic ray labeling of erosion surfaces. *In situ* nuclide production rates and erosion. *Earth and Planetary Science Letters*, **104**, 424–439.

Lamb, C.F. (1980) Painter reservoir field: giant in the Wyoming thrust belt. *Bulletin American Association of Petroleum Geologists*, **64**, 638–644.

Lambeck, K. (1983) Structure and evolution of intracratonic basins in central Australia. *Geophysical Journal of Royal Astronomical Society*, **74**, 843–886.

Langford, R.P. (1989) Fluvial-aeolian interactions. Part I: modern systems. *Sedimentology*, **36**, 1023–1035.

Langford, R.P. and Chan, M.A. (1989) Fluvial-aeolian interactions. Part II: ancient system. *Sedimentology*, **36**, 1037–1051.

Larsen, P.H. (1988) Relay structures in a Lower Permian basement-involved extension system, East Greenland. *Journal of Structural Geology*, **10**, 3–8.

Larson, R.L. and Pitman, W.C. (1972) Worldwide correlation of Mesozoic magnetic anomalies and its implications. *Bulletin Geological Society of America*, **83**, 3645–3662.

Lash, G.G. (1987) Longitudinal petrographic variations in a Middle Ordovician trench deposit, central Appalachian orogen. *Sedimentology*, **34**, 227–235.

Laslett, G.M., Green, P.F., Duddy, I.R. and Gleadow, A.J.W. (1987) Thermal annealing of fission tracks in apatite, 2. A quantitative analysis. *Chemical Geology*, **65**, 1–13.

Latin, D. and White, N. (1990) Generating melt during lithospheric extensions: Pure shear vs. simple shear. *Geology*, **18**, 327–331.

Latin, D.M., Dixon, J.E. and Fitton, J.G. (1990) Rift-related magmatism in the North Sea basin. In: D.J. Blundell and A.D. Gibbs (eds.) *Tectonic Evolution of the North Sea Rifts*. Clarendon Press, Oxford, 102–144.

Lavier, L.L. and Steckler, M.S. (1997) The effect of sedimentary cover on the flexural strength of continental lithosphere. *Nature*, **389**, 476–479.

Lawrence, D.T., Doyle, M. and Aigner, T. (1990) Stratigraphic simulation of sedimentary basins: concepts and calibration. *Bulletin American Association of Petroleum Geologists*, **74**, 273–295.

Le Pichon, X. and Francheteau, J. (1978) A plate tectonic analysis of the Red Sea – Gulf of Aden area. *Tectonophysics*, **46**, 369–406.

Le Pichon, X. and Sibuet, J.-C. (1981) Passive margins: a model of formation. *Journal of Geophysical Research*, **86**, 3708–3720.

Le Pichon, X., Fournier, M. and Jolivet, L. (1992) Kinematics, topography, shortening, and extrusion in the India-Eurasia collision. *Tectonics*, **11**, 1085–1098.

Le Pichon, X., Francheteau, J. and Bonnin, J. (1973) *Plate Tectonics*. Elsevier, New York.

Le Stunff, Y. and Ricard, Y (1995) Topography and geoid due to lithospheric mass anomalies. *Geophysical Journal International*, **122**, 982–990.

Leeder, M.R. (1978) A quantitative stratigraphic model for alluvium, with special reference to channel deposit density and interconnectedness. In: *Fluvial Sedimentology* (ed. by A.D. Miall) *Canadian Society Petroleum Geologists Memoir*, **5**, 587–596.

Leeder, M.R. (1993) Tectonic controls upon drainage basin development, river channel migration and alluvial architecture: Implications for hydrocarbon reservoir development and characterization. *Special Publication Geological Society of London*, **73**, 7–22.

Leeder, M.R. (1995) Contintental rifts and proto-oceanic rift troughs. In: *Tectonics of Sedimentary Basins* (eds. C. Busby and R. Ingersoll). Blackwell Science, Oxford, 119–148.

Leeder, M.R. (1999) *Sedimentology and Sedimentary Basins: From Turbulence to Tectonics*. Blackwell Science, Oxford.

Leeder, M.R. and Alexander, J. (1987) The origin and tectonic significance of asymmetrical meander-belts. *Sedimentology*, **34**, 217–226.

Leeder, M.R. and Gawthrope, R.L. (1987) Sedimentary models for extensional tilt-block/half-graben basins. In: *Continental Extensional Tectonics* (eds. M.P. Coward, J.F. Dewey and P.L. Hancock) *Geological Society London Special Publication* **28**, 139–152.

Leeder, M.R., Harris, T. and Kirkby, M.J. (1998) Sediment supply and climate change: implications for basin stratigraphy. *Basin Research*, **10**, 7–18.

Leeds, A.R., Knopoff, L. and Kausel, E.G. (1974) Variations of upper mantle structure under the Pacific Ocean. *Science*, **186**, 141–143.

Lefort, J.P. and Agarwal, B.N.P. (1996) Gravity evidence for an Alpine buckling of the crust beneath the Paris Basin. *Tectonophysics*, **258**, 1–14.

Leighton, M.W., Kolata, D.R., Oltz, D.R. and Eidel, J.J. (1990) *Interior Cratonic Basins. American Association of Petroleum Geologists Memoir* **51**.

Lemoine, F.G., Kenyon, S.C., Factor, J.K., Trimmer, R.G., Pavlis, N.K. Chinn, D.S., Cox, S.M. Klosko, S.M., Luthcke, S.B., Torrence, M.H. Wang, Y.M. Williamson, R.G., Pavlis, E.C., Rapp, R.H. and Olson, T.R. (1998) The development of the joint NASA GSFC and the National Imagery and Mapping Agency (NIMA) geopotential model EGM96. *NASA Technical Paper*.

Lerch, F.J., Klosko, S.M. and Patch, G.B. (1983) A refined gravity model from LAGEOS (GEM-L2), NASA *Tech. Memo.*, 84986.

Lerche, I., Dromgoole, E., Kendall, C.G.S.C., Walter, L.M. and Scaturo, D. (1987) Geometry of carbonate bodies: a quantitative investigation of factors influencing their evolution. *Carbonates and Evaporites*, **2**, 15–42.

Lerche, I., Yarzab, R.F. and Kendell, C.G.St. (1984) Determination of paleoheat flux from vitrinite reflectance data. *American Association Petroleum Geologists Bulletin*, **69**, 1709–1717.

Leythaeuser, D., Schaefer, R.G. and Yukler, A. (1982) Role of diffusion in primary migration of hydrocarbons. *Bulletin American Association of Petroleum Geologists*, **66**, 408–429.

Li, Y. and Yang, J. (1998) Tectonic geomorphology in the Hexi Corridor, north-west China. *Basin Research*, **10**, 345–352.

Lin, J.C. (2000) Morphotectonic evolution of Taiwan. In: *Geomorphology and Global Tectonics* (ed. by M.A. Summerfield), *Wiley*, 135–146.

Link, M.H. (1982) Provenance, palaeocurrents and palaeogeography of Ridge Basin, southern California. In: *Geologic History of Ridge Basin, Southern California* (eds. J.C. Crowell and M.H. Link), 265–276, *Society of Economic Paleontologists Mineralogists, Pacific Section*.

Link, M.H. and Osborne, R.H. (1978) Lacustrine facies in the Pliocene Ridge Basin Group: Ridge Basin, California. In: *Modern and Ancient Lake Sediments* (eds. A. Matter and M.E. Tucker), 169–187, *Special Publication International Association of Sedimentol.* **2**, Blackwell Scientific, Oxford.

Lister, G.S. and Davis, G.A. (1989) The origin of metamorphic core complexes and detachment faults formed during Tertiary continental extension in the northern Colorado River region, USA. *Journal of Structural Geology*, **11**, 65–94.

Lister, G.S., Banga, G. and Feenstra, A. (1984) Metamorphic core complexes of Cordilleran type in the Cyclades, Aegean Sea, Greece. *Geology*, **12**, 221–225.

Lister, G.S., Etheridge, M.A. and Symonds, P.A. (1986) Detachment faulting and the evolution of passive continental margins. *Geology*, **14**, 890–892.

Lister, C.R.B., Sclater, J.G., Davis, E.E., Villinger, H. and Nagihara, S. (1990) Heat flow maintained in ocean basins of great age: Investigations in the north-equatorial west Pacific. *Geophysical Journal International*, **102**, 603–630.

Lithgow-Bertelloni, C. and Gurnis, M. (1997) Cenozoic subsidence and uplift of continents from time-varying dynamic topography. *Geology*, **25**, 735–738.

Livingstone, D.A. (1963) Chemical composition of rivers and lakes. Data of geochemistry. *U.S. Geology Survey Prof. Paper*, **440G**, 1–64.

Lopatin, N.V. (1971) Temperature and geologic time as factors in coalification (in Russian). *Akad. Nauk SSSR Izvestiya, Seriya Geologicheskaya*, **3**, 95–106.

Lopes, J.A. (1990) Structural styles of growth faults in the US Gulf Coast Basin. In: *Classic Petroleum Provinces* (ed. by J. Brooks). *Special Publication Geological Society of London*, **50**, 203–219.

Loucks, R.G. and Anderson, J.H. (1985) Depositional facies, diagenetic terranes, and porosity development in Lower Ordovician EllenburgerDolomite, Puckett Field, west Texas. In: *Carbonate Petroleum Reservoirs*. (eds. P.O. Roehl and P.W. Choquette) Springer-Verlag, New York, 19–37.

Louden, K.E. and Chian, D. (1999) The deep structure of non-volcanic rifted continental margins. *Philosophical Transactions of the Royal Society, London*, **A357**, 767–804.

Loutit, T.S., Hardenbol, J., Vail, P.R. and Baum, G.R. (1988) Condensed sections: the key to age dating of continental margin sequences. In: *Sea Level Changes: an Integrated Approach* (eds. B.S. Wilgus, H.W. Hastings, J.C. Posamentier, C.A. van Wagoner, Ross and G.C. St.C. Kendall), *Special Publication Society of Economic Paleontologists and Mineralogists* **42**, 183–213.

Lowell, J.D. and Genik, G.J. (1972) Sea floor spreading and structural evolution of southern Red Sea. *Bulletin American Association of Petroleum Geologists*, **56**, 247–259.

Lowry, A.R. and Smith, R.B. (1994) Flexural rigidity of the Basin and Range-Colorado Plateau-Rocky Mountain transition from coherence analysis of gravity and topography. *Journal of Geophysical Research*, **99**, B10, 20123–20140.

Lucia, F. (1983) Petrophysical parameters estimated from visual descriptions of carbonate rocks: A field classification of carbonate pore space. *Journal of Petroleum Technology*, **35**, 629–637.

Lucia, F. (1995) Rock-fabric/petrophysical classification of carbonate pore space for reservoir characterization. *American Association of Petroleum Geologists Bulletin*, **79**, 1275–1300.

Lucia, F.J. (1999) *Carbonate Reservoir Characterization*. Springer-Verlag, Berlin.

Lucia, F.J. and Major, R.P. (1994) Porosity evolution through hypersaline reflux dolomitization. In: *Dolomites. International Association of Sedimentologists Special Publication*, (eds. B. Purser, M. Tucker and D. Zenger, **21**, 325–341.

Luheshi, M.N. and Jackson, D. (1986) Conductive and convective heat transfer in sedimentary basins. In: *Thermal Modeling in Sedimentary Basins* (ed. by J. Burrus), 219–234, *1st IFP Exploration Research Conference, Carcans, France, June 3–7, 1985*. Editions Technip, Paris.

Lvovich, M.I., Karasik, G. Ya, Bratseva, N.L., Medvedeva, G.P. and Maleshko, A.V. (1991) Contemporary Intensity of the World Land Intracontinental Erosion. *USSR Academy of Sciences, Moscow*.

Lynch, H.D. and Morgan, P. (1987) The tensile strength of the lithosphere and the localization of extension. In: *Continental Extensional Tectonics* (eds. M.P. Coward, J.F. Dewey and P.L. Hancock), 53–65, *Special Publication Geological Society of London*, **28**.

Lynch, H.D. and Morgan, P. (1990) Finite-element models of continental extension. *Tectonophysics*, **174**, 115–135.

Lyon-Caen, H. and Molnar, P. (1985) Gravity anomalies, flexure of the Indian plate, and the structure, support and evolution of the Himalaya and Ganga Basin. *Tectonics*, **4**, 513–538.

Lyon-Caen, H. and Molnar, P. (1989) Constraints on the deep structure and dynamic processes beneath the Alps and adjacent regions from an analysis of gravity anomalies. *Geophysical Journal International*, **99**, 19–32.

Mack, G.H. and Seager, W.R. (1990) Tectonic control on facies distribution of the Camp Rice and Palomas Formations (Pliocene-Pleistocene) in the southern Rio Grande rift. *Bulletin of the Geological Society of America*, **102**, 45–53.

Mackenzie, A.S. (1984) Applications of biological markers to petroleum geochemistry. In: *Advances in Petroleum Geochemistry* (eds. J. Brooks and D.H. Welte), Vol. 1, 115–214, Academic Press, London.

Mackenzie, A.S. and McKenzie, D. (1983) Isomerization and aromatization by hydrocarbons in sedimentary basins formed by extension. *Geological Magazine*, **120**, 417–528.

Mackenzie, A.S. and Quigley, T.M. (1988) Principles of geochemical prospect appraisal. *Bulletin American Association of Petroleum Geologists*, **72**, 399–415.

Mackey, S.D. and Bridge, J.S. (1995) Three-dimensional model of alluvial stratigraphy: Theory and application. *Journal of Environment*, **23**, 83–106.

Magara, K. (1976) Thickness of removed sedimentary rocks, paleopore pressure and paleotemperatures, southwestern part of western Canada Basin. *Bulletin American Association of Petroleum Geologists*, **60**, 554–565.

Maggi, A., Jackson, J.A., McKenzie, D. and Preistley, K. (2000) Earthquake focal depths, effective elastic thickness, and the strength of the continental lithosphere. *Geology*, **28**, 495–498.

Magoon, L.B. and Dow, W.G. (1994) The petroleum system. In: *The Petroleum System – From Source To Trap* (eds. L.B. Magoon and W.G. Dow). *American Association Petroleum Geologists Memoir*.

Majorowicz, J.A. and Jessop, A.M. (1981) Present heat flow and a preliminary geothermal history of the central Prairies Basin, Canada. *Geothermics*, **10**, 81–93.

Majorowicz, J.A., Jones, F.W., Lam, H.L. and Jessop, A.M. (1984) The variability of heat flow both regional and with depth in southern Alberta, Canada: effect of groundwater flow? *Tectonophysics*, **106**, 1–29.

Malavieille, J. (1984) Modélisation expérimentale des chevauchements imbriqués: Application aux chaînes des montagnes. *Société Géologique de France, Bulletin*, **26**, 129–138.

Malinverno, A. (1997) On the power-law size distribution of turbidite beds. *Basin Research*, **9**, 263–274.

Malinverno, A. and Ryan, W.B.F. (1986) Extension in the Tyrrhenian Sea and shortening in the Apennines as result of arc migration driven by sinking of the lithosphere. *Tectonics*, **5**, 227–245.

Mancktelow, N. S. (1985) The Simplon Line: A major displacement zone in the western Lepontine Alps. *Eclogae Geologicae Helvetiae*, **78**, 73–96.

Mancktelow, N.S. and Grasemann, B. (1997) Time-dependent effects of heat advection and topography on cooling histories during erosion. *Tectonophysics*, **270**, 167–195.

Mange, M.A. and Maurer, H.F.W. (1993) Heavy minerals in colour. Chapman and Hall, London.

Mann, C.D. and Vita-Finzi, C. (1988) Holocene serial folding in the Zagros. In: *Gondwana and Tethys* (eds. M. Audley-Charles and A. Hallam). *Special Publication Geological Society London*, **37**, 51–59.

Mann, P., Draper, G. and Burke, K. (1985) Neotectonics of a strike-slip restraining bend system, Jamaica. In: *Strike-Slip Deformation, Basin Formation, and Sedimentation* (eds. K.T. Biddle and N. Christie-Blick), *Special Publication Society of Economic Paleontologists and Mineralogists* **37**, 211–226.

Mann, P., Hempton, M.R., Bradley, D.C. and Burke, K. (1983) Development of pull-apart basins. *Journal of Geology*, **91**, 529–554.

Manspeizer, W. (1985) The Dead Sea rift: impact of climate and tectonism on Pleistocene and Holocene sedimentation. In: *Strike-Slip Deformation, Basin Formation, and Sedimentation* (eds. K.T. Biddle and N. Christie-Blick), 143–158, *Special Publication, Society of Economic Paleontologists and Mineralogists*, **37**.

Marr, J.G., Swenson, J.B., Paola, C. and Voller, V.R. (2000) A two-diffusion model of fluvial stratigraphy in closed depositional basins. *Basin Research*, **12**, 381–398.

Marsaglia, K.M. (1995) Interarc and backarc basins. In: *Tectonics of Sedimentary Basins* (eds. C. Busby and R. Ingersoll). Blackwell Science, Oxford, 299–329.

Marsden, G., Yielding, G., Roberts, A.M. and Kusznir, N.J. (1990) Application of a flexural cantilever simple-shear/pure-shear model of continental lithosphere to the formation of the northern North Sea Basin. In: *Tectonic Evolution of the North Sea Rifts* (eds. D.J. Blundell and A.D. Gibbs). Oxford University Press, 236–257.

Marzo, M. and Puigdefabregas, C. (1993) *Alluvial Sedimentation. Special Publication International Association of Sedimentologists*, **17**. Blackwell Scientific Publications, Oxford.

Masson, D.G. (1996) Catastrophic collapse of the volcanic island of Hierro 15 ka ago and the history of landslides in the Canary Islands. *Geology*, **24**, 231–234.

Matsuzawa, T. Umino, N. Hasegawa, A. and Takagi, A. (1986) Upper mantle velocity structure estimated from PS-converted waves beneath the northeastern Japan Arc. *Geophysical Journal of the Royal Astronomical Society*, **86**, 767–787.

Matter, A., Homewood, P., Caron, C., van Stuijvenberg, J., Weidmann, M. and Winkler, W. (1980) Flysch and Molasse of western and central Switzerland. In: *Geology of Switzerland, a Guide Book* (ed. by R. Trümpy). *Swiss Geological Commission*, 261–293.

Matthews, R.K. (1974) *Dynamic Stratigraphy*. Prentice-Hall, New Jersey.

Mayuga, M.N. (1970) Geology and development of California's giant Wilmington oil field. In: *Geology of Giant Petroleum Fields*, 158–184, *American Association Petroleum Geologists Memoir* **14**.

McCave, I.N. and Tucholke, B.E. (1986) Deep-current-controlled sedimentation in the western North Atlantic. In: *The Geology of North America*, vol. M. *The Western North Atlantic Region, Decade of North America Geology* (eds. P.R. Vogt and B.E. Tucholke), *Geological Society of America*, Boulder, Colorado, 451–468.

McConnell, R.B. (1977) East African rift system dynamics in view of Mesozoic apparent polar wander. *Journal Geological Society of London*, **134**, 33–39.

McConnell, R.B. (1980) A resurgent taphrogenic lineament of Precambrian origin in eastern Africa. *Journal Geological Society of London*, **137**, 483–489.

McConnell, R.K. (1968) Viscosity of the mantle from relaxation time spectra of isostatic adjustment. *Journal of Geophysical Research*, **73**, 7089–7105.

McCubbin, D.G. (1982) Barrier island and strand plain facies. In: *Sandstone Depositional Environments* (eds. P.A. Scholle and D. Spearing), 247–279, *American Association of Petroleum Geologists*, Tulsa, Oklahoma.

McKenzie, D. and Bickle, M.J. (1988) The volume and composition of melt generated by extension of the lithosphere. *Journal of Petrology*, **29**, 625–679.

McKenzie, D., Watts, A., Parsons, B. and Roufosse, M. (1980) Planform of mantle convection beneath the Pacific Ocean. *Nature*, **288**, 442–446.

McKenzie, D.P. (1978a) Some remarks on the development of sedimentary basins. *Earth and Planetary Science Letters.*, **40**, 25–32.

McKenzie, D.P. (1978b) Active tectonics of the Alpine–Himalayan belt: the Aegean and surrounding regions. *Geophysical Journal Royal Astronomical Society* **55**, 217–254.

McKenzie, D.P. (1983) The Earth's mantle. *Scientific American*, **249**, 66–113.

McLeod, A.E., Dawers, N.H. and Underhill, J.R. (2000) The propagation and linkage of normal faults; insights from the Strathspey-Brent-Statfjord fault array, northern North Sea.: *Basin Research*, **12**, 263–284.

McNutt, M.K. (1984) Lithospheric flexure and thermal anomalies. *Journal of Geophysical Research*, **89**, 11180–11194.

McNutt, M.K. and Kogan, M.G. (1987) Isostasy in the USSR, 2, Interpretation of admittance data. In: *The Composition, Structure, Dynamics of the Lithosphere–Aesthenosphere System* (eds.

K. Fuchs and C. Froideveaux), *Geodyn. Ser.*, **16**, 309–327, American Geophysical Union, Washington D.C.

McNutt, M.K., Diament, M. and Kogan, M.G. (1988) Variations of elastic plate thickness at continental thrust belts. *Journal of Geophysical Research*, **93**, 8825–8838.

McQuillan, H. (1985) Fracture-controlled production from the Oligo-Miocene Asmari Formation in Gachsaran and Bibi Hakimeh Fields, southwest Iran. In: *Carbonate Petroleum Reservoirs* (eds. P.O. Roehl and P.W. Choquette) Springer-Verlag, New York, 511–523.

Meissner, F.F., Woodward, J. and Clayton, J.L. (1984) Stratigraphic relationships and distribution of source rocks in the greater Rocky Mountain region. In: *Hydrocarbon Source Rocks of the Greater Rocky Mountain Region* (eds. J. Woodward, F.F. Meissner and J.L. Clayton) *Rocky Mountain Association of Geologists*, Denver, Colorado, 1–34.

Meissner, R. (1986) *The Continental Crust: A Geophysical Approach*. Academic, Orlando.

Menard, H.W. (1964) *Marine Geology of the Pacific*. McGraw-Hill, New York.

Menpes, R.J. and Hillis, R.R. (1995) Quantification of Tertiary exhumation from sonic velocity log data, Celtic Sea/Southwestern Approaches. In: *Basin Inversion* (eds. J.G. Buchanan and P.G. Buchanan), 191–210, *Special Publication Geological Society of London*, **88**.

Métivier, F. and Gaudemer, Y. (1999) Stability of output fluxes of large rivers in South and East Asia during the last 2 million years: implications for floodplain processes. *Basin Research*, **11**, 293–304.

Métivier, F., Gaudemer, Y., Tapponier, P. and Klein, M. (1999) Mass accumulation rates in Asia during the Cenozoic. *Geophysical Journal International*, **137**, 280–318.

Meybeck, M. (1979) Concentration des eaux fluviales en éléments majeurs et apports en solution aux océans. *Rev. Géologie Dynamique et Géographie Physique*, **21**, 215–246.

Meybeck, M. (1987) Global chemical weathering of surficial rocks estimated from river dissolved loads. *American Journal of Science*, **287**, 401–428.

Meyers, J.H., Suttner, L.J., Furer, L.C., May, M.T. and Soreghan, M.J. (1992) Intrabasinal tectonic control on fluvial sandstone bodies in the Cloverly Formation (Early Cretaceous) east-central Wyoming, USA. *Basin Research*, **4**, 315–333.

Miall, A.D. (1984) *Principles of Sedimentary Basin Analysis*. New York, Springer-Verlag, 490 pp.

Miall, A. D. (1991) Stratigraphic sequences and their chronostratigraphic correlation. *Journal of Sedimentary Petrology*, **61**, 497–505.

Miall, A. D. (1992) The Exxon global cycle chart: An event for every occasion. *Geology*, **20**, 787–790.

Miall, A. D. (1997) *The Geology of Stratigraphic Sequences*. Springer-Verlag, Berlin.

Miall, A.D. (1994) Sequence stratigraphy and chronostratigraphy: Problems of definition and precision in correlation, and their implications for global eustasy. *Geoscience Canada*, **21**, 1–26.

Miall, A.D. (2000) *Principles of Sedimentary Basin Analysis*. 3rd Edition, Springer-Verlag, New York.

Miall, A.D. and Miall, C.E. (2001) Sequence stratigraphy as a scientific enterprise: The evolution and persistence of conflicting paradigms. *Earth Science Reviews*, **54**, 321–348.

Middleton, G.V. (1978) Facies. In: *Encyclopaedia of Sedimentology* (eds. R.W. Fairbridge and J. Bourgeois), 323–325, Dowden, Hutchinson and Ross, Stroudsburg, Penn.

Middleton, G.V. and Wilcock, P.R. (1994) *Mechanics in the Earth and Environmental Sciences*. Cambridge University Press, Cambridge.

Middleton, M.F. (1982) Tectonic history from vitrinite reflectance. *Geophysical J.R. astr. Society*, **68**, 121–132.

Mike, K. (1975) Utilization of the analysis of ancient river beds for the detection of Holocene crustal movements. In: *Recent Crustal Movements* (eds. N. Pavoni and R. Green), *Tectonophysics*, **29**, 359–368.

Miller, J.A. (1985) Depositional and reservoir facies of the Mississippian Leadville Formation, Northwest Lisbon Field, Utah. In: *Carbonate Petroleum Reservoirs* (eds. P.O. Roehl and P.W. Choquette) Springer-Verlag, New York, 161–173.

Miller, K.G., Mountain, G.S., Browning, J.V., Kominz, M., Sugarman, P.J., Christie-Blick, N., Katz, M.E. and Wright, J.D. (1998) Cenozoic global sea level, sequences, and the New Jersey transect: Results from coastal plain and continental slope drilling. *Reviews of Geophysics*, **36**, 569–601.

Miller, K.G., Wright, J.D. and Fairbanks, R.G. (1991) Unlocking the ice house: Oligocene-Miocene oxygen isotopes, eustasy and margin erosion. *Journal of Geophysical Research*, **96**, 6829–6848.

Milliman, J.D. and Meade, R.H. (1983) Worldwide delivery of river sediment to the oceans. *Journal of Geology*, **91**, 1–21.

Milliman, J.D. and Syvitski, J.P.M. (1992) Geomorphic/tectonic control of sediment discharge to the ocean: the importance of small mountainous streams. *Journal of Geology*, **100**, 525–544.

Minster, J.B. and Jordan, T.H. (1978) Present-day plate motions. *Journal of Geophysical Research*, **83**, 5331–5354.

Minster, J.B., Jordan, T.H., Molnar, P. and Haines E. (1974) Numerical modelling of instantaneous plate tectonics. *Geophysical Journal of Royal Astronomical Society* **36**, 553–562.

Mitchum, R.M. Jr, Vail, P.E. and Thompson, S. III (1977) The depositional sequence as a basic unit for stratigraphic analysis. In: *Seismic Stratigraphy: Applications to Hydrocarbon Exploration* (ed. by C.E. Payton), *American Association Petroleum Geologists Memoir*, **26**, 53–62.

Mitrovica, J.X. and Jarvis, G.T. (1985) Surface deflections due to transient subduction in a convecting mantle. *Tectonophysics*, **120**, 211–237.

Mitrovica, J.X., Beaumont, C. and Jarvis G.T. (1989) Tilting of continental interiors by the dynamical effects of subduction. *Tectonics*, **8**, 1079–1094.

Molnar, P. (1988) Continental tectonics in the aftermath of plate tectonics. *Nature*, **335**, 131–137.

Molnar, P. (1992) Brace-Goetze strength profiles, the partitioning of strike-slip and thrust faulting at zones of oblique

convergence, and the stress-heat flow paradox of the San Andreas fault. In: *Fault Mechanics and Transport Properties of Rocks* (eds. T.F. Wong and B. Evans), 435–459, San Diego, California.

Molnar, P. and Atwater, T. (1978) Interarc spreading and Cordilleran tectonics as alternates related to the age of subducted oceanic lithosphere. *Earth and Planetary Science Letters*, **41**, 330–340.

Molnar, P. and Chen, W.P. (1982) Seismicity and mountain building. In: *Mountain Building Processes* (ed. by K.G. Hsü). Academic Press, London, 41–57.

Molnar, P. and England, P. (1990) Late Cenozoic uplift of mountain ranges and global climate change: chicken or egg? *Nature*, **346**, 29–34.

Molnar, P. and Tapponnier, P. (1975) Cenozoic tectonics of Asia: effects of a continental collision. *Science*, **189**, 419–426.

Montadert, L., Roberts, D.G., de Charpal, O. and Guennoc, P. (1979) Rifting and subsidence of the northern continental margin of the Bay of Biscay. *Init. Rep. Deep Sea Drilling Project*, **48**, 1025–1060.

Montanez, I.P. (1994) Late diagenetic dolomitization of Lower Ordovician, Upper Knox carbonates: A record of the hydrodynamic evolution of the southern Appalachian Basin. *American Association of Petroleum Geologists Bulletin*, **78**, 1210–1239.

Montgomery, D.R. (1994) Valley incision and uplift of mountain peaks. *Journal of Geophysical Research*, **99**, 13913–13921.

Montgomery, D.R. and Brandon, M.T. (2002) Topographic controls on erosion rates in tectonically active mountain ranges. *Earth and Planetary Science Letters*, **201**, 481–489.

Montgomery, D.R. and Dietrich, W.E. (1988) Where do channels begin? *Nature*, **336**, 232–234.

Montgomery, D.R. and Dietrich, W.E. (1992) Channel initiation and the problem of landscape scale. *Science*, **255**, 826–830.

Moore, C.H. (1989) *Carbonate Diagenesis and Porosity*. Elsevier, New York.

Moore, C.H. (2001) *Carbonate Reservoirs*. Elsevier Science, Amsterdam.

Moore, C.H. and Heydari, E. (1993) Burial diagenesis and hydrocarbon migration in platform limestones: A conceptual model based on the Upper Jurassic of Gulf Coast of USA. In: *Diagenesis and Basin Development* (eds. A.D. Horbury and A.G. Robinson), *American Association of Petroleum Geologists Studies in Geology* **36**, Tulsa, Oklahoma, 213–229.

Moore, D.G. (1969) Reflection profiling studies of the California continental borderlands. *Special Paper, Geological Society of America*, **107**, 138 pp.

Moore, W.S. (1982) Late Pleistocene sea level history. In: *Uranium Series Disequilibrium: Application to Environmental Problems* (eds. M. Ivanovich and R.S. Harmon), 481–496, Clarendon Press, Oxford.

Morad, S., Ketzer, J.M. and De Ros, L.F. (2000) Spatial and temporal distribution of diagenetic alterations in siliciclastic rocks. Implications for mass transfer in sedimentary basins. *Sedimentology*, **47** (Millenium Reviews), 95–120.

Morelli, C., Gantar, G. and Pisani, M. (1975) Bathymetry, gravity and magmatism in the Strait of Sicily and in the Ionian Sea. *Bolletino di Geoftsica, Teorica ed Applicala*, **11**, 3–190.

Moretti, I. and Turcotte, D.L. (1985) A model for erosion, sedimentation, and flexure with application to New Caledonia. *Journal of Geodynamics*, **3**, 155–168.

Morgan, P. and Baker, B.H. (1983) Introduction: processes of continental rifting. *Tectonophysics*, **94**, 1–10.

Morgan, W.J. (1981) Hotspot tracks and the opening of the Atlantic and Indian Oceans. In: *The Sea*, **7** (ed. by C. Emiliani), 443–487, Wiley Interscience, New York.

Morgan, W.J. (1983) Hotspot tracks and the early rifting of the Atlantic. *Tectonophysics*, **94,** 123–139.

Morley, C.K. (2001) *Geoscience of Rift-Systems: Evolution of East Africa. American Association Petroleum Geologists Studies in Geology*, **44**, Oklahoma.

Morton, A.C., Haszeldine, R.S., Giles, M.R. and Brown, S. (eds.) (1992) *Geology of the Brent Group. Geological Society of London Special Publication*, **61.**

Morton, R.A. and Price, W.A. (1987) Late Quaternary sea level fluctuations and sedimentary phases of the Texas coastal plain and shelf. In: *Sea Level Fluctuation and Coastal Evolution* (eds. D. Nummedal, O.H. Pilkey and J.D. Howard), *Special Publication, Society of Economic Paleontologists and Mineralogists*, **41**, 181–198.

Mueller, S., Peterschmitt, E., Fuchs, K., Emter, D. and Ansorge, J. (1973) Crustal structure of the Rhine graben area. *Tectonophysics*, **20**, 381–391.

Multer, H.G. (1971) *Field Guide in some Carbonate Rock Environments, Florida Keys and Western Bahamas*. Fairleigh Dickinson University, Madison, New Jersey, 158 pp.

Murris, R.J. (1980) Middle East: stratigraphic evolution and oil habitat. *Bulletin American Association of Petroleum Geologists*, **64**, 597–618.

Mussett, A.E., Dagley, P. and Skelhorn, R.R. (1988) Time and duration of activity in the British Tertiary Igneous Province, Early Tertiary volcanism and the opening of the North Atlantic. *Special Publication, Geological Society London*, **39**, 201–214.

Nadeau, P.H. and Reynolds, R.C. (1981) Burial and contact metamorphism in the Mancos shale. *Clays and Clay Minerals*, **29**, 249–259.

Naeser, C.W. (1979) Thermal history of sedimentary basins: fission track dating of subsurface rocks. In: *Aspects of Diagenesis* (eds. P.A. Scholle and P.R. Schluger), *Society Economic Paleontologists and Mineralogists Special Publication*, **26**, 109–112.

Nakiboglu, S.M. and Lambeck, K. (1983) A re-evaluation of the isostatic rebound of Lake Bonneville. *Journal of Geophysical Research*, **88**, 10439–10448.

Nederlof, M.H. and Mohler, H.P. (1981) Quantitative investigation of trapping effect of unfaulted caprock (abstr.). *Bulletin American Association of Petroleum Geologists*, **65**, 964.

Nemec, W. and Steel, R.J. (eds.) (1988) *Fan Deltas: Sedimentology and Tectonic Settings*. Blackie, London.

Neugebauer, H.J. (1983) Mechanical aspects of continental rifting. *Tectonophysics*, **94**, 91–108.

Newell, N.A. (1999) Water washing in the northern Bonaparte Basin. *Journal of the Australian Petroleum Exploration Association (APEA)*, 227–247.

Newman, R. and White, N. (1999) The dynamics of extensional sedimentary basins: Constraints from subsidence inversion. *Philosophical Transactions Royal Society of London*, **A357**, 805–834.

Nicholson, C., Seeber, L., Williams, P. and Sykes, L.R. (1986) Seismic evidence for conjugate slip and block rotation within the San Andreas fault system, southern California. *Tectonics*, **5**, 629–648.

Nicholson, C., Seeber, L., Williams, P. and Sykes, L.R. (1985a) Seismicity and fault kinematics through the eastern Transverse Ranges, California: block rotation, strike-slip faulting and shallow-angel thrusts. *Journal of Geophysical Research*, **91**, 4891–4908.

Nicholson, C., Seeber, L., Williams, P.L. and Sykes, L.R. (1985b) Seismic deformation along the southern San Andreas fault, California: Implications for conjugate slip rotational block tectonics. *Tectonics*, **5**, 629–648.

Niedoroda, A.M., Reed, C.W., Swift, D.J.P., Arata, H. and Hoyanagi, K. (1995) Modeling shore-normal large-scale coastal evolution. *Marine Geology*, **126**, 181–199.

Nienhuis, P.H. (1981) Distribution of organic matter in living marine organisms. In: *Marine Organic Chemistry* (eds. E.K. Duursma and R. Dawson), 31–69, Elsevier, Amsterdam.

Nilsen, T.H. and McLaughlin, R.J. (1985) Comparison of tectonic framework and depositional patterns of the Hornelen strike-slip basin of Norway and the Ridge and Little Sulphur Creek strike-slip basins of California. In: *Strike-Slip Deformation, Basin Formation and Sedimentation* (eds. K.T. Biddle and N. ChristieBlick), 79–103, *Special Publication Society of Economic Paleontologists and Mineralogists*, **37**.

Nilsen, T.H. and Sylvester, A.G. (1995) Strike-slip basins. In: *Tectonics of Sedimentary Basins* (eds. C.J. Busby and R.V. Ingersoll), 425–457, Blackwell Science, Oxford.

Noller, J.S., Sowers, J.M. and Lettis, W.R. (2000) *Quaternary Geochronology: Methods and Applications*. American Geophysical Union, Washington, D.C.

Normark, W.R. and Gutmacher, C.E. (1988) Sur submarine slide, Monterey Fan, central California. *Sedimentology*, **35**, 629–648.

Norris, R.J., Koons, P.O. and Cooper, A.F. (1990) The obliquely-convergent plate boundary in the South Island of New Zealand: Implications for ancient collision zones. *Journal of Structural Geology*, **12**, 715–725.

O'Sullivan, P.B. and Brown, R.W. (1998) Effects of surface cooling on apatite fission track data: evidence for Miocene climate change, North Slope, Alaska. In: *Advances in Fission Track Geochronology* (eds. P. van den Haute and F. De Corte), 255–267, Kluwer Academic Publishers, The Netherlands.

Odin, G.S. and Matter, A. (1981) De glauconiarum origine. *Sedimentology*, **28**, 611–641.

Odinsen, T., Reemst, P., van der Beek, P., Faleide, J.I. and Gabrielsen, R.H. (2000) Permo-Triassic and Jurassic extension in the northern North Sea: Results from tectonostratigraphic forward modelling. In: *Dynamics of the Norwegian Margin* (ed. by A. Nottvedt), 83–103, *Special Publication Geological Society of London*, **167**.

Odonne, F. and Vialon, P. (1983) Analogue models of folds above a wrench fault. *Tectonophysics*, **99**, 31–46.

Ogniben, L., Parotto, M. and Praturion, A. (eds.) (1975) *Structural Model of Italy*. Consiglio Nazionale delle Ricerche, **90**.

Okay, A., Demirbag, E., Kurt, H., Okay, N. and Kuscu, I. (1999) An active, deep marine strike-slip basin along the North Anatolian fault in Turkey. *Tectonics*, **18**, 129–147.

Olson, H.C. and Leckie, R.M. (2003) *Micropaleontologic Proxies for Sea-Level Change and Stratigraphic Discontinuities. Society for Sedimentary Geology Special Publication.*

Olsen, H.W. (1960) Hydraulic flow through saturated clays. *Clays and Clay Minerals*, **11**, 131–161.

Ori, G.G. and Friend, P.F. (1984) Sedimentary basins, formed and carried piggyback on active thrust sheets. *Geology*, **12**, 475–478.

Ori, G.G., Roveri, M. and Valloni, F. (1986) Plio-Pleistocene sedimentation in the Apenninic-Adriatic foredeep (central Adriatic Sea, Italy). In: *Foreland Basins* (eds. P.A. Allen and P. Homewood), 183–198, *Special Publication International Association of Sedimentol.*, **8**, Blackwell Scientific, Oxford.

Orowan, E. (1967) Seismic damping and creep in the mantle. *Geophysical Journal of Royal Astronomical Society*, **14**, 191–218.

Osleger, D.A. (1990) Subtidal carbonate cycles: implications for allocyclic versus autocyclic controls. *Geology*, **19**, 917–920.

Overeem, J., Weltje, G.J., Bishop-Kay, C. and Krooenenberg, S.B. (2001) The late Cenozoic Eridanos delta system in the southern North Sea Basin: A climate signal in sediment supply. *Basin Research*, **13**, 293–312.

Owen, R.B., Crossley, R., Johnson, T.C., Tweddle, D., Kornfield, I., Davison, S. and Eccles, D.H. (1990) Major low levels of Lake Malawi and their implications for speciation rates in cichlid fishes. *Proceedings Royal Society London B: Biological Sciences*, **B 240**, 519–553.

Palciauskas, V.V. (1986) Models for thermal conductivity and permeability in normally compacting basins. In: *Thermal Modeling in Sedimentary Basins* (ed. by J. Burrus), 323–336, *1st IFP Exploration Research Conference, Carcans, France, June 3–7, 1985*. Editions Technip, Paris.

Pallatt, N., Wilson, M.J. and McHardy, W.J. (1984) The relationship between permeability and the morphology of diagenetic illite in reservoir rocks. *Journal of Petroleum Technology*, **36**, 2225–2227.

Paola, C. (2000) Quantitative models of sedimentary basin filling. *Sedimentology*, **47** (Suppl. 1), 121–178.

Paola, C. and Seal, R. (1995) Grain-size patchiness as a cause of selective deposition and downstream fining. *Water Resources Research*, **31**, 1395–1407.

Paola, C., Heller, P.L. and Angevine, C.L. (1992) The large-scale dynamics of grain size variation in alluvial basins. 1. Theory. *Basin Research*, **4**, 73–90.

Parker, G. (1978a) Self-formed straight rivers with equilibrium banks and mobile bed. Part 1. The sand-silt river. *Journal of Fluid Mechanics*, **89**, 109–125.

Parker, G. (1978b) Self-formed straight rivers with equilibrium banks and mobile bed. Part 2. The gravel river. *Journal of Fluid Mechanics*, **89**, 127–146.

Parker, G., Paola, C., Whipple, K.X. and Mohrig, D.C. (1998) Alluvial fans formed by channelized fluvial and sheet flow. I: Theory. *Journal of Hydraulic Engineering*, **124**, 985–995.

Parkinson, N. and Summerhayes, C. (1985) Synchronous global sequence boundaries. *Bulletin American Association of Petroleum Geologists*, **69**, 685–687.

Parrish, J.T., Ziegler, A.M. and Scotese, C.R. (1982) Rainfall patterns and the distributions of coals and evaporites in the Mesozoic and Cenozoic. *Palaeogeography, Palaeoclimatology, Palaeoecology*, **40**, 67–101.

Parsons, B. (1982) Causes and consequences of the relation between area and age of the ocean floor. *Journal of Geophysical Research*, **87**, 289–302.

Parsons, B. and Daly, S. (1983) The relationship between surface topography, gravity anomalies, and the temperature structure of convection. *Journal of Geophysical Research*, **88**, 1129–1144.

Parsons, B. and Sclater, J.G. (1977) An analysis of the variation of ocean floor bathymetry with heat flow and age. *Journal of Geophysical Research*, **82**, 803–827.

Partington, M.A., Mitchener, B.C., Milton, N.J. and Fraser, A.J. (1993) Genetic sequence stratigraphy of the North Sea Late Jurassic and Early Cretaceous; distribution and prediction of Kimmeridgian-Late Ryazanian reservoirs in the North Sea and adjacent areas. In: *Petroleum Geology of Northwest Europe*: Proceedings 4th Conference (ed. by J.R. Parker), 347–370, *Geological Society of London*, Bath.

Paterson, M.S. (1958) Experimental deformation and faulting in Wombeyan marble. *Bulletin Geological Society of America*, **69**, 465–476.

Payton, C.E. (Editor) (1977) *Seismic Stratigraphy: Applications to Hydrocarbon Exploration. American Association Petroleum Geologists Memoir*, **26**.

Pazzaglia, F.J. and Brandon, M.T. (1996) Macrogeomorphic evolution of the post-Triassic Appalachian mountains determined by deconvolution of the offshore basin sedimentary record. *Basin Research*, **8**, 255–278.

Peakall, J., Leeder, M., Best, J. and Ashworth, P. (2000) River response to lateral ground tilting: A synthesis and some implications for the modelling of alluvial architecture in extensional basins. *Basin Research*, **12**, 413–424.

Peltier, W.R. (1980) Models of glacial isostasy and relative sea level. In: *Dynamics of Plate Interiors* (eds. A.W. Ball, P.L. Bender, T.R. McGetchin and R.I. Walcott), *American Geophysi-cal Union Geodynamics Ser.*, **1**, 111–127.

Peltzer, G. and Tapponnier, P. (1988) Formation and evolution of strike-slip faults, rifts, and basins during the India-Asia collision: An experimental approach. *Journal of Geophysical Research*, **93**, 15085–15118.

Peper, T. (1993) *Tectonic Control on the Sedimentary Record in Foreland Basins*. PhD thesis, Free University, Amsterdam.

Peterson, F. (1988) Pennsylvanian to Jurassic eolian transportation systems in the western United States. *Sedimentary Geology*, **56**, 207–260.

Pettijohn, F.J. (1975) *Sedimentary Rocks* (3rd Edition). Harper and Row, New York.

Pettijohn, F.J., Potter, P.E. and Siever, R. (1973) *Sand and Sandstone*. Springer-Verlag, New York.

Philippi, G.T. (1965) On the depth, time and mechanism of petroleum generation. *Geochimica et Cosmochimica Acta*, **29**, 1021–1049.

Pickup, S.L.B., Whitmarsh, R.B., Fowler, C.M.R. and Reston, T.J. (1996) Insight into the nature of the ocean-continent transition off west Iberia from a deep multichannel seismic reflection profile. *Geology*, **24**, 1079–1082.

Pilger, R.H. (1984) Cenozoic plate kinematics, subduction and magmatism, South American Andes. *Journal Geological Society of London*, **141**, 793–802.

Pilkey, O.H., Locker, S.D. and Cleary, W.J. (1980) Comparison of sand-layer geometry on flat floors of ten modern depositional basins. *Bulletin American Association of Petroleum Geologists*, **64**, 841–856.

Pinet, C., Jaupart, C., Mareschal, J.-C., Gariépy, C., Bienfait, G. and Lapointe, R. (1991) Heat flow and lithospheric structure of the eastern Canadian shield. *Journal of Geophysical Research*, **96**, 19923–19941.

Pinet, P. and Souriau, M. (1988) Continental erosion and large-scale relief. *Tectonics*, **7**, 563–582.

Pitman, W.C. (1978) Relationship between eustasy and stratigraphic sequences of passive margins. *Bulletin Geological Society of America*, **89**, 1389–1403.

Pitman, W.C. (1979) The effect of eustatic sea level changes on stratigraphic sequences at Atlantic margins. In: *Geological and Geophysical Investigations of Continental Margins. American Association Petroleum Geologists Memoir*, **29**, 453–460.

Pitman, W.C. and Andrews, J.A. (1985) Subsidence and thermal history of small pull-apart basins. In: *Strike-Slip Deformation, Basin Formation and Sedimentation* (eds. K.T. Biddle and N. Christie-Blick), *Special Publication Society of Economic Paleontologists and Mineralogists*, **37**, 45–49.

Platt, J.P. (1986) Dynamics of orogenic wedges and the uplift of high-pressure metamorphic rocks. *Bulletin Geological Society of America*, **97**, 1037–1053.

Plummer, N., Busby, J., Lee, R. and Hanshaw, B. (1990) Geochemical modeling of the Madison Aquifer in parts of Montana, Wyoming, and South Dakota. *Water Resources Research*, **26**, 1981–2014.

Poag, C.W. (1980) Foraminiferal stratigraphy, palaeoenvironments and depositional cycles in the Outer Baltimore Canyon Trough. In: *Geological Studies of the COST B-3 Well, US Mid-Atlantic Continental Slope Area* (ed. by P.A. Scholle), *US Geological Survey Circular*, **833**, 44–65.

Pollack, H.N. and Chapman, D.S. (1977) On the regional variation of heat flow, geotherms and lithospheric thickness. *Tectonophysics*, **38**, 279–296.

Pomar, L. (2001) Types of carbonate platforms: a genetic approach. *Basin Research*, **13**, 313–334.

Porter, M.L. (1987) Sedimentology of an ancient erg margin: the Lower Jurassic Aztec Sandstone, southern Nevada and southern California. *Sedimentology*, **34**, 661–680.

Posamentier, H.W. and Chamberlain, C.J. (1993) Sequence stratigraphic analysis of Viking Formation lowstand beach deposits in the Joarcam field, Alberta. In: *Sequence Stratigraphy and Facies Associations* (eds. H.W. Posamentier, C.P. Summerhayes, B.U. Haq and G.P. Allen), *Special Publication International Association of Sedimentologists*, **18**, 469–486, Blackwell Scientific Publications, Oxford.

Posamentier, H.W. and James, D.P. (1993) An overview of sequence stratigraphic concepts: Uses and abuses. In: *Sequence Stratigraphy and Facies Associations* (eds. H.W. Posamentier, C.P. Summerhayes, B.U. Haq and G.P. Allen), *Special Publications, International Association of Sedimentologists*, **18**, 3–18, Blackwell Scientific Publications, Oxford.

Posamentier, H.W. and Vail, P.R. (1988) Eustatic controls on clastic deposition, II, sequence and systems tract models. In: *Sea Level Changes: An Integrated Approach* (eds. C.K. Wilgus et al.), 125–154, *Special Publication Society of Economic Paleontologists and Mineralogists*, **42**.

Posamentier, H.W., Allen, G.P., James, D.P. and Tesson, M. (1992) Forced regressions in a sequence stratigraphic framework: concepts, examples and sequence stratigraphic significance. *Bulletin American Association of Petroleum Geologists*, **76**, 1687–1709.

Posamentier, H.W., Jervey, M.T. and Vail, P.R. (1988) Eustatic controls on eustatic deposition, I, conceptual framework. In: *Sea Level Changes: An Integrated Approach* (eds. C.K. Wilgus, B.S. Hastings, C.G. St.C. Kendall, H.W. Posamentier, C.A. Ross and J.C. Van Wagoner), 109–124, *Special Publ. Society of Economic Paleontologists and Mineralogists*, **42**.

Postma, G. (1990) Depositional architecture and facies of river and fan deltas: A synthesis. In: *Coarse-grained Deltas* (eds. A. Colella and D.B. Prior). *Special Publication International Association Sedimentologists*, **10**, 13–27.

Potter, P.E. (1978) Petrology and chemistry of modern big river sands. *Journal of Geology*, **86**, 423–449.

Potter, P.E. (1984) South American modern beach sand and plate tectonics. *Nature*, **311**, 645–648.

Powell, T.G., Foscolos, A.E., Gunther, P.R. and Snowdon, L.R. (1978) Diagenesis of organic matter and fine clay minerals: a comparative study. *Geochimica et Cosmochimica Acta*, **42**, 1181–1197.

Pratt, B.R. and James, N.P. (1986) The St. George Group (Lower Ordovician) of western Newfoundland: tidal flat island model for carbonate sedimentation in shallow epeiric seas. *Sedimentology*, **33**, 313–343.

Price, R.A. (1973) Large-scale gravitational flow of supracrustal rocks, southern Canadian Rockies. In: *Gravity and Tectonics* (eds. K. de Jong and R. Scholten), 491–502, Wiley, New York.

Price, R.A. and Hatcher, R.D. (1983) Tectonic significance of similarities in the evolution of the Alabama–Pennsylvania Appalachians and the Alberta–British Columbia Canadian Cordillera. In: *Contributions to the Tectonics and Geophysics of Mountain Chains* (eds. R.D. Hatcher, H. Williams and I. Zietz), *Geology Society of America Memoir* **158**, 149–160.

Primmer, T.J., Cade, C.A., Evans, J., Gluyas, J.G., Hopkins, M.S., Oxtoby, N.H., Smalley, P.C., Warren, E.A. and Worden, R.H. (1997) Global patterns in sandstone diagenesis: Their application to reservoir quality prediction for petroleum exploration. In: *Reservoir Quality Prediction in Sandstones and Carbonates* (eds. J.A. Kupecz, J. Gluyas and S. Bloch), *American Association of Petroleum Geologists Memoir*, **69**, 61–77.

Prins, M.A. and Weltje, G.J. (1999) End-member modeling of siliciclastic grain-size distributions: The Late Quaternary record of eolian and fluvial sediment supply to the Arabian Sea and its paleoclimatic significance. In: *Numerical Experiments in Stratigraphy: Recent Advances in Stratigraphic and Sedimentologic Computer Simulations. Society for Sedimentary Geology Special Publications*, **63**, 91–111.

Prosser, S. (1993) Rift-related linked depositional systems and their seismic expression. In: *Tectonics and Seismic Sequence Stratigraphy* (eds. G.D. Williams and A. Dobbs) *Geological Society of London Special Publication London* **71**, 35–66.

Purser, B.H., Brown, A. and Aissaoui, D.M. (1994) Nature, origins and evolution of porosity in dolomites. In: *Dolomites* (eds. B. Purser, M. Tucker and D. Zenger), *International Association of Sedimentologists Special Publication*, **21**, 283–308.

Quinlan, G.M. and Beaumont, C. (1984) Appalachian thrusting, lithospheric flexure, and the Paleozoic stratigraphy of the eastern interior of North America. *Canadian Journal of Earth Sciences*, **21**, 973–996.

Ragotzkie, R.A. (1978) Heat budgets of lakes. In: *Lakes: Chemistry, Geology, Physics* (ed. by A. Lerman), 1–20, Springer-Verlag, Berlin.

Raiverman, V., Kunte, S.V. and Mukherjea, A. (1983) Basin geometry, Cenozoic sedimentation and hydrocarbons in north western Himalaya and Indo-Gangetic plains. *Petroleum Asia Journal*, **6**, 67–92.

Ramberg, I.B. (1978) Comparison of the Oslo Graben with the Rio Grande Rift. *Conference Proceedings: Los Alamos Scientific Laboratory*, **7487**, 68–71.

Ranalli, G. (1995) *Rheology of the Earth*. Chapman and Hall, London.

Ratcliff, J.T., Tackler, P.J., Schubert, G. and Zebib, A. (1997) Transitions in thermal convection with strongly variable viscosity. *Physics Earth Planetary Interiors*, **102**, 201–212.

Read, J.F., Grotzinger, J.P., Bova, J.A. and Koerschner, W.F. (1986) Models for generation of carbonate cycles. *Geology*, **14**, 107–110.

Read, J.F., Osleger, D. and Elrich, M. (1991) Two-dimensional modelling of carbonate ramp sequences and component cycles. In: *Sedimentary Modeling: Computer Simulations and Methods for Improved Parameter Definition* (eds. E.K. Franseen, W.L. Watney, G.G.S.C. Kendall and W. Ross), *Bulletin Kansas, State Geological Survey*, **233**, 473–488.

Reading, H.G. (1980) Characteristics and recognition of strike-slip fault systems. In: *Sedimentation in Oblique-Slip Mobile Zones* (eds. P.F. Ballance and H.G. Reading), *Special Publication International Association of Sedimentologists*, **4**, 7–26.

Reading, H.G. (1982) Sedimentary basins and global tectonics. *Proceedings Geological Association*, **93**, 321–350.

Reading, H.G. (ed.) (1996) *Sedimentary Environments: Processes, Facies and Stratigraphy* (Third Edition), Blackwell Science, Oxford.

Reading, H.G. (ed.) (1986) *Sedimentary Environments and Facies*, 2nd edition. Blackwell Scientific, Oxford.

Reading, H.G. and Collinson, J.D. (1996) Clastic coasts. In: *Sedimentary Environments, processes, facies and stratigraphy, 3rd Edition* (ed. H.G. Reading), pp. 154–231, Blackwell Science.

Reasenberg, P. and Ellsworth, W.L. (1982) Aftershocks of the Coyote Lake, California earthquake of August 6, 1979: a detailed study. *Journal of Geophysical Research*, **87**, 10637–10655.

Reineck, H.E. and Singh, I.B. (1980) *Depositional Sedimentary Environments*, 2nd edn. Springer, Berlin Heidelberg New York, 549 p.

Reiners, P.W. (2002) (U-Th)/He chronometry experiences a renaissance. *EOS*, Transactions, American Geophysical Union, **83**, 26–27.

Ricci Lucchi, F. (1986) The Oligocene to Recent foreland basins of the northern Apennines. In: *Foreland Basins* (eds. P.A. Allen and P. Homewood), 105–140, *Special Publication International Association of Sedimentologists* **8**, Blackwell Scientific, Oxford.

Richards, M.A. and Hager, B.H. (1984) Geoid anomalies in a dynamic Earth. *Journal of Geophysical Research*, **89**, 5487–6002.

Rider, M.H. (1996) *The Geological Interpretation of Well Logs*. Rider-French Publications.

Riedel, W. (1929) Zur Mechanik geologischer Brucherscheinungen. *Zentralblatt fur Mineralogie, Geologie und Palaeontologie*, **1929B**, 354–368.

Risk, M.J. and Rhodes E.G. (1985) From mangroves to petroleum precursors: an example from tropical N.E. Australia. *Bulletin American Association of Petroleum Geologists*, **69**, 1230–1240.

Rittenhouse, G. (1972) Stratigraphic trap classification. In: *Stratigraphic Oil and Gas Fields: Classification, Exploration Methods and Case Histories* (ed. by R.E. King), 14–28, *American Association of Petroleum Geologists Memoir*, **16**.

Rivenaes, J.C. (1992) Application of a dual-lithology, depth-dependent diffusion equation in stratigraphic simulation. *Basin Research*, **4**, 133–146.

Rivenaes, J.C. (1997) Impact of sediment transport efficiency on large-scale sequence architecture: results from stratigraphic computer stimulation. *Basin Research*, **9**, 91–105.

Robert, P. (1988) *Organic Metamorphism and Geothermal History*. Elf-Aquitaine and Reidel Publishing, Dordrecht.

Robinson, A.G., Coleman, M.L. and Gluyas, J.G. (1993) The age of illite cement growth, Village Fields area, southern North Sea: Evidence from K-Ar ages and $^{18}O/^{16}O$ ratios. *American Association Petroleum Geologists Bulletin*, **77**, 68–80.

Rodgers, D.A. (1980) Analysis of pull-apart basin development produced by en echelon strike-slip faults. *Special Publication International Association of Sedimentologists*, **4**, 27–41, Blackwell Scientific Publications, Oxford.

Romankevich, E.A. (1984) *Geochemistry of Organic Matter in the Ocean*. Springer-Verlag, Berlin.

Rona, P.A. (1982) Evaporites at passive margins. In: *Dynamics of Passive Margins* (ed. by R.A. Scrutton), 116–132, *American Geophysical Union* and *Geological Society of America Geodynamics Series*, **6**.

Rosenbloom, N.A. and Anderson, R.S. (1994) Hillslope and channel evolution in a marine terraced landscape, Santa Cruz, California. *Journal of Geophysical Research*, **99**, 14013–14029.

Rosendahl, B.R., Reynolds, D.J., Lorber, P.M., Burgess, C.F., McGill, J., Scott, D., Lambiase, J.J. and Derksen, S.J. (1986) Structural expressions of rifting: lessons from Lake Tanganyika, Africa. In: *Sedimentation in the African Rifts* (ed. by L.E. Frostick et al.), 29–43, *Special Publication Geological Society of London* **25**.

Ross, W.C., Watts, D.E. and May, J.A. (1995) Insights from stratigraphic modelling: mud-limited versus sand-limited depositional systems. *Bulletin American Association of Petroleum Geologists*, **79**, 231–258.

Rothman, D.H., Grotzinger, J.P. and Flemings, P. (1994) Scaling in turbidite deposition. *Journal of Sedimentary Research*, **64**, 59–67.

Rowley, D.B. and Sahagian, D. (1986) Depth-dependent stretching: a different approach. *Geology*, **14**, 32–35.

Rowley, E. and White, N. (1998) Inverse modelling of extension and denudation in the East Irish Sea and surrounding areas. *Earth and Planetary Science Letters*, **161**, 57–71.

Roy, R.F., Decker, E.R., Blackwell, D.D. and Birch, F. (1968) Heat flow in the United States. *Journal of Geophysical Research*, **73**, 5207–5221.

Royden, L. (1993) The tectonic expression of slab pull at convergent plate boundaries. *Tectonics*, **12**, 303–325.

Royden, L. and Karner, G.D. (1984) Flexure of the continental lithosphere beneath Apennine and Carpathian foredeep basins: evidence for an insufficient topographic load. *Bulletin American Association of Petroleum Geologists*, **68**, 704–712.

Royden, L. and Keen, C.E. (1980) Rifting processes and thermal evolution of the continental margin of eastern Canada determined from subsidence curves. *Earth and Planetary Science Letters*, **51**, 343–361.

Royden, L., Patacca, E. and Scandone, P. (1987) Segmentation and configuration of subducted lithosphere in Italy; an important control on thrust-belt and foredeep basin evolution. *Geology*, **15**, 714–717.

Royden, L., Sclater, J.G. and Von Herzen, R.P. (1980) Continental margin subsidence and heat flow: important parameters in formation of petroleum hydrocarbons. *Bulletin American Association of Petroleum Geologists*, **64**, 173–187.

Royden, L.H. (1985) The Vienna Basin: a thin-skinned pull-apart basin. In: *Strike-Slip Deformation, Basin Formation and Sedimentation* (eds. K.T. Biddle and N. Christie-Blick), *Special*

Publication Society of Economic Paleontologists and Mineralogists, **37**, 319–338.

Runcorn, S.K. (1967). Flow in the mantle inferred from the low degree harmonics of the geopotential. *Journal of the Royal Astronomical Society*, **14**, 375–384.

Russell, K.L. (1968) Oceanic ridges and eustatic changes in sea level. *Nature*, **218**, 861–862.

Rutter, E.H. (1976) The kinetics of rock deformation by pressure solution. *Philosophical Transactions of the Royal Society, London*, **A283**, 203–219.

Rutter, E.H. (1983) Pressure solution in nature, theory and experiment. *Journal Geological Society of London*, **140**, 725–740.

Rutter, E.H. and Brodie, K.H. (1988) The role of tectonic grain size reduction in the rheological stratification of the lithosphere. *Geologische Rundschau*, **77**, 295–308.

Ruzyla, K. and Friedman, G.M. (1985) Factors controlling porosity in dolomite reservoirs of the Ordovician Red River Formation, Cabin Creek Field, Montana. In: *Carbonate Petroleum Reservoirs* (eds. P.O. Roehl and P.W. Choquette), Springer-Verlag, New York, 39–58.

Rybach, L. (1986) Amount and significance of radioactive heat sources in sediments. In: *Thermal Modelling in Sedimentary Basins* (ed. by J. Burrus), 311–322, *1st IFP Exploration Research Conference, Carcans, France, June 3–7, 1985*. Editions Technip.

Rybach, L. and Cermak, V. (1982) Radioactive heat generation in rocks. In: *Physical Properties of Rocks* (ed. by G. Angenheister), 353–371. Vol. 1b, Springer-Verlag, Berlin.

Sahagian, D. (1980) Sublithospheric upwelling distribution. *Nature (London)*, **287**, 217–218.

Sahagian D.L. (1993) Structural evolution of African basins; stratigraphic synthesis. *Basin Research.*, **5**, 41–54.

Saller, A.H., Buded, D.A. and Harris, P.M. (1994) Unconformities and porosity development in carbonate strata: Ideas from a Hedberg Conference. *American Association of Petroleum Geologists Bulletin*, **78**, 857–872.

Sambrook-Smith, G.H. and Ferguson, R.I. (1995) The gravel-sand transition along river channels. *Journal of Sedimentary Research*, **65**, 423–430.

Sammonds, P.R. (1999) Understanding the fundamental physics governing the evolution and dynamics of the Earth's crust and ice sheets. *Philosophical Transactions of the Royal Society, London*, **357**, 3377–3401.

Sarg, J.F. (1981) Petrology of the carbonate-evaporite facies transition of the Seven Rivers Formation (Guadalupian, Permian), southeast New Mexico. *Journal of Sedimentary Petrology*, **51**, 73–95.

Sarg, J.F. (1988) Carbonate sequence stratigraphy. In: *Sea Level Changes: An Integrated Approach* (eds. C.K. Wilgus, B.S. Hastings, C.G.St.C. Kendall, H.W. Posamentier, C.A. Ross and J.C. van Wagoner), *Special Publication, Society of Economic Paleontologists and Mineralogists*, Tulsa, Oklahoma, **42**, 155–181.

Sarg, J.F. and Skjold, L.J. (1982) Stratigraphic traps in Palaeocene sands in the Balder area, North Sea. In: *The Deliberate Search for the Subtle Trap* (ed. by M.T. Halbouty), 197–206, *American Association of Petroleum Geologists Memoir*, **32**.

Sass, J.H., Lachenbruch, A.H. and Munroe, R.J. (1971) Thermal conductivities of rocks from measurements on fragments and its application to heat flow determination. *Journal of Geophysical Research*, **76**, 3391–3401.

Schaller, M., von-Blanckenburg, F., Hovius, N. and Kubik, P.W. (2001) Large-scale erosion rates from in situ-produced cosmogenic nuclides in European river sediments. *Earth and Planetary Science Letters*, **188**, 3–4.

Schedl, A. and Wiltschko, D.V. (1984) Sedimentological effects of a moving terrain. *Journal of Geology*, **92**, 273–287.

Scherer, M. (1987) Parameters influencing porosity in sandstones: A model for sandstone porosity prediction. *Bulletin American Association of Petroleum Geologists*, **71(5)**, 485–491.

Schlager, W. (1981) The paradox of drowned reefs and carbonate platforms. *Geological Society of America Bulletin*, **92**, 197–211.

Schlager, W. (1992) *Sedimentology and Sequence Stratigraphy of Reefs and Carbonate Platforms*. American Association of Petroleum Geologists Continuing Education Course Notes Series, **34**, Tulsa, Oklahoma.

Schlische, R.W. (1991) Half-graben basin filling models: New constraints on continental extensional basin development. *Basin Research*, **3**, 123–141.

Schlumberger (1974) *Well Evaluation Conference, North Sea* (ed. by R. Campbell et al.), Schlumberger, France.

Schlunegger, F. and Willett, S. (1999) Spatial and temporal variations in exhumation of the central Swiss Alps and implications for exhumation mechanisms. *Geological Society of London, Special Publication*, **154**, 157–179.

Schneider, F., Burrus, J. and Wolf, S. (1993) Modelling overpressures by effective stress/porosity relationships in low permeable rocks: empirical artifact or physical reality? In: *Basin Modelling; Advances and Applications. Norwegian Petroleum Society, Special Publication*, **3**, Elsevier, New York, 333–341.

Schlunegger, F., Jordan, T.E. and Klaper, E.M. (1997a) Controls of erosional denudation in the orogen on foreland basin evolution: The Oligocene central Swiss Molasse Basin as an example. *Tectonics*, **16**, 823–840.

Schlunegger, F., Leu, W. and Matter, A. (1997b) Sedimentary sequences, seismofacies, subsidence analysis, and evolution of the Burdigalian Upper Marine Molasse Group (OMM) of central Switzerland. *Bulletin American Association of Petroleum Geologists*, **81**, 1185–1207.

Scholz, C.A., Moore, Jr. T.C., Hutchinson, D.R., Gomschtok, A.J., Klitgord, K.D. and Kurotchkin, A.G. (1998) Comparative sequence stratigraphy of low-latitude versus high-latitude lacustrine rift basins: Seismic data examples from the East African and Baikal rifts. *Palaeogeography, Palaeoclimatology, Palaeoecology*, **140**, 401–420.

Scholz, C.H. (1988) The brittle-plastic transition and the depth of seismic faulting. *Geologische Rundschau*, **77**, 319–328.

Scholz, C.H. (1990) *The Mechanics of Earthquakes and Faulting*. Cambridge University Press.

Schowalter, T.T. (1976) The mechanics of secondary hydrocarbon migration and entrapment. *Wyoming Geology Association of Earth Science Bulletin*, **9**, 1–43.

Schröder, K.W. and Theune, C. (1984) Festoffabtrag und Stauraumsverlandung in Mitteleuropa. *Wasserwirstschaft*, **74**, 374–379.

Schubert, C. (1982) Origin of Cariaco Basin, southern Caribbean Sea. *Marine Geology*, **47**, 345–360.

Schwartz, R.K. and DeCelles, P.G. (1988) Cordilleran foreland basin evolution in response to interactive Cretaceous thrusting and foreland partitioning, southwestern Montana. *Memoir Geological Society of America*, **171**, 489–513.

Sclater, J.G. and Christie, P.A.F. (1980) Continental stretching: an explanation of the post Mid-Cretaceous subsidence of the central North Sea basin. *Journal of Geophysical Research*, **85**, 3711–3739.

Sclater, J.G., Jaupart, C. and Galson, D. (1980a) The heat flow through oceanic and continental crust and the heat loss of the Earth. *Reviews Geophysics and Space Physics*, **18**, 269–311.

Sclater, J.G., Parsons, B. and Jaupart, C. (1981) Oceans and continents: similarities and differences in the mechanisms of heat loss. *Journal of Geophysical Research*, **86**, 11535–11552.

Sclater, J.G., Royden, L., Horvath, F., Burchfiel, B.C., Semken, S. and Stegena, L. (1980b) The formation of the intra-Carpathian basins as determined from subsidence data. *Earth and Planetary Science Letters*, **51**, 139–162.

Sears, S.O. and Lucia, F.J. (1979) Reef-growth model for Silurian pinnacle reefs, northern Michigan reef trend. *Geology*, **3**, 299–302.

Sears, S.O. and Lucia, F.J. (1980) Dolomitization of northern Michigan Niagara reefs by brine refluxion and fresh water/sea water mixing. In: *Concepts and Models of Dolomitization* (eds. D.H. Zenger, J.B. Dunham and R.C. Ethington), 215–235, *Special Publication Society of Economic Paleontologists and Mineralogists*, **28**.

Seeber, L., Armbruster, J.G. and Quittmeyer, R.C. (1981) Seismicity and continental subduction in the Himalayan arc. In: *Zagros, Hindu Kush, Himalaya Geodynamic Evolution* (eds. H.K. Gupta and F.M. Delany), American Geophysical Union Geodynamics Series, **3**, 215–242.

Segall, P. and Pollard, D.D. (1980) Mechanics of discontinuous faults. *Journal of Geophysical Research*, **85**, 4337–4350.

Seidl, M.A. and Dietrich, W.E. (1992) The problem of channel erosion into bedrock. *Catena Supplement*, **23**, 101–124.

Seidl, M.A., Weissel, J.K. and Pratson, L.F. (1996) The kinematics and pattern of escarpment retreat across the rifted continental margin of SE Australia. *Basin Research*, **12**, 301–316.

Selley, R.C. (1985) *Elements of Petroleum Geology*. W.H. Freeman, New York.

Sellwood, B.W. (1986) Shallow marine carbonate environments. In: *Sedimentary Environments and Facies, 2nd Edition* (ed. H.G. Reading), 283–342, Blackwell Scientific, Oxford, 615 pp.

Sengör, A.M.C. and Burke, K. (1978) Relative timing of rifting and volcanism on Earth and its tectonic implications. *Geophysical Research Letters*, **5**, 419–421.

Sengör, A.M.C., Burke, K. and Dewey, J.F. (1978) Rifts at high angles to orogenic belts: tests for their origin and the Upper Rhine Graben as an example. *American Journal of Science*, **278**, 24–40.

Sengör, A.M.C., Gorur, N. and Saroglu, F. (1985) Strike-slip faulting and related basin formation in zones of tectonic escape: Turkey as a case study. In: *Strike-Slip Deformation, Basin Formation and Sedimentation* (eds. K.T. Biddle and N. Christie-Blick), *Special Publication Society of Economic Paleontologists and Mineralogists*, **37**, 227–264.

Seni, S.J. and Jackson, M.P.A. (1984) Sedimentary record of Cretaceous and Tertiary salt movement, East Texas Basins. *Report of Investigations, Texas University, Bureau of Economic Geology*, **139**, 89 pp.

Serra, O. (1984) *Fundamentals of Well-log Interpretation. 1. Acquisition of Logging Data*. Elsevier.

Serra, O. (1986) *Fundamentals of Well-log Interpretation. 2. The Interpretation of Logging Data*. Elsevier.

Shackleton, N.J. (1977) Oxygen isotope and palaeomagnetic evidence for early northern hemisphere glaciation. *Nature*, **270**, 216–219.

Shackleton, N.J. and Opdyke, N.D. (1973) Oxygen isotope and palaeomagnetic stratigraphy of equatorial Pacific core V28–V2381: oxygen isotope temperatures and ice volumes on a 10^5 year and 10^6 year scale. *Quaternary Research*, **3**, 339–355.

Shanley, K.W. and McCabe, P.J. (1998) *Relative Role of Eustasy, Climate, and Tectonism in Continental Rocks. Society for Sedimentary Geology Special Publication*, **54**, 234 p.

Shanmugam, G. (1985) Significance of coniferous rain forests and related organic matter in generating commercial quantities of oil, Gippsland Basin, Australia. *Bulletin American Association of Petroleum Geologists*, **69**, 1241–1254.

Sharp, I.R., Gawthorpe, R.L., Armstrong, B. and Underhill, J.R. (2000) Propagation history and passive rotation of mesoscale normal faults: implications for syn-rift stratigraphic development. *Basin Research*, **12**, 285–306.

Sharp, R.V. (1976) Surface faulting in Imperial Valley during the earthquake swarm of January–February, 1975. *Bulletin Seismological Society America*, **66**, 1145–1154.

Shibaoka, M. and Bennett, A.J.R. (1977) Patterns of diagenesis in some Australian sedimentary basins. *Journal of Australian Petroleum Exploration Association*, **17**, 58–63.

Shinn, E.A. (1986) Modern carbonate tidal flats; their diagnostic features. *Quarterly Journal of Colorado School of Mines*, **81**, 7–35.

Shor, G.G. and Pollard, D.D. (1964) Mohole site selection studies north of Maui. *Journal of Geophysical Research*, **69**, 1627–1637.

Shuster, M.W. and Aigner, T. (1994) Two-dimensional synthetic seismic and log cross-sections from stratigraphic forward models. *Bulletin American Association of Petroleum Geologists*, **78**, 409–431.

Sibson, R.H. (1983) Continental fault structure and the shallow earthquake source. *Journal of Geological Society of London*, **140**, 741–768.

Silver, B.A. and Todd, R.G. (1969) Permian cyclic strata, northern Midland and Delaware Basins, west Texas and

southeastern New Mexico. *American Association of Petroleum Geologists Bulletin*, **53**, 2223–2251.

Silver, P.G., Carlson, R.W. and Olson, P. (1988) Deep slabs, geochemical heterogeneity, and the large-scale structure of mantle convection; investigation of an enduring paradox. *Annual Review of Earth and Planetary Sciences*, **16**, 477–541.

Sinclair, H.D. (1994) The influence of lateral basin slopes on turbidite sandstone deposition in the Annot sandstones of SE France. *Journal of Sedimentary Research*, **64**, 42–64.

Sinclair, H.D. (1996) Plan-view curvature of foreland basins and its implications for the palaeostrength of the lithosphere underlying the western Alps. *Basin Research*, **8**, 173–182.

Sinclair, H.D. (1997) Tectono-stratigraphic model for underfilled peripheral foreland basins: An Alpine perspective. *Geological Society of America Bulletin* **109**, 324–346.

Sinclair, H.D. and Allen, P.A. (1992) Vertical versus horizontal motions in the Alpine orogenic wedge: stratigraphic response in the foreland basin. *Basin Research*, **4**, 215–232.

Sinclair, H.D., Coakley, B.J., Allen, P.A. and Watts, A.B. (1991) Simulation of foreland basin stratigraphy using a diffusion model of mountain belt uplift and erosion: An example from the central Alps, Switzerland. *Tectonics*, **10**, 599–620.

Sinclair, H.D. and Cowie, P.A. (2003) Basin-floor topography and the scaling of turbidites. *Journal of Geology*, **111**, 277–299.

Skogseid, J., Planke, S., Faleide, J.I., Pedersen, T., Eldholm, O. and Neverdal, F. (2000) NE Atlantic continental rifting and volcanic margin formation. In: *Dynamics of the Norwegian Margin* (ed. by A. Nottvedt), *Special Publication Geological Society London*, **167**, 295–326.

Sleep, N.H. (1990) Hotspots and mantle plumes: Some phenomenology. *Journal of Geophysical Research*, **95**, 6715–6736.

Sleep, N.H. and Sloss, L.L. (1978) A deep borehole in the Michigan Basin. *Journal of Geophysical Research*, **83**, 5815–5819.

Sleep, N.H. and Snell, N.S. (1976) Thermal contraction and flexure of midcontinent and Atlantic marginal basins. *Geophysical Journal of the Royal Astronomical Society*, **45**, 125–154.

Sloss, L.L. (1950) Paleozoic stratigraphy in the Montana area. *Bulletin American Association of Petroleum Geologists*, **34**, 423–451.

Sloss, L.L. (1962) Stratigraphic models in exploration. *Journal of Sedimentary Petrology*, **32**, 415–422.

Sloss, L.L. (1963) Sequences in the cratonic interior of North America. *Bulletin Geological Society of America*, **74**, 93–114.

Sloss, L.L. (1988) Forty years of sequence stratigraphy. *Bulletin Geological Society of America*, **100**, 1661–1665.

Sloss, L.L. and Speed, R.C. (1974) Relationships of cratonic and continental-margin tectonic episodes. In: *Tectonics and Sedimentation* (ed. by W.R. Dickinson), 98–119, *Special Publication Society of Economic Paleontologists and Mineralogists* **22**.

Small, E.E. and Anderson, R.S. (1995) Geomorphically driven Late Cenozoic rock uplift in the Sierra Nevada, California. *Science*, **270**, 277–280.

Small, E.E. and Anderson, R.A. (1998) Pleistocene relief production in Laramide mountain ranges, western United States. *Geology*, **26**, 123–136.

Small, E.E., Anderson, R.S., Hancock, G.S. and Finkel, R.C. (1999) Estimates of regolith production from ^{10}Be and ^{26}Al: Evidence for steady state alpine hillslopes. *Geomorphology*, **27**, 131–150.

Smith, A.G. (1976) Plate tectonics and orogeny: a review. *Tectonophysics*, **33**, 215–285.

Smith, D.A. (1980) Sealing and non-sealing faults in Louisiana Gulf Coast Salt Basin. *Bulletin American Association of Petroleum Geologists*, **64**, 145–172.

Smith, G.A. and Landis, C.A. (1995) Intra-arc basins. In: *Tectonics of Sedimentary Basins* (eds. C. Busby and R. Ingersoll). *Blackwell Science, Oxford*, 263–298.

Smith, L. and Chapman, D.S. (1983) On the thermal effects of groundwater flow, 1. Regional scale systems. *Journal of Geophysical Research*, **88**, 593–608.

Smith, L.A. (1965) Paleoenvironmental variation curves and palaeoeustatics. *Transactions Gulf Coast Association of Geological Societies*, **15**, 47–60.

Smoot, J.P. (1983) Depositional subenvironments in an arid closed basin; the Wilkins Peak Member of the Green River Formation (Eocene), Wyoming, USA. *Sedimentology*, **30**, 801–828.

Snyder, D.B. and Barazangi, M. (1986) Deep crustal structure and flexure of the Arabian plate beneath the Zagros collisional mountain belt as inferred from gravity observations. *Tectonics*, **5**, 361–373.

Sonder, L. and England, P.C. (1989) Effects of a temperature-dependent rheology on large-scale continental extension. *Journal of Geophysical Research*, **94**, 7603–7619.

Spence, W. (1987) Slab pull and the seismotectonics of subducting lithosphere. *Reviews of Geophysics*, **25**, 55–69.

Spohn, L. and Schubert, G. (1983) Convective thinning of the lithosphere: a mechanism for rifting and midplate volcanism on Earth, Venus and Mars. *Tectonophysics*, **94**, 67–90.

St John, B., Bally, A.W. and Klemme, H.D. (1984) *Sedimentary Provinces of the World: Hydrocarbon Productive and Non-productive.* American Association of Petroleum Geologists, Tulsa, Oklahoma.

Stach, E., MacKowsky, M.-Th., Teichmüller, M., Teichmüller, R., Taylor, G.H. and Chandra, D. (1982) *Stach's Textbook of Coal Petrology (3rd Edition)*. Gebrüder Borntraeger, Berlin-Stuttgart.

Stallard, R.F. (1995) Tectonic, environmental and human aspects of weathering and erosion: a global review using a steady-state perspective. *Annual Reviews of Earth and Planetary Sciences* **23**, 11–39.

Stallard, R.F. and Edmond, J.M. (1983) Geochemistry of the Amazon; 2, The influence of geology and weathering environment on the dissolved load. *Journal of Geophysical Research, Oceans and Atmospheres*, **88**, 9671–9688.

Steckler, M.S. (1981) *Thermal and Mechanical Evolution of Atlantic-type Margins*. Unpubl. PhD thesis, Columbia University, New York.

Steckler, M.S. (1985) Uplift and extension at the Gulf of Suez: indications of induced mantle convection. *Nature*, **317**, 135–139.

Steckler, M.S. (1999) High resolution sequence stratigraphic modeling: 1. The interplay of sedimentation, erosion and subsidence. In: *Numerical Experiments in Stratigraphy* (eds. J. Harbaugh, L. Watney, G. Rankey, R. Slingerland, R. Goldstein and E. Franseen). *Special Publication Society of Economic Paleontologists and Mineralogists*, **62**, 139–150.

Steckler, M.S. and ten Brink, U.S. (1986) Lithospheric strength variations as a control on new plate boundaries: examples from the northern Red Sea region. *Earth and Planetary Science Letters*, **79**, 120–132.

Steckler, M.S. and Watts, A.B. (1978) Subsidence of the Atlantic-type continental margin off New York. *Earth and Planetary Science Letters*, **41**, 1–13.

Steckler, M.S. and Watts, A.B. (1981) Subsidence history and tectonic evolution of Atlantic-type continental margins. In: *Dynamics of Passive Margins* (ed. by R.A. Scrutton), *American Geophysical Union Geodynamics Series* **6**, 184–196.

Steckler, M.S., Watts, A.B. and Thorne, J.A. (1988) Subsidence and basin modelling at the U.S. Atlantic continental margin. In: *The Atlantic Continental Margin, U.S.*, Vol. 1–2, *The Geology of North America* (eds. R.E. Sheridan and J.A. Grow), 199–416, Geological Society of America.

Stein, C.A., Cloetingh, S. and Wortel, R. (1989) SEASAT-derived gravity constraints on stress and deformation in the northeastern Indian Ocean. *Geophysical Research Letters*, **16**, 823–826.

Stein, R.W., King, G.C.P. and Rundle, J.B. (1988) The growth of geological structure by repeated earthquakes 2. Field examples of continental dip-slip faults. *Journal of Geophysical Research*, **93**, 13319–13331.

Stern, R. J. (2002) Subduction zones. *Reviews of Geophysics*, **40**, DOI 10.1029/2001RG000108.

Stern, T.A., Quinlan, G.M. and Holt, W.E. (1992) Basin formation behind an active subduction zone: 3-dimensional flexural modelling of Wanganui Basin, New Zealand. *Basin Research*, **4**, 197–214.

Stevenson, C.J and Turner, J.S. (1977) Angle of subduction. *Nature (London)*, **270**, 334–336.

Stewart, J. and Watts, A.B. (1997) Gravity anomalies and spatial variations of flexural rigidity at mountain ranges. *Journal of Geophysical Research*, **102**, B3, 5327–5352.

Stock, J.D. and Montgomery, D.R. (1999) Geologic constraints on bedrock river incision using the streampower law. *Journal of Geophysical Research*, **104**, 4983–4993.

Stöckli, D.F., Farley, K.A. and Dumitru, T.A. (2000) Calibration of the apatite (U-Th)/He thermochronometer on an exhumed fault block, White Mountains, California. *Geology*, **28**, 983–986.

Stockmal, G.S., Beaumont, C. and Boutilier, R. (1986) Geodynamic models of convergent tectonics: the transition from rifted margin to overthrust belt and consequences for foreland basin development. *Bulletin American Association of Petroleum Geologists*, **70**, 181–190.

Stow, D.A.V. (1985) Deep sea clastics: where are we and where are we going? In: *Sedimentology: Recent Developments and Applied Aspects* (eds. P.J. Brenchley and B.P.J. Williams), 67–93, *Special Publication Geological Society of London* **18**, Blackwell Scientific, Oxford.

Strakhov, N.M. (1967) *Principles of Lithogenesis*, Vol. 1. Oliver and Boyd, Edinburgh.

Straub, C. and Kahle, H.G. (1995) Active crustal deformation in the Marmara Sea region, NW Anatolia, inferred from GPS measurements. *Geophysical Research Letters*, **22**, 2533–2536.

Stuart, C.A. (1970) Geopressures. *Proceedings 2nd Symp. Abnormal Subsurface Pressure*, Louisiana State University, Baton Rouge, Louisiana, Supplement.

Stüwe, K., White, L. and Brown, R. (1994) The influence of eroding topography on steady state isotherms; applications to fission track analysis. *Earth and Planetary Science Letters*, **124**, 63–74.

Su, W. J. and Dziewonski, A.M. (1992) On the scale of mantle heterogeneity. *Physics of the Earth and Planetary Interiors*, **74**, 29–54.

Su, W.J., Woodward, R.L. and Dziewonski, A.M. (1994) Degree 12 model of shear velocity heterogeneity in the mantle. *Journal of Geophysical Research*, **99**, 6945–6980.

Summerfield, M.A. (1991) *Global Geomorphology*. Longman, London.

Summerfield, M.A. and Hulton, N.J. (1994) Natural controls on fluvial denudation rates in major world drainage basins. *Journal of Geophysical Research*, **99**, 13871–13883.

Suppe, J. (1983) Geometry and kinematics of fault-bend folding. *American Journal of Science*, **283**, 684–721.

Surlyk, F. (1990) Mid-Mesozoic synrift turbidite systems: Controls and predictions. In: *Correlation in Hydrocarbon Production* (ed. by J.D. Collinson) Graham and Trotman, London, 231–241.

Surlyk, F., Clemmensen, L.B. and Larsen, H.C. (1981) Post-Palaeozoic evolution of the East Greenland continental margin. In: *Geology of the North Atlantic Borderlands* (eds. J.W. Kerr and A.J. Fergusson), 611–646, *Canadian Society Petroleum Geologists Memoir* **7**.

Suter, JR., Berryhill, H.L Jr. and Penland, S. (1987) Late Quaternary sea level fluctuations and depositional sequences, southwest Louisiana continental shelf. In: *Sea Level Fluctuation and Coastal Evolution* (eds. D. Nummedal, O.H. Pilkey and J.D. Howard), *Special Publication Society of Economic Paleontologists and Mineralogists* **41**, 199–219.

Sweeney, J.J. and Burnham, A.K. (1990) Evaluation of a simple model of vitrinite reflectance based on chemical kinetics. *Bulletin American Association of Petroleum Geologists*, **74**, 1559–1570.

Swift, D.J.P. (1974) Continental shelf sedimentation. In: *The Geology of Continental Margins* (eds. C.A. Burk and C. L. Drake), 117–135, Springer-Verlag, Berlin.

Swift, D.J.P., Han, G. and Vincent, C.E. (1986) Fluid processes and seafloor responses on a modern storm-dominated shelf: Middle Atlantic shelf of North America. Part I. The Storm Current Regime. In: *Shelf Sands and Sandstones* (eds. R.J. Knight

and J.R. McLean) *Memoir Canadian Society Petroleum Geologists Calgary*, **11**, 99–119.

Sykes, L. (1967) Mechanisms of earthquakes and nature of faulting on the mid-ocean ridges. *Journal of Geophysical Research*, **72**, 2131–2153.

Sylvester, A.G. (1988) Strike-slip faults. *Bulletin Geological Society of America*, **100**, 1666–1703.

Talbot, M.R. and Allen, P.A. (1996) Lakes. In: *Sedimentary Environments: Processes, Facies and Stratigraphy* (ed. by H.G. Reading). 3rd Ed., 83–124, Blackwell Scientific Publications.

Talling, P.J. (2001) On the frequency distribution of turbidite thickness. *Sedimentology*, **48**, 1297–1331.

Talling, P.J., Lawton, T.F., Burbank, D.W. and Hobbs, R.S. (1995) Evolution of latest Cretaceous-Eocene nonmarine deposystems in the Axhandle piggyback basin of central Utah. *Bulletin Geological Society of America*, **107**, 297–315.

Tamaki,K. and Honza, E. (1991) Global tectonics and formation of marginal basins: Role of the Western Pacific. *Episodes*, **14**, 224–230.

Tankard, A.J. (1986) On the depositional response to thrusting and lithospheric flexure: examples from the Appalachian and Rocky Mountain basins. In: *Foreland Basins* (eds. P.A. Allen and P. Homewood), *Special Publication International Association of Sedimentologists* **8**, 369–394.

Tankard, A.J., Jackson, M.P.A., Eriksson, K.A., Hobday, D.K., Hunter, D.R. and Minter, W.E.L. (1982) *Crustal Evolution of Southern Africa*. Springer-Verlag, New York.

Tapponnier, P. and Molnar, P. (1976) Slip-line field theory and large-scale continental tectonics. *Nature*, **264**, 319–324.

Taymaz, T., Jackson, J. and McKenzie, D. (1991) Active tectonics of the north and central Aegean Sea. *Geophysical Journal International*, **106**, 433–490.

Tchalenko, J. S. (1970) Similarities between shear zones of different magnitudes. *Bulletin Geological Society of America*, **81**, 1625–1640.

Tchalenko, J.S. and Ambraseys, N.N. (1970) Structural analyses of the Dasht-e Baÿaz (Iran) earthquake fractures. *Bulletin Geological Society of America*, **81**, 1625–1640.

Teichmüller, M. (1970) Bestimmung des Inkohlungsgrades von kohligen Einschlussen in Sedimenten des Oberrheingrabens: ein Hilfsmittel bei der Klärung geothermischer Fragen. In: *Graben Problems* (eds. J.H. Illies and S. Müller), *Upper Mantle Science Proj. Science Rept.*, **27**, 124–142.

Teichmüller, M. (1982) Fluoreszenz von Liptiniten und Vitriniten in Bezichung zu Inkohlungsgrad und Verkokungsverhalten. *Geologie Landesamt Nordrhein-Westfalen. Special Paper.*

Teichmüller, M. and Teichmüller, R. (1975) Inkohlungsuntersuchungen in der Molasse des Alpenvorlands. *Geologica bavar.*, **73**, 123–142.

ten Brink, U.S. and Ben-Avraham, Z. (1989) The anatomy of a pull-apart basin: Seismic reflection observations of the Dead Sea basin. *Tectonics*, **8**, 333–350.

ten Brink, U.S., Ben-Avraham, Z., Bell, R.E., Hassouneh, M., Coleman, D.F., Andreasen, G., Tibor, G. and Coakley, B.J. Structure of the Dead Sea pull-apart basin from gravity analyses. *Journal of Geophysical Research, B* **98**, 21,877–21, 894.

ter Voorde, M. and Cloetingh, S. (1996) Numerical modelling of extension in faulted crust: Effects of localized and regional deformation on basin stratigraphy. *Geological Society of London Special Publication* **99**, 283–296.

Terres, R.R. and Sylvester, A.G. (1981) Kinematic analysis of rotated fractures and blocks in simple shear. *Bulletin Seismological Society America*, **71**, 1593–1605.

Terzaghi, K. (1936) The shearing resistance of saturated soils. In: *Proceedings of the 1st International Conference on Soil Mechanics*, Harvard **1**, 54–56.

Terzaghi, K. and Peck, R.B. (1948) *Soil Mechanics in Engineering Practice*. Wiley.

Thiessen, R., Burke, K. and Kidd, W.S.F. (1979) African hotspots and their relation to the underlying mantle. *Geology*, **7**, 263–266.

Thomas, B.M. (1982) Land plant source rocks for oil and their significance in Australian basins. *Journal of Australian Petroleum Exploration Association*, **22**, 164–178.

Tissot, B. (1969) Premières données sur les mécanismes et le cinétique de la formation du pétrole dans les sédiments; simulation d'un schéma reactionnel sur ordinateur. *Revue de l'Institut Français du Pétrole*, **24**, 470–501.

Tissot, B. and Espitalié, J. (1975) L'evolution thermique de la matière organique des sediments: applications d'une simulation mathématique. *Revue de l'Institut Français du Pétrole*, **30**, 743–777.

Tissot, B. (1973) Vers l'évaluation quantitative du pétrole formé dans les bassins sédimentaires. *Petrole et Techniques*, **222**, 27–31.

Tissot, B.P. and Welte, D.H. (1978) *Petroleum Formation and Occurrence: A New Approach to Oil and Gas Exploration*. Springer-Verlag, Berlin.

Tissot, B.P. and Welte, D.H. (1984) *Petroleum Formation and Occurrence* (2nd edition). Springer-Verlag, New York.

Toksöz, M.N. and Bird, P. (1977) Formation and evolution of marginal basins and continental plateaus. In: *Island Arcs, Deep Sea Trenches and Back arc Basins* (eds. M. Talwani and W.C. Pitman), 379–393, *Maurice Ewing Series*, **1**, American Geophysical Union.

Trudgill, B. (2002) Structural controls on drainage development in the Canyonlands grabens. In: *Bulletin American Association of Petroleum Geologists*, **86**, 1095.

Tucker, G.E. (1996) *Modelling the Large-scale Interaction of Climate, Tectonics, and Topography*. PhD dissertation, Pennsylvania State University, University Park, P.A.

Tucker, G.E. and Slingerland, R. (1996) Predicting sediment flux from fold and thrust belts. *Basin Research*, **8**, 329–349.

Turcotte, D.L. (1983) Driving mechanisms of mountain building. In: *Mountain Building Processes* (ed. by K.J. Hsu), 141–146, Academic Press, Orlando, Florida.

Turcotte, D.L. and Bernthal, M.J. (1984) Synthetic coral reef terraces and variations of Quaternary sea level. *Earth and Planetary Science Letters*, **70**, 121–128.

Turcotte, D.L. and Kenyon, P.M. (1984) Synthetic passive margin stratigraphy. *Bulletin American Association of Petroleum Geologists*, **68**, 768–775.

Turcotte, D.L. and Schubert, G. (1982) *Geodynamics: Applications of Continuum Mechanics to Geological Problems*. Wiley, New York.

Turcotte, D.L. and Schubert, G. (2002) *Geodynamics* (Second Edition). Cambridge University Press, Cambridge.

Turcotte, D.L. and Willeman, R.J. (1983) Synthetic cyclic stratigraphy. *Earth and Planetary Science Letters*, **63**, 89–96.

Ulmishek, G. (1986) Stratigraphic aspects of petroleum resource assessment. In: *Oil and Gas Assessment: Methods and Applications* (ed. by D.D. Rice) *American Association Petroleum Geologists Studies in Geology*, **21**, 59–68.

Underhill, J.R. (1991) Controls on Late Jurassic seismic sequences, Inner Moray Firth, UK North Sea: A critical test of a key segment of Exxon's original global cycle chart. *Basin Research*, **3**, 79–98.

Underhill, J.R. (2001) Controls on the genesis and prospectivity of Palaeogene palaeogeomorphic traps, East Shetland Platform, UK North Sea. *Journal of Marine and Petroleum Geology*, **18**, 259–281.

Underwood, M.B. and Moore, G.F. (1995) Trenches and trench slope basins. In: *Tectonics of Sedimentary Basins* (eds. C. Busby and R. Ingersoll). Blackwell Science, Oxford, 179–220.

Upcott, N.M., Mukasa, R.K., Ebinger, C.J. and Karner, G.D. (1996) Along-axis segmentation and isostasy in the Western Rift, East Africa. *Journal of Geophysical Research*, **101,** 3247–3268.

Ussami, N., Shiraiwa, S. and Landin-Dominguez, J.M. (1999) Basement reactivation in a sub-Andean foreland flexural bulge: The Pantanal wetland, SW Brazil. *Tectonics*, **18**, 25–39.

Uyeda, S. and Kanamori, H. (1979) Back-arc opening and the mode of subduction. *Journal of Geophysical Research*, **84**, 1049–1061.

Vail, P.E. Mitchum, R.M. Jr. and Thompson, S. III (1977a) Relative changes of sea level from coastal onlap. In: *Seismic Stratigraphy: Applications to Hydrocarbon Exploration* (ed. by C.E. Payton), *American Association of Petroleum Geologists Memoir* **26**, 63–82.

Vail, P.R., Mitchum, R.M. Jr. and Thompson S. (1977b) Seismic stratigraphy and global changes of sea level, Part 4: Global cycles of relative changes of sea level. In: *Seismic Stratigraphy: Applications to Hydrocarbon Exploration* (ed. by C.E. Payton), *American Association of Petroleum Geologists Memoir*, **26**, 83–97.

Valentine, JW. and Moores, E.M. (1970) Plate tectonic regulation of faunal diversity and sea level. *Nature*, **228**, 657–669.

Van Balen, R.T., Podladchikov, Y.Y. and Cloetingh, S. (1998) A new multilayered model for intraplate stress-induced differential subsidence of faulted lithosphere applied to rifted basins. *Tectonics*, **17**, 938–954.

Van Balen, R.T., Van der Beek, P.A. and Cloetingh, S. (1995) The effect of rift shoulder erosion on stratal patterns at passive margins: Implications for sequence stratigraphy. *Earth and Planetary Science Letters*, **134**, 532–544.

van den Beukel, J. and Wortel, R. (1986) Thermal modelling of arc-trench regions. *Geologie en Mijnbouw*, **65**, 133–43.

van Gijzel, P. (1982) Characterization and identification of kerogen and bitumen and determination of thermal maturation by means of qualitative and quantitative microscopical techniques. In: *How to Assess Maturation and Paleotemperatures, Society of Economic Paleontologists and Mineralogists Short Course Notes*, **7**, 159–216.

van Hinte, J.E. (1978) Geohistory analysis: application of micropalaeontology in exploration geology. *Bulletin American Association of Petroleum Geologists*, **62**, 201–222.

Van Wagoner, J.C., Mitchum, R.M. Jr., Campion, K.M. and Rahmanian, V.D. (1990) *Siliciclastic Sequence Stratigraphy in Well Logs, Cores and Outcrop: Concepts for High Resolution Correlation of Time and Facies. American Association of Petroleum Geologists Methods in Exploration Series*, **7**, Tulsa.

Van Wagoner, J.C., Posamentier, H.W., Mitchum, R.M., Vail, P.R., Sarg, J.F., Loutit, T.S. and Handenbol, J. (1988) An overview of the fundamentals of sequence stratigraphy and key definitions. In: *Sea-Level Changes: An Integrated Approach. Special Publication Society of Economic Paleontologists and Mineralogists*, **42**, 39–45.

Van Wees, J.D. and Cloetingh, S. (1996) 3-D modelling of stress-induced subsidence in the North Sea basin. *Tectonophysics*, **266**, 343–359.

Van West, F.P. (1972) Trapping mechanisms of Minnelusa oil accumulations, northeastern Powder River basin, Wyoming. *Mountain Geologist*, **9**, 3–20.

Vassoevich, N.B., Visotskij, I.V., Guseva, A.N. and Olenin, V.B. (1967) Hydrocarbons in the sedimentary mantle of the Earth. *Proceedings 7th World Petroleum Congress*, **2**, 37–45.

Veevers, J.J. (1981) Morphotectonics of rifted continental margins in embryo (East Africa), youth (Africa-Arabia), and maturity (Australia). *Journal of Geology*, **89**, 57–82.

Vening-Meinesz, F.A. (1941) Gravity over the Hawaiian Archipelago and over the Madeira area. *Proceedings Netherlands Acad, Wetensia.*

Vening-Meinesz, F.A. (1948) *Gravity Expeditions at Sea*, 1923–1938. Netherlands Geodetic Commission, Waltman, Delft.

Vincent, S.J. (2001) The Sis palaeovalley: A record of proximal fluvial sedimentation and drainage basin development in response to Pyrenean mountain building. *Sedimentology*, **48**, 1235–1276.

Vine, F. and Matthews, D.H. (1963) Magnetic anomalies over ocean ridges. *Nature*, **199**, 947–949.

Vinogradov, L.S., Aver'yanov, I.S. and Nigmati, I.S. (1983) Catagenetically sealed oil pools of the Volga–Ural region. *Petroleum Geology*, **19**, 266–268.

Wagner, C.W. and Van der Togt, C. (1973) Holocene sediment types and their distribution in the Southern Persian Gulf. In: *The Persian Gulf: Holocene Carbonate Sedimentation and Diagenesis in a Shallow Epicontinental Sea* (ed. B.H. Purser), 123–156, Springer-Verlag, Berlin, 471 pp.

Walcott, R.I. (1970) Flexural rigidity, thickness and viscosity of the lithosphere. *Journal of Geophysical Research*, **75**, 3941–3954.

Walderhaug, O. (1996) Kinetic modeling of quartz cementation and porosity loss in deeply buried sandstone reservoirs. *American Association Petroleum Geologists Bulletin*, **80**, 731–745.

Walker, R.G. (Ed.) (1984) *Facies Models* (2nd Edition). Geoscience Canada Reprint Series, **1**.

Walling, D.E. and Webb, B.W. (1996) Erosion and sediment yield: a global overview. In: *Erosion and Sediment Yield: Global and Regional Perspectives* (eds. D.E. Walling and B.W. Webb), *International Association of of Hydrological Sciences Publ.*, **236**, 3–19.

Walling, D.E. and Webb, B.W., (1983) Patterns of sediment yield. In: *Background to Palaeohydrology* (ed. by K.J. Gregory), John Wiley & Sons. Chichester, United Kingdom, 69–100.

Wangen, M. (1995) The blanketing effect in sedimentary basins. *Basin Research*, **7**, 283–298.

Waples, D.W. (1980) Time and temperature in petroleum formation: application of Lopatin's method to petroleum exploration. *Bulletin American Association of Petroleum Geologists*, **64**, 916–926.

Ware, P.D. and Turner, J.P. (2002) Sonic velocity analysis of the Tertiary denudation of the Irish Sea basin. In: *Exhumation of the North Atlantic Margin: Timing, Mechanisms and Implications for Petroleum Exploration* (eds. A.G. Doré, J.A. Cartwright, M.S. Stoker, J.P. Turner and N. White). *Geological Society of London Special Publication* **196**, 355–370.

Waschbusch, P.J. and Royden, L.H. (1992) Spatial and temporal evolution of foredeep basins: Lateral strength variations and inelastic yielding in continental lithosphere. *Basin Research*, **4**, 179–196.

Watson, H.J. (1981) Casablanca field, offshore Spain, a palaeogeomorphic trap. *Bulletin American Association of Petroleum Geologists Abstr.*, **65**, 1005–1006.

Watts A.B. (1992) The effective elastic thickness of the lithosphere and the evolution of foreland basins. *Basin Research*, **4**, 169–178.

Watts, A.B. (1978) An analysis of isostasy in the world's oceans: 1. Hawaiian-Emperor seamount chain. *Journal of Geophysical Research*, **83**, 5989–6004.

Watts, A.B. (1982) Tectonic subsidence, flexure and global changes in sea level. *Nature*, **297**, 469–474.

Watts, A.B. (1988) Gravity anomalies, crustal structure and flexure of the lithosphere at the Baltimore Canyon Trough. *Earth and Planetary Science Letters*, **89**, 221–238.

Watts, A.B. (2001) *Isostasy and Flexure of the Lithosphere*. Cambridge University Press, Cambridge.

Watts, A.B. and Cochran, JR. (1974) Gravity anomalies and flexure of the lithosphere along the Hawaiian–Emperor seamount chain. *Geophysical Journal of Royal Astronomical Society*, **38**, 119–141.

Watts, A.B. and Ryan, W.B.F. (1976) Flexure of the lithosphere and continental margin basins. *Tectonophysics*, **36**, 25–44.

Watts, A.B. and Steckler, M.S. (1979) Subsidence and eustasy at the continental margin of eastern North America. *American Geophysical Union, Maurice Ewing Ser.*, **3**, 218–239.

Watts, A.B. and Talwani, M. (1974) Gravity anomalies seaward of trenches and their tectonic implications. *Geophysical Journal of R. astr. Society*, **36**, 57–90.

Watts, A.B. and Thorne, J. (1984) Tectonics, global changes in sea level and their relationship to stratigraphic sequences at the US Atlantic continental margin. *Marine and Petroleum Geology*, **1**, 319–339.

Watts, A.B. and Torné, M. (1992) Subsidence history, crustal structure and thermal evolution of the Valencia Trough: a young extensional basin in the western Mediterranean. *Journal of Geophysical Research*, **97**, 20021–20041.

Watts, A.B., Karner, G.D. and Steckler, M.S. (1982) Lithospheric flexure and the evolution of sedimentary basins. *Phil. Trans. R. Society London*, **A305**, 249–281.

Weaver, P.P.E., Rothwell, R.G., Ebbing, J., Gunn, D. and Hunter, P.M. (1992) Correlation, frequency of emplacement and source directions of megaturbidites on the Madeira Abyssal Plain. *Marine Geology*, **109**, 1–20.

Weber, K.J. (1986) How heterogeneity affects oil recovery. In: *Reservoir Characterization* (eds. L.W. Lake and H.B. Carroll, Jr), 487–544, Academic Press, Orlando.

Weber, K.J. (1987) Computation of initial well productivities in aeolian sandstone on the basis of a geological model, Leman Gas Field, U.K. In: *Reservoir Sedimentology* (eds. R.W. Tillmann and K.J. Weber), 333–354, *Special Publication Society of Economic Paleontologists and Mineralogists*, **40**.

Weber, K.J., Mandl, G., Pilaar, W.F., Lehner, F. and Precious, R.G. (1978) The role of faults in hydrocarbon migration and trapping in Nigerian growth fault structures, 2643–2651, *Offshore Tech. Conf, Houston, paper OTC* 3356.

Weber, V.V. and Maximov, S.P. (1976) Early diagenetic generation of hydrocarbon gases and their variations dependent on initial organic composition. *Bulletin American Association of Petroleum Geologists*, **60**, 287–293.

Weinstein, S.A. and Olson, P. (1992) Thermal convection with non-Newtonian plates. *Geophysical Journal International.*, **111**, 515–530.

Weissel, J.K. and Karner, G.D. (1989) Flexural uplift of rift flanks due to mechanical unloading of the lithosphere during extension. *Journal of Geophysical Research*, **94**, 13919–13950.

Wen, L. and Anderson, D.L. (1995) The fate of slabs inferred from seismic tomography and 130 million years of subduction. *Earth and Planetary Science Letters*, **133**, 185–198.

Wernicke, B. (1981) Low-angle normal faults in the Basin and Range province: nappe tectonics in an extending orogen. *Nature*, **291**, 645–648.

Wernicke, B. (1985) Uniform-sense normal simple shear of the continental lithosphere. *Canadian Journal of Earth Sciences*, **22**, 108–125.

Wesson, R.L., Helley, E.J., Lajoie, K.R. and Wentworth, C.M. (1975) Faults and future earthquakes. In: R.D. Borchardt (ed.) *Studies for Seismic Zonation of the San Francisco Bay Region, U.S. Geological Survey Professional Paper*, **941A**, 5–30.

Wheeler, H.E. (1958) Time stratigraphy. *Bulletin American Association of Petroleum Geologists*, **42**, 1047–1063.

Wheeler, H.O. (1964) Baselevel, lithosphere surface, and time-stratigraphy. *Geological Society of America Bulletin*, **75**, 599–610.

Wheeler, P. and White, N. (2000) Quest for dynamic topgraphy: observations from southeast Asia. *Geology*, **28**, 963–966.

Whelan, J.K. and Thomson-Rizer, C.L. (1993) Chemical methods for assessing kerogen and protokerogen types and maturity. In: *Organic Geochemistry*, (eds. M.H. Engel and S.A. Macko), Plenum Presss, New York, 289–346.

Whipple, K.X. and Trayler, C.R. (1996) Tectonic control on fan size: the importance of spatially-variable subsidence rates. *Basin Research*, **8**, 351–366.

White, A.F. and Blum, A.E. (1995) Effects of climate on chemical weathering in watersheds. *Geochimica et Cosmochimica Acta*, **59**, 1729–1747.

White, D.A. (1980) Assessing oil and gas plays in facies cycle wedges. *Bulletin American Association of Petroleum Geologists*, **64**, 1158–1178.

White, D.A. (1988) Oil and gas play maps in exploration and assessment. *Bulletin American Association of Petroleum Geologists*, **72**, 944–949.

White, N. (1993) Recovery of strain rate variation from inversion of subsidence data. *Nature*, **366**, 449–452.

White, N. (1994) An inverse method for determining lithospheric strain rate variation on geological timescales. *Earth and Planetary Science Letters*, **122**, 351–371.

White, N. and Lovell, B. (1997) Measuring the pulse of a plume with the sedimentary record. *Nature*, **387**, 888–891.

White, N. and McKenzie, D.P. (1988) Formation of the steer's head geometry of sedimentary basins by differential stretching of the crust and mantle. *Geology*, **16**, 250–253.

White, R.S. and McKenzie, D. (1989) Magmatism at rift zones: the generation of volcanic continental margins and flood basalts. *Journal of Geophysical Research*, **94**, 7685–7729.

Wilcox, R.E., Harding, T.P. and Seely, D.R. (1973) Basin wrench tectonics. *Bulletin American Association of Petroleum Geologists*, **57**, 74–96.

Wilgus, C.K., Hastings, B.S., Kendall, C.G. St. C., Posamentier, H.W., Ross, C.A. and Van Wagoner, J.C. (eds.) (1988) *Sea-level Changes: An Integrated Approach. Special Publication Society of Economic Paleontologists and Mineralogists*, Tulsa, Oklahoma, **42**.

Wilhelm, O. (1945) Classification of petroleum reservoirs. *Bulletin American Association of Petroleum Geologists*, **29**, 1537–1580.

Wilkinson, B.H., Diedrich, N.W. and Drummond, C.N. (1996) Facies successions in peritidal carbonate sequences. *Journal of Sedimentary Research*, **66**, 1065–1078.

Wilkinson, B.H., Diedrich, N.W., Drummond, C.N. and Rothman, E.D. (1998) Michigan hockey, meteoric precipitation, and rhythmicity of accumulation on peritidal carbonate platforms. *Bulletin Geological Society of America*, **110**, 1075–1093.

Wilkinson, B.H., Drummond, C.N., Rothman, E.D. and Diedrich, N.W. (1997) Stratal order in peritidal carbonate sequences. *Journal of Sedimentary Research*, **67**, 1068–1082.

Willett, S. (1999) Orogeny and orography: the effects of erosion on the structure of mountain belts. *Journal of Geophysical Research*, **104**, 28957–28981.

Willett, S.D. (1992) Dynamic and kinematic growth and change of a Coulomb wedge. In: *Thrust Tectonics*. Chapman & Hall. London, 19–31.

Willett, S.D., Beaumont, C. and Fullsack, P. (1993) Mechanical model for the tectonics of doubly vergent compressional orogens. *Geology*, **21**, 371–374.

Willett, S.D., Chapman, D.S. and Neugebauer, H.J. (1985) A thermo-mechanical model of continental lithosphere. *Nature*, **314**, 520–523.

Williams, C.A., Connors, C., Dahlen, F.A., Price, E.J. and Suppe, J. (1994) Effect of the brittle-ductile transition on the topography of compressive mountain belts on Earth and Venus. *Journal of Geophysical Research*, **99**, B10, 19947–19974.

Williams, D.G. (1984) Correlation of Pleistocene marine sediments of the Gulf of Mexico and other basins using oxygen isotope stratigraphy. In: *Principles of Pleistocene Stratigraphy Applied to the Gulf of Mexico* (ed. by N. Healy-Williams), 65–118, International Human Resources Development Corporation, Boston.

Williams, H.H., Kelley, P.A., Janks, J.S. and Christensen, R.M. (1985) The Palaeogene rift basin source rocks of Central Sumatra. *Proceedings Indonesia Petroleum Association. 14th Annual Convention, October, 1985.*

Williams, J.J. (1968) The stratigraphy and igneous reservoirs of the Angila field, Libya. In: *Geology and Archaeology of Northern Cyrenaica, Libya* (ed. by T.F. Baff), 197–206.

Wilson, J.L (1975) *Carbonate Facies in Geologic History*. Springer-Verlag, Berlin.

Wilson, J.T. (1963) A possible origin of the Hawaiian Islands. *Canadian Journal of Physics*, **41**, 863–870.

Wilson, J.T. (1966) Did the Atlantic close and then re-open? *Nature*, **211**, 676–681.

Wilson, J.T. and Burke, K. (1972) Two types of mountain building. *Nature*, **239**, 448–449.

Wise, D.U. (1974) Continental margins; freeboard and volumes of continents and oceans through time. In: *The Geology of Continental Margins* (eds. C.A. Burk and C.L. Drake), 45–58, Springer-Verlag, New York.

Wolf, R., Farley, K. and Kass, D. (1998) A sensitivity analysis of the apatite (U-Th)/He thermochronometer. *Chemical Geology*, **148**, 105–114.

Wolf, R., Farley, K. and Silver, L. (1996) Assessment of (U-Th)/He thermochronometry: the low temperature history of the San Jacinto Mountains, California. *Geology*, **25**, 65–68.

Wood & P.J. Barton (1983) Crustal thinning and subsidence in the North Sea. *Nature*, **302**, 134–136.

Woodcock, N.H. (1986) The role of strike-slip fault systems at plate boundaries. *Philosophical Transactions of the Royal Society, London*, **A317**, 13–29.

Woodside, W. and Messmer, J.H. (1961) Thermal conductivity of porous media (parts I and II). *Applied Physics*, **32**(9), 1688–1707.

Woodwell, G.M., Whittaker, R.H., Reiners, W.A., Likens, G.E., Delwiche, C.C. and Botkin, D.B. (1978) The biota and the world carbon budget. *Science*, **199**, 141–146.

Worden, R.H. and Morad, S. (2003) Clay minerals in sandstones: controls on formation, distribution and evolution. In: R.H. Worden and S. Morad (eds.) *Clay Mineral Cements in Sandstones, International Association of Sedimentologists, Special Publication*, **34**, 3–41 Blackwell Publishing, Oxford.

Wright, L.D. (1977) Sediment transport and deposition at river mouths: a synthesis. *Bulletin Geological Society of America*, **88**, 857–868.

Wright, L.D. and Coleman, J.M. (1974) Mississippi River mouth processes; effluent dynamics and morphologic development. *Journal of Geology*, **82**, 751–778.

Wyllie, P.J. (1971) *The Dynamic Earth*. Wiley, New York.

Yong, L., Allen, P.A., Densmore, A.L. and Qiang, X. (2003) Evolution of the Longmen Shan Foreland Basin (Western Sichuan, China) during the Late Triassic Indosinian orogeny. *Basin Research*, **15**, 117–138.

Yoshii, T. (1979) Compilation of geophysical data around the Japanese Islands. *Bulletin of the Earthquake Research Institute, Tokyo*, **54**, Part 1, 75–117.

Young, M.J., Gawthorpe, R.L. and Sharp. I.R. (2000) Sedimentology and sequence stratigraphy of a transfer zone coarse grained delta. Miocene Suez Rift, Egypt. *Sedimentology*, **47**, 1081–1104.

Zak, I. and Freund, R. (1981) Asymmetry and basin migration in the Dead Sea rift. *Tectonophysics*, **80**, 27–38.

Zeitler, P.K., Herczig, A.L., McDougall, I. and Honda, M. (1987) U-Th–He dating of apatite: a potential thermochronometer. *Geochimica et Cosmochimica Acta*, **51**, 2865–2868.

Zhong, S., Gurnis, M. and Moresi, L. (1996) Free-surface formulation of mantle convection. I. Basic theory and application to plumes. *Geophysical Journal International*, **127**, 708–718.

Ziegler, P.A., Cloetingh, S. and van J.D. Wees (1995) Dynamics of intra-plate compressional deformation: the Alpine foreland and other examples. *Tectonophysics*, **252**, 7–60.

Zoback et al. (1987) New evidence on the state of stress of the San Andreas fault system. *Science*, **238**, 1105–1111.

Zoback, M.L. (1992) First and second order patterns of stress in the lithosphere: The World Stress Map Project. *Journal of Geophysical Research*, **97**, 11703–11728.

Zweigel, J. and Zweigel, P. (1998) Plan-view curvature of foreland basins and its implications for the palaeostrength of the lithosphere underlying the Western Alps. Discussion of Sinclair (1996), with reply. *Basin Research*, **10**, 271–278.

Index

Note: page numbers in italics refer to figures; those in bold to tables.

Basin Analysis is an up-to-date overview of the essential processes of the formation and evolution of sedimentary basins, and their implications for the development of hydrocarbon resources. Since the first edition of this important and popular text, there has been an explosion of new data, new technology, and new concepts in the field. This new edition takes account of these developments while retaining the successful structure and philosophy of the original text.

Basin Analysis builds an understanding of sedimentary basins by examining the principles underlying how basins function by looking at their structure, thermal and subsidence history, and stratigraphic architecture.

The new edition features:

- a discussion on the major types of lithospheric deformation relevant to basin development – stretching and flexure;
- a new chapter on the effects of mantle dynamics;
- radically revised chapters on the basin-fill;
- a new chapter on the erosional engine for sediment delivery to basins, reflecting the massive and exciting advances in this area in the last decade;
- expansion of the techniques used in approaching problems in basin analysis;
- updated chapters on subsidence analysis and measurements of thermal maturity of organic and nonorganic components of the basin-fill;
- new material on thermochronological and exposure dating tools; and
- inclusion of the important petroleum system concept in the updated section on the application to the petroleum play.

This book is essential reading for advanced undergraduates, graduate students, and professional earth scientists interested in basin analysis and petroleum geology.

Philip Allen (right) is a sedimentary geologist with research interests in sedimentology, stratigraphy, physical Earth surface processes, and basin analysis. He has held University appointments at Cardiff, Oxford, and Trinity College, Dublin, and is currently a Professor in the Geological Institute of the Swiss Federal Polytechnic (ETH) in Zürich.

John Allen (left) has 25 years experience as a petroleum geologist in the international oil and gas industry, initially with British Petroleum (BP) and then with BHP Billiton as an exploration advisor and Chief Geologist. He is currently a global business strategist in BHP Billiton's Petroleum division, based in Melbourne, Australia.

Cover design by Code 5 Design Associates Ltd
Printed in Singapore

Visit our websites at
www.blackwellpublishing.com
www.earth-pages.com

Blackwell Publishing

ISBN 0-632-05207-4
9 780632 052073
90000>